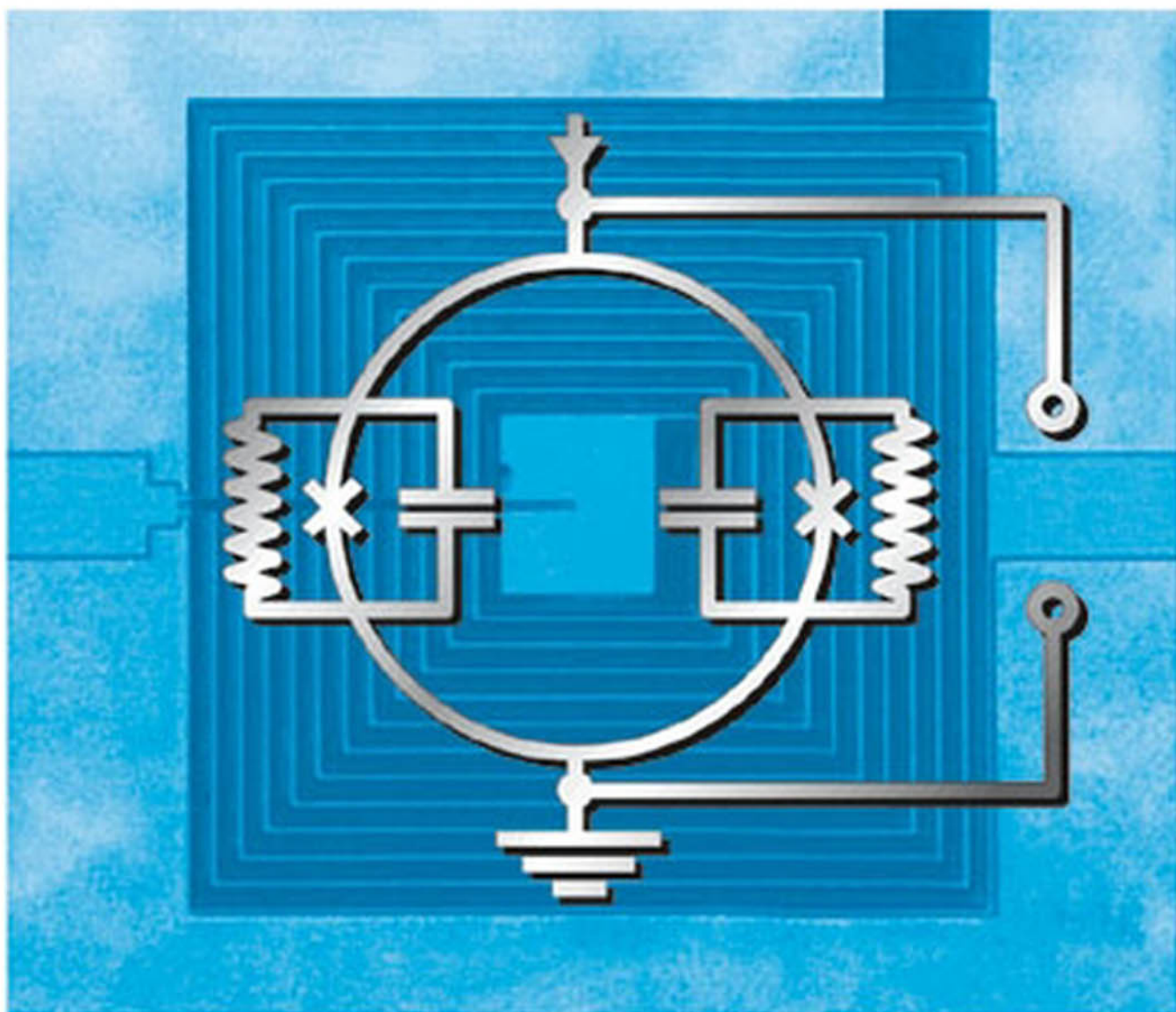


Edited by
John Clarke and Alex I. Braginski

WILEY-VCH

The SQUID Handbook

Vol. II Applications of SQUIDs and SQUID Systems



John Clarke, Alex I. Braginski (Eds.)

The SQUID Handbook

Vol. II Applications of SQUIDs
and SQUID Systems



WILEY-VCH Verlag GmbH & Co. KGaA

J. Clarke, A. I. Braginski (Eds.)

The SQUID Handbook

Vol. II

Related Titles

Buckel, W., Kleiner, R.

Superconductivity Fundamentals and Applications

Second Edition

475 pages with approx. 247 figures

2004

Hardcover

ISBN 3-527-40349-3

Andrä, W., Nowak, H. (eds.)

Magnetism in Medicine A Handbook

Second Edition

550 pages with 155 figures and 11 tables

2006

Hardcover

ISBN 3-527-40558-5

John Clarke, Alex I. Braginski (Eds.)

The SQUID Handbook

Vol. II Applications of SQUIDs
and SQUID Systems



WILEY-VCH Verlag GmbH & Co. KGaA

The Editors

Prof. John Clarke

Department of Physics
366 LeConte Hall
University of California
Berkeley, CA 94720-7300
USA
and

Materials Science Division
Lawrence Berkeley National Laboratory
One Cyclotron Road
Berkeley, CA 94720
jclarke@berkeley.edu

Prof. Dr. Alex I. Braginski

Research Center Jülich
IBN-2
D-52425 Jülich
Germany
a.braginski@fz-juelich.de

All books published by Wiley-VCH are carefully produced. Nevertheless, authors, editors, and publisher do not warrant the information contained in these books, including this book, to be free of errors. Readers are advised to keep in mind that statements, data, illustrations, procedural details or other items may inadvertently be inaccurate.

Library of Congress Card No.: applied for

British Library Cataloguing-in-Publication Data

A catalogue record for this book is available from the British Library.

Bibliographic information published by

Die Deutsche Bibliothek

Die Deutsche Bibliothek lists this publication in the Deutsche Nationalbibliografie; detailed bibliographic data is available in the Internet at <<http://dnb.ddb.de>>.

© 2006 WILEY-VCH Verlag GmbH & Co. KGaA,
Weinheim

All rights reserved (including those of translation into other languages).
No part of this book may be reproduced in any form – nor transmitted or translated into machine language without written permission from the publishers. Registered names, trademarks, etc. used in this book, even when not specifically marked as such, are not to be considered unprotected by law.

Typesetting Kühn & Weyh, Satz und Medien,
Freiburg

Printing Strauss GmbH, Mörlenbach

Bookbinding Litges & Dopf Buchbinderei GmbH,
Heppenheim

Printed in the Federal Republic of Germany.
Printed on acid-free paper.

ISBN-13: 978-3-527-40408-7

ISBN-10: 3-527-40408-2

This Handbook is dedicated to the memory of

*Robin P. Giffard, Christoph Heiden and
James E. Zimmerman.*

Contents

Volume I

Preface XI

| | | |
|----------|---|-----|
| 1 | Introduction | 1 |
| 1.1 | The Beginning | 2 |
| 1.2 | Subsequent Developments | 5 |
| 1.3 | The dc SQUID: A First Look | 7 |
| 1.4 | The rf SQUID: A First Look | 12 |
| 1.5 | Cryogenics and Systems | 16 |
| 1.6 | Instruments: Amplifiers, Magnetometers and Gradiometers | 17 |
| 1.7 | Applications | 21 |
| 1.8 | Challenges and Perspectives | 24 |
| 1.9 | Acknowledgment | 26 |
| 2 | SQUID Theory | 29 |
| 2.1 | Josephson Junctions | 30 |
| 2.2 | Theory of the dc SQUID | 43 |
| 2.3 | Theory of the rf SQUID | 70 |
| 3 | SQUID Fabrication Technology | 93 |
| 3.1 | Junction Electrode Materials and Tunnel Barriers | 94 |
| 3.2 | Low-temperature SQUID Devices | 96 |
| 3.3 | High-temperature SQUID Devices | 107 |
| 3.4 | Future Trends | 118 |
| 4 | SQUID Electronics | 127 |
| 4.1 | General | 128 |
| 4.2 | Basic Principle of a Flux-locked Loop | 128 |
| 4.3 | The dc SQUID Readout | 137 |
| 4.4 | The rf SQUID Readout | 155 |
| 4.5 | Trends in SQUID Electronics | 165 |

| | | |
|---------------------------------------|---|-----|
| 5 | Practical DC SQUIDS: Configuration and Performance | 171 |
| 5.1 | Introduction | 172 |
| 5.2 | Basic dc SQUID Design | 175 |
| 5.3 | Magnetometers | 186 |
| 5.4 | Gradiometers | 193 |
| 5.5 | 1/f Noise and Operation in Ambient Field | 200 |
| 5.6 | Other Performance Degrading Effects | 208 |
| 6 | Practical RF SQUIDs: Configuration and Performance | 219 |
| 6.1 | Introduction | 220 |
| 6.2 | Rf SQUID Magnetometers | 220 |
| 6.3 | Rf SQUID Gradiometers | 236 |
| 6.4 | Low-Frequency Excess Noise in rf SQUIDS | 237 |
| 6.5 | Response of rf SQUIDS to High-frequency Electromagnetic Interference | 239 |
| 6.6 | Characterization and Adjustment of rf SQUIDS | 241 |
| 6.7 | The rf SQUID <i>versus</i> the dc SQUID | 244 |
| 6.8 | Concluding Remarks and Outlook | 246 |
| 7 | SQUID System Issues | 251 |
| 7.1 | Introduction | 254 |
| 7.2 | Cryogenics | 255 |
| 7.3 | Cabling and Electronics | 272 |
| 7.4 | Data Acquisition and Rudimentary Signal Processing | 289 |
| 7.5 | Characterization, Calibration and Testing | 292 |
| 7.6 | Conditions Imposed on SQUID Systems by the Environment and Applications | 309 |
| 7.7 | Noise Suppression | 315 |
| 7.8 | Signal and Noise Implications for the SQUID System Design | 335 |
| 7.9 | Concluding Remarks and System Trends | 344 |
| Appendix 1 357 | | |
| Basic Properties of Superconductivity | | |
| Appendix 2 367 | | |
| Abbreviations, Constants and Symbols | | |
| Index 383 | | |

Volume II**Preface** XI**List of Contributors** XV

| | | |
|-----------|--|-----|
| 8 | SQUID Voltmeters and Amplifiers | 1 |
| | <i>J. Clarke, A. T. Lee, M. Mück and P. L. Richards</i> | |
| 8.1 | Introduction | 3 |
| 8.2 | Voltmeters | 4 |
| 8.3 | The SQUID as a Radiofrequency Amplifier | 5 |
| 8.4 | Microstrip SQUID Amplifier | 20 |
| 8.5 | SQUID Readout of Thermal Detectors | 32 |
| 8.6 | Nuclear Magnetic and Quadrupole Resonance and Magnetic Resonance Imaging | 56 |
| 8.7 | The Axion Detector | 81 |
| 9 | SQUIDs for Standards and Metrology | 95 |
| | <i>J. Gallop and F. Piquemal</i> | |
| 9.1 | Introduction | 96 |
| 9.2 | SQUIDs in Voltage Metrology | 97 |
| 9.3 | Cryogenic Current Comparator (CCC) | 101 |
| 9.4 | Other Current Metrological Applications of SQUIDS | 123 |
| 9.5 | Future Trends and Conclusion | 129 |
| 10 | The Magnetic Inverse Problem | 139 |
| | <i>E. A. Lima, A. Irimia and J. P. Wikswo</i> | |
| 10.1 | The Peculiarities of the Magnetic Inverse Problem | 141 |
| 10.2 | The Magnetic Forward Problem | 145 |
| 10.3 | The Magnetic Inverse Problem | 168 |
| 10.4 | Conclusions | 254 |
| 11 | Biomagnetism | 269 |
| | <i>J. Vrba, J. Nenonen and L. Trahms</i> | |
| 11.1 | Introduction | 271 |
| 11.2 | Magnetoencephalography | 274 |
| 11.3 | Magnetocardiography | 321 |
| 11.4 | Quasistatic Field Magnetometry | 342 |
| 11.5 | Magnetoneurography | 346 |
| 11.6 | Liver Susceptometry | 351 |
| 11.7 | Gastromagnetometry | 356 |
| 11.8 | Magnetic Relaxation Immunoassays | 360 |

| | | |
|-----------|---|-----|
| 12 | Measurements of Magnetism and Magnetic Properties of Matter | 391 |
| | <i>R. C. Black and F. C. Wellstood</i> | |
| 12.1 | Introduction | 392 |
| 12.2 | The SQUID Magnetometer–Susceptometer | 392 |
| 12.3 | Scanning SQUID Microscopy | 409 |
| 13 | Nondestructive Evaluation of Materials and Structures using SQUIDs | 441 |
| | <i>H.-J. Krause and G. Donaldson</i> | |
| 13.1 | Introduction | 442 |
| 13.2 | Detection of Magnetic Moments | 445 |
| 13.3 | Magnetic Flux Leakage Technique | 448 |
| 13.4 | Static Current Distribution Mapping | 452 |
| 13.5 | Eddy Current Technique | 453 |
| 13.6 | Alternative Excitation Techniques | 467 |
| 13.7 | Conclusion and Prospects | 472 |
| 14 | SQUIDs for Geophysical Survey and Magnetic Anomaly Detection | 481 |
| | <i>T. R. Clem, C. P. Foley, M. N. Keene</i> | |
| 14.1 | Introduction | 483 |
| 14.2 | Magnetic Measurements in the Earth’s Field | 484 |
| 14.3 | Operation of SQUIDs in Real World Environments | 494 |
| 14.4 | Data Acquisition and Signal Processing | 499 |
| 14.5 | Geophysical Applications of SQUIDs | 504 |
| 14.6 | Magnetic Anomaly Detection Systems using SQUIDs | 527 |
| 14.7 | Future Prospects | 536 |
| 15 | Gravity and Motion Sensors | 545 |
| | <i>Ho J. Paik</i> | |
| 15.1 | Introduction | 546 |
| 15.2 | The Superconducting Accelerometer | 547 |
| 15.3 | Superconducting Transducer for Gravitational-Wave Detectors | 548 |
| 15.4 | Superconducting Gravity Gradiometers (SGGs) | 554 |
| 15.5 | Applications of the SGG Technology | 563 |
| 15.6 | Outlook | 575 |
| | Appendix | 581 |
| | Physical Constants, Abbreviations and Symbols | |
| | Index | 617 |

Preface

We hope that this two-volume Handbook will provide an in-depth, systematic treatment of Superconducting QUantum Interference Devices (SQUIDs) and their many applications. Our intent is to offer the reader a reasonably complete, balanced and up-to-date presentation of the entire field, with as few omissions and duplications as possible. Although our publisher initially suggested that one or two of us write the Handbook, we pointed out that the field had become so large and diverse that this would be an almost impossible undertaking. Many aspects of SQUIDs, especially applications, have become so specialized that no single person can realistically provide adequate coverage. Consequently, we invited various colleagues collectively to write a comprehensive treatise. Fortunately, virtually everyone we asked graciously agreed to participate.

The first volume of the Handbook, published in 2004, contained seven chapters devoted to the fundamental science, fabrication and operation of low- T_c and high- T_c , dc and rf SQUIDs. After an introductory overview, subsequent chapters were entitled SQUID Theory, SQUID Fabrication Technology, SQUID Electronics, Practical DC SQUIDs: Configuration and Performance, Practical RF SQUIDs: Configuration and Performance, and SQUID System Issues. Appendix 1 briefly described the Basic Properties of Superconductivity and Appendix 2 listed the acronyms and symbols used in the Handbook.

Volume II contains eight chapters concerned with applications using SQUIDs as sensors and readout devices.

In Chapter 8, Clarke, Lee, Mück and Richards describe the theory and implementation of SQUID voltmeters and amplifiers. The first sections describe measurements of quasistatic voltages, the use of the dc SQUID as a radiofrequency amplifier, and the extension of the frequency range into the microwave regime by means of a microstrip input circuit. Subsequently, the application of SQUIDs to read out thermal detectors and their multiplexing in the time- and frequency-domains are discussed. SQUID amplifiers for nuclear magnetic resonance and magnetic resonance imaging are reviewed, and various examples are presented. The chapter concludes with a brief discussion of the implementation of a near-quantum-limited SQUID amplifier on a detector to search for the axion, a candidate for cold dark matter.

In Chapter 9, Gallop and Piquemal describe the role of SQUIDs in standards and metrology. After a brief discussion of highly accurate voltage measurement, the authors focus on the principles and accuracy limits of the cryogenic current comparator (CCC). Among its applications are measurements of resistance ratios, very low currents from superconducting electron transistors, and currents in beams of charged particles. Other metrology applications include secondary thermometers based on magnetic susceptibility and resistance, and a primary thermometer based on Nyquist noise.

In Chapter 10, Lima, Irimia and Wikswo tackle the magnetic inverse problem that is central to interpreting measurements in biomagnetism, geophysics and nondestructive evaluation. They first describe the forward problem – the determination of magnetic fields produced by distributions of magnetization and current and by multipoles. They begin their discussion of the inverse problem with the law of Biot and Savart, and go on to discuss the imaging of distributions of magnetization. An important aspect of the inverse problem is “silent sources” – for example, source configurations that produce either an electric or a magnetic field but not both. They conclude with a treatment of the three-dimensional inverse problem – which, in general, has no unique solution – that highlights some of the most widely used algorithms.

In Chapter 11, Vrba, Nenonen and Trahms address biomagnetism, unquestionably the largest single consumer of SQUIDs. They begin with magnetoencephalography (MEG) – magnetic signals from the brain – and describe whole cortex systems, types of sensors, fetal MEG, and data analysis with clinical examples. They continue with magnetocardiography, describing the kinds of instrumentation, types of sensors, and clinical applications. There follows a miscellany of topics in biomagnetism, including the measurement of static fields from the body, detecting signals propagating along nerves, the susceptibility of the liver as a diagnostic tool, gastro-magnetometry, and immunoassay using magnetic labeling of cells.

In Chapter 12, Black and Wellstood describe measurements of magnetism and magnetic properties of matter. The first part describes the history, development and operation of the most widely used SQUID system, namely a commercially available magnetometer and susceptometer. Issues of accuracy and sensitivity are discussed. The second part of the chapter is concerned with the scanning SQUID microscope. The authors outline the special requirements for the SQUIDs and cryogenics, describe the techniques for scanning and image processing, and discuss issues of spatial resolution. They conclude with a review of current and potential applications.

In Chapter 13, Krause and Donaldson give an overview of methods for nondestructive evaluation. These include the detection of static magnetic moments, the magnetic flux leakage technique, static current distribution mapping, and the eddy current technique. A number of examples is presented. The chapter concludes with a brief discussion of alternative ways of exciting a magnetic response.

In Chapter 14, Clem, Foley and Keene describe the application of SQUIDs to geophysical survey and magnetic anomaly detection. They begin with issues of magnetic measurements in the presence of the Earth’s field and operating

SQUIDS in harsh environments, and continue with data acquisition and signal processing. A major portion of the chapter is concerned with geophysical applications, ranging from rock magnetometry to a variety of prospecting and surveying methods. They conclude with an overview of the detection of magnetic anomalies, for example, buried ordnance.

Finally, in Chapter 15, Paik addresses gravity and motion sensors. He describes in turn a superconducting accelerometer, a superconducting transducer for gravitational-wave detectors, and the superconducting gravity gradiometer (SGG). Applications of the SGG include precision tests of the laws of gravity, searching for new weak forces, gravity mapping and mass detection, and inertial navigation and survey.

In the Appendix, we duplicate Appendix 2 of Volume I and provide a list of additional acronyms and symbols for each chapter of Volume II.

This very brief survey illustrates the remarkable diversity of the SQUID, which finds applications to physics, astrophysics, cosmology, chemistry, materials science, standards, biology and medicine. We would like to believe that the Handbook will be of use not only to practitioners of the art of SQUIDs but also to students and professionals working in these fields.

In conclusion, we express our heartfelt thanks to the authors of both volumes of the Handbook for their hard work, their attention to quality and accuracy and not least for their patience and perseverance during our editing of their manuscripts. One of us (JC) expresses his grateful thanks to his assistant, Barbara Salisbury, for her unflagging help with all the manuscripts for both volumes. We owe an enormous debt of gratitude to the staff at Wiley-VCH, particularly to Dr. Michael Bär, who first asked us to co-write the Handbook, and to Mrs. Vera Palmer and Mrs. Ulrike Werner without whose expert guidance and extraordinary patience the Handbook would never have seen the light of day. Finally, we thank our wives Maria Teresa and Grethe for their patience and understanding during our editing of both volumes of the Handbook, which took much of our time away from them.

Alex Braginski and John Clarke

List of Contributors

Volume I

Alex I. Braginski

(Chapters 1 and 6)

Research Centre Jülich, ISG-2, D-52425
Jülich, Germany, (retired), and
Physics Department, University of
Wuppertal, 42097 Wuppertal, Germany
A.Braginski@fz-juelich.de

Dietmar Drung

(Chapter 4, Appendix 2)

Physikalisch-Technische Bundesanstalt,
Abbestrasse 2-12, 10587 Berlin,
Germany
Dietmar.Drung@ptb.de

Robin Cantor

(Chapters 3 and 5)

STAR Cryoelectronics, 25-A Bisbee
Court, NM 87508 Santa Fe, USA
rcantor@starcryo.com

Catherine P. Foley

(Chapter 7)

CSIRO Industrial Physics, P.O. Box
218, Lindfield, NSW 2070 Australia
Cathy.Foley@csiro.au

Boris Chesca

(Chapter 2)

Institute of Physics, University of
Tübingen, Auf der Morgenstelle 14,
72076 Tübingen, Germany
boris.chesca@uni-tuebingen.de

Mark N. Keene

(Chapter 7)

QinetiQ Ltd., St. Andrews Road,
Malvern, Worcestershire WR14 3PS,
UK
mnkeene@qinetiq.com

John Clarke

(Chapter 1)

Department of Physics, 366 LeConte
Hall, University of California, Berkeley
CA 94720-7300, USA, and
Materials Sciences Division, Lawrence
Berkeley National Laboratory,
1 Cyclotron Road, Berkeley CA 94720,
USA
jclarke@berkeley.edu

Reinhold Kleiner

(Chapter 2, Appendix 1)

Institute of Physics, University of
Tübingen, Auf der Morgenstelle 14,
72076 Tübingen, Germany
kleiner@uni-tuebingen.de

Dieter Koelle

(Chapter 2 and 5 and
Appendices 1 and 2)
Institute of Physics, University of
Tübingen, Auf der Morgenstelle 14,
72076 Tübingen, Germany
koelle@uni-tuebingen.de

Frank Ludwig

(Chapter 3)
Institute of Electrical Metrology and
Electrical Engineering, Technical
University of Braunschweig, 38092
Braunschweig, Germany
f.ludwig@tu-bs.de

Michael Mück

(Chapter 4)
Institute of Applied Physics, University
of Giessen, Heinrich-Buff-Ring 16,
35392 Giessen, Germany
Michael.Mueck@ap.physik.uni-
giessen.de

H. J. M. ter Brake

(Chapter 7)
Department of Applied Physics, Twente
University of Technology, P.O. Box 217,
7500AE Enschede, The Netherlands
H.J.M.terBrake@tn.utwente.nl

Jiri Vrba

(Chapter 7)
VSM MedTech Ltd, 9 Burbidge Street,
Coquitlam, B.C., Canada
jvrba@vsmmedtech.com

Yi Zhang

(Chapter 6)
Research Centre Jülich, ISG-2, 52425
Jülich, Germany
y.zhang@fz-juelich.de

Volume II

Randall C. Black

(Chapter 12)
Quantum Design, Inc., 6325 Lusk Blvd.,
San Diego CA 92121, USA
randy@blacksdesign.com

Ted R. Clem

(Chapter 14)
Naval Surface Warfare Center Panama
City, 110 Vernon Avenue, Panama City
FL 32407-7001, USA
ted.clem@navy.mil

John Clarke

(Chapter 8)
Department of Physics, 366 LeConte
Hall, University of California, Berkeley
CA 94720-7300, USA, and
Materials Sciences Division, Lawrence
Berkeley National Laboratory,
1 Cyclotron Road, Berkeley CA 94720,
USA
jclarke@berkeley.edu

Gordon B. Donaldson

(Chapter 13)
Department of Physics, University of
Strathclyde, Glasgow G4 0NG, UK
g.b.donaldson@strath.ac.uk

Catherine P. Foley

(Chapter 14)
CSIRO Industrial Physics, P.O. Box
218, Lindfield, NSW 2070 Australia
Cathy.Foley@csiro.au

John Gallop

(Chapter 9)

National Physical Laboratory, Hampton Rd., Teddington TW11 0LW, UK
John.Gallop@npl.co.uk

Andrei Irimia

(Chapter 10)

Department of Physics and Astronomy,
Vanderbilt University, VU Station B
351807, Nashville TN 37235, USA
andrei.irimia@vanderbilt.edu

Mark N. Keene

(Chapter 14)

QinetiQ Ltd., St. Andrews Road,
Malvern, Worcestershire WR14 3PS,
UK
mnkeene@qinetiq.com

Hans-Joachim Krause

(Chapter 13)

Institute of Thin Films and Interfaces,
Research Center Jülich, 52425 Jülich,
Germany
h.-j.krause@fz-juelich.de

Adrian T. Lee

(Chapter 8)

Department of Physics, University of
California, 363 LeConte Hall, Berkeley
CA 94720-7300, USA
atl@physics7.berkeley.edu

Eduardo Andrade Lima

(Chapter 10)

Department of Biomedical Engineering,
Vanderbilt University, VU Station B
351807, Nashville TN 37235, USA
eduardo.a.lima@vanderbilt.edu

Michael Mück

(Chapter 8)

Institute of Applied Physics, University
of Giessen, Heinrich-Buff-Ring 16,
35392 Giessen, Germany
Michael.Mueck@ap.physik.uni-
giessen.de

Jukka Nenonen

(Chapter 11)

Laboratory of Biomedical Engineering,
Helsinki University of Technology,
Espoo, Finland

Jukka.Nenonen@neuromag.fi

Ho Jung Paik

(Chapter 15)

Department of Physics, University of
Maryland, College Park MD 20742,
USA

hpaik@physics.umd.edu

François Piquemal

(Chapter 9)

Bureau National de Métrologie, LNE:
Laboratoire National de Métrologie et
d'Essais, Avenue Roger Hennequin 29,
78197 Trappes cedex, France
francois.piquemal@lne.fr

Paul L. Richards

(Chapter 8)

Department of Physics, University of
California, 363 LeConte Hall, Berkeley
CA 94720-7300, USA
richards@physics.berkeley.edu

Lutz Trahms

(Chapter 11)

Department of Bioelectricity and
Biomagnetism, Physikalisch-
Technische Bundesanstalt,
Abbestr. 2-12, 10587 Berlin, Germany
lutz.trahms@ptb.de

Jiri Vrba

(Chapter 11)
VSM MedTech Ltd., 9 Burbidge Street,
Coquitlam, B.C., Canada
jvrba@vsymmmedtech.com

Frederick C. Wellstood

(Chapter 12)
Center for Superconductivity Research,
Department of Physics, University of
Maryland, College Park MD 20742-
4111, USA
well@squid.umd.edu

John P. Wikswo

(Chapter 10)
Departments of Biomedical
Engineering, Physics and Astronomy,
Molecular Physiology and Biophysics,
Vanderbilt University, VU Station B
351807, Nashville TN 37235, USA
john.wikswo@vanderbilt.edu

8**SQUID Voltmeters and Amplifiers**

John Clarke, Adrian T. Lee, Michael Mück and Paul L. Richards

| | | |
|---------|---|----|
| 8.1 | Introduction | 3 |
| 8.2 | Voltmeters | 4 |
| 8.3 | The SQUID as a Radiofrequency Amplifier | 5 |
| 8.3.1 | Introduction | 5 |
| 8.3.2 | Mutual Interaction of SQUID and Input Circuit | 6 |
| 8.3.3 | Tuned Amplifier: Theory | 10 |
| 8.3.4 | Untuned Amplifier: Theory | 12 |
| 8.3.5 | Tuned and Untuned Amplifiers: Experiment | 13 |
| 8.3.6 | To Tune or Not to Tune? | 16 |
| 8.3.7 | SQUID Series Array Amplifier | 17 |
| 8.3.8 | The Quantum Limit | 18 |
| 8.3.9 | Future Outlook | 19 |
| 8.4 | Microstrip SQUID Amplifier | 20 |
| 8.4.1 | Introduction | 20 |
| 8.4.2 | The Microstrip | 21 |
| 8.4.3 | The Microstrip SQUID Amplifier: Gain | 21 |
| 8.4.4 | The Microstrip SQUID Amplifier: Noise Temperature | 26 |
| 8.4.5 | High- T_c Microstrip SQUID Amplifier | 31 |
| 8.4.6 | Future Outlook | 31 |
| 8.5 | SQUID Readout of Thermal Detectors | 32 |
| 8.5.1 | Introduction | 32 |
| 8.5.2 | Transition-Edge Sensors | 33 |
| 8.5.3 | SQUID Multiplexers | 35 |
| 8.5.3.1 | Time-Domain Multiplexing | 35 |
| 8.5.3.2 | Frequency-Domain Multiplexing | 39 |
| 8.5.4 | TES Bolometers | 45 |
| 8.5.4.1 | TES Bolometer Designs | 46 |
| 8.5.4.2 | Bolometer Performance | 49 |
| 8.5.5 | TES Calorimeters and Nonequilibrium Detectors | 50 |
| 8.5.5.1 | Calorimeter Designs | 51 |
| 8.5.5.2 | Calorimeter Noise Performance | 52 |

2 | 8 SQUID Voltmeters and Amplifiers

| | | |
|---------|--|----|
| 8.5.6 | SQUID Readout of Non-TES Detectors | 53 |
| 8.5.6.1 | Magnetic Calorimeter | 53 |
| 8.5.6.2 | SIS Tunnel Junction | 54 |
| 8.5.6.3 | NIS Junctions | 55 |
| 8.5.6.4 | Kinetic-Inductance Thermometer | 55 |
| 8.5.7 | Future Outlook | 56 |
| 8.6 | Nuclear Magnetic and Quadrupole Resonance and Magnetic Resonance Imaging | 56 |
| 8.6.1 | Introduction | 56 |
| 8.6.2 | Principles of NMR and NQR | 57 |
| 8.6.3 | SQUID-Detected NMR and NQR | 61 |
| 8.6.3.1 | NQR of ^{14}N | 61 |
| 8.6.3.2 | Spin Noise | 64 |
| 8.6.3.3 | NMR of Hyperpolarized ^{129}Xe | 67 |
| 8.6.3.4 | Liquid-State Proton NMR and MRI | 69 |
| 8.6.4 | Future Outlook | 80 |
| 8.7 | The Axion Detector | 81 |

8.1

Introduction

Volume I of this handbook is concerned with the theory, fabrication and performance of dc and rf SQUIDS, and with the implementation of SQUIDS as magnetometers and gradiometers using appropriate superconducting input circuits. Most of these devices are used at frequencies ranging from zero to a few kilohertz, for example for quasistatic measurements of susceptibility, for geophysical applications and for biomagnetism. In this chapter we are concerned with the use of SQUIDS as voltmeters and amplifiers. Since rf SQUIDS are almost never used for such purposes, we confine ourselves to dc SQUIDS.

Broadly speaking, we can divide these applications into three frequency ranges. The first is the measurement of quasistatic voltages – for example, thermoelectric voltage and the voltage generated by quasiparticle charge imbalance in a superconductor. These voltmeters are described briefly in Section 8.2. The second frequency range extends from a few tens or hundreds of hertz to perhaps 100 MHz, and is discussed in Section 8.3. Major applications include readout schemes for bolometers and calorimeters for particle detectors, discussed in Section 8.5, and nuclear magnetic resonance (NMR), nuclear quadrupole resonance (NQR) and magnetic resonance imaging (MRI), discussed in Section 8.6. In the frequency range up to a few megahertz, the SQUID is generally operated in a flux-locked loop, while at higher frequencies it is operated open-loop, with an applied flux near $(2n + 1)\Phi_0/4$ ($\Phi_0 = h/2e \approx 2.07 \times 10^{-15}$ Wb is the flux quantum and n is an integer) chosen to maximize the flux-to-voltage transfer coefficient $(\partial V/\partial\Phi)_I \equiv V_\Phi$. At frequencies up to, say, 100 MHz, the conventional square-washer SQUID design described in Chapter 5 is entirely adequate. In the third range of frequencies, a few hundred megahertz to a few gigahertz, however, the parasitic capacitance between the input coil and the SQUID washer can substantially reduce the gain of the conventional design. An alternative option is the so-called microstrip SQUID amplifier, in which the input coil is used as a resonant microstrip. This device is described in Section 8.4. Applications of the microstrip amplifier include the axion detector described in Section 8.7 and a postamplifier for the radiofrequency single-electron transistor (RFSET).

8.2

Voltmeters

One of the earliest applications of the dc SQUID was as a voltmeter. The sensor was in fact a SLUG (superconducting low-inductance undulatory galvanometer) [1] described briefly in Chapter 5. In essence, the SLUG consists of a bead of PbSn solder frozen around a length of Nb wire. The critical current measured between the two superconductors is periodic (often multiply periodic) in the supercurrent passed along the Nb wire. In the early days of this device, it was possible to measure changes in this current of about $1 \mu\text{A Hz}^{-1/2}$. The fact that the input circuit had a low inductance – a few nanohenries – enabled one to measure voltages developed by much smaller resistances than had been previously possible since the time constant of the measurement could be kept to below one second.

Figure 8.1 shows the original voltmeter circuit used with a SLUG. The voltage source V_s was connected in series with a standard resistor r_s and the Nb wire of the SLUG. The SLUG was operated in a flux-locked loop (Section 4.2) that fed a current i_s into r_s to maintain a null current in the Nb wire: evidently the value of V_s is given by $i_s r_s$. With a SLUG current resolution of $1 \mu\text{A Hz}^{-1/2}$ determined by the readout electronics, the voltage resolution for $r_s = 10^{-8} \Omega$ was $10^{-14} \text{ V Hz}^{-1/2}$. This represented a five orders of magnitude improvement over the resolution of semiconductor amplifiers. Since the Nyquist voltage noise across a $10^{-8} \Omega$ resistance at 4.2 K is about $1.5 \text{ fV Hz}^{-1/2}$, these early measurements were not Nyquist noise limited. Nonetheless, the SLUG voltmeter was used successfully to make measurements of the characteristics of superconductor–normal metal–superconductor (SNS) Josephson junctions [2] and of thermoelectric voltages [3]. Subsequently, it was used in studies of the resistance of the SN interface [4] and to make the first measurements of quasiparticle charge imbalance in superconductors [5].

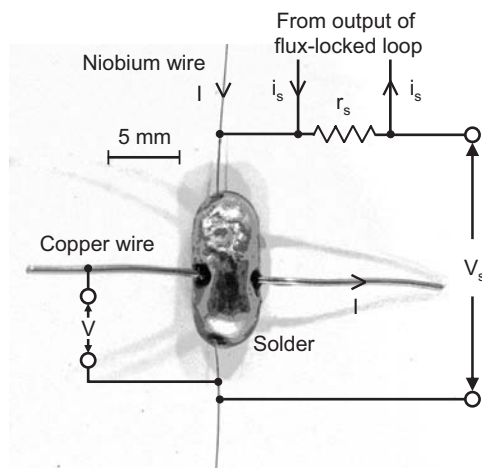


Fig. 8.1 The SLUG. The configuration of a voltmeter measuring a voltage source V_s has been superimposed on a photograph.

The development of much lower noise SQUIDs with multiturn input coils, notably the Ketchen Jaycox square-washer design [6], has greatly reduced the equivalent current noise. For example, for a low- T_c SQUID with a flux noise of $2 \times 10^{-6}\Phi_0$ Hz $^{-1/2}$ at frequencies above the $1/f$ knee (f is frequency) of typically 1 Hz, coupled to an input coil with a mutual inductance of 5 nH, the current noise $S_I^{1/2}(f) \approx 1 \text{ pA Hz}^{-1/2}$. At 4.2 K, this resolution enables one to make Nyquist-noise-limited measurements in resistors

$$r \lesssim 4k_B T / S_I(f) \approx 200 \Omega. \quad (8.1)$$

In making this estimate, we have neglected the effects of current noise in the SQUID loop which induces noise voltages into the input circuit. This subject is discussed at length in Section 8.3. These devices are generally used with current feedback to the standard resistor to obtain a null balancing voltmeter [7].

Voltmeters have also been based on high- T_c SQUIDs operating at 77 K [8–10]. The unavailability of flexible, bondable wire made from a high- T_c superconductor means that normal wire must be used to connect the components in the input circuit. Contact resistance between this wire and the $\text{YBa}_2\text{Cu}_3\text{O}_{7-x}$ (YBCO) input coil adds to the total resistance. As a result, the voltage resolution is limited to roughly 1 pV Hz $^{-1/2}$.

SQUID packages suitable for use as voltmeters are available commercially from several companies. The SQUID is enclosed in a niobium can to shield it from ambient magnetic noise. The two ends of the input coil are connected to niobium pads to which external niobium wires can be clamped with screws to produce superconducting contacts. Thus, the user can readily couple any desired external circuit to the SQUID.

8.3

The SQUID as a Radiofrequency Amplifier

8.3.1

Introduction

This section is concerned with the use of the dc SQUID as a radiofrequency (rf) amplifier. We confine our attention to the situation in which the SQUID is operated open loop, biased near $(2n + 1)\Phi_0/4$ to maximize V_ϕ . A thorough discussion of such amplifiers is quite complicated. Although these issues are often ignored in the design of SQUID input circuits, the coupling of a circuit to a SQUID may modify its properties significantly, while at the same time the SQUID reflects both a nonlinear impedance and a voltage noise source into the input circuit. The modification of the SQUID by a coupled inductance was pointed out by Zimmerman [11], and studied extensively in a series of papers by Clarke and coworkers [12–14]. The fact that the SQUID loop contains a noise current that is partially correlated with the voltage noise [15] across the SQUID was computed by Tesche

and Clarke [16], and subsequently used by various authors to calculate the noise temperature of amplifiers [13, 14, 17–20]. A complete treatment of these issues would make this chapter unwieldy, and we limit ourselves to summarizing the key theoretical results and to describing some experimental amplifiers.

8.3.2

Mutual Interaction of SQUID and Input Circuit

Consider a SQUID with loop inductance L and two identical Josephson junctions each with critical current I_0 , self capacitance C and shunt resistance R . For a typical SQUID in the ${}^4\text{He}$ temperature range, the noise parameter $\Gamma \equiv 2\pi k_{\text{B}}T / I_0\Phi_0 \sim 0.05$. The noise energy $\varepsilon(f) \equiv S_{\phi}(f)/2L$ is optimized [15] when $\beta_L \equiv 2LI_0/\Phi_0 = 1$. The Stewart–McCumber parameter [21, 22] $\beta_C \equiv 2\pi I_0 R^2 C / \Phi_0$ should be somewhat less than unity to avoid hysteresis in the current voltage (I - V) characteristic (see Chapters 1 and 2). Under these conditions, one finds the following results [15]. The maximum flux-to-voltage transfer coefficient is

$$V_{\phi} \equiv |\partial V / \partial \Phi|_{I_{\text{B}}} \approx R/L \quad (8.2)$$

where I_{B} is the value of the bias current that maximizes V_{ϕ} , and the flux in the SQUID is near $(2n + 1)\Phi_0/4$ (n is an integer). When V_{ϕ} is maximized, the spectral density of the voltage noise across the SQUID, which is assumed to arise from Nyquist noise in the shunt resistors, is [15]

$$S_V(f) \approx 16 k_{\text{B}} T R. \quad (8.3)$$

The current noise in the SQUID loop has a spectral density [16]

$$S_J(f) \approx 11 k_{\text{B}} T / R \quad (8.4)$$

and is partially correlated with the voltage noise with the cross spectral density [16]

$$S_{VJ}(f) \approx 12 k_{\text{B}} T. \quad (8.5)$$

Figure 8.2(a) shows an input circuit consisting of a voltage source V_i in series with a resistance R_i , the inductance L_p of a pickup coil, a stray inductance L_s , a capacitor C_i and the input inductance L_i of the SQUID. Depending on the application, some of the components may be omitted. The mutual inductance to the SQUID is $M_i = k_i(L_i)^{1/2}$, where $k_i \leq 1$ is the coupling coefficient. The SQUID reflects a complex impedance into the input circuit which is derived from the dynamic input impedance Z of the SQUID; in turn, Z can be related to the flux-to-current transfer function $J_{\phi} \equiv (\partial J / \partial \Phi)_{I_{\text{B}}}$ by the equation [18]

$$-J_{\phi} = j\omega/Z = 1/L + j\omega/R. \quad (8.6)$$

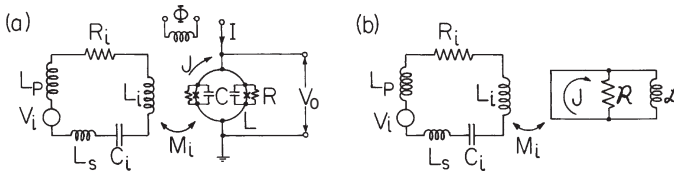


Fig. 8.2 (a) Schematic of a generic tuned amplifier. The voltage source V_i is connected in series with a pickup loop of inductance L_p , a stray inductance L_s , a capacitor C_i , a resistance R_i and the input inductance L_i of the SQUID. (b) Dynamic input impedance of the

SQUID represented by an inductance \mathcal{L} and resistance \mathcal{R} . In both figures, J is the current induced in the SQUID loop by signal and noise sources in the input circuit. (Reproduced with permission from ref. [13].)

The parameters \mathcal{Z} , \mathcal{L} and \mathcal{R} refer to currents flowing around the SQUID loop. At $\omega = 0$, $-J\phi$ reduces to the inverse of the dynamic input inductance \mathcal{L} , while for $\omega > 0$ there are resistive losses, represented by the dynamic input resistance \mathcal{R} . Figure 2(b) shows a schematic representation of \mathcal{L} and \mathcal{R} , which define the response of the SQUID to an applied flux Φ .

Figure 8.3 shows the variation of L/\mathcal{L} and R/\mathcal{R} with applied flux [13] for four values of bias current. Typically, SQUIDs are operated with $I_B \approx 2I_0$. We observe that both parameters depend strongly on Φ , with L/\mathcal{L} becoming negative in some regions.

We next discuss the effect of the input circuit on the SQUID parameters. Throughout this discussion we assume that the SQUID is operated open-loop, with its current and flux biases adjusted to maximize V_ϕ . We also assume that the loading of the readout amplifier on the SQUID is negligible. To illustrate the point, consider a superconducting pickup inductance L_p in series with a stray inductance L_s connected across the input inductance L_i , as in a magnetometer. We assume that the SQUID is current-biased at a voltage corresponding to a Josephson angular frequency ω_J . In the absence of parasitic capacitance, currents in the

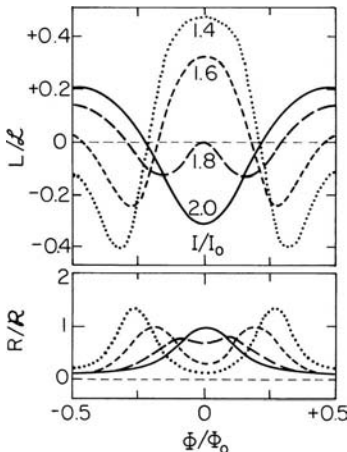


Fig. 8.3 Simulated values of L/\mathcal{L} and R/\mathcal{R} versus reduced flux Φ/Φ_0 for a bare SQUID versus flux Φ for four values of bias current. SQUID parameters were $\beta_L = 1.0$, $\beta_C = 0.2$ and $\Gamma \approx 0.06$ (Reproduced with permission from ref. [13].)

SQUID loop at ω_l and its harmonics will induce currents into the input circuit. It is easy to show that the SQUID loop inductance will be *reduced* by the presence of the input circuit to a value

$$L^r = (1 - k_{ie}^2)L, \quad (8.7)$$

where

$$k_{ie} = k_i[(L_i + L_p + L_s)/L_i]^{-1/2} \quad (8.8)$$

is the effective coupling coefficient between the SQUID and the total inductance of the input circuit. Other parameters of the SQUID take the reduced values V_ϕ^r , J_ϕ^r , Z^r and R^r corresponding to a SQUID with loop inductance L^r . In practice, things may be not so simple: parasitic capacitance between the coil and the SQUID washer modifies the coupling between them at the Josephson frequency and its harmonics. In the limiting case where this parasitic capacitance prevents any high-frequency currents from flowing in the input circuit, the SQUID parameters are unaffected by the input circuit [12]. In a real system, the result is likely to be somewhere between the two extremes; it will also depend, for example, on the number of turns in the input coil which determines the parasitic capacitance. By studying a series of SQUIDs with 20-turn input coils, Hilbert and Clarke [13] found that V_ϕ was increased by roughly the expected amount (corresponding to the reduced loop inductance) when the previously open coil was shorted.

We are now in a position to consider the modification of the input circuit by the SQUID impedance reflected into it. A productive way of writing the result is in terms of the output voltage across the SQUID in the presence of a signal applied to the input circuit shown in Figure 8.2(a). After some calculation, one finds [12]

$$V(\omega) = V_N^r(\omega) + M_i V_\phi^r \left[\frac{V_i(\omega) + M_i J_N^r(\omega)(R_i + 1/j\omega C_i)/L_T}{Z_T(\omega) - J_\phi^r M_i^2(R_i + 1/j\omega C_i)/L_T} \right]. \quad (8.9)$$

Here, $V_N^r(\omega)$ and $J_N^r(\omega)$ are the reduced voltage and current noises of the SQUID, and $V_i(\omega)$ is the input voltage applied to the resistance R_i and capacitance C_i in series with the total inductance of the input circuit $L_T = L_i + L_p + L_s$. The total impedance of the (uncoupled) input circuit is

$$Z_T(\omega) = R_i + j\omega(L_i + L_p + L_s) + 1/j\omega C_i. \quad (8.10)$$

The denominator of Eq. (8.9) contains the term $-J_\phi^r M_i^2(R_i + 1/j\omega C_i)/L_T$ that represents the impedance reflected into the input circuit from the SQUID. The term involving $J_N^r(\omega)$ in the square brackets is the noise current generated in the input circuit by the SQUID. We can readily derive the voltage gain for a SQUID amplifier from Eq. (8.9):

$$G_v = \frac{M_i V_\phi^r}{Z_T - k_{ie}^2 L J_\phi^r (R_i + 1/j\omega C_i)} \equiv \frac{M_i V_\phi^r}{Z_T^*}. \quad (8.11)$$

Using Eq. (8.6), we see that the impedance can be written in the form

$$Z_T^* = R_i \left(1 + \frac{k_{ie}^2 L}{\mathcal{L}^r} \right) + \frac{k_{ie}^2 L}{\mathcal{R}^r C_i} + j\omega \left[L_i + a_e^2 L \left(\frac{R_i}{\mathcal{R}^r} - \frac{1}{\omega^2 C_i \mathcal{L}^r} \right) + L_p + L_s \right] + \frac{1}{j\omega C_i}. \quad (8.12)$$

We note that \mathcal{R}^r and \mathcal{L}^r contribute to both the real and imaginary parts of Z_T^* .

Hilbert and Clarke [13] made extensive measurements of J_ϕ^r as a function of Φ by connecting a capacitor C_i across the input coil of both a 4-turn and a 20-turn SQUID. The resonant frequency f_0^0 and full width at half maximum (FWHM) of this tank circuit were measured directly with the SQUID biased with a large current ($\gg 2I_0$) where the SQUID has negligible inductive screening and a dynamic input impedance of approximately $2\mathcal{R}^r$. The SQUID was then biased at its usual operating point, and the Nyquist noise power $P(f_0)$ generated by the tank circuit was measured at the output of the SQUID with a spectrum analyzer. The value of V_ϕ^r was determined from the height of the peak. The frequency f_0 at which the noise power peaked generally differed from f_0^0 , and yielded the inductance change ΔL_i reflected into the tank circuit. Similarly, the value of the FWHM, Δf , yielded the resistance change ΔR_i . From these values, it was straightforward to infer the values of L/L^r and R/R^r from Eq. (8.12) inserted into Eq. (8.11).

The results for a 20-turn SQUID are shown in Figure 8.4 for three values of bias current. The behavior of $|V_\phi|$ is much as expected. However, the magnitudes of the curves suggest that the inductive screening of the SQUID is more effective at the lowest bias current than at the highest bias current; this result is consistent with a reduction in screening by the parasitic capacitance as the Josephson frequency increases. The measured values of L/L^r follow the trends in the simulations quite well. For example, at the lowest bias current there is a broad maximum at $\Phi = 0$ and a negative region around $\Phi = \pm\Phi_0/2$. The overall magnitude of L/L^r

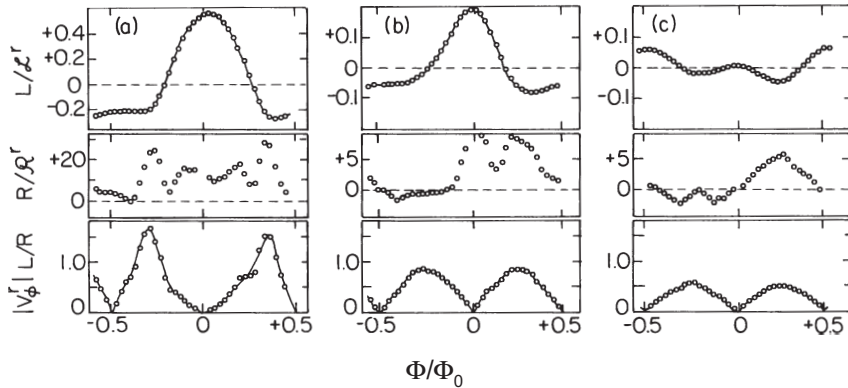


Fig. 8.4 Measured values of L/L^r , R/R^r and $|V_\phi|L/R$ versus reduced flux Φ/Φ_0 for a SQUID with $L \approx 400$ pH, $2I_0 \approx 6 \pm 1$ μA , $C \approx 0.5$ pF and $R \approx 8 \Omega$, corresponding to $\beta_L \approx 1$ and $\beta_C \approx 0.2$. The temperature was 4.2 K corresponding to $\Gamma \approx 0.06$. Bias current: (a) 4.0 μA , (b) 5.0 μA , (c) 6.0 μA . (Reproduced with permission from ref. [13].)

is generally in fair agreement with the simulations. On the other hand, the measured values of R/R^r , which vary between +30 and -5, are in sharp disagreement with the simulated values, which are always positive, with a maximum of about 2. Thus, ΔR_i is evidently dominated by a mechanism other than the resistance reflected from the SQUID.

Further investigation showed that the change in resistance in the tank circuit was dominated by feedback from the output of the SQUID via the parasitic capacitance between the washer and the input coil. Approximating the distributed capacitance with a lumped capacitor, Hilbert and Clarke [13] were able to account for the observed change in resistance in the input circuit to within a factor of 2. The reader is referred to the original paper for details.

This concludes our discussion of the input impedance of the dc SQUID and of the mutual loading of the SQUID and input circuit. We next apply these ideas to the design of SQUID amplifiers.

8.3.3

Tuned Amplifier: Theory

To simplify our initial discussion we first neglect capacitive feedback, and later return briefly to this issue. The circuit is shown schematically in Figure 8.2(a); we interpret R_i as the impedance of the voltage source V_i . For $V_i = 0$, the noise voltage at the SQUID output can be written from Eqs. (8.8) and (8.9) as

$$V_N(\omega) = V_N^r(\omega) + k_{ie}^2 L V_\phi^r (R_i + 1/j\omega C_i) J_N^r(\omega) / Z_T^*(\omega) \quad (8.13)$$

where $Z_T^*(\omega)$ is given by Eq. (8.12). We now assume that the amplifier is operated at the resonant frequency $f_0 = \omega_0/2\pi$ at which the imaginary terms in Z_T^* tune to zero:

$$\omega_0 = [(L_i + L_s + k_{ie}^2 L R_i / R^r) C_i / (1 + k_{ie}^2 L / L^r)]^{-1/2}. \quad (8.14)$$

Thus, at the resonant frequency, Eq. (8.13) reduces to

$$V_N(\omega_0) = V_N^r(\omega_0) + \frac{k_{ie}^2 L (R_i + 1/j\omega_0 C_i) J_N^r(\omega_0) V_\phi^r}{R_i + \Delta R_i} \quad (8.15)$$

where

$$\Delta R_i = k_{ie}^2 L (R_i / L^r + 1 / R^r C_i). \quad (8.16)$$

To simplify matters, we now assume that Q is high so that $R_i \ll 1/j\omega C_i$. As we shall see later, optimization of the noise temperature implies that $k_{ie}^2 Q \approx 1$, so that $k_{ie}^2 \ll 1$. Thus, to an excellent approximation the SQUID parameters assume their bare values, the resonant frequency becomes $\omega_0 \approx [(L_i + L_s) C_i]^{-1/2}$ and Eq. (8.15) reduces to

$$V_N(\omega_0) \approx V_N^0(\omega_0) - j\omega_0 M_i^2 V_\phi J_N(\omega_0)/(R_i + \Delta R_i). \quad (8.17)$$

Here, $V_N^0(\omega_0)$ is the voltage noise across the bare SQUID. We have retained the term ΔR_i for later discussion, since in practice it is dominated by capacitive feedback. Neglecting ΔR_i for the moment, we can interpret Eq. (8.17) quite simply. The current noise $J_N(\omega)$ produces a voltage noise $-j\omega M_i J_N(\omega)$ into the input circuit which, on resonance, yields a current noise $-j\omega M_i J_N(\omega)/R_i$ and hence a flux noise $-j\omega M_i^2 J_N(\omega)/R_i$ in the SQUID. Multiplying this term by V_ϕ yields the second term in Eq. (8.17).

We now introduce the noise temperature $T_N(f_0)$ of the SQUID amplifier on resonance through the definition

$$4k_B T_N(f_0) R_i G_V^2(f_0) = S_V(f_0). \quad (8.18)$$

Here, $S_V(f_0)$ is the spectral density of the voltage noise at the output of the SQUID amplifier, which we can readily calculate from Eq. (8.17). We find the value of R_i that optimizes $T_N(f_0)$ by calculating $\partial T_N(f_0)/\partial R_i = 0$ from Eq. (8.18):

$$R_i^{\text{opt}} = [(R_{i0}^{\text{opt}})^2 + (\Delta R_i)^2]^{1/2}. \quad (8.19)$$

Here,

$$R_{i0}^{\text{opt}} = (S_J/S_V)^{1/2} \omega_0 M_i^2 V_\phi. \quad (8.20)$$

This result can also be obtained from the usual [23] treatment of an amplifier with a voltage noise source $-j\omega M_i J_N(\omega)$ and a current noise source $V_N(\omega)/M_i V_\phi$ placed at its input terminals. With $\Delta R_i \ll R_{i0}^{\text{opt}}$, the corresponding optimized noise temperature is

$$T_N^{\text{opt}}(f_0)/T = 8RR_i^{\text{opt}}/M_i^2 V_\phi^2. \quad (8.21)$$

Finally, setting $V_\phi \approx R/L$, we find

$$R_{i0}^{\text{opt}} \approx k_i^2 \omega_0 L_i \quad (8.22)$$

and

$$T_N^{\text{opt}} \approx (S_V S_J)^{1/2} \omega_0 / 2k_B V_\phi \approx 7T\omega_0/V_\phi. \quad (8.23)$$

We note that T_N^{opt} scales as the ratio ω_0/V_ϕ .

Furthermore, neglecting ΔR_i we can readily show from Eq. (8.22) that the optimum value of $Q \approx \omega_0(L_i + L_s)/R_i$ is $Q^{\text{opt}} \approx (1 + L_s/L_i)/k_i^2$, or

$$Q^{\text{opt}} k_{ie}^2 \approx 1. \quad (8.24)$$

In general, for reasonably high values of Q this result implies that if necessary one should add inductance to the input circuit to reduce k_{ei} . The resulting weak

coupling justifies the use of the bare SQUID parameters. Finally, the optimized power gain at resonance, $|V_0/V_i|^2 R_i/R_{\text{dyn}}$ (V_0 is the output signal voltage), is found from the square of Eq. (8.11) to be

$$G_p^{\text{opt}} \approx M_i^2 V_\phi^2 / R_i R_{\text{dyn}} \approx V_\phi / \omega_0 \quad (8.25)$$

where we have set the dynamic resistance of the SQUID $R_{\text{dyn}} \approx R$. Combining Eqs. (8.23) and (8.25), we find the gain noise temperature product

$$G_p^{\text{opt}} T_N^{\text{opt}} \approx 7T. \quad (8.26)$$

Thus, high gain is synonymous with low noise temperature.

The results given in Eqs. (8.15)–(8.26) are at the resonant frequency. We observe that the cross spectral density $S_{VJ}(f)$ does not enter the noise temperature, for the following reason. The noise voltage induced into the input circuit is in quadrature with the current noise $J_N(t)$ in the SQUID that generates it. On resonance the input circuit has a real impedance, so that the noise produced at the SQUID output by this voltage noise is also in quadrature with that component of the output noise produced by the circulating current. As a result, the cross-correlation term vanishes. However, in principle one can obtain a lower noise temperature [17] by operating the amplifier off resonance, so that the noise at the SQUID output produced by the voltage noise in the input circuit partially cancels the component due to the current noise in the SQUID. It is straightforward to show that the minimum noise temperature so obtained is given by replacing $(S_V S_J)^{1/2}$ in Eq. (8.23) by $(S_V S_J - S_{VJ}^2)^{1/2}$. However, in practice the gain of the amplifier may well be too low to make operation off resonance realistic.

To give an example of the predicted performance of a tuned amplifier on resonance, we assume $L \approx 400$ pH, $R \approx 8 \Omega$, $L_i \approx 160$ nH, $k_i^2 = 0.7$, $\beta_L = 1$, $V_\phi \approx R/L \approx 2 \times 10^{10} \text{ s}^{-1}$, $S_V \approx 16 k_B T R$, $S_J \approx 11 k_B T/R$ and $f_0 = 100$ MHz to find $R_i^{\text{opt}} \approx 70 \Omega$, $G_p^{\text{opt}} \approx 15$ dB and $T_N^{\text{opt}} \approx T/5$.

To conclude the discussion of the tuned amplifier, we note that the resistance induced into the input circuit in practical devices is dominated by capacitive feedback. This effect modifies both the resonant frequency and the Q of the amplifier [14]. This frequency shift is of the order of $1/Q$ and thus is small for high values of Q . The effect on Q , on the other hand, may be much larger, and could be a factor of 2 for the numerical example considered above [14].

8.3.4

Untuned Amplifier: Theory

To represent an untuned amplifier, we set $L_p = 1/j\omega C_i = 0$. The analysis proceeds along the same lines as that for the tuned case. Thus, we set $1/j\omega C_i = 0$ in Eq. (8.13) for $V(\omega)$ and $1/j\omega C_i = L_p = 0$ in Eq. (8.12) for $Z_T^*(\omega)$. After some calculation, we find the following expression for the noise temperature:

$$T_N(f) = \frac{S_V^r |Z_T^*|^2 + 2S_{VJ}^r k_{ie}^2 LR_i V_\phi^r \operatorname{Re}(Z_T^*) + S_J^r (k_{ie}^2 V_\phi^r LR_i)^2}{4k_B R_i M_i^2 (V_\phi^r)^2}. \quad (8.27)$$

To make progress, we neglect the terms $k_{ie}^2 L / L^r$ and $k_{ie}^2 LR_i / L_i R^r$ in $Z_T^*(\omega)$. These are reasonable approximations since $L / L^r \leq 1/10$ for Φ near $\Phi_0/4$ or $3\Phi_0/4$, and $LR_i / L_i R^r \sim \omega L / R \ll 1$. We can now optimize $T_N(f)$ with respect to R_i to find

$$R_i^{\text{opt}}(f) \approx 2\pi f(L_i + L_s) \left[1 + \frac{2k_{ie}^2 LV_\phi^r S_{VJ}^r}{S_V^r} + (k_{ie}^2 LV_\phi^r)^2 \frac{S_J^r}{S_V^r} \right]^{-1/2}. \quad (8.28)$$

The corresponding optimized noise temperature is

$$T_N^{\text{opt}}(f) \approx 4\pi^2 f^2 (L_i + L_s) S_V^r / 2k_B k_{ie}^2 L (V_\phi^r)^2 R_i^{\text{opt}}(f). \quad (8.29)$$

In contrast to the tuned case, where $k_e \ll 1$ and we could replace the reduced SQUID parameters with their corresponding bare parameters, we now need to estimate the reduced parameters. We assume the same bare SQUID parameters used for the example of a tuned amplifier in Section 8.3.3, and take $L_s = 20$ nH, corresponding to the case of the particular amplifier discussed in Section 8.3.5. We find $k_{ie}^2 \approx 0.6$ and hence $\beta_L^r = (1 - k_{ie}^2)\beta_L \approx 0.4$. From simulations we find $V_\phi^r \approx 2.5 \times 10^{10}$ s⁻¹, $S_V^r \approx 18$ $k_B T R$, $S_J^r \approx 12$ $k_B T / R$ and $S_{VJ}^r \approx 12$ $k_B T$ [15, 16]. Inserting these values into Eq. (8.28) we find $R_i^{\text{opt}} \approx 0.7\omega(L_i + L_s)$, which differs little from the value for the tuned case provided $L_s \lesssim L_i$. From Eq. (8.29) we find $T_N^{\text{opt}} \approx 0.6T$, three times greater than the value for the tuned amplifier.

As a final remark, we note that the reduced SQUID parameters, even for a value of k_{ie}^2 as large as 0.6, differ little from the bare parameters. Given that capacitive feedback, which we have neglected, also modifies the gain and noise temperature to some extent [14], it appears that the trouble of calculating the reduced parameters is not really justified unless k_{ie}^2 becomes rather close to unity.

8.3.5

Tuned and Untuned Amplifiers: Experiment

Hilbert and Clarke [14] measured the gain and noise temperature of a SQUID used as a tuned and an untuned amplifier. The configurations used to measure the power gain G_p and noise temperature T_N are shown in Figure 8.5. The output of the SQUID, which was enclosed in a superconducting shield, was coupled to a low-noise, room-temperature amplifier followed by a spectrum analyzer and a power meter. To measure the gain, a calibrated signal was coupled to a cold attenuator that presented an impedance R_i to the input coil. To measure the noise temperature, the input coil was connected to a resistor R_i , the temperature T_i of which could be raised above the bath temperature with a heater. The total noise temperature referred to the input of the amplifier is

$$T_N^T = T_N + T_i + T_N^P/G_p \quad (8.30)$$

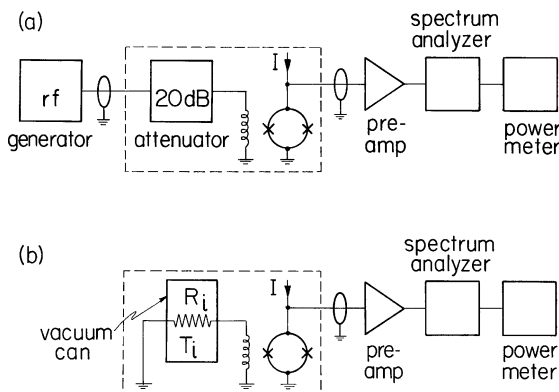


Fig. 8.5 Circuit used to measure (a) the power gain and (b) the noise temperature of an untuned SQUID amplifier. Components in the dashed boxes are immersed in liquid helium. (Reproduced with permission from ref. [14].)

where T_N^P is the noise temperature of the postamplifier. By measuring the output noise power as a function of T_i one can obtain T_N .

In the case of the tuned amplifier, the four-turn input coil with $L_i \approx 5.6$ nH was connected in series with a capacitor $C_i \approx 20$ pF and the source resistance R_i . The measured resonant frequency was about 93 MHz and Q was about 45. The corresponding optimized value of R_i (Eq. (8.22)) is about 2Ω . The resonant frequency implies a large stray inductance, $L_s \approx 140$ pH. Thus, from Eq. (8.8) we find $k_{ie}^2 \approx 0.023$, so that $Qk_{ie}^2 \approx 1$, as required by Eq. (8.24). The measured gain of 18.6 dB was in quite good agreement with the predicted value (see Table 8.1). The measured output noise power as a function of T_i is shown in Figure 8.6, and leads to $T_N = 1.7 \pm 0.5$ K, slightly above the predicted value. The shift in resonant frequency with flux bias was less than 1%, as expected given the low value of k_{ie}^2 . The change in Q when the flux bias was changed from $(n + 1/4)\Phi_0$ to $(n + 1/2)\Phi_0$ was substantially higher, about 25%, and demonstrated that the additional resistance in the input circuit due to the SQUID was dominated by capacitive feedback.

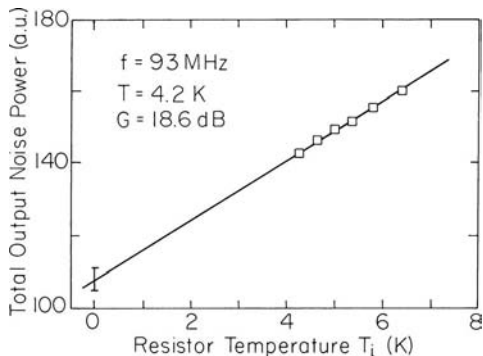


Fig. 8.6 Total output noise power (arbitrary units) versus T_i at 93 MHz for a tuned SQUID amplifier at 4.2 K. (Reproduced with permission from ref. [14].)

Table 8.1 Measured and predicted power gain G_p and noise temperature T_N for a dc SQUID radiofrequency amplifier.

| Frequency (MHz) | G_p (dB) | | T_N (K) | |
|-----------------------|------------|----------------|-----------|---------------|
| | Measured | Predicted | Measured | Predicted |
| $T = 4.2$ K (tuned) | 93 | 18.6 ± 0.5 | 17 | 1.7 ± 0.5 |
| $T = 1.5$ K (untuned) | 60 | 24.0 ± 0.5 | — | 1.2 ± 0.3 |
| | 80 | 21.5 ± 0.5 | — | 0.9 ± 0.3 |
| | 100 | 19.5 ± 0.5 | 18.5 | 1.0 ± 0.4 |
| $T = 4.2$ K (untuned) | 60 | 20.5 ± 0.5 | — | 4.5 ± 0.6 |
| | 80 | 18.0 ± 0.5 | — | 4.1 ± 0.7 |
| | 100 | 16.5 ± 0.5 | 16.5 | 3.8 ± 0.9 |

For the untuned amplifier, the SQUID had a 20-turn input coil, with $L_i \approx 120$ nH and $M_i \approx 6$ nH. The estimated value of k_{ie}^2 was about 0.6. At 80 MHz, the total inductance $L_i + L_s \approx 140$ nH was approximately optimized to a 50- Ω source impedance. Figure 8.7 shows the gain *versus* frequency for positive and negative values of V_ϕ . In each case, the gain drops by about 5 dB as the frequency is increased from 10 to 100 MHz as a result of the increasing impedance of the input coil. There is a resonance around 150 MHz that produces a dip in the gain for negative V_ϕ and a peak for positive V_ϕ . This resonance corresponds to the self-resonance of the input coil, and corresponds to a parasitic capacitance of about 8 pF. The measured values of gain and noise temperature at three frequencies and two temperatures are listed in Table 8.1, and are in quite good agreement with predictions.

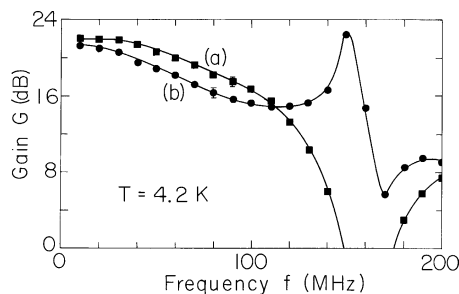


Fig. 8.7 Gain *versus* frequency for an untuned SQUID amplifier for (a) negative and (b) positive V_ϕ . (Reproduced with permission from ref. [14].)

8.3.6

To Tune or Not to Tune?

Given the preceding discussion of tuned and untuned amplifiers, it is natural to ask which type one should use under a given set of conditions. This question becomes particularly relevant for the case of NMR discussed in Section 8.6, and it is convenient to discuss it at this juncture. We again consider the configuration of Figure 8.2, but now assume that the voltage source V_i is generated by an oscillating magnetic flux in the pickup loop which has an inductance L_p . The untuned amplifier is obtained by setting $R_i = 1/C_i = 0$. The issue is the following. On resonance, the tuned input circuit enhances the signal amplitude by a factor Q , but the Nyquist noise in the input circuit also peaks at the resonance frequency. This noise may well overwhelm the intrinsic noise of the SQUID. In the untuned case, there is no resonant enhancement of the signal, but the input circuit, at least at low frequencies, is noiseless, and the SQUID noise determines the noise in the input circuit. Which of the two cases offers the higher signal-to-noise ratio? To discuss this question, it is convenient to focus on the signal energy in the pickup loop

$$E = \langle V_i^2 \rangle / 2\omega^2 L_p \quad (8.31)$$

where $\langle V_i^2 \rangle$ is the mean square voltage induced by the oscillating flux.

We first consider the tuned amplifier, operated at the resonant frequency ω_0 . If we assume an optimized input circuit at 4.2 K, the situation is very simple at frequencies below 100 MHz where $T_N^{\text{opt}} \ll T$ (Section 8.3.3). The minimum detectable signal energy in a bandwidth $\delta f \ll f_0/Q$ is found by setting $\langle V_i^2 \rangle = 4k_B T R_i \delta f$ in Eq. (8.31) to find

$$E_{\min}^{\text{tuned}} = 2k_B T R_i \delta f / 4\pi^2 f^2 L_p \approx k_B T (L_i + L_p + L_s) \delta f / \pi f Q L_p . \quad (8.32)$$

We have neglected the impedance reflected into the input circuit by the SQUID, which is a reasonable approximation for $Q \gg 1$ so that $k_{ie}^2 \ll 1$ (Eq. (8.24)), and we thus set $Q = \omega_0 (L_i + L_p + L_s) / R_i$.

For the untuned case, the situation is more complicated. Strictly speaking, we should optimize the parameters of the input circuit in a manner analogous to that for the untuned amplifier in Section 8.3.4. However, since we are concerned with finding only an order of magnitude result, we shall resort to the following *approximate*, but much simpler, estimate. The mean square flux induced in the SQUID is given approximately by

$$\frac{M_i^2 \langle V_i^2 \rangle}{\omega^2 (L_i + L_p + L_s)^2} = \frac{2k_i^2 L_i L L_p E}{(L_i + L_p + L_s)^2} \quad (8.33)$$

where we have neglected the impedance reflected into the input circuit from the SQUID. We now assume $L_s \ll L_i + L_p$ and $L_p \sim L_i$ so that the output voltage noise

of the SQUID is not too far from its value in the absence of the input circuit and we may neglect the distinction between V_ϕ and V_ϕ^r . These approximations enable us to find the minimum detectable signal energy simply by setting Eq. (8.33) equal to the mean square flux noise of the bare SQUID, $16k_B T R \delta f / V_\phi^2$, to find

$$E_{\min}^{\text{untuned}} \approx 32k_B T \delta f / k_i^2 V_\phi . \quad (8.34)$$

We have set $V_\phi = R/L$.

From Eqs. (8.32) and (8.34), we see that it is advantageous to use a tuned circuit provided $E_{\min}^{\text{tuned}} < E_{\min}^{\text{untuned}}$, that is, with $k_i \sim 1$,

$$f_0 Q > V_\phi / 16\pi . \quad (8.35)$$

For $V_\phi \sim 2 \times 10^{10}$ s⁻¹, this result implies that it is desirable to use a tuned circuit only if $f_0 Q > 400$ MHz. For frequencies of a few megahertz, this implies a tuned circuit with Q of a few hundred, which is generally realistic. On the other hand, for a frequency of (say) 10 kHz, it would be quite impractical to tune – the required $Q \sim 4 \times 10^4$ would imply a bandwidth of 0.25 Hz – and one should clearly use an untuned circuit. The crossover from untuned to tuned circuits is likely to occur around 1 MHz, at which frequency a more careful evaluation of the untuned case would be warranted.

8.3.7

SQUID Series Array Amplifier

A very useful extension of the basic design of the dc SQUID is the SQUID series array [24]. The array consists of N_s SQUIDs with their current leads connected in series; N_s is typically 100. The SQUIDs are biased with a single current and the voltage is measured across the entire array. The input coils to the SQUIDs are similarly connected in series. Provided the flux in each SQUID is the same, the value of V_ϕ is increased to $N_s V_\phi$, which is thus typically 5 mV/ Φ_0 . Since the noise voltages $V_N(f)$ across the SQUIDs are incoherent, the voltage noise is increased by the factor $N_s^{1/2}$ to $N_s^{1/2} V_N(f)$. The large flux-to-voltage transfer coefficient enables one to connect the array directly to a low-noise, room-temperature amplifier while having the SQUID noise dominate over the amplifier noise.

The SQUID array can readily be used as an amplifier. Following the discussion in Section 8.3.3, we can write the voltage noise induced into the input circuit as $-j\omega M_i N_s^{1/2} J_N(\omega)$, where $N_s^{1/2} J_N(\omega)$ is the contribution of the N_s incoherent current noise sources in the SQUIDs. The equivalent current noise in the input circuit due to the voltage noise across the array is $N_s^{1/2} V_N(\omega) / M_i N_s V_\phi$. We observe that the product of the current and noise sources in the input circuit is *independent* of N_s . Consequently, for an array SQUID used as an amplifier with a tuned input circuit, one expects the optimized noise temperature to be the same as for a single SQUID, Eq. (8.23).

Huber *et al.* [25] fabricated SQUID arrays with 10, 30 and 100 SQUIDs. A novel feature of their design was that the flux focusing washer of each SQUID was electrically isolated from the SQUID itself. The relatively small capacitance between the SQUID and washer was substantially less than that between the input coil and the washer. Since these two capacitances are in series, the effective parasitic capacitance between the input coil and the SQUID was substantially reduced, largely eliminating resonances induced on the current–voltage characteristic. The 3-dB point of a 100-SQUID array was 120 MHz. The fact that no coupling network is required between the array and the room-temperature amplifier makes this configuration particularly appealing for radiofrequency applications.

8.3.8

The Quantum Limit

At signal frequencies greater than $k_B T/h$, one expects quantum effects to become important. For a device cooled in a dilution refrigerator to 20 mK, the corresponding frequency is about 0.4 GHz so that the quantum limit is likely to be relevant only to the microstrip SQUID amplifier (Section 8.4). We briefly discuss quantum effects in Josephson junctions and SQUIDs.

In the case of a single resistively shunted junction (RSJ) (Section 2.1.1), quantum effects become significant when $hf_j > k_B T$, where $f_j = 2eV/h$ is the Josephson frequency and V is the time-averaged voltage across the junction. In this limit, one replaces the spectral density of the current noise in the shunt resistor with $(2hf_j/R) \coth(hf_j/k_B T)$ [26, 27]. In the limit $hf_j \gg k_B T$ this spectral density reduces to $2hf_j/R$, representing the zero-point fluctuations of an ensemble of harmonic oscillators with random phases. This term can be observed by measuring the voltage noise across a junction at a frequency f_m much less than f_j . This noise is predicted to have a spectral density

$$S_V(f_m) = [4k_B T + \frac{1}{2} (I/I_0)^2 2eV \coth(eV/k_B T)] R_{\text{dyn}}^2 \quad (8.36)$$

where $I > I_0$. The first term in brackets arises from noise generated at frequency f_m . The second term arises from noise generated at the Josephson frequency $2eV/h$ and mixed down to the measurement frequency by the nonlinearity of the junction; the mixing coefficient is $\frac{1}{2}(I_0/I)^2$. Equation (8.36) represents the solution of a quantum Langevin equation in which one uses zero-point fluctuations in the classical equation of motion for the RSJ (Eq. (2.22)). Koch *et al.* [28] measured the voltage noise at a frequency of about 100 kHz for Josephson frequencies up to about 500 GHz, and found good agreement with Eq. (8.36).

At sufficiently low temperatures and high signal frequencies, one would expect quantum effects to become important in the dc SQUID. Unfortunately, since SQUIDs are typically operated at a bias current rather close to the (non-noise-rounded) value of their critical current, the quantum Langevin equation is of dubious validity and one should instead undertake a full quantum mechanical treatment of the SQUID as an amplifier. This problem turns out to be remarkably

challenging, and, to date, remains unsolved. Despite the questionable validity of the quantum Langevin approach, a quarter of a century ago Koch *et al.* [29] carried out a series of simulations for noise in a SQUID coupled to a tuned input circuit to make an amplifier (as in Figure 8.2 with $L_p = L_s = 0$). They computed the spectral densities $S_V(f)$, $S_J(f)$ and $S_{VJ}(f)$ at $T = 0$ assuming that the noise arose from uncorrelated zero-point fluctuations in the two shunt resistors. As a figure of merit they defined the quality $n^{(i)}(f)hf = S_V^{(i)}(f)/4R_i$ as the mean photon energy in the input circuit due to intrinsic SQUID noise; $S_V^{(i)}(f)$ is the spectral density of the voltage noise referred to the input terminals of the amplifier. When the amplifier is operated off resonance (Section 8.3.3) to minimize the noise temperature, one finds

$$n^{(i)} = \pi[S_V(f) S_J(f) - S_{VJ}^2(f)] h/V_\phi. \quad (8.37)$$

For an optimized SQUID, Koch *et al.* [29] found $n^{(i)} \approx \frac{1}{2}$, that is to say, on the average the SQUID adds one half photon of noise to the input circuit. When this energy is added to the zero-point energy $\frac{1}{2}hf$ of the resonant circuit, the total noise of the amplifier becomes hf , the result for any quantum-limited amplifier.

Since, as we shall see in Section 8.4.4, the microstrip SQUID amplifier is within a factor of two of this quantum limit, it would be of great interest to perform a full quantum mechanical treatment of the SQUID amplifier to find out whether or not it is indeed strictly quantum-limited and to examine the validity of the quantum Langevin approach.

8.3.9 Future Outlook

The theory and operation of single dc SQUIDs used as radiofrequency amplifiers at frequencies up to about 100 MHz are well in hand. The measured gain and noise temperature are in quite good agreement with predictions. However, a complication in the understanding of these amplifiers is the presence of parasitic capacitance between the input coil and the SQUID washer. This capacitance not only introduces resonance on the current–voltage characteristic but also partially screens currents at the Josephson frequency from the input circuit, making it difficult to calculate the effects of mutual coupling between the SQUID and input circuit with any precision (Section 8.3.2). The use of a design in which the flux-focusing washer is electrically isolated from the SQUID [25] can substantially reduce the parasitic capacitance between the SQUID and the input coil (Section 8.3.7). This decreases the magnitude of resonances on the current–voltage characteristic and at the same time largely eliminates the interaction between the SQUID and input circuit at the Josephson frequency. As a result, the effect of the input circuit on the SQUID parameters may become relatively unimportant. These effects are well worth exploring experimentally. The use of SQUID series array amplifiers, with their substantially enhanced output signal voltage, allows one to use a low-noise amplifier at room temperature without the need of an

impedance-matching network between them. This simplification is very appealing for radiofrequency applications.

Although the theory of the SQUID amplifier in the classical regime is well understood, the same cannot be said for the quantum limit. A theory that fully accounts for the quantum mechanical nature of the SQUID is very much needed, particularly to understand whether or not the SQUID is truly a quantum-limited amplifier.

8.4

Microstrip SQUID Amplifier

8.4.1

Introduction

As we have seen in Section 8.3, the conventional square-washer SQUID configuration [6] can be operated as a low-noise amplifier at frequencies up to about 100 MHz. As the frequency is increased, however, parasitic capacitance between the input coil and the square washer causes the gain to fall off to levels that are no longer useful. This problem was addressed by Tarasov *et al.* [30] who made a four-loop SQUID with input coils in series deposited inside the loops rather than on top of the superconducting washer. As a result, the parasitic capacitance is reduced, and the operating frequency range is substantially extended. For example, in a tuned amplifier configuration a gain of nearly 20 dB was achieved at 420 MHz. The development of this amplifier was described in a subsequent series of publications [31–35], and its frequency range increased by reducing the number of SQUID loops to two. For an operating temperature of 4.2 K and a frequency of 3.65 GHz, a gain of (11 ± 1) dB and a noise temperature of (4 ± 1) K were achieved [34]. A two-stage amplifier at the same frequency achieved a gain of (17.5 ± 1) dB [33]. This research is currently focused on developing an intermediate-frequency amplifier to follow an SIS (superconductor–insulator–superconductor) mixer for radio astronomy.

In an alternative approach, one makes a virtue of the capacitance between the coil and the washer by using it to form a resonant microstrip [36]. The signal to be amplified is applied between one end of the coil and the washer, while the other end of the coil is left open. Provided that the source impedance is greater than the characteristic impedance of the microstrip, there is a peak in the gain when a half wavelength of the standing wave is approximately (but not exactly) equal to the length of the coil. Gains of well over 20 dB and noise temperatures well below the bath temperature can be achieved. However, as we shall see, the actual behavior of the device differs markedly from that of a simple microstrip because the inductance coupled into the input coil from the SQUID is generally substantially greater than the intrinsic microstrip inductance.

8.4.2

The Microstrip

A microstrip consists of a superconducting strip of width w separated from an infinite superconducting sheet by an insulator with dielectric constant ϵ and thickness d . We assume that the thicknesses of the two superconductors are much greater than the superconducting penetration depth λ , and that $w \gg d$. The capacitance and inductance per unit length of the microstrip are given by $C_0 = \epsilon \epsilon_0 w/d$ (F m^{-1}) and $L_0 = (\mu_0 d/w)(1 + 2\lambda/d)$ (H m^{-1}) [37]. Here, $\epsilon_0 = 8.85 \times 10^{-12} \text{ F m}^{-1}$ and $\mu_0 = 4\pi \times 10^{-7} \text{ H m}^{-1}$ are the permittivity and permeability of free space, and $c = 1/(\epsilon_0 \mu_0)^{1/2} = 3 \times 10^8 \text{ m s}^{-1}$ is the velocity of light in vacuum. The factor $(1 + 2\lambda/d)$ accounts for the penetration of the magnetic field into the (identical) superconductors. The velocity of an electromagnetic wave on the microstrip is thus given by $\bar{c} = c/[\epsilon(1 + 2\lambda/d)]^{1/2}$, and its characteristic impedance by

$$Z_0 = \left(\frac{L_0}{C_0} \right)^{1/2} = \frac{d}{w} \left[\frac{\mu_0 (1 + 2\lambda/d)}{\epsilon \epsilon_0} \right]^{1/2}. \quad (8.38)$$

The microstrip represents an electromagnetic resonator. For a microstrip of length ℓ with its two ends either open or terminated with resistances greater than Z_0 , the fundamental frequency occurs when ℓ is equal to a half wavelength [37],

$$f_0(L_0) = c/2 \ell [\epsilon(1 + 2\lambda/d)]^{1/2}. \quad (8.39)$$

In this mode, the resonator is analogous to a parallel tuned circuit, and, for a resistance $R_i > Z_0$ connected to one end, the quality factor of the resonance is given by $Q = \pi R_i / 2Z_0$.

8.4.3

The Microstrip SQUID Amplifier: Gain

The microstrip SQUID has the conventional square-washer configuration (Figure 8.8). However, in contrast to the conventional input scheme in which the signal is connected to the two ends of the coil, the signal is instead coupled between one end of the coil and the square washer, which provides the groundplane for the microstrip. In an early set of experiments [36], the square washer had inner and outer dimensions of $0.2 \times 0.2 \text{ mm}^2$ and $1 \times 1 \text{ mm}^2$, and the input coil had $n = 31$ turns, a width $w = 5 \mu\text{m}$ and a length $\ell = 71 \text{ mm}$. Estimated parameters were $L \approx 320 \text{ pH}$, $L_i \approx 300 \text{ nH}$ and $M_i \approx 10 \text{ nH}$. The critical current and shunt resistance per junction were typically $5 \mu\text{A}$ and 10Ω , and the maximum value of V_ϕ was about $60 \mu\text{V}\Phi_0^{-1}$. At 4.2 K , the white flux noise measured in a flux-locked loop at low frequencies was typically $2\text{--}3 \mu\Phi_0 \text{ Hz}^{-1/2}$. We note that virtually the entire length of the coil overlays the washer, which is at a uniform potential. The SQUID chip was mounted on a printed circuit board, and each pad was wire bonded to a $50\text{-}\Omega$ trace patterned on the board. The grounds of the input and output SMA con-

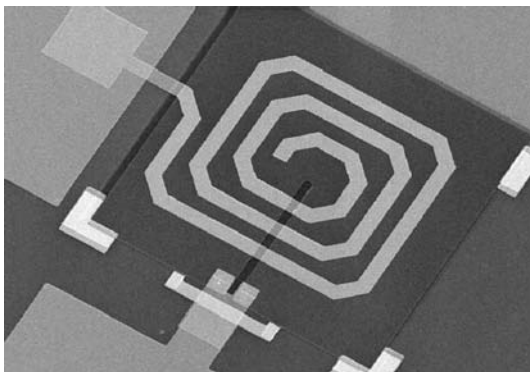


Fig. 8.8 Configuration of microstrip SQUID amplifier. The input signal is connected between one end of the coil and the square washer.

nectors were soldered to a groundplane on the reverse side of the board, and their center conductors were soldered to the traces coupled to the input of the microstrip and to the output from the SQUID, respectively. The assembly was rigidly mounted inside a superconducting box that eliminated fluctuations in the ambient magnetic field. Most measurements were made with the package immersed in liquid ${}^4\text{He}$.

The circuit shown in Figure 8.9 was used to measure the gain; the input coil over the square washer is shown as a distributed line. The current bias was supplied by batteries. In later versions of the device, the flux bias was provided by a directly coupled flux-locked loop that maintains the SQUID near its maximum gain [38]. The loop rolls off at frequencies above a few kilohertz, and has no effect on the high-frequency performance. A sweep oscillator was coupled to the microstrip via a room-temperature 100-dB attenuator and a cold 20-dB attenuator that prevented noise produced by the generator from saturating the SQUID. The cold attenuator also presented an impedance of 50Ω to both the input coaxial line and the microstrip. A second cold, 4-dB attenuator coupled the output of the SQUID to a room-temperature postamplifier. The gain of the system excluding the SQUID was calibrated by disconnecting the SQUID and connecting together the input and output attenuators. All measurements of the gain of the SQUID amplifier were referred to the baseline so obtained. Because the washer SQUID is an asymmetric device – the two Josephson junctions are situated close together rather than on opposite sides of the SQUID loop – one can either ground the washer or ground the counter-electrode close to the Josephson junctions. Since the washer acts as a groundplane for the input coil, at first sight it might seem plausible to ground the washer. However, it is also possible to ground the counter-electrode and have the washer at output potential. In the latter case, there is feedback from the output voltage generated on the washer to the input coil, via the capacitance between them. If the sign of V_ϕ is such that the output voltage has

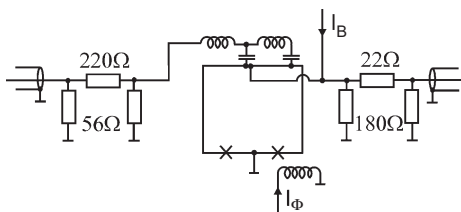


Fig. 8.9 Circuit used to determine the gain of the microstrip SQUID, which is shown with counter-electrode grounded. I_B is the current bias, and I_ϕ provides the flux bias. The input and output π -networks have attenuations of 20 dB and 5 dB, respectively. (Reproduced with permission from ref. [36].)

the same sign as the input voltage, the feedback is positive; if the signs are opposite, the feedback is negative. We designate the flux-to-voltage transfer coefficients as V_ϕ^+ and V_ϕ^- , respectively.

Figure 8.10 shows the gain as a function of frequency for six devices with coil lengths ranging from 98 mm to 3 mm. The two SQUID configurations are shown in the figure: for the four longer coils the hole in the washer was $200 \times 200 \mu\text{m}^2$ and the estimated inductance was 350 pH; for the two shorter coils, the hole was $10 \times 200 \mu\text{m}^2$ and the estimated inductance was 90 pH. These inductances, the number of turns on the coils and the length of the coils are listed in Table 8.2. The peak gains achieved with SQUIDs 5 and 6 are lower than for the other four devices because of the reduced mutual inductance between the input coil and the washer.

Table 8.2 Measured and calculated frequency of the fundamental resonance (half-wavelength) for six microstrip SQUIDs with inductance L and coils of n turns and length ℓ ^a.

| SQUID | L (pH) | n | ℓ (mm) | f_0 (MHz) | $f_0^{\text{calc}}(L_0)$ (MHz) | $f_0^{\text{calc}}(n^2 L)$ (MHz) |
|-------|-------------|-----|----------------|----------------|-----------------------------------|-------------------------------------|
| 1 | 350 | 40 | 98 | 105 | 500 | 91 |
| 2 | 350 | 15 | 23 | 370 | 2100 | 500 |
| 3 | 350 | 11 | 16 | 590 | 3000 | 820 |
| 4 | 350 | 6 | 8 | 1200 | 6200 | 2200 |
| 5 | 90 | 8 | 4 | 2200 | 12330 | 4400 |
| 6 | 90 | 7 | 3 | 2650 | 15000 | 5300 |

^a The measured values f_0 were obtained with a reverse gain technique. The calculated value $f_0^{\text{calc}}(L_0)$ was obtained from Eq. (8.39) with $\epsilon = 5.5$, $\lambda = 0.15 \mu\text{m}$ and $d = 0.4 \mu\text{m}$. The calculated value $f_0^{\text{calc}}(n^2 L)$ was obtained from Eq. (8.40) with $C_0 = 0.6 \text{ nF m}^{-1}$.

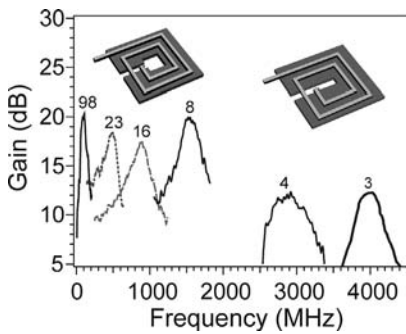


Fig. 8.10 Gain *versus* frequency for six microstrip SQUID amplifiers in two different configurations with counter-electrode grounded and V_ϕ^+ . Numbers refer to coil lengths in millimeters.

In a more recent set of devices [39], the peak in the gain was moved to high frequency by scaling down the hole in the SQUID to $10 \times 200 \mu\text{m}^2$, and reducing the dimensions of the coils. The gains achieved ranged from 12 ± 1 dB at 2.2 GHz to 6 ± 1 dB at 7.4 GHz. The reduction in gain compared with devices operating at lower frequencies was due largely to the lower mutual inductance between the coil and the SQUID which, in turn, arose from the smaller SQUID inductance. Nonetheless, it is encouraging that useful levels of gain can be achieved at frequencies well into the gigahertz range.

It is important to realize that the peak in the gain is shifted to a frequency higher than the resonant frequency of the coil – typically by 30% – by positive feedback [40]. The true resonant frequency f_0 can be determined by a reverse gain technique [40] as follows. With the SQUID washer grounded, a signal source is connected across the SQUID and the signal transmitted through the SQUID into the coil resonator is measured with a spectrum analyzer. The current flux biases are adjusted to their usual operating values, that is, to produce maximum forward gain. At the resonant frequency of the resonator, where $\ell = \lambda/2$, there is a minimum in the observed power. This minimum arises from the asymmetric voltage distribution on the resonator, which induces a positive current in one half of the resonator and an equal, negative current in the other half. The measured values of f_0 are listed in Table 8.2.

Also listed in Table 8.2 are the resonant frequencies $f_0(L_0)$ predicted by the microstrip formula, Eq. (8.39), using $\epsilon = 5.5$, $d = 0.4 \mu\text{m}$ and $\lambda = 0.15 \mu\text{m}$. We see that in all cases these exceed the measured value by a factor of roughly 5. Thus, the input coil does not behave as a simple microstrip resonator. A much better agreement between the measured and predicted resonant frequencies is obtained by taking $n^2 L/\ell$ as the inductance per unit length, instead of L_0 ; here, we have used $n^2 L$ as the inductance of the input coil (Chapter 5). This assumption leads to the predicted resonant frequency [40]

$$f_0(n^2 L) = 1/2n(\ell LC_0)^{1/2}. \quad (8.40)$$

The resonant frequencies predicted by this model are also listed in Table 8.2. The agreement with the measured values is acceptable for the longer coils, but becomes progressively worse as the coil length is reduced. This trend may possibly be explained by the fact that the parasitic inductance of the wiring to the chip becomes progressively more important as the length of the coil is shortened.

The electromagnetic behavior of the microstrip SQUID amplifier has been studied using both an analog model and numerical calculations [40]. The analog model confirmed the validity of Eq. (8.40) for the resonant frequency. The numerical simulations, using both lumped circuit and distributed element models, were used to study the effects of positive and negative feedback, corresponding to a grounded electrode with transfer functions V_ϕ^+ and V_ϕ^- . These simulations agree well with the observation that the peak in the gain occurs at a frequency above and below the resonance, respectively. The same model was used to investigate the input impedance of the microstrip, which is dominated by the complex impedance of the SQUID. For V_ϕ^+ the input resistance becomes negative below the $\lambda/2$ resonance in the frequency range where the gain is high. Correspondingly, for V_ϕ^- the input resistance is negative above the $\lambda/2$ resonance, where the gain is also high. For low gains (above the resonance for V_ϕ^- and below the resonance for V_ϕ^+), the input resistance is positive and the return loss is high. These simulations followed the trends in measured values of the input impedance remarkably well.

In a further series of experiments, the harmonic distortion and intermodulation distortion were investigated [41]. Biased for maximum gain, the microstrip SQUID amplifier generates third harmonic signals with an amplitude in good agreement with a model based on a sinusoidal flux-to-voltage transfer function. The amplitude of the third harmonic is less than 1% of the fundamental for a flux amplitude of $0.1 \Phi_0$. However, under the same bias conditions, departures from a sinusoidal transfer function produce a second harmonic signal. This signal can be reduced or even eliminated by adjusting the flux bias empirically away from the point of maximum gain. Similarly, the third- and fifth-order intermodulation products can be non-negligible with the SQUID biased for maximum gain, but one or the other can be reduced if the flux bias is adjusted appropriately.

We have seen that substantial levels of gain can be achieved with the microstrip SQUID amplifier. However, the frequency at which the gain peaks is evidently fixed by the length of the microstrip, whereas some applications demand tuneability. Fortunately, one can tune the frequency quite simply by connecting a varactor diode between the otherwise open end of the input coil and the washer [42]. The capacitance of the diode can be varied by changing the value of the reverse bias voltage. Changing the capacitance modifies the phase shift of the electromagnetic wave when it is reflected, thereby increasing or decreasing the effective length of the microstrip and lowering or raising the peak frequency.

Experiments were carried out with a GaAs varactor diode, the capacitance of which could be varied from 1 to 10 pF by changing the bias voltage from 1 V to -22 V. Two diodes in parallel were used to increase the tuning range. The diodes,

in series with a capacitor, were connected between the washer and the end of the input coil not connected to the signal source. The gain for optimized current and flux biases for a SQUID with 31 turns is shown in Figure 8.11 for 9 values of the capacitance of the two diodes. We see that the peak frequency is progressively lowered, from 195 MHz to 117 MHz, as the capacitance is increased. The maximum gain is constant to within 1 dB over this range. In the absence of the varactor, the peak frequency is about 200 MHz. In fact, the presence of the varactors increases the gain, most likely by increasing the degree of positive feedback. The dependence of the peak frequency on the varactor capacitance is in reasonable agreement with a simple model [42].

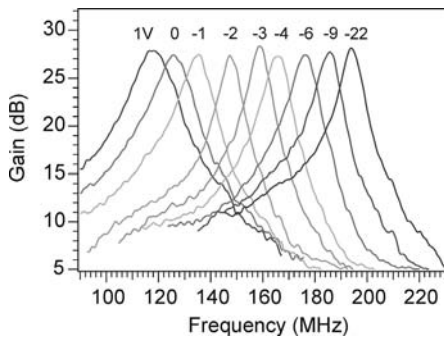


Fig. 8.11 Tuning the microstrip SQUID amplifier. Gain *versus* frequency for a 31-turn SQUID at 4.2 K for 9 values of reverse bias voltage applied to the varactor diodes connected between the open end of the coil and the washer. (Reproduced with permission from ref. [42].)

A potential concern is whether the varactor diode can introduce additional noise into the amplifier. Estimates of the contributions of the Nyquist noise and shot noise of the diode and of the noise on the bias voltage indicate that they should not be significant. The measured noise temperatures of a particular device with and without the varactor diodes were identical to within the uncertainties.

8.4.4

The Microstrip SQUID Amplifier: Noise Temperature

We turn now to the central issue, the noise temperature. An accurate way of measuring T_N is to increase the temperature T of the input load by means of a heater, so that the resistor provides a well-defined source of Nyquist noise power. The noise power at the output of the postamplifier is given by

$$P_N(f) = k_B(T + T_N)R_iGG_p + k_B T_p R_i G_p , \quad (8.41)$$

where G and G_p are the (power) gains of the SQUID amplifier and postamplifier, and T_p is the noise temperature of the postamplifier. By measuring the output

noise power with a spectrum analyzer for several values of T , one can infer $T_N + T_p/G$. Measuring T_p separately using a similar method, one can deduce T_N . This discussion also makes it clear that one requires $T_p/G \ll T_N$ to ensure that the postamplifier noise does not contribute significantly to the system noise temperature.

In preliminary experiments, the postamplifier was at room temperature and had a noise temperature of about 80 K. Thus, with a typical SQUID power gain of 200 at the peak, the postamplifier contributed a noise temperature of about 0.4 K. Subsequent experiments made use of a single-stage postamplifier using a heterojunction field effect transistor (HFET – Fujitsu FHX 13LG) operated in the ${}^4\text{He}$ bath. This postamplifier had a noise temperature of 10 ± 1.5 K. Figure 8.12 shows the system noise temperature *versus* frequency for a device with a peak frequency near 365 MHz, cooled to 1.8 K. The peak gain of the microstrip SQUID was 24.5 ± 0.5 dB. The noise temperature increases rapidly as the frequency moves away from the resonance; this effect is due largely to the resonant network used to couple the SQUID to the HFET. The minimum system noise temperature is 0.28 ± 0.06 K, to which the postamplifier contributes 0.09 ± 0.02 K. Thus, the intrinsic noise temperature is 0.19 ± 0.06 K, an order of magnitude lower than the bath temperature. The noise temperature is also an order of magnitude lower than that of state-of-the-art, cooled semiconductor amplifiers [43].

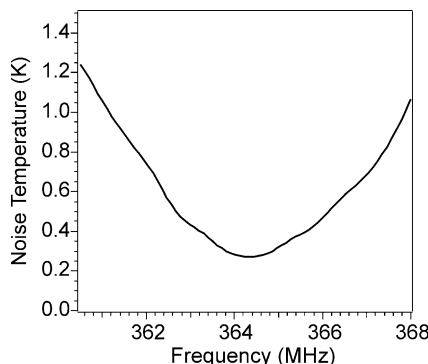


Fig. 8.12 Noise temperature for a microstrip SQUID amplifier with 29-turn spiral input coil. The device and its HFET postamplifier were cooled to 1.8 K. (Reproduced with permission from ref. [44].)

An alternative way to determine T_N is to couple the input of the microstrip to a tuned circuit, as shown in Figure 8.13 [44]. The tuned circuit consisted of a 1 pF capacitor and a four-turn copper coil, about 4 mm in diameter, inductively coupled to the microstrip by means of a loop of wire. The resonant frequency was about 438 MHz. In a separate experiment, the loop was connected to a 50Ω cable, and the distance between the coil and the loop was adjusted to produce a 2-dB loss, thus reducing Q by a factor of about two. To determine the gain and Q , a second loop, with a coupling loss of 10 dB to the tuned circuit, was connected to a signal generator via a cold 20-dB attenuator and a stainless steel cable with a loss of 3 dB. The measured transmitted power at 4.2 K is shown in Figure 8.14 (upper trace).

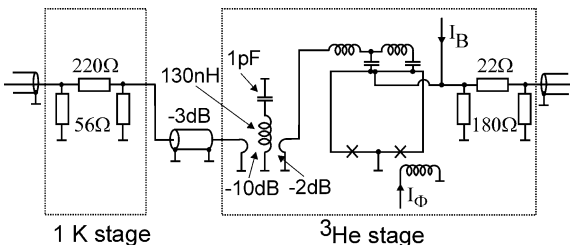


Fig. 8.13 Configuration of circuit used to detect Nyquist noise in a resonant circuit inductively coupled to the input of the microstrip amplifier. (Reproduced with permission from ref. [44].)

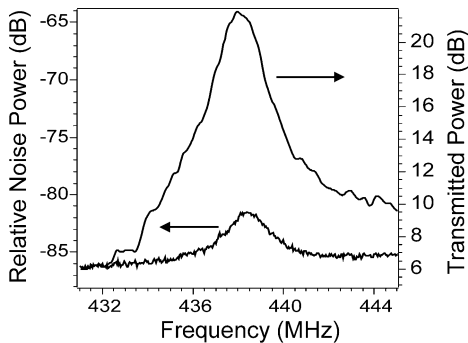


Fig. 8.14 Microstrip SQUID amplifier coupled to the resonant circuit of Figure 8.13. Transmitted power (referred to the loop that couples signal into the resonant circuit) and relative noise power with no input signal at 4.2 K. (Reproduced with permission from ref. [44].)

The Q is about 270 and the maximum gain is 22 dB. The gain is referred to the input coupling loop of the resonant circuit, and includes an added 12 dB to account for the coupling losses.

The noise generated by the resonant circuit, with the generator disconnected, is shown in the lower trace of Figure 8.14. The measured peak is 4.7 dB above the (nearly white) noise at 432 MHz. This peak contains contributions from the Nyquist noise of the resonant circuit and from the system noise of the SQUID amplifier. Although it is not entirely straightforward to separate these contributions, using the following *approximate* argument one can show that this result is consistent with the measured noise temperature. On resonance, since the microstrip reduces Q of the resonant circuit to approximately half of its unloaded value, the source impedance presented to the microstrip is roughly equal to the characteristic impedance of the microstrip. At frequencies well below resonance, the magnitude of the source impedance is approximately ωL_ℓ , where L_ℓ is the inductance of the coupling loop. Estimating $L_\ell \sim 10$ nH, we find $\omega L_\ell \sim 25 \Omega$ at 400 MHz. Since $T_N \ll T$, to a first approximation one can ignore any variation in the noise power with source impedance. Thus, referred to the input of the preamplifier, the

total noise on resonance can be characterized by the temperature $[G'(T/1.58) + G'T_N + T_p]$; off-resonance, where we assume the noise from the resonant circuit to be negligible, the corresponding temperature is $(G'T_N + T_p)$. Here $G' = 16$ dB is the gain of the microstrip SQUID amplifier reduced by the 4-dB loss in the attenuator coupling it to the HFET, and $T_p = 15$ K is the measured noise temperature of the HFET of 438 MHz. The factor of 1/1.58 accounts for the 2-dB loss between the resonant circuit and the input to the microstrip SQUID amplifier. We can deduce $T_S = T_N + T_p/G'$ from the relation $10 \log_{10} \{[G'(T/1.58) + G'T_S]/G'T_S\} = 4.7$, and find $T_S = 1.4$ K. For the given values of T_p and G' we calculate $T_N = 1$ K.

It is evident from Eq. (8.23) that T_N should scale with the bath temperature. Thus, even lower noise temperatures should be possible with the device cooled to millikelvin temperatures in a dilution refrigerator. However, the contribution of the HFET amplifier, about 0.1 K, would then become dominant. To circumvent this problem, a second microstrip SQUID amplifier was used as a postamplifier [44]. If necessary, the peak frequency of the second SQUID could be tuned with a varactor diode to coincide with that of the first. To prevent the two SQUIDs from interacting with each other, it was necessary to separate them with an attenuating network. For a particular pair of SQUIDs at 4.2 K, the maximum gain was 33.5 ± 1 dB.

Such a system was cooled in a dilution refrigerator [45]. The two peak frequencies were made to coincide by means of small changes in the bias fluxes. All leads connected directly to the SQUIDs were very heavily filtered over a wide frequency range using a combination of lumped circuit and copper powder filters, and a superconducting shield surrounding the SQUIDs eliminated ambient magnetic field fluctuations. The overall gain of the two SQUIDs at 538 MHz was 30 ± 1 dB and 32 ± 1 dB at 4.2 K and 100 mK, respectively. A third stage of amplification was provided by an HFET with a resonant input circuit, cooled to 4.2 K and connected to the SQUID postamplifier via a cryogenic cable with a loss of 6 dB. At 550 MHz, the gain of the HFET was 22 ± 1 dB, and its noise temperature T_p about 6 K. At the lowest temperatures, the cable loss reduced the effective gain G' of the two SQUIDs to 26 ± 1 dB so that the HFET contributed a noise temperature $T_p/G' \approx 15$ mK referred to the input of the first SQUID. Two different input circuits were used to measure the noise: one involved measuring the signal-to-noise ratio in the presence of an accurately known signal, and the other measuring the noise from a resonant circuit. The two methods gave nearly identical results, and we describe only the second.

During the measurement, a small (about -140 dBm) signal was applied to the tuned circuit, via the coupling loop, at a frequency about 2 MHz above its 519 MHz resonant frequency. This signal was used to optimize the bias currents and fluxes of the two SQUIDs for maximum gain and optimum signal-to-noise ratio. The peak was monitored throughout the measurements to verify that the gain did not drift. The inset in Figure 8.15 shows this peak, together with the noise peak from the resonant circuit. The value of T_N is extracted from the peak using the method described above, with the Nyquist noise power replaced by $(hf/2k_B)\coth(hf/2k_B T)$. Figure 8.15 shows the inferred values of T_N versus T . The

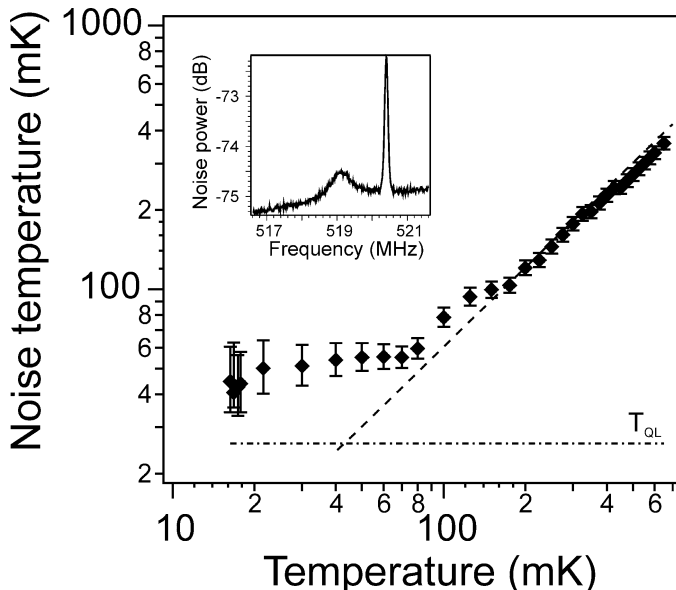


Fig. 8.15 Noise temperature of input micro-strip SQUID at 519 MHz *versus* temperature measured with a resonant source. The dashed line through the data corresponds to $T_N \propto T$, and the dot-dash line indicates $T_Q = h/f/k_B$

≈ 25 mK. The inset shows the noise peak produced by an LC-tuned circuit at 20 mK. The peak at 520.4 MHz is a calibrating signal. (Reproduced with permission from ref. [45].)

error bars are determined solely by the uncertainty in the spectrum analyzer measurement. We see that T_N scales as T above about 150 mK, and flattens off at temperatures below about 70 mK to 47 ± 10 mK; by comparison, the quantum-limited noise temperature, $T_Q \approx h/f/k_B$, is about 25 mK.

A potential source of the low-temperature saturation of T_N is hot electrons produced in the resistive shunts by bias current heating. Wellstood *et al.* [46] obtained remarkably similar results for the noise spectral density measured at frequencies below about 50 kHz in SQUIDs cooled to around 20 mK, and found good agreement with a model in which the temperature of the electrons is determined by their coupling to the phonons. To investigate whether hot electrons were indeed responsible for the saturation in Figure 8.15, Mück *et al.* [45] remeasured the noise of the same SQUID at 140 kHz, where $T_Q < 10 \mu\text{K}$. For this experiment, the output of the first SQUID was coupled to the two ends of the input coil of a second SQUID, via a superconducting transformer with a current gain of about 3. The output of the second SQUID was coupled to a room-temperature amplifier with a noise temperature of about 3 K. The temperature dependence of the noise energy at 140 kHz mimicked that plotted in Figure 8.15 quite remarkably, leveling off to $7.5 \pm 1.3 \hbar$ at low temperatures, thus providing strong evidence that the low-temperature saturation of T_N indeed arose from hot electrons.

8.4.5

High- T_c Microstrip SQUID Amplifier

Tarasov and coworkers [47–50] fabricated and tested microstrip SQUID amplifiers involving YBCO SQUIDs with grain boundary junctions. The spiral microstrip was made either of YBCO, deposited on a separate substrate and coupled to the SQUID in a flip-chip arrangement, or of Au, deposited on the SQUID washer with an intervening layer of insulator. The maximum gain of these devices to date is a few decibels at frequencies of around 1 GHz. However, it is possible that such amplifiers operated at low temperature could achieve very high levels of gain. For example, Tarasov and coworkers [49, 50] fabricated YBCO devices with 0.5 μm grain boundary junctions, and achieved values of I_0R_n as high as 8 mV and values of V_ϕ as high as $1 \text{ mV}\Phi_0^{-1}$ at 20 K. These values are substantially higher than those achieved with low- T_c devices, where the external resistive shunts drastically reduce the values of I_0R that can be achieved. Since the relatively high levels of 1/f noise observed in high- T_c SQUIDs (Chapter 5) are not an issue at high frequencies, the high- T_c microstrip amplifier is worthy of further investigation for use at or below ^4He temperatures.

8.4.6

Future Outlook

Several challenges remain for the microstrip SQUID amplifier. Although substantial levels of gain have been achieved at frequencies up to 3 or 4 GHz [39], one would like to extend this frequency range up to (say) 10 GHz. Another interesting endeavor would be the development of high- T_c SQUIDs with low critical current – and correspondingly high resistance – at 4.2 K. Such SQUIDs might well have substantially higher values of I_0R_n than resistively shunted low- T_c SQUIDs, and thus higher levels of gain as microstrip amplifiers. Perhaps the biggest challenge, however, is to achieve the quantum-limited noise temperature at frequencies of 0.5–1 GHz. The lowest noise temperature yet achieved [45], $47 \pm 10 \text{ mK}$ at 0.519 GHz, was in fact limited by hot electrons in the resistive shunts [46]. It would thus be of great interest to reduce the hot electron temperature by means of cooling fins to attempt to attain the quantum limit.

The current understanding of the operation of the microstrip SQUID amplifier [40] is largely empirical. Although this model is adequate for the design of new devices, it would be a significant advance if a first-principles theory were to be developed that would enable one to calculate with reasonable accuracy the gain, frequency response and input impedance.

The original motivation for the development of the microstrip SQUID amplifier was to improve the performance of an axion detector (Section 8.7). However, another intriguing application is as a postamplifier for the radiofrequency single-electron transistor (RFSET) [51]. This device is a charge detector typically operating at frequencies of several hundred megahertz. Although potentially very sensitive, the RFSET has relatively low gain and its noise temperature is generally lim-

ited by noise in the HFET to which its output is coupled. It appears likely that the use of a microstrip SQUID as a postamplifier will enable the RFSET to reach the quantum limit of charge detection [52], and several groups are working towards this goal.

8.5

SQUID Readout of Thermal Detectors

8.5.1

Introduction

The detection of electromagnetic waves plays an important role in science, technology and everyday life. Several types of cooled sensor for the detection of millimeter-wave to X-ray radiation are being developed which use a SQUID readout. The development of these sensors is strongly motivated by the requirements for astrophysical observations. A particularly promising development is the use of the voltage-biased superconducting transition-edge sensor (TES) for thermal detectors [53]. Several types of readout multiplexer for TESs are under development with the near-term goal of producing imaging arrays with 10^4 elements. In the following sections, we discuss the operation of the voltage-biased TES and the requirements for the SQUID readout, including SQUID output multiplexers. We then describe the application, design, and performance of far-infrared to millimeter-wave bolometers and X-ray calorimeters. These devices have been the focus of intensive recent development. Finally, we briefly describe several other types of sensor that use SQUID readouts, including magnetic calorimeters, SIS tunnel junction sensors, normal-insulator-superconductor (NIS) tunnel junction sensors and kinetic inductance sensors.

In a thermal detector, a photon absorbing layer is attached to a low-temperature heat sink by a weak thermal conductance. A thermistor, such as a TES, is attached to the absorber which senses the energy released by one (or more) absorbed photon(s). At far-infrared to millimeter wavelengths, TES thermal detectors are used to measure the rate of arrival of photons. In this mode, the characteristic time for energy deposition is long compared with the thermal relaxation time, so that the temperature rise is proportional to the absorbed power. Thermal detectors operated in this mode are called bolometers. Arrays of TES bolometers are being developed for ground-based, airborne, balloon-borne and space telescopes for use at millimeter to far-infrared wavelengths.

From near-infrared to X-ray wavelengths, the temperature pulse from a single absorbed photon is detected. The characteristic time for energy deposition is short compared with the thermal relaxation time of the device, so that the height of the temperature pulse is proportional to the total energy of the absorbed photon. Thermal detectors operated in this mode are called calorimeters. They are used to measure the spectrum of a source as well as its flux. Individual TES calorimeters are used for laboratory X-ray spectroscopy. Arrays of TES calorimeters are being

developed for spectroscopic imaging on major forthcoming astrophysical space X-ray missions.

8.5.2

Transition-Edge Sensors

A TES consists of a superconducting film biased within its superconducting to normal state transition. The large positive derivative of resistance with respect to temperature dR_{TES}/dT for such a transition results in a strong feedback between thermal and electrical power dissipated in the detector. With current bias, this “electrothermal” feedback is positive and can result in thermal runaway. With voltage bias, by contrast, the electrothermal feedback is negative and stabilizes the operating point of the device. Voltage-bias of a TES gives many of the traditional advantages of a system with strong negative feedback, including improved linearity and bandwidth, and immunity of the response to changes in the external parameters. Irwin first proposed the operation of a TES in the voltage-biased mode [53]. From here, we will only refer to the voltage-biased operation of a TES.

The strong negative electrothermal feedback keeps the total power P_{tot} dissipated in the TES constant at the value required to heat the TES to the superconducting critical temperature T_c . This total power can be written $P_o + P_{\text{bias}}$, where P_o is the optical power, $P_{\text{bias}} = V_b^2/R_{\text{TES}}$ is the bias power and V_b is the bias voltage across the TES. The electrothermal feedback varies the current to keep the total power constant when P_o changes. An increase in P_o increases R_{TES} and decreases the bias power P_{bias} . The change of the TES current I_{TES} divided by the change in photon power at angular frequency ω is called the current responsivity S_i . For a thermal circuit with a single thermal time constant (a single pole response),

$$S_i \equiv \frac{dI_{\text{TES}}}{dP_{\text{tot}}} = -\frac{1}{V_b} \frac{\mathcal{L}_{\text{TES}}}{\mathcal{L}_{\text{TES}} + 1} \frac{1}{(1 + i\omega\tau_{\text{eff}})} \quad (8.42)$$

where $\mathcal{L}_{\text{TES}} = \alpha_{\text{TES}} P_b/GT$ is the loop gain, $\alpha_{\text{TES}} = T dR_{\text{TES}}/R_{\text{TES}} dT$, $G = dP_{\text{tot}}/dT$ is the differential thermal conductance, and τ_{eff} is the effective time constant [54]. In the high loop gain limit, the low-frequency responsivity becomes $S_i = -1/V_b$. The responsivity depends only on the bias voltage and so is independent of both P_o and the heat sink temperature T_0 . A loop gain of ~ 100 is typical. The time constant set by the heat capacity C_h without feedback is $\tau_0 = C_h/G$. The effective time constant $\tau_{\text{eff}} = \tau_0/(1 + \mathcal{L}_{\text{TES}})$ is much shorter than τ_0 . In practice, the full reduction in τ_{eff} is rarely seen because most devices have complicated thermal circuits with multiple time constants. Delay in the transfer of heat from the absorber to the TES (an internal time constant) is not reduced by feedback.

The input noise of a TES can be described by the noise equivalent power (NEP), which can be written as a quadrature sum of contributions from the TES thermal fluctuation noise, the spectral density of the equivalent SQUID current noise i_n referred to the input of the amplifier and the TES Johnson noise:

$$NEP^2 = 4k_B T^2 G + (i_n + 4k_B T / R_{\text{TES}}) / S_i. \quad (8.43)$$

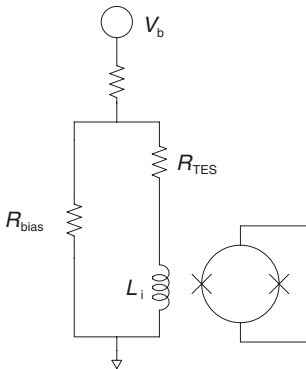


Fig. 8.16 A typical TES bias circuit. A voltage bias is achieved by current bias of the cold shunt resistor R_{bias} , which is much smaller than the resistance R_{TES} of the TES. The current through the TES is measured with a SQUID ammeter whose input coil is in series with the TES.

At frequencies below $\omega = 1/\tau_{\text{eff}}$ thermal fluctuation noise usually dominates and at higher frequencies Johnson noise usually dominates. Other noise sources, when present, are called excess noise.

As shown in Figure 8.16, the TES resistance R_{TES} is coupled to a SQUID via an input coil with impedance $\omega L_i < R_{\text{TES}}$. A cold, current-biased shunt resistor, R_{bias} , is used to provide voltage bias to the TES. The noise contribution from the bias network is negligible when R_{bias} is operated close to the detector temperature.

A SQUID with a current-coupling input coil is a natural readout device for a TES sensor. The operating impedance of a TES generally falls in the range of $1 \text{ m}\Omega$ to several ohms. The noise temperature of an appropriate SQUID is much smaller than the typical TES operating temperatures of $60\text{--}300 \text{ mK}$. There will therefore be a wide range of resistance where the SQUID noise will be less than that of the TES. This flexibility is important since stability of the detector places an additional constraint on the resistance of the TES. Electrothermal oscillations, where the electrothermal feedback becomes positive due to a phase shift caused by reactance in series with the TES, can occur unless $L_i/R_{\text{TES}} < \tau_{\text{eff}}$ [55, 56]. In some devices, it is necessary to add extra heat capacity, such as a gold film, to the TES, or to warm the detector somewhat to meet this condition. Furthermore, since the ratio of TES thermal noise to SQUID noise power itself is proportional to the ratio L_i/R_{TES} , there is a lower limit on the effective time-constant for which the TES noise can dominate the SQUID noise. Typically, this limit is $\sim 1 \mu\text{s}$ which is sufficient for many applications [55]. The time constant requirement can depend on the electronic feedback used to linearize the SQUID. Standard flux-locked loop feedback systems can reduce the effective input inductance, but strong coupling is required between the input and feedback coils. The special shunt feedback circuit described in Section 8.5.3.2 provides a virtual ground at the amplifier input [57]. Finally, the slew rate requirement on the SQUID readout system increases with decreasing detector time constant and can be the limiting factor in total system bandwidth.

Detectors that count photons or other particles often require a short response time to keep dead time to a minimum. In this case, the thermal conductance

across the TES must be sufficiently large that the internal thermalization time is as short as the required response time. This requirement is generally satisfied by a relatively small sensor resistance. There are several factors that bound R_{TES} on the low side in addition to the electrothermal stability criterion given above. First, any parasitic resistance in series with the TES must be much less than the resistance of the TES. Of course the wires and connections can be made fully superconducting, but this is sometimes inconvenient since, for example, it eliminates the possibility of using standard connectors. Second, some excess noise sources have been found to increase with decreasing resistance [58–61]. Finally, lower operating resistances may result in higher microphonic response from variations in wire self-inductance due to motion relative to local groundplanes. The TES resistance is bounded at the high end by the requirement that the TES noise dominates the SQUID noise for a given set of SQUID parameters. The TES performance characteristics specific to bolometers and calorimeters will be discussed in Sections 8.5.4 and 8.5.5.

8.5.3

SQUID Multiplexers

The size of a TES array can be limited by the practical difficulty of instrumenting each pixel with a SQUID readout. The heat load onto the cryogenic stages and complexity of the wiring are particularly serious limits. Readout multiplexing, where signals from multiple detectors are combined at low temperature and then separated again at ambient temperature, greatly eases the difficulty of reading out a large array. Several groups are developing SQUID readout multiplexers (MUX), with the goal of reducing the number of wires from a large TES array by two orders of magnitude. Two complementary methods are being pursued at present. The first multiplexes the signals in the time domain, where detectors are read out sequentially in time by one amplifier. The second multiplexes in the frequency domain, where detector signals are encoded by amplitude modulation of a set of ac carriers. Kivaranta *et al.* [62] have pointed out that these two multiplexing schemes can both be described by one fundamental process where each signal is multiplied by one of a set of orthogonal functions, the signals are added together, and then each signal is recovered by multiplication by the same function at the output. In this description, there are several possible choices of orthogonal functions including those of the Hadamard encoding scheme discussed by Karasik and McGrath [63]. Irwin [64] and Kivaranta *et al.* [62] have compared also time- and frequency-domain multiplexing.

8.5.3.1 Time-Domain Multiplexing

The time-domain approach has been developed by the cryoelectronics group at the National Institute for Science and Technology (NIST), Boulder [64–68]. The signals from a set of detectors are measured by sequentially selecting one TES at a time using SQUIDs as switches as described below. A schematic circuit diagram

of an early version is shown in Figure 8.17 and the overall system topology is shown in Figure 8.18. The SQUIDS in the column are connected in series and each SQUID has an input coil to read the flux from a single TES. The TESs are biased continuously, and the current from each TES is sampled periodically by using bias on the address line to turn “on” the appropriate SQUID switch. Bias current flows only through the active SQUID. The remainder of the SQUID switches are “off” since they are in the zero voltage state. The voltage across the entire line of SQUIDS is therefore equal to the voltage across the active SQUID alone.

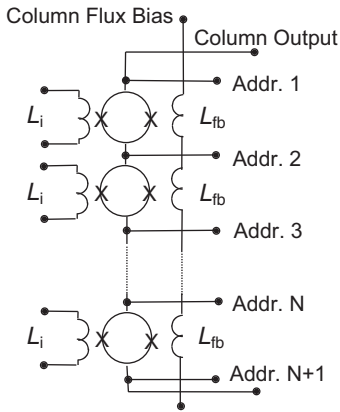


Fig. 8.17 Circuit schematic for an early version of NIST time-domain SQUID multiplexer, showing its basic functions. The TES detector is always biased and a bias resistor (both not shown) are connected to the terminals marked L_i . The column of SQUIDS is connected in series. (Reproduced with permission from ref. [65].)

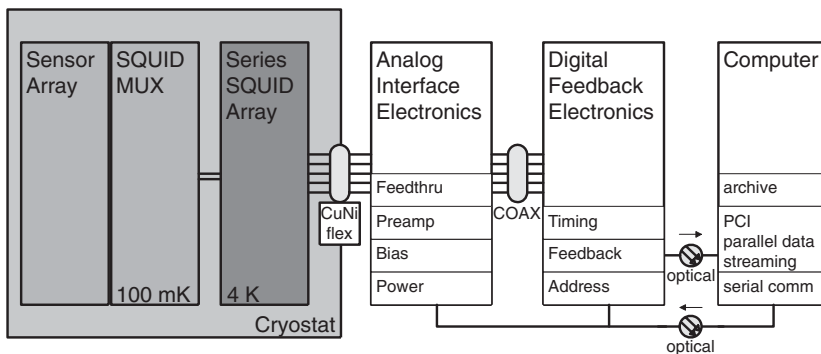


Fig. 8.18 Complete SQUID time-domain multiplexer system. The TES sensor array and the SQUID MUX chip operate at the detector temperature.

Flux feedback, with a feedback coil for each SQUID, is used to linearize the response of the SQUIDS. To reduce the number of wires required, all of the feedback coils are wired in series and only the current required for the active SQUID is applied. The instantaneous values of the time-varying feedback currents required for all the SQUIDS are stored in a digital circuit, as described by Reintsema *et al.* [68].

A large array of time-domain multiplexed sensors is organized into rows and columns; SQUIDS connected in series form a column as is shown in Figure 8.17.

The number of wires from low temperatures to 300 K required to instrument N_{row} SQUIDs in a column is $N_{\text{row}} + 5$ as shown in Figure 8.17 [65]. Two more wires are required per column to provide a common bias to the TESs as can be seen in Figure 8.19. The total number of wires for a TES array is reduced by using multiple rows and sharing address lines across the rows. For N_{col} columns and N_{row} rows, the number of wires required is then $4N_{\text{col}} + N_{\text{row}}$ (this number includes a reduction in wire number achieved by sharing ground wires as in Figure 8.19). For large N_{col} and N_{row} , this number represents a large reduction compared to an unmultiplexed system where the number of wires scales as $N_{\text{col}} \times N_{\text{row}}$. If the SQUIDs are placed on a separate wafer, the number of connections from the detector wafer is proportional to $N_{\text{col}} \times N_{\text{row}}$. These connections can be made using indium bump-bonds. In principle, the SQUID switches could be fabricated on the same wafer as the sensors. In this case, the number of connections from the detector and SQUID wafer to the next stage is reduced by multiplexing.

The sampling rate for each detector must be higher than the Nyquist frequency for the detector bandwidth $f = (2\pi\tau_{\text{eff}})^{-1}$. Some extra bandwidth may be desirable to ensure that the electrothermal stability criterion discussed earlier $L_i/R_{\text{TES}} < \tau_{\text{eff}}$

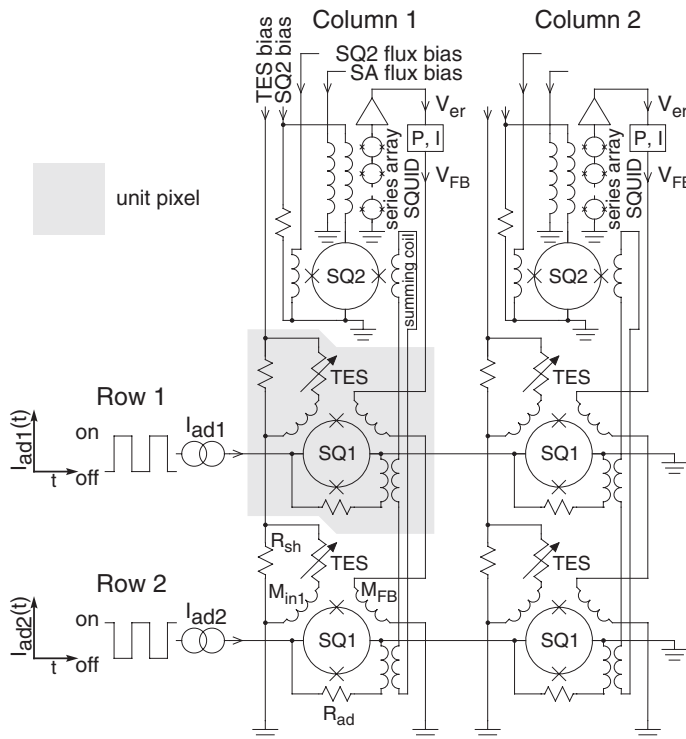


Fig. 8.19 Schematic for a two-dimensional time-domain multiplexer. Each column corresponds to one set of multiplexed sensors. Columns with up to 32 TESs have been tested. (Figure courtesy of Randy Doriese (NIST)).

is always met [56]. This extra bandwidth is achieved by decreasing the L_i/R_{TES} time constant and increasing the sampling rate by the same factor. The “clock” rate for switching from one SQUID to the next in a column is given by the single detector sampling rate times the number of SQUIDs in the column. Any noise from the detector at frequencies higher than the Nyquist frequency can be aliased back into the detector bandwidth and give excess noise. No additional filtering is required to avoid aliasing of the thermal fluctuation noise when the bandwidth is limited by the detector time constant. Johnson noise has no such bandwidth limit, so a low-pass filter is necessary to prevent excess Johnson noise. The input inductance of the SQUID and the TES resistance automatically form an L_i/R_{TES} low-pass filter, which can be close to the required value. If necessary, an additional inductor that is not coupled to the SQUID loop can be added in series with the input coil without changing the noise contribution from the SQUID.

Multiplexed operation with eight TES bolometers has been demonstrated including observation of the sky at submillimeter wavelengths with the Fabry–Perot Interferometer Bolometer Research Experiment (FIBRE) instrument at the Caltech Submillimeter Observatory. Sample output using mock signals is shown in Figure 8.20. A second-generation configuration is being developed with 32-channel multiplexing that is appropriate for science projects such as the Submillimetre Common-User Bolometer Array-2 (SCUBA-2) submillimeter camera and the Constellation-X X-ray satellite [67, 68]. Figure 8.19 shows a schematic circuit diagram for the 32-channel multiplexer.

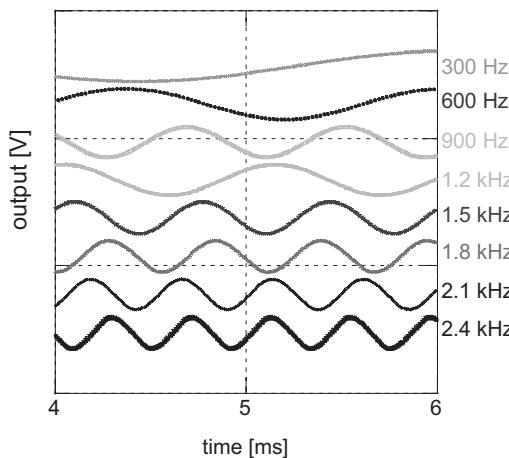


Fig. 8.20 Output of an eight-channel time-domain multiplexer resulting from injecting different sinusoidal signals into each input.

The power dissipated by the multiplexer at the detector temperature arises from the SQUID switches and the address circuits. The first-stage SQUID switch dissipation is very low, since only one SQUID is biased “on” per row. In early designs, the resistors in the address lines dominated the power dissipated at the detector

temperature [65, 66]. In contemporary designs, however, the address circuit power is comparable to the SQUID dissipation [67, 68]. The power dissipation of the address circuits has been reduced in this generation by changing from a current bias of the SQUID to a bias intermediate between constant current and constant voltage. The total dissipation is ~ 4 nW per column, so that a 32×32 array would dissipate 128 nW. For most applications this power dissipation is negligible, but it could be significant for a long-term space mission with very large arrays.

This change in the address circuit reduces the gain of the first stage, and therefore a transformer-coupled second-stage SQUID has been implemented. All SQUID switches in one column are coupled by one transformer to a single second-stage SQUID. Both the first- and second-stage SQUIDs are operated at the detector temperature. A series array SQUID operated at ~ 4 K reads the signal from the second-stage SQUID and is used to drive the cable that runs to ambient temperature. A photograph of a second-generation 32-channel MUX chip is shown in Figure 8.21.

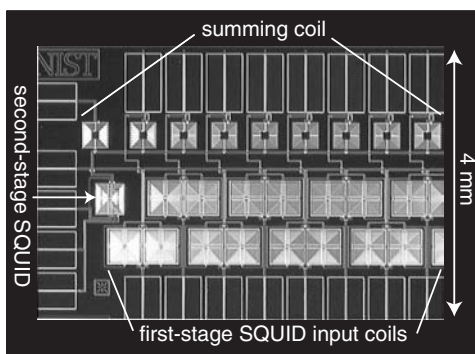


Fig. 8.21 Photograph of a 32-channel time-domain multiplexer chip. The circuit topology is shown in Figure 8.17. The first-stage SQUIDs are coupled to the second-stage SQUID via a single transformer loop labeled the “summing coil” in the photograph.

The present system samples at 6 MHz and has a total bandwidth of 3 MHz. This sampling rate is adequate for bolometric arrays, but an improvement by a factor of 4 is required for Constellation-X calorimeters with $\tau_{\text{eff}} \sim 100$ μ s [67]. The ultimate performance is limited by the slew rate and dynamic range of the SQUID readout.

8.5.3.2 Frequency-Domain Multiplexing

Frequency-domain multiplexing has been developed by several groups [57, 69–75]. Each TES in a multiplexed set is biased with an oscillating current with a unique frequency. When the sensor absorbs signal power, its resistance changes and modulates the signal current. This amplitude modulation transfers the signal spectrum to sidebands above and below the bias frequency. The output currents from the set of TESs are summed and amplified by a SQUID. Since each sensor

is operated at a different bias frequency, the currents from different sensors are uniquely distributed in frequency and can be combined in a common readout line. The signals from the individual sensors are recovered by a bank of frequency-selective demodulators in the ambient electronics.

Two topologies have been explored which can be termed “current summing” and “voltage summing.” A schematic circuit diagram of the two multiplexing circuits is shown in Figure 8.22. Early work focused on the voltage-summing scheme as shown in Figure 8.22(a) [69, 70]. Here, the sensors are coupled to the summing loop by transformers, with their secondaries connected in series and fed to an output amplifier. To maintain constant voltage bias, the impedance presented by the transformer primary must be much smaller than the sensor resistance. In the current-summing scheme as shown in Figure 8.22(b), the individual sensor circuits are added at a current-summing node at the input of the readout amplifier. To maintain constant voltage on the sensor, the input impedance of the amplifier must be much smaller than the sensor resistance. The low input impedance of the SQUID makes it appropriate for detecting the signal currents from the sensors.

The voltage- and current-summing schemes are fully equivalent with respect to electronic noise, dynamic range and all other performance parameters. The choice between the two is determined by practical considerations. The current-summing scheme is used by most groups now. It does not require the transformers required for voltage summing, and therefore it is easier to implement. Unless specified, all discussions below describe the current-summing scheme.

As with the time-domain multiplexer, filters are required to avoid an increase in noise caused by the accumulation of Johnson noise from adjacent detectors. An inductive-capacitive (L_fC_f) resonant filter is added in series with the TES. This filter suppresses noise current outside the resonant bandpass. It also reduces the

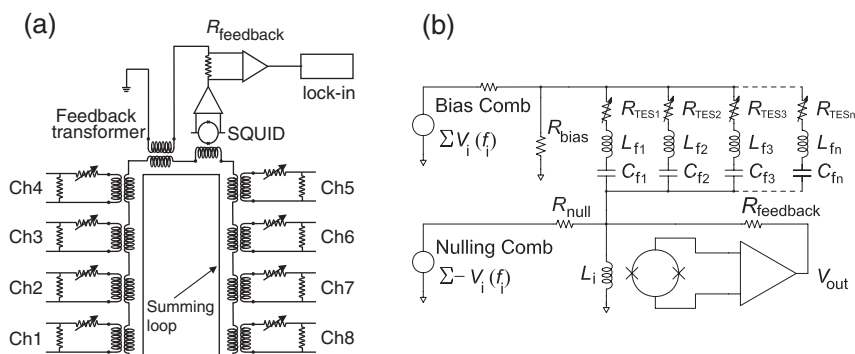


Fig. 8.22 Schematics of voltage-summing and current-summing frequency-domain multiplexer circuits. In both circuits, TESs (represented as variable resistors) are sinusoidally biased, each with a unique frequency. In the voltage-summing circuit (a), the sensor

current is transformer coupled to a “summing loop” where the voltages from all the secondary coils are added together. In the current-summing circuit (b), the currents from all multiplexed TESs are added together at the input inductor of the SQUID amplifier.

dominant source of crosstalk between channels since each TES is essentially biased by only the relevant frequency.

The number of channels which can be multiplexed is maximized by choosing the same bandwidth for each channel. The full-width bandwidth b_{LC} must be a factor of two larger than $f_{\max} = 1/2\pi\tau_{\text{eff}}$ to ensure both constant voltage bias and electrothermal stability [56, 71]. (The factor of two comes from the fact that there are two sidebands, one above and one below the carrier.) As with the time-domain multiplexer, some additional bandwidth may be desirable to ensure electro-thermal stability. Constant bandwidth implies that the circuit Q is proportional to frequency, which is automatically fulfilled if L_f is kept constant. The spacing between individual frequency “bins” is determined by the required neighbor-channel attenuation.

The circuit parameters are interrelated and determined in the following sequence [71]:

1. The maximum Q is determined by the maximum frequency f_{\max} and the required bandwidth b_{LC} , $Q = f_{\max}/b_{LC}$. A lower Q can be chosen at the expense of channel density.
2. The inductance is set by the adopted Q and the total resistance $R_{\text{tot}} \sim R_{\text{TES}}$ in the circuit: $L_f = R_{\text{tot}}Q/2\pi f_{\max}$.
3. The frequency spacing Δf is determined by the allowable cross-talk. All neighbors m will couple into a given channel n , so the ratio of cross-talk signal to primary signal is $I_{c,n}/I_n = \sum_{m \neq n} (I_m/I_n)$ and the ratio of total accumulated noise to intrinsic TES noise is $(N_c/N_r)_n = \sqrt{\sum_{m \neq n} (I_m/I_n)^2}$.
4. The minimum frequency $f_{\min} = 1/2\pi\sqrt{LC_{\max}}$ is given by the thermal time constant of the sensor and by the maximum practical capacitance together with the inductance calculated in step 2.
5. The number of channels that can be multiplexed is then $(f_{\max} - f_{\min})/\Delta f$.

Microphonic response due to wire vibrations has been a serious problem for bolometer and calorimeter arrays using high-impedance semiconducting sensors. Systems using TESs are much better in this regard due to the low impedance of the TES. Frequency-domain multiplexing, in particular, gives high immunity to microphonic response due to the combination of the narrow-band filters and the fact that the bias frequencies are much higher than those of mechanical resonances. Only currents generated very near the bias frequency can inject heat into the TES or be measured by the SQUID.

An L_fC_f filter chip with photolithographed inductors and capacitors has been implemented for the frequency range 380 kHz to 1 MHz [71], as shown in Figure 8.23. The set of eight filters is fabricated on a 10 mm × 20 mm chip. Higher frequency operation would lead to smaller areas. Four different configurations of

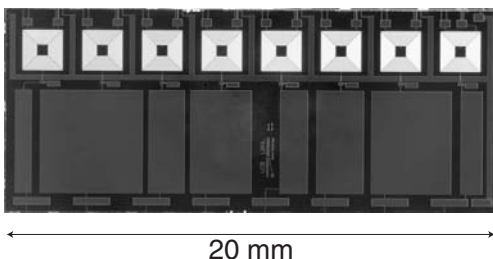


Fig. 8.23 Photograph of niobium L,C_f filter chip fabricated by TRW (now Northrop–Grumman). The eight inductors at the top are spiral wound and fabricated on a split washer, similar to those used for SQUIDs, to reduce coupling between inductors. The capacitors

use a sandwich of anodized 50-nm thick Nb_2O_5 oxide and 50-nm thick silicon dioxide giving a specific capacitance of 0.8 nF mm^{-2} . The loss tangent of these capacitors is < 0.001 , which is adequate for the multiplexer circuit.

filter chip have been fabricated which can be combined to build a 32-channel multiplexer.

The SQUID readout system must have a high dynamic range for frequency multiplexing, since the ratio of the bias carrier amplitude to the TES noise is typically 10^6 . The combination of this large dynamic range and the large required bandwidth pushes the performance of the SQUID readout system and gives the primary limitation on the total number of TESs that can be multiplexed. However, since all the time-varying signals are contained in the sidebands of the carrier, it is possible to null the carrier itself without any loss of data except for the static resistance of the TES, which is encoded at the carrier frequency. The static resistance can be recovered by measuring the required nulling current. Carrier nulling can be accomplished by adding a sinusoidal current at the input of the SQUID with the same amplitude as the carrier but of opposite phase. The amplitude can be simply adjusted with a feedback system at frequencies below those characteristic of the signals from the observations. In principle, nulling at frequencies up to the TES time constant is also possible. Carrier nulling can reduce the dynamic range requirements of the SQUID readout system dramatically. It also reduces the importance of spurious signals produced by the SQUID amplifier at combination frequencies. This intermodulation distortion can give increased crosstalk and noise if the intermodulation products appear near the frequency of another carrier. Carrier nulling can reduce or eliminate the need to widen the carrier spacing to avoid the effects of this type of distortion.

It is natural to use shunt feedback, which nulls the current through the input inductor, to produce a virtual ground at the SQUID input as shown in Figure 8.22(b) [57]. This configuration reduces the effective impedance of the input inductor and reduces crosstalk. As discussed in the previous paragraph, the main challenge for the SQUID readout system is the difficult combination of relatively high frequencies and the large dynamic range between the level of the carrier and the noise level. A controller with a high gain–bandwidth product is required to

keep the SQUID in the linear regime. One possible implementation is shown in Figure 8.22(b). This configuration uses a series array SQUID which eliminates the need for a coupling transformer and gives a wide bandwidth [24]. This controller uses a single operational amplifier with low noise and high gain-bandwidth product, which introduces only a single pole. In this configuration, the wires from the SQUID to the controller have to be short enough that the transit time permits stable feedback. The wire length in the current Berkeley (University of California and Lawrence Berkeley National Laboratory (LBNL)) system is 0.2 m. Linear operation with a peak-to-peak flux of $4\Phi_0$ has been measured at 1 MHz, corresponding to a slew rate of $10^7 \Phi_0 s^{-1}$. With this slew rate, 32 TES sensors with 100- μ s time constants can be multiplexed assuming the carriers are nulled within 10% of their original amplitude. Cold feedback electronics for the SQUID could reduce this wire length and thus increase the bandwidth and the number of multiplexed detectors.

In the simplest scheme, shown in Figure 8.22(b), four wires to room temperature are used to instrument a single SQUID or SQUID array. For convenience when discussing large two-dimensional arrays, we use the word column to describe the set of TESs that are multiplexed together. Since the $L_f C_f$ filters select only one bias frequency, two wires can provide bias to an entire column of N_{row} TESs. Two wires are required for carrier nulling. The total number of wires exiting the cryostat is $8N_{\text{col}}$ for N_{col} columns. In this scheme, the columns have no common connections, so the total number of wires for an $N_{\text{col}} \times N_{\text{row}}$ array is simply $8N_{\text{col}}$. Obviously, the minimum number of wires comes from maximizing N_{row} , which is constrained by the performance of the SQUID readout as discussed above. One advantage of this scheme compared with time-domain multiplexing is that each detector can have a different bias amplitude with only two bias wires per column.

The number of connections from the TESs to the summing nodes for a $N_{\text{col}} \times N_{\text{row}}$ array is $2N_{\text{col}} \times N_{\text{row}}$ but this number is reduced to $2N_{\text{col}}$ between the summing coil and the SQUIDs. It is plausible that the filters could be integrated into the detector wafer. If so, the number of connections to the wafer and subsequent stages would be greatly reduced. It is practical to have all SQUIDs on a temperature stage near 4 K and to have virtually no multiplexer power dissipation at the lower detector temperature.

Bias generators with the same frequency can be shared, but this requires the dispersion of the central frequencies of the resonators to be <1%. It is not prohibitive to use individual bias generators for each TES, since direct-digital synthesis (DDS) generators are low in cost and have adequate stability. If analog synchronous demodulation is used, one detection circuit is required for each TES. This can be done with a single inexpensive integrated circuit. In the future, digitization of the multiplexed signal would allow an entire column or more to be read with a single circuit with all the demodulations performed simultaneously in the digital domain.

Multiplexing of two TES microcalorimeters with no loss in energy resolution has been achieved using the voltage-summing approach [70]. A resolution of 60 eV was observed in the multiplexed mode, which is identical to the value observed with individual readouts. The detector time constant was ~ 1 ms, and the bias frequencies were 124 and 154 kHz. More recently, the preferred current-summing approach has been demonstrated with an eight-channel system [72]. Data from seven TES bolometers and one resistor (mock bolometer) show $< 0.3\%$ crosstalk between nearest neighbors as shown in Figure 8.24. The measured noise of the multiplexed detectors is equal to the expected detector noise.

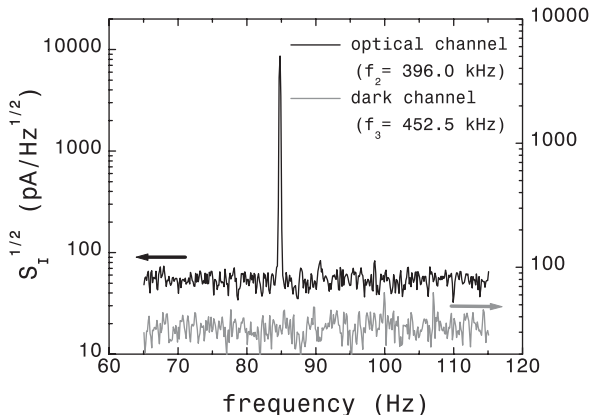


Fig. 8.24 Crosstalk data from two of seven frequency-multiplexed bolometers. Eight channels in total are multiplexed including one resistor (mock bolometer). One of the seven TES bolometers is modulated optically at 84 Hz (indicated) using a cold LED. The other bolometers show no measurable crosstalk, giving an upper limit of 0.3%. (Reproduced with permission from ref. [72].)

Finally, a new type of SQUID frequency-domain multiplexer is being developed with the goal of greatly increasing the combination of detector bandwidth and number of multiplexed detectors compared to current technology [76]. In the new concept, each TES is biased with a static voltage and instrumented with a SQUID. The output of the SQUID for each multiplexed detector is used to load a resonant circuit operated at microwave frequencies (with a different frequency for each TES), and the Q of all the resonant circuits for the set are continuously measured using a single high-electron-mobility transistor (HEMT) amplifier. As the signal varies on a TES, the impedance seen at the output of its SQUID and therefore the Q of its resonant circuit varies. Multiplexing of two TESs has been demonstrated thus far, and the expected number of multiplexed detectors is in the range 10^2 – 10^3 [76].

8.5.4

TES Bolometers

The most demanding application for bolometers is astrophysical observation at far-infrared to millimeter wavelengths, where the early universe radiates very strongly. For example, the strongest signal reaching us from the earliest galaxies is starlight which has been absorbed by galactic dust and re-radiated in the far-infrared [77, 78]. The cosmic microwave background (CMB) is the remnant black-body radiation left over from the Big Bang. It has cooled as the universe has expanded for 14 billion years, and it now has a temperature of 2.7 K. The peak of the CMB frequency spectrum is at about 150 GHz, and it dominates the electromagnetic energy in the universe. The spatial variation of the CMB on the sky provides a snapshot of the early universe 400,000 years after the Big Bang. Measurements of these spatial fluctuations in the CMB radiation have shown that the geometry of the universe is Euclidean (space is flat), have provided the most accurate values for several important cosmological parameters and have provided very strong support for an inflation-driven cosmological model dominated by dark energy and containing substantial dark matter [79–85]. Inflation is a model where the universe expands exponentially for a short period at the very first instant after the Big Bang; it naturally explains many properties of the observed universe including its spatial flatness. Future measurements of the polarization of the CMB may help discriminate between competing models of inflation. For some models, inflation occurs at the energy scale for Grand Unification ($\sim 10^{16}$ GeV where the electromagnetic, strong, and weak forces are unified), and therefore CMB polarization measurements could provide a glimpse into an unexplored energy scale. [86]. Finally, surveys of clusters of galaxies via their scattering of the CMB (the Sunyaev–Zel'dovich effect) promise to test models of structure formation and characterize the expansion history of the universe [87].

Bolometers are the most sensitive detectors for astronomical photometry and low-resolution spectroscopy from ~ 200 μm to ~ 3 mm wavelength. This range of wavelengths lies between the millimeter-wave technology of monolithic microwave integrated circuit (MMIC) amplifiers and the infrared technology of close-packed arrays of photon detectors [88, 89]. The scientific goals mentioned above will require ground-based observations and space missions with arrays of 10^3 – 10^5 pixels. Current astronomical bolometers use thermistors of heavily doped Si or Ge with junction field-effect transistor (JFET) amplifiers. Arrays of several hundred pixels are in use with one amplifier per pixel. Issues associated with amplifier operating temperature, power dissipation and noise margin make it difficult to extend the conventional technology to much larger arrays. The development of TES bolometers is being driven by the requirements for these future astronomical measurements. They offer a number of important practical advantages compared with conventional technology. The large negative electrothermal feedback improves the linearity, stability and speed. Fabrication is entirely by thin-film deposition and optical lithography. The SQUID amplifiers have low power dissipation, have large noise margin and operate at or near the bolometer temperature.

The low impedance of a TES and the simplification of cryogenic layout reduce microphonic noise. Finally, the SQUID output multiplexers described above can be used to simplify the readout electronics greatly.

8.5.4.1 TES Bolometer Designs

Some of the most successful conventional submillimeter- and millimeter-wave bolometer systems use an array of close-packed conical horn antennas in the focal plane. Horn antennas restrict the solid angle seen by the bolometer, which is important at millimeter wavelengths where a 4 K cryostat can be as bright as the astronomical source. Scalar horn antennas have very low sidelobes which translates to low sidelobe response for the entire telescope. The bolometers, which are located at the small ends of the horns, are separated sufficiently for easy support and wiring. The TES spiderweb bolometer structures shown in Figure 8.25 (right), which have radial support legs, are appropriate for horn-antenna coupled systems. The spiderweb absorber geometry was originated by Bock *et al.* [90], and early versions of the TES spider-web bolometer have been reported by Gildemeister *et al.* [91]. The absorbing element is a mesh of 1- μm thick low-stress silicon nitride several wavelengths across, which is metallized with gold to produce an average sheet resistance of 377Ω per square. The silicon is etched away from the front side to a depth of $\sim 20 \mu\text{m}$ to release the silicon nitride membrane. A conducting backshort is located on the back of the silicon substrate at an optical distance of one quarter wavelength behind the mesh (including the retardation in the silicon substrate). The mesh absorber is designed for low heat capacity and low cosmic ray cross-section. The thermistor located near the edge of the mesh is made from a superconducting proximity-effect sandwich of Al and Ti with $T_c \sim 400 \text{ mK}$. This transition temperature is appropriate for bolometers operated using ^3He sorption refrigerators, which produce heat sink temperatures of $\sim 270 \text{ mK}$. Fully superconducting leads are used from the thermistor to the edge of the array. Arrays of 300 to

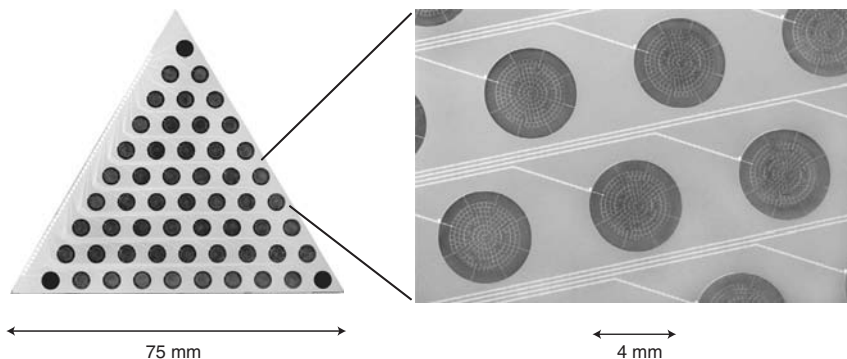


Fig. 8.25 Array of 55 TES spiderweb bolometers (left) and close up of bolometers (right). Six identical wedges of the type shown are assembled to form a 330-element hexagonal close-packed array. The bolometers are 4 mm in diameter with leg lengths of 0.5 mm.

1000 TES spider-web bolometers are being fabricated for ground-based surveys of galaxy clusters using the Sunyaev–Zel'dovich effect.

Interest is developing in the use of planar antennas lithographed on the silicon substrate to couple bolometers to telescopes. The use of planar antennas in conjunction with lithographed band-defining filters and rf-multiplexing networks opens the possibility of a fully lithographed array with multiple frequency bands and polarizations for each pixel. This approach is very promising for CMB polarization measurements. Figure 8.26 shows TES bolometers coupled by dual-polarization double-slot dipole antennas in a Nb ground plane [92–94]. Antennas of this type couple to the telescope optics by way of extended hemispherical Si lenses. Another technique is to use a “phased-array” antenna where the outputs of many small antennas are combined with the proper phases to produce a narrower antenna pattern which can couple directly to the telescope optics as shown in Figure 8.27 [95]. In the bolometers shown in Figures 8.26 and 8.27, Nb microstrip lines couple the signals from the antenna to a set of microstrip filters, which are used to define the measured frequency band, and then to a small resistive termination which forms the absorbing element of a leg-isolated TES bolometer. Much of the technology for the superconducting antennas, microstrips and filters used for these bolometers has been previously developed for SIS heterodyne mixers at submillimeter and millimeter wavelengths and for picosecond Josephson digital logic.

Close-packed arrays of bolometers are used at submillimeter and far-infrared frequencies where radiation from the cryostat is not such a serious problem [96–98]. For a given field of view, these arrays can have a somewhat higher sensitivity than horn or planar antenna coupled bolometers and fully sample (two pixels per FWHM beamsize) the sky at the cost of a much larger number of detectors. A

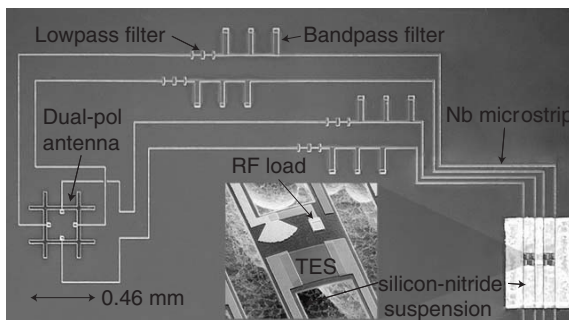


Fig. 8.26 Photograph of planar-antenna-coupled bolometer chip. A dual-polarization antenna is on the left. Each double-slot dipole antenna coherently adds the signal from two slot dipoles to form a relatively symmetric antenna pattern. The slots in this chip are lithographed in a superconducting Nb groundplane. The antennas have a resonant response centered at 220 GHz. Microstrip

transmission lines and distributed transmission line filters are used. The design bandpass is centered at 220 GHz with a 30% bandwidth. The transmission lines terminate in the matched loads on the leg-isolated TES bolometers at the lower right. The inset shows the middle of the silicon nitride bridge with a TES, a microwave load resistor and a microwave tuning stub.

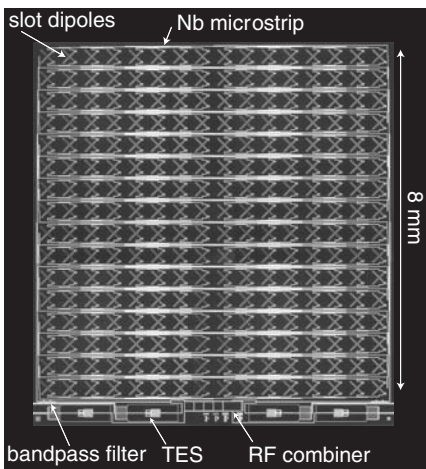


Fig. 8.27 Photograph of JPL/CIT antenna-coupled bolometer prototype. The dual-polarization antenna is a phased array of slot dipoles. The slot dipoles are an array of crosses, and the two dipoles in each cross give the two orthogonal polarizations. The $8\text{ mm} \times 8\text{ mm}$ phased-array antenna has a large effective area giving a highly directional

antenna pattern without using the traditional substrate-mounted lens to couple to the telescope beam. The two polarizations are split into two differential Stokes parameters using a microwave combiner (hybrid) circuit. Two silicon nitride suspended bolometers each are used for Stokes parameters Q and U . (Figure courtesy of Jamie Bock (JPL/CIT).)

bolometer structure is shown in Figure 8.28 (left) which can support a close-packed array of 1024 TES mesh bolometers. The mesh is supported by beams of silicon nitride. The leads reach the edges of the array along narrow dividing strips between the pixels. A single pixel shown in Figure 8.28 (right) has been successfully tested [96]. A prototype for a 1600-element far-infrared array for the SCUBA-2

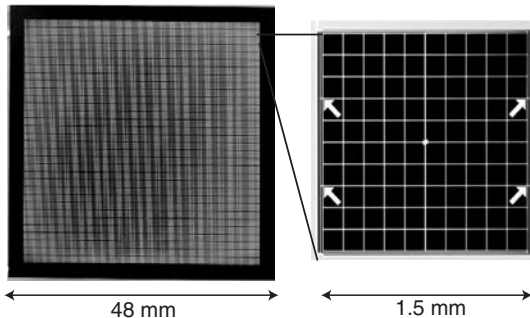


Fig. 8.28 Photographs of filled-array prototype. A single TES bolometer pixel with TES sensor and metallized mesh is shown at right. The single pixel fills a square area of $1.5\text{ mm} \times 1.5\text{ mm}$. It consists of a rigid square grid (light lines) of 11×11 beams, each $7\text{-}\mu\text{m}$ wide and metallized for optical

absorption. The grid is suspended at four points (arrows) by $7\text{-}\mu\text{m}$ wide free-standing tensioned silicon nitride beams which run along the left and right sides. A 1024-element array of membrane structures with no sensors or metallization is shown to the left.

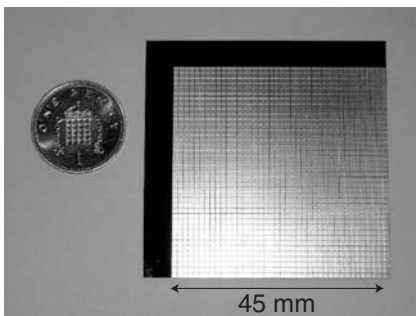


Fig. 8.29 Photograph of bolometer test structures for the SCUBA-2 array. The free-standing membranes are $100\text{ }\mu\text{m}$ wide.

instrument is shown in Figure 8.29 [98]. This array uses continuous absorber films rather than a mesh. A second wafer, which contains the wiring and the back-short, is attached using In bump-bonds.

8.5.4.2 Bolometer Performance

The noise in a bolometric measurement increases with the total absorbed radiant power, $P_o = P_s + P_b$, which is sum of the signal power P_s and any background power P_b from other sources such as the cryostat, the optics, and the atmosphere. Cold baffles and filters are used to minimize P_b . The fluctuations (photon noise) from P_o set a lower limit to the noise. If the SQUID noise is negligible, then the TES noise given in Eq. (8.43) depends on the operating temperature. Bolometers are optimized to minimize all these sources of additional noise. Ideally they are reduced to less than the photon noise as long as the required base temperature T_0 can be practically achieved. The TES thermistor is chosen to have T_c between $1.5T_0$ and $2T_0$. The exact value depends on the temperature dependence of G . Below the optimum value, the thermal conductance G in the thermal noise term in Eq. (8.43) is too large. Above this optimum, the temperature in the same term is too large. The thermal conductance G is chosen so that the bolometer temperature will rise to close to T_c with the largest anticipated photon power $P_o = P_{\max}$. Higher power will cause the bolometer to saturate.

As mentioned above, the noise in bolometer systems is usually specified by a noise equivalent power referred to the bolometer input. Bolometers for ground based observations typically have noise levels in the range $\text{NEP} \sim 10^{-17}\text{--}10^{-16}\text{ W Hz}^{-1/2}$, which can be achieved with a heat sink temperature of $\sim 0.3\text{ K}$. The most stringent requirements are for bolometers operated on cooled orbiting telescopes viewing dark regions of the sky. For photometry with 30% bandwidths, an intrinsic bolometer $\text{NEP} \sim 10^{-18}\text{ W Hz}^{-1/2}$ is required, which can be achieved with a heat sink temperature of $\sim 0.1\text{ K}$. For spectroscopy with bandwidths of 0.1%, an $\text{NEP} \sim 10^{-20}\text{ W Hz}^{-1/2}$ is required, which is not commonly achieved with silicon nitride suspensions. The required ultralow thermal conductance can be achieved with a hot-electron TES bolometer [99, 100]. A small-area TES is deposited directly on the Si substrate without any legs for thermal isolation. At temperatures $\leq 0.1\text{ K}$,

the weakness of the electron-phonon interaction impedes the flow of heat from the metal into the dielectric substrate and can provide suitably low values of thermal conductance G . Hot-electron bolometers are well suited for antenna coupling, since a transmission line can terminate directly into the small-area TES.

8.5.5

TES Calorimeters and Nonequilibrium Detectors

Calorimetry is important for counting photons and measuring their energy, from optical to gamma-ray frequencies. There are applications both to astrophysics and laboratory spectroscopy [101]. Within astrophysics, X-ray astronomy has driven much of the development of high-resolution calorimeters [102]. X-ray observations play a fundamental role in the study of hot and energetic objects such as the coronae of stars, gas in galaxies and clusters of galaxies, supernovae, gamma-ray bursts and accretion disks around black holes and neutron stars. Temperatures of 10^6 to 10^8 K correspond to 0.1 to 10 keV. Microcalorimeters achieve sufficiently high spectral resolution ($100 < \Delta\lambda/\lambda < 10,000$) that atomic lines can be resolved. Flux measurements of these lines give chemical abundances and spectral Doppler shifts give velocities.

Calorimeters are also being developed for optical to ultraviolet astronomy [103]. These calorimeters can be built in arrays that promise simultaneous imaging, low-resolution spectroscopy and timing. A 24-element array of tungsten TESs for UV-optical wavelengths is shown in Figure 8.30. A resolution of 0.15 eV at an energy of 3 eV has been achieved with $T_c = 90$ mK. Count rates of 30 kHz and photon timing of 300 ns have been achieved. The quantum efficiency of the bare tungsten pixels is 50%.

Calorimeters are also used in searches for weakly interacting massive particles (WIMPs) which are candidates for the dark matter which makes up ~25% of the mass-energy of the universe. Detectors for WIMP dark matter as shown in Figure 8.31 have been developed that sense the athermal phonon flux produced in a

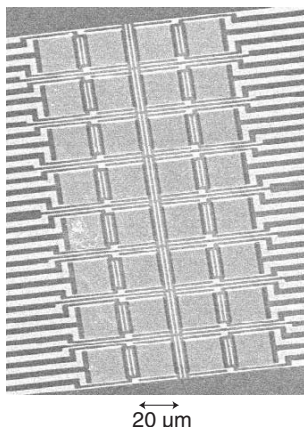


Fig. 8.30 Photograph of a 24-element array of tungsten TESs for UV-optical wavelengths.

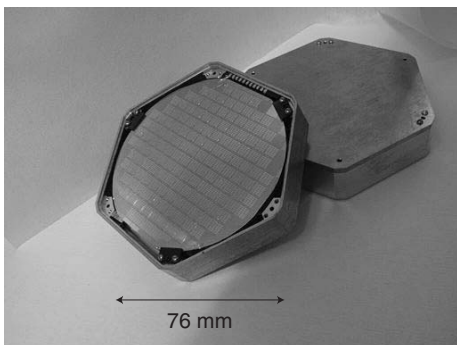


Fig. 8.31 Photograph of a TES-based direct dark matter detector.
The substrate is 10-mm thick Si.

semiconductor target by the scattering of WIMPs from nuclei [104, 105]. The detector substrate shown is 1-cm thick Si. Nuclear recoils in the substrate produce phonons, which in turn break Cooper pairs in superconducting Al phonon absorbers on the surface. The resulting quasiparticles are trapped in a tungsten TES giving signals proportional to the energy deposition. Nuclear and electron recoils are discriminated by comparing the phonon signal to the ionization signal detected by ionization electrodes on the surface.

In the laboratory, X-ray calorimeters are valuable for materials analysis given their ability to measure high-resolution atomic spectra [106]. Finally, calorimeters have been used to distinguish between singly and doubly charged fragments of DNA in time-of-flight mass spectroscopy [107].

8.5.5.1 Calorimeter Designs

The design of an X-ray calorimeter has several conflicting requirements. There must be an absorber with sufficient stopping power to absorb the energy of the X-ray photon. There must be a weak thermal link to the heat sink to allow them to thermalize the photon energy. The time constant of the calorimeter has to be short to avoid overlapping of pulses. For imaging arrays, the filling factor of the array should be high. The requirement for a fast response conflicts with the need for enough material to stop the X-ray photon and a sufficiently weak link to thermalize the absorbed energy. Calorimeter design, therefore, requires a high level of optimization.

The weak link in X-ray calorimeters is typically implemented using a thin membrane of silicon nitride. The absorber and TES sensor must be well coupled thermally on an island in the silicon nitride. The absorber is usually made from a non-superconducting metal such as Bi which has low heat capacity, Cu which has high thermal conductivity or a combination of Bi and Cu. The TES itself can be used as the absorber, but this does not allow the highest possible filling factor.

An array of TES microcalorimeters fabricated at NIST is shown in Figure 8.32. The TES, which acts as the absorber, covers the entire suspended membrane. Microcalorimeters with similar construction have a reported resolution of 4.5 eV FWHM for 6 keV X-rays [59, 108]. A more recent result gives 2.4 eV resolution at 6 keV with a TES calorimeter [109]. An array with a high filling factor can be achieved using “mushroom” shaped absorbers as in the array shown in Figure 8.33 [110]. The absorber can overhang the suspension without thermally shorting it.

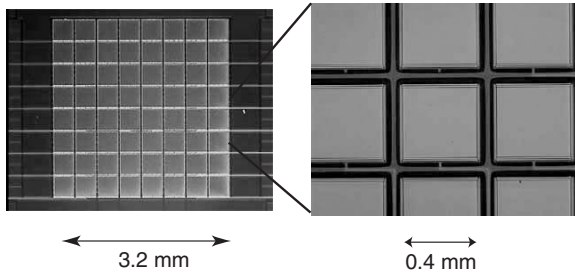


Fig. 8.32 Photographs of an 8×8 array of TES microcalorimeters for X-ray observations fabricated at NIST Boulder. The entire array is shown at left and a close-up view is shown on the right. Each pixel is $400 \mu\text{m}$ on a side. The TESs are Mo/Cu proximity effect sandwiches.

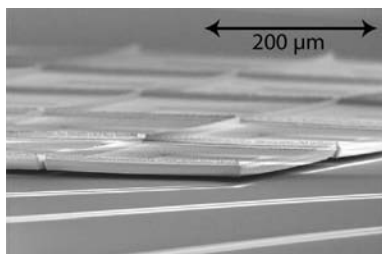


Fig. 8.33 Angled scanning electron micrograph of 5×5 array of TES microcalorimeters with “mushroom absorbers” made at NASA Goddard Space Flight Center. The pixels are 0.25 mm squares. These Bi/Cu absorbers contact the Mo/Au TES in the center, but overhang the nitride membrane weak link and

the solid substrate and electrical contacts between pixels. The absorbers are 4 layers of Bi and 4 layers of Cu alternated. Each Cu layer is $0.2 \mu\text{m}$ thick. Each Bi layer is 2.25 or $2.0 \mu\text{m}$, for a total of $8.5 \mu\text{m}$ of Bi. (Figure courtesy of Caroline Kilbourne (Goddard Space Flight Center, NASA).)

8.5.5.2 Calorimeter Noise Performance

The energy resolution for a calorimeter with a thermometer using a temperature-dependent resistance can be written

$$\Delta E_{\text{FWHM}} = 2.35 \sqrt{k_B T^2 C_h \sqrt{8n_g} / a_{\text{TES}}} \quad (8.44)$$

where C_h is the heat capacity of the device, $n_g = d \log P_{\text{bias}} / d \log T$ is the logarithmic derivative of the bias power with respect to the detector temperature, and $a_{\text{TES}} =$

$TdR_{\text{TES}}/R_{\text{TES}}dT$ as previously defined [111]. Since this resolution is proportional to $a_{\text{TES}}^{-1/2}$, TES calorimeters with a_{TES} as large as 10^3 have a potential advantage over calorimeters with semiconductor thermistors. This advantage is partly offset by the need to avoid saturation of the detector. Although the pulse area remains proportional to the deposited energy in a saturated TES calorimeter, pulses can become unacceptably long. TES calorimeters therefore need to be optimized for a maximum X-ray energy E_{max} and have constant resolution for all energies below the selected E_{max} . The main benefit of the high a_{TES} of a TES is that higher heat capacity materials can be used to absorb the X-rays.

Excess noise has been reported with TES calorimeters, which is not yet fully understood [58–61]. It appears that there is more than one mechanism since different devices give noise that depends differently on bias, geometry *etc.* For many, but not all, devices, the excess noise increases with increased a_{TES} [61]. Although the mechanisms are not fully understood, advances have been made by several groups. If this excess noise can be eliminated, the resolution of TES calorimeters can be improved by a factor 2–3, which would be a dramatic improvement.

8.5.6

SQUID Readout of Non-TES Detectors

In this section we summarize non-TES radiation sensing detectors that can be read out using a SQUID.

8.5.6.1 Magnetic Calorimeter

The magnetic calorimeter uses the temperature-dependent magnetization of a paramagnetic material in a small applied magnetic field as a thermometer [112]. The magnetization is monitored by a dc SQUID. The thermometer is made with a metallic host doped with a dilute concentration of paramagnetic ions, such as gold doped with a few hundred ppm of erbium. The flux signal can be written

$$\frac{d\Phi}{dT} = G_1(r_t, h_t, R_s) \frac{1}{R_s} \mu_0 V_t \frac{\partial M_t}{\partial T} \quad (8.45)$$

where Φ is the magnetic flux, G_1 is a dimensionless prefactor that depends on the radius r_t and height h_t of the thermometer, R_s is the radius of the sensor loop, V_t is the volume of the thermometer and M_t is the magnetization. One application of magnetic calorimeters is soft x-ray detection. As shown in Figure 8.34, a resolution of 3.4 eV for 6-keV X-rays has been obtained [113]. The noise of this detector has contributions from the SQUID readout, magnetic Johnson noise and 1/ f noise of unknown origin. The intrinsic thermodynamic noise of this detector is estimated to be 0.7 eV.

The energy resolution of a thermal noise-limited magnetic calorimeter is given by

$$\Delta E_{\text{FWHM}} \approx 2.36\sqrt{2}\sqrt{4k_B C_a T^2}(\tau_s/\tau_d)^{1/4} \quad (8.46)$$

where C_a is the heat capacity of the absorber, τ_s is the relaxation time of the sensor (internal time constant) and τ_d is the relaxation time of the entire detector. This equation assumes that the heat capacities of the absorber and the thermometer are equal, a condition that gives the optimum resolution. In contrast to the TES calorimeter, the resolution improves with slower detectors. Therefore, the magnetic calorimeter may be preferred for slow count rates and for detectors with high heat capacity absorbers.

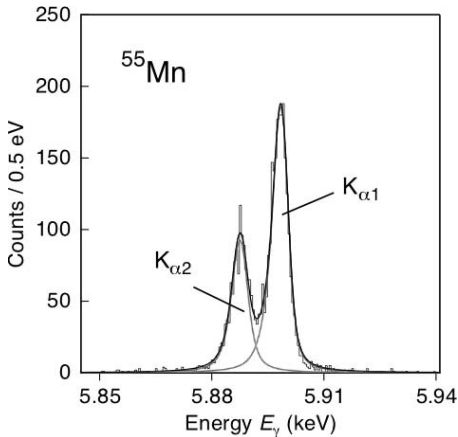


Fig. 8.34 Energy spectrum measured with a magnetic calorimeter using a ^{55}Mn source. The resolution is 3.4 eV FWHM.

8.5.6.2 SIS Tunnel Junction

When an energetic particle, such as an X-ray photon, is absorbed in a superconductor, the number of quasiparticles created is proportional to the absorbed energy. SIS tunnel junctions can be used to measure the excited quasiparticles. The Josephson supercurrent is suppressed by applying a weak magnetic field. One of the superconducting electrodes can be used to absorb the X-rays, or the electrodes can be used as a quasiparticle trap for a separate superconducting absorber with a higher critical temperature. When the tunnel junction is biased with a voltage, the quasiparticles are detected by a current-sensitive or integrating charge-sensitive amplifier. Most work has been done with transistor-based amplifiers, but SQUIDS are a good match for large-area junctions as pointed out by Mears *et al.* [114]. The benefit of instrumenting a large area junction is that it can act as the absorber, thereby avoiding the use of a separate absorber that increases the calorimeter time constant. The capacitance C_j of the tunnel junction increases and the dynamical resistance R_d decreases linearly with increasing area. Mears *et al.* argue that SQUID amplifiers are suitable for junctions larger than $\sim 100 \mu\text{m} \times 100 \mu\text{m}$ where $R_d < 10,000 \Omega$ and $C_j > 400 \text{ pF}$ [114]. The Lawrence Livermore National Laboratory group has used a series array SQUID readout to instrument tunnel junctions with areas up to $282 \mu\text{m} \times 282 \mu\text{m}$.

The resolution of an SIS X-ray detector is fundamentally limited by the statistics of the number of quasiparticles produced, which in turn depends on the energy

gap of the superconducting absorber. Niobium devices have a energy resolution limit of ~ 3 eV for 6-keV X-rays. Statistical fluctuations in the recombination and tunneling processes degrade the resolution below this fundamental limit and set a limit of ~ 10 eV at 6 keV. The energy resolution of SIS junction detectors improves with decreasing T_c . Tunnel junctions are being developed for optical wavelengths where a resolution of 8 nm at 200 nm and 80 nm at 1000 nm wavelengths has been achieved using a $20 \mu\text{m} \times 20 \mu\text{m}$ tantalum SIS tunnel junction [115].

8.5.6.3 NIS Junctions

NIS junctions have an exponential dependence of current on the normal electrode temperature which makes them useful sensors for bolometers and calorimeters. As with SIS tunnel junctions, both transistor and SQUID amplifiers have been used. The impedance of NIS junctions is low enough that SQUIDs can give a good match, provided an input network is used that has a high current-to-flux ratio. For a $100 \text{ mm} \times 100 \text{ mm}$ NIS junction the normal resistance is typically $\sim 50 \text{ m}\Omega$, and the dynamic resistance is $\sim 50 \Omega$. X-ray calorimeters based on NIS junctions have achieved a resolution of 20 eV at 6 keV [116].

In addition, NIS junctions are well suited for millimeter-wave bolometers. The normal metal electrode can be used as the terminating resistor for a planar antenna or waveguide probe. Very low thermal conductance to the heat sink can be achieved with an NIS junction where the normal metal electrode operates as a hot-electron device and has a small volume. A thermal conductance of $\sim 10^{-14} \text{ W K}^{-1}$ had been achieved at 100 mK [117]. Such low thermal conductances and the associated low NEPs ($10^{-19} \text{ W Hz}^{-1/2}$) are suitable for cooled space-borne telescopes observing dim sources at submillimeter wavelengths.

8.5.6.4 Kinetic-Inductance Thermometer

The kinetic-inductance thermometer relies on the temperature dependence of the superconducting penetration depth. In the original proposal by McDonald, four kinetic inductance thermometers are used in an alternating current bridge with a SQUID reading out the bridge current [118]. One of the thermometers is attached to a bolometer substrate and power incident on that substrate unbalances the bridge giving a signal. A superconducting meander over a thin groundplane was chosen to give a high ratio of kinetic to magnetic inductance. This interesting technique has not yet been fully explored.

The Zmuidzinas group at Caltech have explored the dependence of the kinetic inductance on the quasiparticle density at temperatures far below T_c [119]. Photons break Cooper pairs and change both the quasiparticle density and the kinetic inductance. This detector operates like a photodetector rather than a bolometer. In the original concept, these detectors form part of a microwave frequency resonant circuit that is read out in multiplexed fashion with a HEMT amplifier. SQUID readouts can also be used.

8.5.7

Future Outlook

In the future, SQUID multiplexers will enable increasingly more ambitious array instruments. Arrays for CMB observations, for example, can grow by a factor of 100 before the array size will become limited by telescope optics. Optical arrays, by contrast, can grow by at least a factor of 10^6 before reaching similar constraints. New multiplexer technologies will have to be developed to increase array sizes by many orders of magnitude, although the new technologies could be based on the current concepts.

Another important future trend will be the optimization of SQUID multiplexers for specific applications. For example, space-based array instruments will have tight requirements on cryogenic and ambient power dissipation, radiation hardness and physical size of components. Robust packaging that facilitates simple assembly will also be important.

In the future, SQUID multiplexers will become increasingly integrated with detector arrays. SQUIDs can be designed to operate at the detector temperature (>50 mK), which opens the possibility of integrating all the multiplexer circuitry directly on the detector wafer. An entire detector system could consist of a lithographed array, a relatively small number of wires to ambient temperature, and the cryogenic system.

Finally, as thermal detector array technology matures, costs will drop and arrays may become practical for applications beyond scientific research. Thermal imaging for security and medical applications, gamma-ray detectors for isotope identification and X-ray scattering measurements for material analysis are some of the intriguing areas for the future.

8.6

Nuclear Magnetic and Quadrupole Resonance and Magnetic Resonance Imaging

8.6.1

Introduction

Nuclear magnetic resonance (NMR) is one of the most powerful techniques to emerge from basic physics. It is widely used as a tool to investigate the structure of new materials – for example, pharmaceuticals – at frequencies that range up to 900 MHz. The high magnetic field required – 21.1 T for protons at 900 MHz – is generated by superconducting magnets in large systems that cost millions of dollars. The NMR frequency is a direct measure of the local magnetic field experienced by a given nucleus, giving one an exquisite tool to measure magnetic interactions. This same property is exploited in magnetic resonance imaging (MRI) where the application of magnetic field gradients enables one to image the human body with extraordinary fidelity. Again, the required magnetic field, typically 1.5 T, is maintained by a superconducting magnet. Today, there are roughly 20,000 MRI

machines worldwide, providing noninvasive diagnosis of virtually all parts of the body. Finally, although much less widely used, nuclear quadrupole resonance (NQR) provides a spectroscopic means of determining local electric field gradients.

In view of the importance of these techniques and the high sensitivity of SQUID-based amplifiers, it is hardly surprising that SQUID detection has been widely exploited for the detection of resonance signals. In his 1998 comprehensive review, Greenberg [120] lists some 100 different SQUID-based experiments, demonstrating the extraordinary diversity of the field. Nuclei for NMR include ^1H , ^3He , ^{19}F , ^{65}Cu , ^{107}Ag , ^{195}Pt , and ^{129}Xe and for NQR ^2D , ^{14}N , and ^{27}Al . The samples have variously been gases, liquids and solids and their nuclear temperatures have ranged from 300 K down to below 1 μK . Relatively recently, significant advances have been made in low-field MRI of room-temperature samples.

Given the plethora of topics, it is clear that this brief section must necessarily be highly selective. We first give a thumbnail sketch of the principles of magnetic resonance; for a thorough treatment the reader is referred to two classic textbooks [121, 122]. We then briefly discuss four examples of SQUID-based detection of NMR, NQR and MRI, chosen to illustrate the diversity of this burgeoning field.

8.6.2

Principles of NMR and NQR

Many nuclei have a magnetic moment

$$\vec{\mu} = \gamma \hbar \vec{I}, \quad (8.47)$$

where \vec{I} is the nuclear angular momentum in units of \hbar and γ is the gyromagnetic ratio. The projection of \vec{I} on the z -axis, I_z , takes one of the $(2I + 1)$ allowed values $m_I = -I, (-I + 1), \dots, +I$. In the presence of a magnetic field B_0 along the z -axis, the potential energy of the nucleus is

$$\vec{\mu} \cdot \vec{B}_0 = -\mu_z B_0 = -\gamma \hbar I_z B_0. \quad (8.48)$$

Many of the nuclei of interest have spin $\frac{1}{2}$, in which case there are just two energy levels, an upper one corresponding to $m_I = -\frac{1}{2}$ and the lower corresponding to $m_I = +\frac{1}{2}$, with a separation (in angular frequency units)

$$\omega_0 = \gamma B_0. \quad (8.49)$$

Equation (8.49) is the frequency of magnetic resonance in a magnetic field B_0 ; for protons, $\omega_0/2\pi B_0 = 42.58 \text{ MHz T}^{-1}$.

We now consider N identical, noninteracting, spin- $\frac{1}{2}$ nuclei per unit volume, in thermal equilibrium at a temperature T in a magnetic field B_0 . From elementary statistical mechanics, for example [123], the magnetization of the ensemble along the direction of B_0 is given by

$$M_0 = N\mu \tanh(\mu B_0/k_B T) \quad (I = \frac{1}{2}). \quad (8.50)$$

In the limit $\mu B_0 \ll k_B T$, Eq. (8.50) reduces to

$$M_0 = N\mu^2 B_0/k_B T \quad (I = \frac{1}{2}). \quad (8.51)$$

It is important to realize that at room temperature in achievable magnetic fields the fractional magnetization is very small. For example, for protons ($\mu_p = 1.41 \times 10^{-26} \text{ JT}^{-1}$) at 300 K in a field of 1T, $M_0/N\mu_p \approx 3.4 \times 10^{-6}$.

Some SQUID measurements of NMR involve measuring the reduction in the longitudinal magnetization, M_z , in the presence of a magnetic field B_0 and a continuous rf magnetic field. When the resonance condition $\omega_0 = \gamma B_0$ is satisfied, absorption of energy from the rf field tends to equalize the populations of the two levels of a spin- $\frac{1}{2}$ system (for example), reducing the static magnetization. Thus, the resonant frequency can be readily found from a static measurement.

Most NMR measurements, however, are made with a pulse technique and involve detection at the frequency $\omega_0/2\pi$. In the presence of a static field B_0 in the z -direction, one applies an oscillating field $B_1 \cos \omega_0 t$ perpendicular to B_0 , with the appropriate amplitude and duration to tip the magnetic moment into the $x-y$ plane. The resulting torque causes the magnetic moment to precess about B_0 at frequency $\omega_0/2\pi$. As it precesses, the magnetic moment undergoes two relaxation processes. The first is a relaxation of its direction towards the z -axis, where it will eventually regain equilibrium, in the longitudinal or spin-lattice relaxation time T_1 . The second process is the dephasing of the individual nuclear spins by the local field produced at each site by neighboring spins in the transverse or spin-spin relaxation time T_2 . The values of T_1 and T_2 vary greatly but $T_1 \geq T_2$ always. In solids T_1 can be extremely long – even months – at low temperatures, whereas T_2 is short, perhaps only microseconds. In contrast, in a nonviscous liquid at room temperature T_1 and T_2 may be on the order of 1 s; the spin-spin interaction is greatly reduced by motional narrowing. The FWHM linewidth of the NMR line is $\Delta\nu = 1/\pi T_2$, (“homogeneous broadening”), so that liquids have narrow linewidths whereas solids have broad linewidths. However, inhomogeneities in the applied magnetic field can substantially broaden the linewidth (“inhomogeneous broadening”) and reduce T_2 to a value T_2^* given by

$$\frac{1}{T_2^*} = \frac{1}{T_2} + \frac{1}{T_2'}. \quad (8.52)$$

The time T_2' is the inhomogeneous lifetime.

Virtually all pulsed NMR spectra are obtained using the very important spin echo technique invented by Hahn [124]. Figure 8.35(a) shows the pulse sequence and detected NMR signal, and Figures 8.35(b)–(f) show the behavior of the spins in the rotating frame; the frame rotates at frequency ω_0 so that the spins appear to be stationary. Initially, (Figure 8.35(b)), the net magnetization M_0 is aligned along B_0 (z -axis) in thermal equilibrium. As described above, a $\pi/2$ -pulse along the x -axis (Figure 8.35(a)) tips the magnetization along the $-y$ -axis (Figure 8.35(c)),

whereupon it begins to precess about the z -axis, producing the free-induction decay (FID) shown in Figure 8.35(a). Because different spins precess at slightly different rates, in the rotating frame (Figure 8.35(d)) the effective magnetization begins to spread out, causing the FID to relax with a time constant T_2^* . At a time τ_e after the $\pi/2$ -pulse (Figure 8.35(a)), a π -pulse along the x -axis flips the magnetization through 180° (Figure 8.35(e)). Because the spins retain their sense of rotation, their subsequent time evolution in the rotating frame causes them to refocus. At a time $2\tau_e$ after the $\pi/2$ -pulse, the signal appears as an echo (Figures 8.35(a) and (f)). We note that only inhomogeneous broadening is reduced by the spin echo; homogeneous broadening, which is due to interactions between randomly fluctuating spins, is not affected.

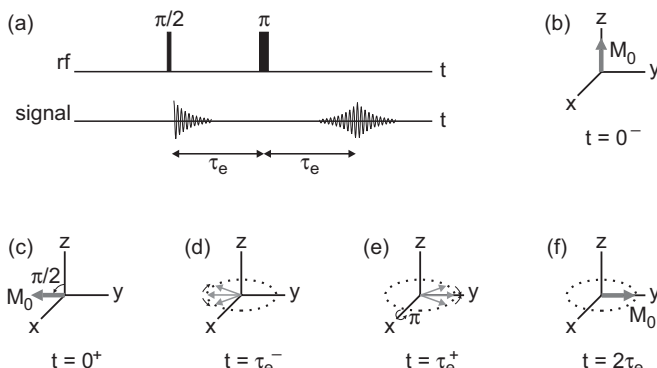


Fig. 8.35 Spin echo. (a) Pulse sequence and signal from detector; (b) equilibrium magnetization M_0 at time $t = 0^-$; (c) M_0 in the $x-y$ plane at $t = 0^+$ after application of $\pi/2$ pulse; (d) dispersion of spins at $t = \tau_e^-$; (e) spins at $t = \tau_e^+$ after application of π pulse; (f) recovery of M_0 at time $t = 2\tau_e$. The coordinate system in (b)–(f) rotates at the Larmor frequency.

In MRI, one uses NMR to determine the spatial structure of specimens by means of three orthogonal magnetic field gradients that define a “voxel.” There are many imaging schemes for attaining this goal, but they all rely on the idea that a unique value of magnetic field established in a small region produces a unique NMR frequency of – almost always – the protons contained in it. The amplitude of the signal is a measure of the number of protons; in addition, “ T_1 -weighted contrast” can be used to distinguish the protons in different environments, for example, in healthy and cancerous tissue.

NQR involves nuclei with $I \geq 1$, which have an electric quadrupole moment eQ_e that is a measure of the departure of the nuclear charge distribution from spherical symmetry. A comprehensive review of NQR is to be found in the classic text by Das and Hahn [125]. The quadrupole moment is positive for “cigar-shaped” nuclei and negative for “door-knob-shaped” nuclei. Values of Q_e range from 0.003 barns for the deuteron to about 5 barns for heavy nuclei (1 barn = 10^{-28} m 2). The electric quadrupole moment interacts with the local electric field gradient at the nucleus,

and as a result precesses about the major axis of the field gradient. This motion is analogous to the precession of the magnetic moment of a nucleus about an applied magnetic field. However, the quadrupole precession requires no externally applied electric or magnetic field, and arises solely from the electric field gradient produced inside the solid.

The electric field gradient is a second-rank tensor composed of the nine second-order derivatives $V_{ij} = \partial^2 V / \partial x_i \partial x_j$ ($i, j = 1, 2, 3$) of the electrostatic potential V at the nucleus arising from all the charges external to the nucleus. In fact, one can always choose principal axes for the potential V such that only the diagonal components V_{xx} , V_{yy} and V_{zz} are nonzero. Furthermore, to satisfy Laplace's equation at the nucleus, the diagonal terms must sum to zero: $V_{xx} + V_{yy} + V_{zz} = 0$ [121, 122, 125]. Consequently, there are only two independent parameters that characterize the derivatives, which by convention are defined as the field gradient

$$eq = V_{zz} \quad (8.53)$$

and the asymmetry parameter

$$\eta = (V_{xx} - V_{yy})/V_{zz}. \quad (8.54)$$

We note that if the nucleus is at a cubic symmetry point, this symmetry implies that $V_{xx} = V_{yy} = V_{zz} = 0$ so that the quadrupole interaction vanishes. Thus, the nucleus must be at a site that does not possess cubic symmetry in order for η to be nonzero.

In contrast to the magnetic moment of a nucleus, the symmetry of the electric quadrupole moment is such that its energy is unchanged when the direction of the nucleus is changed by 180° . Consequently, the quadrupole energy levels are independent of the sign of m_I , and in fact depend on m_I^2 . As an example, we consider the ^{14}N nucleus with $I = 1$. In zero magnetic field and for $\eta \neq 0$, the nucleus has $(2I + 1) = 3$ distinct energy levels, shown in Figure 8.36. In terms of the eigenstates $|I, m_I\rangle$, the states are $|1, 0\rangle$, $(|1, 1\rangle - |1, -1\rangle)/\sqrt{2}$ and $(|1, 1\rangle + |1, -1\rangle)/\sqrt{2}$, with corresponding energies $-2hv_Q$, $hv_Q(1 - \eta)$ and $hv_Q(1 + \eta)$. Here, following convention, we have defined the frequency $v_Q = |eV_{zz}Q_e/4\hbar|$. Thus, one expects to observe three distinct frequencies in the NQR spectrum, corresponding to the transitions among energy levels shown in Figure 8.36.

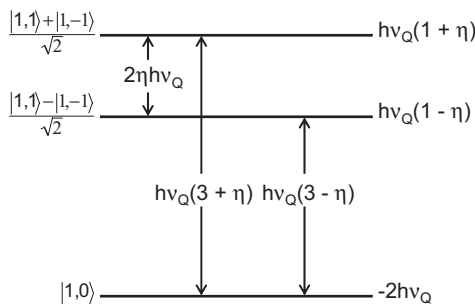


Fig. 8.36 Energy levels of ^{14}N in zero applied magnetic and electric fields for nonzero asymmetry parameter η .

NQR frequencies range from tens of kilohertz to hundreds of megahertz. Since the precessing nuclei have magnetic moments and thus produce an oscillating magnetic field, high-frequency NQR can be observed in solids in zero magnetic field with essentially the same techniques used for high-field NMR. In the case of conventional spectrometers, low-frequency NQR is usually observed as a perturbation on the high-field NMR spectrum. The fact that these low-frequency signals can readily be detected directly by means of a SQUID makes this method particularly attractive. Measurements of the NQR frequencies enable one to deduce the quadrupole coupling constant $|eV_{zz}Q_e/h|$ and η ; the value of Q_e has to be determined independently. Thus, NQR provides a direct measure of the local field gradient at the nucleus in question.

8.6.3

SQUID-Detected NMR and NQR

A wide variety of measurements have been made possible by the use of a SQUID to detect NMR [120]. Examples include the discovery of nuclear spin ordering in ^{63}Cu at temperatures below 100 nK [126, 127], the determination of the NMR susceptibility [128] and of ferromagnetic resonance behavior [129] in superfluid $^3\text{He-B}$, measurements of zero-field magnetic order in a few monolayers of ^3He absorbed on a surface [130], observations of methyl quantum tunneling [131], the detection of NMR in a single, 50- μm -diameter particle of ^{195}Pt [132], absolute measurements of magnetic field using ^3He [133] and thermometry [134]. In the following sections we briefly describe four very different applications: NQR of ^{14}N , spin noise, NMR and MRI of hyperpolarized ^{129}Xe and NMR and MRI of ^1H .

8.6.3.1 NQR of ^{14}N

Changes in z-magnetization induced by NMR or NQR can readily be observed with a SQUID magnetometer in a relatively simple arrangement. As an illustration, in early work Day [135] measured the NMR spectra of ^1H , ^7Li and ^{19}F . Much useful work has been performed on the NQR of ^{14}N , using, for example, the experimental configuration shown in Figure 8.37 [136, 137]. The sample, contained in a glass tube, can be inserted into and removed from the apparatus while it is immersed in liquid ^4He . A solenoid, wound on a lead tube, supplies a magnetic field of up to 30 mT before the ^4He is transferred; subsequently the current in the solenoid is removed and a very stable static field is maintained by a supercurrent in the lead shield. Changes in the static magnetization M_z parallel to the applied field are coupled into the SQUID via a NbTi flux transformer with a 14-turn pickup coil. A saddle coil is used to apply a continuous rf magnetic field perpendicular to the static field, with a frequency that is swept through the NMR and NQR resonance. In this particular case, a shunt resistor R_s across the terminals of the input coil to the SQUID was used to provide a low-pass filter to reduce interference from rf fields.

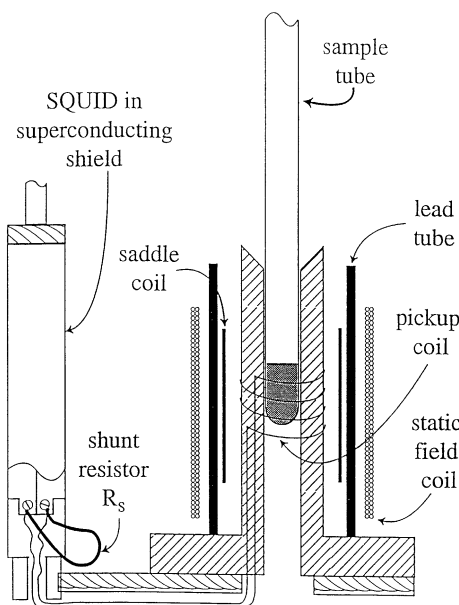


Fig. 8.37 Configuration of spectrometer for the measurement of longitudinal magnetization in the presence of continuous microwave irradiation. (Reproduced with permission from ref. [136].)

Figure 8.38 shows the ^{14}N spectrum obtained for cocaine hydrochloride, with resonances at 815 and 965 kHz. The experiment is based on a technique involving cross-relaxation between ^{14}N and ^1H , and the detected magnetization is due to the protons [138]. One measures the ^1H magnetization in a small applied magnetic field while exciting the population of the ^{14}N levels with an rf field. This strategy has the advantage of increasing the signal amplitude by the ratio $\gamma_{\text{H}}/\gamma_{\text{N}} \sim 15$, where γ_{H} and γ_{N} are the gyromagnetic ratios of ^1H and ^{14}N . The magnetic field is adjusted so that a multiple of the ^1H transition frequency is matched to one of the three possible ^{14}N transition frequencies v_+ , v_- , or v_0 . The inset of Figure 8.38 corresponds to the case where the v_- transition frequency is equal to three times the ^1H transition frequency. As the nonmatched ^{14}N transitions are excited with the rf signal, the populations of the energy levels change. Since there is dipolar coupling between the ^{14}N and ^1H nuclei, the change in the population of the matched levels is reflected in the ^1H magnetization which, in turn, is detected by the SQUID. As a result, by varying the applied magnetic field, one can map the ^{14}N NQR spectrum onto a detectable change in the proton magnetization. In the particular example shown in Figure 8.38, only the $v_- = 815$ kHz and $v_+ = 965$ kHz transitions could be observed. Fortunately, with the aid of the level scheme shown in Figure 8.36 for $I = 1$ nuclei, these are sufficient to obtain the quadrupole coupling constant $|eV_{zz}Q_e/h| = 1.186$ MHz and asymmetry parameter $\eta = 0.252$. NQR of ^{14}N in peptides and amino acids is a powerful tool for structural determination [120, 139].

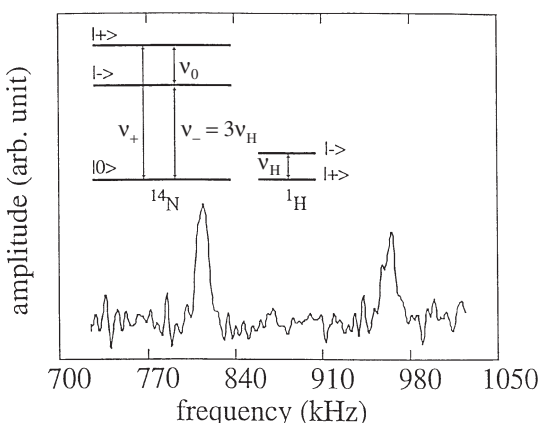


Fig. 8.38 ^{14}N NQR spectrum of cocaine hydrochloride showing resonance at $\nu_0 = 815$ kHz and $\nu_+ = 965$ kHz. Inset energy level diagrams show that ν_- is matched to three times the proton Larmor frequency ν_H . (Reproduced with permission from ref. [138].)

As an example of pulsed ^{14}N NQR, experiments have been performed on powdered ammonium perchlorate, NH_4ClO_4 [140]. The sample, at ^4He temperatures, was placed in one loop of a first-derivative axial gradiometer, and rf pulses were applied by means of a solenoid wound coaxially with the gradiometer. The dc SQUID was operated in a flux-locked loop which – as in most pulsed experiments – was disabled during the application of the rf pulse. The gradiometer was untuned, giving wideband detection. All the experiments were carried out in nominally zero magnetic field. Figure 8.39(a) shows the echo formed by the application of two rf pulses, 4 ms apart. The first, $\pi/2$ -pulse, had an amplitude of 3.8 mT and the second, π -pulse, of 6.5 mT; each consisted of a single 45-kHz cycle. The signal shown was demodulated at 35 kHz and averaged over 16,000 accumulations. The Fourier transform (Figure 8.39(b)) shows three NQR resonances at 17.4, 38.8 and 56.2 kHz, corresponding to the level splittings shown in the inset. Combined with the level scheme of Figure 8.36, these data yield an ^{14}N quadrupole coupling constant $|eV_{zz}Q_e/h| = 63.3$ kHz, and an asymmetry parameter $\eta = 0.550$.

These experiments show that a broadband detector enables one to excite and observe the three transitions of a three-level system simultaneously. The fact that one can observe narrow linewidths in a polycrystalline material results from the lack of an applied magnetic field to define a direction in space. As a result, all equivalent ^{14}N sites have the same resonant frequency regardless of spatial orientation. If one were to perform high-field NMR on the same sample, the random orientation of the molecules with respect to the applied field would produce a “powder pattern” in which the NMR lines would broaden, making it difficult or impossible to discern the NQR lines.

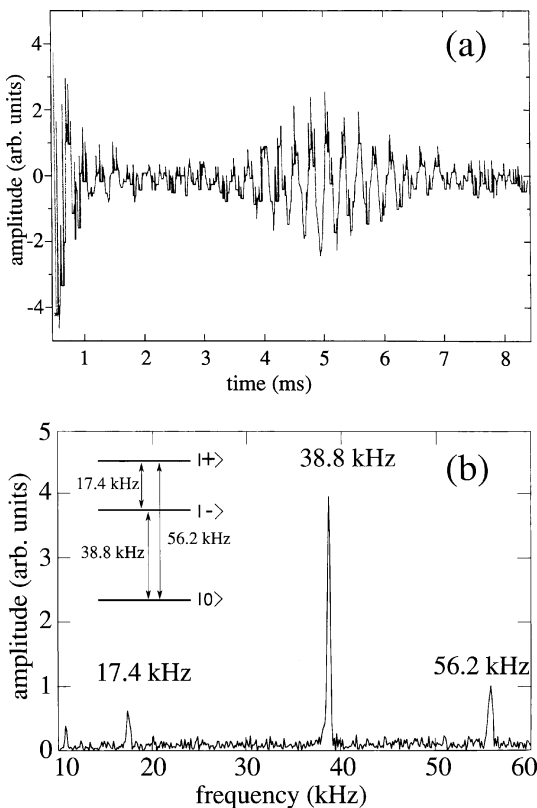


Fig. 8.39 NQR of ^{14}N in NH_4ClO_4 at 1.5 K. (a) Spin echo produced by two pulses 4 ms apart, demodulated at 35 kHz. (b) Fourier transform of the echo, showing three peaks corresponding to the energy level splittings shown in the inset. (Reproduced with permission from ref. [140].)

8.6.3.2 Spin Noise

A quite different example of NQR is the observation of “spin noise” produced by ^{35}Cl in NaClO_3 or KClO_3 [141, 142]. The ^{35}Cl nucleus has spin $3/2$, and the nuclear quadrupole interaction produces two doubly degenerate energy levels with a splitting of 30.6859 MHz. The sample is inserted into a superconducting solenoid that is part of the tuned input circuit of a SQUID amplifier (Section 8.3.5), and the experiment consists of measuring the current noise in this circuit. There are two versions of the experiment: measurements of the spin fluctuations in thermal equilibrium and spontaneous emission from the spin ensemble when the two populations are initially equalized by means of rf irradiation at the NQR frequency.

In the absence of the sample, the tuned input circuit produces noise with a Lorentzian power spectrum. This noise originates as Nyquist noise in the circuit resistance, which results in a quality factor Q of typically 5000. The presence of the sample modifies this spectrum in the vicinity of the NQR frequency. The sam-

ple has a complex spin susceptibility: the real part modifies the inductance of the pickup coil, shifting the resonant frequency, while the imaginary part modifies the damping, acting as a source of Nyquist noise. A straightforward analysis shows that the spectral density of the current noise produced in the input circuit is

$$S_i(\omega) = \frac{(2/\pi)k_B[R_i T + R_s(\omega)T_s]}{(R_i + R_s)^2 + [\omega(L_T + L_s) - 1/\omega C_i]^2}. \quad (8.55)$$

Here, R_i and L_T are the total resistance and inductance in the input circuit (including contributions from the SQUID), R_s and L_s are the resistance and inductance induced into the input circuit by the spins and C_i is the series capacitance. The temperature T_s of the spin is not necessarily equal to the bath temperature T . The term $(2/\pi)k_B R_s(\omega) T_s$ is the spectral density of the Nyquist noise voltage produced by the spins, and represents fluctuations in the magnetization of the sample. In the absence of the sample ($R_s = L_s = 0$), Eq. (8.55) reduces to the expected Lorentzian power spectrum for current noise in a tuned circuit.

In the experiments, the powdered sample was inserted into the Nb solenoid, and the SQUID was operated open-loop. The temperature was 1.5 K. The spectral density of the noise at the output of the SQUID was monitored, and the tuning capacitor in the input circuit was adjusted from outside the cryostat so that the resonant frequency was close to the NQR frequency. The quality factor Q was about 5000. In the first experiment, the spins of a sample of NaClO_3 were in thermal equilibrium with the bath temperature ($T_s = T$). The spectral density of the current noise, shown in Figure 8.40, reveals a dip in the power spectrum due to the spin fluctuations. The origin of the dip is readily discerned from Eq. (8.55): on resonance, $S_i(\omega) = 2k_B T / \pi(R_i + R_s)$, and the presence of the resistance R_s reduces the noise over that expected in the absence of the sample (shown as a dotted curve in Figure 8.40).

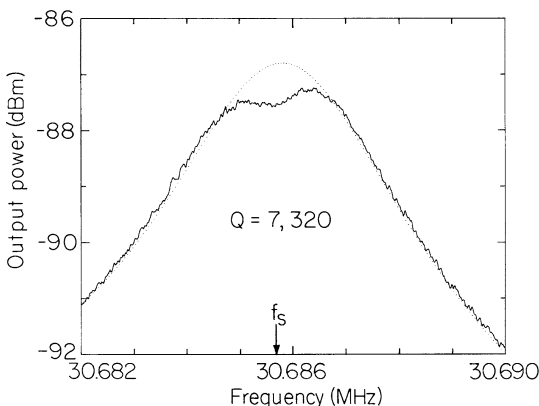


Fig. 8.40 Spectral density of current noise in the tuned input circuit of a SQUID amplifier due to fluctuating spins of ^{35}Cl in NaClO_3 in thermal equilibrium at 1.5 K. The data were averaged over 3 h. The NQR frequency f_s is indicated. The solid line is the power spectrum of the noise in the tuned circuit in the absence of the sample. (Reproduced with permission from ref. [142].)

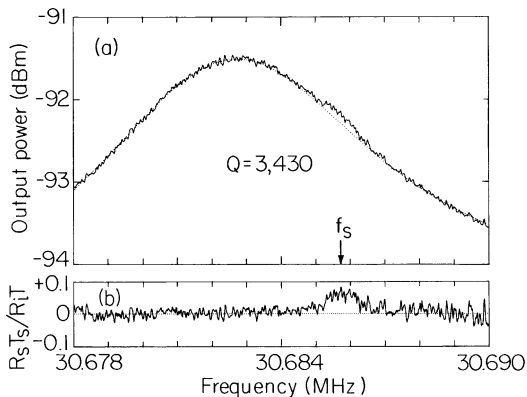


Fig. 8.41 Spectral density of current noise in the tuned input circuit of a SQUID amplifier due to the spontaneous emission of photons from the saturated spins of ^{35}Cl in KClO_3 . The bath temperature was 1.5 K. The data were averaged over 2.3 h. (a) Measured spectrum, with noise due to the tuned circuit alone

shown as a solid line; NQR frequency f_s is indicated. (b) Spectral density with sample subtracted from spectral density without sample to leave the spontaneous emission contribution. (Reproduced with permission from ref. [142].)

In the second experiment, the spin populations of a sample of KClO_3 were equalized by continuous rf excitation at the NQR frequency. For this sample, T_1 was extremely long – several days. After the rf excitation was turned off, the noise power spectrum was measured. In this condition of spin saturation, $M_z = R_s = L_s = 0$, and $T_s = \infty$. However, it can be shown that the product $R_s T_s$ is constant, independent of the difference in the spin populations. Thus, at resonance, Eq. (8.55) reduces to $S_i(\omega) = (2/\pi)k_B[R_I T + R_s(\omega)T_s]/R_I^2$, and we expect a “bump” in the noise. This feature is shown in Figure 8.41. Physically, the increase in the noise over the thermal equilibrium value arises from the spontaneous emission of photons into the tuned circuit as the excess spin population of the upper level relaxes to its equilibrium value.

It is noteworthy that the spontaneous emission rate A for one spin is extremely low, about $2 \times 10^{-16} \text{ s}^{-1}$, or roughly one spin flip every one million centuries. Since there are about $N = 2 \times 10^{21}$ spins, the total emission rate $NA/2 \approx 2 \times 10^5 \text{ s}^{-1}$, corresponding to a power of $5 \times 10^{-21} \text{ W}$. This is about 5% of the Nyquist noise power $4k_B T / \pi T_2 \approx 10^{-19} \text{ W}$ generated in the bandwidth $1/\pi T_2$ of the spin noise.

These first observations of spin fluctuations and spontaneous emission were made possible in a conceptually simple experiment by the fact that the noise temperature of the tuned SQUID amplifier, about 0.2 K, was substantially lower than the bath temperature. Although such measurements will of course never supplant the conventional methods of performing magnetic resonance, they demonstrate that an ensemble of spins exhibits resonance effects even in the absence of magnetic pulses to establish spin precession.

8.6.3.3 NMR of Hyperpolarized ^{129}Xe

As we see from Eq. (8.51), the equilibrium magnetization of an ensemble of spins at 300 K in low magnetic fields is exceedingly small. An important method of increasing the magnetization of certain gases – notably ^3He and ^{129}Xe – is by optical pumping [143]. The resulting enhancement in the NMR signal due to this “hyperpolarization” has made possible a number of novel experiments, including enhanced MRI of organisms [144–146] and enhanced NMR of surfaces and solutions [147–149]. Of particular interest is the use of hyperpolarized gas to obtain high-resolution MRI of the lungs, which are otherwise difficult to image. In all these applications, the hyperpolarized gas is prepared in one system, and subsequently transferred to another location for imaging. Consequently, the lifetime T_1 is of critical importance. In the case of solid ^{129}Xe , Gatzke *et al.* [150] made NMR measurements at 4.2 K in magnetic fields ranging from 0.2 T to 5 mT, and found that T_1 varied from roughly 10^6 to 10^4 s. Since one would prefer to store ^{129}Xe in as low a magnetic field as possible while preserving a long T_1 , the extension of the NMR measurements to much lower fields is of both practical and fundamental interest. Thus, TonThat *et al.* [151] used an untuned SQUID magnetometer to detect NMR in ^{129}Xe at fields as low as 0.019 mT, and we briefly describe these experiments.

Experiments were performed on both naturally abundant ^{129}Xe (26.4%) and isotopically enriched ^{129}Xe (80%). The procedure to pump ^{129}Xe optically was as follows [152]. The Xe gas was admitted into a glass cell containing Rb, the temperature of which was raised subsequently to 70–90 °C to establish a high vapor pressure. The cell was illuminated with circularly polarized light at the wavelength of the D₁ line in Rb, 794.74 nm, while a 3-mT magnetic field split the Rb and Xe levels. The optical pumping induced a large electron polarization in the Rb vapor which was transferred via collisions to the ^{129}Xe nuclei. After about an hour of optical pumping, the cell was cooled and the hyperpolarized ^{129}Xe gas was drawn into a sample tube immersed in liquid N₂, where it was frozen in a field of 0.1 T. It was estimated that the enhanced polarization of the ^{129}Xe was 10%. Finally, the sample tube was transferred to a ^4He cryostat containing the SQUID-based spectrometer shown in Figure 8.42. The Nb pickup saddle coil was connected to the input coil of a dc SQUID, and the superconducting solenoid generating B_0 was equipped with a thermal switch to enable it to be operated in the persistent current mode.

NMR was performed with a single excitation pulse at fields ranging from 0.019 to 8.9 mT, corresponding to Larmor frequencies of about 0.2 to 110 kHz. Representative spectra are shown in Figure 8.43. The signal-to-noise ratio for these single-shot spectra is very high, reflecting the high degree of polarization. At low fields, the FWHM linewidth approached 520 ± 60 Hz for the isotopically enriched samples and 340 ± 20 Hz for the naturally abundant samples. These values agreed well with the values of 616 and 350 Hz, respectively, calculated for nuclear dipole-dipole interactions [143].

Values of T_1 were determined by measuring a series of ^{129}Xe NMR signals at different times after the sample was inserted in the spectrometer. It was found

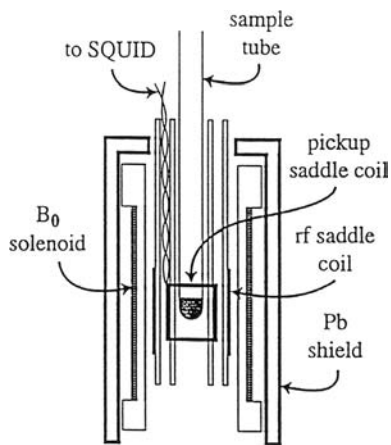


Fig. 8.42 Schematic of a SQUID-based NMR spectrometer. The sample is at the center of the orthogonal pickup and excitation coils. A persistent current solenoid provides a static field B_0 along the axis of the sample tube. Coils and sample are enclosed in a Pb tube, and the dewar is surrounded by a double μ -metal shield that reduces the ambient field to below 0.1 μ T. (Reproduced with permission from ref. [151].)

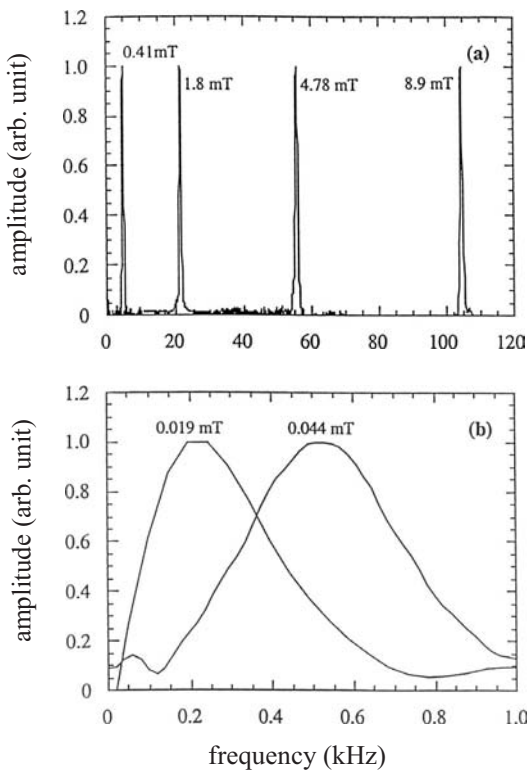


Fig. 8.43 SQUID-detected ^{129}Xe NMR. (a) Isotopically enriched ^{129}Xe (80%) for four magnetic fields, and (b) isotopically enriched sample at 0.044 mT and naturally abundant sample at 0.019 mT. (Reproduced with permission from ref. [151].)

that T_1 decreased with decreasing field above about 2 mT, and remained more or less constant at about 2000 s as the field was lowered to 0.019 mT. This long relaxation time even in fields comparable to that of the Earth implies that ^{129}Xe can be stored and used in a variety of experiments without the need for high magnetic fields to inhibit relaxation.

In further experiments [153], a second set of coils was added to provide a magnetic field gradient along the direction of the magnetic field. A two-dimensional MRI of frozen ^{129}Xe was obtained at 1 mT by progressively rotating the sample tube through 12 angular steps of 30° each, and reconstructing the image. Subsequently, images of ^{129}Xe in porous materials at room temperature were obtained at 2.3 mT with a high- T_c SQUID [154]. It was even possible to observe the chemical shift of hyperpolarized ^{129}Xe adsorbed onto polypropylene [155]. In a field of about 2.5 mT, the NMR peak from the adsorbed ^{129}Xe at 30.077 kHz was readily resolved from the peak at 30.071 kHz from free ^{129}Xe gas, a shift of about 200 ppm.

These low-field experiments on hyperpolarized ^{129}Xe demonstrate that the techniques developed with high-field NMR can be extended to millitesla fields. They represent a step towards the use of xenon chemical shifts for diagnostic chemical and biomedical NMR analysis, and chemical-shift-resolved MRI in molecules, materials and organisms at ultralow magnetic fields.

8.6.3.4 Liquid-State Proton NMR and MRI

In this last example, we discuss an application of the NMR technique that is of great importance in medicine, namely MRI. Given the incredible success of high-field NMR and MRI, why would one consider low fields and SQUID detection? To answer this question, we first note that in the conventional method of detection – a resonant circuit followed by an amplifier – the induced voltage scales as the magnetization M_0 , which in turn scales with the static field B_0 (Eq. (8.51)), and by Faraday's law with the precession frequency ω_0 , which also scales with B_0 . Thus, the voltage scales as B_0^2 or ω_0^2 . Consequently, the power signal-to-noise ratio increases as B_0^4 ; by the same token, it also decreases as B_0^4 making low-field NMR seemingly unappealing. In contrast, if one detects the signal with an untuned flux transformer coupled to a SQUID, which responds to flux rather than rate of change of flux, the output voltage scales with B_0 or ω_0 . Thus, the signal falls off linearly with B_0 , rather than quadratically, as is the case for Faraday detectors. However, it is well known that one can dramatically increase the magnetization above its equilibrium value by one of several means, including dynamic nuclear polarization [122, 156] optical pumping (as in Section 8.6.3.3) [157] or prepolarization in a much larger magnetic field B_p [158]. In the last case, for precession fields B_0 less than B_p , the SQUID-detected NMR signal becomes independent of B_0 . Given the very high intrinsic sensitivity of the SQUID, it is then possible to achieve high signal-to-noise ratios in very low magnetic fields.

There is, furthermore, a major advantage of low-field NMR or MRI. At high fields, in order to obtain high spectral resolution (narrow linewidths) or high spa-

tial resolution, it is necessary to “shim” B_0 to very high precision. For example in a 900-MHz system, to obtain a 1-Hz linewidth one needs to achieve a magnetic field homogeneity of about 1 part in 10^9 across the dimensions of the sample. This is achievable, but at some cost. Furthermore, spatial variations in the magnetic susceptibility across the sample produce a linewidth broadening, or a loss of spatial resolution in MRI, that cannot be compensated. In contrast, at an NMR frequency of (say) 2 kHz (corresponding roughly to the Earth’s field), the field homogeneity required for a 1-Hz linewidth is only 1 part in 2000, which is very easy to obtain; furthermore, the effects of susceptibility variation become negligible.

Clearly, to perform NMR or MRI on protons in (say) water, the sample cannot be cooled to liquid helium or nitrogen temperatures but must be maintained above 0°C. Early imaging experiments with untuned SQUID detection were carried out by Kumar *et al.* [159, 160] and by Schlenga *et al.* [161], the latter with a high- T_c SQUID. Neither experiment involved prepolarization. In the experiment of Schlenga *et al.*, the applied field was about 2 mT, corresponding to an NMR frequency of about 85 kHz, and the linewidth was broadened to about 70 Hz by field inhomogeneities. Spatial resolution of better than 1 mm was achieved in phantoms containing mineral oil, but the averaging time was extremely long, eight hours.

Subsequently, McDermott *et al.* studied proton NMR [162] and MRI [163, 164] in microtesla fields using prepolarization. The circuit diagram of their NMR experiment is shown schematically in Figure 8.44(a). The gradiometer was wound around the tail section of a double-walled Pyrex insert that was immersed in liquid ^4He in a fiberglass dewar (not shown in the figure). The liquid sample in a Pyrex cell was lowered into the insert, and was maintained at about 300 K by a resistive heater. A single-layer solenoid of copper wound around the sample cell provided the polarizing field B_p , while a set of coils (not shown) in the ^4He bath provided the measurement field B_0 , perpendicular to B_p . The belly of the ^4He dewar was lined with a sheet of Pb, and the dewar was surrounded by a single-layer mu-metal shield. The SQUID was operated in a conventional flux-locked loop. The measurement involved the following sequence of pulses (Figure 8.44(b)). The sample was polarized in a field $B_p \sim 1$ mT for a time longer than T_1 (typically several seconds), with the measurement field B_0 of a few microteslas turned on. When the polarizing field was turned off nonadiabatically (in a time short compared with the NMR period), the spins precessed about the measurement field. After a time τ_e the direction of B_0 was abruptly reversed, causing the spins to reverse their sense of the precession and producing a spin echo that peaked at time $2\tau_e$. This “field inversion spin echo” differs from the conventional “Hahn spin echo” in which the phase of the spins is inverted by means of an rf pulse while the sense of the precession is preserved. The sequence of pulses is repeated and the signals are averaged; the time series is Fourier transformed to produce a spectrum. The entire procedure is controlled by a computer, which also disables the flux-locked loop during the application and removal of the polarizing field.

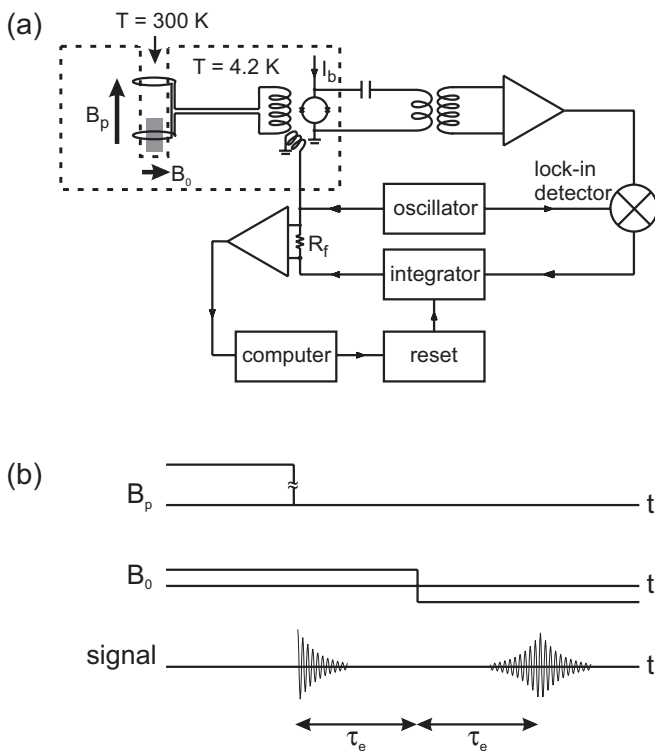


Fig. 8.44 Low-field NMR. (a) Configuration of system to detect NMR signals in microtesla magnetic fields. Dashed lines enclose components at 4.2 K. (b) Pulse sequence to prepolarize spins and to obtain a spin echo using magnetic field inversion. (Reproduced with permission from ref. [162].)

Two results are shown in Figure 8.45 that illustrate the great advantage of operating in a low magnetic field [162]. Figure 8.45(a) shows the spectrum of protons in mineral oil obtained without prepolarization in a measurement field of 1.8 mT, using a Hahn spin echo sequence. The spectrum is averaged over 10,000 transients. The linewidth is about 1 kHz, indicating that the field homogeneity over the volume of the sample is about 1%. Figure 8.45(b) shows the spectrum from the same sample in a field of 1.8 μT with a polarizing field of 2 mT and a field inversion spin echo. The spectrum was averaged over only 100 transients. We see immediately that the 1000-fold reduction in B_0 has reduced the linewidth from about 1 kHz to about 1 Hz, and that the signal-to-noise ratio has been increased despite the fact that the number of averages has been reduced by a factor of 100. The increase in signal-to-noise arises from the fact that the total energy under the peak is about the same in the two spectra (the polarizing field in Figure 8.45(b) and the static field in Figure 8.45(a) are almost identical): thus, the 1000-fold reduction in linewidth in Figure 8.45(b) produces a 1000-fold increase in the amplitude of the peak.

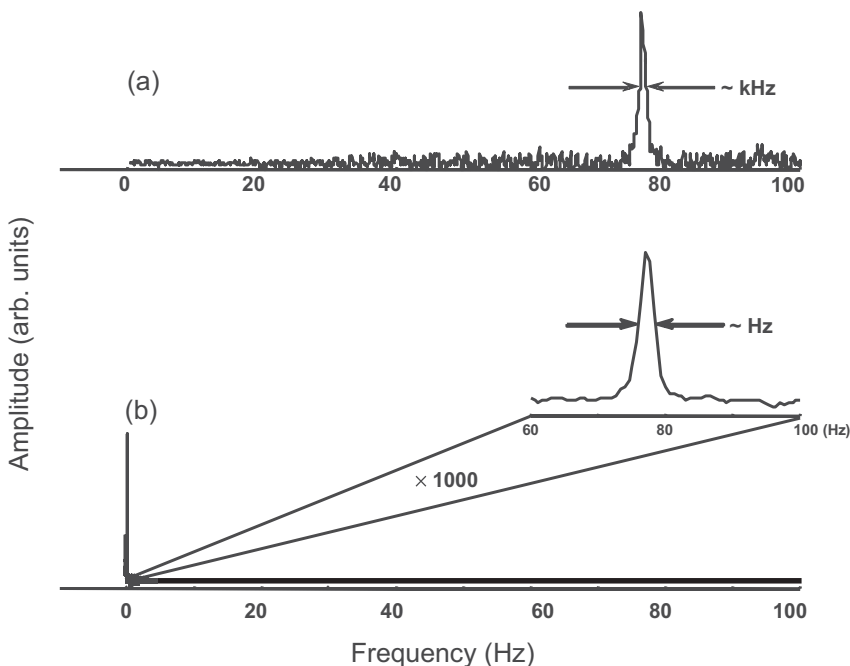


Fig. 8.45 NMR spectra of protons in 5 ml of mineral oil. (a) Spectrum obtained in a 1.8-mT static field with a Hahn spin echo sequence, using 10,000 averages. (b) Spectrum obtained in a 1.8- μ T static field with spin prepolarization in 2 mT, using 100 averages. The inset shows the spectrum on an expanded frequency scale. (Reproduced with permission from ref. [162].)

The enhanced spectral resolution achieved in microtesla fields can be exploited to detect scalar coupling (also known as J -coupling) in heteronuclear spin systems [162, 165]. As an example, we consider trimethyl phosphate, which contains a single ^{31}P atom and nine equivalent protons (Figure 8.46). The nuclear spin of the ^{31}P interacts with the proton spins via the chemical bonds, producing a very small splitting of the proton levels. Figure 8.46 shows the 10.4 ± 0.6 Hz splitting obtained in a magnetic field of $4.8 \mu\text{T}$, averaged over 100 transients. The splitting is very clearly resolved. Since electron-mediated scalar couplings between nuclear spins yield splittings that are specific to a particular chemical bond, this technique could be used as a low-field NMR “bond detector.” Subsequently, Burghoff *et al.* [166] operated a similar system in the very low field environment ($< 10 \text{nT}$) of the Berlin magnetically shielded room [167]. For protons in water, they achieved a linewidth of 0.17 Hz at a Larmor frequency of 19 Hz. To achieve the same linewidth in a 900-MHz NMR spectrometer, one would require a relative field homogeneity of 0.2 parts per billion, which is beyond the current state of the art. The authors used the same system to observe the spectral lines due to J -coupling in trifluoroethanol with a linewidth of about 0.3 Hz in a magnetic field of $0.993 \mu\text{T}$.

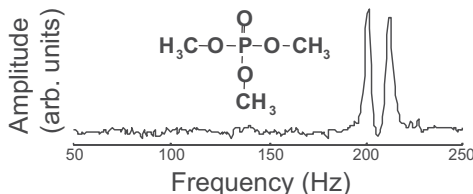


Fig. 8.46 NMR spectrum of 3 ml of neat trimethyl phosphate. The measurement field was 4.8 μT , and the spectrum was averaged over 100 transients. (Reproduced with permission from ref. [162].)

The narrow linewidth achievable in a low magnetic field has an immediate applicability to MRI. When the NMR linewidth Δf is determined by magnetic field inhomogeneity, the spatial resolution that can be achieved in an MRI experiment is $\Delta z = 2\pi\Delta f/\gamma G_z$, where G_z is the magnetic field gradient. For a measurement field B_0 with fixed relative homogeneity, Δf scales linearly with B_0 . Thus, in an MRI experiment performed in low field with linewidths approaching the lifetime limit, high spatial resolution can be achieved with relatively small field gradients, which disperse the NMR signal over a quite small bandwidth.

Low-field MRI [163, 164] has been performed using the set of coils shown schematically in Figure 8.47. The wooden cube, 1.8 m on a side, supports three pairs of coils that are used to cancel the Earth's magnetic field. A Helmholtz pair with a radius of 0.6 m provides a horizontal measurement field of about 100 μT at the center of the cube. The cube also supports three orthogonal sets of gradient coils. A Maxwell pair, with a radius of 0.6 m, produces the gradient $G_z = \partial B_z/\partial z$. Two sets of saddle coils produce the off-diagonal encoding gradients $G_x = \partial B_z/\partial x$ and $G_y = \partial B_z/\partial y$ [168]. A copper-wire coil, placed immediately below the sample, produces a polarizing field along the axis of the gradiometer; the spin excitation coil surrounds the polarizing coil. The entire system is surrounded by an eddy-current shield, made from 3-mm-thick Al sheet, that attenuates magnetic noise at the measurement frequency by an order of magnitude and essentially eliminates rf interference. Finally, the fiberglass dewar contains a second-derivative gradiometer that is situated so that the sample, which is placed immediately below the dewar, is at the center of the cube. The dewar, built in-house to have very low magnetic noise, was copied from a design by Seton *et al.* [169]. The upper cooled shield is made from an electrically insulating ceramic, and the superinsulation consists of aluminized polyester cloth. The fine structure of this material results in a finely divided aluminum coating that reflects well in the infrared while producing much lower magnetic noise due to Nyquist noise currents than is the case for the aluminized mylar conventionally used. An array of 25 Josephson tunnel junctions [170] is connected in series with the gradiometer and the input coil of the SQUID to protect the SQUID from the large changes in magnetic flux produced when the polarizing field is switched on or off. Any current induced in the gradiometer circuit is limited to the induced voltage divided by the normal state resistance of the

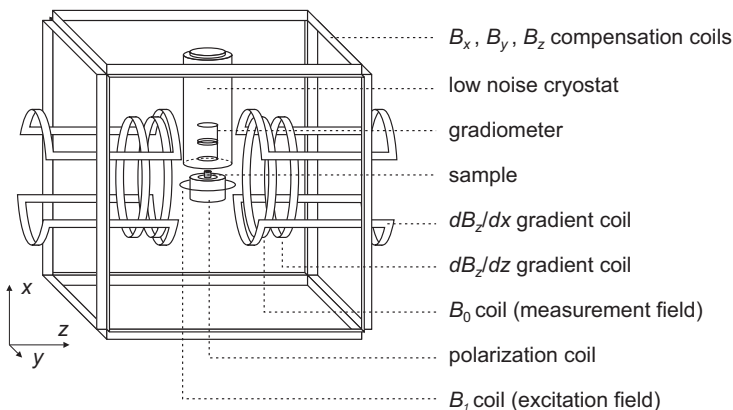


Fig. 8.47 Configuration of coils used to produce magnetic fields and magnetic field gradients for MRI. For clarity, the G_y coils are not shown. (Reproduced with permission from ref. [164].)

array. The magnetic field noise referred to the lowest loop of the gradiometer is $1.7 \text{ fT Hz}^{-1/2}$

There are various methods that can be used to obtain images [171]. An appropriate pulse sequence for two-dimensional (2D) imaging is shown in Figure 8.48. In the x -direction, the image is frequency encoded, that is, a gradient G_x produces a frequency variation $\omega = \gamma(B_0 + xG_x)$. In the y -direction, the image is phase encoded, that is, a gradient G_y produces a phase change $\Delta\phi = \gamma z G_y \tau_e$, where τ_e is the spin echo time. The data are subsequently decoded to reconstruct the image. Each complete pulse sequence involves one value of G_x and one value of G_y . The measurement field B_0 , about $100 \mu\text{T}$, is applied along the z -axis throughout the image acquisition. The pulse sequence begins with the application of the polarizing field along the x -axis for a time t_p several times longer than T_1 , so that the proton spins are fully polarized. This field is turned off adiabatically (that is, in a time long compared with the period of the NMR signal) so that the spins reorient to align with B_0 , retaining their initial polarization. After a predetermined delay time t_d a $\pi/2$ pulse is applied along the x -axis, causing the spins to precess about the z -axis. Shortly after, the frequency encoding and phase encoding gradients are switched on; these persist until the π pulse is applied to form the spin echo. The SQUID electronics is enabled shortly after the π pulse is complete, so that it is not saturated when the magnetic fields are switched. The entire sequence is repeated as necessary to improve the signal-to-noise ratio.

Figure 8.49 shows 2D images of two “phantoms,” both acquired in a measurement field of $132 \mu\text{T}$, corresponding to an NMR frequency of 5.6 kHz , and a magnetic field gradient of $200 \mu\text{T m}^{-1}$. In Figure 8.49(a), the phantom consisted of 13 columns of mineral oil contained in holes drilled in a block of plastic with diameters of 3.2, 6.3 and 9.6 mm [163]. In Figure 8.49(b), the phantom was a plastic grid placed in a shallow tray of water; the spatial resolution is 0.8 mm.

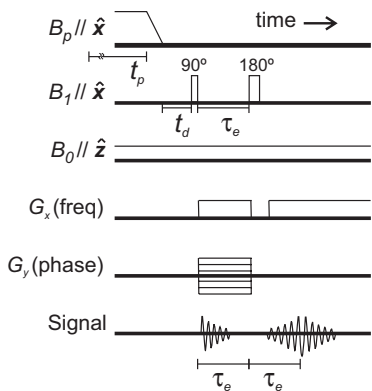


Fig. 8.48 Pulse sequence for two-dimensional imaging. (Reproduced with permission from ref. [172].)

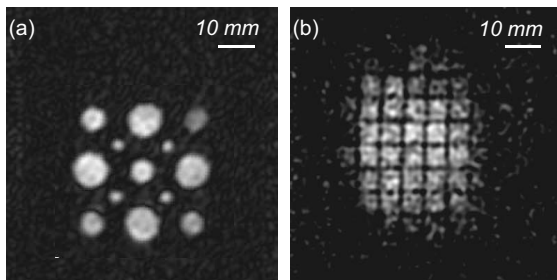


Fig. 8.49 Two-dimensional images of phantoms. (a) Plastic block with 13 holes with diameters of 3.2, 6.3 and 9.6 mm filled with mineral oil. (Reproduced with permission from ref. [163].) (b) Plastic grid placed in a shallow tray of water; the resolution is 0.8 mm. (Courtesy M. Hatridge, M. Mössle and W.R. Myers.)

In virtually all clinical applications, however, one requires three-dimensional images. The third dimension can be obtained by adding a second phase encoding gradient sequence G_z , simultaneously with G_y , to the 2D imaging sequence of Figure 8.48. Figure 8.50 shows six image slices obtained from an intact bell pepper, with a resolution of about 1 mm [172]. Figure 8.51 shows a 20-mm-thick image slice of a human forearm. For technical reasons, the polarizing field was reduced to 40 mT and the resolution is not as good as in the preceding images, about 3 mm [172]. Nonetheless, one clearly sees the bone marrow within the radius and ulna; the bone itself appears black because T_1 and T_2 are very short in solid material. A layer of subcutaneous fat is also visible.

Subsequently, Matlachov *et al.* [173] constructed a similar system and were able to observe the proton NMR signal at about 450 Hz from a live frog. Volegov *et al.* [174] fabricated a system with a first-order gradiometer and operated it in a magnetically shielded room. They were able to make simultaneous measurements of the proton NMR and magnetoencephalography (MEG) signals (see Chapter 11). To achieve these results, they first prepolarized the subject's cortex in a field of

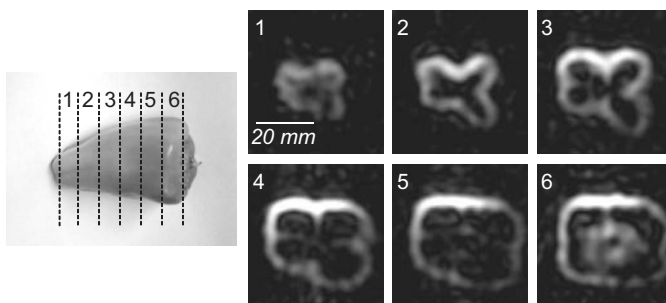


Fig. 8.50 Three-dimensional image of an intact pepper. The slices are made in software after the complete image has been acquired. (Reproduced with permission from ref. [172].)

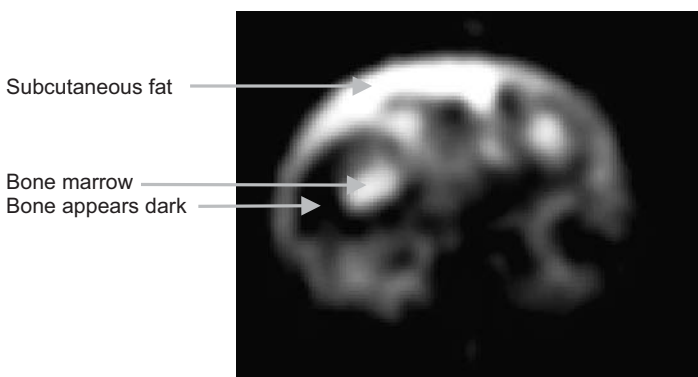


Fig. 8.51 Image of a forearm, 20-mm slice thickness. The polarizing field was 40 mT, the Larmor frequency was 5.6 kHz and the gradients were approximately $70 \mu\text{T m}^{-1}$. (Reproduced with permission from ref. [172].)

5 mT for 1.5 s. After the polarizing field was removed, the SQUID feedback loop was turned on after 10 ms and the median nerve of the subject was electrically stimulated after typically 100 ms. The free-induction decay of the protons at about 270 Hz and the MEG somatosensory response were measured simultaneously and then separated by means of filters. While these first experiments had no imaging capability, they demonstrate the feasibility of combining MEG and microtesla MRI capabilities into a single system. The ultimate goal of such a system would be to combine the fast temporal response of MEG with the high spatial resolution of the magnetic resonance image that is always required to interpret MEG signals. Another challenging possibility is the imaging of neural currents using microtesla MRI.

An important issue in MRI is the ability to distinguish two (or more) tissue types – for example, white and gray matter in the brain – even though the proton densities may be identical. This distinction can often be made if the values of T_1 in the two tissues are different; this technique is known as T_1 -weighted contrast

imaging. Low-field MRI can readily be adapted to this modality, and, as we shall see, has the important virtue of offering much higher contrast than high-field MRI in many situations.

Figure 8.52(a) shows a pulse sequence suitable for T_1 -weighted contrast imaging of two samples with the same values of T_1 in a relatively high field but different values in lower fields [175]. Both samples are fully magnetized in a polarizing field B_{p1} which is then reduced adiabatically to an intermediate value B_{p2} . The two magnetizations decay towards equilibrium at different rates in the intermediate field $B_{\text{int}} = (B_{p2}^2 + B_0^2)^{1/2}$; both B_{p2} and B_0 can be adjusted as necessary. In Figure 8.52(a), B_{p2} is reduced adiabatically to zero after a time t_{int} while B_0 is kept constant at 132 μT . Subsequently, a $\pi/2$ pulse is applied followed by an imaging sequence. The brightness of the image of a particular region depends on the value of the magnetization when the $\pi/2$ pulse is applied. As a demonstration, images were acquired of phantoms consisting of 0.25% and 0.50% solutions of agarose gel in water. Figure 8.53(a) shows the variation of the relaxation rate $1/T_1$ versus the intermediate magnetic field and Larmor frequency in which the spins were allowed to relax; for reference, the relaxation rate of protons in water has been included. We see immediately that while $1/T_1$ in water remains constant, in the two gel solutions the rates are almost identical at high field (above about 30 mT) but differ by a factor of two at low fields, below a few hundred microteslas. This striking difference is illustrated in the images of the two phantoms in Figures 8.53(b) and (c) obtained at intermediate field values of 10 μT and 300 mT, respectively. At 300 mT, the two phantoms are indistinguishable, whereas at 10 μT the 0.25% gel solution is much brighter than the 0.5% solution.

A somewhat simplified explanation of the differences in T_1 at high and low fields is as follows. The relaxation rate scales approximately as

$$1/T_1 \propto \langle B_{\text{loc}}^2 \rangle \times 2\tau_c / (1 + \omega_0^2 \tau_c^2) \quad (8.56)$$

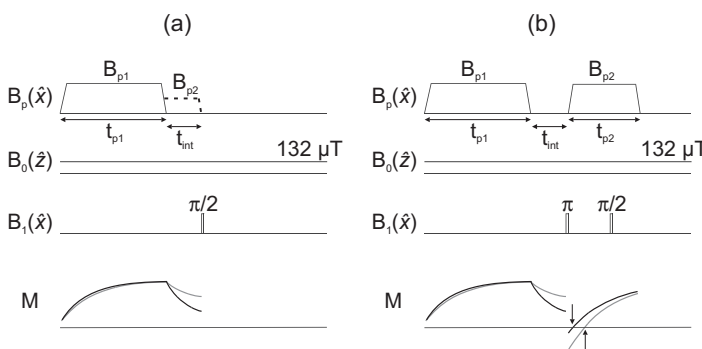


Fig. 8.52 Pulse sequences. (a) Pulse sequence for T_1 -weighted contrast imaging in an adjustable field with corresponding evolution of longitudinal magnetization (two values of T_1 are shown). (b) Field cycling

inversion recovery sequence. Magnetization evolutions are shown for two samples that have identical values of T_1 in B_{p1} and B_{p2} , but very different values in B_0 . (Reproduced with permission from ref. [175].)

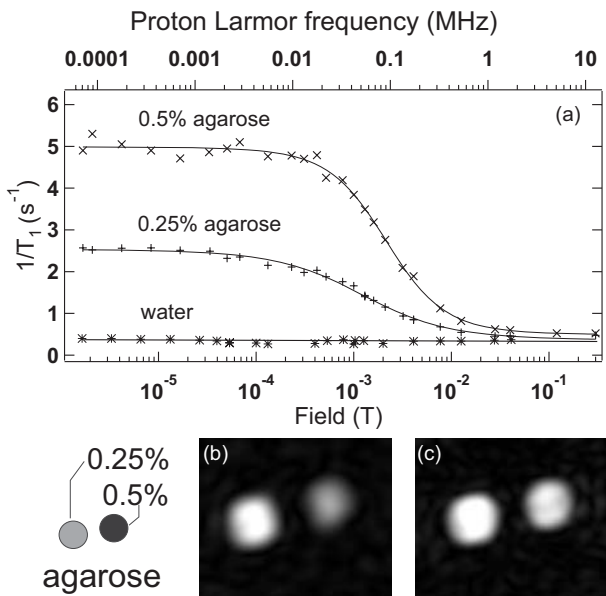


Fig. 8.53 Dependence of relaxation times on magnetic field for two different samples of agarose gel dissolved in water. Data and images were acquired using the pulse sequence of Figure 8.53(a). (a) $1/T_1$ versus magnetic field and Larmor frequency; for

comparison, the results for water are also shown. Images are of two glass tubes filled with the two different solutions, obtained for intermediate fields of (b) $10 \mu\text{T}$ and (c) 300 mT . (Reproduced with permission from ref. [175].)

where $\langle B_{\text{loc}}^2 \rangle$ is the mean square fluctuation in the local field and τ_c is a characteristic correlation time at which molecules rotate. For water, τ_c is of the order of picoseconds, $\omega_0 \tau_c \ll 1$ and $1/T_1$ is independent of frequency. However, in the gel solution, some fraction b of the water molecules is bound to cross-linked polymer chains, which are slow moving and have long correlation times of the order of $1 \mu\text{s}$, similar to those found in tissue. The overall relaxation rate is given by

$$1/T_1 = (1 - b)/T_{1f} + b/T_{1b} \quad (8.57)$$

where T_{1f} and T_{1b} are the relaxation times of free water and water bound to the gel. Thus, for the bound water, there is a marked increase in $1/T_1$ as the NMR frequency is lowered through a value of $1/2\pi\tau_c \sim 10^5 \text{ Hz}$. This is indeed the behavior observed in Figure 8.53(a).

A further refinement in enhancing the contrast of images of samples with different relaxation times is T_1 -inversion recovery [175]. The pulse sequence is shown in Figure 8.52(b). After the magnetizations of two different samples have decayed to different degrees in the intermediate field, a π -pulse inverts the spins and the polarizing field is reapplied. The spin populations recover towards their equilibrium values in this field, but in doing so they cross zero at different times. Thus, by

removing the polarizing field adiabatically at the appropriate value of t_{p2} for which the magnetization of one of the samples is zero and applying the imaging sequence, one observes no NMR signal from that sample. The results of applying this technique to three tubes containing water and 0.25% and 0.5% concentrations of agarose gel in water are shown in Figure 8.54. Evidently, any one of the three samples can be made to vanish by choosing t_{p2} appropriately.

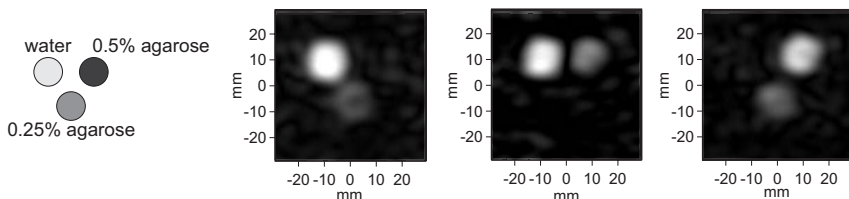


Fig. 8.54 Inversion recovery images of three glass tubes filled with water, 0.25% gel in water and 0.5% gel in water, using the pulse sequence of Figure 8.52(b). Each image was suppressed in turn by initiating the imaging sequence at the time when its magnetization was zero. (Reproduced with permission from ref. [175].)

As a final illustration of the enhanced T_1 -weighted contrast achievable at low fields, Figure 8.55(a) shows a phantom consisting of a tube of 0.5% agarose gel containing nine plastic straws filled with water. The inner diameter of the tubes ranges from 1 mm to 6 mm. Figure 8.55(b) shows an image of the phantom acquired with an intermediate field of 100 mT where the T_1 -values of water and gel are approximately 1.6 s and 1.5 s, respectively. The largest of the water columns is barely distinguished. In contrast, in the image acquired with an intermediate field of 132 μ T where $T_1 \approx 0.3$ s for gel, all nine straws are clearly visible. All these results indicate the potential of T_1 -weighted contrast imaging at low fields for distinguishing different tissue types in the human body, for example in screening for tumors.

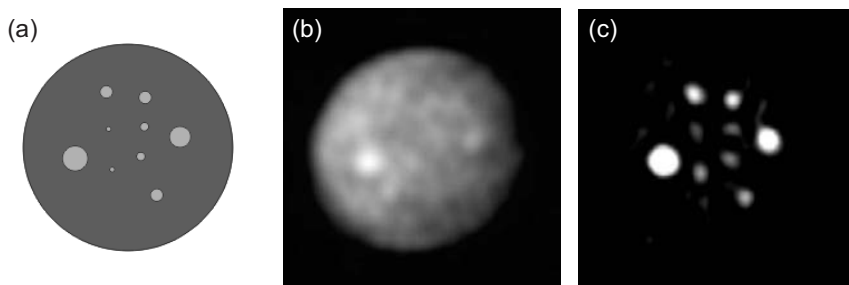


Fig. 8.55 Images of a phantom consisting of water columns in 0.50% agarose gel in water. (a) Schematic showing nine plastic straws with internal diameters ranging from 1 mm to 6 mm. Image obtained at an intermediate field of (b) 100 mT and (c) 132 μ T. (Courtesy M. Hatridge, M. Mössle and W.R. Myers.)

The NMR and MRI results described above involved spin prepolarization in a relatively high field and detection of the precessing spins in a very low field using an untuned magnetometer. In a prior approach, Seton and coworkers [176–182] used a SQUID with a tuned input circuit to acquire *in vivo* images, without the aid of prepolarization. The imaging field was 10 mT, corresponding to a Larmor frequency of 425 kHz. The 30-turn pickup coil was connected in series with a tuning capacitor, the input coil of the SQUID and an array of Josephson junctions that in this case acted as a “Q-spoiler” [170]. When an rf pulse was applied to initiate spin precession, the large current induced in the input circuit exceeded the critical current of the array, and the ensuing dissipation reduced Q to a low value. This technique enabled Seton and coworkers to achieve high Q -values – typically ~30,000 – with a very short recovery time after the rf pulse has been turned off. The SQUID was operated in a directly coupled, flux-locked loop [178] with additional positive feedback [183, 184] (see Chapter 4). For the imaging experiments, the bandwidth was enhanced to about 5 kHz by means of feedback inductively coupled to the inductor of the tuned circuit. The noise at the resonant frequency was extraordinarily low, $0.08 \text{ fT Hz}^{-1/2}$. This noise level is substantially lower than that of a conventional fiberglass dewar, typically $3\text{--}5 \text{ fT Hz}^{-1/2}$, and was achieved with the custom-made dewar [169] mentioned earlier. Seton and coworkers obtained good-quality images of phantoms consisting of columns of water.

To reduce noise picked up from the room-temperature coils supplying the imaging field, Seton and coworkers subsequently used a gradiometer to detect the NMR signal [182], and were thus able to image a human forearm.

It is interesting to compare the two approaches to MRI. The 425-kHz images demand a field homogeneity of about 2 ppm to achieve a 1-Hz linewidth. Although straightforward by the standards of high-field MRI, this homogeneity is more demanding than the 200 ppm required by the 5.6-kHz system. The sensitivity of the tuned magnetometer is roughly 30 times more than the untuned magnetometer, but this difference is offset by the much higher magnetization due to prepolarization which was used in the latter case.

8.6.4 Future Outlook

The prospects for low-frequency NQR, NMR and MRI based on SQUID detection are encouraging. Measurements of low-frequency NQR are relatively difficult with conventional detection but very straightforward with the aid of a SQUID (Figures 8.38 and 8.39). Such techniques are particularly useful when applied to peptides and amino acids as they provide powerful tools for structural determination. Low-frequency, broadband NMR spectroscopy enables one to investigate two or more nuclei simultaneously [162] and is a simple means of determining J -coupling (Figure 8.46). Since the splitting due to J -coupling is unique to a given chemical compound, this method could be used to detect the formation of certain substances, for example in the analysis of blood samples.

The largest impact of this technology, however, may be with low-field MRI, for which there would seem to be a number of potential clinical applications. One intriguing possibility is to integrate the required field and gradient coils with existing systems for MEG (Chapter 11). The large number of sensors means that the NMR signal could be averaged over many of them, thus improving the signal-to-noise ratio. Since the interpretation of MEG data inevitably requires a magnetic resonance image, the merging of the two SQUID-based technologies would enable one to acquire both sets of data during the same session and at potentially lower cost. An even more challenging potential application is the use of microtesla MRI to image neural currents in the brain.

The cost of a SQUID-based MRI system with, say, seven channels is likely to be appreciably lower than a conventional MRI system. A further advantage is that the SQUID system would be much more open than the conventional system, not only making it less confining for patients but also opening the possibility of using it during medical procedures. SQUID-based MRI could readily be configured to image limbs, for example to examine joints such as knees and elbows. Finally, as we have seen, the particular strengths of low-field MRI are its enhanced T_1 -weighted contrast and the ease with which low fields can be switched to different values for field cycling. This advantage could be exploited to screen for breast cancer, for example where the T_1 -contrast between tumors and healthy tissue is expected to be much higher than with high-field MRI. Furthermore, since imaging in low fields is much less sensitive to susceptibility variations within the sample than in high fields (the induced field gradient scales with the measurement field), one could hope to use it to guide a (nonmagnetic) metal needle for biopsy of breast or prostate tumors. Other possibilities include guiding cryosurgery of tumors, exploiting the temperature dependence of T_1 to monitor the temperature of a tumor during treatment with ultrasonic heating, and guiding the insertion of radioactive seeds into a tumor.

Needless to say, the introduction of these clinical techniques would require a great deal of system development, particularly with regard to lower noise sensors and suitable polarizing coils, but the result might well be significant improvements in healthcare at lower cost.

8.7

The Axion Detector

The original impetus for the development of the microstrip SQUID amplifier was the need for a lower-noise amplifier for the axion detector at Lawrence Livermore National Laboratory (LLNL), and we briefly describe this application [185].

There is overwhelming cosmological evidence that about 22% of the mass of the universe is cold dark matter (CDM); the corresponding density is 0.3–0.45 MeV mm^{−3}. Two leading contenders for CDM are the WIMP, which supersymmetry theories predict to have a mass of 10–100 GeV, and the axion. The axion was originally postulated to satisfy a requirement in particle theory. The upper

limit measured for the electric dipole moment on the neutron is 10^{11} smaller than the value expected from the Standard Model of particle physics. This result implies that CP conservation is vastly stronger than predicted. (Here, C is charge conjugation and P is parity inversion.) Peccei and Quinn [186] extended the Standard Model to suppress strong CP violation, and subsequently Weinberg [187] and Wilczek [188] independently postulated the axion – a neutral, spinless particle – to resolve the CP problem. It is predicted that the rest mass m_a of the axion lies between $1 \mu\text{eV}c^{-2}$ and $1 \text{ meV}c^{-2}$ (approximately 240 MHz and 240 GHz). For $m_a = 1 \mu\text{eV}c^{-2}$, the corresponding number density is $n_a = (3-4.5) \times 10^{11} \text{ mm}^{-3}$.

In 1983 Sikivie [189, 190] showed that in the presence of a high magnetic field the axion should undergo Primakoff conversion into a real photon, with energy equal to the rest mass of the axion, and a virtual photon. This prediction has led to the construction of an axion detector – intended to search for the real photon – at LLNL [185]. The detector consists of a cavity 1 m long and 0.6 m in diameter cooled to about 1.5 K in a magnetic field of 8 T. The cavity has a Q value of about 10^5 and can currently be tuned over the range 0.7–0.8 GHz. The output from the cavity is coupled into a cooled HEMT amplifier with a noise temperature of 1.7 K; thus the system noise temperature T_s is about 3.2 K. The goal of the experiment is to look for a signal above the blackbody noise of the cavity that would signify the presence of the photon produced by the decay of an axion. Since the axion energy is unknown, one must sweep the frequency of the cavity.

The expected signal is exceedingly small. The photon power generated in the cavity by the decay of the axions scales as $m_a n_a \times (\text{magnetic field})^2 \times (\text{cavity volume})$. There are two theories for the scaling coefficient, which involves the coupling strength of the axion to the two photons. The KSVZ (Kim–Shifman–Vainshtein–Zakharov) model [191, 192] yields a photon power $\delta P \approx 5 \times 10^{-22} \text{ W}$, while the DFSZ (Dine–Fischler–Srednicki–Zhitnitsky) model [193, 194], which leads to a weaker coupling, predicts $\delta P \approx 5 \times 10^{-23} \text{ W}$. To achieve the DFSZ limit with a signal-to-noise ratio (SNR) of 4, one can show that the frequency scan rate is given by

$$\frac{df}{dt} \approx (80 \text{ MHz/yr})(f/1 \text{ GHz})^2. \quad (8.58)$$

Equation (8.58) can be rewritten as $df/f^2 \approx 2.5 \times 10^{-18} dt$, where f is in hertz and t is in seconds. This result, in turn, can be integrated to find the time $\tau(f_1, f_2)$ to scan from a lower frequency f_1 to an upper frequency f_2 :

$$\tau(f_1, f_2) \approx 4 \times 10^{17} (1/f_1 - 1/f_2) \text{ s}. \quad (8.59)$$

For the frequency decade $f_1 = 0.24 \text{ GHz}$ to $f_2 = 2.4 \text{ GHz}$, one finds a scan time of about 45 years.

Fortunately, there is every reason to believe that this unrealistically long scan time can be drastically reduced. For a power detector with noise temperature T_s and bandwidth Δf , the Dicke radiometer equation [195] yields an integration time $\tau(f_1, f_2)$ given by

$$\text{SNR} = (\delta P / k_B T_s) [\tau(f_1 f_2) / \Delta f]^{1/2}. \quad (8.60)$$

Thus, for given values of SNR, δP and Δf , we see that $\tau(f_1 f_2) \propto T_s^2$. If one were to cool the cavity with a dilution refrigerator to (say) 50 mK while retaining the existing amplifier, the value of T_s would be reduced by a factor of about 2 and hence $\tau(f_1 f_2)$ would be shortened by a factor of about 4. However, if instead one were to cool the cavity to 50 mK and replace the HEMT amplifier with a microstrip SQUID amplifier, also cooled to 50 mK to produce a noise temperature of 50 mK, the system noise temperature would be reduced to 100 mK. Consequently, the scan time would be reduced from 45 years by a factor of $(3.2/0.1)^2$ to about 16 days! Thus, the potential impact of the microstrip SQUID on this important cosmological experiment is extraordinary, and would enable one to test the DFSZ limit over a decade of frequency in a very accessible time.

The LLNL detector is to be upgraded with a microstrip SQUID amplifier, while continuing to operate at 1.5 K, in the fall of 2006. If this feasibility test is successful, it is expected that funding will be provided to cool the detector with a dilution refrigerator, thus taking full advantage of the low noise temperature offered by the microstrip SQUID amplifier.

Acknowledgments

The authors thank Matt Dobbs, Stephan Friedrich and Caroline Kilbourne for suggesting improvements to this chapter. Figures and comments were provided by Jamie Bock, Blas Cabrera, Hsiao-Mei Cho, Randy Doriese, Michael Hatridge, Kent Irwin, Trevor Lanting, Jared Mehl, Michael Mössle, Mike Myers, Whit Myers, Carl Reintsema, Andy Smith, Helmuth Spieler and Joel Ullom.

This work was supported by the Director, Office of Science, Office of Basic Energy Sciences, Materials Sciences and Engineering Division (JC) and the Director, Office of Science, Office of High Energy and Nuclear Physics (ATL) of the US Department of Energy under contract number DE-AC02-05CH11231, by the National Science Foundation under grant number AST-0096933 (ATL and PLR), and by the National Aeronautics and Space Administration under grant number NAG5-11422 (ATL and PLR).

References

- 1 Clarke, J. (1996) A superconducting galvanometer employing Josephson tunneling, *Phil. Mag.* **13**, 115–127.
- 2 Clarke, J. (1969) Supercurrents in lead–copper–lead sandwiches, *Proc. Roy. Soc. A* **308**, 447–471.
- 3 Rumbo, E. (1969) Measurement of thermoelectric power at low temperatures, *Phil. Mag.* **13**, 689–691.
- 4 Pippard, A.B., Shepherd, J.G., Tindall, D.A. (1971) Resistance of superconductor-normal interfaces, *Proc. Roy. Soc. I A* **324**, 17–35.
- 5 Clarke, J. (1972) Experimental observation of pair-quasiparticle potential difference in nonequilibrium superconductors, *Phys. Rev. Lett.* **28**, 1363–1366.
- 6 Ketchen, M.B., Jaycox, J.M. (1982) Ultralow noise tunnel junction dc SQUID with a tightly coupled planar input coil, *Appl. Phys. Lett.* **40**, 736–738.
- 7 Polushkin, V., Drung, D., Koch, H. (1994) A broadband picovoltmeter based on the direct current superconducting quantum interference device with additional positive feedback, *Rev. Sci. Instrum.* **65**, 3005–3011.
- 8 Miklich, A.H., Koelle, D., Ludwig, F., Nemeth, D.T., Dantsker, E., Clarke, J. (1995) Picovoltmeter based on a high transition temperature SQUID, *Appl. Phys. Lett.* **66**, 230–232.
- 9 Eriksson, T., Blomgren, J., Winkler, D., Holst, T., Shen, Y.Q. (1999) A SQUID picovoltmeter working at 77 K, *IEEE Trans. Appl. Supercond.* **9**, 3495–3498.
- 10 Blomgren, J., Eriksson, T., Winkler, D. (2001) An HTS SQUID picovoltmeter with a flip-chip transformer, *IEEE Trans. Appl. Supercond.* **11**, 892–895.
- 11 Zimmerman, J.E. (1971) Sensitivity enhancement of superconducting quantum interference devices through the use of fractional-turn loops, *J. Appl. Phys.* **42**, 4483–4487.
- 12 Martinis, J.M., Clarke, J. (1985) Signal and noise theory for the dc SQUID, *J. Low Temp. Phys.* **61**, 227–236, and references therein.
- 13 Hilbert, C., Clarke, J. (1985) Measurements of the dynamic input impedance of a dc SQUID, *J. Low Temp. Phys.* **61**, 237–262.
- 14 Hilbert, C. and Clarke, J. (1985) DC SQUIDs as radiofrequency amplifiers, *J. Low Temp. Phys.* **61**, 263–280.
- 15 Tesche, C.D., Clarke, J. (1977) DC SQUID: noise and optimization, *J. Low Temp. Phys.* **27**, 301–331.
- 16 Tesche, C.D., Clarke, J. (1979) DC SQUID: current noise, *J. Low Temp. Phys.* **37**, 397–403.
- 17 Clarke, J., Tesche, C.D., Giffard, R.P. (1979) Optimization of dc SQUID voltmeter and magnetometer circuits, *J. Low Temp. Phys.* **37**, 405–419.
- 18 Koch, R.H. (1982) Ph.D. thesis, University of California, Berkeley.
- 19 Tesche, C.D. (1982) Optimization of dc SQUID linear amplifiers and the quantum noise limit, *Appl. Phys. Lett.* **41**, 490–492.
- 20 Tesche, C.D. (1983) Analysis of strong inductive coupling on SQUID systems, *IEEE Trans. Mag. MAG-19*, 458–460.
- 21 Stewart, W.C. (1968) Current-voltage characteristics of Josephson junctions, *Appl. Phys. Lett.* **12**, 277–280.
- 22 McCumber, D.E. (1968) Effect of ac impedance on dc voltage-current characteristics of Josephson junctions, *J. Appl. Phys.* **39**, 3113–3118.
- 23 Robinson, F.N.H. (1974) *Noise and Fluctuations in Electronic Devices and Circuits*. Oxford University Press.
- 24 Welty, R.P., Martinis, J.M. (1991) A series array of dc SQUIDS, *IEEE Trans. Magn.* **27**, 2924–2926.
- 25 Huber, M.E., Neil, P.A., Benson, R.G., Burns, D.A., Corey, A.M., Flynn, C.S., Kitaygorodskaya, Y., Massihzadeh, O., Martinis, J.M., Hilton, G.C. (2001) DC SQUID series array amplifiers with 120 MHz bandwidth, *IEEE Trans. Appl. Supercond.* **11**, 1251–1256.
- 26 Likharev, K.K., Semenov, V.K. (1972) Fluctuation spectrum in superconducting point junctions, *Pis'ma Zh. Eksp. Teor. Fiz.* **15**, 625–629.
- 27 Koch, R.H., Van Harlingen, D.J., Clarke, J. (1980) Quantum noise theory

- for the resistively shunted Josephson junction, *Phys. Rev. Lett.* **45**, 2132–2135.
- 28** Koch, R.H., Van Harlingen, D.J., Clarke, J. (1982) Measurements of quantum noise in resistively-shunted Josephson junctions, *Phys. Rev. B* **26**, 74–87.
- 29** Koch, R.H., Van Harlingen, D.J., Clarke, J. (1981) Quantum noise theory for the dc SQUID, *Appl. Phys. Lett.* **38**, 380–382.
- 30** Tarasov, M.A., Belitsky, V.Yu., Prokopenko, G.V. (1992) DC SQUID rf amplifiers, *IEEE Trans. Appl. Supercond.* **2**, 79–83.
- 31** Tarasov, M.A., Prokopenko, G.V., Koshelets, V.P., Lapitskaya, I.L., Filippenko, L.V. (1995) Integrated rf amplifier based on dc SQUID, *IEEE Trans. Appl. Supercond.* **5**, 3226–3229.
- 32** Prokopenko, G.V., Shitov, S.V., Koshelets, V.P., Balashov, D.B. (1997) A dc SQUID based low-noise 4-GHz amplifier, *IEEE Trans. Appl. Supercond.* **7**, 3496–3499.
- 33** Prokopenko, G.V., Balashov, D.V., Shitov, S.V., Koshelets, V.P. (1999) Two-stage S-band dc SQUID amplifier, *IEEE Trans. Appl. Supercond.* **9**, 2902–2905.
- 34** Prokopenko, G.V., Shitov, S.V., Balashov, D.V., Dmtriev, P.N., Koshelets, V.P., Mygind, J. (2001) Low-noise s-band dc SQUID based amplifier, *IEEE Trans. Appl. Supercond.* **11**, 1239–1242.
- 35** Prokopenko, G.V., Shitov, S.V., Mygind, J. (2002) A broadband dc SQUID based rf amplifier: experimental basics and development concept, *Physica* **372–376**, 229–232.
- 36** Mück, M., André, M–O., Clarke, J., Gail, J., Heiden, Ch. (1998) Radio frequency amplifier based on a niobium dc superconducting quantum interference device with microstrip input coupling, *Appl. Phys. Lett.* **72**, 2885–2887.
- 37** Ramo, S., Whinnery, J.R., van Duzer, T. (1965) *Fields and Waves in Communication Electronics* New York: J. Wiley & Sons.
- 38** Mück, M., Clarke, J. (2001) Flux-bias stabilization scheme for a radio-frequency amplifier based on a superconducting quantum interference device, *Rev. Sci. Instrum.* **72**, 3691–3693.
- 39** Mück, M., Welzel, C., Clarke, J. (2003) Superconducting quantum interference device amplifiers at gigahertz frequencies, *Appl. Phys. Lett.* **82**, 3266–3268.
- 40** Mück, M., Clarke, J. (2000) The superconducting quantum interference device microstrip amplifier: computer models, *J. Appl. Phys.* **88**, 6910–6918.
- 41** Mück, M., Clarke, J. (2001) Harmonic distortion and intermodulation products in the microstrip amplifier based on a superconducting quantum interference device, *Appl. Phys. Lett.* **78**, 3666–3668.
- 42** Mück, M., André, M–O., Clarke, J., Gail, J., Heiden, Ch. (1999) The microstrip superconducting quantum interference device rf amplifier: tuning and cascading, *Appl. Phys. Lett.* **75**, 3545–3547.
- 43** Bradley, R.F. (1999) Cryogenic, low-noise, balanced amplifiers for the 300–1200 MHz band using heterostructure field-effect transistors, *Nucl. Phys. B (Proc. Suppl.)* **72**, 137–144.
- 44** André, M–O., Mück, M., Clarke, J., Gail, J., Heiden, Ch. (1999) Microstrip dc superconducting quantum interference device radio-frequency amplifier with tenth-kelvin noise temperature, *Appl. Phys. Lett.* **75**, 698–700.
- 45** Mück, M., Kycia, J.B., Clarke, J. (2001) Superconducting quantum interference device as a near-quantum-limited amplifier at 0.5 GHz, *Appl. Phys. Lett.* **78**, 967–969.
- 46** Wellstood, F.C., Urbina, C., Clarke, J. (1994) Hot-electron effects in metals, *Phys. Rev. B* **49**, 5942–5955.
- 47** Tarasov, M.A., Kalabukhov, A.S., Snigirev, O.V., Krasnosvobodtsev, S.I., Stepansov, E.A. (1999) A radiofrequency dc SQUID amplifier with a microstrip input coil: simulations and experiment, *7th International Superconductive Electronics Conference Extended Abstracts*, pp. 540–542.
- 48** Tarasov, M.A., Snigirev, O.V., Kalabukhov, A.S., Krasnosvobodtsev, S.I., Stepansov, E.A. (1999) Design and fabrication of the high- T_c radiofrequency amplifier with the microstrip input coil based on bicrystal dc SQUIDS (EUCAS, Spain), *Inst. Phys. Conf. Ser.* **167**, 533–536.
- 49** Tarasov, M.A., Kalabukhov, A.S., Snigirev, O.V., Krasnosvobodtsev, S.I., Stepansov, E.A. (2000) UHF amplifier

- based on a high- T_c dc SQUID with a microstrip input coupler, *J. Commun. Technol. Electron.* **45**, 1147–1152.
- 50** Stepansov, E., Tarasov, M.A., Kalabukhov, A.S. (2002) Submicron YBCO Josephson junctions on sapphire bicrystal substrates for microwave devices, *Physica C* **372–376**, 76–79.
- 51** Schoelkopf, R.J., Wahlgren, P., Kozhevnikov, A.A., Delsing, P., Prober, D.E. (1998) The radio-frequency single-electron transistor (RF-SET): a fast and ultrasensitive electrometer, *Science* **280**, 1238–1242.
- 52** Devoret, M.H., Schoelkopf, R.J. (2000) Amplifying quantum signals with the single-electron transistor, *Nature* (London) **406**, 1039–1046.
- 53** Irwin, K.D. (1995) An application of electrothermal feedback for high resolution cryogenic particle detection, *Appl. Phys. Lett.* **66**, 1998–2000.
- 54** Lee, S.-F., Gildemeister, J. M., Holmes, W., Lee, A. T., Richards, P. L. (1998) Voltage-biased superconducting transition-edge bolometer with strong electrothermal feedback operated at 370 mK, *Appl. Optics* **37**, 3391–3397.
- 55** Irwin, K.D., Hilton, G.C., Wollman, D.A., Martinis, J.M. (1998) Thermal-response time of superconducting transition-edge microcalorimeters, *J. Appl. Phys.* **83**, 3978–3985.
- 56** Irwin, K.D., Hilton, G.C. (2005) Cryogenic particle detection, *Topics Appl. Phys.* **99**, 63–149.
- 57** Spieler, H. (2003) Frequency domain multiplexing for large-scale bolometer arrays, *Proc. Far-IR, Sub-mm & mm Detector Technology Workshop*, J. Wolf, J. Farhoond and C.R. McCreight (eds.), NASA/CP-211408, pp. 243–249.
- 58** Gildemeister, J.M., Lee, A.T., Richards, P.L. (2001) Model for excess noise in voltage-biased superconducting bolometers, *Appl. Optics* **40**, 6229–6235.
- 59** Bergmann Tiest, W.M., Hoevers, H.F.C., Mels, W.A., Ridder, M.L., Bruijn, M.P., de Korte, P.A.J., Huber M.E. (2002) Performance of X-ray microcalorimeters with an energy resolution below 4.5 eV and 100 μ s response time, *Proc. Low-Temperature Detectors IX*, F.S. Porter et al. (eds.), pp. 199–202.
- 60** Lindeman, M.A., Brekosky, R.P., Figueroa-Feliciano, E., Finkbeiner, F.M., Li, M., Stahle, C.K., Stahle, C.M., Tralsawala, N. (2002) Performance of Mo/Au TES microcalorimeters, *Proc. Low-Temperature Detectors IX*, F.S. Porter et al. (eds.), pp. 203–206.
- 61** Ullom, J.N., Doriese, W.B., Hilton, G.C., Beall, J.A., Deiker, S., Duncan, W.D., Ferreira, L., Irwin, K. D., Reintsema, C. D., Vale, L.R. (1999) Characterization and reduction of unexplained noise in superconducting transition-edge sensors, *Appl. Phys. Lett.* **84**, 4206–4208.
- 62** Kiviranta, M., Seppä, H., van der Kuur, J., de Korte, P. (2002) SQUID-based readout schemes for microcalorimeter arrays, *AIP Conf. Proc.* **605**, 295–300.
- 63** Karasik, B.S., McGrath, W.R. (2001) Novel multiplexing technique for detector and mixer arrays, *Proc. 12th Int. Symp. on Space Terahertz Technology*, Humphrey's Half Moon Inn, Shelter Island, San Diego, CA, pp. 336–345.
- 64** Irwin, K.D. (2002) Review: SQUID multiplexers for transition-edge sensors, *Physica C* **368**, 203–210.
- 65** Chervenak, J.A., Irwin, K.D., Grossman, E.N., Martinis, J.M., Reintsema, C.D., Huber, M.E. (1999) Superconducting multiplexer for arrays of transition edge sensors, *Appl. Phys. Lett.* **74**, 4043–4045.
- 66** Chervenak, J.A., Grossman, E.N., Irwin, K.D., Martinis, J.M., Reintsema, C.D. (2000) Performance of multiplexed SQUID readout for cryogenic sensor arrays, *Nucl. Instrum. Meth. A* **444**, 107–110.
- 67** de Korte, P.A.J., Beyer, J., Deiker, S., Hilton, G.C., Irwin, K.D., MacIntosh, M., Nam, S.W., Reintsema, C.D., Vale, L.R., Huber, M.E. (2003) Time-division superconducting quantum interference device multiplexer for transition-edge sensors, *Rev. Sci. Instrum.* **74**, 3807–3815.
- 68** Reintsema, C.D., Beyer, J., Nam, S.W., Deiker, S., Hilton, G.C., Irwin, K.D., Martinis, J.M., Ullom, J., Vale, L.R., MacIntosh, M. (2003) A prototype system for SQUID multiplexing of large-format transition-edge sensor arrays, *Rev. Sci. Instrum.* **74**, 4500–4580.

- 69** Yoon, J., Clarke, J., Gildemeister, J.M., Lee, A.T., Myers, M.J., Richards, P.L., Skidmore, J.T. (2001) Single superconducting quantum interference device multiplexer for arrays of low-temperature sensors, *Appl. Phys. Lett.* **78**, 371–373.
- 70** Cunningham, M.F., Ullom, J.N., Miyazaki, T., Labov, S.E., Clarke, J., Lanting, T.M., Lee, A.T., Richards, P.L., Yoon, J., Spieler, H. (2002) High-resolution operation of frequency-multiplexed transition-edge photon sensors, *Appl. Phys. Lett.* **81**, 159–161.
- 71** Lanting, T.M., Cho, H.-M., Clarke, J., Dobbs, M.A., Lee, A.T., Richards, P.L., Spieler, H., Smith, A. (2003) Frequency-domain multiplexing for large-scale bolometer arrays, *Proc. SPIE* **4855**, 172–181.
- 72** Lanting, T., Cho, H.-M., Clarke, J., Dobbs, M.A., Holzapfel, W., Lee, A.T., Lueker, M., Richards, P.L., Smith, A.D., Spieler, H., Tran, H. (2005) Frequency-domain multiplexed readout of transition-edge sensor arrays using a superconducting quantum interference device, *Appl. Phys. Lett.* **86**, 112511–1–3.
- 73** van der Kuur, J., Kampen, W. van, Bergmann Tiest, W.M., Bruijn, M.P., Hoevers, H.F.C., Mels, W.A., Weijs, L., de Korte, P.A.J. (2000) SQUID read-out concepts for imaging arrays of microcalorimeters, *Proc. 4th European Workshop on Low Temperature Electronics (WOLTE-4)*, Noordwijk, The Netherlands, ESA WPP-171, pp. 319–329.
- 74** van der Kuur, J., de Korte, P., Hoevers, H., Kiviranta, M., Seppä, H. (2002) Performance of an X-ray microcalorimeter under AC-biasing, *Appl. Phys. Lett.* **81**, 4467–4469.
- 75** Miyazaki, T., Yamazaki, M., Futamoto, K., Mitsuda, K., Fujimoto, R., Iyomoto, N., Oshima, T., Audley, D., Ishisaki, Y., Kagei, T., Ohashi, T., Yamasaki, N., Shoji, S., Kudo, H., Yokoyama, Y. (2002) AC calorimeter bridge; a new multi-pixel readout method for TES calorimeter arrays, *AIP Conf. Proc.* **605**, 313–316.
- 76** Irwin, K.D., and Lehnert, K.W. (2004) Microwave SQUID multiplexer, *Appl. Phys. Lett.* **85**, 2107–2109.
- 77** Hughes, D. H., Serjeant, S., Dunlop, J., Rowan-Robinson, M., Blain, A., Mann, R. G., Ivison, R., Peacock, J., Efstathiou, A., Gear, W., Oliver, S., Lawrence, A., Longair, M., Goldschmidt, P., Jenness, T. (1998) High-redshift star formation in the Hubble Deep Field revealed by a submillimetre-wavelength survey, *Nature* **394**, 241–247.
- 78** Barger, A. J., Cowie, L. L., Sanders, D. B., Fulton, E., Taniguchi, Y., Sato, Y., Kawara, K., Okuda, H. (1998) Submillimetre-wavelength detection of dusty star-forming galaxies at high redshift, *Nature* **394**, 248–251.
- 79** de Bernardis, P., Ade, P.A.R., Bock, J.J., Bond, J.R., Borrill, J., Boscaleri, A., Coble, K., Crill, B.P., De Gasperis, G., Farese, P.C., Ferreira, P.G., Ganga, K., Giacometti, M., Hivon, E., Hristov, V.V., Iacoangeli, A., Jaffe, A.H., Lange, A.E., Martinis, L., Masi, S., Mason, P.V., Mauskopf, P.D., Melchiorri, A., Miglio, L., Montroy, T., Netterfield, C.B., Pascale, E., Piacentini, F., Pogosyan, D., Prunet, S., Rao, S., Romeo, G., Ruhl, J.E., Scaramuzzi, F., Sforna, D., Vittorio, N. (2000) A flat Universe from high-resolution maps of the cosmic microwave background radiation, *Nature* **404**, 955–959.
- 80** Mauskopf, P.D., Ade, P.A.R., de Bernardis, P., Bock, J.J., Borrill, J., Boscaleri, A., Crill, B.P., DeGasperis, G., De Troia, G., Farese, P., Ferreira, P.G., Ganga, K., Giacometti, M., Hanany, S., Hristov, V.V., Iacoangeli, A., Jaffe, A.H., Lange, A. E., Lee, A.T., Masi, S., Melchiorri, A., Melchiorri, F., Miglio, L., Montroy, T., Netterfield, C.B., Pascale, E., Piacentini, F., Richards, P.L., Romeo, G., Ruhl, J.E., Scannapieco, E., Scaramuzzi, F., Stompor, R., Vittorio, N. (2000) Measurement of a peak in the cosmic microwave background power spectrum from the north american test flight of Boomerang, *Astrophys. J.* **536**, L59–L62.
- 81** Hanany, S., Ade, P., Balbi, A., Bock, J., Borrill, J., Boscaleri, A., de Bernardis, P., Ferreira, P.G., Hristov, V.V., Jaffe, A.H., Lange, A.E., Lee, A.T., Mauskopf, P.D., Netterfield, C.B., Oh, S., Pascale, E., Rabii, B., Richards, P.L.,

- Smoot, G.F., Stompor, R., Winant, C.D., Wu, J.H.P. (2000) MAXIMA-1: a measurement of the cosmic microwave background anisotropy on angular scales of $10' - 5^\circ$, *Astrophys. J.* **545**, L5–L9.
- 82** Lee, A.T., Ade, P., Balbi, A., Bock, J.J., Borrill, J., Boscaleri, A., de Bernardis, P., Ferreira, P.G., Hanany, S., Hristov, V.V., Jaffe, A.H., Mauskopf, P.D., Netterfield, C.B., Pascale, E., Rabii, B., Richards, P.L., Smoot, G.F., Stompor, R., Winant, C.D., Wu, J.H.P. (2001) A high spatial resolution analysis of the MAXIMA-1 cosmic microwave background anisotropy data, *Astrophys. J.* **561**, L1–L5.
- 83** Halverson, N.W., Leitch, E.M., Pryke, C., Kovac, J., Carlstrom, J.E., Holzapfel, W.L., Dragovan, M., Cartwright, J.K., Mason, B.S., Padin, S., Pearson, T.J., Readhead, A.C.S., Shepherd, M.C. (2002) Degree Angular Scale Interferometer first results: a measurement of the cosmic microwave background angular power spectrum, *Astrophys. J.* **568**, 38–45.
- 84** Netterfield, C.B., Ade, P.A.R., Bock, J.J., Bond, J.R., Borrill, J., Boscaleri, A., Coble, K., Contaldi, C.R., Crill, B.P., de Bernardis, P., Farese, P., Ganga, K., Giacometti, M., Hivon, E., Hristov, V.V., Iacoangeli, A., Jaffe, A.H., Jones, W.C., Lange, A.E., Martinis, L., Masi, S., Mason, P., Mauskopf, P.D., Melchiorri, A., Montroy, T., Pascale, E., Piacentini, F., Pogosyan, D., Pongetti, F., Prunet, S., Romeo, G., Ruhl, J.E., Scaramuzzi, F. (2002) A measurement by BOOMERANG of multiple peaks in the angular power spectrum of the cosmic microwave background, *Astrophys. J.* **571**, 604–614.
- 85** Bennett, C.L., Halpern, M., Hinshaw, G., Jarosik, N., Kogut, A., Limon, M., Meyer, S.S., Page, L., Spergel, D.N., Tucker G.S., Wollack, E., Wright, E.L., Barnes, C., Greason, M.R., Hill, R.S., Komatsu, E., Nolta, M.R., Odegard, N., Peirs, H.V., Verde, L., Weiland, J.L. (2003) First year Wilkinson microwave anisotropy probe (WMAP) observations: preliminary maps and basic results, *Astrophys. J. Suppl.*, **148**, 1–27.
- 86** Kinney, W.H. (1998) Constraining inflation with cosmic microwave background polarization, *Phys. Rev. D* **58**, 1–10.
- 87** Carlstrom, J.E., Holder, G.P., Reese, E.D. (2002) Cosmology with the Sunyaev-Zel'dovich Effect, *Ann. Rev. Astron. Astrophys.* **40**, 643–680.
- 88** Richards, P.L. (1994) Bolometers for infrared and millimeter waves, *J. Appl. Phys.* **76**, 1–24.
- 89** Rieke, G.H. (1994) *Detection of Light: From the Ultraviolet to the Submillimeter*, Cambridge University Press.
- 90** Bock, J.J., Chen, D., Mauskopf, P.D., and Lange, A.E. (1995) A novel bolometer for infrared and millimeter-wave astrophysics, *Space Sci. Rev.* **74**, 229–235.
- 91** Gildemeister, J.M., Lee, A.T., Richards, P.L. (1999) A fully lithographed voltage-biased superconducting spiderweb bolometer, *Appl. Phys. Lett.* **74**, 868–870.
- 92** Myers, M., Lee, A.T., Richards, P.L., Schwan, D., Skidmore, J.T., Smith, A.D., Spieler, H., Yoon, J. (2002) Antenna-coupled arrays of voltage-biased superconducting bolometers, *AIP Conf. Proc.* **605**, 247–250.
- 93** Myers, M., Lee, A.T., Engargiola, G., Holzapfel, W., Lee, A.T., O'Brient, R., Richards, P.L., Smith, A.D., Spieler, H., Tran, H. (2005) An antenna-coupled bolometer with integrated microstrip bandpass filter, *Appl. Phys. Lett.* **86**, 114103–1–3.
- 94** Chattopadhyay, G., Miller, D., LeDuc, H.G., Zmuidzinas, J. (2000) A dual polarized quasi-optical SIS Mixer at 550 GHz, *IEEE Trans. Microwave Theory Techn.* **48**, 1680–1686.
- 95** Goldin, A., Bock, J.J., Hunt, C., Lange, A.E., LeDuc, H., Vayonakis, A., Zmuidzinas, J. (2002) SAMBA: superconducting antenna-coupled, multi-frequency, bolometric array, *AIP Conf. Proc.* **605**, 251–254.
- 96** Gildemeister, J.M., Lee, A.T., Richards, P.L. (2000) Monolithic arrays of absorber-coupled voltage-biased superconducting bolometers, *Appl. Phys. Lett.* **77**, 4040–4042.
- 97** Agnese, P., Cigna, C., Pornin, J.-L., Accomo, R., Bonnin, C., Colombel, N.,

- Delcourt, M., Doumayrou, E., Lepenec, J., Martignac, J., Reveret, V., Rodriguez L., Vigroux, L.G. (2003) Filled bolometer arrays for Herschel/PACS, *Proc. SPIE* **4855**, 108–114.
- 98** Duncan, W., Holland, W.S., Audley, M.D., Cliffe, M., Hodson, T., Kelly, B.D., Gao, X., Gostick, D.C., MacIn-tosh, M., McGregor, H., Peacocke, T., Irwin, K. D., Hilton, G.C., Deiker, S.W., Beier, J., Reintsema, C.D., Walton, A.J., Parkes, W., Stevenson, T., Gundlach, A.M., Dunare, C., Ade, P.A.R (2003) SCUBA-2: developing the detectors, *Proc. SPIE* **4855**, 19–29.
- 99** Lee, A.T., Richards, P.L., Nam, S.W., Cabrera, B., Irwin, K.D. (1996) A superconducting bolometer with strong electrothermal feedback, *Appl. Phys. Lett.* **69**, 1801–1803.
- 100** Karasik, B.S., Sergeev, A.V., Gershenson, M.E. (2002) Electron–phonon relaxation in hot-electron detectors below 1K, *AIP Conf. Proc.* **605**, 75–78.
- 101** Stahle, C.K., McCammon, D., Irwin, K.D. (1999) Quantum calorimetry, *Phys. Today*, **52**, 32–37.
- 102** Paerels, F.B.S., Kahn, S.M. (2003) High-resolution X-ray spectroscopy with Chandra and XMM–Newton, *Ann. Rev. Astron. Astrophys.* **41**, 291–342.
- 103** Cabrera, B., Clarke, R.M., Colling, P., Miller, A.J., Nam, S., Romani, R.W. (1998) Detection of single infrared, optical, and ultraviolet photons using superconducting transition edge sensors, *Appl. Phys. Lett.* **73**, 735–737.
- 104** Hellmig, J., Gaitskell, R., Abusaidi, R.A., Cabrera, B., Clarke, R.M., Emes, J., Nam, S.W., Saab, T., Sadoulet, B., Seitz, D., Young, B.A. (1999) CDMS II Z-sensitive ionization and phonon germanium detector, *Proc. VIII International Workshop on Low Temperature Detectors*, Dalfsen, The Netherlands, pp. 308–312.
- 105** Booth, N.E., Cabrera, B., Fiorini, E. (1996) Low-temperature particle detectors, *Ann. Rev. Nucl. Part. Sci.* **46**, 471–532.
- 106** Wollman, D.A., Hilton, G.C., Irwin, K.D., Bergren, N.F., Rudman, D.A., Newbury, D.E., Martinis, J.M. (1999) Cryogenic microcalorimeters for X-ray microanalysis, *Proc. 1999 NCSL Workshop and Symposium (National Conference of Standards Laboratories)*, pp. 811–819.
- 107** Rabin, M. W., Hilton, G. C., Martinis, J.M. (2001) Application of microcalorimeter energy measurement to biopolymer mass spectrometry, *IEEE Trans. Appl. Supercond.* **11**, 242–247.
- 108** Irwin, K.D., Hilton, G.C., Martinis, J.M., Deiker, S., Bergren, N.F., Nam, S.W., Rudman, D.A., Wollman, D.A. (2000) A Mo–Cu superconducting transition–edge microcalorimeter with 4.5 eV energy resolution at 6 keV, *Nucl. Instrum. Meth. Phys. Res.* **444**, 184–187.
- 109** Kent Irwin, NIST, private communication.
- 110** Chervenak, J.A., Finkbeiner, F.M., Stevenson, T.R., Tally, D.J., Brekosky, R.P., Bandler, S.R., Figueroa–Feliciano, E., Lindeman, M.A., Kelley, R.L., Saab, T., Stahle, C.K. (2004) Fabrication of transition edge sensor X-ray microcalorimeters for Constellation–X, *Nucl. Instrum. Meth. Phys. Res. A* **520**, 460–462.
- 111** Irwin, K.D., Hilton, G.C., Wollman, D.A., Martinis, J.M. (1996) X-ray detection using a superconducting transition–edge sensor microcalorimeter with electrothermal feedback, *Appl. Phys. Lett.* **69**, 1945–1947.
- 112** Enss, C., Fleischmann, A., Horst, K., Schonefeld, J., Sollner, J., Adams, J.S., Huang, Y.H., Kim, Y.H., Seidel, G.M. (2000) Metallic magnetic calorimeters for particle detection, *J. Low Temp. Phys.* **121**, 137–176.
- 113** Fleischmann, A., Link, M., Daniyarov, T., Rotzinger, H., Enss, C., Seidel G.M., (2004) Metallic magnetic calorimeters (MMC): detectors for high–resolution x-ray spectroscopy, *Nucl. Instrum. Meth. Phys. Res. A* **520**, 27–31.
- 114** Mears, C.A., Labov S.E., Frank, M., Netel, H., Hiller L.J., Lindeman M.A., Chow D., Barfknecht A.T. (1997) High-resolution superconducting X-ray spectrometers with an active area of 282 $\mu\text{m} \times 282 \mu\text{m}$, *IEEE Trans. Appl. Supercond.* **7**, 3415–3418.
- 115** Peacock, T., Verhoeve, P., Rando, N., Erd, C., Bavdaz, M., Taylor, B.G., Per-

- ez, D. (1998) Recent developments in superconducting tunnel junctions for ultraviolet, optical and near infrared astronomy, *Astron. Astrophys. Suppl.* **127**, 497–504.
- 116** Ullom, J.N. (2002) Physics and applications of NIS junctions, *AIP Conf. Proc.* **605**, 135–140.
- 117** Nahum, M., Martinis, J.M. (1993) Ultra-sensitive–hot–electron microbolometer, *Appl. Phys. Lett.* **63**, 3075–3077.
- 118** McDonald, D.G. (1987) Novel superconducting thermometer for bolometric applications, *Appl. Phys. Lett.* **50**, 775–777.
- 119** Mazin, B.A., Day, P.K., LeDuc, H.G., Vayonakis, A., Zmuidzinas, J. (2002) Superconducting kinetic inductance photon detectors, *Proc. SPIE* **4849**, 283–293.
- 120** Greenberg, Ya. S. (1998) Application of superconducting quantum interference devices to nuclear magnetic resonance, *Rev. Mod. Phys.* **70**, 175–222.
- 121** Abragam, A. (1961) *The Principles of Nuclear Magnetism*, Oxford: Clarendon Press.
- 122** Slichter, C.P. (1989) *Principles of Magnetic Resonance*, 3rd edition, New York: Springer.
- 123** Kittel, C., Kroemer, H. (1980) *Thermal Physics*, 2nd edition, San Francisco: W.H. Freeman.
- 124** Hahn, E.L. (1950) Spin echoes, *Phys. Rev.* **80**, 580–594.
- 125** Das, T.P., Hahn, E.L. (1958) *Nuclear Quadrupole Resonance Spectroscopy*, New York: Academic Press.
- 126** Huiku, M.T., Loponen, M.T. (1982) Observation of a magnetic phase transition in the nuclear spin system of metallic copper at nanokelvin temperatures, *Phys. Rev. Lett.* **49**, 1288–1291.
- 127** Huiku, M.T., Loponen, M.T. (1983) Experimental curve of entropy and susceptibility versus temperature for copper nuclear spin down to the ordered state, *Phys. Rev. Lett.* **50**, 1516–1519.
- 128** Webb, R.A. (1977) Measurements of difference between the dynamic NMR and static susceptibility of superfluid He–B using a rf SQUID, *Phys. Rev. Lett.* **38**, 1151–1155.
- 129** Webb, R.A. (1977) Ferromagnetic resonance behavior in superfluid ^3He –B, *Phys. Rev. Lett.* **39**, 1008–1011.
- 130** Friedman, L.J., Thomson, A.L., Gould, C.M., Bozler, H.M., Weichman, P.B., Cross, M.C. (1989) Zero-field magnetic order in the boundary layers of ^3He on grafoil, *Phys. Rev. Lett.* **62**, 1635–1638.
- 131** Black, B., Majer, G., Pines, A. (1993) SQUID NMR study of methyl quantum tunneling in a series of carboxylic acids, *Chem. Rev. Lett.* **201**, 550–554.
- 132** Narasimhan, L.R., Takigawa, M., Ketchen, M.B. (1994) Magnetic resonance of a small platinum particle using an integrated dc SQUID, *Appl. Phys. Lett.* **65**, 1305–1307.
- 133** Gallop, J.C., Radcliffe, W.J. (1978) Cryogenic free precession He magnetometer using a SQUID, *J. Phys. D.* **11**, L203–L206.
- 134** Hirschkoff, E.C., Symko, O.G., Vant-Hull, L.L., Wheatley, J.C. (1970) Observation of the static nuclear magnetism of pure metallic copper in low magnetic fields, *J. Low Temp. Phys.* **2**, 653–665.
- 135** Day, E.P. (1972) Detection of NMR using a Josephson junction magnetometer, *Phys. Rev. Lett.* **29**, 540–542.
- 136** Connor, C., Chang, J., Pines, A. (1990) Magnetic resonance spectrometer with a dc SQUID detector, *Rev. Sci. Instrum.* **61** 1059–1063.
- 137** Connor, C., Chang, J., Pines, A. (1990) Aluminum and boron nuclear quadrupole resonance with a dc SQUID, *J. Chem. Phys.* **93** 7639–7646.
- 138** Yesinowski, J.P., Buess, M.L., Garroway, A.N., Ziegeweid, M., Pines, A. (1995) Detection of ^{14}N and ^{35}Cl in cocaine base and hydrochloride using NQR, NMR, and SQUID techniques, *Anal. Chem.* **67**, 2256–2263.
- 139** Augustine, M.P., TonThat, D.M., Clarke, J. (1998) SQUID detected NMR and NQR, *Solid State NMR* **11**, 139–156.
- 140** Hürlimann, M.D., Pennington, C.H., Fan, N.Q., Clarke, J., Pines, A., Hahn, E.L. (1992) Pulsed Fourier–transform NQR of ^{14}N with a dc SQUID, *Phys. Rev. Lett.* **69**, 684–687.
- 141** Sleator, T., Hahn, E.L., Hilbert, C., Clarke, J. (1985) Nuclear spin noise, *Phys. Rev. Lett.* **55**, 1742–1745.

- 142** Sleator, T., Hahn, E.L., Hilbert, C., Clarke, J. (1987) Nuclear spin noise and spontaneous emission, *Phys. Rev. B* **36**, 1969–1980.
- 143** Happer, W. (1972) Optical pumping, *Rev. Mod. Phys.* **44**, 169–188.
- 144** Albert, M.S., Cates, G.D., Driehuys, B., Happer, W., Saam, B., Springer, C. S., Wishnia, A. (1994) Biological magnetic resonance imaging using laser-polarized ^{129}Xe , *Nature* **370**, 199–201.
- 145** Middleton, H., Black, R.D., Saam, B., Cates, G.D., Cofer, G.P., Guenther, R., Happer, W., Hedlund, L.W., Johnson, G.A., Juvan, K., Swartz, J. (1995) MR imaging with hyperpolarized ^3He gas, *J. Magn. Reson. Med.* **33**, 271–275.
- 146** Sakai, K., Bilek, A.M., Oteiza, E., Walsworth, R.L., Balamore, D., Jolesz, F.A., Albert, M.S. (1996) Temporal dynamics of hyperpolarized ^{129}Xe resonances in living rats, *J. Mag. Res. B* **111**, 300–304.
- 147** Navon, G., Song, Y.-Q., Room, T., Appelt, S., Taylor, R.E., Pines, A. (1996) Enhancement of solution NMR and MRI with laser-polarized xenon, *Science* **271**, 1848–1851.
- 148** Bifone, A., Song, Y.-Q., Seydoux, R., Taylor, R.E., Goodson, B.M., Pietrass, T., Budinger, T.F., Navon, G., Pines, A. (1996) NMR of laser-polarized xenon in human blood, *Proc. Natl. Acad. Sci.* **93**, 12932–12936.
- 149** Room, T., Appelt, S., Seydoux, R., Hahn, E.L., Pines, A. (1999) Enhancement of surface NMR by laser-polarized noble gases, *Phys. Rev. B* **59**, 1157–1161.
- 150** Gatzke, M., Cates, G.D., Driehuys, B., Fox, D., Happer, W., Saam, B. (1993) Extraordinarily slow nuclear spin relaxation in frozen laser-polarized ^{129}Xe , *Phys. Rev. Lett.* **70**, 690–693.
- 151** TonThat, D.M., Ziegeweid, M., Song, Y.-Q., Munson, E.J., Appelt, S., Pines, A., Clarke, J. (1997) SQUID detected NMR of laser-polarized xenon at 4.2 K and at frequencies down to 200 Hz, *Chem. Phys. Lett.* **272**, 245–249.
- 152** Augustine, M.P., Zilm, K.W. (1996) Optical pumping magnetic resonance in high magnetic fields: characterization of nuclear relaxation during pumping, *J. Chem. Phys.* **105**, 2998–3011.
- 153** Augustine, M.P., Wong-Foy, A., Yarger, J.L., Tomaselli, M., Pines, A., TonThat, D.M., Clarke, J. (1998) Low field magnetic resonance images of polarized noble gases obtained with a dc superconducting quantum interference device, *Appl. Phys. Lett.* **72**, 1908–1910.
- 154** Wong-Foy, A., Saxena, S., Moulé, A.J., Bitter, H.-M.L., Seeley, J.A., McDermott, R., Clarke, J., Pines, A. (2002) Laser polarized ^{129}Xe NMR and MRI at ultralow magnetic fields, *J. Magn. Res.* **157**, 235–241.
- 155** Saxena, S., Wong-Foy, A., Moule, A.J., Seeley, J.A., McDermott, R., Clarke, J., Pines, A. (2001) Resolution of ^{129}Xe chemical shifts at ultralow magnetic field, *J. Am. Chem. Soc.* **123**, 8133–8134.
- 156** Abragam, A. (1982) *Order and Disorder*, Oxford: Clarendon Press.
- 157** Happer, W., Miron, E., Schaefer, S., Schreiber, D., van Wijngaarden, W.A., Zeng, X. (1984) Polarization of the nuclear spins of noble-gas atoms by spin exchange with optically pumped alkali-metal atoms, *Phys. Rev. A* **29**, 3092–3110.
- 158** Packard, M., Varian, R. (1954) Free nuclear induction in the earth's magnetic field, *Phys. Rev.* **93**, 941–941.
- 159** Kumar, S., Thorson, B.D., Avrin, W.F. (1995) Broadband SQUID NMR with room temperature samples, *J. Magn. Reson., Ser. B* **107**, 252–259.
- 160** Kumar, S., Avrin, W.F., Whitecotton, B.R. (1996) NMR of room temperature samples with a flux-locked dc SQUID, *IEEE. Trans. Magn.*, **32**, 5261–5264.
- 161** Schlenge, K., McDermott, R., Clarke, J., de Souza, R.E., Wong-Foy, A., Pines, A. (1999) Low-field magnetic resonance imaging with a high- T_c superconducting quantum interference device, *Appl. Phys. Lett.* **75**, 3695–3697.
- 162** McDermott, R., Trabesinger, A.H., Mück, M., Hahn, E.L., Pines, A., Clarke, J. (2002) Liquid state NMR and scalar couplings in microtesla magnetic fields, *Science* **295**, 2247–2249.
- 163** McDermott, R., Lee, S.-K., ten Haken, B., Trabesinger, A.H., Pines, A., Clarke, J. (2004) Microtesla magnetic resonance imaging with a Superconducting QUan-

- tum Interference Device, *Proc. Natl. Acad. Sci.* **101**, 7857–7861.
- 164** McDermott, R., Kelso, N., Lee, S.-K., Mössle, M., Mück, M., Myers, W., ten Haken, B., Seton, H.C., Trabesinger, A.H., Pines, A., Clarke, J. (2004) SQUID-detected magnetic resonance imaging in microtesla magnetic fields, *J. Low Temp. Phys.* **135**, 793–821.
- 165** Trabesinger, A.H., McDermott, R., Lee, S.-K., Mück, M., Clarke, J., Pines, A. (2004) SQUID-detected liquid state NMR in microtesla fields, *J. Phys. Chem. A* **108**, 957–963.
- 166** Burghoff, M., Hartwig, S., Trahms, L., Bernardino, J. (2005) Nuclear magnetic resonance in the nanoTesla range, *Appl. Phys. Lett.* **87**, 054103–1–3.
- 167** Erné, S.N., Hahlbohm, H.D., Scheer, J., Trontelj, Z. (1981) The Berlin magnetically shielded room (BMSR), in *Biomagnetism*, S.N. Erné, H.D. Hahlbohm, and H. Lübbig (eds.), Berlin, W. de Gruyter, pp. 79–87.
- 168** Bottomley, P.A. (1981) A versatile magnetic-field gradient control-system for NMR imaging, *J. Phys. E. Sci. Instrum.* **14**, 1081–1087.
- 169** Seton, H.C., Hutchison, J.M.S., Bussell, D.M. (2005) Liquid helium cryostat for SQUID-based MRI receivers, *Cryogenics* **45**, 348–355.
- 170** Hilbert, C., Clarke, J., Sleator, T., Hahn, E.L. (1985) Nuclear quadrupole resonance detected at 30 MHz with a dc SQUID, *Appl. Phys. Lett.* **47**, 637–639.
- 171** Haacke, E.M., Brown, R.W., Thompson, M.R., Venkatesan, R. (1999) *Magnetic Resonance Imaging: Physical Principles and Sequence Design*, New York: J. Wiley & Sons.
- 172** Mössle, M., Myers, W.R., Lee, S.-K., Kelso, N., Hatridge, M., Pines, A., Clarke, J. (2005) SQUID-detected *in vivo* MRI at microtesla magnetic fields, *IEEE Trans. Appl. Supercond.* **15**, 757–760.
- 173** Matlachov, A.N., Volegov, P.L., Espy, M.A., George, J.S., Kraus Jr., R.H. (2004) SQUID detected NMR in microtesla magnetic fields, *J. Magn. Reson.* **170**, 1–7.
- 174** Volegov, P.L., Matlachov, A.N., Espy, M.A., George, J.S., Kraus Jr., R.H. (2004) Simultaneous magnetoencepha-
- lography and SQUID detected NMR in microtesla magnetic fields, *Magn. Reson. Med.* **52**, 467–470.
- 175** Lee, S.-K., Mössle, M., Myers, W., Kelso, N., Trabesinger, A.H., Pines, A., Clarke, J. (2005) SQUID-detected MRI at 132 µT with T_1 contrast weighted at 10 µT–300 mT, *Magn. Reson. Med.* **53**, 9–14.
- 176** Seton, H.C., Bussell, D.M., Hutchison, J.M.S., Nicholson, I., Lurie, D.J. (1992) DC SQUID based NMR detection from room temperature samples, *Phys. Med. Biol.* **37**, 2133–2138.
- 177** Seton, H.C., Bussell, D.M., Hutchison, J.M.S., Lurie, D.J. (1995) Use of dc SQUID receiver preamplifier in a low field MRI system, *IEEE. Trans. Appl. Supercond.* **5**, 3218–3221.
- 178** Seton, H.C., Bussell, D.M., Hutchison, J.M.S. (1995) A dc SQUID rf amplifier used in low field MRI system, in *Proc. 2nd European Conference on Applied Superconductivity*, D. Dew-Hughes (ed.), Bristol: IOP, pp. 1487–1490.
- 179** Seton, H.C., Bussell, D.M., Hutchison, J.M.S. (1995) A liquid helium cooled rf coil and SQUID amplifier for MRI at 0.01 T, *Proc. Soc. Magn. Res.* **2**, 959.
- 180** Seton, H.C., Bussell, D.M., Hutchison, J.M.S. (1997) A tuned SQUID amplifier for MRI based on a DOIT flux locked loop, *IEEE Trans. Appl. Supercond.* **7**, 3213–3216.
- 181** Seton, H.C., Hutchison, J.M.S., Bussell, D.M., (1997) A 4.2-K receiver coil and SQUID amplifier used to improve the SNR of low field magnetic resonance images of the human arm, *Meas. Sci. Technol.* **8**, 198–207.
- 182** Seton, H.C., Hutchison, J.M.S., Bussell, D.M., (1999) Gradiometer pick-up coil design for a low field SQUID-MRI system, *MAGMA* **8**, 116–120.
- 183** Drung, D., Cantor, R., Peters, M., Scheer, H. J., Koch, H. (1990) Low noise high speed dc SQUID magnetometer with simplified feedback electronics, *Appl. Phys. Lett.* **57**, 406–408.
- 184** Drung, D., Matz, H., Koch, H. (1995) A 5 MHz bandwidth magnetometer with additional positive feedback, *Rev. Sci. Instrum.* **66**, 3008–3015.

- 185 Bradley, R., Clarke, J., Kinion, D., Rosenberg, L.J., van Bibber, K., Matsuki, S., Mück, M., Sikivie, P. (2003) Micro-wave cavity searches for dark-matter axions, *Rev. Mod. Phys.* **75**, 777–817.
- 186 Peccei, R. and Quinn, H. (1977) CP conservation in the presence of pseudoparticles, *Phys. Rev. Lett.* **38**, 1440–1443.
- 187 Weinberg, S. (1978) A new light boson?, *Phys. Rev. Lett.* **40**, 223–226.
- 188 Wilczek, F. (1978) Problem of strong P- and T-invariance in the presence of instantons, *Phys. Rev. Lett.* **40**, 279–282.
- 189 Sikivie, P. (1983) Experimental tests of the ‘invisible’ axion, *Phys. Rev. Lett.* **51**, 1415–1417.
- 190 Sikivie, P. (1985) Detection rates for ‘invisible’-axion searches, *Phys. Rev. D* **32**, 2988–2991.
- 191 Kim, J.E. (1979) Weak-interaction singlet and strong CP invariance, *Phys. Rev. Lett.* **43**, 103–107.
- 192 Shifman, M.A., Vainshtein, A.I., Zakharov, V.I. (1980) Can confinement ensure natural CP invariance of strong interactions?, *Nucl. Phys. B* **166**, 493–506.
- 193 Dine, M., Fischler, W., Srednicki, M., (1981) A simple solution to the strong CP problem with a harmless axion, *Phys. Lett. B* **104**, 199–202.
- 194 Zhitnitsky, A.P.(1980) On the possible suppression of axion–hadron interactions, (1980) *Yad. Fiz.* **31**, 497 [*Sov. J. Nucl. Phys.* **31**, 260–263].
- 195 Dicke, R.H. (1946) The measurement of thermal radiation at microwave frequencies, *Rev. Sci. Instrum.* **17**, 268–275.

9**SQUIDs for Standards and Metrology***John Gallop and François Piquemal*

| | | |
|---------|---|-----|
| 9.1 | Introduction | 96 |
| 9.2 | SQUIDS in Voltage Metrology | 97 |
| 9.2.1 | SQUID Femtovoltmeter: Highly Accurate Voltage Measurement | 97 |
| 9.2.1.1 | Principle | 97 |
| 9.2.1.2 | Femtovoltmeter for Verifying the Universality of Josephson Constant | 98 |
| 9.2.2 | SQUID Ampermeter for linking the Volt to Mechanical SI Units | 98 |
| 9.2.3 | Other Precise SQUID-Based Voltage Measurements | 100 |
| 9.3 | Cryogenic Current Comparator (CCC) | 101 |
| 9.3.1 | Principle of the CCC | 101 |
| 9.3.2 | Limits to Accuracy of CCC Ratio Measurements | 104 |
| 9.3.2.1 | Sensitivity and Current Resolution | 104 |
| 9.3.2.2 | Exactness of the CCC Current Ratio | 108 |
| 9.3.3 | Resistance Ratio Measurement | 111 |
| 9.3.3.1 | Introductory | 111 |
| 9.3.3.2 | Resistance Bridge Based on Type I CCC | 113 |
| 9.3.3.3 | Some Remarks on Construction | 114 |
| 9.3.4 | Measurements of Very Low Currents from SET Sources | 115 |
| 9.3.4.1 | Introduction | 115 |
| 9.3.4.2 | Design and Performance of the CCC as an Ultra-Low-Current Amplifier | 118 |
| 9.3.4.3 | Measurements of SET Current Sources | 119 |
| 9.3.5 | Type II CCC for Resistance Measurements at Very High Currents | 121 |
| 9.3.6 | CCC for Non-Invasive Sensing of Charged Particle Beams | 122 |
| 9.4 | Other Current Metrological Applications of SQUIDS | 123 |
| 9.4.1 | Thermometry Using SQUIDS | 123 |
| 9.4.1.1 | Introduction | 123 |
| 9.4.1.2 | Magnetic Susceptibility Measurement for a Secondary Thermometer | 124 |
| 9.4.1.3 | The SQUID as a Sensor for a Resistance Thermometer | 125 |
| 9.4.1.4 | Noise Measurement for a “Primary” Thermometer | 125 |
| 9.4.2 | Radio-Frequency Attenuation with SQUIDS | 127 |
| 9.5 | Future Trends and Conclusion | 129 |

9.1

Introduction

Metrology is the science of precise measurement. SQUIDS, combining the two properties of extraordinary sensitivity together with a periodic response to an input signal which is based on a quantum standard (the flux quantum $\Phi_0 = h/2e$), are particularly well suited for metrology applications, and especially for quantum electrical metrology. As simple as a superconducting ring interrupted by one or two Josephson junctions, the working principle of SQUID is based on double quantum phenomena both involving the same quantum Φ_0 : the quantization of magnetic flux across the ring and the oscillation of the supercurrent circulating across the junction. The first metrological use of the SQUID as a voltmeter (a null detector in the sub-femtovolt range) for testing the universality of the current–phase relationship of a Josephson junction hardly comes as a surprise (see Section 8.2). The second important application of the SQUID in metrology is its use as a magnetic flux detector combined with a marvellous tool: the cryogenic current comparator (CCC). This is the instrument used in a resistance bridge which has allowed National Metrology Institutes (NMIs) to establish the high reproducibility of the quantum resistance standard based on the quantum Hall effect (QHE) (see Section 9.3.3). The CCC can also operate as an ultra low current amplifier with a very highly accurate gain. CCCs have been developed for measuring the very small current delivered by single electron tunneling (SET) sources, (for example: a few picoamps for a single-electron pump). The aim is firstly to establish if SET devices could generate highly quantized current and therefore if a quantum standard of current could be available especially for amplitudes less than 1 nA (see Section 9.3.4). Then the important issue will be the closure of the quantum metrological triangle with a very high precision, by directly combining the ac Josephson effect (ac JE), QHE and SET.

There are at least two other applications of CCCs in electrical metrology nowadays. The first involves a second type of CCC particularly designed to measure direct currents with an amplitude as high as 100 A (see Section 9.3.5). The second, which implies a CCC based on the initial concept of a superconducting tube, is devoted to noninvasive sensing of charged particle beams.

Other current applications of SQUIDS in metrology concern thermometry (Section 9.4.1) and a former metrological application of SQUIDS in the field of microwave measurement which may come back to prominence in the future (Section

9.42). The wide domain of X-ray and γ -ray spectrometry where SQUIDs are used for metrological purposes is dealt with in Chapter 8.

It has to be pointed out that many of the metrological applications presented are still in the development phase and this chapter represents a snapshot in time. The chapter ends with an assessment of future trends (see Section 9.5), especially those of single-particle detection, quantum measurement and the requirements of metrology at the nanometer scale.

9.2

SQUIDs in Voltage Metrology

9.2.1

SQUID Femtovoltmeter: Highly Accurate Voltage Measurement

9.2.1.1 Principle

A SQUID magnetometer may be converted very simply to a highly sensitive femtovoltmeter [1], as already discussed in Section 8.2. It is only necessary to take a coil of inductance L_i and a low resistance R_i , which is magnetically coupled to the SQUID loop *via* the mutual inductance M_i and to apply the voltage V_s to be measured across it as shown in Figure 9.1. The current I_i , which flows in the input coil, will apply flux to the SQUID loop. This flux may be then detected in the usual way using the flux-locked loop feedback circuit. Of course the input coil may be made of a superconductor, having essentially zero resistance. Then the steady state current flowing is determined by the voltage applied and the internal resistance of the voltage source.

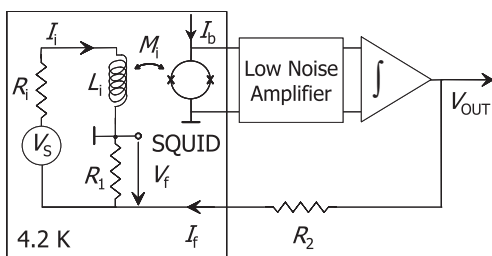


Fig. 9.1 Basic circuit of a picovoltmeter based on a dc SQUID. The feedback current I_f flowing through the resistor R_1 develops a voltage drop V_f which tends to null I_i . Then the signal voltage V_s equals the product $R_1 I_f$, and the output voltage V_{OUT} is given by $V_{\text{OUT}} = V_s R_2 / R_1$, typically $R_2 / R_1 \gg 1$. I_b denotes the SQUID bias current.

9.2.1.2 Femtovoltmeter for Verifying the Universality of Josephson Constant

In an extreme case, the voltage source may have truly zero resistance. An example would be a Josephson junction irradiated with a spectrally pure microwave source having frequency f and biased on one of the induced Shapiro steps which exhibit quantized voltages at $n\Phi_0 f$ (n is an integer), but which have zero differential resistance against small changes in bias current. In this case a steady state current will not be attained: instead an input current increasing linearly in time will be produced at a rate $dI/dt = \Delta V_s/L_i$, where ΔV_s is the constant applied voltage and L_i is the inductance of the input coil [2]. The extreme sensitivity of SQUIDs when used in this way (with vanishingly small input resistance sources) was demonstrated to be at the level of 10^{-22} V [3]. Tsai *et al.* used the same principle, where two Josephson junctions made of different materials are biased with the same frequency on the same integer Shapiro step, while they are joined through a superconducting input coil coupled to a SQUID. By attempting to observe the time-dependent signal expected at the SQUID output Tsai *et al.* were able to put an upper limit on the material dependence of the frequency to voltage ratio [4]. The so defined Josephson constant $K_J^{1)}$, is less than 2 parts in 10^{16} . That strengthens our confidence in the universal aspect of K_J and hence in the equality $K_J = 2e/h$.

However, even if strong theoretical arguments exist, from a strictly metrological point of view, this relation is not proven. Moreover, this result does not mean an upper deviation of the ratio $K_J/(2e/h)$ from one is of the order indicated above. The exactness of this relation has been recently tested by the CODATA task group in the framework of the 2002 fundamental constant adjustment [6]. It was shown that there is no significant deviation between K_J and $2e/h$, but with an uncertainty of 8 parts in $10^{82})$.

9.2.2

SQUID Ampermeter for linking the Volt to Mechanical SI Units

In the SI system, the electrical quantities are defined so that force and energy generated in electrical systems are measured in the same units as in mechanical systems. For linking the volt and ampere to mechanical SI units, one needs some electromechanical system in which electrical and mechanical energies can be compared directly. Several kinds of experiments contribute to providing values of

- 1) The determinations of $2e/h$ in SI units performed in the 1980s, which were found in better agreement than the previous ones, allowed the Comité International des Poids et Mesures (CIPM) to recommend implementing the Josephson effect as a voltage standard, to use the Josephson constant K_J as an estimate of $2e/h$ and for calibration purposes by assigning to it one single exact value of $K_{J,90} = 483\,597.9\text{ GHz/V}$ [5]. Note that the uncertainty on K_J presently given by the CIPM is 4 parts in 10^7 *in terms of SI units*.
- 2) This is a fairly large value compared to the agreement of one part in 10^{10} routinely found by the NMIs in direct comparisons of 1 V and 10 V Josephson voltage standards based on series arrays of large numbers of underdamped junctions (superconductor-insulator-superconductor technology). The arrays contain 2000 to 3000 junctions for 1 V, to more than 10 000 junctions for 10 V (for a review of Josephson standards, see for instance [7, 8]).

K_J or $2e/h$ in SI units (if one assumes the equality $K_J = 2e/h$ to be valid). The moving coil Watt balance is the technique of highest accuracy so far. This method could be the origin of a new SI definition of the kilogram if an uncertainty of one part in 10^8 is reached, the definition possibly based on the Planck constant. A review of Watt balance experiments is given in [9]. Another method, currently investigated by some NMIs with the same objective, involves a SQUID ampermeter [1–13]. This method consists of levitating a superconducting body successively at different equilibrium positions in a non-uniform magnetic field³⁾.

Figure 9.2 (a) shows a schematic of the experimental setup currently developed at NMIJ⁴⁾ [10,11]. A body of small mass $m = 25$ g, a phosphor-bronze thin wall cone covered with lead, reaches stable levitation positions in the magnetic field induced by the conical superconducting coil. The levitation occurs when the magnetic flux is large enough for the force due to the Meissner effect to balance the weight of the body. The current source is controlled by a SQUID ampermeter to keep always at zero the current I_S in such a way that the coil current is permanently equal to the drive current I . The experiment consists of two working phases:

1. In a “flux-up” mode, the Josephson device irradiated by microwaves at frequency f is biased on the $n=1$ Shapiro step for a time interval t . Consequently, the flux in the coil is increased by a known amount $\Delta\Phi = f\Phi_0 t$ since the emf of the superconducting coil is maintained equal to the Josephson voltage during the process.
2. Then the Josephson device is biased on the $n=0$ step to keep Φ constant so that the floated body reaches an equilibrium position. The vertical position of the center of gravity of the body is then measured by laser interferometry while the drive current is measured by recording the voltage drop V across a calibrated resistor R .

The energy supplied by the external source between any two equilibrium positions at heights z_L and z_H , with subscripts L and H corresponding to low and high positions respectively, is

$$\int_{\Phi_L}^{\Phi_H} I d\Phi = \frac{1}{2} (\Phi_H I_H - \Phi_L I_L) + mg(z_H - z_L). \quad (9.1)$$

The first term on the right-hand side corresponds to the increase of the magnetic energy of the coil-floating body system, and the second term is the work provided by the magnetic field to increase the gravitational energy of the body.

3) The experiments using the Watt balance or the floating body method lead to the determination of the Planck constant in terms of the kilogram with the double assumption

that $2e/h$ and h/e^2 are the true constants involved in the acJE and QHE.

4) NMIJ is the National Metrology Institute of Japan.

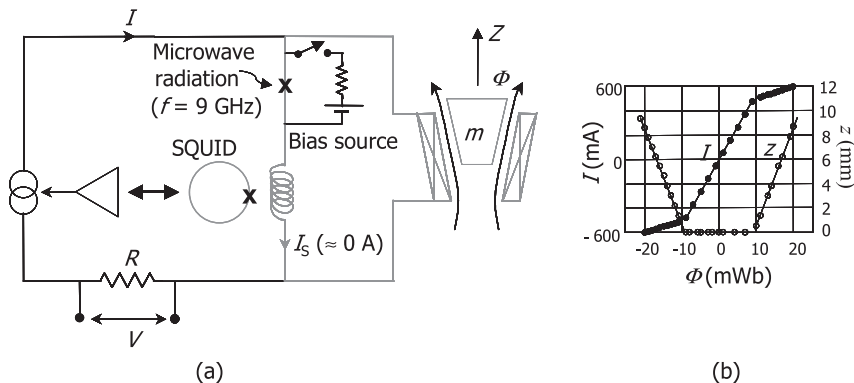


Fig. 9.2 Principle of the floating superconductor body method for the determination of Φ_0 in SI units. (a) Schematic of the experimental set-up at NMIJ. The superconducting part of the circuit is in gray. (b) Equilibrium trajectory: coil current I and vertical displacement z as functions of the magnetic flux Φ induced by the coil.

The process of repeating successively the “flux up” and “constant flux” modes provides a set of data (I, z) as a function of Φ which describe a so-called equilibrium trajectory [10], as shown in Figure 9.2 (b). The trajectory data allow one to calculate an SI value of Φ_0 and thus $2e/h$ or K_J . From the energy Eq. (9.1), a value of Φ_0^2 is indeed deduced in terms of kilogram, meter and second since both the flux change and the current can be expressed in units of Φ_0 .

The main obstacles to reducing the uncertainty level to well below one part in 10^6 presently reached at NMIJ reside in unwanted energy losses, insufficient understanding of mass metrology in the low temperature environment, and imperfect diamagnetism. The uncertainty component related to null current detection is estimated to be of the order of one part in 10^7 with a SQUID ammeter whose current sensitivity has been adjusted to $110 \mu\text{A}/\Phi_0$ [11].

9.2.3

Other Precise SQUID-Based Voltage Measurements

SQUID picovoltmeters have been used in precise comparisons of low-resistance-value standard resistors in standards laboratory applications but are generally only useful where cryogenic resistors are involved (R_i in Figure 9.1) [14]. For comparing resistance standards of 100Ω at room temperature or quantum Hall resistance standards operating on the $i = 2$ or $i = 4$ plateau ($12\,906 \Omega$ and $6\,453 \Omega$, respectively) at very low temperature ($T < 1 \text{ K}$), it is important to develop SQUID-based null detectors with a noise equivalent resistance (R_N) at 300 K less than that of the best nanovoltmeter commercially available ($R_N \approx 20 \Omega$). The SQUID has thus been used as a null detector in a CCC-based resistance bridge in which a $100\text{-}\Omega$ resistance standard placed at room temperature was calibrated against quantum Hall resistance standards operating on the $i = 2$ or $i = 4$ plateau at 1.3 K with an uncertainty of a few parts in 10^9 [15].

Picovoltmeters have also been fabricated using cuprate high-temperature superconductor (HTS) SQUIDS. Miklich *et al.* fabricated a YBCO SQUID with a YBCO input coil which demonstrated a $2.3 \text{ pV/Hz}^{1/2}$ sensitivity for signals at 1 Hz [16]. Eriksson *et al.* were able to demonstrate a possible application of an HTS SQUID picovoltmeter as a means of testing for transients on high-voltage power supply transmission lines, with a speed of response which was superior to conventional methods [17].

The early work on the CCC described in the next section was aimed at Josephson voltage measurements, using cryogenic resistors to scale the voltage to higher levels [18, 19]. In the 1970s, the primary voltage standards were indeed based on single overdamped Josephson junctions which generated a voltage of only a few millivolts (typically working on high-order steps, $n > 500$ at frequency $f \approx 10 \text{ GHz}$). By means of this cryogenic voltage comparator, it was possible to calibrate secondary standards such as the well-known 1.018-V saturated Weston cells (still in use nowadays) with an uncertainty of 10 nV , 10 times lower than the uncertainty obtained with the method employing voltage dividers.

9.3

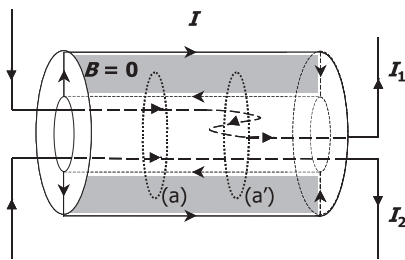
Cryogenic Current Comparator (CCC)

9.3.1

Principle of the CCC

The CCC was invented by Harvey in 1972 [20]. The principle rests on Ampère's law and perfect diamagnetism of the superconductor in the Meissner state. Consider two wires inserted into a superconducting tube of wall thickness several times larger than the London penetration depth (Figure 9.3). Currents I_1 and I_2 circulating through these wires will induce a supercurrent I flowing up the inner surface of the tube and back down the outer surface in such a way that a null magnetic flux density is maintained inside the tube. By applying Ampère's law to a contour in the bulk, labelled a in Figure 9.3, we find that

$$\oint_a B dl = 0 = \mu_0(I_1 + I_2 - I) \quad (9.2)$$



$$I = -(I_1 + I_2)$$

Fig. 9.3 Principle of a CCC.

which yields the equality of the currents:

$$I = I_1 + I_2. \quad (9.3)$$

If the wires carrying I_1 and I_2 pass through the tube N_1 and N_2 times respectively, the supercurrent I is equal to

$$I = N_1 I_1 + N_2 I_2. \quad (9.4)$$

These equalities are valid independent of the position of the wires inside the tube, even if the wires describe some "S" path (Figure 9.3, case a'). Only the current density distribution on the inner surface of the tube can be inhomogeneous in the case of asymmetric positioning of the wires, whereas the current density distribution on the outer surface stays homogeneous. Here is the key reason for the high level of precision of the CCC.

In the real case of a tube of finite length, the equalities above are in fact altered by the unscreened magnetic flux induced by the currents I_1 and I_2 at the ends. To overcome these end effects and at the same time to make the device practical with a limited size, the tube is shaped in a torus with its ends being overlapped (but electrically insulated) like a "snake swallowing its tail" (Figure 9.4). The longer is the overlap, the more efficient is the screening of the magnetic flux which tends to leak through the gap of the overlap. This is the method proposed by Sullivan and Dziuba for improving the exactness of the CCC current ratio [21]. Currents I_1 and I_2 of opposite direction flowing in two windings of number of turns N_1 and N_2 induce a supercurrent $I = N_1 I_1 - N_2 I_2$. The external magnetic flux Φ , which results only from the supercurrent, is detected by a SQUID through a flux transformer composed of a pickup coil wound very close to the toroidal shield (on its inner or outer surface) and the input coil of the SQUID. The output voltage of the SQUID is then converted to a current which feeds back one of the two windings

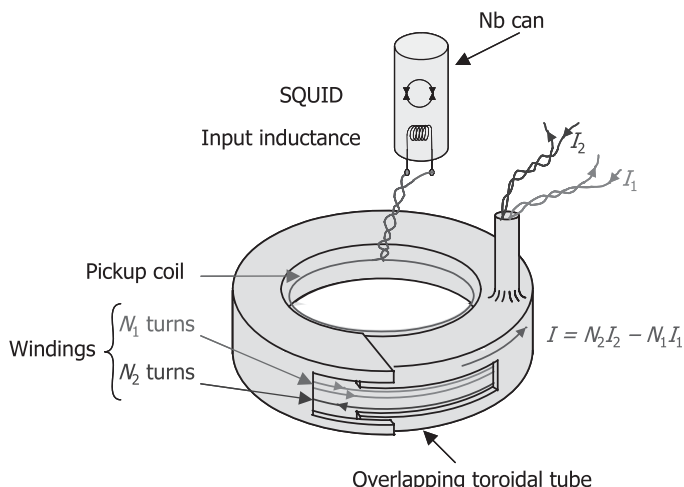


Fig. 9.4 Schematic of a type I CCC.

to null the magnetomotive forces. From this ampere turn balance results the equality of the ratios:

$$I_1/I_2 = N_2 / N_1. \quad (9.5)$$

A second type (II) of CCC, proposed by Grohmann and coworkers in 1973, can also be constructed by placing the pickup coil inside the toroidal superconducting shield and by wrapping the windings outside, like a conventional transformer with windings around the ferromagnetic torus [22]. The superconducting shield also overlaps itself around the torus. Figure 9.5 shows an example of a type II CCC which is presently used in metrology and is described in Section 9.3.5 [23]. Note that in this configuration, the SQUID could be placed inside a superconducting shield and thus become completely immune to parasitic magnetic flux.

All CCCs currently used in NMIs are based on low-temperature superconducting (LTS) materials, particularly lead for the overlapping shield, because these materials guarantee high current resolution (reduced Johnson noise due to low working temperature, high level of screening against unwanted magnetic fields), and high accuracy (because their high critical current density allows a complete Meissner effect in the bulk). However investigations have been carried on HTS-based CCCs and some promising results have been reported [24–28]. Different geometries have been designed depending on the particular application. For instance, Early *et al.* have been able to fabricate a split-toroid YBCO CCC which could be suitable for resistance ratio or low current measurements [28]. Another example, which is described in Section 9.3.6, is a CCC made of a YBCO-coated tube. It has been developed at the National Physical Laboratory (NPL) for measuring charged particle beams.

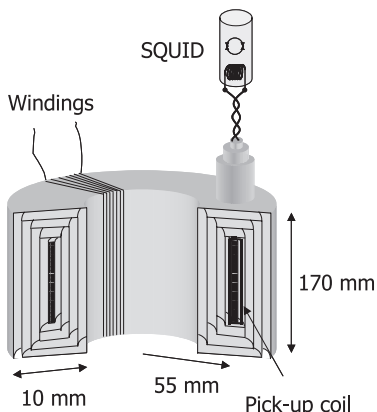


Fig. 9.5 Schematic of a type II CCC.

9.3.2

Limits to Accuracy of CCC Ratio Measurements**9.3.2.1 Sensitivity and Current Resolution**

The performance of the CCC in terms of sensitivity and noise depends strongly on the flux transformer (FT), which has to match the SQUID to the overlapping toroidal shield as well as possible, as shown schematically in Figure 9.6.

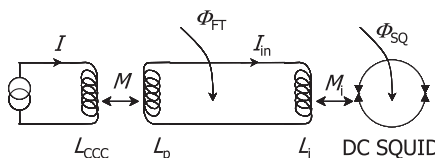


Fig. 9.6 Basic flux transformer (FT) circuit.

Sensitivity of the CCC

The sensitivity of the CCC, S_{CCC} , is defined as the variation of the supercurrent I circulating on the surface of the overlapping tube which creates a magnetic flux variation Φ_{SQ} of one Φ_0 across the SQUID ring. In ampereturn/ Φ_0

$$S_{\text{CCC}} = |\partial \Phi_{\text{SQ}} / \partial I|^{-1} = |\partial I / \partial I_{\text{in}}| / M_i \quad (9.6)$$

where M_i is the mutual inductance of the SQUID loop and input coil and I_{in} is the circulating current in the flux transformer. Applying conservation of magnetic flux to the superconducting flux transformer, assuming zero initial flux, $\Phi_{\text{FT}} = (L_p + L_i)I_{\text{in}} + MI = 0$, gives

$$S_{\text{CCC}} = (L_p + L_i) / MM_i, \quad (9.7)$$

where L_p is the inductance of the pickup coil, L_i is the input inductance of the SQUID and M is the mutual inductance between the overlapping toroidal tube and the pickup coil. It is easy to show that the sensitivity reaches the optimal value

$$S_{\text{CCC}}^{\text{opt}} = (2/k) (L_i / L_{\text{CCC}})^{1/2} / M_i \quad (9.8)$$

where L_{CCC} is the inductance of the overlapping toroidal tube, for a number of turns of the pickup coil

$$N^{\text{opt}} = (L_i / l_p)^{1/2}. \quad (9.9)$$

Here k is the coupling constant between the pickup coil and the overlapping shield ($M = k(L_p L_{\text{CCC}})^{1/2}$) and l_p is the inductance corresponding to a single turn of the pickup coil ($L_p = N^2 l_p$).

In practice, the overall CCC and SQUID⁵⁾ system is surrounded by (at least) one external superconducting shield to obtain an environmental magnetic field weak enough and essentially very stable. Consequently the inductive coupling between this external shield and both the overlapping shield and the pickup coil has to be taken into account to calculate N^{opt} and $S_{\text{CCC}}^{\text{opt}}$ and Eq. (9.9) is no longer valid⁶⁾.

Several numerical methods have been proposed in the literature to calculate S_{CCC} of type I CCCs and good agreement has been generally found between calculated and measured values [29–31]. From the method proposed by Sesé and co-workers analytical formulae for S_{CCC} can be derived, provided some realistic conditions are fulfilled [32,33]. This method, based on a finite element calculation, takes into account not only the influence of the external shield but also the mirror effect of the overlapping toroidal shield on the pickup coil. The perpendicular magnetic field induced by the coil on the wall of the shield is cancelled by the superconducting material, like an image coil which generates an opposite magnetic field. This effect results in an effective inductance L'_p and a mutual inductance M given by the relations:

$$L'_p = (1 - k') L_p + k N^2 L'_{\text{CCC}}, \quad (9.10)$$

$$M = k N L'_{\text{CCC}}, \quad (9.11)$$

provided k' , the coupling constant between the pickup coil and its image, is close to 1 [32]. Here k is a coupling parameter between the pickup coil and the overlapping toroidal shield characterized by an effective inductance L'_{CCC} . In the ideal case where $k'=1$, the optimal number of turns N^{opt} and the optimal sensitivity $S_{\text{CCC}}^{\text{opt}}$ are given by

$$N^{\text{opt}} = (L_i / L'_{\text{CCC}})^{1/2} \quad (9.12)$$

and

$$S_{\text{CCC}}^{\text{opt}} = (2/k) (L_i / L'_{\text{CCC}})^{1/2} / M_i = (2/k) N^{\text{opt}} / M_i. \quad (9.13)$$

In practice, Eq. (9.12) combined with the calculated value of the effective inductance L'_{CCC} provide a good estimate to the designer of the number of turns required on the pickup coil. Note that, for Eqs. (9.12) and (9.13) to be valid, L_i has to be larger than L'_{CCC} which is often the case.

- 5) In general, the SQUID itself is inserted inside a superconducting shield (typically a Nb can) as shown in Figure 9.3.
- 6) If the SQUID is mounted very close to the overlapping tube, the influence of the superconducting shield of the SQUID on the calculation of S_{CCC} would also have to be taken into account: an example is a Nb can which largely occupies the central zone of the torus (Figure 9.4).

Current Resolution

The most relevant characteristic of the CCC is its current resolution δI in terms of A/Hz^{1/2} and is defined as the square root of the power spectral density of current noise referred to the CCC input, or equivalently as the minimum measurable supercurrent circulating per Hz^{1/2} in the overlapping tube of the CCC. The complete expression for δI is given by the relation

$$\delta I = [4k_B T/R_{in} + 8\varepsilon/N_1^2 k^2 L'_{CCC} + (S_{\phi ext}/N_1 L'_{CCC})^2]^{1/2} \quad (9.14)$$

where N_1 is the number of turns of the primary winding of the CCC. The first term corresponds to the Johnson noise of the input resistor at temperature T . The second term is the contribution of the SQUID with an energy resolution ε when the optimal sensitivity of the CCC is reached. The third term comes from the external magnetic flux noise with a power spectral density $S_{\phi ext}$ [34]. This last term becomes negligible with careful shielding as described below. The dominant noise arises from one of the two first terms, depending on the CCC application. When a CCC is used for comparing resistance standards (Section 9.3.3), the Johnson noise they deliver cannot be avoided and consequently the number of turns of the primary winding is increased to a limiting value (typically around 2000) above which the noise contribution of the SQUID becomes negligible. For low current measurements (Section 9.3.4), where high input resistances are involved, only the SQUID noise contributes.

The current resolution of a CCC fitted with a high-permeability toroidal core is given by a relation which slightly differs from Eq. (9.14), in which L'_{CCC} will be replaced by another effective inductance including the permeability of the ferromagnetic core. The power spectral density of the current noise of the core itself, $(\delta I_C)^2$, obviously has to be added.

Some Details on Design

From the reported results of various calculations and measurements of the effective inductances, L'_{CCC} and L'_p , and of the sensitivity and current resolution a preliminary design for a type I CCC can be made as follows [29–37].

The overlapping toroidal shield has to be designed with a mean radius a as high as possible and a section $h \times w$ (see Figure 9.7) as small as possible since a maximum inductance is required. These requirements are evident from the relation below, which gives L_{CCC} without taking into account the surrounding external shield

$$L_{CCC} = \mu_0 a [\ln(8a/r) - 2] \quad (9.15)$$

where $r = (wh/\pi)^{1/2}$ is the radius of a circular section whose area is equal to that of the rectangular section of the toroidal shield (Figure 9.7). In fact, this relation has been found to be in good agreement, to within a few per cent, of the value found by numerical calculations of the distribution of the current circulating on the surface of the overlapping shield [36].

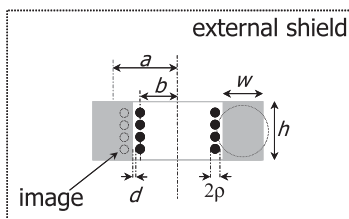


Fig. 9.7 Parameters of a toroidal shield and pickup coil for a type I CCC.

However, these two parameters are fixed by the experimental constraints, the section $h \times w$ by the total number of turns of the winding and the mean radius a by the radius of the external shield, which is itself limited by the size of the cryostat neck.

By considering the system as a magnetic circuit and introducing the relevant reluctances, Sesé *et al.* have proposed a simple rule to optimize to a good approximation the size of the overlapping shield with respect to the external shield [37]. They find that L_{CCC} is maximized when the internal area A_{int} ($= \pi b^2$) enclosed by the torus is equal to the external area between the torus and the external shield A_{ext} ($= \pi R_{\text{shield}}^2 - \pi(b + w)^2$), as illustrated in Figure 9.8. This result follows from the equality of the reluctances $\mathcal{R}_1 = h/(\mu_0 A_{\text{int}})$ and $\mathcal{R}_2 = h/(\mu_0 A_{\text{ext}})$, with $A_{\text{int}} + A_{\text{ext}}$ kept constant.

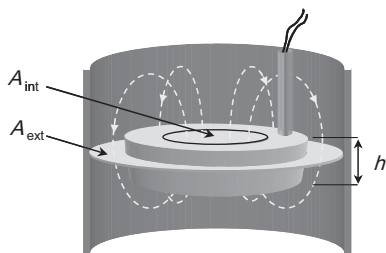


Fig. 9.8 Effect of external shield on type I CCC.

The optimal value of the mean radius of the toroidal shield is given by

$$a^{\text{opt}} = [(R_{\text{shield}}^2 - w^2/2)/2]^{1/2}. \quad (9.16)$$

It is noteworthy that the mean radius a could be made larger if the axis of the toroidal shield is made perpendicular to the external shield axis.

The pickup coil has to be wound as close as possible to the inner or outer surface of the overlapping shield ($d/a \ll 1$, see Figure 9.7) and the turns have to be suitably spaced, as described below. The coupling between the overlapping shield and the pickup coil is indeed much improved by minimizing the coupling of each turn to the rest of the turns, each turn being coupled only to its own image [32]. Several possibilities have been proposed: individually shielding the turns by means of superconducting sheath, placing the wire inside a superconducting tube

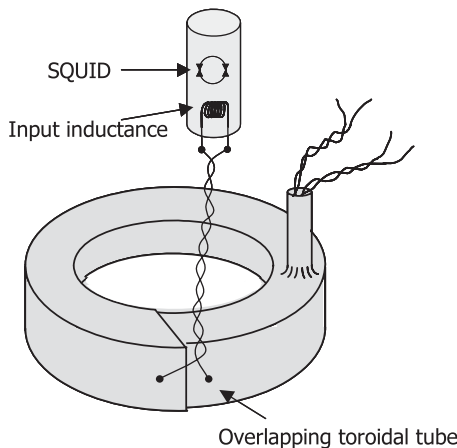


Fig. 9.9 Overlapping toroidal shield used as a pickup coil.

or using a wide tape instead of a wire [33]. Another way is to use a SQUID with an input inductance $L_i = L'_{\text{CCC}}$, equivalent to that of a single-turn pickup coil. A perfect matching has thus been achieved by connecting the input coil of the SQUID directly to the overlapping shield as shown on Figure 9.9 [38].

For a good current resolution the SQUID has to be chosen with high energy resolution, but without a severe restriction on the input inductance (provided that $L_i \geq L'_{\text{CCC}}$) since this inductance has no influence on δI .

Good current resolution strongly depends on the screening of environmental magnetic fields by additional external shields. The shields are used more for obtaining high stability of the residual magnetic field rather than for reducing the latter down to a non measurable level. The condition to be fulfilled is $S_{\phi_{\text{ext}}}^{1/2} < 10^{-4} \Phi_0/\text{Hz}^{1/2}$, given the typical values $\epsilon = 10^{-31} \text{ J/Hz}$ (in the white noise regime) and $L'_{\text{CCC}} = 10 \text{ nH}$ in Eq. (9.14). In terms of magnetic flux density, the condition becomes $S_{B_{\text{ext}}}^{1/2} < 0.3 \text{ fT/Hz}^{1/2}$ for a typical CCC with a 20-mm inner diameter. Here, $S_{\phi_{\text{ext}}}$ and $S_{B_{\text{ext}}}$ are the spectral densities of the external magnetic flux and field noise. Consequently, the total attenuation required for screening a parasitic magnetic field like that of the Earth's ($|B_{\text{Earth}}| \approx 50 \mu\text{T}$) should exceed 220 dB. This value can then be considered as an upper limit value for obtaining a highly stable magnetic environment.

9.3.2.2 Exactness of the CCC Current Ratio

Uncertainty of the Winding Ratio

A high accuracy of current ratio measurement is reached when the superconducting tube covering the windings overlaps itself over a length l large enough to minimize the flux Φ_l leaking through the gap of the overlap. This leakage flux carries the information on the position of the windings. Theoretical error values of the order of one part in 10^{10} or less have been reported for both types of CCC [39].

The relationship below, which is a simplified form of the relation proposed by Seppä for a type I CCC, gives the maximum error in terms of magnetic flux:

$$\Phi_l/\Phi = [\delta \exp(-l/r)] [a \ln(a/r)]^{-1} \quad (9.17)$$

where Φ is the total magnetic flux, δ is the gap thickness, r is the equivalent radius of the tube ($r = (wh/\pi)^{1/2}$ with the same notations as in Figure 9.7) and a is the mean radius of the torus [40].

For a one-turn overlap of the shield ($l = 2\pi a$), with typical values $a = 15$ mm, $r = 3$ mm and maximum value $\delta = 1$ mm, the error is around 10^{-16} , smaller than the least measurable values which have been reported to be 10^{-11} .

Note that a possible error on the winding ratio could exist due to the natural imperfection of the ends of each winding, which may form kinks. In practice, this error is nulled first by twisting the output wires and then, in the case of a type I CCC, by inserting the output wires in the superconducting coaxial tubes forming a chimney, such as that shown in Figure 9.4, for example. The resulting magnetic flux due to the winding ends is indeed strongly screened by the superconducting tube, the efficiency increasing as a function of the height/diameter ratio of the tube.

In practice, a CCC is generally made of a series of windings with numbers of turns in an arithmetic progression and two identical windings (for instance 15, 15, 30, 60, 120, ...). This enables one to test the efficiency of the superconducting toroidal shield by a self-calibration of the ratio 1:1. A current passing through two windings with the same number of turns connected in series-opposition can induce an ampere-turn imbalance, which gives the ratio error [41]. Superconducting wires are generally used for the CCC windings in order to make static leakage currents negligible and to reduce to a few ohms the resistance of links between current sources and resistances to be compared.

Frequency Effect

Most of the measurements involving CCCs are carried out at ultralow frequencies between 10 mHz and 0.5 Hz with the expectation that the results will not be altered by any frequency effect. A few measurements carried out at frequencies from 1 Hz to 10 kHz produced interesting results and enable one to establish an upper limit on the error in the current ratio and to reduce it. According to Grohmann *et al.*, the error sources arise from various capacitances inside the CCC (shunting capacitance between the leads, stray capacitance between ground and leads, shunting capacitances between the turns of the winding and stray capacitance between ground and winding) [42]. They may partly cancel each other out due to opposite signs. For example, consider two windings shown schematically in Figure 9.10. The true value of the current crossing the winding labelled 1 is given by

$$I_{1T} = I_1 - I_1' + I_2'', \quad (9.18)$$

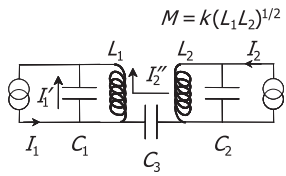


Fig. 9.10 Schematic of two windings with leakage currents crossing the shunt capacitances C_1 and C_3 .

where I_1' denotes the leakage oscillating current crossing the shunt capacitance of the winding and I_2'' corresponds to the oscillating current leaking through the capacitance between the two windings. It seems possible to cancel the errors, at least partly, by means of coaxial windings for type II CCCs or by placing a supplementary capacitor in parallel to the winding or between one of the winding terminals and the ground for type I CCCs [43]. The type II geometry is the most suited for ac applications of CCC. Errors reduced to one part in 10^8 at 10 kHz have been reported [39].

For a type I CCC, a simple approximate expression for the error on the current ratio I_1/I_2 can be given, in terms of the self-inductance of the windings L_1 and L_2 and their mutual inductance $M = k (L_1 L_2)^{1/2}$ with a coupling factor k

$$\delta(I_1/I_2)/(I_1/I_2) = (1-k)L_1 C \omega^2 \quad (9.19)$$

for the case of large ratio $I_1/I_2 \gg 1$ (*i.e.* $L_1 \gg L_2$). Here C denotes the leakage capacitance (shunt or stray) and ω is the frequency [44]. The term $(1-k) L_1$ can be deduced from the measurement of the emf across winding 1 induced by an alternating current passing through it. The measurement of the capacitance between winding 1 on one side and winding 2 and ground on the other leads to an approximate value of C . Another possible way to estimate the ratio error is *via* the determination of the lowest resonance frequency of the CCC f_{res} given by

$$\delta(I_1/I_2)/(I_1/I_2) = (1-k)(f/f_{\text{res}})^2. \quad (9.20)$$

We have assumed that each winding combined with its leakage capacitance behaves as an LC tank circuit, where the lowest resonance frequency is $f_{\text{res}} \approx 1/2\pi L_1 C$ (*if* $L_1 \gg L_2$). The resonant peaks can easily be observed on the current (or flux) noise spectrum recorded at the system output [35, 45–47].

Finite Open Loop Feedback Gain

An uncertainty in the value of the current ratio measured by the CCC arises from the finite open loop gain of the SQUID operating in a flux-locked loop mode. The error in current ratio can be easily deduced from the simplified block diagram shown in Figure 9.11. Currents I_1 and I_2 applied to the CCC through its (primary) winding of N_1 turns and (secondary) winding of N_2 turns respectively, induce a magnetic flux difference $\delta\Phi = \Phi_1 - \Phi_2$ at the SQUID. The loop gain of the CCC, G_L , which corresponds to the ratio $\Phi_1/\delta\Phi \approx \Phi_2/\delta\Phi$, is given by

$$G_L = N_2 G_{\text{Electronics}} V_d / R_f S_{\text{CCC}} \quad (9.21)$$

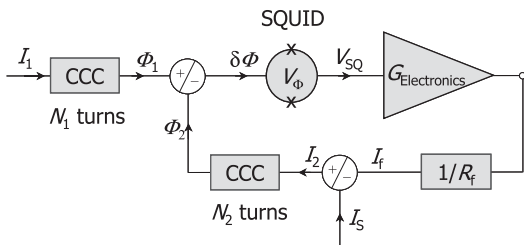


Fig. 9.11 CCC block diagram.

where $G_{\text{Electronics}}$ is the gain of the feedback electronics (see Chapter 4), V_ϕ is the optimized transfer coefficient of the SQUID and R_f is the feedback resistance.

First, consider the case of current I_2 only delivered by the SQUID feedback electronics. The error in current ratio is simply equal to the reverse of the loop gain,

$$I_2 = I_f = (N_1/N_2)I_1(1 - 1/G_L). \quad (9.22)$$

Typically, G_L reaches 100 dB at a frequency of 10 mHz for a bandwidth of 1 kHz (in dynamic mode, $G_L(f) \propto f_{\text{cut-off}}/f$), and so induces an error of one part in 10^5 . Second, consider the case of current I_S delivered by a secondary current source which is servo-controlled by the primary source in such a way that I_S/I_1 is preliminarily adjusted: $I_S/I_1 = N_1/N_2(1 \pm x)$. The sum of currents circulating through the secondary winding is thus given by

$$I_2 = (N_1/N_2)I_1(1 \pm x/G_L). \quad (9.23)$$

The error x/G_L becomes insignificant if $x < 10^{-5}$, an adjustment value not so difficult to achieve. The error decreases if N_2 increases but the stability margin decreases as well.

9.3.3

Resistance Ratio Measurement

9.3.3.1 Introductory

The resistance bridges currently used in NMIs to calibrate material resistance standards (wire-wound resistors) against quantum Hall resistance standards (QHRS) are based on the type I CCC and generally this CCC is coupled to a commercial rf or dc SQUID. Precise resistance ratio measurement is made possible via the current ratio measurement made with a very high accuracy. The CCC presents two advantages compared to the conventional direct current comparators, commercially available and operating with ferromagnetic cores:

- The resolution is markedly improved, by a factor of 100 at least. For a CCC, the square root of the noise power spectral density in terms of ampereturns is typically between 10^{-9} and 10^{-10} ampereturn/Hz $^{1/2}$ in the white noise region, or of the order of 100 fA/Hz $^{1/2}$ for the largest windings. This low noise level is mainly due to the SQUID used as magnetic flux detector.

- The uncertainty in current ratio does not exceed one part in 10^9 (more often than not, it is reduced down to one part in 10^{10}) compared to a few parts in 10^8 with a ferromagnetic-core-based direct current comparator⁷⁾ operating at room temperature.

With such properties, the CCC allows one to demonstrate the universality of the von Klitzing constant R_K (corresponding to h/e^2) derived from the QHE through the relation $R_H(i) = R_K / i$ where R_H is the quantum Hall resistance and i is an integer corresponding to the Hall quantum plateau number (see [49, 50] and references therein). Under some experimental conditions and following specific technical guidelines [51], the independence of R_K on QHE device characteristics (type, materials, channel width, contacts), the number i and experimental parameters (temperature, measuring current, magnetic field) has been demonstrated at levels down to a few parts in 10^{10} [52, 53].

Moreover, on-site bilateral comparisons of complete QHE systems carried out between the Bureau International des Poids et Mesures (BIPM) and some NMIs during the past decades [54–58] or more recent comparisons via $1\ \Omega$ or $100\ \Omega$ travelling standards have shown excellent agreement of a few parts in 10^9 [59, 60]. These results, which have to be ascribed to the use of CCC bridges in such comparisons, strongly support the universality of R_K ⁸⁾.

Typically, the secondary resistance standards which are calibrated against QHRS have nominal values of $1\ \Omega$ and $10\ k\Omega$. They are used as reference standards for routine calibration purposes. Their values are rather far from that of $R_K/4$ and $R_K/2$ (around $6453\ \Omega$ and $12\ 906\ \Omega$, respectively) quantum values which are the most often used with single QHE devices. Consequently, their calibration against QHRS has to be carried out in several steps. In contrast, for example, to the method involving resistance build-up networks, the CCC bridge described below makes the calibration process of these secondary standards more simple, restricted to only two steps, by means of transfer standards such as $100\ \Omega$ and $1\ k\Omega$ resistance standards.

Note that some NMIs have developed specific CCC bridges to cover a more extended measurement range, up to $100\ M\Omega$ *via* a direct comparison with QHR [47, 62], and even up to $1\ G\Omega$ [63]⁹⁾.

- 7) In the best case, measurement uncertainties of the order of one part in 10^9 have been reported with a non-commercial room-temperature current comparator working at $1\ Hz$ [48].
- 8) That confirms the validity of the international recommendation in 1988 for the use of the quantum Hall resistance as the primary resistance standard, too. As for the ac Josephson effect (see footnote 1), CIPM has defined the von Klitzing constant R_K as an estimate of h/e^2 and for calibration purposes has assigned to it one single value $R_{K,90} =$

$25\ 812.807\ \Omega$ [61]. Note that the uncertainty on R_K presently given by the CIPM is 1 part in 10^7 *in terms of SI units*.

- 9) With the same aim of scaling the resistance in terms of R_K over a wide range, quantum Hall array resistance standards (QHARS) with nominal quantum values from $100\ \Omega$ to $1.29\ M\Omega$ ($50\ R_K$) are currently developed. The arrays are composed of a large number of single Hall bars connected in series or in parallel with multiple links (see for instance [64, 65] and references therein).

9.3.3.2 Resistance Bridge Based on Type I CCC

The CCC is connected to a double constant current source which feeds resistors of resistances R_1 and R_2 to be compared, with primary and secondary currents I_1 and I_2 respectively, as shown in Figure 9.12. Here, the secondary current source is slaved on the primary current source in such a way that the current ratio can be reliably adjusted allowing the SQUID to be properly and accurately flux locked, as discussed in Section 9.3.2.2 [41, 49].

In the ideal case, the operation should consist of setting the current ratio to equal the voltage drops across the resistances, *i.e.*, to null the voltage drop through a detector connected to the low voltage terminals of the resistances: $R_1 I_1 = R_2 I_2$. Consequently the resistance ratio R_1/R_2 will be equal to the winding ratio N_1/N_2 .

In real cases, a fraction ε of the current I_2 has to be diverted to an auxiliary winding of N_a number of turns to balance the bridge both in voltage and in ampereturns:

$$N_1 I_1 - N_2 I_2 + \varepsilon N_a I_2 = 0, \quad (9.24)$$

$$R_1 I_1 - R_2 I_2 = 0. \quad (9.25)$$

Elimination of the currents from these two relations gives the resistance ratio:

$$\frac{R_1}{R_2} = \frac{N_1}{N_2} \left(1 + \frac{N_a}{N_2} \varepsilon \right). \quad (9.26)$$

In the bridge illustrated in Figure 9.12, the deviation ε is obtained by recording the output voltages of the null detector which correspond to the two positions of the resistive divider $\varepsilon_{\pm} = \varepsilon \pm x$ where x is typically of the order of one part in 10^7 . Thus ε is given by

$$\varepsilon = (\varepsilon_- V_+ - \varepsilon_+ V_-) / (V_+ - V_-), \quad (9.27)$$

where the voltages V_+ and V_- of opposite signs correspond to ε_+ and ε_- respectively [49]. This deviation ε can also be obtained by using an amplifier at the output of the detector which generates a current through the auxiliary winding and a resistor placed in series. The value of ε is thus deduced by measuring the voltage drop across the resistor [66]. The advantage of this second method is the ability to automate the bridge fully.

Either way, the voltages are measured by periodically reversing the current polarity in order to compensate for the unwanted thermal electromotive forces. The typical working frequency is of the order of 0.1 Hz or less and might be in the range where the SQUID generates $1/f$ noise. This flicker noise may be avoided by operating the bridge at 1 Hz [44]. However, the current ratio has to be preadjusted both in phase and out of phase and the CCC needs a supplementary winding. Moreover, the dependence of the resistance standard on frequency has to be known. As previously mentioned, working frequencies higher than 1 Hz might induce significant error ($> 10^{-9}$) in the current ratio due to finite capacitive leakage and shunt between the CCC windings.

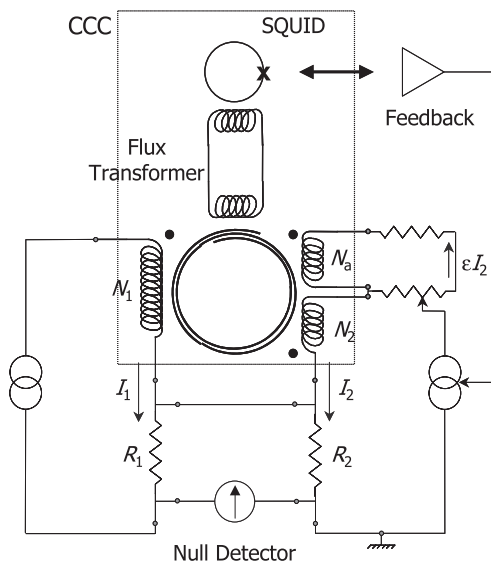


Fig. 9.12 Circuit diagram for a CCC-based resistance bridge.
The toroidal shield of the CCC is symbolized by a two-turn spiral. The three dots indicate the input of coils for applying currents, which induce magnetic fields of the same polarity.

9.3.3.3 Some Remarks on Construction

The CCC has to be composed of a series of windings allowing any kind of current ratios, 1, 2, 4, ..., 100 and particularly the ratios 64.532 and 129.064 used for measuring resistance ratios $R_H(i)/100 \Omega$ with $i = 4$ or 2. In the case of $R_H(i=2)/100 \Omega$, the numbers of turns N_1 and N_2 are usually equal to 1936 or 2065 and 15 or 16, respectively, so that the winding ratio does not deviate by more than 2×10^{-5} from the ratio of the nominal values of resistances (12 906.4035:100). Moreover, the choice of N_1 values of around 2000 is well suited to reduce the SQUID noise to a level less than the Johnson noise of the resistances to be compared.

To take full advantage of the high performance of the CCC, great care has to be taken in the construction of the bridge. For example, the bridge must have low leakage currents and good insulation between the primary and secondary circuits. The current ratio will be precisely preadjusted taking into account the finite open loop gain of the SQUID. The potentiometer must be calibrated and the nonlinearity of the nanovoltmeter used as null detector has to be measured. It is strongly recommended that the complete bridge has a unique ground point. Optocoupler isolation amplifiers are commonly used, for instance at the external feedback output of the SQUID electronics and at the output of the null detector. The IEEE transmission line through which the computer monitors the bridge and acquires data is an optical fiber.

9.3.4

Measurements of Very Low Currents from SET Sources

9.3.4.1 Introduction

By extending the concept of the sensitive current detector as proposed by Harvey in his original paper, one can use the CCC as a low-current amplifier with two characteristics never reached by any conventional device [20]. As shown below, the CCC may exhibit a current resolution around $1 \text{ fA}/\text{Hz}^{1/2}$ or less over the white noise frequency range. This excellent resolution is mainly due to the low noise properties of the SQUID. The second extraordinary feature of this cryogenic amplifier is the exactness of the current gain. The metrological needs of such a CCC emerged in the 1990s when the first SET current sources, electron turnstile [67] and electron pump [68], were demonstrated and exhibited quantization of the current they deliver. These SET devices allow control of elementary charge transfer at the rate of a clock signal [69]. The amplitude of the delivered current is simply given by the product of the elementary charge e and frequency f . Its value is rather low, of the order of 1 pA or, at best, less than 1 nA for more recent SET devices based on surface acoustic waves (SAW) [70]. Therefore, measurement of this current with metrological accuracy, for example within an uncertainty of one part in 10^6 , requires a highly accurate amplifier and the CCC is the most appropriate instrument. The development of a CCC-based current amplifier has been greatly stimulated by the demonstration of a SET-based quantum current standard (especially for subnanoampere range). The motivation is above all to close the quantum metrological triangle (QMT) (Figure 9.13) which experimentally consists of applying Ohm's law $V = RI$ directly to the voltage, resistance and current related to the ac JE, QHE and SET respectively, as first proposed by Likharev and Zorin, noting that voltage and current are both in terms of a frequency, a physical quantity which is measured with the highest accuracy nowadays [71]. Another experimental way for the closure of the QMT consists of following $Q = CV$ from the realization of a quantum capacitance standard from SET devices without, however, involving a SQUID [72, 73].

The aim of the QMT experiments is to check the consistency of the constants involved in the three quantum phenomena which are strongly believed to provide the free space values of h/e^2 , $2e/h$ and e . In practice, the experiments determine the dimensionless product $R_K K_J Q_X$, expected to be equal to 2, where the constant Q_X is defined as an estimate of the elementary charge, $Q_X = e|_{\text{SET}}$, by analogy to the definitions of Josephson and von Klitzing constants, $K_J = 2e/h|_{\text{JE}}$ and $R_K = h/e^2|_{\text{QHE}}$ [74, 75]. Checking the equality $R_K K_J Q_X = 2$ with an uncertainty of one part in 10^8 will be a relevant test of the validity of the three theories.

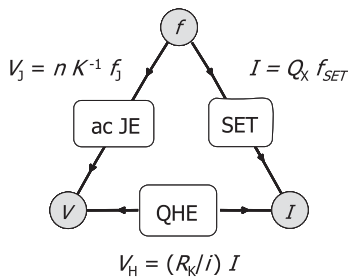


Fig. 9.13 Quantum metrological triangle. Theory predicts that R_K , K_j and Q_x correspond to the fundamental constants h/e^2 , $2e/h$ and e .

The principle of the QMT experiment in following Ohm's law rests on the direct comparison of the voltage V_J delivered by a Josephson junction array (JJA) biased on the n -th Shapiro step to the Hall voltage V_H of a QHE sample operating on the i -th plateau and fed with a current I_1 generated by a SET current source¹⁰. The current I_1 is amplified by a factor G_{CCC} , the gain of the CCC. From this voltage comparison one finds

$$V_J = R_H(i) G_{CCC} I. \quad (9.28)$$

Taking into account the relationships given by acJE, QHE and SET and using the same notation as in [74], $R_K = h/e^2 (1 + r)$, $K_j = 2e/h (1 + k)$ and $Q_x = e (1 + q)$, one finds that Eq. (9.28) becomes

$$s = (n/2)(i/G_{CCC})(f_j/f_{SET}) \quad (9.29)$$

where $s = r + q + k$ to first order, and f_j and f_{SET} are the irradiation and operation frequencies of the JJA and SET devices, respectively. Measurement of the residual term s will give information on the level of consistency of the three quantum phenomena.

An experimental set-up for testing the QMT is sketched in Figure 9.14. The current amplifier is composed of a type I CCC of high winding ratio, $G_{CCC} = N_1/N_2$, a dc SQUID with low white noise level and low corner frequency f_c , and a secondary current source, servo-controlled by the SQUID in such a way that the latter works at null magnetic flux [74]. In order to minimize the contribution from $1/f$ flicker noise, the polarity of the current to be amplified is periodically reversed. The Hall voltage is simultaneously compared to the voltage of a programmable Josephson junction array voltage standard (JAVS), well suited here because of the low voltage level and the requirement of periodic reversal of polarity [77]. The null detector will be balanced by adjusting the operating frequency of the SET source, f_{SET} . This

¹⁰) Another approach consists of balancing the current delivered by the SET device against the current applied to a cryogenic resistor of high resistance ($100\text{ M}\Omega$) by a Josephson voltage. The current is detected by a CCC

operating as a SQUID ammeter, the primary winding being the input coil coupled to the SQUID via a flux transformer [76]. Then the same CCC is used for calibrating directly the $100\text{ M}\Omega$ resistance with the QHRS [47].

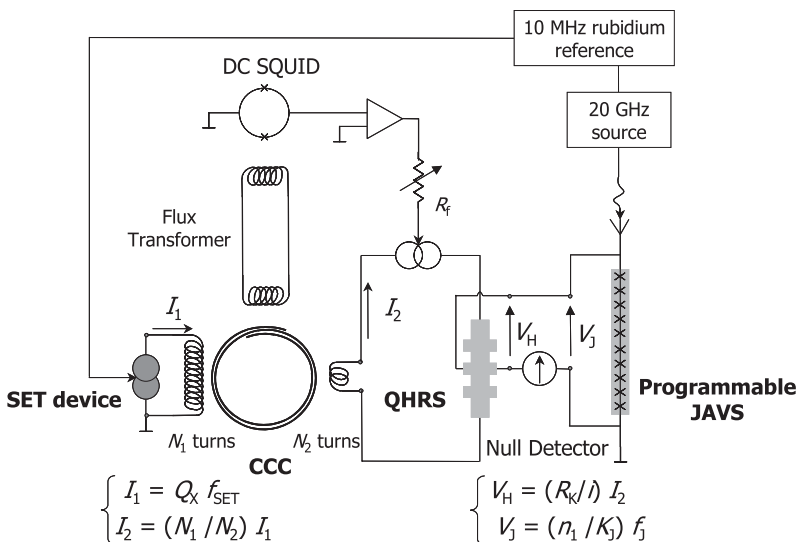


Fig. 9.14 Basic circuit for closing the quantum metrological triangle.

frequency and the irradiation frequency of the JJA are both referred to a 10 MHz rubidium clock.

The great challenge of this experiment is to reduce the “random” uncertainties¹¹⁾ to the lowest possible level, one part in 10^6 or maybe less, taking into account the current of a few picoamps delivered by the electron pumps which are at present assumed to be the most accurate current sources. Indeed, Keller *et al.* have demonstrated that single electrons can be pumped very accurately, *i.e.*, with an uncertainty of one part in 10^8 , at frequencies of a few megahertz [78].

The QMT has been successfully closed within an uncertainty of one part in 10^6 at the National Institute of Standards and Technology (NIST) by constructing an electron counting capacitance standard (ECCS) [72]. This method consists of charging with an electron pump a cryogenic capacitor of known capacitance calibrated in terms of R_k from a QHRs. The voltage drop across the capacitance is controlled with a Josephson array voltage standard. The uncertainty of one part in 10^6 is mainly due to the calibration of a conventional commercial bridge used for measuring the capacitance ratio between the cryogenic capacitor and a room temperature capacitor. In the near future, the uncertainty on the closure of the QMT by this method could be reduced down to one part in 10^7 . We note that developments of ECCSs are in progress at other NMIs (METAS, NPL, PTB)¹²⁾.

11) The largest uncertainties in the instruments used (uncertainties related here to errors coming from systematic effects) are estimated to be of the order of one part in 10^8 , and depend weakly on current level. They arise from the finite open loop

feedback gain and from leakage currents.

12) METAS (Metrologie und Akreditierung Schweiz) and PTB (Physicalisch Technische Bundesanstalt) are the NMIs of Switzerland and Germany, respectively.

9.3.4.2 Design and Performance of the CCC as an Ultra-Low-Current Amplifier

The first way to amplify currents as low as a few picoamps with good accuracy is a CCC with very high winding ratio and with a large inner radius to maximize its inductance. In his pioneering work, Hartland developed a 109 999:1 ratio CCC with an overall diameter of 160 mm leading to a theoretical current resolution $\delta I = 80 \text{ aA/Hz}^{1/2}$ [79]. However, this CCC has never operated properly. One suggested problem is the effect of instability of the helium bath temperature. Another problem might be due to self-resonance. Actually, a compromise on the size of the CCC and on the number of turns of its windings has to be found. The larger these two parameters are, the better the current resolution, but the stronger the influence of external magnetic fields and the lower the self-resonance frequency. The problem relating to the magnetic field is not insurmountable. It can be solved by enhancing the efficiency of the shielding system. For example, the CCC can be enclosed inside two concentric superconducting shields, the inner shield of niobium and the outer shield of lead, the overall system being located in a closed ferromagnetic cylinder. The theoretical attenuation of such a shielding system is 210 dB [34].

However, the self-resonance problem is difficult to overcome, especially when it occurs at low frequency, in the bandwidth of the SQUID. For the CCCs of high winding ratio reported below, self-resonances have been observed at frequencies down to a few kilohertz due to the large inductance of the primary winding (of the order of 1 to 10 H) combined with stray or shunt capacitance (about 100 pF to 1 nF) [35, 45–47]. This has to be compared with the self-resonance frequencies higher than 30 kHz observed for CCCs of small number of turns (2000 turns at most), such as those used for resistance measurements. A solution to damp the resonating LC oscillations consists of providing the CCC with a resistive primary winding, for example of phosphor-bronze wire [47].

Subsequently, several operating CCCs have been developed. Two of them are coupled to a commercial dc SQUID. One is a 40 960:1 ratio CCC with an overall diameter of 64 mm; a current resolution of $\delta I = 800 \text{ aA/Hz}^{1/2}$ has been measured as the white noise floor. The $1/f$ noise occurs at the corner frequency $f_c = 0.3 \text{ Hz}$ [80].

The other is a 20 000:2 ratio CCC with a smaller diameter, 46 mm. It achieves a current resolution of $\delta I = 4 \text{ fA/Hz}^{1/2}$ in the white noise domain and a corner frequency $f_c \approx 0.5 \text{ Hz}$ [34]. The ability to measure currents from 1 pA to a few

femtoamps with a Type A uncertainty¹³⁾ of 50 aA (one standard deviation estimate) over a one hour period has been demonstrated with this CCC [35].

A 45 000:1 ratio CCC coupled to a commercial dc SQUID is still in development at the Laboratoire National de Métrologie et d'Essais (LNE) [82]. With an overall diameter of 114 mm, its current resolution is expected to reach $\delta I \approx 100 \text{ aA/Hz}^{1/2}$ at 1 Hz [83].

This CCC is placed in a temperature-stabilized enclosure at 1.5 K. This enclosure is attached to the bottom part of the dilution refrigerator allowing direct access to the SET device. A more compact CCC will be easier to use at very low temperature, for example by placing it inside a dilution unit very close to the SET device. Based on this idea and the proposal of Seppä *et al.* for a thin-film CCC [84], a CCC with windings based on microlithographic superconducting paths of 2 μm width and spaced by the same width is being investigated at LNE.

A fourth CCC is directly and optimally coupled to a home-made low noise dc SQUID [45,46]. This CCC is provided with a 30 000:1 winding ratio and its overall diameter is 100 mm. The current resolution corresponds to a white noise floor at about $\delta I = 2.1 \text{ fA/Hz}^{1/2}$ over a frequency range down to a surprisingly low corner frequency, $f_c = 0.1 \text{ Hz}$.

A second approach to developing a large-gain CCC while designing it with a small size, as suggested by Sesé *et al.*, is to use a strip-wound ferromagnetic core which increases the inductance of the overlapping tube and maximizes its coupling to the pickup coil [85]. Unlike several earlier reports that the sensitivity of a ferromagnetic core-based CCC is limited by the SQUID's sensitivity, the authors demonstrated that the sensitivity can be preserved or enhanced by introducing a pickup coil with fractional turn loops. However, the dominant $1/f$ noise due to the ferromagnetic core remains too large (the best material currently used is an amorphous CoNiFe alloy) so that there are no realistic chances for improvement.

9.3.4.3 Measurements of SET Current Sources

A few laboratories have been able to carry out measurements of current delivered by SET devices directly by means of a CCC. For instance, the current delivered by a SETSAW device has been measured at NPL by means of a 40 960:1 ratio CCC [80]. However, despite the low uncertainties achieved (3 fA for a 1 nA current), measurements are currently being made using a commercial electrometer, cali-

¹³⁾ Following well established guidelines, for instance the "GUM" [81] which are recommended for properly expressing and estimating the uncertainties of measurements, there are two categories of statistical methods for evaluating the uncertainties, classified as Type A and Type B. Indeed, it is more suitable to distinguish methods of evaluation rather than uncertainties (by separating them into "random" and "systematic" uncertainties depending on whether the errors come from random and systematic effects)

which could lead to ambiguity [82]. The uncertainty evaluated by a Type A method is obtained from a probability density deduced from observed distribution of data. The standard deviation is given by the root square of the usual variance calculated on repeated sets of observations. In contrast to the Type A uncertainties, the uncertainties evaluated by a Type B method are obtained from an assumed probability density based on some level of confidence that an event occurs.

brated to 15 fA for the 2 nA range, accurate enough for testing the SETSAW device.

LNE has reported the first measurements on SET transistors [86] and SET pumps [87] with a 10 000:1 ratio CCC. For these measurements, the SQUID is flux-locked by feeding the current to its modulation coil. By means of a simplified bridge, this internal feedback mode allows one to characterize the SET devices, to measure the noise properties of the complete system with sufficient signal-to-noise ratio and, as reported below, to verify the feasibility of operating SET devices over long periods. In this mode, the gain of the CCC is no longer equal to N_1/N_2 but much smaller and is given by the relation

$$G_{\text{CCC}} = (M_i/M_f)(k/2)(L_{\text{CCC}}/L_i)^{1/2}N_1. \quad (9.30)$$

In practice G_{CCC} amounts to 5800 with a primary winding of $N_1 = 10\,000$ turns compared with a 10 000:1 ratio in the usual external feedback mode.

In the first experiments with SET transistors, well-defined Coulomb oscillations (peaks of 200 fA) have been recorded by voltage biasing the transistor with only 100 nV [83, 86]. For SET pump experiments, flat and extended current steps have been observed at frequencies even as high as 30 MHz ($I = 4.8$ pA) [87]. Preliminary current measurements have been carried out in the electron pumping mode over periods of 30 minutes to 12 hours. An unexpected excess noise was revealed, reaching a level of 130 fA/Hz $^{1/2}$ compared with the CCC noise of 4 fA/Hz $^{1/2}$ (see Figure 9.15). This has led to, for instance, Type A uncertainties of around two parts in 10^4 for the longest measurement time, 12 hours [83].

We note that SET devices operate at very low temperature (< 100 mK) where the thermal fluctuation energy of electrons is negligible compared with the Coulomb energy. In order to prevent any assisted photon tunneling processes [88], it is strongly recommended that one filters out any microwave radiation coming from the rest of the system (kept at higher temperature) [83], particularly radiation generated by the Josephson junctions of the SQUID [87]. This requires specific cables

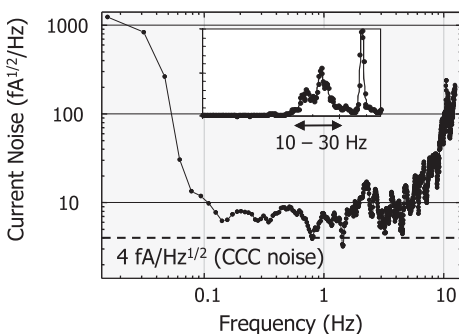


Fig. 9.15 Current noise spectrum of a CCC with an electron pump connected. The insert shows peaks observed around 10 Hz due to environment mechanical vibrations [87].

(some are commercially available) and microwave filters described in detail elsewhere [86, 89].

The measurement time for low currents has to be particularly long in order to reduce the random uncertainties. Special attention has to be paid to the nature of the noise. If the condition of uncorrelated noise is fulfilled, Type A uncertainties may be estimated by calculating the experimental standard deviation of the mean of all data [81]. Statistical methods may be helpful, for example Allan variance analysis, which is widely used in the time and frequency domains and also in the field of electrical metrology [90, 91].

The fact that a SET pump can operate over a time as long as 12 hours as shown by these first measurements is very promising [83, 85]. This confirms the stability time for the background charges (whose change affects the pump accuracy) reported by Keller *et al.* [78]. They found a stability time between one hour and a few tens of hours on a 7-junction pump, which, however, was not connected to an external circuit (including coil, resistor, filter *etc.*) contrary to the case in [83, 85].

This stability permits one to expect a reduction of uncertainties down to a few tens of attoamps with a similar 10 000:1 ratio CCC. In particular, the standard deviation of the mean given by

$$\sigma = \delta I [(f_s - f_R)/N]^{1/2}, \quad (9.31)$$

where $2N$ is the total number of current reversals over this measurement time, may reach 20 aA, for $\delta I = 4 \text{ fA}/\text{Hz}^{1/2}$, a repetition frequency f_R of a single measurement (two current reversals) equal to the corner frequency $f_c = 0.5 \text{ Hz}$ and, in the optimal case, a frequency twice that of the sampling, $f_s = 1 \text{ Hz}$. Improved CCCs, combined with new SET devices able to supply quantized current at least ten times higher than existing SET pumps, should make the closure of the metrological triangle feasible with an uncertainty level of few parts in 10^8 .

9.3.5

Type II CCC for Resistance Measurements at Very High Currents

The flexibility of the CCC concept is illustrated by the high measurement accuracy (achieving a relative uncertainty $\sigma < 10^{-7}$) of high currents (up to 100 A) in the calibration of resistors down to values of $100 \mu\Omega$ [23]. Here, the type II CCC configuration has the advantage over type I that the current-carrying windings may be positioned further away from the superconducting shield. This is required since the surface magnetic field of the high-current-carrying wires could be large enough to exceed the lower critical field H_{c1} of the superconducting shield. In turn this could lead to flux penetration or trapped flux movement, both of which would lead to errors in the CCC current ratio.

CCCs are normally optimized for sensitivity. However, in this high-current application sensitivity to current changes in the windings is not the dominant issue. Instead, there is a risk that background noise in the high-current source will be too large to allow stable SQUID operation. The authors, therefore, deliberately

reduced the SQUID sensitivity by introducing a short loop of superconducting wire in parallel with the SQUID input.

The dimensions of the CCC are shown in Figure 9.5, where it is indicated how the current-carrying windings may be relatively simply changed to allow changes in ratio or of conductor material. Indeed it is easy to wind and rewind over a toroidal shield. For currents up to 1 A superconducting NbTi wire (0.125 mm in diameter) is used whereas for currents up to 100 A six Cu wires are used in parallel, each with a diameter of 0.6 mm. The hatched region within the superconducting shield represents the region occupied by the Nb wire pickup coil. The ends of this coil are taken out through superconducting shields concentric to the SQUID.

The prototype system has a sensitivity of $S_{\text{CCC}} = 13 \times 10^{-6}$ ampereturn/ Φ_0 , with a current detection level of $\delta I/I = 2 \times 10^{-8}/\text{Hz}^{1/2}$. The limiting accuracy for the calibration of low value resistors is currently determined by the temperature coefficient of the resistors themselves, which sets a practical limit of $\sigma \approx 4 \times 10^{-7}$.

9.3.6

CCC for Non-Invasive Sensing of Charged Particle Beams

Another metrological application of the CCC aims at real-time non-invasive measurement of charged particle beams in the range 10 pA–10 mA. Apart from applications in fields such as high energy accelerators, ion implantation and other charged particle beam instruments [92] this use is directed in the longer term at a precision measurement of the Faraday constant F which relates to the SI definition of the amount of substance and the Avogadro constant N via the relationship

$$N = F/e. \quad (9.32)$$

Investigations at NPL [27] into HTS current comparator designs, including a readout SQUID also made from HTS material, are aimed at producing a system capable of good accuracy non-invasive measurement of an ion beam current in the range 1 μA to 10 mA, such as could be integrated with the isotopically pure Au ion beam of the type being used for a Faraday constant measurement at PTB [93]. A tube coated with HTS material, inside and out, forms the CCC. A charged particle beam flows along the axis of the tube and the induced screening currents flow on the inside and outside surfaces; the outer current generates a magnetic field which may be sensed by an external SQUID. Again, as in the other CCC applications, the external field is extremely insensitive to the distribution of the charged particle beam over the cross-section of the tube. The mechanical inflexibility and problems with joining currently available HTS materials means that the design of HTS CCC and readout SQUID are severely constrained: only single-layer systems are feasible with existing technology. A schematic of the prototype device is shown in Figure 9.16.

A further important advantage, not apparently demonstrated in conventional superconductor CCCs, is gained when the tube (which is itself made from an insulating material) is coated both inside and outside by a continuous supercon-

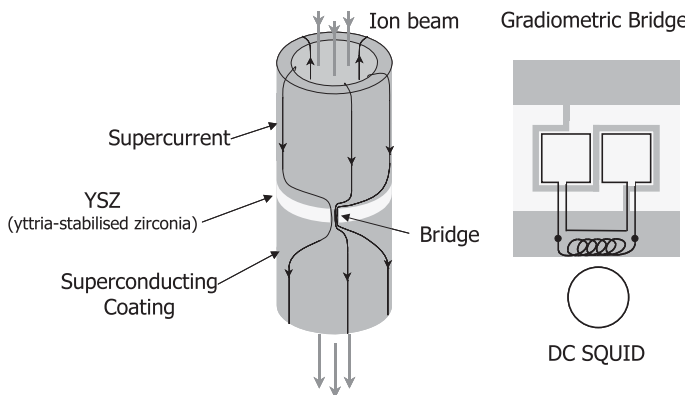


Fig. 9.16 HTS CCC based on YBCO – yttria-stabilized zirconia (YSZ) coated tube coupled to a SQUID gradiometer. The size of the CCC developed at NPL is length = 120 mm, inner diameter = 20 mm, outer diameter = 29 mm.

ducting film. The outer superconducting layer can then be patterned into a narrow bridge structure crossing its median plane, through which a current will flow equal to the entire beam current (as indicated diagrammatically in Figure 9.16). This region of high current density can provide greatly improved coupling to a SQUID detector located near the beam, so that the sensitivity is no longer limited by the need to locate the detector at a distance from the beam which is usually dictated by the tube diameter. The only limits on the dimensions of this bridge are that, first, the total current flowing through it must not exceed the critical current density j_c of the superconducting bridge. A second limit arises when the inductance of the bridge exceeds the inductance of the two-layer superconducting tube in which case current will tend to flow up the inside surfaces of the comparator tube, rather than through the bridge, thereby reducing the sensitivity. Preliminary experiments suggests that δI may be as small as $10 \text{ pA/Hz}^{1/2}$ for simple single-layer HTS structures.

9.4 Other Current Metrological Applications of SQUIDs

9.4.1 Thermometry Using SQUIDs

9.4.1.1 Introduction

Temperature is an unusual physical parameter in that it is not an extensive quantity. Thermodynamic temperature is defined in terms of two fixed points: the absolute zero of temperature (0 K) and the triple point of water (defined to be 273.16 K). There exist a number of primary thermometers which are able to sense

thermodynamic temperatures, but can usually operate over only a limited range of temperature. Thus the best known thermodynamic thermometer is the ideal gas scale. There exists also an International Temperature Scale (ITS-90); it extends down to 0.65 K and is in close agreement with thermodynamic temperatures throughout its range. A number of different thermometers and fixed points are used to realize the scale. SQUIDs may also be used to indicate either thermodynamic temperatures (through the use of the Josephson effects or magnetic flux fluctuations, in various manifestations of primary noise thermometry) or very small temperature changes.

9.4.1.2 Magnetic Susceptibility Measurement for a Secondary Thermometer

There are at least two quite distinct forms of sensitive temperature sensors based on SQUIDs. The first measures the change of susceptibility $\chi(T)$ with the temperature of a paramagnetic system coupled to a SQUID, where the Curie–Weiss law dependence of the susceptibility

$$\chi(T) = C_s/(T - T_c) \quad (9.33)$$

allows very small changes to be detected. Here C_s is a constant dependent on the paramagnetic system used and T_c is the ordering temperature of the dilute spins. This system can be used over a relatively wide temperature range. The method may be extended into the millikelvin temperature range by using very dilute paramagnetic salts (cerium magnesium nitrate (CMN) or lanthanum-diluted CMN, for which $T_c < 2\text{mK}$) by means of a SQUID-based mutual inductance bridge.

It has long been recognized that for a system with heat capacity C there is a Gaussian probability distribution for the mean square temperature fluctuations given by

$$\langle (\Delta T)^2 \rangle = k_B T^2 / C_s. \quad (9.34)$$

When this is converted to a power spectral density $S_T(f)$ of temperature fluctuation in unit bandwidth it is transformed to

$$S_T(f) = 4k_B T^2 / G \quad (9.35)$$

where now G is the thermal conductance to a heat sink controlled at $\langle T \rangle$. This sets a lower limit on the temperature precision which can be achieved with a single measurement within unit bandwidth. Note that the uncertainty scales as T^2 and that the thermal link between thermometer and heat bath should be as strong as possible in order to minimize temperature fluctuations. Readout sensitivity of such a high-resolution thermometer based on a SQUID is a few pK/Hz^{1/2}, easily capable of measuring ΔT for real systems, which is more typically 100 pK/Hz^{1/2}, so the reality of this practical limit to temperature measurement has been demonstrated [94].

9.4.1.3 The SQUID as a Sensor for a Resistance Thermometer

A second method of measuring temperature senses the change in resistance of a thin film superconductor, which is biased (and maintained by negative feedback) at the mid-point of its superconducting transition. The SQUID senses the small change in feedback current which occurs when the temperature of the thin film changes. Since the width of a metallic-superconductor transition can be much less than 1 mK, and a change corresponding to a very small fraction of this width is readily detectable (because of the SQUID's ability to detect sub femtovolt voltage changes), this is an extremely sensitive technique, though of much more limited temperature range. It is clearly related to the bolometric sensor application described in Chapter 8.

9.4.1.4 Noise Measurement for a “Primary” Thermometer

Nyquist's theorem states that the power spectral density of noise voltage S_V across a resistor R at temperature T (in the classical regime) is given by the simple expression

$$S_V = 4k_B T R. \quad (9.36)$$

In principle, this provides a method to measure temperature based only on a determination of noise, a simple resistance measurement and knowledge of Boltzmann's constant k_B . Thermometers based on this expression have been developed mainly for high temperature use, but it turns out that the necessary characterization of the system bandwidth and gain are too difficult to allow the required millikelvin precision at ambient temperatures. However, in the cryogenic regime the extreme sensitivity of SQUIDs may be used to good effect. In this case, the low input impedance of the SQUID means that a more sensitive thermometer may be developed by using the expression for the current noise spectral density S_I associated with a resistance R at temperature T

$$S_I = 4k_B T / R. \quad (9.37)$$

Early work by Webb *et al.* showed that measurements made between 5 mK and 4.2 K agreed within 3% with a magnetic temperature scale derived from the susceptibility of a dilute paramagnetic material [95]. This thermometer does not provide a primary thermometric method since the bandwidth of the SQUID and the flatness of the current gain across the entire bandwidth are required to be known. Rather, it provides a sensitive cryogenic thermometer which may provide rapid measurements down to the lowest temperatures. More recent work by Lusher *et al.* has further improved on the performance [96].

Kamper and Zimmerman suggested that the subtlety of the Josephson effects could provide a true SQUID-based primary noise thermometer [97]. A Josephson junction is shunted by the low resistance R (in the range $1\mu\Omega$ to $1\text{m}\Omega$), forming a resistive SQUID configuration. The essential feature of their proposal was that

the thermally generated voltage fluctuations across the resistor could be used to frequency modulate an oscillating Josephson junction. The observed Lorentzian lineshape Δf of the Josephson oscillation could be accurately measured to provide a measure of the temperature, assuming that R can be accurately measured. A simple and fast way to measure the linewidth of the oscillation is to feed the output from the amplifier to a frequency counter capable of measuring the count variance. In this way, the need to characterize accurately the gain and bandwidth of an amplifier is avoided. In fact the linewidth involves the flux quantum thus:

$$\Delta f = 4\pi k_B T R / \Phi_0^2 . \quad (9.38)$$

The circuit for such a measurement system is shown schematically in Figure 9.17(a).

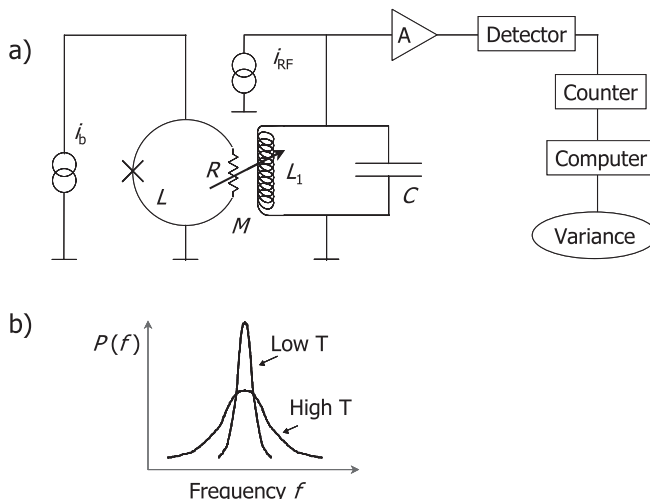


Fig. 9.17 Noise measurement system for a “primary” thermometer.
 (a) Schematic of Josephson line width thermometer with rf SQUID readout. (b) Schematic of probability distribution of Josephson oscillation frequency at low and high temperatures.

This behavior has been accurately verified and compared with other primary thermometers at NIST and forms the basis of one of two primary thermometers available for use below 1 K [98]. A second type of noise thermometer based on flux quantization and superconductivity has also been demonstrated by Lee *et al.* [99]. This is the so-called quantum-roulette noise thermometer in which the probability distribution of the quantized fluxon states of a superconducting ring is experimentally established by repeatedly interrupting the superconducting circuit of the ring and measuring the thermal fluctuation current. A SQUID, magnetically coupled to the superconducting ring, reads out the flux state of the ring following each opening and closing of the switch, allowing a histogram of states to be built

up. The width of this probability distribution in units of flux quanta allows the temperature to be deduced [99]. Such a single-entity thermometer requires that the *principle of ergodicity* is satisfied, that is, the long-time average over an arbitrary function of the phase space coordinates is equal to the average of the same function taken over all possible and equally probable states that the system can go through. This principle is becoming increasingly significant in a variety of fields of temperature measurement, especially where the size of the systems is being reduced towards the nanoscale. When the number of individual entities (such as atoms or molecules) in the system falls below a length-dependent number, the definition of temperature itself becomes problematic. As well as providing a potentially valuable primary noise thermometer using high-temperature superconductors, the quantum-roulette noise thermometer provides a test-bed for investigations of the applicability of this principle of ergodicity.

9.4.2

Radio-Frequency Attenuation with SQUIDs

An rf SQUID pumped (biased) at microwave frequency f presents an impedance which is a function, periodic in Φ_0 , of the instantaneous magnetic flux Φ_a applied to the SQUID ring. This property can be used for calibrating attenuators at radio frequencies.

In the ideal case and for a non hysteretic SQUID, *i.e.*, one characterized by a small critical current $I_0 < \Phi_0/2\pi L$, operating in the non-adiabatic regime ($f > R/2\pi L$), the output voltage of the SQUID is a perfect sinusoidal function of Φ_a :

$$V_{\text{out}}(\Phi_a) = V_0 \sin(2\pi\Phi_a/\Phi_0). \quad (9.39)$$

Similarly, the power reflected by the SQUID will also vary as a sinusoid:

$$P(\Phi_a) = P_{\text{offset}} + P_0 \sin(2\pi\Phi_a/\Phi_0). \quad (9.40)$$

Consider now an applied flux $\Phi_a(t) = \Phi_a \cos(2\pi f_a t)$ varying in time at a frequency f_a much less than the pumping frequency (typically $f_a \approx f/10$), but much greater than the cut-off frequency of the detection circuit bandwidth. It is easy to show that the time-averaged reflected power is given by

$$P = P_{\text{offset}} + P_0 J_0(2\pi\Phi_a/\Phi_0), \quad (9.41)$$

where J_0 is the zeroth-order Bessel function.

As shown in Figure 9.18, the applied flux is created through a mutual inductance by the current I which flows across the attenuator A to be calibrated. The main part of the reflected power will follow the zeroth-order Bessel function of this current $J_0(2\pi I/I_0)$. The detection and counting of the zero crossings of $J_0(2\pi I/I_0)$ allow one to calculate rf current ratios and thus to calibrate the attenuator accurately. The zero crossings of the Bessel function are detected by supplying

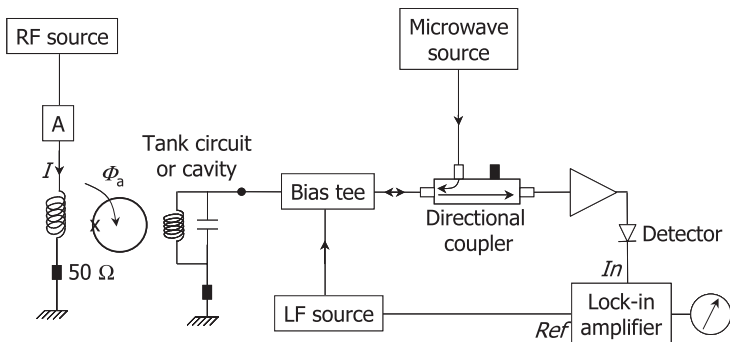


Fig. 9.18 Basic circuit for rf attenuation measurement with microwave pumped SQUID.

the SQUID with a low-frequency (1 kHz) signal and by recording the zeros at the output of a phase-locked amplifier.

Several decades ago, NMIs used such methods to calibrate rf attenuators [100–103]. The microwave-pumped SQUID typically consisted of an adjustable point contact mounted in a superconducting waveguide close to its short-circuited end at a distance of a quarter of a wavelength¹⁴⁾. The best results were an uncertainty of 0.001 dB with a dynamic range of more than 100 dB at frequencies from 0 to 1 GHz. Based on these past experiences with this first generation of microwave pumped SQUIDs, two possible sources were known to create deviations of the instantaneous output voltage of the SQUID from a perfect sinusoid, and thus linearity errors in the measured attenuation. The first possibility was the poor quality of the junction itself, which resulted in an inhomogeneous critical current and, therefore, caused departures from the Josephson relation linking the supercurrent to the phase through a perfect sinusoid.

The second cause was the influence of the measurement signal power on the tunnel resistance of the quasiparticles, *i.e.*, the resistance R of the Josephson junction described by the RCSJ model. This effect becomes significant at high frequencies [102]. Moreover the routine of attenuation measurement was compromised by unreliability of the junction.

The drawbacks above could be solved today with a better understanding of SQUID devices and with improved technology for junction and SQUID fabrication. The use of microwave-pumped SQUIDs¹⁵⁾ for improving attenuation measurement with an uncertainty less than 0.001 dB could be reconsidered as an alternative to the method presently used, which involves the waveguide beyond cut-off (WBCO) attenuator as primary standard.

14) Adjustable point contacts (in niobium or tantalum) were preferably used rather than microbridges, for which some results reported significant error in attenuation, partly due to the bad thermal contact of the junction with the helium bath.

15) This will probably be limited to LTS SQUIDs since high-temperature (cuprate) SQUIDs with grain-boundary junctions have been shown to exhibit a nonsinusoidal Josephson relationship [104].

9.5

Future Trends and Conclusion

This chapter has demonstrated that the best developed and most widely used applications of SQUIDs to metrology occur in the fields of electrical measurements (over a range of frequency and scales) and thermometry (at cryogenic temperatures). This may not always remain the case. It has been observed that metrology (encompassing both precision measurement and standards) provides the earliest applications of many areas of new physics. Examples of this include not only the Josephson effects and the QHE but also many non-SQUID-related innovations in physics such as laser cooling of atoms and the Bose-Einstein condensation. Below we discuss what the authors regard as potentially important future metrological applications of SQUIDs.

As SQUIDs allow the uncertainty principle dominated regime to be investigated, the relationship between quantum measurement fundamentals and quantum metrology comes into focus. At the same time the requirement to make precise measurements at ever smaller length scales initiated a paradigm shift in the nature of electrical (and other) metrology. Thus, as has been made clear above, when SET devices are involved the electrical parameter to be measured is no longer the continuous classical quantity – the electrical current – but rather the quantized electrical charge. Similarly in weakly superconducting electronic circuits it is the passage of single flux quanta which represents the basic electrical measurement not the classical continuous variable which is voltage. Metrology must address the needs of the quantum and nanoscale regimes and SQUIDs are well placed to enable the transition, as we shall see below.

With the increasing importance of the spin component of electron transport for future devices (giant and colossal magnetoresistance effects (GMR, CMR), spin valves, magnetic tunnel junctions, etc.) the capability of the SQUID to detect the smallest level of spin polarization will require optimization. Here, the requirements for SQUIDs are the opposite to those for magnetic field sensing: the SQUID loop directly senses the spin and its area must be minimized, subject to optimal coupling to spins.

The most common applications of SQUIDs have involved measurement of magnetic flux density changes with extreme sensitivity. In such cases, it is important to maximize the sensing area of the input coil coupled to the SQUID. In an increasingly important range of newer applications, relating mainly to spintronics and quantum computing, the SQUID is used to detect magnetization or magnetization changes in a micrometer- or sub-micrometer-size sample. In these cases a quite different set of conditions applies [105–107]. There are two major issues which have to be considered in order to develop further such devices and extend their applicability to the study of samples of nanoscale dimension. Firstly, achieving the required sensitivity for the detection of a low number of spins and secondly, facilitating the deposition of such a small sample within the loop of the SQUID. This will enable many of the standards applications outlined in previous sections to be transferred to the nanoscale in future.

Ultimately, the SQUID may enable single electronic spin flips to be detected, allowing electronic spin resonance (ESR) and other spin manipulations to be done on a single spin. (Recently single spin detection has been achieved using a mechanical magnetic resonance detection device [108] but this technique is rather specialized and of limited applicability). As well as setting the lower limiting size of a single magnetic domain storage element, single spins are also regarded as one of the most promising possible realizations of the *qubits* on which quantum computation will depend, if it becomes feasible. In such a single-spin detection situation the input coil and flux transformer are dispensed with and a “bare” SQUID is used. Reducing the loop area of the SQUID, which reduces its inductance, can increase the energy resolution of the device to near quantum limit operation. Furthermore, a device incorporating a SQUID of small loop area is less sensitive to external magnetic fields, making it an ideal probe of samples situated within the SQUID loop. In the thermal limit, the energy resolution of a SQUID, of capacitance C and inductance L , operating at a temperature T is given by [109]

$$\varepsilon = 16 k_B T (LC)^{1/2}. \quad (9.42)$$

The electronic spin resolution is given by

$$S_n = d \frac{\sqrt{S_\phi}}{2\pi\mu_B\mu_0} \quad (9.43)$$

in units of spins (of moment μ_B) per $\sqrt{\text{Hz}}$, where S_ϕ is the power spectral density of flux noise, related to the energy resolution by $S_\phi = 2\varepsilon L$, and d is the dimension of the SQUID loop, scaled by a geometry-dependent factor between 1 and 10. In measurements made on a set of Nb dc SQUID devices ranging from $d = 100 \mu\text{m}$ down to $3 \mu\text{m}$ it has been demonstrated that the flux noise resolution exhibits the expected linear scaling with d . The smallest device has a spin resolution of about 40 spins in a 1 Hz bandwidth limited by noise in the first-stage room temperature preamplifier. Extension of this scaling to SQUIDs with $d \approx 100 \text{ nm}$ should enable single electronic spin flips to be detected. This work has been extended recently by Jamet *et al.* to barely submicrometer SQUIDs (made using long Dayem bridge Nb Josephson junctions) to investigate the magnetic anisotropy of nanoscale particles containing just 10^3 atoms of Co [110].

The overall aim of the QMT experiments is to verify with a very low uncertainty the coherency of the deduced values of the constants involved in these three quantum phenomena or, in other words, to confirm that these condensed matter physics phenomena, in which interparticle interactions are undoubtedly strong, yield the free space values of constants $2e/h$, h/e^2 and e . The target uncertainty needs to be around one part in 10^8 . If there is no deviation, our confidence in the three phenomena to provide us with $2e/h$, h/e^2 and e will be considerably enhanced. Any significant discrepancy will prompt further experimental and theoretical work. The closure of the QMT, at the required uncertainty of one part in 10^8 or less, should be assisted by improvements in SQUIDs, microlithography techniques and new SET devices which could generate accurate currents as high as

100 pA. Ideas currently under investigation for the implementation of a higher-frequency-locked current source include improved SETSAW devices [111] and superconducting Cooper pair pumps as a generalization of a single electron pump [112].

Very recently, a Cooper pair “sluice” has been proposed. It consists of two mesoscopic SQUIDS forming between them a superconducting island which is fitted with a gate [113] (Figure 9.19). The gate provides the possibility of coherent transfer of Cooper pair charges, one at a time, under the influence of an applied rf signal, with higher accuracy and at higher frequency than has been demonstrated with electron pumps, turnstiles or SETSAW devices. The closure of the QMT to enhance our confidence of the acJE, QHE and SET providing the ratios of fundamental constants h/e^2 , $2e/h$ and e can be viewed as *a bridge between microscopic and macroscopic physics* [114]. This bridge is needed to establish a new structure of the SI units, fully based on fundamental constants. It is not clear when we can expect this new formulation of the SI to be implemented. However, it can be expected that SQUIDs will play an important role in these developments.

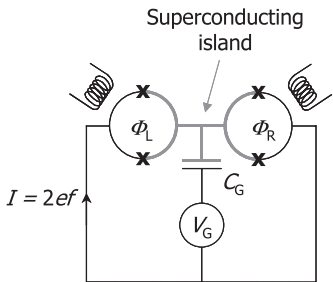


Fig. 9.19 Schematic of a Cooper pair sluice. The flow of Cooper pairs is controlled by varying periodically both the gate voltage V_G applied to the island via a capacitor (C_G) and the magnetic fluxes Φ_R and Φ_L through the SQUID loops. The superconducting island is shown as a thick gray line.

References

- 1 Clarke, J. (1966) A superconducting galvanometer employing Josephson tunnelling, *Phil. Mag.* **13**, 115–127.
- 2 Clarke, J. (1968) An experimental comparison of the Josephson voltage frequency relation in different superconductors, *Phys. Rev. Lett.* **21**, 1566–1569.
- 3 Jain, A. K., Lukens, J. E., and Tsai, J. S. (1987) Test for relativistic gravitational effects on charged particles, *Phys. Rev. Lett.* **58**, 1165–1168.
- 4 Tsai, J. S., Jain, A. K. and Lukens, J. E., (1983) High precision test of the universality of the Josephson voltage-frequency relation, *Phys. Rev. Lett.* **51**, 316–319.
- 5 CIPM (1988) Représentation du volt au moyen de l'effet Josephson [Representation of the volt by means of Josephson effect], Recommandation 1 (CI – 1988), 77ème session, (1988).
- 6 Mohr, P. J., and Taylor, B. N., (2005) CODATA (Committee on Data for Science and Technology) recommended values of the fundamental physical constants: 2002, *Rev. Mod. Phys.* **77**, 1–107.
- 7 Pöpel, R. (1992) The Josephson effect and voltage standards, *Metrologia* **29**, n°2, 153–174.
- 8 Hamilton, C. A. (2000) Josephson voltage standards, *Rev. Sci. Instrum.* **71**, 3611–3623.
- 9 Eichenberger, A., Jeckelmann, B., and Richard, P., (2003) Tracing Planck's constant to the kilogram by electromechanical method, *Metrologia* **40**, 356–365.
- 10 Shiota, F., Miki, Y., Namba, A., Nezu, Y., Sakamoto, Y., Morokuma, T., and Hara, K., (1995) Absolute determination of the magnetic flux quantum using superconducting magnetic levitation, *IEEE Trans. I&M* **44**, 583–586.
- 11 Shiota, F., Miki, Y., Fuji, Y., Morokuma, T., and Nezu, Y. (2000) Evaluation of equilibrium trajectory of superconducting magnetic levitation system for the future kg unit of mass, *IEEE Trans. I&M* **49**, 1117–1121.
- 12 Frantsuz, E. F., Gorchakov, Y. D., and Khavinson, V. M. (1992) Measurements of the magnetic flux quantum, Planck constant, and elementary charge using superconducting magnetic levitation, *IEEE Trans. I&M* **41**, 482–485.
- 13 Riski, K., Heikkilä, P., Kajastie, H., Manninen, J., Rossi, H., Nummila, K., Frantsuz, E., and Khavinson, V. (2001) Design of a superconducting magnetic levitation system, in *Proc. IMEKO TC3 2001*, pp.239–246.
- 14 Sachslehner, F. (1998) Two-channel DC-SQUID picovoltmeter for the measurement of low-field Hall coefficient and electrical resistance from 4.2 to 100 K, *Cryogenics* **38**, 293–298.
- 15 Delahaye, F., and Bournaud, D. (1991) Low noise measurements of the quantized Hall resistance using an improved cryogenic current comparator bridge, *IEEE Trans. I&M* **40**, 237–240.
- 16 Miklich, A. H., Koelle, D., Ludwig, F., Nemeth, D. T., Dantsker E., and Clarke, J. (1995) Picovoltmeter based on a high transition temperature SQUID, *Appl. Phys. Lett.* **66**, 230–232.
- 17 Eriksson, T. Blomgren, J., and Winkler, D. (2002) An HTS SQUID picovoltmeter used as preamplifier for Rogowski coil sensors, *Physica C* **368**, 130–133.
- 18 Dziuba, R. F., Field, B. F., and Finnegan, T. F. (1974) Cryogenic voltage comparator system for $2e/h$ measurement, *IEEE Trans. I&M* **23**, 264–267.
- 19 Harvey, I. K. (1976) Cryogenic ac Josephson effect emf standard using a superconducting current comparator, *Metrologia* **12**, 47–54.
- 20 Harvey, I. K. (1972) Precise low temperature DC ratio transformer, *Rev. Sci. Instrum.* **43**, 1626–1629.
- 21 Sullivan, D. B., and Dziuba, R. F. (1974) Low temperature direct current comparator, *Rev. Sci. Instrum.* **45**, 517–519.
- 22 Grohmann, K., Hahlbohm, H. D., Lübbig, H., and Ramin, H. (1973) Construction principles and properties of ironless DC and AC current comparators with superconducting shields, *PTB Mitt.* **83**, 313–318.
- 23 Williams, J. M., and Kleinschmidt P. (1999) A cryogenic current comparator

- bridge for resistance measurements at currents of up to 100 A, *IEEE Trans. I&M* **48**, 375–378.
- 24** Elmqvist, R. E. (1999) Cryogenic current comparator measurements at 77 K using thallium-2223 thick-film shields, *IEEE Trans. I&M* **48**, 383–386.
- 25** Elmqvist, R. E., and Dziuba, R. F. (1995) High-temperature superconductor cryogenic current comparator, *IEEE Trans. I&M* **44**, 262–264.
- 26** Arri, E., Boella, G., Pavese, F., Negro, A., Vanolo, M., Dagnino, C., and Lamberti, P. (1998) Improved studies on an HTS current cryocomparator with thick-film YBCO toroidal shield, in *Proc. CPEM'98*, Washington DC, pp. 221–222.
- 27** Hao, L., Macfarlane, J. C., and Gallop, J. C. (1999) Ion beam measurement with a high-temperature superconductor SQUID and current comparator, *IEEE Trans. I&M* **48**, 302–305.
- 28** Early, M. D., Jones, K., Staines, M. P., and Exley, R. R. (1999) Development of a split-toroid high-temperature superconducting cryogenic current comparator, *IEEE Trans. I&M* **48**, 306–309.
- 29** Early, M. D., and Jones, K. (1997) Optimum sensitivity of an externally shielded cryogenic current comparator, *IEEE Trans. I&M* **46**, 459–462.
- 30** Frantsuz, E. T. (1998) On forward estimate of the sensitivity of a cryogenic current comparator, *Metrologia* **35**, 847–851.
- 31** Early, M. D., and van Dam, M.A. (1999) Results from a detailed calculation of the sensitivity of a cryogenic current comparator, *IEEE Trans. I&M* **48**, 379–382.
- 32** Sesé, J., Lera, F., Camon, G. and Rillo, C. (1999) Calculation of effective inductances of superconducting devices. Application to the cryogenic current comparator, *IEEE Trans. Appl. Supercon.* **9**, 58–62.
- 33** Rillo, C., Sesé, J., Bartolomé, E., Flokstra, J., Camon, A., and Rietveld, G. (2003) On the sensitivity of cryogenic current comparators : theory and experiments, *Metrologia* **40**, 51–56.
- 34** Gay, F., Piquemal, F., and Genevès, G. (2000) Ultra low noise current amplifier based on a cryogenic current comparator, *Rev. of Sci. Instrum.* **71**, 4592–4595.
- 35** Gay, F. (2000) Un comparateur cryogénique de courants pour la réalisation d'un étalon quantique basé sur l'effet tunnel monoélectron [Cryogenic current comparator for the realisation of a quantum standard based on single electron tunneling], *PhD Thesis*, Conservatoire National des Arts et Métiers, Paris, France (in French).
- 36** Symm, G. T. (1992) Design of a cryogenic current comparator, in *Proc. Boundary Elements XIV*, 1, Brebbia, C. A., Dominguez, J., and Paris, F. (Eds), pp. 519–526.
- 37** Sesé, J., Bartolomé, E., Flokstra, J., Rietveld, G., Camon, A., and Rillo, C. (2003) Simplified calculus for the design of a cryogenic current comparator, *IEEE Trans. I&M* **52**, 612–616.
- 38** Sesé, J. (1999) Optimacion del patron cuantico de resistencia [Optimisation of the quantum resistance standard], *PhD Thesis*, Saragossa University, Spain, in Spanish.
- 39** Grohmann, K., Hahlbohm, H.D., and Hechtfischer, D. (1979) The cryocurrent comparator as a calculable dc ratio standard, *IEEE Trans. I&M* **28**, 205–211.
- 40** Seppä, H. (1990) The ratio error of the overlapped-tube cryogenic current comparator, *IEEE Trans. I&M* **39**, 689–697.
- 41** Delahaye, F., and Reymann, D. (1985) Progress in resistance ratio measurements using a cryogenic current comparator at LCIE, *IEEE Trans. I&M* **34**, 316–319.
- 42** Grohmann, K., and Hechtfischer, D. (1984) Self calibrating cryo current comparators for ac applications, *IEEE Trans. I&M* **33**, 91–96.
- 43** Seppä, H., and Satrapinski, A. (1997) AC resistance bridge based on the cryogenic current comparator, *IEEE Trans. I&M* **46**, 463–466.
- 44** Delahaye, F. (1991) An ac-bridge for low frequency measurements of the quantized Hall resistance, *IEEE Trans. I&M* **40**, 883–888.
- 45** Bartolomé, E. (2002) Cryogenic current comparators with optimum SQUID readout for current and resistance quan-

- tum metrology, *PhD Thesis*, Twente University, The Netherlands.
- 46** Rietveld, G., Bartolomé, H., Sesé, J., de la Court, P., Flokstra, J., Rillo, C., and Camon, A. (2003) 1:30 000 cryogenic current comparator with optimum SQUID readout, *IEEE Trans. I&M* **52**, 621–625.
- 47** Elmquist, R. E., Hourdakis, E., Jarret, D. G., and Zimmerman, N. M. (2005) Direct resistance comparisons from the QHR to 100 MΩ using a cryogenic current comparator, *IEEE Trans. I&M* **54**, 525–528.
- 48** Delahaye, F., and Bournaud, D. (1993) Accurate AC measurements of standard resistors between 1Hz and 20 Hz, *IEEE Trans. I&M* **42**, 287–291.
- 49** Piquemal, F. (1999) L'effet Hall quantique en métrologie [Quantum Hall effect in metrology], *Bulletin du BNM* **116**, 5–57 (in French).
- 50** Jeckelmann, B., and Jeanneret, B. (2000) The quantum Hall effect as an electrical resistance standard, *Rep. Prog. Phys.* **64**, 1603–1655.
- 51** Delahaye, F., and Jeckelmann, B. (2003) Revised technical guidelines for reliable dc measurements of the quantized Hall resistance, *Metrologia* **40**, 217–223.
- 52** Hartland, A., Jones, K., Williams, J. M., Gallagher, B. L., and Galloway, T. (1991) Direct comparison of the quantized Hall resistance in gallium arsenide and silicon, *Phys. Rev. Lett.* **66**, 969–973.
- 53** Jeckelmann, B., Inglis, A. D., and Jeanneret, B. (1995) Material, device, and step independence of the quantized Hall resistance, *IEEE Trans. I&M* **44**, 269–272.
- 54** Data can be found on BIPM website: <http://bipm.fr/>.
- 55** Delahaye, F., Witt, T., Piquemal, F., and Genevès, G. (1995) Comparison of quantum Hall effect resistance standards of the BNM-LCIE and the BIPM, *IEEE Trans. I&M* **44**, 258–261.
- 56** Delahaye, F., Witt, T., Jeckelmann, B., and Jeanneret, B. (1996) Comparison of quantum Hall effect resistance standards of the OFMET and the BIPM, *Metrologia* **32**, 385–388.
- 57** Delahaye, F., Witt, T., Pesel, E., Schumacher, B., and Warnecke, P. (1997) Comparison of quantum Hall effect resistance standards of the PTB and the BIPM, *Metrologia* **34**, 211–214.
- 58** Delahaye, F., Witt, T., Elmquist, R., and Dziuba, R. F. (2000) Comparison of quantum Hall effect resistance standards of the NIST and the BIPM, *Metrologia* **37**, 173–176.
- 59** Satrapinski, A., Seppä, H., Schumacher, B., Warnecke, P., Delahaye, F., Poirier, W., and Piquemal, F. (2001) Comparison of four QHR systems within one month using a temperature and pressure stabilized 100 Ω resistor, *IEEE Trans. I&M* **50**, 238–241.
- 60** Nakanishi, M., Kinoshita, J., Endo, T., Zhang, Z., Shao, H., He, Q., and Liang, B. (2002) Comparison of resistance standards between the National Institute of Metrology (China) and the Electrotechnical Laboratory (Japan), *Metrologia* **39**, 207–212.
- 61** CIPM (1988) Représentation de l'ohm au moyen de l'effet Hall quantique [Representation of the ohm by means of quantum Hall effect], Recommandation 2 (CI – 1988), 77^{ème} session.
- 62** Pesel, E., Schumacher, B., and Warnecke, P. (1995) Resistance scaling up to 1 MΩ with a cryogenic current comparator, *IEEE Trans. I&M* **44**, 273–275.
- 63** Fletcher, N., Janssen, J. T., and Williams, J. (2001) A cryogenic current comparator based resistance bridge for the range 10 kΩ to 1 GΩ, in *Proc. British Electro-Magnetic Conference BEMC'01*, Harrogate, UK.
- 64** Poirier, W., Bounouh, A., Hayashi, K., Fhima, H., Piquemal, F., Genevès, G., and André, J. P. (2002) $R_K/100$ and $R_K/200$ quantum Hall array resistance standards, *J. Appl. Phys.* **92**, 2844–2854.
- 65** Poirier, W., Bounouh, A., Piquemal, F., and André, J. P. (2004) A new generation of QHARS : Discussion about the technical criteria for quantization, *Metrologia* **41**, 285–294.
- 66** Hartland, A. (1992) The quantum Hall effect and resistance standards, *Metrologia* **29**, 175–190.
- 67** Geerligs, L. J., Anderegg, V. F., Holweg, P. A., Mooij, J. E., Pothier, H., Estève, D., and Devoret, M. H. (1990) Fre-

- quency-locked turnstile device for single electrons, *Phys. Rev. Lett.* **64**, 2691–2694.
- 68** Pothier, H., Lafarge, P., Estève, D., Urbina, C., and Devoret, M. H. (1992) Single electron pump based on charging effects, *Europhys. Lett.* **17**, 249–254.
- 69** Grabert H., and Devoret M. H (eds.) (1991) *Single charge Tunneling Coulomb Blockade Phenomena in Nanostructures, Nato ASI series*, New York Plenum Press., B294.
- 70** Shilton, J. M., Talyanskii, V. I., Pepper, M., Ritchie, D.A., Frost, J. E. F., Ford, C. J. B., Smith, C. G., and Jones, A.C. (1996) High-frequency single-electron transport in a quasi-one-dimensional GaAs channel induced by surface acoustic waves, *Journal of Physics : Condensed Matter* **8**, L531–L539.
- 71** Likharev, K., and Zorin, A. (1985) Theory of the Bloch-wave Oscillations in small Josephson junctions, *J. Low Temp. Phys.* **59**, 347–382.
- 72** Keller, M. W., Eichenberger, A. L., Martinis, J. M., and Zimmerman, N. M. (1999) A capacitance standard based in counting electrons, *Science* **285**, 1706–1709.
- 73** Keller, M. W. (2001) Standards of current and capacitance based on single-electron tunneling devices, in *Recent Advances in Metrology and Fundamental Constants, FERMI School CXLVI*, Varenna, Italy, pp. 291–316.
- 74** Piquemal, F., and Genevès, G. (2000) Argument for a direct realization of the quantum metrological triangle, *Metrologia* **37**, 207–211.
- 75** Piquemal, F., Bounouh A., Devoille L., Feltin N., Thevenot O., and Trapon G. (2004) Fundamental electrical standards and the quantum metrological triangle, *C. R. Physique* **5**, 857–879.
- 76** Elmquist, R., Zimmerman, N. M., and Huber, W. H. (2003) Using a high-value resistor in triangle comparisons of electrical standards, *IEEE Trans. I&M* **52**, 590–593.
- 77** Hamilton, C. A., Burroughs, C. J., and Kautz, R. L. (1995) Josephson D/A converter with fundamental accuracy, *IEEE Trans. I&M* **44**, 223–225.
- 78** Keller, M. W., Martinis, J. M., Zimmerman, N. M., and Steinbach, A. H. (1996) Accuracy of electron counting using a 7-junction electron pump, *Appl. Phys. Lett.* **69**, 1804–1807.
- 79** Hartland, A. (1993) Development of a cryogenic current comparator for the measurement of small current, in *Proc. British Electro-Magnetic Conference BEMC'93*, UK, pp. 18/1–18/4.
- 80** Janssen, T. B. J. M., and Hartland, A. (2000) Accuracy of quantized single electron current in a one dimensional channel, *Phys. B.* **284-288**, 1790–1791.
- 81** ISO (1993) *Guide to the Expression of Uncertainty in Measurement*, International Standardization Organisation (ISO).
- 82** Following some changes of French metrological organization (2001–2005), the same group reported on its works under successive labels BNM-LCIE (Bureau National de Métrologie – Laboratoire Central des Industries Electriques) then BNM-LNE (Laboratoire National d'Essais) and since 2005 LNE (Laboratoire National de Métrologie et d'Essais).
- 83** Feltin, N., Devoille, L., and Piquemal, F. (2004) Contribution of LNE within the COUNT project, In *COUNT final report*, van den Brom, H., Coord., contract no. G6RD-CT 1999-00046 (unpublished).
- 84** Seppä, H., Satrapinski, A., Kiviranta, M., and Virkki, V. (1999) Thin-film cryogenic current comparator, *IEEE Trans. I&M* **48**, 365–369.
- 85** Sesé, J., Camon, A., Rillo, C., and Rietveld, G. (1999) Ultimate current resolution of a cryogenic current comparator, *IEEE Trans. I&M* **48**, 1306–1313.
- 86** De Wilde, Y., Gay, F., Piquemal, F., and Genevès, G. (2001) Measurements of single electron transistor devices combined with a CCC: progress report, *IEEE Trans. I&M* **50**, 231–234.
- 87** Feltin, N., Devoille, L., Piquemal, F., Lotkhov, S., and Zorin, A. (2003) Progress in measurements of single electron pump by means of a CCC, *IEEE Trans. I&M* **52**, 599–603.
- 88** Covington, M., Keller, M. W., Kautz, R. L., and Martinis, J. M. (2000) Noise-induced leakage and counting errors in the electron pump, *Phys. Rev. Lett.* **84**, 5192–5195.

- 89** Vion, D., Orfila, P. F., Joyez, P., Estève, D., and Devoret, M. H. (1995) Miniature electrical filters for single electron devices, *J. Appl. Phys.* **77**, 2519–2524.
- 90** Allan, D. W. (1987) Should the classical variance be used as a basic measure in standards metrology, *IEEE Trans. I&M* **36**, 646–654.
- 91** Witt, T. J. (2000) Testing for correlations in measurements, in *Advanced Mathematical and Computational techniques in Metrology IV*, Ciarlini, P., Paves, F. and Richter, D., (Eds.), Singapore: World Scientific, pp. 273–288.
- 92** See for instance: Peters, A., Vodel, W., Koch, H., Neubert, R., Reeg, H., and Schroeder, C. H. (1998) A Cryogenic Current Comparator for the absolute measurement of nA beams, *AIP Conference Proc.* **451**, 163–180.
- 93** Ratschko, D., Zhou, B. G., Knolle, D. and Glaeser, M. (1997) Investigations on ion beams from a high current ion source, *IEEE Trans. I&M* **46**, 588–591.
- 94** Day, P., Hahn, I., Talso, C. P., Chui, Harter, A. W., Rowe, D., and Lipa, J. A. (1997) The fluctuation-imposed limit for temperature measurement, *J. Low Temp. Phys.* **107**, 359–370.
- 95** Webb, R. A., Giffard, R. P., and Wheatley, J. C. (1973) Noise thermometry at ultra low temperatures, *J. Low Temp. Phys.* **13**, 383–429.
- 96** Lusher, C. P., Junyun, Li, Maidanov, V. A., Digby, M. E., Dyball, H., Casey, A., Nyéki, J., Dmitriev, V. V., Cowan, B. P., and Saunders, J. (2001) Current sensing noise thermometry using a low T_c DC SQUID preamplifier, *Meas. Sci. Technol.* **12**, 1–15.
- 97** Kamper, R. A., and Zimmerman, J. E. (1971) Noise thermometry with the Josephson effect, *J. Appl. Phys.* **42**, 132–136.
- 98** Hudson, R. P., Marshak, H., Soulén, R. J., and Utton, D. B. (1975) Recent advances in thermometry below 300mK, *J. Low Temp. Phys.* **20**, 1–102.
- 99** Lee, R. A. M., Macfarlane, J., Romans, E., Ling Hao, Peden, D., and Gallop, J. (2001) Quantum Roulette Noise Thermometer: progress and prospects, *IEEE Trans. Appl. Supercond.* **11**, 859–862.
- 100** Kamper, R. A., Simmonds, M. B., Adair, R. T., and Hoer, C. A. (1973) A new technique for rf measurements using superconductors, in *Proceedings of IEEE* **61**, 121–122.
- 101** Sullivan, D. B., Adair, R., and Frederick, N. V. (1978) RF instrumentation based on superconducting quantum interference, in *Proc. IEEE* **66**, 454–463.
- 102** Petley, B. W., Morris, K., Yell, R. W., and Clarke, R. N. (1976) Moulded microwave SQUID for RF attenuation calibration, *Electron. Lett.* **12**, 237–238.
- 103** Seppä, H. (1983) Some new aspects concerning the X band SQUID for the measurement of RF attenuation, *IEEE Trans. I&M* **32**, 253–259.
- 104** Il'ichev, E., Zakosarenko, V., Ijsselsteijn, R., Schultze, V., Meyer, H., Hoenig, H., Hilgenkamp, H., and Mannhart, J. (1998) Nonsinusoidal Current-Phase Relationship of Grain Boundary Josephson Junctions in High-Tc Superconductors, *Phys. Rev. Lett.* **81**, 894–897.
- 105** Gallop, J. C., and Radcliffe, W. J. (1985) An absolute SQUID magnetometer, *IEEE Trans. Magn.* **21**, 602–605.
- 106** Ketchen, M. B., Awschalom, D. D., and Gallagher, W. J. et al. (1989) Design, fabrication, and performance of integrated miniature SQUID susceptometers, *IEEE Trans. Magn.*, **25** n° 2, 1212–1215.
- 107** Narasimhan, L. R., Takigawa M., and Ketchen M. B. (1994) Magnetic resonance of a small platinum particle using an integrated dc SQUID, *Appl. Phys. Lett.* **65**, 1305–1307.
- 108** Rugar, D., Budakian, R., Mamin, H. J., and Chui, B. W. (2004) Single spin detection by magnetic resonance force microscopy, *Nature* **430**, 329–332.
- 109** Tesche, C. D., and Clarke, J. (1977) DC SQUID: Noise and Optimization, *J. Low Temp. Phys.* **29**, 301–331.
- 110** Jamet, M., Wernsdorfer, W., Thirion, C., Mailly, D., Dupuis, V., Mélinon, P., and Pérez, A. (2001) Magnetic Anisotropy of a Single Cobalt Nanocluster, *Phys. Rev. Lett.* **86**, 4676–4679.
- 111** Fletcher, N. E., Ebbecke, J., Janssen, T. J. B. M., Ahlers, F., Pepper, M., Beere, H. E., and Ritchie, D. A. (2003) Quantized acoustoelectric current transport through a static quantum dot using a

- surface acoustic wave, *Phys. Rev. B* **68**, 245310/1–3.
- 112** Zorin, A., B., Lotkhov, S. V., Bogoslovsky, S. A., and Niemeyer, J. (2001) Radio-frequency-driven motion of single Cooper pairs across the superconducting single-electron transistor with dissipative environment, *cond-mat*/0105211.
- 113** Niskanen, A. O., Pekola, J., P., and Seppä, H. (2003) Fast and accurate single-island charge pump: Implementation of a Cooper pair pump, *Phys. Rev. Lett.* **91**, 177003/1–4.
- 114** Bordé, C., private communication.

10

The Magnetic Inverse Problem

Eduardo Andrade Lima, Andrei Irimia and John P. Wikswo

| | | |
|----------|--|-----|
| 10.1 | The Peculiarities of the Magnetic Inverse Problem | 141 |
| 10.2 | The Magnetic Forward Problem | 145 |
| 10.2.1 | Introduction | 145 |
| 10.2.2 | Magnetic Fields from Magnetization Distributions | 146 |
| 10.2.2.1 | Field and Moment of a Magnetic Dipole | 146 |
| 10.2.2.2 | Magnetic Fields from Ferromagnetic Materials | 147 |
| 10.2.2.3 | Magnetic Fields from Paramagnetic and Diamagnetic Materials | 148 |
| 10.2.3 | Magnetic Fields from Current Distributions | 149 |
| 10.2.4 | Magnetic Fields from Multipole Sources | 152 |
| 10.2.4.1 | Introduction | 152 |
| 10.2.4.2 | Poisson's and Laplace's Equations | 152 |
| 10.2.4.3 | Magnetic Multipoles | 159 |
| 10.2.4.4 | Current Multipoles in Conducting Media | 165 |
| 10.3 | The Magnetic Inverse Problem | 168 |
| 10.3.1 | Introduction | 168 |
| 10.3.2 | Inverting the Law of Biot and Savart | 168 |
| 10.3.2.1 | Nonuniqueness of Inverse Solutions | 168 |
| 10.3.2.2 | The Spatial Filtering Approach | 169 |
| 10.3.2.3 | Dipole Fitting | 208 |
| 10.3.2.4 | Methods for Regularization | 209 |
| 10.3.2.5 | Lead Field Analysis | 210 |
| 10.3.2.6 | The Finite-Element Method | 216 |
| 10.3.2.7 | Phase-Sensitive Eddy-Current Analysis | 226 |
| 10.3.2.8 | Summary of Inverse Magnetic Imaging of Current Distributions | 227 |
| 10.3.3 | Imaging Magnetization Distributions | 227 |
| 10.3.3.1 | The Dipole Field Equation | 227 |
| 10.3.3.2 | Inverting the Dipole Field Equation for Diamagnetic and Paramagnetic Materials | 230 |
| 10.3.3.3 | Two-Dimensional Magnetization Imaging | 231 |
| 10.3.3.4 | Magnetic Susceptibility Tomography | 232 |
| 10.3.4 | The Inverse Problem and Silent Sources | 237 |

- 10.3.4.1 Introduction 237
- 10.3.4.2 The Helmholtz Decomposition 237
- 10.3.4.3 Electrically Silent Sources 239
- 10.3.4.4 Multipole Expansions 241
- 10.3.4.5 Multiple Dipole Models 243
- 10.3.5 Three-Dimensional Inverse Algorithms 245
 - 10.3.5.1 Introduction 245
 - 10.3.5.2 Beamformers 245
 - 10.3.5.3 Minimum Norm Techniques 246
 - 10.3.5.4 FOCUSS 248
 - 10.3.5.5 MUSIC 249
 - 10.3.5.6 Principal and Independent Component Analysis 251
 - 10.3.5.7 Signal Space Projection 252
 - 10.3.5.8 Other Three-Dimensional Methods 253
- 10.4 Conclusions 254

10.1

The Peculiarities of the Magnetic Inverse Problem

In the early days of SQUID magnetometry, a researcher was fortunate to have a single SQUID magnetometer to measure the magnetic field at a small number of locations outside of an object such as the human head or chest, a rock, a thin metal film, or a block of superconductor. The nature of the source being studied and the type of information being obtained would dictate the number of locations where the field had to be measured and how the data were to be analyzed. The fact that the magnetic field was measured from outside the object rather than from within meant that the description of the object was in fact inferred from the magnetic field by using the measurements to specify a limited number of parameters of a model that might describe the object. This process is known as the “magnetic inverse problem” and involves obtaining a description of the magnetic sources from measurements of their magnetic field.

An extremely simple example of the magnetic inverse problem would be to determine the average remanent magnetization of a large spherical object from an external magnetic field measurement. If the sphere were known to be homogeneously magnetized, the magnetic field outside of the sphere would be identical to that of a point magnetic dipole located at the center of the sphere. The magnetic field \vec{B} at the point \vec{r} produced by a point magnetic dipole \vec{m} at the point \vec{r}' is given by

$$\vec{B}(\vec{r}) = \frac{\mu_0}{4\pi} \left\{ \frac{3\vec{m} \cdot (\vec{r} - \vec{r}')}{|\vec{r} - \vec{r}'|^5} (\vec{r} - \vec{r}') - \frac{\vec{m}}{|\vec{r} - \vec{r}'|^3} \right\}. \quad (10.1)$$

Since this equation is linear in the dipole moment \vec{m} , if the location of the dipole is known, this equation can be inverted to obtain the three components of \vec{m} from measurement of the three components of \vec{B} at a single point \vec{r} ¹⁾

1) Taking the dot product of (10.1) with

$(\vec{r} - \vec{r}')$ and rearranging terms, we get

$$\vec{m} \cdot (\vec{r} - \vec{r}') = \frac{2\pi}{\mu_0} |\vec{r} - \vec{r}'|^3 \vec{B}(\vec{r}') \cdot (\vec{r} - \vec{r}').$$

By substituting this expression into (10.1) we obtain (10.2) after some manipulation (Mark Leifer, personal communication).

$$\vec{m} = \frac{4\pi}{\mu_0} |\vec{r} - \vec{r}'|^3 \left\{ \frac{3}{2} \frac{\vec{B}(\vec{r}') \cdot (\vec{r} - \vec{r}')}{|\vec{r} - \vec{r}'|^2} (\vec{r} - \vec{r}') - \vec{B}(\vec{r}') \right\}. \quad (10.2)$$

Hence it is sufficient to measure the magnetic field \vec{B} at a single known location \vec{r} outside of the sphere. However, if our sphere has only a small number of small regions that are magnetized but at unknown locations within the sphere, we would need multiple dipoles to describe the field. Since the location of these dipoles is unknown, the nonlinearity of (10.1) in \vec{r} and \vec{r}' makes the inverse process much harder; in general, there is no closed-form analytical solution for determining both \vec{m} and \vec{r}' from measurements of \vec{B} at multiple locations. In this context, there is another serious implication of (10.1): the fall-off of the field with distance serves as a harsh low-pass spatial filter, so that the further a magnetic object is from the measurement location, the greater is the spatial blurring of the contribution of adjacent source regions. The loss of information with distance is so rapid that it often cannot be balanced by realistic reductions of sensor noise.

More importantly, were the object we were studying to contain a spherical shell of uniform radial magnetization, the integration of (10.1) over that shell would produce a zero magnetic field outside of the shell. Hence no magnetic measurements and inverse process would be able to detect the presence of such a closed shell were it somewhere inside the object. Similar problems occur in the interpretation of magnetic fields from current sources in conducting objects, whether they are a heart, a brain, or a corroding aircraft wing: whenever a measured field obeys Laplace's equation, there exists the possibility of source distributions with symmetries such that they produce no externally detectable fields. The ability to add or subtract such silent sources at will without altering the measured field corresponds to the lack of a unique solution to an inverse problem.

The nonuniqueness of the solution to the inverse problem was first realized by Helmholtz [1] in 1853, but was described in the context of electrostatics. Helmholtz stated [2], in now-archaic terminology, that "... the same electromotoric surface may correspond to infinitely many distributions of electromotoric forces inside the conductors, which have only in common that they produce the same tensions (voltages) between given points on the surface." As we will see in the following sections, both electric and magnetic fields satisfy Laplace's and Poisson's equations in the static limit and, consequently, have many properties in common, such as nonuniqueness. We will weave aspects of silent source distributions throughout this chapter.

Added problems, or at least confusion, can arise from the vector nature of the magnetic field, in that often an array of SQUIDs may not measure all three components of the magnetic field vector. To explore this, let us consider an infinite volume divided into upper and lower semi-infinite half spaces. Current and magnetization distributions occupy the lower half space, while the upper half space is vacuum. We further restrict our problem by placing our SQUIDs only on a hori-

zontal plane in the upper half space, as shown in Figure 10.1. In theory, a measurement of a *single component* of the vector magnetic field everywhere over this infinite horizontal plane will contain all of the information about the magnetic field everywhere in the upper half space, consistent with the magnetic field obeying Laplace's equation. Upward or downward continuation of the measured magnetic field above or below the measurement plane will allow one to specify the magnetic field everywhere in the upper half space. In practice, however, one can measure the magnetic field at only a finite number of locations in the plane. In this case, there are not only issues regarding the Shannon sampling theorem and the maximum allowable separation between field measurements for a given source distribution, but also questions as to how best to distribute a collection of one-, two-, and three-axis SQUIDs over the measurement plane. For example, the accuracy of solutions to the inverse problem for the head or abdomen using a moderate number of SQUID channels may well be improved by allocation of some SQUIDs to vector magnetometers at the edge of a finite array and single-component SQUIDs elsewhere [3, 4].

These and other limitations of the magnetic inverse problem arise from the presence of scalar and vector products inherent in Maxwell's equations, and produce inverse challenges that are not encountered in optical, X-ray, ultrasound, NMR, or tactile images. Generally, the interpretation of optical images in terms of the sources that produce the image, *i.e.*, the optical inverse problem, may require

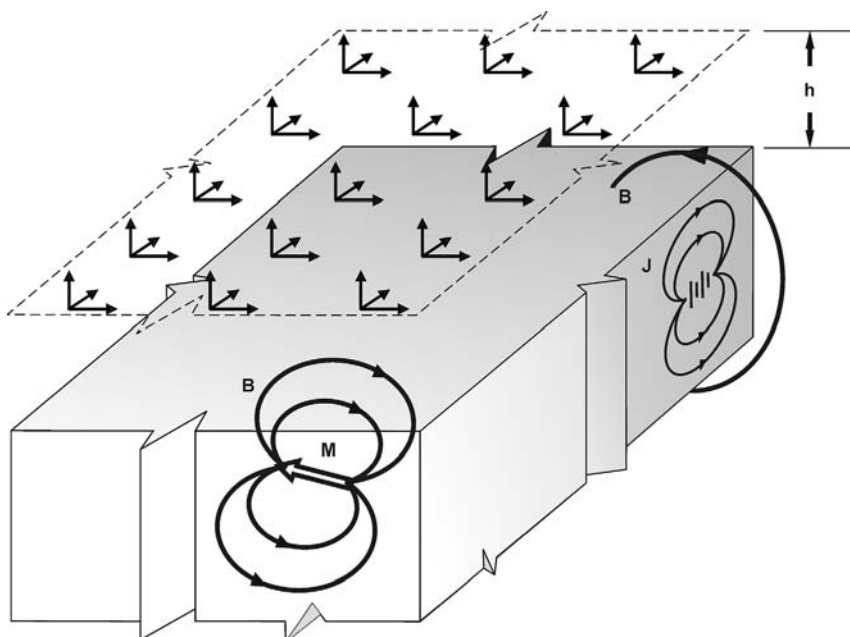


Fig. 10.1 A semi-infinite half space containing current and magnetization distributions, whose associated magnetic field is measured by a planar array of vector SQUID magnetometers in the upper, source-free half space.

deconvolution but will not require the inversion of a Laplacian field, but the magnetic inverse problem does. This should give an indication of the difficulties that will be encountered in attempting to use magnetic field measurements to discern the magnetic or electric sources hidden from direct view within an object.

In the days of a single SQUID and simple models, or instruments dedicated to measuring a single physical property, the appropriate equation for a simple model could be selected with care and intuition to obtain the required information. However, complex models, as would be required to describe spatially distributed heterogeneous sources in the brain or a thin slice of a meteorite, require measurement of the magnetic field at the least at as many points as there are model parameters. If the source distribution is either time-independent or periodic, a single magnetometer can be used to make sequential measurements at multiple locations. Today, the number of points where a scanned SQUID measures the magnetic field may exceed 125 000 [5, 6]. If the time-varying source distribution is aperiodic with a time variation that exceeds the rate at which the SQUID can be moved, one has no choice but to use multiple SQUIDs to record simultaneously the field at the required number of locations. For this reason, the number of SQUID sensors in a magnetoencephalogram (MEG) system is now approaching 1000. In these two cases it is reasonable to consider this as a problem in magnetic imaging: a magnetometer produces a vector or scalar “image” of the magnetic field, and the magnetic inverse problem becomes one of determining an “image” of the associated source distribution. In many situations, a source image can be obtained only after performing some sort of vector processing, as both the sources and their fields usually have a vector nature and are not colinear. In the limit of magnetic imaging of distributed, vector sources, our intuition based upon single point dipoles may fail us and there may not be a simple vector manipulation that can provide us with the answer.

What began 35 years ago as a SQUID measurement of the magnetic field at a single point above the human chest [7] has now progressed to the point of true magnetic images created by scanning a high-resolution SQUID microscope over a highly heterogeneous section of a Martian meteorite [8]. Hence the magnetic inverse problem has now evolved to include problems in image deconvolution that are potentially complicated by the nonuniqueness of the magnetic inverse problem. In this chapter, we establish a firm mathematical foundation for the magnetic inverse problem and present a number of simple examples, drawn primarily from our research in the field, borrowing extensively from and building upon an earlier book chapter [9]. We concentrate on the general issues of the magnetic inverse problem, and leave the discussion of MEG and magnetocardiogram (MCG) applications of three-dimensional inverse algorithms to Chapter 11. The present chapter is intended to serve as a tutorial, and not an all-inclusive review of the literature.

10.2

The Magnetic Forward Problem

10.2.1

Introduction

In order to explain the magnetic inverse problem, it is important first to define the forward one: the calculation of the magnetic field given a complete description of the sources. As shown in Figure 10.2, there are a number of different mechanisms by which magnetic fields can be generated. From the perspective of the forward problem, these can be grouped by which of two formulas govern the field production. The first, the law of Biot and Savart, is used to describe the magnetic

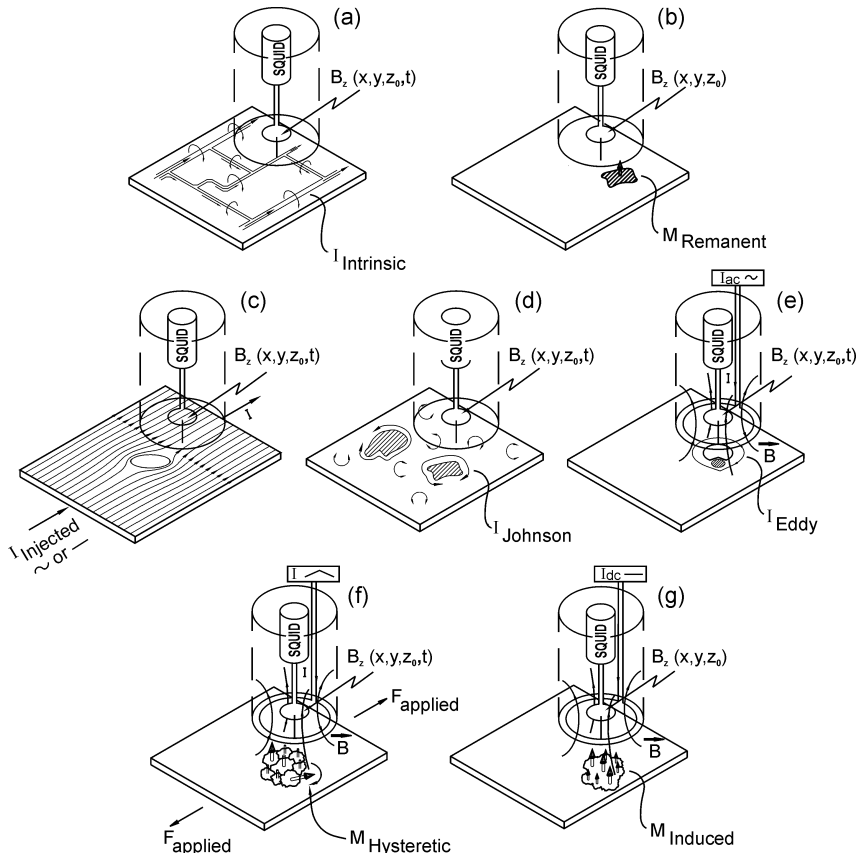


Fig. 10.2 Various mechanisms by which a scanning SQUID magnetometer can produce an image: (a) intrinsic currents, (b) remanent magnetization, (c) flaw-induced perturbations in applied currents, (d) Johnson noise in conductors, (e) eddy currents and their

perturbations by flaws, (f) hysteretic magnetization in ferromagnetic materials in the presence of an applied stress, and (g) diamagnetic and paramagnetic materials in an applied field. (Adapted from Ref. [141], with permission.)

fields produced by intrinsic currents, for example the magnetocardiogram (MCG) and MEG produced by current sources in the heart and brain, or from currents applied to a printed or integrated circuit, as is shown in Figure 10.2(a). Johnson noise arising from thermal motion of electrons in a conductor (Figure 10.2(d)) can produce measurable magnetic fields, as can inhomogeneity-induced perturbations in applied currents (Figure 10.2(c)). The second, the equation for the magnetic field of a point magnetic dipole, governs the field from remanent magnetization from ferromagnetic objects or inclusions (Figure 10.2(b)), ferromagnetic materials under stress, with or without an applied field (Figure 10.2(f)), or from paramagnetic or diamagnetic objects in an applied, static magnetic field (Figure 10.2(g)). If one applies an oscillating field, SQUIDs can be used to image the eddy currents (Figure 10.2(e)). After we examine the two governing equations in some detail, *i.e.*, the magnetic forward problem, we will then examine their inversion, *i.e.*, the magnetic inverse problem.

In this chapter, we will limit our discussion to the quasistatic magnetic field, *i.e.*, the field determined by the instantaneous sources. We do not consider the rate of change of the magnetic field, retarded potentials, *etc.* The time variation must be slow enough that inductive effects can be ignored, appropriate for most low-frequency SQUID applications except those involving eddy currents in metals.

In this chapter, we also do not address the numerous computational techniques that have been developed for the forward problem of calculating the magnetic field from current and magnetization distributions, but instead will outline the general principles that govern the forward problem for a variety of source and sample geometries.

10.2.2

Magnetic Fields from Magnetization Distributions

10.2.2.1 Field and Moment of a Magnetic Dipole

In the quasistatic limit, the magnetic field of a magnetostatic dipole is given by (10.1). For an object with a distributed magnetization $\vec{M}(\vec{r})$, which is equivalent to a dipole density, each differential volume element d^3r' in the object is assigned a dipole moment $\vec{m}(\vec{r}')$ that is equal to $\vec{M}(\vec{r}')d^3r'$, so that we can simply integrate (10.1)

$$\vec{B}(\vec{r}) = \frac{\mu_0}{4\pi} \int_V \left\{ \frac{3\vec{M}(\vec{r}') \cdot (\vec{r} - \vec{r}')}{{|\vec{r} - \vec{r}'|}^5} (\vec{r} - \vec{r}') - \frac{\vec{M}(\vec{r}')}{|{\vec{r} - \vec{r}'}|^3} \right\} d^3r'. \quad (10.3)$$

The magnetization can either be permanent, *e.g.*, ferromagnetic remanent magnetization, or induced through diamagnetic, paramagnetic, or ferromagnetic effects. Let us suppose that an object made of magnetically linear, isotropic material is

placed in a magnetic field produced by a distant electromagnet. The magnetization $\vec{M}(\vec{r})$ at a source point \vec{r} is determined by the product of the magnetic susceptibility $\chi(\vec{r})$ and the applied magnetic field intensity $\vec{H}(\vec{r})$

$$\vec{M}(\vec{r}) = \chi(\vec{r})\vec{H}(\vec{r}). \quad (10.4)$$

The magnetic induction field \vec{B} , hereafter referred to as the “magnetic field,” at the same source point \vec{r} is given by

$$\vec{B}(\vec{r}) = \mu_0 \left\{ \vec{H}(\vec{r}) + \vec{M}(\vec{r}) \right\}, \quad (10.5)$$

where μ_0 is the permeability of free space. We can express this in terms of the susceptibility χ by substituting (10.4) into (10.5) to obtain

$$\vec{B}(\vec{r}) = \mu_0 \left\{ 1 + \chi(\vec{r}) \right\} \vec{H}(\vec{r}) \quad (10.6)$$

$$= \mu_0 \mu_r(\vec{r}) \vec{H}(\vec{r}) \quad (10.7)$$

$$= \mu(\vec{r}) \vec{H}(\vec{r}), \quad (10.8)$$

where the relative permeability μ_r is given by

$$\mu_r(\vec{r}) = 1 + \chi(\vec{r}) \quad (10.9)$$

and the absolute permeability μ is

$$\mu(\vec{r}) = \mu_0 \mu_r(\vec{r}). \quad (10.10)$$

As we shall see, the difficulty with susceptibility and magnetization imaging is that the field measured by the SQUID is not the local field within the object, but the field in the source-free region outside of the object.

10.2.2.2 Magnetic Fields from Ferromagnetic Materials

Soft ferromagnetic materials have high permeabilities, in the approximate range $10^3 \leq \mu_r \leq 10^5$, so that

$$\mu_r = 1 + \chi \approx \chi. \quad (10.11)$$

In general for these materials, χ , and hence μ_r , are functions of the applied field. If the materials are “hard,” they exhibit significant hysteresis; if they are “soft,”

they do not. Soft materials may exhibit a range of fields for which χ is approximately constant, but in general for ferromagnetic materials, χ has a strong dependence on the applied field. In either case, there is an applied \vec{H} above which the material saturates and the magnetization \vec{M} in (10.4) attains a maximum value. Above that value, any increases in \vec{B} in (10.5) are due only to the increase in \vec{H} . Since the magnetic field within soft ferromagnetic materials can be from 10^3 to 10^5 times the applied field, the determination of the magnetization within a ferromagnetic material must be made in the strong-field limit: $\vec{B} = \mu_0(\vec{H} + \vec{M}) = \mu\vec{H}$ at any point in the material, so that \vec{M} at one point is affected by \vec{M} at other points in the material. Self-consistency requires simultaneous solution of \vec{H} and \vec{M} everywhere, since $\vec{M}(\vec{r})$ is determined by both $\vec{H}(\vec{r})$ and $\chi(\vec{r})$, even if the applied field \vec{H} was initially uniform before the object was placed in the field. In this strong-field case, the magnetic inverse problem, *i.e.*, the inversion of (10.3) to determine $\vec{M}(\vec{r})$, is difficult to impossible, particularly if there is a remanent (hard) magnetization superimposed upon the induced (soft) magnetization. While it is difficult to induce a soft, spherically symmetric, magnetically silent magnet with external fields, it is in principle possible to have such a distribution in a hard component of magnetization, and this leads to the previously discussed nonuniqueness problem.

10.2.2.3 Magnetic Fields from Paramagnetic and Diamagnetic Materials

The situation is much friendlier for the magnetic imaging of paramagnetic ($0 \leq \chi \leq 10^{-3}$) and diamagnetic ($-10^{-6} \leq \chi \leq 0$) materials, in that

$$\mu_r = 1 + \chi \approx 1. \quad (10.12)$$

As a result, the variation in the magnitude of the induced magnetic field \vec{B} is 10^{-6} to 10^{-3} times the magnetic field in free space, and is proportional to the applied field, since paramagnetic and diamagnetic materials are linear and nonhysteretic at practical applied fields. The most significant feature of the low susceptibility of these materials is that (10.3) can be evaluated in the weak-field limit, also known as the Born approximation: at any point in the material we can ignore the contributions to the applied field at \vec{r}' from the magnetization elsewhere in the object and consider the applied magnetic intensity \vec{H} as it would be in the absence of the magnetic material. In that case, we immediately know the magnetic field \vec{B} everywhere as well. In the Born approximation, the magnetization is independent of the magnetization elsewhere in the sample, and hence is a local phenomenon, in contrast to ferromagnetism. Because \vec{M} is so weak for diamagnetic and paramagnetic materials, if we know \vec{H} everywhere, we shall then know \vec{B} to at least one part in 10^3 for a paramagnetic material with $\chi = 10^{-3}$, and to one part in 10^6 for a diamagnetic one with $\chi = -10^{-6}$. Thus, we have eliminated a major problem in obtaining a self-consistent, macroscopic solution that is based upon the microscopic constitutive equation given by (10.5). Because of their periodic flux-voltage characteristic, and the ability to thermally release magnetic flux trapped in pickup

coils, SQUID magnetometers readily can measure only the very small perturbation $\vec{B}_p(\vec{r})$ in the applied magnetic field [10]. We thereby can eliminate \vec{B} and \vec{H} from the imaging problem, and need them only to determine the magnetization. The measured magnetic field, $\vec{B}_p(\vec{r})$, thus is given by (10.3) where

$$\vec{M}(\vec{r}) = \frac{\chi(\vec{r})}{\mu_0} \vec{B}(\vec{r}) = \chi(\vec{r}) \vec{H}(\vec{r}). \quad (10.13)$$

If $\vec{H}(\vec{r})$ is uniform, then the spatial variation of $\vec{M}(\vec{r})$ is determined only by $\chi(\vec{r})$. For isotropic materials, χ is a scalar, and the direction of \vec{M} is the same as that of \vec{B} ; otherwise, a tensor susceptibility is required.

10.2.3

Magnetic Fields from Current Distributions

The calculation of the magnetic fields from magnetizations is conceptually straightforward because the only vector operation is the dot product in the first term of (10.3). In contrast, the law of Biot and Savart contains a vector cross product which complicates the problem. Let us start with the simplest case of determining the distribution of currents in a planar circuit, as shown, for example, in Figures 10.2(a), 10.3, and 10.4. In general, the magnetic field $\vec{B}(\vec{r})$ at the point \vec{r} is given by the law of Biot and Savart

$$\vec{B}(\vec{r}) = \frac{\mu_0}{4\pi} \int_V \frac{\vec{J}(\vec{r}') \times (\vec{r} - \vec{r}')}{|\vec{r} - \vec{r}'|^3} d^3 r', \quad (10.14)$$

where $\vec{J}(\vec{r}')$ is the current density at point \vec{r}' . It is also instructive to rewrite (10.14) in terms of the curl of the current distribution [11, 12]

$$\vec{B}(\vec{r}) = \frac{\mu_0}{4\pi} \int_S \frac{\vec{J}(\vec{r}') \times \hat{n}}{|\vec{r} - \vec{r}'|} d^2 r' + \frac{\mu_0}{4\pi} \int_V \frac{\nabla' \times \vec{J}(\vec{r}')}{|\vec{r} - \vec{r}'|} d^3 r', \quad (10.15)$$

where \hat{n} is the normal to the surface S that bounds the object or regions within the object with differing conductivities. The first integral represents the magnetic field due to the discontinuity of the tangential component of the current at any external or internal boundaries of the object, and the second is that produced by any curl within the object. Note that within a homogeneous conductor, any current distribution that has zero curl will not contribute to the external magnetic field and, hence, will be magnetically silent [13–15]. This implies that in homogeneous, three-dimensional conductors, currents that obey Ohm's law, relating the current density to either the electric field \vec{E} or the electric scalar potential V , e.g.,

$$\vec{J}(\vec{r}) = \sigma \vec{E}(\vec{r}) = -\sigma \nabla V(\vec{r}), \quad (10.16)$$

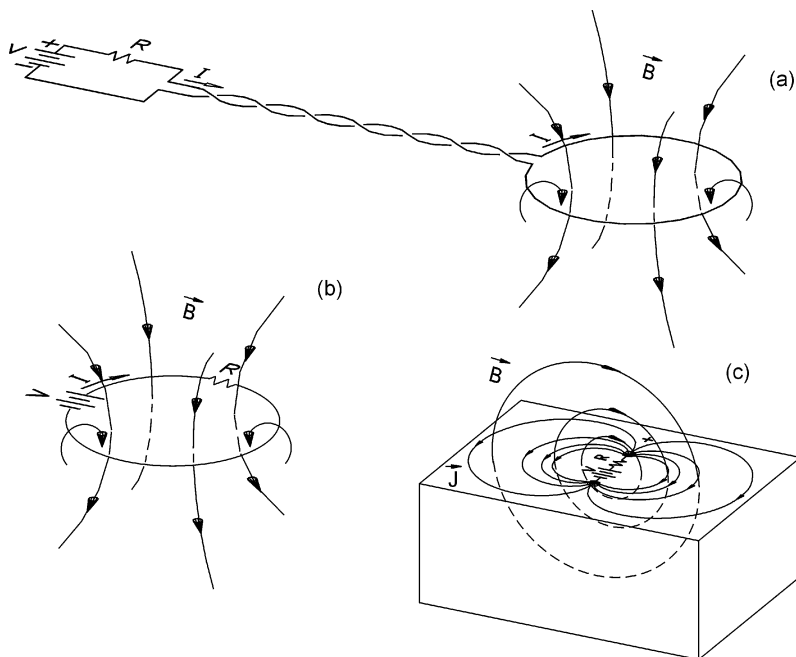


Fig. 10.3 Currents and their magnetic fields: (a) a loop of wire and its magnetic field \vec{B} , when the battery is far away. It follows from Ampère's law that the magnetic field from the leads connecting the battery to the loop is negligible because the leads are tightly twisted; (b) a loop of wire that contains a voltage source and a current-limiting resistor; (c) the current and magnetic field distribu-

tions from a current source located on the surface of a conducting bath of saline. The source can be thought of as a current dipole whose moment (*i.e.*, strength) is the product of the spacing between the positive and negative electrodes times the current passing between them. (Adapted from Ref. [243], with permission.)

do not contribute to the magnetic field because the curl of a gradient is identically zero, and the conductivity σ is a constant within the volume V and passes through the curl operator. Batteries, such as a dry cell dropped into a conducting medium (Figure 10.4), or the microscopic equivalent, a current dipole [16, 17], are non-Ohmic and hence can have curl. The first term in (10.15) would indicate that whenever Ohmic currents encounter a boundary or a discontinuity in conductivity, a magnetic field could be produced, since a discontinuity in the component of the current density tangential to a boundary is equivalent to a curl.²⁾ In a thin sheet that would approximate a two-dimensional conductor, the sample has two parallel surfaces in proximity that have curls of opposite sign which cancel each

- 2) The insulating boundary on the side of the cylindrical battery in Figure 10.4 produces a discontinuity of tangential current, and this provides an alternative description for the magnetic field produced by a battery in a

homogeneous conducting medium. Whether or not this approach is taken, it is extremely important to recognize the importance of insulating layers such as those outside of batteries and wires.

other far from the sheet; the curl that contributes most strongly to the magnetic field is that from any edges in the conductor. A current-carrying wire, bent into a pattern, has a curl all along its surface. We shall address the role of spatial variations in the conductivity σ in two-dimensional conductors in a later section. For now, we shall concentrate on sheet conductors with a constant (homogeneous) conductivity σ .

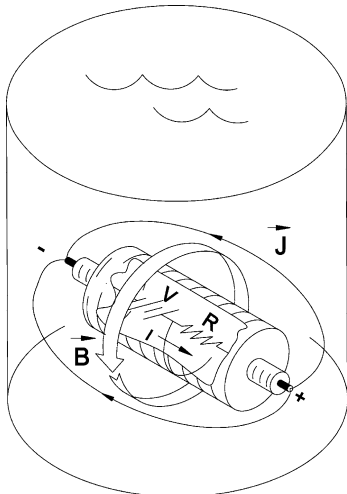


Fig. 10.4 A simple current source in the form of a battery in a bucket of saline. Currents flow in the saline, and a magnetic field encircles the battery. (Adapted from Ref. [243], with permission.)

In typical measurements, the component of the magnetic field normal to the sample, B_z , is mapped by scanning the SQUID pickup coil of radius a over the sample, at a fixed height z_0 , as shown in Figure 10.5. In this case, we can expand the cross product in (10.14) and rewrite the law of Biot and Savart as a pair of integrals

$$B_z(\vec{r}) = \frac{\mu_0}{4\pi} \int_V \frac{J_x(\vec{r}') (y - y')}{|\vec{r} - \vec{r}'|^3} d^3 r' - \frac{\mu_0}{4\pi} \int_V \frac{J_y(\vec{r}') (x - x')}{|\vec{r} - \vec{r}'|^3} d^3 r'. \quad (10.17)$$

Equations (10.14) and (10.17) are convolution integrals. The source of the field is the current density $\vec{J}(\vec{r}')$; the remaining terms of the integrand are a function of both \vec{r} and \vec{r}' and form the Green's function $G(\vec{r} - \vec{r}')$. To calculate the magnetic field, we integrate the product of \vec{J} and G over the entire region where \vec{J} is non-zero, *i.e.*, we convolve \vec{J} and G to determine \vec{B} . Note that in (10.14), G is a vector function that contains the cross product, but in (10.17), it is a pair of scalar functions. It is worth noting that identical arguments starting with (10.3) show that the magnetic field from a magnetization distribution can be expressed as the convolution of $\vec{M}(\vec{r}')$ with another vector Green's function.

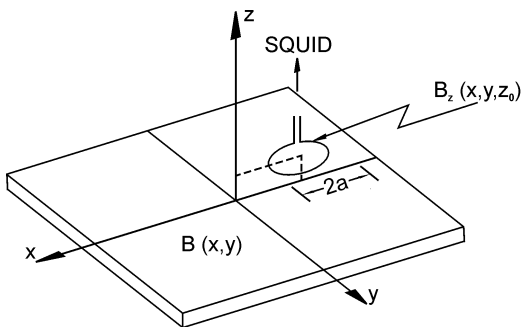


Fig. 10.5 The geometric arrangement and coordinates for a SQUID that is scanned over a current-carrying sample. (Adapted from Ref. [56], with permission.)

10.2.4

Magnetic Fields from Multipole Sources

10.2.4.1 Introduction

Any discussion of the forward problem would not be complete without a description of the relationship between multipole sources and their fields. In the following sections, we discuss the commonalities of the magnetic fields associated with a number of different sources, how the magnetic field can be described in terms of the gradient of a scalar magnetic potential, and how this in turn provides the basis for multipole expansions of either the sources or their fields. While this last topic is intimately connected with the inverse problem, we present it first under the forward problem because physical representations of magnetic dipoles and quadrupoles (in contrast to their abstract mathematical equivalents) are often the actual sources of magnetic fields, and hence a description of the spatial dependence of these fields is critical to understanding their measurement and mapping.

10.2.4.2 Poisson's and Laplace's Equations

In contrast to ray-based imaging modalities that involve the focusing of electromagnetic or acoustic waves onto detector arrays, and are hence governed by the equations of propagating waves, a magnetic field is governed by the laws of Biot and Savart, Ampère, and Gauss (which are the static limits of the dynamic Maxwell equations that govern electromagnetic wave propagation). We have already presented the equations that describe the relation between an electric or magnetic source distribution and the associated magnetic field ((10.1), (10.3), (10.14), (10.15), (10.17)). Now we need to show how the magnetic field in the source-free region occupied by the SQUID obeys the much simpler Laplace's equation. As we will see later in this chapter, this simplification carries with it a cost in a reduction

of the information contained in the field and a corresponding restriction on the invertibility of the field equations and the solution to the inverse problem. This section draws extensively from Ref. [18].

To aid in our development of an intuition regarding Laplace's equation, it is worthwhile to begin with electrostatic fields. Let us first consider a quasistatic charge distribution given by the charge density $\rho(\vec{r})$. In vacuum, Gauss' law for the electric field \vec{E} reduces to

$$\nabla \cdot \vec{E}(\vec{r}) = \rho(\vec{r})/\epsilon_0 , \quad (10.18)$$

where ϵ_0 is the electrical permittivity of free space. Because the differential form of Faraday's law reduces to $\nabla \times \vec{E}(\vec{r}) = \vec{0}$ for a quasistatic charge distribution, the electric field can be described as the negative gradient of the scalar electrostatic potential $V(\vec{r})$, where

$$\vec{E}(\vec{r}) = -\nabla V(\vec{r}) . \quad (10.19)$$

Equations (10.18) and (10.19) can be combined to obtain Poisson's equation

$$\nabla^2 V(\vec{r}) = -\rho(\vec{r})/\epsilon_0 , \quad (10.20)$$

which is known to have the solution

$$V(\vec{r}) = \frac{1}{4\pi\epsilon_0} \int_V \frac{\rho(\vec{r}')}{|\vec{r} - \vec{r}'|} d^3 r' . \quad (10.21)$$

This equation shows that, in the mathematical sense, the charge density $\rho(\vec{r})$ is the “source” of the scalar potential.³⁾ Most importantly, if we restrict our attention to source-free regions where $\rho(\vec{r}) = 0$, we find that the electrostatic potential obeys Laplace's equation

$$\nabla^2 V(\vec{r}) = 0 , \quad (10.22)$$

and the entire armamentarium of techniques to solve Laplace's equation can be brought to bear on the problem.

We can now extend our analysis to consider the electric field of current sources in a homogeneous conductor. In an infinite, homogeneous, isotropic, linear conductor, containing sources of electromotive force (EMF), the quasistatic current density $\vec{J}(\vec{r})$ obeys Ohm's law, which can be written as

$$\vec{J}(\vec{r}) = \sigma \vec{E}(\vec{r}) + \sigma \vec{E}^i(\vec{r}) = \sigma \vec{E}(\vec{r}) + \vec{J}^i(\vec{r}) , \quad (10.23)$$

³⁾ A purist would argue that one cannot have the electrostatic potential without the charge, and vice versa, so that it is better to describe the charge and the potential as

being “associated” with each other, rather than having the charge as the “source” of a field.

where the impressed voltage $\vec{E}^i(\vec{r})$ is zero, where there are no EMFs, and σ is the electrical conductivity of the conductor. Alternatively, the effect of the EMFs can be described in terms of the impressed current density \vec{j}^i . It can be shown that \vec{E}^i can be described as an EMF dipole density and \vec{j}^i can be interpreted as a current dipole density [19]. Because of the high impedance of the cellular membranes across which bioelectric currents are driven by transmembrane concentration gradients, bioelectric sources are almost always described in terms of \vec{j}^i rather than \vec{E}^i . It is important to note that in the quasistatic limit conservation of charge requires that $\nabla \cdot \vec{j}(\vec{r}) = 0$. Taking the divergence of (10.23) and using (10.19), we once again obtain Poisson's equation

$$\nabla^2 V(\vec{r}) = \frac{1}{\sigma} \nabla \cdot \vec{j}^i(\vec{r}), \quad (10.24)$$

which has the solution

$$V(\vec{r}) = \frac{1}{4\pi\sigma} \int_V \frac{-\nabla' \cdot \vec{j}^i(\vec{r}')}{|\vec{r} - \vec{r}'|} d^3 r', \quad (10.25)$$

and we see that $\nabla \cdot \vec{j}^i(\vec{r})$ is the source of the scalar potential. In regions within the conductor where $\nabla \cdot \vec{j}^i = 0$, this reduces to Laplace's equation.

The extension of this formalism to the magnetic field of steady-state current distributions is straightforward. We have already shown that the law of Biot and Savart can be written as

$$\vec{B}(\vec{r}) = \frac{\mu_0}{4\pi} \int_V \frac{\nabla' \times \vec{j}^i(\vec{r}')}{|\vec{r} - \vec{r}'|} d^3 r'. \quad (10.26)$$

We now recognize this as the solution to a vector form of Poisson's equation,

$$\nabla^2 \vec{B}(\vec{r}) = -\mu_0 \nabla \times \vec{j}^i(\vec{r}), \quad (10.27)$$

wherein each Cartesian component of \vec{B} is Laplacian, with a source that is the corresponding Cartesian component of $\nabla \times \vec{j}$. In the event that the current density is produced by impressed current sources in an unbounded homogeneous medium that obeys Ohm's law, (10.23) reduces to

$$\vec{j}(\vec{r}) = -\sigma \nabla V(\vec{r}) + \vec{j}^i(\vec{r}), \quad (10.28)$$

such that

$$\nabla \times \vec{j}(\vec{r}) = \nabla \times \vec{j}^i(\vec{r}), \quad (10.29)$$

so that the solution for infinite homogeneous conductors reduces to Poisson's equation for which the integration can be restricted to the region containing impressed currents

$$\vec{B}(\vec{r}) = \frac{\mu_0}{4\pi} \int_V \frac{\nabla' \times \vec{J}^i(\vec{r}')}{|\vec{r} - \vec{r}'|} d^3 r'. \quad (10.30)$$

This equation is particularly significant in that it shows that for unbounded conductors, the Ohmic currents do not contribute to the magnetic field, and the field is determined by the impressed currents alone.

This result also leads to an important equation for the case where the source is a current dipole \vec{P} located at \vec{r}'' , i.e.,

$$\vec{J}^i(\vec{r}) = \vec{P} \delta(\vec{r} - \vec{r}''), \quad (10.31)$$

where $\delta(\vec{r} - \vec{r}'')$ is the Dirac delta function. We can apply (10.31) to (10.23) to write (10.14) as

$$\vec{B}(\vec{r}) = \frac{\mu_0}{4\pi} \frac{\vec{P} \times (\vec{r} - \vec{r}'')}{|\vec{r} - \vec{r}''|^3}. \quad (10.32)$$

It is vital to note that deeply embedded in the derivation of this equation is the assumption that we are dealing with an unbounded homogeneous conductor. The fascinating aspect of this equation is that it is, in effect, a differential form of the law of Biot and Savart, operating on only one portion of the complete "circuit." While in general this would raise concerns over current continuity and Newton's third law, in this special case of an unbounded conductor, \vec{P} is a point source of current, and the magnetic field contributions of each differential element of the return Ohmic current integrate exactly to zero. Figure 10.4 shows how a current dipole or a small battery has an encircling magnetic field, which in an unbounded conductor would be given by (10.32). In the limit of a very large bucket and a battery that reduces to a current dipole, the magnetic field can be calculated by considering only the current dipole moment of the battery. For small buckets, the discontinuity in the tangential current at the wall of the bucket will also contribute to the magnetic field. As will be apparent in the subsequent discussion of edge effects, it is important to appreciate that magnetic fields can be exquisitely sensitive to discontinuities in the tangential current!

For completeness, it is important to point out that the addition of boundary surfaces S_j within the conductor, thereby making the conductor only *piecewise* homogeneous, will add secondary current sources \vec{K}^i that are given by the product of the difference in conductivities across the boundary with the potential at the

boundary, with an orientation specified by the normal \hat{n}_j to the boundary [20], such that

$$\vec{K}^i(\vec{r}) = -(\sigma' - \sigma'')V(\vec{r})\hat{n}_j(\vec{r}) \quad \text{for } \vec{r} \text{ on all } S_j, \quad (10.33)$$

$$\vec{K}^i(\vec{r}) = \vec{0} \quad \text{for } \vec{r} \text{ not on any } S_j$$

In this case, our equations for the electric potential and magnetic field become [21, 22]

$$V(\vec{r}) = \frac{1}{4\pi\sigma} \int_V \frac{-\nabla' \cdot \{\vec{J}^i(\vec{r}') + \vec{K}^i(\vec{r}')\}}{|\vec{r} - \vec{r}'|} d^3 r', \quad (10.35)$$

$$\vec{B}(\vec{r}) = \frac{\mu_0}{4\pi} \int_V \frac{\nabla' \times \{\vec{J}^i(\vec{r}') + \vec{K}^i(\vec{r}')\}}{|\vec{r} - \vec{r}'|} d^3 r'. \quad (10.36)$$

As we will see later, these two equations are critical in understanding the relation between bioelectric and biomagnetic fields.

If the current distribution is bounded, as it would be for a conductor bounded by a surface S , the curl of \vec{B} , as given by Maxwell's fourth equation, must be zero outside of S , *i.e.*,

$$\nabla \times \vec{B}(\vec{r}) = \vec{0}. \quad (10.37)$$

Any field that has no curl can be described in terms of the gradient of the magnetic scalar potential, so that we can now write

$$\vec{B}(\vec{r}) = -\mu_0 \nabla V_m(\vec{r}) \quad \text{outside } S. \quad (10.38)$$

Since $\nabla \cdot \vec{B}(\vec{r})$ is zero everywhere,

$$\nabla^2 V_m = 0 \quad \text{outside } S, \quad (10.39)$$

and we see that the quasistatic magnetic field in a current-free region can be derived from a scalar potential obeying Laplace's equation. The identical result applies to a bounded object with a quasistatic magnetization $\vec{M}(\vec{r})$: the magnetic induction *outside* the object must satisfy (10.39).

Inside a magnetized object, $\vec{B}(\vec{r})$ is given by

$$\vec{B}(\vec{r}) = -\mu_0 \nabla V_m(\vec{r}) + \mu_0 \vec{M}(\vec{r}). \quad (10.40)$$

If we take the divergence of each term and note that $\nabla \cdot \vec{B}(\vec{r}) = 0$, we obtain Poisson's equation for V_m

$$\nabla^2 V_m(\vec{r}) = \nabla \cdot \vec{M}(\vec{r}) . \quad (10.41)$$

This has the solution

$$V_m(\vec{r}) = \frac{1}{4\pi} \int_V \frac{-\nabla' \cdot \vec{M}(\vec{r}')}{|\vec{r} - \vec{r}'|} d^3 r', \quad (10.42)$$

which shows that $-\nabla' \cdot \vec{M}(\vec{r}')$ can be interpreted as an effective magnetic charge density that is the source of V_m . Similar to the constraint on $\nabla \cdot \vec{J}$ for the electric field of a distributed current, the condition that $\nabla \cdot \vec{B} = 0$ implies that

$$\int_V \nabla' \cdot \vec{M}(\vec{r}') d^3 r' = 0 . \quad (10.43)$$

Equation (10.41) shows that the magnetic field outside of a magnetized object is also Laplacian, so we can describe the current-related source of V_m in (10.38) as an effective magnetization given by [18, 23]

$$\vec{M}(\vec{r}) = \frac{1}{2} \vec{r} \times \vec{J}(\vec{r}) . \quad (10.44)$$

The divergence of \vec{M} becomes

$$\nabla \cdot \vec{M}(\vec{r}) = \nabla \cdot \left[\frac{1}{2} \vec{r} \times \vec{J}(\vec{r}) \right] = -\frac{1}{2} \vec{r} \cdot [\nabla \times \vec{J}(\vec{r})] . \quad (10.45)$$

Thus the magnetic scalar potential outside the bounded current distribution satisfies the equation

$$V_m(\vec{r}) = \frac{1}{4\pi} \int_V \frac{\frac{1}{2} \vec{r}' \cdot \nabla' \times \vec{J}(\vec{r}')}{|\vec{r} - \vec{r}'|} d^3 r', \quad (10.46)$$

and we identify the source of V_m to be one-half the radial component of the curl of \vec{J} . In unbounded homogeneous media with impressed current sources, \vec{J} can be replaced by \vec{J}^i . In the piecewise homogeneous case, it is necessary to include the secondary sources \vec{K}^i .

We close the loop on boundary effects by noting that the symmetry of a bounded conductor may lead to several interesting results. A radial current dipole in a spherical conductor and a current dipole perpendicular to the surface of a semi-infinite conductor produce *no* magnetic field *outside* the conductor. A current

dipole parallel to and below the surface of a conducting half space produces a magnetic field in the upper half space given by (10.32), as if the boundary did not exist [24]!

The equations derived in this section, summarized in Table 10.1, can be used to calculate the electric and magnetic fields from various sources. The problem of greater complexity is the inverse one of fitting a model of the source to observed field data.

Table 10.1 Summary of the electric and magnetic Poisson's equations [18]

$$\text{General form: } \nabla^2 \Psi(\vec{r}) = -s(\vec{r}), \quad \Psi(\vec{r}) = \frac{1}{4\pi} \int_V \frac{s(\vec{r}')}{|\vec{r} - \vec{r}'|} d^3 r'$$

| Field | Sources, s | Solution to Poisson's equations |
|---|---|---|
| Electric scalar potential $V(\vec{r})$ from a quasistatic charge distribution $\rho(\vec{r})$ | $s(\vec{r}) = \frac{1}{\epsilon_0} \rho(\vec{r}) = \nabla \cdot \vec{E}(\vec{r})$ | $V(\vec{r}) = \frac{1}{4\pi\epsilon_0} \int_V \frac{\rho(\vec{r}')}{ \vec{r} - \vec{r}' } d^3 r'$ |
| Electric scalar potential $V(\vec{r})$ from a quasistatic current distribution in a medium of conductivity σ | $s(\vec{r}) = -\frac{1}{\sigma} \nabla \cdot \vec{J}(\vec{r})$ | $V(\vec{r}) = \frac{1}{4\pi\sigma} \int_V \frac{-\nabla' \cdot \vec{J}(\vec{r}')}{ \vec{r} - \vec{r}' } d^3 r'$ |
| Magnetic scalar potential $V_m(\vec{r})$ from a quasistatic magnetization $\vec{M}(\vec{r})$ | $s(\vec{r}) = -\nabla \cdot \vec{M}(\vec{r})$ | $V_m(\vec{r}) = \frac{1}{4\pi} \int_V \frac{-\nabla' \cdot \vec{M}(\vec{r}')}{ \vec{r} - \vec{r}' } d^3 r'$ |
| Magnetic induction $\vec{B}(\vec{r})$ from a quasistatic current distribution $\vec{J}(\vec{r})$ | For each component B_j $s_j(\vec{r}) = \mu_0 [\nabla \times \vec{J}(\vec{r})]_j$ | $B(\vec{r}) = \frac{\mu_0}{4\pi} \int_V \frac{\nabla' \times \vec{J}(\vec{r}')}{ \vec{r} - \vec{r}' } d^3 r'$ |
| Magnetic scalar potential $V_m(\vec{r})$ outside a bounded quasistatic current distribution $\vec{J}(\vec{r})$ | $s(\vec{r}) = \frac{1}{2} \vec{r} \cdot [\nabla \times \vec{J}(\vec{r})] = -\nabla \cdot \vec{M}_{\text{eff}}(\vec{r})$ | $V_m(\vec{r}) = \frac{1}{4\pi} \int_V \frac{\frac{1}{2} \vec{r} \cdot [\nabla' \times \vec{J}(\vec{r}')]}{ \vec{r} - \vec{r}' } d^3 r'$ |

10.2.4.3 Magnetic Multipoles

Given our understanding of the sources of electric and magnetic fields, we can now draw from Ref. [25] to describe these sources and their associated fields in terms of equivalent multipoles. A vector field with zero curl, termed conservative or irrotational, can be described as the negative gradient of a scalar potential $\Psi(\vec{r})$ which satisfies Poisson's equation

$$\nabla^2 \Psi(\vec{r}) = -s(\vec{r}), \quad (10.47)$$

where $s(\vec{r})$ describes the source distribution in terms of another scalar field, and in our case $\Psi(\vec{r})$ can be either $V(\vec{r})$ or $V_m(\vec{r})$. As we saw above, this equation is known to have a solution of the form

$$\Psi(\vec{r}) = \frac{1}{4\pi} \int_V \frac{s(\vec{r}')}{|\vec{r} - \vec{r}'|} d^3 r', \quad (10.48)$$

where the integral must be evaluated over all regions where s is nonzero. If the source distribution s can be bounded by a closed surface S , then $\Psi(\vec{r})$ outside of S satisfies Laplace's equation

$$\nabla^2 \Psi(\vec{r}) = 0, \quad \vec{r} \text{ outside of } S, \quad (10.49)$$

which can be solved using multipole expansion techniques. If the surface that most closely bounds the sources is spherical, it is most convenient to use expansions based on Cartesian [26] or spherical coordinates. Nevertheless, from a theoretical perspective, it is interesting to note that, even in spherical geometry, spherical harmonic theory is not required to derive the multipole formalism [27]. If the best bounding surface is, for example, a prolate spheroid, it may be advantageous to use a prolate spheroidal expansion. Here we will consider only the case where the bounding surface is a sphere of radius a , so that

$$\nabla^2 \Psi(\vec{r}) = 0, \quad |\vec{r}| > a. \quad (10.50)$$

There are several equivalent series expansions for Ψ in the region $|\vec{r}| > a$ [28]

$$4\pi \Psi = \sum_{n=0}^{\infty} \sum_{m=0}^n \frac{1}{r^{n+1}} (a_{nm} \cos m\phi + b_{nm} \sin m\phi) P_n^m(\cos \theta) \quad (10.51)$$

$$= \sum_{n=0}^{\infty} p^{(n)} \frac{(-1)^n}{n!} \frac{\partial^n}{\partial l_{n1} \partial l_{n2} \dots \partial l_{nn}} \left(\frac{1}{r} \right) \quad (10.52)$$

$$= \sum_{n=0}^{\infty} \sum_{l=0}^n \sum_{k=0}^{n-l} \frac{(-1)^n}{l!k!(n-l-k)!} c_{nkl} \frac{\partial^n}{\partial x^l \partial y^k \partial z^{n-l-k}} \times \left(\frac{1}{r} \right), \quad (10.53)$$

where $P_n^m(\cdot)$ is an associated Legendre polynomial, r , θ , and ϕ are the spherical coordinates, a_{nm} , b_{nm} , $p^{(n)}$, and c_{nkl} are all coefficients of the expansion, and k , l , n , and m are indices. The index n determines the order of the multipole ($n = 0$ is a monopole, $n = 1$ is a dipole, etc.). In (10.52), $p^{(n)}$ may be interpreted as the magnitude of the n th multipole, which has $3n$ associated direction cosines, $a_{n1}, \beta_{n1}, \gamma_{n1}, \dots, a_{nn}, \beta_{nn}, \gamma_{nn}$, and

$$\frac{\partial}{\partial l_{ni}} = a_{ni} \frac{\partial}{\partial x} + \beta_{ni} \frac{\partial}{\partial y} + \gamma_{ni} \frac{\partial}{\partial z} \quad (10.54)$$

and

$$a_{ni}^2 + \beta_{ni}^2 + \gamma_{ni}^2 = 1. \quad (10.55)$$

The theoretical derivations of Gray [29–31] and Nolte [32] are excellent sources of reference regarding magnetic multipolar expansions, including useful alternative derivations of Ψ based on the scalar, vector, and Debye potentials. In Ref. [27], a spherical tensor approach is employed to derive a multipole expansion similar to (10.53), but involving instead the magnetic vector potential. Reference [25] discusses each expansion in some detail, provides the formulas for each of the coefficients, and determines the relationship of the various expansions. The most important result to come from that discussion is the realization that the intuitively obvious and easy-to-draw Taylor's series multipole expansion includes terms for the quadrupole and higher moments that correspond to externally silent spherical capacitors. These terms are valid representations of particular degrees of freedom of the source distribution, but do not produce external fields. They can be removed in the traceless tensor representation that is derived from the Taylor's series, and are by design absent in the spherical harmonic expansion, which is based in effect upon the representation of the external fields as a solution to Laplace's equation. The distinction between silent and nonsilent in this case is whether one is using the multipoles to represent the source itself, or the associated external fields. A forward calculation must show that a silent component of a source will not contribute to the field; an inverse calculation could never specify a silent source term from the external fields. For this chapter, we will limit ourselves to the spherical harmonic expansion summarized in Table 10.2. This table shows that the expansion can be described as a series of even and odd unit potentials $\Psi_{nm}^e(r)$ and $\Psi_{nm}^o(r)$ multiplied by the corresponding multipole strengths a_{nm} and b_{nm} .

Table 10.2 Spherical harmonic multipole expansion [18]

$$\Psi(\vec{r}) = \sum_{n=0}^{\infty} \sum_{m=0}^n [a_{nm} \Psi_{mn}^e(r)(\vec{r}) + b_{nm} \Psi_{mn}^o(r)(\vec{r})], \quad r > a$$

| Monopole | |
|---|---|
| $\Psi_{00}^e = \frac{1}{4\pi} \frac{1}{r}$ | $a_{00} = \int_V s(\vec{r}') d^3 r'$ |
| $\Psi_{10}^e = \frac{1}{4\pi} \frac{z}{r^3}$ | $a_{10} = \int_V s(\vec{r}') z' d^3 r'$ |
| Dipole | |
| $\Psi_{11}^e = \frac{1}{4\pi} \frac{x}{r^3}$ | $a_{11} = \int_V s(\vec{r}') x' d^3 r'$ |
| $\Psi_{11}^o = \frac{1}{4\pi} \frac{y}{r^3}$ | $b_{11} = \int_V s(\vec{r}') y' d^3 r'$ |
| Quadrupole | |
| $\Psi_{20}^e = \frac{1}{4\pi} \frac{3z^2 - r^2}{2r^5}$ | $a_{20} = \frac{1}{2} \int_V s(\vec{r}') (3z'^2 - r'^2) d^3 r'$ |
| $\Psi_{21}^e = \frac{1}{4\pi} \frac{3xz}{r^5}$ | $a_{21} = \int_V s(\vec{r}') x' z' d^3 r'$ |
| $\Psi_{21}^o = \frac{1}{4\pi} \frac{3yz}{r^5}$ | $b_{21} = \int_V s(\vec{r}') y' z' d^3 r'$ |
| $\Psi_{22}^e = \frac{1}{4\pi} \frac{3(x^2 - y^2)}{r^5}$ | $a_{22} = \frac{1}{4} \int_V s(\vec{r}') (x'^2 - y'^2) d^3 r'$ |
| $\Psi_{22}^o = \frac{1}{4\pi} \frac{6xy}{r^5}$ | $b_{22} = \frac{1}{2} \int_V s(\vec{r}') x' y' d^3 r'$ |
| Octupole | |
| $\Psi_{30}^e = \frac{1}{4\pi} \frac{z}{2r^7} (5z^2 - 3r^2)$ | $a_{30} = \frac{1}{2} \int s(\vec{r}') z' (5z'^2 - 3r'^2) d^3 r'$ |
| $\Psi_{31}^e = \frac{1}{4\pi} \frac{3x}{2r^7} (5z^2 - r^2)$ | $a_{31} = \frac{1}{4} \int s(\vec{r}') x' (5z'^2 - 4r'^2) d^3 r'$ |
| $\Psi_{31}^o = \frac{1}{4\pi} \frac{3y}{2r^7} (5z^2 - r^2)$ | $b_{31} = \frac{1}{4} \int s(\vec{r}') y' (5z'^2 - r'^2) d^3 r'$ |
| $\Psi_{32}^e = \frac{1}{4\pi} \frac{15z}{r^7} (x^2 - y^2)$ | $a_{32} = \frac{1}{4} \int s(\vec{r}') z' (x'^2 - y'^2) d^3 r'$ |
| $\Psi_{32}^o = \frac{1}{4\pi} \frac{30xyz}{r^7}$ | $b_{32} = \frac{1}{2} \int s(\vec{r}') x' y' z' d^3 r'$ |
| $\Psi_{33}^e = \frac{1}{4\pi} \frac{15x}{r^7} (x^2 - 3y^2)$ | $a_{33} = \frac{1}{24} \int s(\vec{r}') x' (x'^2 - 3y'^2) d^3 r'$ |
| $\Psi_{33}^o = \frac{1}{4\pi} \frac{15y}{r^7} (3x^2 - y^2)$ | $b_{33} = \frac{1}{24} \int s(\vec{r}') y' (3x'^2 - y'^2) d^3 r'$ |

Four of the source terms listed in Table 10.1 are the divergence of a vector and thus provide the opportunity to simplify the multipole moment integrals listed in Table 10.2. Again following Ref. [18], we find that the moments of the spherical harmonic multipole expansion are of the form

$$A_{nm}^p = \int_V s(\vec{r}') f(\vec{r}') d^3 r', \quad (10.56)$$

where p is either e or o , A_{nm}^e is a_{nm} , A_{nm}^o is b_{nm} , and $f(\vec{r}')$ is the weight function which is different for each moment. When we consider the sources s that are the negative divergence of a vector field \vec{F} , i.e., $s = -\nabla \cdot \vec{F}$, (10.56) can be written as

$$A_{nm}^p = - \int_V f(\vec{r}') \nabla' \cdot \vec{F}(\vec{r}') d^3 r'. \quad (10.57)$$

The vector identity

$$f \nabla \cdot \vec{F} = \nabla \cdot (f \vec{F}) - \vec{F} \cdot \nabla f \quad (10.58)$$

can be used to rewrite (10.57) as

$$A_{nm}^p = - \int_V \nabla \cdot (f \vec{F}) d^3 r' + \int_V \vec{F} \cdot \nabla f d^3 r'. \quad (10.59)$$

The first integral vanishes when it is transformed into a surface integral outside the source region. Thus the moments reduce to the simpler form

$$A_{nm}^p = - \int_V \vec{F} \cdot \nabla f d^3 r' \quad (10.60)$$

which is tabulated in Table 10.3. As an example, the dipole moment \vec{m} for a distributed magnetization \vec{M} is greatly simplified by this technique

$$\vec{m} = - \int_V \nabla' \cdot \vec{M}(\vec{r}') \vec{r}' d^3 r' = \int_V \vec{M}(\vec{r}') d^3 r'. \quad (10.61)$$

The field at \vec{r} produced by a dipole located at \vec{r}' is obtained by computing the gradient of the dipole potentials in Table 10.3

$$\vec{B}(\vec{r}) = -\nabla \Psi(\vec{r}) = \frac{\mu_0}{4\pi} \left(\frac{3\vec{m} \cdot (\vec{r} - \vec{r}')}{|\vec{r} - \vec{r}'|^5} (\vec{r} - \vec{r}') - \frac{\vec{m}}{|\vec{r} - \vec{r}'|^3} \right). \quad (10.62)$$

Table 10.3 Spherical harmonic multipole strengths [18] in terms of dipole density S

$$A_{nm}^p = \int_V S(\vec{r}') \cdot \nabla f(\vec{r}') d^3 r'$$

| | |
|------------|---|
| Monopole | $a_{00} = \int_V \nabla \cdot S(\vec{r}') d^3 r' = 0$ |
| Dipole | $a_{10} = \int_V S_z(\vec{r}') d^3 r'$ $a_{11} = \int_V S_x(\vec{r}') d^3 r'$ $b_{11} = \int_V S_y(\vec{r}') d^3 r'$ |
| Quadrupole | $a_{20} = \int_V [3z'S_z(\vec{r}') - \vec{r}' \cdot S(\vec{r}')] d^3 r'$ $a_{21} = \int_V [x'S_z(\vec{r}') + z'S_x(\vec{r}')] d^3 r'$ $b_{21} = \int_V [\gamma'S_z(\vec{r}') + z'S_y(\vec{r}')] d^3 r'$ $a_{22} = \frac{1}{2} \int_V [x'S_x(\vec{r}') - \gamma'S_y(\vec{r}')] d^3 r'$ $b_{22} = \frac{1}{2} \int_V [x'S_y(\vec{r}') + \gamma'S_x(\vec{r}')] d^3 r'$ |
| Octupole | $a_{30} = \frac{3}{2} \int_V [S_z(\vec{r}') (5z'^2 - r'^2) - 2z'r' \cdot S(\vec{r}')] d^3 r'$ $a_{31} = \frac{1}{4} \int_V [S_x(\vec{r}') (5z'^2 - r'^2) + 2x' (5z'S_z(\vec{r}') - S(\vec{r}') \cdot \vec{r}')] d^3 r'$ $b_{31} = \frac{1}{4} \int_V [S_y(\vec{r}') (5z'^2 - r'^2) + 2y' (5z'S_z(\vec{r}') - S(\vec{r}') \cdot \vec{r}')] d^3 r'$ $a_{32} = \frac{1}{4} \int_V [2z' (x'S_x(\vec{r}') - y'S_y(\vec{r}')) + S_z(\vec{r}') (x'^2 - y'^2)] d^3 r'$ $b_{32} = \frac{1}{2} \int_V [y'z'S_x(\vec{r}') + x'z'S_y(\vec{r}') + x'y'S_z(\vec{r}')] d^3 r'$ $a_{33} = \frac{1}{8} [(x'^2 - y'^2) S_x(\vec{r}') - 2x'y'S_y(\vec{r}')] d^3 r'$ $b_{33} = \frac{1}{8} [2x'y'S_x + (x'^2 - y'^2) S_y(\vec{r}')] d^3 r'$ |

The end result of this exercise is a series of dipole pictures for the spherical harmonic multipole series, as shown in Figure 10.6. It is important to recognize that in the limit as the dipole spacing becomes small, the two alternative configurations, shown for example by the black and gray arrows in a_{21} , produce the same field. We will address the implications of these pictures when we later discuss the information content of biomagnetic signals.

If an electric or magnetic source consists of N dipoles \vec{M}_a at locations $\vec{r}_a (a = 1, N)$, then it is straightforward to relate this model to a multipole series computed about the origin [19, 28]. For a single magnetic dipole \vec{m} at the point \vec{r} , the magnetization is given by

$$\vec{M}(\vec{r}) = \vec{m} \delta(\vec{r} - \vec{r}), \quad (10.63)$$

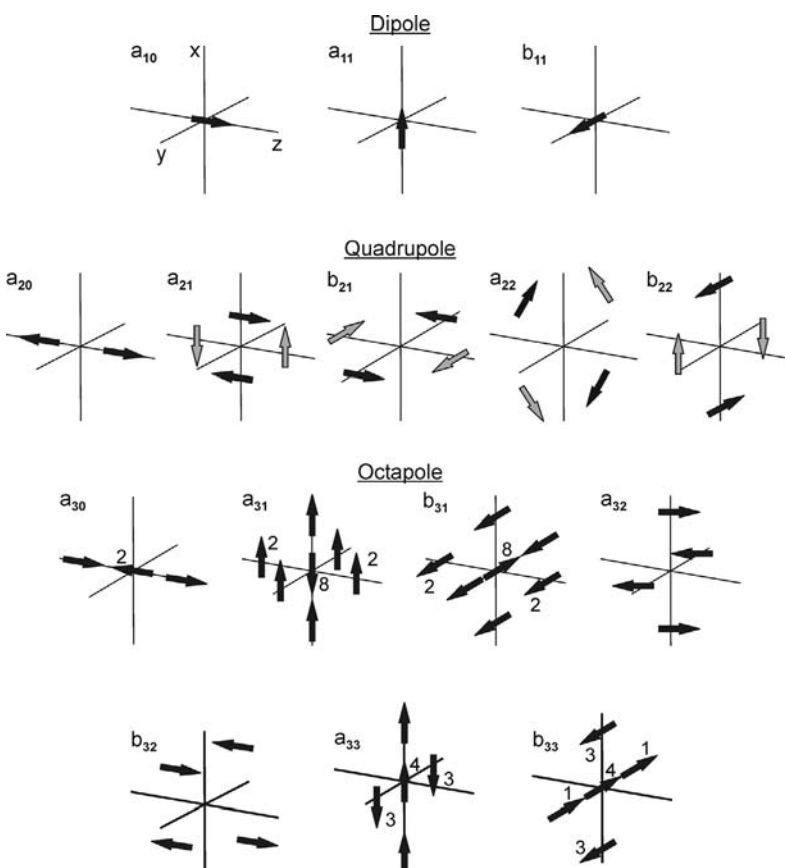


Fig. 10.6 The dipole models that correspond to the various multiple moments in Tables 10.2 and 10.3. The gray and black arrows in the quadrupole moments describe two current source distributions that are electrically identical but magnetically different. (Adapted from Ref. [18], with permission.)

where $\delta(\vec{r} - \vec{r}')$ is the Dirac delta function. Substitution of this into the integrals in Table 10.3 can be used to obtain the dipole through octapole moments of a dipole displaced from the origin [18].

10.2.4.4 Current Multipoles in Conducting Media

The advantage of the multipole approach is that it provides a mathematically compact, orthogonal description of a source distribution, which is particularly advantageous in an inverse calculation. Moreover, it has been pointed out in the literature [33–35] that the classic equivalent current dipole model can sometimes lead to dangerous oversimplification of the inverse problem, partly because dipoles alone describe spatially extended sources rather poorly. We refer the reader to the work of Mosher *et al.* [33, 34, 36] for excellent and up-to-date reviews of MEG forward modeling using multipole expansions.

The challenge is to establish an appropriate interpretation of the higher order multipole moments. To explore the relationship between multipole moments and distributed dipole sources, we draw from a detailed discussion of the uniform double-layer model [22].

Figure 10.7 shows a schematic representation of a cardiac activation wave front. In the uniform double-layer model of cardiac activation, the active sources of the cardiac electric and magnetic fields are constrained to an expanding wave front, which is assumed to be thin, and have an impressed current density \vec{j} that is everywhere uniform and perpendicular to the wave front [37]. It is termed a double layer because current is injected by the wave front into the medium at the outer surface, and withdrawn with an equal strength at the inner one. In this case, the solid angle theorem [23] states that the electric potential at any point in an infinite, homogeneous conductor containing such a uniform double-layer source is determined by the solid angle subtended by the rim of the double layer. The projected area of this rim is proportional to the dipole moment of this source and field; the curvature and detailed shape of the rim contribute to the quadrupole and higher moments [22]. It also follows that the external potential is independent of any perturbations of the layer that do not affect the shape or location of the rim, in that they are equivalent to the addition or subtraction of closed double layers, which are equivalent to externally silent, spherical capacitors. If the origin of the multipole series does not correspond to the center of the surface enclosed by the rim, there will be additional terms to the multipole expansion that are described by the dipole shift equations [18, 28]. Conversely, the center of the wave front can in principle be located by determining the location for the multipole origin that minimizes higher order moments [22]. Interpretation is even more complicated when, late in cardiac depolarization, the wave front expands until it breaks through the epicardial surface, adding a second, or third rim to the wave front, each with its own shifted multipole series!

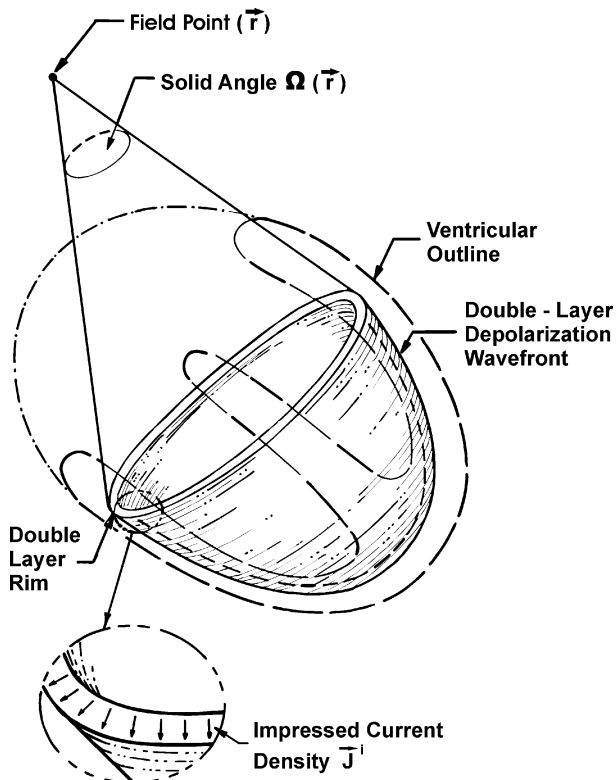


Fig. 10.7 The double-layer model of ventricular activation.
(Adapted from Ref. [22], with permission.)

Given the difficulty in picturing the rim topology that corresponds to higher order moments, it is tempting to ignore multipole series from the outset and use only a distributed dipole source, as shown in Figure 10.8. While this approach provides a straightforward means of computing the electric and magnetic fields from *a priori* knowledge of the spatiotemporal behavior of the wave front, we will show later in the chapter that it fails as an inverse model because the dipoles are not independent or orthogonal. As discovered when first attempted by Holt *et al.* [38–40], there are instabilities in the solutions that correspond to the addition and subtraction of dipole representations of spherical capacitors. Perturbing one dipole can be balanced by a corresponding antiperturbation of all other dipoles. The obvious solution is to constrain the orientation of the dipole, through quadratic programming, so that their orientation cannot reverse. This corresponds to the addition of physiological constraints to a model, something that has been popular in MEG analyses of cortical sources.

While the preceding discussion was directed towards cardiac sources, it applies equally well to distributed sources in the brain and gastrointestinal (GI) system,

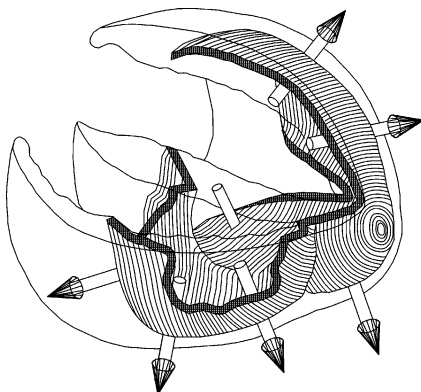


Fig. 10.8 A multiple-dipole representation of the cardiac activation.
(Adapted from Ref. [243], with permission.)

which can have a significant spatial extent [41]. The issue of MEG sensitivity to cortical sources as a function of their depth is addressed in work of Hillebrand [42] and Okada [43, 44]. Fourier inverse techniques, discussed in a later section, have been used to determine how the magnetic field of cortical sources is affected by their linear extent [45–48]. It has also been shown that higher order current multipole coefficients can provide supplementary information on characteristics of the source, in addition to the location and magnitude of the source extracted from the dipolar terms. There is an increasing body of evidence suggesting that multipole fitting in realistic head models may be required to accurately estimate and characterize neuronal activity [49]. Specifically, quadrupoles can be related to source curvature and octupoles to spatial extent. However, large (yet feasible) signal-to-noise ratios (SNRs) are required to detect such components. For example, using a 49-channel SQUID system, the highest SNR should be of the order of 60 to detect a spatial extent of 20 mm.

The application of forward and inverse models to the study of the GI system was pioneered by Allescher et al. [50] and by Irimia and Bradshaw [51–53], who showed that inverse solutions can be used to detect the pathological uncoupling of electric sources due to gastroparesis and ischemia. In spite of considerable progress in this area, solving the GI inverse problem remains difficult, mainly because the system being studied has a large spatial extent and is populated with many distinct sources that have very different frequency characteristics.

10.3

The Magnetic Inverse Problem

10.3.1

Introduction

Given our brief introduction to the magnetic forward problem, we now address the inverse problem of determining sources from fields. We showed above that the magnetic field represents a convolution of a source distribution with a Green's function. In this light, the inverse problem simply reduces to the deconvolution of these convolution integrals. Therein lies the challenge.

10.3.2

Inverting the Law of Biot and Savart

10.3.2.1 Nonuniqueness of Inverse Solutions

The fundamental difficulty in magnetic imaging of currents is that there is no unique solution to the inverse problem of determining the three-dimensional current distribution in (10.14) from the measurements of the magnetic field outside of the object. As mentioned in Section 10.1, the easiest proof of nonuniqueness is to note that it is possible to superimpose on any three-dimensional current distribution another source distribution that is magnetically silent, such as when the radial internal currents of a spherically symmetric battery are superimposed upon an infinite, homogeneous conductor. This is exactly analogous to the electrostatic case where there is no electric field outside a spherical capacitor formed by a pair of concentric spherical shells carrying opposite charge. In an electrostatics inverse problem, spherical capacitors of arbitrary radius, charge, and sphere separation can be added or subtracted from the source distribution without changing the potentials measured on the surface that bounds all sources. Hence, any attempt to solve such an inverse problem will be unable to determine which spherical capacitor configurations exist, and which do not. Constraints might be used to prevent the inverse algorithm from creating spherical capacitors *de novo*, but there is a whole class of higher-order silent sources. As we saw above, the spherical harmonic multipole solution to Laplace's equation is designed specifically to eliminate those silent sources [18, 25]. The usual approach to this problem for either the electric or magnetic inverse is to restrict the possible sources and invert the resulting set of constrained equations.

In contrast to the three-dimensional current-imaging problem, the two-dimensional problem does have a unique inverse. As we shall see in this chapter, there is a wide variety of inverse algorithms for magnetic imaging of two-dimensional current distributions, including spatial filtering, dipole fitting, the Hosaka-Cohen transformation, alternating projections, lead-field analysis, the finite-element method, and blind deconvolution. While there may be a unique inverse solution, even the two-dimensional inverse problem can be ill-conditioned, in that the abil-

ity to determine the inverse solution with the desired accuracy or spatial resolution can be strongly dependent upon measurement noise, source-detector distance, and the exact nature of the source current distribution. We shall show that this can be overcome in part by applying constraints to limit the effects of noise or to utilize most fully *a priori* knowledge of the current distribution.

10.3.2.2 The Spatial Filtering Approach

The most elegant method to obtain a two-dimensional current image from a magnetic field map is to use Fourier-transform deconvolution (inversion) of the law of Biot and Savart [54–59]. Following the notation of Roth [56], let us assume that we are imaging the magnetic field produced by a two-dimensional current $\vec{J}(x, y)$ distributed through a slab of conducting material of thickness d that extends to infinity in the xy -plane. We shall assume that we measure the component B_x at a height $z \gg d$, so that we can integrate (10.14) over z' and immediately obtain⁴

$$B_x(x, y, z) = \frac{\mu_0 d}{4\pi} z \int_{-\infty}^{\infty} \int_{-\infty}^{\infty} \frac{J_y(x', y')}{[(x - x')^2 + (y - y')^2 + z^2]^{3/2}} dx' dy'. \quad (10.64)$$

We can write this equation as the convolution of the current distribution with a Green's function that represents the magnetic source-to-field transfer function:

$$B_x(x, y, z) = \int_{-\infty}^{\infty} \int_{-\infty}^{\infty} J_y(x', y') G((x - x'), (y - y'), z) dx' dy', \quad (10.65)$$

where the Green's function is given by

$$G((x - x'), (y - y'), z) = \frac{\mu_0 d}{4\pi} \frac{z}{[(x - x')^2 + (y - y')^2 + z^2]^{3/2}}. \quad (10.66)$$

Rather than computing this through integration in Cartesian space, we can instead compute the spatial Fourier transform (*FT*)⁵ of J_y using the fast Fourier transform (FFT) or more accurate techniques [60], so that

- 4) Hereafter, when we are discussing the two-dimensional current image, we shall assume that the sample has a thickness d that is negligible compared to z , so that \vec{J} has neither a z -component nor z -dependence. Thus, we shall be able to use the standard current density \vec{J} , with units of amperes/meter², rather than a two-dimensional equivalent. The thickness d will be written explicitly in the equations. $\vec{J}d$ is simply a two-dimensional current density with units of amperes/meter.

- 5) We use the following definition of the two-dimensional Fourier transform pair in this chapter:

$$f(k_x, k_y) = \int_{-\infty}^{+\infty} \int_{-\infty}^{+\infty} F(x, y) e^{-i(k_x x + k_y y)} dx dy$$

$$F(x, y) = \frac{1}{(2\pi)^2} \int_{-\infty}^{+\infty} \int_{-\infty}^{+\infty} f(k_x, k_y) e^{i(k_x x + k_y y)} dk_x dk_y$$

This may lead to slight differences between some of the equations presented herein and those in the original papers.

$$j_y(k_x, k_y) = FT\{J_y(x, y)\}. \quad (10.67)$$

Similarly, we can write

$$b_x(k_x, k_y, z) = FT\{B_x(x, y, z)\}. \quad (10.68)$$

The Green's function has the Fourier transform [56]

$$g(k_x, k_y, z) = \frac{\mu_0 d}{2} e^{-z\sqrt{k_x^2 + k_y^2}}, \quad (10.69)$$

where $k_x = 2\pi/x$ and $k_y = 2\pi/y$ are the spatial frequencies, in m^{-1} , in the x and y directions. We can then use the convolution theorem to write the law of Biot and Savart as a simple multiplication in the spatial frequency domain

$$b_x(k_x, k_y, z) = g(k_x, k_y, z) j_y(k_x, k_y). \quad (10.70)$$

This process allows us to start with a known y component of the current density, $J_y(x, y)$, and then calculate the x component of the magnetic field, $B_x(x, y, z)$. Note that the spatial filter that corresponds to the magnetic forward problem, g , falls exponentially with both k and z , so that the high-spatial-frequency contributions to the current distribution are attenuated in the magnetic field, *i.e.*, the Green's function acts as a spatial low-pass filter. The farther the magnetometer is from the current distribution, the harsher is the filtering.

Inverse Spatial Filtering

A supposedly simple division allows us to solve (10.70) for $j_y(k_x, k_y)$ and hence solve in Fourier space the inverse imaging problem of determining \vec{J} from \vec{B}

$$j_y(k_x, k_y) = \frac{b_x(k_x, k_y, z)}{g(k_x, k_y, z)}. \quad (10.71)$$

The desired image of $J_y(x', y')$ is obtained with the inverse Fourier transform

$$J_y = FT^{-1}\{j_y(k_x, k_y)\}. \quad (10.72)$$

A similar set of equations would allow us to determine J_x from a map of B_y . This inverse solution is unique [56].

As we shall see in more detail shortly, the problem with this inverse process, in general, is in the division in (10.71). If g is small, but nonzero, at spatial frequencies for which $1/g$ is large, j_y tends toward infinity. Unfortunately, g falls exponentially with k , so that $1/g$ diverges exponentially. Since noise is always present in experimental data, b_x is certainly nonzero at high frequencies, even if the theoretical magnetic field associated with the source does not contain high-spatial-fre-

quency components. Therefore, (10.71) is destined to “blow up” due to excessive amplification of noise. Before we see how this can be avoided, it is useful to look at the z component of the field.

From (10.17), it follows that the Fourier transform of B_z is [56]

$$b_z(k_x, k_y, z) = i \frac{\mu_0 d}{2} e^{-z\sqrt{k_x^2+k_y^2}} \left(\frac{k_x j_y(k_x, k_y)}{\sqrt{k_x^2 + k_y^2}} - \frac{k_y j_x(k_x, k_y)}{\sqrt{k_x^2 + k_y^2}} \right). \quad (10.73)$$

This shows us, in general, that a single image of B_z would be inadequate to determine both J_x and J_y , and would provide only a linear combination of the two. However, if we assume that the current distribution is continuous, it must have zero divergence in the quasistatic limit, *i.e.*,

$$\nabla \cdot \vec{J}(x, y) = 0. \quad (10.74)$$

For two-dimensional current with no source or sinks, this reduces to

$$\frac{\partial J_x}{\partial x} + \frac{\partial J_y}{\partial y} = 0. \quad (10.75)$$

If we compute the Fourier transform of this equation, we then have the added constraint

$$ik_x j_x(k_x, k_y) + ik_y j_y(k_x, k_y) = 0, \quad (10.76)$$

which allows us to solve (10.73) for either J_x or J_y and then use the continuity equation to obtain the other. While this procedure works well for planar current distributions, it may not be applicable for mapping effective surface currents on the upper boundary of three-dimensional current distributions in thick objects, since current flowing on the surface can disappear as J_z into the bulk conductor of the object without affecting B_z .

Noise and Windowing

We now can address briefly the issue of noise and windowing, which is treated in greater detail elsewhere for two-dimensional imaging [56], for fetal MCG noise removal [61], and for cylindrical models of the head [45, 47, 48] and abdomen [62]. The value of j_y in (10.71) will diverge if there is noise in the absence of signal, *i.e.*, if the denominator goes to zero faster than does the numerator. However, because the noise in a SQUID measurement is white at high temporal frequencies, a scanned SQUID image will have white noise at high spatial frequencies. The low-pass characteristic of the law of Biot and Savart is manifest as a Green’s function that tends towards zero exponentially at high spatial frequencies, so that an unstable inverse is almost guaranteed except in cases where the magnetometer is very close to the current distribution. The solution to this dilemma is to filter spatially the magnetic field data by eliminating all contributions at high spatial frequencies, so that the numerator is identically zero above a frequency k_c . The pro-

cess of low-pass filtering in the frequency domain (or windowing in the temporal domain) will ensure a stable inverse, but at the cost of losing high-spatial-frequency information.

The steps in this process, and how it affects the image quality, are shown in Figures 10.9 and 10.10, in which we simulate the forward problem of conversion of a current source distribution into a magnetic field map (down the left column) and, after adding noise, the inverse problem of converting the field map into a reconstructed source image (up the right column), which includes the windowing that is usually required to provide a stable inverse solution.

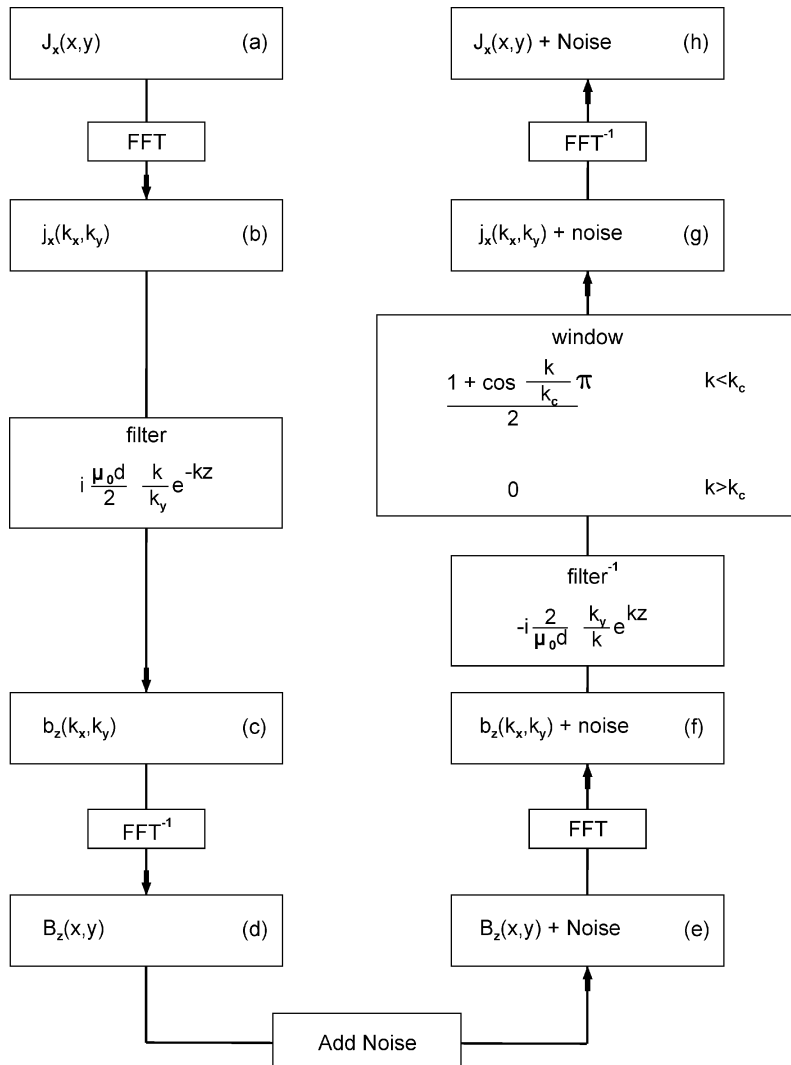


Fig. 10.9 Schematic outlining the forward and inverse Fourier imaging process. (Adapted from Ref. [56], with permission.)

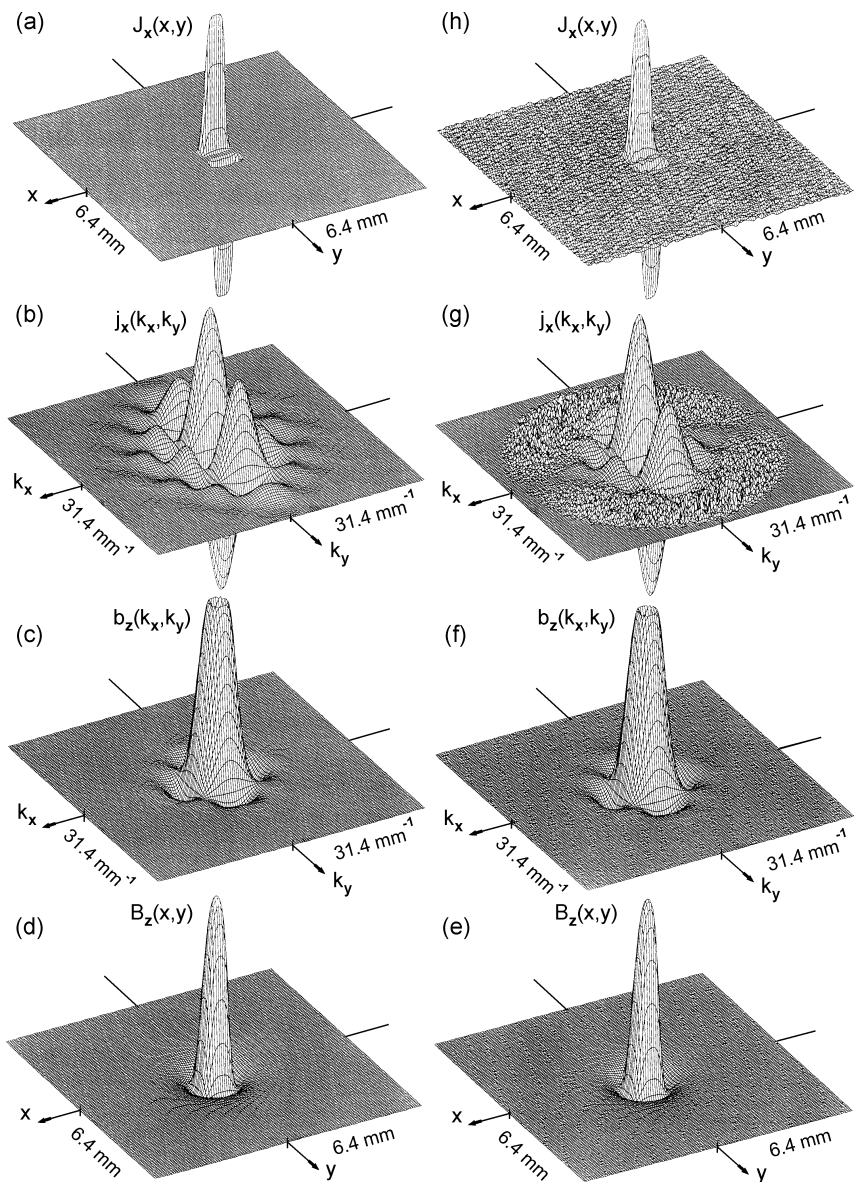


Fig. 10.10 Forward and inverse spatial filtering/Fourier transform calculations for $z = 0.3$ mm. See text for details. (Adapted from Ref. [56], with permission.)

In Figure 10.10(a), we start with the x component of the current density, $J_x(x, y)$, for a square loop of current and compute in Figure 10.10(b) the imaginary part of the Fourier transform of $J_x(x, y)$, i.e., $j_x(k_x, k_y)$. The real part of the Fourier transform of $B_z(x, y, z)$, $b_z(k_x, k_y)$, at $z = 0.3$ mm is shown in Figure 10.10(c), and

from this we compute in Figure 10.10(d) the z -component of the magnetic field, $B_z(x, y, z)$, with peak amplitude of 756 pT. To simulate measurement noise in Figure 10.10(e), we add to B_z in Figure 10.10(d) a 0.5-pT amplitude white noise. From this, we compute the real part of the Fourier transform of B_z with added noise in Figure 10.10(f), the imaginary part of the Fourier transform of the J_x image multiplied by a Hanning window with a low-pass filter with $k_c = 30 \text{ mm}^{-1}$ (Figure 10.10(g)), to produce in Figure 10.10(h) the current-density image J_x .

Figure 10.11 shows a comparison of the results of the spatial filtering/Fourier transform inverse approach for equivalent theoretical and experimental images for a current test pattern. This magnetic imaging approach is the basis for extensive work on the magnetic detection of current distributions within integrated circuits [63, 64].

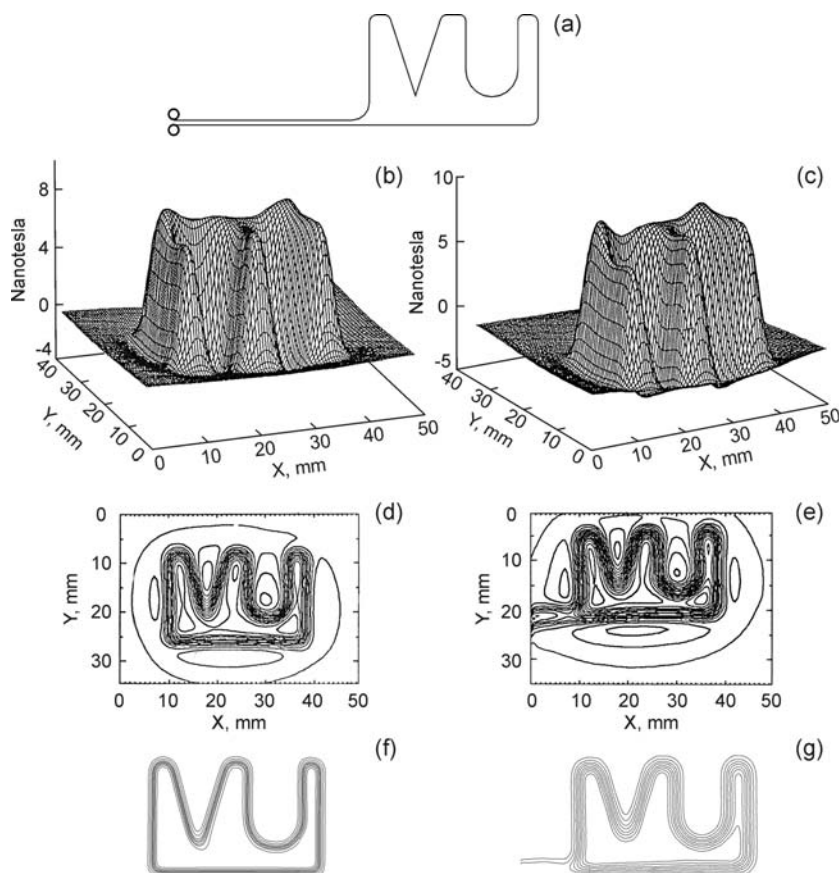


Fig. 10.11 Magnetic imaging of a current pattern: (left) theoretical and (right) experimental images. (a) The source current; (b) and (c) surface plots of the magnetic field; (d) and (e) isocontour plots; and (f) and (g) the deconvolved current images. (Adapted from Ref. [244], with permission.)

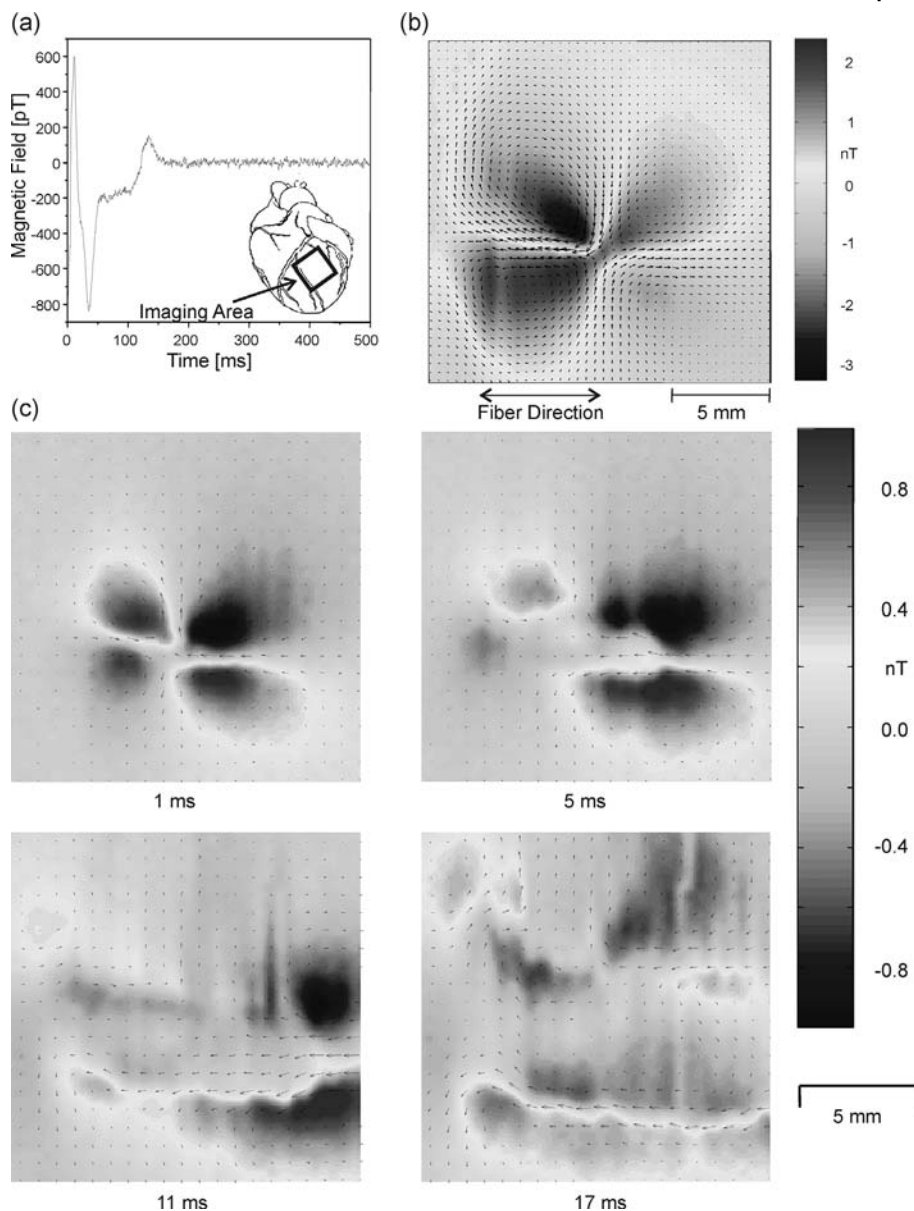


Fig. 10.12 Magnetic imaging of cardiac action currents. (a) MCG taken at a location on the scanning grid. Inset: anterior view of the heart showing the location of the $16 \times 16 \text{ mm}^2$ scanning area. (b) Magnetic field resulting from a cathodal stimulus current of 1.5 mA. The overlaid arrows schematically represent the current distribution under the assumption of two-dimensional sheet currents as determined by inverse Fourier

imaging. (c) Magnetic fields generated by the propagation of action currents resulting from a cathodal point stimulus. The arrows show schematically the current distribution. The octupolar pattern with four current loops can be explained in the framework of a bidomain model with an unequal anisotropy ratio in the intra- and extracellular space. (Adapted from Ref. [174], with permission.)

Figure 10.12 shows a magnetic field map obtained with the original Micro-SQUID magnetometer and the corresponding current image for a slice of isolated cardiac tissue [65, 66]. These measurements provided some of the first proof that cardiac tissue is best described by bidomain models⁶ with unequal anisotropy ratios in the intracellular and extracellular spaces [67].

Magnetometer Separation

The trade-off between stability of the inverse and the cutoff of high spatial frequencies is unfortunate, in that the presence of noise limits the ability to enhance the spatial resolution of a current image obtained with a distant magnetometer. Figure 10.13 shows how the quality of an image is degraded as the magnetometer is moved away from the source distribution. The mean square deviation (MSD) of the image from the modeled source is 0.03 at 0.1 mm with $k_c = 10 \text{ mm}^{-1}$ (Figure 10.13(a)); 0.07 at 0.3 mm with $k_c = 30 \text{ mm}^{-1}$ (Figure 10.13(b)); 0.44 at 1.0 mm with $k_c = 10 \text{ mm}^{-1}$ (Figure 10.13(c)); and 0.95 at 3 mm with $k_c = 3 \text{ mm}^{-1}$ (Figure 10.13(d)).

The primary strengths of the technique are the speed with which the field map can be deconvolved and the ease with which it can be low-pass filtered: a fast Fourier transform of the data is computed, the data are multiplied in the frequency domain by the low-pass filtered Green's function, and the inverse FFT is computed. For a particular measurement geometry, the Green's function needs to be computed only once.

Apodizing

The discussion so far has assumed that the magnetic field is measured at a point. In practice, SQUID magnetometers have pickup coils whose diameter is comparable to the spacing between the coil and the sample, consistent with optimizing the trade-offs between sensitivity and spatial resolution [68]. Since the SQUID measures flux, the pickup coil integrates the magnetic field that threads the coil, and thus the shape of the coil is convolved with the field distribution in a manner that results in further low-pass spatial filtering of the field. The relationship between coil diameter, spatial resolution, and sensitivity is nontrivial. A spatial-filtering analysis can be used to show that a noisier (less sensitive), smaller pickup coil placed close to a sample can in certain circumstances provide better images than a larger, quieter SQUID further away [69, 70].

- 6) The bidomain model of cardiac tissue addresses the limitations of the uniform double-layer model by treating cardiac tissue as an active, anisotropic, three-dimensional cable, in which the intracellular and extracellular spaces of the interconnected (syncytial) cardiac cells, with their differing electrical anisotropies, are separated by the nonlinear membrane that serves as the current source that drives action currents from the intracel-

lular to extracellular spaces, and vice versa. The double-layer representation corresponds to what would be seen in the extracellular space alone: the appearance and disappearance of the current from opposite surfaces of the wave front. The bidomain model casts this in terms of known membrane electrophysiology and homogenizes the problem to avoid the details of individual cells.

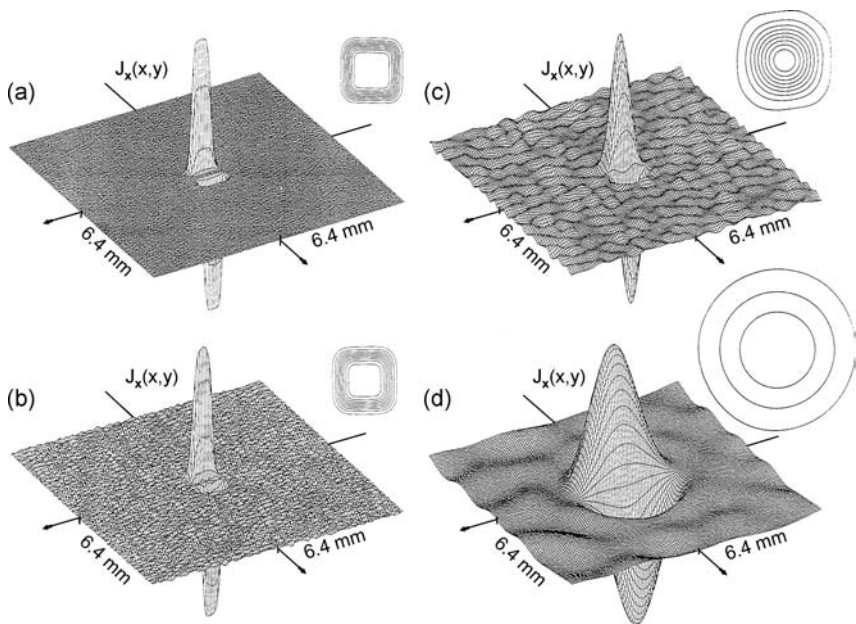


Fig. 10.13 Spatial filtering/Fourier transform inverse image of the current density for four different values of $h(k_x, k_y)$, calculated from the $e^{-Q^2 R^2}$ component of the magnetic field produced by the square current loop used in the simulations of Fig. 10.10 after magnetometer noise of 0.5 pT has been added to the

magnetic field. Plots of both $J_x(x, y)$ and the current lines (upper right inset) are shown. Each line corresponds to 0.1 μA, except in (d), where each line is 0.05 μA. (a) $z = 0.1$ mm, (b) 0.3 mm, (c) 1.0 mm, (d) 3.0 mm.
(Adapted from Ref. [56], with permission.)

One would suspect that a deconvolution approach could be used to eliminate the effect of the finite coil area. The image processing approach can be extended to examine and correct for the effects of finite-diameter pickup coils [71]. We discuss the flux-field deconvolution in greater detail later in this chapter. For a SQUID with a finite-diameter pickup coil, the magnetic field B_z will be convolved with the spatial sampling (or turns) function H of the coil to give the detected flux Φ . Figure 10.14 shows four different pickup coils [71]. In Fourier space, the magnetic field distribution from the sample $b(k_x, k_y)$ will be multiplied by the turns function $h(k_x, k_y)$ to give the flux $\phi(k_x, k_y)$. Ideally, the effect of the coil could be corrected by dividing $\phi(k_x, k_y)$ by $h(k_x, k_y)$ to obtain $b(k_x, k_y)$, so that an inverse Fourier transform would give the coil-corrected B_z . Unfortunately, for typical coils, the edges of the coil introduce zeros in their spatial frequency transfer function, $h(k_x, k_y)$, which complicate deconvolution of the images at high spatial frequencies: the zero in the forward transfer function produces an infinity in the inverse function, making it difficult to obtain any information from the field at or even near that spatial frequency. This could be ameliorated with windowing, as before, but this leads once again to the loss of high-frequency information instead of to

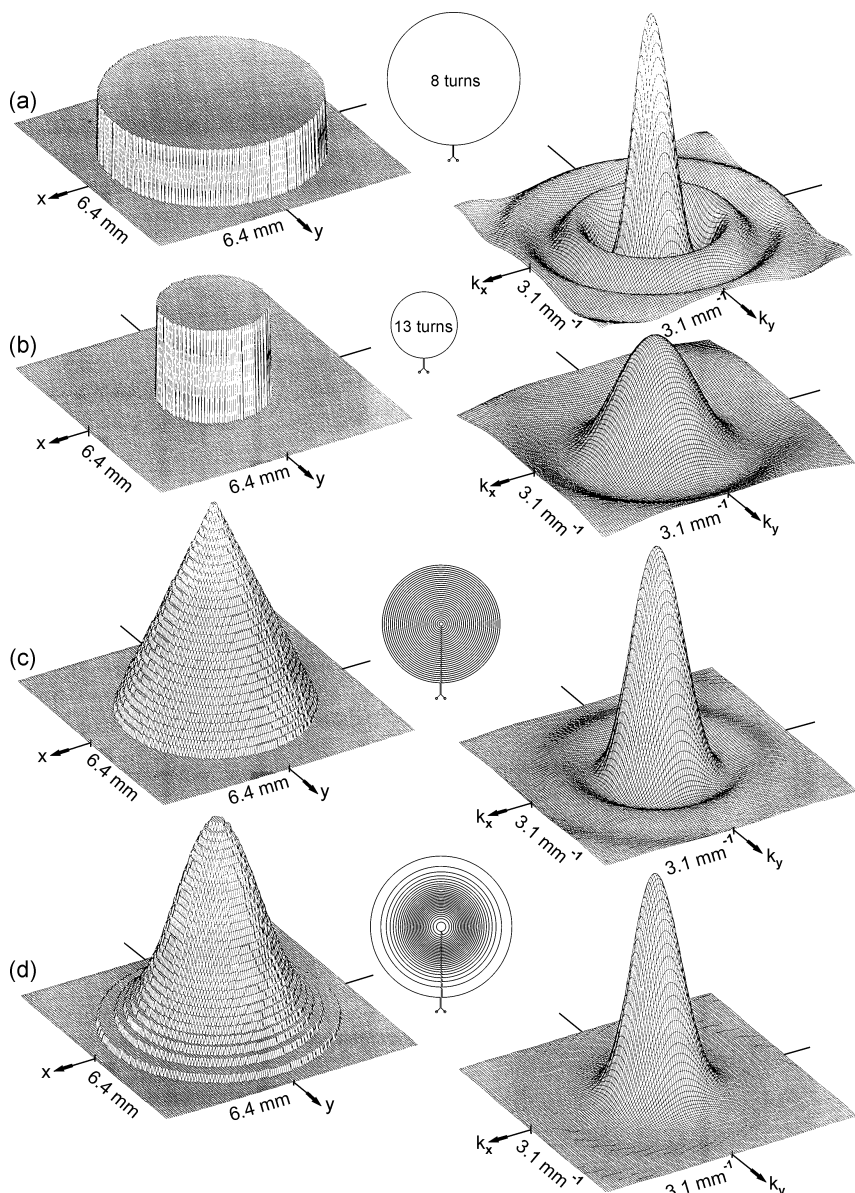


Fig. 10.14 Four SQUID pickup coils with different separations of the turns. Left: the turns function $H(r)$; middle: the coil; right: the Fourier transform of the turns function $h(k_x, k_y)$. The coils are (a) 8 turns with a

5-mm diameter, (b) 13 turns with a 2.5-mm diameter, (c) a pancake coil with 29 turns, and (d) an apodized coil with 29 turns and a turns functions given by $e^{-\alpha^2 r^2}$. (Adapted from Ref. [71], with permission.)

the desired extent of resolution enhancement. As shown in Figure 10.15, even with windowing, the contribution near the zeros produces spikes that appear in the frequency domain at the edge of the window, and these spikes produce noise in the spatial images.

A solution to this problem that has been demonstrated theoretically [71] but not yet implemented is to adjust the spacing of individual turns in a planar coil, as shown in Figures 10.14(c) and (d), so that the zeros in the transfer function

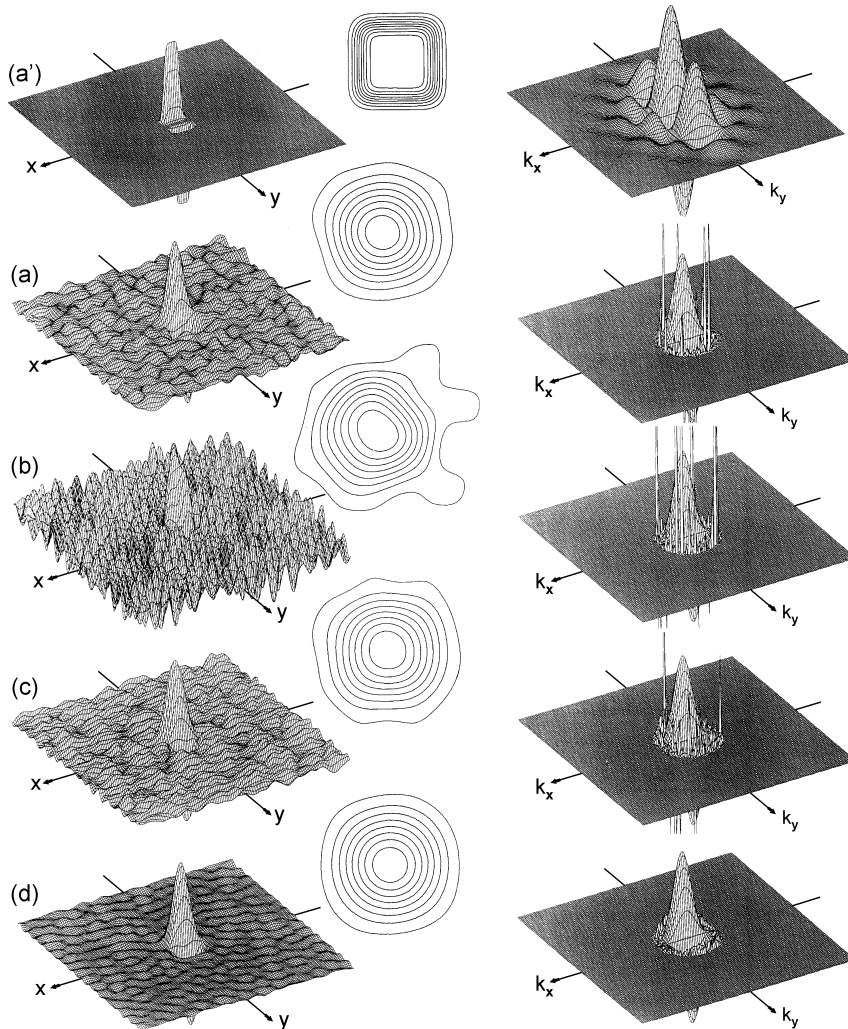


Fig. 10.15 A comparison of the imaging ability of the four different SQUID pickup coils in Fig. 10.14. Left: the x -component of the current density; center: current lines of the image of the current; right: the imaginary part of the

Fourier transform of the current density images. The source current is (a'), and (a)–(d) are the density images from the four coils. (Adapted from Ref. [71], with permission.)

$h(k_x, k_y)$, shown in the right-hand column, are either eliminated or forced to very high spatial frequencies. This process, termed apodizing, could provide a significant enhancement in spatial resolution for certain SQUID imaging applications, particularly SQUID microscopy.⁷⁾ Figure 10.15 illustrates the process. Figure 10.15(a') shows the x -component of a 5 mm square current loop with a 0.75 mm Gaussian width (left), the image of these currents (center), and the spatial Fourier transform of the current. We then used this current to compute magnetic fields at a height of 5 mm above this loop, with a current noise of 15 pA and a k_c of 1.8 mm^{-1} . The current image in Figure 10.15(d) from the apodized coil has lower noise yet provides excellent spatial resolution, despite the fact that the apodized coil has a larger outer diameter than the other three coils.

Estimation of the Maximum Spatial Frequency

While the Nyquist sampling limit is well understood for time-series signal analysis, the extension of this concept to spatial frequencies of magnetic field distribution deserves some explanation, particularly with regard to the complementary issues of maximum spatial frequency in the measured magnetic field, and the spatial sampling generally used in measuring it. The estimation of the maximum spatial frequency of the magnetic field produced by a particular source configuration is of utmost importance, as it determines whether severe information loss happens in the field integration along the coils of a SQUID sensor. In addition, it determines the region in the spatial frequency plane over which the deconvolution has to be calculated and it imposes restrictions on the step size of the mapping grid so as to avoid aliasing, as explained in the next subsection. While a precise value for this frequency is sometimes difficult to obtain, since it requires a detailed model of the field source, an estimate may provide enough information to achieve reliable deconvolutions. Because the spectrum of magnetic fields usually extends towards infinity, some criterion should be used to define a “maximum” frequency. We consider as maximum spatial frequencies the frequencies encompassing 99% of the total field energy. To calculate the maximum spatial frequencies, we first compute the total field energy

$$\mathcal{E} = \int_{-\infty}^{+\infty} \int_{-\infty}^{+\infty} |B_z(x, y, z)|^2 dx dy. \quad (10.77)$$

Then, for fields without circular symmetry, we suppose the maximum frequencies to be the same in both x and y directions, and use Parseval’s theorem to obtain

- 7) At present, most biomagnetic SQUID systems are limited by the low-pass filtering of the Green’s function, associated with the liftoff, and not by the coil size. However, for SQUID microscopes, apodized coils may provide much better sensitivity than bare SQUIDs and yet offer comparable spatial

resolution. In addition, apodized coils are flat, multturn coils, thereby avoiding the strong blurring effect associated with the coil thickness of hand-wound coils in SQUID microscopes. Usually, coil thickness is much greater than liftoff in SQUID microscopes.

$$\int_0^{k_{\max}} \int_0^{k_{\max}} \left| b_z(k_x, k_y, z) \right|^2 dk_x dk_y = (1/4) \times 4\pi^2 \times 0.99 \times E. \quad (10.78)$$

However, for circularly symmetric fields we can obtain a one-dimensional relation by using the zeroth-order Hankel transform [72] (in this case, k_{\max} is the same in all directions)

$$\int_0^{k_{\max}} k_\rho |b_z(k_\rho, z)|^2 dk_\rho = 4\pi^2 \times 0.99 \times E, \quad (10.79)$$

where $k_\rho = (k_x^2 + k_y^2)^{1/2}$. Equations (10.78) and (10.79) can be numerically solved for k_{\max} .

As an example, consider a current dipole pointing in the x -direction. Then, we have that

$$B_z(x, y, z) = \frac{\mu_0 p_x}{4\pi} \left[\frac{y}{(x^2 + y^2 + z^2)^{3/2}} \right], \quad (10.80)$$

which has a two-dimensional Fourier transform given by

$$b_z(k_x, k_y, z) = \begin{cases} -i\mu_0 p_x \frac{k_y e^{-z\sqrt{k_x^2+k_y^2}}}{2\sqrt{k_x^2+k_y^2}} & \text{for } k_x \neq 0 \text{ and } k_y \neq 0, \\ 0 & \text{otherwise.} \end{cases} \quad (10.81)$$

Thus, the total field energy is related to the liftoff distance z by

$$\mathcal{E} = \frac{(\mu_0 p_x)^2}{64\pi z^2}. \quad (10.82)$$

For a magnetic dipole source pointing in the z -direction, the field exhibits circular symmetry

$$B_z(x, y, z) = \frac{\mu_0 m_z}{4\pi} \left[\frac{3z^2}{(x^2 + y^2 + z^2)^{5/2}} - \frac{1}{(x^2 + y^2 + z^2)^{3/2}} \right], \quad (10.83)$$

and the Fourier transform is

$$b_z(k_\rho, z) = \begin{cases} \mu_0 m_z \left[2\sqrt{2\pi} z^2 (k_\rho/z)^{3/2} K_{3/2}(z k_\rho) - (2\pi/z) e^{-z k_\rho} \right], & \text{for } k_\rho \neq 0 \\ 0 & \text{otherwise,} \end{cases} \quad (10.84)$$

where $K_{3/2}(\cdot)$ is the modified Bessel function of order 3/2. In this case, the total field energy is given by

$$\mathcal{E} = \frac{3(\mu_0 m_z)^2}{64\pi z^4}. \quad (10.85)$$

The plots of the maximum frequency against liftoff distance for the two dipolar sources are shown in Figure 10.16. We observe that the maximum frequency for a 5-mm liftoff, as used in the examples, ranges from 90 to 160 m⁻¹. Other field sources can be used to estimate more closely the maximum spatial frequencies, depending on the experiment in question.

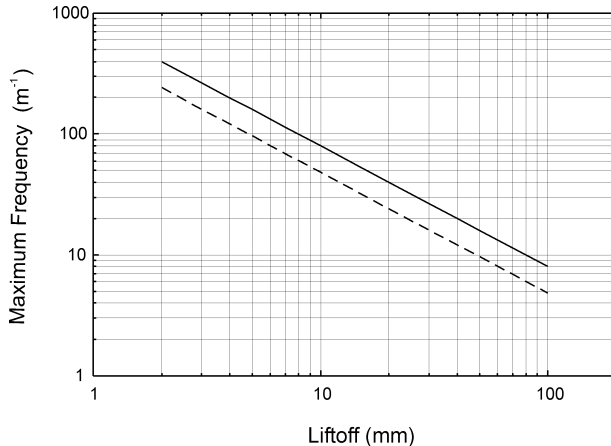


Fig. 10.16 Maximum spatial frequency of the magnetic field as a function of the liftoff for a current dipole (dashed line) on the xy -plane, and a magnetic dipole (solid line) pointing in the z -direction. (Adapted from Ref. [87], with permission.)

Sampling Frequency and Step Size

Before we can proceed further with our analysis of spatial filtering, we must clarify several important issues in spatial sampling, particularly in the context of a scanning magnetometer or a SQUID array used to record a time-varying field. It is important to consider the trade-offs between scanning velocity, SQUID separation, temporal sampling rate, integration time constant, temporal response, spatial resolution, and sensitivity [73]. We will analyze the more complex case of a scanned SQUID, but many of our observations apply to SQUID arrays as well.

The temporal sampling frequency used to construct a magnetic field map should satisfy the Nyquist theorem

$$f_s > 2f_{\max}, \quad (10.86)$$

where f_{\max} is the maximum temporal frequency present in the magnetic field signal. For time-varying fields, f_{\max} is determined either by the SQUID electronics filter cutoff frequency (for low signal-to-noise ratios) or by the field sources. For static fields, f_{\max} is related to the scanning speed and to the maximum spatial fre-

quency k_{\max} of the magnetic field. More accurately, f_{\max} depends on the maximum spatial frequency of the flux, since this is the quantity being sampled. However, because the flux is a low-pass or band-pass filtered version of the magnetic field, ensuring that the field is sampled without aliasing implies that the flux is also correctly sampled. If the scanning speed is v and $s(k)$ is the spectrum of the magnetic field along a scan line in the x -direction, by using the transformation of variables $x = vt$ and the “time-scaling” property of Fourier transforms we obtain

$$s(k) = FT\{S(x)\} = FT\{S(vt)\} = \frac{1}{v} s\left(\frac{\omega}{v}\right) = \frac{1}{v} s\left(\frac{2\pi f}{v}\right). \quad (10.87)$$

Thus, the spatial and temporal frequencies are related by the following expression

$$k = \frac{2\pi f}{v}, \text{ or } f = \frac{kv}{2\pi}, \quad (10.88)$$

meaning that the faster the scan is performed, the higher the temporal frequencies that must be recorded, as expected. That also means, however, that one has to increase the bandwidth of the SQUID system, and that leads to increased noise. To avoid spatial aliasing, the temporal sampling frequency should satisfy

$$f_s > \frac{k_{\max} v}{\pi}. \quad (10.89)$$

The scanning step size Δ , or the reciprocal of the spatial sampling frequency, is also governed by the Nyquist theorem. The maximum step size (or SQUID separation in an array) that can be used without the occurrence of aliasing is given by

$$\Delta \leq \frac{\pi}{k_{\max}} \quad (10.90)$$

Inward Continuation

Because there is no unique solution to the three-dimensional magnetic inverse problem, most solutions to this inverse problem use heavily constrained models for the sources. Alternatively, if the sources are restricted to a well-defined, bounded volume, Laplace’s equation can be used to continue fields observed at some distance inward to the bounding surface, thereby sharpening or deblurring the field. The continuation can also be performed in the opposite direction: upward continuation transforms the magnetic field measured on one surface to the field that would be measured at another surface farther from the sources. As was discussed in Section 10.1, there is no need to sample the field over the entire volume above the source distribution. The best results, however, will be obtained if the magnetometer is placed as close as possible to the sources so as to minimize the noise-enhancing amplification of high spatial frequencies associated with inward continuation.

As discussed in more detail elsewhere [46–48, 74, 75], this approach can be used to convert, in a model-independent manner, a map of the magnetic field measured 10–20 mm from the surface of the scalp into a sharper map of the mag-

netic field on the surface of the cortex, without having to utilize any physical or physiological constraints. Inward continuation deeper into the cortex could be invalidated by active current sources near the cortical surface.

Both inward and upward continuations are unique. Upward continuation is a stable transformation, as it performs a low-pass attenuation on the original field, whereas inward (or downward) continuation tends to be unstable, because it consists of exponentially boosting high spatial frequencies. In the latter case, the stability of the calculation can be affected by measurement geometry, source configuration, and noise. While inward continuation has not been utilized heavily in biomagnetism, it is a common technique in geophysics to sharpen geomagnetic features deep beneath the soil surface. In the spatial frequency domain, the inward continuation of the field measured at z_1 to the point z_2 is [56]

$$b_z(k_x, k_y, z_2) = e^{(z_1-z_2)\sqrt{k_x^2+k_y^2}} b_z(k_x, k_y, z_1). \quad (10.91)$$

When z_2 is less than z_1 , the exponential term acts as a high-pass amplifier, amplifying the high-spatial-frequency components of the image. The advantage of this approach is that it allows sharpening of the image without a specific model for the source. In addition, it preserves the physical dimensions of the original data, unlike other derivative-based techniques used to enhance the spatial resolution of magnetic fields. Therefore, the same analysis tools used on the original data can also be applied to the transformed data. The disadvantages are that it works only between two values of z for which there are no current sources or magnetization, and that it is subject to instabilities due to excessive amplification of high-spatial-frequency noise.

Several techniques have been developed to overcome the instability problem, and the literature in geophysics is abundant in papers dealing with this subject. We just mention two of those techniques, which improve the quality of continued field maps. The integrated second vertical derivative (ISVD) method proposed by Fedi and Florio [76] combines frequency and spatial domain transformations to achieve better stability. The idea is to use a Taylor series expansion in z to continue the field, but to utilize frequency methods in the calculations of derivatives. The first vertical derivative is obtained by initially integrating the field along the z -direction, by means of a frequency-domain operator, and then by computing the second vertical derivative from the horizontal second derivatives, as given by Laplace's equation. All other high-order vertical derivatives can be obtained from Laplace's equation applied to either the field (even-order derivatives) or the first derivative (odd-order derivatives). Because the integration performed in the frequency domain is a stable operation and the second horizontal derivatives are approximated by finite differences, the Taylor series is fairly stable. However, the influence of the low-pass filtering associated with integration on the final spatial resolution of the continued field still has to be assessed.

Using a different approach based on Wiener filter theory, Pawłowski [77] proposed the preferential continuation method, which stabilizes the inward continua-

tion and allows for a discriminated processing of shallow and deep sources. In this method, a band-pass amplification is applied to the original field map, enhancing deep sources while keeping shallow sources (high spatial frequencies) unchanged. The overall effect for nonplanar source distributions is equivalent to “compressing” the map, with shallow and deep sources presenting similar sharpness. Even though this feature is useful in many applications, care should be taken when interpreting or further processing the continued fields. For planar sources, the resulting effect is a controlled increase in the sharpness, while avoiding excess of noise, but compromising spatial resolution.

It is worthwhile noticing that the exponential factor $e^{\pm z\sqrt{k_x^2+k_y^2}}$ associated with inward and upward continuations is already embedded in the expressions of the inverse problem in the spatial frequency domain (e.g., (10.73), (10.207) and (10.209)). Thus, when calculating the solution to the inverse problem by spatial frequency methods we are implicitly performing an inward continuation all the way down to the sources. Consequently, the inward continuation at a smaller lift-off is quite useful when an inverse solution with adequate resolution could not be obtained due to the need of severe regularization (*i.e.*, low-pass filtering), or when just a sharper magnetic map is sufficient to provide the desired information.

To illustrate the capabilities of the method, we used one of the Vanderbilt SQUID microscope systems (monolithic SQUID with $40 \mu\text{m} \times 40 \mu\text{m}$ effective area) to scan a sample consisting of a piece of paper containing small symbols printed by two different printers. The original magnetic map is shown in Figure 10.17(a), while an inward continued map is shown in Figure 10.17(b). The

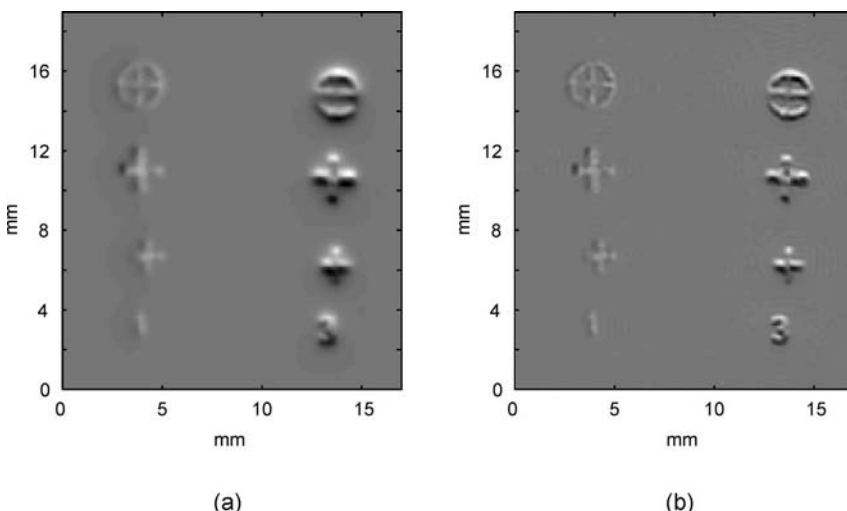


Fig. 10.17 Increasing the spatial resolution of a magnetic map by means of downward continuation techniques. (a) Original magnetic map of a pattern of small symbols printed on a sheet of paper, obtained with one of the

Vanderbilt SQUID microscopes; (b) magnetic map processed by a downward continuation technique. Notice the increase in spatial resolution (deblurring), particularly evident for the right-hand column of symbols.

deblurring effect of the inward continuation is readily apparent, corresponding to an increase in the spatial resolution, particularly for the top and bottom symbols in the right-hand column.

Imaging Discontinuous Currents

In the spatial frequency domain, the z component of the magnetic field from a current-carrying plate of thickness d is given by (10.73), which can be written in a more compact form as

$$b_z = \frac{i\mu_0 d}{2} \left(\frac{k_x}{k} j_y - \frac{k_y}{k} j_x \right) e^{-kz}, \quad z \gg d, \quad (10.92)$$

where

$$k = \sqrt{k_x^2 + k_y^2}. \quad (10.93)$$

Let us consider a measurement of the distortions of the magnetic field associated with discontinuities or heterogeneities in a planar sample, such as a high-temperature superconductor. If current is injected into a planar sample through vertical wires and bus structures on the edges, the current would be uniform were it not for the discontinuities. As shown in Figure 10.18, the magnetic field from the vertical wires is horizontal and does not contribute to the vertical magnetic field B_z . Were the sample homogenous and continuous, the current in the sheet would be uniform, and the magnetic field would be determined solely by the curl of the current associated with the current discontinuity at the edges. Similarly, if we did not choose to use the bus structures, we could include our knowledge of the location of the wires that inject the current by modifying the two-dimensional continuity condition ((10.75)) to include this information [78, 79] as follows:

$$\nabla \cdot \vec{J}(x, y) = F(x, y), \quad (10.94)$$

where $F(x, y)$ describes the current source and sink distribution in the sheet, *i.e.*, I_z in the wires as it enters the sheet. In the spatial frequency domain, our magnetic imaging problem becomes

$$ik_x j_x + ik_y j_y = f(k_x, k_y). \quad (10.95)$$

We then obtain

$$J_x = FT^{-1}\{j_x\} \quad (10.96)$$

$$= FT^{-1} \left\{ i \frac{2k_y}{\mu_0 kd} e^{kz} b_z - i \frac{k_x f}{k^2} \right\}, \quad (10.97)$$

and

$$J_y = FT^{-1} \left\{ j_y \right\} \quad (10.98)$$

$$= FT^{-1} \left\{ -i \frac{2k_x}{\mu_0 k d} e^{kz} b_z - i \frac{k_y f}{k^2} \right\}. \quad (10.99)$$

These equations break down for $k = 0$; one cannot recover uniform components of current distributions. This corresponds to an infinite sheet of uniform current producing no perpendicular magnetic field, *i.e.*, with the two edges infinitely far away and the magnetic field being parallel to the sheet.

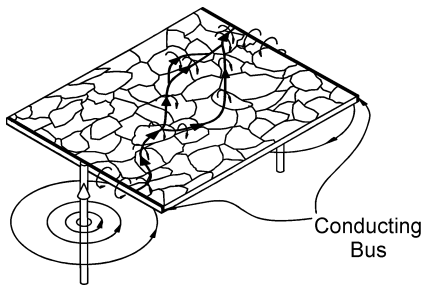
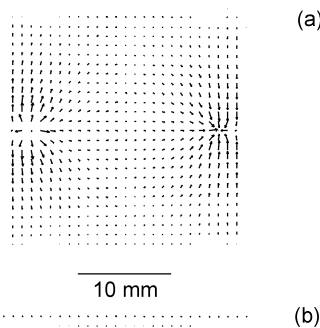


Fig. 10.18 Current injection into a granular substrate. (Adapted from Ref. [9], with permission.)



(a)

(b)

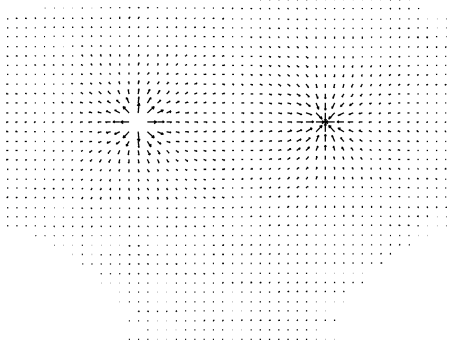


Fig. 10.19 The results of using an unconstrained filtering technique to solve a bounded current source: (a) the original current distribution; (b) the reconstruction using inverse spatial filtering. (Adapted from Ref. [79], with permission.)

Figure 10.19 shows a comparison of the original current distribution and the distribution reconstructed by this approach. Note that the source and the image are in good agreement in the immediate vicinity of the current-injection electrodes. As we shall see later, the inability of the spatial filtering technique to constrain currents to flow within known boundaries limits this technique to situations where the magnetometer is very close to the current distribution.

Planar Current-Injection Tomography

We can extend this approach and use magnetic imaging and the Fourier transform/spatial filtering approach to determine the conductivity distribution within a planar conducting object [60]. We start with Ohm's law, which gives us the current density $\vec{J}(\vec{r})$ in an inhomogeneous, isotropic conductor with conductivity distribution $\sigma(\vec{r})$,

$$\vec{J}(\vec{r}) = \sigma(\vec{r}) \vec{E}(\vec{r}). \quad (10.100)$$

As we saw in (10.15), the curl of the current density can be thought of as the “source” of the magnetic field. In inhomogeneous conductors, $\nabla \times \vec{J}$ has two contributions: one from spatial variations, $\nabla \sigma$, and another from EMFs, $\nabla \times \vec{E}$,

$$\nabla \times \vec{J} = \nabla \sigma \times \vec{E} + \sigma \nabla \times \vec{E}. \quad (10.101)$$

A boundary between conducting and insulating regions is simply a sudden spatial variation in σ , at which the discontinuity in the tangential current produces a magnetic field. In the quasistatic limit with no sources of EMF within the conductor, *i.e.*, with currents injected and removed only on the surface of the object, the curl of \vec{E} must be zero, since it is derivable from a scalar potential. In this case, $\nabla \times \vec{J}$ becomes

$$\nabla \times \vec{J}(\vec{r}) = \frac{\nabla \sigma(\vec{r})}{\sigma} (\vec{r}) \times \vec{J}(\vec{r}), \quad (10.102)$$

which can be written as

$$\nabla \times \vec{J}(\vec{r}) = (\nabla \ln \sigma(\vec{r})) \times \vec{J}(\vec{r}). \quad (10.103)$$

As pointed out by Staton [60], the strategy of conductivity imaging via current-injection tomography is to reconstruct $\sigma(\vec{r})$ from a known $\vec{J}(\vec{r})$ using (10.103). However, it is not possible to reconstruct the conductivity distribution using a single distribution of injected current. One problem with a single configuration of injected current is that it is possible to have a nonzero $\nabla \ln \sigma$ and nonzero \vec{J} , but have zero $\nabla \times \vec{J}$. This occurs if both $\nabla \ln \sigma$ and \vec{J} are parallel, for example in a rectangular conducting bar in which the conductivity varies only in one direction, but the current flows uniformly in the bar along that direction. In this case, the currents do not indicate the presence of gradients in the conductivity distribution, and the current distribution could be the result of uniform current injection into

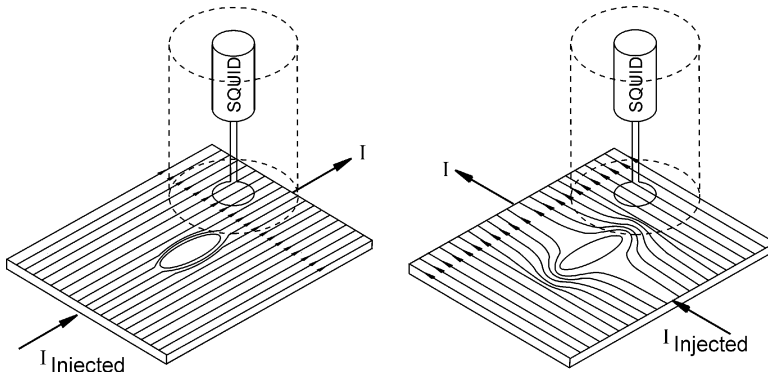


Fig. 10.20 Current-injection tomography in a thin, conducting plate.
(Adapted from Ref. [60], with permission.)

an isotropic homogeneous bar. It is thus important that tomography be employed by injecting current into the sample from multiple directions, with magnetic imaging of the current distribution for each configuration of current injection. At the very least, current should be injected in orthogonal directions: two directions for a thin conducting plate and three directions for a rectangular conducting slab, as illustrated in Figure 10.20. When current is injected (left) along the major axis of an elliptical flaw (x direction), the current is perturbed less than when injected (right) orthogonally along the minor axis (y direction). The combined magnetic imaging of both current distributions contains information on the length and width of the flaw.

As should be familiar by now, if the current density \vec{J} were known everywhere in a three-dimensional conducting sample, then it would in principle be possible to solve (10.102). However, there is no unique solution to the general three-dimensional magnetic inverse problem for currents, and hence determination of a three-dimensional conductivity distribution from magnetic measurements alone will, in general, be impossible. However, the two-dimensional current inverse problem does have a unique solution [56], and we can use current tomography with magnetic measurements of $J(\vec{r})$ to determine the conductivity distribution in a planar sample.

To illustrate this approach, let us examine the minimal case of using only two orthogonal distributions of injected current for a planar sample. We can use magnetometer and spatial filtering inverse techniques described previously to obtain images of the two resulting current distributions

$$\vec{J}_1(x, y) = J_{1x}(x, y)\hat{x} + J_{1y}(x, y)\hat{y}, \quad (10.104)$$

$$\vec{J}_2(x, y) = J_{2x}(x, y)\hat{x} + J_{2y}(x, y)\hat{y}. \quad (10.105)$$

For our two-dimensional case, the normal component of the curl of each current-density distribution obeys (10.103), which becomes

$$\begin{aligned}\nabla \times \vec{J}_1(x, y) \cdot \hat{n} &= J_{1y} \left(\frac{\partial \ln \sigma(x, y)}{\partial x} \right) - J_{1x} \left(\frac{\partial \ln \sigma(x, y)}{\partial y} \right) \\ &\equiv c_1(x, y),\end{aligned}\quad (10.106)$$

$$\begin{aligned}\nabla \times \vec{J}_2(x, y) \cdot \hat{n} &= J_{2y} \left(\frac{\partial \ln \sigma(x, y)}{\partial x} \right) - J_{2x} \left(\frac{\partial \ln \sigma(x, y)}{\partial y} \right) \\ &\equiv c_2(x, y).\end{aligned}\quad (10.107)$$

The unknown quantities in this pair of equations are $\partial \ln \sigma(x, y)/\partial x$ and $\partial \ln \sigma(x, y)/\partial y$. In tomography, with a large number of directions of injected current, there will be a highly overdetermined set of equations for these two unknown distributions that would be solved numerically. In our simple two-current example, we can reduce the pair of equations into a more tractable form analytically

$$\frac{\partial \ln \sigma(x, y)}{\partial x} = (J_{x1}c_2 - J_{x2}c_1) / (J_{x1}J_{y2} - J_{x2}J_{y1}) \equiv f_x(x, y), \quad (10.108)$$

and

$$\frac{\partial \ln \sigma(x, y)}{\partial y} = (J_{y1}c_2 - J_{y2}c_1) / (J_{x1}J_{y2} - J_{x2}J_{y1}) \equiv f_y(x, y). \quad (10.109)$$

To obtain the conductivity distribution, we simply numerically integrate each of these equations

$$\ln \sigma(x, y) = \ln \sigma(x_0, y_0) + \int_{x_0}^x f_x(x', y) dx' + \int_{y_0}^y f_y(x_0, y') dy'. \quad (10.110)$$

The conductivity distribution is thus

$$\sigma(x, y) = \sigma(x_0, y_0) e^{\left(\int_{x_0}^x f_x(x', y) dx' + \int_{y_0}^y f_y(x_0, y') dy' \right)}. \quad (10.111)$$

Note that in the integration, we include explicitly as a constant of integration the conductivity $\sigma(x_0, y_0)$ at the single point where we began the integration. If that conductivity is not known, we can determine only normalized conductivity $\sigma(x, y)/\sigma(x_0, y_0)$. Alternatively, if we measure the resistance between the current injection electrodes, we should be able to obtain a value for $\sigma(x_0, y_0)$. Figure 10.21

shows the results of a numerical simulation of this process for an elliptically shaped, Gaussian flaw in a copper plate, given by

$$\sigma(x, y) = \sigma_0 \left(1 - 0.8 e^{-\frac{1}{2} \left[\left(\frac{x}{a} \right)^2 + \left(\frac{y}{b} \right)^2 \right]} \right) \quad (10.112)$$

where $\sigma_0 = 5.8 \times 10^7$ S/m, $a = 5$ mm, and $b = 2$ mm. The thin, conducting plate is of length $l = 0.1$ m, width $w = 0.1$ m, and thickness 100 μ m. For the simulation, a total of 10 mA of current was injected uniformly into the plate along the major axis of the elliptical flaw (x -direction), and also in a separate current injection along the minor axis of the elliptical flaw (y -direction) as illustrated in Figure 10.21. The forward problem consisted of calculating the electrical potentials, current densities, curl of the current densities, and magnetic fields. The inverse problem consisted of reconstructing the conductivity distribution from the magnetic fields. As discussed in more detail by Staton [60] the accuracy of this method is determined by the ability to image current densities and curl distributions from the magnetic fields. The error in the inverse procedure depends on a variety of factors: the distance between the current distribution and detector, the signal-to-noise ratio of the measurement, the distance between magnetic measurements, and the spatial extent of the measurement. This calculation demonstrates the fea-

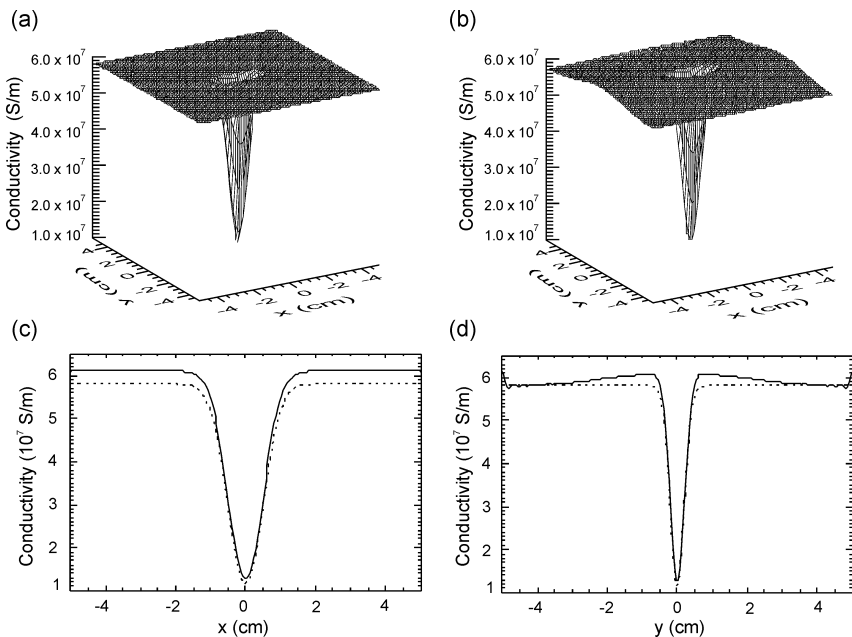


Fig. 10.21 A comparison of (a) original conductivity distribution and (b) magnetically reconstructed solution using current-injection tomography, and cross-section comparison of original conductivity distribution (dotted line)

and reconstructed solution (solid line) along the (c) major axis and (d) minor axis of the elliptically shaped, Gaussian flaw. (Adapted from Ref. [60], with permission.)

sibility of the technique; further studies will require adding noise and varying the sampling parameters, and should also address the possible advantages of applying current to the sample from multiple directions (more than the minimally required number of two or three).

The Hosaka-Cohen Transformation

A “current pattern” in the xy -plane can be obtained from B_z by the Hosaka-Cohen (HC) transformation [80]

$$HC \equiv \frac{\partial B_z}{\partial y} \hat{x} - \frac{\partial B_z}{\partial x} \hat{y}, \quad (10.113)$$

where the field is measured a distance z above the currents. The components of HC resemble the currents, *i.e.*,

$$J_x \propto \frac{\partial B_z}{\partial y} \equiv HC_x \quad (10.114)$$

$$J_y \propto \frac{\partial B_z}{\partial x} \equiv HC_y. \quad (10.115)$$

The HC transformation is believed valid for two-dimensional current distributions, but has been applied to data from three-dimensional sources [80, 81]. The uncertainty lies with the derivation of the HC transformation, which is based upon the curl of \vec{B} . Ampère’s law states that

$$\begin{aligned} \vec{J} &= \frac{1}{\mu_0} \nabla \times \vec{B} \\ &= \frac{1}{\mu_0} \left\{ \left(\frac{\partial B_z}{\partial y} - \frac{\partial B_y}{\partial z} \right) \hat{x} - \left(\frac{\partial B_z}{\partial x} - \frac{\partial B_x}{\partial z} \right) \hat{y} + \left(\frac{\partial B_y}{\partial x} - \frac{\partial B_x}{\partial y} \right) \hat{z} \right\}. \end{aligned} \quad (10.116)$$

Within a current distribution of infinite extent with no z -dependence,

$$\frac{\partial B_y}{\partial z} \simeq \frac{\partial B_x}{\partial z} \simeq 0. \quad (10.117)$$

If we add the tighter constraint that $J_z = 0$ everywhere, then

$$\vec{J} \simeq \frac{1}{\mu_0} \left\{ \frac{\partial B_z}{\partial y} \hat{x} - \frac{\partial B_z}{\partial x} \hat{y} \right\}. \quad (10.118)$$

Within a constant, this is the same as (10.113). However, this equation, as derived, applies only within the conductor, since outside a conductor both \vec{J} and $\nabla \times \vec{B}$ are everywhere zero in the quasistatic limit. In practice, one cannot readily measure \vec{B} inside a conductor. However, the symmetry for a two-dimensional planar current distribution is the same as for a three-dimensional current distribution with no J_z

and no z -dependence of either J_x or J_y . The validity of the HC transformation is unclear when it is possible only to measure \vec{B} at height z above the xy -plane.

We can shed some light on the meaning of the HC transformation by using Fourier spatial filtering [78]. In the spatial-frequency domain, we had the exact inverse solution for two-dimensional current distributions

$$j_x(k_x, k_y) = i \frac{2}{\mu_0 d} \frac{k_y}{\sqrt{k_x^2 + k_y^2}} e^{z\sqrt{k_x^2 + k_y^2}} b_z(k_x, k_y) \quad (10.119)$$

$$j_y(k_x, k_y) = -i \frac{2}{\mu_0 d} \frac{k_x}{\sqrt{k_x^2 + k_y^2}} e^{z\sqrt{k_x^2 + k_y^2}} b_z(k_x, k_y). \quad (10.120)$$

This can be expanded in a Taylor series

$$j_x(k_x, k_y) = i \frac{2}{\mu_0 d} \frac{k_y b_z(k_x, k_y)}{k} \left(1 + kz + \frac{1}{2!} k^2 z^2 + \dots \right), \quad (10.121)$$

where

$$k = \sqrt{k_x^2 + k_y^2}. \quad (10.122)$$

If k and z are sufficiently small, then

$$j_x(k_x, k_y) \approx i \frac{2}{\mu_0 d} k_y b_z(k_x, k_y) f, \quad (10.123)$$

where

$$f = 1/k + z + kz^2/2. \quad (10.124)$$

Similarly,

$$j_y(k_x, k_y) \approx -i \left(\frac{2}{\mu_0 d} \right) k_x b_z(k_x, k_y) f. \quad (10.125)$$

For comparison, the two-dimensional Fourier transform of HC is

$$j_x(k_x, k_y) \propto ik_y b_z(k_x, k_y) \quad (10.126)$$

$$j_y(k_x, k_y) \propto -ik_x b_z(k_x, k_y). \quad (10.127)$$

By fitting a straight line to the exact expression, we obtain [78]

$$j_x \simeq i \frac{2\pi z}{\mu_0 d} k_y b_z(k_x, k_y) \quad (10.128)$$

$$j_y \simeq -i \frac{2\pi z}{\mu_0 d} k_x b_z(k_x, k_y). \quad (10.129)$$

By taking the inverse Fourier transform, we can find the relation between the current density and the field gradients

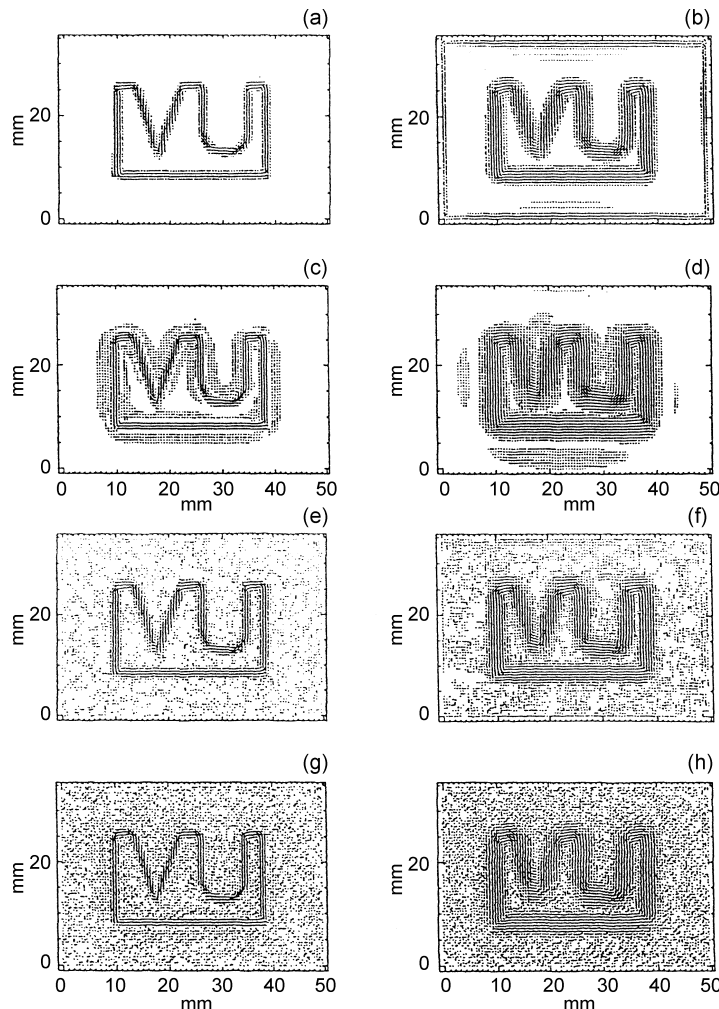


Fig. 10.22 A comparison of the exact and HC reconstructions for a “VU” current source similar to that in Fig. 10.11. Left: $z = 1.5$ mm; right: $z = 3.0$ mm. (a,b,c,d) No noise; (e,f,g,h) SNR = 10. (a,b,e,f) Exact reconstruction; (c,d,g,h) HC reconstruction. (Adapted from Ref. [78], with permission.)

$$J_x \simeq \frac{2\pi z}{\mu_0 d} \frac{\partial B_z}{\partial y} \quad (10.130)$$

$$J_y \simeq -\frac{2\pi z}{\mu_0 d} \frac{\partial B_z}{\partial x}, \quad (10.131)$$

and we see that the HC transformation is the first-order approximation to the exact inverse result. The approximation is best for small z and k . Figure 10.22 compares the results of the HC transformation and the exact result for data similar to those in Figure 10.12.

Alternating Projections to Enhance High-Frequency Information

A variety of general-purpose techniques common to image processing can be used to enhance the magnetic images obtained with scanning magnetometers. Examples include high- and low-pass spatial filtering [82], and background subtraction using polynomial fits. Alternating projections is a useful iterative technique to apply either constraints or *a priori* knowledge about the source [83]. As an example of this approach, suppose that we have an unknown current distribution, $\vec{j}^u(x, y)$, that corresponds to a wire of unknown shape. This current produces a magnetic field $B_z(x, y)$ by a known Green's function $G(x - x', y - y')$. In the spatial frequency domain, we have that

$$b_z(k_x, k_y) = FT\{B_z(x, y)\} \quad (10.132)$$

$$g(k_x, k_y) = FT\{G(x - x', y - y')\}. \quad (10.133)$$

The inverse problem is simply

$$j_x(k_x, k_y) = \frac{b_z(k_x, k_y)}{g(k_x, k_y)}. \quad (10.134)$$

However, as we discussed before, this results in numerical instabilities when $g(k_x, k_y)$ is small at large k . We avoid this problem by low-pass filtering the inverse process to obtain an approximate current image $\hat{j}_x(k_x, k_y)$, where

$$\hat{j}_x(k_x, k_y) = LPF \left\{ \frac{b_z(k_x, k_y)}{g(k_x, k_y)} \right\} \quad (10.135)$$

with the low-pass filter function $LPF = 0$ when $k_{LPF} < \sqrt{k_x^2 + k_y^2} < \infty$, and $LPF = 1$ otherwise. However, a spatial low-pass filter blurs the image and reduces the spatial resolution. The challenge is to return as much of the high-frequency information as possible while avoiding the instabilities that plague the Fourier inverse

approach. Because we know that the current is contained in a wire, we can sharpen the image by assuming that signals below a certain amplitude in the spatial domain are noise and eliminate them by a thresholding operation. We then use the added high-frequency information in the spatial-frequency domain to replace the high-frequency information that was lost in the low-pass filtering operation. Iteration between the spatial and spatial-frequency domains is why this approach is termed alternating projections.

We prepare for the iteration by assuming that our zeroth current distribution is the one that was obtained by the low-pass filtered Fourier inverse

$$j_x^0(k_x, k_y) = \hat{j}_x(k_x, k_y). \quad (10.136)$$

We select a threshold T and let $n = 1$. As step 1, we compute

$$J_x^n(x, y) = FT^{-1} \{ j_x^{n-1}(k_x, k_y) \}. \quad (10.137)$$

Step 2 is to form the thresholded image $\tilde{J}_x^n(x, y)$ by setting to zero all the values of $J_x^n(x, y)$ whose amplitudes are less than T , which sharpens the current distribution and adds high-frequency information. Step 3 converts this image into the spatial-frequency domain,

$$j_x^n(k_x, k_y) = FT \{ \tilde{J}_x^n(x, y) \}. \quad (10.138)$$

The difficulty is that the low-frequency information in this image is not as accurate as that in the original $\hat{j}_x(k_x, k_y)$. We correct for this with step 4: we substitute the more accurate $\hat{j}_x(k_x, k_y)$ for the less accurate $j_x^n(k_x, k_y)$ in the region $0 < \sqrt{k_x^2 + k_y^2} < k_{LPF}$. We keep the sharpened $\hat{j}_x^n(k_x, k_y)$ in the region $\sqrt{k_x^2 + k_y^2} > k_{LPF}$. Finally, we decide whether or not to terminate the iteration, and if not, we let $n \leftarrow n + 1$ and return to step 1. The results of this process are shown in Figure 10.23. This is but one example of alternating projections. The technique can be further improved by adding a current-continuity constraint as a third projection [84]. Other criteria can be used to sharpen or modify the image, such as the selective enhancement of line-like structures in the image [83]. As with other sharpening algorithms, it is important to realize that the alternating projection approach does not reconstruct the original current distribution in a quantitative manner as do the other techniques we have reviewed, but instead processes the observed field pattern in a manner that can make it resemble more closely the original currents, with no guarantee of quantitative accuracy.

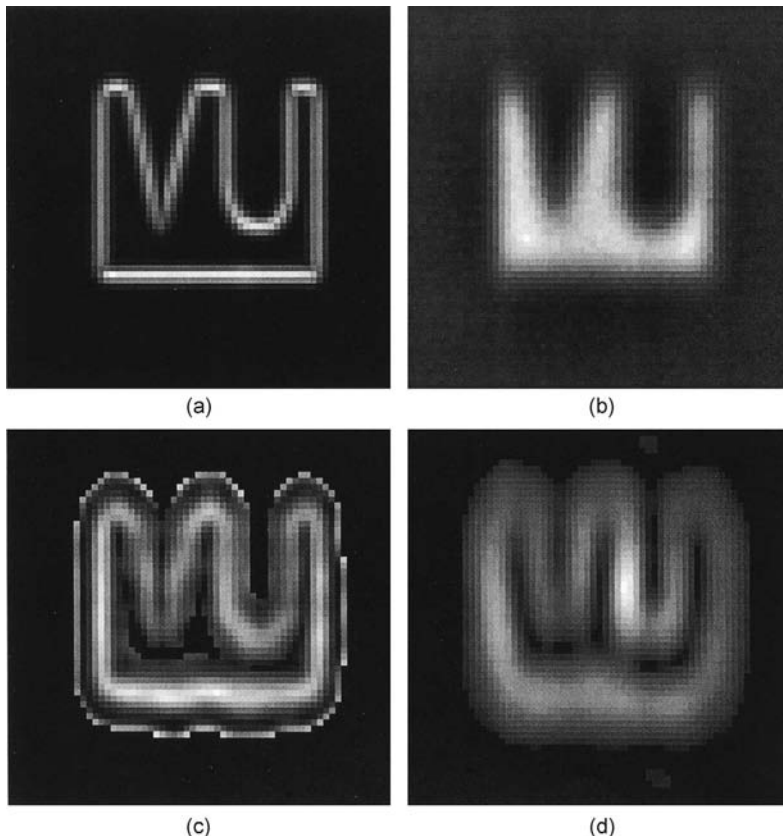


Fig. 10.23 Alternating projection enhancement of magnetic field maps: (a) the original current image; (b) the magnetic field at 1.5 mm with noise; (c) the recovered image after the first iteration; (d) after ten iterations. (Adapted from Ref. [84], with permission.)

Flux-Field Deconvolution

When inverting experimental data, often one cannot neglect the effects of the field integration over SQUID pickup and compensation coils. Since SQUID sensors detect magnetic flux and not magnetic field directly, the approximation $\Phi = \vec{B} \cdot \vec{A}$ is only valid if the field is uniform or the sources of the magnetic field are located far away from the coils, so that \vec{B} can be considered constant within the integration area. In many situations, especially with planar gradiometers, this is a coarse approximation and it can lead to substantial error in the solution of the inverse problem. In order to avoid this issue, we can try to incorporate sensor modeling into the formulation of the inverse problem. Unfortunately, for some common coil layouts this results in cumbersome calculations that frequently do not have a closed-form solution.

In cases where the magnetic field mapping area is not very restricted, it is possible to use spatial filtering tools to formulate the flux integral as a convolution and undo the integration by means of a deconvolution. By extending the approach used to analyze and design apodized coils, we can obtain models associated with different SQUID magnetometer and gradiometer designs. In addition to allowing for the recovery of magnetic field maps from magnetic flux measurements, such models can be a valuable aid in tailoring the geometry and arrangement of coils so as to optimize the SQUID performance for particular applications. Furthermore, spatial filtering models make it possible to effectively compare a multitude of magnetometer and gradiometer designs independent of any particular magnetic field source distribution, by using a common mathematical framework [85–89].

To demonstrate the relevance of modeling field integration in SQUID sensors, compare Figures 10.24(a) and (b). Figure 10.24(a) shows the simulated vertical component of the magnetic field produced by a single current dipole placed on the xy plane, at a 5-mm liftoff. Figure 10.24(b) shows the map that is obtained if a first-order planar gradiometer with square coils is used to scan the field. It is clear that both graphs bear little resemblance to one another and one cannot expect to obtain consistent solutions to inverse problems by disregarding such transformations to the magnetic field.

We begin by analyzing planar gradiometer designs and then extend the formulation to include axial gradiometers. We will not discuss magnetometer designs in this subsection, as they can be considered a special case of a planar gradiometer, and also to avoid repeating information presented in previous sections. However, we highlight that the formalism presented herein can be directly applied to magnetometers, since gradiometers are intrinsically more complex. Part of this section draws extensively from Ref. [87].

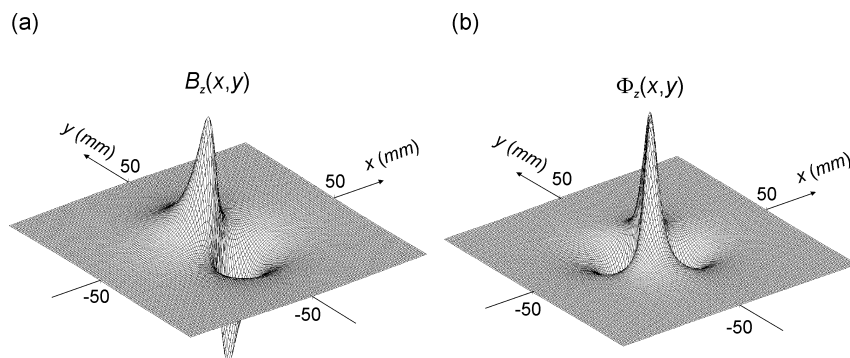


Fig. 10.24 Differences between the magnetic field map associated with a current dipole and the corresponding magnetic flux map obtained with a planar SQUID gradiometer: (a) vertical (z) component of the magnetic field generated by a current dipole located on

the xy -plane, at a 5-mm liftoff; (b) net magnetic flux through a first-order planar gradiometer with 5-mm square coils and 5-mm baseline in the x -direction. (Adapted from Ref. [87], with permission.)

Planar Gradiometers. The key idea behind modeling gradiometers through the use of frequency methods is the manipulation of the magnetic flux definition, so as to express the net flux through the gradiometer as the two-dimensional convolution of the magnetic field with a stepwise function F_G (the planar gradiometer is assumed to be parallel to the xy -plane)

$$\begin{aligned}\Phi(x, y, z) &= \iint_S \vec{B} \cdot \hat{n} \, da = \int_{-\infty}^{+\infty} \int_{-\infty}^{+\infty} B_z(x', y', z) F_G(x - x', y - y') \, dx' dy' \\ &= F_G(x, y)^* B_z(x, y, z).\end{aligned}\quad (10.139)$$

This stepwise function accounts for the region of integration S , which in turn is related to the geometrical characteristics of the gradiometer. The function F_G is defined for an arbitrary point on the gradiometer plane as the number of turns of the coils enclosing the point, taking into account the winding direction.

The deconvolution operation aims to invert (10.139), thereby obtaining the magnetic field B_z associated with a known net flux through a specific gradiometer. Taking the two-dimensional Fourier transform on (10.139) and using the convolution property, we obtain

$$\varphi(k_x, k_y, z) = f_G(k_x, k_y) b_z(k_x, k_y, z). \quad (10.140)$$

Hence, gradiometers can be characterized in the frequency domain by a function f_G known as the spatial frequency response. In order to obtain the recovered field \tilde{B}_z , we first divide the Fourier transform of the flux by the frequency response, and then take the inverse Fourier transform:

$$\tilde{B}_z(x, y, z) = FT^{-1} \left[\frac{\varphi(k_x, k_y, z)}{f_G(k_x, k_y)} \right] = FT^{-1} \left[f_G^1(k_x, k_y) \varphi(k_x, k_y, z) \right], \quad (10.141)$$

where $f_G^1 = 1/f_G$ is the inverse spatial filter.

As an example, consider a first-order planar gradiometer with baseline d in the x -direction, comprised of two identical N -turn square coils with sides of length L wound in opposite directions. The stepwise function, also known as the turns function, is given by

$$F_G(x, y) = \begin{cases} N, & |x - d/2| \leq L/2 \text{ and } |y| \leq L/2 \\ -N, & |x + d/2| \leq L/2 \text{ and } |y| \leq L/2 \\ 0, & \text{otherwise,} \end{cases} \quad (10.142)$$

and the gradiometer frequency response is

$$f_G(k_x, k_y) = -2iL^2 N \sin(k_x d/2) \operatorname{sinc}\left(\frac{k_x L}{2\pi}\right) \operatorname{sinc}\left(\frac{k_y L}{2\pi}\right), \quad (10.143)$$

where $\text{sinc}(u) = \sin(\pi u)/\pi u$. Figure 10.25(a) shows the graph of the magnitude of the frequency response for $L=5$ mm, $d=5$ mm, and $N=1$.

Several characteristics can be observed from both the graph and (10.143). First, this gradiometer configuration lacks circular symmetry, which means that the gradiometer effects are not the same along different directions. Therefore, direct interpretation of maps can be difficult if the source arrangement is not known *a priori*: if the sample is scanned with the sensor oriented in different ways, different maps will be obtained. Moreover, (10.143) is separable, which means that the effects in the x and y directions are independent.

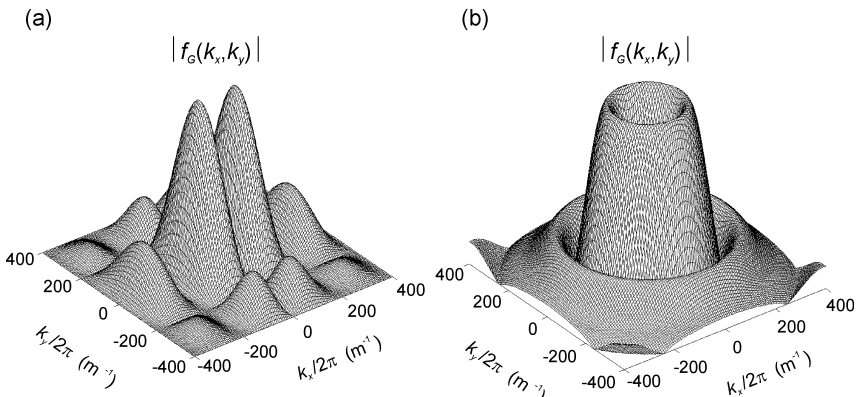


Fig. 10.25 Magnitude of the normalized gradiometer spatial frequency response: (a) first-order planar gradiometer comprised of two 5-mm single-turn square coils and 5-mm baseline in the x direction; (b) first-order

concentric planar gradiometer made up of a four-turn 2.5-mm radius circular coil and a single-turn 5-mm radius circular coil.
(Adapted from Ref. [87], with permission.)

Second, there exists a line of zeros $k_x = 0$ through the origin of the spatial frequency plane which is associated with the sine term in (10.143). As discussed in previous sections, a zero in the frequency domain corresponds to permanent loss of information. Because gradiometers are intended to selectively reject some information, such as uniform fields, inevitably zeros will appear in the frequency response. A rejection of uniform fields is equivalent to a zero at the origin of the frequency plane $k_x = k_y = 0$, and therefore the mean value of the field cannot be recovered by the deconvolution procedure. However, the line of zeros $k_x = 0$ intrinsic to this configuration (note that changing L or d will produce no change on that line) corresponds to a rejection of any field that is constant in the x direction but not necessarily in the y direction. Although this can be useful in some specific applications [86], it leads to severe distortions in the recovered field. Figure 10.26(a) shows the magnetic field recovered from the flux depicted in Figure 10.24(b).

Third, the baseline introduces lines of zeros $k_x = \pm 2\pi(n-1)/d$, for $n = 1, 2, \dots$, whereas the coil introduces lines of zeros $k_x = \pm 2\pi m/L$ and $k_y = \pm 2\pi m/L$, for $m = 1, 2, \dots$. If $L=d$, as in our example design, then the lines of zeros associated

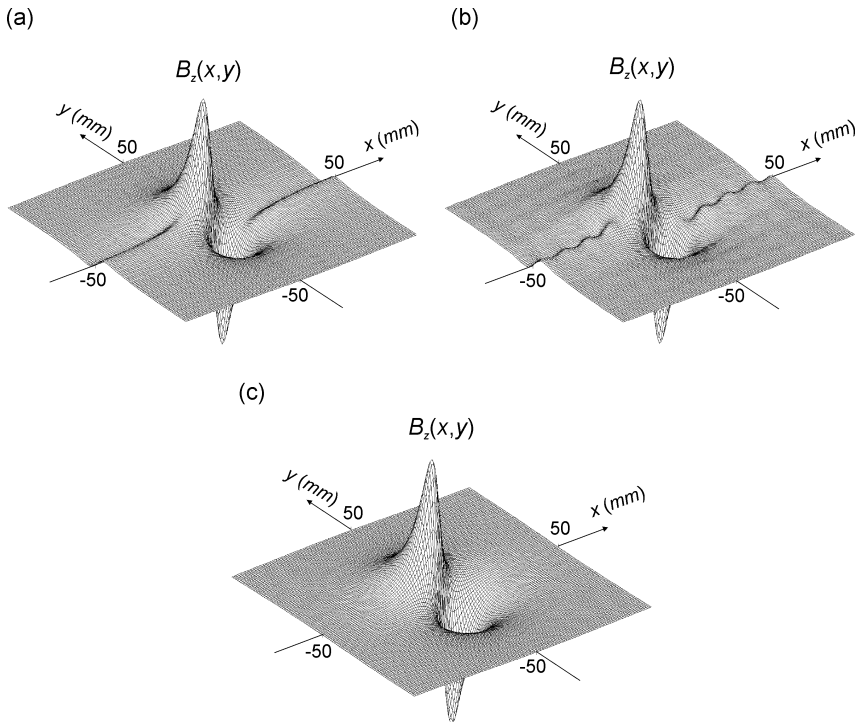


Fig. 10.26 Magnetic field maps recovered by the flux-field deconvolution for different gradiometer designs: (a) first-order gradiometer comprised of 5-mm single-turn square coils and 5-mm baseline in the x direction; (b) same as (a) except for 10-mm coils and

10-mm baseline; (c) first-order concentric planar gradiometer made up of a four-turn 2.5-mm radius circular coil and a single-turn 5-mm radius circular coil. (Adapted from Ref. [87], with permission.)

with the baseline (for $n \geq 2$) coincide with the lines of zeros in the same direction which are related to the coil geometry. If the source distribution generates a magnetic field with information at higher spatial frequencies, reaching those other lines of zeros, then additional information is lost and more distortion is introduced in the recovered field. Figure 10.26(b) shows the recovered field obtained from the same flux map, but with a gradiometer with $L = d = 10$ mm. (Note that increasing L or d results in moving the lines of zeros closer to the origin.)

It is worthwhile observing that other configurations of planar gradiometers have better spatial frequency characteristics and do not suffer from some of the pathologies described above. For instance, Figure 10.26(c) shows the recovered field obtained using a concentric planar design with circular coils (four-turn 5-mm radius coil surrounded by a single-turn 10-mm coil). It can be seen that an excellent recovery of the magnetic field could be obtained in this case. For this configuration, we have

$$F_G(x, y) = \begin{cases} N_1 - N_2, & \sqrt{x^2 + y^2} \leq a_1 \\ -N_2, & a_1 < \sqrt{x^2 + y^2} \leq a_2 \\ 0, & \text{otherwise,} \end{cases} \quad (10.144)$$

and

$$f_G(k_x, k_y) = \frac{2\pi N_1 a_1}{\sqrt{k_x^2 + k_y^2}} \left[J_1(a_1 \sqrt{k_x^2 + k_y^2}) - J_1(a \cdot a_1 \sqrt{k_x^2 + k_y^2}) / a \right], \quad (10.145)$$

where the condition $N_1 / N_2 = (a_2 / a_1)^2$ must be satisfied to reject uniform fields, $J_1(\cdot)$ is the Bessel function of first kind and first order, and $a = a_2 / a_1$. Observe that the frequency response is circularly symmetrical, as it depends on $\sqrt{k_x^2 + k_y^2}$ only, as shown in Figure 10.25(b). There is a zero at the origin, with the subsequent zeros appearing at circles around the origin of the spatial frequency plane.

Differently from the inverse problem, we always have to handle zeros in the division operation in (10.141), because gradiometers have at least one zero at the origin of the frequency plane. If noise is present in the flux map at moderate to high levels, improper handling of the zeros in the gradiometer frequency response can lead to noisy recovered fields. To address this issue by reducing the sensitivity of the inverse filter to noise and assigning to the inverse filter frequency response a defined value at the zeros of the gradiometer frequency response, we use a pseudoinverse filter defined as follows:

$$f_G^I(k_x, k_y) = \begin{cases} \frac{1}{f_G(k_x, k_y)}, & \text{if } |f_G(k_x, k_y)| > \gamma \\ \frac{1}{\gamma} \frac{|f_G(k_x, k_y)|}{f_G(k_x, k_y)}, & \text{otherwise,} \end{cases} \quad (10.146)$$

where γ is an adjustable threshold value. Equation (10.146) shows that the pseudoinverse filter limits $|1/f_G|$ to a maximum value of $1/\gamma$, while preserving the phase information. If the threshold is too small then the recovered field can be noisy, whereas making it too big can lead to loss of information on large regions of the frequency plane around the zeros.

However, even with the pseudoinverse approach, the recovered field may still be noisy due to the amplification of the noise component by a factor of $1/\gamma$ near the lines or circles of zeros. In order to tame noise amplification, we only calculate the deconvolution for spatial frequencies in the first lobe of the frequency response, that is, in the region of the frequency plane delimited by the first line or circle of zeros. As discussed before, gradiometers and magnetometers should ideally be designed so that the relevant information in the spectrum of the magnetic field does not extend past lines or circles of zeros. This way, we ensure that only the noise component is discarded.

Figure 10.27(a) shows the recovered field obtained by deconvolving the flux map shown in Figure 10.24(b), with white noise added to the flux so as to provide a

signal-to-noise ratio of 30 dB. The solution was obtained by calculating the deconvolution over the whole frequency plane, leading to degradation by noise amplification. By restricting the computation of the deconvolution to the first lobe of the gradiometer frequency response, we get the result shown in Figure 10.27(b). Similar recovery quality can be achieved for other sources, provided the spectrum of interest lies within the first lobe. Figure 10.27(c) shows the magnetic field produced by a magnetic dipole pointing in the z -direction, at a 5-mm liftoff, and Figure 10.27(d) shows the recovered field.

Note that restricting the calculation of the convolution to a region in the frequency plane is equivalent to applying a filter $h(k_x, k_y)$:

$$\tilde{\mathbf{b}}_z(k_x, k_y, z) = \left[f_G^1(k_x, k_y) \varphi(k_x, k_y, z) \right] h(k_x, k_y) = \tilde{\mathbf{b}}_z(k_x, k_y, z) h(k_x, k_y). \quad (10.147)$$

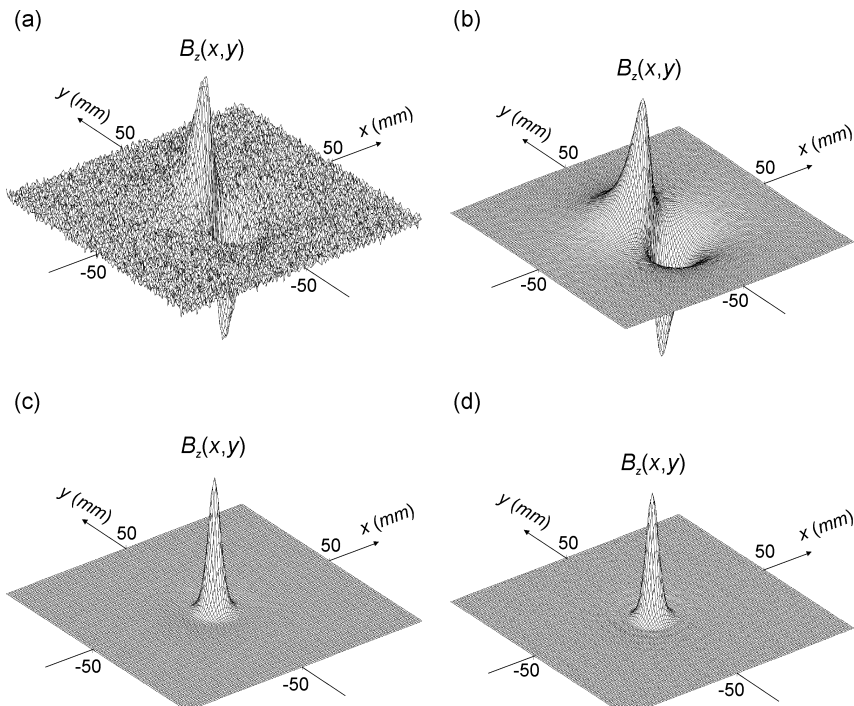


Fig. 10.27 Magnetic field recovered from flux maps with a 30-dB signal-to-noise ratio using the concentric planar design described before: (a) magnetic field map obtained by calculating the deconvolution over the whole spatial frequency plane; (b) magnetic field map obtained by restricting the calculation of the deconvolution to the first lobe of the

gradiometer spatial frequency response; (c) original magnetic field map associated with a magnetic dipole pointing in the z -direction, at a 5-mm liftoff; (d) recovered magnetic field map using the same concentric gradiometer as before, and restricting the deconvolution to the first lobe of the frequency response.
(Adapted from Ref. [87], with permission.)

In the simplest case, h is a two-dimensional rectangular window: $h(k_x, k_y) = 1$ within the first lobe and $h(k_x, k_y) = 0$ everywhere else. In the space domain, this is equivalent to convolving the recovered field $\tilde{B}_z(x, y, z)$ with the inverse Fourier transform of $h(k_x, k_y)$, yielding $\tilde{\tilde{B}}_z(x, y, z)$. Depending on how narrow this window is, perceptible ringing can be introduced in $\tilde{\tilde{B}}_z(x, y, z)$, as a consequence of convolving with sinc or jinc⁸⁾ functions associated with the impulse response of ideal low-pass filters. Choosing other window types with smaller sidelobes or two-dimensional nonrecursive filters may considerably improve the quality of the recovered field.

Axial Gradiometers. In order to extend the modeling to include axial gradiometers, we first realize that the baseline effect is now decoupled from the field integration. Therefore, it is necessary to increase the dimension of the model. Let us suppose a generic axial gradiometer made up of N identically shaped coils with negligible thickness along the z -direction. The net flux in the gradiometer can then be expressed as

$$\Phi(x, y, z) = \int_{-\infty}^{+\infty} \int_{-\infty}^{+\infty} \int_{-\infty}^{+\infty} B_z(x', y', z') F_G(x - x', y - y', z - z') dx' dy' dz' \quad (10.148)$$

where

$$F_G(x, y, z) = \hat{F}(x, y) \sum_{j=0}^{N-1} n_j \delta(z - d_j). \quad (10.149)$$

The stepwise function $\hat{F}(x, y)$ is related to a normalized (single-turn) coil, while the number of turns and winding direction of each coil is given by n_j . Assuming the origin of the coordinate system at the center of the bottommost (pickup) coil, we have $d_0 = 0$ and each d_j is the distance of the j th coil to the pickup coil. Note that the delta function represents that the coils have no thickness, and therefore are “concentrated” at discrete values of z .

Taking the three-dimensional Fourier transform on (10.149), we obtain

$$f_G(k_x, k_y, k_z) = \hat{f}(k_x, k_y) \left(\sum_{j=0}^{N-1} n_j e^{-ik_z d_j} \right) = f_1(k_x, k_y) f_2(k_z), \quad (10.150)$$

which is the general expression for the spatial frequency response of an axial gradiometer. Even though f_G is separable, it is also a function of three variables, and therefore a graphic visualization is difficult to attain. However, if the coils are circular, (10.150) can be further simplified, since it becomes a function of just two spatial variables $k_\rho = \sqrt{k_x^2 + k_y^2}$ and k_z .

8) $\text{jinc}(x) = J_1(x)/x$.

As an example, consider an ordinary second-order axial gradiometer design, comprised of three circular coils of radius a , with N , $2N$, and N turns, separated by a baseline d . In this case, the gradiometer frequency response is given by

$$\begin{aligned} f_G(k_\rho, k_z) &= \hat{f}(k_\rho) N (1 - 2e^{-ik_z d} + e^{-i2k_z d}) \\ &= 4\pi a N \frac{J_1(ak_\rho)}{k_\rho} e^{-ik_z} [\cos(k_z d) - 1]. \end{aligned} \quad (10.151)$$

Should we wish to take the coil thickness into account, (10.150) can still be used, provided that we model a multi-turn coil as a stack of single-turn coils. In this way, j now sequentially indexes the turns of the coils and d_j stands for the distance between the (cumulative) j th turn and the first turn of the pickup coil. We observe that only f_2 is affected by this change.

It should be highlighted that (10.148) and (10.149) can also be used to model planar gradiometers, providing a way to compare the frequency responses of axial and planar configurations. By having $N=1$ and $d_0=0$ in (10.150), and having $\hat{f}(k_x, k_y)$ represent the two-dimensional planar gradiometer frequency response, we obtain the simple equation

$$f_G(k_x, k_y, k_z) = \hat{f}(k_x, k_y). \quad (10.152)$$

This equation expresses that the three-dimensional gradiometer frequency response is independent of k_z . Thus, the gradiometer behaves as an all-pass filter in the z -direction.

The deconvolution of (10.148) is much more complex than the two-dimensional case. In principle, a two-dimensional map is not enough to invert the equation and the flux must be known in a volume. This poses some serious experimental problems, as it requires mapping the field at several liftoffs and then interpolating the scans in order to generate a uniform three-dimensional grid of data. However, for deconvolution purposes an alternative approach is possible. Although it is not suitable to analyze the spatial frequency characteristics of gradiometers, it enables us to perform a two-dimensional deconvolution of a single flux map obtained with an axial gradiometer.

Let $\Phi(x, y, z_0)$ denote the net magnetic flux through the generic axial gradiometer described above, whose pickup coil is placed at a fixed height z_0 :

$$\Phi(x, y, z_0) = \sum_{j=0}^{N-1} n_j \int_{-\infty}^{\infty} \int_{-\infty}^{\infty} B_z(x', y', z_0 + d_j) \hat{F}(x - x', y - y') dx' dy'. \quad (10.153)$$

We can take the Fourier transform to obtain

$$\varphi(k_x, k_y, z_0) = \sum_{j=0}^{N-1} n_j b_z(k_x, k_y, z_0 + d_j) \hat{f}(k_x, k_y). \quad (10.154)$$

At first glance, it would appear that we cannot invert (10.154), since it relates (in the spatial frequency domain) magnetic fields at different heights $z_0 + d_j$ with a single flux at z_0 . Nevertheless, upward continuation can solve this problem, allowing us to bring all of the fields to a common single height z_0 :

$$\varphi(k_x, k_y, z_0) = \sum_{j=0}^{N-1} n_j b_z(k_x, k_y, z_0) e^{-d_j \sqrt{k_x^2 + k_y^2}} \hat{f}(k_x, k_y). \quad (10.155)$$

Therefore, (10.155) can now be inverted and solved for the field

$$\tilde{B}_z(x, y, z_0) = FT^{-1} \left\{ \frac{\varphi(k_x, k_y, z_0)}{\hat{f}(k_x, k_y) \left[\sum_{j=0}^{N-1} n_j e^{-d_j \sqrt{k_x^2 + k_y^2}} \right]} \right\}. \quad (10.156)$$

Note that, depending on the values of n_j and d_j , the term in square brackets may introduce other zeros in the deconvolution problem, in addition to the zero at the origin present in all gradiometer frequency responses. Also note that the deconvolution of the field integration and the deconvolution of the baseline can be carried out independently. In this way, depending on the parameter values associated with the experimental setup and the sensor, we can choose to undo just the predominant effect.

The model can be readily extended to incorporate axial gradiometers made up of coils of different sizes and/or shapes [68] if we assume different stepwise functions for each coil in (10.148). Similarly, (10.153) can be generalized to handle such designs.

Mapping Area. In addition to the sampling frequency and the scanning step size, discussed before, the mapping area also plays a significant influence on the quality of deconvolutions and solutions to the inverse problem. Let $\Phi(x, y, z)$ denote the magnetic flux through a gradiometer at a height z , associated with an arbitrary source distribution, and $\Phi'(x, y, z)$ denote the actual finite-length flux map. We define Φ' as

$$\Phi'(x, y, z) = \begin{cases} \Phi(x, y, z) & , \text{ for } (x, y) \text{ within the mapping area} \\ 0 & , \text{ otherwise.} \end{cases} \quad (10.157)$$

Equivalently,

$$\Phi'(x, y, z) = \Phi(x, y, z) W(x, y), \quad (10.158)$$

where $W(x, y)$ is a rectangular window representing the mapping area. Therefore, to determine the effect of using the truncated flux map Φ' instead of Φ on the recovered field $\tilde{B}_z(x, y, z)$, we replace φ by φ' in (10.141):

$$\begin{aligned}\tilde{\tilde{B}}_z(x, y, z) &= FT^{-1} \left[f_G^1(k_x, k_y) \varphi'(k_x, k_y, z) \right] \\ &= FT^{-1} \left[f_G^1(k_x, k_y) \left(\varphi(k_x, k_y, z) \otimes w(k_x, k_y) \right) \right],\end{aligned}\quad (10.159)$$

where \otimes represents a convolution performed in the frequency domain. If the mapping area is large enough to ensure that $\Phi'(x, y, z) \approx \Phi(x, y, z)$ then the convolution with the product of sinc functions, which is associated with a two-dimensional rectangular window, can be neglected. Otherwise, significant distortion may be introduced in the recovered field, as it creates edges in the flux map and oscillations in the spectrum due to the sincs. An artifice that can be used to decrease this sort of distortion consists of generating a larger map by appending flipped/mirrored versions of the original map at its edges. Additional nonrectangular windows may then be applied to the enlarged map so as to taper the edges, thereby decreasing ringing in the recovered map.

A final remark is in order regarding computer implementation of deconvolution algorithms: when using FFT algorithms, one should be careful to sample (in the frequency domain) the continuous transforms, such as (10.143) and (10.145), the same way the FFT does. Otherwise, symmetries in the spectrum are broken and the recovered field contains a large complex component, besides being inaccurate.

Other Applications of Spatial Filtering

As can be seen from the breadth of applications we have just outlined, spatial filtering is a powerful approach. There are further applications of the technique relevant to magnetic imaging, including the interpretation of gradiometers as one-dimensional spatial filters, neglecting area effects [90–93], and the use of filters to determine multipole moments from measurement of the normal component of the field above the surface of a sphere or plane [94]. As a final remark, several improvements have been made to the inverse filtering method, notably for applications in magneto-optical imaging. In particular, Jooss and co-workers [95] extended the method to handle samples with finite thickness, and corrections have been introduced for the in-plane field effect [96]. In addition, there have been detailed studies of the influence of noise on the spatial resolution of the inverse filtering method [97].

Summary of Findings for Spatial Filtering

From this overview and the more detailed analyses of spatial filtering in the literature, we find that the coil-to-source spacing limits spatial resolution, that coil diameter should equal coil-to-source spacing, that inverse spatial filtering is unique in one and two dimensions, that inward continuation separates the problems of uniqueness from those of instability, that noise limits stability, that apodizing can improve spatial resolution and sensitivity, and that windowing to filter out noise and improve stability compromises spatial resolution. The spatial filtering approach is powerful and easy to implement with commercial software packages,

but it is limited primarily by the difficulty in applying specialized boundary conditions and utilizing other *a priori* knowledge of the sources. Planar current tomography offers promise for the characterization of the conductivity distribution within a planar conducting object, but further algorithm development is required. While spatial filtering at first glance is limited to two-dimensional problems, the use of inward and outward continuation makes it a versatile approach for some three-dimensional problems. Alas, it does not provide a solution to the nonuniqueness of the three-dimensional magnetic inverse problem.

10.3.2.3 Dipole Fitting

The conceptually easiest inverse solution is to divide the two-dimensional object into N elements, and then to assign an unknown current dipole to each element, *i.e.*, $p_{x,i}$ and $p_{y,i}$, where the magnetic field from the i th elemental current dipole is given by our differential form of the law of Biot and Savart ((10.32))

$$B_{z,i}(\vec{r}) = \frac{\mu_0}{4\pi} \frac{p_{x,i}(\vec{r}_i)(y - y'_i) - p_{y,i}(\vec{r}_i)(x - x'_i)}{\left| \vec{r} - \vec{r}'_i \right|^3}. \quad (10.160)$$

A least-squares solution, singular-value decomposition,⁹⁾ or an iterative approach can be used to determine the components of each elemental dipole [100]. The solution will be most stable when the magnetometer is close to the sample. While this approach can be used in three dimensions, troublesome instabilities can occur if more than a few dipoles are used. Even in two dimensions, there are several problems with this approach. For a large number of dipoles, the approach is computationally demanding. If there are no constraints between the adjacent dipoles, current will not be conserved. While a stable solution to the equation may be obtained, interpretation of the results in such a situation may be unclear. Furthermore, the presence of noise can lead to instabilities in the solution, particularly if a very fine discretization is used, and it can become necessary to devise constraints to avoid the appearance of large opposing dipoles in adjacent elements. Minimum norm techniques, discussed in Section 10.3.5 and in Chapter 11, may improve the performance of this approach [101], but at the risk of smoothing features in the inverse solution.

9) Let $\tilde{\mathbf{A}}$ be an $m \times n$ real matrix with $m > n$. Then $\tilde{\mathbf{A}}$ can be decomposed into a product of three matrices, using singular-value decomposition (SVD), $\tilde{\mathbf{A}} = \tilde{\mathbf{U}} \tilde{\Sigma} \tilde{\mathbf{V}}^T$, where $\tilde{\mathbf{U}}$, $\tilde{\Sigma}$, and $\tilde{\mathbf{V}}$ are matrices of dimensionality $m \times n$, $n \times n$, and $n \times n$, respectively. The

matrix $\tilde{\Sigma}$ is diagonal and contains the singular values of $\tilde{\mathbf{A}}$ arranged in decreasing magnitude. Both $\tilde{\mathbf{U}}$ and $\tilde{\mathbf{V}}$ are unitary. For a detailed account of how to compute the SVD, see Refs. [98,99].

10.3.2.4 Methods for Regularization

Recently, Feldmann addressed the inversion of the Biot–Savart law with a more general method [102]. In this approach, the problem is formulated as a Fredholm integral equation of the first kind by expressing the current density in terms of a scalar field $F(x, y)$

$$\vec{J} = \nabla \times [F(x, y) \hat{z}], \quad (10.161)$$

which was proposed beforehand by Brandt [103]. Therefore, the z -component of the magnetic field is given by

$$B_z(x, y) = \int_{-\infty}^{+\infty} \int_{-\infty}^{+\infty} H(x - x', y - y') F(x', y') dx' dy'. \quad (10.162)$$

Three different kernels H were analyzed, depending on the geometry: slab, thin films of finite thickness, and sheet currents. Note that, in this method, we first obtain $F(x, y)$ and then we determine J_x and J_y by means of (10.161). Since (10.162) is an ill-posed problem, the Tikhonov–Philips regularization method is used to impose smoothness on the solution. Thus, the inversion of (10.162) is replaced by the minimization of

$$C(F, \lambda) = \left\| \int_{-\infty}^{+\infty} \int_{-\infty}^{+\infty} H(x - x', y - y') F(x', y') dx' dy' - B_z(x, y) \right\|_2^2 + \lambda \Omega[F], \quad (10.163)$$

with respect to F , where λ is the regularization parameter, the L^2 -norm of a function f of two variables is given by $\|f\|_2 = \sqrt{\int_{-\infty}^{+\infty} \int_{-\infty}^{+\infty} |f(x, y)|^2 dx dy}$, and the operator Ω , which measures the smoothness of F , is

$$\Omega[F] = \left\| \frac{\partial^2 F}{\partial x^2} + \frac{\partial^2 F}{\partial y^2} \right\|_2^2 \quad (10.164)$$

The minimizer of (10.163) is given by

$$F_\lambda(x, y) = \int_{-\infty}^{+\infty} \int_{-\infty}^{+\infty} \frac{|h(k_x, k_y)|^2}{|h(k_x, k_y)|^2 + \lambda(2\pi)^4 (k_x^2 + k_y^2)^2} \left[\frac{b_z(k_x, k_y)}{h(k_x, k_y)} \right] e^{i2\pi(k_x x + k_y y)} dk_x dk_y. \quad (10.165)$$

A (sub)optimal value for λ can be found by means of the generalized cross-validation (GCV) method, which is based on statistical considerations. Therefore, in contrast to the inverse spatial filtering method presented before, in principle it is not necessary to obtain the regularization parameter (k_c for the inverse filtering) empirically.

A thorough comparison of inversion methods for the Biot–Savart law is also presented in Ref. [102], where the regularized integral equation, the inverse spatial filtering and the conjugate gradient (CG) methods were analyzed under noiseless and noisy conditions. (The iterative CG method is presented in Ref. [104].) The overall conclusion is that for noiseless and high-precision data, the CG method produces the best inversions, since it can automatically choose an optimal value for the regularization parameter directly from the data by means of the GCV method. In contrast, the automatic choice of the parameter for the integral equation method is far from the optimal value for noiseless data. It is important to highlight, though, that given the optimal values for the regularization parameters, all three methods yield excellent results in the noiseless case.

When data with realistic signal-to-noise ratios are used, the performance of the CG method is severely compromised, due to the lack of regularizing effect. However, excellent results were obtained over a broad range of signal-to-noise ratios with both the regularized integral equation and the inverse spatial filtering methods, and only slight differences in the quality of the inversions could be perceived. Consequently, the main drawback of the inverse filtering method is the lack of a criterion to determine the spatial frequency k_c . Although there are no theoretical impediments to automatically obtaining this parameter from the data, a reliable method has yet to be developed. Recently, a criterion has been proposed by Soika and Möller [105], but further systematic analyses are required to determine its applicability to different source distributions. Therefore, depending on the problem at hand, one may opt to use the more complex method of the regularized integral equation.

10.3.2.5 Lead Field Analysis

The intrinsic limitation of the three-dimensional magnetic inverse problem is the presence of degrees of freedom in the hypothetical current source distribution that are magnetically silent, such as spherical batteries or radially symmetric arrays of current dipoles. One particularly useful method to prevent the mathematical instabilities associated with the potential existence of silent sources is to use lead-field expansions to constrain the inverse problem so as to limit the set of sources only to those that produce measurable magnetic fields in the particular magnetometer arrangement used. Figure 10.28(a) shows how the energization of an ECG lead will produce a current distribution in the torso that provides information about the spatial sensitivity of that lead to current sources, while Figure 10.28(b) shows the same when an alternating current in a magnetometer pickup coil induces circulating currents in the torso, also providing information about the sensitivity of the magnetometer to cardiac current sources.

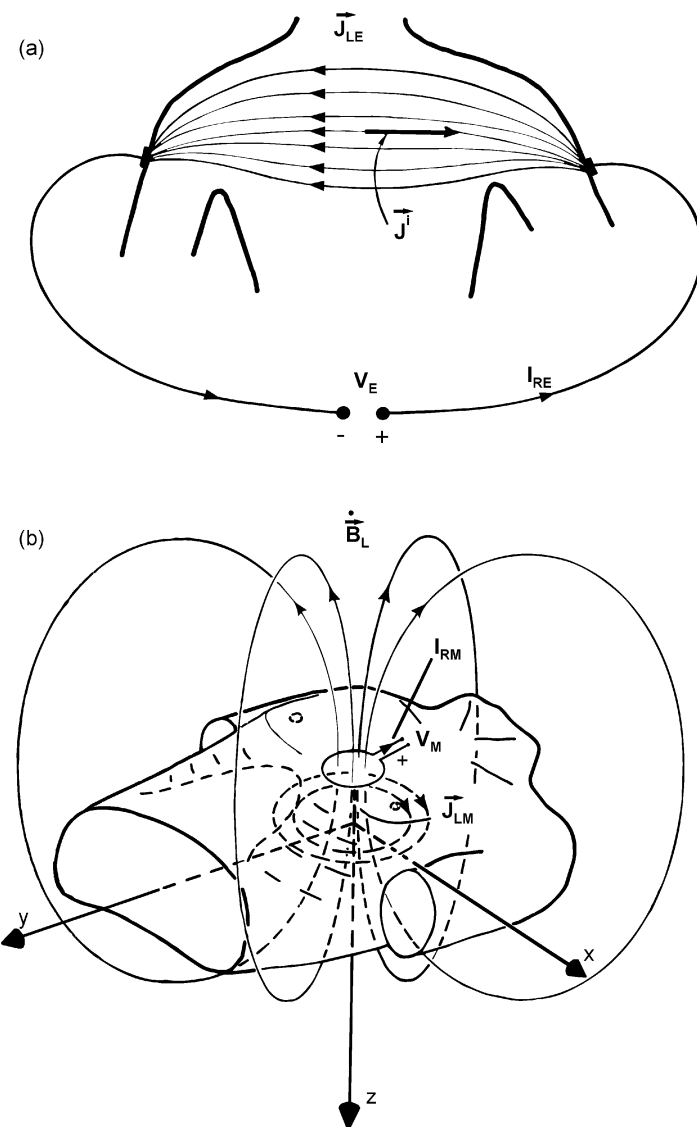


Fig. 10.28 A schematic representation of simple ECG and MCG leads and lead fields. Here, I_{RE} is the current used to “reciprocally” energize the electric lead and produce the electric lead field \vec{J}_{LE} . In the magnetic lead, a time-varying current I_{RM} produces a time-varying magnetic field B_L which by Faraday

induction produces the magnetic lead field. The outputs of the electric and magnetic leads, V_E and V_M , respectively, can be determined by summing the projection of each element of the impressed current density \vec{J}_i on the lead field current densities. (Adapted from Ref. [22], with permission.)

Lead Fields

To understand quantitatively the process outlined in Figure 10.28, we first need to define the lead fields [22, 106, 107]. Note that this analysis is valid either for a fixed array of N sensors, or for a scanning SQUID sensor that samples the magnetic field at N different positions \vec{r}_i . Suppose that a magnetometer measures B_z at a specific point \vec{r} . As shown in (10.65), this measurement represents a convolution of the source current distribution $\vec{J}(\vec{r}')$ and the Green's function $G(\vec{r}, \vec{r}')$ over the points \vec{r}' where both \vec{J} and G are nonzero. This Green's function is equivalent to a mutual inductance, M_{pq} , between a particular source element, $d\vec{p}$, of a current dipole distribution and a single, specific pick-up coil, q . The principle of reciprocity states that M_{pq} equals M_{qp} , which is equivalent to saying that the Green's function is the same whether the current source is at \vec{r} and the coil is at \vec{r}' or visa versa, i.e., $G(\vec{r}, \vec{r}') = G(\vec{r}', \vec{r})$. The lead field $\vec{L}_i^J(\vec{r}')$ for the i th magnetometer at \vec{r}_i is simply the current distribution \vec{J} that would be produced were the magnetometer pickup loop replaced by a coil carrying a low-frequency ac current. In this approach, the output of the i th SQUID magnetometer, a scalar variable, is simply the convolution of the source currents and the lead field for that magnetometer

$$B_i(\vec{r}) = \int_V \vec{L}_i^J(\vec{r}') \cdot \vec{J}(\vec{r}') d^3 r'. \quad (10.166)$$

Note the index i in \vec{L}_i^J contains within it the location \vec{r}_i , and hence we need not carry the dual-position notation of $G(\vec{r}, \vec{r}')$. If a current source at a particular point \vec{r}' is orthogonal to $\vec{L}_i^J(\vec{r}')$ at that same point, then that source cannot contribute to the field detected by the SQUID at \vec{r}_i . Reciprocally, a measurement of that component of the magnetic field cannot determine the strength of that component of the current source at \vec{r}' , although it may be able to detect another component at that location.¹⁰ The requirement that the solution set is to be restricted to those currents that produce fields that can be measured by the chosen magnetometers is equivalent to stating that all of the imaged currents have to lie along the lines of the lead fields of one or more of the magnetometers.

Lead Field Expansions

Equation (10.166) suggests that we use the set of lead fields for our N magnetometers to constrain the inverse source distribution [78, 107, 108]. While lead-field expansions were originally developed for three-dimensional inverse problems, to maintain the consistency of our derivations we shall restrict ourselves to measurement of two-dimensional current distributions. We begin with the law of Biot and

¹⁰ This is an easy explanation for the inability of a SQUID to measure magnetic fields from radial dipoles in a conducting sphere: it is impossible, by means of external coils, to induce in the sphere eddy currents with radial components, i.e., radial lead fields. For this reason, it is impossible to use exter-

nal coils to create a lead field that would detect a spherical battery. Also note that were we trying to measure a magnetization \vec{M} rather than a current \vec{J} , we would utilize the magnetic lead field \vec{L}^B , rather than the current lead field \vec{L} .

Savart for B_x at the i th measurement point above a two-dimensional current distribution

$$B_{x,i}(\vec{r}_i) = \left(\frac{\mu_0 d}{4\pi} \right) \int_S \frac{J_y(\vec{r}') (z_i - z')}{|\vec{r}_i - \vec{r}'|^3} dx' dy', \quad (10.167)$$

where S is the surface containing the sources. We can write this in terms of the lead field for that magnetometer

$$B_{x,i}(\vec{r}_i) = \int_S \vec{L}_i^J(\vec{r}') \cdot \vec{J}(\vec{r}') d^2 r'. \quad (10.168)$$

The dot product and the orientation of the lead field automatically selects the J_y component of the source current.

Let us suppose that we can expand $\vec{J}(\vec{r}')$ in terms of the nonorthogonal set of m lead-field functions \vec{L}_i^J

$$\vec{J}(\vec{r}') = \sum_{k=1}^m A_k \vec{L}_k^J(\vec{r}') w(\vec{r}'), \quad (10.169)$$

where $w(\vec{r}')$ is the *a priori* probability density for the current density, and A_k are the expansion coefficients. If we know, for example, that the currents in a particular region are zero, then we can at the beginning of our calculation set $w(\vec{r}')$ to zero at those locations. To determine A_k , we substitute (10.169) into (10.168), and exchange the order of summation and integration

$$B_{x,i}(\vec{r}_i) = \sum_{k=1}^m A_k \int_S \vec{L}_i^J(\vec{r}') \cdot \vec{L}_k^J(\vec{r}') w(\vec{r}') d^2 r'. \quad (10.170)$$

The field is thus

$$B_{x,i} = \sum_{k=1}^m P_{ik} A_k \quad (i = 1, 2, \dots, N) \quad (10.171)$$

where

$$P_{ik} = \int_S \vec{L}_i^J(\vec{r}') \cdot \vec{L}_k^J(\vec{r}') w(\vec{r}') d^2 r'. \quad (10.172)$$

While computation of P_{ik} can be tedious, it needs to be done only once for a particular measurement geometry. Singular-value decomposition or some other numerical technique is used to solve this set of linear equations for A_k , which are then

substituted into (10.169) to find $\vec{J}(\vec{r})$. The process can be iterated to refine the images, where $w(\vec{r})$ is adjusted each time. Figure 10.29 shows how this can be used to determine the distribution of currents flowing on the surface of a current-carrying tube with a small flaw [78, 108, 109]. This approach has the advantage that constraints can be applied through both the lead fields and the weighting function $w(\vec{r})$, but it is difficult to apply boundary conditions and other *a priori* knowledge of the source. In the case of the current-carrying tube, the lack of an analytical expression for the Fourier transform of the Green's function for currents flowing on the cylinder precludes the easy application of the Fourier transform approach. One limitation of the approach is that if there are too many magnetic field points, or too many basis functions are chosen, then the inner products used to determine P_{ik} are so similar to each other that the related matrix equation (10.171) becomes highly singular. Thus, for this approach, the number of magnetic field data points and basis functions must be limited [78].

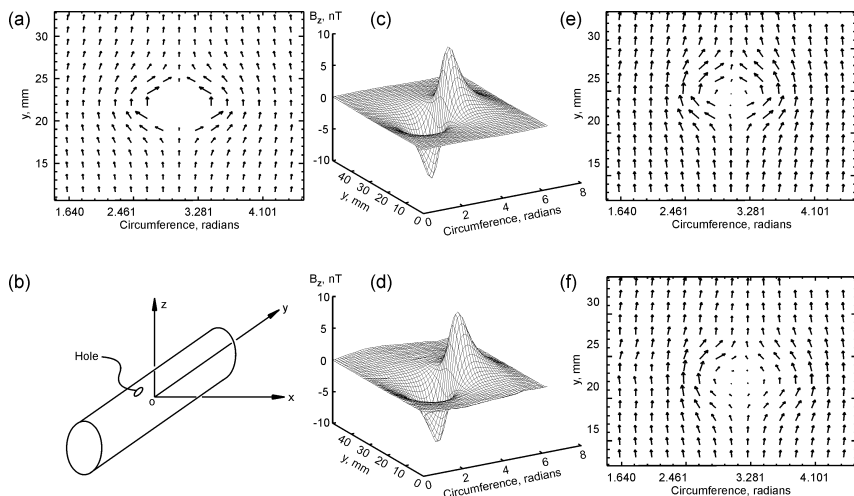


Fig. 10.29 An example of a lead-field inverse for a current-carrying tube with a small hole: (a) original current distribution; (b) geometry; (c) calculated magnetic field; (d) measured magnetic field; (e) currents reconstructed from theoretical magnetic field; (f) currents reconstructed from measured magnetic field. (Adapted from Ref. [136], with permission.)

As summarized by Tan [78], the lead-field analysis introduced by Ioannides [110] provides a method to constrain the current-imaging space. However, because the lead-field functions are defined over all space by using the *a priori* probability density function $w(\vec{r})$, lead-field analysis can incorporate only a constraint condition, such as the absence of current from a particular region, but not boundary conditions, such as the specification that current can flow only tangentially to an insulating boundary. Also, the lead-field interpolation functions are neither complete nor orthogonal, and this approach can recover only the components of the

current distribution to which the pickup coil is sensitive. Therefore, the reconstructions are sensitive to the choice of the measurement locations and hence the lead-field functions.

Sensor Array Optimization

The lead-field approach can be used to optimize sensor arrays for optimum inverse solutions [3], particularly with regard to the distribution of single-component *versus* vector magnetometers. Nalbach and Dössel analyzed the distribution of the sensors in a multichannel SQUID system and showed that fewer sensors nonuniformly distributed can provide better information to the inverse problem in MCG and ECG than a larger number of sensors distributed over a regular grid [4]. The lead-field method combined with realistic torso modeling was used to compare different sensor arrangements. In essence, the inverse problem consists of inverting the lead-field matrix, which in this analysis maps cardiac sources onto body surface potentials \tilde{b}_{el} or magnetic fields \tilde{b}_{mag}

$$\tilde{\tilde{A}}\tilde{x} = \tilde{b}_{\text{mag},\text{el}} \therefore \tilde{x} = \tilde{\tilde{A}}^{-1}\tilde{b}_{\text{mag},\text{el}}. \quad (10.173)$$

Since the lead-field matrix is ill-conditioned, singular-value decomposition (SVD) is used to decompose $\tilde{\tilde{A}}$, and to obtain an inverse solution

$$\tilde{\tilde{A}} = \tilde{\tilde{U}} \tilde{\tilde{\Sigma}} \tilde{\tilde{V}}. \quad (10.174)$$

The matrix $\tilde{\tilde{U}}$ can be seen as an orthonormal basis for the measurement space, and the matrix $\tilde{\tilde{V}}$ as an orthonormal basis of the source space. The singular values, which are sorted in descending order in $\tilde{\tilde{\Sigma}}$, represent the magnitude with which vectors in the source space base are mapped into the measurement space base. Because a division by the singular values is performed in the calculation of the inverse solution, the slope of the singular value curve is related to the ill-posedness of the problem.

To obtain a sensor arrangement that is optimized for the inverse MCG, the calculation started with an even distribution of 990 sensors on a grid comprised of 15 elliptical layers surrounding the torso and containing 66 sensors each. If the canceling of a sensor did not change the set of maximal reconstructible base vectors, then such a sensor was discarded. Following this procedure, an optimized 32-channel arrangement was obtained. This configuration allowed the reconstruction of a larger number of base vectors than a 99-channel arrangement of evenly distributed sensors, comprised of 33 magnetometers, 33 planar gradiometers in the x -direction, and 33 planar gradiometers in the y -direction. It should be taken into account, though, that not every optimized configuration is feasible, due to constraints imposed by Dewar design.

10.3.2.6 The Finite-Element Method

One of the potentially most powerful approaches to the two-dimensional magnetic inverse problem may be the finite-element inverse, which can readily incorporate known source geometry and a wide variety of boundary conditions [78, 79]. Constrained reconstruction was originally proposed to solve the unbounded inverse Fourier transform problem in magnetic resonance imaging [111]. This method used a series of box-car functions as the interpolation functions to represent the original function, so that the solution of the inverse Fourier transform is bounded. Tan *et al.* [79] examined the applicability of this approach to the magnetic imaging problem and then developed a more flexible approach that utilized the finite-element interpolation functions. A recent comparison of the finite-element method (FEM) *versus* the boundary-element method (BEM) for lead-field computation in ECG is provided in Ref. [112].

We can write the Biot-Savart law for the z -component of the magnetic field above a two-dimensional current distribution $\vec{J}(x, y)$ in the xy -plane at $z = 0$ in the expanded form

$$B_z(x, y, z) = \frac{\mu_0 d}{4\pi} \int \frac{J_x(x', y')(y - y') - J_y(x', y')(x - x')}{[(x - x')^2 + (y - y')^2 + z^2]^{3/2}} dx' dy'. \quad (10.175)$$

In order to reconstruct the current image \vec{J} from the magnetic field data recorded in the xy -plane at a height z above the current distribution, we section the current-source space into a mesh of elements, as shown in Figure 10.30, that represents our prior knowledge about the conductor geometry.

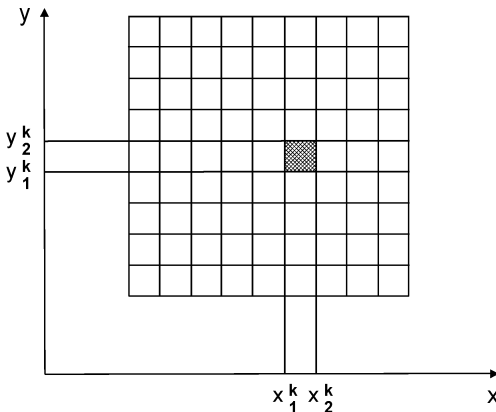


Fig. 10.30 A finite-element mesh describing a square conducting sheet.
(Adapted from Ref. [79], with permission.)

We can represent the current distribution $\vec{J}(\vec{r})$ anywhere within an element k by using a set of two-dimensional interpolation functions and the values of the current at the nodes in the mesh

$$\begin{aligned} J_x^k &= \sum_j J_{xj}^k N_j^k(x', y') \\ J_y^k &= \sum_j J_{yj}^k N_j^k(x', y'), \end{aligned} \quad (10.176)$$

where N_j^k are the two-dimensional interpolation functions for the k th element, J_{xj}^k , J_{yj}^k is the set of the nodal values that need to be determined, and j is the index for all interpolation functions in a single element. With this approach, we need to specify the values of the currents only at the nodes of the mesh; the interpolation functions provide us with analytical expressions for determining the current at all other points in the sample. As we did with the lead-field expansion for the current, we substitute (10.176) into (10.175), sum up all the elements, and reverse the order of summation and integration to obtain a set of linear equations that describe the magnetic field

$$[B_{zi}] = \sum_k [A_{zi,xj}^k] [J_{xj}^k] - [A_{zi,yj}^k] [J_{yj}^k], \quad (10.177)$$

where the subscript i stands for the i th measurement point and

$$A_{zi,xj}^k = \frac{\mu_0 d}{4\pi} \int \int_{(k)} \frac{N_j^k(x', y')(y_i - y')}{[(x_i - x')^2 + (y_i - y')^2 + z^2]^{3/2}} dx' dy' \quad (10.178)$$

$$A_{zi,yj}^k = \frac{\mu_0 d}{4\pi} \int \int_{(k)} \frac{N_j^k(x', y')(x_i - x')}{[(x_i - x')^2 + (y_i - y')^2 + z^2]^{3/2}} dx' dy'. \quad (10.179)$$

If we measure B_{zi} , calculate all A^k and invert (10.177), we should be able to solve for J_{xj}^k and J_{yj}^k . However, because we are measuring only one variable (B_z) over the mesh of the field map and are trying to determine two variables (J_x) and (J_y) over a coarser mesh of a current map, it may be difficult or impossible to solve (10.177) for J_x and J_y , since the equations can be highly singular and unstable. As before, we can incorporate the current-continuity condition to improve greatly the stability of the solution from B_z . Similar equations can be derived for measurement of either B_x or B_y

$$[B_{xi}] = \sum_k [A_{xi,yj}^k] [J_{yj}^k] \quad (10.180)$$

$$\begin{bmatrix} B_{yi} \end{bmatrix} = \sum_k \begin{bmatrix} A_{yi,xj}^k \end{bmatrix} \begin{bmatrix} J_{xj}^k \end{bmatrix}, \quad (10.181)$$

where

$$A_{xi,yj}^k = -A_{yi,xj}^k = \frac{\mu_0 d}{4\pi} \int \int_{(k)} \frac{N_j^k(x', y') z}{[(x_i - x')^2 + (y_i - y')^2 + z^2]^{3/2}} dx' dy'. \quad (10.182)$$

Because B_x is determined solely by J_y and B_y by J_x , the determination of a single component by the measurement of only one tangential component is straightforward. The continuity equation can be used to determine the other component. Alternatively, the independent measurement of B_x and B_y would allow the imaging of both J_x and J_y , and hence the determination of whether or not current was conserved on the surface being mapped. This may be of great practical importance for the creation of maps of an effective surface corrosion current for three-dimensional objects, since the surface-current distribution will be determined by underlying galvanic activity.

It is time consuming to calculate A^k and their inverses, but since they depend only upon the geometry of the finite-element mesh and the measurement arrangement, they must be calculated only once for each measurement configuration. On the other hand, once the inverses are determined, calculating a particular solution is computationally modest.

Continuous Two-Dimensional Current Distributions

In SQUID nondestructive evaluation (NDE), we encounter two types of current-imaging problems: those with a continuous current distribution, such as when a uniform current sheet is perturbed by a localized flaw, for which the electrodes used to apply the current to the test object are distant and can be ignored; and those problems with a discontinuous current distribution, as would occur when current is injected into the planar sample by vertical wires, as shown in Figure 10.18. As an example of the first case, Figure 10.31 shows a simulation using the square current pattern.

For this application, we can use a bilinear finite element with an interpolation function of the form [79]

$$N_j^k(x, y) = a_j^k + b_j^k x + c_j^k y + d_j^k xy, \quad (10.183)$$

where a_j^k, b_j^k, c_j^k and d_j^k are the parameters specific to the k th element. Inside the k th element, the current distribution $\vec{J}(x, y)$ can be expressed in terms of the vector current density \vec{S}_n at the four corners

$$\begin{aligned} J_x^k &= \mathfrak{S}_{x1}^k N_1^k + \mathfrak{S}_{x2}^k N_2^k + \mathfrak{S}_{x3}^k N_3^k + \mathfrak{S}_{x4}^k N_4^k \\ J_y^k &= \mathfrak{S}_{y1}^k N_1^k + \mathfrak{S}_{y2}^k N_2^k + \mathfrak{S}_{y3}^k N_3^k + \mathfrak{S}_{y4}^k N_4^k. \end{aligned} \quad (10.184)$$

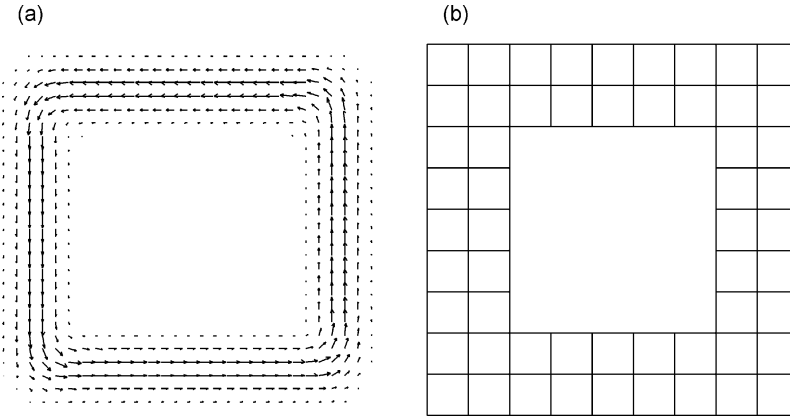


Fig. 10.31 Finite-element model for a bounded source: (a) the simulated current source used to test the continuous-current reconstruction algorithm; (b) the grid used to section the current space corresponding to (a). (Adapted from Ref. [79], with permission.)

We can utilize within each element a set of normalized, local coordinates, termed natural coordinates η and ξ , that range from +1 to -1, so that we can write the continuity condition ((10.75)) as

$$\frac{\partial J_x}{\partial \xi} \frac{\partial \xi}{\partial x} + \frac{\partial J_y}{\partial \eta} \frac{\partial \eta}{\partial y} = 0. \quad (10.185)$$

Substituting (10.184) into the above equation and sorting the coefficients by the order of the polynomial, we obtain a polynomial expression for the continuity equation [79]

$$\begin{aligned} & \frac{1}{a^k} \left(-\mathfrak{J}_{x1}^k + \mathfrak{J}_{x2}^k - \mathfrak{J}_{x3}^k + \mathfrak{J}_{x4}^k \right) + \frac{1}{b^k} \left(-\mathfrak{J}_{y1}^k - \mathfrak{J}_{y2}^k + \mathfrak{J}_{y3}^k + \mathfrak{J}_{y4}^k \right) + \\ & \frac{1}{a^k} \left(\mathfrak{J}_{x1}^k - \mathfrak{J}_{x2}^k - \mathfrak{J}_{x3}^k + \mathfrak{J}_{x4}^k \right) \eta + \frac{1}{b^k} \left(\mathfrak{J}_{y1}^k - \mathfrak{J}_{y2}^k - \mathfrak{J}_{y3}^k + \mathfrak{J}_{y4}^k \right) \xi = 0. \end{aligned} \quad (10.186)$$

Since the coordinates ξ and η are independent of each other, each term of the polynomial must be individually zero to ensure that the continuity condition is satisfied in every element. Thus, we obtain a set of equations governing the coefficients J_{xj}^k and J_{yj}^k

$$\begin{aligned} & \frac{1}{a^k} \left(-\mathfrak{J}_{x1}^k + \mathfrak{J}_{x2}^k - \mathfrak{J}_{x3}^k + \mathfrak{J}_{x4}^k \right) + \frac{1}{b^k} \left(-\mathfrak{J}_{y1}^k - \mathfrak{J}_{y2}^k + \mathfrak{J}_{y3}^k + \mathfrak{J}_{y4}^k \right) = 0 \\ & \left(\mathfrak{J}_{x1}^k - \mathfrak{J}_{x2}^k - \mathfrak{J}_{x3}^k + \mathfrak{J}_{x4}^k \right) = 0 \\ & \left(\mathfrak{J}_{y1}^k - \mathfrak{J}_{y2}^k - \mathfrak{J}_{y3}^k + \mathfrak{J}_{y4}^k \right) = 0. \end{aligned} \quad (10.187)$$

By incorporating the continuity condition ((10.187)) into one of the reconstruction equations ((10.177), (10.180), or (10.181)), we can obtain the images of the current density using only one component of the magnetic field [78, 79].

Since the finite-element method can deal with each individual element, any kind of boundary condition is easy to incorporate into the solution. For instance, a bounded current source usually will not allow current to flow out of the edge, which corresponds to the boundary condition

$$\vec{J} \cdot \hat{n} = 0. \quad (10.188)$$

Because the interpolation functions in the finite-element method are designed so that the nodal values are simply the current densities at the nodes, if the nodal values of the current component normal to the edge are zero, then this boundary condition is satisfied along that edge.

To demonstrate this approach, consider a 11.7 mm \times 12.6 mm current loop as shown in Figure 10.31(a). The current distribution does not have sharp edges to avoid problems with spatial aliasing that would occur with the spatial-filtering inverse. We assume that the shape of the conductor is known, and hence we can create the finite-element mesh shown in Figure 10.31(b). In an ideal case, when no noise is present in the data and the magnetic field is recorded very close to the current source, the filtering technique, which involves only a fast Fourier transform (FFT), a two-dimensional multiplication, and an inverse FFT, has the advantages of dealing with a large amount of data quickly and provides an excellent result. However, even a small amount of noise will reduce severely the quality of the image produced by the filtering technique, producing current noise over the entire image plane, while the finite-element method controls the effects of the noise in the magnetic field by restricting the current to within the correct boundary.

To demonstrate this, we calculate the z -component of the magnetic field as would be measured at $z = 1.5$ mm and at $z = 3$ mm, and then add spatially white noise so that the signal-to-noise ratios (SNRs) are 20-to-1 and 5-to-1, respectively. For the finite-element inverse, we sample the magnetic field over a 25 mm \times 25 mm area with 1 mm spacing, *i.e.*, 26 \times 26 points. Since the spatial-filtering inverse can readily use more data points without requiring the inversion of a giant matrix, we can sample the field over the same region with a 60 \times 60 mesh. Figures 10.32(a) and (b) show the results of the filtering technique and the finite-element method, respectively, for $z = 1.5$ mm and a SNR of 20. The mean-square deviation (MSD) for the result from the filtering technique (Figure 10.32(a)) increases from 0.002 to 0.133, which means that even a 5% noise level will degrade the quality by a factor of 60 over the reconstruction from the noise-free data. In contrast, the MSD for the finite-element method (Figure 10.32(b)) increases only from 0.026 to 0.040. While the finite-element approach with 26 \times 26 noise-free field points at 1.5 mm provides images that are coarser than obtained by the 60 \times 60 data used with the filtering approach, the image quality is degraded less quickly by noise for the finite-element approach, so that in the presence of only a small amount of noise, the finite-element approach provides superior results.

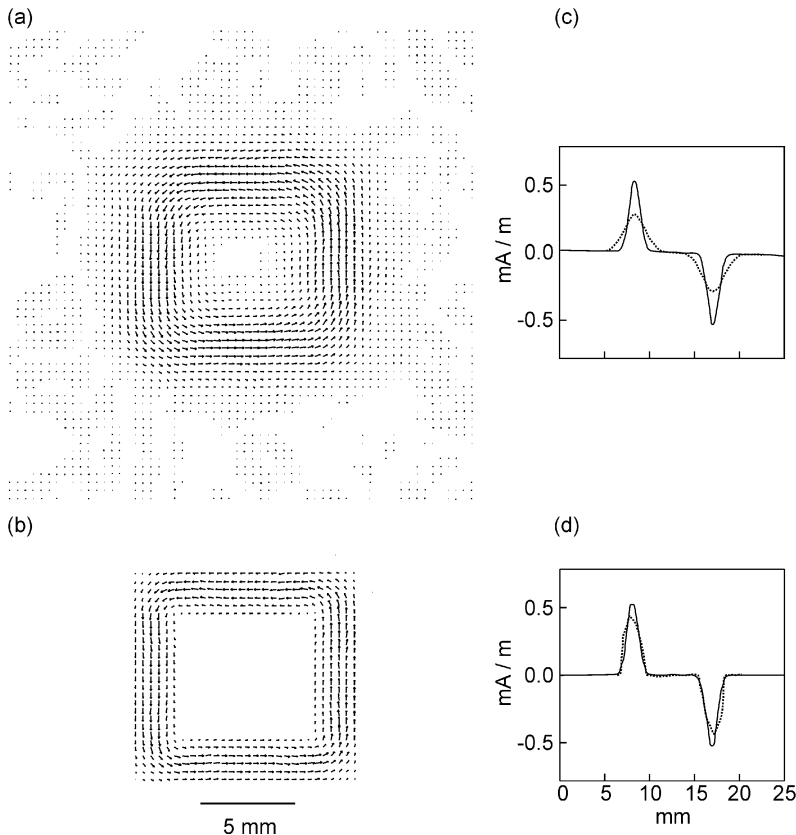


Fig. 10.32 The reconstructions by the filtering technique (a,c) and the finite-element method (b,d) at $z = 1.5$ mm with SNR = 20. (a,b) Reconstructed images of the current; (c,d) cross-section of J_x . The solid and dotted lines in (c) and (d) are the original current distribution and the reconstruction. (Adapted from Ref. [79], with permission.)

The advantage of the finite-element approach is even more apparent for B_z measured at 3 mm with a SNR of 5, shown in Figure 10.33. The filtering result in Figure 10.33(a) has an MSD of 0.42, whereas the finite-element method, shown in Figure 10.33(b), has an MSD of 0.12.

Discontinuous Two-Dimensional Current Sources

In measurements when current is injected into a conductor, as in Figure 10.18, there is a discontinuity in the current in the plane at the location of the two electrodes. In the filtering technique, we can address this with source/sink terms in the equation of continuity; in the finite-element approach, the continuity equation (10.187) can be modified for the elements containing the sources [79]. However, the accuracy of the reconstruction in the immediate vicinity of the electrode may be unsatisfactory. The usual approach would be to modify the mesh to have a very

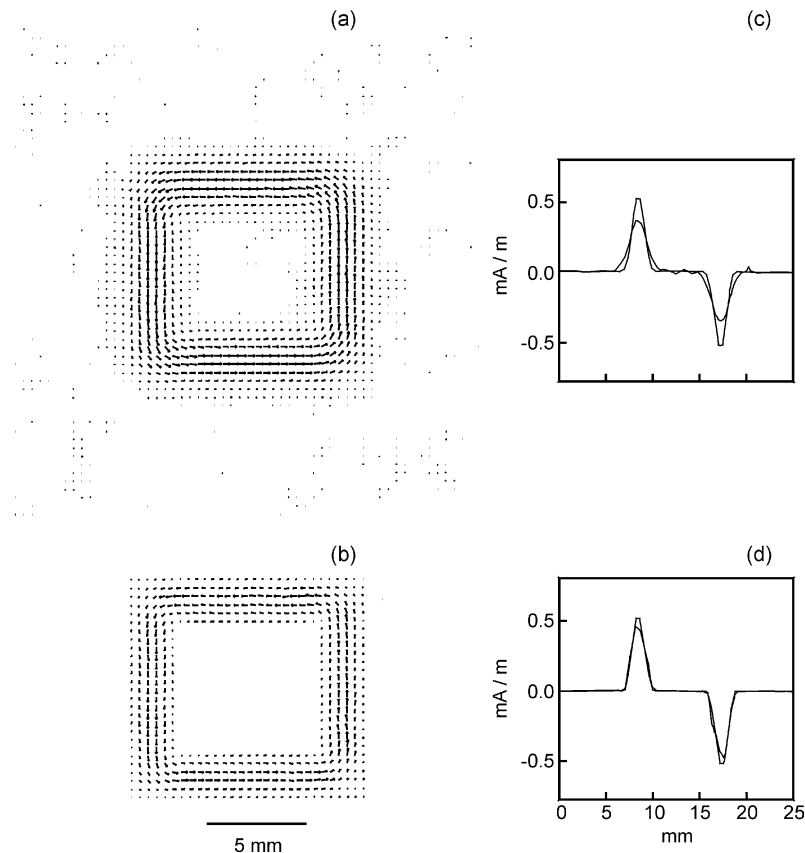


Fig. 10.33 The reconstructions by the filtering technique (a,c) and the finite-element method (b,d) at $z = 3.0$ mm with SNR = 5. (a,b) Reconstructed images of the current; (c,d) cross-section of J_x . The solid and dotted lines in (c) and (d) are the original current distribution and the reconstruction. (Adapted from Ref. [79], with permission.)

fine discretization in the immediate vicinity of the electrodes. However, with the finite-element inverse approach, such mesh refinement would drastically increase the size of the matrix that had to be inverted by singular-value decomposition or some other solver. An alternative approach is to superimpose two currents: a divergent current \vec{J}_d that correctly represents the current in the immediate vicinity of the two electrodes, and a continuous component \vec{J}_c , such that

$$\vec{J} = \vec{J}_d + \vec{J}_c. \quad (10.189)$$

For the divergent part, we assume that the current corresponds to that associated with the potential V produced by a pair of point electrodes at voltages $\pm U$ in an unbounded homogeneous conducting sheet, where

$$V = U \log \sqrt{(x - x_1)^2 + (y - y_1)^2} - U \log \sqrt{(x - x_2)^2 + (y - y_2)^2}, \quad (10.190)$$

so that

$$\begin{aligned} J_{dx} &= \frac{\partial V}{\partial x} \\ &= \frac{U(x - x_1)}{(x - x_1)^2 + (y - y_1)^2} - \frac{U(x - x_2)}{(x - x_2)^2 + (y - y_2)^2}, \end{aligned} \quad (10.191)$$

$$\begin{aligned} J_{dy} &= \frac{\partial V}{\partial y} \\ &= \frac{U(y - y_1)}{(x - x_1)^2 + (y - y_1)^2} - \frac{U(y - y_2)}{(x - x_2)^2 + (y - y_2)^2}. \end{aligned} \quad (10.192)$$

Then the deconvolution problem reduces to trying to find the divergence-free component \vec{J}_c such that the total current \vec{J} will produce the correct magnetic field while satisfying both the boundary condition

$$(\vec{J}_d + \vec{J}_c) \cdot \hat{n} = 0, \quad (10.193)$$

and also the continuity condition

$$\nabla \cdot \vec{J}_d = U\delta(\vec{r} - \vec{r}_1) - U\delta(\vec{r} - \vec{r}_2), \quad (10.194)$$

$$\nabla \cdot \vec{J}_c = 0. \quad (10.195)$$

Examples of this approach are presented in [79].

Eliminating Edge Fields

When current is passed through a conducting object of finite dimension, the discontinuity of the current at the edges of the object can produce large magnetic fields whose gradients will limit the ability to detect small flaws or field perturbations within the object either by direct imaging or by inverse solution. In terms of the inverse problem, the presence of the edges produces a large signal that could dominate the inverse process to the exclusion of smaller features. This was first recognized when trying to determine the smallest possible hole in a plate that could be detected by SQUID imaging of injected currents. There are a number of solutions to this problem involving either software preprocessing before an inverse calculation, or even with hardware at the time of data acquisition. Figure 10.34 shows how this can be accomplished by using a canceling plate that has a uniform current distribution passing beneath the sample, but in the opposite direction [113]. This approach may be useful for SQUID NDE measurements on

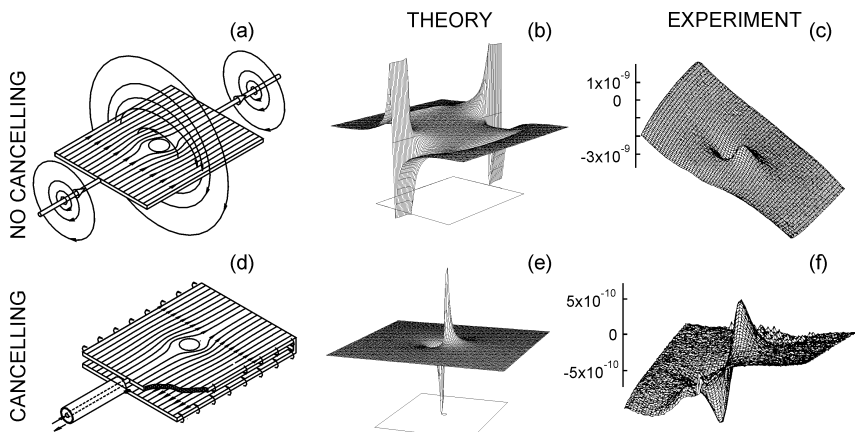


Fig. 10.34 The effects of conductor edges and the use of a canceling plate in the detection of small flaws in a conducting object: (a) the injection of current into a planar conductor with a hole; (b) the predicted magnetic field; (c) the magnetic signature of the hole; (d) the use of a canceling plate and a coaxial cable to deliver the current to the sample; (e,f) the measured magnetic field (scale range 1 nT). (Adapted from Ref. [113], with permission.)

long samples, such as at the end of a continuous aluminum extruder or rolling mill. As software preprocessing, the calculated magnetic field from an appropriately shaped plate can be subtracted from the recorded magnetic image, with the caveat that the SQUID must have an adequate field resolution (e.g., low digitization error) and linearity so as to not introduce additional artifacts.

An alternative approach is to use spatial filters, which can take the form of physical gradiometers, or synthetic ones (consistent with the limitations imposed by resolution and linearity) that are matched to the magnetic signature of the flaw of interest [114]. Figure 10.35 shows a simulation of how the edge effects of the internal structure of the lower wing splice of an F-15 aircraft can be eliminated by digital filtering. More importantly, this study also demonstrates that physical or synthetic planar gradiometers can be designed to detect small flaws in large background signals. A spatial filter that is matched to the magnetic signature of the flaw of interest represents a physical detector or algorithm that is sensitive to a particular inverse solution but insensitive to others. This approach can be generalized to any situation where a desired signature may be buried within a larger background field. A gradiometer might be configured, either in hardware or software, to optimize detection of that signature. Scanning of this synthetic gradiometer corresponds to the convolution of the gradiometer transfer function with the magnetic field. The advantage of doing this as a preprocessing step in the inverse solution is that different filters can be compared since all of the original field distribution was recorded prior to analysis.

The finite-element technique also can be used to eliminate edge fields from recorded field distributions, thereby enhancing the signals from any interior

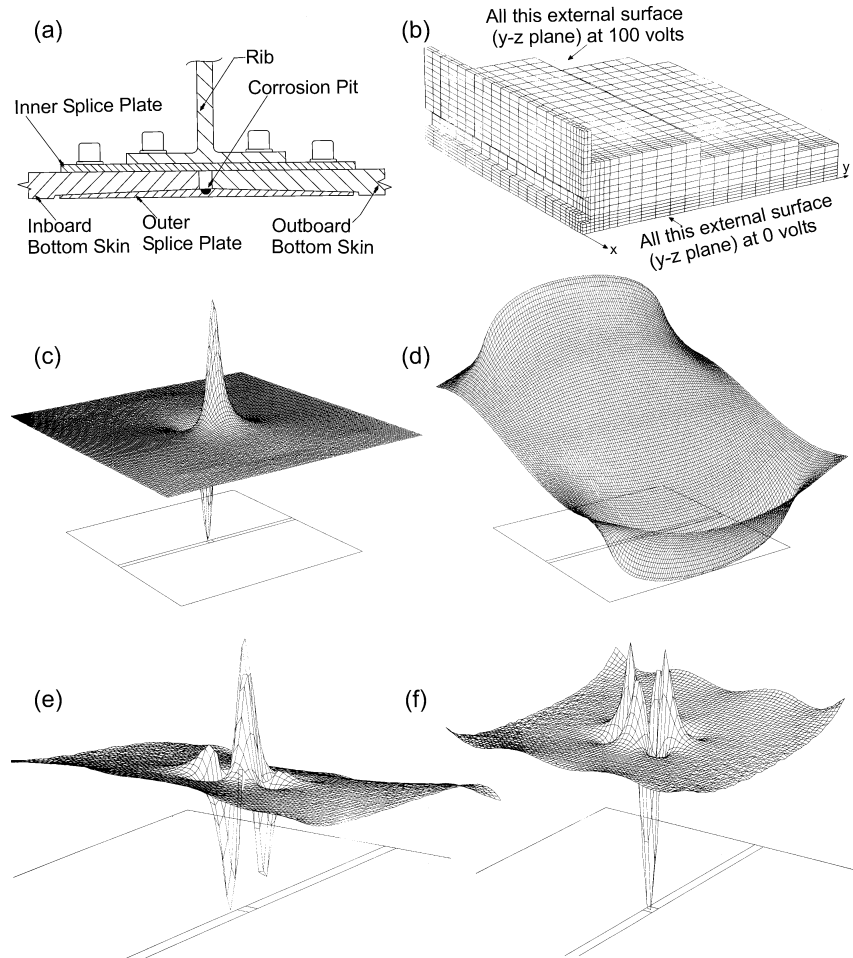


Fig. 10.35 Simulations of the magnetic signature of a small region of hidden corrosion in an F-15 lower wing splice. (a) Schematic cross-section of the splice. (b) The finite-element mesh describing one-quarter of a section of wing splice. A uniform current is applied parallel to the x -axis. (c) The magnetic signature of the flaw alone. (d) The magnetic field from the wing structure and the flaw. The

peak-to-peak signal arising from the edges of the various plates in the splice is 400 times larger than that of the flaw. (e,f) The simulated output of a SQUID gradiometer configured to reject large-scale spatial variations such as from the wing structure and selectively detect fields from localized flaws.
(Adapted from Ref. [114], with permission.)

structure [79]. Equation (10.15) shows that we can write the law of Biot and Savart in terms of a surface integral of the discontinuity in the tangential component of the current density \vec{J} , and the volume integral of the curl of \vec{J} . In two dimensions, the surface integral reduces to a line integral over the boundary b of the sample, and the volume integral to an integral over the two-dimensional surface S , so that

$$B_z(\vec{r}) = \frac{\mu_0 d}{4\pi} \oint_b \frac{\vec{J}(\vec{r}') \cdot d\vec{l}'}{|\vec{r} - \vec{r}'|} + \frac{\mu_0 d}{4\pi} \int_S \frac{[\nabla' \times \vec{J}(\vec{r}')]_z}{|\vec{r} - \vec{r}'|} dx' dy'. \quad (10.196)$$

Following the approach in Tan *et al.* [79], we can use Ohm's law

$$\vec{J} = -\sigma \nabla V, \quad (10.197)$$

the curl of this expression,

$$\begin{aligned} \nabla \times \vec{J} &= -\nabla \times (\sigma \nabla V) \\ &= -\nabla \sigma \times \nabla V \\ &= \nabla \times (V \nabla \sigma), \end{aligned} \quad (10.198)$$

and standard vector identities to rewrite (10.196) as

$$B_z(\vec{r}) = \frac{\mu_0 d}{4\pi} \oint_b \frac{\vec{J}(\vec{r}') \cdot d\vec{l}'}{|\vec{r} - \vec{r}'|} + \frac{\mu_0 d}{4\pi} \int_S \frac{[V(\vec{r}') \nabla' \sigma(\vec{r}') \times \vec{r}]_z}{|\vec{r} - \vec{r}'|} dx' dy'. \quad (10.199)$$

If the medium is homogeneous and isotropic, $\nabla' \sigma = \vec{0}$, and the second integral is zero, which means that the magnetic field depends only on the current tangential to the edge, *i.e.*, the first integral. If the test object has a nonuniform or anisotropic conductivity, the second term will contribute. The finite-element technique provides us with a powerful tool for separating these two contributions: the magnetic field is used with the finite-element inverse to determine the current distribution in a homogeneous, isotropic sample of the correct shape. This current is then used with the first integral of (10.199) to compute the magnetic field produced by the edges. If this is identical to the measured field, the sample is homogeneous and isotropic. If the two fields differ, then there are internal inhomogeneities or anisotropies. This approach may provide a means for enhancing the sensitivity of SQUID imaging to detect internal flaws in metallic structures.

10.3.2.7 Phase-Sensitive Eddy-Current Analysis

So far, we have discussed only the injection of current into conducting samples. While the injected-current technique is useful for high-precision measurements on test samples, the need to make good electrical contact with the sample would make it difficult to use on painted structures such as airplanes. It is also possible to use sheet inducers, first demonstrated with the MagnetoOptic Imager (MOI) [115, 116] in which the oscillating magnetic field is applied tangential to the surface of the test object by a sheet conductor or set of wires parallel to the test surface. This induces a large-extent sheet current in the test specimen, and thus produces flaw perturbation fields quite similar to those obtained with direct-current

injection. While beyond the scope of this chapter, it is important to recognize that this approach can be applied to inverse determinations, wherein SQUID data from this technique produce images suitable for deconvolution, and phase-sensitive analysis techniques can provide an additional degree of feature discrimination based upon flaw depth [117–120]. In this situation, the phase of the eddy current induced in a planar sample is a function of depth. At the surface of the sample, the eddy currents lead the magnetic field by approximately 90° . At low frequencies, the eddy-current phase is reasonably constant within the sample. At frequencies such that the skin depth is one-tenth of the thickness of the plate, there are large changes in the phase shift between the surface and the center of the sample. By using a vector lock-in amplifier and software phase-rotation techniques, we can image the component of the magnetic signal from the eddy currents at any desired phase relative to the applied field [119, 120]. Because of a frequency-dependent reversal of the sign of the eddy currents with depth, this technique also offers the possibility of three-dimensional current tomography [119, 120].

10.3.2.8 Summary of Inverse Magnetic Imaging of Current Distributions

As can be seen from the preceding analyses, the deconvolution of magnetic field maps to obtain images of current distributions can be addressed with a wide variety of mathematical techniques. There are others, such as an iterative perturbative approach using cubic splines [121] and a volume-integral approach [122], that have not been discussed here, and undoubtedly more techniques will be developed. In the perturbative approach, for example, the monopole and dipole terms of the electric potential can be computed analytically [123]. Likely candidates for further development as an inverse technique are the boundary integral [124–126] and resolution field [127, 128] methods. The geophysics literature is rich in sophisticated techniques [129–132]. A major limitation of the entire deconvolution process is that it is still more of an art than a science: there is no simple recipe to determine which approach is preferable for a particular combination of measurement geometry, noise, and current distribution. Until such a recipe is developed, it may be necessary to determine empirically the optimal technique for a particular application.

10.3.3

Imaging Magnetization Distributions

10.3.3.1 The Dipole Field Equation

Virtually all materials are magnetic, *i.e.*, they perturb to some extent an applied magnetic field. The perturbation is large if the material is iron, and very small if it is water or plastic. The perturbations of this field can be imaged, as shown schematically in Figures 10.2(b) and (g) and in the data in Figures 10.36 and 10.37. Such data can be used to determine the nature of the object that produced the perturbation, generally in terms of the magnetization or magnetic susceptibility

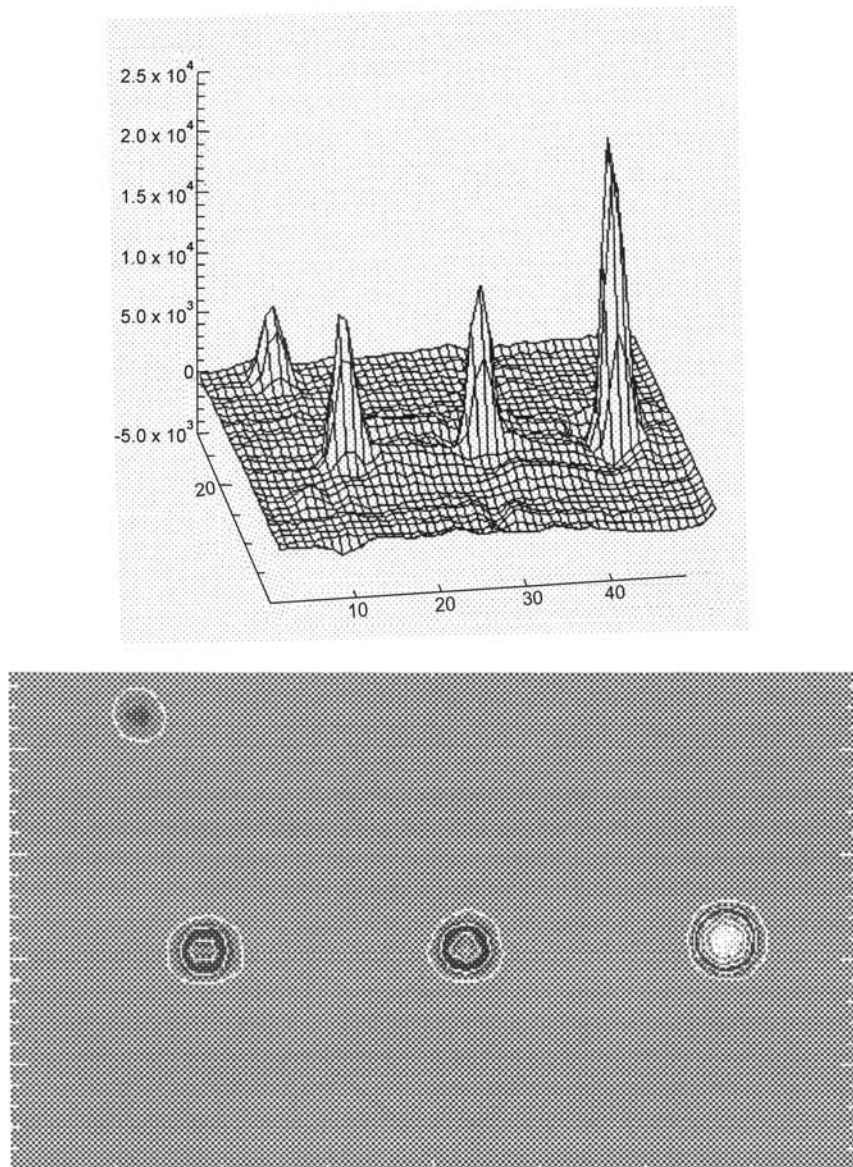


Fig. 10.36 Magnetic decoration of surface defects. A nickel NDE sample had electric discharge machined (EDM) slots with dimensions of $\sim 100 \mu\text{m}$, that were filled with a superparamagnetic tracer. The magnetic field was recorded 2.0 mm from the sample with a $174\text{-}\mu\text{T}$ applied field. These susceptibility

images display the location and size of surface defects, including one (upper left) that was the result of a previously undetected scratch. MicroSQUID can find flaws as small as $2 \times 10^{-12} \text{ m}^3$. (Adapted from Ref. [137], with permission.)

of the object. To see how this is accomplished, we need to start with a single magnetic dipole, whose field is given by (10.1), and whose inverse is given by (10.2). While this approach is appropriate for Figure 10.36, it may not work when we have multiple dipoles, or a distribution of dipoles in the form of a dipole density or magnetization as in Figure 10.37. In these latter cases, the inversion process is not so straightforward.

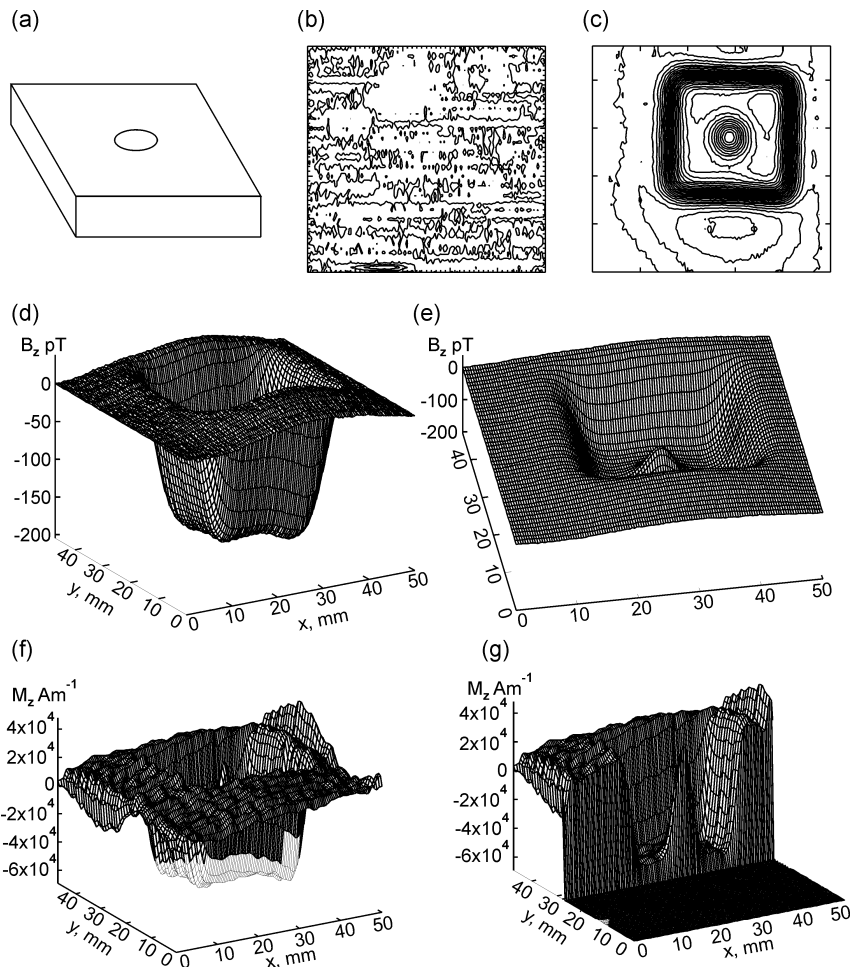


Fig. 10.37 Susceptibility images of Plexiglas. A 25.4-mm square sample of Plexiglas containing a 4.5-mm diameter hole was magnetized in a 110- μT applied field and scanned at a distance of 2.0 mm. (a) The sample; (b,c) contour maps of the recorded field B_z with (b) $B_{\text{app}} = 0 \mu\text{T}$ and (c) $B_{\text{app}} = 100 \mu\text{T}$;

(d,e) surface maps of the recorded field $B_{\text{app}} = 100 \mu\text{T}$ from two perspectives; (f,g) magnetization distributions computed from the measured field for (f) the entire sample and (g) a section of the sample. (Adapted from Ref. [138], with permission.)

10.3.3.2 Inverting the Dipole Field Equation for Diamagnetic and Paramagnetic Materials

The general inverse problem for magnetic media involves solving for the vector magnetization $\vec{M}(\vec{r}')$ in (10.3), or, after dividing by the applied field, the susceptibility $\chi(\vec{r}')$. This inverse problem has no unique solution. In the quasistatic limit, the curl of \vec{B} is zero in a current-free region, indicating that the field can be expressed as the gradient of the magnetic scalar potential V_m , where $\vec{B} = -\mu_0 \nabla V_m$. The magnetic potential outside of the surface S that bounds the sample of volume V is given by [133]

$$V_m(\vec{r}) = \frac{1}{4\pi} \int_S \frac{\vec{M}(\vec{r}) \cdot \hat{n}}{|\vec{r} - \vec{r}'|} d^2 r' + \frac{1}{4\pi} \int_V \frac{\nabla' \cdot \vec{M}(\vec{r}')}{|\vec{r} - \vec{r}'|} d^3 r'. \quad (10.200)$$

Hence, we see that measurements of quasistatic magnetic fields in free space outside a magnetized body provide information about the divergence of the magnetization distribution, rather than the magnetization itself, just as measurements of the magnetic field outside of a current distribution provide information only about the curl of the currents ((10.15)). Thus, any magnetization distribution that is divergence-free will be magnetically silent and cannot affect the external magnetic field. Beardsley [134] points out that in special cases, such as in a film with a magnetization that does not vary with thickness, the combined measurement of the external magnetic field and the angular deflection of an electron beam passing through the sample (differential phase contrast Lorentz microscopy) can provide the requisite information required to determine unambiguously the magnetization within the film. In this chapter, we restrict ourselves to SQUID measurements alone, and hence are faced, once again, with a potentially unsolvable inverse problem.

For magnetically soft materials, the magnetization is provided by external magnetic fields, and hence divergence-free magnetizations are avoided. This provides an important constraint to the problem. If we apply only a uniform H_z field, and if we know that for our sample $\vec{M}(\vec{r}') = \chi \vec{H}(\vec{r}')$, we need to solve for the scalar magnetization $M_z(\vec{r}')$ in the slightly simpler equation

$$\vec{B}(\vec{r}) = \frac{\mu_0}{4\pi} \int_V \left\{ \frac{3M_z(\vec{r}')(z - z')}{|\vec{r} - \vec{r}'|^5} (\vec{r} - \vec{r}') - \frac{M_z(\vec{r}')\hat{z}}{|\vec{r} - \vec{r}'|^3} \right\} d^3 r'. \quad (10.201)$$

In two dimensions, there is a unique inverse solution to this problem, to be presented in the next section. After that discussion, we shall show that in three dimensions, however, there is still a problem with nonuniqueness.

10.3.3.3 Two-Dimensional Magnetization Imaging

For two-dimensional samples, we can apply our inverse spatial filtering approach to determine the magnetization or susceptibility distributions from the magnetic field [78, 135, 136]. If the source is restricted to two dimensions, such as a thin sheet of diamagnetic or paramagnetic material, (10.201) reduces to a two-dimensional surface integral. We shall for now assume that we are applying only a z -component field $H_0\hat{z}$, and are measuring only the z -component of the sample-induced magnetic field \vec{B} at a height $(z - z')$ above the two-dimensional sample of infinite extent, so that we have

$$B_z(\vec{r}) = \frac{\mu_0}{4\pi} \int_{x'=-\infty}^{\infty} \int_{y'=-\infty}^{\infty} \left\{ \frac{3M_z(\vec{r}') (z - z')^2}{|\vec{r} - \vec{r}'|^5} - \frac{M_z(\vec{r}')}{|\vec{r} - \vec{r}'|^3} \right\} dx' dy'. \quad (10.202)$$

In practice, the integrals need not extend beyond the boundary of the source object, outside of which $\vec{M} \equiv \vec{0}$. In order to solve this equation for $M_z(\vec{r}')$, we define a Green's function

$$G_z(\vec{r} - \vec{r}') = \frac{\mu_0}{4\pi} \left\{ \frac{3(z - z')^2}{|\vec{r} - \vec{r}'|^5} - \frac{1}{|\vec{r} - \vec{r}'|^3} \right\}, \quad (10.203)$$

so that (10.202) becomes

$$B_z(\vec{r}) = \int_{-\infty}^{\infty} \int_{-\infty}^{\infty} M_z(\vec{r}') G_z(\vec{r} - \vec{r}') dx' dy'. \quad (10.204)$$

We compute the two-dimensional spatial Fourier transform of the magnetic field

$$b_z(k_x, k_y, z) = FT\{B_z(x, y, z)\}, \quad (10.205)$$

so that we can use the convolution theorem to express (10.202) in the spatial frequency domain as

$$b_z(k_x, k_y, z) = g_z(k_x, k_y, z - z') m_z(k_x, k_y), \quad (10.206)$$

where $g_z(k_x, k_y, z - z')$ is the two-dimensional spatial Fourier transform of the Green's function, i.e.,

$$g_z(k_x, k_y, z - z') = \frac{\mu_0}{4\pi} \left\{ 2\pi k e^{-k(z-z')} \right\}, \quad (10.207)$$

with

$$k = \left(k_x^2 + k_y^2 \right)^{\frac{1}{2}} \quad (10.208)$$

and $m_z(k_x, k_y)$ is the Fourier transform of the magnetization $M_z(x, y)$. The inverse problem then reduces to a division in the spatial frequency domain

$$m_z(k_x, k_y) = \frac{b_z(k_x, k_y, z)}{g_z(k_x, k_y, z - z')} \cdot \quad (10.209)$$

As we have seen before, it may be necessary to use windowing techniques to prevent this equation from “blowing up” because of zeros in the Green’s function occurring at spatial frequencies for which there is a contribution to the magnetic field from either the sample or from noise. Typically, the window $w(k_x, k_y)$ is a low-pass filter which attenuates high-frequency noise in the vicinity of the zeros of g_z , so that (10.209) becomes

$$m_z(k_x, k_y) = \frac{b_z(k_x, k_y, z)}{g_z(k_x, k_y, z - z')} w(k_x, k_y). \quad (10.210)$$

As the final step, we use the inverse Fourier Transform (FT^{-1}) to obtain an image of the magnetization distribution

$$M_z(x, y) = FT^{-1} \left\{ m_z(k_x, k_y) \right\}, \quad (10.211)$$

which can then be used to obtain the desired susceptibility image

$$\chi(x, y) = \frac{M_z(x, y)}{H_0(\vec{r})}. \quad (10.212)$$

This outlines the basic approach to two-dimensional magnetic susceptibility imaging; many of the techniques demonstrated for current-density imaging also will be applicable. It is important to note that once the Green’s function (and its inverse) and the window have been specified, it also is possible to proceed directly from $B_z(x, y)$ to $\chi(x, y)$ by evaluating the appropriate convolution integral in xy -space. Applications of this technique include localizing dilute paramagnetic tracers [137] and the imaging of plastic [138] (as shown in Figure 10.37), rock [8, 139, 140], and even water [141].

10.3.3.4 Magnetic Susceptibility Tomography

If the source is three-dimensional, a somewhat more general approach must be taken. We can start with (10.1), the dipole field equation for the magnetic field

$d\vec{B}(\vec{r})$ produced by a single magnetic dipole $d\vec{m}(\vec{r}')$. If the dipole moment arises from the magnetization of an incremental volume $d\nu$ in an applied field $\vec{H}(\vec{r}')$, we have that

$$d\vec{m}(\vec{r}') = \chi(\vec{r}') \vec{H}(\vec{r}') d\nu'. \quad (10.213)$$

The dipole field equation then becomes

$$d\vec{B}(\vec{r}) = \frac{\mu_0 \chi(\vec{r}')}{4\pi} \left\{ \frac{3\vec{H}(\vec{r}') \cdot (\vec{r} - \vec{r}')}{|\vec{r} - \vec{r}'|^5} (\vec{r} - \vec{r}') - \frac{\vec{H}(\vec{r}')}{|\vec{r} - \vec{r}'|^3} \right\} d\nu'. \quad (10.214)$$

This equation can be written as

$$d\vec{B}(\vec{r}) = \vec{G}(\vec{r}, \vec{r}', \vec{H}) \chi(\vec{r}') d\nu', \quad (10.215)$$

where we introduce a vector Green's function

$$\vec{G}(\vec{r}, \vec{r}', \vec{H}) = \frac{\mu_0}{4\pi} \left\{ \frac{3\vec{H}(\vec{r}') \cdot (\vec{r} - \vec{r}')}{|\vec{r} - \vec{r}'|^5} (\vec{r} - \vec{r}') - \frac{\vec{H}(\vec{r}')}{|\vec{r} - \vec{r}'|^3} \right\}. \quad (10.216)$$

The components of \vec{G} are simply

$$\vec{G} = G_x \hat{x} + G_y \hat{y} + G_z \hat{z}, \quad (10.217)$$

where

$$G_x(\vec{r}, \vec{r}', \vec{H}) = \frac{\mu_0}{4\pi} \left\{ \frac{3\vec{H} \cdot (\vec{r} - \vec{r}')}{|\vec{r} - \vec{r}'|^5} (x - x') - \frac{H_x}{|\vec{r} - \vec{r}'|^3} \right\}, \quad (10.218)$$

$$G_y(\vec{r}, \vec{r}', \vec{H}) = \frac{\mu_0}{4\pi} \left\{ \frac{3\vec{H} \cdot (\vec{r} - \vec{r}')}{|\vec{r} - \vec{r}'|^5} (y - y') - \frac{H_y}{|\vec{r} - \vec{r}'|^3} \right\}, \quad (10.219)$$

$$G_z(\vec{r}, \vec{r}', \vec{H}) = \frac{\mu_0}{4\pi} \left\{ \frac{3\vec{H} \cdot (\vec{r} - \vec{r}')}{|\vec{r} - \vec{r}'|^5} (z - z') - \frac{H_z}{|\vec{r} - \vec{r}'|^3} \right\}. \quad (10.220)$$

The three components of the magnetic field in (10.215) now can be written as

$$dB_x(\vec{r}) = \chi(\vec{r}') G_x(\vec{r}, \vec{r}', \vec{H}), \quad (10.221)$$

$$dB_y(\vec{r}) = \chi(\vec{r}') G_y(\vec{r}, \vec{r}', \vec{H}), \quad (10.222)$$

$$dB_z(\vec{r}) = \chi(\vec{r}') G_z(\vec{r}, \vec{r}', \vec{H}). \quad (10.223)$$

Note that \vec{H} may in turn be a function of x' , y' , and z' . In contrast, the Green's function in (10.203) does not contain \vec{H} . However, \vec{H} is assumed to be known and only adds a geometrically variable scale factor into the Green's function. The increased complexity of (10.218) through (10.220) arises from our desire to include \vec{H} as a vector field with three independently specified components.

If we know both the location \vec{r}' of a source that is only a single dipole, and also the strength and direction of \vec{H} at that point, we can make a single measurement of the magnetic field at \vec{r} to determine $\chi(\vec{r}')$. It is adequate to measure only a single component of $\vec{B}(\vec{r})$ as long as that component is nonzero. The problem becomes somewhat more complex when there are either multiple dipoles or a continuous distribution of dipoles. In that case, we need to sum or integrate (10.215) over the entire source object

$$\vec{B}(\vec{r}) = \int_{x'} \int_{y'} \int_{z'} \vec{G}(\vec{r}, \vec{r}', \vec{H}) \chi(\vec{r}') d\nu' \quad (10.224)$$

To proceed numerically, we shall assume that we can discretize the source object into m elements of volume or voxels v_j , where $1 \leq j \leq m$. The field from this object is then

$$\vec{B}(\vec{r}) = \sum_{j=1}^m \vec{G}(\vec{r}, \vec{r}_j, \vec{H}) \chi(\vec{r}_j) v_j. \quad (10.225)$$

A single measurement of \vec{B} will be inadequate to determine the susceptibility values for the m elements. Thus, we must make our measurements at n measurement points \vec{r}_i , where $1 \leq i \leq n$ identifies each such measurement. The three field components measured at a single point would constitute, in this notation, three independent scalar measurements which happen to have the same value for \vec{r} . Equation (10.225) becomes

$$\vec{B}_i(\vec{r}_i) = \sum_{j=1}^m \vec{G}(\vec{r}_i, \vec{r}_j, \vec{H}) \chi(\vec{r}_j) v_j. \quad (10.226)$$

To simplify the analysis, we can convert to matrix notation. In this case, the vector Green's function \vec{G} becomes an $n \times m$ matrix $\tilde{\vec{G}}$ that contains as each of its rows the Green's functions that relate a single measurement to every source element, *i.e.*, (10.221) – (10.223). The n field measurements can be written as the n elements of an $n \times 1$ column matrix $\tilde{\vec{B}}$. The magnetic susceptibility of each of the m

source elements can be described by an $m \times 1$ column matrix $\tilde{\chi}$. The volume of each source element can be incorporated into either the \tilde{G} or $\tilde{\chi}$ matrices. The measurements are related to the sources by

$$\tilde{B} = \tilde{G}\tilde{\chi}. \quad (10.227)$$

If $n = m$ the system of equations will be exactly determined, but it may not be possible to obtain a solution because of measurement noise or nonorthogonality, *i.e.*, linear dependence of the n equations. The alternative is to choose $n > m$, so that the system becomes overdetermined, and a least-squares solution can be attempted. Ideally, only those measurements needed to increase the independence of the equations will be added. While there are several ways to proceed, we shall consider only the general approach of multiplying both sides of (10.227) by \tilde{G}^T , the transpose of \tilde{G} , also known as the normal equations

$$\tilde{G}^T \tilde{B} = \tilde{G}^T \tilde{G}\tilde{\chi}. \quad (10.228)$$

The product $\tilde{G}^T \tilde{G}$ is now an $m \times m$ matrix that in principle can be inverted. This allows us to solve for $\tilde{\chi}$

$$\left[\tilde{G}^T \tilde{G} \right]^{-1} \tilde{G}^T \tilde{B} = \tilde{\chi}. \quad (10.229)$$

The ability to compute the inverse of the $\tilde{G}^T \tilde{G}$ matrix is determined by the measurement noise, by how well the measurements span the source space, and by the well-conditioning of the G matrix. Typically, if this inversion process is attempted for measurements made in a single plane over a complex source, the near elements of the source will dominate, and the matrix will be ill-conditioned.

Magnetic susceptibility tomography [142–147] can be used to avoid the ill-conditioned nature of (10.229) by applying the magnetic field from a number of different directions and by measuring the magnetic field at multiple locations all around the object. Since $n \gg m$, the system of equations becomes highly overdetermined, and standard techniques, such as singular value decomposition, can be used to determine the susceptibility of each voxel. Since the direction of the magnetization of each voxel of the material is known for every measurement, and this direction is varied, the domination of the $\tilde{G}^T \tilde{G}$ matrix by a small set of measurements can be avoided. The stability of the inversion of (10.229) can be enhanced by using nonuniform magnetizing fields [142]. The first demonstration of this technique, shown in Figure 10.38, used a uniform magnetizing field and a 64-voxel cube [145]. The reconstruction was reasonably accurate in the absence of noise, but the matrix was sufficiently ill-conditioned that stable inverse solutions were difficult to obtain with modest amounts of noise. The matrix will be more readily inverted if nonuniform magnetizing fields are utilized, since there are only three independent uniform fields that can be applied to an object [142–144],

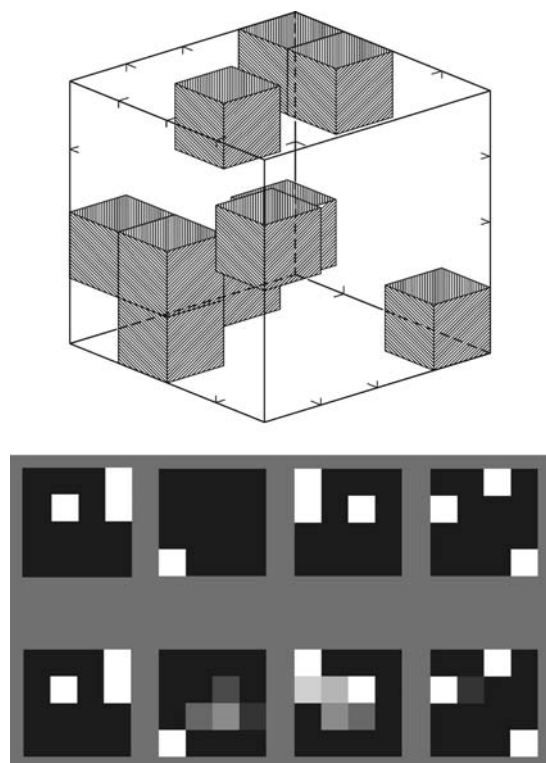


Fig. 10.38 Susceptibility tomography to reconstruct a simulated 64-element cube. Top: the ten shaded elements have a susceptibility of $+2.5 \times 10^{-5}$; all others have a susceptibility of $+2.0 \times 10^{-5}$. Bottom (upper): gray-scale representation of the actual susceptibility distribution; bottom (lower): the

distribution determined by a simulated susceptibility tomography measurement using a fixed magnetizing field and maps of the normal component of the perturbation field over the six faces of the cube. (Adapted from Ref. [145], with permission.)

and since a nonuniform magnetizing field eliminates the uncertainty of equivalent spherical sources with identical dipole moments.¹¹⁾

11) Suppose that we consider two uniformly magnetized spheres, centered at the origin, that have different radii but with magnetizations that are scaled such that the two spheres have the same magnetic dipole moment. Because the magnetic field outside of a uniformly magnetized sphere is perfectly dipolar, it is impossible to distinguish between these two sources by means of magnetic measurements made beyond the radius of the larger sphere. The existence of two different source distributions with identical fields in the region outside of all possi-

ble sources is the death knell for the inverse problem: without additional constraints, an inverse algorithm will be unable to control the degree of freedom within the source that corresponds to the radius of a uniformly magnetized sphere whose susceptibility scales inversely with the sphere volume. A multipole analysis of the external fields can give the dipole moment of the source to an arbitrary accuracy, but cannot determine both the radius of a uniformly magnetized sphere and its susceptibility if they are scaled for a constant dipole moment.

Two- and three-dimensional magnetic susceptibility imaging offers potential advantages for imaging magnetically labeled flaws or composites impregnated with dilute magnetic tracers [137, 148, 149], for magnetic imaging of materials such as plastic, titanium, or aluminum that are normally considered nonmagnetic, monitoring macrophage activity [150, 151], and, with susceptibility tomography, three-dimensional magnetic images of metabolism and iron storage in the liver and possibly regional oxygenation of the brain. In particular, while magnetic resonance imaging (MRI) is highly sensitive to spatial variations in magnetic susceptibility [152–155], the calibration of MRI susceptibility measurements for iron storage or other measurements of susceptibility effects in the body remains elusive, and hence SQUID susceptometry remains the gold standard [156–158]. However, additional improvements to both SQUID instruments and algorithms [142–144, 159] will be required before magnetic susceptibility tomography can compete with the more conventional, nonimaging methods for SQUID measurements of biosusceptibilities. Ongoing work in MRI inverse models and measurement protocols may eventually provide a noninvasive means for measuring biosusceptibility distributions in humans [160].

10.3.4

The Inverse Problem and Silent Sources

10.3.4.1 Introduction

In the preceding sections, we presented a wide variety of techniques for addressing the magnetic inverse problem. The lack of a unique solution to the magnetic or electric inverse problems is a general issue that applies to either field alone. However, in biomagnetism, the electric sources produce both electric and magnetic fields. This coupling of the fields in turn leads to new complexities that we will now explore. Sections 10.3.4.2 and 10.3.4.4 draw extensively from Ref. [13].

10.3.4.2 The Helmholtz Decomposition

In Section 10.2.4.2, we saw that the electric potential in an infinite homogeneous conductor is determined solely by the divergence of the primary current, while the magnetic field is determined by its curl. This leads to an interesting, and somewhat controversial, observation about the primary current distribution. If $\vec{J}^i(\vec{r})$ is an arbitrary vector field, it can be represented by a Helmholtz decomposition [161]

$$\vec{J}^i(\vec{r}) = \vec{J}_F^i(\vec{r}) + \vec{J}_V^i(\vec{r}), \quad \text{where } \nabla \times \vec{J}_F^i(\vec{r}) = \vec{0} \text{ and } \nabla \cdot \vec{J}_V^i(\vec{r}) = 0. \quad (10.230)$$

Thus \vec{J}_F^i has no curl and is called a “flow field,” while \vec{J}_V^i has no divergence and is called a “vortex field.” In an infinite homogeneous conductor, represented by only the first terms in (10.35) and (10.36) (*i.e.*, $\vec{K}^i = \vec{0}$), the electric potential is thereby determined solely by the pattern of \vec{J}_F^i and the magnetic field only by the

pattern of \vec{J}_V^i ; if \vec{J}_F^i and \vec{J}_V^i are independent, then V and \vec{B} will likewise be independent. This observation has been the basis for the controversy regarding possible independent information in the MCG. As we will see, the answer to this controversy may lie in the clarification of either the physiological constraints on \vec{J}^i , since any constraint that prevents \vec{J}^i from being the most general form of vector field will also cause \vec{J}_F^i and \vec{J}_V^i to be related, or in the effects of inhomogeneities at the cellular level.

The question of constraints on \vec{J}^i can be addressed using a simple variable-counting argument [22]. If the primary current distribution is a general vector field, it will have three degrees of freedom. The Helmholtz decomposition is simply a statement that such a vector field can be described by a scalar potential with one degree of freedom (consistent with \vec{J}_F^i having no curl), and a vector potential with two degrees of freedom (consistent with \vec{J}_V^i having no divergence). As first pointed out by Rush [162], there are physiological constraints on \vec{J}^i that leave it with less than three degrees of freedom. As a result, the electric and magnetic fields cannot be completely independent.

The question of independence becomes more complicated in a conductor with boundaries or internal inhomogeneities. Then V is still determined solely by \vec{J}_F^i , but \vec{B} now receives contributions from both \vec{J}_V^i and \vec{J}_F^i through the appearance of V in the second term of the integrand in (10.36). The magnetic field contribution from \vec{J}_V^i may still contain independent information consistent with our preceding discussion, but the contribution associated with the inhomogeneities is determined by \vec{J}_F^i . This would provide a mixing of the information in the MCG and ECG, which could be particularly important in situations where the second term of the integrand in (10.36) dominates the first. At first glance the second term is governed by V , which is described by \vec{J}_F^i . However, the integration of \vec{K}^i in both equations incorporates the boundary geometry differently and the effect of the geometry on the relative information content of these two integrals is not yet understood. Using the variable counting approach, the secondary source contribution should contain at least two degrees of freedom, since V contains one and the boundary that specifies the orientation of the secondary sources will contain another. How these two or more degrees of freedom couple to the ECG and the MCG is in need of clarification.

The ideal way to demonstrate the independence (or dependence) of the two integrals on the boundary geometry would be to demonstrate (or to prove the nonexistence of) examples in which a particular boundary or internal inhomogeneity affects either the electric field or the magnetic field from a particular source but not both, *i.e.*, an inhomogeneity that would be silent to only one of the two fields. A simple example is a horizontal current dipole in a conducting half space beneath a horizontal boundary: the normal component of the magnetic field in the air above the boundary is not affected by the inhomogeneity but the electric field above is. Many theoretical and experimental studies have compared the effects of the geometry of macroscopic inhomogeneities on the MCG and ECG with the hope of determining which measurement is least sensitive to the boundary and most sensitive to the primary sources. The situation is reversed at the cel-

lular level, since the inhomogeneity of the membrane dominates both the electric and magnetic fields and the active currents within the membrane do not directly affect either field to an appreciable degree.

The realization that the ECG and MCG *might be* independent, *i.e.*, the MCG might contain new information not present in the ECG, led to an intense debate. Rush claimed that there was no new information in the MCG [162], Plonsey responded [163] by noting that the uniform double layer provided a physiological constraint that reduced $\mathbf{J}^*(\vec{r})$ to having a single degree of freedom. Wikswo *et al.* demonstrated that the uniform double layer model led to differing sensitivities of the ECG and MCG to both the configuration of the double-layer rim and the effect of boundaries in (10.35) and (10.36) [22]. As summarized by Gulrajani [164], the initial arguments then reduced to one of differential sensitivities. The issue of physiological constraints remained unaddressed [165].

10.3.4.3 Electrically Silent Sources

In 1982, Wikswo and Barach realized, based upon pioneering work by Corbin, Scherr, and Roberts [166–168], that the anisotropy of cardiac tissue could create current sources that had a magnetically detectable but electrically silent component [14], as shown in Figure 10.39. These sources were then realized to be examples of a general class of sources, as illustrated in Figure 10.40, where the electric field reflects irrotational components of the source, and the magnetic field reflects both.

Plonsey and Barr then showed, in a ground-breaking pair of papers, that the cardiac bidomain should support circulating currents that could not be readily detected from measurements of the extracellular potential [169, 170]. An analytical examination of the role of tissue anisotropy demonstrated that the bidomain model had within it electrical anisotropies that might support currents that were electrically silent but magnetically detectable [15], and that much of the argument

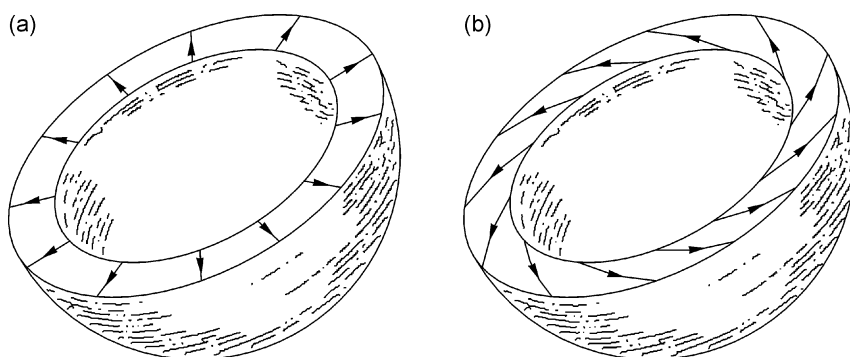


Fig. 10.39 Two models of the cardiac activation wave front: (a) a uniform double-layer model of cardiac activation; (b) another double-layer model of cardiac activation that would be electrically identical to that in (a) but magnetically different. (Adapted from Ref. [14], with permission.)

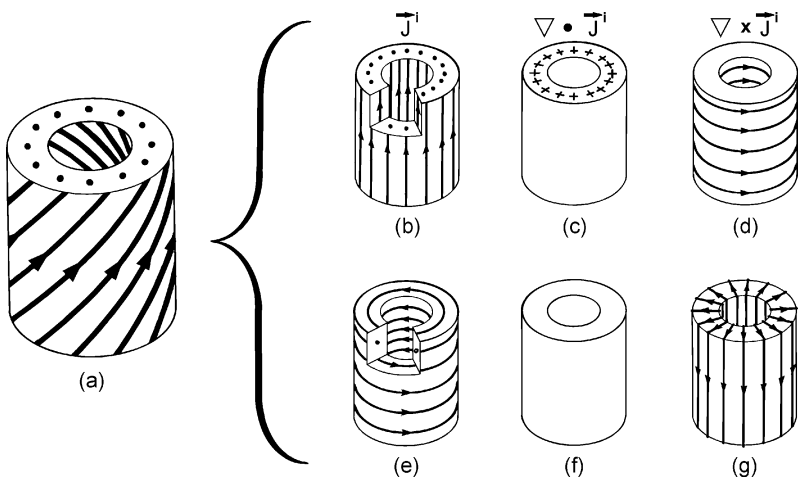


Fig. 10.40 (a) A general, hypothetical impressed current distribution in a tubular region of biologically active tissue; (b) the impressed currents \vec{J}^i are uniformly distributed in the z direction and have the divergence and curl shown in (c) and (d). The \vec{J}^i in (e) are tangential and have curl, as in (g), but no

divergence, as in (f). The cut-outs are to show that the impressed current is distributed throughout the wall of the tube, while the curls and divergences are nonzero only on surfaces. (Adapted from Ref. [14], with permission.)

reduced to one of off-diagonal terms in the two anisotropy tensors that were required to describe cardiac tissue. The question of whether or not these toy models would survive in realistic geometries was assessed by a modeling study of the magnetic field that would be recorded at the ventricular apex [171], as shown in Figure 10.41.

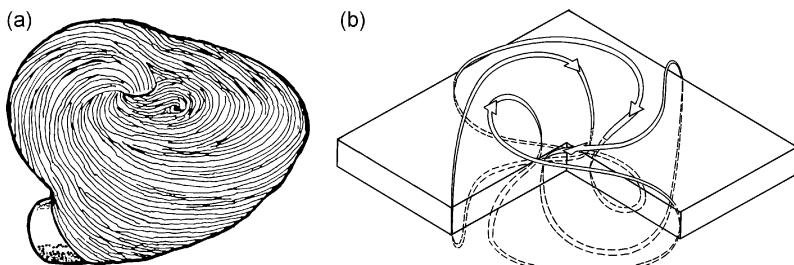


Fig. 10.41 The effects of spiral tissue architecture at the cardiac apex: (a) the fiber orientation at the apex (adapted from Ref. [245], with permission); (b) the apical magnetic field predicted for a bidomain model of a planar slab of tissue with spiral tissue architecture having a circularly symmetric cylindrical

wave front propagating outwards from the center. The field pattern is quite different from that produced by expanding wave fronts in tissue with parallel fibers, shown in Figs. 10.7 and 10.39. (Adapted from Ref. [171], with permission.)

From the perspective of the inverse problem, the issue then reduces to whether the appropriate model fitted to magnetic and electric data could distinguish between these two types of cardiac sources, *i.e.*, use the MCG to detect the effects of spiral anisotropy that could not be discerned from the ECG [70]. To date, there have yet to be incontrovertible demonstrations of new information in the human MCG, although magnetic fields recorded from the surface of an isolated rabbit heart during stimulation and propagation of action potentials clearly support the bidomain model and its representation of the magnetic field [65, 172–175].

10.3.4.4 Multipole Expansions

The relation of the electric and magnetic fields of current sources is also present in multipole expansions, as evidenced by the gray and black arrows representing dipole models in Figure 10.6. Both sets of current dipoles in the quadrupole expansion produce, in the appropriate limit, indistinguishable electric fields, but different magnetic fields. In the simple multipole expansions discussed in Ref. [18], there is in fact a series of electrically silent multipole terms. To better demonstrate this point, we analyze the current multipole expansions for the electric potential and magnetic field, such as the ones derived by Katila and Karp [176]. These authors emphasized that the leading term of each expansion has the current dipole as its source, and therefore to first order the two measures of cardiac activity yield identical information. Independently we have noted that the next term of the expansion has the current quadrupole coefficients a_{ij} appearing as the source, but different combinations of a_{ij} enter the expression for $V(\vec{r})$ than for $\vec{B}(\vec{r})$. In particular, the field depends on asymmetric terms of the quadrupole tensor that do not contribute to the potential. We shall briefly elaborate on this point of view.

The a_{ij} represent particular integrals of each Cartesian component of the current density [176]

$$a_{ij} = \int r'{}_i J_j^i(\vec{r}') dv', \quad (10.231)$$

where both indexes i and j stand for any of the three axes x , y , and z , leading to nine possible combinations. The set of quadrupole terms can be arrayed in a matrix denoted by the symbol $\tilde{\tilde{A}}$

$$\tilde{\tilde{A}} = \begin{bmatrix} a_{xx} & a_{xy} & a_{xz} \\ a_{yx} & a_{yy} & a_{yz} \\ a_{zx} & a_{zy} & a_{zz} \end{bmatrix}. \quad (10.232)$$

Each of the terms can be represented by a pair of opposing dipoles placed side-by-side or in a line, with an appropriate distance of separation. The terms of the quadrupole tensor of (10.232) can thus be displayed pictorially as in Figure 10.42(a). This tensor at first glance appears to have nine independent terms.

However, the sum of a_{xx} , a_{yy} and a_{zz} , known as the “trace” of the tensor, must be set equal to zero, because this sum must be electrically silent, *i.e.*, the electric potential outside this combined source would be zero everywhere, and the sum of a_{xx} , a_{yy} and a_{zz} would otherwise be indeterminate. Because of this constraint, there are only eight independent terms in the tensor. While the act of setting the trace to zero will also modify the pictures in Figure 10.42(a) [177], we shall not do this so as to simplify the discussion.

We can write $\tilde{\mathbf{A}}$ as the sum of symmetric and antisymmetric tensors

$$\tilde{\mathbf{A}} = \tilde{\mathbf{A}}^s + \tilde{\mathbf{A}}^a, \quad (10.233)$$

where $\tilde{\mathbf{A}}^s$ and $\tilde{\mathbf{A}}^a$ are given by combining $\tilde{\mathbf{A}}$ with its mathematical transpose, indicated by $\tilde{\mathbf{A}}^T$

$$\begin{aligned} \tilde{\mathbf{A}}^s &= \frac{1}{2} (\tilde{\mathbf{A}} + \tilde{\mathbf{A}}^T) \\ \tilde{\mathbf{A}}^a &= \frac{1}{2} (\tilde{\mathbf{A}} - \tilde{\mathbf{A}}^T). \end{aligned} \quad (10.234)$$

The pictorial representation of $\tilde{\mathbf{A}}$ and $\tilde{\mathbf{A}}^T$ is shown in Figures 10.42(b) and (c), respectively. The symmetric tensor $\tilde{\mathbf{A}}^s$ contains combinations of a_{ij} that appear in the current multipole expansion for the electrical potential distribution from a primary current source. It contains five independent terms, when we take account of the constraint that the trace must be zero. The antisymmetric tensor $\tilde{\mathbf{A}}^a$ contains three independent terms, since the three terms in the lower left corner of Figure 10.42(c) are simply the negative of the respective three terms in the upper right corner across the diagonal. We also see that these three terms in the current quadrupole tensor represent current loops (magnetic dipoles) oriented normal to the three axes of the Cartesian coordinate system. Each is electrically “silent,” so it is apparent that these three terms can be determined only by magnetic measurements and not by electric ones. One advantage of analyzing a field pattern with the current multipole expansion, as opposed to the magnetic multipole expansion, is that it allows extraction of the maximal information from the magnetic field while also providing equivalent primary current generators that can be readily interpreted in terms of various physiological current source distributions.

More sophisticated vector expansions of the source can also be obtained, which contain electric-like and magnetic-like terms. The electric field depends only on the former, whereas the magnetic field depends on both [165].

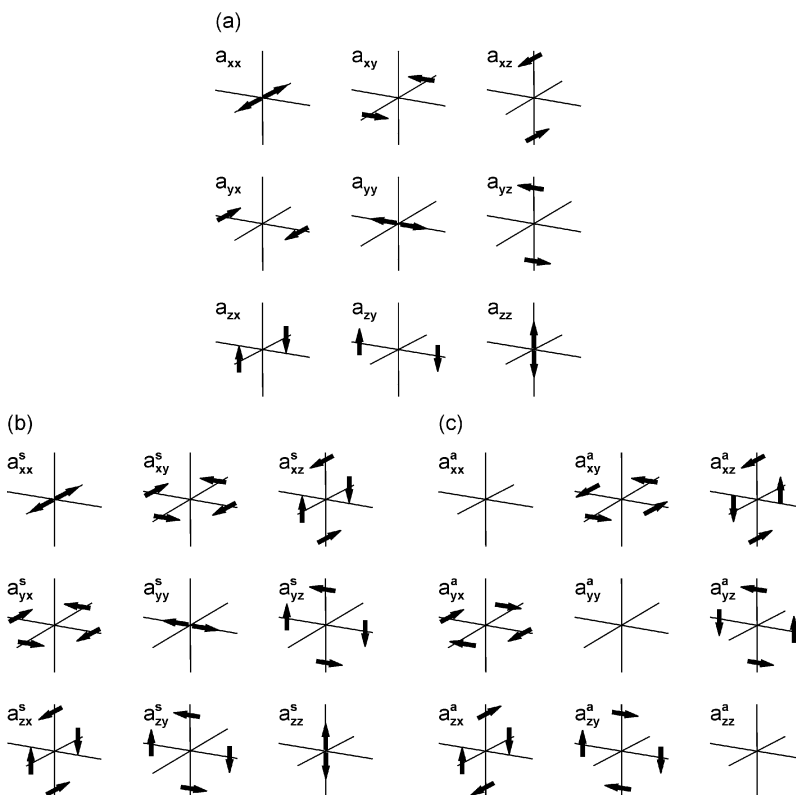


Fig. 10.42 Pictorial representation of the current quadrupole tensor: (a) the complete tensor; (b) symmetric part of the tensor; (c) antisymmetric part of the tensor. (Adapted from Ref. [13], with permission.)

10.3.4.5 Multiple Dipole Models

We presented Figure 10.8 in the context of the forward model of computing the cardiac magnetic field from a distributed dipole model of the cardiac activation wave front. From the point of view of the inverse model, this picture is dangerously deceptive. We demonstrate this by referring to the classic example by Holt *et al.* that demonstrated the limitations of multiple dipole models for inverse electrocardiography [38–40]. The effectiveness of various inverse algorithms that employ the multiple dipole model was investigated, among others, by Uutela *et al.* [178].

Least-Squares Fitting and the Generalized Inverse

We can now come full circle and reexamine the problems of fitting magnetic fields to a set of magnetic or electric dipoles. Earlier, we showed that the fields from a single dipole were given by (10.1) or (10.160). Following the convention we had in our discussion of magnetic susceptibility tomography, we can use matrix

notation to write the magnetic field as the product of a Green's function matrix and a source vector

$$\vec{B}(\vec{r}) = \sum_{j=1}^m \vec{G}(\vec{r}, \vec{r}_j) S(\vec{r}_j) v_j, \quad (10.235)$$

where $S(\vec{r}_j)$ is either an electric or magnetic dipole at point \vec{r}_j . This becomes

$$\tilde{\vec{B}} = \tilde{\vec{G}} \tilde{\vec{S}}. \quad (10.236)$$

As before, if $n = m$ the system of equations will be exactly determined, but it may not be possible to obtain a solution because of measurement noise, *i.e.*, linear dependence of the n rows of $\tilde{\vec{G}}$. The alternative is to choose $n > m$, so that the system becomes over-determined, and we can proceed with the least-squares generalized inverse solution

$$\tilde{\vec{S}} = [\tilde{\vec{G}}^\top \tilde{\vec{G}}]^{-1} \tilde{\vec{G}}^\top \tilde{\vec{B}}. \quad (10.237)$$

The ability to compute the inverse of the $\tilde{\vec{G}}^\top \tilde{\vec{G}}$ matrix is determined by the measurement noise, by how well the measurements span the source space, and by the well-conditioning of the G matrix. It may be that $\tilde{\vec{G}}^\top \tilde{\vec{G}}$ is sufficiently ill-conditioned or singular that its inverse cannot be computed, in which case one must resort to SVD or some other regularization technique to determine those contributions to $\tilde{\vec{G}}^\top \tilde{\vec{G}}$ that can be determined by the measurement set. However, as we will now show, physiological constraints on the source distribution may produce computational problems far beyond what might be addressed with SVD. To show this, we will now examine the multiple-dipole model of the cardiac activation wave front as shown in Figure 10.8.

Multiple Dipoles and Cardiac Activation

As electrocardiography became more sophisticated and multiple recording leads became available, there was great interest in moving beyond the simple dipole model of the heart [179–181]. The obvious next step was to use two dipoles, one for each ventricle, and then multiple dipoles, such that the time dependence of a single dipole might reflect regional ischemia or infarction, and hence the inversion of Figure 10.8 comes to the fore. As discovered when first attempted by Holt *et al.* [38–40], there are instabilities in the solutions that correspond to the addition and subtraction of dipole representations of spherical capacitors. Perturbing one dipole can be balanced by a corresponding antiperturbation of all other dipoles. The obvious solution is to constrain the orientation of the dipole, through quadratic programming, so that their orientation cannot reverse. This corresponds to the addition of physiological constraints to a model, something that has been popular in MEG analyses of cortical sources. However, it must be remembered that at least in the uniform double-layer model of cardiac activation, any perturbation of the wave

front that does not affect the shape of the rim will not affect the external potentials, so physiological constraints such as *a priori* knowledge of wave front geometry will help, if at all, only as long as the actual geometry for the disease subject is close to what was assumed in creating the model. The situation is even more complicated when we consider the bidomain effects discussed above.

10.3.5

Three-Dimensional Inverse Algorithms

10.3.5.1 **Introduction**

In the cases presented up to this point, we generally considered only the simplest constraints with respect to whether an object is two- or three-dimensional, or whether we know where the current is injected and withdrawn, or what the boundary conditions are. For the MEG and to some extent the MCG, physiological information, obtained by MRI or other imaging modalities, can provide valuable information. One must be cautious, particularly when dealing with pathological conditions, that the data from a patient are not interpreted solely on the basis of a model designed for normal subjects. The question then reduces to one of deciding where best to place the uncertainties intrinsic to the magnetic inverse problem: stable solutions that specify diffuse effective sources, or highly localized models that may be overly simplistic. Undoubtedly, the best results will be obtained if the greatest amount of complementary information can be included in the analysis.

There are a number of three-dimensional inverse algorithms, such as beamformers, minimum norm techniques, the focal undetermined system solver, multiple signal classification, principal and independent component analysis, low-resolution electromagnetic tomography, magnetic field tomography, *etc.* (Some of those techniques have been reviewed in the context of magnetocardiography in Ref. [182].) The remainder of this section briefly reviews these important methods, which are further discussed in Chapter 11. It must be emphasized that none of these techniques can create new information beyond what is provided to the model. It should also be mentioned that the three-dimensional techniques discussed below can be applied in the context of both the current and magnetic dipole models, provided of course that appropriate modifications are made to accommodate the two formalisms.

10.3.5.2 **Beamformers**

Beamformers [183, 184] are spatial filters that were originally introduced in telecommunications [185] to provide an efficient method for the estimation of signals originating from a source located in a certain direction in the presence of noise and other signals. Their purpose is to spatially filter signals that have overlapping temporal frequencies but distinct sources. Historically, the term originates from the fact that early spatial filters were akin to pencil beams that preferentially allowed signals from a specific location to be received by a detector, while others

were attenuated [183]. The use of beamformers in biomagnetism was pioneered by van Veen, van Drongelen et al. [183, 186], and Robinson and Vrba [187].

Through the use of multiple beamformers with different passbands, one can construct a neural power map that depicts neural power as a function of passband location [183]. Beamformer outputs are formed as weighted sums of sensor responses that specify spatial filtering features and increase sensitivity to signals from a preferred location. Strategies for determining the optimal set of weights lead to various distinct implementations of the beamformer method, including the linearly constrained minimum-variance (LCMV) [188] and nonlinearly constrained beamformers [187] used in synthetic aperture magnetometry (SAM). In the latter case, weights are computed for a unique orientation of the target source via a nonlinear optimization process that seeks to maximize the neural activity index, also known as the pseudo-Z statistic [189]. Various other adaptations of this method exist, including, for example, adaptive beamformers [190, 191].

10.3.5.3 Minimum Norm Techniques

Minimum norm techniques are optimal when minimal *a priori* information about the source is provided [192]. In this approach, the inverse problem is addressed using a combination of magnetometer lead fields to estimate the primary current distribution. As already explained in this chapter, one can write, in terms of the current dipole \vec{P} ,

$$B_i(\vec{r}') = \vec{L}_i(\vec{r}') \cdot \vec{P},$$

where B_i is the field component parallel to \vec{L}_i measured at location i of the magnetometer coil, and \vec{L}_i is the lead field associated with that location. Primary current distributions can be considered as elements of a so-called current space F that includes all square-integrable current distributions whose locations are limited to the conductor V . Since the field measurements B_i only convey information about a subspace F' of F , it follows that this subspace is spanned by the lead fields. One can define the inner product of two currents \vec{J}_1 and \vec{J}_2 in F as

$$\langle \vec{J}_1, \vec{J}_2 \rangle = \int_V \vec{J}_1(\vec{r}) \cdot \vec{J}_2(\vec{r}) d^3 r \quad (10.238)$$

with norm

$$\|\vec{J}_k\|^2 = \int_V |\vec{J}_k(\vec{r})|^2 d^3 r \quad (10.239)$$

The basic idea of the minimum norm technique is to identify an estimate J^* that is a linear combination of lead fields

$$\vec{J}^* = \sum_{j=1}^M w_j \vec{L}_j, \quad (10.240)$$

where w_j are real coefficients. Such an estimate must be confined to F' and must also reproduce the measured signals B_i . The process described above can be carried out by solving the set of linear equations

$$\tilde{\mathbf{b}} = \tilde{\tilde{\Gamma}} \tilde{\mathbf{w}}, \quad (10.241)$$

where

$$\tilde{\mathbf{b}} = (B_1, \dots, B_m)^T \quad (10.242)$$

is the set of measured data,

$$\tilde{\mathbf{w}} = (w_1, \dots, w_m)^T \quad (10.243)$$

is the set of lead field coefficients to be found, and $\tilde{\tilde{\Gamma}}$ is an $m \times m$ matrix with entries that are lead field inner products of the form

$$\Gamma_{ij} = \langle \vec{L}_i, \vec{L}_j \rangle \quad (10.244)$$

Solutions to this set of equations are not unique because any current \vec{J}_\perp satisfying the equality $\langle \vec{J}_\perp, \vec{L}_i \rangle = 0$ (i.e., perpendicular to the lead field \vec{L}_i) can be added to \vec{J}^* , yielding another solution to our set of equations. The physical meaning of this statement is that any current distribution that the magnetometer cannot detect can be added to the solution [192]. Mathematically, $\tilde{\tilde{\Gamma}}$ is nonsingular if the lead fields are linearly independent. In practical situations, however, this is not the case: $\tilde{\tilde{\Gamma}}$ can have very small eigenvalues, which leads to large errors in the calculation of the lead field coefficients w_j . In such cases, a regularization method can be applied, as discussed in a previous section of this chapter. Two minimum norm algorithms worth mentioning are the L1 and L2 norms, where L1 is characterized by a limited number of focused sources, while L2 (also known as minimum norm least squares or MNLS) is associated with a broad distribution of many sources [193].

The value and effectiveness of classic minimum norm techniques has been recognized in the EEG and MEG community particularly in cases where *a priori* source information is not available and/or very noisy data are analyzed. It has been shown that, although these methods are generally unable to accurately retrieve the depth of sources, they are quite effective at reconstructing two-dimensional projections of current distributions [192, 194–196].

10.3.5.4 FOCUSS

The FOCal Undetermined System Solver (FOCUSS) algorithm [197, 198] is a tomographic reconstruction method that aims to tame the major problem associated with typical minimum norm techniques: the lack of spatial resolution resulting in diffuse solutions, especially for deeper sources. In this method, a dipole is assigned to each voxel of the reconstruction volume, meaning that the nonlinear position parameters are completely specified. The Cartesian components of the dipole moments are thus the only unknowns to be estimated, and they are linearly related to the measurements. Provided that we make a sufficiently fine sampling of the volume relative to the spatial smoothness of the source distribution, the accuracy of the method is limited mainly by noise and other modeling errors. In some applications, such as MEG, it may be advantageous to use spherical coordinates and to recover only the two orthogonal vector components of the moment tangential to the radius of the sphere. In this way, we avoid the ill-posedness associated with radially oriented currents in the head, which cannot be observed with external field measurements, as discussed previously. For time-varying fields, reconstructions are calculated for each time slice.

The major strength of the FOCUSS algorithm lies in the reconstruction of localized sources. Unlike minimum norm estimates, which tend to produce many nonzero dipoles corresponding to a dispersion of the sources over a large volume, FOCUSS only selects a small number of elements that can generate the observed field.

We can express the system of linear equations in matrix form. Assuming a Cartesian coordinate system and numbering the dipole components sequentially, we have

$$\tilde{\mathbf{b}} = \tilde{\mathbf{G}}\tilde{\mathbf{p}}, \quad (10.245)$$

or

$$\begin{bmatrix} b_1 \\ \vdots \\ b_m \end{bmatrix} = \begin{bmatrix} G_{1,x} & G_{1,y} & G_{1,z} & G_{2,x} & G_{2,y} & \dots & G_{n/3,z} \end{bmatrix} \begin{bmatrix} p_1 \\ \vdots \\ p_n \end{bmatrix} \quad (10.246)$$

where $\tilde{\mathbf{b}}$ is an $m \times 1$ vector containing m measurements of a magnetic field component, $\tilde{\mathbf{G}}$ is the $m \times n$ basis matrix or Green's function matrix, whose elements are determined by the model geometry, and $\tilde{\mathbf{p}}$ is an $n \times 1$ vector containing the n unknown components of $n/3$ dipoles. Since $\tilde{\mathbf{G}}$ depends solely on the geometry of the sources and sensors, it needs to be calculated only once for a particular configuration, allowing for realistic, complex, and detailed modeling.

In essence, the algorithm starts with a distributed estimate, which can be obtained, for example, by the minimum norm method. Then, FOCUSS recursively enhances some of the sources while attenuating the rest of the elements until they become zero. Only a small number of dipoles is therefore selected,

yielding a localized energy solution. Specifically, at each iteration of the algorithm, a solution is obtained by means of the weighted minimum norm

$$\tilde{\mathbf{p}} = \tilde{\mathbf{W}} \left(\tilde{\mathbf{G}} \tilde{\mathbf{W}} \right)^+ \tilde{\mathbf{b}} = \tilde{\mathbf{W}} \tilde{\mathbf{W}}^T \tilde{\mathbf{G}}^T \left(\tilde{\mathbf{G}} \tilde{\mathbf{W}} \tilde{\mathbf{W}}^T \tilde{\mathbf{G}}^T \right)^{-1} \tilde{\mathbf{b}}, \quad (10.247)$$

where $+$ stands for the Moore–Penrose inverse, or pseudo-inverse, of a matrix and $\tilde{\mathbf{W}}$ is an $n \times n$ weighting matrix comprised of dimensionless scaling factors, whose purpose is to enhance some of the elements in $\tilde{\mathbf{p}}$. At each step, only $\tilde{\mathbf{W}}$ is changed, leading to a new (partial) solution.

Different definitions of $\tilde{\mathbf{W}}$ are possible, but a common choice is to make it a diagonal matrix whose elements are the elements of $\tilde{\mathbf{p}}$ obtained in the previous iteration. Another choice, which proves to be more robust, consists of defining $\tilde{\mathbf{W}}$ as the compound product of the weighting matrices obtained in the preceding steps. FOCUSS stops when the solution $\tilde{\mathbf{p}}$ no longer changes, and it has been shown that the algorithm always converges to a localized solution with no more than m nonzero elements [198].

Since FOCUSS is an initialization-dependent algorithm, care should be taken in calculating this particular step. An unbiased minimum norm solution, which compensates for the bias associated with the magnetic field falloff, may be used to provide an initialization within proximity of the true sources. In addition, in many applications, the matrix $\tilde{\mathbf{G}}$ is ill-conditioned, thereby requiring the use of some regularization technique to achieve a compromise between stability and a close fit to the data. Truncated SVD, where singular values below a certain threshold are discarded, may be used to address this problem.

10.3.5.5 MUSIC

The MUSIC algorithm was first proposed by Schmidt [199] to address the processing of signals from sensors with arbitrary locations and directional characteristics. It was then applied to biomagnetism by Mosher and co-workers [200, 201]; in our description of this method, we rely heavily on their work. Because our discussion is nevertheless introductory in nature, we refer the reader to the original literature [199, 200] for a detailed description of the method.

Let the $m \times n$ matrix $\tilde{\mathbf{F}}$ contain the spatiotemporal data for n time samples and m SQUID magnetometer channels. One can define an $m \times r$ “hybrid” gain matrix $\tilde{\mathbf{H}}$ that represents some mix of rotating or fixed dipoles in a noisy data model; the rank of $\tilde{\mathbf{H}}$ is equal to $R = 2p_R + p_F$, where p_R and p_F represent the number of rotating and fixed dipoles, respectively, for a total number of p dipoles. $\tilde{\mathbf{H}}$ contains the $3p$ unknown location parameters of these dipoles as well as the corresponding p_F unknown constraint moment parameters.

The matrix equation for this model assumes the form

$$\tilde{\mathbf{F}} = \tilde{\mathbf{H}} \tilde{\mathbf{S}} + \tilde{\mathbf{N}}, \quad (10.248)$$

where $\tilde{\tilde{F}}$ contains the magnetometer data, \tilde{S} is a scalar time series matrix, and \tilde{N} represents the error between the measurements and our model; dimensionally, \tilde{S} is $r \times n$. In MUSIC, \tilde{H} is assumed to be of full column rank r for p dipoles. Let $\tilde{\tilde{R}}_F$ denote a square symmetric matrix representing the spatial autocorrelation of the data, which can be computed using

$$\tilde{\tilde{R}}_F = E\left\{\tilde{\tilde{F}}\tilde{\tilde{F}}^T\right\}, \quad (10.249)$$

where $E\{\cdot\}$ is the expectation operator. Then $\tilde{\tilde{R}}_F$ can be written in terms of its eigendecomposition

$$\tilde{\tilde{R}}_F = \tilde{\tilde{\Phi}}\tilde{\tilde{\Lambda}}\tilde{\tilde{\Phi}}^T = \begin{bmatrix} \tilde{\tilde{\Phi}}_s & \tilde{\tilde{\Phi}}_n \end{bmatrix} \begin{bmatrix} \tilde{\tilde{\Lambda}}_s & \\ & \tilde{\tilde{\Lambda}}_n \end{bmatrix} \begin{bmatrix} \tilde{\tilde{\Phi}}_s & \tilde{\tilde{\Phi}}_n \end{bmatrix}^T, \quad (10.250)$$

where $\tilde{\tilde{\Lambda}}_s$ is a diagonal matrix containing the largest R eigenvalues, while $\tilde{\tilde{\Phi}}_s$ contains the corresponding eigenvectors. One assumption of the MUSIC algorithm is that the additive noise in the data is white and that it has a temporal and spatial mean of zero; this condition can be used to show that $\tilde{\tilde{\Lambda}}_n = \sigma\tilde{I}$, where σ is the noise variance [200]. This variance is also equal to an eigenvalue λ with multiplicity $m-r$, which can be used to show that $\tilde{\tilde{\Phi}}_n$ contains the remaining $m-r$ eigenvalues. The MUSIC algorithm computes the eigendecomposition

$$\hat{\tilde{R}}_F = \frac{1}{N}\tilde{\tilde{F}}\tilde{\tilde{F}}^T = \hat{\tilde{\tilde{\Phi}}}\hat{\tilde{\tilde{\Lambda}}}\hat{\tilde{\tilde{\Phi}}}^T, \quad (10.251)$$

where $\hat{\tilde{\tilde{R}}}_F$ is the data estimate of $\tilde{\tilde{R}}_F$ (the caret throughout this section refers to data estimate matrices of statistical quantities). The algorithm then orders the eigenvalues $\lambda_1, \dots, \lambda_m$ thus computed in descending order of their magnitude and finds a separation point D between the signal and noise subspace eigenvalues (where $1 \leq D < m$) based on the criterion that a distinct drop in eigenvalue magnitude occurs between λ_D and λ_{D+1} (see also Ref. [202] on alternative criteria for selecting the separation point). Next, the $m \times 2$ gain matrix \tilde{G}_i is computed over a fine grid of three-dimensional locations. For each entry in this matrix, the principal left eigenvectors \tilde{U}_{G_i} of $\tilde{\tilde{G}}_i$ are computed using an SVD of the form

$$\tilde{G}_i = \tilde{U}_{G_i} \tilde{\tilde{\Sigma}}_{G_i} \tilde{V}_{G_i}^T. \quad (10.252)$$

This in turn allows one to compute

$$J_h(i) = \lambda_{\min}\left\{\tilde{U}_{G_i}^T \hat{\tilde{\tilde{\Phi}}}^T \hat{\tilde{\tilde{\Phi}}}_n \tilde{U}_{G_i}\right\}, \quad (10.253)$$

i.e., the minimum eigenvalue of the expression in brackets. If, at each minimum of J_h , the subspace of $\tilde{\tilde{G}}_i$ is orthogonal to the noise subspace, then the dipole is rotating. An alternative way of determining this is by computing the cost function

$$J_r(i) = \frac{\left\| \hat{\tilde{\Phi}}_n^T \tilde{\tilde{U}}_{G_i} \tilde{\tilde{\Sigma}}_{G_i} \right\|_F^2}{\left\| \tilde{\tilde{\Sigma}}_{G_i} \right\|_F^2}, \quad (10.254)$$

where the subscript F refers to the Frobenius norm;¹² in this case, a rotating dipole satisfies $J_h(i) \approx J_r(i) \approx 0$. If the location of the dipole is fixed ($J_h(i) \approx 0$, $J_r(i) \neq 0$), its orientation can be estimated by computing the eigenvector of λ_{\min} . The process described above is then repeated until p_R rotating dipoles and p_F fixed dipoles are found such that $R = 2p_R + p_F$. Refinement of the solution can be achieved by further application of the same algorithm on a finer local grid.

10.3.5.6 Principal and Independent Component Analysis

Another method related to MUSIC that has been used perhaps less successfully [203, 204] is the principal component analysis (PCA) algorithm. In this approach, the data matrix \tilde{F} is first decomposed using the SVD

$$\tilde{F} = \tilde{U} \tilde{\tilde{\Sigma}} \tilde{V}^T. \quad (10.255)$$

The columns of \tilde{U} contain information referring to the spatial distribution of principal components while those of \tilde{V} are the corresponding time functions. If one forms the matrix $\tilde{\tilde{\Sigma}}'$ containing only the R principal singular terms, the i th dipole location and moment can be found from a least squares minimization of the quantity

$$\min_{\vec{L}_i, \vec{Q}_i} \left\| \tilde{\tilde{G}}_i(\vec{L}_i) \vec{Q}_i - \tilde{U} \tilde{\tilde{\Sigma}}' \tilde{C}_i \right\|_2^2, \quad (10.256)$$

where $\tilde{\tilde{G}}_i(\vec{L}_i)$ is the usual gain matrix for a dipole at location \vec{L}_i with components specified by \vec{Q}_i . Several methods exist for choosing the so-called rotation factors $\{C_{lm}\}$ [205, 206]; the error in the equation above can be written as [200]

$$J_{\text{PCA}}(i) = \left\| \tilde{U} \tilde{\tilde{\Sigma}}' \tilde{C}_i - \tilde{\tilde{G}}_i \vec{Q}_i \right\|_2^2 = \left\| \tilde{\tilde{P}}_{G_i}^\perp \tilde{U} \tilde{\tilde{\Sigma}}' \tilde{C}_i \right\|_2^2, \quad (10.257)$$

where $\tilde{\tilde{P}}_{G_i}^\perp$ is the orthogonal projection for a unique dipole.

¹²) The Frobenius norm of an $m \times n$ matrix \tilde{A} is

$$\text{defined as } \left\| \tilde{A} \right\|_F = \sqrt{\sum_{i=1}^m \sum_{j=1}^n |a_{ij}|^2}.$$

Independent component analysis (ICA) is an extension of PCA that was developed in relation to the blind source separation (BSS) problem, where ICA is very common [207, 208]. Several ICA algorithms exist, such as SOBI [209], Infomax [210], and fICA [211]; the fundamental assumption common to all of these, however, is that distinct sources generate uncorrelated (*i.e.*, unrelated) and statistically independent signals. The process of finding an appropriate set of such signals is carried out in ICA by minimizing a measure of joint entropy of the signals under consideration. Another assumption of this technique which has been criticized as a weakness is that the number of sources cannot exceed the number of sensors [212]. However, to have more sources than sensors (as in a fixed MEG measurement, for example) would violate our principle of a model not creating new information.

Two phases are involved in ICA: learning and processing. In the first of these, a weighting matrix $\tilde{\mathbf{W}}$ is found, which minimizes the mutual information between channels. This process effectively makes output signals that are statistically independent, such that the multivariate probability density function of the input signals f becomes equal to

$$f = \prod_i f_i, \quad (10.258)$$

i.e., to the product of probability density functions of every independent variable [213]. In the second phase of ICA, the matrix $\tilde{\mathbf{W}}$ is applied to the signal subspace data and the parameters of the dipoles are found using a search method (*e.g.*, the simplex algorithm). A very common application of ICA is in EEG, where the method is used, for example, to recover brain signals associated with the detection of visual targets [212, 214] or to extract ocular artifacts from EEG data [215, 216]. Detailed theoretical discussions of both BSS and ICA are provided in Refs. [208, 217, 218].

10.3.5.7 Signal Space Projection

In the signal space projection (SSP) approach, the magnetic field signals m_i , $i = 1, \dots, m$, are assumed to form a time-dependent signal vector $\tilde{\mathbf{m}}(t)$ in an m -dimensional signal space. The measured signal vector $\tilde{\mathbf{m}}(t)$ can be written as

$$\tilde{\mathbf{m}}(t) = \sum_{i=1}^M a_i(t) \tilde{s}_i + \tilde{n}(t), \quad (10.259)$$

where \tilde{s}_i are the elements of an orthonormal basis spanning the m -dimensional magnetic signal space F , $a_i(t)$ contains the time-dependence information of \tilde{s}_i , and $\tilde{n}(t)$ is the noise. Because \tilde{s}_i are basis objects spanning F that specify the orientations of the field vectors, the former are held fixed. In other words, as Hämäläinen and Ilmoniemi put it, “each source corresponds to a constant output pattern whose amplitude changes with time” [192]. One advantage of this approach over

other methods such as PCA is that, if the $a_i(t)$ coefficients are estimated directly from $\tilde{m}(t)$, no conductivity or source model is required [219].

The SSP method was introduced by Ilmoniemi et al. [220] and was applied for the first time by Miettinen [221]. To carry out SSP, two projection operators, $\tilde{\tilde{P}}_{\perp}$ and $\tilde{\tilde{P}}_{\parallel}$, are required to divide the signal $\tilde{m}(t)$ into two parts \tilde{s}_{\perp} and \tilde{s}_{\parallel} , respectively. The first part contains information belonging to the subspace spanned by component vectors $1, \dots, k$ and the matrix $\tilde{\tilde{K}} = (\tilde{s}_1 \ \tilde{s}_2 \ \dots \ \tilde{s}_k)$ is associated with it. The second part \tilde{s}_{\parallel} cannot be reproduced by any of the sources in $\tilde{\tilde{K}}$. Thus

$$\tilde{s}_{\parallel} = \tilde{\tilde{P}}_{\parallel} \tilde{m} \quad \text{and} \quad \tilde{s}_{\perp} = \tilde{\tilde{P}}_{\perp} \tilde{m}. \quad (10.260)$$

The matrix representations of the operators $\tilde{\tilde{P}}_{\perp}$ and $\tilde{\tilde{P}}_{\parallel}$ can be computed using the SVD of $\tilde{\tilde{K}}$

$$\tilde{\tilde{K}} = \tilde{\tilde{U}} \tilde{\tilde{\Lambda}} \tilde{\tilde{V}}^T. \quad (10.261)$$

The first k columns of the matrix $\tilde{\tilde{U}}$ form an orthonormal basis for the column space of $\tilde{\tilde{K}}$, yielding the results

$$\tilde{\tilde{P}}_{\parallel} = \tilde{\tilde{U}}_k \tilde{\tilde{U}}_k^T \quad (10.262)$$

and

$$\tilde{\tilde{P}}_{\perp} = \tilde{\tilde{I}} - \tilde{\tilde{P}}_{\parallel}. \quad (10.263)$$

The data estimates $\hat{\tilde{a}}(t)$ of the theoretical amplitudes $a_i(t)$ are then computed from

$$\hat{\tilde{a}}(t) = \tilde{\tilde{V}} \tilde{\tilde{\Lambda}}^{-1} \tilde{\tilde{U}}^T \tilde{m}(t). \quad (10.264)$$

The operators $\tilde{\tilde{P}}_{\perp}$ and $\tilde{\tilde{P}}_{\parallel}$ effectively form a spatial filter since they allow one to isolate signals that were generated only by the sources of interest. If the sources included in $\tilde{\tilde{K}}$ are only artifact-related, the information contained in the artifact-free signal can be separated into \tilde{s}_{\perp} . For this reason, the SSP method is particularly valuable as an artifact removal tool [222, 223] and has been used as such in a variety of applications [192, 224–226] including, among others, neuronal source characterization [227] and gastrointestinal inverses [47].

10.3.5.8 Other Three-Dimensional Methods

LORETA (low resolution electromagnetic tomography) was introduced by Pascual-Marqui et al. [228], who proposed that the inverse solution describing the current density throughout the full volume of the conductor can be selected based on the criterion of smoothness associated with the spatial distribution of sources. Mathematically, this method minimizes the squared norm of the Laplacian of the

weighted three-dimensional current density vector field [229]. One of the demonstrated advantages of this algorithm is that it provides small localization errors for deep sources; the method has been applied successfully to study auditory event-related potentials [230] and epileptiform activity [229]. A more recent algorithm, dubbed standardized LORETA (sLORETA) [191, 231, 232], does not use the Laplacian as a measure of spatial smoothness in computing the inverse solution. It relies instead on the calculation of statistical maps indicating the probable locations of sources. The performance of this method under the presence of noise is evaluated in Ref. [232].

Many other inverse techniques exist, such as the maximum entropy of the mean (MEM) method of Clarke and Janday [233, 234], probabilistic reconstruction of multiple sources (PROMS) [235], and magnetic field tomography (MFT) [236], all of which make use of probabilistic methods to estimate the detectable impressed current \vec{j}^i . In MFT [110], the value of the impressed current is computed independently for each time slice; the method is also best adapted to the detection of distributed sources. In the Bayesian approach [237, 238] the prior knowledge regarding the nature of the sources is represented as a prior probability, which is combined with a probabilistic description of the data to compute a posterior distribution by making use of Bayes' theorem; the optimal distribution of sources maximizes this probabilistic quantity.

As a final remark, it is interesting to note that most common linear inverse algorithms are highly related at a theoretical level and differ mostly in how the source covariance matrix of the data is constructed. As demonstrated by Mosher et al. [239], the method of estimating data and noise covariances used in a particular technique is important because many minimum norm algorithms are intimately dependent on these parameters. Conceptually, this is essential because the estimation of covariances is strongly related to the distinction between data and noise, which plays a vital role in the source recovery process.

10.4 Conclusions

Very few of the peculiarities or techniques described above to solve the magnetic inverse problem are unique to SQUID magnetometers, but in fact arise from the nature of the fields themselves. SQUIDs are among the most sensitive magnetometers, and all of this sensitivity is generally required to measure biomagnetic fields. With few exceptions, the biomagnetic inverse problem is a three-dimensional one, and has no unique solution. As a result, a wide range of techniques is utilized to convert biomagnetic images into approximations or constrained descriptions of bioelectric sources. The NDE and geomagnetic applications of SQUIDs are more forgiving, in that often the samples are two-dimensional, for which there are unique inverse solutions, or applied fields can be controlled in a manner that provides additional information required to solve the inverse problem. It is important to realize, however, that many of the techniques outlined in

this chapter, even in their present rudimentary state of development, can be used to analyze field images obtained from optical, fluxgate, Hall probe, and magnetoresistive magnetometers. Given the promise of these and other advanced imaging techniques, it is enticing to consider the future use of SQUID cameras based upon digital SQUID techniques to provide a thousand integrated digital magnetometers on a single chip [240, 241], or imaging optical magnetometers [242]. Meanwhile, there is much work that can be done to explore even more fully the mathematics and experimental techniques of magnetic imaging with SQUIDs and other magnetometers.

Acknowledgments

Much of the research described within this chapter was funded by grants from the Air Force Office of Scientific Research, the Electric Power Research Institute, and the National Institutes of Health. We are indebted to Afshin Abedi, John Barach, Alan Bradshaw, James Cadzow, Anthony Ewing, Luis Fong, Jenny Holzer, William Jenks, Xangkang Li, Yu Pei Ma, Bradley Roth, Nestor Sepulveda, Daniel Staton, Shaofen Tan, and Ian Thomas for their major contributions to the Vanderbilt magnetic imaging effort, and their papers from which we have drawn heavily in preparing this chapter. We thank Hans Koch and Wolfgang Haberkorn for providing the historical background on the nonuniqueness of the inverse problem solution. We also thank William Jenks, Margaret Khayat, Eduardo Parente Ribeiro, Daniel Staton, and Leonora Wikswo for their comments on predecessors of this manuscript, and Licheng Li for her care in preparing many of the illustrations. We especially thank Harold Weinstock for his encouragement and support of this research. We are deeply indebted to Don Berry, Cheryl Cosby, and Allison Price for their unflagging assistance and attention to detail in preparing the manuscript for this chapter, including but not limited to maintaining the reference database, typing the many equations, revising or creating each of the drawings, and very careful editing.

References

- 1** Helmholtz, H. (1853) Ueber einige Gesetze der Vertheilung elektrischer Ströme in körperlichen Leitern mit Anwendung auf die thierisch-elektrischen Versuche, *Ann. Phys. Chem.* **89**, 211–233, 353–377.
- 2** Braginski, A.I. (2005) Personal communication.
- 3** Bradshaw, L.A. and Wikswo, J.P., Jr. (1999) Vector or scalar magnetometer arrays?, in *Proceedings of the First Joint BMES/EMBS Conference*, Vol. 2, Atlanta, GA, p. 888.
- 4** Nalbach, M. and Dossel, O. (2002) Comparison of sensor arrangements of MCG and ECG with respect to information content, *Physica C* **372**, 254–258.
- 5** Baudenbacher, F., Peters, N. T. and Wikswo, J. P., Jr. (2002) High resolution low-temperature superconductivity superconducting quantum interference device microscope for imaging mag-

- netic fields of samples at room temperatures, *Rev. Sci. Instrum.* **73**, 1247–1254.
- 6** Fong, L. E., Holzer, J. R., McBride, K. K., Lima, E. A., Baudenbacher, F. and Radparvar, M. (2005) High-resolution room-temperature sample scanning superconducting quantum interference device microscope configurable for geological and biomagnetic applications, *Rev. Sci. Instrum.* **76**, 053703.
- 7** Cohen, D., Edelsack, E. A. and Zimmerman, J. E. (1970) Magnetocardiograms taken inside a shielded room with a superconducting point-contact magnetometer, *Appl. Phys. Lett.* **16**, 278–280.
- 8** Weiss, B. P., Kirschvink, J. L., Baudenbacher, F. J., Vali, H., Peters, N. T., Macdonald, F. A. and Wikswo, J. P. (2000) A low temperature transfer of ALH84001 from Mars to Earth, *Science* **290**, 791–795.
- 9** Wikswo, J. P., Jr. (1996) The magnetic inverse problem for NDE, in *SQUID Sensors: Fundamentals, Fabrication and Applications*, Weinstock, H. (ed.), Kluwer, The Netherlands, pp. 629–695.
- 10** Ma, Y. P., Thomas, I. M., Lauder, A. and Wikswo, J. P., Jr. (1993) A high resolution imaging susceptometer, *IEEE Trans. Appl. Supercond.* **3**, 1941–1944.
- 11** Wikswo, J. P., Jr. (1978) The calculation of the magnetic field from a current distribution: application to finite element techniques, *IEEE Trans. Magn. Mag* **14**, 1076–1077.
- 12** Geselowitz, D. B. (1970) On the magnetic field generated outside an inhomogeneous volume conductor by internal current sources, *IEEE Trans. Magn. Mag* **6**, 346–347.
- 13** Wikswo, J. P., Jr. (1983) Theoretical aspects of the EEG-MEG relationship, in *Biomagnetism: An Interdisciplinary Approach*, Williamson, S. J., Romani, G.-L., Kaufman, L. and Modena, I. (eds.), Plenum, New York, pp. 311–326.
- 14** Wikswo, J. P., Jr. and Barach, J. P. (1982) Possible sources of new information in the magnetocardiogram, *J. Theor. Biol.* **95**, 721–729.
- 15** Roth, B. J. and Wikswo, J. P., Jr. (1986) Electrically silent magnetic fields, *Biophys. J.* **50**, 739–745.
- 16** Demunck, J. C., Vandijk, B. W. and Spekreijse, H. (1988) Mathematical dipoles are adequate to describe realistic generators of human-brain activity, *IEEE Trans. Biomed. Eng.* **35**, 960–966.
- 17** Williamson, S. J. and Kaufman, L. (1981) Biomagnetism topical review, *J. Magn. Magn. Mater.* **22**, 129–201.
- 18** Wikswo, J. P., Jr. and Swinney, K. R. (1985) Scalar multipole expansions and their dipole equivalents, *J. Appl. Phys.* **57**, 4301–4308.
- 19** Brody, D. A. (1968) The inverse determination of simple generator configurations from equivalent dipole and multipole information, *IEEE Trans. Biomed. Eng.* **BME15**, 106–110.
- 20** Horacek, B. M. (1973) Digital model for studies in magnetocardiography, *IEEE Trans. Magn. Mag* **9**, 440–444.
- 21** Grynszpan, F. (1971) Relationship between the surface electromagnetic fields and the electrical activity of the heart, Ph.D. Dissertation, University of Pennsylvania.
- 22** Wikswo, J. P., Jr., Malmivuo, J. A. V., Barry, W. H., Leifer, M. C. and Fairbank, W. M. (1979) The theory and application of magnetocardiography, in *Advances in Cardiovascular Physics*, Vol. 2. Ghista, D. N., Vollenhoven, V. E. and Yang, W. (eds.), Karger, Basel/New York, pp. 1–67.
- 23** Jackson, J. D. (1975) *Classical Electrodynamics*, Wiley, New York.
- 24** Cohen, D. and Hosaka, H. (1976) Magnetic field produced by a current dipole, *J. Electrocardiol.* **9**, 409–417.
- 25** Wikswo, J. P., Jr. and Swinney, K. R. (1984) A comparison of scalar multipole expansions, *J. Appl. Phys.* **56**, 3039–3049.
- 26** Castellanos, A., Panizo, M. and Rivas, J. (1978) Magnetostatic multipoles in cartesian coordinates, *Am. J. Phys.* **46**, 1116–1117.
- 27** Gonzalez, H., Juarez, S. R., Kielnowski, P. and Loewe, M. (1998) Multipole expansion in magnetostatics, *Am. J. Phys.* **66**, 228–231.
- 28** Geselowitz, D. B. (1965) Two theorems concerning the quadrupole applicable to electrocardiography, *IEEE Trans. Biomed. Eng.* **BM12**, 164–168.

- 29** Gray, C. G. (1978) Simplified derivation of magnetostatic multipole expansion using scalar potential, *Am. J. Phys.* **46**, 582–583.
- 30** Gray, C. G. (1979) Magnetic multipole expansions using the scalar potential, *Am. J. Phys.* **47**, 457–459.
- 31** Gray, C. G. (1980) Definition of the magnetic quadrupole-moment, *Am. J. Phys.* **48**, 984–985.
- 32** Nolte, G. and Curio, G. (1997) On the calculation of magnetic fields based on multipole modeling of focal biological current sources, *Biophys. J.* **73**, 1253–1262.
- 33** Mosher, J. C., Leahy, R. M., Shattuck, D. W. and Baillet, S. (1999) MEG source imaging using multipolar expansions, in *Information Processing in Medical Imaging: 16th International Conference, IPMI '99*, Visegrad, Hungary, Kuba, A., Samal, M. and Todd-Pokropek, A. (eds.), Springer, Berlin/New York, pp. 15–28.
- 34** Jerbi, K., Mosher, J. C., Baillet, S. and Leahy, R. M. (2002) On MEG forward modelling using multipolar expansions, *Phys. Med. Biol.* **47**, 523–555.
- 35** Jerbi, K., Baillet, S., Mosher, J. C., Nolte, G., Garnero, L. and Leahy, R. M. (2004) Localization of realistic cortical activity in MEG using current multipoles, *NeuroImage* **22**, 779–793.
- 36** Ermer, J. J., Mosher, J. C., Baillet, S. and Leahy, R. M. (2001) Rapidly recomputable EEG forward models for realistic head shapes, *Phys. Med. Biol.* **46**, 1265–1281.
- 37** Brody, D. A. and Bradshaw, J. C. (1962) The equivalent generator components of uniform double layers, *Bull. Math. Biophys.* **24**, 183–195.
- 38** Lynn, M. S., Barnard, A. C. L. and Holt, J. H. (1967) A proposed method for the inverse problem in electrocardiology, *Biophys. J.* **7**, 925–945.
- 39** Holt, J. H., Barnard, A. C. L. and Lynn, M. S. (1969) A study of the human heart as a multiple dipole electrical source; II. Diagnosis and quantitation of left ventricular hypertrophy, *Circulation* **40**, 697–718.
- 40** Holt, J. H. and Barnard, A. C. L. (1973) Body surface potentials in ventricular hypertrophy – analysis using a multi-pole dipole model of the heart, in *Computer application on ECG and VCG analysis, Proceedings of the 2nd IFIP TC-4 Working Conference on Computer Application on ECG and VCG Analysis*, North Holland, Amsterdam, pp. 333–349.
- 41** Wikswo, J. P., Jr., Gevins, A. and Williamson, S. J. (1993) The future of the EEG and MEG, *Electroencephalogr. Clin. Neurophysiol.* **87**, 1–9.
- 42** Hillebrand, A. and Barnes, G. R. (2002) A quantitative assessment of the sensitivity of whole-head MEG to activity in the adult human cortex, *NeuroImage* **16**, 638–650.
- 43** Okada, Y., Lauritzen, M. and Nicholson, C. (1987) MEG source models and physiology, *Phys. Med. Biol.* **32**, 43–51.
- 44** Okada, Y. C., Lahteenmaki, A. and Xu, C. B. (1999) Experimental analysis of distortion of magnetoencephalography signals by the skull, *Clin. Neurophysiol.* **110**, 230–238.
- 45** Wikswo, J. P., Jr. and Roth, B. J. (1988) Magnetic determination of the spatial extent of a single cortical current source: a theoretical analysis, *Electroencephalogr. Clin. Neurophysiol.* **69**, 266–276.
- 46** Bradshaw, L. A. and Wikswo, J. P. (2001) Spatial filter approach for evaluation of the surface Laplacian of the electroencephalogram and magnetoencephalogram, *Ann. Biomed. Eng.* **29**, 202–213.
- 47** Bradshaw, L. A., Wijesinghe, R. S. and Wikswo, J. P. (2001) Spatial filter approach for comparison of the forward and inverse problems of electroencephalography and magnetoencephalography, *Ann. Biomed. Eng.* **29**, 214–226.
- 48** Tan, S., Roth, B. J. and Wikswo, J. P., Jr. (1990) The magnetic field of cortical current sources: the application of a spatial filtering model to the forward and inverse problems, *Electroencephalogr. Clin. Neurophysiol.* **76**, 73–85.
- 49** Nolte, G. and Curio, G. (2000) Current multipole expansion to estimate lateral extent of neuronal activity: a theoretical analysis, *IEEE Trans. Biomed. Eng.* **47**, 1347–1355.
- 50** Allescher, H. D., Abraham-Fuchs, K., Dunkel, R. E. and Classen, M. (1998)

- Biomagnetic 3-dimensional spatial and temporal characterization of electrical activity of human stomach, *Dig. Dis. Sci.* **43**, 683–693.
- 51** Irimia, A. and Bradshaw, L. A. (2003) Theoretical ellipsoidal model of gastric electrical control activity propagation, *Phys. Rev. E* **68**, 051905.
- 52** Irimia, A., Beauchamp, J. J. and Bradshaw, L. A. (2004) Theoretical and computational multiple regression study of gastric electrical activity using dipole tracing from magnetic field measurements, *J. Biol. Phys.* **30**, 239–259.
- 53** Irimia, A. and Bradshaw, L. A. (2004) Theoretical and computational methods for the noninvasive detection of gastric electrical source coupling, *Phys. Rev. E* **69**, 051920.
- 54** Dallas, W. J. (1985) Fourier space solution to the magnetostatic imaging problem, *Appl. Opt.* **24**, 4543–4546.
- 55** Kullmann, W. H. and Dallas, W. J. (1987) Fourier imaging of electrical currents in the human brain from their magnetic fields, *IEEE Trans. Biomed. Eng.* **BME34**, 837–842.
- 56** Roth, B. J., Sepulveda, N. G. and Wikswo, J. P., Jr. (1989) Using a magnetometer to image a two-dimensional current distribution, *J. Appl. Phys.* **65**, 361–372.
- 57** Alvarez, R. E. (1990) Biomagnetic Fourier imaging, *IEEE Trans. Med. Imaging* **9**, 299–304.
- 58** Smith, W. E., Dallas, W. J., Kullmann, W. H. and Schlitt, H. A. (1990) Linear estimation theory applied to the reconstruction of a 3-D vector current distribution, *Appl. Opt.* **29**, 658–667.
- 59** Alvarez, R. E. (1991) Filter functions for computing multipole moments from the magnetic-field normal to a plane, *IEEE Trans. Med. Imaging* **10**, 375–381.
- 60** Staton, D. J., Rousakov, S. V. and Wikswo, J. P., Jr. (1996) Conductivity imaging in plates using current injection tomography, *Rev. Prog. Quant. Non-destr. Eval.* **15**, 845–851.
- 61** Wakai, R. T. and Lutter, W. J. (2002) Matched-filter template generation via spatial filtering: application to fetal biomagnetic recordings, *IEEE Trans. Biomed. Eng.* **49**, 1214–1217.
- 62** Bradshaw, L. A., Richards, W. O. and Wikswo, J. P., Jr. (2001) Volume conductor effects on the spatial resolution of magnetic fields and electric potentials from gastrointestinal electrical activity, *Med. Biol. Eng. Comp.* **39**, 35–43.
- 63** Chatraphorn, S., Fleet, E. F. and Wellstood, F. C. (1999) High-Tc scanning SQUID microscopy: imaging integrated circuits beyond the standard near-field limit, *Bull. APS* **44**, 1554.
- 64** Chatraphorn, S., Fleet, E. F., Wellstood, F. C., Knauss, L. A. and Eiles, T. M. (2000) Scanning SQUID microscopy of integrated circuits, *Appl. Phys. Lett.* **76**, 2304–2306.
- 65** Staton, D. J., Friedman, R. N. and Wikswo, J. P., Jr. (1993) High-resolution SQUID imaging of octupolar currents in anisotropic cardiac tissue, *IEEE Trans. Appl. Supercond.* **3**, 1934–1936.
- 66** Staton, D. J. (1994) Magnetic imaging of applied and propagating action current in cardiac tissue slices: determination of anisotropic electrical conductivities in a two dimensional bidomain, Ph.D. Dissertation, Vanderbilt University.
- 67** Wikswo, J. P., Jr. (1994) The complexities of cardiac cables: virtual electrode effects, *Biophys. J.* **66**, 551–553.
- 68** Wikswo, J. P., Jr. (1978) Optimization of SQUID differential magnetometers, *AIP Conf. Proc.* **44**, 145–149.
- 69** Wikswo, J. P., Jr. (1988) High-resolution measurements of biomagnetic fields, in *Advances in Cryogenic Engineering*, Fast, R. W. (ed.), Plenum, pp. 107–116.
- 70** Wikswo, J. P., Jr. (1996) High-resolution magnetic imaging: cellular action currents and other applications, in *SQUID Sensors: Fundamentals, Fabrication and Applications*, Weinstock, H. (ed.), Kluwer, The Netherlands, pp. 307–360.
- 71** Roth, B. J. and Wikswo, J. P., Jr. (1990) Apodized pickup coils for improved spatial resolution of SQUID magnetometers, *Rev. Sci. Instrum.* **61**, 2439–2448.
- 72** Poularikas, A. D. (1996) *The Transforms and Applications Handbook*, CRC Press, Boca Raton, FL.
- 73** Abedi, A., Fellenstein, J., Lucas, A. J. and Wikswo, J. P., Jr. (1999) A superconducting quantum interference device

- magnetometer system for quantitative analysis and imaging of hidden corrosion activity in aircraft aluminum structures, *Rev. Sci. Instrum.* **70**, 4640–4651.
- 74** Bradshaw, L.A. (1995) Measurement and modeling of gastrointestinal bioelectric and biomagnetic fields, Ph.D. Dissertation, Vanderbilt University.
- 75** Blakely, R. J. (1995) *Potential Theory in Gravity and Magnetic Applications*, Cambridge University Press, New York.
- 76** Fedi, M. and Florio, G. (2002) A stable downward continuation by using the ISVD method, *Geophys. J. Int.* **151**, 146–156.
- 77** Pawłowski, R. S. (1995) Preferential continuation for potential-field anomaly enhancement, *Geophysics* **60**, 390–398.
- 78** Tan, S. (1992) Linear system imaging and its applications to magnetic measurements by SQUID magnetometers, Ph.D. Dissertation, Vanderbilt University.
- 79** Tan, S., Sepulveda, N. G. and Wikswo, J. P., Jr. (1995) A new finite-element approach to reconstruct a bounded and discontinuous two-dimensional current image from a magnetic field map, *J. Comput. Phys.* **122**, 150–164.
- 80** Hosaka, H. and Cohen, D. (1976) Visual determination of generators of the magnetoangiogram, *J. Electrocardiol.* **9**, 426–432.
- 81** Thomas, I. M., Freake, S. M., Swithenby, S. J. and Wikswo, J. P., Jr. (1993) A distributed quasi-static ionic current source in the 3–4 day old chicken embryo, *Phys. Med. Biol.* **38**, 1311–1328.
- 82** Barbosa, C. H., Bruno, A. C., Scavarda, L. F., Lima, E. A., Ribeiro, P. C. and Kelber, C. (1995) Image-processing techniques for NDE SQUID systems, *IEEE Trans. Appl. Supercond.* **5**, 2478–2481.
- 83** Oh, S., Ramon, C., Marks, R. J., II, Nelson, A. C. and Meyer, M. G. (1993) Resolution enhancement of biomagnetic images using the method of alternating projections, *IEEE Trans. Biomed. Eng.* **40**, 323–328.
- 84** Li, X., Cadzow, J.A. and Wikswo, J.P. (1996) Reconstruction of electric current density distribution from magnetometer measurements (unpublished).
- 85** Lima, E. A., Bruno, A. C. and Szczupak, J. (1999) Two-dimensional spatial frequency response of SQUID planar gradiometers, *Supercond. Sci. Technol.* **12**, 949–952.
- 86** Lima, E. A. and Bruno, A. C. (2001) Improving the detection of flaws in steel pipes using SQUID planar gradiometers, *IEEE Trans. Appl. Supercond.* **11**, 1299–1302.
- 87** Lima, E. A., Bruno, A. C. and Szczupak, J. (2002) Two-dimensional deconvolution technique to recover the original magnetic field from the flux measured by SQUID planar gradiometers, *Supercond. Sci. Technol.* **15**, 1259–1267.
- 88** Lima, E. A. and Bruno, A. C. (2002) Experimental verification of a spatial deconvolution procedure for planar gradiometer configurations, *Physica C* **368**, 100–104.
- 89** Lima, E. A. and Bruno, A. C. (2003) Spatial frequency response of conventional and non-conventional SQUID gradiometers, *IEEE Trans. Appl. Supercond.* **13**, 735–738.
- 90** Bruno, A. C., Ribeiro, P. C., von der Weid, J. P. and Symko, O. G. (1986) Discrete spatial filtering with SQUID gradiometers in biomagnetism, *J. Appl. Phys.* **59**, 2584–2589.
- 91** Bruno, A.C., Guida, A.V. and Ribeiro, P.C. (1987) Planar gradiometer input signal recovery using a Fourier technique, in *Biomagnetism '87, 6th Int. Conf.*, Tokyo, pp. 454–457.
- 92** Ribeiro, P. C., Bruno, A. C., Paulsen, C. C. and Symko, O. G. (1987) Spatial Fourier transform method for evaluating SQUID gradiometers, *Rev. Sci. Instrum.* **58**, 1510–1513.
- 93** Bruno, A. C. and Ribeiro, P. C. (1989) Spatial deconvolution algorithm for superconducting planar gradiometer arrays, *IEEE Trans. Magn.* **25**, 1219–1222.
- 94** Alvarez, R. E. (1991) Filter functions for computing multipole moments from the magnetic-field normal to a plane, *IEEE Trans. Med. Imaging* **10**, 375–381.
- 95** Jooss, C., Warthmann, R., Forkl, A. and Kronmuller, H. (1998) High-resolution magneto-optical imaging of critical cur-

- rents in $\text{YBa}_2\text{Cu}_3\text{O}_{7-\delta}$ thin films, *Physica C* **299**, 215–230.
- 96** Laviano, F., Botta, D., Chioldoni, A., Gerbaldo, R., Ghigo, G., Gozzelino, L., Zanella, S. and Mezzetti, E. (2003) An improved method for quantitative magneto-optical analysis of superconductors, *Supercond. Sci. Technol.* **16**, 71–79.
- 97** Chatraphorn, S., Fleet, E. F. and Wellstood, F. C. (2002) Relationship between spatial resolution and noise in scanning superconducting quantum interference device microscopy, *J. Appl. Phys.* **92**, 4731–4740.
- 98** Press, W. H., Flannery, B. P. and Teukolsky, S. A. (1992) Singular value decomposition, in *Numerical Recipes in FORTRAN: The Art of Scientific Computing*. Press, W. H. (ed.), Cambridge University Press, Cambridge, UK/New York, pp. 51–63.
- 99** Golub, G. H. and Van Loan, C. F. (1996) *Matrix Computations*, Johns Hopkins University Press, Baltimore, MD.
- 100** Benzing, W., Scherer, T. and Jutzi, W. (1993) Inversion calculation of two dimensional current distributions from their magnetic field, *IEEE Trans. Appl. Supercond.* **3**, 1902–1905.
- 101** Ramon, C., Meyer, M. G., Nelson, A. C., Spelman, F. A. and Lampert, J. (1993) Simulation studies of biomagnetic computed tomography, *IEEE Trans. Biomed. Eng.* **40**, 317–322.
- 102** Feldmann, D. M. (2004) Resolution of two-dimensional currents in superconductors from a two-dimensional magnetic field measurement by the method of regularization, *Phys. Rev. B* **69**, 144515.
- 103** Brandt, E. H. (1995) Square and rectangular thin superconductors in a transverse magnetic-field, *Phys. Rev. Lett.* **74**, 3025–3028.
- 104** Wijngaarden, R. J., Heeck, K., Spoelder, H. J. W., Surdeanu, R. and Griessen, R. (1998) Fast determination of 2D current patterns in flat conductors from measurement of their magnetic field, *Physica C* **295**, 177–185.
- 105** Soika, E. and Moller, H. J. (2004) Magnetic field measurements and numerical simulation of the current distribution in the emitter region of solar cells, *J. Magn. Magn. Mater.* **272–276**, 667–668.
- 106** Tripp, J. H. (1983) Physical concepts and mathematical models, in *Biomagnetism: An Interdisciplinary Approach*, Williamson, S. J. (ed.), Plenum, New York, pp. 101–138.
- 107** Jenkins, J., Wu, D. and Arzbaecher, R. (1976) Use of the atrial electrogram in computer detection and classification of cardiac arrhythmias, in *Proceedings of the 29th ACEMB Conference*, Boston, MA, p. 128.
- 108** Hurley, D. C., Ma, Y. P., Tan, S. and Wikswo, J. P., Jr. (1993) Imaging of small defects in nonmagnetic tubing using a SQUID magnetometer, *Res. Nondestr. Eval.* **5**, 1–29.
- 109** Hurley, D. C., Ma, Y. P., Tan, S. and Wikswo, J. P., Jr. (1993) A comparison of SQUID imaging techniques for small defects in nonmagnetic tubes, *Rev. Prog. Quant. Nondestr. Eval.* **12**, 633–640.
- 110** Ioannides, A. A., Bolton, J. P. R. and Clarke, C. J. S. (1990) Continuous probabilistic solutions to the biomagnetic inverse problem, *Inverse Problems* **6**, 523–542.
- 111** Haacke, E. M., Liang, Z. P. and Izen, S. H. (1989) Constrained reconstruction – a superresolution, optimal signal-to-noise alternative to the Fourier-transform in magnetic-resonance imaging, *Med. Phys.* **16**, 388–397.
- 112** Seger, M., Fischer, G., Modre, R., Messnarz, B., Hanser, F. and Tilg, B. (2005) Lead field computation for the electrocardiographic inverse problem – finite elements versus boundary elements, *Comp. Meth. Programs Biomed.* **77**, 241–252.
- 113** Wikswo, J. P., Jr., Sepulveda, N. G., Ma, Y. P., Henry, W. P., Crum, D. B. and Stanton, D. J. (1993) An improved method for magnetic identification and localization of cracks in conductors, *J. Nondestr. Eval.* **12**, 109–119.
- 114** Sepulveda, N. G. and Wikswo, J. P. (1994) Differential operators and their applications to magnetic measurements using SQUID magnetometers (unpublished).
- 115** Thome, D. K., Fitzpatrick, G. L. and Skaugset, R. L. (1996) Aircraft corrosion

- and crack inspection using advanced magneto-optic imaging technology, *Proc. SPIE* **2945**, 365–373.
- 116** Fitzpatrick, G. L., Thome, D. K., Skaugset, R. L., Shih, E. Y. C. and Shih, W. C. L. (1993) Magnetooptic eddy-current imaging of aging aircraft – a new NDI technique, *Mater. Eval.* **51**, 1402–1407.
- 117** Ma, Y. P. and Wikswo, J. P., Jr. (1994) SQUID eddy current techniques for detection of second layer flaws, *Rev. Prog. Quant. Nondestruct. Eval.* **13**, 303–309.
- 118** Ma, Y. P. and Wikswo, J. P., Jr. (1995) Techniques for depth-selective, low-frequency eddy current analysis for SQUID-based nondestructive testing, *J. Nondestruct. Eval.* **14**, 149–167.
- 119** Ma, Y. P. and Wikswo, J. P., Jr. (1996) Depth-selective SQUID eddy current techniques for second layer flaw detection, *Rev. Prog. Quant. Nondestruct. Eval.* **15**, 401–408.
- 120** Ma, Y. P. and Wikswo, J. P., Jr. (1998) SQUID magnetometers for depth-selective, oriented eddy current imaging, *Rev. Prog. Quant. Nondestruct. Eval.* **17A**, 1067–1074.
- 121** Ioannides, A. A. and Grimes, D. I. F. (1987) Line current source reconstructions from magnetic-flux measurements, *Phys. Med. Biol.* **32**, 146.
- 122** McKirdy, D. M., Cochran, A. and Donaldson, G. B. (1996) Forward and inverse processing in electromagnetic NDE using SQUIDs, *Rev. Prog. Quant. Nondestruct. Eval.* **15A**, 347–354.
- 123** Nolte, G. and Curio, G. (1999) Perturbative analytical solutions of the electric forward problem for realistic volume conductors, *J. Appl. Phys.* **86**, 2800–2811.
- 124** Cruse, T. A., Ewing, A. P. and Wikswo, J. P., Jr. (1999) Green's function formulation of Laplace's equation for electromagnetic crack detection, *Computat. Mech.* **23**, 420–429.
- 125** Ewing, A. P., Cruse, T. A. and Wikswo, J. P., Jr. (1998) A SQUID NDE measurement model using BEM, *Rev. Prog. Quant. Nondestruct. Eval.* **17A**, 1083–1090.
- 126** Ewing, A. P., Barbosa, C. H., Cruse, T. A., Bruno, A. C. and Wikswo, J. P., Jr. (1998) Boundary integral equations for modeling arbitrary flaw geometries in electric current injection NDE, *Rev. Prog. Quant. Nondestruct. Eval.* **17A**, 1011–1015.
- 127** Lutkenhoner, B. and Menendez, R. G. D. P. (1997) The resolution-field concept, *Electroencephalogr. Clin. Neurophysiol.* **102**, 326–334.
- 128** Lutkenhoner, B. (2003) Magnetoencephalography and its Achilles' heel, *J. Physiol. Paris* **97**, 641–658.
- 129** Lines, L. R. and Treitel, S. (1984) Tutorial, a review of least-squares inversion and its application to geophysical problems, *Geophys. Prospect.* **32**, 159–186.
- 130** Oldenburg, D. (1990) Inversion of electromagnetic data: an overview of new techniques, *Surv. Geophys.* **11**, 231–270.
- 131** Marcuello-Pascual, A., Kaikkonen, P. and Pous, J. (1992) 2-D inversion of MT data with a variable model geometry, *Geophys. J. Int.* **110**, 297–304.
- 132** Parker, R. L. (1977) Understanding inverse theory, *Annu. Rev. Earth Planetary Sci.* **5**, 35–64.
- 133** Reitz, J. R. and Milford, F. J. (1967) *Foundations of Electromagnetic Theory*, Addison-Wesley, Reading, MA.
- 134** Beardsley, I. A. (1989) Reconstruction of the magnetization in a thin film by a combination of Lorentz microscopy and field measurements, *IEEE Trans. Magn.* **25**, 671–677.
- 135** Tan, S., Ma, Y. P., Thomas, I. M. and Wikswo, J. P., Jr. (1996) Reconstruction of two-dimensional magnetization and susceptibility distributions from the magnetic field of soft magnetic materials, *IEEE Trans. Magn.* **32**, 230–234.
- 136** Tan, S., Ma, Y. P., Thomas, I. M. and Wikswo, J. P., Jr. (1993) High resolution SQUID imaging of current and magnetization distributions, *IEEE Trans. Appl. Supercond.* **3**, 1945–1948.
- 137** Thomas, I. M., Ma, Y. P. and Wikswo, J. P., Jr. (1993) SQUID NDE: detection of surface flaws by magnetic decoration, *IEEE Trans. Appl. Supercond.* **3**, 1949–1952.
- 138** Thomas, I. M., Ma, Y. P., Tan, S. and Wikswo, J. P., Jr. (1993) Spatial resolution and sensitivity of magnetic susceptibility imaging, *IEEE Trans. Appl. Supercond.* **3**, 1937–1940.

- 139** Thomas, I. M., Moyer, T. C. and Wikswo, J. P., Jr. (1992) High resolution magnetic susceptibility imaging of geological thin sections: pilot study of a pyroclastic sample from the Bishop Tuff, California, U.S.A., *Geophys. Res. Lett.* **19**, 2139–2142.
- 140** Weiss, B. P., Baudenbacher, F. J., Wikswo, J. P. and Kirschvink, J. L. (2001) Magnetic microscopy promises a leap in sensitivity and resolution, *EoS Trans. AGU* **82**, 513–518.
- 141** Wikswo, J. P., Jr., Ma, Y. P., Sepulveda, N. G., Tan, S., Thomas, I. M. and Launder, A. (1993) Magnetic susceptibility imaging for nondestructive evaluation, *IEEE Trans. Appl. Supercond.* **3**, 1995–2002.
- 142** Ribeiro, E. P., Wikswo, J. P., Jr., Ribeiro, P. C. and Szczupak, J. (1996) Magnetic susceptibility tomography with nonuniform field, in *Biomag 96: Proceedings of the 10th Int. Conf. on Biomagnetism*, Aine, C. J., Okada, Y. C., Stroink, G. and Switzenby, S. J. (eds.), Springer, New York, pp. 671–674.
- 143** Ribeiro, E.P., Wikswo, J.P., Jr., Ribeiro, P.C. and Szczupak, J. (1997) Magnetic susceptibility tomography with filtered singular values, *Med. Biol. Eng. Comp.* **35** (Suppl. I), 14.
- 144** Ribeiro, E.P. (1996) Magnetic susceptibility tomography with superconducting magnetometer SQUID, Ph.D. Dissertation, PUC-Rio, Rio de Janeiro.
- 145** Sepulveda, N. G., Thomas, I. M. and Wikswo, J. P., Jr. (1994) Magnetic susceptibility tomography for three-dimensional imaging of diamagnetic and paramagnetic objects, *IEEE Trans. Magn.* **30**, 5062–5069.
- 146** Thomas, I.M., Sepulveda, N.G. and Wikswo, J.P., Jr. (1993) Magnetic susceptibility tomography: a new modality for three-dimensional biomedical imaging, in *Proceedings of the 15th Annual International Conference of the IEEE Engineering in Medicine and Biology Society, Engineering Solutions to Current Health Care Problems*, Vol. 15, Part I, San Diego, CA, pp. 94–95.
- 147** Wikswo, J. P., Jr., Sepulveda, N. G. and Thomas, I. M. (1995) Three-dimensional biomagnetic imaging with magnetic susceptibility tomography, in *Biomagnetism: Fundamental Research and Clinical Applications: Proceedings of the 9th International Conference on Biomagnetism*, Baumgartner, C., Deecke, L., Stroink, G. and Williamson, S. J. (eds.), IOS Press, Burk, VA, pp. 780–784.
- 148** Jenks, W. G., Sadeghi, S. S. H. and Wikswo, J. P., Jr. (1997) SQUIDs for nondestructive evaluation, *J. Phys. D: Appl. Phys.* **30**, 293–323.
- 149** Jenks, W.G., Ma, Y.P., Parente Ribeiro, E. and Wikswo, J.P. (1997) SQUID NDE of composite materials with magnetic tracers (unpublished).
- 150** Thomas, I. M. and Friedman, R. N. (1993) Magnetic susceptibility imaging of macrophage activity in rat liver using intravenous superparamagnetic tracers, in *Proceedings of the Annual International Conference of the IEEE Engineering in Medicine and Biology Society*, Szeto, A. Y. J. and Rangayyan, R. M. (eds.), IEEE, San Diego, CA, pp. 503–504.
- 151** Thomas, I. M. and Friedman, R. N. (1995) Study of macrophage activity in rat liver using intravenous superparamagnetic tracers, in *Biomagnetism: Fundamental Research and Clinical Applications*, Baumgartner, C. (ed.), Elsevier Science, pp. 809–813.
- 152** Weisskoff, R. M. and Kiihne, S. (1992) MRI susceptometry – image-based measurement of absolute susceptibility of MR contrast agents and human blood, *Magn. Reson. Med.* **24**, 375–383.
- 153** Yamada, N., Imakita, S., Sakuma, T., Nishimura, Y., Yamada, Y., Naito, H., Nishimura, T. and Takamiya, M. (1990) Evaluation of the susceptibility effect on the phase images of a simple gradient echo, *Radiology* **175**, 561–565.
- 154** Weis, J., Nilsson, S., Ericsson, A., Wikstrom, M., Sperber, G. O. and Hemmingsson, A. (1994) Measurement of magnetic-susceptibility and MR contrast agent concentration, *Magn. Reson. Imaging* **12**, 859–864.
- 155** Chu, S. C. K., Xu, Y., Balschi, J. A. and Springer, C. S. (1990) Bulk magnetic-susceptibility shifts in NMR-studies of compartmentalized samples – use of paramagnetic reagents, *Magn. Reson. Med.* **13**, 239–262.

- 156** Farrell, D. E. (1993) Assessment of iron in human tissue: the magnetic biopsy, in *Biomagnetism: An Interdisciplinary Approach*, Williamson, S. J. (ed.), Plenum Press, New York, pp. 483–499.
- 157** Brittenham, G. M., Sheth, S., Allen, C. J. and Farrell, D. E. (2001) Noninvasive methods for quantitative assessment of transfusional iron overload in sickle cell disease, *Semin. Hematol.* **38**, 37–56.
- 158** Paulson, D. N., Engelhardt, R., Fischer, R. and Heinrich, H. C. (1989) The Hamburg biosusceptometer for liver iron quantification, in *Advances in Biomagnetism*, Williamson, S. J., Hoke, M., Stroink, G. and Kotani, M. (eds.), Plenum Press, New York, pp. 497–500.
- 159** Ribeiro, E.P., Wikswo, J.P., Jr., Ribeiro, P.C., Monteiro, E.C., Bruno, A.C. and Szczupak, J. (1996) Tomografia de susceptibilidade magnética com campo gradiente, in *III National Forum on Science and Technology in Health*, Campos Do Jordao, SP, Brazil.
- 160** Wang, Z. Y. J., Li, S. C. and Haselgrove, J. C. (1999) Magnetic resonance imaging measurement of volume magnetic susceptibility using a boundary condition, *J. Magn. Reson.* **140**, 477–481.
- 161** Plonsey, R. (1972) Capability and limitations of electrocardiography and magnetocardiography, *IEEE Trans. Biomed. Eng.* **BM19**, 239–244.
- 162** Rush, S. (1975) Independence of magnetic and electric body surface recordings, *IEEE Trans. Biomed. Eng.* **BME22**, 157–167.
- 163** Plonsey, R. and Barr, R. C. (1982) The four-electrode resistivity technique as applied to cardiac muscle, *IEEE Trans. Biomed. Eng.* **BME29**, 541–546.
- 164** Gulrajani, R. M. (1998) *Bioelectricity and Biomagnetism*, Wiley, New York.
- 165** Koch, H. and Haberkorn, W. (2001) Magnetic field mapping of cardiac electrophysiological function, *Philos. Trans. R. Soc. London A* **359**, 1287–1298.
- 166** Corbin, L. V., II and Scher, A. M. (1977) The canine heart as an electrocardiographic generator. Dependence on cardiac cell orientation, *Circ. Res.* **41**, 58–67.
- 167** Roberts, D. E., Hersh, L. T. and Scher, A. M. (1979) Influence of cardiac fiber orientation on wavefront voltage, conduction velocity, and tissue resistivity in the dog, *Circ. Res.* **44**, 701–712.
- 168** Roberts, D. E. and Scher, A. M. (1982) Effect of tissue anisotropy on extracellular potential fields in canine myocardium in situ, *Circ. Res.* **50**, 342–351.
- 169** Plonsey, R. and Barr, R. C. (1984) Current flow patterns in two-dimensional anisotropic bisyncytia with normal and extreme conductivities, *Biophys. J.* **45**, 557–571.
- 170** Barr, R. C. and Plonsey, R. (1984) Propagation of excitation in idealized anisotropic two-dimensional tissue, *Biophys. J.* **45**, 1191–1202.
- 171** Roth, B. J., Guo, W.-Q. and Wikswo, J. P., Jr. (1988) The effects of spiral anisotropy on the electric potential and the magnetic field at the apex of the heart, *Math. Biosci.* **88**, 191–221.
- 172** Staton, D. J. and Wikswo, J. P., Jr. (1995) High-resolution imaging of magnetic fields from injected and action currents in slices of anisotropic cardiac tissue, in *Biomagnetism: Fundamental Research and Clinical Applications: Proceedings of the 9th International Conference on Biomagnetism*, Baumgartner, C., Deecke, L., Stroink, G. and Williamson, S. J. (eds.), IOS Press, Amsterdam, pp. 684–687.
- 173** Staton, D. J. and Wikswo, J. P., Jr. (1995) Magnetic imaging of currents in two-dimensional cardiac tissue: experimental and theoretical studies of electrical activity in mammalian cardiac slices, in *Biomagnetism: Fundamental Research and Clinical Applications: Proceedings of the 9th International Conference on Biomagnetism*, Baumgartner, C., Deecke, L., Stroink, G. and Williamson, S. J. (eds.), IOS Press, Amsterdam, pp. 647–651.
- 174** Baudenbacher, F., Peters, N. T., Baudenbacher, P. and Wikswo, J. P. (2002) High resolution imaging of biomagnetic fields generated by action currents in cardiac tissue using a LTS-SQUID microscope, *Physica C* **368**, 24–31.
- 175** Fong, L. E., Holzer, J. R., McBride, K., Lima, E. A., Baudenbacher, F. and Radparvar, M. (2004) High-resolution imaging of cardiac biomagnetic fields using a low-transition-temperature supercon-

- ducting quantum interference device microscope, *Appl. Phys. Lett.* **84**, 3190–3192.
- 176** Katila, T. and Karp, P. (1983) Magneto-cardiography: morphology and multipole presentations, in *Biomagnetism: An Interdisciplinary Approach*, Williamson, S. J. (ed.), Plenum Press, New York, pp. 237–263.
- 177** Wikswo, J.P., Jr., Griffin, J.C., Leifer, M.C. and Harrison, D.C. (1978) Vector magnetocardiography: the effect of the heart lung boundary, *Clin. Res.* **26**, 486a.
- 178** Uutela, K., Hamalainen, M. and Salmin, R. (1998) Global optimization in the localization of neuromagnetic sources, *IEEE Trans. Biomed. Eng.* **45**, 716–723.
- 179** Wilson, F. N., Johnston, F. D., Rosenbaum, F. F. and Barker, P. S. (1946) On Einthoven's triangle, the theory of unipolar electrocardiographic leads, and the interpretation of the precordial electrocardiogram, *Am. Heart J.* **32**, 277–310.
- 180** Wilson, F. N. and Bayley, R. H. (1950) The electric field of an eccentric dipole in a homogeneous spherical conducting medium, *Circulation* **1**, 84–92.
- 181** Gonnelli, R. S. and Agnello, M. (1987) Inverse problem solution in cardiomagnetism using a current multipole expansion of the primary sources, *Phys. Med. Biol.* **32**, 133–142.
- 182** Dossel, O. (2000) Inverse problem of electro- and magnetocardiography: review and recent progress, URL: http://www.ijbem.org/volume2/number2/doessel/paper_ijbem.htm.
- 183** VanVeen, B. D. and Buckley, K. M. (1988) Beamforming: a versatile approach to spatial filtering, *IEEE ASSP Magazine* **5**, 4–24.
- 184** Liu, T. C. and VanVeen, B. D. (1992) Multiple window based minimum variance spectrum estimation for multidimensional random-fields, *IEEE Trans. Signal Process.* **40**, 578–589.
- 185** Lacoss, R. T. (1968) Adaptive combining of wideband array data for optimal reception, *IEEE Trans. Geosci. Electron. GE* **6**, 78–86.
- 186** van Drongelen, W., Yuchtman, M., VanVeen, B. D. and van Huffelen, A. C. (1996) A spatial filtering technique to detect and localize multiple sources in the brain, *Brain Topogr.* **9**, 39–49.
- 187** Robinson, S.E. and Vrba, J. (1999) Functional neuroimaging by synthetic aperture magnetometry (SAM), in *Bio-mag98: 11th International Conference on Biomagnetism*, Sendai, Japan, Tohoku University Press, pp. 302–305.
- 188** VanVeen, B. D., van Drongelen, W., Yuchtman, M. and Suzuki, A. (1997) Localization of brain electrical activity via linearly constrained minimum variance spatial filtering, *IEEE Trans. Biomed. Eng.* **44**, 867–880.
- 189** Hillebrand, A. and Barnes, G. R. (2003) The use of anatomical constraints with MEG beamformers, *NeuroImage* **20**, 2302–2313.
- 190** Sekihara, K., Nagarajan, S. S., Poeppel, D. and Marantz, A. (2004) Performance of an MEG adaptive-beamformer source reconstruction technique in the presence of additive low-rank interference, *IEEE Trans. Biomed. Eng.* **51**, 90–99.
- 191** Schimpf, P. H., Liu, H. S., Ramon, C. and Haueisen, J. (2005) Efficient electromagnetic source imaging with adaptive standardized LORETA/FOCUSS, *IEEE Trans. Biomed. Eng.* **52**, 901–908.
- 192** Hamalainen, M. S. and Ilmoniemi, R. J. (1994) Interpreting magnetic-fields of the brain – minimum norm estimates, *Med. Biol. Eng. Comp.* **32**, 35–42.
- 193** Haan, H., Streb, J., Bien, S. and Rosler, F. (2000) Individual cortical current density reconstructions of the semantic N400 effect: using a generalized minimum norm model with different constraints (L1 and L2 norm), *Hum. Brain Mapp.* **11**, 178–192.
- 194** Hauk, O. (2004) Keep it simple: a case for using classical minimum norm estimation in the analysis of EEG and MEG data, *NeuroImage* **21**, 1612–1621.
- 195** Hamalainen, M., Hari, R., Ilmoniemi, R. J., Knuutila, J. and Lounasmaa, O. V. (1993) Magnetoencephalography – theory, instrumentation, and applications to noninvasive studies of the working human brain, *Rev. Mod. Phys.* **65**, 413–497.
- 196** Uutela, K., Hamalainen, M. and Somersalo, E. (1999) Visualization of magnetoencephalographic data using mini-

- mum current estimates, *NeuroImage* **10**, 173–180.
- 197** Gorodnitsky, I. F., George, J. S. and Rao, B. D. (1995) Neuromagnetic source imaging with FOCUSS – a recursive weighted minimum norm algorithm, *Electroencephalogr. Clin. Neurophysiol.* **95**, 231–251.
- 198** Gorodnitsky, I. F. and Rao, B. D. (1997) Sparse signal reconstruction from limited data using FOCUSS: a re-weighted minimum norm algorithm, *IEEE Trans. Signal Process.* **45**, 600–616.
- 199** Schmidt, R. O. (1986) Multiple emitter location and signal parameter-estimation, *IEEE Trans. Antenn. Propag.* **AP-34**, 276–280.
- 200** Mosher, J. C., Lewis, P. S. and Leahy, R. M. (1992) Multiple dipole modeling and localization from spatio-temporal MEG data, *IEEE Trans. Biomed. Eng.* **39**, 541–557.
- 201** Mosher, J. C. and Leahy, R. M. (1998) Recursive MUSIC: a framework for EEG and MEG source localization, *IEEE Trans. Biomed. Eng.* **45**, 1342–1354.
- 202** Chen, W. G., Wong, K. M. and Reilly, J. P. (1991) Detection of the number of signals – a predicted eigen-threshold approach, *IEEE Trans. Signal Process.* **39**, 1088–1098.
- 203** Maier, J., Dagnelie, G., Spekreijse, H. and Vandijk, B. W. (1987) Principal components-analysis for source localization of veps in man, *Vision Res.* **27**, 165–177.
- 204** Achim, A., Richer, F. and Saint-Hilaire, J. M. (1988) Methods for separating temporally overlapping sources of neu-roelectric data, *Brain Topogr.* **1**, 22–28.
- 205** Mocks, J. and Verleger, R. (1986) Principal component analysis of event-related potentials – a note on misallocation of variance, *Electroencephalogr. Clin. Neurophysiol.* **65**, 393–398.
- 206** Wood, C. C. and Mccarthy, G. (1984) Principal component analysis of event-related potentials – simulation studies demonstrate misallocation of variance across components, *Electroencephalogr. Clin. Neurophysiol.* **59**, 249–260.
- 207** Jutten, C. and Herault, J. (1991) Blind separation of sources: 1. An adaptive algorithm based on neuromimetic architecture, *Signal Process.* **24**, 1–10.
- 208** Comon, P. (1994) Independent component analysis, a new concept?, *Signal Process.* **36**, 287–314.
- 209** Tang, A. C., Pearlmutter, B. A., Malaszenko, N. A., Phung, D. B. and Reeb, B. C. (2002) Independent components of magnetoencephalography: localization, *Neural Comput.* **14**, 1827–1858.
- 210** Bell, A. J. and Sejnowski, T. J. (1995) An information maximization approach to blind separation and blind deconvolution, *Neural Comput.* **7**, 1129–1159.
- 211** Hyvärinen, A. (1999) Survey on independent component analysis, *Neural Comput. Surv.* **2**, 94–128.
- 212** Stone, J. V. (2002) Independent component analysis: an introduction, *Trends Cognitive Sci.* **6**, 59–64.
- 213** Zhukov, L., Weinstein, D. and Johnson, C. (2000) Independent component analysis for EEG source localization – an algorithm that reduces the complexity of localizing multiple neural sources, *IEEE Eng. Med. Biol. Magazine* **19**, 87–96.
- 214** Makeig, S., Jung, T. P., Bell, A. J., Ghahremani, D. and Sejnowski, T. J. (1997) Blind separation of auditory event-related brain responses into independent components, *Proc. Nat. Acad. Sci. USA* **94**, 10979–10984.
- 215** Vigario, R. N. (1997) Extraction of ocular artefacts from EEG using independent component analysis, *Electroencephalogr. Clin. Neurophysiol.* **103**, 395–404.
- 216** Vigario, R., Sarela, J., Jousmaki, V., Hamalainen, M. and Oja, E. (2000) Independent component approach to the analysis of EEG and MEG recordings, *IEEE Trans. Biomed. Eng.* **47**, 589–593.
- 217** Amari, S. and Cardoso, J. F. (1997) Blind source separation – semiparametric statistical approach, *IEEE Trans. Signal Process.* **45**, 2692–2700.
- 218** Ikeda, S. and Toyama, K. (2000) Independent component analysis for noisy data – MEG data analysis, *Neural Networks* **13**, 1063–1074.
- 219** Uusitalo, M. A. and Ilmoniemi, R. J. (1997) Signal-space projection method for separating MEG or EEG into compo-

- nents, *Med. Biol. Eng. Comp.* **35**, 135–140.
- 220** Ilmoniemi, R. (1997) Method and apparatus for separating the different components of evoked response and spontaneous activity brain signals as well as of signals measured from the heart, US Patent 5655534, PCT/F193/00504.
- 221** Miettinen, M. (1992) Magnetic measurements of visually evoked responses, M.Sc. Thesis, Helsinki University of Technology.
- 222** Nolte, G. and Curio, G. (1999) The effect of artifact rejection by signal-space projection on source localization accuracy in MEG measurements, *IEEE Trans. Biomed. Eng.* **46**, 400–408.
- 223** Nolte, G. and Hamalainen, M. S. (2001) Partial signal space projection for artefact removal in MEG measurements: a theoretical analysis, *Phys. Med. Biol.* **46**, 2873–2887.
- 224** Huotilainen, M., Ilmoniemi, R. J., Tiitinen, H., Lavikainen, J., Alho, K., Kajola, M., Simola, M. and Naatanen, R. (1993) Eye-blink removal for multichannel MEG measurements, in *Recent Advances in Biomagnetism: 9th International Conference on Biomagnetism*, Deecke, L., Baumgartner, C., Stroink, G. and Williamson, S. J. (eds.), Vienna, Austria, pp. 209–210.
- 225** Vrba, J., Robinson, S. E., McCubbin, J., Lowery, C. L., Eswaran, H., Wilson, J. D., Murphy, P. and Preissl, H. (2004) Fetal MEG redistribution by projection operators, *IEEE Trans. Biomed. Eng.* **51**, 1207–1218.
- 226** Hamalainen, M. S. (1995) Functional localization based on measurements with a whole-head magnetometer system, *Brain Topogr.* **7**, 283–289.
- 227** Tesche, C. D., Uusitalo, M. A., Ilmoniemi, R. J., Huotilainen, M., Kajola, M. and Salonen, O. (1995) Signal-space projections of MEG data characterize both distributed and well-localized neuronal sources, *Electroencephalogr. Clin. Neurophysiol.* **95**, 189–200.
- 228** Pascual-Marqui, R. D., Michel, C. M. and Lehmann, D. (1994) Low-resolution electromagnetic tomography – a new method for localizing electrical-activity in the brain, *Int. J. Psychophysiol.* **18**, 49–65.
- 229** Lantz, G., Michel, C. M., Pascual-Marqui, R. D., Spinelli, L., Seeck, M., Seri, S., Landis, T. and Rosen, I. (1997) Extracranial localization of intracranial interictal epileptiform activity using LOR-ETA (low resolution electromagnetic tomography), *Electroencephalogr. Clin. Neurophysiol.* **102**, 414–422.
- 230** Anderer, P., Pascual-Marqui, R. D., Semlitsch, H. V. and Saletu, B. (1998) Differential effects of normal aging on sources of standard N1, target N1 and target P300 auditory event-related brain potentials revealed by low resolution electromagnetic tomography (LORETA), *Electroencephalogr. Clin. Neurophysiol./ Evoked Potent.* **108**, 160–174.
- 231** Pascual-Marqui, R. D. (2002) Standardized low-resolution brain electromagnetic tomography (sLORETA): technical details, *Methods Findings Exp. Clin. Pharmacol.* **24**, 5–12.
- 232** Wagner, M., Fuchs, M. and Kastner, J. (2004) Evaluation of sLORETA in the presence of noise and multiple sources, *Brain Topogr.* **16**, 277–280.
- 233** Clarke, C. J. S. and Janday, B. S. (1989) The solution of the biomagnetic inverse problem by maximum statistical entropy, *Inverse Problems* **5**, 483–500.
- 234** Amblard, U., Lapalme, E. and Lina, J. M. (2004) Biomagnetic source detection by maximum entropy and graphical models, *IEEE Trans. Biomed. Eng.* **51**, 427–442.
- 235** Greenblatt, R. E. (1993) Probabilistic reconstruction of multiple sources in the bioelectromagnetic inverse problem, *Inverse Problems* **9**, 271–284.
- 236** Gross, J., Ioannides, A. A., Dammers, J., Maess, B., Friederici, A. D. and Muller-Gartner, H. W. (1998) Magnetic field tomography analysis of continuous speech, *Brain Topogr.* **10**, 273–281.
- 237** Phillips, J. W., Leahy, R. M., Mosher, J. C. and Timsari, B. (1997) Imaging neural activity using MEG and EEG, *IEEE Eng. Med. Biol.* **16**, 34–42.
- 238** Baillet, S. and Garnero, L. (1997) A Bayesian approach to introducing anatomical priors in the EEG/MEG

- inverse problem, *IEEE Trans. Biomed. Eng.* **44**, 374–385.
- 239** Mosher, J.C., Baillet, S. and Leahy, R.M. (2003) Equivalence of linear approaches in bioelectromagnetic inverse solutions, in *IEEE Workshop on Statistical Signal Processing*, St. Louis, MO, pp. 294–297.
- 240** Wikswo, J. P., Jr. (1995) SQUID magnetometers for biomagnetism and non-destructive testing: important questions and initial answers, *IEEE Trans. Appl. Supercond.* **5**, 74–120.
- 241** Wikswo, J. P., Jr. (2000) Applications of SQUID magnetometers to biomagnetism and nondestructive evaluation, in *Applications of Superconductivity*, Weinstock, H. (ed.), Kluwer Netherlands, pp. 139–228.
- 242** Kominis, I. K., Kornack, T. W., Allred, J. C. and Romalis, M. V. (2003) A sub-femtotesla multichannel atomic magnetometer, *Nature* **422**, 596–599.
- 243** Wikswo, J. P., Jr. (1990) Biomagnetic sources and their models, in *Advances in Biomagnetism*, Williamson, S. J. (ed.), Plenum Press, New York, pp. 1–18.
- 244** Wikswo, J. P., Jr., van Egeraat, J. M., Ma, Y. P., Sepulveda, N. G., Staton, D. J., Tan, S. and Wijesinghe, R. S. (1990) Instrumentation and techniques for high-resolution magnetic imaging, *Proc. SPIE* **1351**, 438–470.
- 245** Mall, F. P. (1911) On the muscular architecture of the ventricles of the human heart, *Am. J. Anat.* **11**, 211–266.

11

Biomagnetism

Jiri Vrba, Jukka Nenonen and Lutz Trahms

- 11.1 Introduction 271
- 11.2 Magnetoencephalography 274
 - 11.2.1 Introduction 274
 - 11.2.2 MEG Signals 276
 - 11.2.3 Whole-Cortex MEG Systems 279
 - 11.2.3.1 Preface 279
 - 11.2.3.2 MEG System Description 279
 - 11.2.3.3 MEG and EEG 284
 - 11.2.3.4 MEG Peripherals 286
 - 11.2.4 Sensor Types for MEG 288
 - 11.2.4.1 Introduction 288
 - 11.2.4.2 Baseline Optimization for Radial Devices 290
 - 11.2.4.3 Radial and Planar Gradiometers 291
 - 11.2.4.4 Radial and Vector Magnetometers 296
 - 11.2.4.5 Comparison of Various Devices in the Presence of Environmental Noise 297
 - 11.2.5 Fetal MEG Systems 299
 - 11.2.5.1 Introduction 299
 - 11.2.5.2 Design Philosophy 300
 - 11.2.5.3 Construction of fMEG System 300
 - 11.2.6 MEG Data Analysis 302
 - 11.2.6.1 General Principles 302
 - 11.2.6.2 MEG Data Interpretation (MEG Source Imaging) 303
 - 11.2.6.3 Examples of MEG and fMEG Results 314
 - 11.2.6.4 Clinical MEG 319
 - 11.2.7 Conclusions and Outlook 320
 - 11.3 Magnetocardiography 321
 - 11.3.1 Introduction 321
 - 11.3.2 Sources of MCG Signals 322
 - 11.3.3 Cardiomagnetic Instrumentation 324
 - 11.3.3.1 General System Description and Sensor Array Configurations 324

- 11.3.3.2 Multichannel Low-Temperature Systems 325
- 11.3.3.3 Systems Operating Outside Magnetically Shielded Rooms 328
- 11.3.3.4 High-Temperature SQUIDs 329
- 11.3.3.5 Multichannel High- T_c Systems 330
- 11.3.4 Comparisons of Sensor Types 331
 - 11.3.4.1 Sensitivity 331
 - 11.3.4.2 Axial and Planar Sensors 332
 - 11.3.4.3 Vector Magnetometers 332
 - 11.3.4.4 Conversion of Signals from Different Sensor Arrays 333
- 11.3.5 Applications of MCG 334
 - 11.3.5.1 Introduction 334
 - 11.3.5.2 Arrhythmia Risk Stratification 334
 - 11.3.5.3 Studies on Myocardial Ischemia 336
 - 11.3.5.4 Cardiac Source Imaging 337
 - 11.3.5.5 Fetal MCG 339
 - 11.3.6 Discussion 339
 - 11.3.6.1 Statistical Validation of MCG Results 339
 - 11.3.6.2 Improvement of Clinical Applicability 340
 - 11.3.6.3 Conclusion and Outlook 341
- 11.4 Quasistatic Field Magnetometry 342
 - 11.4.1 Opening the Near-dc Window 342
 - 11.4.2 Quasistatic Field Magnetometer 343
 - 11.4.3 Applications 344
- 11.5 Magnetoneurography 346
 - 11.5.1 The Long History of Measuring Signal Propagation in Nerves 346
 - 11.5.2 Measurement Technique and Signal Processing 348
 - 11.5.3 Source Modeling for Magnetoneurography 349
 - 11.5.4 Clinical Perspective 350
- 11.6 Liver Susceptometry 351
 - 11.6.1 Incorporated Magnetism as a Source of Diagnostic Information 351
 - 11.6.2 Measurement Technique 352
 - 11.6.3 Applications 354
 - 11.6.4 Outlook 355
- 11.7 Gastromagnetometry 356
 - 11.7.1 Magnetogastrography (MGG) and Magnetoenterography (MENG) 356
 - 11.7.2 Magnetic Marker Monitoring (MMM) 357
- 11.8 Magnetic Relaxation Immunoassays 360
 - 11.8.1 Immunoassays and Superparamagnetic Particles 360
 - 11.8.2 MARIA 361
 - 11.8.3 Instrumental Developments 363
 - 11.8.4 Applications 364

11.1

Introduction

Measurement of bioelectric fields associated with the human body dates to 1887 when the first electrocardiogram (ECG) was recorded [1]. This was followed in the 1920s by the electrogastrogram (EGG) [2] and the electroencephalogram (EEG) [3]. The magnetic fields of the human heart and brain were first recorded during the 1960s [4, 5] and the first magnetic recordings using SQUIDs were published in the early 1970s [6, 7]. Since then, magnetic fields from numerous other body organs have been recorded, for example from the eye, the stomach (magnetogastrogram, MGG), the small intestine (magnetoenterogram, MENG), the skeletal muscles (magnetomyogram, MMG), the peripheral nerves (magnetoneurogram, MNG), the liver, the fetal heart (fMCG) and fetal brain (fMEG), and the lungs. Most of these pioneering applications were made using single-channel SQUID devices. Modern, highly sensitive biomagnetic instruments are designed for clinical applications and may have up to several hundred channels. Basically, two geometrical configurations have emerged: nearly flat sensor arrays have been designed for magnetocardiography (MCG), and this layout appears to be well suited for most other human organs of interest, whereas the helmet-type sensor arrays are well established for magnetoencephalography (MEG).

Biomagnetometers are complex instruments and their construction requires multidisciplinary engineering efforts in hardware, system design, and data handling and interpretation: specifically in sensor development (Chapters 2, 3, 5, and 6), cryogenics (Section 7.2), noise cancellation (Section 7.7), electronics (Chapter 4), and modeling and inverse problem (Chapters 10 and 11). Biomagnetism has also stimulated intense commercial activity, which has led to the development of reliable and easy-to-use systems with large numbers of channels [8–18]. Magnetic field detectors for most biomagnetic applications operate on the same principles, although the sensor types and their configuration and number may be different.

Even though the magnetic field has been detected from many organs, so far the most extensive application of biomagnetism has been to the brain and MEG investigations have been gradually moving from research laboratories to clinical practice. At the time of writing there are about 100 large-scale MEG systems installed worldwide, out of which about 90 are whole-cortex MEG. Additionally more than 10 large-scale systems have a planar arrangement of SQUIDs so that they can also be used for MCG. These numbers are steadily growing (see Figure 11.1). In addi-

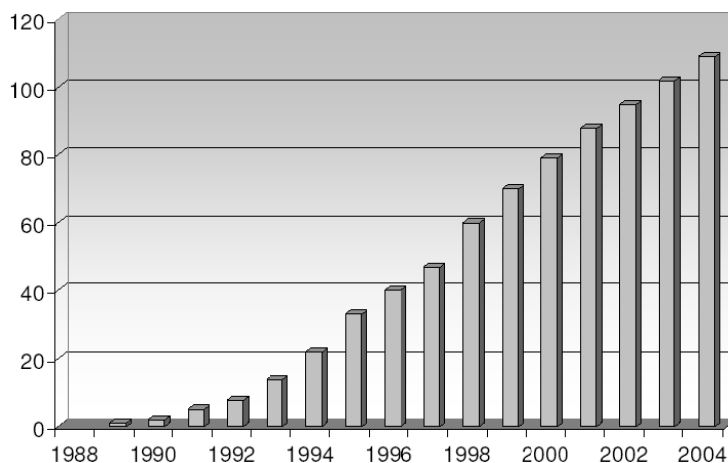


Fig. 11.1 Number of large-scale biomagnetic devices in operation worldwide.

tion, there are numerous systems with smaller number of channels for other biomagnetic applications. The number of SQUIDs installed by the end of 2004 in MEG and MCG applications alone was over 20,000.

High- T_c SQUIDs have been also successfully used for almost all biomagnetic applications. They still are not as reliable as and are more difficult to produce than low- T_c SQUIDs, and, of course, their noise is higher. Consequently, the performance of high- T_c SQUIDs is not considered sufficient for large-scale MEG devices. However, the high- T_c SQUIDs are penetrating into MCG and other applications where the required number of channels is smaller and high sensitivity is not always required.

The magnetic field distribution measured above the body surface not always provides sufficient information for most diagnostic or research applications, and it is often desirable to reconstruct the location and structure of currents which generated the observed magnetic field. Deduction of the current distribution from the measured magnetic fields, is an inverse problem (Chapter 10), which is unfortunately nonunique and often ill-posed. Inversion methods are an important part of biomagnetic investigations and considerable effort is expended on their development and perfection.

This chapter touches on the major biomagnetic applications and contains sections dealing with MEG, MCG, DC-magnetometry, MNG, liver susceptometry, and MGG. In particular for MEG and MCG, which have a history of more than 30 years, it is hardly possible to cover the entire volume of literature which is continuously increasing (see Figure 11.2). In contrast, Sections 11.4 to 11.7 deal with much more recent applications some of which still have to show their clinical potential. Liver susceptometry was recognized in 1995 when it became accepted for reimbursement by health insurers. The chapter closes with a section on magnetic immunoassays, a newly developed application of SQUIDs for *in vitro* diagnostics, which may also find its way into an *in vivo* application in the future.

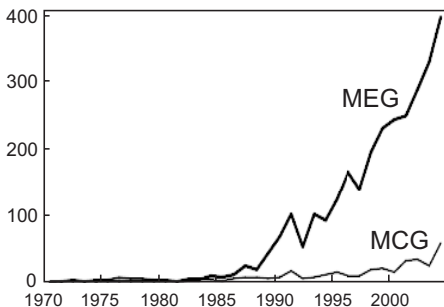


Fig. 11.2 Publications per year on MEG and MCG (from MedLine).

Until now, biomagnetic measurements have been entirely dominated by SQUID magnetometers. Recently, sub-femtotesla, spin-exchange, relaxation-free atomic magnetometers were proposed and demonstrated [19]. The operation of atomic magnetometers is based on detection of Larmor spin precession of optically pumped atoms (usually K, Rb, Cs). Their sensitivity is limited by spin-exchange collisions between the alkali atoms. The newly proposed magnetometers eliminate the sensitivity reduction due to the spin-exchange by operating at high alkali atom density in very low fields. The demonstration used a magnetometer cell heated to about 180 °C, a potassium atom density of about $6 \times 10^{19} \text{ m}^{-3}$, and a magnetic shield with a shielding factor of about 10^6 . A noise level $<1 \text{ fT}/\sqrt{\text{Hz}}$ in a bandwidth of 10 to 150 Hz was demonstrated. It was suggested that such magnetometers may potentially replace SQUIDs in biomagnetic applications, because they do not require expensive cryogenic cooling.

However, several important technical obstacles must be overcome before such magnetometers can be successfully applied to biomagnetic applications [20]. The proposed magnetometers must be operated in magnetic shields with a shielding factor about 10^4 times larger than that of the magnetically shielded rooms presently used for biomagnetic measurements. Construction of such shields for non-claustrphobic use with human subjects may be challenging. In contrast, SQUIDs can successfully operate in the presence of tesla-strength steady fields and microtesla time-varying fields. The optical magnetometers operate in a hot oven and the brain (or other biological tissues) must be protected from the heat. It may be more difficult to devise a low-noise “hot” insulator than to design a low-noise “cold” insulator (dewar) for the SQUIDs. Nevertheless, a 256-channel atomic magnetometer for human MEG is presently under construction [21].

A more conventional atomic magnetometer based on Cs vapors pumped by resonant laser radiation was demonstrated to operate in weak magnetic shielding with a resolution of $63 \text{ fT}/\sqrt{\text{Hz}}$ in a detection bandwidth of 140 Hz. Such a magnetometer is not as sensitive as a SQUID detector, but it has already been successfully used in a gradiometer arrangement to detect time-averaged MCG [22].

Biomagnetic measurements (MEG, MCG) are usually combined with anatomical tomographic information, typically obtained from high-field magnetic reso-

nance imaging (MRI). The MRI images are reconstructed from nuclear magnetic resonance (NMR) signals generated by nuclear spins that precess in static magnetic fields and magnetic gradients. It was recently demonstrated [23] that NMR detection with untuned SQUID magnetometers in ultralow magnetic fields (microtesla range) can be used to enhance spectral resolution and signal-to-noise ratio (SNR). The ability to measure NMR (and MRI) in low fields opens up the possibility of acquiring anatomical images in the same machine as that used for biomagnetic measurements.

The proposed method has several advantages [24, 25]. The untuned SQUID detector yields a signal that is independent of frequency. Thus even low-frequency NMR signals which correspond to low magnetic fields can be detected with high SNR. In addition, reduction of the measurement field strength reduces inhomogeneous broadening of NMR lines, thus increasing SNR and spatial resolution. Susceptibility artifacts that cause spurious gradients that broaden NMR lines are also reduced. Furthermore, there is an exciting prospect that the technique may ultimately lead to direct imaging of local magnetic fields caused by bioelectric currents [26]. Low-field MRI will never supplant high-field scanners. However, microtesla MRI could be combined with multichannel biomagnetometers and could provide an anatomical substrate for correlation with magnetic sources. Use of multichannel SQUID systems for low-field MRI also could greatly enhance SNR through various signal processing methods [23]. Single-channel simultaneous MCG and NMR data have already been demonstrated [27].

Throughout this chapter, plain symbols will denote scalar quantities and bold symbols vectors and matrices.

11.2

Magnetoencephalography

11.2.1

Introduction

Electromagnetic activity associated with ionic currents flowing within a functioning brain produces electric and magnetic fields which can be measured on and around the scalp. These fields can be utilized to deduce what parts of the brain were activated. The interest in the electromagnetic activity of the human brain has a long history. The first recording of the human brain electric fields (electroencephalograph, or EEG) was reported in 1929 [3] and its magnetic counterpart (magnetoencephalograph, or MEG), was first measured in 1968 using room-temperature coils [5]. The low sensitivity of these early MEG measurements was dramatically improved with the advent of SQUID sensors, which were first used for detection of MEG in 1972 [7]. After this pioneering work, the field of MEG developed first by using single-channel devices, followed by somewhat larger systems with 5 to 7 channels in the mid-1980s, then systems with about 20 to 40 sensors in the late 1980s and early 1990s, and finally the first helmet whole-cortex MEG systems

were introduced in 1992. Present MEG systems have several hundred channels in a helmet arrangement and operate in either sitting or supine positions.

Presently, MEG is the most important biomagnetic application and its technology has been intensely developed in the commercial sector, resulting in complex systems with large numbers of channels covering the whole cortex surface. The first whole-cortex MEG systems [28–31] were introduced in 1992 by VSM Med-Tech Ltd (then CTF Systems Inc.) [8] and Elekta Neuromag Oy [9], and later on by 4D Neuroimaging [10]. In addition to these three major suppliers, whole-cortex MEG systems are also manufactured in Japan [11] and in Italy [12]. Flat-bottom commercial multichannel systems are described in Section 11.3. Noncommercial SQUID magnetometers with large numbers of channels were also constructed in a number of laboratories around the world, using both low- and high-temperature superconductors. Some examples, not intended to be exhaustive, can be found in [32–43].

The introduction of the helmet-type MEG systems has led to a dramatic increase in the use of SQUID sensors. It was estimated that the number of SQUID sensors installed in commercial whole-cortex MEG systems from 1992 to the end of 2004 was in excess of 20,000, while the total number of functional SQUIDs in all applications before 1992 (a period of 20 years since the first SQUID recording of the human brain magnetic fields in 1972) was only slightly more than 1000 [45].

The existing commercial MEG instruments are based on low- T_c SQUIDS. Systems based on high- T_c superconductors are also being developed, however, mostly for MCG applications [43, 44], see Section 11.3. The present high- T_c SQUIDS cannot be reliably manufactured in large quantities, are not as sensitive as their low- T_c counterparts, and require better shielding. However, their performance is steadily improving and they already are suitable for some applications.

The MEG measures magnetic fields on the scalp surface. However, the brain current distribution, which is responsible for the observed fields, is usually more interesting to the user. Unfortunately, the inversion problem (computation of the current distribution from the measured magnetic field) is nonunique [46] and ill-posed and the MEG data must be supplemented by additional information, physiological constraints, or mathematical models and simplifications. Additional information to assist the field inversion can also be supplied by other measuring modalities.

One such modality is EEG [47]. Both MEG and EEG measure the same sources of neuronal activity and their information is complementary and additive [48]. Both MEG and EEG have excellent temporal resolution and provide functional information which is usually combined with anatomical images, obtained, for example, from MRI [49–51] or computed axial tomography (CAT or CT) [50, 52]. Additional functional information from positron emission tomography (PET) [53, 54], single-photon emission computed tomography (SPECT), *e.g.* [54, 55], or functional MRI (fMRI), *e.g.* [49, 54, 56, 57], can also be combined with MEG and EEG to characterize the brain sources more fully.

In summary, MEG and EEG provide a direct measure of the neuronal activity with excellent temporal resolution, but with spatial localization dependent on the

nonunique inversion problem. Both MRI and CT provide high-resolution spatial anatomic images and fMRI, PET and SPECT provide three-dimensional functional characterization of the brain activity in terms of metabolic and hemodynamic processes. In comparison with MEG and EEG, fMRI, PET and SPECT are limited by the long time constants of the metabolic and hemodynamic processes and by the poorly defined relationship between them and neuronal processes.

11.2.2

MEG Signals

In this section the origins of MEG signals will be briefly reviewed. More detailed exposition of the cellular mechanism of the magnetic field generation can be found elsewhere [58–61].

The MEG fields are generated by currents flowing within the brain, especially the cortex. The cortex contains well-aligned pyramidal cells, which consist of dendrites, a cell body, and an axon, and there are approximately 10^5 to 10^6 cells in an area of about 10 mm^2 of the cortex [62]. The cells are interconnected by nerve fibers which are connected to dendrites and cell bodies by synapses, as in Figure 11.3(a). In the human brain there are approximately 10^{10} neurons and 10^{14} synaptic connections.

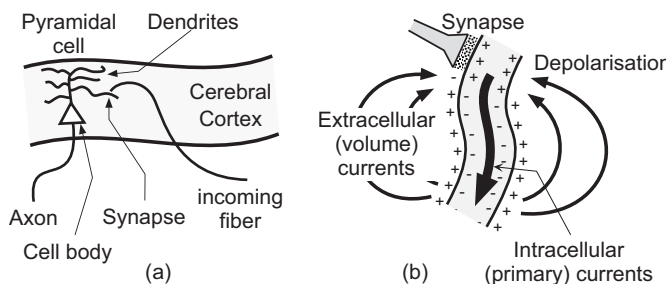


Fig. 11.3 Origins of the brain magnetic field. (a) Small section of cortex expanded to indicate pyramidal cell, dendrites, and synaptic connection. (b) Intracellular and extracellular dendritic currents. (c) Activation can be located either in sulci, resulting in tangential current, or in gyri, resulting in radial currents, (CSF, cerebrospinal fluid). (d) Cortical currents produce fields detectable outside the head.

The dendrite (or a cell body) can be thought of as a tubular volume surrounded by a membrane. Because of the Na–K pump mechanism [58], there is an excess concentration of K⁺ ions inside and of Na⁺ ions outside the cell. These concentration gradients and the difference of the membrane permeability for K and Na ions cause diffusion of the positive ions across the membrane. A competition between the electrical and the diffusion forces (Nernst equation [58]) establishes a negative equilibrium potential of about –70 mV within the cell. Cell stimulation (chemical, electrical, or mechanical) can cause alteration of the cell transmembrane potential and can lead to cell depolarization (or hyperpolarization), as shown in Figure 11.3(b). Because the cell is conductive, the polarization change induces current flow within the cell (intracellular current) and a return current outside the cell through the brain.

The transmembrane currents are called the impressed currents, J^i and they drive passive volume currents in the conducting tissues outside the membrane. The contribution of the volume currents to the magnetic field can be expressed as a sum of terms over all surfaces of conductivity discontinuities, including the cell membranes and the macroscopic volume of the brain itself. Summation over the cell boundary terms can be shown to be equivalent to a sum of dipole sources and can be expressed as a cellular-average current dipole density, J^c . From a macroscopic point of view, the combination of J^i and J^c behaves as an effective current source, and it is convenient to call it the primary source of biomagnetic fields, $J^p = J^i + J^c$. The secondary sources then correspond to the terms associated with macroscopic discontinuities, for example the brain boundary [64]. The goal of magnetic imaging studies is to find J^p from measurements. Since the membrane volume is small, the contribution of J^i to the magnetic field is negligible and the primary sources can be expressed as $J^p \approx J^c$.

The action potentials or axonal currents are usually not observable magnetically, because they consist of propagating depolarization and repolarization regions, equivalent to two, close-spaced, opposing polarity, in-line current dipoles (quadrupolar source) [64, 65], which give rise to magnetic fields with fast spatial decay. Therefore, observed MEG signals are often thought to arise from postsynaptic currents [61].

The postsynaptic dendritic depolarization currents flow roughly perpendicular to the cortex. However, the cortex is highly convoluted with numerous sulci and gyri and, depending on where the cell stimulation occurred, the current flow can be either tangential or radial to the scalp, as shown in Figure 11.3(c). If the brain were modeled as a conducting sphere, due to symmetry only the tangential currents would produce fields outside the brain, Figure 11.3(d), while there would be no contribution from radial currents [63, 66]. This would seem to indicate that the MEG is not sensitive to gyral sources. However, it has been shown on a purely anatomical basis that only 5% of the whole cortical area is within 15° of the radial direction, and that it is the source depth, rather than orientation, that limits the sensitivity of MEG to the electrical activity of the cortical surface [67]. In addition, radial magnetic fields, which are often measured by MEG, are mostly caused by

the tangential primary currents, while the electric potentials (or EEG) are affected also by the volume currents.

Current flow within a single cell is too small to produce observable fields outside the scalp. The detectable fields are a result of nearly simultaneous activation of a large number of cells, typically 10^4 to 10^5 [59]. Generally, the MEG sources are distributed; however, activation of even a large number of cells is often spatially small and can be modeled by a point equivalent current dipole (ECD) [68]. As an example, consider auditory evoked fields (AEF) which are typically caused by sources with an equivalent dipole strength of the order of 20 to 80 nA m [69]. Since the current dipole density in the brain tissue is nearly constant and in the range from about 0.5 to 2 nA m/mm² [70], the AEF dipole magnitude corresponds to the order of 100 mm² area of activated cortical tissue.

Typical ranges of frequencies and amplitudes encountered in MEG are shown by solid lines in Figure 11.4(a). The field magnitudes range from low 10 fT for the spinal chord to about 1 pT for α or δ rhythms, and in frequency from a fraction of a hertz to about 1 kHz.

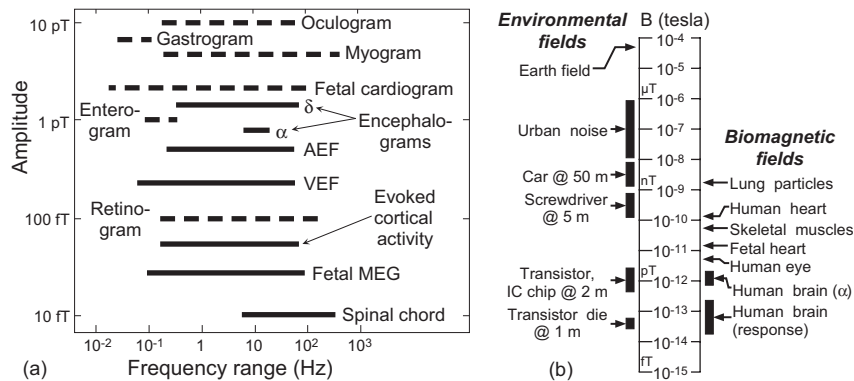


Fig. 11.4 (a) Representative biomagnetic fields and their frequency and amplitude ranges. Solid lines indicate brain fields, dashed lines fields from other body parts.
(Adapted from [71]). (b) Comparison of biomagnetic fields and environmental noise.

The MEG signals are small in comparison with environmental noise. This is illustrated in Figure 11.4(b), where selected biomagnetic fields are compared with noise caused by magnetic field sources commonly found in typical environments. Figure 11.4(b) is on a logarithmic scale and it is evident that the brain fields are many orders of magnitude smaller than the environmental noise. This disparity between the brain fields and the environmental noise magnitudes underlines the necessity of efficient noise cancellation (Section 7.7).

11.2.3

Whole-Cortex MEG Systems

11.2.3.1 Preface

MEG systems are complex installations involving multidisciplinary engineering spanning diverse fields including SQUID sensors (Chapters 2, 3, 5, and 6), cryogenics (Section 7.2), noise cancellation (Section 7.7), electronics (Chapter 4), system design (Chapter 7), software, data handling and interpretation (Chapter 10 and this chapter, Section 11.2.6), and neurosciences. Even though SQUIDS are the necessary components without which MEG systems would not be possible, they represent only a small part of the system. Various other issues, like noise cancellation, flux transformer optimization, patient support, head positioning within the helmet, and so forth, are equally important.

Modern MEG investigations utilize whole-cortex helmet-type MEG instrumentation with large numbers of channels. These instruments are not only highly sensitive, but they also enhance their detection capability by employing sophisticated array-based signal processing. The whole-cortex MEG systems are qualitatively different from the conventional devices having small numbers of channels, and are the subject of the present section.

11.2.3.2 MEG System Description

A schematic of a generic MEG system is shown in Figure 11.5. The SQUID sensors and their associated flux transformers are mounted within a liquid He dewar, which is usually suspended in a movable gantry for a supine or seated patient position. The present generation of dewars contributes about 2 to 3 fT rms/ $\sqrt{\text{Hz}}$ noise and limits the sensitivity of shielded MEG systems. This noise is generated by thermal fluctuations in various conducting materials in the dewar vacuum space and its method of computation and characterization are discussed in [72, 73]. There is no fundamental reason why the present dewar noise could not be reduced. A low-noise dewar, employing superinsulation with finely divided metallization and a vapor-cooled shield made from an electrically insulating ceramic was shown to achieve noise as low as 0.08 fT rms/ $\sqrt{\text{Hz}}$ [74].

The patient rests on an adjustable chair or a bed. The SQUID system and patient are usually positioned within a shielded room. At present, the majority of MEG installations use shielded rooms, however, progress is being made towards unshielded operation. The MEG measurements are usually complemented by EEG, and both MEG and EEG signals are preamplified and transmitted from the shielded room for further processing. The MEG installations also have provisions for stimulus delivery and typically have an intercom and a video camera for observation of and communication with the subject within the shielded room.

The electronics architecture provides for the management of large numbers of channels (as an example, an MEG system may have over 300 SQUID channels and 128 or even 256 EEG channels, plus 16 or 32 general purpose analog-to-digi-

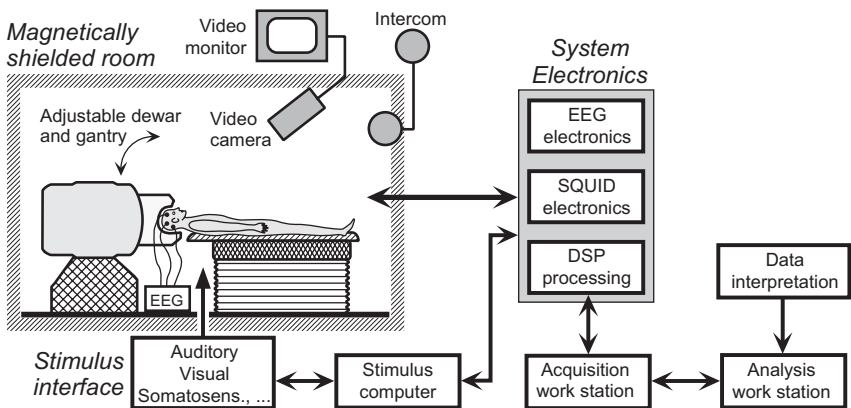


Fig. 11.5 Schematic of a typical MEG system. The MEG dewar is mounted in a gantry suitable for seated or horizontal patient positions. The MEG and EEG detectors are usually located within a shielded room and are interfaced to electronics located outside the room.

The MEG and EEG signals may be preprocessed with a digital signal processor (DSP) before they are acquired by a computer. There are also provisions for various stimuli and for communication with and observation of the patient.

tal-converter (ADC) channels and typically 16 or 32 trigger channels). The data are often preprocessed before acquisition by a computer. The preprocessing may simply consist of resampling and filtering, or it may also provide noise cancellation (for example, higher-order gradiometer synthesis [30, 75, 132] or signal space noise cancellation [76]), or it may allow high-speed execution of computationally expensive tasks (covariance updates, spatial processing, and so forth).

It should be emphasized that even though the MEG signals are small, typically no more than about 1 pT, it is necessary to maintain a high dynamic range of the MEG electronics. This is because the environmental noise is present even within the shielded rooms, and, at lower frequencies, it can have a dynamic range as large as 20 to 22 bits for gradiometers and 26 bits for magnetometers [77] (gradiometers with longer baseline are subjected to larger dynamic range). For unshielded operation, the dynamic ranges are 23 to 25 and 31 bits for gradiometers and magnetometers, respectively. Systems with lower dynamic range must necessarily compromise flux resolution and are not suitable for investigation of paradigms where unaveraged data with narrow bandwidth are required, or where differences between data sets are investigated.

The dewar tail end, which is in contact with the patient, has a helmet shape and the inner vessel of the dewar is covered with the primary sensor flux transformers, as shown in Figure 11.6. The helmet covers approximately 0.1 to 0.12 m² of the scalp. The flux transformers can be magnetometers, radial or planar gradiometers, or their combinations. The number of sensing channels is widely variable, and systems with 64, 122, 143, 148, 151, 153, 160, 248, 275, and 306 channels have been produced [8–12], and a system with 492 vector magnetometers (at 164 sites) was recently introduced [12, 78]. The MEG sensor noise is usually in the

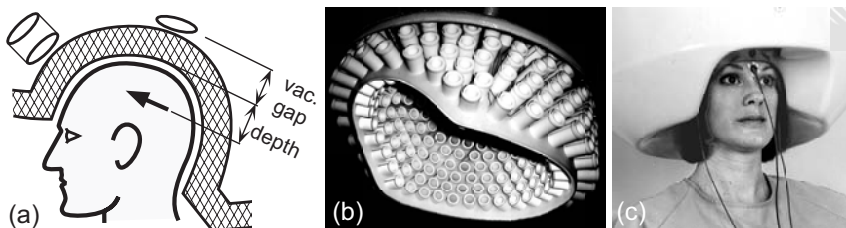


Fig. 11.6 Sensor arrangement around the head. (a) Sensors are separated from the scalp surface by a vacuum gap in the dewar and the signal sources are positioned at a certain depth below the scalp surface. (b) Photograph of a 275-channel radial

gradiometer sensor array. (c) View of the dewar tail and the subject head. The coils attached to the subject head are used for the determination of the head position relative to the sensors.

range from 3 to <10 fT rms/ $\sqrt{\text{Hz}}$ for radial gradiometers or magnetometers [8–12] and about 0.3 fT/mm rms/ $\sqrt{\text{Hz}}$ for planar gradiometers [9].

The sensing coils are separated from the scalp surface by the vacuum gap in the dewar, which is typically 15 to 20 mm (Figure 11.6(a)). References for noise cancellation, if present, are located some distance away from the primary sensors so that they detect the environmental noise, and are not sensitive to the brain signals. Various noise cancellation methods are described in Section 7.7. Examples of commercial whole-cortex MEG systems are shown in Figures 11.7 and 11.8.

The CTF MEG system in Figure 11.7 [8] uses radial gradiometers with a 50-mm baseline as primary sensors and references suitable for noise cancellation by up to third-order synthetic gradiometers (29 references); the number of sensing channels is either 151 or 275. The dewar orientation is adjustable between the vertical and horizontal positions. The system uses a digital SQUID feedback loop with its dynamic range extended by utilizing the periodicity of the SQUID transfer function [79]. The SQUID feedback loop is completed with digital integrator [80]. The loop remains locked for the applied flux in the range $\pm\Phi_0$. When this range is exceeded, the locking point shifts by one Φ_0 along the transfer function and the shifts are counted. The system exhibits a dynamic range of 32 bits, with approximately 0.3 fT per least significant bit (LSB). A computer processing cluster (four dual Intel Xenon processors) is incorporated into the electronics for implementation of various real-time processing tasks [81]. With 304 SQUID channels (275 sensors and 29 references), up to 128 EEG, and 16 ADC, 4 DAC, and miscellaneous other channels, the maximum sample rate is 12 kHz.

4D Neuroimaging [10] produces the Magneis MEG whole-cortex systems. The Magneis system is pictured in Figure 11.8(a). The primary sensors are radial magnetometers, or axial gradiometers (with 50 mm baseline), or a combination of the two, with 23 remote references for noise reduction. The magnetometer flux transformers are mounted on the vacuum side of the liquid He reservoir. These systems can have either 148 or 248 sensors for models 2500WH or 3600WH, respectively. The dewar is elbow-shaped and accomplishes the vertical and horizontal

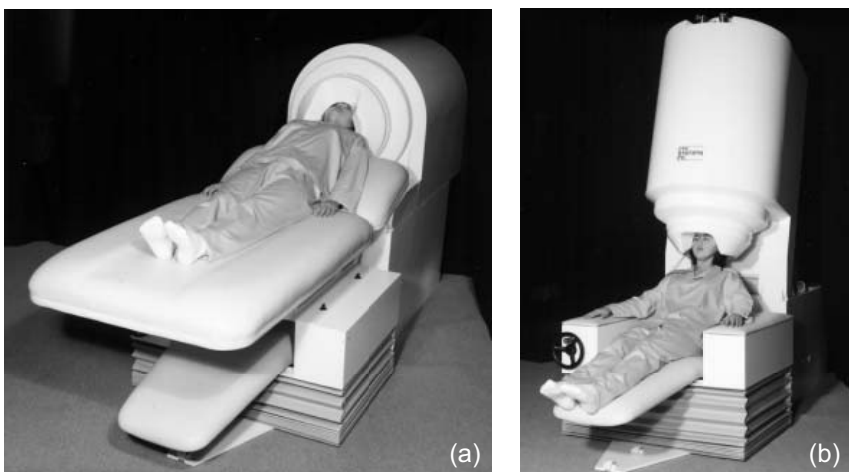


Fig. 11.7 CTF whole-cortex MEG system with 151 or 275 channels [8].

(a) Fully supine position; (b) upright position.

helmet positions by tilting in the range of $\pm 45^\circ$ from the vertical. This system has 24-bit digitization with up to 8-kHz sample rates.

The Elekta Neuromag® system is shown in Figure 11.8(b). The sensor samples the neuromagnetic field by means of 204 planar gradiometers (baseline 17 mm), organized in orthogonal pairs, and 102 radial magnetometers centered on the midpoint of each planar gradiometer pair. Altogether 306 independent signals are thus acquired. The sensor components are made on a silicon chip using thin-film photolithography to provide a high degree of geometrical precision and balance. The sensor combines the focal sensitivity of the planar detectors and the widespread sensitivity of the magnetometers in an optimal fashion. The system is also mounted in an elbow-shaped dewar which allows a rapid change between sitting and supine position measurements. The maximum sample rate with 306 MEG and 64 EEG channels is up to 10 kHz and the signals are digitized to 24 bits [9].

Eagle Technology Inc. [11] produces a 64- to 208-channel whole-cortex compact MEG system for subjects in the supine position only. The sensors are radial gradiometers with 50-mm baseline and 15.5-mm diameter coils. The sensor separation is approximately 25 mm. The system is operated using a Windows NT platform.

ATB Srl. [12, 83] produces a whole-cortex MEG system with 165 radial magnetometers uniformly distributed on the scalp surface with a spacing of about 32 mm. The company also recently installed a system with 492 vector magnetometers (at 164 sites) [12, 78]. The system uses an additional 12 references (4 vector magnetometers, placed about 70 mm away from the helmet support) for noise cancellation. The system allows up to 128 EEG channels. The sample rates are up to 8.4 kHz with a maximum of 330 channels and up to 4.2 kHz with a maximum of 660 channels. The digitization resolution is 18 bits.

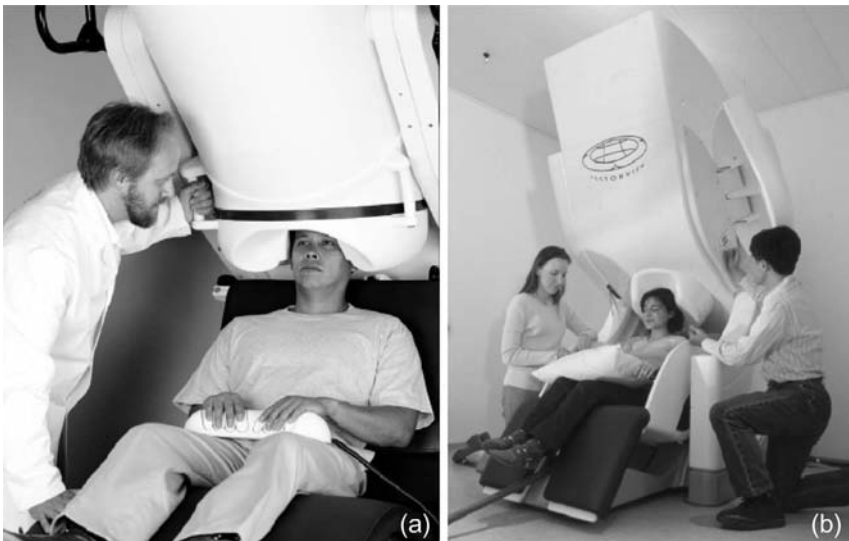


Fig. 11.8 Whole-cortex MEG instrumentation of 4D Neuroimaging [10] and Elektas Neuromag Oy [9] for seated or supine subjects: (a) Magnes 2500WH or Magnes 3600WH (courtesy of 4D Neuroimaging Inc.); (b) Elektas Neuromag® (courtesy of Elektas Neuromag Oy).

A summary of sensor and electronic parameters of existing commercial MEG systems is shown in Table 11.1.

A whole-cortex MEG system based on a superconducting imaging-surface concept (SIS-MEG) has been constructed and operated [84, 85]. The SIS-MEG consists of 149 low- T_c SQUID magnetometers surrounded by a superconducting helmet-like structure fabricated from lead. Sensors inside the helmet are shielded from environmental noise by 25 to 60 dB, depending on whether the sensors are close to the superconducting helmet brim or near the apex. In addition to the sensors, there are also four reference vector magnetometers (12 sensors) located outside the SIS helmet. The SIS almost completely shields the references from the brain signals, and the references are used in an adaptive noise cancellation approach to reduce the environmental noise. In addition to the passive shielding by SIS, the adaptive noise cancellation reduces the environmental noise by another 60 to 90 dB. Residual sensor noise is in the range from 2 to 10 fT/ $\sqrt{\text{Hz}}$, depending on the sensor position relative to the SIS helmet.

MEG measurements result in large volumes of data. To give an example of the data throughput, consider a system with 300 SQUID channels with 4 bytes per data point, 128 EEG channels with 2 bytes per data point, and 16 additional ADC channels with 2 bytes per data point, or in total 1488 bytes per data point. With a sample rate of 1 kHz, such a system will generate roughly 1.5 Mbytes per second (and higher sample rates are usually available). One hour of recording at such a data rate will produce about 5.5 Gbytes of data.

Table 11.1 Comparison of commercial MEG system parameters (SSP – signal space separation, SSP – signal space projection, CALM – continuously adjusted least square method).

| | Units | Elekta Neuromag Oy | VSM MedTech Ltd (CTF MEG) | 4D Neuroimaging (Magnes) | Eagle Technology Inc. | Advanced Technologies Biomagnetics |
|--|--------|---|-----------------------------------|--|----------------------------------|---|
| Sensing channels | – | 102 radial mags. and 204 planar grads. | 151 or 275 radial gradiometers | 148 or 248 radial mags. (or radial grads., or a combin.) | 64 to 208 radial gradiometers | 165 radial mags., or 164 vector mags. (492 ch) |
| Primary sensor baseline (if applicable) | mm | 17 for gradiometers | 50 | 50 for gradiometers | 50 | – |
| References for noise cancellation | – | 0 | 29 | 23 | 3 | 12 |
| Typical system noise | fT/√Hz | 3 ^a | 5 ^b | 5 ^b | 5 ^b | 5 ^b |
| Data dynamic range | bits | 27/32 ^e | 32 | 24 | 12 (16 optional) | 18 |
| EEG/EMG channels | – | 64 or 128 | 32, 64 or 128 | 96 | 0 ^c | 128 |
| ADC channels | – | 8 or 16 | 16 | 32 | 32 | 367 for 165 ch MEG, 40 for 429 ch MEG ^d |
| DAC channels | – | 12 | 4 | 4 | None | – |
| Trigger channels | – | 32 | 48 | 16 | 16 | 16 |
| Max. sample rate | kHz | 10 | 12 | 8 | 10 | 8.4 |

| Units | Elekta Neuromag Oy | VSM MedTech Ltd (CTF MEG) | 4D Neuroimaging (Magnes) | Eagle Technology Inc. | Advanced Technologies Biomagnetics |
|----------------------------------|--------------------|---|--|-----------------------------|---------------------------------------|
| Environmental noise cancellation | — | SSS ^f or SSP ^g , active compensation optional | Synthetic third-order spatial gradient | CALM ^h | Adaptive noise cancellation |
| Acquisition computer | — | HP C8000 | HP XW8200 | Sun Microsystems UltraSPARC | Multiple Pentium IV's PC |
| Operating system | — | HPUX 11 and LINUX Enterprise 3.0 | LINUX RedHat Enterprise 3.0 | UNIX Solaris 8 | Windows 2000 Linux/Windows |

a 3 fT/ $\sqrt{\text{Hz}}$ for magnetometers and 0.3 fT/mm/ $\sqrt{\text{Hz}}$ for planar gradiometers.

b Noise for gradiometers corresponds to the gradient noise multiplied by gradiometer baseline and is quoted in fT/ $\sqrt{\text{Hz}}$.

c Can connect third-party EEG into ADC channels.

d There are 660 ADCs for MEG, EEG, and auxiliary inputs. Thus for 128 EEG channels and 165 MEG channels there are 367 free ADC channels, and for 492 MEG channels system there are $660 - 492 = 40$ free ADC channels.

e with active compensation

f SSS – Signal Space Separation

g SSP – Signal Space Projection

h CALM – Continuously Adjusted Least Squares Method

11.2.3.3 MEG and EEG

The primary currents discussed in Section 11.2.2 will generate return currents in the conducting volume of the brain. The magnetic fields due to the primary and volume currents are detected by MEG, and their corresponding electric potentials on the scalp surface by EEG. Were the brain modeled by a perfectly spherical conductor, the radial primary currents would generate no magnetic field outside the head, but the electric potentials on the scalp surface would be nonzero (however, the head is not spherical and in practice the majority of the cortex surface is accessible to MEG measurement [67]). If only radial magnetic fields were measured, then MEG would be sensitive to the tangential primary currents, while EEG would be affected by the volume currents. In this case maps of the radial magnetic field and electric potentials on the scalp surface would be orthogonal, as shown schematically in Figure 11.9(a) [86, 87]. Tangential MEG measurement would be sensitive to both the primary and volume currents [63, 66].

EEG and MEG must be measured simultaneously in order to take advantage of their complementary information. The EEG electrodes and all their connections must be nonmagnetic to avoid generation of MEG artifacts. The currents in the EEG electrode leads will not generate MEG artifacts if the EEG preamplifier impedance is greater than about $1 \text{ M}\Omega$ (easily satisfied in practice). A view of a subject with EEG electrodes attached and with the head partially withdrawn from the MEG helmet is shown in Figure 11.9(b).

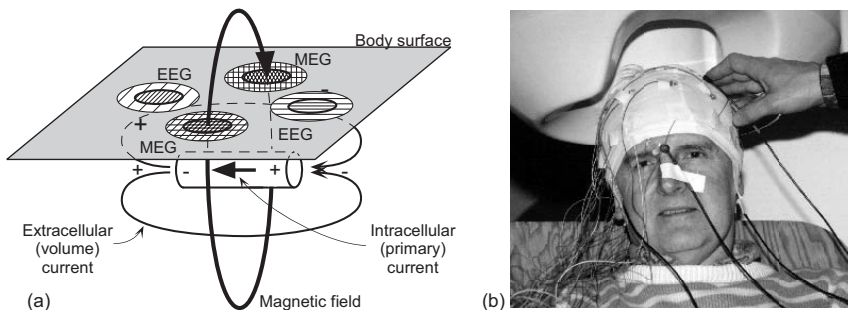


Fig. 11.9 EEG and MEG. (a) Orthogonal relationship between EEG and MEG signals. (b) A subject with attached EEG electrodes and with the head partially withdrawn from the MEG helmet.

11.2.3.4 MEG Peripherals

In addition to EEG, there are other important peripherals used in MEG: shielded rooms, head positioning equipment, and stimulation equipment.

Shielded Rooms

Shielded room performance is discussed in Section 7.3. Typical rooms used for MEG are the “modestly” shielded μ -metal rooms corresponding to curve (2) in Figure 7.7(a). These rooms usually contain a thick Al layer positioned between two

μ -metal layers. The rooms can be obtained commercially from a number of manufacturers [88–91].

High attenuation magnetically shielded μ -metal rooms [92–95] or high attenuation whole-body superconducting shields [96] have been used at several installations. However, such installations are not typical because the high-performance shielding is complicated and expensive (Sections 7.3 and 7.6.3).

Head Positioning

Even though the patient's head is located within the MEG helmet, the patient can still move it and accurate determination of its position and orientation relative to the MEG array is necessary. The position information is used to register the MEG results relative to the brain anatomy (for example to MRI images).

The most common and simplest head positioning method uses a small number of easily identifiable anatomical landmarks (for example nasion and preauricular points). Special markers are placed at these landmark points (for example small coils for MEG, Figure 11.6(c), and oil capsules for MRI), their positions are determined, and used to derive a transformation between the MEG and MRI systems of coordinates. The accuracy of this method is of the order of a few millimeters because the placement errors of the MEG and MRI markers compound. Continuous head position monitoring, utilizing MEG sensors, is also available [97, 98].

To reduce these registration problems, the partial- or whole-head surface is digitized in the MEG system of coordinates. The head surface digitization can be done either by moving a small coil on the head surface and detecting its position by MEG sensors as in Figure 11.9(b) [99], or using a dedicated electromagnetic tracking device, *e.g.* [100]. The surface of the head is also determined from the MRI image and the transformation between the two systems is obtained by matching the two head shapes [101–103].

Stimulation Equipment

Evoked MEG measurements are carried out with a wide range of stimulation equipment. The visual stimulators may use nonmagnetic goggles, projection screens, or computer monitors. The sound stimulators usually deliver sound from remote speakers to the ear(s) by means of nonmagnetic plastic tubing, or the stimulation sound can be directly piped to the shielded room. Somatosensory experiments use electrical stimulators or various tactile stimulation schemes. Also, various switches and detectors are used for voluntary or forced finger movements. Regardless of the stimulation method, care must be taken not to introduce stimulation artifacts. The wires of the electrical stimulators should be tightly twisted, computer monitors (LCD) must be tested for magnetic noise and synchronous artifacts, switches must be nonmagnetic (usually an interruptible optical beam), and speakers must be sufficiently far from the MEG system not to produce magnetic noise.

11.2.4

Sensor Types for MEG**11.2.4.1 Introduction**

MEG sensing arrays consist of primary sensors and, optionally, references for environmental noise cancellation. The primary sensor flux transformers are located in close proximity to the scalp surface, where they couple to the magnetic field of the brain. The references are located at some distance away from the brain, and are designed mostly to detect the environmental noise while being nearly insensitive to the brain signals. The primary sensors are subjected to noise which can be either correlated or uncorrelated among the channels. The correlated noise is either the environmental noise, or noise from electrically active tissues other than brain (for example muscles, MCG), or unwanted brain signals. The uncorrelated noise is the random noise generated in the SQUIDs and their electronics.

It will be assumed that all sensor types (with or without the reference noise cancellation) can be designed for the same white noise levels (see Chapter 5 for magnetometer and gradiometer design procedures). This section will thus focus on the comparison of the sensor types from the point of view of their response to the brain signals and their ability to reject the environmental and the brain-generated noise.

Several variations of the primary flux transformers commonly used in MEG practice are shown in Figure 11.10(a). Flux transformers (1), (2), and (6) are magnetometers, which have the highest sensitivity to both the near- and far-field sources. This property makes them highly sensitive to the environmental noise and they depend on other techniques for noise cancellation. The flux transformers (3), (4), and (5) in Figure 11.10(a) are hardware first-order gradiometers. If the gradiometers (4) and (5) were positioned at the same location and if their dimensions were infinitesimally small, they would produce identical signals because outside the head $\text{curl } \mathbf{B} = 0$. The gradiometers provide reduced sensitivity to the environmental noise while maintaining good sensitivity to the near-field brain signals. Hardware gradiometers may also require supplemental noise cancellation.

If we disregard both SQUID and environmental noise, the peak signals detected by various primary flux transformers in response to a single equivalent current dipole (ECD) are shown in Figure 11.10(b) for a spherical conducting medium [63, 66] as a function of the ECD distance from the model sphere center (or as a function of the ECD depth below the scalp surface) [104]. Since the brain field magnitude is a strong function of the ECD depth, the peak signals have been normalized by the radial magnetometer peak signal to make differences between various flux transformers clearer. As a result, the normalized magnetometer response is unity for all ECD depths.

The radial gradiometer peak signal strength declines with decreasing baseline and increasing ECD depth. For example, in the limit where the dipole source approaches the sphere center (and when the signal for all devices approaches zero,

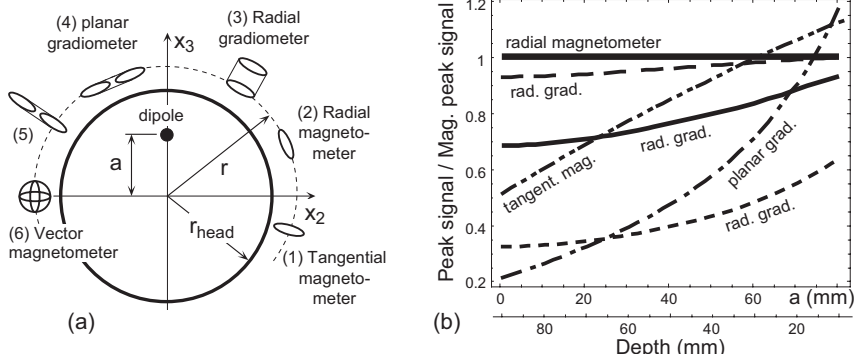


Fig. 11.10 Sensor types and comparison of a single ECD source peak signal strengths detected by different noiseless flux transformer types. An ECD source oriented along x_1 is positioned at a distance a from the model sphere center, sensors are located on a spherical shell with radius $r = 0.11$ m, the head radius is $r_{\text{head}} = 90$ mm, and all sensors are assumed to have infinitesimally small coil diameters. (a) Illustration of various sensor types: 1, tangential magnetometer, 2, radial magnetometer, 3, radial gradiometer,

4, planar gradiometer, 5, radial–tangential gradiometer, 6, vector magnetometer.
 (b) Peak signal normalized by magnetometer peak signal, plotted as a function of the ECD source distance from the model sphere center, or a depth below the head surface:

- radial magnetometers,
- - - tangential magnetometers,
- - - radial gradiometers $b_{\text{rad}} = 0.15$ m,
- radial gradiometers $b_{\text{rad}} = 50$ mm,
- - - radial gradiometers $b_{\text{rad}} = 15$ mm,
- - - planar gradiometers $b_{\text{pln}} = 15$ mm.

see Section 11.2.6.1), a 50-mm baseline radial gradiometer will detect a signal about 30% smaller than a magnetometer. For more superficial sources the difference is smaller; for example when the source is about 10 mm deep ($a = 80$ mm), the 50-mm baseline radial gradiometer signal is only about 5% smaller than that of a magnetometer. The peak signal magnitude of a tangential magnetometer decays with depth much faster than that of radial gradiometer, and the loss of the signal magnitude as a function of the dipole depth is fastest for planar gradiometers with 15-mm baseline. When the dipole position approaches the sphere center, the planar gradiometer signal is about 80% smaller than that of a magnetometer.

In the absence of noise and provided that the measured fields are not undersampled, arrays of different flux transformers are equivalent and it is possible to predict signals detected by one flux transformer array type from the measurement of another [142, 143]. However, in realistic measurement situations, the sensors are exposed not only to the wanted brain signals, but also to the environmental noise, noise from electrically active tissues other than brain, unwanted brain signals, and the SQUID and electronics noise. The presence of noise removes the equivalence among different flux transformer arrays, since information that is lost in the noise cannot be recovered. Thus the noiseless flux transformer behavior, as shown in Figure 11.10(b), is not sufficient for the determination of the optimum flux transformer configuration. In the presence of noise, the most important parameter is the SNR, and the flux transformer arrays must be optimized for

a maximum SNR. In addition to noise suppression, sensor arrays must also be designed to extract the maximum possible information from the measured signal. Noise suppression is discussed in Chapter 7; here we discuss optimization of radial devices from the noise point of view, compare arrays of various sensor types, and conclude the section with a brief discussion of the information content.

11.2.4.2 Baseline Optimization for Radial Devices

First, let us consider optimization of radial magnetometers and gradiometers (the magnetometers can be considered as gradiometers with infinitely long baseline). This problem has already been discussed in Section 7.4.3 where it was shown that SNR maximization leads to a certain optimum baseline length [106]. In this section specific optimization curves are shown, and the derivation of the optimum baseline lengths from the environmental noise parameters determined at various MEG sites around the world is discussed.

Examples of single-channel SNRs for radial gradiometers as a function of the baseline length for different onsets of low-frequency noise, f_o (Section 7.7.3) are shown in Figure 11.11(a). The SNR in Figure 11.11(a) is defined as a ratio of the forward solution norm per channel to the rms noise per channel (while in [104, 106] the SNR was defined in terms of signal peaks). For large values of f_o , the optimum baselines are short. As f_o decreases, the position of the maximum SNR moves towards longer baselines. For no low-frequency noise ($f_o = 0$ in Figure 11.11(a)), the optimum baseline would be infinitely long and the magnetometers would produce the best results.

The low-frequency noise onset was measured at real MEG installations, and the results indicate that the optimum baselines are short, less than about 80 mm. This is further illustrated for MEG sites in Europe, North America, and Japan in Figure 11.11(b), where the optimum baseline is plotted as a function of the minimum frequency of interest, f_{\min} (see Section 7.4.3). Five sites ranging from the “quietest” to the “noisiest” were selected [107]. The width of different bands in Figure 11.11(b) corresponds to the variation of the dipole distance from the model sphere center in the range from 30 to 80 mm (the upper band edges correspond to a deeper dipole at $a = 30$ mm). The narrow width of the bands reflects the relatively weak dependence of the optimum baseline on the source depth.

A very quiet site is represented by band (1) in Figure 11.11(b). In this case the optimum baseline is ≈ 60 mm for $f_{\min} \approx 0.1$ Hz and it increases to about 200 mm for $f_{\min} \approx 1$ Hz. Such quiet performance is not matched at any other sites, even when the MEG systems are operated at night. Band (5) in Figure 11.11(b) represents one of the noisiest sites, where even for large f_{\min} the optimum baselines are short (for quite large minimum frequency of interest, $f_{\min} = 3$ Hz, the optimum baseline is only 50 mm). Other urban locations, for example Vienna, Paris, and others, correspond to a noise situation in the vicinity of bands (3) and (4). Note that the short baselines designed for the noisy sites will also work well at the quieter sites, because for smaller f_o , the optimization curves in Figure 11.11(b) are only weakly dependent on the baseline.

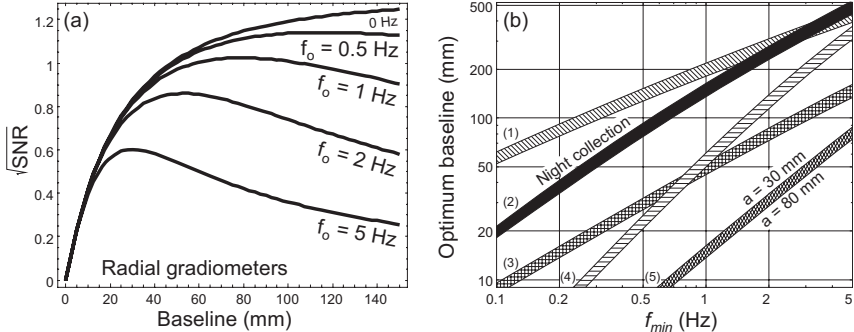


Fig. 11.11 Optimization of the radial gradiometer baseline length. $r = 0.11$ m, $v_w = 5$ fT rms/ $\sqrt{\text{Hz}}$, number of averages $N_{\text{ave}} = 1$, $b_o = 50$ mm. (a) Square root of the radial gradiometer signal-to-noise ratio as a function of the baseline length for different onsets of low-frequency noise, f_o , $q = 10$ nA m, low-frequency noise slope $k = 1.5$, minimum frequency of interest $f_{min} = 0.3$ Hz, $\Delta f = 50$ Hz, dipole distance from the model sphere center $a = 50$ mm. (b) Optimum radial gradiometer

baseline as a function of the minimum frequency of interest for several MEG sites (within the standard shielded rooms [88]). $\Delta f = 30$ Hz, upper rim of each band corresponds to the dipole distance from the model sphere center of $a = 30$ mm, lower rim to $a = 80$ mm. (1) $f_o = 0.6$ Hz, $k = 1.5$, Tuebingen; (2) $f_o = 1$ Hz, $k = 2$, Osaka, night-time; (3) $f_o = 3$ Hz, $k = 1.7$, Tokyo; (4) $f_o = 2.1$ Hz, $k = 2.6$, Amsterdam; (5) $f_o = 6$ Hz, $k = 2.2$, Toronto.

11.2.4.3 Radial and Planar Gradiometers

Radial and planar gradiometers are compared by Monte Carlo simulations for the ECDs located at different depths in a model sphere and for random and correlated noise. Simulations for numbers of channels ranging from 20 to 300 produce a cluster of localized dipole positions, where the standard deviation of the cluster, σ , is different along the depth, and along the longitudinal and the transverse directions relative to the dipole [61]. To simplify the presentation, these three standard deviations will be replaced by their rms average and denoted by σ_V [104]. The parameter σ_V is representative of the dipole localization accuracy and will be used to compare different sensor types.

It will be assumed that random SQUID noise is the same for both types of gradiometers. This noise will be cited in fT/ $\sqrt{\text{Hz}}$ and will correspond to the gradient noise multiplied by the gradiometer baseline. If evoked experiments are performed, one is usually interested in magnetic signals originating from focal sources and the brain activity outside these sources is considered a noise. This “brain noise” is correlated among sensors and the radial and planar gradiometer responses to it are different. It was shown by simulation that because of their “near-sightedness” (see Figure 11.10(b)) planar gradiometers with a baseline of about 16.5 mm detect about 50% less brain noise than radial gradiometers with 50-mm baseline [31]. Radial gradiometers with a short baseline also become “near-sighted”, Figure 11.10(b), and if their baseline is made as short as that of the planar gradiometers, they detect similarly low noise. On the other hand, if the

baseline is very long (as for magnetometers), the detected brain noise is about 20% larger than that for the 50-mm baseline radial gradiometers [104].

The localization error, σ_v , for different noise situations as a function of the dipole distance from the model sphere center is shown in Figure 11.12 for planar gradiometers with 16.5-mm baseline, hardware radial gradiometers with 50-mm baseline, and magnetometers with reference noise cancellation (equivalent to radial gradiometers with the long baseline of 0.26 m – these devices will be referred to as magnetometer-based systems). Since the hardware radial gradiometers in the CTF MEG systems are usually operated in conjunction with synthetic third-order gradiometer noise cancellation, these devices are also included in the comparison and will be called third-order gradiometers for brevity. Noise cancellation for a combination of planar gradiometers and magnetometers using signal space separation (SSS) was introduced recently, but no comparable plots were available at the time of writing.

In Figure 11.12(a) σ_v is shown for random SQUID noise. Since this noise was assumed to be the same for all types of sensors, this figure mimics the results in Figure 11.10(b). The magnetometer-based systems exhibit the smallest error, followed by the radial gradiometers with 50-mm baseline (with or without the third-order gradiometer noise cancellation), and the planar gradiometers exhibit the largest localization error.

The situation is quite different when the brain noise is considered in Figure 11.12(b). In this case and for the dipole distances from the model sphere center > 40 mm, the planar gradiometers exhibit slightly smaller localization error than the radial gradiometers or magnetometer-based systems. This result is independent of the noise cancellation by the third-order gradiometers, because no far-field noise sources are present. The better planar gradiometer performance is a consequence of its lower detected brain noise. This conclusion was first derived by Knuutila et al [31], where the error ratios were plotted, while here the absolute error values are shown [104].

When a typical environmental noise is also present in addition to the white and brain noise, the realistic situation is shown in Figure 11.12(c). The environmental noise is similar to that in Figure 11.11(b), bands (3) and (4). In this case the localization errors are smallest for the third-order gradiometers, then for the planar gradiometers, then for the bare radial gradiometers, and the magnetometers exhibit the largest errors. The third-order gradiometers exhibit the best performance because they eliminate almost all environmental noise and their localization errors are roughly the same as in Figure 11.12(b). The planar gradiometers have less error than the bare radial gradiometers because they have shorter baseline and admit less environmental noise (see Section 7.7.3). The magnetometer-based systems have the longest effective baseline and are most sensitive to the environmental noise and therefore produce the largest errors.

The difference between the planar gradiometers and the radial gradiometers with synthetic third-order gradiometer noise cancellation is shown in Figure 11.12(d). For the white noise and the combination of white, environmental, and brain noise the difference is positive, indicating that the third-order gradiometers

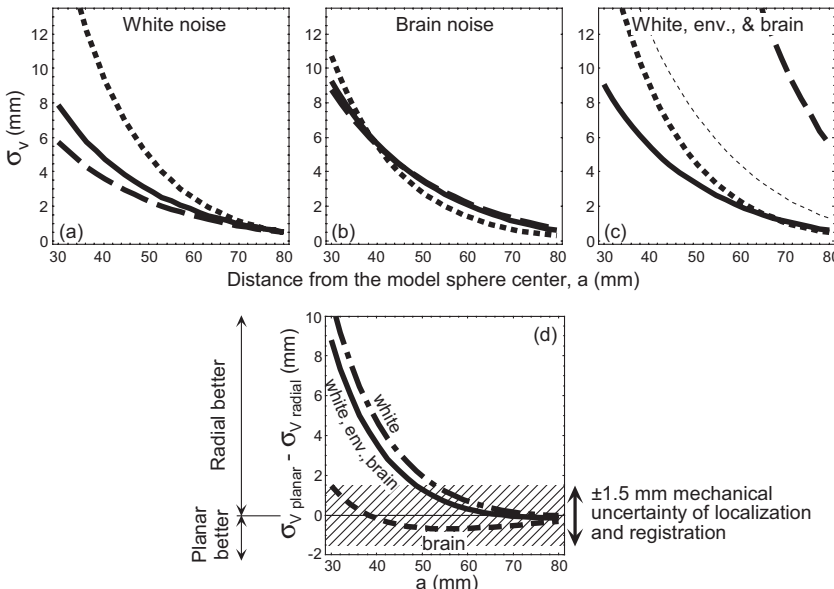


Fig. 11.12 Comparison of σ_v for magnetometers with reference noise cancellation, radial first-order gradiometers, synthetic third-order gradiometers with radial first-order gradiometer primary sensors, and planar gradiometers. Spherical sensor shell with radius $r = 0.11$ m, extending from vertex to $3\pi/4$ from vertex, number of channels $K = 150$, dipole moment $q = 20$ nA m, radial gradiometer coils: square with 17.7 mm edge, planar gradiometer coils: rectangle 16.5 mm \times 33 mm, minimum frequency of interest $f_{min} = 0.3$ Hz, $\Delta f = 30$ Hz. (a, b, c) —— magnetometer-based with baseline $b_{rad} = 0.26$ m, - - - first-order radial gradiometer with baseline $b_{rad} = 50$ mm, — third-order synthetic gradiometer with first-order radial gradiometer primary sensors with $b_{rad} = 50$ mm, - - - planar gradiometers with baseline $b_{pln} = 16.5$ mm. (a) Uncorrelated white noise,

$N_w = 5$ ft rms/ $\sqrt{\text{Hz}}$, number of averages $N_{ave} = 1$. (b) Correlated brain noise, $v_{brain\ b=5} = 25.6$ ft rms/ $\sqrt{\text{Hz}}$, $v_{brain\ b=26} = 33.2$ ft rms/ $\sqrt{\text{Hz}}$, $v_{brain\ pln} = 12.5$ ft rms/ $\sqrt{\text{Hz}}$ for radial gradiometers with 50, 260 mm and planar gradiometers, respectively, $N_{ave} = 100$. (c) Environmental, white, and brain noise. The environmental noise is similar to that shown by lines 3 and 4 in Figure 11.11(b). (d) Difference between the localization errors of planar gradiometers and radial gradiometers with synthetic third-order gradiometer noise cancellation. Positive difference — radial gradiometers with synthetic third-order gradiometers produce smaller localization error, negative difference — planar gradiometers produce smaller localization error. Shaded band indicates the approximate mechanical uncertainty of the localization and registration.

produce smaller errors than the planar gradiometers. For the brain noise the difference is negative, indicating that the planar gradiometers produce smaller errors. However, in this case the difference is small and in practice it is overshadowed by various other uncertainties, for example, accuracy of the localization coil placement. The same SNR argument can also be applied to the evaluation of two-dipole resolution, and it can be similarly shown that the ability to cancel the environmental noise is the dominant performance parameter. Similar calculations have not been carried out for arrays combining planar gradiometers and magnetometers.

An alternative noise cancellation method was recently proposed for MEG and applied to sensor arrays consisting of a combination of magnetometers and planar gradiometers (triple-sensor array) [108–110]. Because the MEG sensors are located in a source-free volume, the magnetic field, B , can be expressed as a gradient of a scalar potential, Ψ , $B = -\nabla\Psi$, which is a solution of the Laplace equation, $\nabla^2\Psi = 0$. Such a solution can be represented as a linear combination of basis functions, e.g., spherical harmonics, as

$$\Psi(r) = \sum_{n=0}^{\infty} \sum_{m=-n}^n a_{nm} \frac{Y_{nm}(\theta, \varphi)}{r^{n+1}} + \sum_{n=0}^{\infty} \sum_{m=-n}^n b_{nm} r^n Y_{nm}(\theta, \varphi) \quad (11.1)$$

where Y_{nm} are spherical harmonic functions, θ and φ denote spherical angles, $r = |\mathbf{r}|$ is the distance from the expansion center, and a_{nm} and b_{nm} are expansion coefficients. The first term on the right-hand side of Eq. (11.1) diverges at the origin and it represents sources within the sensor shell; the second term diverges at infinity and corresponds to sources outside the sensor shell. Contributions of the internal and external sources can be separated and the external terms can be discarded to reduce the environmental noise. The method is named SSS. The approach of separating the internal and external terms was first proposed in 1838 by Gauss [111, 112] to show that the Earth's magnetic field originates from within the Earth.

To implement the SSS method, the expansion in Eq. (11.1) is truncated to retain only the necessary expansion orders, N_{int} and N_{ext} , and the monopole term $n = 0$ is left out. The expression for the potential is converted to that for the magnetic field by computing gradients of the relevant terms in Eq. (11.1) and accounting for all coils corresponding to each MEG sensor. The MEG measurement is expanded into this truncated series, external terms are discarded to reduce the environmental noise, and only the internal terms are retained. The MEG measurement can be approximated as $\mathbf{m} \approx \mathbf{S}_Y \mathbf{X}_Y$ where \mathbf{S}_Y is a $K \times N_Y$ matrix of spherical harmonic terms (this matrix is computed from the sensor geometry and is independent of source configuration), $N_Y = (N_{\text{int}} + 1)^2 + (N_{\text{ext}} + 1)^2 - 2$ is the number of spherical harmonic expansion terms, K is number of MEG channels, and \mathbf{X}_Y is a $N_Y \times 1$ vector of expansion coefficients. The \mathbf{X}_Y can be found from $\mathbf{X}_Y = \mathbf{S}_Y^+ \mathbf{m}$, where \mathbf{S}_Y^+ is the pseudoinverse of \mathbf{S}_Y (see Section 7.7.5), giving an approximation $\hat{\mathbf{m}}$ to the measured signal, $\hat{\mathbf{m}} = \mathbf{S}_Y \mathbf{S}_Y^+ \mathbf{m}$. The environmental interference is reduced by retaining only the internal terms in the matrices \mathbf{S}_Y and \mathbf{S}_Y^+ . Alternatively, if only the external terms in the matrices \mathbf{S}_Y and \mathbf{S}_Y^+ are retained, the resulting approximation of the environmental interference is free of brain signal, and can be used for active shielding [113]. The required expansion order for most situations is $N_{\text{int}} = 8$ or 9 and $N_{\text{ext}} \leq 6$, corresponding to $N_Y \leq 147$ expansion terms. MEG systems with channel number $K > 147$ can take advantage of this technique.

SSS shielding may be defined as the ratio of the measured and reconstructed signal vector norms. The achievable shielding is critically dependent on how accurately the MEG system is constructed, calibrated, and balanced. When the combined magnetometer and planar gradiometer array is considered and if $N_{\text{int}} = 8$

and $N_{\text{ext}} = 4$, then 0.1% relative gain error among channels reduces the shielding to about 150, and 1% gain error to about 15 [109]. This SSS shielding dependence on the relative gain error can be utilized to improve the MEG sensor calibration accuracy [110]. Both the SSS effect on the sensor noise and the ultimate shielding depend on the sensor array geometry, which determines the condition number of the matrices used for calculation of S_Y^+ [110].

The SSS can provide good shielding against near sources located within shielded rooms. An example is shown in Figure 11.13, where SSS was applied on a MEG recording of an epilepsy patient with a vagus nerve stimulator (VNS). Such a stimulator is located on the patient's chest very close to the sensor array, and generates very large disturbances even if it does not pace the brain. In this example, some of the magnetometers were saturated by the VNS disturbance, but SSS was still capable of showing the epileptic activity.

In addition to the environmental noise cancellation, the spherical harmonic expansion can be used to correct the MEG recorded during the head motion to that which would be obtained if the head were stationary. This is accomplished by extrapolating the measured fields, through the spherical harmonic expansion, to coordinates rigidly connected to the head [108, 114]. This last feature can also be used for conversion of MEG data to user-defined virtual sensor arrays, for separating the brain activity signals from the interference due to various contaminants on the scalp surface when the subject's head is moving [108], and for recording neuromagnetic quasistatic phenomena using voluntary head movement [115]. Because SSS is a new method, thorough evaluation of its applicability is still ongoing.

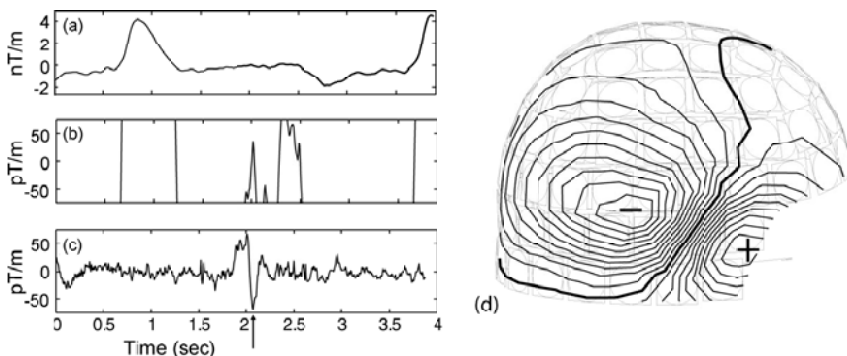


Fig. 11.13 An example of SSS noise suppression in an epilepsy patient with a vagus nerve stimulator (VNS). (a) A trace of a planar gradiometer channel over the right frontal lobe on a scale ($\pm 5 \times 10^{-9}$ T/m) before the SSS noise suppression. (b) The same signal on a

'physiological' scale (magnified by 100).
 (c) The signal after SSS shows an epileptic spike with a magnitude of about ± 50 pT/m.
 (d) Isocontour field at the peak of the epileptic spike (time = 2 s in (c)). (Courtesy of Dr. M. Funke, University of Utah).

11.2.4.4 Radial and Vector Magnetometers

Most MEG systems use radial gradiometers, magnetometers, planar gradiometers, or combinations of magnetometers and planar gradiometers. It has been suggested, for example [42, 38, 117], that the vector magnetometers (or “vector” gradiometers) would produce more information because the tangential field components would also be measured.

For random SQUID noise and a single dipole it was shown by Monte Carlo simulations, by expansion of the dipole equations in the vicinity of the correct dipole position, and by considering the information content that for a given number of channels it is best to deploy all channels as radial rather than vector devices [118, 119]. This is illustrated in Figure 11.14(b), where the dipole localization error, σ_v , multiplied by \sqrt{K} , where K is the number of channels, is shown as a function of the dipole position relative to a hemispherical sensor shell [104]. Each value of σ_v was determined by 200 Monte Carlo simulations and the correlated noise was simulated using 1000 random magnitude and randomly distributed and oriented dipoles in the model sphere. The figure indicates that if the dipole is within the helmet or even slightly outside it, the radial magnetometers produce smaller localization error, independent of the number of channels used.

If the correlated brain noise and a single dipole are considered, as in Figure 11.14(c), the conclusions are different. For dipoles well within the sensor shell, the localization errors for both radial and vector devices are similar. However, when the dipole is moved to the sensor shell rim or slightly outside it, the vector magnetometers produce smaller localization errors (vector magnetometers can

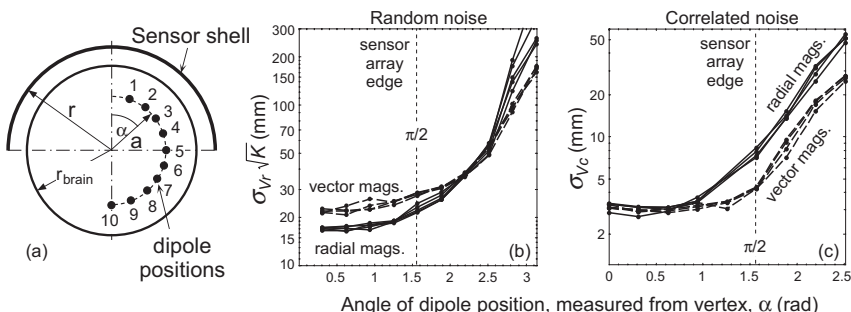


Fig. 11.14 Comparison of radial and vector magnetometer dipole localization accuracy, σ_v as a function of the ECD position relative to the sensor array edge, $r_{\text{brain}} = 80$ mm, hemispherical sensor shell, $r = 107$ mm, $a = 70$ mm, point magnetometers, dipole positions in 18° increments, position 5 corresponds to the dipole at the sensor array edge. Number of investigated magnetometers: radial $K = 97$, 142, 190, 289, 586, vector: $K = 96$, 141, 291, 570 (numbers of the vector magnetometer sites 32, 47, 97, 190). Lines in (b) and (c) correspond to constant number of channels;

solid lines – radial magnetometers; dashed lines – vector magnetometers. Vertical dashed line marks the array edge. (a) Simulation geometry. (b) Random noise of 30 fT rms (5 fT/√Hz in 36 Hz bandwidth). (c) Correlated noise simulated to resemble brain noise in 1-Hz bandwidth. Radial magnetometers: 30.4 fT rms; vector magnetometers: 22.5 fT rms (rms value was computed over all three vector components). The two different noise values correspond to the same random distribution of dipoles (used for the brain noise simulation).

extrapolate better in the vicinity of the sensor array edge). This conclusion was reached assuming that the centers of the vector and radial magnetometers are at the same distance from the head (point coils). Since this is physically not possible, the vector magnetometer centers must be moved slightly farther away from the head in order to accommodate the coil dimension (see Figure 11.10(a)). If the vector magnetometer centers were, for example, 10 mm farther from the head than the radial magnetometer centers, all advantage of the vector magnetometers in the presence of the correlated noise would be lost, that is, the vector and radial magnetometer performances for sources outside the helmet would be comparable, while for the sources within the helmet the vector magnetometer localization error would be larger.

It has been argued [117] that if multiple sources with overlapping waveforms are present, then the vector magnetometer information can result in better localization. However, the experiments were performed with a relatively small-area array (not a whole-cortex system) and no comparative analysis of the radial and vector devices with equal number of channels was performed.

It is sometimes argued that measurement of the radial field components is preferable because they are less dependent on the volume currents than the tangential components [137]. However, simulations with realistically shaped conductor models showed that the disturbances of the conductor shape produce equal distortions in all three field components [139]. This conclusion is to be expected because any field component can be computed from the distribution of any other component by integrating $\text{curl } \mathbf{B} = 0$ in the current-free space outside the source region [61].

11.2.4.5 Comparison of Various Devices in the Presence of Environmental Noise

Finally, the performance of various devices is compared using detection probability curves (DPCs). The DPCs express the probability of finding a dipole within a specified volume as a function of the dipole magnitude [120]. The high-probability region of the DPCs for 1000-mm³ localization volume and for different device types are shown in Figure 11.15(a). The DPCs are steep and the dipole magnitude depends only weakly on the selected probability value. The environmental noise corresponds to typical MEG installations (curves (3) and (4) in Figure 11.11(b)) and is characterized in terms of parameters defined in Section 7.6.2. Generally, devices with longer baselines detect higher noise and their DPCs are shifted to larger dipole moments. Thus the magnetometer-based systems have the worst detection capability, and for simple first-order hardware gradiometers the detection capability improves with decreasing baseline (similar to that discussed in Section 9.2.4.2). The devices with efficient noise cancellation (for example synthetic third-order gradiometers), resolve the smallest dipoles. Similar curves for a combination of planar gradiometers and magnetometers with SSS noise cancellation were not available at the time of writing.

The minimum resolvable dipole as a function of the dipole distance from the model sphere center is shown in Figure 11.15(b). The curves for all devices have a

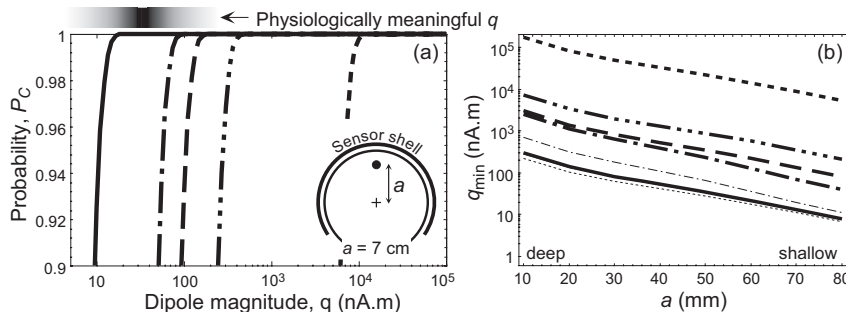


Fig. 11.15 Minimum detectable dipole magnitude. The symbols have the same meaning as in Figure 11.12. Simulated sensors, sensor shell radius $r = 110\text{ mm}$, extending from vertex to $11\pi/16$, the environmental noise parameters were collected with radial gradiometer with 50-mm baseline, onset of low-frequency noise for magnetometers $f_{o0} = 35\text{ Hz}$, first-order gradiometers $f_{o1} = 4\text{ Hz}$, and third-order gradiometers $f_{o3} = 0.7\text{ Hz}$, log-log low-frequency noise slope for all sensor types was 2, white sensor noise $v_w = 5\text{ fT rms}/\sqrt{\text{Hz}}$, $\Delta f = 30\text{ Hz}$, $N_{\text{ave}} = 1$, minimum frequency of interest $f_{\min} = 0.3\text{ Hz}$. Heavy lines – typical environmental and white noise; thin lines – perfectly shielded systems (no environmental noise,

white noise only). - - - radial magnetometers, - - - first-order hardware radial gradiometer $b_{\text{rad}} = 150\text{ mm}$, - - - first-order hardware radial gradiometer $b_{\text{rad}} = 50\text{ mm}$, - - - planar gradiometer $b_{\text{pln}} = 16.5\text{ mm}$, — third-order synthetic gradiometer based on first-order hardware gradiometer primary sensors with 50 mm baseline, - - - radial magnetometers and first-order hardware gradiometers $b_{\text{rad}} = 150\text{ mm}$, - - - planar gradiometer $b_{\text{pln}} = 16.5\text{ mm}$. (a) High probability end of DPCs for dipole detection within 1000 mm^3 . (b) Minimum resolvable dipole magnitude (99% probability of detection within 1000 mm^3 volume) as a function of the dipole distance from the model sphere center.

similar dependence on distance, but their magnitudes are different. The curve for the perfectly shielded radial first-order hardware gradiometer with $b_{\text{rad}} = 50\text{ mm}$ is hidden behind the heavy solid line for the third-order synthetic gradiometers (the synthetic gradiometers eliminate almost all environmental noise and their resolution is nearly the same as that of a perfectly shielded first-order gradiometer). Figure 11.15(b) extends the findings of Figure 11.15(a) and indicates that the relative behavior of different sensors is not affected much by the dipole position.

The thin lines in Figure 11.15(b) show what would happen if the MEG system were placed within a perfect shield (no environmental or brain noise, random noise only). In this case the magnetometers and long-baseline gradiometers would produce the best resolution (thin dashed line, the two devices are nearly indistinguishable). The radial gradiometer with 50-mm baseline would perform roughly the same as the third-order synthetic gradiometer (because there is no environmental noise to cancel). The performance curves of these devices are hidden behind the heavy third-order gradiometer line computed in the presence of noise. The difference between the thin dashed line (magnetometer in noiseless case) and the heavy solid line (synthetic third-order gradiometer in the presence of noise or radial gradiometer with 50-mm baseline in the absence of noise) is the basis for occasional claims that magnetometers resolve smaller dipoles than gradi-

ometers. However, even in the noiseless situation the difference is very small and since in practice perfect shielding is never realized, shorter-baseline gradiometers consistently outperform the long-baseline devices or magnetometers. The perfectly shielded planar gradiometer is also shown by thin dash-dot-dash line. Its performance is poorer than that of the perfectly shielded radial devices because it is less sensitive to deep sources (see Figure 11.10(b)).

In addition to the sensor array ability to localize dipole sources, the total information obtained by the available number of SQUID sensors can also be examined. According to Shannon's theory of information transmission [121], the information gained through one sample in a single MEG channel is $I = 1/2 \log_2 (P + 1)$. Here P is the power SNR, which can be calculated as the ratio of the signal power of the activity due to random current density throughout the brain to the mean square noise power of the sensors [122].

To obtain the total information of multisensor arrays covering the whole head, the overlapping lead fields of the channels need to be orthogonalized. The total information per sample in the whole array is then obtained by adding the information conveyed by each of the orthogonalized channels, $I_{\text{tot}} = 1/2 \sum_k \log_2 (P_k' + 1)$, where P_k' is the power SNR of the k th orthogonalized channel [122]. These calculations were recently utilized to find the optimal number of sensors and to compare arrays containing sensors of different type [123]. The conclusions reached in the paper illustrate applications of this method, and show that if the sensor noise is scaled to increase with increasing channel density, then for each MEG system there exists a limiting number of channels beyond which the total information cannot be increased. If the sensor noise is independent of the number of channels, the sensor array information increases monotonically with the increasing number of channels. The information calculations, however, cannot be used to deduce the MEG resolution at a particular location in the brain.

11.2.5

Fetal MEG Systems

11.2.5.1 Introduction

Fetal MEG (fMEG) is closely related to MEG. The objective of fMEG is to measure the brain activity of unborn fetuses. It is a difficult task, because fetal brain signals are small in comparison with adult signals, the fetal brain is typically more distant from the sensor array than the adult brain, and further, detection is performed in the presence of strong interference from the maternal and fetal hearts and various abdominal signals (intestinal electrical activity, uterine contractions, and so forth). Additional artifacts are produced by fetal (and maternal) motion and the fact that the locations of the fMEG signal maxima depend on the fetal head position.

Averaged fMEG signals in response to auditory stimuli were first reported by Blum *et al.* [124] and repeated later at several laboratories [125–128]. In order to eliminate successfully the interference due to cardiac signals (which could be more than 100 times larger than the fMEG signals), later efforts employed various

signal extraction methods (spatial filtering, PCA, and so forth) in addition to averaging. Magnitudes of the reported fMEG signals for transient tone bursts are in the range of 8 to 180 fT and the latencies range from about 125 to nearly 300 ms, decreasing with increasing gestation age [126]. The response is typically observed in not more than about 50% of examined subjects. Fetal responses to steady-state auditory clicks has also been reported [129].

Early experiments used single- or multiple-channel probes with relatively small coverage area, requiring a search for the region with the largest fMEG signals. In this section the design philosophy and construction of optimized fMEG instrumentation are described [130].

11.2.5.2 Design Philosophy

Even though modern SQUID sensors have sufficiently low noise, the SNR of fMEG is usually poor because of various interferences and motion artifacts. The ability to remove the interference is one of the more important fMEG requirements and it clearly leads to the need for large signal space where the interference signals are easier to separate from the fetal brain signals. Large signal space implies a large number of channels. The presence of motion artifacts (fetal, and to a certain extent also maternal) suggests that the measurements should be performed rapidly while the mother is in a comfortable position.

Smaller, conventional SQUID probes suspended above the mother's abdomen by a gantry often require repeated repositioning to locate the region of maximum signal and the mothers must be supine (or nearly supine) which is difficult to maintain over an extended period of time. The suspended probe can be constructed to cover most areas of the abdominal surface; however, physically larger probes would preclude mapping below the pubic symphysis (joint located in the front of the pelvis), where the fMEG signals may be largest during late gestation periods. On the other hand, the suspended probe should be sufficiently large to satisfy the requirement of a large number of channels and large signal space.

A better choice than a suspended probe seems to be a floor-mounted stationary SQUID system, on which the mother sits and leans her abdomen against a suitably shaped sensing surface. Such a design can cover all required areas including the perineum, is inherently safe, and the mother is comfortable and can easily mount or dismount the system [130]. Having the mother seated on the dewar has the potential disadvantage of adding vibrational noise from the mother to the sensors. However, such noise can be eliminated using synthetic higher-order gradiometer noise cancellation [131, 132].

11.2.5.3 Construction of fMEG System

Relatively small-area, gantry-suspended probes for fMEG do not differ much from general-purpose SQUID systems, and will not be discussed here. Instead, specialized fMEG instrumentation designed according to the principles stated in Section 11.2.5.2 will be described [130].

An array of 151 SQUID sensors is shaped to cover the mother's anterior abdominal surface, from the perineum to the top of the uterus (in late gestation) and is shown in Figure 11.16. The primary flux transformers are radial first-order gradiometers with 80-mm baseline and 20-mm coil diameter. The nominal system white noise levels are 4 fT rms/ $\sqrt{\text{Hz}}$. The sensor array surface is curved to fit the pregnant abdomen, covering a region ≈ 0.45 m high and ≈ 0.33 m wide with an area of about 0.13 m^2 , and inclined at roughly 45° (the sensor layout with a narrow perineal region is shown in Figure 11.16(c)). The dewar is horizontal and it also contains a set of 29 references for noise cancellation with higher-order gradiometer synthesis (see Section 7.4.3). The fMEG system is operated under the same shielding conditions as the standard MEG systems (Section 9.2.3.3). An adjustable padded seat matches the height of the perineal dewar extension, so that the mother can sit upon and lean against the sensor surface, as shown in Figures 11.16(a) and (b).

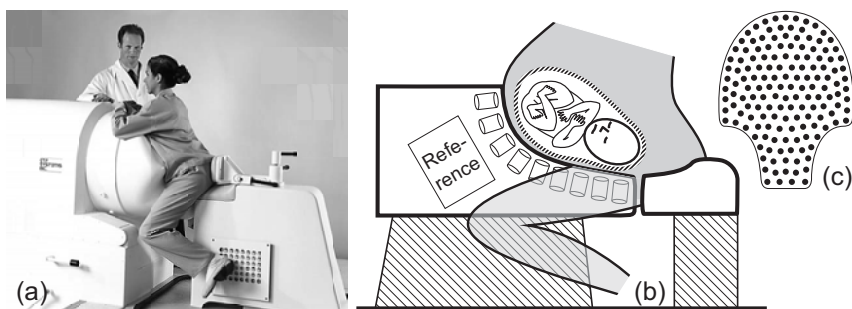


Fig. 11.16 Fetal MEG system, SARA (SQUID Array for Reproductive Assessment) [8].
(a) Photograph of the system where mothers sits on and lean against the fMEG sensor array.
(b) Schematic showing sensor and reference positions in relation to fetus.
(c) Sensor layout in the 151-channel fMEG system.

The auditory stimuli are generated by a speaker mounted outside the shielded room. The sound is either transmitted directly into the shielded room with an intensity of about 100 dB [125, 128], or conducted to the mother's abdomen by internal 25-mm diameter flexible plastic tubing and terminated by a soft-rimmed anesthesia mask [130]. In the latter configuration, the sound pressure level at the exit from the mask is 120 dB resulting in estimated sound pressure within the abdomen of 70 to 80 dB. Visual stimulation is accomplished by a light emitting diode (LED) source located outside the shielded room. The light flash from the LED is conducted to the room through a 7.7-m long fiber-optic cable terminated over the maternal abdomen by a plastic multifiber dispersing device placed above the fetal eye [133].

11.2.6

MEG Data Analysis**11.2.6.1 General Principles**

MEG measures the distribution of magnetic field on the scalp surface. However, it is often required to invert the magnetic field and provide information about the current distribution within the brain. It was shown in Chapter 10 that such an inversion problem is ill-defined and non-unique, and that, in order to succeed, MEG data must be supplemented by additional information, additional physiological constraints, or simplified mathematical models of the sources. While fundamentals of a generic inversion problem are outlined in Chapter 10, this section surveys methods used in MEG practice, including current dipoles, various flavors of minimum norm techniques, beamformers, multiple signal classification (MUSIC), principal component analysis (PCA), independent component analysis (ICA), and Bayesian methods. Since the literature associated with various techniques presented in this chapter is voluminous, the references are not exhaustive and only a selected few typical works are cited.

The different inversion methods used in MEG can be theoretically unified if the same second-order statistics are uniformly applied [134]. Generally, we wish to determine the current distribution in the brain, or distribution of current dipoles, \mathbf{q} , from the measured magnetic field, \mathbf{m} . The problem can be stated as

$$\mathbf{m} = \mathbf{L}\mathbf{q} + \mathbf{v} \quad (11.2)$$

where \mathbf{m} is a $K \times 1$ vector of the measurement, K is the number of MEG channels, \mathbf{L} is a $K \times p_c$ lead field matrix [86] relating p_c cortical dipoles to K measurements, \mathbf{q} is the $p_c \times 1$ vector of signed current dipole amplitudes, and \mathbf{v} is the $K \times 1$ vector of noise (anything not accounted for by $\mathbf{L}\mathbf{q}$). Assuming independence between noise and dipoles, it is shown in [134] that the generalized linear solution of Eq. (11.2) for current dipole amplitudes is

$$\hat{\mathbf{q}} = \mathbf{C}_q \mathbf{L}^T \mathbf{C}_m^{-1} \mathbf{m} = \mathbf{C}_q \mathbf{L}^T (\mathbf{L} \mathbf{C}_q \mathbf{L}^T + \mathbf{C}_v)^{-1} \mathbf{m} = (\mathbf{L}^T \mathbf{C}_v^{-1} \mathbf{L} + \mathbf{C}_q^{-1}) \mathbf{L}^T \mathbf{C}_v^{-1} \mathbf{m} \quad (11.3)$$

where \mathbf{C}_q is the source covariance matrix, \mathbf{C}_v is the noise covariance matrix, and \mathbf{C}_m is the data covariance matrix given by $\mathbf{C}_m = \mathbf{L} \mathbf{C}_q \mathbf{L}^T + \mathbf{C}_v$; here noise and dipoles were assumed to be independent. The superscript ‘T’ denotes matrix transpose. Even though Eq. (11.3) represents the general linear solution of the inversion problem and various inversion approaches can be related to it, it is still insightful to show alternative approaches to and specific properties of various flavors of the inversion methods. This will be done in this section where connections to Eq. (11.3) will be noted.

It is assumed that the MEG data were subjected to noise cancellation and were prepared according to the requirements imposed by various experiments. For example, relevant time segments were selected (*e.g.*, in epilepsy studies), artifacts

were removed (eye blinks, motion artifacts, or bursts of power line amplitudes if unshielded, and so forth), data were filtered to the required bandwidth, data were averaged if applicable (*e.g.* in evoked studies), any offset was removed, and in special situations a subset of channels was selected. Various analytic techniques require a different degree of data preparation. In one extreme, the dipole or minimum norm analyses require meticulous removal of artifacts and environmental noise. In the opposite extreme, spatial methods such as, for example, beamformers, are relatively insensitive to environmental noise or artifacts because such disturbances are usually represented by different signal space vectors from the signal.

11.2.6.2 MEG Data Interpretation (MEG Source Imaging)

Equivalent Current Dipole

The simplest brain source model is an infinitely small current element embedded within the conducting medium of the brain (ECD), representing coherent activation of neurons located within a small area, *e.g.* [61, 64, 86, 135, 136]. The ECD corresponds to the intracellular current in Figure 11.3 and it induces volume return currents in the conducting medium. The model is especially simple if the brain can be represented by a uniformly conducting sphere [59, 61, 63, 66]; however, the model has also been extended to spheroidal counducting media [137], multiple local sphere approximation [138], or realistic head shapes, *e.g.* [139, 140].

Assume a current dipole, \mathbf{q} , in a spherical conducting medium, positioned at a distance \mathbf{a} from the model sphere center. If the sphere center is at the origin, then the magnetic field at a position \mathbf{r} can be expressed analytically as [66]

$$\mathbf{B}(\mathbf{r}) = \frac{\mu_0}{4\pi F^2} \{ F \mathbf{q} \times \mathbf{a} - [(\mathbf{q} \times \mathbf{a}) \cdot \mathbf{r}] \nabla F \}, \quad (11.4)$$

where

$$F = r_o(r_o + r^2 - \mathbf{a} \cdot \mathbf{r}), \quad (\mathbf{r}_o = \mathbf{r} - \mathbf{a}) \quad (11.5)$$

and

$$\nabla F = (r^{-1}r_o^2 + r_o^{-1}\mathbf{r}_o \cdot \mathbf{r} + 2r_o + 2r) \mathbf{r} - (r_o + 2r + r_o^{-1}\mathbf{r}_o \cdot \mathbf{r}) \mathbf{a}. \quad (11.6)$$

If, in addition, the field is measured only in radial directions, then Eq. (11.4) simplifies to the radial component of the Biot–Savart law for the dipole current, and the volume currents do not contribute any field [61, 64, 141]. The tangential fields, however, depend on the volume currents and the full expression in Eq. (11.4) must be used. Only the tangential current dipole components will produce field outside the model sphere; the radial components will produce zero field. This implies that the current dipole located at the center of the model sphere will produce zero field outside the sphere because its orientation is always radial.

The responses of various flux transformer arrays to one ECD are shown in Figure 11.17. For the radial devices, that is radial magnetometers or gradiometers, the field patterns exhibit two opposite polarity extrema, one on each side of the dipole. The measured field strength and its spatial extent are slightly smaller for the radial gradiometer than for the radial magnetometer, and the difference decreases with increasing baseline length. The tangential magnetometers and planar gradiometers, oriented as in Figure 11.10(a), exhibit a single extremum directly above the dipole. The peak-to-peak signals of radial devices are roughly a factor of two larger than those of the tangential magnetometers or planar gradiometers.

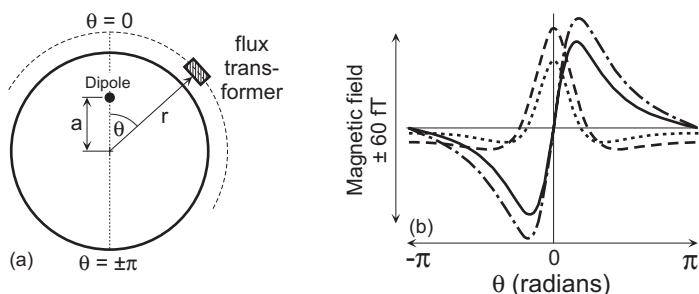


Fig. 11.17 Response of various sensor types to an equivalent current dipole. The dipole is located on the x_3 axis and oriented along the x_1 axis. The sensors are located on a circle concentric with the model sphere and located in the x_2-x_3 plane, $a = 50$ mm, $r = 110$ mm, dipole magnitude $q = 10$ nA m. (a) Geometry of the model. (b) Sensor response: — radial

magnetometers, — radial gradiometers with 50-mm baseline, - - - tangential magnetometers, - · - - planar gradiometers with 16.5-mm baseline. The tangential magnetometer coil orientation and the planar gradiometer baseline direction are in the x_2-x_3 plane in order to intercept the extrema of the dipole fields and gradients.

If the measured magnetic field is dipolar (see Section 11.2.6.3 for an example), the position and orientation of a single or multiple dipole can be determined by a nonlinear fit. The number of dipoles and their initial positions are guessed and the dipole parameters are determined by a nonlinear search designed to minimize differences between the computed and measured fields, e.g. [135, 144–146]. Such a procedure works well for one or two dipoles; however, when more dipoles are used the solutions often get trapped in local minima. In such situations global optimization methods [147], including clustering methods [148], genetic algorithms [149], or simulated annealing [150] may be used.

Signal Space Projection

Signal space projection (SSP) [151, 152] is an analysis method where the measured fields are expressed in terms of vectors in a K -dimensional signal space (K is the number of sensors). It is assumed that component vectors corresponding to different neuronal sources have distinct and stable (fixed) orientations and only their magnitudes are functions of time. If the directions of some of the vectors

forming the multichannel signal can be determined from the data (or are known otherwise), the SSP can be used to separate the data into two orthogonal parts: a subspace which contains time-varying contributions from sources with known signal space directions, and an orthogonal subspace containing the rest of the signal. Both signal subspaces can be studied separately. Separating strong signals can reveal activity which may have been masked by them, or sources with known signal space direction can be examined with enhanced SNR. If the vectors are formed by forward modeling corresponding to known sources, the SSP can be used as a spatial filter that passes only signals corresponding to these known sources. Alternatively, if the vectors associated with artifacts are known, the SSP can be used to eliminate these artifacts from the signal [153]. If the signal vectors are determined from the data, the source model need not be known. Restricting all sources to current dipoles in a known volume conductor model reduces the SSP to the multiple dipole approximations [152]. The SSP method is used not only for MEG, but also for other biomagnetic data analysis (for example MCG).

Minimum Norm

The dipole model assumes that the brain activity is localized in one or several small areas of the brain. Sometimes it is required to obtain a more general inverse solution without *a priori* assumptions about the source current distribution. Such an inverse problem can be linearized by dividing the investigated volume into a grid and assigning an unknown current to each grid element (voxel). The problem is highly underdetermined, that is, there are many more parameters than measurements. However, it can be solved uniquely if it is also required that the current vector norm be minimized. Such solutions belong to the family of minimum norm methods, first proposed for MEG applications by Hamalainen and Ilmoniemi [154]. The mathematically unique solution to the minimum norm problem is obtained by the Moore–Penrose inverse, also known as minimum norm least squares (MNLS) inverse, or pseudoinverse [155, 156].

The minimum norm procedure usually places three orthogonal current dipoles at each voxel. If there are n voxels, then the number of dipoles is $p_c = 3n$. The lead field element L_{ij} describes the relationship between a voxel current component j and the sensor i . In its simplest form the minimum norm solution for the currents is $\mathbf{q} = \mathbf{L}^+ \mathbf{m} = \mathbf{L}^T (\mathbf{L}\mathbf{L}^T)^{-1} \mathbf{m}$, where the superscript ‘ $+$ ’ denotes the pseudoinverse. This solution is obtained from Eq. (11.3) by setting $\mathbf{C}_q = \mathbf{I}$ and neglecting the noise covariance matrix \mathbf{C}_v . Minimum norm solutions are generally diffuse and the lead field matrix favors solutions closest to the sensors.

This bias can be removed by a suitable weighting (unbiased solution). If \mathbf{W} is the weighting matrix, then the weighted minimum norm solution is, e. g. [157, 158]

$$\mathbf{q} = \mathbf{W}\mathbf{W}^T \mathbf{L}^T (\mathbf{L}\mathbf{W}\mathbf{W}^T \mathbf{L}^T)^{-1} \mathbf{m}. \quad (11.7)$$

Equation (11.7) can be obtained from Eq. (11.3) by setting $\mathbf{C}_q = \mathbf{W}\mathbf{W}^T$ and neglecting \mathbf{C}_v . The elements of the weighting matrix can be chosen to compensate for the

undesirable depth dependency (for example, lead field normalization [157]). Such weighting reduces the minimum norm tendency to push the solutions towards the surface, but the solutions are still diffuse.

The minimum norm method has also been adapted to produce sparse localized solutions [159]. The resulting algorithm, FOCUSS (FOCal Undetermined System Solution), is a recursive linear estimation based on the weighted pseudoinverse solution. The weights at each step are derived from the solutions of the previous step. The algorithm proceeds from an initial estimate to a source distribution where the number of system parameters does not exceed the number of measurements. The weights are contained in the matrix W (Eq. (11.7)). The FOCUSS weighting matrix usually contains the currents derived in the previous step as its diagonal elements, or the weights can be compound products of all previous solutions. The matrix W also contains weights for correction of the depth bias due to the lead field matrix L . A related method, magnetic field tomography (MFT) [160, 161], utilizes weights (and regularization parameters) which are optimized according to the given experimental geometry and noise. The MFT has been successfully used to analyze unaveraged single trial data.

An illustration of the characteristic behavior of several minimum norm methods is shown in Figure 11.18 [157]. The minimum norm solutions are diffuse and superficial, even for the deepest sources. The unbiased minimum norm solutions are diffuse, but no longer superficial, and FOCUSS reconstructs the source exactly at all investigated depths.

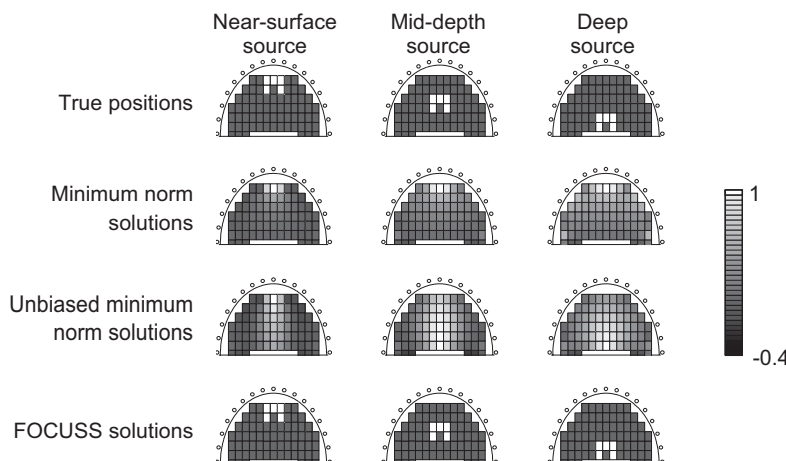


Fig. 11.18 Resolution achieved with different minimum norm techniques for an extended source at different depths. Each column illustrates a different depth source (near-surface, mid-depth, and deep) and each row illustrates a different reconstruction method (minimum norm, unbiased minimum norm, and FOCUSS). Simulated current distributions are

illustrated in the top row. The compound version of FOCUSS with bias compensation was used. Each subimage was normalized by dividing each element by the maximum value in the image. (Courtesy of Irina Gorodnitsky, Cognitive Science Dept., University of California, San Diego. Adapted from [157] with permission.)

It was proposed to normalize the MNLS current dipole distribution estimate, Eq. (11.3), by the standard error due to the additive noise [162]. Such normalization produces a statistical parametric map (SPM) for each time point, and the SPMs for multiple time points were combined to obtain dynamic SPM mapping of cortical activity. The approach is similar to the construction of SPMs for functional MRI.

Another approach to the minimum norm is the algorithm LORETA (low-resolution electromagnetic tomography) [163]. This algorithm introduces a spatial second derivative operator (Laplacian) into the weighting function and seeks the minimum norm solution subject to the maximum smoothness condition. This requirement is justified on a physiological basis by assuming that the neighboring points in the brain tissue are likely to be synchronized. This method produces low spatial resolution which is a consequence of the smoothness constraint. The standardized LORETA (sLORETA) [164] is a MNLS method where the resulting current density power is weighted, on a location-dependent basis, by the estimates of its variance. The sLORETA is not affected by source correlations, but in the presence of random noise it produces small localization errors. Simultaneously active sources can be separated only if their fields are distinct and of similar strength; weak or deep sources remain invisible in the presence of a strong superficial source, and nearby sources of similar orientation are interpreted as one source roughly located between them [165].

The standard MNLS methods belong to the class of L_2 norms. To improve on their general blurriness, approaches based on the L_1 norm (absolute value) were proposed [166–168]. For norms other than L_2 , nonlinear minimization is necessary. One approach is to seek a maximally sparse solution [166] where the number of nonzero current dipoles is equal to the number of MEG channels. There are many maximally sparse solutions available and the acceptable one corresponds to the minimum norm of the selected nonzero dipoles. The L_1 norm can be found efficiently using linear programming methods [169]. A “standard” L_1 norm technique [167] assumes that the current dipole orientations are known in advance. The orientations can be obtained either from MRI images or from a weighted MNLS estimate. The L_1 norm current dipole estimation is then performed by linear programming relative to the known orientations. The method was named minimum current estimate (MCE). Because the estimation of the current distribution is ill-posed, it is necessary to regularize the estimate. The MCE uses the singular value decomposition regularization method and the number of located current dipoles is equal to the regularization cut-off index. The nonlinear L_1 approaches exhibit better localization accuracy and improved spatial resolution at high SNR. At low SNR, these algorithms tend to show scattered and spurious results for deeper source locations.

Beamformers

The current distribution in the brain can also be obtained using beamformers. The beamformer is a spatial filter designed to extract electrical activity from a target location in the brain while suppressing contributions originating outside the

target. Thus beamformers can reduce interference from other parts of the brain, from other electrically active tissues in the human body, and from the environment. The beamformer can be used to construct a volumetric image of the averaged local electrical activity (power or some other related parameter), or to extract the time course of the activity originating from a target location (synthetic channel). The beamformer spatial resolution depends on the SNR of the target current source. For low SNR the beamformer spatial resolution is low and a point current dipole is detected as an extended three-dimensional spot. Conversely, for high SNR, a point source is manifested as a spatially small high-power point in the investigated region of interest (ROI).

The beamformers utilize spatial and temporal correlations to obtain information about uncorrelated dipolar sources. The linearly constrained minimum variance (LCMV) beamformers in the form which is now used in MEG were first described in 1972 [170]. The beamformer literature is vast and only a few selected references are given here. An introduction to beamformers may be found in, for example, [171] and a relatively recent review of various beamforming techniques in [172]. Two beamformer types are discussed in this section: the LCMV beamformers [173–176], which can be operated without specific information about the source orientation, and beamformers which include the source orientation either by performing a four-dimensional search for three coordinates and one orientation (synthetic aperture magnetometry, SAM [177]), or by determining the orientation directly [178].

To describe the beamformer mathematics, assume that the MEG measurement can be modeled by fixed and uncorrelated multiple dipoles in a homogeneous, spherical, conducting medium. Also, assume that the data correspond to MEG, where only the tangential dipole components contribute to the signal (extension to EEG where all three dipole components contribute is straightforward). To localize all dipoles, we divide the ROI into a three-dimensional grid, where each grid cell is called a voxel. The beamformer is then successively scanned through all the voxels within the ROI, the beamformer parameters corresponding to all voxels are determined, and the dipole positions are identified as the voxels at which the volumetric image of some beamformer parameter peaks.

The geometry for the beamformer (and MUSIC) analysis is shown in Figure 11.19(a). There is one dipole (or more) positioned within a spherical conducting medium. One current dipole, \mathbf{q}_o , is shown at a location O. The beamformer probes a location denoted by θ , which may or may not be coincident with the dipole \mathbf{q}_o . First, consider the LCMV beamformer. The dipole moment at the voxel θ can be decomposed into two orthogonal tangential components, $\mathbf{q}_{\theta 1}$ and $\mathbf{q}_{\theta 2}$, shown in Figure 11.19(b). The forward solutions per unit dipole for these two components, $L_{\theta k}$, $k = 1, 2$, can be combined into a gain matrix, $H_\theta = [L_{\theta 1}, L_{\theta 2}]$. Let the vector $\mathbf{m}(t)$ represent an instantaneous MEG measurement; the number of components in \mathbf{m} is equal to the number of channels, K. Define a spatial filter centered on the location θ as $y_\theta(t) = \mathbf{W}_\theta^T \mathbf{m}(t)$, where \mathbf{W}_θ is the weight matrix. The elements of $\mathbf{m}(t)$ are assumed to be zero mean stationary processes and the beamformer weights are determined by minimizing the power projected from the location θ ,

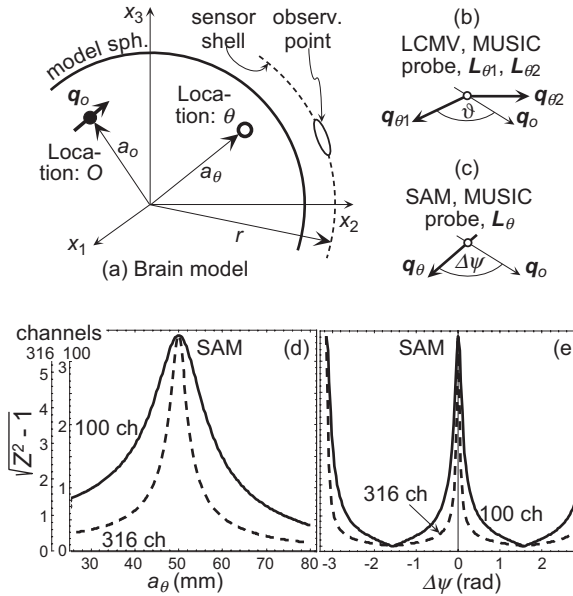


Fig. 11.19 (a) Geometry for analysis of beamformers and MUSIC. Sensor shell with radius r is concentric with the model sphere. Dipole \mathbf{q}_o is positioned at a distance a_o from the model sphere center (position O) and the probe is positioned at a distance a_θ from the model sphere center (position θ). (b) The LCMV probe has two orthogonal directions \mathbf{q}_{o1} and \mathbf{q}_{o2} . (c) The MEG dipoles are probed in the tangential plane; the SAM probe is oriented at an angle $\Delta\psi$ relative to the \mathbf{q}_o .

(d) Analytically computed SAM depth profile when a dipole is on x_3 axis, the sensor shell is rotationally symmetric around x_3 axis, and the probe is aligned with the dipole. Hemispherical sensor shell, $r = 110$ mm, $v = 3$ fT/Hz, $\Delta f = 15$ Hz, $q_o = 1$ nAm, $a_o = 50$ mm, 100 and 316 channels, scales are different for different number of channels. (e) SAM dependence on the probe orientation when the probe is at the dipole location. $a_o = a_\theta$; same parameters as in (d).

$P_\theta = \mathbf{W}_\theta^T \mathbf{C}_m \mathbf{W}_\theta$, subject to the unity gain condition, $\mathbf{W}_\theta^T \mathbf{H}_\theta = \mathbf{I}$, where \mathbf{C}_m is the covariance matrix of the measurement and \mathbf{I} is the identity matrix. The weights are given as [176]

$$\mathbf{W}_\theta = \mathbf{C}_m^{-1} \mathbf{H}_\theta (\mathbf{H}_\theta^T \mathbf{C}_m^{-1} \mathbf{H}_\theta)^{-1}. \quad (11.8)$$

The weights can be used to compute the time course of the dipole magnitude variation at voxel θ , $\gamma_\theta(t)$ – the synthetic channel, or the local power, P_θ , or an especially useful quantity, the power normalized by the noise projected by the beamformer [176]. This will be called a pseudo- Z^2 quantity [177], $Z_\theta^2 = P_\theta / N_\theta$, where $N_\theta = \mathbf{W}_\theta^T \mathbf{C}_v \mathbf{W}_\theta$ is the sensor noise projected by the beamformer from location θ , and \mathbf{C}_v is the sensor noise covariance matrix. The normalization by noise is important because it removes divergence of the projected power when the beamformer target voxel approaches the model sphere center (where the forward solution ap-

proaches zero). The ratio P_θ/N_θ removes the divergence because both P_θ and N_θ exhibit singularities of the same type.

An alternative approach is to construct a beamformer where at each three-dimensional location the power or noise projected by the beamformer is probed only for one tangential current dipole direction as in Figure 11.19(c). This direction is rotated in the tangential plane and the orientation at which some beamformer parameter (for example P_θ or Z_θ^2) is maximized corresponds to a solution for that location [177]. In such case the location indicator θ is four-dimensional (three spatial coordinates and one orientation) and the procedure corresponds to SAM. Alternatively, the preferred orientation can be determined from a 2×2 matrix computed from the covariance matrix and the lead fields [178]. By retaining only one vector in the gain matrix, $H_\theta = L_\theta$, the SAM weights are obtained from Eq. (11.5) as $W_\theta = C_m^{-1}L_\theta/L_\theta^T C_m^{-1}L_\theta$. Note that the weights in the form $C_m^{-1}L_\theta$ (that is without the scaling factor $L_\theta^T C_m^{-1}L_\theta$) were already proposed for MEG applications in 1992 [179].

The beamformer formalism can also be derived from Eq. (11.3) [134] by assuming that the dipole sources are independent. Then the source covariance matrix C_q is diagonal and, by adjusting the diagonal elements of C_q for perfect resolution, it can be shown that Eq. (11.8) is related to Eq. (11.3). The relationship among the beamformers and other linear estimation methods are also reviewed in [180].

So far the discussion has dealt with beamformers configured for maximum spatial resolution. The beamformer equations can be regularized by adding an additional condition that the sensor noise projected by the beamformer does not exceed a certain specified limit [177]. The completely regularized SAM beamformer is equivalent to the projection of the measurement to the target vector (or SSP, discussed above); it projects minimum sensor noise but its spatial resolution is poor. The slight noise increase is usually not a problem and unregularized beamformers are mostly used in practical applications.

The sensor array sensitivity patterns can provide a useful insight into beamformer functioning. The sensitivity pattern of a single radial gradiometer is shown in Figure 11.20(a) for three interference sources and one target source. The single channel exhibits a sensitivity null (white region) directly under the sensor. All three interferers and the target are in nonzero sensitivity regions and their signals will be intermixed in the single channel output. The situation for the unregularized SAM is shown in Figure 11.20(b). In this case the SAM weights, W_{target} , were determined for the target voxel in the presence of the three interference sources. The SAM sensitivity to a dipole source at location x is then $W_{\text{target}}^T L_x$, where L_x denotes the forward solution for dipole at x . The SAM beamformer projects sensitivity nulls to the vicinity of the interferers, while maintaining unit sensitivity to the target. The closeness of the nulls to the interferers depends on the SNR. For decreasing SNR, the nulls move away from the interferers and the interferer power begins to leak into the SAM output. Information about the nulls is in the covariance matrix of the measurement. The sensitivity pattern of a fully regularized SAM is shown in Figure 11.20(c). In this case the SAM is equivalent to SSP,

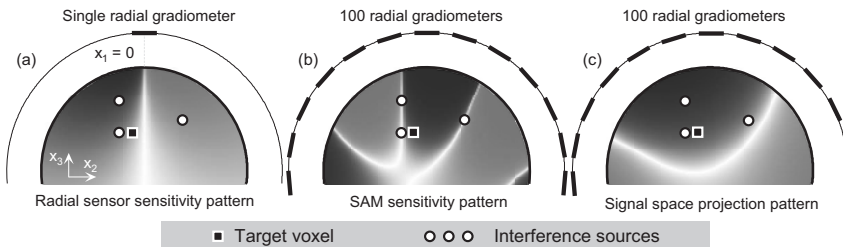


Fig. 11.20 SAM sensitivity patterns. The SAM weights were determined for the indicated target voxel and the interference sources. $K = 100$ channels, sensor shell radius $r = 107$ mm, conducting sphere radius = 80 mm, sensor white noise $v_w = 3$ fT rms/ $\sqrt{\text{Hz}}$, bandwidth $\Delta f = 15$ Hz, no brain noise. Sensors are radial gradiometers with 50-mm baseline, only the proximal coils are shown symbolically by

short thick lines. Interferers: $q_1 = 35$ nA m at $(0, -20, 55)$ mm, $q_2 = 120$ nA m at $(0, -20, 30)$ mm, $q_3 = 50$ nA m at $(0, 30, 40)$ mm, all perpendicular to the figure plane. Target voxel at $(0, -10, 30)$ mm. Origin is at the sphere center, sensitivity is shown as gray-scale shading. (a) Single radial gradiometer. (b) unregularized SAM. (c) fully regularized SAM (SSP).

the spatial resolution is poor, the sensitivity null is far from the interferers, and the interferers and the target signals are mixed together.

Examples of the SAM beamformer response to one dipole are shown in Figures 11.19(d) and (e). The variation of Z_θ obtained by SAM as a function of the probe orientation when the probe is located on the dipole is shown in Figure 11.19(e) for the simulation of one dipole and sensor noise (no brain noise). The figure illustrates sharp selectivity of SAM relative to the dipole orientation. The SAM depth profile through the same dipole is shown in Figure 11.19(d). Even though the dipole is spatially point-like, the SAM (and also LCMV) responses are broadened, indicating the power leakage to the neighboring voxels. Such broadening can be reduced (or spatial resolution increased) by increasing the SNR or by increasing the number of channels (Figures 11.19(d) and (e)).

The effect of the number of channels on the SAM spatial resolution is further illustrated in Figure 11.21 [181] for a more realistic situation. Brain noise was measured in an unshielded environment by a 275 MEG system [8]. An ECD signal was added to the measured brain noise, the volumetric SAM Z^2 image was computed by unregularized SAM, and its three-dimensional contours at full-width-half-maximum (FWHM) were computed. Then the 275-channel sensor array was roughly uniformly spatially resampled to 138 channels and the SAM Z^2 FWHM contours were again constructed using the same, but resampled, data. It is evident that the increase in the number of channels from 138 to 275 increases the spatial resolution by more than a factor of two. In addition, the beamformer is more accurate for the larger number of channels, because the FWHM Z^2 contour center of gravity is closer to the true dipole position.

It has been shown by simulation, analytically, and on real MEG data that the SAM peak width is narrower than the LCMV peak width by a factor of $\sqrt{2}$ [182, 183]. Thus, even though the SAM is computationally more expensive than the

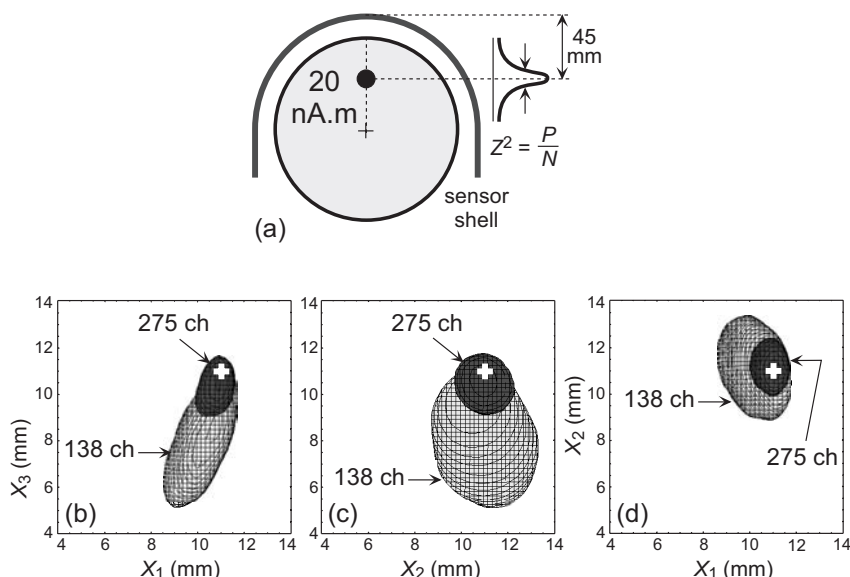


Fig. 11.21 Effect of spatial resampling on the SAM beamformer spatial resolution. (a) Experimental geometry. An ECD with 20 nA m magnitude and positioned about 45 mm below the sensor array was added to the measured brain noise; the ECD orientation was parallel to the prevailing local brain noise source orientation. (b, c, d) Three-dimensional contours of SAM Z^2 images

corresponding to the original 275-channel (dark) and the resampled 138-channel (light) sensor arrays. White "+" indicates the true source position, dark region corresponds to the 275-channel 3D contours, and the light gray region to the 138-channel 3D contour; 3D contours projected (b) to the x_1 - x_3 plane; (c) to the x_2 - x_3 plane; (d) to the x_1 - x_2 plane.

LCMV beamformer, it is a preferred choice for MEG because it produces better spatial resolution. Both SAM and LCMV can be treated analytically for one or two dipole sources if it is assumed that only the random noise is present, the problem has axial symmetry, and the sensor density is large [182, 183].

When the MEG measurements in two different states are available (*e.g.*, control and active states), it is often useful to compute pseudo-*T* or pseudo-*F* parameters in addition to the pseudo-*Z* parameter [177, 130, 184]. If the variance of the SAM image is computed instead of the projected noise (for example by bootstrap methods [185]), the true *Z*-, *T*, or *F*-statistics for the SAM result can be obtained [184].

The beamformers can also be constructed in the frequency domain [186], and the method is called dynamic imaging of coherent sources (DICS). DICS allows studies of cortico-cortical and cortico-muscular interactions by imaging power and coherence estimates within the human brain.

Multiple Signal Classification

The MUSIC method is related to beamformers [187–189]. MUSIC is a subspace scanning method. It determines the dipole parameters by requiring that the dipole forward solution be orthogonal to the noise subspace (or parallel to the sig-

nal subspace). MUSIC requires an additional nonlinear step of determining where to partition the covariance matrix into signal and noise subspaces. MUSIC assumes that there are fewer sources than sensors, the sources are uncorrelated and the noise is white. Sources are located by three-dimensional (or four-dimensional) scanning of the MUSIC probe through the brain volume (see Figure 11.19(a)–(c)) and at each location orthogonalizing the single dipole gain matrix to the noise subspace. The dipole orientation can be taken into consideration by evaluating the eigenvalue decomposition of a 2×2 matrix computed from the covariance matrix and lead fields [188].

In the limit of high SNR, small number of sources, and white noise, the MUSIC localizer function and the SAM projected power differ only by a scaling factor (because the contribution of the signal subspace to the inverse covariance matrix in the expression for the SAM power can be neglected). If the integration time were infinite, the MUSIC localizer would be singular while the SAM power would not. In this case neglecting the signal subspace would introduce excessive error.

If the MUSIC assumptions are not satisfied, that is, when multiple dipoles are active in the presence of spontaneous brain activity, the MUSIC results fluctuate widely as a function of subspace partitioning and no clear indication of the correct subspace partitioning can be obtained from the eigenspectra [183, 190]. MUSIC performs best when distinct transitions between the noise and signal subspaces can be identified. The beamformers behave gracefully even when multiple dipoles are active in the presence of spontaneous background brain activity and the covariance matrix is full rank.

To reduce the ill-posedness of the MEG inversion problem, a method was proposed to combine time–frequency analysis with MEG MUSIC and to estimate neural sources from each time–frequency component [191]. The algorithm is suited for localizing sources of nonstationary and transient MEG signals. Under the assumption that the brain responses to different stimuli are additive and the correlation between these responses is zero, and if separate control and active task measurements are available, MUSIC was modified to include a covariance subtraction method [192, 193]. Such a method was shown to be superior to a simple waveform subtraction and can handle situations where some of the control sources do not appear in the task measurement.

To conclude the discussion of beamformers and MUSIC, it should be pointed out that beamformers can also be modified to operate on signal subspaces and are sometimes called eigenspace beamformers, *e.g.* [194, 195]. The eigenspace beamformers can reduce background variations; however, the problem with determining the subspace partitioning is similar to that for MUSIC.

Principal Component Analysis

PCA, *e.g.* [196, 197], also determines the signal and noise subspaces. The method attempts to fit dipoles into the orthogonal principal spatial vectors of the singular value decomposition of the data. PCA has been shown to be potentially inaccurate, as it can mislocalize dipoles even in noiseless simulations.

Independent Component Analysis

ICA is a relatively new technique which allows separation of sources which are linearly mixed at the sensors. The method is also called blind separation, because the source signals are not directly observed and nothing is known about their mixture, *e.g.* [198, 199]. The mixing model used for the separation is usually stated as $\mathbf{m}(t) = \mathbf{A}_{\text{ICA}}\mathbf{s}(t)$, where $\mathbf{m}(t)$ is the instantaneous vector of the measurement, $\mathbf{s}(t)$ is the instantaneous source activity vector, and \mathbf{A}_{ICA} is the mixing matrix. The procedure provides solution for an unmixing matrix \mathbf{B}_{ICA} , such that the estimated source activity is given as $\hat{\mathbf{s}}(t) = \mathbf{B}_{\text{ICA}}\mathbf{m}(t)$, where $\hat{\mathbf{s}}$ is the estimate of the source vector \mathbf{s} . The sources are assumed to be statistically independent and the separation is obtained by optimizing a contrast function, that is, a scalar measure of some distributional property of the output $\hat{\mathbf{s}}$. The contrast functions are based on entropy, mutual independence, high-order decorrelations, and so forth. ICA has been applied to MEG and EEG either to remove artifacts or to extract desired signals, *e.g.* [200–202].

Bayesian Inference

Finally, the method based on Bayesian inference will be mentioned, *e.g.* [203–205]. The method determines expectation and variance of the *a posteriori* source current probability distribution given a source prior probability distribution and data set. The model can include probability weightings determined from fMRI or PET to influence the MEG current images. The method can be extended to include the parallel tempering for evading local convergence and the reversible jump procedure to facilitate the MEG inverse solution even when the number of neuromagnetic sources is not known [206].

11.2.6.3 Examples of MEG and fMEG Results

Adult MEG

The MEG time traces corresponding to mechanically stimulated somatosensory evoked fields (SEF) are shown in Figures 11.22(a) and (b). The data were collected in an unshielded environment by hardware first-order gradiometers and the large noise fluctuations (even after averaging) correspond mostly to the low-frequency background, not to the power lines at 60 Hz. The environmental noise is nearly completely cancelled by the third-order synthetic gradiometers in Figure 11.22(b), and the SEF response becomes clearly visible.

The SEF response is a good example of a single dipole signal. This is illustrated in Figure 11.22(c), where the magnetic field map corresponding to an averaged response from an electrically stimulated median nerve, collected within a shielded room, is shown. The map exhibits two extrema, one corresponding to the field exiting from the head and the other to the field entering the head. The dipole projected to the map surface is shown by an arrow located between the two field extrema. More examples of SEF, auditory, and visual fields can be found, for example, in [207].

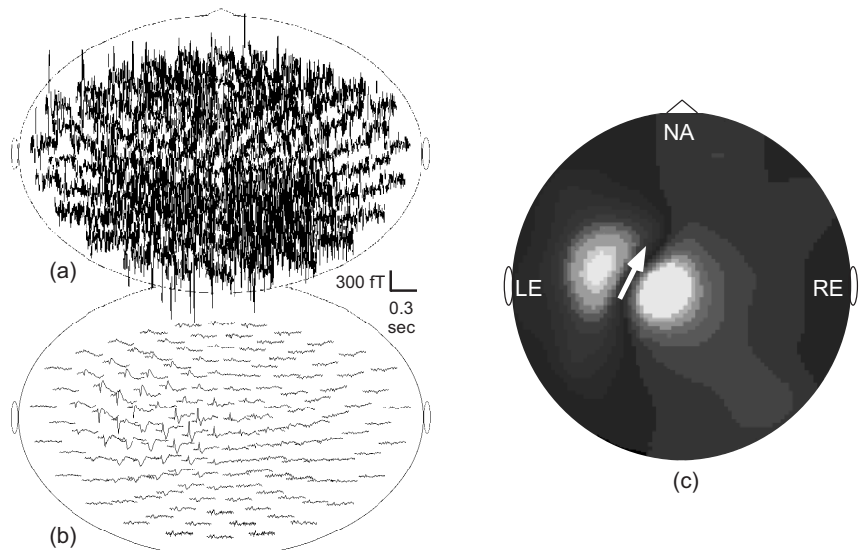


Fig. 11.22 Examples of MEG response to SEF stimulation. Results in (a) and (b) correspond to a different collection from the result in (c). (a, b) SEF data, unshielded, mechanical stimulation of the right index finger tip, randomized interstimulus interval = 0.6 to 0.9 s, 300 averages, trial duration 0.41 s, bandwidth 0 to 50 Hz. (a) First-order hardware

gradiometers with 50-mm baseline; (b) the same SEF data after noise cancellation with synthetic third-order gradiometers. (Courtesy of Dr. D. Cheyne, CTF Systems Inc.) (c) Dipole analysis of the SEF data; LE, RE – left and right ear, NA – nasion. (Courtesy of Dr. N. Nakasato, Kohnan Hospital, Sendai.)

Several examples of MEG data analysis using SAM are shown in Figure 11.23. Figures 11.23(a) and (b) correspond to an electrically stimulated median nerve, which yields a field map similar to that shown in Figure 11.22(c). The unaveraged signals were analyzed by SAM and are superposed on an MRI slice. The data were also averaged and the P50 feature was fitted by a single dipole (3.4% fit error), shown by a black-rimmed white dot. The dipole fit and the active region outlined by the SAM are in good agreement.

The left hemisphere changes of the source activity in the β -band (15 to 30 Hz) during silent tachistoscopic reading are shown in Figure 11.23(c). A nine-year-old subject was instructed to read a short story silently, and, after the data collection was completed, the subject was asked to summarize the story. Additional “nonsense” words containing no vowels were randomly inserted into the story with 50% probability. MEG data were partitioned by word category (readable or nonsense) and T -pseudo statistics were computed. Activation in the Vernike area (B) and suppression in the frontal area (A) are shown.

A SAM statistical image showing the brain region activated during auditory hallucinations in schizophrenia is shown in Figure 11.23(d) [208]. The subject could distinguish the “normal” and “hallucinogenic” states. The hallucinations usually

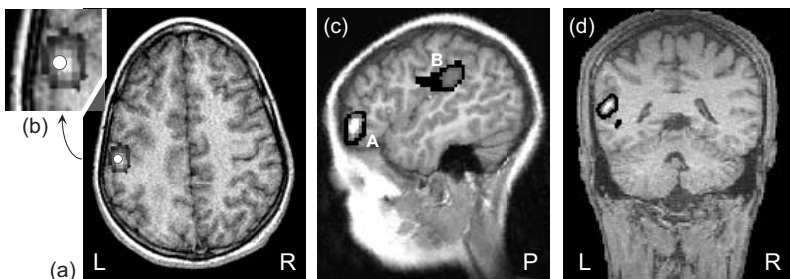


Fig. 11.23 Examples of SAM results. (a) SAM and dipole analyses of SEF data evoked by electrical stimulation of the right median nerve, bandwidth 30 to 100 Hz. The dipole is represented by a black-rimmed white dot overlaid on the SAM result. (Courtesy of Drs. D. Cheyne and S.E. Robinson, CTF Systems Inc.). (b) Enlarged region around the source in (a). (c) Left-hemisphere changes in the 15 to 30 Hz band during silent tachistoscopic

reading of a story randomly interspersed with 50% “nonsense” words (nine-year-old subject, text displayed at a rate of one word per sec, *T*-pseudo statistics. (Courtesy of Dr. S.E. Robinson, CTF Systems Inc.). (d) SAM image showing a region of brain activated during auditory hallucinations, in schizophrenia (*T*-statistics, logarithm of *p*-values is plotted for $p < 10^{-3}$, adapted from [208]).

lasted about 15 s. The subject was asked to press a button when the hallucination stopped. The active segment (-10 to -0.5 s) and control segment (0.5 to 10 s) were collected. Eight repetitions were available. *T*-statistics images¹⁾ were computed using the bootstrap method, known as jack-knife, and only the values of $p < 10^{-3}$ are shown. (Jack-knife is a special bootstrap method. The bootstrap techniques are used for assessing the accuracy of a parameter estimator in situations where conventional techniques are not valid, for example, there are not enough data [209].)

The application of the frequency-dependent beamformer and determination of synchronization and directionality indices by DICS [186] to demonstrate that slow finger movements are controlled by a cerebello–thalamo–cortical loop, synchronized at about 8 Hz [210], is shown in Figure 11.24. Subjects were asked to perform continuous sinusoidal flexion and extension movements in a horizontal plane with their right index finger. The MEG signals were recorded with 122 planar gradiometers and DICS was used to determine spatial distribution of coherent oscillatory activity.

Examples of applications of SAM and ECD fits to epilepsy are shown in Figure 11.25 [211]. SAM has been modified to the so-called SAM(g2) [212] to detect interictal spikes more clearly. In this method the brain volume is divided into voxels, synthetic channels $y_\theta(t) = \mathbf{W}_\theta^T \mathbf{m}(t)$ are computed at each voxel, and excess kurtosis is determined for each synthetic channel. The excess kurtosis is defined as $\sum_N [y_\theta(n) - \bar{y}]^4 / (\sigma_y^4 N) - 3$, where $n = 1, \dots, N$, N is the number of samples, and \bar{y} and σ_y are the mean and standard deviation of the synthetic channel. The excess

1) The *T*- and *F*-tests are statistical methods for hypotheses testing. The *T*-test compares the means of two groups when samples are or

are not from the same population. The *F*-test can, e.g., be used to determine if variances of two populations are equal.

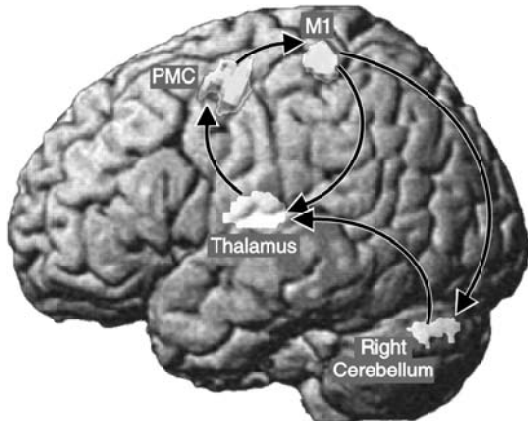


Fig. 11.24 Map of 6- to 9-Hz cerebral connectivities. The map represents spatial distribution of coherence with the left primary motor cortex (PMC) as a reference region. Only areas with $P < 0.05$ are shown. Note that the left thalamus and right cerebellum are projected to the left surface for easier visualization. The dominant coupling direction is indicated by arrows. Adapted from [210].

kurtosis is a normalized sum of the fourth powers of all samples of the synthetic channel and it emphasizes the spiking activity. Hot-spots in the volumetric image of the excess kurtosis represent regions in the brain where the spiking activity is large. Standard SAM synthetic channels are then derived for these hot-spots and the epileptic activity is displayed.

An example of a patient with a single interictal spike locus is shown in Figures 11.25(a) and (b). SAM(g_2) detected a single maximum near the left central sulcus in Figure 11.25(a). The interictal spikes were also fitted by ECDs and the corresponding dipole fit scattergram is shown in Figure 11.25(b). There is little difference between the two methods, other than the fact that the dipole fits indicate a slightly deeper source [211]. The result demonstrates that SAM(g_2) is equivalent

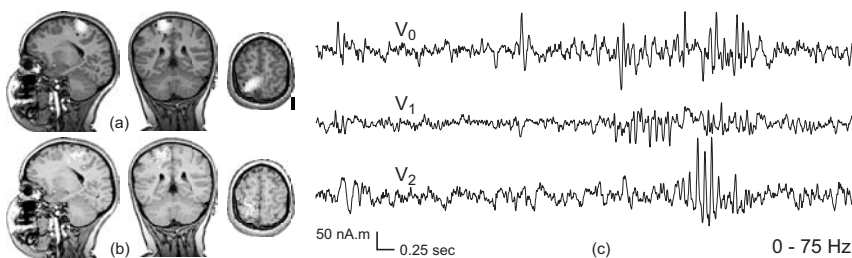


Fig. 11.25 Examples of MEG epilepsy recordings. (a, b) A patient with a single interictal spike locus detected by (a) SAM(g_2) and (b) dipole fits. (the dipoles with residual variance of $< 10\%$ are shown). (c) A patient with three SAM virtual sensors V_0 , V_1 , and V_2 , corresponding to the three maxima in the SAM(g_2) image, bandwidth 0 to 75 Hz.

to the ECD fit when there is a single-spike locus and good SNR. When multiple independent interictal spike loci were present, there was some disagreement between SAM(g_2) and the ECD scatter in the case of low SNR. Synthetic channel waveforms for the example of multiple-spike loci are shown in Figure 11.25(c). The source waveforms have little correlation with one another, although several spikes are coincident in time.

Fetal MEG

A review of recent work on fMEG is presented in [213]. Most research has concentrated on auditory evoked fields (fAEF), because the sound propagates well through the maternal abdomen and can reach the fetus. There are numerous reports of fAEF measurements, *e.g.* [128, 214, 215], and the detection rate is generally found to be about 50%. The detection rate depends on several factors, including fetal position and fetal state. The detection rate can be increased to about 80% by multiple recordings [215]. Detection of fetal visual evoked fields (fVEF) was also successfully demonstrated [133] and [216] starting from 28 weeks of gestation, and it was shown that the multimodal approach of applying both auditory and visual paradigms in successive recording sessions increases the detection success rate of one or both stimuli to 91% [217].

Averaged fetal evoked fields are very low in amplitude, typically 10 to 100 fT. In contrast, spontaneous, well-localized, low-frequency signals of 1 to 6 Hz with an amplitude of several hundred femtotesla were observed. The topography of these spontaneous signals is consistent with the location of the fetal head. The recordings of this spontaneous activity at less than 36 weeks of gestation are characterized by alternating bursts of low frequencies and intervals of relative silence, similar to the patterns observed by EEG in premature infants aged 28 to 36 weeks. Recordings at greater than 36 weeks of gestation showed the continuous background activity similar to that described in EEG studies of premature infants at 36 to 40 weeks [218].

A dedicated fMEG system, described in Section 11.2.5.2, provides not only the fetal brain measurement, but also the fetal heart and uterine contraction signals as a byproduct. The contractile activity of the uterus is accompanied by excitation and propagation of electrical activity, which occurs in bursts. The frequency, duration, and strength of the bursts directly relate to the frequency, duration, and amplitude of the contraction. The feasibility of recording magnetic fields corresponding to the electrical activity of the uterine smooth muscle (magnetomyography, MMG) was recently demonstrated [219]. The MMG evaluation provides a new noninvasive method for predicting labor.

The fMEG is measured in the presence of environmental noise and various near-field biological signals and other interference: *e.g.*, maternal magnetocardiogram (mMCG), fetal magnetocardiogram (fMCG), uterine smooth muscle MMG, and motion artifacts. In the majority of reported work, the MCG was reduced by adaptive filtering and/or noise estimation techniques [220, 221]. The fMCG and mMCG interference can be significantly reduced by projecting them out of the data by orthogonal projection [151–153, 222]. The projection operator application,

however, redistributes fMEG signals among sensors [223], but the redistribution can be corrected provided that the sensing array has sufficiently large coverage [224]. To demonstrate that the fMEG signals indeed originate within the fetal head, they were combined with a fetal brain model and used to localize fMEG sources. The localized sources were found in locations consistent with the known position of the fetal head determined by ultrasound [225].

Without going into details, the consistency of the fMEG signals is illustrated in Figure 11.26. In this case the visual flash evoked fMEG response and spontaneous fMEG signals, including sharp waves and burst-suppression waves, were visible during one measurement. The time traces of these signals, after projecting out mMEG and fMEG and correcting for redistribution, are shown in Figure 11.26 [225]. All three types of signal in Figure 11.26 occupy sensors located above the fetal head and, when modeled, are localized into the known position of the fetal head. Slight differences between the signal locations in Figure 11.26 are due to signals originating at different parts of the fetal brain.

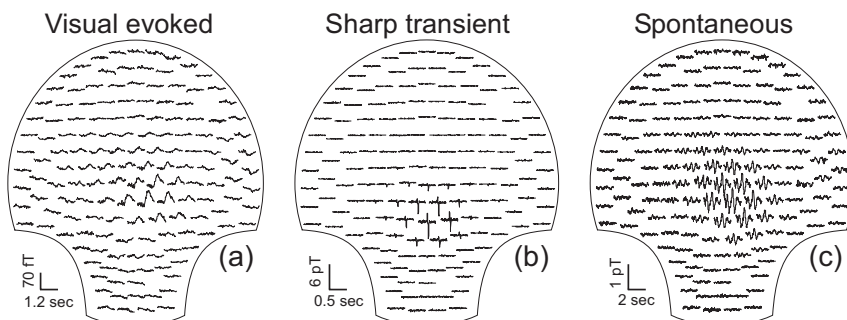


Fig 11.26 Three types of signal observed in visual flash evoked fMEG recording.
(a) Flash evoked fMEG; (b) sharp transient wave fMEG; (c) spontaneous fMEG.

11.2.6.4 Clinical MEG

The MEG market is evolving from research applications into clinical and for-profit MEG centers. This evolution is driven in part by the adoption by the US Centers for Medicare and Medicaid Services (CMS) of the American Medical Association's Current Procedural Terminologies® (CPT codes) for MEG procedures. These codes permit charging of MEG procedures for recording and analysis of spontaneous MEG data, for example epileptic activity, and for recording and analysis of single and multiple evoked magnetic fields, for example auditory, visual, sensory, motor, and language cortices. An example of spontaneous epilepsy MEG data is given in Figure 11.25 and of evoked MEG fields in Figures 11.22 and 11.23.

11.2.7

Conclusions and Outlook

MEG is presently the most successful biomagnetic application, and about 90 whole-cortex MEG systems were installed around the world by the end of 2004. MEG is finding its way into clinical applications in the areas of presurgical mapping and epilepsy, and is employed in numerous research investigations, including pathological functional deficits, neuropharmacology, and a growing list of applications in neurosciences and psychiatry. The number of instruments is steadily increasing, and some MEG examinations are already covered by insurance and can be done on a cost recovery basis.

All present commercial whole-cortex MEG systems utilize low- T_c SQUIDS, because the high- T_c devices cannot yet be reproducibly manufactured in large quantities and their noise performance and linearity are not as good as those of the low- T_c devices.

MEG provides brain signals on a millisecond scale and it complements other functional imaging techniques like fMRI and PET, which can provide location information but their time resolution is limited. MEG is also complementary to its older counterpart, EEG. Both methods measure the same current sources and their simultaneous utilization can increase the overall diagnostic accuracy.

The use of MEG was recently extended to studies of unborn fetuses, or fMEG. There are presently no other techniques for noninvasive assessment of fetal neurological status. fMEG has a potential to provide assessment of the fetal brain state and to assist physicians to make informed decisions during high-risk pregnancies and diagnosis associated with infection, toxic insult, hypoxia, ischemia, and hemorrhage. In addition, the same instrument provides assessment of fetal heart activity and various other abdominal electrical activity (for example uterine contractions).

Even though the task of measuring the magnetic fields of the human brain in the presence of high environmental noise is challenging, the technology is well understood and MEG instruments are reliable and relatively easy to use. Modern instruments have a large number of channels and generate an enormous quantity of data. It is becoming virtually impossible to examine all recorded traces visually, so that various interpretational methods are used to convert the collected data into a simpler presentation, which a clinician or a researcher can utilize more easily. Such techniques attempt to invert the magnetic fields recorded around the scalp into information about the electrical activity within the brain. Since the MEG inversion problem is nonunique and highly undetermined, various simplifying assumptions and constraints must be introduced. Because of this, a wide range of inversion methods has been devised. The methods differ in the assumptions they make about the brain and current sources and in mathematical details. The most frequently used methods are the ECD, various flavors of minimum norm, MUSIC, and beamformers.

The MEG signal interpretation and its separation from unwanted brain activity or other interferences (for example heart or muscles) is still a remaining chal-

lence. There is, however, encouraging progress in the signal processing area, which, in combination with the large number of channels in modern MEG instruments, provide powerful processing capability and can handle difficult interpretational tasks with increasing success. Examples are the ability of MEG to interpret single-trial unaveraged data, more accurate epilepsy analysis, and the ability to map the signal propagation paths within the brain.

11.3

Magnetocardiography

11.3.1

Introduction

Measurements of electric potential differences on the body surface that arise from the heart (electrocardiography, ECG) have an important and established role in clinical diagnosis and research of the cardiac function. Both the 12-lead ECG and multilead body surface potential mapping (BSPM) are used [226]. The same bioelectric activity in the body that generates electric potentials also gives rise to biomagnetic fields, which are extremely low in magnitude (0.1 to 100 pT; see Figure 11.4), although much stronger than the MEG signals. The first successful recording of the MCG was reported in 1963 [4]. However, it was only after the development of SQUID sensors at the beginning of the 1970s that accurate detection of MCG signals became possible [6].

Until the 1990s, most MCG studies were performed with single-channel devices, by moving the system sequentially over the thorax and measuring signals from one location at time. Today, noninvasive MCG mapping recordings are carried out with multichannel systems, acquiring the signals simultaneously over the whole chest of the patient or at least a good part of it [36, 227–233]. More information can thus be acquired than with the standard 12-lead ECG. Furthermore, vector-type gradiometers detecting all three field components were demonstrated, possibly offering additional advantages [117, 234, 235]. Efficient conversion methods from one sensor configuration to another facilitate accurate comparisons of data between different sensor arrays [143, 236, 237]. In addition, difficulties with skin-electrode contact are avoided, which sometimes causes problems in ECG studies. However, one should not consider MCG to be a possible replacement of ECG. The much higher equipment cost and the necessity of cooling to liquid helium temperatures would make it impractical. High- T_c SQUID systems operating in liquid nitrogen can somewhat reduce the cost of cooling, but at a price of reduced sensitivity [43, 44, 238].

Although MCG has not yet been established as a routine clinical tool, successful results have been reported in several clinically important problems, including assessment of the risk of life-threatening arrhythmias, detection and characterization of coronary diseases, noninvasive localization of cardiac activation, such as arrhythmia-causing regions or ischemic currents, and studies of fetal heart func-

tion. This section considers the basic principles of cardiomagnetism, focusing on MCG instrumentation and measurements. A short outline is also given of approaches to MCG signal processing and source imaging. Finally, the validation of MCG results is discussed, and future trends are outlined.

11.3.2

Sources of MCG Signals

This section gives a brief outline of the genesis of ECG and MCG. A more detailed description can be found in textbooks, *e.g.* [226], and in reviews, *e.g.* [239–241].

MCG and ECG arise primarily from electric currents in the body associated with flow of charged ions (such as Na^+ , K^+ , Ca^{2+}) in the myocardium. If we consider electromagnetic fields relatively far from myocardial cells, electric currents associated with their activation can be characterized by an elementary current dipole. Myocardial muscle cells are interconnected to form a complex fibrous and anisotropic three-dimensional structure. A large number of elementary sources are activated simultaneously and appear as a wavefront during ventricular depolarization and repolarization (Figures 11.27(a) and (b)).

The cardiac cycle (normally about 1 second) is manifested as distinct deflections on the body-surface ECG and MCG signals: the P-wave arises from the atrial activation, the QRS-complex reflects the ventricular depolarization, and the T-wave results from the ventricular repolarization. Both amplitudes and durations of the P–QRS–T signals depend greatly on the type of the sensor (Figures 11.27(c) and (d)).

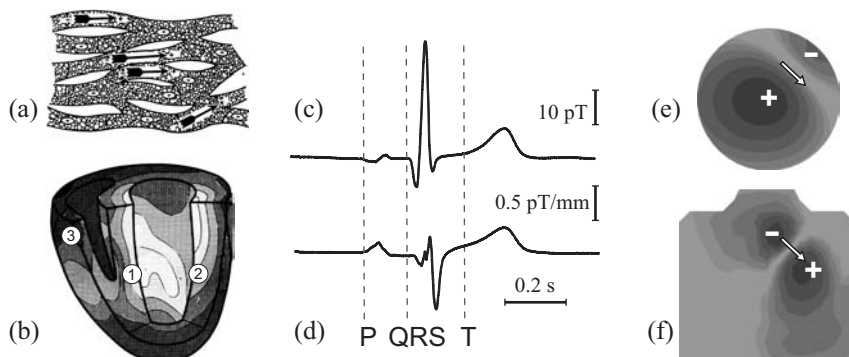


Fig. 11.27 (a) A small group of interconnected myocardial muscle cells. The arrows indicate elementary current dipoles modeling the excitation of individual cells. (b) In the normal heart, the ventricular depolarization starts in the left ventricular septum (1) and propagates as a wavefront over the ventricular walls (2), terminating at the right ventricle free wall (3) [242]. MCG signal measured

(c) with an axial gradiometer ($\partial B_z / \partial z$) and (d) with a planar gradiometer ($\partial B_z / \partial x$). The onsets of the P-, QRS-, and T-waves are depicted with dashed lines. (e) Isocontours of the magnetic field component B_z , and (f) of the potential on the anterior thorax surface, generated by a tangential current dipole (denoted by the arrow) in a homogeneous thorax model.

In MCG and ECG source modeling studies cellular-level details are usually left without explicit attention, and the active source regions are characterized by the concept of the *primary* current density, J^P [64]. It comprises the ionic currents inside and in the vicinity of excited cells. The primary current causes an electric potential V , which in turn generates passive volume currents $J^V = -\sigma \nabla V$ everywhere in the body with electric conductivity σ . The total current density inside the body can be expressed as a sum $J = J^P - \sigma \nabla V$. By finding the primary current we locate the source of myocardial activity.

The electric field, E , and the magnetic field, B , of J can be determined from quasistatic Maxwell equations. A very large number of cells has to be excited to obtain a measurable signal. Thus it is convenient to introduce a macroscopic equivalent current dipole (ECD):

$$\mathbf{q} = \int_V \mathbf{J}^P(\mathbf{r}') d^3 r' \quad (11.9)$$

where the integration extends over the excited source volume. Cohen and Hosaka [243] were the first to study an ECD in connection with measured MCG maps. The ECD can be regarded as the lowest-order equivalent source both of the ECG and the MCG. One can also derive higher-order equivalent generators, such as quadrupoles and octupoles, by using multipole expansions [244] (see also Section 10.3.4.4).

Instead of a single current dipole, distributed source currents associated with a propagating cardiac excitation wavefront can be represented by a large number of individual current dipoles, or more often in terms of a uniform double layer (see Figures 10.7 and 10.8). This representation consists of a sheet of dipoles with equivalent strengths, which are oriented perpendicularly to the surface of the propagation wavefront. The propagated excitation wavefront can also be described in terms of bidomain models (see Section 10.3.2.2 footnote 6), which can take the anisotropic properties of the myocardium properly into account.

It can be shown that the volume currents in an infinite homogeneous volume conductor give no contribution to the electric potential nor to the magnetic field, and the fields are solely due to the primary currents, J^P . In addition, the electric potential and magnetic field should be independent of each other. In the case of a homogeneous semi-infinite space with a plane boundary, it is possible to derive simple analytic expressions for the magnetic field of a current dipole. Furthermore, radial currents do not produce any magnetic field outside the semi-infinite volume conductor. MCG is thus to a great extent selectively sensitive to tangential current sources.

In reality, however, the situation is more complicated due to macroscopic interfaces of electrical conductivity. Assume that the body is a homogeneous volume conductor, bound by the surface S . The magnetic field can be obtained in this case from an integral equation [245]:

$$\mathbf{B}(\mathbf{r}) = \mathbf{B}_\infty(\mathbf{r}) + \frac{\mu_0}{4\pi} \int_S \sigma V(\mathbf{r}') d\mathbf{S} \times (\mathbf{r} - \mathbf{r}') / |\mathbf{r} - \mathbf{r}'|^3, \quad (11.10)$$

where the surface potential, $V(\mathbf{r}')$, is first solved from another integral equation and σ is the conductivity inside of the surface S . Vector \mathbf{r} refers to the observation point, while vector \mathbf{r}' points to an integration point on the surface S . The term \mathbf{B}_{∞} denotes the magnetic field in an infinite homogeneous medium (in the absence of the boundary S), and the surface integral accounts for the contribution of the conductivity change on the boundary S .

In the boundary element method (BEM), the magnetic field is calculated from a linear matrix equation obtained by discretization of Eq. (11.10) [246, 247]. The calculation can also be extended to torso models with more complex inhomogeneities. In most BEM applications to the bioelectromagnetic forward problem, the surfaces are tessellated with triangular elements. Realistically shaped geometries of each patient are usually extracted from MRI data. The regions of interest (for example the heart, the lungs, and the thorax) need first to be segmented from the data. The surfaces of these volumes are then discretized for numerical calculations. The segmentation and tessellation problems are tedious, but nearly automated computer methods have been developed, e.g. [248].

Figures 11.27(e) and (f) show the distributions of B_z and the surface potential computed for a tangential dipole $\mathbf{q} = q_x \mathbf{e}_x + q_y \mathbf{e}_y$ in a homogeneous BEM torso model. The main features in these maps are similar to those in the case of semi-infinite volume conductor maps: the dipolar pattern of B_z is very similar to the potential map pattern which has been rotated by 90°. A radial current dipole $\mathbf{q} = q_z \mathbf{e}_z$ produces a nearly zero magnetic field \mathbf{B} outside the thorax, while a unipolar potential pattern appears on the anterior chest surface.

11.3.3

Cardiomagnetic Instrumentation

11.3.3.1 General System Description and Sensor Array Configurations

Cardiomagnetic SQUID systems follow similar basic principles to the multichannel MEG sensors (see Section 11.2.3). The dc SQUID sensors offer the best sensitivity for the measurement of cardiomagnetic fields. Still, strong environmental magnetic noise, unavoidable at urban hospitals and laboratories, makes the detection of biomagnetic signals impossible without special techniques for environmental interference suppression. The environmental magnetic noise is reduced by magnetically shielded rooms (MSR), which typically consist of a combination of μ -metal and eddy current shields. In addition, gradiometer coils are used to diminish residual magnetic noise within the shields. Alternatively, high-order gradiometers can be utilized if no magnetic shielding is employed. The shielding and noise rejection techniques are discussed in detail in Sections 7.6 and 7.7.

Besides wire-wound gradiometer coils, arrays of magnetometer sensors can be utilized to compose differences between one or several coils electronically (e.g. [36, 231]). Alternatively, software-based interference suppression methods can be applied, such as synthetic gradiometers or signal space projection (see Section

7.7.5), noise reduction with wavelets [249], or the signal space separation technique [108].

Conventionally, sensors in MCG instruments are positioned in one plane (or nearly so) to detect the magnetic field component perpendicular to the chest surface of a subject in the supine position. This field component, usually denoted as B_z , is analogous to the radial field component in MEG studies (see Section 11.2). Several MCG instruments have utilized first-order axial gradiometers with relatively large coils [36, 37, 227–231]. However, planar magnetometers and gradiometers on integrated thin-film chips use less space and are easier to manufacture [232, 233]. Their small pickup area and the short baseline of gradiometers are not a problem if a sufficient SNR reserve exists, as is the case in a good-quality MSR. Sensor configurations measuring all three field components have also been constructed (*e.g.* [117, 234, 235]). Different sensor types are introduced in detail in Chapter 5, and briefly discussed in the next section. Examples of sensor layouts are shown in Figure 11.28.

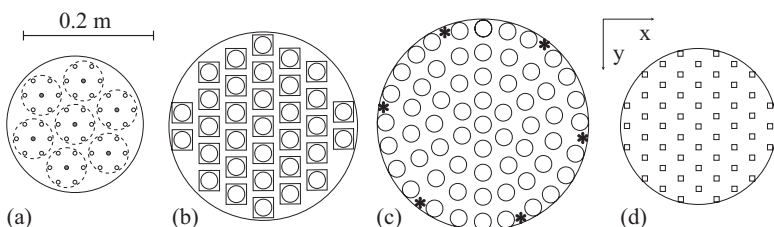


Fig. 11.28 Sensor layouts in some multichannel dc SQUID systems. (a) PTB Berlin (Figure 11.29(b)), 83 sensors, 49 MCG channels on a plane. Each set of seven pickup coils (dashed circles) shares a common compensation coil 70 mm above the central coil (filled circles). (b) VectorView (Figure 11.29(c)), 99 MCG channels in a slightly curved hexagonal grid. (c) Magnes 1300 C (Figure 11.29(d)), 61 MCG channels for normal and 6 channels (marked by *) for tangential field components in a curved concentric grid. (d) Argos 55 (Figure 11.29(e)), 55 MCG channels in a flat hexagonal grid. Each square denotes two orthogonal planar

gradiometers, and the circles refer to a magnetometer integrated on the same chip.

(c) Magnes 1300 C (Figure 11.29(d)), 61 MCG channels for normal and 6 channels (marked by *) for tangential field components in a curved concentric grid. (d) Argos 55 (Figure 11.29(e)), 55 MCG channels in a flat hexagonal grid.

11.3.3.2 Multichannel Low-Temperature Systems

Until the 1990s, biomagnetic measurements were usually performed with single- or at most few-channel instruments cooled by liquid helium, *e.g.* [227]. However, most MCG applications require mapping over multiple locations of the thorax surface. With only one channel this is time-consuming and cannot provide simultaneous recordings, which are preferable or necessary in most clinical applications. Therefore, in the past decade, true multichannel systems were developed. Furthermore, the sensitivity of sensors has been improved. Typical noise levels for magnetometers or axial gradiometers range between 5 and 10 fT/√Hz at low frequencies inside a MSR [37, 227 to 233] and a sensitivity as low as 2 fT/√Hz has been reported [36, 235].

Large-array multichannel MCG systems may contain more than 60 SQUID sensors in an array covering an area of up to 0.3 m in diameter over the subject's chest. The sensors are placed at the bottom part of a large cylindrical dewar with a flat or slightly curved bottom to fit the chest surface. The boil-off rate of helium in such a dewar is typically a few liters per day. The dewar is attached to a gantry system, which allows easy positioning of the sensor above the subject's thorax (see Figure 11.29). It is often also possible to move the subject bed horizontally and vertically.

The position of the sensor array with respect to the subject's thorax can be determined, for example, by using special marker coils attached to the skin (see Section 11.2.3.4). The positions of these coils are determined by a three-dimensional digitizer before the measurement (in torso coordinates), and from the MCG recordings (in device coordinates) when electric current is fed to the coils.

The MCG recordings are usually triggered by ECG (using nonmagnetic electrodes). For this purpose, a three-lead ECG is sufficient. However, in research studies the measurements are often accompanied by 12-lead ECG or 32- to 128-channel BSPM recordings with the same or separate data acquisition as in MCG. Furthermore, nonmagnetic exercise ergometers have been developed to perform physical stress-testing in the supine position [228, 232, 233].

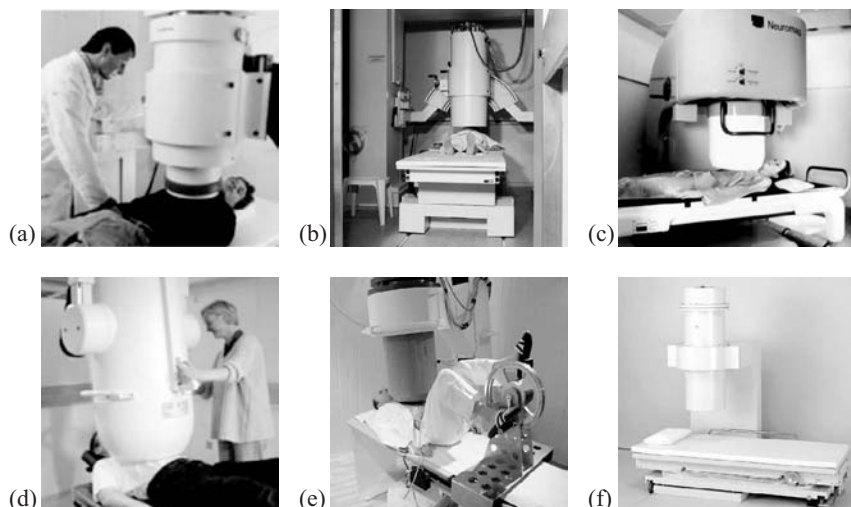


Fig. 11.29 Multichannel MCG systems inside magnetically shielded rooms. (a) Siemens Krenikon. (Courtesy of Siemens AG.) (b) The 63-channel noncommercial PTB system. (Courtesy of Physikalisch-Technische Bundesanstalt Berlin.) (c) Vectorview. (Courtesy of

Elektro Neuromag Oy.) (d) Magnes 1300C. (Courtesy of 4D Neuroimaging.) (e) Argos 55. (Courtesy of Advanced Technologies Biomagnetics.) (f) MC-6400. (Courtesy of Hitachi, Ltd.)

Figure 11.29 displays six different multichannel dc SQUID systems (R – sensor array diameter; d – sensor spacing, b_{rad} – gradiometer baseline):

- Siemens Krenikon had 37 first-order axial gradiometers arranged on a flat hexagonal grid [228]. The gradiometers and feedback transformers are first placed on flexible two-dimensional printed circuits, which are then folded to form the final three-dimensional structure. The pickup coil area was 600 mm^2 . $R = 0.19 \text{ m}$, $d = 30 \text{ mm}$, $b_{\text{rad}} = 70 \text{ mm}$. Altogether, five commercial systems were operational between 1989 and 1995.
- A noncommercial 63-channel system was constructed at PTB Berlin, Germany [36]. Altogether, 49 sensors in a hexagonal array detect the B_z component, while 14 sensors detect the B_x and B_y components. The pickup coil area is 52 mm^2 , and 20 reference channels are used to form electronically first- or second-order gradiometers. $R = 0.21 \text{ m}$, $d = 30 \text{ mm}$, $b_{\text{rad}} = 70 \text{ mm}$. The system has been operational at the University Clinic Benjamin Franklin in Steglitz, Berlin, since 1994.
- Elekta Neuromag VectorView [232]. The system has 33 magnetometer and 66 planar gradiometer channels (detecting $\partial B_z / \partial x$ and $\partial B_z / \partial y$). Noise suppression is based on signal space projection [152] (software gradiometers, see Section 7.7.5), or the signal space separation method [108]. $R = 0.3 \text{ m}$, $d = 40 \text{ mm}$, $b_{\text{pln}} = 16.5 \text{ mm}$ (planar gradiometers). The system is installed at the BioMag Laboratory, Helsinki University Central Hospital, Finland.
- 4-D NeuroImaging Magne 1300 C [231]. The system has 67 magnetometers, arranged on a slightly curved surface. $R = 0.32 \text{ mm}$, $d = 28 \text{ mm}$. Electronic noise reduction is carried out with the aid of an array of ambient noise detectors. The system was installed at the Research and Development Center for Microtherapy (EFMT) in Bochum, Germany, in 1998.
- Advanced Technologies Biomagnetics (AtB), Argos 50 [233]. The basic component is an integrated planar SQUID magnetometer with a sensing area of $8 \times 8 \text{ mm}^2$. The sensor array consists of 55 SQUID sensors covering a circular planar surface. Noise cancellation is based on a combination of a cost-optimized shielded room and real-time compensation (software gradiometers) using reference magnetometers detecting environmental noise. $R = 0.23 \text{ m}$, $d = 30 \text{ mm}$. The system can be operated together with a specially designed nonmagnetic ergometer for exercise MCG studies. The system was installed at the University of Ulm, Germany, and at the University of Chieti, Italy, in 1999. A vector-gradiometer system consisting of 55 SQUID sensor triplets, Argos 200, is in use at the Biomagnetic Centre at the Friedrich-Schiller University of Jena, Germany.

- Hitachi Ltd, MC-6400 [230] has 64 first-order axial gradiometers in a regular 8×8 square grid. The pickup coil area is 250 mm^2 . $R = 0.2 \text{ m}$, $d = 25 \text{ mm}$, $b_{\text{rad}} = 50 \text{ mm}$. Tangential derivatives $\partial B_z / \partial x$ and $\partial B_z / \partial y$ at each measuring site are calculated from the measured B_z . The system bed can be moved in three directions to adjust the position of the dewar.

In addition, several other systems have been employed in MCG studies [227]. For example, Philips developed a twin-dewar system [37], which can be utilized both in MEG and MCG studies. Each dewar has 31 first-order axial gradiometers ($b_{\text{rad}} = 70 \text{ mm}$, pickup coil area 300 mm^2) on a curved surface ($R = 0.135 \text{ m}$). BTi introduced a dual 37-channel system, each one covering roughly 0.15 m diameter area [229]. In addition, Cryoton [18] has developed 7- and 19-channel MCG systems. Recently, PTB Berlin has developed a non-commercial vector magnetometer and gradiometer system [234, 235].

Besides cardiomagnetism, all of the systems introduced in this section can be employed in other biomagnetic studies, including fetal MCG, magnetoneurography, and gastromagnetism (see Sections 11.5 and 11.7). A large-array dc SQUID system specially designed for fetal MEG, also well suited for fetal MCG (fMCG) studies, is shown in Figure 11.16.

11.3.3.3 Systems Operating Outside Magnetically Shielded Rooms

The first multichannel low- T_c and high- T_c SQUID systems operating without magnetic shielding have been developed for possible clinical use rather than research. Most of these have low channel numbers. The SNR of such systems is, unfortunately, lower than that of conventional low-temperature dc SQUID systems, which operate in MSRs, while the electromagnetic interference inside a hospital is usually much stronger than the noise in research laboratories. These disadvantages can be partially compensated by an appropriate construction of the measurement system and by post processing of the measured data, beginning with mandatory filtering and signal averaging over sufficiently long time sequences. MCG mapping with systems having a low number of channels requires recordings from several positions over the chest.

The CMI-2409 system (Figure 11.30(a)) has nine second-order axial low- T_c dc SQUID gradiometers in a square 3×3 grid in one plane [14]. In addition, three vectorial reference channels (xyz) are utilized for electronic noise suppression. A 36-channel version has been installed at the Catholic University of Rome (see [271]). The Squid International MCG7 system (Figure 11.30(b)) has four measurement channels and three low- T_c SQUID detectors for environmental noise cancellation [15].

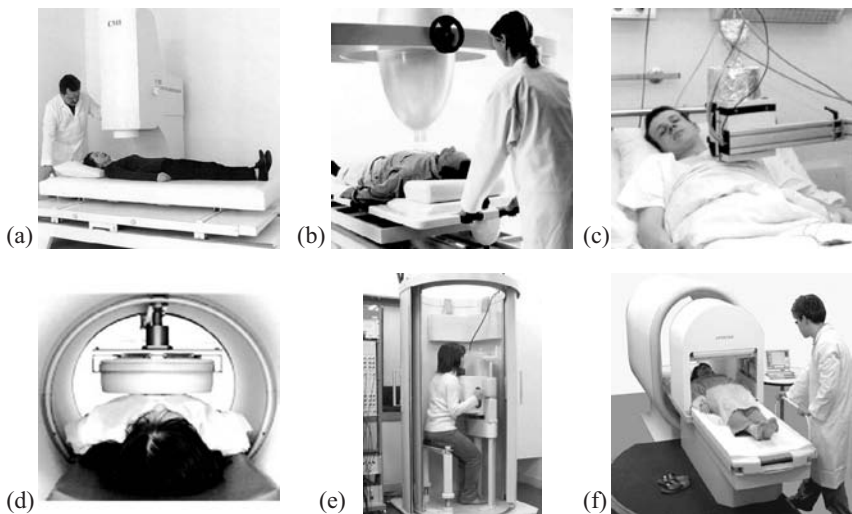


Fig. 11.30 Multichannel MCG systems operated without magnetically shielded rooms (a) CMI-2409. (Courtesy of CardioMag Imaging Inc.) (b) Squid International, MCG7 system. (c) Three-channel high- T_c system at the University of Jena, Germany. (Courtesy of Friedr. Schiller Universität Jena.) (d) A 32-channel high- T_c system operated inside an open-

ended cylindrical shield. (Courtesy of Sumitomo Electric Hightechs Ltd.) (e) A 16-channel high- T_c system operated inside a vertical shielding cylinder. (Courtesy of Hitachi Ltd.) (f) A 51-channel high- T_c system operated inside a horizontal cylindrical shield. (Courtesy of Hitachi Ltd.)

11.3.3.4 High-Temperature SQUIDS

In the 1990s, many SQUID researchers believed that the field of MCG would expand during the next few years with the implementation of low-noise high- T_c SQUID arrays that can be operated at the temperature of liquid nitrogen (see Section 3.3). Liquid nitrogen is substantially cheaper and easier to handle and more generally available at hospitals than liquid helium. Also, the liquid nitrogen heat of evaporation is 62 times larger than that of liquid He. Therefore, liquid-nitrogen-cooled systems require less frequent filling and are more convenient for the operator. Furthermore, cryogenic dewars are easier to manufacture, and the higher noise level of the high- T_c SQUIDs is partly compensated by the smaller distance between the sensors and the chest. At present, however, low-temperature SQUIDS are easier to produce and thus cheaper than the high- T_c sensors. Other current drawbacks are the insufficient reproducibility of high-quality sensors, their higher noise, and the lack of appropriate high- T_c wires from which large-coil gradiometers can be wound and bonded to the SQUID chip in such a way that the contacts remain superconducting.

Still, high- T_c SQUID sensors are being steadily improved, and the number of reports where they are applied to the recording of human MCG is increasing. The SQUID fabrication technique, number of sensors, and noise compensation meth-

ods vary, and studies have been carried out in very differing environments. Some systems are operated in a MSR or inside a cylindrical enclosure, while some of the currently operating systems allow MCG recordings without any magnetic shielding. Therefore, direct comparison of the system performances is difficult.

Large-area multilayer flux transformers and the flip-chip technique were utilized in [250] to construct a variety of dc SQUID magnetometers and planar gradiometers with good noise properties. The white noise levels at 77 K down to few hertz of $6 \text{ fT}/\sqrt{\text{Hz}}$ for a magnetometer and $3 \text{ fT/mm}/\sqrt{\text{Hz}}$ for a planar gradiometer were achieved with a bias reversal scheme inside a three-layer MSR.

Typically, high- T_c systems are operated without magnetic shielding. Unshielded recordings utilize gradiometric configurations and additional reference sensors. For example, the outputs of two planar first-order gradiometers – directly bonded to a dc SQUID magnetometer – were subtracted digitally to construct a second-order gradiometer [251]. Additionally, three orthogonal magnetometers were applied in reducing homogeneous interferences. Detection of MCG signals was feasible even in a very noisy laboratory environment. The noise of the unshielded gradiometers at 10 Hz was above $100 \text{ fT}/\sqrt{\text{Hz}}$.

Alternatively, three high- T_c rf SQUID magnetometers were mounted in an axial gradiometer arrangement ($b_{\text{rad}} = 75 \text{ mm}$) [252]. The MCG signal was derived electronically from the magnetometer outputs. The white noise at 77 K was about $130 \text{ fT}/\sqrt{\text{Hz}}$. Recording of sequential MCG mapping was demonstrated at a grid of 6×6 locations.

An optimized second-order gradiometer was reported in [253]. Direct-coupled dc SQUID magnetometers were inserted in a 45° inclined dewar for measuring the MCGs in a sitting position. Two first-order gradiometers ($b_{\text{rad}} = 75 \text{ mm}$) were first constructed electronically from three z -axis magnetometers, and a second-order software gradiometer (combination of an axial and a planar one) was balanced using the two first-order gradiometers and two reference (B_x , B_y) magnetometers. The noise level of the balanced gradiometer was about $180 \text{ fT}/\sqrt{\text{Hz}}$ at 100 Hz.

Other electronic gradiometers have also been reported, *e.g.*, utilizing a first-order axial gradiometer with active noise control [254], an off-axis second-order axial gradiometer [255], or a second-order planar gradiometer [256].

11.3.3.5 Multichannel High- T_c Systems

Multichannel thin-film high- T_c SQUID systems were already reported in 1996 [43]. A 32-channel system has magnetometers on a regular 6×6 grid ($d = 40 \text{ mm}$) in a flat-bottom liquid-nitrogen dewar with a diameter of 0.4 m and height of 0.20 m . In another 16-channel system the SQUID sensors are arranged on a 4×4 grid ($d = 40 \text{ mm}$). The dewar and the gantry are located inside an open-end cylindrical permalloy magnetic shield (Figure 11.30(d)). The magnetic field resolution of the SQUIDs at 10 Hz is 150 to $450 \text{ fT}/\sqrt{\text{Hz}}$.

A 7-channel magnetometer system was reported in [257]. Six YBCO dc SQUID magnetometers (pick-up area $10 \times 10 \text{ mm}^2$) are on a circle, and one at the center

($d = 36$ mm). The average noise level of the sensors was $120 \text{ fT}/\sqrt{\text{Hz}}$ down to 1 Hz inside a MSR. Operation outside of the shielded room was possible by using electronic first-order gradiometers.

A compact 8-channel high- T_c dc SQUID was reported in [44]. Altogether 24 SQUID magnetometers can be mounted on three levels to compose electronic axial gradiometers. In a MSR, the noise level of $50 \text{ fT}/\sqrt{\text{Hz}}$ at 10 Hz was achieved for first-order gradiometers. Measurements in an unshielded environment can be performed with different gradiometric arrangements.

Planar thin-film gradiometers integrated on the dc SQUID chip have been applied for bedside MCG recordings without magnetic shielding [258] (Figure 11.30(c)). Two first-order planar gradiometers ($b_{\text{pln}} = 4$ mm) detected $\partial B_x/\partial z$ and $\partial B_y/\partial z$, and one SQUID was used for detecting environmental noise. The field gradient noise in an unshielded environment in that study was $0.5 \text{ pT/mm}/\sqrt{\text{Hz}}$ at 1 Hz. Recently, an improved SQUID design resulted in a drastically reduced system noise, $31 \text{ fT/mm}/\sqrt{\text{Hz}}$ in an unshielded laboratory environment [259]; the gradient resolution inside the magnetic shield was $1.2 \text{ fT/mm}/\sqrt{\text{Hz}}$ in the white noise region.

A 4-channel rf SQUID high- T_c system was described in [260]. The system has four sensing magnetometers near the bottom of the liquid nitrogen dewar, and two reference magnetometers for forming electronic first- or second-order axial gradiometers ($b_{\text{rad}} = 100$ mm or 200 mm). Inside a MSR, the magnetometers reached a field sensitivity of 20 to $30 \text{ fT}/\sqrt{\text{Hz}}$.

Hitachi Ltd has developed a system with 16 high- T_c SQUID magnetometers operated inside a vertical three-layer open-ended magnetic shielding cylinder constructed of flexible magnetic sheets [261]. The walls of the cylinder are made of 20- μm -thick nanocrystalline soft magnetic material ribbon. Its shielding factors in the radial direction at the center of the cylinder are better than 35 dB in the low-frequency region (see Figure 11.30(e)). Recently, they have developed a system with 51 channels [262], using the same directly coupled magnetometers as in the 16-channel system. The system is operated inside a horizontal cylindrical shield (Figure 11.30(f)). The white noise of the magnetometers was 50 to $100 \text{ fT}/\sqrt{\text{Hz}}$.

The performance of high- T_c SQUID sensors is steadily improving. All the systems described above are demonstrations in gradual development towards an MCG system which would offer a steady and robust performance in an unshielded clinical environment.

11.3.4 Comparisons of Sensor Types

11.3.4.1 Sensitivity

In the following a brief outline is given of the use of differing sensor configurations. Similar basic principles are valid as in MEG studies, and a more detailed comparison between sensor types can be found in Section 11.2.4. Basically, the most important differences when compared to MEG are that the distance from

the cardiac sources to the pickup coils is larger (50 to 150 mm) than in the head (\sim 40 to 60 mm). Usually, the SNR in MCG is higher than in MEG due to stronger source-current magnitudes. In studies of patients with, for example, myocardial infarctions the interesting pathology is, however, manifested as small-amplitude signals ($< 0.5 \text{ pT}$). If one requires an SNR of 10, for example, that would require a sensitivity of $50 \text{ fT}/\sqrt{\text{Hz}}$. This is a level that is achievable by good high- T_c systems, at least with some magnetic shielding. The issues of baseline length for optimum SNR and effects of environmental noise are basically similar to those presented in Section 11.2.4, and they are not addressed here.

11.3.4.2 Axial and Planar Sensors

Magnetometer sensors have the highest sensitivity for nearby and far-field sources. Therefore, gradiometric noise compensation is required to reduce the unwanted external noise components, especially the 50-Hz line frequency or 60-Hz line frequency. Typically, MCG instruments operating inside a MSR employ first-order axial gradiometers with relatively long baseline (50 to 100 mm) optimized for the distance between the pickup coil and the heart [36, 37, 227–230]. In an unshielded environment, second-order axial gradiometers reduce the external noise more efficiently.

Axial gradiometers are more complicated than magnetometers and planar gradiometers integrated on thin-film chips [232, 233]. Short-baseline planar gradiometers (10 to 20 mm) are optimal for nearby sources (such as the cortex in MEG), thus reducing the signal amplitudes from cardiac sources located relatively far from the sensor (for example, Figures 11.27(c) and (d)). Due to their short baseline and high balance, planar gradiometers are very robust against external disturbances. The balance of axial gradiometers can be improved synthetically (see Sections 7.7 and 11.2).

11.3.4.3 Vector Magnetometers

Multichannel sensor configurations measuring all three field components have also been constructed [117, 234, 235]. It has been shown that such measurements may produce significantly more information than recordings of one field component [266, 267] (see also Section 10.1). An experiment of measuring vector-field components at several positions and distances over the anterior parts of the thorax surfaces was reported recently [235].

Because the biomagnetic fields are quasistatic ($\nabla \times \mathbf{B} = 0$), it is directly seen that $\partial B_z / \partial x = \partial B_x / \partial z$. In other words, measurements of the tangential gradients yield information about the tangential field components. The Hosaka–Cohen transformation (Section 10.3.2.2) utilizes this fact and rotates the tangential gradients by 90° to form a so-called current arrow map (CAM):

$$\mathbf{HC} = (\partial B_z / \partial y) \mathbf{e}_x - (\partial B_z / \partial x) \mathbf{e}_y. \quad (11.11)$$

Here e_x, e_y are the perpendicular unit vectors on the sensor array plane. Strictly taken, the Hosaka–Cohen transformation is valid for two-dimensional current distributions, but CAM estimated from Eq. (11.11) has proved to be a useful approximation (pseudo current pattern) for the underlying current sources (e.g. [241, 263–265], see Figures 11.31(c) and 11.32(b)).

It still remains to be seen in a larger number of patient measurements whether the complete vector-field information outweighs the increased complexity in the sensor configurations and electronics of vector systems. In any event, such measurements are, however, valuable in defining optimal sensor locations and orientations, for example for high- T_c systems with a relatively small number of channels, and in experimenting and testing forward and inverse modeling approaches. In addition, knowledge of the tangential field components can improve the localization accuracy of focal and distributed sources [241, 266, 267].

So far, few studies have attempted to record MCGs on more than one sensor plane (e.g. [235, 241, 268]). Recordings from the left or back of the thorax may be able to provide more accurate information, especially from the inferior regions of the heart deep in the chest, than vector measurements above the anterior side only.

11.3.4.4 Conversion of Signals from Different Sensor Arrays

Comparison of biomagnetic measurements performed with different multichannel magnetometers is difficult, because the sensor configurations have large variations among the individual systems. Multichannel MCG signals exhibit significant differences, both in the spatial distribution and in the time domain. For example, the amplitudes and even durations of the signal waveforms may vary considerably between planar and axial gradiometers. Thus, direct comparison of MCG recordings with different devices is problematic.

As a result, transformation procedures have been proposed [143, 236, 237] to reconstruct signals in any multichannel sensor array from recordings with different multisensor systems. The signals from seven healthy volunteers were recorded with two systems (Figures 11.29(b) and (c)) in [237]. Signals from one sensor array were employed to compute parameters of a multipole expansion or minimum norm estimates at 1-ms steps over the cardiac cycle. The signals of the second sensor array were then simulated from the computed estimates and compared against measured data. Both the multipole- and the minimum norm-based transformation methods yielded good results; the average correlation between simulated and measured signals was >93%. Thus, the methods are useful for comparison of MCG data recorded with differing sensor configurations, for example for multicenter patient studies.

11.3.5

Applications of MCG

11.3.5.1 Introduction

Because of the demands posed by cryogenics and magnetic shielding, MCG has been applied – until recent years – mainly as a laboratory research tool. Still, successful results have been reported in clinically important problems, such as: (a) assessment of the risk of life-threatening arrhythmias, (b) detection and characterization of ischemic heart diseases, (c) noninvasive localization of cardiac activation, such as arrhythmia-causing regions, a pacing catheter and cardiac evoked field, or ischemic currents, and (d) studies of fetal heart function. Recent reviews present a covering evaluation of the clinical applications of MCG [269–271].

11.3.5.2 Arrhythmia Risk Stratification

There is continuing clinical interest in noninvasive identification of cardiac patients at risk of fatal arrhythmias. In MCG and ECG studies, the main approaches for arrhythmia risk stratification can be divided into three categories according to their physiological scope of interest: (a) activation discontinuities during the ventricular depolarization, (b) heterogeneity during the ventricular repolarization, and (c) the function of the autonomic nervous system in heart rate variation analysis. All these methods can be used as arrhythmia risk indicators either separately or by combining the independent components of each method.

Arrhythmogenic regions cause disturbances in the ventricular depolarization. They are usually studied after applying signal averaging, and detecting low-amplitude late potential and late field signals at the end of the QRS complex, *e.g.* [272]. Intra-QRS changes can be detected with the so-called Berlin fragmentation analysis method [273], where a nonrecursive binomial filter from 37 to 90 Hz is used. The filtered QRS complex is characterized by finding the number of signal extrema during the QRS, and by calculating their product with the sum of the amplitude differences between neighbouring extrema, resulting in a fragmentation index. Also other approaches have been suggested, such as wavelet decomposition and spectral turbulence analysis, *e.g.* [270]. Figure 11.31(a) shows examples of the QRS fragmentation scores plotted over the measurement area. Myocardial infarction (MI) patients without arrhythmias showed typically much less fragmentation than MI patients with documented arrhythmias [273].

The vulnerability of patients to malignant arrhythmias is also manifested during the ventricular repolarization. It can be studied with automated algorithms to define the dispersion of QT-durations in multichannel MCG signals (that is, the intervals from the QRS onset to offsets of the T-wave) [274, 275].

Besides analyses of morphological MCG tracings, extraction of spatial features in MCG mappings provide valuable information of the arrhythmia vulnerability. Integral maps over the whole QRST interval and extrema trajectory plots revealing the spatial route of the maxima and the minima in MCG distributions have been

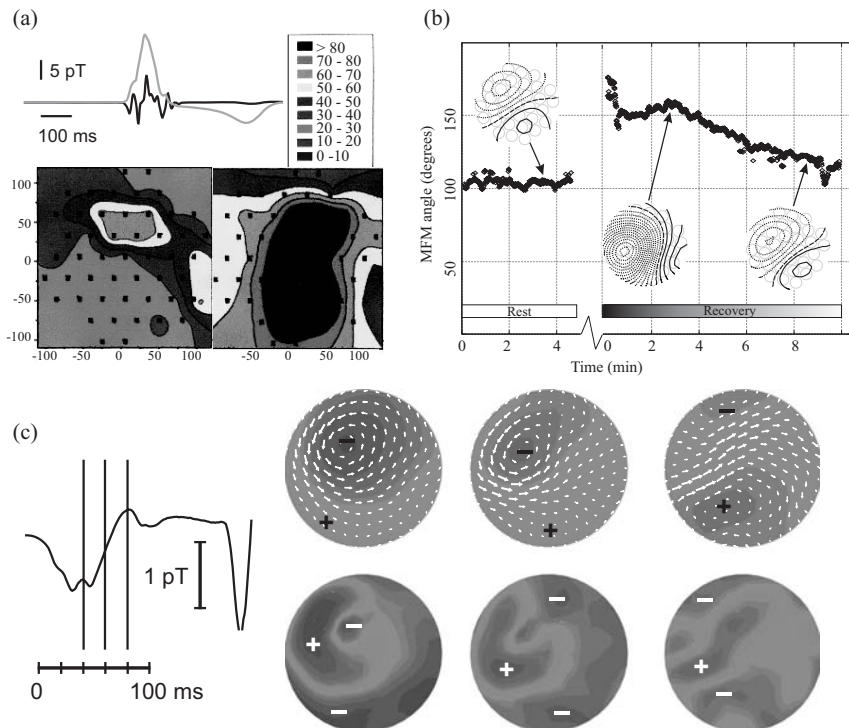


Fig. 11.31 Examples of multichannel MCG signal processing. (a) Arrhythmia risk assessment using the QRS fragmentation score. (Adapted from [273] with permission of IOP Publishing Ltd.) (b) Ischemia studies: rotation of the MCG field pattern at the ST-segment in patients with coronary artery disease. (Adapted from [282] with permission of IOP Publishing Ltd.) (c) Current arrow maps (CAMs) at three time instants when the activation propagates from the left to the right atrium. Top row: CAMs (white arrows) are overlaid on top of the isocontours of B_z (+ and – denote, respectively, largest magnetic flux into and out of the chest). Bottom row: isocontours of the CAM magnitude values.

used in arrhythmia risk evaluation [239, 276]. The complexity of spatial features can be assessed with orthogonal expansion methods (principal component analysis) [277]. The current arrow maps can also be used to search for MCG markers of the arrhythmia vulnerability, e.g. in patients with abnormal repolarization [278].

Recently, MCG studies of atrial function and arrhythmias have become the subject of increasing interest [269–271]. In addition to time-domain analyses, the current arrow maps and three-dimensional current density reconstruction [279] have provided useful information of the spatiotemporal characteristics of atrial arrhythmias.

11.3.5.3 Studies on Myocardial Ischemia

According to the National Institute of Health (USA), ischemic heart disease is the leading cause of death in the developed countries. Exercise ECG is a well-standardized and widely used diagnostic and prognostic test for the evaluation of patients with ischemic heart disease. The pioneering studies of Savard *et al.* [280] showed that MCG is able to reveal near-dc changes related to ischemic injury currents, which cannot be detected by ECG (see also [241] and Section 11.4). Recently, MCG mapping during pharmacologically or physically induced stress has received a steadily increasing attention, *e.g.* [263, 281]. An accurate noninvasive method for recognition of acute and chronic ischemia would have important clinical applications, due to the development of novel therapeutic interventions for revascularization.

The improved multichannel systems have brought MCG mapping during interventions technically closer to clinical feasibility. First pharmacological MCG stress testing in three normal subjects showed significantly more distinct repolarization changes in multichannel MCG data than in simultaneously recorded 32-lead BSPM [281]. Specially designed nonmagnetic ergometers facilitate exercise testing during MCG measurements [233, 282] (Figure 11.29(e)). Studies of patients with coronary artery disease (CAD) at rest and stress have also demonstrated differences between spatial as well as temporal aspects of the magnetic maps of patients with and without significant stenosis of coronary arteries [283–285], and in assessment of myocardial viability in patients with chronic ischemia [286].

The properties of planar gradiometers were utilized in [263] in defining the rotation of the MCG pattern as the orientation of the maximum surface gradient. The rotation angle of the maps between rest and post exercise can be used to identify the patients in three subgroups of single-vessel CAD. Similar principles have been applied also in [264, 265] to compose CAM images in patients with ischemic heart disease. The gradient analysis was extended in [282] to detect beat-to-beat variations of the rotation angle as a function of the heart rate. Physical exercise caused rotation of the MCG field pattern at the ST-segment in patients with CAD. The rotation angle measured after the stress slowly recovered back to the rest situation (Figure 11.31(b)). The rotation angle parameter could separate different types of CAD patients from each other. The rotation angle was also applied in a study where age- and sex-dependent variations of MCG in normal subjects and CAD patients were compared [283].

Analyses based on the CAM have become a particularly useful tool in detection of CAD from simple rest MCG recordings – on the basis of the pseudo-current distribution during the ST-segment – even with systems operated without magnetic shielding [271, 284, 285]. In addition, machine learning based on self-organizing maps has been investigated to facilitate automated data analysis and classification of MCG patterns [287].

11.3.5.4 Cardiac Source Imaging

Inverse Problem

The estimation of bioelectric current sources in the body is often called magnetic source imaging (see Section 10.1 and [239, 240]). To relate the functional information provided by MCG (and ECG) source imaging to underlying cardiac anatomy, other imaging methods are employed, such as MRI and X-rays (fluoroscopy and computer tomography). Cardiac source imaging studies require the solution of an *inverse problem* (see Section 10.3). Because the inverse problem does not have a unique solution in three dimensions, one has to replace the actual current sources by equivalent generators that are characterized by a few parameters. Thus, the solution of the forward problem of Eq. (11.10) is first needed.

Equivalent Current Dipole

The simplest physiologically sound model for the myocardial current distribution is the best-fitting ECD, Eq. (11.9). In cardiac studies, an ECD is applicable to approximate the location and strength of the net primary current density confined to a small volume of tissue. Myocardial depolarization initiated at a single site spreads at a velocity of about 0.4 to 0.8 mm/ms, and the ECD can be thought to be moving along the “center of mass” of the excitation. In practice, localization based on a single ECD is meaningful only during the first 10 to 20 ms of excitation. The ECD model has been used to characterize small source regions such as the conduction system activation, infarction area, arrhythmia-causing ventricular pre-excitation site in Wolff–Parkinson–White (WPW) syndrome, and other arrhythmogenic regions [239, 240, 247, 288, 289]. Localizations of pacing catheters have also been reported [289–291]. In the above mentioned studies, accuracies of 5 to 25 mm have been reported by comparing the MCG localization results to: (a) cardiac surgery, (b) catheter ablation, (c) the results of invasive electrophysiological studies, (d) ECG localization results, and (e) physiological knowledge (X-ray or MRI data). Examples of the ECD localizations are presented in Figure 11.32.

Distributed Source Models

In reality, ECG and MCG arise from *distributed* current sources. Because the use of two or more ECDs becomes very complicated in cardiac studies, it is more convenient to solve the inverse problem for a current distribution in terms of the lead fields (minimum norm estimation, see Sections 10.3.5.3 and 11.2.6). The lead fields are provided by the forward solution in the selected torso and sensor geometry. Because even small contributions of the measurement noise make the solution ill-posed, suitable regularization techniques are needed to stabilize the solution [292–296]. MCG current density reconstruction has been applied for locating the origin of ventricular late fields [292], and in estimation of ischemic regions induced by ergometer exercise in patients with CAD [293–295]. Figure 11.32(c) shows an example of current density estimated from exercise MCG data in a patient with CAD. PET data were used as a reference. The current density and PET maps were scaled to the maximum magnitude and are displayed on a polar

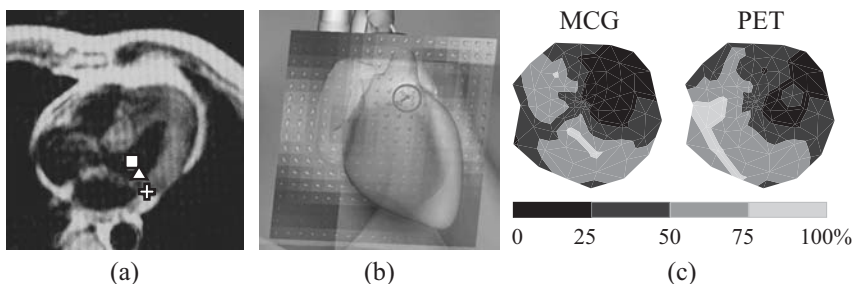


Fig. 11.32 Examples of MCG source localizations. (a) Localization of an accessory pathway in a patient suffering from pre-excitation syndrome. The cross points to an invasively obtained reference, the square marks an ECD solution with a semi-infinite homogeneous space, and the triangle pinpoints the solution with a boundary element torso model. (Adapted from [288] with permission of IOP Publishing Ltd.) (b) Current arrow map (white arrows) and the ECD location (circled arrow).

at 20 ms after the onset of a ventricular extrasystolic beat. The results are overlaid on a three-dimensional visualization of the heart (Courtesy of Prof. Riccardo Fenici, Catholic University of Rome.) (c) Regularized current-density magnitude estimated from a difference MCG map (stress–rest) [295], and the glucose uptake distribution from PET images on the surface of the left ventricle in a patient with three-vessel CAD.

projection: the apex of the heart is at the center and the atrio-ventricular level on the edge of the map. The darkest regions indicate scar tissue (PET) and low current density, while the lightest regions point to high metabolic activity and high current densities.

Besides single-layer sources, such as the equivalent current density above, uniform double-layer sources can be applied. The lead fields from each point on the endo- and epicardial surfaces of the heart to the MCG sensors are utilized in defining the sequence of cardiac excitation during the QRS complex. The quality of such solutions, utilizing simultaneously both MCG and BSPM data, has been verified with intraoperative epicardial recordings in patients undergoing open-chest surgery [296].

Phantom Studies

Besides patient studies, the ability of the MCG to locate artificial current dipoles has been tested with physical thorax phantoms (*e.g.* [297, 298]). A nonmagnetic pacing catheter in a realistically shaped thorax phantom resulted in equal accuracies of 5 to 10 mm from MCG and BSPM data [297]. Reconstructions of current densities in phantom experiments have showed that the conventional minimum norm solution produces usually a too widely spread solution, while the assumption of maximum sparseness may compress the source image too much [298].

Integration with Medical Imaging Data

Cardiac source imaging studies require a realistic description of the geometry and volume-conductor properties of the thorax [239, 240]. Usually, MRI data of the patients are applied, and the heart, the lungs, and the thorax are segmented. The

surfaces of the segmented objects are then triangulated for numerical BEM calculations [248]. Because MRI data are often costly and not available for all patients, methods based on more generally available imaging facilities, such as thorax X-ray and cardiac fluoroscopy, have recently been developed [299].

An essential part of cardiac source imaging is to combine the computed source estimations accurately with the cardiac anatomy. Therefore, external markers attached to the skin are often applied both to define the position of the sensor array with respect to the subject's thorax, and to align the medical image data with the thorax coordinate system in the MCG recording (e.g. [290, 291, 300]).

11.3.5.5 Fetal MCG

The first fMCG recording was reported in 1974 [301]. fMCG has a relatively high SNR and is remarkably free of maternal interference compared to the fetal electrocardiogram. fMCG can be reliably monitored beginning at 20 weeks of gestation, and can be detected at as early as 16 weeks of gestation [302]. The maternal MCG and other interferences can be removed by independent components analysis [303]. Fetal heart rate variability (fHRV), the change in the amount of time between fetal heartbeats, and reliable extraction of time intervals marking the onset and offset of depolarization and repolarization have been shown to be important measures of fetal well-being [304, 305]. In addition, fMCG has been used to classify arrhythmias, to study congenital heart disease, and to observe fetal well-being during growth retardation or (abnormal) twin pregnancy (e.g. [306, 307]). Recommendations for standardization of fMCG have been published in [308]. Also, the feasibility of high- T_c SQUID systems has been investigated for fMCG [260, 309].

11.3.6

Discussion

11.3.6.1 Statistical Validation of MCG Results

Despite over 30 years of MCG research, common standards of measurement techniques, data processing and presentation are still lacking. Suggestions for such standards are emerging, but there are large differences between sensors and their arrangement in the multichannel magnetometers as well as in recording conditions, ranging from quiet MSRs to very noisy unshielded hospital environments. Fortunately, tools have been developed and tested to transform MCG signals recorded with a multichannel SQUID array to signals of different sensor types and arrays. These kinds of conversion methods are a necessary requirement to perform multicenter MCG studies.

Invasively recorded cardiac signals, such as potentials measured from the heart during electrophysiological studies, provide the gold standard for validation of MCG source imaging. Even though patient populations studied by MCG before or during invasive catheterization are still relatively small, the localization studies of various cardiac arrhythmias have shown encouraging results. Multichannel sys-

tems and accurate combination of the results with cardiac anatomy have improved the accuracy to the order of 5 to 10 mm, which is sufficient to aid in planning and delivering the curative therapy of arrhythmia patients. Further validation of the MCG localization accuracy has been obtained by locating artificial dipole sources, such as pacing catheters inserted into the heart during electrophysiological studies.

For arrhythmia risk evaluation and studies of ischemic heart disease, MCG mapping is an attractive alternative for two reasons: first, the ease of measurement makes it well-suited for screening purposes; and second, several approaches in the analysis can be applied to a single recording. Time-domain analyses of both late fields and intra-QRS fragmentation have performed well in comparison to ECG. Further improvement may be obtained by combination of the analysis of ventricular depolarization, of spatial heterogeneity in MCG repolarization, and of short-term heart rate variability – all possible with one MCG mapping recording. The first systematic evaluations of the prospective prediction value of MCG in clinical studies are being carried out (e.g. [271, 284, 285]).

11.3.6.2 Improvement of Clinical Applicability

Several MCG systems have been installed in hospitals, which exhibit magnetically harsh environments due to strong and rapidly varying ambient electromagnetic noise (power cables, elevators, imaging systems and other hospital apparatus, large magnetizable objects, traffic on nearby streets, and so forth). Electromagnetic pollution is steadily increasing, and therefore operation of an MCG system without any shielding becomes more and more difficult. Most MCG systems are still operated inside a MSR. A more economical and flexible shielding can, however, be achieved using active compensation of low-frequency interference and eddy-current screens build into the walls of rooms housing the systems.

The arrhythmogenic substrate is not manifested in all normal sinus rhythm recordings, and interventions may be needed during MCG to stimulate extrasystolic beats and controlled arrhythmias to locate them. Thus, MCG should be available in a catheterization laboratory, but the demands of magnetical shielding and liquid helium presently limit the use of MCG mapping in many clinical applications, such as guiding invasive arrhythmia localization.

The first multisensor low- T_c and high- T_c SQUID systems operating without magnetic shielding have become commercially available. Such systems can bring MCG applications closer to clinical practice [260–262, 309, 310]. Further technical development of the systems and effective signal processing algorithms are still necessary to improve the SNR.

In the 1970s and 1980s MCG data were usually recorded by engineers with single-channel devices. Multichannel systems and improved data acquisition in the 1990s have made the devices more suitable and easier to use for medical researchers. In the next phase, system development combined with improved signal analysis and source modeling software are becoming increasingly important for extraction and combination of all available MCG and other functional data.

11.3.6.3 Conclusion and Outlook

It can be concluded from all MCG studies published so far that for some applications the diagnostic performance of MCG is superior to the conventional 12-lead ECG. However, this advantage has not yet driven clinicians to accept widely and utilize the method, mostly because of the high cost and low availability. Nevertheless, there is a growing interest in clinical applications of MCG to screening, monitoring, and diagnosis of cardiac diseases.

The localization of arrhythmias and the detection of arrhythmia risk are already established therapy-related applications. Detection and localization of ischemia and viability would be applicable to numerous cardiac patients. Ongoing studies of the prognostic value of MCG for statistical validation may lead to new applications, especially in prediction of CAD or infarction in intensive care patients with chest pain (*e.g.* [271, 284, 285]). However, all these studies will be strongly dependent on the availability of high-performance multichannel MCG systems in clinical environments, and on combining the efforts of physicists and engineers in system development and cardiologists in patient data collection and analysis.

The technology trend in MCG is aiming at low-cost multichannel detector arrays operated with minimal magnetic shielding. Technically, biomagnetic recordings are possible today even without SQUIDs by using optical (atomic) magnetometers and gradiometers [22] (see Section 11.1), or with magnetoresistive sensors [311]. New sensors – as well as multichannel high- T_c SQUID systems – may provide an easier solution to the challenge of having sensors in more than one plane. Besides anterior locations, recordings from the left or back of the chest can significantly improve the detection and localization problems of abnormal cardiac function.

Studies combining MCG and imaging of cardiac anatomy in the same recording session are also under way. For example, SQUID sensors in microtesla MRI can provide anatomical substrate for correlation with magnetic sources (see Section 11.1). Single-channel simultaneous MCG and NMR were reported in [27]. Information about cardiac anatomy can be obtained less ideally but relatively inexpensively with low-cost fluoroscopy and/or echocardiography. Electroanatomic mapping would solve the precise localization difficulties and contribute to the acceptance of MCG mapping.

Finally, the use of magnetic nanoparticle labels *in vivo* (see Section 11.8) could be a very powerful new tool, *e.g.*, for localization on inflammation or infection in heart arteries – preceding (thus predicting the risk of) vulnerable plaque rupture.

11.4

Quasistatic Field Magnetometry

11.4.1

Opening the Near-dc Window

Physiological and pathophysiological activity of the brain at low frequencies has been of continuous interest for some 50 years [312]. Physiological investigations using direct-coupled EEG have shown that sustained activity may endure for several seconds during the application of a permanent acoustic stimulus [313]. Pathophysiological conditions, such as metabolic injuries of brain cells due to stroke or migraine, are believed to be accompanied by slow depolarization processes.

In the frequency range below 1 Hz, noise makes EEG measurements difficult. In this so-called near-dc range, voltage instabilities at the electrode–skin interface are an inevitable source of perturbation for EEG. Invasive approaches, such as vibrating probes inserted in the nerve tissue, have provided local information about the low-frequency activity [314], but their applicability to humans is limited. For MEG, near-dc measurements are spoiled by signals originating from the geo-physical and urban environment that are suppressed only insufficiently by conventional μ -metal-shielded rooms. Also SQUIDs themselves exhibit $1/f$ noise, which complicates the recording of slow processes of the brain, heart, muscles, and nerves. The conventional application of a high-pass filter with a cut-off frequency somewhere below 1 Hz in most EEG and MEG recordings appears to be the engineer’s surrender to the noise that increases so dramatically at low frequencies.

Nevertheless, MEG recording has been employed successfully to study slow brain activity. Sustained magnetic fields [315], as well as the magnetic equivalent of the “Bereitschaftspotential” measured using single-channel SQUIDs [316], were already being reported in the early 1980s. Slow field changes during migraine [317] and epileptic activity were observed [318, 319] as a pathophysiological effect associated with relatively strong near-dc signals. Sustained auditory evoked fields upon stimuli lasting several seconds have been investigated by conventional MEG recording using no high-pass filter [320] or a high-pass filter with a 0.03-Hz cut-off frequency [321]. For recording weak near-dc MEG signals for even longer times or lower frequencies, a special biomagnetic recording technique has been developed, quasistatic field magnetometry, commonly referred to as dc magnetometry.

The general idea of dc magnetometry is to improve the measurement condition further by transforming the recording frequency to higher frequencies using a mechanical modulation technique. Even before he introduced SQUIDs to biomagnetism, Cohen suggested moving the entire source, in this case the human thorax, with respect to the magnetic sensor in order to transform the low-frequency signal from the near-dc range to a higher frequency [322]. The concept of mechanical modulation for dc magnetometry was subsequently used and modified by a number of researchers. The near-dc field of the human leg was studied

by lateral scanning of a single SQUID gradiometer [323]. With the aid of a pendulum gantry, the biomagnetic field of injury currents induced by an incision through the muscle tissue of a rabbit could be recorded [324]. Near-dc activity of the brain was investigated using a stepwise motion of the head with respect to the sensor [325]. Today, the concept of dc magnetometry is refined to a robust system for mechanically driven periodic modulation. Its first version was developed to record the minute fields generated by muscle and nerve tissue specimens [326]. Refinement of this design resulted in two dedicated configurations for near-dc measurements, a small one for specimen and limbs [327] and a large one for whole-body magnetometry [328], both using the same multichannel system with 49 SQUIDs in a flat hexagonal arrangement as described in Section 11.3 (see Figure 11.28(a)). With a resolution of 10 fT in a frequency range down to at least a few millihertz, this system is the state of the art for near-dc measurements, and it is described in the following section.

11.4.2 Quasistatic Field Magnetometer

To reduce external perturbations, the measurement is performed in a magnetically shielded room (AK3b by Vacuumschmelze, Hanau [88]). Interference from the engine driving the mechanical modulation is eliminated by positioning it outside the room. The mechanical motion is transmitted to the modulation device inside the room by an oil-filled hydraulic mechanism. In the small modulation device a vertically mounted cylinder transforms the oil pressure into a vertical oscillation of the scissor-lift construction. The whole-body modulation device is operated in a horizontal direction to increase its stability (see Figure 11.33).

Both devices are made of materials containing low concentrations of ferromagnetic impurities, and titanium nitride-coated tools are used to avoid further contamination during the manufacturing procedure. Cylinder and piston are made of glass-fiber-reinforced plastic or zirconium dioxide ceramics, guided by bronze-reinforced Teflon gaskets to reduce friction.

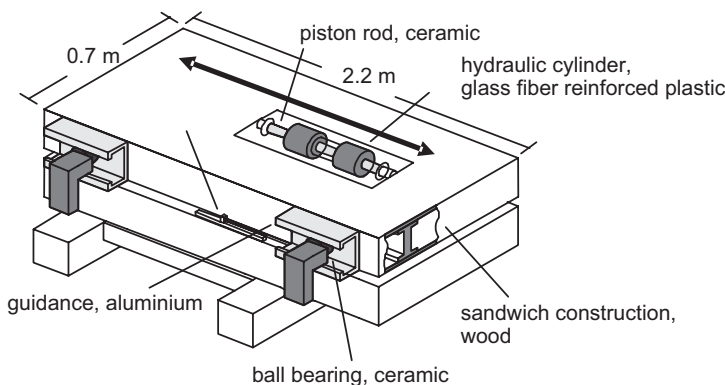


Fig. 11.33 Schematic of a whole-body modulation device for dc magnetometry.

Periodic motion is achieved by feeding the control unit with an alternating voltage. A potentiometer reads the actual position of the table and residual deviations from the sinusoidal shape are corrected by a feedback circuit. To prevent collisions of the patient with the dewar, a fast safety mechanism is installed at the dewar bottom that switches off the modulation motion immediately upon a slight touch. Typical parameters for the horizontal modulation are a frequency of 0.4 Hz and an amplitude of 75 mm.

The magnetic signals are recorded by the multichannel SQUID flat sensor array using a 64-Hz low-pass filter and a sampling rate of 250 Hz. Note that a dc coupled input is not required because low frequencies are shifted into the sidebands of the modulation frequency and its harmonics. One way to retrieve the underlying dc field is to demodulate the recorded signal B_k for each channel k by using a modified cross-correlation with the position y of the modulation

$$A_k = \frac{\sqrt{2}}{N} \frac{\sum_{i=1}^N B_{ik}(y_i - \bar{y})}{\sqrt{\frac{1}{N} \sum_{i=1}^N (y_i - \bar{y})^2}}, \quad (11.12)$$

where the index i runs over the N data points of one modulation period.

By measuring in a shielded environment, para- and diamagnetism may be ruled out as sources of slowly varying or steady biomagnetic fields, but the possibility of ferromagnetic contaminations must still be considered. Ferromagnetic particles may have entered the lungs and the intestine and their field may interfere with dc signals of these or other nearby organs. Some effort may be necessary to reduce the signal of these ferromagnetic sources, such as an iron-free diet for days or weeks before the investigation. For brain studies, much difficulty can be avoided if the subject's hair is washed immediately before dc magnetometry. In addition, it is recommended that the investigated organ be demagnetized by applying an alternating magnetic field to the region of interest. A field amplitude of some 25 mT at a distance of 10 mm should be sufficient for this task.

11.4.3

Applications

Ionic flow due to tissue lesions was among the first bioelectric currents studied by near-dc magnetometry. An injury in a dog's heart, induced by artery occlusion, was shown to lead to a change of the resting potential of the affected cardiac tissue, which in turn resulted in a corresponding slowly varying current and, at the same time, a change of the MCG ST level [329]. Soon it was found that there are additional natural sources of dc currents in the body that may be related to growth or healing processes or to relaxation or stimulation of muscle tissue [330, 331].

Nerve and muscle tissue specimens served for the study of the temporal behavior of injury currents *ex vivo* and the relationship between the structure of artificial

tissue lesions and the dc fields they generate [332]. This improved the understanding of the patterns of the dc fields measured *in vivo* above injuries after human muscle biopsies [327]. In these studies it was possible to monitor the decay of the injury current of an artificial lesion for more than two hours after surgery, thereby providing a methodical background for developing a diagnostic procedure to assess traumatic nerve injuries.

More recently dc magnetometry was applied to study the low-frequency behavior of the brain. The fields generated by physiologic activity of the brain after the beginning of sustained auditory stimulation as well as upon finger movements was shown to endure for at least 30 seconds [333, 334]. Interestingly, in both cases the measured dc field has a simple structure that can be modeled by a dipolar source only a few millimeters away from the well-known generators of the corresponding short-term response occurring 100 ms after an auditory or 20 ms after a somatosensory stimulation pulse. These first studies demonstrate that dc magnetometry can extend the frequency range for electrophysiologic investigations of the brain to frequencies several orders of magnitude below 1 Hz.

Quasistatic field MEG has also revealed slow cortical changes which are induced by hyperventilation [335]. A study of nine subjects showed that the temporal development of this artificial state of increased brain excitability could be monitored for more than ten minutes [336]. On the basis of studies such as these one may envision dc magnetometry becoming a diagnostic tool for patients suffering from acute diseases. In particular, regional metabolic injuries in the brain due to stroke are assumed to be accompanied by slowly changing currents that reveal information on the actual condition of the tissue.

In these long-term recordings signal averaging was the conventional tool to reduce noise and obtain a significant signal. However, without subsequent averaging, single-trial analysis of these slow varying brain activities was possible after the application of an ICA. It is shown in Section 11.2.6 that ICA is a powerful signal processing tool for the separation of components in spatiotemporal MEG data, which uses the assumption of spatially stationary and statistically independent sources [198, 199]. For these multichannel dc MEG recordings, ICA allows separation of different contributing sources: in Figure 11.34 the alternating time course of an unaveraged ICA component of the brain activity corresponding to 30 s periods of finger movement and 30 s of rest is evident with adequate SNR [337]. Closely related to the ICA approach is SSS, which was also successfully applied to improve the SNR in dc MEG [338].

At its present state of development, dc magnetometry, utilizing a flat multichannel SQUID array and a mechanical modulation device, makes it possible to study various slow activities of human tissues, in particular of the brain, with time constants of several minutes. There does not seem to be any technical limit on how slow the investigated activity can be. Attempts have also been made to incorporate dc magnetometry into whole-cortex SQUID devices [339]. However, the mechanical constraints of the whole-cortex helmet dewar limit the modulation amplitude and, thereby, the sensitivity.

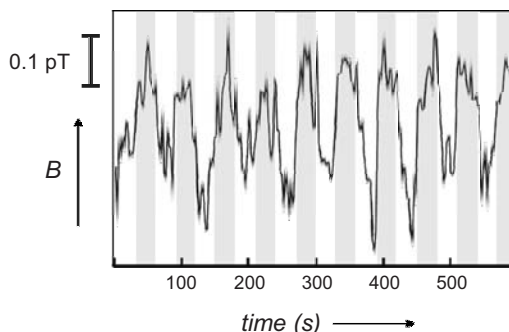


Fig. 11.34 Time course of the ICA component of the dc signal, which correlates in phase and frequency with 30 s of periodic finger movement (shaded areas) and 30 s of rest. Note that this recording was obtained without averaging.

Recent progress in low-field measurement technology has enabled sensitive quasistatic field magnetometry without mechanical modulation. Using massive mu-metal shielding, near-dc MEG changes of a few hundred femtotesla were recorded with a wide bandpass from dc to 100 Hz [340].

Functional MRI and PET are well established for functional brain research and diagnostics in the near-dc range. These methods utilize neurovascular coupling, which provides an indirect access to brain function. With the advent of dc magnetometry, this frequency range of brain activity has become accessible to direct observation. MEG is now the only method for monitoring brain function that covers the entire temporal range from a few milliseconds to several minutes.

11.5 Magnetoneurography

11.5.1 The Long History of Measuring Signal Propagation in Nerves

In 1850 Hermann Helmholtz described an experiment that enabled him to determine the velocity of impulse propagation along a frog's nerve fiber to be 27 m/s [341]. This study of a peripheral nerve may be considered the beginning of quantitative experimental electrophysiology, which later included study of the brain and the heart. Biomagnetic research focused first on the stronger signals of the heart and the brain and it took a number of attempts by several investigators before Wikswo *et al.* finally succeeded in measuring the magnetic field generated by a frog's sciatic nerve [342]. In this experiment, the isolated nerve was kept at room temperature in a saline solution and was threaded through a ferrite ring. The toroidal pickup coil wound around this ring was coupled to a helium-cooled SQUID. This design concentrated the nerve's magnetic flux in the ferrite ring and its sig-

nal was multiplied by the toroidal coil. Although at first sight this approach appeared to be restricted to *in vitro* or *ex vivo* preparations, a modification was developed that allowed this technique to be applied *in vivo* and in humans. To this end, an openable clip-on toroid was constructed that could be closed around a human nerve exposed in a saline solution during a surgical intervention [343]. In this arrangement, helium-cooled devices could be kept at a distance from the investigated subject. This concept was developed even further and resulted in the low-cost biomagnetic current probe system, an alternative recording technique that did not even need a SQUID [344].

The first noninvasive *in vivo* recordings of the magnetic field of action currents of the human median nerve were reported a few years after this pioneering work [345–348]. These studies were designed along the established paradigm for conventional neuroelectric recordings: a peripheral nerve in the arm of a human subject was stimulated at the wrist by an electric current impulse of about 15 mA amplitude and 100 µs duration mediated by a bipolar electrode that was decoupled from the ground to prevent power line interference. The nerve's signal was recorded as it propagated toward the brain by a single- or multichannel SQUID device in a conventional dewar operated in a MSR. When it was positioned above the upper arm of a healthy subject, a deflection of about 100 fT amplitude and about 1 to 2 ms duration was recorded a few milliseconds after the stimulation pulse.

Studies on other nerves followed, in particular on the ulnar nerve in the arm and the tibial nerve in the leg [349, 350]. Different regions along the propagation path of these nerves were measured, such as the lumbar region for the tibial nerve and the plexus in the shoulder where the arm nerves divide into several branches [351 – 353]. Further investigations were on the cervical region where the particular features of the neck as a volume conductor make straightforward interpretation of the data difficult [354, 355].

It became evident during early investigations (and remains still valid today) that:

- MNG signals are among the weakest biomagnetic signals studied so far. Their amplitude is only about 5 to 10 fT in the lumbar region, which is the area of most interest for diagnostic applications. This requires high sensitivity measurements and sophisticated signal processing technology.
- Because the generators in peripheral nerves have a relatively simple structure, peripheral nerve studies may serve as a test bed for biomagnetic measurement techniques and biomagnetic modeling.
- The simple source structure makes it relatively easy to find the corresponding physical models and to extract a number of diagnostically relevant features of peripheral nerve function from MNG data.
- MNG allows one to proceed from the level of the signal to the level of generators. Functional information in terms of current

distributions inside the nerve tissue, as obtained with noninvasive MNG, complements the surface information measured by conventional electroneurography (ENG).

11.5.2

Measurement Technique and Signal Processing

MNG fields have to be recorded with a bandwidth of several kilohertz, because of their short time constants. This implies that a large broadband noise is added to the MNG data and reduces their SNR. An obvious, but important approach to noise reduction is the use of high-performance recording devices for MNG, that is, low-noise SQUIDs including low-noise electronics, and good shielding. Fortunately, MNG is not too affected by low-frequency noise because the MNG signals usually do not extend below 20 Hz. In fact, it was shown that an eddy current shielding provided by a room made of one-inch-thick aluminum may attenuate the environmental noise sufficiently for recording MNG [356]. It is advisable to use low- T_c SQUIDs for MNG, but it illustrates the good performance of modern high- T_c SQUIDs that they also can meet the requirements for MNG [357]. However, the best possible field sensitivity of low- T_c devices is clearly desirable for MNG.

Noise can be reduced by extensive averaging. Since impulse propagation in peripheral nerves is known to be stable and reproducible, there is no technical or physiological limit to this approach. Practical experience has shown, however, that even healthy volunteers are hardly able to undergo this uncomfortable and stressful investigation in a relaxed condition for much more than 15 minutes. With a stimulus repetition rate of about 10 Hz this limits the recording capacity to about 10,000 events. Assuming an instrumental noise of $3 \text{ fT}/\sqrt{\text{Hz}}$ and a recording bandwidth of 2.5 kHz, this results in an rms value of noise of around 1.5 fT. This does not look too bad for analyzing MNG signals of 5 to 10 fT amplitude, but, unfortunately, there is additional noise originating from physiological sources.

Even if patients are cooperative and remain motionless with relaxed muscles, the remaining muscle activities produce strong unstable and nonstationary perturbations in the MNG frequency range of interest. In addition, the periodic perturbation due to heart signals usually has an amplitude that is orders of magnitude larger than the MNG. The presence of these perturbations of physiological sources requires special signal processing tools. To this end, the concept of weighted averaging has proved to be most useful [358]. The main idea of weighted averaging is to weight each epoch in the averaging procedure by its signal power. This method reduces the impact of noisy samples in the averaging procedure, but it also results in an attenuation of the signal. The unwanted effect of signal underestimation can be compensated by an iterative procedure [359]. To suppress the periodical interference by heart signals in the triggered recordings, it is also helpful to include the noise covariance in the weighted averaging [360]. All together, these signal processing tools have provided field distributions with a sufficient

SNR to allow an analysis of MNG signals in terms of dedicated mathematical and physical models.

11.5.3

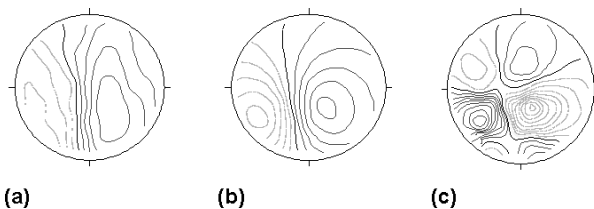
Source Modeling for Magnetoneurography

Approximately 1000 to 10,000 axons are bundled to make up a peripheral nerve, which may branch toward the periphery, for example to the fingers, as well as toward the spine, where three or four branches enter the spinal cord through different intervertebral root entrances. Individual axons have different conduction velocities, which, after a few tens of millimeters of propagation, may lead to a dispersion of the so-called compound action current, that is, the net current of the nerve bundle. The corresponding superposition of depolarization and repolarization currents may lead to partial cancellation of the net current and blurring of the corresponding neuromagnetic field, which can no longer be ascribed to a single current dipole. For the analysis of these fields, the current multipole expansion is a useful concept.

It is well understood from theoretical considerations that different multipole components display different structural properties of the source. The equivalent current dipole corresponds to the integral current intensity. A typical human peripheral nerve, like the tibial nerve, exhibits a current dipole moment of about 10 nA m. Note that this value is derived from MNG studies [350]. A measurement of the electric potential cannot provide this information directly, because body tissue conductivities must also be known for the current strength to be calculated.

The quadrupolar term represents the inhomogeneity of the current distribution. For a linearly extended nerve, such inhomogeneity corresponds to two nearby nerve regions carrying currents in opposing directions (such as the currents corresponding to the depolarization and repolarization of the transmembrane potential). It was shown experimentally that these quadrupolar features are present in MNG recordings [361]. In particular, micro-SQUID MNG at the wrist, where the median nerve is close to the skin surface and the distance between the pickup coil and the nerve bundle is small, provided detailed spatial resolution of the compound action field structure [362].

Higher multipole expansion terms are of even more practical significance for gaining diagnostically relevant information from MNG. One of the octopole components represents the linear extent of a current distribution, which is important for understanding the effects of dispersion of the net current in the nerve bundle. By estimating this component from MNG data, the linear extent of the compound action current of the tibial nerve in the lumbar region, that is, after ~1 m propagation through the leg, was determined to be 140 mm [350], which is in agreement with physiological expectations (see Figure 11.35).



(a) (b) (c)

Fig. 11.35 Magnetic field over an area of 210 mm in diameter generated by the depolarization front of a peripheral nerve having a longitudinal extension of about 140 mm. (a) Measured field (0.5-fT contour step), (b) approximated field of the dipolar component (0.5 fT), (c) approximated field of the octopolar component (0.1 fT). (From M. Burghoff's (PTB-Berlin) unpublished results.)

11.5.4

Clinical Perspective

Peripheral nervous system diseases may be manifested as disturbances of the conduction velocity, distributed homogeneously or inhomogeneously along the conduction path. For these diseases, MNG is a diagnostic tool for which there is no counterpart in conventional electrophysiology. It was shown recently that MNG allows a much better reconstruction of the propagation path in stimulated nerves than multichannel ENG [363]. In terms of a current distribution model reconstructed from the MNG, better assessment of the affected function, that is the instantaneous conduction velocity, is possible. It would be worthwhile to find out whether this methodological advantage of MNG can provide additional diagnostic value for the treatment of diseases such as Guillan–Barré syndrome.

A frequent disturbance in the peripheral nerve function is a conduction block due to a lesion, for instance, a nerve root compression. For a considerable percentage of affected patients, conventional imaging techniques display the structural lesions, but do not provide an unambiguous picture of the functional defect location. In such cases, MNG may provide additional information on the functional disturbance. Figure 11.36 illustrates the result of an MNG investigation of a patient suffering from a nerve root compression generated by a herniated intervertebral disk: a functional image of impulse propagation in a leg nerve that identifies and localizes a conduction block [364].

Magnetoneurography is a powerful tool for diagnosing localized malfunctions of the peripheral nervous system. Considering the frequency of such diseases in the population of industrialized countries one may envision its high clinical potential. However, MNG requires the use of sophisticated data processing techniques, as well as a multichannel device having a flat array of SQUIDS with a noise level well below $5 \text{ fT}/\sqrt{\text{Hz}}$. Such instruments are not widely distributed so that these requirements may delay the application of MNG as a routine clinical diagnostic tool.

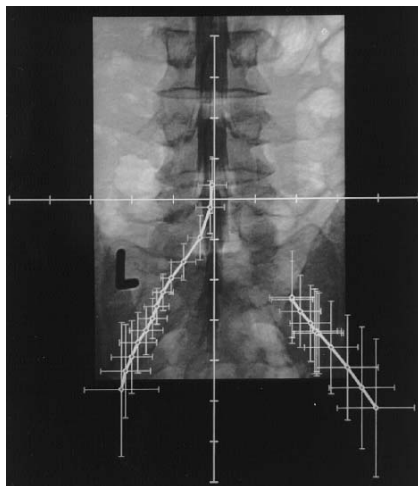


Fig. 11.36 Propagation of the equivalent current dipole along the tibial nerve of a patient suffering from a nerve root compression leading to a conduction block on the right side. The localizations in steps of 0.25 ms are superimposed on an X-ray image of the patient's lumbar region. The tics on the grid are separated by 20 mm. (From [364].)

11.6 Liver Susceptometry

11.6.1 Incorporated Magnetism as a Source of Diagnostic Information

Ionic currents flowing through living tissue are by no means the only origin of biomagnetic fields. Magnetic fields can also be generated by ferro- or paramagnetic particles that are incorporated into biologic tissue.

On the one hand, ferromagnetic contamination may perturb the measurements. For example, it was pointed out in Section 11.4 that permanent fields from ferromagnetic contamination in the hair, stomach, intestine, lungs, or liver are particularly perturbing for biomagnetic measurements in the low-frequency range. This contamination has become an even more serious problem as the application of magnetic resonance imaging in strong static magnetic fields becomes more widespread.

On the other hand, biomagnetic fields due to incorporated magnetism may provide diagnostically relevant information. It is well known that ferromagnetic iron particles accumulate in the lungs of iron welders and give rise to an increased magnetism. Investigations of the temporal behavior of the lung magnetization allow one to monitor noninvasively the amount in and effect of the iron load on the pulmonary systems of such patients.

Liver is another human organ for which knowledge of the iron content is diagnostically relevant. Together with red cells of the blood, liver serves as a store for iron in the human body. In a healthy adult, daily uptake and release of 1 to 2 mg iron keep the iron content at a constant level of some 2700 mg for the blood and some 800 mg in the liver [365]. If the iron uptake is pathologically increased, for

instance due to a disturbed metabolism or frequent blood transfusions, iron accumulates mainly in the liver, but also in the spleen and some other organs. Conventionally, this pathological overload is quantitatively assessed by liver biopsies, but it was recognized even before the advent of SQUIDs that noninvasive susceptibility measurement may offer a reliable alternative to this invasive procedure [366]. The use of SQUIDs for the assessment of iron overload was first suggested by Wikswo *et al.* [367, 368], and the development of an adequate SQUID-based measurement technique started with the pioneering work of a clinical research group in Cleveland [369 – 371]. Today, liver susceptometry helps thousands of patients in the world every year, and is performed using commercial devices [17, 372, 373].

11.6.2

Measurement Technique

While most other biomagnetic applications of SQUIDs detect the magnetic fields generated by ionic currents within the body, the content of paramagnetic iron in the liver is determined by a susceptibility measurement, that is, by measuring the response of the tissue to an applied magnetic field. A dedicated biomagnetic measurement setup needed for liver iron susceptometry is commonly referred to as a biosusceptometer. A schematic of a state-of-the-art liver susceptometer is shown in Figure 11.37. It consists of the following elements:

- Second-order gradiometers coupled to a helium-cooled SQUID for measuring the variation of the magnetic flux during the measurement procedure.

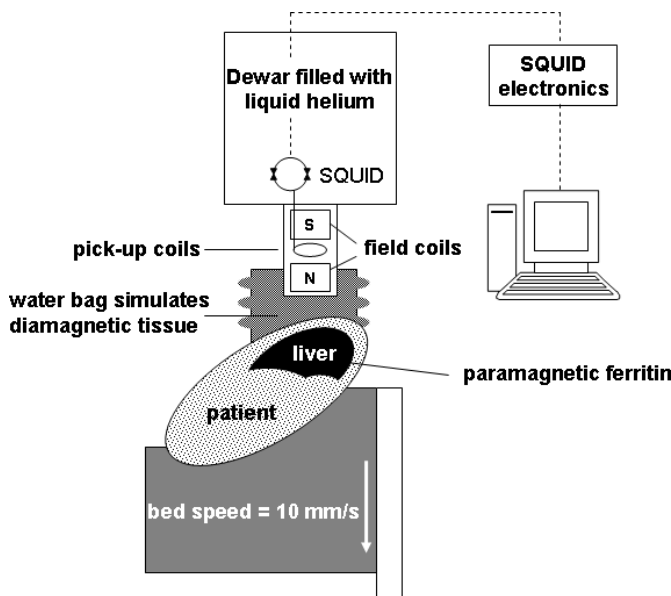


Fig. 11.37 Schematic of a liver susceptometer. (Modified from [373].)

- A superconducting magnet generating a field of ~ 3 mT at the liver tissue.
- A bed for positioning the patient horizontally; in addition the bed should be movable vertically under motor control.
- A bag filled with water simulating the diamagnetism of human body tissue.

The patient is laid in supine position with the left side elevated and the thorax touching the water bag. With this arrangement, the flux change, $\Delta\phi(z)$, due to the susceptibility of the liver tissue that is registered by the detector coils of the gradiometers is given by [372, 374]

$$\Delta\Phi(z) = \left(\frac{1}{\mu_0 I_d} \right) \int_V \chi(\mathbf{r}) \mathbf{B}_f(\mathbf{r}) \cdot \mathbf{B}_d(\mathbf{r}) d^3r \quad (11.13)$$

where $\chi(\mathbf{r})$ is the magnetic susceptibility of the tissue, $\mathbf{B}_f(\mathbf{r})$ is the inhomogeneous magnetizing field, and $\mathbf{B}_d(\mathbf{r})$ is the magnetic field generated by a current I_d in the detector coil. For the volume integral only nearby regions below the detector are relevant, because of the fast spatial decay of the applied inhomogeneous field.

The changing flux is measured by the gradiometer with a low pass at a few hertz while the body is moved away from the device in a vertical direction at a speed of about 10 mm/s. During this motion the position of the body is monitored by measuring the magnetic field of a locator device consisting of a loop fed by an alternating current. At the same time the bag is continuously filled with water to provide a homogeneous reference medium, which is considered to represent the average susceptibility of the body tissue. This procedure changes the susceptibility of the relevant integration region from the value of the liver to the reference value of the water bag. The measurement is usually repeated several times to obtain an averaged signal with improved SNR. Susceptibility of the liver tissue can be estimated from the measured flux changes and the position of the body relative to the susceptometer by using Eq. (11.13). It is useful to complement liver susceptometry by ultrasonic imaging of the abdomen, in order to obtain more accurate information about the liver's position, size, and shape.

Systems such as that described above have been operated for more than 20 years and shown to be robust and to provide reliable diagnostic information. The linear relation between the concentration of paramagnetic compounds in the investigated volume and the corresponding susceptibility change makes quantitative measurements possible. This linear relationship can easily be established experimentally by calibrating the biosusceptometer using phantoms with well-defined volumes and susceptibilities. Biosusceptometers have a sensitivity of 20 $\mu\text{g/g}$ when calibrated with a ferric chloride solution in a cylindrical phantom tank [372]. In a real *in vivo* measurement, the situation is somewhat worse because of inhomogeneities of the surrounding tissue and limited knowledge about the magnetic properties of the iron particles, which have uncertainties between 50 $\mu\text{g/g}$ and 300 $\mu\text{g/g}$ [373]. This is sufficient for iron overload patients

with pathologically increased concentrations of up to 5000 µg/g. For quantifying the liver iron load of healthy subjects or of patients with an iron deficiency a better sensitivity would be helpful. Increasing the sensitivity of biosusceptometers to make the quantification of low susceptibilities possible remains a challenge to the developers of SQUID instrumentation.

Several alternatives have been developed that meet the special demands for bio-susceptometry. In particular, omitting the water bag facilitates the investigation of small children who may not tolerate its heavy weight [375]. However, decreased sensitivity due to the uncompensated signal from the body tissue limits the applicability to patients suffering from severe iron overload. Also, an ac susceptometer was developed in which the magnetizing field was driven at a frequency of 14 Hz by Helmholtz coils [376]. This system exhibited good sensitivity but relatively poor spatial resolution, which may result in difficulties in discriminating liver tissue from the surrounding tissue of the lungs or the intestine.

11.6.3

Applications

In the population of European descent one out of 400 subjects is affected by genetic hemochromatosis (GH) [377]. This metabolic disease leads to an inadequate uptake of iron which is then stored mainly in the liver. If the disease remains untreated, irreversible defects such as diabetes, arthropathies, or liver cirrhosis may appear simultaneously with or even before the first unambiguous laboratory findings. This alone may call for screening of the general population. With the advent of modern genetic diagnosis, it has become possible to recognize the genetic defect responsible for GH [378]. It is not difficult to predict that in the near future this knowledge will be used to identify the carriers of this genetic defect at an early age, before their disease becomes symptomatic. In these patients, iron depletion therapy has to be started before the onset of iron-induced liver damage and this will require adequate diagnostic monitoring of iron stores.

In Mediterranean countries, anemias such as β -thalassemia major and sickle cell disease have a high prevalence. Affected patients are treated by blood transfusions which may cause a secondary iron overload in the liver and spleen. To avoid the corresponding side effects and to maximize the patient's life expectancy it is essential to balance this overload by iron chelation treatment. The efficacy of this treatment has to be reliably controlled. Liver susceptometry was demonstrated to be superior to the conventional determination of the concentration of serum ferritin in a study on several hundred patients of iron-loading anemias as well as of GH, [379, 380]. Also for the assessment of the efficacy of novel iron chelating agents for iron chelation treatment, liver susceptometry has proved to be the appropriate tool [381, 382].

After the clinical use of liver iron susceptometry was introduced in the 1980s in Cleveland, it has been routinely applied at the university hospital in Hamburg-Eppendorf, where several thousands of patients have been examined during the past 15 years. Most of the patients had GH and thalassemia, but basic studies

were also performed, for example, the investigation of iron metabolism in athletes [383]. These investigations have shown that liver susceptometry meets the requirements for a reliable quantitative diagnosis of iron overload [384]. This was clearly recognized when liver susceptometric investigations were accepted for reimbursement by health insurers in the middle of the 1990s. A number of new biosusceptometry centers are being established in Europe and in the USA that will be equipped with commercial susceptometer systems. This reflects both the progress in SQUID measurement technology, and the increasing need for reliable determination of liver iron content.

11.6.4

Outlook

Other noninvasive approaches used to determine the iron content of specific organs are based on imaging techniques and provide a comprehensive assessment of the organs affected by iron overload, including also spleen, pancreas, and muscles. In particular, X-ray CT and MRI have been suggested as alternatives to SQUID-based liver susceptometry [384, 385]. However, quantitative determination of iron overload by these methods is difficult. X-ray absorption displayed by CT appears to be a poor quantitative measure of the iron concentration. For MRI the relation between the concentration of the paramagnetic relaxation centers in the liver and their induced relaxivity to the nuclear magnetization in different types of tissue is not yet fully understood [386]. Nevertheless it appears likely that MRI will become an increasingly important diagnostic tool for assessing iron overload and may complement the quantitative information provided by liver susceptometry [387]. On the basis of calibrations using SQUID susceptometry, MRI could provide even quantitative information on iron overload.

While MRI provides a spatially resolved image of the affected organs, SQUID-based susceptometry provides an integral assessment of the iron load. Separate investigation of an enlarged spleen in several patients has shown that discrimination of various organs by SQUID susceptometry is possible [388]. This option may become important in assessing the iron load in heart tissue where an overload may cause serious malfunctions. Such measurements could be complemented by ultrasound images or by establishing a combined investigation using both SQUID-based susceptometry and MRI.

SQUID-based liver susceptometry is commonly accepted today as the reference measurement for determining the iron content of the liver. Based on calibrations using well-defined phantoms it provides a quantitative measure of the concentration of the hemosiderin/ferritin iron complex. It is an integral measurement that avoids uncertainties that may arise in small liver tissue biopsies due to local fluctuations of the iron concentration [389]. Above all, it is noninvasive and may be applied repeatedly to a patient with a chronic disease without the risk of side effects. Because of these benefits liver susceptometry has become the first medical application of SQUIDs accepted as a routine clinical diagnostic tool.

11.7

Gastromagnetometry

11.7.1

Magnetogastrography (MGG) and Magnetoenterography (MENG)

Two functions of the gastrointestinal organs have been studied with SQUID detectors [390]: (a) the spontaneous activity of the smooth muscles of the stomach and intestine, by measuring the biomagnetic field of the corresponding electrophysiological currents; and (b) gastrointestinal motility and transport, by measuring the temporal variation of the magnetostatic fields generated by ingested ferromagnetic markers. The two study types are commonly referred to as (a) MGG and MENG for spontaneous signals of stomach and intestine, respectively, and (b) magnetic marker monitoring (MMM).

Electric signals from the stomach, that is, electrogastrograms (EGG), were first recognized by Alvarez in 1922 who deduced the transcutaneous surface potential related to gastric motion [2]. As the electrocardiogram does for the heart, the EGG directly and noninvasively measures the electrophysiologic reflection of gastric muscular activity. For the stomach, the dominant frequency is the basic electrical rhythm (BER) of about 50 mHz, or 3 cycles/minute. A change of this frequency may indicate a disturbance of gastric function, that is, so-called bradygastria or tachygastria. At the present time, EGG has been accepted as a research tool, which provides direct access to the electrophysiologic function of the stomach, but it is not yet established for routine gastroenterological diagnostics. However, the modern signal acquisition devices available today at low cost coupled with sophisticated signal processing may lead to wider acceptance of EGG, which may emerge as a relatively simple tool for diagnosis of diseases such as dyspepsia or irritable bowel syndrome.

Like EGG, its magnetic counterpart, the magnetogastrogram, offers the opportunity to monitor gastric rhythms. While EGG has gained only limited acceptance in routine clinical diagnostics, the prospects for MGG may be better considering the wealth of spatiotemporal information on gastric activity available in MGG data. It was pointed out by Bradshaw *et al.* that by using vector magnetometry it may be possible to distinguish locations of gastromagnetic generators and, thereby, separate gastric activity from other sources [391] and characterize the propagation of the gastric slow wave [392].

The situation appears to be even more favorable for MENG, the measurement of the biomagnetic field generated by the small intestine. An electrical counterpart of MENG has not been established, because of the poor conduction properties of the abdomen. Layers of skeletal muscle and fat isolate the volume currents in the gut and weaken the intensity of the transcutaneous potential at the skin's surface. This is the classic situation in which the SQUID-based measurement technique benefits from the practically undisturbed transmission of the biomagnetic field through body tissue. With the first detection of biomagnetic signals from the small intestine in the picotesla range, a window was opened for studying and

diagnosing the electrophysiology of this organ [394]. Noninvasive biomagnetic measurements of the small intestine's BER in a number of subjects using conventional multichannel SQUID systems identified bioelectrical currents with a frequency that decreases along the small intestine from 0.2 Hz in the duodenum [393, 394] to 0.16 Hz in the ileum [393].

A close correlation between the bioelectric and biomagnetic signals was found by simultaneous invasive electroenterography using implanted electrodes placed at the small intestine and noninvasive MENG in an animal model [395, 396]. By identifying a frequency change of the BER, MENG can diagnose mesenteric ischemia in the small intestine, with a high sensitivity and specificity, before irreversible damage occurs [397]. Considering that mesenteric arterial occlusion is a life-threatening disorder that urgently requires an early and reliable diagnosis, it is evident that noninvasive MENG may have great potential for clinical application in humans.

11.7.2

Magnetic Marker Monitoring (MMM)

The function of the gastrointestinal tract can also be studied by measuring the signal of ingested ferromagnetic material. One way is to administer a test meal containing a few grams of ferromagnetic particles of ~0.1 mm grain size. If a magnetizing impulse of, for example, 60 mT is applied for 70 ms to the stomach, the particles obtain a net magnetization that generates a field of several hundred nanotesla above the abdomen. Recording such a strong field usually does not require SQUIDs but can be done with flux-gate magnetometers [398, 399]. As an alternative approach, an ac susceptometer has been used to measure the ferromagnetic load inside the stomach [400]. Such measurements provide an estimate of the gastric emptying time, or an assessment of the mixing power of the stomach on the basis of the decay constant of the signal following the magnetization impulse [401]. Interestingly, the signals display the typical gastric contraction rhythm of about 3 cycles/minute that is correlated to the EGG signal.

Another way to use magnetic material for SQUID-based gastroenterologic studies is to administer the patient or volunteer a single oral dosage form that carries a magnetic moment. The magnetic moment of such an ingested magnetic marker generates a dipolar magnetic field which is determined by its location and orientation. The marker's path through the entire gastrointestinal tract can be reconstructed by solving the inverse problem for a magnetic dipole [402, 403]. For this approach, which is commonly referred to as MMM, the magnetic marker capsule should have the following properties: (a) a permanent magnetic moment in the range between 100 nAm² and 10 µAm² and (b) a specific weight around 1.0 g/cm³. The latter condition is necessary to ensure that the magnetic marker behaves like a drug capsule or a conventional food. By coating a saccharose pellet of ~1 mm diameter with a few micrograms of magnetite and by magnetizing this marker in a field of about 100 mT, both conditions can be fulfilled [404]. To simulate drug capsules having dimensions of a few millimeters, the coated pellet can

be enclosed in a larger cylindrically shaped capsule of appropriate material that is resistant to digestion, such as silicone rubber.

The field above the stomach or abdomen, generated after ingestion of such a capsule, is usually in the range of several picotesla, which makes it easily measurable by conventional SQUID instruments. Theoretically, six independent magnetic field measurements at different locations are needed to determine the magnetic dipole moment, $\mu = (\mu_x, \mu_y, \mu_z)$, and its location, $\mathbf{r} = (x, y, z)$. This number can be reduced to five, if the absolute value of the magnetic moment, μ , is determined before the capsule is ingested. For practical applications in the presence of noise, usually more than ten magnetic field values are required for the marker localization. A SQUID device with fewer channels is of only a limited use for MMM, since the field of a magnetic marker measured sequentially at a number of sensor positions represents a consistent registration of a dipolar field only when the marker remains immobilized for the duration of the scan [405, 406]. To track a moving marker, a multichannel system of 37 SQUIDs distributed over an area of 230 mm diameter was shown to be sufficient [407]. Furthermore, it was pointed out mathematically that for a flat system measuring only one (z -) component of the biomagnetic field, the inverse problem for vertical (z -) orientations of a magnetic dipole may be ill-conditioned [408]. As in the case for MGG, the inverse solution becomes more stable when x - and y -components are also measured and included in the localization procedure.

Once the technical requirements are met, the MMM is straightforward. The subject is positioned within a shielded room and the magnetic capsule is brought from a remote location to ensure that the initial magnetic signal can be used as a reference baseline. The magnetic field generated by the marker, while it is passing through the esophagus, stomach, duodenum, and small and large intestine, is recorded by a multichannel SQUID device with a temporal resolution of a few milliseconds.

The data analysis is also simple. At the location \mathbf{r} with respect to a magnetic dipole with a moment \mathbf{M} , a field

$$\mathbf{B}(\mathbf{M}, \mathbf{r}) = \left(\frac{\mu_0}{4\pi r^5} \right) [3\mathbf{r} \cdot (\mathbf{r} \cdot \mathbf{M}) - r^2 \mathbf{M}] \quad (11.14)$$

is generated. This is virtually a perfect approximation of the physical situation, since the spatial extent of the dipole source is negligible, and for the magnetic dipole model, in contrast to the current dipole model, the problem of volume currents is irrelevant. As a side effect of this simplicity, MMM may serve as a test bed for numerical procedures which are well established in biomagnetism, such as localization algorithms. If the method is applied to a phantom measurement where the location of the marker can be validated by independent means, deviations from reality may be traced back to shortcomings of the algorithm or the measurement conditions [409]. For practical biomagnetic applications, noise generated by the environment and the body (produced by, for instance, heart or stomach) has to be considered a source of deviation from the ideal situation.

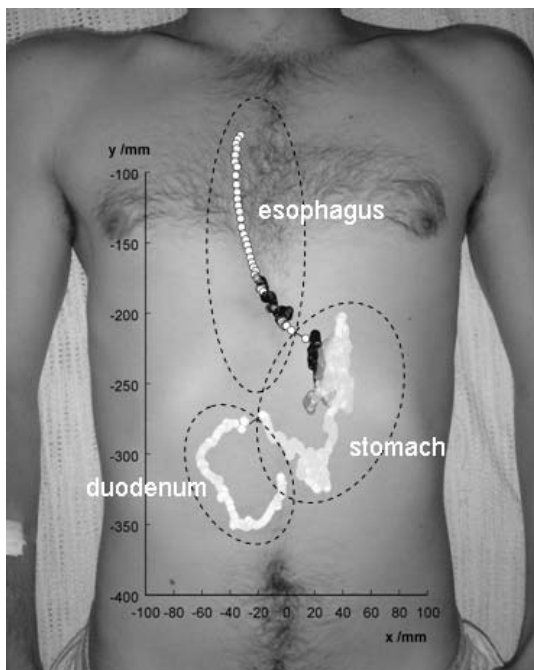


Fig. 11.38 Transport of a magnetic marker through esophagus, stomach, and duodenum in a frontal projection. The dots represent marker localizations in time steps of 40 ms; altogether 40 minutes of the transport are displayed.

Virtually all sections of gastrointestinal transport have been studied by MMM in healthy human subjects [410–413]. This includes the few seconds of passage through the esophagus, gastric emptying through the “house-keeper wave”, irregular motion through the small intestine, and slow motion through the transverse colon. As an example, Figure 11.38 depicts the transportation of the marker through esophagus, stomach, and the c-shaped duodenum in a two-dimensional projection. More impressive than static pictures are animations of marker motions which can be obtained from MMM data and be displayed on a computer screen.

MMM is noninvasive, does not cause any discomfort and does not expose the subjects to any kind of radiation as does γ -scintigraphy. Therefore, it is also suitable for testing the resorption of drug substances from pharmaceutical preparations by healthy human volunteers. When studying the erosion or dissolution of oral drugs, analysis of the MMM signal has to consider the decay of the magnetic moment along its path through the gastrointestinal tract. In such situations, the number of unknown dipole parameters is increased to six [409].

Gastromagnetism may also provide a number of benefits for medical research and diagnosis. In addition to its noninvasiveness, it has excellent temporal and spatial resolution which permits one to analyze gastrointestinal wall motility. Transit times as well as transport patterns for different sections of the gastrointest-

inal system can be studied. Combined with minimally invasive procedures such as intraluminal manometry, MMM may help the study of the function and efficacy of the peristaltic activity of the gastrointestinal organs under both physiological and pathophysiological conditions.

The statistical yield of MMM investigations could be significantly increased if more than a single marker were employed. However, the resulting complex multiple-marker field patterns destabilize the inverse solution. It is not known how this problem can be resolved, but there is reason to expect that introduction of vector magnetometry and more sophisticated signal processing tools may make possible simultaneous monitoring of two or three markers.

Considering that gastromagnetometry is potentially applicable to a wide range of relevant investigations, it is surprising that comparatively few studies of the gastrointestinal organs have been pursued during the 30 years of biomagnetic research and development. The technical requirements for MMM are similar to those for MGG and MENG, and multichannel SQUID devices can be easily designed for all gastromagnetometry applications. In principle, a device similar to a conventional commercial multichannel MCG system with a few additional tangential channels for the x - and y -components would be satisfactory. When MCG devices become more common in clinical research institutions, gastromagnetometry may be considered an additional internal medicine application with large clinical potential.

11.8

Magnetic Relaxation Immunoassays

11.8.1

Immunoassays and Superparamagnetic Particles

Immunoassays are an analytical tool that is well established in medicine and biology for the qualitative and quantitative detection of analytes in complex biological liquids, such as plasma. They play an outstanding role in medical diagnosis whenever the identification of small amounts of substances (for example hormones, viruses) is required. Immunoassays are based on the specificity of the binding reaction between the two reaction components. Usually, an immunoassay uses some sort of label that is attached to one of the reaction components. If the unlabeled reaction component is attached to a solid phase, for example to the wall of the reaction vessel, the binding reaction results in the fixation of both reaction components including the label. After washing, the bound reaction components remain in the vessel and can be identified by some physical signal of the attached label. For instance, in a radioisotope immunoassay (RIA), which uses radioactive isotopes as labels, the radiation intensity is a measure of the amount of molecules that took part in the binding reaction. Other assays, such as the enzyme-linked immunosorbent assay (ELISA) or the fluorescence dye immunoassay (FIA) use optical interactions for the quantitative detection of reaction components.

In the case of magnetic relaxation immunoassays, magnetic nanoparticles are used as labels. Magnetic nanoparticles consist of a material that is ferri- or ferromagnetic as bulk, and have a size in the nanometer range, that is, diameters from a few nanometers to about 50 nm. They are too small to be ferromagnetic, but exhibit a single domain of homogeneous magnetization. In its equilibrium state, the magnetization of a magnetic nanoparticle is aligned along the particle's "easy axis". Exposure to an external magnetic field may tilt the magnetization vector with respect to the easy axis. The characteristic time constant for a thermally activated relaxation of the magnetization vector to the easy axis is the Néel relaxation time $\tau_N = \tau_0 \exp(E/k_B T)$, where $k_B T$ is the thermal energy, and E is the energy barrier which is proportional to the particle volume [414].

Magnetic nanoparticles can be coated by a layer of an organic material, such as dextrane. This may increase the hydrodynamic diameter of the particle by a factor of two or more. The corresponding decrease of the particle's specific weight makes these particles suitable for a stable suspension in a liquid carrier medium such as water. In these so-called ferrofluids, the magnetization can relax via an additional mechanism due to the thermally activated rotational diffusion of the particles in the suspension. The corresponding Brownian relaxation time, $\tau_B = 3\eta_0 V_h / k_B T$, depends on the viscosity of the carrier liquid, η_0 , and hydrodynamic volume, V_h , which includes the volume of the coating layer.

For observation times much longer than the relaxation time, magnetic nanoparticles, whether they are solid or suspended in a solution, behave like paramagnetic material. However, the susceptibility they exhibit is orders of magnitude stronger than for any conventional paramagnetic substance. This is why their extraordinary magnetic properties are commonly referred to by the notion of superparamagnetism.

A number of biologic applications for superparamagnetic particles have been established such as cell separation using magnetic field gradients [415]. To this end, specific antibodies were coupled to the organic coating layer of the particle. On the basis of this technology, the magnetic relaxation immunoassay (MARIA) was developed, which exploits the superparamagnetic properties of the nanoparticle labels using the outstanding sensitivity of SQUIDs [416].

11.8.2

MARIA

The coating layers of the magnetic labels of MARIA are coupled to one or more specific antibodies. If the corresponding antigens are attached to a solid phase, such as the wall of the sample tube, then the binding reaction between the antibody and antigen reduces the mobility of the magnetic label. As the preparation step of a MARIA measurement, an external magnetic field is applied for a few seconds to the sample which generates a net magnetization. After the magnetic field is switched off, SQUIDs are used to measure the decay of the sample's magnetization.

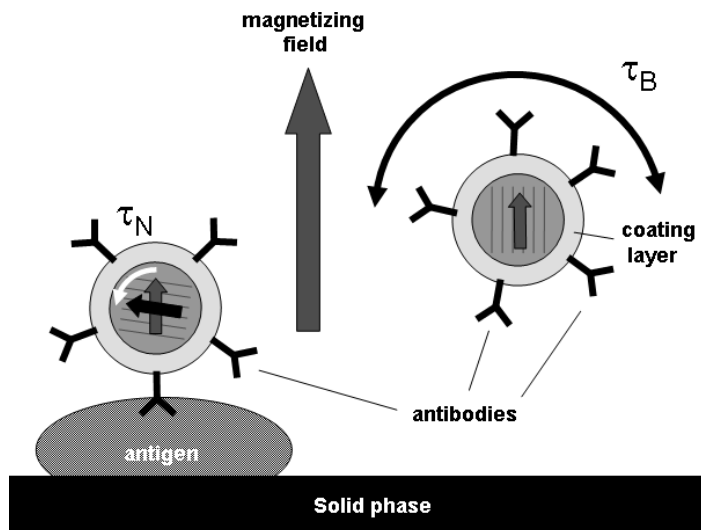


Fig. 11.39 Relaxation mechanisms for magnetic nanoparticles after the magnetizing field is switched off. Brownian relaxation is due to the rotational diffusion of the entire particle in the solution (right side). Néel relaxation is due to the reorientation of the magnetization

vector to the easy axis of the particle core (left side). Covalent binding of the attached antibody, indicated by the Y-shaped structure, to its specific antigen may cause a transition of the effective relaxation from the Brownian mechanism to the Néel mechanism.

An aqueous sample of diluted magnetic nanoparticles can lose its net magnetization by two mechanisms (see Figure 11.39). One mechanism is the Néel relaxation of the magnetization vectors within the cores of the particles, which is discussed above. A second mechanism is the thermal reorientation of the labels by their rotational diffusion in the solution [417]. For an ensemble of identical noninteracting particles, the effective relaxation is an exponential decay with a rate given by the sum of the Néel and Brownian relaxation rates [418]:

$$\tau^{-1} = \tau_N^{-1} + \tau_B^{-1}. \quad (11.15)$$

Figure 11.40 illustrates this behavior for magnetite particles having a spherical shape. For most sizes one of the two relaxation mechanisms dominates, so that only one relaxation rate has to be considered, that is, τ_N^{-1} for small particles and τ_B^{-1} for larger particles. In this example, particles having a hydrodynamic diameter of 24 nm relax by the Brownian mechanism. If, however, these particles become immobilized by their binding to a solid phase, this relaxation process becomes inhibited, so that only the slower Néel relaxation remains. The corresponding increase of the relaxation time is utilized by MARIA for detecting and quantifying binding reactions.

The amplitude increase of the Néel part of the relaxation is a measure of the number of particles that are immobilized by the binding reaction. Note that this

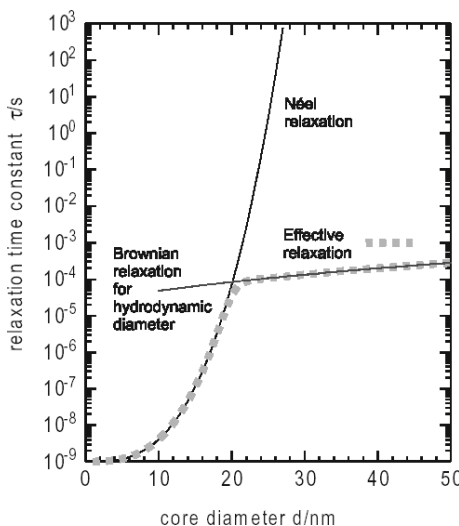


Fig. 11.40 Dependence of Brownian and Néel relaxation on the diameter of spherical magnetite particles in a solution. In this example, particles smaller than 19 nm relax solely by the Néel process and particles larger than 22 nm relax solely by the Brownian mechanism. For particles with a coating layer, the hydrodynamic diameter is assumed to be ~40 nm larger than the core diameter.

information can be obtained in the presence of the unbound reaction components that remain in the solution and still exhibit Brownian relaxation behavior. Unlike conventional immunoassays, MARIA provides a binding-specific signal and, therefore, does not require any washing and rinsing procedure to remove signals from unbound labels. This simplification makes possible continuous monitoring of the kinetics of a binding reaction with a time resolution of a few seconds [419].

11.8.3

Instrumental Developments

A number of different instruments for the realization of a magnetic relaxation immunoassay have been developed. Some of them are based on “conventional” low- T_c SQUID technology [420–422], while other approaches use modifications of a high- T_c SQUID microscope [423, 424]. The basic features of these instruments are briefly described.

The SQUIDS of a MARIA instrument have to tolerate exposure to a magnetizing field amounting to a few millitesla at the site of the sample. By the use of twin coils, *i.e.*, parallel coils with opposite polarity, the stray field at the SQUID can be reduced by several orders of magnitude. However, a delay between magnetization switch-off and the start of the signal registration cannot be avoided. A dead time of less than 100 μs was attained by using a low- T_c dc SQUID with a bandwidth of several megahertz and a wide dynamic range of ±235 nT. In the first version, a

MARIA device based on a vertical gradiometer design was operated in a MSR [421]. By using the three-SQUID concept [427] or, alternatively, an electronic second-order gradiometer, a MARIA device was designed that can be operated without a passive μ -metal shielding [428].

Unwanted interference from the magnetizing field can also be reduced by applying the magnetization field perpendicular to the orientation of the SQUID pickup area [422–424]. The field generated by a sample magnetized in the horizontal direction is most favorably recorded by an integrated planar gradiometer, which ensures effective coupling to the SQUID. This MARIA configuration can be combined with a horizontal positioning system which additionally makes possible a spatially resolved registration of magnetic relaxation processes [429].

SQUID microscopes can be also used for magnetic relaxation immunoassays. By using high- T_c SQUIDs, the sample to sensor distance can be significantly reduced to 1.5 mm [424, 425] or even to 200 μm [423]. Compared with the low- T_c devices discussed above, which typically provide SQUID to sample distances around 10 mm, this distance reduction results in an increase of the magnetic signal, which depends on the details of the geometrical arrangement of pickup coil, magnetizing field, and sample shape [426]. In terms of the number of measured particles, high sensitivities were obtained by these systems, *i.e.*, about 10^6 [424] or even 5×10^4 [423] particles could be detected by SQUID microscopy.

11.8.4

Applications

MARIA has been applied to a number of different binding reactions between antibodies and antigens, such as collagen III, human immunoglobulin G (hIgG), and many others, using different preparations of magnetic nanoparticles [414, 421, 423, 424]. In all of these applications, the specific binding reaction resulted in the appearance or an increase of a slow relaxation signal which can be attributed to the Néel relaxation process of the bound particles. In addition to the solid-phase immunoassay, the aggregation of biotinylated magnetic nanoparticles, where biotin is coupled to the shell and causes a specific binding to avidin, was investigated in the liquid phase [430]. Here, the reduced mobility of large aggregates in the solution leads to suppression of the Brownian relaxation. These experiments demonstrated that the MARIA signal allows one to monitor the sample at sequential titration stages without the need for interruption by a washing procedure. It was even possible to monitor the temporal development of the aggregation for about 30 minutes with a resolution of a few seconds.

By using biotinylated magnetic nanoparticles, that is, by coupling the magnetic nanoparticle to one of the reaction components via the universal biotin–avidin interface, made MARIA applicable to a variety of biomolecules. On the basis of the biotin–avidin interface, the binding reaction of virtually any avidin-coupled biomolecule can now be studied by MARIA [431, 432].

To date, it has been demonstrated that MARIA has a number of advantages over conventional approaches to immunoassays:

- The binding specificity of the signal simplifies the procedure, because the residual unbound molecules do not have to be removed.
- Convenient successive and time-dependent monitoring of binding reactions by sequential measurements is possible.
- The Néel relaxation amplitude is a linear measure of the immobilized particles, which facilitates a quantitative analysis.
- In its SQUID microscope version, MARIA makes possible observation of the behavior of a very small number of reaction components.
- MARIA is applicable to turbid media such as blood, where optical methods often fail.

MARIA can also be applied to detect suspensions of bacteria. It was estimated that, depending on the sample size, a few hundreds of magnetically labeled *Listeria monocytogenes* should be detectable for a MARIA SQUID microscope [433].

There appears to be a great potential of the magnetorelaxometric technique for *in vivo* applications to humans, in particular for cancer imaging [434]. Local enrichments of magnetic nanoparticles somewhere in the living tissue may become visible and localized by multichannel SQUID devices. As for the *in vitro* experiment, the specific relaxation signal of the bound particles could be separated from an unspecific background signal. A well-established *in vivo* application of magnetic nanoparticles is MRI, where proton relaxation time reductions induced by the field distortion of magnetic nanoparticles are visualized as a change of contrast. While MRI provides spatially resolved images, magnetic relaxation provides an integrated view on the localization of the particles. Thus, for *in vivo* applications, these two methods could complement each other perfectly.

In spite of all the advantages mentioned above, MARIA suffers from a limitation. The present MARIA sensitivity to low concentration of reaction components is slightly less, or at best equal, to that of the conventional ELISA. This drawback is mainly caused by the broad size distribution of the magnetic nanoparticles which are used as labels. Because of the dramatic variation of the Néel relaxation time with the particle diameter (see Figure 11.40), the method is highly sensitive to the particle size distribution, and the majority of particles exhibits Néel relaxation times outside the range of measurable relaxation times, that is, $\tau_N < 100 \mu\text{s}$ or $\tau_N > 10 \text{ s}$. Thus, most binding sites are occupied by “silent” labels and only a small percentage of the bound labels contribute to the Néel relaxation signal. The sensitivity of a MARIA could be increased by several orders of magnitude if the physical properties and the homogeneity of the ferrofluid composition could be optimized for the application in a magnetic immunoassay. Once this is accomplished, MARIA could resolve very low biomolecular concentrations, perhaps even a few single molecules in the sample tube.

Acknowledgments

We would like to thank our colleagues for their help with experiments, data processing, simulations, and preparation of some parts of this presentation material, and for numerous stimulating discussions and fruitful collaboration on ideas associated with this chapter. Namely, we would like to thank Drs. S. E. Robinson, H. Wilson, A. A. Fife, P. Kubik, J. McCubbin and Messrs. B. Taylor, J. McKay, T. Bardouille, and M. Tillotson at VSM MedTech Ltd; Drs. C. Lowery, H. Eswaran, and R. N. P. Murphy at the University of Arkansas Medical School, Dr. H. Preissl at the University of Arkansas Medical School and MEG Center at Tuebingen; Drs. A. Ahonen, J. Simola, and S. Taulu at Elektta Neuromag Oy; Drs. K. Tsukada and A. Kandori, Hitachi Ltd; Dr. H. Itozaki, Osaka University; Dr. S. Erne, Advanced Technologies Biomagnetics; Dr. P. Seidel, Friedrich Schiller Universität Jena; Prof. R. Fenici, Catholic University of Rome; Drs. M. Burghoff, H. Koch, and G. Wübbeler from PTB Berlin; Dr. G. Curio from Charité, Berlin; Dr. R. Fischer from University Hospital Eppendorf, Hamburg; and to Dr. W. Weitschies from the University of Greifswald.

References

- 1 Waller, A.D. (1887) A demonstration on man of electromotive changes accompanying the heart's beat, *J. Physiol.* **8**, 229–234.
- 2 Alvarez, W.C. (1922) The electrogastrogram and what it shows. *J. Am. Med. Assoc.* **78**, 1116–1119.
- 3 Berger, H. (1929) Über das Electrenkephalogramm des Menschen, *Arch. Psychiat. Nervenkr.* **7**, 527–570.
- 4 Baule, G.M. and McFee, R. (1963) Detection of the magnetic field of the heart, *Am. Heart J.* **66**, 95–96.
- 5 Cohen, D. (1968) Magnetoencephalography: evidence of magnetic fields produced by alpha-rhythm current, *Science* **161**, 784–786.
- 6 Cohen, D., Edelsack, E.A., and Zimmerman, J.E. (1970) Magnetocardiograms taken inside a shielded room with a superconducting point-contact magnetometer, *Appl. Phys. Lett.* **16**, 278–280.
- 7 Cohen, D. (1972) Magnetoencephalography: detection of the brain's electrical activity with a superconducting magnetometer, *Science* **175**, 664–666.
- 8 VSM MedTech Ltd (CTF MEG), 9 Burbridge Street, Coquitlam, BC, Canada V3K 7B2 , www.vsmmedtech.com (cited material from August 2005).
- 9 Elektta Neuromag Oy., PO Box 68, FIN-00511 Helsinki, Finland, www.neuromag.com (cited material from August 2005).
- 10 4D Neuroimaging, 9727 Pacific Heights Blvd., San Diego, CA 92121, USA www.4dneuroimaging.com (cited material from August 2005).
- 11 Eagle Technology Inc., 1-2-23 Hirosaka, Kanazawa, Japan, www.eagle-tek.com (cited material from August 2005).
- 12 AtB, Advanced Technologies Biomagnetics S.r.l., Via Martiri di Pietransieri 2, 65129 Pescara, Italy, www.atb-it.com (cited material from August 2005).
- 13 Hitachi Ltd, www.hqrdr.hitachi.co.jp/crle (cited material from August 2005).
- 14 CardioMag Imaging Inc. (CMI), 450 Duane Av, Schenectady, NY 12304, USA, www.cardiomag.com (cited material from August 2005).
- 15 SQUID International AG, Kruppstr. 82–100, D-45145, Essen, Germany, www.squid.de (cited material from August 2005).

- 16** Sumitomo Electric Hightechs, Co., 2-60 Nanko-higasi 8-chome, Suminoe-ku, Osaka 559-0031, Japan, www.shs.co.jp/en/products/p_05_03.html and www.shs.co.jp/b/us_h/rev_e.html (cited material from August 2005).
- 17** Tristan Technologies Inc., San Diego, CA, USA, www.tristantech.com/prod-biomagnet.html (cited material from August 2005).
- 18** Cryoton Co. Ltd, 12, Solnechnaja Avenue, Troitsk, Moscow Region, 142190, Russia, www.cryoton.webzone.ru/ (cited material from August 2005).
- 19** Kominis, I.K., Kornack, T.W., Allred, J.C., and Romalis, M.V. (2003) A sub-femtotesla multichannel atomic magnetometer, *Nature* **422**, 596–599.
- 20** Wikswo, J.P. (2004) SQUIDS remain best tool for measuring brain's magnetic fields, *Physics Today* **57**, 15.
- 21** Romalis, M.V., Baranga, B.-A.A., and Hoffman, D.E. (2004) Magnetoencephalography with an atomic magnetometer, in Halgren, E., Ahlfors, S., Hämäläinen, M. and Cohen, D. (eds.), *Biomag2004, Proc. 14th Internat. Conf. on Biomagnetism*, Biomag2004 Ltd, Boston, MA, p. 661.
- 22** Weis, A., Wynands, R., and Bison, G. (2004) Dynamical MCG mapping with an atomic vapor magnetometer, in Halgren, E., Ahlfors, S., Hämäläinen, M. and Cohen, D. (eds.), *Biomag2004, Proc. 14th Internat. Conf. on Biomagnetism*, Biomag2004 Ltd., Boston MA, pp. 646–647.
- 23** McDermott, R., Trabesinger, A.H., Muck, M., Hahn, E.L., Pines, A., and Clarke, J. (2002) Liquid-state NMR and scalar couplings in microtesla magnetic fields, *Science* **295**, 2247–2249.
- 24** McDermott, R., Lee, S.K., ten Haken, B., Trabesinger, A.H., Pines, A., and Clarke, J. (2004) Microtesla MRI with superconducting quantum interference device, *Proc. Nat. Acad. Sci.* **101**, 7857–7861.
- 25** Volegov, P., Matlachov, A.N., Espy, M.A., George, J.S., and Kraus, Jr., R.H. (2004) Simultaneous magnetoencephalography and SQUID detected nuclear MR in microtesla magnetic fields, *Magn. Reson. Med.* **52**, 467–470.
- 26** Xiong, J., Fox, P.T., and Gao, J.-H. (2003) Directly mapping magnetic field effects of neuronal activity by magnetic resonance imaging, *Human Brain Mapping* **20**, 41–49.
- 27** Espy, M.A., Volegov, P.L., Matlachov, A.N., George, J.S., and Kraus, Jr., R.H. (2004) Simultaneously detected biomagnetic signals and NMR, in Halgren, E., Ahlfors, S., Hämäläinen, M. and Cohen, D. (eds.), *Biomag2004, Proc. 14th Internat. Conf. on Biomagnetism*, Biomag2004 Ltd, Boston, MA, pp. 621–622.
- 28** Cheyne, D., Vrba, J., Crisp, D., Betts, K., Burbank, M., Cheung, T., Fife, A.A., Haid, G., Kubik, P., Lee, S., McCubbin, J., McKay, J., McKenzie, D., Spear, P., Taylor, B., Tillotson, M., Weinberg, H., Basar, E., and Tsutada, T. (1992) Use of an unshielded, 64-channel whole-cortex MEG system in the study of normal and pathological brain function, in A. Dittmar and J.C. Froment (eds.), *Proc. Satellite Symposium on Neuroscience and Technology, Proc. IEEE-EMBS*, Lyon, France, pp. 46–50.
- 29** Ahonen, A., Hämäläinen, M., Kajola, M. et al. (1992) A 122-channel magnetometer covering the whole head, in A. Dittmar and J.C. Froment (eds.), *Proc. Satellite Symposium on Neuroscience and Technology, Proc. IEEE-EMBS*, Lyon, France, pp. 16–20.
- 30** Vrba, J., Betts, K., Burbank, M.B., Cheung, T., Fife, A.A., Haid, G., Kubik, P.R., Lee, S., McCubbin, J., McKay, J., McKenzie, D., Spear, P., Taylor, B., Tillotson, M., Cheyne, D., and Weinberg, H. (1993) whole cortex, 64 channel SQUID biomagnetic system, *IEEE Trans. Appl. Supercond.* **3**, 1878–1882.
- 31** Knuutila, K.E.T., Ahonen, A.I., Hämäläinen, M.S., Kajola, M.J., Laine, P.P., Lounasmaa, O.V., Parkkonen, L.T., Simola, J.T.A., and Tesche, C.D. (1993) A 122-channel whole-cortex SQUID system for measuring the brain's magnetic fields, *IEEE Trans. Mag.* **29**, 3315–3320.
- 32** ter Brake, H.J. M., Flokstra, J., Jaszcuk, W., Stammis, R., van Ancum, G.K., and Martinez, A. (1991) The UT 19-channel dcSQUID based neuromagnetometer, *Clin. Phys. Physiol. Meas.* **12B**, 45–50.

- 33** Becker, W., Dickmann, V., Jurgens, R. and Kornhuber, C. (1993) First experiences with a multichannel software gradiometer recording normal and tangential components of MEG, *Physiol. Meas.* **14**, A45–A50.
- 34** Dieckmann, V., Jurgens, R., Becker, W., Elias, H., Ludwig, W. and Vodel, W. (1996) RF-SQUID to DC-SQUID Upgrade of a 28-Channel Magnetoencephalography (MEG) System, *Meas. Sci. Technol.* **7**, 844–852.
- 35** Matlashov, A.N., Slobodchikov, V.Y., Bakharev, A.A., Zhuravlev, Yu., and Bondarenko, N. (1995) Biomagnetic multichannel system built with 19 cryogenic probes, in C. Baumgartner *et al.* (eds.), *Biomagnetism: Fundamental Research and Clinical Applications*, Elsevier Science, IOS Press, pp. 493–496.
- 36** Drung, D., Absmann, Curio, G., Mackert, B.-M., Matthies, K.-P., Matz, H., Peters, M., Scheer, H.-J. and Koch, H. (1995) The PTB 83-SQUID system for biomagnetic applications in a clinic, *IEEE Trans. Appl. Supercond.* **5**, 2112–2117.
- 37** Dossel, O., David, B., Fuchs, M., Kruger, J., Ludeke, K.-M., and Wischmann, H.-A. (1993) A modular 31-channel SQUID system for biomagnetic measurements, *IEEE Trans. Appl. Supercond.* **3**, 1883–1886.
- 38** Yoshida, Y., Arakawa, A., Kondo, Y., Kajihara, S., Tomita, S., Tomita, T., Takashii, Y., and Matsuda, N. (2000) A 129 channel vector neuromagnetic imaging system, in C. Aine *et al.* (eds.), *Biomag96: Advances in Biomagnetism Research*, Springer-Verlag, pp. 154–157.
- 39** Ueda, M., Kandori, A., Ogata, H., Takada, Y., Komuro, T., Kazami, K., Ito, T. and Kado, H. (1995) Development of a biomagnetic measurement system for brain research, *IEEE Trans. Appl. Supercond.* **5**, 2465–2469.
- 40** Sata, K., Fujimoto, S., Fukui, N., Haraguchi, E., Kido, T., Nishiguchi, N., and Kang, Y.M. (2000) Development of a 61-channel MEG system cooled by a GM/JT cryocooler, in C. Aine *et al.* (eds.), *Biomag96: Advances in Biomagnetism Research*, Springer-Verlag, pp. 114–117.
- 41** Fujimoto, S., Sata, K., Fukui, N., Haraguchi, E., Kido, T., Nishiguchi, K., and Kang, Y.M. (2000) A 32-channel MCG system cooled by a GM/JT cryocooler, in C. Aine *et al.* (eds.), *Biomag96: Advances in Biomagnetism Research*, Springer-Verlag, pp. 43–46.
- 42** Kotani, M., Uchikawa, Y., Kawakatsu, M., Tsukada, K., Kandori, A., Sasabuti, H., Suzuki, H., Kondo, S., Matsuda, N., Shinada, K., and Yamada, Y. (1998) A whole-head SQUID system for detecting vector components, *Appl. Supercond.* **5**, 399–403.
- 43** Itozaki, H., Tanaka, T., Toyoda, S., Hirano, Haruta, Y., Nomura, M., Saijou, T., and Kado, H. (1996) A multi-channel high- T_c SQUID system and its applications, *Supercond. Sci. Technol.* **9**, A38–A41.
- 44** Barthelmess, H.-J., Halverscheid, M., Schiefenhovel, B., Heim, E., Schilling, M., and Zimmermann, R. (2001) Low-noise biomagnetic measurements with a multichannel dc-SQUID system at 77 K, *IEEE Trans. Appl. Supercond.* **11**, 657–660.
- 45** Wikswo, Jr., J.P. (1995) SQUID magnetometers for biomagnetism and nondestructive testing: important questions and initial answers, *IEEE Trans. Appl. Supercond.* **5**, 74–120.
- 46** Helmholz, H. (1835) Über einige Gesetze der Vertheilung elektrischer Strome in körperlichen Leitern mit Anwendung auf die thierisch-elektrischen Versuche, *Ann. Phys. Chem.* **89**, 211–233, 353–377.
- 47** Pflieger, M.E., Simpson, G.V., Ahlfors, S.P. and Ilmoniemi, R.J. (2000) Superadditive information from simultaneous MEG/EEG data, in C. Aine *et al.* (eds.), *Biomag96: Advances in Biomagnetism Research*, Springer-Verlag, pp. 1154–1157.
- 48** Cohen, D. and Cuffin, B.N. (1987) A method of combining MEG and EEG to determine the sources, *Phys. Med. Biol.* **32**, 85–89.
- 49** Wright, G.A. (1997) Magnetic resonance imaging, *IEEE Signal Processing* **14**, No.1, 56–66.
- 50** Lauterbur, P.C. (1973) Image formation by induced local interactions: examples

- employing nuclear magnetic resonance, *Nature* **242**, 190–191.
- 51** Hinshaw, W.S. and Lent, A.H. (1983) An introduction to NMR imaging: from the Bloch equations to the imaging equation, *Proc. IEEE* **71**, 338–350.
- 52** Hinz, T. (1988) Utilization of reconstruction algorithm in transmission and emission computed tomography, in C.E. Swenberg and J.J. Contlin (eds.), *Imaging Techniques in Biology and Medicine*, Academic Press, New York, pp. 257–299.
- 53** ter Poggiani, M.M., Phelps, M.E., Hoffman, E.J., and Mullani, N.A. (1975) A positron emission transaxial tomography for nuclear medicine imaging (PETT), *Radiology* **114**, 89–98.
- 54** Gilardi, M.C., Rizzo, G., Lucignani, G., and Fazio, F. (1996) Integrating competing technologies with MEG, in H. Weinstock (ed.), *SQUID Sensors: Fundamentals, Fabrication and Applications*, NATO ASI Series E: Applied Sciences, Vol. 329, Kluwer Academic, Dordrecht, pp. 491–516.
- 55** Knoll, G.F. (1983) Single photon emission computed tomography, *Proc. IEEE* **71**, 320–329.
- 56** Stehling, M.K., Turner, R., and Mansfield, P. (1991) Echo-planar imaging: magnetic resonance imaging in a fraction of a second, *Science* **254**, 43–50.
- 57** Belliveau, J.W., Kenedy, D.N., McKinsky, R.C., Buchbinder, B.R., Weisskoff, R.M., Cohen, M.S., Vevea, J.M., Brady, T.J., and Rosen, B.R., (1991) Functional mapping of the human visual cortex by magnetic resonance imaging, *Science* **254**, 716–719.
- 58** Partridge, L.D. and Partridge, L.D. (1993) *The Nervous System, Its Function and Its Interaction with the World*, A Bradford Book, MIT Press, Cambridge, MA.
- 59** Wikswo, Jr, J.P. (1989) Biomagnetic sources and their models, in S.J. Williamson *et al.* (eds.), *Advances in Biomagnetism*, Plenum Press, New York and London, pp. 1–18.
- 60** Taccardi, B. (1982) Electrophysiology of excitable cells and tissues, with special consideration of the heart muscle, in S.J. Williamson *et al.* (eds.), *Biomagnetism: An Interdisciplinary Approach*, NATO ASI Series A: Life Sciences, Vol. 66, Plenum Press, New York and London, pp. 141–171.
- 61** Hämäläinen, M., Hari, R., Ilmoniemi, R.J., Knuutila, J., and Lounasmaa, O.V. (1993) Magnetoencephalography – theory, instrumentation, and applications to noninvasive studies of the working human brain, *Rev. Mod. Phys.* **65**, 413–497.
- 62** Carpenter M.B. (1985) *Core Text of Neuroanatomy*, Williams & Wilkins, Baltimore, London, Sydney.
- 63** Grynszpan F. and Geselowitz, D.B. (1973) Model studies of the magnetocardiogram, *Biophys. J.* **13**, 911–925.
- 64** Trip, J.H. (1982) Physical concepts and mathematical models, in S.J. Williamson *et al.* (eds.), *Biomagnetism: An Interdisciplinary Approach*, NATO ASI Series A: Life Sciences, Vol. 66, Plenum Press, New York and London, pp. 101–149.
- 65** Swinney, K.R. and Wikswo, Jr, J.P. (1980) A calculation of magnetic field of a nerve action potential, *Biophys. J.* **32**, 719–732.
- 66** Sarvas, J. (1987) Basic mathematical and electromagnetic concepts of the biomagnetic inverse problem, *Phys. Med. Biol.* **32**, 11–22.
- 67** Hillebrand, A. and Barnes, G.R. (2002) A quantitative assessment of the sensitivity of whole-head MEG to activity in the adult human cortex, *NeuroImage* **16**, 638–650.
- 68** Williamson, S.J. and Kaufman, L. (1981) Biomagnetism, *J. Mag. Mag. Mater.* **22**, 129–201.
- 69** Nakasato, N., Fujita, S., Seki, K., Kawamura, T., Matani, A., Tamura, I., Fujiwara, S., and Yoshimoto, T. (1995) Functional localization of bilateral auditory cortices using an MRI-linked whole head magnetoencephalography (MEG) system, *Electroencephalogr. Clin. Neurophysiol.* **94**, 183–190.
- 70** Okada, Y.C. (2003) Toward understanding the physiological origins of neuro-magnetic signals, in Z.-L. Lu and L. Kaufman (eds.), *Magnetic Source Imaging of the Human Brain*. Lawrence Erlbaum Associates, Mahwah, NJ and London, pp. 43–76.

- 71** Fagaly, R.L. (1990) Neuromagnetic instrumentation, in S. Sato (ed.), *Advances in Neurology*, Vol. 54, Magnetoencephalography, Raven Press, New York, pp. 11–32.
- 72** Varpula, T. and Poutanen, T. (1984) Magnetic field fluctuations arising from thermal motion of electric charge in conductors, *J. Appl. Phys.* **55**, 4015–4021.
- 73** Nenonen, J., Montonen, J., and Katila, T. (1996) Thermal noise of biomagnetic measurements, *Rev. Sci. Instrum.* **67**, 2397–2405.
- 74** Seton, H.C., Hutchison, J.M.S., and Bussell, D.M. (1997) A 4.2 K receiver coil and SQUID amplifier used to improve the SNR of low-field magnetic resonance images of the human arm, *Meas. Sci. Technol.* **8**, 198–207.
- 75** Vrba, J., Betts, K., Burbank, M., Cheung, T., Cheyne, D., Fife, A.A., Haid, G., Kubik, P.R., Lee, S., McCubbin, J., McKay, J., McKenzie, D., Mori, K., Spear, P., Taylor, B., Tillotson, M., and Xu, G. (1995) Whole cortex 64 channel system for shielded and unshielded environments, in C. Baumgartner *et al.* (eds.), *Biomagnetism: Fundamental Research and Clinical Applications*, Elsevier Science, IOS Press, pp. 521–525.
- 76** Parkkonen, L.T., Simola, J.T., Tuoriniemi, J.T., and Ahonen, A.I. (1999) An interference suppression system for multichannel magnetic field detector arrays, in T. Yoshimoto *et al.* (eds.), *Recent Advances in Biomagnetism*, Tohoku University Press, pp. 13–16.
- 77** Vrba, J. and McKay, J. (1998) Character and acquisition of multichannel biomagnetic data, *Appl. Supercond.* **5**, 431–439.
- 78** Pasquarelli, R., De Melis, M., Marzetti, L., Trebeschi, A., and Erne, S.N. (2004) Argos 500: operation of a helmet vector-MEG, in Halgren, E., Ahlfors, S., Härmäläinen, M. and Cohen, D. (eds.), *Biomag2004, Proc. 14th Internat. Conf. on Biomagnetism*, Biomag2004 Ltd, Boston, MA, pp. 34–35.
- 79** Vrba, J., Fife, A.A., Burbank, M.B. (1981) Digital SQUID electronics in geophysical applications, in H. Weinstock and W.C. Overton, (eds.), *SQUID Applications to Geophysics*, Society of Exploration Geophysicists, Tulsa, OK, pp. 31–34.
- 80** McKay, J., Vrba, J., Betts, K., Burbank, M.B., Lee, S., Mori, K., Nonis, D., Spear, P., and Uriel, Y. (1993) Implementation of a multi-channel biomagnetic measurement system using DSP technology, *Proc. of 1993 Canadian Conference on Electrical and Computer Engineering*, vol. II, pp. 1090–1093.
- 81** McCubbin, J., Vrba, J., Spear, P., McKenzie, D., Willis, R., Loewen, R., Robinson, S.E., and Fife, A.A. (2004) Advanced electronics for the CTF MEG system, in Halgren, E., Ahlfors, S., Härmäläinen, M. and Cohen, D. (eds.), *Biomag2004, Proc. 14th Internat. Conf. on Biomagnetism*, Biomag2004 Ltd, Boston MA, pp. 36–37.
- 82** Laine, P.P., Härmäläinen, M.S., and Ahonen, A.I. (1997) Essential figures of merit for clinical MEG, *Biomedizinische Technik*, **42**, 209–212.
- 83** Pizzella, V., Della Penna, S., Erne, S.N., Granata, C., Pasquarelli, A., Torquati, K., Rossi, R., and Russo, M. (2001) A 165-channel neuromagnetometer for multimodal brain imaging, in J. Nenonen, R. Ilmoniemi, and T. Katila (eds.), *Biomag2000, Proc. 12th Int. Conf. on Biomagnetism*, Helsinki University of Technology, Espoo, Finland, pp. 939–942.
- 84** Kraus, Jr., R.H., Volegov, P., Maharajh, K., Matlachov, A., Espy, M., and Flynn, E.R. (2002) Source localization using a novel SQUID-based superconducting imaging-surface system, *Physica C* **368**, 18–23.
- 85** Volegov, P., Matlachov, A., Mosher, J., Espy, M.A., and Kraus, Jr., R.H. (2004) Noise-free magnetoencephalography recordings of brain function, *Phys. Med. Biol.* **49**, 2117–2128.
- 86** Williamson, S.J. and Kaufman, L. (1981) Biomagnetic fields of the cerebral cortex, in S.N. Erne *et al.* (eds.), *Biomagnetism*, Walter de Gruyter, Berlin and New York, pp. 353–402.
- 87** Cheyne, D., Roberts, L.E., Gaetz, W., Bosnyak, D., Weinberg, H., Johnson, B., Nahmias, C., and Deecke, L. (2000) EEG and MEG source analysis of somatosensory evoked responses to mechanical

- stimulation of the fingers, in C. Aine *et al.* (eds.), *Biomag96: Advances in Biomagnetism Research*, Springer-Verlag, pp. 1130–1133.
- 98** Vacuumschmelze GmbH, Hanau, Germany, Shielded Room model AK-3.
- 99** Amuneal Manufacturing Corp., 4737 Darrah Street, Philadelphia, PA 19124, USA.
- 100** Tokin Corporation, 6-7-1 Koriyama Tihakuku, Sendai-City, Miyagi-pref, 982, Japan.
- 101** Lindgren RF Enclosures, Inc., 400 High Grove Boulevard, Glendale Heights, IL, 60139, USA.
- 102** Kelha, V.O. (1981) Construction and performance of the Otaniemi magnetically shielded room, in S.N. Erne *et al.* (eds.), *Biomagnetism*, Walter de Gruyter, Berlin and New York, pp. 33–50.
- 103** Erne, S. N., Hahlbohm, H.-D., Scheer, H. and Trontelj, Z. (1981) The Berlin magnetically shielded room (BMSR) Section B – performances, in S.N. Erne *et al.* (eds.), *Biomagnetism*, Walter de Gruyter, Berlin and New York, pp. 79–87.
- 104** Harakawa, K., Kajiwara, G., Kazami, K., Ogata, H., and Kado, H. (1996) Evaluation of a high-performance magnetically shielded room for biomagnetic measurement, *IEEE Trans. Mag.* **32**, 5226–5259.
- 105** Bork, J., Hahlbohm, H.-D., Klein, R., and Schnabel, A. (2001) The 8-layered magnetically shielded room of the PTB: design and construction, in J. Nenonen, R. Ilmoniemi, and T. Katila (eds.), *Biomag2000, Proc. 12th Int. Conf. on Biomagnetism*, Helsinki University of Technology, Espoo, Finland, pp. 970–973.
- 106** Matsuba, H., Shintomi, K., Yahara, A., Irisawa, D., Imai, K., Yoshida, H. and Seike, S. (1995) Superconducting shield enclosing a human body for biomagnetic measurement, in C. Baumgartner *et al.* (eds.), *Biomagnetism: Fundamental Research and Clinical Applications*, Elsevier Science, IOS Press, pp. 483–489.
- 107** Utela, K., Taulu, S., and Hämäläinen, M. (2001) Detecting and correcting for head movements in neuromagnetic measurements, *NeuroImage* **14**, 1424–1431.
- 98** de Munck, J.C., Verbunt, J.P.A., Van't Ent, D., and Van Dijk, B.W. (2001) The use of an MEG device as a 3D digitizer and a motion monitoring system, *Phys. Med. Biol.* **46**, 2041–2052.
- 99** Erne, S.N., Narici, L., Pizzella, V., and Romani, G.L. (1987) The positioning problem in biomagnetic measurements: a solution for arrays of superconducting sensors, *IEEE Trans. Magn. MAG-23*, 1319.
- 100** Polhemus Inc., 1 Hercules drive, PO Box 560, Colchester, VT 05446, USA.
- 101** Bamidis, P.D. and Ioannides, A.A. (2000) Combination of point and surface matching techniques for accurate registration of MEG and MRI, in C. Aine *et al.* (eds.), *Biomag96: Advances in Biomagnetism Research*, Springer-Verlag, pp. 1126–1129.
- 102** Abraham-Fuchs, K., Lindner, L., Wegener, P., Nestel, F., and Schneider, S. (1991) Fusion of biomagnetism with MRI or CT images by contour-fitting, *Biomed. Eng.* **36** (Suppl.), 88–89.
- 103** Kober, H., Grummich, P., and Vieth, J. (1995) Fit of the digitized head surface with the surface reconstructed from MRI-tomography, in C. Baumgartner *et al.* (eds.), *Biomagnetism: Fundamental Research and Clinical Applications*, Elsevier Science, IOS Press, pp. 309–312.
- 104** Vrba, J. (2000) Multichannel SQUID biomagnetic systems, in H. Weinstock (ed.), *Applications of Superconductivity*, Kluwer Academic, Dordrecht, pp. 61–138.
- 105** Vrba, J. and Robinson, S.E. (2002) SQUID sensor array configurations for magnetoencephalography applications, *Supercond. Sci. Technol.* **15**, R51–R89.
- 106** Vrba, J. (1997) Baseline optimization for noise cancellation systems, *Proc. 19th Int. Conf. IEEE-EMBS*, Chicago, IL, pp. 1240–1243.
- 107** Vrba, J. and Robinson, S.E. (2001) The effect of environmental noise on magnetometer- and gradiometer-based MEG systems, in J. Nenonen, R. Ilmoniemi, and T. Katila (eds.), *Biomag2000, Proc. 12th Int. Conf. on Biomagnetism*, Helsinki University of Technology, Espoo, Finland, pp. 953–956.

- 108** Taulu, S., Kajola, M., and Simola, J. (2004) Suppression of interference and artifacts by the signal space separation method, *Brain Topography*, **16**, 269–275.
- 109** Taulu, S., Simola, J., Kajola, M., and Nenonen, J. (2004) Software magnetic shield by signal space separation (SSS), in Halgren, E., Ahlfors, S., Hämäläinen, M. and Cohen, D. (eds.), *Biomag2004, Proc. 14th Internat. Conf. on Biomagnetism*, Biomag2004 Ltd, Boston, MA, pp. 186–187.
- 110** Taulu, S., Simola, J., and Kajola, M. (2005) Application of the signal space separation method, *IEEE Trans. Sig. Process.* **53**, 3359–3372.
- 111** Gauss, C.F. (1839) *Allgemeine Theorie des Erdmagnetismus, in Resultate aus den Beobachtungen des Magnitischen Vereins im Jahre 1838*, Leipzig.
- 112** Garland, G.D. (1979) The contributions of Carl Friedrich Gauss to geomagnetism, *Historia Mathematica* **6**, 5–29.
- 113** Simola, J., Taulu, S., Parkkonen, L., and Kajola, M. (2004) Active shielding method for an MEG device, in Halgren, E., Ahlfors, S., Hämäläinen, M. and Cohen, D. (eds.), *Biomag2004, Proc. 14th Internat. Conf. on Biomagnetism*, Biomag2004 Ltd, Boston, MA, p. 38.
- 114** Wilson, H.S. (2004) Continuous head-localization and data correction in whole-cortex MEG sensor, in Halgren, E., Ahlfors, S., Hämäläinen, M. and Cohen, D. (eds.), *Biomag2004, Proc. 14th Internat. Conf. on Biomagnetism*, Biomag2004 Ltd, Boston, MA, pp. 648–649.
- 115** Taulu, S. and Kajola, M. (2005) Presentation of electromagnetic multichannel data: the signal space separation method, *J. Appl. Phys.* **97**, 124905 (10 pages).
- 116** Vrba, J., Taylor, B., Cheung, T., Fife, A.A., Haid, G., Kubik, P.R., Lee, S., McCubbin, and J., Burbank, M.B. (1995) Noise cancellation by a whole-cortex SQUID MEG system, *IEEE Trans. Appl. Supercond.* **5**, 2118–2123.
- 117** Uchikawa, Y., Kobayashi, K., Kawakatsu, M., and Kotani, M. (2001) A 3-D vector measurement and its application on biomagnetic signals, in J. Nenonen, R. Ilmoniemi, and T. Katila (eds.), *Biomag2000, Proc. 12th Int. Conf. on Biomagnetism*, Helsinki University of Technology, Espoo, Finland, pp. 915–918.
- 118** Hughett, P. and Miyauchi, S. (2000) A comparison of vector and radial magnetometer arrays for whole-head magnetoencephalography, in Aine, C.J. et al. (eds.), *Biomag 96: Proc. 10th Int. Conference on Biomagnetism*, Springer-Verlag, New York, pp. 51–54.
- 119** Matsuba, H., Vrba, J., and Cheung, T. (2000) Current dipole localization errors as a function of the system noise and the number of sensors, in Aine, C.J. et al (eds.), *Biomag 96: Proc. 10th Int. Conference on Biomagnetism*, Springer-Verlag, New York, pp. 79–82.
- 120** Vrba, J. and Robinson, S.E. (1999) Detection probability curves for evaluating localization algorithms and comparing sensor array types, in T. Yoshimoto et al. (eds.), *Recent Advances in Biomagnetism*, Tohoku University Press, pp. 97–100.
- 121** Shannon, C., and Weaver, W. (1949) *The Mathematical Theory of Communication*. University Illinois Press, Urbana, IL.
- 122** Kemppainen, P.K., and Ilmoniemi, R.J. (1989) Channel capacity of multichannel magnetometers, in S.J. Williamson et al. (eds.) *Advances in Biomagnetism*, Plenum Press, New York, pp. 635–638.
- 123** Nenonen, J., Kajola, M., Simola, J., and Ahonen, A. (2004) Total information of multichannel MEG sensor arrays, in Halgren, E., Ahlfors, S., Hämäläinen, M. and Cohen, D. (eds.), *Biomag2004, Proc. 14th Internat. Conf. on Biomagnetism*, Biomag2004 Ltd, Boston, MA, pp. 630–631.
- 124** Blum, T., Salig, E., and Bauer, R. (1985) First magnetoencephalographic recording of the brain activity of the human fetus, *British J. Obstet. Gynaecol.* **92**, 1224–1229.
- 125** Wakai, R.T., Leuthold, A.C., and Martin, Jr. C.B. (1996) Fetal auditory evoked responses detected by magnetoencephalography, *Am. J. Obstet. Gynecol.* **174**, 1484–1486.
- 126** Schleussner, E., Schneider, U., Olbertz, D., Kahler, R., Huonker, R., Michels, W., Nowak, H., and Seewald, H.-J. (1999) Assessment of the fetal neuronal

- maturity using auditory evoked fields in fetal magnetoencephalography, in T. Yoshimoto *et al.* (eds.), *Recent Advances in Biomagnetism*, Tohoku University Press, pp. 975–977.
- 127** Eswaran, H., Lowery, C.L., Robinson, S.E., Cheyne, D., Haid, V., McKenzie, D., Vrba, J., and Wilson, J.D. (1992) Recording of human fetal auditory evoked fields, in T. Yoshimoto *et al.* (eds.), *Recent Advances in Biomagnetism*, Tohoku University Press, pp. 959–962.
- 128** Lengle, J.M., Chen, M., and Wakai, R.T. (2001) Improved neuromagnetic detection of fetal and neonatal auditory evoked responses, *Clin. Neurophys.* **112**, 785–792.
- 129** Lowery, C., Robinson, S., Eswaran, H., Vrba, J., Haid, V., and Cheung, T. (1999) Detection of the transient and steady-state auditory evoked responses in the human fetus, in T. Yoshimoto *et al.* (eds.), *Recent Advances in Biomagnetism*, Tohoku University Press, pp. 963–966.
- 130** Robinson, S.E., Burbank, M.B., Fife, A.A., Haid, G., Kubik, P.R., Sekachev, I., Taylor, B., Tillotson, M., Vrba, J., Wong, G., Lowery, C., Eswaran, H., Wilson, D., Murphy, P., and Preissl, H. (2001) A biomagnetic instrument for human reproductive assessment, in J. Nenonen, R. Ilmoniemi, and T. Katila (eds.), *Bio-mag2000, Proc. 12th Int. Conf. on Biomagnetism*, Helsinki University of Technology, Espoo, Finland, pp. 919–922.
- 131** Vrba, J., McCubbin, J., and Robinson, S.E. (1999) Vibration analysis of MEG systems, in T. Yoshimoto *et al.* (eds.), *Recent Advances in Biomagnetism*, Tohoku University Press, pp. 109–112.
- 132** Vrba, J. (1996) SQUID gradiometers in real environments, in H. Weinstock (ed.), *SQUID Sensors: Fundamentals, Fabrication and Applications*, Kluwer Academic, Dordrecht, pp. 117–178.
- 133** Eswaran, H., Wilson, J.D., Preissl, H., Robinson, S.E., Vrba, J., Murphy, P., Rose, D.F., and Lowery, C.L. (2002) Magnetoencephalographic recording of visual evoked brain activity in the human fetus, *The Lancet* **360**, 779–780.
- 134** Mosher, J.C., Baillet, S., Leahy, R.M. (2003) Equivalence of linear approaches in bioelectromagnetic inverse solutions, 2003 *IEEE Workshop on Statistical Signal Processing*, St. Louis, MO, pp. 294–297.
- 135** Scherg, M. and von Cramon, D. (1985) Two bilateral sources of the late AEP as identified by a spatio-temporal dipole model, *Electroencephalogr. Clin. Neurophysiol.* **62**, 32–44.
- 136** Brenner, D., Lipton, J., Kaufman, L., and Williamson, S.J. (1978) Somatically evoked magnetic fields of the human brain, *Science* **199**, 81–83.
- 137** Cuffin, B.N. and Cohen, D. (1977) Magnetic fields of a dipole in a special volume conductor shapes, *IEEE Trans. Biomed. Eng.* **BME-24**, 372–381.
- 138** Huang, M.X., Mosher, J.C., and Leahy, R.M. (1999) A sensor-weighted overlapping-sphere head model and exhaustive head model comparison for MEG, *Phys. Med. Biol.* **44**, 423–440.
- 139** Hämäläinen, M.S. and Sarvas, J. (1989) Realistic conductivity geometry model of the human head for interpretation of neuromagnetic data, *IEEE Trans. Biomed. Eng.* **36**, 165–171.
- 140** Holroyd, T., Endo, H., and Takeda, T. (1999) Creation of cortical surface models from MRI data for dipole fitting of MEG data, in T. Yoshimoto *et al.* (eds.), *Recent Advances in Biomagnetism*, Tohoku University Press, pp. 220–223.
- 141** Ilmoniemi, R.J., Hämäläinen, M.S., and Knuutila, J. (1985) The forward and inverse problems in the spherical model, in H. Weinberg *et al.* (eds.), *Biomagnetism: Application and Theory*, Pergamon Press, New York, pp. 278–282.
- 142** Ahonen, A.I., Hämäläinen, M.S., Ilmoniemi, R.J., Kajola, M.J., Knuutila, J.E.T., Simola, J.T., and Vilkman, V.A. (1993) Sampling theory for neuromagnetic detector arrays, *IEEE Trans. Biomed. Eng.* **40**, 859–869.
- 143** Ilmoniemi, R.J. and Numminen, J.K. (1992) Synthetic magnetometer channels for standard representation of data, in M. Hoke *et al.* (eds.), *Biomagnetism: Clinical Aspects*, Elsevier Science Publishers, Amsterdam, pp. 793–796.
- 144** Romani, G.L. and Leon, R. (1984) Localization of cerebral sources by neuromagnetic measurements, in H. Weinberg *et al.* (eds.), *Biomagnetism: Application*

- tion and Theory, Pergamon Press, New York, pp. 205–220.
- 145 Nelder, J.A. and Mead, R. (1965) A simplex method for function minimization, *Comput. J.* **7**, 308–313.
- 146 Marquardt, D.W. (1963) An algorithm for least squares estimation of nonlinear parameters, *J. Soc. Indust. Appl. Math.* **11**, 431–441.
- 147 Uutela, K., Hämäläinen, M., and Salminen, R. (1998) Global optimization in the localization of neuromagnetic sources, *IEEE Trans. Biomed. Eng.* **45**, 716–723.
- 148 Torn, A. and Zhilinskas, A. (1989) Global optimization, in *Lecture Notes in Computer Science*, Springer-Verlag, Berlin, no. 350.
- 149 Holland, J.H. (1975) *Adaptation in Natural and Artificial Systems*, University of Michigan, Ann Arbor, MI.
- 150 Kirkpatrick, K., Gelatt, Jr. C.D., and Vecchi, M.P. (1983) Optimization by simulated annealing, *Science* **220**, 671–680.
- 151 Tesche, C.D., Uusitalo, M.A., Ilmoniemi, R.J., Huotilainen, M., Kajola, M., and Salonen, O. (1995) Signal-space projections of MEG data characterize both distributed and well-localized neuronal sources, *Electroencephalogr. Clin. Neurophysiol.* **95**, 189–200.
- 152 Uusitalo, M.A. and Ilmoniemi, R.J. (1997) Signal-space projection method for separating MEG or EEG into components, *Med. Biol. Eng. Comput.* **35**, 135–140.
- 153 Huotilainen, M., Ilmoniemi, R.J., Tiitinen, H., Lavikainen, J., Alho, K., Kajola, M., and Naatanen, R. (1995) The projection method in removing eye-blink artifacts from multichannel MEG measurements, in C. Baumgartner *et al.* (eds.), *Biomagnetism: Fundamental Research and Clinical Applications*, Elsevier Science, IOS Press, pp. 363–367.
- 154 Hämäläinen, M.S. and Ilmoniemi, R.J. (1984) Interpreting measured magnetic fields of the brain: estimates of current distribution, *Report TKK-F-A559*, Helsinki University of Technology, Espoo, Finland.
- 155 Penrose, R. (1955) A generalized inverse for matrices, *Proc. Cambridge Philos. Soc.* **51**, 406–413.
- 156 Wang, J.-Z., Williamson, S.J., and Kaufman, L. (1992) Magnetic source images determined by a lead-field analysis: the unique minimum norm least squares estimation, *IEEE Trans. Biomed. Eng.* **39**, 665–675.
- 157 Gorodnitsky, I.F., George, J.S., and Rao, B.D. (1995) Neuromagnetic source imaging with FOCUSS: a recursive weighted minimum norm algorithm, *Electroencephalogr. Clin. Neurophysiol.* **95**, 231–251.
- 158 Fuchs, M., Wagner, M., Kohler, T., and Wischmann, H.-A. (1999) Linear and nonlinear current density reconstructions, *J. Clin. Neurophys.* **16**, 267–195.
- 159 Gorodnitsky, I.F. and Rao, B.D. (1992) A new iterative weighted norm minimization algorithm and its applications, in *Proc. 6th SP Workshop on Statistical Signal and Array Processing*, pp. 412–415.
- 160 Ioannides, A.A., Bolton, J.P.R., and Clarke, C.J.S. (1990) Continuous probabilistic solutions to the biomagnetic inverse problem, *Inverse Problems* **6**, 523–542.
- 161 Ioannides, A.A. and Tylor, J.G. (1999) Minimum norm, magnetic field tomography (MTF) and FOCUSS, in T. Yoshimoto *et al.* (eds.), *Recent Advances in Biomagnetism*, Tohoku University Press, pp. 228–231.
- 162 Dale, A.M., Liu, A.K., Fischl, B.R., Buckner, R.L., Belliveau, J.W., Lewine, J.D., and Halgren, E. (2000) Dynamic statistical parametric mapping: combining fMRI and MEG for high-resolution imaging of cortical activity, *Neuron* **26**, 55–67.
- 163 Pascual-Marqui, R.D., Michel, C.M., and Lehmann, D. (1994) Low resolution electromagnetic tomography: a new method for localizing electrical activity in the brain, *Int. J. Psychophysiol.* **18**, 49–65.
- 164 Pascual-Marqui, R.D. (2002) Standardized low resolution electromagnetic tomography (sLORETA): technical details, *Meth. Findings Exp. & Clin. Pharmacol* **24**, 5–12.
- 165 Wagner, M., Fuchs, M., and Kastner, J. (2004) Evaluation of sLORETA in the presence of noise and multiple sources, *Brain Topography* **16**, 277–280.

- 166** Matsuura, K. and Okabe, Y. (1995) Selective minimum-norm solution of the biomagnetic inverse problem, *IEEE Trans. Biomed. Eng.* **42**, 608–615.
- 167** Utela, K., Hämäläinen, M., and Somersalo, E. (1999) Visualization of magnetoencephalographic data using minimum current estimates, *NeuroImage* **10**, 173–180.
- 168** Fuchs, M., Wagner, M., Kohler, T., and Wischmann, H.-A. (1999) Linear and nonlinear current density reconstruction, *J. Clin. Neurophysiol.* **16**, 267–295.
- 169** Luenberger, D.G. and Kuenberger, D.G. (1984) *Linear and Nonlinear Programming*, Addison-Wesley.
- 170** Frost, O.L. (1972) An algorithm for linearly constrained adaptive array processing, *Proc. IEEE* **60**, 926–935.
- 171** Van Veen, B. and Buckley, K. (1988) Beamforming: a versatile approach to spatial filtering, *IEEE ASSP Magazine* **5**, 4–24.
- 172** Godara, L.C. (1997) Application of antenna array to mobile communications: II. Beam-forming and direction-of-arrival considerations, *Proc. IEEE* **85**, 1195–1245.
- 173** Van Veen, B., Joseph, J., and Hecox, K. (1992) Localization of intra-cerebral sources of electrical activity via linearly constrained minimum variance spatial filtering, *IEEE 6th SP Workshop on Statistical Signal & Array Processing*, pp. 526–529.
- 174** Spencer, M.E., Leahy, R.M., Mosher, J.C., and Lewis, P.S. (1992) Adaptive filters for monitoring localized brain activity from surface potential time series, *26th Asilomar Conf. on Signals, Systems and Computers*, Pacific Grove, CA, Vol. 1, pp. 156–161.
- 175** Sekihara, K. and Scholz, B. (1996) Generalized Wiener estimation of three-dimensional current distribution from biomagnetic measurements, *IEEE Trans. Biomed. Eng.* **43**, 281–291.
- 176** Van Veen, B.D., Van Drongelen, W., Yuchtman, M., and Suzuki, A. (1997) Localization of brain electrical activity via linearly constrained minimum variance spatial filtering, *IEEE Trans. Biomed. Eng.* **44**, 867–880.
- 177** Robinson, S.E. and Vrba, J. (1999) Functional neuroimaging by synthetic aperture magnetometry (SAM), in T. Yoshimoto *et al.* (eds.), *Recent Advances in Biomagnetism*, Tohoku University Press, Sendai, pp. 302–305.
- 178** Sekihara, K. and Scholz, B. (2000) Generalized Wiener estimation of three-dimensional current distribution from biomagnetic measurements, in C. Aine *et al.* (eds.), *Biomag96: Advances in Biomagnetism Research*, Springer-Verlag, pp. 338–341.
- 179** Robinson, S.E. and Rose, D.F. (1992) Current source image estimation by spatially filtered MEG, in M. Hoke *et al.* (eds.), *Biomagnetism: Clinical Aspects*, Elsevier Science, pp. 761–765.
- 180** Greenblatt, R.E., Ossadtchi, A., and Pflieger, M.E. (2005) Local linear estimators for the bioelectromagnetic inverse problem, *IEEE Trans. Signal Process.* **53**, 3403–3412.
- 181** Vrba, J., Robinson, S.E., and McCubbin, J. (2004) How many channels are needed for MEG?, in Halgren, E., Ahlfors, S., Hämäläinen, M. and Cohen, D. (eds.), *Biomag2004, Proc. 14th Internat. Conf. on Biomagnetism*, Biomag2004 Ltd, Boston, MA, p. 601–602.
- 182** Vrba, J. and Robinson, S.E. (2001) Differences between synthetic aperture magnetometry (SAM) and linear beamformers, in J. Nenonen, R. Ilmoniemi, and T. Katila (eds.), *Biomag2000, Proc. 12th Int. Conf. on Biomagnetism*, Helsinki University of Technology, Espoo, Finland, pp. 681–684.
- 183** Vrba, J. and Robinson, S.E. (2000) Linearly constrained minimum variance beamformers, synthetic aperture magnetometry, and MUSIC in MEG applications, in M.B. Mathews (ed.), *34th Asilomar Conf. on Signals, Systems, and Computers*, Pacific Grove, CA, IEEE Omnipress, Vol. 1, pp. 313–317.
- 184** Vrba, J. and Robinson, S.E. (2001) Signal processing in MEG, *Methods* **25**, 249–271.
- 185** Politis, D.N. (1998) Computer-intensive methods in statistical analysis, *IEEE Signal Process. Magazine* **15**, 39–55.
- 186** Gross, J., Kujala, J., Hämäläinen, M., Timmermann, L., Schnitzler, A., and

- Salmelin, R. (2001) Dynamic imaging of coherent sources: studying neural interactions in the human brain, *PNAS* **98**, 694–699.
- 187** Schmidt, R.O. (1986) Multiple emitter location and signal parameter estimation, *IEEE Trans. Anten. Propagat. AP-34*, 276–280.
- 188** Mosher, J.C., Lewis, P.S., and Leahy, R.M. (1992) Multiple dipole modeling and localization from spatio-temporal MEG data, *IEEE Trans. Biomed. Eng* **39**, 541–557.
- 189** Mosher, J.C. and Leahy, R.M. (1996) EEG and MEG source localization using recursively applied (RAP) MUSIC, *Proc. 30th Annual Asilomar Conf. on Signals, Systems, and Computers*, Pacific Grove, CA, pp. 1201–1207.
- 190** Robinson, S.E. and Vrba, J. (2001) Comparison of SAM and MUSIC performance for unaveraged MEG, in J. Nenonen, R. Ilmoniemi, and T. Katila (eds.), *Biomag2000, Proc. 12th Int. Conf. on Biomagnetism*, Helsinki University of Technology, Espoo, Finland, pp. 685–688.
- 191** Sekihara, K., Nagarajan, S., Poeppel, D., and Miyashita, Y. (1999) Time-frequency MEG-MUSIC algorithm, *IEEE Trans. Med. Imaging* **18**, 92–97.
- 192** Sekihara, K., Poeppel, D., Marantz, A., Phillips, C., Koizumi, H., and Miyashita, Y. (1998) MEG covariance difference analysis: a method to extract target source activities by using task and control measurements, *IEEE Trans. Biomed. Eng.* **45**, 87–97.
- 193** Sekihara, K., Poeppel, D., Marantz, A., C., Koizumi, H., and Miyashita, Y. (1998) Comparison of covariance-based and waveform-based subtraction methods in removing the interference from button-pressing finger movements, *Brain Topography* **11**, 95–102.
- 194** Van Veen, B.D. (1988) Eigenstructure based partially adaptive array design, *IEEE Trans. Anten. Propagat.* **36**, 357–362.
- 195** Yu, J.-L. and Yeh, C.-C. (1995) Generalized eigenspace-based beamformers, *IEEE Trans. Sig. Process.* **43**, 2453–2461.
- 196** Maier, J., Dagnelie, G., Spekreijse, H., and van Dijk, B. (1987) Principal component analysis for source localization of VEPs in man, *Vision Res* **27**, 165–177.
- 197** Achim, A., Richer, F., and Saint-Hilaire, J. (1988) Methods for separating temporally overlapping sources of neuroelectric data, *Brain Topography* **1**, 22–28.
- 198** Cardoso, J.-F. (1998) Blind signal separation: statistical principles, *Proc. IEEE* **86**, 2009–2025.
- 199** Hyvärinen, A. (1999) Fast and robust fixed-point algorithms for independent component analysis, *IEEE Trans. Neural Networks* **10**, 626–634.
- 200** Makeig, S., Jung, T.-P., Bell, A., Ghahremani, D., and Sejnowski, T. (1997) Blind separation of auditory event-related brain responses into independent components, *Proc. Nat. Acad. Sci. USA* **94**, 10979–10984.
- 201** Ziehe, A., Muller, K.-R., Nolte, G., Mackert, B.-M., and Curio, G. (2000) Artifact reduction in magnetoneurography based on time-delayed second-order correlations, *IEEE Biomed. Eng.* **47**, 75–87.
- 202** Vigario, R., Sarela, J., Jousmaki, V., Hämäläinen, M., and Oja, E. (2000) Independent component approach to the analysis of EEG and MEG recordings, *IEEE Biomed. Eng.* **47**, 589–593.
- 203** Hämäläinen, M.S., Haario, H., and Lehtinen, M.S. (1987) Inferences about sources of neuromagnetic fields using Bayesian parameter estimation, *Report TKK-F-A620*, Helsinki University of Technology, Espoo, Finland.
- 204** Phillips, J.W., Leahy, R.M., and Mosher, J.C. (2000) MEG-based imaging of focal neuronal current sources, in C. Aine et al. (eds.), *Biomag96: Advances in Biomagnetism Research*, Springer-Verlag, pp. 310–313.
- 205** Auranen, T., Nummenmaa, A., Hämäläinen, M.S., Jaaskelainen, I.P., Lampinen, J., Vehtari, A., and Sams, M. (2005) Bayesian analysis of the neuromagnetic inverse problem with l_p-norm priors, *Neuroimage* **26**, 870–884.
- 206** Bertrand, C., Ohmi, M., Suzuki, R., and Kado, H. (2001) A probabilistic solution to the MEG inverse problem via MCMC methods: the reversible jump and parallel tempering algorithms, *IEEE Trans. Biomed. Eng.* **48**, 533–542.

- 207** Nakasato, N., Seki, K., Kawamura, T., Ohtomo, S., Kanno, A., Fujita, S., Hatanaka, K., Fujiwara, S., Kayama, T., Takahashi, A., Jokura, H., Kumabe, T., Ikeda, H., Mizoi, K. and Yoshimoto, T. (1996) Cortical mapping using an MRI-linked whole head MEG system and presurgical decision making, *Electroencephalogr. Clin. Neurophysiol. Suppl.* **47**, 333–341.
- 208** Ishii, R., Shinosaki, K., Ikejiri, Y., Ukai, S., Yamashita, K., Iwase, M., Mizuno-Matsumoto, Y., Inouye, T., Yoshimine, T., Hirabuki, N., Robinson, S.E., and Takeda, M. (2000) Theta rhythm increases in left superior temporal cortex during auditory hallucinations in schizophrenia: a case report, *NeuroReport* **11**, 3283–3287.
- 209** Zoubir, A.M. and Boashash, B. (1998) The bootstrap and its application in signal processing, *IEEE Signal Process. Magazine*, **15**, 56–76.
- 210** Gross, J., Timmermann, L., Kujala, J., Dirks, M., Schmitz, F., Salmelin, R., and Schnitzler, A. (2002) The neural basis of intermittent motor control in humans, *Proc. Natl. Acad. Sci. USA* **99**, 2299–2302.
- 211** Robinson, S.E., Nagarajan, S.S., Mantle, M., Gibbons, V., and Kirsch, H. (2004) Localization of interictal spikes using SAM(g2) and dipole fit, in Halgren, E., Ahlfors, S., Hämäläinen, M. and Cohen, D. (eds.), *Biomag2004, Proc. 14th Internat. Conf. on Biomagnetism*, Biomag2004 Ltd, Boston, MA, p.738–739.
- 212** Robinson, S.E., Vrba, J., Otsubo, H., and Ishii, R. (2002) Finding epileptic loci by nonlinear parameterization of source waveforms, in H. Nowak, *et al.* (eds.), *Biomag 2002*, VDE Verlag, Berlin and Offenbach, Germany, pp. 220–222.
- 213** Preissl, H., Lowery, C.L., and Eswaran, H. (2004) Fetal magnetoencephalography: current progress and trends, *Exp. Neurol.* **190**, S28–S36.
- 214** Zappasodi, F., Tecchio, F., Pizzella, V., Cassetta, E., Romano, B.V., Filligoi, P.M., Rossini, P.M. (2001) Detection of fetal auditory evoked responses by means of magnetoencephalography, *Brain Res.* **917**, 167–173.
- 215** Eswaran, H., Preissl, H., Wilson, J.D., Murphy, P., Robinson, S.E., Rose, D., Vrba, J., Lowery, C.L. (2002) Short-term serial magnetoencephalography recordings of fetal auditory evoked responses, *Neurosci. Lett.* **331**, 128–132.
- 216** Eswaran, H., Lowery, C.L., Wilson, J.D., Murphy, P., and Preissl, H. (2004) Functional development of the visual system in human fetus using magnetoencephalography, *Exp. Neurol.* **190**, S52–S58.
- 217** Eswaran, H., Lowery, C.L., Wilson, J.D., Murphy, P., and Preissl, H. (2005) Fetal magnetoencephalography – a multimodal approach, *Devel. Brain Res.* **154**, 57–62.
- 218** Rose, D.F. and Eswaran, H. (2004) Spontaneous neuronal activity in fetuses and newborns, *Exp. Neurol.* **190**, S37–S43.
- 219** Eswaran, H., Preissl, H., Wilson, J.D., Murphy, P., and Lowery, C.L. (2004) Prediction of labor in term and preterm pregnancies using non-invasive magnetoencephalographic recordings of uterine contractions, *Am. J. Obstet. and Gynecol.* **190**, 1598–1603.
- 220** Samonas, M., Petrou, M., and Ioannides, A. A. (1997) Identification and elimination of cardiac contribution in single-trial magnetoencephalographic signals. *IEEE Trans. Biomed. Eng.* **44**, 386–350.
- 221** Strohbach, P., Abraham-Fuchs, K., and Härrer, W. (1994) Event-synchronous cancellation of the heart interference in biomedical signals. *IEEE Trans. Biomed. Eng.* **41**, 343–350.
- 222** Robinson, S.E., Vrba, J., and McCubbin, J. (2002) Separating fetal MEG signals from the noise, in H. Nowak *et al.* (eds.), *Biomag 2002*, VDE Verlag, Berlin and Offenbach, Germany, pp. 665–667.
- 223** Hämäläinen, M.S. (1995) Functional localization based on measurements with a whole-head magnetometers system. *Brain Topography* **7**, 283–289.
- 224** Vrba, J., Robinson, S.E., McCubbin, J., Lowery, C.L., Preißl, H., Eswaran, H., Wilson, D., and Murphy, P. (2004) Fetal MEG redistribution by projection operators, *IEEE Biomed. Eng.* **51**, 1207–1218.
- 225** Vrba, J., Robinson, S.E., McCubbin, J., Murphy, P., Eswaran, H., Wilson, J.D.,

- Preissl, H., and Lowery, C.L. (2004) Human fetal brain imaging by magnetoencephalography: verification of fetal brain signals by comparison with fetal brain models, *NeuroImage* **21**, 1009–1020.
- 226** MacFarlane, P.W. and Lawrie, T.D.W. (eds.) (1989) *Comprehensive Electrocardiology*, Pergamon Press, London.
- 227** Nowak, H. (1998) Biomagnetic instrumentation, in W. Andrä, and H. Nowak (eds.), *Magnetism in Medicine*, Wiley VCH, Berlin, pp. 88–135.
- 228** Schneider, S., Hoenig, E., Reichenberger, H., Abraham-Fuchs, K. et al. (1990) Multichannel biomagnetic system for study of electrical activity in the brain and heart, *Radiology* **176**, 825–830.
- 229** Buchanan, D.S., Warden, L., Johnson, R.T., and Riley, S.W. (1995) A novel approach to extended coverage biomagnetometers, in C. Baumgartner, et al. (eds.), *Biomagnetism: Fundamental Research and Clinical Applications*, Elsevier Science, IOS Press, pp. 497–501.
- 230** Tsukada, K., Kandori, A., Miyashita, T., Sasabuchi, H. et al. (1998) A simplified superconducting quantum interference device system to analyze vector components of a cardiac magnetic field, in *Proc. 20th Ann. Internat. Conf. of IEEE/EMBS* (Hong Kong), pp. 524–527.
- 231** Van Leeuwen, P., Haupt, C., Hoomann, C., Hailer, B. et al. (1999) A 67 channel biomagnetometer designed for cardiology and other applications, in T. Yoshimoto, M. Kotani, S. Kuriki, H. Karibe, and N. Nakasato, (eds.), *Recent Advances in Biomagnetism*, Tohoku University Press, Sendai, pp. 89–92.
- 232** Montonen, J., Ahonen, A., Hämäläinen, M., Ilmoniemi, R. et al. (2000) Magneto-angiographic functional imaging studies in BioMag Laboratory, in C. Aine, Y. Okada, G. Stroink, G. et al. (eds.), *Bio-mag96, Proc. 10th Internat. Conf. on Biomagnetism*, Springer, New York, pp. 494–497.
- 233** Erné, S.N., Pasquarelli, A., Kammerath, H., Della Penna, S. et al. (1999) Argos 55 – the new MCG system in Ulm, in T. Yoshimoto, M. Kotani, S. Kuriki, H. Karibe, and N. Nakasato (eds.), *Recent Advances in Biomagnetism*, Tohoku University Press, Sendai, pp. 27–30.
- 234** Burghoff, M., Schleyerbach, H., Drung, D., Trahms, L. et al. (1999) A vector magnetometer module for biomagnetic application, *IEEE Trans. Appl. Supercond.* **9**, 4069–4072.
- 235** Schnabel, A., Burghoff, M., Hartwig, S., Petsche, F. et al. (2004) A sensor configuration for a 304 SQUID vector magnetometer, in E. Halgren, S. Ahlfors, M. Hämäläinen, and D. Cohen (eds.), *Bio-mag2004, Proc. 14th Internat. Conf. on Biomagnetism*, Biomag2004 Ltd, Boston, MA, pp. 373–374.
- 236** Numminen, J., Ahlfors, S., Ilmoniemi, R., Montonen, J. et al. (1995) Transformation of multichannel magnetocardiographic signals to standard grid form, *IEEE Trans. Biomed. Eng.* **42**, 72–78.
- 237** Burghoff, M., Nenonen, J., Trahms, L. and Katila, T. (2000) Conversion of magnetocardiographic recordings between two different multichannel SQUID devices, *IEEE Trans. Biomed. Eng.* **47**, 869–875.
- 238** Itozaki, H., Sakuta, K., Kobayashi, T., Enpuku, K. et al. (2003) Applications of HTSC SQUIDs, *Topics Appl. Phys.* **91**, 185–248.
- 239** Stroink, G., Moshage, W. and Achembach, S. (1998) Cardiomagnetism, in W. Andrä, and H. Nowak (eds.), *Magnetism in Medicine*, Wiley VCH, Berlin, pp. 136–189.
- 240** Hämäläinen, M.S. and Nenonen, J. (1999) Magnetic source imaging, in J. Webster (ed.), *Encyclopedia of Electrical Engineering*, Vol. 12, Wiley & Sons, New York, pp. 133–148.
- 241** Koch, H. (2001) SQUID magnetocardiography: status and perspectives, *IEEE Trans. Appl. Supercond.* **11**, 49–59.
- 242** Durrer, D., van Dam, R., Freud, G., Janse, M. et al. (1970) Total excitation of the isolated human heart, *Circulation* **41**, 899–912.
- 243** Cohen, D. and Hosaka, H. (1976) Magnetic field produced by a current dipole, *J. Electrocardiol.* **9**, 409–417.
- 244** Katila, T. and Karp, P. (1983) Magneto-angiography: morphology and multipole presentations, in S.J. Williamson,

- G.L. Romani, L. Kaufmann, and I Modena (eds.), *Biomagnetism, An Interdisciplinary Approach*, Plenum Press, New York, pp. 237–263.
- 245** Geselowitz, D.B. (1970) On the magnetic field generated outside an inhomogeneous volume conductor by internal current sources, *IEEE Trans. Magn.* **6**, 346–347.
- 246** Horacek, B.M (1973) Digital model for studies in magnetocardiography, *IEEE Trans. Magn.* **9**, 440–444.
- 247** Nenonen, J., Purcell, C., Horacek, B.M., Stroink, G. *et al.* (1991) Magnetocardiographic functional localization using a current dipole in a realistic torso, *IEEE Trans. Biomed. Eng.* **38**, 658–664.
- 248** Lötvönen, J. (2003) Construction of patient-specific surface models from MR images: application to bioelectromagnetism, *Comput. Methods Programs Biomed.* **72**, 167–178.
- 249** Sternickel, K., Effern, A., Lehnertz, K., Schreiber, T. *et al.* (2001) Nonlinear noise reduction using reference data, *Phys. Rev. E* **63**, 036209.
- 250** Faley, M., Poppe, U., Urban, K., Paulson, D. *et al.* (2001) Low noise HTS dc-SQUID flip-chip magnetometers and gradiometers, *IEEE Trans. Appl. Supercond.* **11**, 1383–1386.
- 251** Kouznetsov, K.A., Borgmann, J., and Clarke, J. (1999) High- T_c second-order gradiometer for magnetocardiography in an unshielded environment, *Appl. Phys. Lett.* **75**, 1979–1981.
- 252** Zhang, Y., Panaitov, G., Wang, S.G., Wolters, N. *et al.* (2000) Second-order, high-temperature superconducting gradiometer for magnetocardiography in an unshielded environment, *Appl. Phys. Lett.* **76**, 906–908.
- 253** Ludwig, F., Jansman, A.B.M., Drung, D., Lindström, M. *et al.* (2001) Optimization of direct-coupled high- T_c SQUID magnetometers for operation in magnetically unshielded environment, *IEEE Trans. Appl. Supercond.* **11**, 1824–1827.
- 254** Mizukami, A., Nishiura, H., Sakuta, K., and Kobayashi, T. (2003) High critical temperature superconducting quantum interference device magnetometer with feedforward active noise control system for magnetocardiographic measurement in unshielded circumstances, *Physica C* **392–396**, 1411–1415.
- 255** Liao, S., Hsu, S., Lin, C., Horng, H. *et al.* (2003) High- T_c SQUID gradiometer system for magnetocardiography in an unshielded environment, *Supercond. Sci. Technol.* **16**, 1426–1429.
- 256** Lee, S., Park, S., Kang, C., Yu, K. *et al.* (2004) Fabrication and magnetocardiography application of the second-order superconducting quantum interference device gradiometer made from a single-layer of $\text{YBa}_2\text{Cu}_3\text{O}_7$ film, *Appl. Phys. Lett.* **84**, 568–570.
- 257** ter Brake, H.J.M., Janssen, N., Flokstra, J., Veldhuis, D. *et al.* (1997) Multichannel heart scanner based on high- T_c SQUIDs, *IEEE Trans. Appl. Supercond.* **7**, 2545–2548.
- 258** Leder, U., Schrey, F., Haueisen, J., Dörner, L. *et al.* (2001) Reproducibility of HTS-SQUID magnetocardiography in an unshielded environment, *Int. J. Cardiol.* **79**, 237–243.
- 259** Peiselt, K., Schmidl, F., Linzen, S., Anton, A. *et al.* (2003) High- T_c dc-SQUID gradiometers in flip-chip configuration, *Supercond. Sci. Technol.* **16**, 1408–1412.
- 260** Zhang, Y., Wolters, N., Lomparski, D., Zander, W. *et al.* (2005) Multichannel HTS rfSQUID gradiometer system recording fetal and adult magnetocardiograms, *IEEE Trans. Appl. Supercond.* **15**, 631–634.
- 261** Suzuki, D., Tsukamoto, A., Yokosawa, K., Kandori, A. *et al.* (2004) A mobile and space-saving high-temperature superconducting multichannel magnetocardiograph in a vertically magnetically shielded cylinder, *Jpn. J. Appl. Phys.* **43**, 117–120.
- 262** Suzuki, D., Tsukamoto, A., Kandori, A., Ogata, K. *et al.* (2004) Development of multichannel compact HTS MCG system using transversal magnetically shielded cylinder, in E. Halgren, S. Ahlfors, M. Hämäläinen, and D. Cohen (eds.), *Biomag2004, Proc. 14th Internat. Conf. on Biomagnetism, Biomag2004 Ltd.*, Boston MA, p. 662.
- 263** Hänninen, H., Takala, P., Mäkipää, M., Montonen, J. *et al.* (2000) Detection of exercise-induced myocardial ischemia

- by multichannel magnetocardiography in single vessel coronary artery disease, *Ann. Noninvasive Electrocardiol.* 5, 147–157.
- 264** Tsukada, K., Miyashita, T., Kandori, A., Mitsui, T. *et al.* (2000) An iso-integral mapping technique using magnetocardiogram, and its possible use for diagnosis of ischemic heart disease, *Int. J. Cardiac Imaging* 16, 55–66.
- 265** Kandori, A., Kanzaki, H., Miyatake, K., Hashimoto, S. *et al.* (2001) A method for detecting myocardial abnormality by using a current-ratio map calculated from an exercise-induced magnetocardiogram, *Med. Biol. Eng. Comput.* 39, 29–34.
- 266** Bradshaw, L., Myers, A., Richards, W., Drake, W. *et al.* (2005) Vector projection of biomagnetic fields, *Med. Biol. Eng. Comput.* 43, 85–93.
- 267** Di Rienzo, L., Haueisen, J. and Arturi, C. (2005) Three component magnetic field data: impact on minimum-norm solutions in a biomedical application, *COMPEL: J. for Computat. and Mathe- mat. in Elect. and Electron. Eng.* 24, 869–881.
- 268** Tsukada, K., Ogata, K., Miyashita, T., Yamada, S. *et al.* (2004) An imaging and quantitative analysis technique for diagnosis of electrophysiological excitation abnormality of heart, in E. Halgren, S. Ahlfors, M. Härmäläinen, and D. Cohen (eds.), *Biomag2004, Proc. 14th Internat. Conf. on Biomagnetism*, Biomag2004 Ltd, Boston, MA, pp. 377–378.
- 269** Tavarozzi, I., Comani, S., del Gatta, C., di Luzio, S. *et al.* (2002) Magnetocardiography: current status and perspectives: II. Clinical applications, *Italian Heart J.* 3, 151–165.
- 270** Mäkijärvi, M., Hänninen, H., Korhonen, P., Montonen, J. *et al.* (2003) Clinical application of magnetocardiographic mapping, in M. Shenasa, M. Borggrefe, and G. Breithardt (eds.), *Cardiac Mapping*, Blackwell/Futura Division, Elmsford, NY, pp. 475–486.
- 271** Fenici, R., Brisinda, D. and Meloni, A.M. (2005) Clinical application of magnetocardiography, *Expert Rev. of Molec. Diagnost.*, 5, 291–313.
- 272** Korhonen, P., Montonen, J., Mäkijärvi, M., Katila, T. *et al.* (2000) Late fields of the magnetocardiographic QRS complex as indicators of propensity to sustained ventricular tachycardia after myocardial infarction, *J. Cardiovasc. Electrophysiol.* 11, 413–420.
- 273** Müller, H. P., Gödde, P., Czerski, K., Oeff, M. *et al.* (1999) Magnetocardiographic analysis of the two-dimensional distribution of intra-QRS fractionated activation, *Phys. Med. Biol.* 44, 105–120.
- 274** van Leeuwen, P., Hailer, B. and Wehr, M. (1996) Spatial distribution of QT intervals: alternative approach to QT dispersion, *Pacing Clin. Electrophysiol.* 19, 1894–1899.
- 275** Oikarinen, L., Viitasalo, M., Korhonen, P., Väänänen, H. *et al.* (2001) Postmyocardial infarction patients susceptible to ventricular tachycardia show increased T wave dispersion independent of delayed ventricular conduction, *J. Cardiovasc. Electrophysiol.* 12, 1115–1120.
- 276** Stroink, G., Meeder, R.J., Elliott, P., Lant, J. *et al.* (1999) Arrhythmia vulnerability assessment using magnetic field maps and body surface potential maps, *Pacing Clin. Electrophysiol.* 22, 1718–1728.
- 277** Hren, R., Steinhoff, U., Gessner, C., Endt, P. *et al.* (1999) Value of magnetocardiographic QRST integral maps in the identification of patients at risk of ventricular arrhythmias, *Pacing Clin. Electrophysiol.* 22, 1292–1304.
- 278** Kandori, A., Shimizu, W., Yokokawa, M., Noda, T. *et al.* (2004) Identifying patterns of spatial current dispersion that characterise and separate the Brugada syndrome and complete right bundle branch block, *Med. Biol. Eng. Comput.* 42, 236–244.
- 279** Nakai, K., Kawazoe, K., Izumoto, H., Tsuboi, J. *et al.* (2004) Three-dimensional electric current density map by 64-channel magnetocardiography in patients with atrial flutter and atrial fibrillation, in E. Halgren, S. Ahlfors, M. Härmäläinen, and D. Cohen (eds.), *Biomag2004, Proc. 14th Internat. Conf. on Biomagnetism*, Biomag2004 Ltd, Boston, MA, pp. 409–410.
- 290** Savard, P., Cohen, D., Lepeschkin, E., Cuffin, B.N. *et al.* (1983) Magnetic mea-

- surement of S-T and T-Q segment shifts in humans, *Circ. Res.* **53**, 264–279.
- 281** Brockmeier, K., Schmitz, L., Chavez, J., Burghoff, M. *et al.* (1997) Magnetocardiography and 32-lead potential mapping: repolarization in normal subjects during pharmacologically induced stress, *J. Cardiovasc. Electrophysiol.* **8**, 615–626.
- 282** Takala, P., Hänninen, H., Montonen, J., Mäkiäärvi, M. *et al.* (2001) Beat-to-beat analysis method for magnetocardiographic recordings during interventions, *Phys. Med. Biol.* **46**, 975–982.
- 283** Chen, J., Thomson, P., Nolan, V., and Clarke, J. (2004) Age and sex dependent variations in the normal magnetocardiogram compared with changes associated with ischemia, *Ann. Biomed. Eng.* **32**, 1088–1099.
- 284** Park, J., Hill, P., Chung, N., Hugenholtz, P., and Jung, F. (2005) Magnetocardiography predicts coronary artery disease in patients with acute chest pain, *Ann. Noninv. Electrocardiol.* **10**, 312–323.
- 285** Hailer, B., Chaikovsky, I., Auth-Eisernitz, S., Schäfer, H. *et al.* (2005) The value of magnetocardiography in patients with and without relevant stenoses of the coronary arteries using and unshielded system, *Pacing Clin. Electrophysiol* **28**, 8–17.
- 286** Morguet, A., Behrens, S., Kosch, O., Lange, C. *et al.* (2004) Myocardial viability evaluation using magnetocardiography in patients with coronary artery disease, *Coronary Artery Dis.* **15**, 155–162.
- 287** Embrechts, M., Szymanski, B., Sternickel, K., Naenna, T. *et al* (2003) Use of machine learning for classification of magnetocardiograms, *IEEE Internat. Conf. on Systems, Man and Cybernetics*, Vol. 2, pp. 1400–1405.
- 288** Bruder, H., Killmann, R., Moshage, W., Weismüller, P. *et al.* (1994) Biomagnetic localization of electrical current sources in the heart with realistic volume conductors using the single-current-dipole model, *Phys. Med. Biol.* **39**, 655–668.
- 289** Moshage, W., Achenbach, S., Göhl, W., and Bachmann, K. (1996) Evaluation of the non-invasive localization of cardiac arrhythmias attainable by multichannel magnetocardiography (MCG), *Int. J. Cardiac Imaging* **12**, 47–59.
- 290** Fenici, R., Nenonen, J., Pesola, K., Korhonen, P. *et al.* (1999) Non-fluoroscopic localization of an amagnetic stimulation catheter by multichannel magnetocardiography, *Pacing Clin. Electrophysiol.* **22**, 1210–1220.
- 291** Pesola, K., Nenonen, J., Fenici, R., Lötjönen, J. *et al.* (1999) Bioelectromagnetic localization of the pacing catheter in the heart, *Phys. Med. Biol.* **44**, 2565–2578.
- 292** Leder, U., Haueisen, J., Huck, M., and Nowak, H. (1998) Non-invasive imaging of arrhythmogenic left ventricular myocardium after infarction, *Lancet* **352**, 1825.
- 293** Seese, B., Moshage, W., Achenbach, S., Killmann, R. *et al.* (1995) Magnetocardiographic (MCG) analysis of myocardial injury currents, in C. Baumgartner, *et al.* (eds.), *Biomagnetism: Fundamental Research and Clinical Applications*, Elsevier, Amsterdam, pp. 628–632.
- 294** Leder, U., Pohl, H.P., Michaelsen, S., Fritschi, T. *et al.* (1998) Noninvasive biomagnetic imaging in coronary artery disease based on individual current density, *Int. J. Cardiol.* **64**, 83–92.
- 295** Nenonen, J., Pesola, K., Hänninen, H., Lauerma, K. *et al.* (2001) Current-density estimation of exercise-induced ischemia in patients with multivessel coronary artery disease, *J. Electrocardiol.* **34**, 37–42.
- 296** Oostendorp, T. and Pesola, K. (2001) Non-invasive determination of the activation sequence of the heart based on combined ECG and MCG measurements, in J. Nenonen, R. Ilmoniemi, and T. Katila, (eds.), *Biomag2000, Proc. 12th Int. Conf. on Biomagnetism*, Helsinki University of Technology, Espoo, Finland, pp. 813–820.
- 297** Fenici, R., Pesola, K., Mäkiäärvi, M., Nenonen, J. *et al.* (1998) Non-fluoroscopic localization of an amagnetic catheter in a realistic torso phantom by magnetocardiographic and body surface potential mapping, *Pacing Clin. Electrophysiol.* **21**, 2482–2491.
- 298** Brauer, H., Haueisen, J., Ziolkowski, M., Tenner, U. *et al.* (2000) Reconstruction of extended current sources in a

- human body phantom applying biomagnetic measuring techniques, *IEEE Trans. Magn.* **36**, 1700–1705.
- 299** Veisterä, H., Fenici, R. and Lötjönen, J. (2004) Online heart model creation for magnetocardiographic measurements, in E. Halgren, S. Ahlfors, M. Härmäläinen, and D. Cohen (eds.), *Biomag2004, Proc. 14th Internat. Conf. on Biomagnetism*, Biomag2004 Ltd, Boston, MA, pp. 415–416.
- 300** Mäkelä, T., Pham, Q.C., Clarysse, P., Nenonen, J., et al. (2003) A 3-D model-based registration approach for the PET, MR and MCG cardiac data fusion, *Med. Image Anal.* **7**, 377–389.
- 301** Kariniemi, V., Ahopelto, J., Karp, P. and Katila, T. (1974) The fetal magnetocardiogram, *J. Perinat. Med.* **2**, 412–216.
- 302** Peters, M., Crowe, J., Pieri, J., et al. (2001) Monitoring the fetal heart non-invasively: a review of methods, *J. Perinat. Med.* **29**, 408–416.
- 303** Comani, S., Mantini, D., Pennesi, P., Lagatta, A. et al (2004) Independent component analysis: fetal signal reconstruction from MCG recordings, *Comput. Meth. Prog. Biomed.* **75**, 163–177.
- 304** Wakai, R.T., Leuthold, A.C., and Martin, C.B. (1998) Atrial and ventricular fetal heart rate patterns in isolated congenital complete heart block detected by magnetocardiography, *Am. J. Obstet. Gynecol.* **179**, 258–260.
- 305** van Leeuwen, P., Lange, S., Klein, A., Geue, D. et al (2004) Reproducibility and reliability of fetal cardiac time intervals using magnetocardiography, *Physiol. Meas.* **25**, 539–552.
- 306** Hamada, H., Horigome, H., Asaka, M., Shigemitsu, S., et al. (1999) Prenatal diagnosis of long QT syndrome using fetal magnetocardiography, *Prenatal Diagn.* **19**, 677–680.
- 307** Hosono, T., Chiba, Y., Shinto, M., Kan-dori, A., et al. (2001) A fetal Wolff-Parkinson-White syndrome diagnosed prenatally by magnetocardiography, *Fetal Diagn. Ther.* **16**, 215–217.
- 308** Grimm, B., Haueisen, J., Huotilainen, M., Lange, S. et al. (2003) Recommended standards for fetal magnetocardiography, *Pacing Clin. Electrophysiol.* **26**, 2121–2126.
- 309** Li, Z., Wakai, R., Paulson, D., Schwartz, N. et al. (2004) HTS magnetometers for fetal magnetocardiography, in E. Halgren, S. Ahlfors, M. Härmäläinen, and D. Cohen (eds.), *Biomag2004, Proc. 14th Internat. Conf. on Biomagnetism*, Biomag2004 Ltd, Boston, MA, pp. 323–324.
- 310** Nomura, M., Nakaya, Y., Ito, S. and Itozaki, H. (2004) Visualization of cardiac electrical current using 32-channel high temperature superconducting quantum interference device, in E. Halgren, S. Ahlfors, M. Härmäläinen, and D. Cohen (eds.), *Biomag2004, Proc. 14th Internat. Conf. on Biomagnetism*, Biomag2004 Ltd, Boston, MA, pp. 632–633.
- 311** Pannetier, M., Fermon, C., Le Goff, G., Simola, J. et al. (2004) Femtotesla magnetic field measurement with magnetoresistive sensors, *Science* **3004**, 1648–1650.
- 312** Köhler, W., Held, R., and O'Connel, D. (1952) An investigation of cortical currents, *Proc. Amer. Philos. Soc.* **96**, 292–330.
- 313** Picton, T.W., Woods, D.L., and Proulx, G.B. (1978) Human auditory sustained response, *Electroenc. Clin. Neurophysiol.* **45**, 186–197.
- 314** Stys, P.K., Ranson, B.R., and Waxman, S.G. (1991) Compound action potential of nerve recorded by a suction electrode: a theoretical and experimental analysis, *Brain Res.* **546**, 18–32.
- 315** Hari, R., Attoniemi, K., Järvinen, M.L., Katila, T., and Varpula, T. (1980) Auditory evoked transient and sustained magnetic fields of the human brain. Localization of neural generators, *Exp. Brain Res.* **40**, 237–240.
- 316** Deecke, L., Weinberg, H., and Brickett, P. (1982) Magnetic fields of the human brain accompanying voluntary movement: Bereitschaftsmagnetfeld, *Exp. Brain Res.* **48**, 144–148.
- 317** Bowyer S.M., Aurora, K.S., Moran, J.E., Tepley, N., and Welch, K.M. (2001) Magnetoencephalographic fields from patients with spontaneous and induced migraine aura, *Ann. Neurol.* **50**, 582–587.
- 318** Barth, D.S., Sutherling, W., and Beatty, J. (1984) Fast and slow magnetic phe-

- nomena in focal epileptic seizures, *Science* **226**, 855–857.
- 319** Vieth, J., Schüler, P., Sack, G., Gansland, O., Dratz, W., Fischer, H., and Grimm, U. (1993) Extracranial slow magnetic field changes during epileptic activity, in W. Haschke *et al.* (eds.), *Slow Cortical changes in the brain*, Birkhäuser, Boston, pp. 243–250.
- 320** Pantev, C., Eulitz, C., Elbert, T., and Hoke, M. (1994) The auditory evoked sustained field: origin and frequency dependence, *Electroenc. Clin. Neurophysiol.* **90**, 82–90.
- 321** Lammertmann, C., and Lütgenhöner, B. (2000) Near-DC magnetic fields following a periodic presentation of long-duration tonebursts, *Clin. Neurophysiol.* **112**, 499–513.
- 322** Cohen, D. (1969) Detection and analysis of magnetic fields produced by bioelectric currents in humans, *J. Appl. Phys.* **40**, 1046–1048.
- 323** Grimes, D., Lennard, R., and Swithenby, S. (1983) DC magnetic fields of the human leg as a function of position and relaxation, *Il Nuovo Cimento* **2D**, 650–659.
- 324** Trontelj, Z., Pirnat, J., Luznik, J., and Jasbinsek, V. (1990) Measurement of magnetic field near an acute surgical injury on the rabbit's thigh, in S.J. Williamson *et al.* (eds.), *Advances in Biomagnetism*, Plenum Press, New York, pp. 517–520.
- 325** Topley, N., Bowyer, S., Clifton, Y., and Saligram, U. (1996) A technique for sequential measurements of dc neuromagnetic fields, *Electroenc. Clin. Neurophysiol.* **99**, 16–18.
- 326** Curio, G., Erne, S.N., Burghoff, M., Wolff, K.-D., and Pilz, A. (1993) Non-invasive neuromagnetic monitoring of nerve and muscle injury currents, *Electroenc. Clin. Neurophysiol.* **89**, 154–160.
- 327** Wübbeler, G., Mackert, J., Armbrust, F., Burghoff, M., Mackert, B.-M., Wolff, K.-D., Ramsbacher, J., Curio, G., and Trahms, L. (1998) SQUID measurements of human nerve and muscle near-dc injury currents using a mechanical modulation of the source position, *Appl. Supercond.* **6**, 559–565.
- 328** Wübbeler, G., Mackert, B.-M., Armbrust, F., Burghoff, M., Marx, P., Curio, G., and Trahms, L. (1999) Measurement of near-DC biomagnetic fields of the head using a horizontal modulation of the body position, in *Recent Advances in Biomagnetism*, Tohoku University Press, pp. 369–372.
- 329** Cohen, D. and Kaufman, L.A. (1975) Magnetic determination of the relationship between the ST-segment shift and the injury current produced by coronary artery occlusion, *Circulation Res.* **36**, 414–424.
- 330** Cohen, D., Palti, Y., Cuffin, B.N., and Schmid, S.J. (1980) Magnetic fields produced by steady currents in the body, *Proc. Natl. Acad. Sci. USA* **77**, 1447–1451.
- 331** Grimes, D.I.F., Lennard, R.F., and Swithenby, S.J. (1985) Macroscopic ionic currents within the human leg, *Phys. Med. Biol.* **30**, 1101–1112.
- 332** Mackert, B.-M., Mackert, J., Wübbeler, G., Armbrust, F., Wolff, K.-D., Burghoff, M., Trahms, L., and Curio, G. (1999) Magnetometry of injury currents from nerve and muscle specimens using superconducting quantum interference devices, *Neurosci. Lett.* **262**, 163–166.
- 333** Mackert, B.-M., Wübbeler, G., Burghoff, M., Marx, P., Trahms, L., and Curio, G. (1999) Non-invasive long-term recordings of cortical 'direct current' (DC-) activity in humans using magnetoencephalography, *Neurosci. Lett.* **273**, 159–162.
- 334** Mackert, B.-M., Wübbeler, G., Leistner, S., Trahms, L., and Curio, G. (2001) Non-invasive single-trial monitoring of human movement-related brain activation based on DC-magnetoencephalography, *Neuroreport* **12**, 1689–1692.
- 335** Elbert, T., Braun, C., Rockstroh, B., and Schneider, S. (1992) The measurement of tonic brain activity by means of magnetoencephalography, in M. Hoke *et al.* (eds.), *Biomagnetism: Clinical Aspects*, Elsevier Science, pp. 337–340.
- 336** Carbon, M., Wübbeler, G., Trahms, L., and Curio, G. (2000) Hyperventilation induced human cerebral magnetic fields non-invasively monitored by mul-

- tichannel 'direct current' magnetoencephalography, *Neurosci. Lett.* **287**, 227–230.
- 337** Wübbeler, G., Ziehe, A., Mackert, B.-M., Müller, K.-R., Trahms, L., and Curio, G. (2000) Independent component analysis of noninvasively recorded cortical magnetic DC-fields, *IEEE Trans. Biomed. Eng.* **47**, 594–599.
- 338** Taulu, S., Simola, J., and Kajola, M. (2004) MEG recordings of dc fields using the signal space separation method (SSS), *Neurol. and Clin. Neurophysiol.* **35**, 1–4.
- 339** Weiskopf, N., Braun, C., and Mathiak, K. (2001) MEG-recordings of DC fields using a 151-channel whole-head device, in J. Nenonen, R. Ilmoniemi, and T. Katila (eds.), *Biomag2000, Proc. 12th Int. Conf. on Biomagnetism*, Helsinki University of Technology, Espoo, Finland, pp. 500–503.
- 340** Burghoff, M., Sander, T., Schnabel, A., Drung, D., Trahms, L., Curio, G., and Mackert, B.M. (2004) dc magnetoencephalography: direct measurement in a magnetically extremely-well shielded room, *Appl. Phys. Lett.* **85**, 6278–6280.
- 341** Helmholz, H. (1850) Messungen über den zeitlichen Verlauf der Zuckung animalischer Muskeln und die Fortpflanzungsgeschwindigkeit der Reizung in den Nerven, *Arch. Anta. Physiol.* 276–364.
- 342** Wikswo, J.P., Barach, J.P., and Freeman, J.A. (1980) The magnetic field of a nerve impulse: first measurements. *Science* **208**, 53–55.
- 343** Leifer, M.E., and Wikswo, J.P. (1983) Optimization of a openable SQUID current probe, *Rev. Sci. Instrum.* **54**, 1017–1022.
- 344** Egeraat, J.M., and Wikswo, J.P. (1992) Measurement of uniform propagation in the squid nervous system with a room temperature magnetic current probe, in M. Hoke *et al.* (eds.), *Biomagnetism: Clinical Aspects*, Elsevier Science Publishers, pp. 385–388.
- 345** Erne, S.N., Curio, G., Trahms, L., Trontelj, Z., and Aust, P. (1988) Magnetic activity of a single peripheral nerve in man, in K. Atsumi *et al.* (eds.), *Biomagnetism'87*, Tokyo Denki University Press, pp. 166–169.
- 346** Trahms, L., Erne, S.N., Trontelj, Z., Curio, G., and Aust, P. (1989) Biomagnetic functional localization of a peripheral nerve in man, *Biophys. J.* **55**, 1145–1153.
- 347** Hari, R., Hällström, J., Tiihonen, J., and Joutsiniemi, S.-L. (1989) Multichannel detection of magnetic compound action fields of median and ulnar nerves, *Electroenc. Clin. Neurophysiol.* **72**, 277–280.
- 348** Hashimoto, I., Okada, K., Gatayama, T., and Yokoyama, S. (1991) Multichannel measurement of magnetic compound action fields of the median nerve in man, *Electroenc. Clin. Neurophysiol.* **81**, 332–326.
- 349** Hashimoto, I., Mashiko, T., Mizuta, T., Imada, T., Iwase, Y., Okazaki, H., and Yoshikawa, K. (1995) Multichannel detection of magnetic compound action fields with stimulation of the index and little fingers, *Electroenc. Clin. Neurophysiol.* **97**, 102–113.
- 350** Burghoff, M., Haberkorn, W., Mackert, B.-M., and Curio, G. (1997) Analysis of magnetic fields recorded from stimulated leg nerves, *J. Clin. Eng.* **22**, 158–162.
- 351** Curio, G., Erne, S.N., Sandfort, J., Scheer, J., Stehr, R., and Trahms, L. (1991) Exploratory mapping of evoked neuromagnetic activity from human peripheral nerve, plexus, and spinal cord, *Electroenc. Clin. Neurophysiol.* **81**, 450–453.
- 352** Curio, G., Reill, L., Sandfort, J., Erne, S.N., Scheer, J., Stehr, R., and Trahms, L. (1993) Nerve, plexus, and spinal cord: possible targets for non-invasive neuromagnetic measurements in man, *Physiol. Meas.* **14**, A91–A94.
- 353** Mackert, B.-M., Burghoff, M., Hiss, L.-H., Nordahn, M., Marx, P., Trahms, L., Curio, G. (2000) Non-invasive magnetoneurography for 3D-monitoring of human compound action current propagation in deep brachial plexus, *Neurosci. Lett.* **289**, 33–36.
- 354** Mackert, B.-M., Curio, G., Burghoff, M., and Marx, P. (1997) Mapping of tibial nerve evoked magnetic fields over the lower spine, *Electroenc. Clin. Neurophysiol.* **104**, 322–327.
- 355** Mackert, B.-M., Burghoff, M., Hiss, L.-H., Nordahn, M., Marx, P., Trahms,

- L., and Curio, G. (2001) Magnetoneurography of evoked compound action currents in human cervical nerve roots, *Clin. Neurophysiol.* **112**, 330–335.
- 356** Lang, G., Shahani, U., Weir, A.I., Maas, P., Pegrum, C.M., and Donaldson, G.D. (1998) Neuromagnetic recordings of the human peripheral nerve with planar SQUID gradiometers, *Phys. Med. Biol.* **43**, 2379–2384.
- 357** Drung, D., Ludwig, F., Müller, W., Steinhoff, U., Trahms, L., Koch, H., Shen, Y.Q., Jensen, M.B., Vase, P., Holst, T., Freloft, T., and Curio, G. (1996) Integrated YBCO magnetometer for biomagnetic measurements, *Appl. Phys. Lett.* **68**, 1421–1423.
- 358** Lütgenhöner, B., Hoke, M., and Pantev, C. (1985) Possibilities and limitations of weighted averaging, *Biol. Cybern.* **52**, 409–416.
- 359** Burghoff, M., Mackert, B.-M., Haberkorn, W., Curio, G., and Trahms, L. (1998) High-resolution magnetoneurography, *Appl. Supercond.* **6**, 567–575.
- 360** Gräbe, T., Burghoff, M., Steinhoff, U., Mackert, B.-M., and Curio, G. (1997) Identifications of signal components by stochastic modeling in measurements of evoked magnetic fields from peripheral nerves, in P. Ciarlini *et al.* (eds.), *Advanced Mathematical Tools in Metrology III*, World Scientific, pp. 178–185.
- 361** Hashimoto, I., Mashiko, T., Mizuta, T., Imada, T., Iwase, K., and Okazaki, H. (1994) Visualization of a moving quadrupole with magnetic measurements of peripheral nerve action fields, *Electroenc. Clin. Neurophysiol.* **93**, 459–467.
- 362** Hoshiyama, M., Kagigi, R., and Nagata, O. (1999) Peripheral nerve conduction recorded by a micro gradiometer system (micro-SQUID) in humans, *Neurosci. Lett.* **272**, 199–202.
- 363** Mackert, B.-M., Burghoff, M., Hiss, L.-H., Trahms, L., and Curio, G. (2001) Tracing of lumbosacral nerve conduction – a comparison of simultaneous magneto- and electroneurography, *Clin. Neurophysiol.* **112**, 1408–1413.
- 364** Mackert, B.-M., Curio, G., Burghoff, M., Trahms, L., and Marx, P. (1998) Magnetonurographic 3D localization of conduction blocks in patients with unilat-
- eral S1 root compression, *Electroenc. Clin. Neurophysiol.* **109**, 315–320.
- 365** Nielsen, P., Fischer, R., Engelhardt, R., Dresow, B., and Gabbe, E.E. (1998) Neue Möglichkeiten in der Diagnose der hereditären Hämochromatose, *Deutsches Ärzteblatt* **46**, C2059–C2065.
- 366** Bauman, J.H., and Harris, J.W. (1967) Estimation of hepatic iron stores by in-vivo measurement of magnetic susceptibility, *J. Lab. Clin. Med.* **70**, 246–257.
- 367** Wikswo, J.P., Fairbank, W.M., and Opfer J.E. (1976) Method for measuring externally of the human body magnetic susceptibility changes, US patent 3980076.
- 368** Wikswo, J.P., Fairbank, W.M., and Opfer J.E. (1978) Apparatus for measuring externally of the human body magnetic susceptibility changes, US patent 4079730.
- 369** Farrell, D.E., Tripp, J.H., and Zanzuchi, P.E. (1980) Magnetic measurements of human iron stores, *IEEE Trans. Magnetics Mag-16*, 818–823.
- 370** Brittenham, G.M., Farrell, D.F., Harris, J.W., Feldmann, E.S., Danish, E.H., Muir, W.A., Tripp, J.H., and Bellon, E.M. (1982) Magnetic susceptibility measurement of human iron stores, *N. Eng. J. Med.* **307**, 1671–1675.
- 371** Farrell, D.E., Tripp, J.H., Brittenham, G.M., Danish, E.H., Harris, J.W., and Tracht, A.E. (1983) A clinical system for accurate assessment of tissue iron concentration, *Il Nuovo Cimento 2D*, 582–593.
- 372** Paulson, D.N., Fagaly, R.L., Toussaint, R.M., and Fischer, R. (1991) Biomagnetic susceptometer with SQUID instrumentation, *IEEE Trans. Magn.* **27**, 3249–3252.
- 373** Fischer, F. (1998) Liver iron susceptibility, in W. Andrä, and H. Nowak (eds.) *Magnetism in Medicine*, Wiley, pp. 286–301.
- 374** Tripp, J.H. (1983) Physical concepts and mathematical models, in S.J. Williamson *et al.* (eds.), *Biomagnetism – An Interdisciplinary Approach*, Plenum, New York, pp. 101–139.
- 375** Hartmann, W., Schneider, L., Wirth, A., Dördelmann, M., Zinser, D., Elias, H., Languth, W., Ludwig, W., and Kleihauer,

- E. (1992) Liver susceptometry for the follow up of transfusional iron overload, in *Advances in Biomagnetism*, M. Hoke *et al.* (eds.), Elsevier Amsterdam, pp. 585–588.
- 376** Sosnitsky, V.N., and Voitovich, I.D. (1996) Application of superconducting electronics to registration of biomagnetic signals, *J. de Physique*, IV **6**, 417–422.
- 377** Powell, L.W. (1994) Primary iron overload, in J.H Brock *et al.* (eds.), *Iron Metabolism in Health and Disease*, Saunders, London, pp. 227–270.
- 378** Feder, J.N., Gnarke, A., Thomas, W., Tsuchihashi, Z., Ruddy, D.A., Basava, A., and Wolff, R.K. (1996) A novel mhc class i-like gene is mutated in patients with hereditary hemochromatosis, *Nature Genetics* **13**, 399–408.
- 379** Brittenham, G.M., Cohen, A.R., McLaren, C.E., Martin, M.B., Griffith, P.M., Nienhuis, A.W., Young, N.S., Allen, C.J., Farrel, D.E., and Harris, J.W. (1993) Hepatic iron stores and plasma ferritin concentrations in patients with sickle cell anemia and thalassemia major, *Am. J. Hematol.* **42**, 81–85.
- 380** Nielsen, P., Engelhardt, R., Duerken, M., Janka, G.E., and Fischer, R. (2000) Using SQUID biomagnetic liver susceptometry in the treatment of thalassemia and other iron loading diseases, *Transfus. Sci.* **23**, 257–258.
- 381** Nielsen, P., Fischer, R., Engelhardt, R., Tondury, P., Gabbe, E.E., and Janka, G.E. (1995) Liver iron stores in patients with secondary hemochromatosis under iron chelation therapy with deferoxamine or deferiprone. *Brit. J. Haematol.* **91**, 827–833.
- 382** Del Vecchio, G.C., Crollo, E., Schettini, F., Fischer, R., and De Mattia, D. (2000) Factors influencing effectiveness of deferiprone in a thalassaemia major clinical setting, *Acta Haematol.* **104**, 99–102.
- 383** Nachtigall, D., Nielsen, P., Fischer, R., Engelhardt, R., and Gabbe, E.E. (1996) Iron deficiency in distance runners – a reinvestigation using ^{59}Fe -labelling and non-invasive liver iron quantification, *Int. J. Sports Med.* **17**, 473–479.
- 384** Kaltwasser, J.P., Gottschalk, R., Schalk, K.P., and Hartl, W. (1990) Non-invasive quantitation of liver iron overload by magnetic resonance imaging, *Brit. J. Haematol.* **74**, 360–363.
- 385** Brittenham, G.M. (1988) Noninvasive methods for the early detection of hereditary hemochromatosis in prospective blood donors, *Ann. N. Y. Acad. Sci.* **526**, 199–208.
- 386** Engelhardt, R., Langkowski, J.H., Fischer, R., Nielsen, P., Kooijman, H., Heinrich, H.C., and Bücheler, E. (1994) MRI-sequences for liver iron quantification: studies in aqueous iron solutions, iron overloaded rats, and patients with hereditary hemochromatosis, *Magn. Reson. Imaging* **12**, 999–1007.
- 387** Clark, P.R., and St Pierre, T.G. (2000) Quantitative mapping of transverse relaxivity ($1/T(2)$) in hepatic iron overload: a single spin-echo imaging methodology, *Magn. Reson. Imaging* **18**, 431–438.
- 388** Fischer, R., Piga, A., Tricta, F., Nielsen, P., Engelhardt, R., Garofalo, F., Di Palma, A., and Vullo, C. (1999) The use of biomagnetic liver susceptometry in the Ferrara-Hamburg-Turin study on thalassemia. in C.J. Aine *et al.* (eds.), *Biomag96*, Springer, pp. 647–650.
- 389** Ambu, R., Crisponi, G., and Sciot, R. (1995) Uneven iron and phosphorus distribution in β -thalassemia, *J. Hepatol.* **23**, 544–549.
- 390** Forsman, M. (1998) Magnetism in gastroenterology, in W. Andrä, and H. Nowak (eds.), Wiley-VCH, *Magnetism in Medicine*, pp. 430–445.
- 391** Bradshaw, L.A., Ladipo, J.K., Staton, D.J., and Wikswo, J.P. (1999) The human vector magnetogastrogram and magnetoenterogram, *IEEE Trans. Biomed. Eng.* **46**, 959–970.
- 392** Bradshaw, L.A., Myers, A.G., Richards, W.O., and Wikswo, J.P. (2003) A spatio-temporal dipole simulation of gastrointestinal magnetic fields, *IEEE Trans. Biomed. Eng.* **50**, 836–847.
- 393** Richards, W.O., Bradshaw, L.A., Staton, D.J., Garrard, C.L., Liu, F., Buchanan, S., and Wikswo, J.P. (1996) Magnetoenterography (MENG), *Dig. Di. Sci.* **41**, 2293–2301.

- 394** Turnbull, G.K., Ritcey, S.P., Stroink, G., Brands, B., and van Leeuwen, P. (1999) Spatial and temporal variations in the magnetic fields produced by human gastrointestinal activity, *Med. Biol. Eng. Comp.* **37**, 549–554.
- 395** Allos, S.H., Staton, D.J., Bradshaw, L.A., Halter, S., Wikswo, J.P., and Richards, W.O. (1997) Superconducting interference device magnetometer for diagnosis of ischemia caused by mesenteric venous thrombosis, *World J. Surg.* **21**, 173–178.
- 396** Bradshaw, L.A., Allos, S.H., Wikswo, J.P., and Richards, W.O. (1997) Correlation and comparison of magnetic and electric detection of small intestine electrical activity, *Am. J. Physiol.* **272** (Gastrointest. Liver Physiol. 35), G1159–G1167.
- 397** Seidel, S.A., Bradshaw, L.A., Ladipo, J.K., Wikswo, J.P., and Richards, W.O. (1999) Noninvasive detection of ischemic bowel, *J. Vasc. Surg.* **30**, 309–319.
- 398** Miranda, J.R.A., Oliveira, R.B., Sousa, P.L., Braga, F.J.H., and Baffa, O. (1997) A novel biomagnetic method to study gastric antral contractions, *Phys. Med. Biol.* **42**, 1791–1799.
- 399** Forsman, M., Hultin, L., and Abrahamsen, H. (1995) Measurements of gastrointestinal transit using fluxgate magnetometers, in C. Baumgartner *et al.* (eds.), *Biomagnetism: Fundamental Research and Clinical Applications*, Elsevier Science, pp. 739–742.
- 400** Forsman, M. (1994) Assessment of gastric movements by monitoring magnetic field decline of magnetized trace particles, *Phys. Med. Biol.* **39a**, 62.
- 401** Carneiro, A.A., Baffa, O., and Oliveira, R.B. (1999) Study of stomach motility using the relaxation of magnetic tracers, *Phys. Med. Biol.* **44**, 1691–1697.
- 402** Weitschies, W., Gröning, R., and Trahms, L. (1989) Verfahren zur Bestimmung des Aufenthaltsorts und der Bewegung von Objekten durch ihr magnetisches Moment, German patent DE 39 40 260.
- 403** Weitschies, W., Kosch, O., Mönnikes, H., and Trahms, L. (2005) Magnetic marker monitoring: an application of biomagnetic measurement instrumentation and principles for the determination of the gastrointestinal behaviour of magnetically marked solid dosage forms, *Adv. Drug Deliv. Rev.* **57**, 1210–1222.
- 404** Weitschies, W., Wedemeyer, J., Stehr, R., and Trahms, L. (1991) Magnetically marked pharmaceutical dosage forms to monitor gastrointestinal transit by biomagnetic measurements, *Pharmac. Pharmacol. Lett.* **1**, 45–48.
- 405** DiLuzio, S., Comani, S., Romani, G.L., Basile, M., DelGratta, C., and Pizzella, V. (1989) A biomagnetic method for studying gastrointestinal activity, *Il Nuovo Cimento D* **11**, 1856–1859.
- 406** Weitschies, W., Wedemeyer, J., Stehr, R., and Trahms, L. (1994) Magnetic markers as noninvasive tool to monitor gastrointestinal transit, *IEEE Trans. Biomed. Eng.* **41**, 192–195.
- 407** Trahms, L., Model, R., Stehr, R., Wedemeyer, J., and Weitschies, W. (1992) Gastrointestinal motility displayed by magnetic marker dislocations monitored by multichannel systems, in M. Hoke *et al.* (eds.), *Biomagnetism: Clinical Aspects*, Elsevier Science, pp. 625–630.
- 408** Model, R. and Trahms, L. (1993) An inverse problem of magnetic source localization, *Numerical Algorithms* **5**, 603–610.
- 409** Weitschies, W., Karaus, M., Cordini, D., Trahms, L., Breitkreutz, J., and Semmler, W. (2001) Magnetic marker monitoring of disintegrating capsules, *Eur. J. Pharm. Sci.* **13**, 411–416.
- 410** Weitschies, W., Kötitz, R., Cordini, D., and Trahms, L. (1997) High-resolution monitoring of the gastrointestinal transport of a magnetically marked capsule, *J. Pharm. Sci.* **86**, 1218–1222.
- 411** Weitschies, W., Cordini, D., Karaus, M., Trahms, L., and Semmler, W. (1999) Magnetic marker monitoring of esophageal, gastric and duodenal transit of non-disintegrating capsules, *Pharmazie* **54**, 426–430.
- 412** Osmanoglu, E., van der Voort, I.R., Fach, K., Kosch, O., Bach, D., Hartmann, V., Strenzke, A., Weitschies, W., Wiedenmann, B., Trahms, L., and Mönnikes, H. (2004) Oesophageal transport

- of solid dosage forms depends on body position, swallowing volume and pharyngeal propulsion velocity, *Neurogastroenterol. Motil.* **16**, 547–556.
- 413** Hu, Z., Mawatari, S., Shibata, N., Takada, K., Yoshikawa, H., Arakawa, A., and Yosida, Y. (2000) Application of a biomagnetic measurement system (BMS) to the evaluation of gastrointestinal transit of intestinal pressure controlled colon delivery capsules (PCDCs) in human subjects, *Pharmac. Res.* **17**, 160–167.
- 414** Néel, L. (1949) Théorie du trainage magnétique des ferromagnétiques en grains fins avec applications aux terres cuites, *Ann. Geophys.* **5**, 99–136.
- 415** Safarik, I. and Safarikova, M. (2002) Magnetic nanoparticles and biosciences, *Monatsh. f. Chem.* **133**, 737–759.
- 416** Weitschies, W., Köttitz, R., Bunte, T., and Trahms L. (1997) Determination of relaxing or remanent nanoparticle magnetization provides a novel binding specific technique for the evaluation of immunoassays, *Pharm. Pharmacol. Lett.* **7**, 5–8.
- 417** Debye, P. (1929) *Polar Molecules*. Chemical Catalog Company, New York.
- 418** Köttitz, R., Fannin, P.C., and Trahms, L. (1995) Time domain study of Brownian and Néel relaxation in ferrofluids, *Magn. Mat. Mat.* **49**, 42–46.
- 419** Eberbeck, D., Bergemann, C., Hartwig, S., Steinhoff, U., and Trahms, L. (2005) Binding kinetics of magnetic nanoparticles on latex beads and yeast cells studied by magnetorelaxometry, *Magn. Mat.* **289**, 435–438.
- 420** Matz, H., Drung, D., Köttitz, R., Trahms, L., Weitschies, W., Koch, H., and Semmler, W. (1996) Gerät zur höchstempfindlichen magnetischen Detektion von Analyten, German patent DE 196 15 254 (WO 97/40377).
- 421** Matz, H., Drung, D., Hartwig, S., Groß, H., Köttitz, R., Müller, W., Vass, A., Weitschies, W., and Trahms, L. (1999) A SQUID measurement system for immunoassays, *IEEE Appl. Supercond.* **6**, 577–583.
- 422** Schambach, J., Warzemann, L., and Weber, P. (1999) SQUID gradiometer measurement system for magnetore-
- laxometry in a disturbed environment, *IEEE Trans. Appl. Supercond.* **9**, 3527–3530.
- 423** Chemla, Y.R., Grossman, H.L., Poon, Y., McDermott, R., Stevens, R., Alper, M.D., and Clarke, J. (2000) Ultrasensitive magnetic biosensor for homogeneous immunoassay, *Proc. Natl. Acad. Sci.* **97**, 14268–14272.
- 424** Enpuku, K. and Minotani, T. (2001) Biological immunoassay with high T_c superconducting quantum interference device (SQUID) magnetometer, *IEICE Trans. Electron.* **E84C**, 43–48.
- 425** Enpuku, K., Minotani, T., Hotta, M., and Makahodo, A. (2001) Application of high T_c SQUID magnetometer to biological immunoassays, *IEEE Appl. Supercond.* **11**, 661–664.
- 426** Enpuku, K., Ohba, A., Inoue, and K., and Soejima, K. (2004) Design for superconducting quantum interference device for magnetic immunoassays, *Jap. J. of Appl. Phys.* **43**, 6044–6049.
- 427** Koch, R., Rozen, J.R., Sun, J.Z., and Gallagher, W.R. (1993) Three SQUID gradiometer, *Appl. Phys. Lett.* **63**, 403–405.
- 428** Haller, H., Matz, H., Hartwig, S., Kerberger, T., Atzpadin, H., and Trahms, L. (2001) Low T_c SQUID measurement system for magnetic relaxation immunoassays in unshielded environment, *IEEE Trans. Appl. Supercond.* **11**, 1371–1374.
- 429** Warzemann, L., Schambach, J., Weber, P., Weitschies, W., and Köttitz, R. (1999) LTS SQUID gradiometer system for in vivo magnetorelaxometry, *Supercond. Sci. Technol.* **12**, 953–955.
- 430** Köttitz, R., Weitschies, W., Trahms, L., Brewer, W., and Semmler, W. (1999) Determination of the binding reaction between avidin and biotin by relaxation measurements of magnetic nanoparticles, *Magn. Mag. Mat.* **194**, 62–68.
- 431** Lange, J. (2001) Spezifisch bindende magnetische Nanopartikel als Signalgeber in magnetischen Relaxationsmessungen, Ph.D. Thesis, Ernst-Moritz-Arndt University, Greifswald.
- 432** Lange, J., Köttitz, R., Haller, A., Trahms, L., Semmler, W., and Weitschies, W. (2002) Magnetorelaxometry – a new

- binding specific detection method based on magnetic nanoparticles, *Magn. Mag. Mat.* **252**, 381–383.
- 433** Grossmann, H.L., Myers, W.R., Vreeland, V.J., Bruehl, R., Alper, M.D., Berrozzi, C.R., and Clarke, J. (2004) Detection of bacteria in suspension by using a superconducting quantum interference device, *Proc. Natl. Acad. Sci.* **101**, 129–134.
- 434** Flynn, E.R. and Bryant, H.C. (2005) A biomagnetic system for *in vivo* cancer imaging, *Phys. Med. Biol.* **50**, 1273–1293.

12

Measurements of Magnetism and Magnetic Properties of Matter

Randall C. Black and Frederick C. Wellstood

| | | |
|---------|--|-----|
| 12.1 | Introduction | 392 |
| 12.2 | The SQUID Magnetometer–Susceptometer | 392 |
| 12.2.1 | Conventional Magnetometry–Susceptometry | 392 |
| 12.2.2 | SQUID-based Magnetometer–Susceptometer | 393 |
| 12.2.3 | History of Development | 394 |
| 12.2.4 | SQUID Magnetometer–Susceptometer Components | 397 |
| 12.2.5 | SQUID Input Circuit | 399 |
| 12.2.6 | Cryocooled MPMS | 400 |
| 12.2.7 | Measurement Sequence | 402 |
| 12.2.8 | Measurement Accuracy: Converting Raw Data to Magnetic Moment | 403 |
| 12.2.9 | Measurement Sensitivity: Magnet and Environment | 404 |
| 12.2.10 | SQUID ac Susceptibility | 405 |
| 12.2.11 | Conclusions and Future Trends | 407 |
| 12.3 | Scanning SQUID Microscopy | 409 |
| 12.3.1 | Basic Principles of SQUID Microscopy | 409 |
| 12.3.2 | SQUIDs for Microscopy | 412 |
| 12.3.3 | Cryogenics | 419 |
| 12.3.4 | Scanning | 422 |
| 12.3.5 | Collecting Data | 425 |
| 12.3.6 | Current Source Image Processing and Spatial Resolution | 426 |
| 12.3.7 | Applications | 429 |
| 12.3.8 | Conclusions and Future Outlook | 435 |

12.1

Introduction

This chapter discusses two distinct types of techniques for making magnetic measurements of small samples: the widely used techniques of SQUID-based small-sample magnetometry and susceptometry and the less well-known technique of scanning SQUID microscopy. In magnetometer–susceptometer systems, measurements of remnant field, magnetization, or magnetic susceptibility are typically made as a function of applied field or temperature. This technique is particularly useful for revealing the presence of magnetic or superconducting phases and providing basic information about the bulk magnetic properties of samples. In contrast, SQUID microscopes are used to measure the local magnetic field just above the surface of a sample. From such data, one can produce images that reveal the strength and location of the sources that produced the fields, whether due to magnetized regions or currents flowing within the sample. The design, construction, and performance of these different types of systems reveal both the challenges of using SQUIDs in practical applications as well as the benefits that can be obtained by doing so.

12.2

The SQUID Magnetometer–Susceptometer

12.2.1

Conventional Magnetometry–Susceptometry

The function of a small-sample magnetometer or susceptometer (MS) is to measure the induced or remnant magnetic moment in a sample, usually as a function of applied magnetic field and temperature. The applications of these instruments are as varied as the study of magnetism itself. They are used widely in basic research and commercial laboratories as well as in industry. Unlike a magnetic microscope, these instruments provide no information on the spatial distribution of magnetization in a sample.

There are almost as many designs for MS systems as there are applications. The most common systems are based on either induction or force-gradient techniques. For the induction-based systems, vibrating sample magnetometers

(VSMs) are the most common [1]. This technique involves vibrating the sample at low frequencies (*e.g.*, 80 Hz) in the gradient region of a copper detection coil and using a lock-in amplifier to detect the response. These instruments achieve sensitivities down to about 10^{-9} A m² for a 1 second average. The sensitivity, accuracy, speed, and ease of use of VSMs have made them the most widely used instrument for magnetic characterization of materials and there are several manufacturers of commercial systems [2].

Of the force-based instruments, the alternating gradient magnetometer (AGM) [3] is the most sensitive of the practical commercial instruments [4]. This technique involves attaching a sample to a mechanical cantilever near coils that apply an alternating gradient field. By applying the alternating field at the cantilever's resonant frequency (*e.g.*, 700 Hz) and detecting the vibration amplitude by some sensitive means (*e.g.*, piezo electric, or optical), an AGM can achieve sensitivity in the 10^{-11} A m² range. However, the need for an oscillating field and a high-*Q* mechanical resonance combine to limit the accuracy and available temperature range of this technique.

12.2.2

SQUID-based Magnetometer–Susceptometer

Both accuracy and sensitivity can be achieved with a SQUID magnetometer–susceptometer (SQUID-MS). A SQUID-MS combines several superconducting components, including a SQUID, superconducting magnet, detection coils, flux transformer, and superconducting shields. To make a measurement, a sample, typically less than a few millimeters in size, is first attached to a sample rod. The sample is then scanned through the center of a first- or second-order superconducting gradiometer (see Figure 12.1). The gradiometer forms a closed flux transformer that is coupled to a SQUID and the signal from the SQUID is typically recorded as a function of sample position. The shape and magnitude of the response curve can then be analyzed using a computer to obtain a corresponding magnetic moment (as explained in Section 12.2.8). To apply a magnetic field to the sample, the detection coils are located in the bore of a superconducting magnet. Temperature control is made possible by placing the sample and sample rod in a sealed variable-temperature insert (not shown in Figure 12.1) which is thermally isolated from the 4.2-K gradiometer and magnet by an annular vacuum space.

Because a SQUID-MS requires a liquid helium cryostat to cool the SQUID, it is relatively little additional expense to provide a superconducting magnet system and helium gas-flow temperature control. As a result, SQUID-MS systems typically offer the ability to measure in applied fields of up to 7 T over a temperature range from above room temperature down to below 2 K.

Measurement accuracy is another characteristic of a SQUID-MS, due to a combination of factors. First, the detection coils are relatively large compared to the sample size, resulting in a relatively small sensitivity to sample geometry. Second, since the detection is done with a nearly static field and sample position, there are negligible effects from eddy currents and microphonics. By comparison, in a

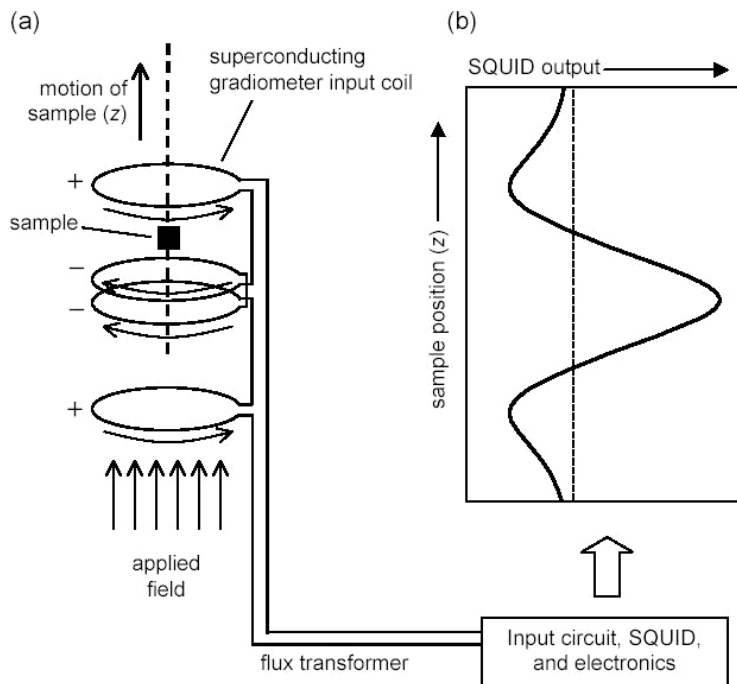


Fig. 12.1 (a) Schematic of SQUID magnetometer–susceptometer.
 (b) Calibrated output from SQUID electronics, recorded as a function of position.

VSM, eddy currents induced in both the sample and surrounding materials can affect the phase and amplitude of the lock-in-detected signal and acoustic coupling between the drive motor and the detection coils produces offsets in the measured moment.

12.2.3

History of Development

The first SQUID-MS systems were built in laboratories in the late 1960s [5] shortly after the invention of the SQUID. The designs evolved significantly through the early 1970s (see Ref. [6] and references therein). These early instruments combined all the key elements of modern commercial systems, including a superconducting magnet, SQUID, gradiometer coil, sample motion, and variable-temperature sample area. The first commercial SQUID-MS system was the SHE Variable Temperature Susceptometer (VTS), first manufactured by S.H.E. Corporation. (S.H.E. Corporation later became Biomagnetic Technologies, Inc.) About 45 of these VTS systems were produced between 1978 and 1987 [7].

The VTS instrument featured a NbTi superconducting shield in a vacuum space between the magnet and the gradiometer coils to attenuate field drift from flux motion in the magnet. In this scheme, the shield is maintained above its transi-

tion temperature while the magnetic field is being changed. Once the field is stable at the set field, the shield is cooled, and a flux corresponding to the set field is captured by the superconducting cylinder. This stabilizes the field inside the cylinder since the flux enclosed by a superconducting loop is conserved. When the field from the magnet drifts due to flux motion, screening currents in the shield oppose any changes in the enclosed flux, thus locking the field. If the screening currents become too large, especially at higher fields, there can be flux motion in the Type-II NbTi shield material and reduced shielding effectiveness [8]. This type of superconducting shield is the most effective means of producing a stable field in a SQUID-MS. However, this technique was abandoned in later commercial SQUID-MS systems because of the system's complexity and the long time required for changing the field.

Quantum Design, Inc. (QD) began producing early versions of their Magnetic Property Measurement System (MPMS) in 1984. The MPMS design incorporated many improvements over the VTS, including more sophisticated computer control, and a second-order gradiometer coil. The computer made possible fully programmed acquisition of magnetization measurements as a function of temperature and field. The second-order gradiometer, being less sensitive to field noise from the magnet, made possible the elimination of the VTS-style superconducting shield and vastly improved the system's reliability and speed. In 1986 high-temperature superconductors were discovered. Since SQUID-MS systems were the most reliable means to identify transition temperatures in superconductors, and production of the VTS was ending, demand for the MPMS soared. Annual shipments of the MPMS went from four systems in 1986 to over 50 per year by 1989. As of this writing (2005), more than 700 MPMS systems have been placed in laboratories around the world [9].

Other companies besides S.H.E. and QD have introduced SQUID instruments. These include the S600X from Cryogenic Limited, previously Cryogenics Consultants Limited (UK, still in production), the Chi-Mag from former Conductus (San Diego), the HSM-2000 from former Hoxan (Japan), and the MS-03 from former Métronique Ingénierie (France). Combined installations of all these systems number about 50 [9]. Since more than 90% of all commercial SQUID-MS systems in use today are from QD, much of the following discussion will focus on specific details of the MPMS (see Figure 12.2).

While the study of superconductors continues to be an important application of the SQUID-MS, these systems have found broad application wherever sensitivity is required. This includes the study of traditional paramagnets, diamagnets, and ferromagnets, as well as more complex structures that display giant and colossal magnetoresistive behaviors, thin-film magnetic media (see Figure 12.3), and biological materials. With the addition of the ac techniques discussed below, SQUID-MS systems have been also used for studies of spin glasses and superparamagnetic particles. Even when the ~100 times sensitivity advantage over a conventional VSM is not needed for a specific measurement, the MPMS is often used because of its accuracy and system-level features, including wide temperature and field range, and ease of use.

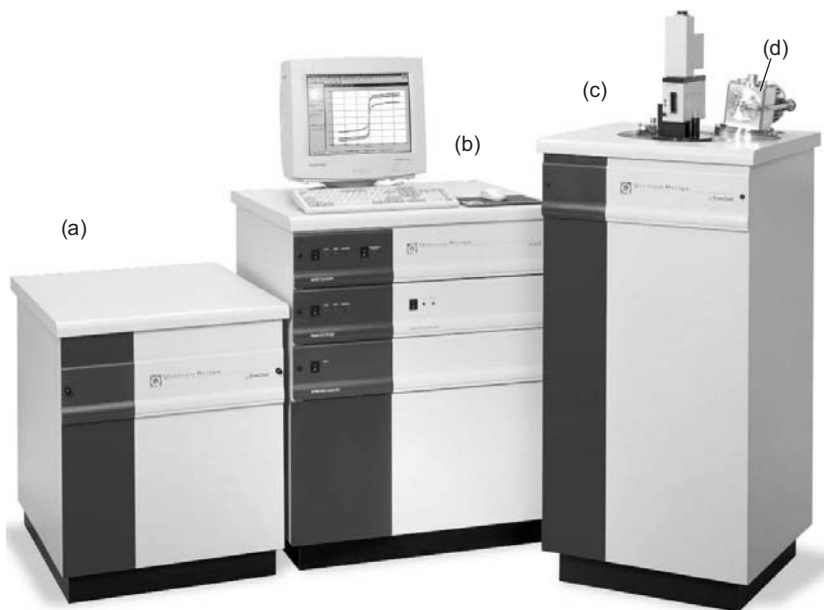


Fig. 12.2 Magnetic Property Measurement System (MPMS) XL, configured with an optional cryocooled dewar (EverCool™). (a) Cabinet for EverCool compressor, (b) computer and cabinet for gas handling and all control electronics, (c) cabinet for dewar, and (d) EverCool cold-head.

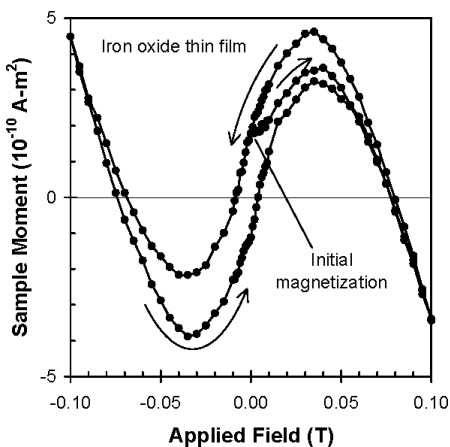


Fig. 12.3 Example of magnetization data obtained using a SQUID magnetometer-susceptometer (MPMS). The sample is a thin film of iron oxide on a silicon substrate [10]. The field is changed from zero (sample initially magnetized), to +0.1 T, to -0.1 T and back to +0.1 T. The diamagnetism of the silicon substrate has superposed a negative slope. Note that the full vertical scale is approximately equal to the noise level on a typical VSM instrument.

12.2.4

SQUID Magnetometer–Susceptometer Components

Figure 12.4 shows a schematic cross-section of the Quantum Design MPMS. The 9-mm diameter sample chamber is cooled by liquid helium that is drawn through a pair of capillary tubes connected to the bottom of the chamber. One capillary is high-flow and thermally switched for rapid cooling. The other enables continuous-filling pumped-helium operation to below 2 K. In operation, cold gas is pumped out of the top of the cryostat through the annular space between the sample chamber and the vacuum sleeve, thus cooling the sample chamber. Heaters and thermometers on the sample chamber (not shown in Figure 12.4) provide temperature control up to 400 K. A mat of vertically oriented copper wires (coil-foil) is wrapped around the lower section of the sample chamber for temperature uniformity in the region of the sample with minimal eddy current induction. An optional oven insert reduces the effective sample chamber diameter to 3.5 mm, but increases the maximum sample temperature to 800 K.

A linear motor attached to the sample rod at the top of the dewar is used to move the sample smoothly within the detection coils. To prevent contamination

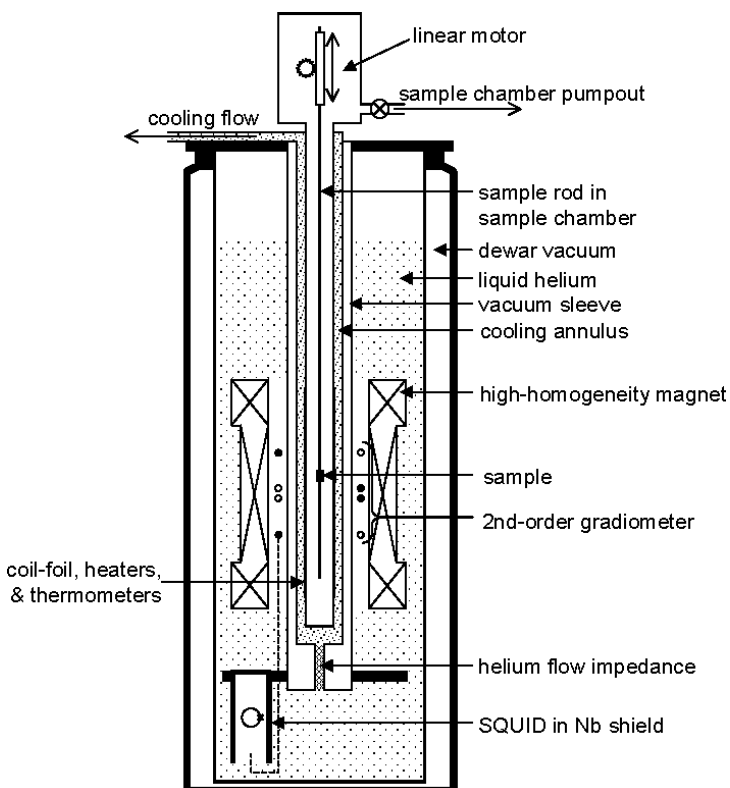


Fig. 12.4 Schematic cross-section of the MPMS.

of the helium exchange gas in the sample chamber, a sliding seal is required if the motor is outside the chamber volume. An alternative is to include the motor and gearing mechanism in the vacuum space. For measuring magnetic anisotropy, a sample rotator is used to rotate the sample *in situ* about a horizontal axis. A different rotator is used to rotate about a vertical axis when the system is configured with optional transverse (saddle) pickup coils.

The MPMS uses an rf SQUID, operating at a 150-MHz bias frequency with a modulation frequency of 100 kHz, in a flux-locked loop. Rf SQUIDs were initially selected for the first MPMS systems because they were cheaper and more readily available than dc SQUIDs. Later, MPMS systems continued to use rf SQUIDS for compatibility with the existing design and control system. As described in Section 12.2.5, the MPMS would not benefit from the increased sensitivity of dc SQUIDS because other noise sources dominate the overall system noise.

Because the SQUID itself cannot tolerate strong fields, it is enclosed in a niobium shield and separated from the magnet region as far as practical in the belly of the dewar. Single-filament superconducting NbTi wires connect the gradiometer to the SQUID capsule. These wires are tightly twisted and immobilized to reduce acoustically induced noise and spurious coupling of the applied field.

While the MPMS has been produced with a number of different magnet configurations, including 1, 2, 5, 5.5, and 7 T versions, the current standard configuration is a high-homogeneity 7 T. The high field homogeneity ($\pm 0.01\%$ over 40 mm length) is necessary because of the relatively large gradiometer baseline (30.4 mm) and the need to scan the sample through the entire gradiometer. The high uniformity ensures that the field variations experienced by the sample during a single scan are low. This is particularly important for samples with irreversible magnetization curves. In the QD system (including the cryocooled version described in Section 12.2.6), the magnet is cooled by direct contact with the helium bath on the outer diameter. On the inner diameter of the magnet, direct contact with the liquid is not used because the magnetic signal from bubbling diamagnetic helium would strongly couple into the gradiometer. Instead, the inner diameter of the magnet is cooled by vertically oriented copper wires embedded in the composite support tube that extends out into the helium bath on both ends of the magnet. The copper wire segments are electrically insulated from each other to eliminate eddy currents. The magnet has a superconducting persistent switch and a quench heater. The switch eliminates current noise from the magnet power supply, thereby providing a very stable measurement field. The field is calibrated based on current in the magnet. Because of trapped flux in the magnet, there can be remnant field errors up to about 1 mT after large field changes. This can be reduced by an order of magnitude by sweeping the field past the set field, several times and by progressively smaller amounts, thus stabilizing flux trapped in the magnet. At zero field, the quench heater can be used to remove trapped flux.

The design and construction of the detection coil are optimized to provide measurement sensitivity, accuracy, and noise immunity, given the mechanical constraints imposed by the other components of the system (e.g., vacuum sleeve). A second-order gradiometer design is used because it significantly reduces noise

contributions from both flux motion in the magnet and from the environment with an order of magnitude improvement compared to a first-order gradiometer [11]. A longitudinal gradiometer (shown in Figure 12.1) detects moments parallel to the applied field, while an optional transverse detection configuration is available that uses saddle coils. The magnet and gradiometer are mechanically rigid to reduce the effects from vibrations, allowing subpicotesla magnetometer sensitivity in tesla-strength fields. In the absence of a vacuum sleeve, the diameter of the detection coils could be optimized for specific sample sizes with a diameter that is small enough for good coupling and large enough that accuracy is not affected by the geometry of the sample. In the MPMS, the smallest diameter coils (20.2 mm) are used which fit on the outside of the vacuum sleeve. Once the coil diameter is determined, the baseline of the gradiometer is optimized for on-axis sensitivity while adequately rejecting field noise from the magnet and environment.

12.2.5 SQUID Input Circuit

To achieve the best overall system performance, the SQUID and input circuit in the MPMS are configured with a combination of shields, filters, and attenuators in a way that sacrifices some sensitivity for enhanced stability. Unlike low-field SQUID magnetometer circuits, this circuit is not strictly optimized to couple the maximum possible flux into the SQUID for a given field at the detection coils. Since the system noise is limited by the magnetic noise from the superconducting magnet anyway, the optimum input circuit design will be such that the SQUID noise contributes only slightly less noise than the magnet, thereby allowing the

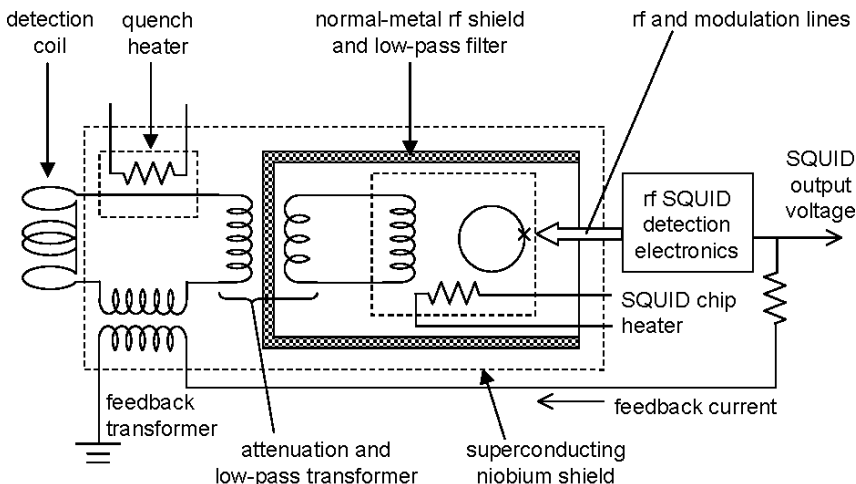


Fig. 12.5 Detection circuit for the MPMS with a double flux transformer and current-nulling (external) feedback. A normal-metal shield separates the primary from the secondary windings of the attenuation transformer, increasing the stability of the feedback loop in the presence of input transients.

maximum dynamic range of operation for the SQUID detection system. Additionally, if other noise sources in the system, such as flux motion in the magnet and environmental rf fields, reach a significant fraction of a flux quantum in the SQUID, the loop will reset, thus spoiling a measurement. Optimizing the overall system performance, including stability, thus requires attenuation and low-pass filtering. As shown in the circuit diagram in Figure 12.5, the input circuit consists of a double flux transformer. The portions of the circuit that are sensitive to static fields are located inside the superconducting niobium shield. Radiofrequency filtering and some signal attenuation are accomplished with a combination of step-down current transformer and continuous normal-metal shield that is inserted between the primary and secondary windings as shown. The continuous shield is a very effective low-pass filter with a rolloff at about 20 kHz. This shield contributes Johnson noise, but is designed to do so at a level below all other accumulated noise sources.

Another feature of the circuit is that the feedback current from the SQUID electronics is applied directly to the detection coil part of the circuit rather than the SQUID. This configuration, which is commonly known as “external” or “current-nulling” feedback, differs from the “internal” or “flux-nulling” feedback configuration in which the feedback flux is applied to the SQUID itself. The problem with using internal feedback in a SQUID-MS is that motion of a magnetized sample produces screening currents in the detection coil and a corresponding change in the field applied to the sample. This is a particular problem for measuring large samples of high susceptibility such as superconductors or soft ferromagnets [6, 12]. Nulling the current directly in the detection coil with the addition of a separate feedback transformer removes this image effect. Note that the 100-kHz modulation signal from the SQUID electronics is still applied directly to the SQUID.

The buildup of persistent currents in the input circuit must also be addressed. During and after applied field changes, imperfections in the gradiometer, field penetration into the niobium shield, and redistribution of trapped flux in the magnet can produce large offset currents in the two closed superconducting loops of the input circuit. Also, flux can become trapped in the SQUID itself, making it noisy. For this, a heater is integrated into the feedback transformer to quench the external input circuit and a second heater is attached to the SQUID chip to quench the SQUID and the internal input circuit. These heaters are turned on whenever the field is changed and prior to each measurement.

12.2.6

Cryocooled MPMS

To eliminate the need for liquid helium transfers, a cryocooled version of the MPMS (MPMS EverCool™) is available. The EverCool uses a GM cryocooler (see Section 7.2.3.4 of volume I of this handbook) combined with a specially designed dewar and gas recirculation system. Like in a standard MPMS, the superconducting components are submerged in a liquid helium bath, which also provides gas-flow cooling of the sample space. A cross-sectional schematic of the EverCool

dewar is shown in Figure 12.6. The GM cryocooler provides >20 W of cooling power at 30 K on the first stage and 1.5 W at 4.2 K on the second stage. The first stage of the GM cooler is linked via flexible copper braids to the thermal shield surrounding the belly of the dewar. A condenser assembly is hard-mounted to the second stage of the cooler, which is further connected to the top of the dewar belly using a soft bellows. This soft mounting reduces the measurement noise caused by the high-frequency components of the ~1-Hz thumping of the cold-head and accommodates differential thermal contraction of the components.

To recover helium gas that is pumped out through the sample-cooling annulus, and to condense helium from an external gas bottle, a gas recirculation system returns helium gas to the dewar belly via the neck. A special baffle in the neck that is thermally anchored to the 30-K shield, serves as a precooler and a purifying coldtrap for the returning gas stream. Once in the belly, the gas is thermally stratified and rises into the condenser assembly through the bellows at the top of the belly. Liquid condensed from the dewar gas drips from the condenser into the belly through the bellows.

The cold head can be cycled on and off either automatically for liquid level control, or manually for performing high-sensitivity measurements. The cold head must be serviced at approximately 10 000-hour intervals. To extend the time be-

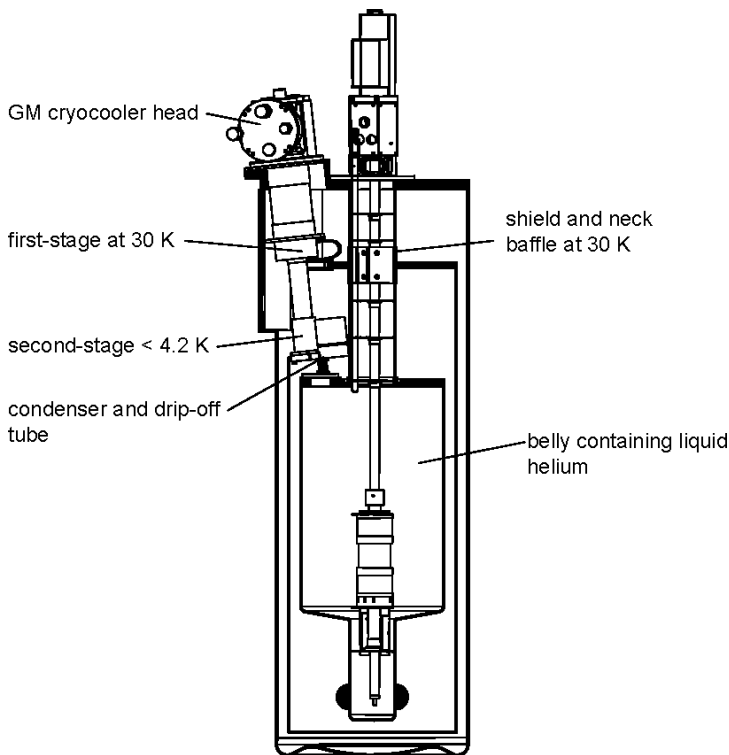


Fig. 12.6 Cross-section of an MPMS EverCool™ dewar.

tween servicing, the head operates at about a 60% duty cycle (10–15 minutes at a time) during periods of low helium boil-off (*e.g.*, no magnet operations). With the cold head running, the noise floor of the instrument is raised by about an order of magnitude. Otherwise, the performance of the EverCool, including temperature and field range, is identical to a standard system.

12.2.7

Measurement Sequence

A measurement is typically performed as a function of applied field or temperature. When measuring at different fields at a fixed temperature, the system performs the following steps for each desired field value:

- Activate the heaters in the SQUID input circuit and hold the SQUID feedback electronics in a reset condition.
- Set the next user-specified field value by ramping the magnet power supply to the persistent current previously stored in the magnet, heating the magnet switch heater, ramping the current in the magnet to the new set-point, holding the current while the persistent switch is cooled, then finally ramping down the applied current.
- Cool the input circuit heaters and reset the SQUID feedback loop.
- Move the sample stepwise through the detection coils, and record the SQUID output as a function of position (*e.g.*, 32 positions over a 40-mm scan length).
- Convert the raw data into a magnetic moment and save the results to a file.

Temperature scans can be performed in a similar way. The temperature can be stabilized at each desired temperature, or measurements can be acquired while sweeping temperature.

In addition to stepwise motion through the detection coils, rapid oscillation of the sample and signal averaging can be used to improve the measurement quality. The Reciprocating Sample Option (RSO) for the MPMS provides this capability. Low-frequency noise, particularly from field redistribution in the magnet caused by flux motion, can cause considerable drift in the SQUID signal, especially in the minutes following a field change. Using a smoothly operating transport mechanism, the lowest frequency noise is avoided by scanning the sample several times per second (up to 4 Hz in the RSO) and averaging the results prior to converting the raw data to a magnetic moment. This frequency is low enough that eddy currents are not important. A variation on this approach is to position the sample at one of the maximum slope positions of the response curve (see Figure 12.1) and oscillate the sample over a much smaller length (a few millimeters). This can be useful if the sample magnetization is highly hysteretic, because this avoids field inhomogeneities present in larger traverses of the magnet.

12.2.8

Measurement Accuracy: Converting Raw Data to Magnetic Moment

Determining the magnetic moment from a measured response curve involves fitting the observed response voltage *versus* axial position z to the theoretical response from a point dipole that is scanned along the axis of the gradiometer. For the MPMS, the fitting function obtained from the Biot–Savart law is given by

$$F(z) = A + Bz + C[g(r, z - D - b/2) - 2g(r, z - D) + g(r, z - D + b/2)], \quad (12.1)$$

where A , B , C , and D are fitting parameters, r is a gradiometer coil radius (10.1 mm), b is the gradiometer baseline (15.2 mm), and the transfer function from each single coil at an axial offset z' is given by

$$g(r, z') = 1/(r^2 + z'^2)^{3/2}. \quad (12.2)$$

The parameters A and B account for any offset and drift in the SQUID signal. The parameter C is proportional to the magnetic moment. The parameter D can be fixed or optionally varied to correct for longitudinal sample centering errors. It must be fixed for small-length RSO scans when there is not enough information in the curve to find the center, or when the moment is very weak compared to the instrument noise or other competing magnetic signals from the sample holder. To account for small system-to-system variations in the gradiometer and input circuit, a 2.5-mm high and 2.5-mm diameter cylinder machined of 99.995%-purity palladium is measured at the factory to obtain an overall calibration factor for each system. This factor is applied to the fit parameter C to get the magnetic moment. This procedure will give an accurate measure of the magnetic moment provided that (1) there is negligible background signal from the sample holder, (2) the sample is small compared to the dimensions of the detection coil, (3) the sample is well-centered radially, and (4) the magnetic moment is not changing during the scan.

For small-moment samples, the background signal from a sample holder may not be neglected and can introduce measurement offsets or incorrect determination of the center position parameter D . All materials used for constructing sample holders have nonzero, though preferably small, susceptibility. Susceptibility variations along the z -direction of the sample holder, including the ends, can produce signals as it is moved through the gradiometer coils during a measurement. An effective way to reduce background signals is to mount a sample in the middle of a holder having uniform susceptibility and cross-section (e.g., a plastic drinking straw) that is long enough for the ends to remain outside of the gradiometer at all points during a measurement scan. If this is not practical, a background subtraction procedure can be used where the raw SQUID signal *versus* position is measured without the sample, and then measured again with the sample. The correct moment is determined by fitting the difference between these two response scans to the ideal dipole response.

In cases where the sample is larger than a few millimeters, or when the sample is not radially centered, the point-dipole analysis will indicate sample moments that are too high or low by up to several percent. For the highest accuracy, the best strategy is to calibrate the system using a sample of known moment and identical size and shape. In practice, it is usually sufficient to look up a correction factor in a table for a standard shape like a cylinder, using the overall dimensions of the sample. For samples up to 3 mm by 3 mm, the corrections are less than 1%. For a 1-mm diameter, vertically oriented cylindrical sample of length 5 mm, the reported moment would be low by almost 4%. For a 1-mm thick disk of diameter 5 mm, the reported moment would be high by almost 4%. If a sample is not radially centered during a scan, the reported moment will be high. For radial offset of less than 1 mm, the error is less than 1%. However, scanning a point dipole along the walls of the sample chamber would result in a +10% error. Also, if the sample is mounted in a way that allows it to rattle back and forth between the walls of the sample chamber, this radial dependence may appear as random noise, or sudden steps in temperature or field scans. In practice, this can be eliminated with careful sample mounting techniques that constrain the radial position during a scan.

12.2.9

Measurement Sensitivity: Magnet and Environment

While sample mounting techniques and instrument calibration techniques determine accuracy, the sensitivity limit for a given measurement is likely to be dominated by either the magnet or the environment. Noise from flux motion in the multi-filament NbTi wire of the magnet is probably the dominant source of measurement noise when environmental sources are minimized. Over most of the magnetic field range, after a new field is set, this flux motion results in an output drift of the SQUID that decays over minutes or hours. When the drift is nearly linear, as it is over most of the field range, the fitting algorithm can compensate for it. Under some circumstances (*e.g.*, small field steps in the range 0.1 to 0.5 T) the drift can have a more complex time dependence, sometime resulting in a several orders of magnitude increase in measurement noise. This is fixed by including wait times at each field for measuring, or by using the rapid oscillation technique described in Section 12.2.7. Using the quench heater imbedded in the magnet is another effective technique for achieving a quiet magnet. A thorough quench, that is, one that heats most of the magnet above its transition temperature, can eliminate the trapped flux, allowing the best sensitivity measurements at zero and small (<0.1 T) fields immediately following the quench. Less thorough quenches, initiated from low or zero field, save helium but are less effective.

In practice, the operating environment may limit the sensitivity. The described instruments typically operate in materials research laboratories. Rarely are facilities like floor vibration isolation, magnetically shielded rooms, or conditioned line power available. Moreover, an MPMS may be located next to high-power materials processing equipment and other unshielded high-field laboratory mag-

nets. In such an environment the second-order gradiometer may not be sufficient to reject the external fields and an optional closed-bottom high-permeability cylindrical magnetic shield around the dewar can be used to shield the detector from the external fields. At high applied fields, vibrations will limit sensitivity. Rubber isolators and thick wooden construction are used in the standard dewar cabinet (see Figure 12.2) to attenuate vibrations from both the floor and the air. This is usually effective in most ground floor or basement laboratories where acoustic noise is dominated by normal voice levels.

12.2.10

SQUID ac Susceptibility

A SQUID-MS system is uniquely adapted to measuring static (dc) magnetization of samples. However, as a general technique for studying magnetic properties, this type of measurement is limited in that it does not directly reveal dynamical information about the magnetic properties of materials. A dynamic (ac) susceptibility measurement is generally required for this.

With an ac susceptometer, a small oscillating field is added to the applied field and a lock-in amplifier used to measure the complex differential susceptibility $\chi_{\text{ac}} = dM/dH$, where M is the magnetization and H the total applied field. Because the measurement is narrow-band, sensitivity is greatly enhanced over a comparable dc technique. At low enough frequencies and small enough oscillation amplitudes, χ_{ac} is real and equal to the slope of the magnetization curve. However, in general there is an imaginary part that contains dynamical information that cannot be found from measurements of the static magnetization.

Most non-SQUID-MS systems use mutual inductance bridges [13] and are limited to frequencies above a few hertz, because the induced signal is proportional to frequency. When configured for ac magnetization measurements, the MPMS has a flat sensitivity of $5 \times 10^{-12} \text{ Am}^2$ down to below 0.1 Hz. On the MPMS system, the ac measurement capability is provided by adding: (1) a separate excitation coil in the bore of the main magnet and (2) electronics capable of driving the excitation coil while also applying a synchronous compensation signal directly to the gradiometer feedback transformer. An oscillating applied field can be produced which ranges in amplitude from 0.1 to 400.0 μT for frequencies from 0.1 to 1000 Hz, on a bias field of ± 7 T. The compensation signal is required because measurements are performed on the most sensitive SQUID range possible. Without the compensation, the 0.1 to 0.2% gradiometer imbalance would couple too much flux directly from the excitation coil.

The system performs the following steps during an ac measurement. First, the sample is positioned in the middle of the lower side coil and the SQUID is then nulled. Nulling involves determining and setting the amplitude and phase of the 50/60-Hz line compensation signal that needs to be injected into the feedback circuit. In addition, a compensation signal is determined and applied to the feedback circuit that reduces the direct coupling of the oscillating field into the imperfect gradiometer. Next, the detected waveform is digitized. Finally, the sample is

moved to the center of the gradiometer and the signal again digitized. A subtraction of the two measurements, properly weighted for the detection coil response function, removes any residual direct coupling between the drive and the detected signal [14].

Because both the drive field and detection coils are outside the sample tube and vacuum sleeve, the effects of eddy currents and the magnetic susceptibility of the tube must be considered. In the MPMS a highly resistive copper alloy with nearly temperature- and field-independent susceptibility, is used for constructing the tubes. Careful frequency-dependent calibration of amplitudes and phase shifts is still required. A further calibration is required to compensate for both field- and frequency-dependent screening of the applied field by the superconducting magnet windings and magnetoresistive effects in the surrounding materials [14].

This technique is very sensitive to differential susceptibility as a function of field and so can detect very weak phase transitions on top of weak background signals. The imaginary component reveals the time-dependent magnetic behavior of spin glasses, superparamagnetic particles, domain-wall motion in ferromagnets, flux motion in superconductors, and other dissipative phenomena in materials. Figure 12.7, for example, shows a superconducting transition in $\text{RuSr}_2\text{GdCu}_2\text{O}_8$ [15]. Both the real and imaginary components of the complex susceptibility χ_{ac} are plotted as a function of temperature. The measurement was performed with an oscillating-field amplitude of 0.1 mT at 1, 10, 100, and 1000 Hz with a static field bias of 1 mT. $\text{Re}(\chi_{ac})$ shows the onset of the Meissner effect below the transition while the peak in $\text{Im}(\chi_{ac})$ occurs at a lower temperature for lower frequencies due to increased coupling of the alternating field to the flux motion at the lower frequency.

Figure 12.8 is another example of an ac susceptibility measurement from a study by Luis *et al.* [42] on horse-spleen ferritin. This protein contains nanometer-size magnetic particles that have been shown to exhibit quantum tunneling

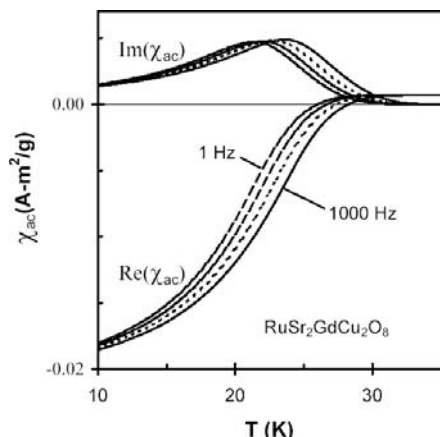


Fig. 12.7 Example of ac magnetization data showing the superconducting transition in $\text{RuSr}_2\text{GdCu}_2\text{O}_8$ [15].

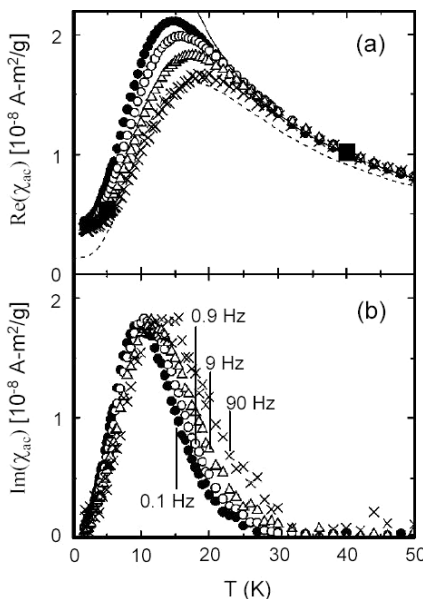


Fig. 12.8 Example of an ac susceptibility measurement on superparamagnetic horse-spleen ferritin at 0.1, 0.9, 9, and 90 Hz.
 (a) Real and (b) imaginary components of χ_{ac} .
 (Reprinted with permission from Ref. [42]. Copyright 1999 by the American Physical Society.)

effects. Above 20 K, ferritin behaves as an ideal superparamagnet, where the moments of the particles are free to rotate in the applied field with characteristic relaxation times. The high-temperature tail of $\text{Re}(\chi_{\text{ac}})$ exhibits Curie-like ($1/T$) paramagnetism, whereas below the peak the moments are progressively frozen. The change in the position of the peak in $\text{Im}(\chi_{\text{ac}})$ with frequency has the logarithmic dependence of a thermally activated Arrhenius process. This frequency dependence was used by Luis *et al.* to verify that the particles were noninteracting. By fitting the temperature dependence of $\text{Im}(\chi_{\text{ac}})$ to a model describing the detailed shape of the curve, they were able to determine the distribution of the particle sizes.

12.2.11 Conclusions and Future Trends

Table 12.1 summarizes the operating specifications for a contemporary MPMS 7-T system. While this table is for the QD instrument, the numbers are representative of other commercial SQUID-MS systems and reflect the design compromises of a general-purpose laboratory instrument meant to be suitable for a broad range of measurement tasks. When increasing, say, the magnet's physical dimensions, one may reduce flux coupling into the gradiometer and improve field uniformity.

However, the larger magnet would be more expensive, helium boil-off would increase, and field changes slowed down due to increased inductance. Increase the sample chamber and vacuum-sleeve diameters to accommodate larger samples and the sensitivity will suffer when smaller samples are measured. The instrument reflects a specific balance of sensitivity, temperature range, field range, field uniformity, accuracy, speed, sample size, instrument cost, operating cost, and so on. For specific measurements, this balance is not always the correct one, and individual researchers will continue to modify commercial systems or build their own. However, changes to the balance in systems like the MPMS are likely to wait for new technological developments in, for example, magnet and cryocooler technologies. Technological developments in these areas could help address some of the most important shortcomings in the current state of the art: measurement speed and sensitivity (limited by the magnet) and operating cost (from helium usage or electricity cost for EverCool).

Tab. 12.1 Performance specifications for the Quantum Design MPMS-XL7.

| Parameter | Value |
|--|--|
| Field range | ± 7.0 T |
| Field stability | 1 ppm/hour |
| Intrinsic field uniformity | 0.01% over 40 mm (± 20 mm from center of pickup coil) |
| Field setting resolution | 0.02 mT up for set fields less than 0.6 T 0.2 mT for set fields greater than 0.6 T |
| Residual field | < 0.5 mT (oscillating approach mode) < 3 mT (no overshoot mode) |
| Maximum sample size (chamber ID) | 9 mm |
| Minimum resolvable change in magnetic moment | < 10^{-11} A m ² up to 0.25 T applied field < 6×10^{-11} A m ² up to 7 T |
| Range of measurement | ± 5×10^{-3} A m ² (option to ±0.3 A m ²) |
| Temperature range | 1.9 to 400 K (800 K with oven insert) |
| Temperature calibration accuracy and stability | ± 0.5% |
| Helium usage | 6 liters/day (superinsulated dewar) |
| Compressor power consumption (EverCool cryocooled dewar option) | 8 kW |

12.3

Scanning SQUID Microscopy

12.3.1

Basic Principles of SQUID Microscopy

Scanning SQUID microscopy [16] involves scanning a sample closely under a SQUID while a computer records the output of the SQUID as a function of the position of the sample. Since a SQUID is extremely sensitive to the perpendicular component of a magnetic field threading its pickup loop, the resulting data can be converted into a false-color image of the magnetic field coming from the sample. Images can be taken of static and audio-frequency magnetic fields, and some work has been also reported on rf and microwave imaging. Compared to other types of magnetic imaging techniques, SQUID microscopes tend to have a wide bandwidth and extremely high flux and field resolution, but only moderate spatial resolution. As with other types of microscopes, SQUID microscopes can be used to examine many different types of samples. They have been used to locate short-circuit faults in semiconductor microchips and multichip modules, study the pairing symmetry of the high- T_c superconductors, find new magnetic materials, image currents from living tissue, and for a variety of other applications-related studies, as discussed at the end of this section.

A SQUID microscope can be built from a few main parts:

- A single small SQUID or array of SQUIDs for detecting the magnetic field.
- A scanning mechanism for positioning the sample at a series of accurately known locations with respect to the SQUID.
- A cryogenic system for keeping the SQUID cold. If the sample is in air at room temperature, this system must also allow the cold SQUID to be brought very close to that sample. Typically this involves a very thin window to separate air from vacuum and a mechanism that allows the window and SQUID to be brought very close together.
- A set of readout electronics for maintaining the SQUID in a flux-locked loop and monitoring its output.
- A computer for recording the output from the feedback loop and controlling the position of the sample.
- Software for processing the data and displaying the results.

The different parts of the microscope must function together and not compromise the performance of the SQUID. Thus, relatively large sources of magnetic field and rf interference, such as pump motors, stepper motors, computers, power supplies, and display monitors should be kept away from the SQUID. For the same reason, only nonmagnetic materials should be used in parts of the apparatus that are close to the SQUID, especially if they experience significant motion with respect to the SQUID. Vibrations and other types of noise in the relative position

of the sample and SQUID must be kept to a minimum, typically below 0.1 μm , in order to not compromise image quality. In addition, if the microscope needs to operate in a relatively harsh rf environment, a Faraday shield should be placed around the SQUID and sample space.

The first fully operational SQUID microscopes were demonstrated in the 1990s [16–39]. Their development was inspired by research on other types of near-field scanned probes, including the scanning tunneling microscope (STM), atomic force microscope (AFM), and magnetic force microscope (MFM) as well as by prior work on SQUID imaging at 1 mm and larger length scales [40]. The field has now advanced to the point where a comprehensive review can no longer be made in a few pages. Many systems have now been built worldwide with notable advances being made in Germany, Japan, France, Russia, and South Korea as well as the USA [41–80]. Despite these advances, most existing systems have performance that is still rather far from optimal. For a typical SQUID-sample separation in the 100 μm range, present high- T_c systems can achieve a spatial resolution of about 20–30 μm , a flux resolution of about $10 \mu\Phi_0 \text{ Hz}^{-1/2}$ and a field resolution of about $30 \text{ pT Hz}^{-1/2}$. The smallest reported coil sizes are now at about 1 μm [41], and proposals for far smaller areas have been made [36]. Spatial resolution of about 100 nm has been achieved using very fine soft magnetic flux guides [48] and the best flux resolution is about $1 \mu\Phi_0 \text{ Hz}^{-1/2}$. In principle much better performance is possible in both respects. Active areas of research in SQUID microscopy include searching for new applications, adding to the capabilities of the instruments, improving the performance, and developing more functional and easily used systems.

SQUID microscopes can be placed into four general categories (see Figure 12.9). In the first type, the sample is at cryogenic temperatures, often at the same temperature as the SQUID (see Figure 12.9(a)). In many of these “cryogenic microscopes,” the sample and SQUID are in vacuum so that a somewhat higher sample temperature can be reached by means of a small sample heater without causing undue heating of the SQUID. Perhaps the most widely known application of this type of microscope has been to basic research on the pairing symmetry of the high- T_c superconductors (see, for example, Refs. [22, 25, 28]); SQUID microscopes have provided strong evidence for $d_{x^2-y^2}$ pairing as well as much information about vortex and current behavior in superconductors [16, 27, 28, 43, 44]. However, since many potentially interesting samples do not function at cryogenic temperatures, this type of microscope has seen less use outside of research laboratories.

The second main type of SQUID microscope is designed specifically for acquiring magnetic images of samples that are in air at room temperature (see Figure 12.9(b)). Of course in these “room temperature” SQUID microscopes, the SQUID still needs to be maintained at cryogenic temperatures. Keeping the SQUID cold, but close to a sample that is in air at room temperature, requires some finesse in design and construction. In practice, these systems are challenging to build, but their ability to examine room-temperature samples has made them more widely used than the other types. The best known application of these systems is in the

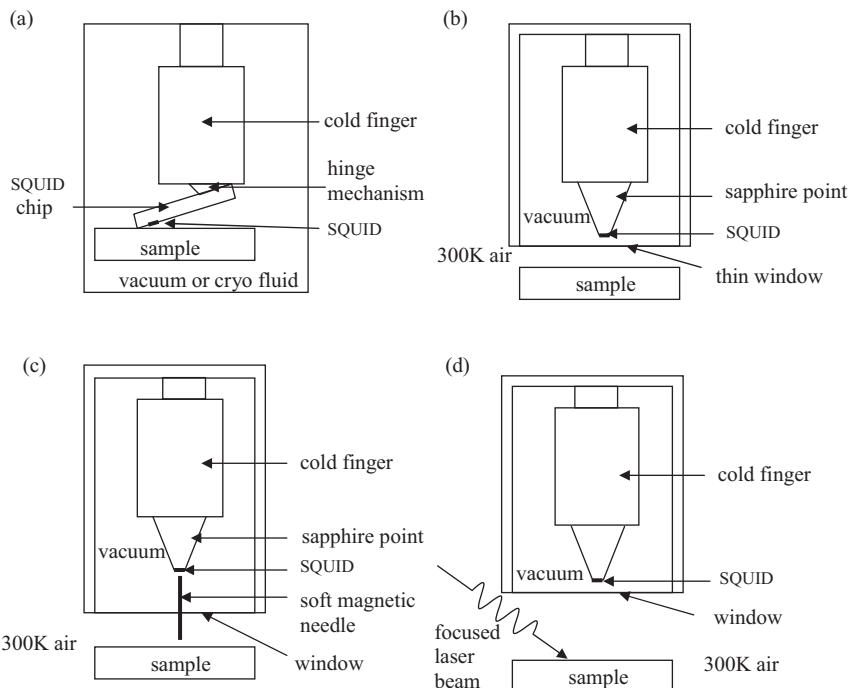


Fig. 12.9 Schematic showing the four main types of SQUID microscopes.
 (a) Cryogenic SQUID microscope, (b) room-temperature SQUID microscope,
 (c) SQUID microscope with a magnetic needle, (d) laser SQUID microscope.

imaging of computer chips and multichip modules for fault analysis, which has been pioneered commercially by Neocera, Inc. [45–47].

The commercialization of room-temperature SQUID microscopes (see Figure 12.10) has been enabled by a convergence of technical and commercial factors. The main commercial factor has been the ability of the microscopes to demonstrate their value by actually helping to solve real manufacturing problems, such as finding short circuits in multichip modules. Working with customers to identify possible situations where the microscopes can help, and then doing the necessary development work to fulfill this possibility, are the key steps in commercialization. For room-temperature systems in particular, important technical factors have been the availability of good high- T_c SQUIDs and cheap magnetically quiet 77-K cryocoolers. Another very significant factor has been the availability of reliable and efficient techniques for converting magnetic field images into images of the source currents that generated the field. For finding the precise location of a short circuit, pictures of the actual current flow, rather than the magnetic field it generates, are much easier to interpret. In addition, it turns out that the spatial resolution of the resulting current images can be up to about an order of magnitude better than the original magnetic field image. Another key factor has been

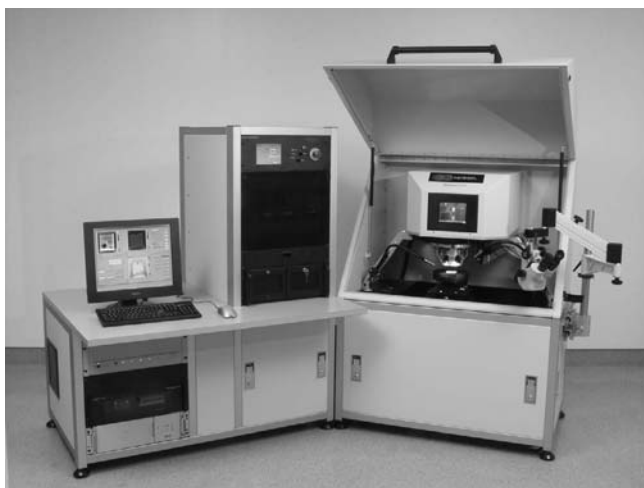


Fig. 12.10 Magma C20™ scanning SQUID microscope used for failure analysis of integrated circuits and multichip modules. (Reproduced with permission from Ref. [47].)

the availability of inexpensive but powerful personal computers that have enabled automation of most of the microscope's operation, including biasing the SQUID, positioning the sample, fine-positioning of the SQUID, data collection, data analysis, and display. The resulting commercial systems are not only relatively easy to operate, but they have been also integrated with other sensors, such as infrared and visible light cameras, and have powerful analysis and display capabilities.

The third main type of SQUID microscope was independently developed by Pitius *et al.* [48–50] and by Tavrin and Siegel at Juelich [51] and involves coupling the SQUID to one end of a high-permeability magnetic needle (see Figure 12.9(c)) [48–60]. The idea is that local magnetic fields from a sample polarize the needle, which then couples this flux to the SQUID. The main advantage of such an approach is the possibility of achieving better spatial resolution of room-temperature objects, although at the price of reduced flux resolution, as discussed below. The fourth main type of SQUID microscope involves using a focused laser beam to generate currents in a sample as shown in Figure 12.9(d). Such “laser-SQUID microscopes” were first developed by Beyer *et al.* [61] and since then have been actively pursued in Japan [62–64]. These systems have been mainly used for examining semiconductor wafers by using the light to generate a current that varies with the local carrier density [61, 63].

12.3.2

SQUIDs for Microscopy

SQUIDs used in microscopy tend to be somewhat different in size and layout than SQUIDs used for more conventional applications. Figure 12.11 shows exam-

ples of low- T_c and high- T_c SQUIDs that have been used in different microscopes [24, 29, 31, 41, 65–67]. There are just a few requirements governing the design of SQUIDs for microscopy. First, the size of the SQUID is one of the main factors that determine the best *spatial resolution* that the system will be able to achieve. SQUIDs used for microscopy tend to be relatively small. Since the SQUID is sensitive to the total flux threading its loop, it measures the average field over the pickup area. If a SQUID is operated very close to a sample, the lateral spatial reso-

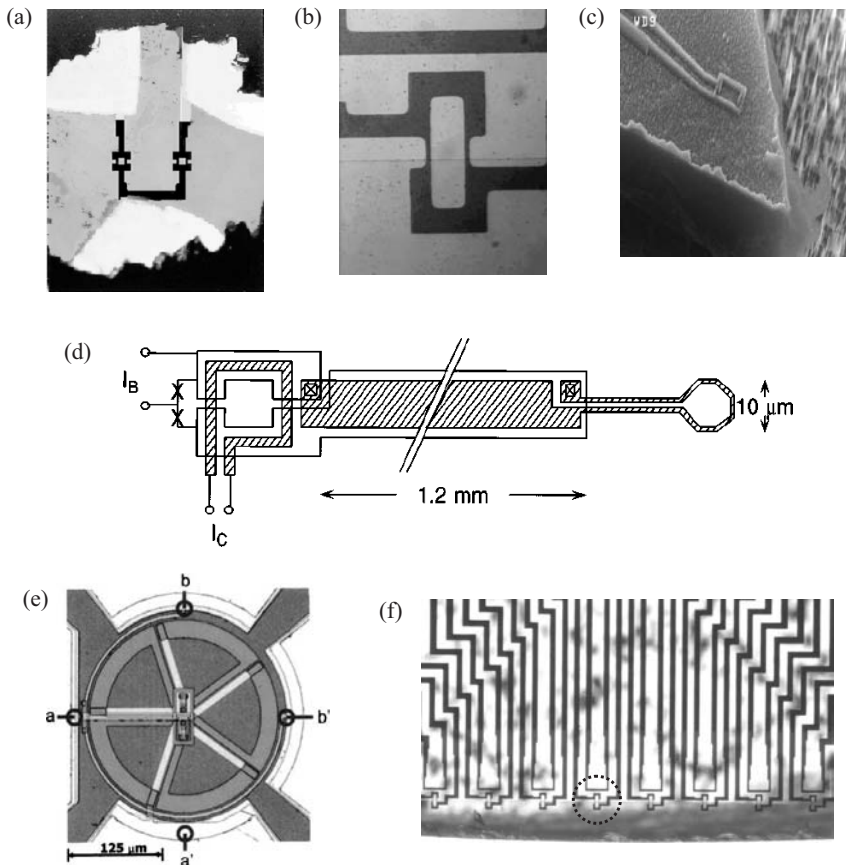


Fig. 12.11 (a) Two YBCO bicrystal z-oriented SQUIDs ($40\text{ }\mu\text{m}$ inside hole length) on the end of a 1-mm tip. (Adapted with permission from Refs. [31] and [65].) (b) $20\text{ }\mu\text{m} \times 60\text{ }\mu\text{m}$ x-oriented SQUID on a SrTiO_3 substrate. (Reproduced with permission from Ref. [67].) (c) Al SQUID with 1- μm pickup close to the edge of shaped chip. (Reprinted with permission from Ref. [41]. Copyright 2002, American Institute of Physics.) (d) Nb SQUID with 10- μm pickup loop close to the edge of

shaped Si chip. (Reprinted with permission from Ref. [24]. Copyright 1995, American Institute of Physics.) (e) 250- μm diameter fractional-turn Nb SQUID for biomagnetic microscopy. (Reprinted with permission from Ref. [66]. Copyright 2004, American Institute of Physics.) (f) Eight $20\text{ }\mu\text{m} \times 60\text{ }\mu\text{m}$ x-oriented YBCO SQUIDS (one circled) on a shaped SrTiO_3 bicrystal substrate. (Reproduced with permission from Ref. [67].)

lution s will be limited to about the side length d of the inner hole of the SQUID. If the SQUID is operated with a separation z from the sample that is much larger than d , then the spatial resolution will be no better than about $4.8z$ because the magnetic field lines spread out as they propagate from the sample (see Eq. (12.14)).

These considerations suggest that in order to achieve the best spatial resolution the SQUID loop should be made as small as possible, have a narrow linewidth to avoid flux-focusing effects, and be operated as close as possible to the sample. However, the smaller the SQUID, the smaller its pickup area and the less sensitive it is to magnetic fields. In addition, it is often the case that one cannot get arbitrarily close to a real source because of an intervening layer of material that is covering the sample. As a rough guide, the best combination of spatial resolution and field resolution can be found by choosing the SQUID to have an inner-hole length d about equal to the minimum achievable separation z between the sources of field in the sample and the SQUID.

The remarks above are what one would naively expect for any near-field probe, *i.e.* where the sample and sensor are separated by distance z that is much less than the wavelength λ of the field being sensed, as is the case for virtually all SQUID microscopes. However, these are only rough rules that are somewhat misleading and far from the complete truth. For example, one can obtain substantially better spatial resolution s than implied above by transforming a magnetic field image into a current density image, as described below.

For applications where the magnetic signals are extremely small, a second key requirement is to obtain the best *magnetic field resolution*. An example of such an application is biomagnetic imaging, where signals of a few picotesla or less are common. In conventional SQUID applications, enhanced field resolution is obtained by using a relatively large-area pickup coil to intercept the flux signal, which is then coupled to the SQUID by means of a flux transformer. However, since microscopy requires fine spatial resolution, it is undesirable to get better field sensitivity by using a large pickup coil. Analysis shows that it is best to use a bare SQUID to detect the field. In fact, a flux transformer actually degrades the field resolution, compared to a bare SQUID of the same size, because of imperfect inductive coupling between the SQUID and the input coil of the flux transformer. For this reason, most SQUID microscopes have been made without using a separate pick up coil and flux transformer. For the best magnetic field sensitivity, a small, low- T_c dc SQUID operated at 4.2 K or below is preferable (see Figure 12.11(c–e)). Such devices can be constructed with noise levels in the range of $1 \mu\Phi_0 \text{ Hz}^{-1/2}$. While high- T_c devices of the same size typically have noise about an order of magnitude higher than this, comparable levels can be achieved. Barthel for example reported a flux noise of about $1.5 \mu\Phi_0 \text{ Hz}^{-1/2}$ in a small narrow-line-width high- T_c SQUID without flux feedback and about twice as high with flux feedback [81]. In fact, one can do better by using a 4.2-K fractional-turn SQUID [82, 83] as Baudenbacher and Wikswo's group at Vanderbilt have demonstrated (see Figure 12.11(e)) [66]. Such devices achieve relatively good performance in a small size by coupling several loops in parallel.

Using an rf SQUID, instead of a dc SQUID, is also possible but has proven to be less popular for microscopy. Use of lower temperatures to achieve even better flux resolution is also possible, but the need for more sophisticated cryogenics and the difficulty of operating the entire system at such low overall noise levels should not be underestimated. Nevertheless, development of a SQUID microscope for operation on a dilution refrigerator has recently been reported by Hasselbach *et al.* [41] at Grenoble [see Figure 12.11(c)] and other systems are now under development [68].

For systems which use low- T_c dc SQUIDs, the best sensitivity occurs for $\beta_L = 2LI_0/\Phi_0 = 1$ and $\beta_C = 2\pi I_0 R^2 C / \Phi_0 < 1$, where I_0 is the critical current of each Josephson junction, L is the SQUID loop inductance, C is the junction capacitance, and R is the resistance shunting each junction. For $\beta_C \ll 1$, Tesche and Clarke found that the magnetic flux noise power spectral density is approximately [70]:

$$S_\phi \approx 16 k_B T L^2 / R, \quad (12.3)$$

where T is the temperature of the SQUID. The minimum detectable magnetic field is the r.m.s. noise in the measured magnetic field:

$$B_n \approx \sqrt{16 k_B T L^2 \Delta f / R A_p^2}, \quad (12.4)$$

where A_p is the pickup area of the SQUID loop and Δf is the measurement bandwidth. From Eq. (12.4), one finds that a 4.2-K SQUID with an inner hole diameter of 10 μm can achieve a field resolution of a few pT $\text{Hz}^{-1/2}$ and a flux noise of less than 1 $\mu\Phi_0 \text{ Hz}^{-1/2}$.

For a SQUID with a square washer layout with an inner hole side length d and an outer side length a , Ketchen and Jaycox [85] found that for $d \ll a$, the pickup area is $A_p \approx ad$ and the inductance is $L \approx 1.25 \mu_0 d$. Substituting these results into Eq. (12.4) reveals that for $d \ll a$:

$$B_n \approx (1.25 \mu_0 / a) \sqrt{16 k_B T \Delta f / R}. \quad (12.5)$$

Thus the minimum detectable field is independent of the inner hole size d and scales inversely with a .

This simple result has two serious shortcomings. First it assumes that the shunting resistance R is independent of the loop inductance L . On the other hand, if the junction capacitance C is constant (fixed junction size), then the constraints $\beta_L = 1$ and $\beta_C < 1$ imply that as L is decreased, I_0 must be increased (to keep $\beta_L = 1$) and R reduced (to keep β_C fixed at a value less than 1). Taking these additional constraints into account, one finds that the minimum detectable field scales inversely with the outer side length a and inversely with the one-quarter power of the inner-hole length d :

$$B_n \approx \sqrt{16 k_B T \Delta f} (1.25 \mu_0)^{3/4} (\pi C / d \beta_C)^{1/4} / a. \quad (12.6)$$

We note that both results imply that the field resolution of a SQUID declines as the SQUID size is reduced, but not as rapidly as the area of the loop.

The second problem with Eq. (12.5) is that the relationship $A_p = ad$ only makes sense for a uniform applied field, and we have not considered what happens if we are close to the source of a spatially varying field. If the SQUID is far from the sample ($z \gg d$) then the field will not vary much over the area of the SQUID and Eqs. (12.5) and (12.6) are appropriate. However, if the SQUID is close to the sample ($z \ll d$), then the amount of flux intercepted at a location depends on the spatial variation of the field as well as the size of the loop. In fact for a point source very close to the SQUID loop, the intercepted flux will be independent of the loop area and thus the average field deduced from that flux will decline inversely with the area. If different types of sources are present, this means that the concept of a pick-up area A_p is ill-defined, or equivalently that the field sensitivity is a poor figure of merit when comparing loops having different sizes. In the limit $z \ll d$, for point-like sources the flux sensitivity is a better figure of merit. We note that for fixed $\beta_C < 1$ and for $\beta_L = 1$, the minimum detectable flux is

$$\Phi_n \approx \sqrt{16 k_B T L^2 \Delta f / R} \approx \sqrt{16 k_B T \Delta f} (\pi C / \beta_C)^{1/4} (1.25 \mu_0 d)^{3/4}. \quad (12.7)$$

Thus the flux resolution improves as the SQUID shrinks as the $3/4$ power of the inner hole size d .

While the above noise expressions are known to work well for describing the white noise in low- T_c SQUIDs, they are not universally valid. Thus, Eqs. (12.3)–(12.7) will fail when the noise becomes so low that quantum effects become important. For typical junction and shunt parameters at 4.2 K, this happens when the SQUID loop diameter reaches about 1 μm . Furthermore, none of these results includes contributions from $1/f$ noise, magnetic noise from the sample itself, external sources of magnetic noise, or rf interference, any of which can dominate the magnetic noise in real systems. Also, Lee *et al.* have shown that surprisingly small random errors in positioning of the sample during scanning (typically below 0.1 μm) can produce large effective magnetic noise in images [69], as discussed in Section 12.3.4. Since there are several different possible causes of noise in SQUID microscope images, the source should be identified before improvements are attempted in a system. Needless to say, if the system's noise is dominated by the effect of position noise, rf interference, or external sources of noise, then very little will be gained by improving the noise due to the SQUID itself.

Additional limitations of these simple relationships become evident if the SQUID is operated close to magnetic materials, normal metals, or superconductors. If $z \ll d$, then inductive coupling to the sample can cause position-dependent variations in parameters such as the SQUID inductance L , the effective pickup area, and the mutual inductance between the SQUID and its feedback coil. Finally, if the SQUID is so small that the width of the lines in the SQUID loop

starts to approach the London penetration depth λ_L of the superconductor, then this must be taken into account when calculating the pickup area and loop inductances.

For microscopes that use high- T_c SQUIDs, the design rules are somewhat different. In particular, typical high- T_c junctions are self-shunted with $\beta_C \ll 1$ and they are usually operated at liquid nitrogen temperatures. The net effect is that a 77-K high- T_c SQUID can typically be expected to have about an order of magnitude worse flux and field resolution than a 4.2-K low- T_c SQUID of the same size. Many high- T_c SQUIDs do not obey Eqs. (12.3)–(12.7) very well. Nevertheless, these simple results are useful for roughing out a design. For a discussion of the behavior of high- T_c SQUIDs and their noise, see Chapters 2 and 5 of volume 1 of this handbook.

If high- T_c SQUIDs are typically less sensitive than low- T_c SQUIDs, why would they be used in a microscope? The main reason is that suitable cryogenic refrigeration is cheaper, simpler, smaller, and less power-hungry at 77 K than at 4.2 K and below. While these differences may be of little consequence for a no-holds-barred laboratory system, they are very significant factors for many laboratories and commercial applications. In addition, high- T_c SQUIDs are still extremely sensitive compared to non-SQUID-based magnetic sensors and any sensor needs only to be “good enough” to do the job at hand.

A third key requirement on the SQUID is that it must be brought in close proximity to the sample to achieve good spatial resolution. Thus, wiring connections to the SQUID must not contact the sample or prevent the SQUID from being brought close to the sample. In z -SQUID systems (the normal to the SQUID pickup loop is parallel to the normal to the sample surface), this problem can be solved by depositing a thin conducting film over the edges of the chip [17–19], and then using silver paint to connect these lines on the edge of the chip to wires that go to the SQUID readout electronics. In this case, one still needs to make the overall size of the SQUID chip small, since it is very difficult to bring the flat face of a large SQUID chip very close to a sample without making contact somewhere.

Another technique involves placing the SQUID near the corner of a substrate and then tilting the substrate so that this corner is brought close to or in contact with the sample (see Figure 12.11(c) and (d)) [20–22, 24]. This technique allows one to use a relatively larger chip, with plenty of room for making SQUID wiring connections. The penalties are minor: one ends up measuring a component of the magnetic field in a noncanonical direction and the chip has to be made so that the SQUID is very near one end. Yet another solution is to adopt an x -SQUID geometry (the normal to the SQUID pickup loop is parallel to the sample surface) (such SQUIDs are shown in Figures 12.11(b) and (f)). Large SQUID chips and simple wire-bond connections can be used, and the orientation is natural for some applications such as imaging current-carrying wires. The disadvantages of this approach are that SQUID chip must be polished carefully to site the SQUID as close as possible to the edge and some applications are not well suited to this orientation, such as imaging samples magnetized in the z -direction.

An alternative approach to achieving very small effective separations for room-temperature samples is to use a magnetic flux guide (see Figure 12.9(c)) [48–60].

In this type of microscope, one end of a sharp magnetizable “needle” is brought in near contact with a sample. The other end of the needle is coupled to a SQUID. Local field from the sample polarizes the needle, producing a signal at the SQUID. This technique can work with room-temperature samples in air if the needle is passed through a window separating air from vacuum (see Figure 12.12). Ideally the spatial resolution is limited by the size of the end of the needle and its proximity to the sample, and not by the size or proximity of the SQUID. The main limitations of the technique are that relatively little of the local flux from the sample may be coupled to the SQUID, and that the guide can produce magnetic noise. Optimizing such systems involves not just the choice of SQUID parameters but also the flux guide geometry, permeability and noise properties and is an active area of research.

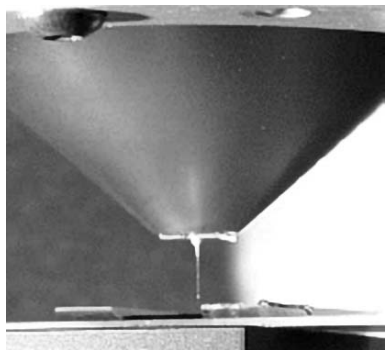


Fig. 12.12 Magnetic needle passing through the window of a room-temperature scanning SQUID microscope. (Reproduced with permission from Ref. [57].)

A fourth key requirement on the SQUID is that it needs to be coupled to a *feedback coil* so that feedback flux is applied to the SQUID to keep the total flux threading the SQUID loop constant. With a flux-locked loop, the output voltage tracks linearly with the applied flux, rather than periodically (see Section 4.2 of volume 1 of this handbook). Ideally, the feedback coil is patterned on the chip to ensure good coupling. It is sometimes useful, and often simpler, to have an external, hand-wired feedback coil. However, such coils tend to be poorly coupled to the SQUID so that larger currents must be used and the resulting flux is applied over a relatively large area. This tends to induce more eddy currents in nearby conducting structures, which can interfere with the operation of the feedback system and imaging.

Finally, for imaging very weak fields, *magnetic shielding* is essential. However, because of its small size, a SQUID used in a scanning microscope will tend to be much less sensitive to magnetic fields than SQUIDs used in most other applications, and the shielding requirements are correspondingly less severe. Thus, a microscope using a high- T_c SQUID a few micrometers on a side would probably only need to be shielded at the level of a few picoteslas. In practice, good audio-frequency images have been obtained using 20-μm inside diameter high- T_c SQUIDs in commercial failure analysis laboratories with only rf shielding.

12.3.3

Cryogenics

All SQUID microscopes require a means for cooling the SQUID below T_c . For cryogenic microscopes (see Figure 12.9(a)), several arrangements are possible. In the simplest systems, the SQUID, sample, and positioning mechanism are cooled by direct immersion in a cryogenic fluid contained in a dewar [17–19]. This has the advantages of simplicity and good thermal contact, and both 77-K and 4.2-K versions of such instruments have been demonstrated. The main disadvantage is that the sample can only be imaged at one temperature. Ice can also accumulate and interfere with the SQUID or positioning mechanism and exchanging samples is likely to be time consuming.

Another approach for cryogenic microscopes is to place the sample and SQUID in a vacuum can which is then cooled in a dewar [20, 21, 24, 25]. This prevents icing and in principle allows the sample and SQUID to be at different temperatures. In such systems, an exchange gas or solid thermal contact is used to cool the SQUID and sample. Figure 12.13 shows two 4.2-K examples of this type of SQUID microscope, one at IBM [32] and one at the University of Maryland [29]. In both cases, the SQUID and positioning mechanism are housed in a vacuum can which is immersed in liquid helium.

Microscopes for imaging room-temperature samples have their own peculiar rules for design and operation. Instruments of this type have been operated using liquid cryogens and cryorefrigerators at both 77 K and 4.2 K. For example, Figure 12.14 shows a schematic of the cryogenic section of a SQUID microscope at the University of Maryland used for imaging room-temperature samples that are in air [29]. The microscope uses a thin-film $\text{YBa}_2\text{Cu}_3\text{O}_7$ high- T_c SQUID which is mounted on the pointed end of a bullet-shaped sapphire rod. The rod is plugged into the end of a liquid-nitrogen-cooled cold finger and projects into the dewar's vacuum space. The SQUID faces a 25- μm thick sapphire window which separates air from vacuum. The diameter of the window (and the end of the point) is about 1 mm to prevent excessive bending under atmospheric pressure. A mechanism allows the window to be moved in the x , y , and z directions and brought up close to the SQUID, ultimately enabling the cold SQUID to be brought within about 25–50 μm of a room-temperature object. The commercial system shown in Figure 12.10 has a similar layout, except that the cold finger is cooled by a Joule–Thomson refrigerator (see Section 7.2.3.2 of volume 1), rather than a liquid nitrogen bath [45–47].

As another example, Figure 12.15 shows a schematic of the lower section of a 4.2-K room-temperature scanning SQUID microscope developed at Vanderbilt University [70, 71]. The Nb SQUID is cooled by solid contact to a copper bracket that is cooled by a liquid helium bath. The SQUID is then coupled via superconducting leads to a multturn pickup coil that is wire-wound on the thinner bottom part of a sapphire cylinder (bobbin) that is at the end of a cold finger. Coil diameters of 250 and 500 μm have been used, with the latter achieving a field sensitivity of 350 $\text{fT Hz}^{-1/2}$ above 1 Hz. The coil faces a 25- μm thick window, which can be

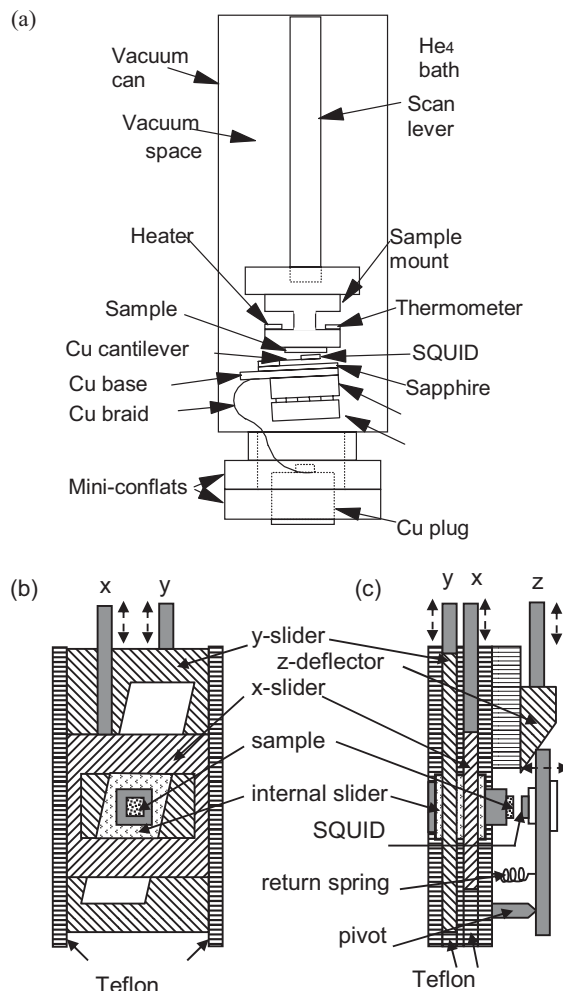


Fig. 12.13 (a) Schematic showing detail of SQUID, sample and scanning mechanism in the IBM 4.2-K scanning SQUID system. (Reprinted with permission from Ref. [32]. Copyright 1999, American Institute of Physics.) Schematics showing (b) front view and (c) side sectional view of scanning section of 4.2-K SQUID system at the University of Maryland. (Adapted with permission from Ref. [29].)

moved close to the SQUID by means of a bellows. The group has exploited the high sensitivity of this system for biomagnetic imaging, as discussed below. This same system was also used with a fractional-turn SQUID (see Figure 12.11(e)) placed at the end of the cold finger. With this 250- μm diameter SQUID, the system achieved a field sensitivity of about 450 fT $\text{Hz}^{-1/2}$ [66].

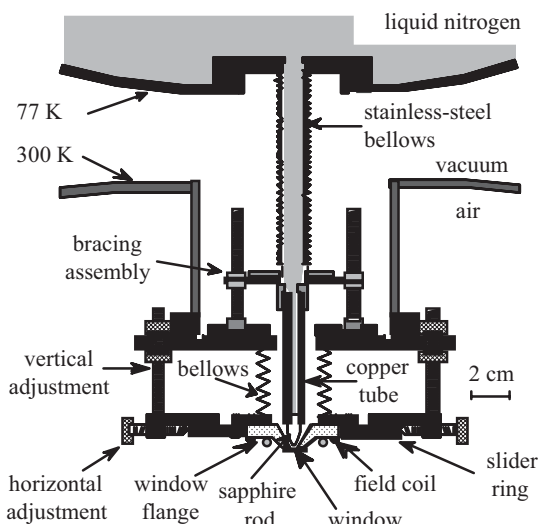


Fig. 12.14 Schematic of lower section of a high- T_c SQUID microscope for imaging room-temperature samples.
(Reproduced with permission from Ref. [29].)

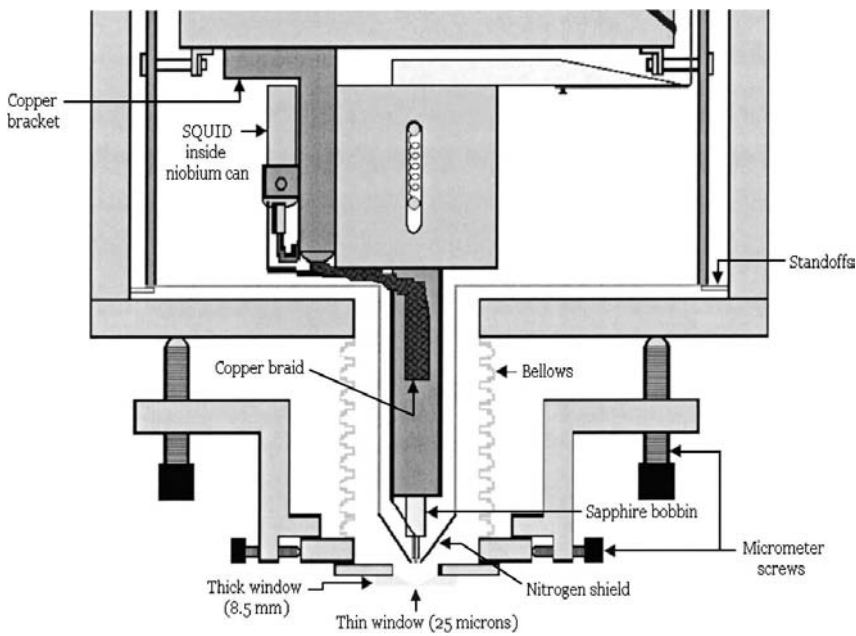


Fig. 12.15 Cross-section of lower section of Vanderbilt LTS-SSM.
(Reprinted from Ref. [71]. Copyright 2002, with permission of Elsevier.)

Finally, some room-temperature microscopes have been built with an “upside down” layout in which the dewar and SQUID are beneath a thin window and the sample above [33, 49]. Figure 12.16 shows an example of such a system built at UC Berkeley, where this design was first developed [33]. The high- T_c SQUID is placed on the end of a cold finger which passes through a vacuum space into liquid nitrogen. The main advantage of such a design is that liquid samples, or samples that are immersed in liquid, can be placed into a well which is closed at the bottom by the thin window. This is particularly convenient for biological samples as it leaves the region above the sample open for optical imaging and the addition of fluid.

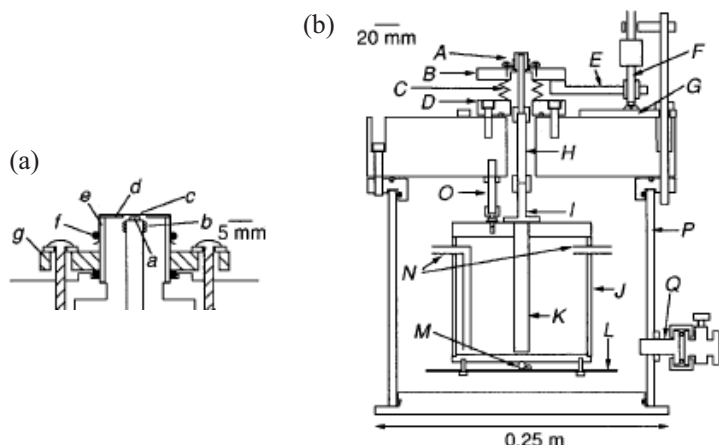


Fig. 12.16 Cross-section of UC Berkley inverted scanning SQUID microscope.
 (a) Detail of thin window *c* and SQUID *a* mounted on vertical cold finger.
 (b) Overall layout of the microscope showing dewar and cold finger beneath the SQUID. (Adapted with permission from Ref. [33]. Copyright 1996, American Institute of Physics.)

12.3.4 Scanning

To obtain clear images, it is essential that the sample positioning mechanism produce smooth, vibration-free, nonhysteretic motion of the sample with respect to the SQUID. In addition, the stage must allow the SQUID to be brought within a few micrometers of the sample and should be non-metallic and non-magnetic so as not to introduce noise, stray magnetic fields, or eddy-current fields. Systems that move the SQUID or that move the sample have both been built. Typically it is preferable to move the sample, because motion of the SQUID tends to introduce tilting of the SQUID loop which in turn can vary the flux coupled into the SQUID from any residual field that is present; such flux variations are undesirable in an image since they do not arise from the sample. In addition, the SQUID must be connected to readout and bias wiring, as well as cryogenics, and

this is most easily done if the SQUID does not move. However, if the sample is large or has many wiring connections of its own, then the best choice may well be to move the SQUID.

The importance of minimizing random errors in the position of the sample while scanning should not be underestimated. Lee *et al.* have pointed out that this “position noise” is likely to be the main source of effective magnetic noise in typical scanning situations [69]. The idea is that if a measurement of magnetic field $B(x)$ is made at the true position x , but the position is recorded as x' , then an error $\Delta x = x' - x$ has been made in the position. Alternatively we could view this as an effective error ΔB in the measurement of the field $B(x')$ at the recorded position x' , where $\Delta B = \Delta x \partial B / \partial x$. For the case of a wire carrying 200 μA of current, and a SQUID measuring the x -component of the field at a distance of $z = 100 \mu\text{m}$, Lee *et al.* find that Δx must be less than about 70 nm in order for the effective noise ΔB to be less than 200 pT [69]. This is a remarkably stringent requirement on positioning, and it becomes much more stringent if the separation is reduced. Furthermore, “position noise” is particularly insidious because its effects are only observable near sharp features, *i.e.* where the spatial gradient of the field is large ($\partial B / \partial x$ or $\partial B / \partial y$). Such features tend to be the very signals one is trying to image. Thus this noise only occurs where it does the most harm, and will not show up if there is no field gradient.

For microscopes that image room-temperature samples, the sample positioning can be accomplished using readily available commercial x - y - z stages. The systems at Maryland have used commercial motor-driven x - y stages made from aluminum. In order to bring a sample up close to the SQUID, a commercial manual z -stage is attached to the top of the x - y stage. We use a 25-mm thick plastic sample stage on top of the z -stage to keep metal portions of the z -stage away from the SQUID.

In cryogenic microscopes, at least part of the positioning mechanism must be cryogenic. Two main techniques have been developed. In one approach the SQUID chip rides above the sample, without making contact [17–19, 29, 30]. For example, in the system shown in Figure 12.13(b), a slider mechanism moves the sample in the x and y directions, while a separate mechanism moves the SQUID in the z -direction, towards or away from the sample. In this system, the positioning mechanism is built from Delrin and Teflon and uses a combination of sliders and wedges to move the sample in the x and y directions. Motion is generated by pushrods that are connected to linear feed-throughs that are driven by stepper motors mounted at the top of the dewar. The SQUID is mounted on a spring-loaded stage which can be moved *in situ* in the z -direction (normal to the sample plane) by means of a simple wedge that is attached to a pushrod and a room-temperature micrometer. For motion in the x -direction (vertical), both the x and y pushrods are raised or lowered together, thereby carrying the x -slider, y -slider, and sample up or down. For y -motion (horizontal), the x -pushrod holds the x -slider fixed and constrains the internal slider and sample to move in the horizontal direction. Pushing down on the y -slider forces the internal slider to the left in Figure 12.13(b) in grooves in the x -slider. The main problem with this approach is

preventing crashing the sensor while scanning during close approaches, especially if the process cannot be monitored visually.

The second main approach for scanning cryogenic samples involves placing the SQUID near the corner of a chip which is mounted on a spring-loaded “hinge mechanism” [20–22, 24]. During scanning, which can involve motion of either the sample or SQUID, the corner of the chip makes soft contact with the sample, thereby holding the SQUID a fixed small distance z above the sample. This approach was pioneered by the Van Harlingen group at the University of Illinois [20, 21] and perfected by Kirtley *et al.* at IBM [22, 24]. Figure 12.13 shows a schematic of the IBM system. The SQUID is mounted on a hinge mechanism at the lower end of the system while the sample is mounted on one end of a scanning lever which extends up to the top of the dewar; the pivot point of the lever is just above the sample holder. Lateral motion of the lever at the top of the dewar produces a much reduced lateral motion of the sample with respect to the SQUID by means of a simple lever arrangement. A few minor disadvantages occur: the sample and SQUID will be in thermal contact, the SQUID chip and sample may tend to get worn away, and the magnetic field component is measured in a direction which is somewhat off the sample normal. Nevertheless, this strategy is the best available scheme for achieving fine spatial resolution over a significant scanning range.

Finally, Hasselbach *et al.* at Grenoble have recently developed a scanning mechanism which borrows techniques from STM and AFM systems to achieve very fine scanning (see Figure 12.17) [41]. In this system, the SQUID is patterned very close to the corner of a shaped Si chip, as shown in Figure 12.11(c). The chip is then glued to one arm of a quartz tuning fork that has a resonance frequency of about 25 kHz (loaded) and a quality factor of 10^4 to 2×10^4 at 0.45 K. The sample is attached to piezoelectric benders that in turn are attached to a linear piezoelectric motor. The benders allow fine control of the separation z between the SQUID and sample, as well as fine x - y scanning over a $\pm 60\text{-}\mu\text{m}$ scan range at 4.2 K. The linear piezoelectric motor is used for making coarse adjustments to z and has a range of ± 5 mm and a resolution of 10 nm. For fine control of z at very close separations, the tuning fork is excited mechanically so that it resonates in a plane perpendicular to the sample. When the corner of the oscillating SQUID chip gets very close to the sample, viscous drag increases and produces a detectable change in the amplitude and phase of the tuning fork’s motion. The phase is detected by monitoring the piezoelectric voltage generated by the tuning fork. For a constant-height scan, the separation is adjusted using the z -piezoelectric bender to keep the drag (phase) constant.

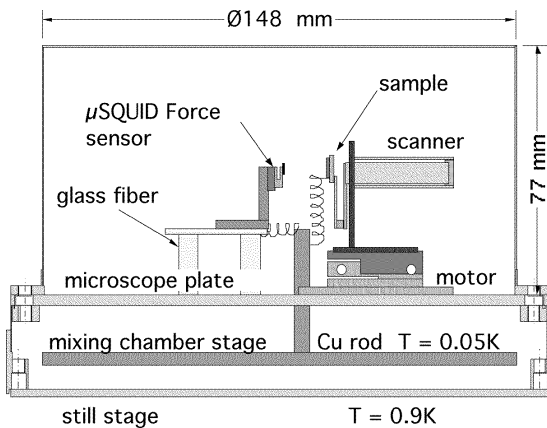


Fig. 12.17 Schematic of Hasselbach *et al.* Micro-SQUID scanning SQUID microscope for an inverted dilution refrigerator. (Reprinted with permission from Ref. [41]. Copyright 2002, American Institute of Physics.)

12.3.5

Collecting Data

The voltage across a SQUID is a periodic function of the applied magnetic flux. To produce an output that is linear in the applied flux, it is necessary to use a null detection scheme or flux-locked loop (see Section 4.2 of volume 1). Microscopes have used both custom-made electronics boxes or commercial SQUID feedback electronics. For example, the systems at Maryland have made use of “Berkeley boxes” [86], feedback electronics that was first developed in John Clarke’s group at Berkeley, or commercial electronics from Star Cryoelectronics [87]. The Berkeley boxes have a bandwidth of about 20 kHz for a 100-kHz modulation frequency and up to about 200 kHz for a 500-kHz modulation frequency. The Star Cryoelectronics systems have a 50–100-kHz bandwidth and a modulation frequency of 256 kHz. The main advantage of the commercial systems is that they interface with a computer and allow for automatic biasing, tuning, and operation of several SQUIDs.

Relatively simple systems can be used to acquire and process SQUID microscope data. Much early data was taken using IBM-compatible 486 personal computers (PC). If large-area images are to be taken at high resolution, it is important to add sufficient memory and hard disk space, although this is not likely to be an issue for a modern PC. An analog-to-digital board is used to acquire data and a motor controller board to run the sample positioning stage. During imaging, we display each individual scan line as it is acquired. The stage position can be acquired by counting the drive pulses supplied to the stepper motors or by reading position encoders. A variety of software programs have been used for controlling the scanning and collecting and displaying data. Most current software of this

type is written using LabView [72] and allows one to take and display data in a variety of ways, including while scanning auxiliary variables such as the amplitude or frequency of an applied field.

12.3.6

Current Source Image Processing and Spatial Resolution

A typical data set from a SQUID microscope includes highly precise values of magnetic field or flux acquired at about 10^5 precise raster scan locations (x, y) above a sample. Such large data sets are most easily understood qualitatively by displaying them as false-color images using readily available visualization software. Images of the raw magnetic field can be very useful for diagnosing problems and providing insight into the behavior of a sample. In some cases, no further analysis may be needed. However, while much can be learned from a magnetic field image, one may ultimately want the location and strength of the sources that generated the field, rather than the field itself. Unfortunately, in general it is not possible to determine uniquely the source strength and location using just magnetic field data; additional information is needed about the nature of the sources. However, in certain favorable cases one can make simple realistic assumptions about the sources and produce a direct transformation of magnetic field data into images of the sources.

The general magnetic inverse problem, and its use in applications such as biomagnetism and nondestructive evaluation (NDE), has been described in detail in Chapter 10. Here we consider the specific case of transforming magnetic data into two-dimensional images of source currents [89] (similar transformation techniques are known for in-plane and out-of-plane magnetization). Such current images are used in SQUID microscopy of integrated circuits because they are not only much more straightforward to interpret than the corresponding magnetic field image, but they can display a considerable enhancement in the spatial resolution.

To understand how the magnetic inverse can improve spatial resolution, Chatraphorn *et al.* analyzed the behavior of the standard inverse map when magnetic noise is present [72]. They found that the resulting current density image will have a mean square current density noise in each pixel given by

$$J_n^2 \equiv (h_0 B_n / \mu_0 d_i z)^2 \cdot [e^{2k_w z} (2k_w z - 1) + 1] / 2\pi, \quad (12.8)$$

where h_0 is the step size (length of a pixel), d_i is the thickness of the conducting layer, B_n is the r.m.s. field noise in each pixel, and k_w is the maximum spatial wave vector (*i.e.*, all spatial Fourier components with wave-vector magnitude greater than k_w are filtered from the image). Examination of this result shows that the noise in the transformed image tends to increase exponentially with $k_w z$. This suggests that if too large a value is used for k_w the resulting current image will be dominated by noise. On the other hand, the spatial resolution in the current image will scale inversely with k_w , since high spatial frequencies are needed to

produce sharp spatial features, so that one would like to choose the largest possible k_w .

Starting from Eq. (12.8), the limit to the spatial resolution can be found readily for specific types of sources. For example, consider an infinitely long wire of thickness d_i carrying current I_y on the y -axis. The true source current density is $J_x = 0$ and $J_y = (I_y/d_i)\delta(x)$, where $\delta(x)$ is the Dirac delta function. This current will generate a magnetic field to which the inversion technique can be applied. The resulting current density image of the wire will be broadened compared to the original delta function due to the cut-off spatial frequency k_w used in the filter function. For a hard cut-off at k_w in Fourier space, the resulting noiseless image is

$$J_y^2(x, y) = \left(I_y k_w / \pi d_i \right)^2 \cdot (\sin(k_w x) / k_w x)^2. \quad (12.9)$$

The spatial resolution s can be defined as the full-width at half-maximum (FWHM) of $J_y^2(x, 0)$:

$$s = 2.783/k_w. \quad (12.10)$$

The maximum signal-to-noise ratio (SNR) for a pixel in the current image is

$$\text{SNR} \equiv \frac{J_y^2(0, 0)}{J_n^2} = 2\pi \frac{\left(\mu_0 I_y k_w z / \pi h_0 B_n \right)^2}{[e^{2k_w z} (2k_w z - 1) + 1]}. \quad (12.11)$$

Thus the peak SNR in the current image decreases exponentially as k_w increases, implying that there is a maximum k_w for which a clear image of the current can be obtained. Using Eq. (12.10) to eliminate k_w , Chatraphorn *et al.* [72] find an implicit function for the ratio z/s :

$$\frac{z}{s} = \frac{1}{2 \cdot 2.783} \ln \left\{ \left(\frac{2\pi}{(S/N)} \left[\frac{2.783 \mu_0 I_y}{\pi h_0 \cdot B_n} (z/s) \right]^2 - 1 \right) / [2 \cdot 2.783(z/s) - 1] \right\}. \quad (12.12)$$

Figure 12.18 shows a plot of z/s versus $I_y/h_0 b_0$ from Eq. (12.12) for $\text{SNR} = 1, 10, 100$, and 1000 (solid diagonal lines) [72]. For a given current I_y , step size h_0 , and noise B_n , the maximum value of z/s will occur when $\text{SNR} = 1$ since for $\text{SNR} < 1$ it will be difficult to distinguish the signal from the noise. The improvement in z/s with decreasing SNR may seem puzzling. However, the SNR here is that of the final transformed current density image, so this behavior just means that as k_w increases (which improves the spatial resolution s) the level of noise in the final picture increases exponentially, and thus poor SNR (more noise) corresponds to better z/s (small s).

From the plot, one also sees that z/s increases (spatial resolution s improves) only logarithmically with increasing $I_y/h_0 B_n$. Thus, to increase z/s from 4 to 5 requires increasing $I_y/h_0 B_n$ by a factor of about 15. Naively, this suggests that little is gained by improving the noise level of the sensor. However, if very large

improvements are made, the sharpening is appreciable. In fact, this is one reason why SQUIDS are so useful for magnetic microscopy; they are so sensitive that they can take advantage of this logarithmic sharpening effect.

For comparison, the naive near-field limit is simply $z/s = 1$ (see Figure 12.18). However, for an infinitely long straight wire that is carrying current I_y along the y -axis, we have

$$B_z(x, z) = \mu_0 I_y x / 2\pi(x^2 + z^2). \quad (12.13)$$

Equating the spatial resolution s_m in the raw magnetic image with the FWHM of B_z^2 , one finds for the magnetic image

$$s_m = 2(1+\sqrt{2})z \approx 4.83 z, \quad (12.14)$$

so that $z/s_m \approx 0.21$ and the B_z image is almost 5 times more blurred than the naive near-field limit. In contrast, Figure 12.18 shows that for $I_y/h_0 B_n > 10^8 \text{ AT}^{-1} \text{ m}^{-1}$, a current image can have $z/s > 1$ and that $z/s > 4$ has been obtained on real samples [72].

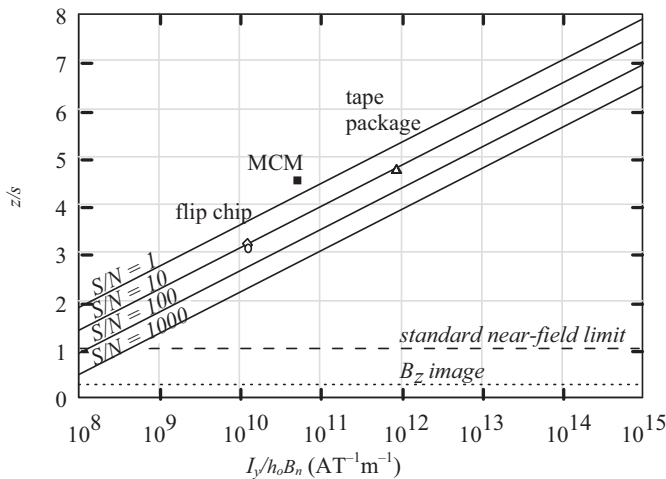


Fig. 12.18 Ratio of SQUID-sample distance z to spatial resolution s versus $I/h_0 B_n$ where I is the current in the sample, h_0 is the step size (pixel size) and B_n is the r.m.s. magnetic field noise in each pixel. Symbols are from real images of different samples. Solid lines correspond to predicted z/s for peak SNR of 1, 10, 100 and 1000 in the final current density image. (Adapted with permission from Ref. [72]. Copyright 2002, American Institute of Physics.)

12.3.7

Applications

SQUID microscopes will be more widely used outside of research laboratories only when they demonstrate their value by solving practical problems. Promising applications typically involve the imaging of small, valuable, room-temperature objects such as magnetic or conducting samples, microelectronic circuits, relatively small metal parts, and biologically active materials or organisms. The common factor is a small sample that not only produces a weak magnetic field but also has a high enough economic value that it is worth spending the time and money needed to acquire a SQUID image.

Some additional general guidelines can be given for evaluating the suitability of SQUID microscopy to an application. Needless to say, the sample needs to produce a magnetic signal that conveys key information that can be spatially resolved by the microscope, but that is not readily observable using any other simple non-magnetic techniques such as visual inspection. Also, the signal strength must be large enough to be measurable (more than about 1 pT), but small enough that key features are not readily observable with simpler and less expensive magnetic sensors (less than about 0.1 mT). Furthermore, the frequency bandwidth where the signal occurs must coincide with the operating bandwidth of the microscope, often below about 100 kHz. It is also important that only a small area needs to be scanned so that the image can be completed in a reasonable amount of time. About 15–20 minutes seems to be the limit for a busy technician, but much less time must be allowed if there are a very large number of samples.

It is usually not a simple task to analyze a new application from the beginning to determine if it is a good candidate for SQUID microscopy. Just considering all of the many possible alternative inspection techniques is a daunting process of elimination. Also, it can be difficult for someone who is not an expert in magnetic fields to determine the expected signal from a sample and how this might be used to produce critical information. However, in many cases, the experts who produce the samples will have already tried all of the more common inspection techniques and found out whether or not they can do the job. Further consideration of SQUID microscopy is likely to be warranted only if no alternative technique is known to work well. In this case, the simplest way to proceed is to contact an existing facility that has a SQUID microscope, discuss the nature of the sample with a SQUID expert, and arrange to have a test image made.

To provide further insight, the following examples illustrate a variety of applications of SQUID microscopes. Since SQUIDs are extremely sensitive to magnetic field, it is easy to image very small amounts of magnetic material. Figures 12.19(a) and (b) show two magnetic images of George Washington's portrait on a US \$1 bill, produced by high- T_c systems at Berkeley [34] and Maryland [29], respectively. The ink used to print the portraits is ferromagnetic and generates an easily measured static field. Producing such images has become something of a tradition in SQUID microscopy for demonstrating that a system is working; the samples are inexpensive, generate relatively robust fields with a range of spatial fea-

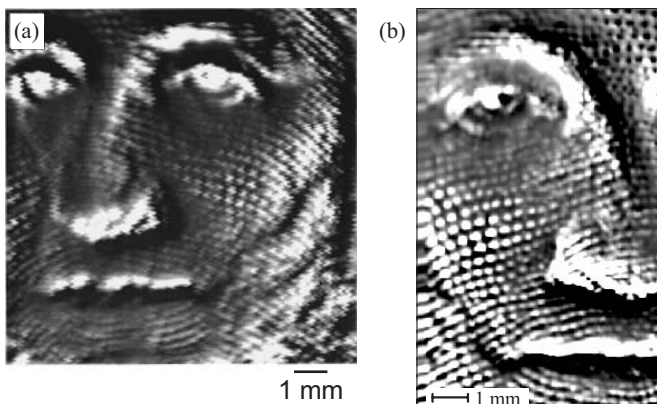


Fig. 12.19 Static magnetic field images of the portrait of George Washington on a US \$1 bill taken using high- T_c SQUID microscopes. (a) Taken using the system at the University of California, Berkeley. White (black) is $+10 \mu\text{T}$ ($-9 \mu\text{T}$). (Reprinted with permission from Ref. [33]. Copyright 1996, American Institute of Physics.) (b) Taken using the system at the University of Maryland. White (black) represents magnetic field pointing out of (into) the page, field range is $\pm 320 \text{ nT}$. (Reproduced with permission from Ref. [26].)

tures, and the resulting images are recognizable to a nonexpert. In Figure 12.19(a) the bill produces a field of about $10 \mu\text{T}$, while in Figure 12.19(b) the bill produces a field of about $\pm 320 \text{ nT}$ at a distance of about $50 \mu\text{m}$ above the sample. The latter image was taken using a high- T_c SQUID with an inner hole diameter of $50 \mu\text{m}$ [18] and the finest features in the image reveals that the spatial resolution is about $70 \mu\text{m}$.

Figure 12.20 shows an image of fields from remnant magnetization in a thin-film Ni–Mn–Ga “combinatorial library” [73], taken using a room-temperature SQUID system. The library is in the form of an array of $2 \text{ mm} \times 2 \text{ mm}$ thin-film squares of differing compositions patterned on a wafer so that the variation of the in-plane magnetization of each square can be detected after the sample is magnetized in an external field. The image was taken with a separation between the SQUID and the sample of $z \approx 0.3 \text{ mm}$. One sees that some squares have a much larger remnant magnetization than others. The idea behind this type of study is to sort through a composition library quickly and accurately with the aim of finding new and interesting magnetic materials. A similar scheme could be exploited to search very large composition libraries for new metals (via eddy current detection), superconductors (via diamagnetic screening), or paramagnetic materials.

Figures 12.21–12.23 show results from a variety of other low-frequency applications. Figure 12.21 shows two remarkable images of half-fluxons in an array of high- T_c corner junctions taken using a 4.2-K scanning SQUID microscope at IBM [75]. Figure 12.21(a) was taken using a Nb SQUID with a $4\text{-}\mu\text{m}$ loop, while an $8\text{-}\mu\text{m}$ loop was used for Figure 12.21(b). Figure 12.22 shows a magnetic field image of the stimulated current flowing in the heart tissue of a rabbit. The data

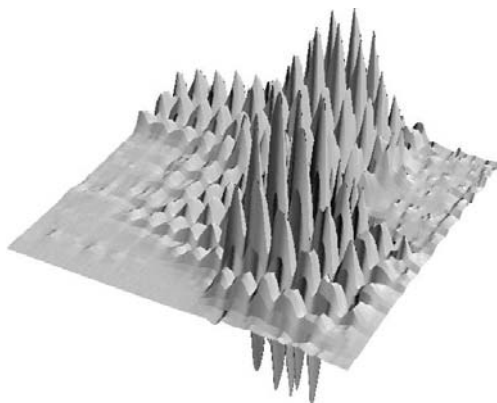


Fig. 12.20 Mapping of magnetic field from a thin-film combinatorial library using a room-temperature scanning SQUID microscope. (Reprinted by permission from Ref. [73]. Copyright 2004, Macmillan Publishers Ltd.)

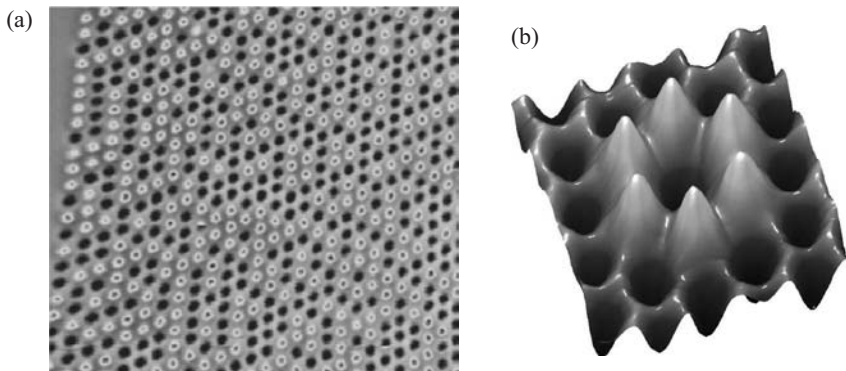


Fig. 12.21 (a) Half-fluxons generated by an array of corner junctions in a high- T_c film. Fluxon to fluxon distance is 12 μm . Taken using IBM 4.2-K scanning SQUID microscope with a 4- μm pickup loop. (b) Six half-fluxons imaged with an 8- μm pickup loop. (Adapted with permission from Ref. [75]. Copyright 2002, Nature Publishing Group.)

were obtained at Vanderbilt using the 4.2-K system shown in Figure 12.15 [70, 71]. In this image, the vectors indicate strength and direction of local current flow. Figure 12.23 shows another type of bio-magnetic measurement, monitoring the magnetic field from a moving magnetotactic bacterium [76]. The magnetic field is produced by a chain of 30–35-nm diameter magnetite particles in the bacterium called magnetosomes. In this case, the bacterium was swimming in a circle, and the resulting variations in field due to the changing orientation and location of the bacterium were detected by a SQUID. These data were collected at Berkeley using the inverted microscope design shown in Figure 12.16.

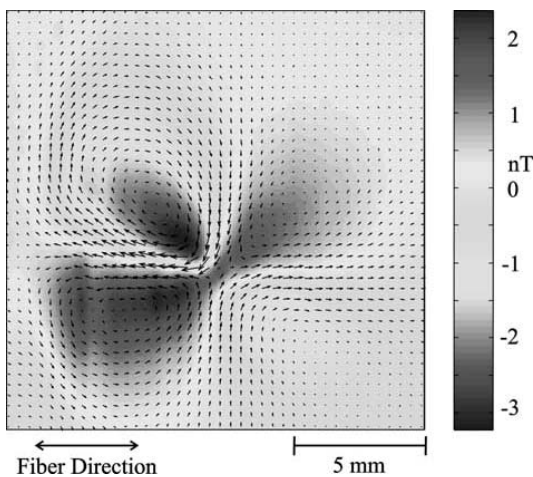


Fig. 12.22 Magnetic field image from a cathodal stimulated current of 1.5 mA in heart tissue. Vectors indicate the strength and direction of local current flow. (Reprinted from Ref. [71]. Copyright 2002, with permission from Elsevier.)

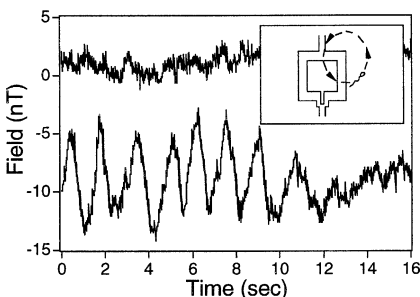


Fig. 12.23 Lower trace shows the magnetic field signal from one magnetotactic bacterium when it happened to swim in a circle close to the SQUID (see inset), measured using the high- T_c SQUID microscope shown in Figure 12.16. Upper trace (offset for clarity) shows the typical small signal from many bacteria. (Reproduced with permission from Ref. [76].)

Figure 12.24(a) shows a magnetic field image from alternating currents flowing in a printed circuit board, taken using the room-temperature system shown in Figure 12.10 [77]. Images of this type have been used to locate shorts in operating multichip modules (MCM) and other circuits [54, 77–80]. In this case, the image has been formed by subtracting two magnetic field images, one from a chip with bump contact damage and the second from the same region on an identical chip that did not have damage. The resulting difference image was then overlaid with a CAD layout showing how the traces in the board connect with the chip, revealing the location of the damage. Figure 12.24(b) shows a $|J(x,y)|^2$ current density image found by performing a magnetic inverse on a high- T_c scanning SQUID image of a portion of a room-temperature multichip module using the system shown in Figure 12.14 [72]. The step size is $h_0 = 20 \mu\text{m}$ and a custom-shaped filter was used with $k_w = 2\pi \times 6 \text{ mm}^{-1}$. An alternating current of 86 μA at 3.354 kHz was used and the SQUID was approximately 340 μm above the (buried) wiring layers. In this

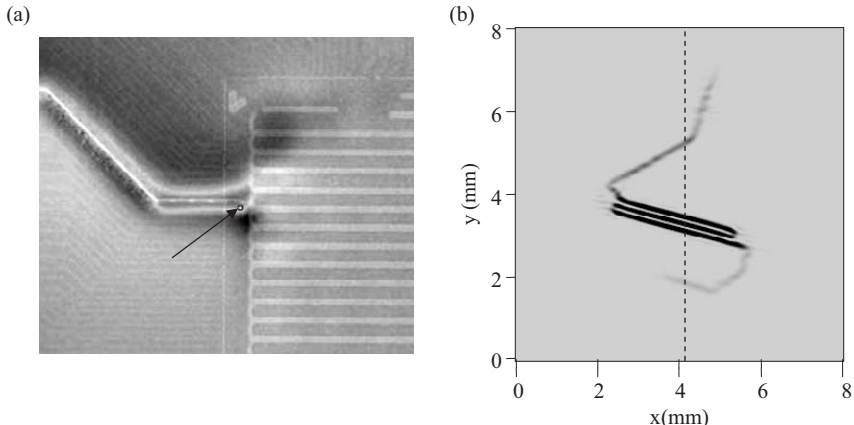


Fig. 12.24 (a) Subtracted magnetic field image from a good and bad current trace going to chip with bump contact damage (see arrow), CAD layout superposed. (Reproduced with permission from Ref. [77].) (b) $|J(x,y)|^2$ current density image found by performing a

magnetic inverse on high- T_c scanning SQUID images of shorted current trace in a room-temperature multichip module. (Reprinted with permission from Ref. [72]. Copyright 2002, American Institute of Physics.)

image, the spatial resolution is about $75\text{ }\mu\text{m}$, so that $z/s = 4.5$ (see the point labeled MCM in Figure 12.18.) This image was compared directly to the CAD layout, allowing the location of the short-circuit connection to be made. With the location known, other techniques can be applied to determine the cause, and fix the underlying steps in the fabrication process to eliminate this type of problem.

Figure 12.25 shows a $|J(x,y)|^2$ current density image (color) of an ASIC (application specific integrated circuit) chip overlaid with an optical image of the chip layout [57]. The image was taken from the backside using the commercial room-temperature system shown in Figure 12.10. The sample had a ground-plane to power-plane short, with the current flowing in two distinct layers. This type of short is often very difficult to find using conventional techniques; since the power and ground planes typically cover the entire sample, the short can be anywhere on the chip, and the high electrical and thermal conductivity of the planes make it difficult to localize the shorts via resistance measurements or thermal imaging.

Another potential application is in NDE of metal parts for small cracks. Application of a magnetic field to a metal induces eddy currents which in turn produce fields which a SQUID can detect. Cracks, thin spots, or other defects which perturb the flow of current will tend to show up in a magnetic image. SQUID systems with detection coils of a few millimeters or larger have been used for NDE for many years [40], as described in Chapter 13. A small SQUID allows the direct imaging of very small buried cracks.

Figure 12.26 shows a 49-kHz eddy-current image of a crack in a riveted aluminum panel taken using the room-temperature microscope shown in Figure 12.14 [23, 29]. The panel has two overlapping 0.2-mm thick aluminum sheets riveted to

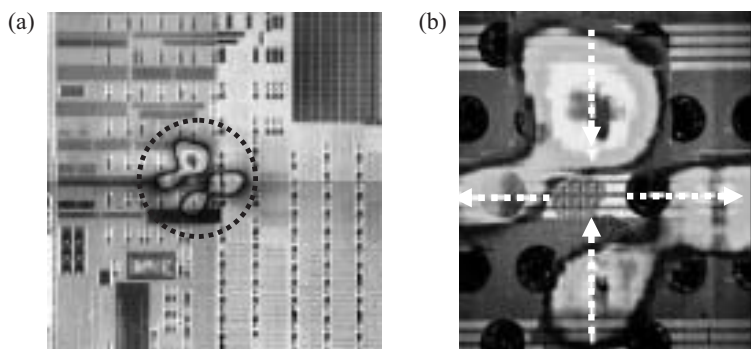


Fig. 12.25 Backside image of current density $J(x,y)^2$ (central four-leaved pattern inside circled region) of ground-plane to power-plane short in an ASIC chip overlaid with an optical image of the chip layout. (b) Detail of circled region in (a) centered on the short. Arrows indicate flow of current into and out of the short on the two layers. (Adapted with permission from Ref. [77].)

a 0.8-mm thick aluminum support strut. The center sheet has a crack which extends diagonally about 2 mm from one of the rivets. The crack was made by shearing the metal apart, and then forcing the two sides back together again leaving no apparent gap between the two sides of the cut. Although not visible to the eye because of the intervening upper aluminum sheet, the crack is readily seen in the eddy-current image.

SQUID microscopes are also capable of imaging high-frequency fields [26], potentially well into the hundreds of gigahertz. This area has been much less developed, however, and only a few demonstrations of such capabilities have been made. In part this is because of the additional complications associated with microwave applications, the lack of suitable readout electronics for the SQUID, and the availability of other simpler techniques such as scanning microwave microscopy. Figure 12.27 shows one example in which the nonlinear response of a high- T_c SQUID was used to image a 400-MHz rf current flowing in a small room-temperature loop at the end of a coaxial line [26]. SQUID microscopy might ultimately be useful for the diagnosis of rf or microwave communication circuits and

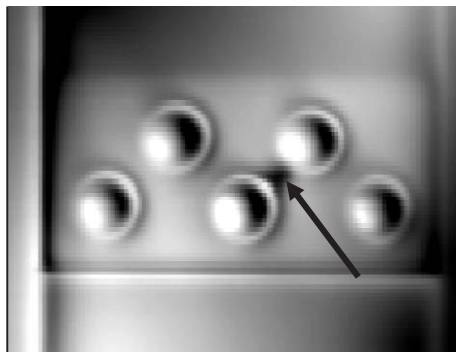


Fig. 12.26 A 49-kHz SQUID eddy-current image of a crack (see arrow) and rivets in 20 mm \times 20 mm section of an aluminum panel. The field was applied using straight wire about 150 μm to one side of the SQUID. The crack is between the center rivet on the bottom row and the rightmost rivet on the top row. (Adapted with permission from Ref. [26].)

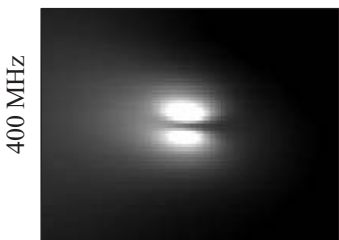


Fig. 12.27 Image of rf field strength just above the edge of a small loop shorting the end of a coaxial cable with a 400-MHz current flowing in the loop. The plane of the loop is perpendicular to the plane of the image. (Reproduced with permission from Ref. [26].)

operating PC chips if the capabilities could be extended to include broadband high-precision readout of nonperiodic signals.

12.3.8

Conclusions and Future Outlook

Whenever considering using a SQUID for a task, it is worth remembering “Weinstock’s Rule”: *Never use a SQUID when a simpler technique will do* [90]. Breaking Weinstock’s rule is folly because SQUIDs tend to be difficult and expensive to use, and in many cases the signals are so large that there is no need for the sensitivity of a SQUID. The main factors that have made SQUID microscopy difficult are the need for cryogenic cooling, the need to bring the cold sensor very near to a warm sample, the complicated nonlinear behavior of the SQUID, and the extreme sensitivity of the SQUID, not just to signals, but to broadband interference and noise.

While the above detrimental factors are readily apparent, it is less obvious that there are some “hidden” factors that convey advantages to SQUID microscopes. Since SQUIDs are extremely sensitive to magnetic fields, and can be made very small or coupled to even smaller flux guides, the resulting microscopes offer a combination of magnetic field and spatial resolution that cannot be obtained in any other way. While conventional SQUIDs tend to be rather large (tens of micrometers to millimeters), there is nothing preventing constructing devices that are submicrometer, except of course having a good reason to do so. Also, the ability to display data pictorially in a simple and intuitive manner is a powerful factor that has helped spread the systems outside the superconducting community; although this is not a unique feature of SQUID microscopes, the lack of such a capability would be extremely detrimental. In addition, data from a scanning SQUID are highly accurate and precise. This not only allows for precise comparisons to be made between theory and experiment, but means that transformed images can have markedly enhanced spatial resolution without introducing much noise or distortion that would occur if the data did not correspond very closely to the field.

Another hidden factor is that although the magnetic field sensitivity of a SQUID becomes worse as the area of a SQUID decreases, it does so only as the square root of the area. This relatively slow decline in performance is not what one might naively expect, and may be missed when comparing SQUID micro-

scopes to other types of magnetic imaging systems. Similarly, the performance of a SQUID depends on parameters such as the operating temperature, shunting resistance and inductance and, particularly for high- T_c SQUIDs, on the quality of the superconducting films and junctions. Comparisons between results for a worst-case SQUID and a best-case alternative technique may not be very revealing.

Finally, in many applications it is impossible to get close to a current source because of an intervening layer of material. Thus comparison with techniques that achieve very high spatial resolution when operating in near-contact with a sample, such as magnetic force microscopy, may be of little practical value.

Some of the obvious difficulties with using a SQUID for microscopy have also turned out to be much less daunting because of technological advances. Thus the availability of cheap but powerful computers has meant that one can automate practically all of the SQUID operation, data collection, and overall system operation in addition to performing complex image processing in real time. Even delicate procedures such as bringing a sample close to the window or a window close to the SQUID have been automated in the most advanced commercial systems. Furthermore there are now many SQUID microscopes in operation worldwide, so that a given application can usually be evaluated using an existing system before any decision is made to construct a new microscope.

Other hidden factors exist that have yet to be exploited. For example, as with any scanned system, high-resolution images of large objects can take a substantial time to acquire. For example, most of the images taken at Maryland used scanning speeds of about 1 mm/s and required 15 minutes to an hour to acquire. However, imaging times can be reduced by a factor of N if an array of N SQUIDs is used. While some work has already been reported along these lines that demonstrates that this approach works, and large arrays of SQUIDs are commonly used in biomagnetic imaging, a clear need has not arisen to drive further progress in this direction. As another example of an unexploited factor, SQUIDs have an extremely large bandwidth of operation, from true dc up to hundreds of gigahertz. Again, the only thing preventing exploitation is a clear application.

The existence of these and other hidden factors implies that considerable care must be taken to obtain meaningful comparisons between SQUID imaging and other types of magnetic imaging. It also suggests that research is likely to continue in this area for some time and that the unique capabilities of the instrument may end up being exploited in unanticipated ways.

References

- 1 Foner, S. (1959) Versatile and sensitive vibrating-sample magnetometer, *Rev. Sci. Instrum.* **30**, 548–557.
- 2 ADE Technologies, Inc., Westwood, MA, has several models including some under the Digital Measurement Systems (DMS) name; Lake Shore Cryotronics, Inc., Westerville, OH, 7400 series; Princeton Measurements Corp., Princeton, NJ, MicroMag series.
- 3 Zijlstra, H. (1970) A vibrating reed magnetometer for microscopic particles, *Rev. Sci. Instrum.* **41**, 1241–1243.
- 4 MicroMag™ Model 2900 AGM System, Princeton Measurements Corp.
- 5 Deaver, B. S., Jr. and Goree, W. S. (1967) Some techniques for sensitive magnetic measurements using superconducting circuits and magnetic shields, *Rev. Sci. Instrum.* **38**, 311–318.
- 6 Zieba, A. (1993) Image and sample geometry effects in SQUID magnetometers, *Rev. Sci. Instrum.* **64**, 3357–3375.
- 7 Robert Fagley, Tristan Technologies, Inc., private communications.
- 8 Philo, J. S. and Fairbank, W. M. (1977) High-sensitivity magnetic susceptometer employing superconducting technology, *Rev. Sci. Instrum.* **48**, 1529–1536.
- 9 Bill Zoekler, Quantum Design, Inc., private communications.
- 10 Measurements courtesy of J. R. O'Brien, Quantum Design, San Diego, CA.
- 11 Vandervoort, K. G., Griffith, G., Claus, H., and Crabtree, G. W. (1991) A low field SQUID magnetometer system for magnetic characterization of high-T_c superconducting samples, *Rev. Sci. Instrum.* **62**, 2271–2275.
- 12 Dummer, D. and Weyhmann, W. (1987) Elimination of the induced current error in magnetometers using superconducting flux transformers, *Rev. Sci. Instrum.* **58**, 1933–1936.
- 13 Deutz, A. F., Hulstman, R. and Kranenburg, F. J. (1989) Automatic mutual inductance bridge for accurate ac susceptibility measurements from 1.2 to 300 K, *Rev. Sci. Instrum.* **60**, 113–120.
- 14 Hibbs, A. D., Sager, R. E., Kumar, S., McArthur, J. E., Singsaas, A. L., Jensen, K. G., Steindorf, M. A., Aukerman, T. A. and Schneider, H. M. (1994) A SQUID-based ac susceptometer, *Rev. Sci. Instrum.* **65**, 2644–2652.
- 15 Sample provided by M. Torikachvili at San Diego State University. Measurements courtesy of J. R. O'Brien, Quantum Design, San Diego, CA.
- 16 Kirtley, J. R. and Wikswo, J. P. (1999) Scanning SQUID microscopy, *Annu. Rev. Mater. Sci.* **29**, 117–148.
- 17 Mathai, A., Song, D., Gim, Y. and Wellstood, F. C. (1992) One-dimensional magnetic flux microscope based on the dc SQUID, *Appl. Phys. Lett.* **61**, 598–600.
- 18 Mathai, A., Song, D., Gim, Y., and Wellstood, F. C. (1993) High resolution magnetic microscopy using a dc SQUID, *IEEE Trans. Appl. Supercond.* **3**, 2609–2612.
- 19 Black, R. C., Mathai, A., Wellstood, F. C. et al. (1993) Magnetic microscopy using a liquid nitrogen cooled YBCO SQUID, *Appl. Phys. Lett.* **62**, 2128–2130.
- 20 Vu, L. N., Wistrom, M. S. and Van Harlingen, D. J. (1993) Imaging of magnetic vortices in superconducting networks and clusters by scanning SQUID microscopy, *Appl. Phys. Lett.* **63**, 1693–1695.
- 21 Vu, L. N., Wistrom, M. S. and Van Harlingen, D. J. (1993) Design and implementation of a scanning SQUID microscope, *IEEE Trans. Appl. Supercond.* **3**, 1918.
- 22 Tsuei, C. C., Kirtley, J. R., Chi, C. C. et al. (1994) Pairing symmetry and flux quantization in a tri-crystal superconducting ring of YBa₂Cu₃O₇, *Phys. Rev. Lett.* **73**, 593–596.
- 23 Black, R. C., Wellstood, F. C., Dantsker, E., et al. (1994) Eddy current microscopy using a 77K superconducting sensor, *Appl. Phys. Lett.* **64**, 100–102.
- 24 Kirtley, J. R., Ketchen, M. B. Stawiasz, K. G. et al. (1995) High-resolution scanning SQUID microscope, *Appl. Phys. Lett.* **66**, 1138–1140.

- 25** Mathai, A., Gim, Y., Black, R. C. *et al.* (1995) Experimental proof of a time-reversal-invariant order parameter with a π shift in $\text{YBa}_2\text{Cu}_3\text{O}_7$, *Phys. Rev. Lett.* **74**, 4523–4526.
- 26** Wellstood, F. C., Gim, Y., Amar, A., Black, R. C. and Mathai, A. (1997) Magnetic microscopy using SQUIDS, *IEEE Trans. Appl. Supercond.* **7**, 3134–3137.
- 27** Jeffery, M., van Duzer, T., Kirtley, J.R. and Ketchen, M.B. (1995) Magnetic imaging of moat-guarded superconducting electronic circuits, *Appl. Phys. Lett.* **67**, 1769–1771.
- 28** Kirtley, J.R., Chaudhari, P., Ketchen, M.B. *et al.* (1995) On the distribution of magnetic flux in high- T_c grain boundary junctions enclosing hexagonal and triangular areas, *Phys. Rev. B* **51**, R12057–12060.
- 29** Black, R. C. (1995) Magnetic microscopy using a superconducting quantum interference device, Ph.D. Dissertation, University of Maryland.
- 30** Mathai, A. (1995) Superconducting quantum interference device microscopy and order parameter symmetry in $\text{YBa}_2\text{Cu}_3\text{O}_7$, Ph.D. Dissertation, University of Maryland.
- 31** Gim, Y. (1996) Novel properties and applications of the high temperature superconductor $\text{YBa}_2\text{Cu}_3\text{O}_7$, Ph.D. Dissertation, University of Maryland.
- 32** Kirtley, J. R., Tsuei, C. C., Moler, K. A. *et al.* (1999) Variable temperature scanning superconducting quantum interference device microscope, *Appl. Phys. Lett.* **74**, 4011–4013.
- 33** Lee, T.S., Chemla, Y. R., Danstker, E. and Clarke, J. (1996) High-transition temperature superconducting quantum interference device microscope, *Rev. Sci. Instrum.* **67**, 4208–4215.
- 34** Lee, T.S., Dantsker, E. and Clarke, J. (1997) High- T_c SQUID microscope for room temperature samples, *IEEE Trans. Appl. Supercond.* **7**, 3147–3150.
- 35** Ketchen, M.B., Kirtley, J. R. and Bhushan, M. (1997) Miniature vector magnetometer for scanning SQUID microscopy, *IEEE Trans. Appl. Supercond.* **7**, 3139–3142.
- 36** Plourde, B. L. T. and Van Harlingen, D. J. (1999) Design of a scanning Josephson junction microscope for sub-micron-resolution magnetic imaging, *Rev. Sci. Instrum.* **70**, 4344–4347.
- 37** Dechert, J., Mück, M. and Heiden, C. (1999) A LTS SQUID microscope for room temperature samples, *IEEE Trans. Appl. Supercond.* **AS-9**, 4111–4114.
- 38** Fleet, E. F., Chatraphorn, S., Wellstood, F. C. *et al.* (1999) HTS scanning SQUID microscope cooled by a closed cycle refrigerator, *IEEE Trans. Appl. Supercond.* **9**, 3704–3707.
- 39** Fleet, E. F. (2000), Design and applications of a cryo-cooled scanning SQUID microscope, Ph.D. Dissertation, University of Maryland.
- 40** See, for example, Wikswo, J. P. (1995) SQUID magnetometers for biomagnetism and nondestructive testing: important questions and initial answers, *IEEE Trans. Appl. Supercond.* **5**, 74–121.
- 41** Veauvy, C., Hasselbach, K. and Mailly, D. (2002) Scanning μ -superconduction quantum interference device force microscope, *Rev. Sci. Instrum.* **73**, 3825–3830.
- 42** Luis, F., del Barco, E., Hernandez, J. M., Remiro, E. *et al.* (1999) Resonant spin tunneling in small antiferromagnetic particles, *Phys. Rev. B* **59**, 11837–11846.
- 43** Plourde, B. L. T., Van Harlingen, D. J., Besselink, R. *et al.* (2000) Vortex dynamics in thin superconducting strips observed by scanning SQUID microscopy, *Physica C* **341–348**, 1023–1026.
- 44** Sugimoto, A., Yamaguchi, T. and Iguchi, I. (2001) Evaluation of supercurrent distribution in high- T_c superconductor by scanning SQUID microscopy, *Physica C* **357–360**, 1473–1477.
- 45** Chatraphorn, S., Fleet, E. F., Wellstood, F. C. *et al.* (2000) Scanning SQUID microscopy of integrated circuits, *Appl. Phys. Lett.* **76**, 2304–2306.
- 46** Fleet, E. F., Chatraphorn, S., Wellstood, F. C. *et al.* (2001) Closed-cycle refrigerator-cooled scanning SQUID microscope for room-temperature samples, *Rev. Sci. Instrum.* **72**, 3281–3290.
- 47** Magma C20™ Scanning HTS SQUID Microscope, Neocera, Inc., 10000 Virginia Manor Road, Beltsville, MD 20705, US Patent 5491411.

- 48** Pitzius, P., Dworak, V., and Hartmann, U. (1997) Ultra-high-resolution scanning SQUID microscopy, *6th Int. Supercond. Electronics Conf. (ISEC '97) Extended Abstracts*, Vol. 3, pp. 395–398.
- 49** Hartmann, U. (2004) Scanning probe methods for magnetic imaging, in *Magnetic Microscopy of Nanostructures*, H. Hopster and H. P. Oepen (eds.), Springer, Heidelberg pp. 285–307.
- 50** Hartmann, U., Wolf, W., and Zhang, Y. (1996) Magnetic flux detector with high spatial resolution, German Patent DE19519480A1.
- 51** Tavrin, Y., and Siegel, M. (1997) New type of HTS SQUID microscope without shielding, *Proc. EUCAS 97, Inst. Phys. Conf. Ser., Appl. Supercond.* **158**, 719–722.
- 52** Tanaka, S., Matsuda, K., Yamazaki, O. et al. (2000) Properties of high T_c superconducting quantum interferences device microscope with high μ -metal needle, *Japan. J. Appl. Phys.* **40**, L431–L433.
- 53** Nagaishi, T., Minamimura, K. and Itozaki, H. (2001) HTS SQUID microscope head with sharp permalloy rod for high spatial resolution, *IEEE Trans. Appl. Supercond.* **11**, 222–225.
- 54** Gudoshnikov, S. A., Deryuzhkina, Y. V., Rudenchik, P. E. et al. (2001) Magnetic flux guide for high-resolution SQUID microscope, *IEEE Trans. Appl. Supercond.* **11**, 219–222.
- 55** Tanaka, S., Matsuda, K., Yamazaki, O. et al. (2002) Development of high- T_c SQUID microscope with flux guide, *Supercond. Sci. Technol.* **15**, 146–149.
- 56** Itozaki, H., Kondo, T., and Nagaishi, T. (2003) HTS scanning SQUID microscope, *Physica C* **392–396**, 1392–1395.
- 57** Woods, S. I., Lettsome, N. M., Cawthorne, A. B. et al. (2003) High resolution current imaging by direct magnetic field sensing, *Proc. 29th Int. Symp. for Testing and Failure Analysis*, ASM International, Materials Park, OH, pp. 6–13.
- 58** Gudoshnikov, S.A. , Liubimov, B.Y., Deryuzhkina, V. et al. (2002) HTS scanning SQUID microscope with high spatial resolution for room temperature samples, *Physica C* **372–376**, 166–169.
- 59** Baek, B., Moon, S. H., Lee, S.-Y. et al. (2004) Investigation of a magnetic flux-guide for a HTS scanning superconducting quantum interference device microscope, *Supercond. Sci. Technol.* **17**, 1022–1025.
- 60** Poppe, U., Faley, M. I., Zimmerman, E. et al. (2004) High temperature superconductor dc-SQUID microscope with a soft magnetic flux guide, *Supercond. Sci. Technol.* **17**, S191–195.
- 61** Beyer, J., Mats, H., Drung, D. and Schurig, T. (1999) Magnetic detection of photogenerated currents in semiconductor wafers using superconducting quantum interference devices, *Appl. Phys. Lett.* **74**, 2863–2865.
- 62** Daibo, M., Kotaka, T. and Shikoda, A. (2002) Photo-induced magnetic field imaging of pn junction using a laser SQUID, *Physica C* **357**, 1483–1487.
- 63** Daibo, M., Shikoda, A. and Yoshizawa, M. (2002) Non-contact evaluation of semiconductors using a laser SQUID microscope, *Physica C* **372–376**, 263–266.
- 64** Nikawa, K. (2002) Laser-SQUID microscopy as a novel tool for inspection, monitoring and analysis of LSI-chip-defects, *IEICE Trans. Electron. E* **85-C**, 746–751.
- 65** Chatraphorn, S. (2000) Room temperature magnetic microscopy using a high- T_c SQUID, Ph.D. Dissertation, University of Maryland.
- 66** Fong, L. E., Holzer, J. R., McBride, K. et al. (2004) High-resolution imaging of cardiac biomagnetic fields using a low-transition-temperature superconducting quantum interference device microscope, *Appl. Phys. Lett.* **84**, 3190–3192.
- 67** Lee, S.-Y. (2004) Multi-channel scanning SQUID microscopy, Ph.D. Dissertation, University of Maryland.
- 68** Liu, Y. (2004) Pennsylvania State University, University Park, private communication.
- 69** Lee, S.-Y., Matthews, J. and Wellstood, F. C. (2004) Position noise in scanning SQUID microscopy, *Appl. Phys. Lett.* **84**, 5001–5003.
- 70** Baudenbacher, F., Peters, N. T., and Wiskwo, J. P. (2002), High resolution low-temperature superconductivity superconducting quantum interference

- device microscope for imaging magnetic fields of samples at room temperatures, *Rev. Sci. Instrum.* **73**, 1247–1254.
- 71** Baudenbacher, F., Peters, N. T., Baudenbacher, P. and Wiksow, J. P. (2002) High resolution imaging of biomagnetic fields generated by action current in cardiac tissue using a LTS-SQUID microscope, *Physica C* **368**, 24–31.
- 72** Chatraphorn, S., Fleet, E. F. and Wellstood, F. C. (2002) The relationship between spatial resolution and noise in scanning SQUID microscopy, *J. Appl. Phys.* **92**, 4731–4740.
- 73** Koinuma, H. and Takeuchi, I. (2004) Combinatorial solid-state chemistry of inorganic materials, *Nature Mater.* **3**, 429–438.
- 74** Takeuchi, I., Famodu, O. O., Read, J. C. et al. (2003) Identification of novel compositions of ferromagnetic shape-memory alloys using composition spreads, *Nature Mater.* **2**, 180–184.
- 75** Hilgenkamp, H. S., Arlando, Smilde, H.-J. H. et al. (2003) Ordering and manipulation of the magnetic moments in large-scale superconducting π -loop arrays, *Nature* **422**, 50–53.
- 76** Chemla, Y. R., Grossman, H. L., Lee, T. S. et al. (1999) A new study of bacterial motion: superconducting quantum interference device microscopy of magnetotactic bacteria, *Biophys. J.* **76**, 3323–3330.
- 77** Knauss, L. A., Woods, S. I. and Orozco, A. (2004) Current imaging using magnetic field sensors, in *Microelectronics Failure Analysis – Desk Reference*, 5th edn, ASM International, Materials Park, OH, pp. 304–312.
- 78** Knauss, L. A., Cawthorne, A. B., Lettsome, N. et al. (2001) Scanning SQUID microscopy for current imaging, *Micro-electron. Reliability* **41**, 1211–1229.
- 79** Orozco, A., Talanova, E., Gilbertson, A. et al. (2003) Fault isolation of high resistance defects using comparative magnetic field imaging, *Proc. 29th Int. Symp. on Testing and Failure Analysis (ISTFA)*, ASM International, Materials Park, OH, pp. 9–13.
- 80** Knauss, L. A., Frazier, B. M., Christen, H. M. et al. (1999) Detecting power shorts from front and backside of IC packages using scanning SQUID microscopy, *ISFTA 99, Proc. Int. Symp. on Testing and Failure Analysis.*, ASM International, Materials Park, OH, pp. 11–16.
- 81** Barthel, K., Koelle, D., Chesca B. et al. (1999) Transfer function and thermal noise of YBCO direct current SQUIDS operated under large thermal fluctuations, *Appl. Phys. Lett.* **74**, 2209–2211.
- 82** Zimmerman, J. E. (1971) Sensitivity enhancement of superconducting quantum interference devices through the use of fractional-turn loops, *J. Appl. Phys.* **42**, 4483–4487.
- 83** Drung, D., Zimmerman, R., Cantor, R. et al. (1991) 37-channel DC SQUID magnetometer system, *Clin. Phys. Physiol. Meas.* **12** (Suppl. B) 21–29.
- 84** Tesche, C. D. and Clarke, J. (1977) dc SQUID: noise and optimization, *J. Low Temp. Phys.* **29**, 301–331; and corrections in Bruines, J. J. P., De Waal, V. J., and Mooij, J. E. (1982) Comment on “dc SQUID: noise and optimization” by Tesche and Clarke, *J. Low Temp. Phys.* **46**, 383–386.
- 85** Ketchen, M. B. and Jaycox, J. M. (1982), Ultra-low-noise tunnel junction dc SQUID with a tightly coupled planar input coil, *Appl. Phys. Lett.* **40**, 736–738.
- 86** Wellstood, F. C., Heiden, C. and Clarke, J. (1984) Integrated dc SQUID magnetometer with a high slew rate, *Rev. Sci. Instrum.* **55**, 952–957.
- 87** pcSQUID System, Star Cryoelectronics, 25-A Bisbee Court, Santa Fe, NM 87508-1412.
- 88** LabVIEW is graphical development software program sold by National Instruments Corporation, 11500 N Mopac Expwy, Austin, TX 78759-3504.
- 89** Roth, B. J., Sepulveda, N. G. and Wikswo, J. P. (1989) Using a magnetometer to image a two-dimensional current distribution, *J. Appl. Phys.* **65**, 361–372.
- 90** Within the SQUID community, this rule is well known and respected due to its wide promulgation by H. Weinstock, see Ref. [47] of Chapter 1 of Volume 1.

13

Nondestructive Evaluation of Materials and Structures using SQUIDs

Hans-Joachim Krause and Gordon Donaldson

| | | |
|----------|---|-----|
| 13.1 | Introduction | 442 |
| 13.1.1 | Motivation | 442 |
| 13.1.2 | History | 443 |
| 13.1.3 | Principles of Operation | 444 |
| 13.2 | Detection of Magnetic Moments | 445 |
| 13.2.1 | Measurement Principle | 445 |
| 13.2.2 | Signal Variation | 445 |
| 13.2.3 | Practical Examples | 446 |
| 13.3 | Magnetic Flux Leakage Technique | 448 |
| 13.3.1 | Measurement Principle | 448 |
| 13.3.2 | Signal Analysis | 450 |
| 13.3.3 | Practical Examples of the Use of SQUIDs | 451 |
| 13.4 | Static Current Distribution Mapping | 452 |
| 13.5 | Eddy Current Technique | 453 |
| 13.5.1 | Measurement Principle | 453 |
| 13.5.2 | Specific Methodology | 455 |
| 13.5.3 | Signal Analysis | 456 |
| 13.5.4 | Practical Examples | 460 |
| 13.5.4.1 | Aluminum Alloy Aircraft Components | 460 |
| 13.5.4.2 | Niobium Sheets for Superconducting Resonators | 463 |
| 13.5.4.3 | Carbon Fiber-Reinforced Polymer | 464 |
| 13.6 | Alternative Excitation Techniques | 467 |
| 13.6.1 | Light: SQUID Photoscanning | 467 |
| 13.6.2 | Heat: Thermoelectric Method | 469 |
| 13.6.3 | Susceptometry | 471 |
| 13.6.4 | Tagging | 471 |
| 13.6.5 | Corrosion | 471 |
| 13.7 | Conclusion and Prospects | 472 |

13.1

Introduction

13.1.1

Motivation

From the time people began to build machines, the need to prevent structural failures was realized. The blanket terms “Nondestructive evaluation” (NDE) and “Nondestructive testing” (NDT) cover the wide variety of inspection schemes which leave the test item intact. The oldest and still most common NDE technique is visual inspection, but since not all defects are visible, more sophisticated passive techniques such as acoustic emission, noise analysis, and leak testing have been developed. Active NDE techniques for finding hidden flaws expose the specimen to some kind of excitation and measure a response. The most common ones include radiography, ultrasonics and electromagnetic techniques. The last denotes the probing of electromagnetic properties of the material under test. In most cases, this probing requires an excitation of the sample and some type of antenna in the vicinity of the sample to record an answer. Except for very high frequencies, the antennae are usually magnetic field sensors. Because of their simplicity and versatility, Faraday (induction) coils are most frequently used, though Hall probes, fluxgates and, following their development for use with computer hard disks, magnetoresistive (MR) devices have all recently become increasingly popular as magnetic field sensors.

The main benefit of using SQUIDs as magnetic field sensors in electromagnetic NDE is their high field sensitivity. Compared to other magnetometers, their sensitivity advantage is particularly pronounced at low frequencies of the order of a few hertz. In addition, SQUIDs offer unsurpassed performance with respect to linearity and dynamic range and they come with an inherent (magnetic flux) calibration.

As NDE applications usually do not require ultimate magnetic field sensitivity but rather demand simple, lightweight systems which are easy to handle, NDE may well become one of the major applications of high- T_c SQUIDs. Indeed, as we will see, there is already one validated procedure in this area involving quality control in the aircraft engine manufacturing industry. In this chapter we explain how this situation has arisen, and then outline three basic techniques by which SQUIDs have been applied in this area. These are the detection of the moments

of magnetic particles in a nonmagnetic base material in Section 13.2, the magnetic flux leakage technique (imaging defects which are magnetic anomalies) in Section 13.3, and the eddy current technique (imaging defects by eddy current mapping) in Section 13.5. The rather academic case of static current distribution mapping is briefly discussed in Section 13.4. Section 13.6 covers a number of special cases which have in common that a magnetic field response is initiated by various other means, such as light, heat, high magnetic fields, marker particles, or electrochemical processes. Finally, we will consider the prospects for future developments.

The first research activities were motivated by interest in exploiting two of the special features of SQUID-based magnetometers, namely their vector properties [1] and their very high sensitivity to *changes* in fields in the presence of large, but constant background fields [2]. However, most later applications have been responses to specific practical needs arising in civil and mechanical engineering structures. Many of these needs have arisen because the structures themselves are aged, and with governments reluctant to commit resources to building new ones, the existing equipment has to be certified for use beyond its original design life.

Most prominent among these problems has been the need to detect deep-lying cracks and corrosion, mostly close to rivet holes, in aircraft structures. The high profile loss of part of the skin of a B737 passenger aircraft above Hawaii has been perhaps the most visible, but the need to extend the life of fleets of military aircraft has been the greater driver. In each case, however, the basic problem was the inability of conventional eddy current methods to penetrate sufficiently deeply to encompass the flaws in question.

Other issues that have attracted the attention of SQUID researchers are cracking and embrittlement of steel in chemical and nuclear plants, cracking in aircraft wheels, and inclusions in high-performance engineering components which can weaken mechanical strength. Apart from purely metallic structures, studies have been made of carbon fiber-reinforced polymer (CFRP) testing, of corrosion, of failure of reinforcing bars in concrete structures such as bridges, and of metal contaminants or lodgements in food and even human bodies.

13.1.2

History

The first activities using SQUIDs for NDE were started in 1982 by H. Weinstock and M. Nisenoff at the Naval Research Laboratory and by G.B. Donaldson *et al.* at the University of Strathclyde. Weinstock and Nisenoff [3, 4] examined anomalies, holes and welds in iron conduits and analyzed magnetic signals of steel bars subjected to tensile stress-strain cycling. Donaldson *et al.* [5, 6] detected flaws in ferromagnetic steel plates; the intended application was underwater inspection of offshore drilling platforms. The first eddy current testing experiments with SQUIDs were carried out by Capobianco *et al.* [7, 8] at the National Bureau of Standards. Wikswo *et al.* from Vanderbilt University were the first group to systematically exploit the possibility of extracting information on the flaw type and geometry

from the measured magnetic field amplitude and phase, thus pioneering the field of solving the inverse problem of SQUID NDE [9, 10].

Prior to 1986, all SQUIDs required the use of liquid helium technology. However high- T_c superconductivity was discovered quite shortly after this and from the NDE point of view this development had two linked effects. First, it became very easy to obtain research funding for all aspect of superconductive applications so that many blue sky ideas found ready resources. Second, although it was thought from theory and from their early performance that high- T_c SQUIDs would inevitably have a sensitivity and noise performance that was inferior to low- T_c devices, this was not seen as a problem for NDE applications which, as we will show, often depend on SQUID features other than extreme field sensitivity. Thus, NDE has become a very important driver for the development of appropriate high- T_c magnetometers and gradiometers, and, because instrument portability is clearly important for many NDE areas, for the development of convenient cryogenic arrangements whether based on liquid nitrogen or other technologies, such as cryocoolers.

The interest in electromagnetic SQUID-based NDE has been growing steadily over the past decade. There is a wide diversity of potentially interesting applications under development. Primarily driven by the challenging demands of aircraft testing and benefiting from steady progress in SQUID sensor and electronics development, SQUID NDE prototype systems were developed to an impressive degree of maturity, as will be shown in subsequent sections.

13.1.3

Principles of Operation

At the outset it is important to realize that all methods of detection ultimately depend on how a flaw in the material under test acts as a source of magnetic field to be detected by a SQUID loop or an associated superconductive pickup coil. The relevant laws are those of low-frequency magnetostatics (except to the extent that the production of a persistent current in a zero-resistance loop is due to Faraday's law). In particular, no phased array techniques such as are found in radar or ultrasonic NDE are available thus far, though it is possible that beam steering techniques, using several SQUID detectors, which have been developed in MEG (Section 11.2), will also be used for NDE purposes. Thus for now, although extremely tiny flaws can be detected, the lateral precision with which they can be *resolved* is at first sight limited to the larger of the pickup coil diameter (D) and the distance between flaw and sensor (h). In fact, as Wellstood has shown (see Chapter 12 on SQUID microscopy), if the image is recorded with high signal-to-noise ratio (which is usually the case when using a SQUID), then the localization precision can be better than that.

In the NDE systems discussed here, coils and distance to sensor are usually larger than a few millimeters: the development of systems in which the superconducting pickup coil is only a few tens of micrometer in diameter, and a matching distance from the room-temperature world, is dealt with in Chapter 12.

13.2

Detection of Magnetic Moments

13.2.1

Measurement Principle

The approach to SQUID NDE, which we first discuss, is the oldest and has its roots in magnetobiology rather than in conventional NDE. It utilizes the fact that a SQUID system is extremely sensitive to tiny changes in flux threading its pickup loops, while being completely insensitive to a large but static magnetic flux threading it. A permanent magnet or a superconducting magnet in the persistent mode therefore produces no time-varying output from a SQUID-based system, provided they are extremely rigidly mounted with respect to it. If, however, a particle, which can be weakly polarized, passes below the magnet and SQUID system, the change in flux linking the SQUID and associated with the field due to the induced dipole moment of the particle may be detected.

13.2.2

Signal Variation

The practical use of NDE tends to rely little on detailed analytical techniques but rather on the recognition of particular signal patterns (signatures) of typical flaws. Nevertheless it is worth considering the algebraic representation of a very basic situation. Consider a small coil of vector area A_p directed along the z -axis, and a magnetic dipole of magnitude M_z , parallel to the z -axis, which moves along the x -axis, passing a distance h directly below the coil. The flux $\Phi(t)$ threading the coil as the dipole moves is easily shown to be given by the simple expression

$$\Phi(t) = \frac{M_z A_p}{4\pi} \left(\frac{3h^2}{r(t)^5} - \frac{1}{r(t)^3} \right) \quad (13.1)$$

where $r(t)$ is the distance of the dipole from the coil at any time. A graph of the magnetic field signal against x shows a broad peak and a zero crossing, to what are always very small negative values, at $x \sim h$. It is also obvious from Fig. 13.1(a) that, if the coil has a diameter d , the graph of the magnetic field signal against x will be broadened by a comparable amount.

As will be seen, the sensing coil is rarely as simple as shown in Fig. 13.1(a), trace M, and is more often a gradiometer consisting of two (as sketched for an axial gradiometer, trace A, and a planar gradiometer, trace P) or more opposing coils, connected in series or parallel. Generally speaking, replacing a magnetometer with a gradiometer will raise the powers of the terms in r by one (e.g., from r^5 to r^6); the numerical coefficients in the two terms will depend on the precise geometry of the gradiometer. For comparison, Fig. 13.1(b) depicts the signal shapes recorded in case of a magnetic dipole oriented in the scanning direction x .

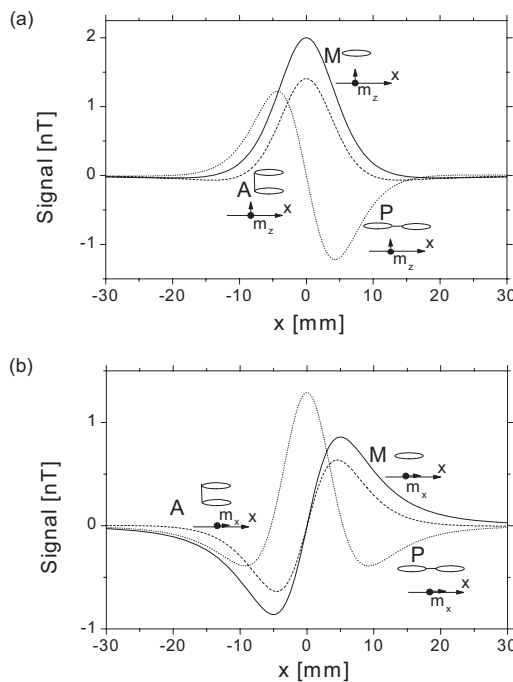


Fig. 13.1 (a) Magnetic field trace of an idealized dipole in the z -direction ($\text{moment } M_z = 10^{-8} \text{ A m}^2$), recorded at a distance $h = 10^{-2} \text{ m}$ with a magnetometer (M, solid line), an axial gradiometer with baseline $5 \times 10^{-3} \text{ m}$ (A, dashed line) and a planar gradiometer with baseline $5 \times 10^{-3} \text{ m}$ (P, dotted line). (b) The same for the dipole oriented in the x -direction.

Note that in usual NDE practice it is the inductive pickup coil of a magnetometer or gradiometer, rather than the dipole or other flaw, which is moved. This has no effect on the basic principles outlined above. However, when the coil is coupled to an unshielded SQUID sensor, such movement through the locally varying static and mains frequency components of the background laboratory fields can present substantial problems: see Section 7.8.3 (volume I) on mobile SQUID systems.

13.2.3 Practical Examples

An early example [11], which illustrates the general principles well, was a biosusceptometer for detecting iron stores in the human liver. It is discussed in detail in Section 11.6.

In the first use of this approach to the detection of flaws in metals, Donaldson *et al.* [5] detected slots in ferric steel plates, with distances of 0.03–0.1 m between slot and sensor, corresponding to the thickness of coatings on typical subsea oil

and gas pipelines. In such a case, the “dipole” moment has a negative sign, produced by a distortion of the polarizing field generated by the magnetostatic boundary conditions at the interface between air and highly polarizable steel (permeability ~ 800) at a rectangular slot. The field is effectively excluded from the slot, so that for a crack of volume V per unit length the effect is to produce an antidipole of magnitude $-B_p V$ per unit length in an otherwise undistorted polarizing field B_p . It was the field at the gradiometer coil (essentially $-3B_p V/h^3$ when the crack is closest to the pickup coil) produced by this “antidipole” that was ultimately detected by the SQUID.

In studies on steel plates, work hardened by repeated bending, but prior to cracking, it was discovered that the resulting dislocation field could also be detected because of the reduction in local permeability $\delta\mu \sim 100\text{--}400$. In the polarizing field, the induced antidipole is of the order of $-(\delta\mu/\mu) B_p V$, where V is the volume of the dislocation field per unit length, smaller than that produced by an open slot, but comparable in magnitude.

The stray fields that are produced by the steel plates, and even effects due to small fluctuations in the distance between excitation coil and surface (lift-off) when a plate is scanned, implied that a resolution as small as $\Delta B_{\min}/B_{\text{pol}} \sim 10^{-5}$ obtained with the liver susceptometer was not achievable, and the limit proved to be two orders of magnitude larger. However, in “structural” NDE, a limit of 10^{-5} was achieved by Wikswo and colleagues [12] while detecting defects and voids in materials such as Plexiglass, but it should be realized that this performance can be achieved only in the presence of negligible drift in the background field. This requires the experiments to be performed in high-quality mu-metal screened enclosures which are expensive.

In the presence of unscreened background drift, one can accept lower resolution if the needs of the application are not compromised. Thus, Tavrin *et al.* have applied the technique to the detection of ferrous inclusions in premagnetized gas turbine discs of aircraft fabricated from a special nonmagnetic alloy [13, 14]. The presence of such inclusions may initiate cracks in these critical parts, and may eventually lead to engine failure. This testing procedure has been commercialized. A second-order unshielded axial gradiometer [15] having $B_N = 130 \text{ fT/Hz}^{1/2}$ (referred to one pickup magnetometer, above 1 Hz) is used to determine quantitatively the mass, radial position, and depth of small ferromagnetic inclusions in the disc. The disc is slowly rotated on a turntable while the SQUID is displaced radially and axially by a mechanically stable arm. The measurement bandwidth is controlled by bandpass filtering in the range between 0.03 and 10 Hz. The measurements of remanent magnetization at two different axial distances from the disc surface are used to calculate the magnetic particle depth utilizing the dipolar $1/R^3$ scaling law. The approximate particle mass is then determined from its dipole strength. A mass of 1 mg is reliably measurable in the depth range up to 70 mm. At a distance of 4 mm, a mass of 10 μg can be resolved. Figure 13.2 shows good experimental agreement between the gradiometer output signal and the mass of artificial inclusions inserted into the disc for the purpose of calibration. Conventional magnetometers were not sensitive enough to provide such a correla-

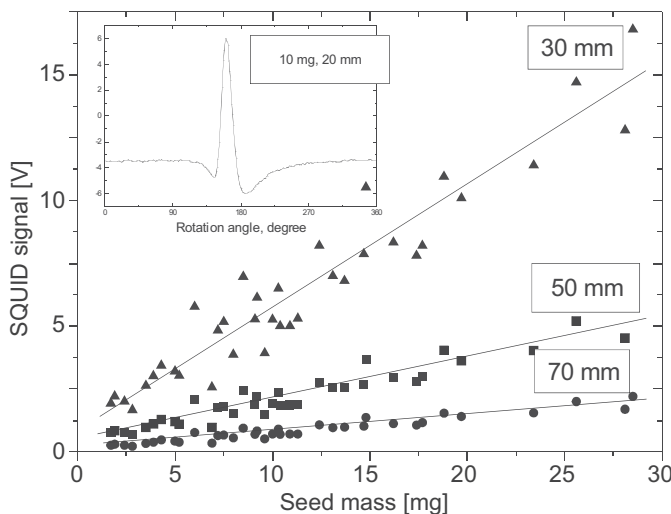


Fig. 13.2 Nondestructive evaluation of aircraft turbine discs. Gradiometer output signal vs. the mass of artificially inserted ferromagnetic inclusions, at three different distances between the sensing SQUID and the inclusion. (From Ref. [17], with permission.)

tion for small inclusions. After several years of commercial turbine disc testing with SQUIDs, a setup comprising of three fluxgate magnetometers was eventually adopted, albeit at the expense of a sensitivity reduction by a factor of 20 [16].

Another example is the detection of small ferromagnetic particles or ferromagnetic inclusions in nonferromagnetic base materials. Nylon fibers and nonmagnetic wires were tested for the presence of such inclusions using a high- T_c SQUID [18]. The wire was moved at speeds up to 800 m/min beneath a 1.3-T magnet and through a magnetic shield surrounding a liquid nitrogen dewar containing the SQUID magnetometer. Ferromagnetic particle sizes down to 47 μm were identified at a distance of 5 mm.

13.3 Magnetic Flux Leakage Technique

13.3.1 Measurement Principle

Surface or subsurface flaws in ferromagnetic materials are usually detected by magnetizing the test sample and monitoring the magnetic flux leakage (MFL) above the surface. Open voids lead to a strong enhancement of the outside stray field due to the local absence of a high-permeability flux guide. Subsurface voids affect the local permeability (magnetization) of the material, and hence also the local stray field. These stray fields are observed either while continuously magne-

tizing the object or by measuring the remanent magnetization. Local changes in the stray field are mapped by scanning the magnetic field sensor over the metal. A few representative examples of applications follow.

The development of an MFL technique using SQUID sensors evolved in the early 1980s as a result of the demand for the detection of flaws in the underwater steel structures of oil platforms [5]. Marine growth prevents close access to the surface of the tested structures so that sensitive far-field techniques were needed. In laboratory tests, low-temperature SQUIDs were used for the detection of flaws in steel plates. The plates were scanned beneath the cryostat containing the SQUID with its pickup coil and a superconducting magnetizing coil generating 10–40 mT in the persistent current mode [19]. The presence of a flaw was manifested by a magnetic dipole signal representing a moment proportional to the flaw volume, the permeability change associated with the flaw, and to the excitation field.

The magnetic stray field measuring method is well suited for the inspection of the prestressed steel tendons in beams forming parts of concrete bridges or roofs [20–23]. Tendon ruptures occur when water penetrates the duct, e.g., due to inadequate grouting, hydrogen-induced corrosion of the steel tendons may be initiated, eventually leading to cracks of single strands and finally to a collapse of the entire structure. For such structures the MFL technique [21, 24] is the only NDT method available.

The principle of the technique is as follows. The tendon hidden in the concrete is magnetized by a field applied outside the concrete by means of a yoke magnet. This exciting field generates a magnetization in the reinforcement bars. The steel acts as a high-permeability magnetic field guide. Ruptures or reductions of the cross-section are local disturbances of the guide, thus giving rise to a magnetic leakage flux (stray field). A probe containing the magnetization device (yoke magnet) and the magnetometer sensors is moved along the direction of the prestressed tendon outside the concrete surface (see Fig. 13.3).

Four high- T_c DC SQUID magnetometers with ramp junctions optimized for high-field performance [26] are used to record the magnetic stray field in the center of the yoke. The magnetic field is recorded while the exciting field is applied (active stray field measurement) and again later when the magnet has been switched off (remanent field measurement). It has been shown that a single

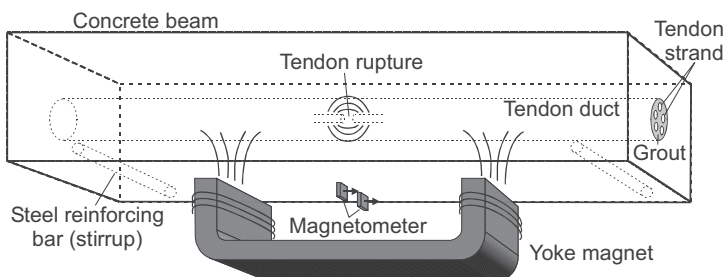


Fig. 13.3 Principle of magnetic detection of ruptures in tendon strands of prestressed concrete beams.

cracked rebar can be found in post-tensioned members, even though the magnetic signature of the crack is attenuated significantly by the shielding effect of the surrounding flawless tendons and the duct around the strands.

13.3.2

Signal Analysis

The stray field signals are affected not only by ruptures of the tendon, but also by the mild steel reinforcing bars (stirrups) close to the probe. Typically, the flaw signal of a tendon rupture is hidden among the signals of stirrups located close to the concrete surface. Provided that the magnetic field sensors have sufficient sensitivity and linearity, flaw signals may be separated from structural disturbance signals by means of a specially developed signal analysis [21]. The magnetic signature of a rebar shows a considerably different shape in the active field, compared to the residual field measurement. The polarity of the residual field measurement signal of the stirrup depends on which pole of the yoke magnet was the last to pass across the stirrup during the magnetization of the member. The residual field measurement R1 is performed after the yoke magnet is switched off at the end of the measurement length. In contrast, the measurement R2 denotes the case where the exciting field is switched off at the starting position after a full magnetization scan. The residual field signature R2 of the stirrup is inverted compared to R1.

This feature directly leads to the first method of stirrup signal suppression: the addition of the two residual field measurements R1 and R2 suppresses the residual field signals of the stirrups, whereas rupture signals are unaffected. Figure 13.4 shows an example of this approach. Nevertheless, the polarity of the residual field signature of a rupture is not well defined.

In order to separate the signals from the reinforcement close to the surface, several active field measurements are conducted at successively increasing magnitude of the exciting field. Because of the strong decrease of the exciting field with distance, the measurement at low excitation fields gives dominant signals from the mild steel reinforcement close to the surface. Because of magnetic saturation, increasing the excitation field only slightly alters the magnetization of the steel close to the surface. The signal increase at higher values of the exciting field B_0 is mainly caused by the steel structures deeper in the concrete.

The second technique to eliminate the signals from the stirrups is direct subtraction of idealized signals. First, the exact position of the stirrups is determined by localizing local maxima (R2) or minima (R1) of the derivative of the axial residual field component. Then, the part of the signal that can be attributed to the stirrups is calculated by fitting the idealized signals of a single stirrup to the measured data (Fig. 13.4, traces F1 and F2). These best-fit stirrup signals are subtracted from the measured signal, yielding corrected signals (C1 and C2 in Fig. 13.4). Adding these two further suppresses remanent signatures of stirrups and brings out the signals of tendon ruptures (Fig. 13.4, center, trace C1+C2). Subsequent correlation analysis with the dipolar signal of a typical void yields the ampli-

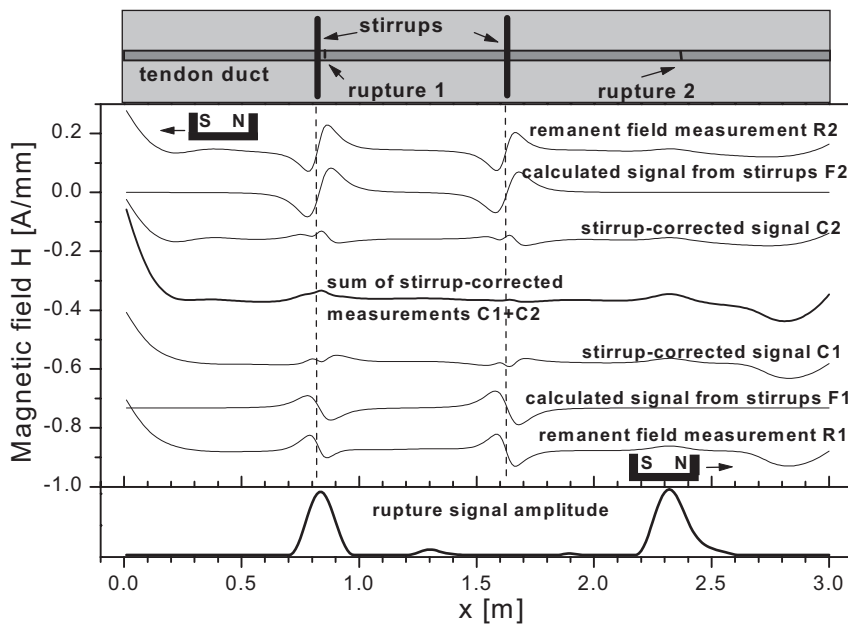


Fig. 13.4 Elimination of stirrup signals using two remanent field measurements after different premagnetization states.

tude of the rupture signal (Fig. 13.4, bottom). The rupture signal amplitude depends on the magnetization of the tendon, on the cross-section of the flaw, and on the distance between the probe and the tendon.

13.3.3

Practical Examples of the Use of SQUIDs

The functionality of the technique has been demonstrated in measurements on German highway bridges. Even though the technique was developed using standard Hall probe sensors, greater linearity and dynamic range was reached with SQUID sensors. Measurements on several bridge structures were carried out. In two such tests conducted in 1995 and 1999, dangerous cracks were detected in a freeway bridge with running car traffic. Rupture indications were verified as originating from broken strands by opening the bridge deck, so that the bridges had to be decommissioned and torn down.

Weinstock and Nisenoff [3] first used SQUID systems to detect anomalous magnetic features. Changes were observed in the remanent magnetic state of steel bars subjected to both elastic and inelastic stress-strain regimes. Barkhausen emission was used to evaluate the magnetic properties of steel [27]. Small, abrupt jumps in the magnetization were characteristic of the transition from reversible to irreversible magnetization states. In a subsequent experiment, the magnetomechanical hysteresis curve of steel was investigated with a SQUID [28]. Prior to

cycling, the stress-induced hysteresis was weak. After 100 000 cycles to 0.7 of the elastic limit, a dramatic increase of the hysteresis was observed.

There are two other potentially important applications of passive methods probing the static magnetic field using a SQUID: (1) testing of nonmagnetic materials, either by probing the susceptibility [29], see Section 13.6.3, or by decorating or tagging the material with magnetic markers to obtain a measurable signal [30–32], see Section 13.6.4, and (2) identification and localization of corrosion by *in-situ* detection of the magnetic signature of the electrical corrosion currents [33–35], see Section 13.6.5.

13.4

Static Current Distribution Mapping

In the case of nonmagnetic but electrically conductive material, the direct current injection scheme can be used. The technique relies strongly on a good electrical contact, and also on the compensation of edge effects and of return current. Injecting or inducing a uniform current distribution in the specimen causes the current to be parallel to the specimen surface under the pickup coil. The ensuing

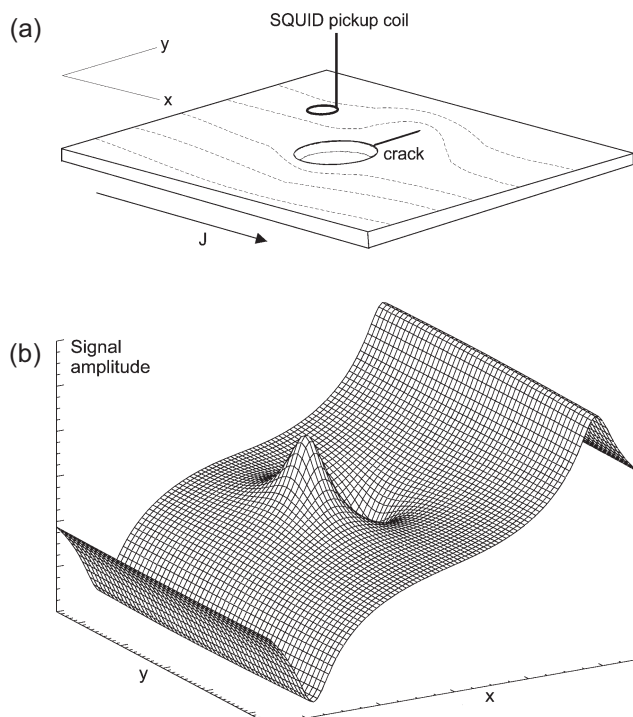


Fig. 13.5 DC current injection: (a) SQUID scan over a sample with a crack adjacent to a hole, (b) resulting B_z magnetic map. (From Ref. [36].)

magnetic field would primarily be parallel to the specimen surface, provided that the scan is carried out close to the center of the sample with a small liftoff distance. The pickup coils measure only the perpendicular component of the magnetic field. A flaw in the specimen will perturb the parallel field and produce a perpendicular component which can then be detected. Figure 13.5 illustrates the SQUID pickup coil being scanned over the sample containing a flaw and the typical magnetic map produced, revealing a signature that commonly has a dipolar shape. Although this technique is not likely to be used in a field instrument, the current distributions produced are similar to those of the planar AC eddy currents produced by sheet inducers (see Section 13.5.2).

For simple flaws in a current-carrying plate, such as flaws with spherical, elliptical or cylindrical shape, the magnetic fields have been calculated analytically [37] and verified experimentally [38]. The analytical solutions, which are possible only for relatively simple geometries, are often more valuable than finite-element calculations of more realistic flaws [39]. However, the results of these analytical calculations are only valid in the case of sufficiently low frequencies.

13.5 Eddy Current Technique

13.5.1 Measurement Principle

Nonmagnetic metallic materials are usually tested by an alternating current technique. Using alternating current has two significant advantages. First, the coupling of the excitation to the material under test can be done inductively, thus eliminating the need for electrical contacts. Second, a narrowband, lock-in readout scheme can be used, resulting in noise reduction. In addition, the quadrature component containing information on excitation energy dissipation can be evaluated. Eddy current testing using a SQUID sensor is of special value in a highly safety-relevant area such as aircraft testing, where small deep flaws need to be localized and sized in aluminum structures [40]. The first demonstration of aircraft lap joint testing was performed in shielding using a low- T_c SQUID system [41]. Subsequently, a cryocooled low- T_c system with remote differential sensing coils was used to demonstrate the detection of very small, hidden flaws without shielding [42].

The penetration depth of the electromagnetic excitation wave, the skin depth

$$\delta = (\pi \mu \sigma f)^{1/2} \quad (13.2)$$

restricts the depth at which flaws may be found. For a plane wave excitation of a medium with conductivity σ and permeability $\mu = \mu_0 \mu_r$ (with the permeability of free space, μ_0 and the relative permeability of the medium, μ_r), δ denotes the depth at which the amplitude decreases to $1/e$. For aluminum, $\delta \approx 2.6$ mm at

1 kHz and ≈ 8.3 mm at 100 Hz. Herein lies one of the advantages of SQUIDs over Faraday coils as sensors for use in aircraft testing. Because SQUIDs sense changes of the magnetic flux whereas induction coils are sensitive to the rate of change of flux, SQUIDs can be used at much lower excitation frequencies than Faraday detectors. Since lower frequencies translate to larger skin depths, it follows that SQUIDs can “see” flaws at greater depths, which is very important given the thickness of the span structures in the next generation of large planes for which it may well be necessary to probe to depths of about 50 mm. Note also that the phase of the penetrating signal changes with depth, and that in particular at δ the phase is rotated by π . Thus, the phase lag of the response signal contains information about the flaw depth.

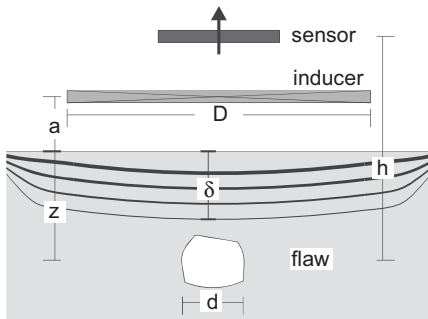


Fig. 13.6 Schematic of the important parameters of eddy current testing: a – liftoff, D – inducer size, d – flaw size, h – distance between flaw and sensor, z – flaw depth, δ – skin depth.

In general, optimum flaw signals are obtained only if the inducer type, the excitation frequency, and geometry details (Figure 13.6) are chosen as the result of an optimization process. The change of response field ΔB_z , as detected by the sensor, can be regarded as consisting of five components, as summarized by the following expression:

$$\Delta B_z = \overbrace{j_{c0}(f, a) \cdot \exp\left(-\frac{\eta(f, z) \cdot z}{\delta(f)}\right)}^{\text{surface current density}} \cdot \overbrace{\lambda}^{\text{current density amplification}} \cdot \underbrace{\exp(-a_{\text{flaw}}(f, z) \cdot z)}_{\text{decay of return field}} \cdot \overbrace{f(d, z)}^{\text{attenuation for small cracks}}. \quad (13.3)$$

The magnetic field change depends on (1) the surface current density, depending on the inducer size D and shape, frequency f , and liftoff a ; (2) the exponential decay of the excitation field, as it penetrates the sample, governed by a decay coefficient δ/η , with a slowly varying function η of frequency f and depth z , describing the decay properties of the inducer field; (3) the interaction process of the current density with the flaw, phenomenologically described by an amplification factor λ ; (4) the decay of the response field, governed by a decay coefficient $1/a_{\text{flaw}}$; and (5) the attenuation of the flaw signal, yielding a d/z dependence in the case when the flaw size d is smaller than its depth z in the material, and unity when $d > z$ [43].

13.5.2

Specific Methodology

Eddy current testing using induction coil sensors is a technique well established in NDE [44]. Since the first demonstration of eddy current testing with a SQUID sensor in the mid-1980s [7, 8], several research groups have developed low- as well as high- T_c SQUID systems for this purpose. Different excitation schemes have been designed, partially in close analogy to conventional eddy current probes.

With the advent of high- T_c SQUID gradiometers for unshielded operation, appropriate excitation–detection schemes were developed [45]. Figure 13.7 depicts a number of exciter types and common excitation–detection schemes frequently used in SQUID NDE. Note that all schemes except one (Fig. 13.7(e)) are differential in nature. Absolute coil excitation denotes excitation with a single coil, differential excitation means excitation with two (or more) spatially separated coils arranged such that their far fields cancel out. The latter yields differential, self-referencing eddy current signals. The technique of self-referencing, *i.e.* comparing signals from two spatially separated areas of the sample against each other, allows one to enhance the sensitivity to small flaws. It can be accomplished either by using a differential exciter such as a double-D coil (Figs. 13.7(a–c)), or a differential readout such as a planar gradiometer parallel to the sample surface (Figs. 13.7(c) and (d)), or by using excitation–detection schemes in which exciter and readout are oriented orthogonal to one another (Fig. 13.7(f)).

The reduction of the distance between the SQUID at cryogenic temperature and the sample at room temperature is of great importance, especially if shallow flaws are to be found. Sophisticated liquid helium cryostat design with the pickup coil mounted on a cold finger in the vacuum space, as close to room temperature as possible [46, 47], led to significant improvements in performance. This and similar concepts were also adapted for liquid nitrogen cryostats [48] (see also Section 12.3.3 on cryogenics for SQUID microscopy).

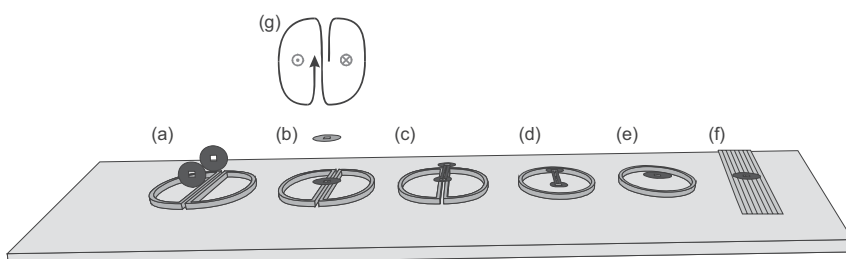


Fig. 13.7 Schematic of different excitors used in eddy current testing with SQUIDS. Double-D excitation with detection using (a) axial gradiometer for tangential field component, (b) magnetometer or axial gradiometer and (c) planar gradiometer, both for vertical field

component. Absolute excitation with (d) planar gradiometer and (e) magnetometer detection. (f) Planar sheet inducer excitation with magnetometer detection. (g) The direction of current flow in a double-D coil and the resultant directions of the magnetic field.

In standard eddy current NDE with single-frequency excitation, the depth of investigation is restricted to a limited range around the skin depth of the chosen excitation frequency. The pulsed eddy current (PEC) NDE technique has the advantage of allowing simultaneous analysis of the sample at all depths, since the Fourier transform of an excitation pulse contains components of all frequencies. For pulsed eddy currents in conjunction with SQUID magnetometers, the advantage over induction coil sensors is that the field does not decay as rapidly as its time derivative, allowing for an even broader range of investigated depths. Note that PEC is analogous to transient electromagnetics (TEM) in geomagnetic prospecting. The disadvantage of pulsed excitation as compared to single-frequency measurement is that the signal-to-noise ratio at any given frequency is lower since the excitation amplitude component at that frequency is smaller. This reduction usually cannot be compensated by increasing the excitation current because of limited current sources, thermal effects, or slew rate limitations of the SQUID.

13.5.3

Signal Analysis

The depth-selective technique for determining the depth of the flaw by means of phase analysis of the response field has been demonstrated by Ma and Wikswo [49]. Their sheet-inducer geometry (Figure 13.7(f)) allowed them to complement their experimental investigations with analytical calculations. By appropriate choice of the phase during evaluation, they were able to suppress signals of surface-breaking cracks and enhance those of deep flaws. The oriented eddy current imaging is feasible using a rotating field scheme [50, 51] or two single measurements with orthogonal excitation [52]. Because the system is linear, two single measurements with orthogonal excitation can be used to reconstruct the signal that would be obtained for an arbitrary orientation of current. The measurements may be performed simultaneously with slightly different frequencies. In their experiments, they used a test sample provided by Lockheed (see Figs. 13.8(a) and (b)), consisting of two 3.2-mm thick aluminum plates bolted together by four 6.4-mm diameter flat-head aluminum fasteners which simulate the rivets. The 6.4-mm long EDM slots simulate the crack defects beneath the rivet. Two separate scans using orthogonal excitation currents were performed, recording both the in-phase and quadrature signals. Figure 13.8(c) shows the resultant signal amplitude at the four rivet locations as a function of phase. At phase 10°, the main contribution to the signal is from the first layer slots, whereas the second layer slots dominate at phase 95°.

Phase analysis has been shown to be applicable also for double-D exciter geometries [53, 54]. Horng *et al.* [55] suggested that one could eliminate the problem of offset fields, which may occur due to the tilting of the exciting coil or other asymmetries, by analyzing the in-phase and quadrature components of the differentiated field with respect to the scanning axis x . To a first-order Taylor expansion, the phase ϕ of the field derivative dB/dx at the location of the flaw center, $x = 0$, is equal to the phase of the field $B(x)$:

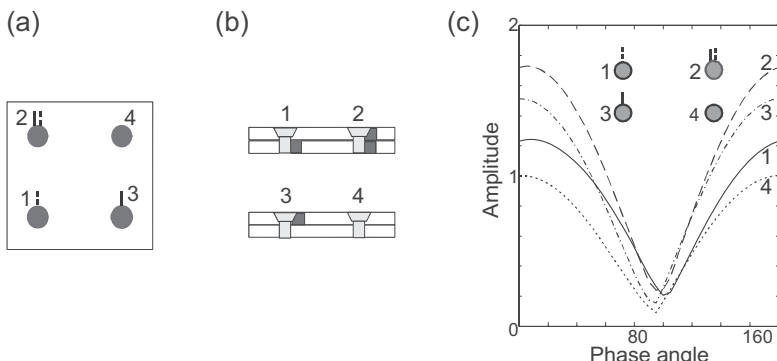


Fig. 13.8 SQUID eddy current detection of second-layer cracks in a riveted test sample using the depth-selective self-referencing method. (a) Top view and (b) cross-sections of the sample. The solid lines denote top-layer cracks, the dashed lines second-layer cracks. (c) Amplitude variation with the phase

angle for the SQUID signals recorded above the four rivets, with the sheet inducer excitation current perpendicular to the cracks. At phase 10°, the rivets with adjacent top-layer cracks yield the highest amplitude; at phase 95°, the rivets with bottom-layer cracks dominate. (From Ref. [52], with permission.)

$$\phi(x \rightarrow 0) = \tan^{-1} \left[\frac{B_{90^\circ}}{B_{0^\circ}} \right]_{x \rightarrow 0} \approx \tan^{-1} \left[\frac{dB_{90^\circ}/dx}{dB_{0^\circ}/dx} \right]_{x=0}. \quad (13.4)$$

Here, B_{0° and B_{90° denote the in-phase and the quadrature components of the magnetic field with respect to the excitation current, as measured by a vector lock-in amplifier. By plotting the phase angle ϕ determined from the field derivatives using (13.4), Fig. 13.9, it was shown that the phase at the location of the flaw varies linearly with the flaw depth.

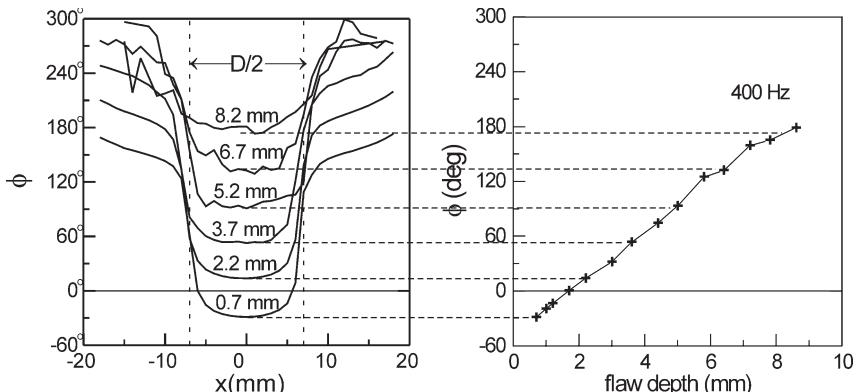


Fig. 13.9 Determination of the flaw depth by phase analysis. The phase of the differential defect field is plotted vs. the scan coordinate x for scans over slots hidden at different depths in stacks of aluminum sheets. On the right, phase calculated from Eq. (13.4) is plotted versus the flaw depth. (From Ref. [55], with permission.)

The signal analysis approaches mentioned above suffer from the fact that they are limited to either simple geometries or to special cases. It is highly desirable to perform a magnetic modeling of the testing problem. Modeling not only gives information for the optimization of system parameters, such as the choice of inducer, excitation geometry, sensor, frequency, and phase, but also yields the signal amplitudes and shapes to be expected from different flaw types [56]. Among the numerical techniques are finite-element and finite difference methods (FEM, FDM), the boundary-element method (BEM), and the volume-integral method (VIM). Most versatile and flexible is FEM. It has been used to resolve numerous complicated questions in SQUID NDE, see, e.g., Refs. [57, 58]. However, FEM is very time consuming even on fast computers and requires a great deal of memory. In order to compute the result of a linear scan, a typical problem in SQUID NDE, one has to re-run the model again, with sample and exciting coil displaced against each other. In contrast, the VIM method requires only a one-time determination of the Green's function for modeling of the defect region. The result of a scan can thus be computed more rapidly and easily. Figure 13.10 gives an example of an eddy current SQUID measurement scan across a flaw in a metal plate and a VIM simulation of the scan which models the experimental result with impressive accuracy [59].

The NDE inspector's dream, however, is to be handed a tomographic 3D analysis of the material under test, an image of the inside of the sample. The electromagnetic 3D inverse problem, i.e., the determination of the source of magnetic fields inside an object by measuring them at several locations outside, does not have a unique solution (*Helmholtz theorem*). In special cases or under special assumptions, inversion is feasible [9]: for example, progress has been made within the biomagnetic and geophysical communities by including realistic physiology and geology within model solutions. It is expected that, for NDE, increasing com-

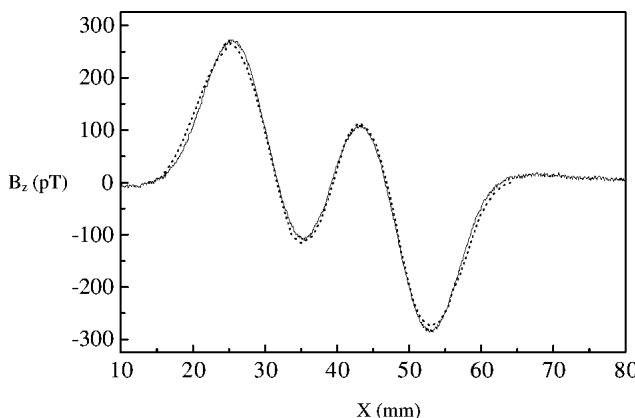


Fig. 13.10 Comparison of experimental data (full line) and VIM simulation results (dotted line) for line scans of the in-phase component of B_z observed above a surface-breaking hole 8 mm \times 2 mm in a 4-mm thick metallic plate. (From Ref. [59], with permission.)

putational power will allow reliable and stable algorithms to be developed for this ill-posed problem. A comprehensive review on techniques for solving the inverse problem in the field of SQUID NDE is given in Chapter 10 and in Ref. [9].

In the case of a current distribution which is confined to a two-dimensional plane, the current density $J(x,y)$ leading to the measured magnetic field distribution $B_z(x,y,z)$, in a plane at a distance z from the current plane, may be derived by means of inverse spatial filtering [60], a technique that is discussed in Section 10.3.2.2.

In standard eddy current NDE, the depth of investigation is restricted to a limited range around the skin depth of the chosen excitation frequency. The PEC technique has the advantage that the excitation pulse can be considered as a large number of single sinusoidal tests at various frequencies, each corresponding to a different standard penetration depth. Therefore, PEC allows simultaneous analysis of the sample at all depths. When analyzing a single pulse response, one can obtain information from both shallow (high-frequency signal components) and deep layers (low-frequency components) simultaneously. It has been demonstrated that PEC testing using a SQUID is feasible [61]. Experiments with PEC for NDE of metals have been demonstrated using a high- T_c SQUID and a commercial data acquisition unit (LAPTEM® from Geoinstruments, Ltd) [62]. Using rectangular excitation pulse trains, eddy currents are induced in the samples. The magnetic field response is recorded in the off-time between the transmitter pulses with a high- T_c SQUID magnetometer. In the case of absolute coil excitation, the recorded PEC data may be inverted, using the formula for the impulse response of a homogeneous half-space known from geophysical data interpretation [63]:

$$B_z(t) = \frac{It}{\sigma a^3} \left[\left(2\theta(t)^2 a^2 - 3 \right) \operatorname{erf}(\theta(t) a) + \frac{6}{\sqrt{\pi}} \theta(t) a \exp(-\theta(t)^2 a^2) \right]. \quad (13.5)$$

Here, I denotes the excitation current in the coil, t is the time after the pulse end, σ denotes the electrical conductivity of the half-space, a is the coil radius, and $\theta(t) = \sqrt{\sigma\mu/4t}$. This conversion yields quasitomographic images of the so-called apparent conductivity of the medium [64] (see Fig. 13.11). From this tomographic conductivity image of the sample, the position and depth of flaws in the material are readily determined.

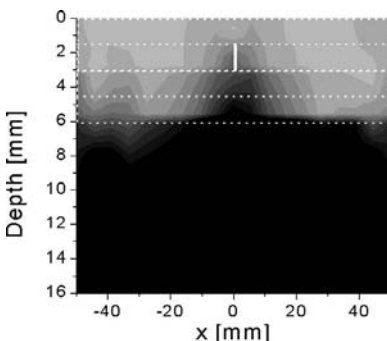


Fig. 13.11 Tomographic B-scan image of the apparent electrical conductivity as a function of position and depth, for a sample of four stacked aluminum plates, with a crack in the second layer. The dotted lines indicate the contours of the sheets, the solid line marks the crack. (From Ref. [62], with permission.)

13.5.4

Practical Examples

13.5.4.1 Aluminum Alloy Aircraft Components

Eddy current testing using a SQUID sensor turns out to be of special value in highly safety-relevant areas such as aircraft testing, where small but deep flaws need to be localized and sized in aluminum structures [40]. The first demonstration of aircraft lap joint testing was performed in a shield using a low- T_c SQUID system [41]. Subsequently, a cryocooled low- T_c system with remote differential sensing coils was used to demonstrate the detection of very small, hidden flaws without shielding [42]. Excitation–detection schemes which are appropriate for high- T_c SQUID electronic gradiometers, consisting of individual magnetometer SQUIDs, were developed by Tavrin *et al.* [65] (see Section 13.5.2). Eddy current detection of flaws as deep as 50 mm in aluminum sheets was demonstrated [45]. For the determination of the crack orientation, to reduce the signal from the rivets of aircraft lap joints, and to account for liftoff variations, two orthogonal sheet inducers were used [52]. Here high dynamic range is more important than a high sensitivity, since the signal amplitude scales with the excitation current. Therefore, even the relatively insensitive high- T_c SQUID can be used in mobile gradiometer configuration to measure eddy currents [58, 66].

Significant progress has been made in developing SQUID systems for the inspection of aging aircraft. Measurements on aircraft lap-joint structures have been conducted [67, 68]. Mobile high- T_c SQUID planar gradiometers [69] with orientation-independent cooling [48] have been developed for eddy current testing of “second-layer” cracks and corrosion in the airplane fuselage [70, 71]. Figure 13.12 shows the results of mapping second-layer defects in a row of rivets using a SQUID. The measured eddy current response signal is significantly enhanced at the locations of the cracks indicated in the sketch below the graph. SQUID inspection of a titanium bolt connection in a 62-mm thick aluminum structure (a design study of the outer wing splice of the Airbus A380) has also been successfully demonstrated using wire excitation at frequencies as low as 22 Hz [72]. Figure 13.13 depicts the SQUID trace recorded during the scan across a titanium bolt with a crack in the second aluminum layer (31 to 46 mm below the surface). The 22-Hz eddy current response is significantly enhanced in comparison to the case without a crack. With conventional eddy current equipment, it was impossible to detect this crack. In both cases, the detectability of deep defects in field conditions (airplane maintenance hangars) is much better than that of conventional eddy current test instruments [43, 73–75]. The aircraft testing program has been performed in cooperation with the aircraft manufacturing and operating industries, and with a manufacturer of conventional test equipment.

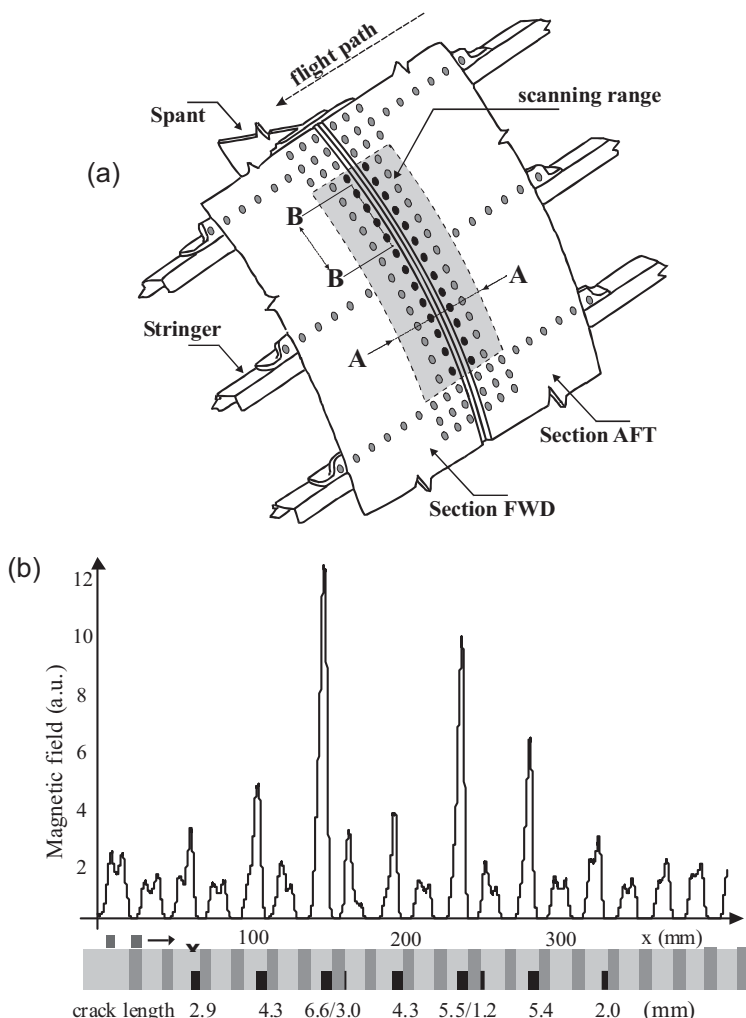


Fig. 13.12 (a) Typical measurement region at a riveted section joint. (b) SQUID measurement of an Airbus A300 sample provided by Airbus, Bremen. Measured signals coincide with the known crack positions and even scale with the lengths given below. (From Ref. [76], with permission.)

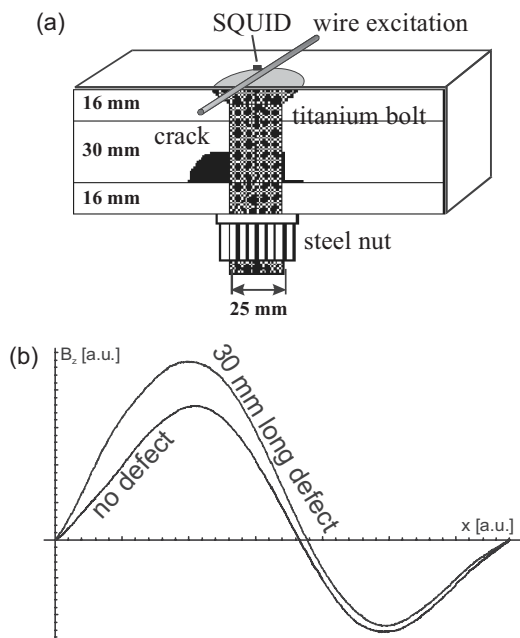


Fig. 13.13 (a) Schematic of the Airbus A380 wing splice sample, with a flaw in the second layer (length 30 mm, depth 31–46 mm). The position of the excitation wire and of the SQUID is indicated. Scanning was performed perpendicular to the wire. (b) Measured SQUID traces of the wing splice sample of a bolt with adjacent flaw and, for comparison, an unflawed bolt connection. Shown are the signals after liftoff correction and phase optimization. The flaw is easily identified. (From Ref. [77], with permission.)

An ambitious approach for airframe testing with PEC was proposed, but never fully developed, by the late Walter Podney [61, 78]. The system was to consist of a hand-held high- T_c SQUID array, involving 16 multiplexed magnetometers, and a Stirling cryocooler for charging a copper cryobattery. During SQUID operation the cryocooler was to be disconnected from the cryobattery and switched off, eliminating all noise due to the vibration and magnetic signal of the cryocooler. Since dissipation in the SQUID is typically tiny (of the order of picowatts), the warm-up time would be entirely determined by radiation from the surrounding envelope and by conduction down electrical leads. Podney predicted that his system would operate for about ten hours before having to be recooled. A similar cryobattery approach has recently been practically demonstrated by Carr *et al.* [79, 80], with the difference that the cryocooler can be completely removed after cooling to about 40 K, leaving a very compact and highly portable system. Warm-up times to 77 K of 90 minutes have been demonstrated and operational times of 12 hours are predicted for future designs.

The ability of high- T_c SQUID magnetometers to test aircraft wheel rims was first demonstrated by Kreutzbrück *et al.* [81]. A suitable system using a high- T_c

SQUID magnetometer with Joule–Thomson cooling in conjunction with remote eddy current (EC) excitation has recently been developed [82, 83]. A routine performance test in the wheel testing facility at the Lufthansa Base, Frankfurt/M., airport proved the stability of operation in electromagnetically disturbed environments.

Analysis of the response field of an inside crack as a function of excitation coil displacement, eddy current frequency, and lock-in phase angle yielded an optimum wheel rotation velocity for deep-lying defects. The technique provides depth selectivity: signals from deep flaws are enhanced over surface flaws. Tests were conducted on aircraft wheels with known flaws. On a Boeing 737 wheel, an inner flaw penetrating only 10% of the wall thickness was detected by scanning the outside surface of the rim (Fig. 13.14). Thus, Lufthansa's specification for manual ultrasonic testing from the inside was reached with the SQUID unit testing automatically from the outside. However, further improvements of reliability and signal analysis are required before commercialization of the system will be feasible.

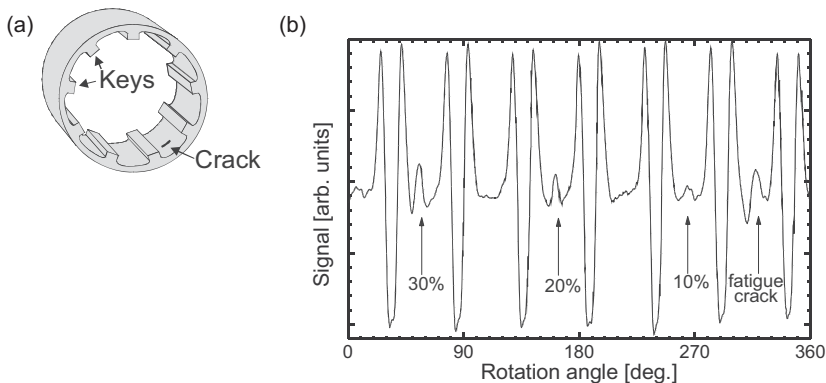


Fig. 13.14 (a) Schematic of an aircraft wheel hub. (b) Single trace measured on a Boeing 737 wheel, using the remote eddy current scheme. The three saw cuts with 30%, 20%, and 10% wall penetration are easily identified among the signals from the seven keys. (From Ref. [77], with permission.)

13.5.4.2 Niobium Sheets for Superconducting Resonators

A very promising application for SQUIDs in NDE is the inspection of niobium sheets for superconducting resonators. The maximum electric field strength that can be sustained in a superconducting microwave cavity is limited by the purity of the niobium from which the cavity is made. For the projected particle accelerator TESLA, even a few very small tantalum inclusions per resonator may lead to a substantial reduction of the projected maximum electrical field strength. Because both the niobium sheets and the cavity manufacturing process are expensive, the sheets need to be inspected for inclusions. Since niobium and tantalum have a similar electrical conductivity, a SQUID sensor with high sensitivity is needed to resolve the slight variations in the eddy current signal originating from tantalum inclusions. Mück *et al.* [84] recently developed an LTS SQUID system for eddy cur-

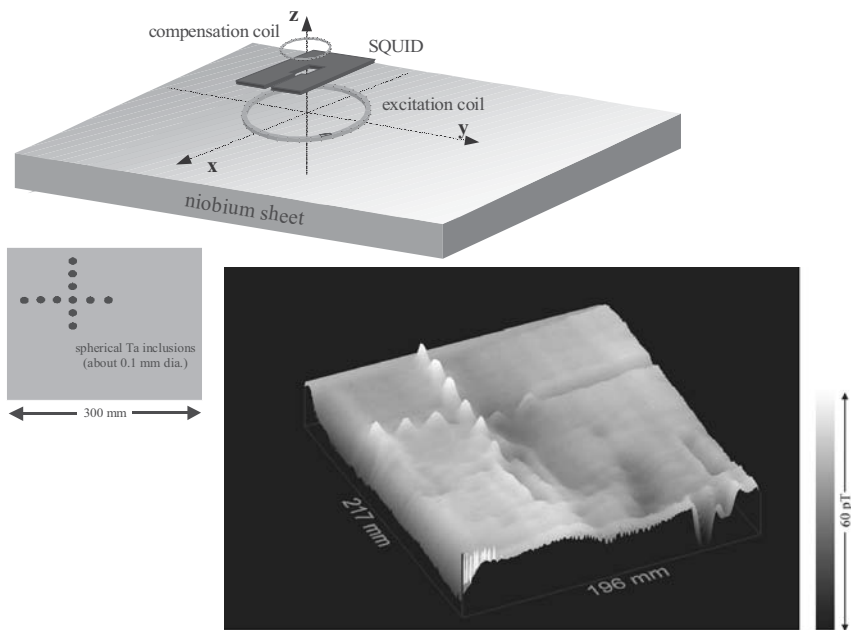


Fig. 13.15 Top: measurement setup for detecting inclusions in niobium sheets with an LTS SQUID eddy current system. Left: the sample was prepared with 11 embedded tantalum spheres of about 0.1 mm in diameter. Bottom: 3D surface plot of the eddy current signal, measured using a 10-kHz, 0.6-mT_{pp} excitation and an LTS SQUID magnetometer. The locations of the spherical inclusions are clearly visible. (From Ref. [84], with permission.)

rent testing of niobium sheets. Figure 13.15 shows a schematic of the measurement setup. A 2-mm thick test sheet of high-purity niobium, prepared with 11 embedded tantalum spheres of about 0.1 mm in diameter, was used as a test sample [84]. The locations of the spherical inclusions were imaged by scanning the sample with the SQUID, as may be seen from the liftoff-corrected and phase-optimized eddy current scan of Fig. 13.15.

13.5.4.3 Carbon Fiber-Reinforced Polymer

Carbon fiber-reinforced polymer (CFRP) materials are rapidly growing in importance for aircraft construction and other industries. For example, they are projected to represent up to 50% of future aircraft such as the Boeing 7E7. There are considerable challenges for NDE presented by CFRPs as a result of the large range of in-service defect scenarios possible compared to conventional metals: for instance, impacts leading to delamination, lamina crushing, matrix cracking, fiber kinking and breaking. These impacts can be of quite low energy: defects can be caused in 2-mm plates by impacts transmitting as little as 10–50 J. This has led to

considerable worldwide effort to develop CFRP NDE using techniques such as X-rays, thermography, and especially ultrasound. Following the first work by Hatuskade *et al.* [85], a number of SQUID researchers have begun to explore opportunities for applying the eddy current technique to such materials [86–91].

Work so far has been performed using the experimental rigs already developed for the SQUID NDE of metals. However, CFRP materials have very different properties. They consist of successive layers of conductive carbon fiber mats embedded in highly resistive epoxy material: their electrical properties are therefore highly anisotropic, and their bulk conductivity ($0.1\text{--}3.6 \times 10^4$ S/m in-plane and $0.01\text{--}0.03 \times 10^4$ S/m perpendicular to it) is much smaller than that of aluminum (3500×10^4 S/m). Skin depths are thus much larger than the thickness of typical sheets at all reasonable eddy current frequencies. In practice, most groups have chosen to work at 10–20 kHz.

Figure 13.16(a) shows the damage visible on the side of a 2-mm thick CFRP plate which has been impacted by a steel bob with 20 J of kinetic energy. Figure 13.16(b) shows how the maximum peak-to-peak SQUID signal, obtained when

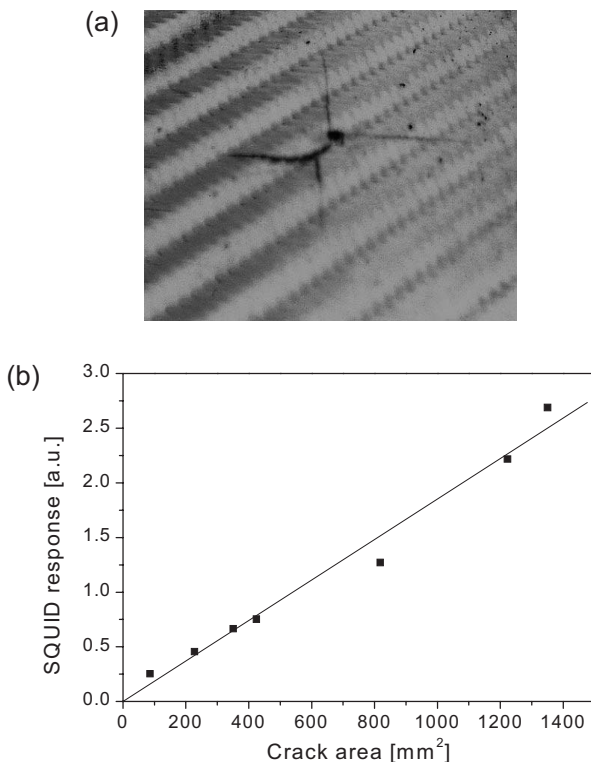


Fig. 13.16 (a) Photograph of the damage of a 2-mm thick CFRP plate which has been impacted by a steel bob with 20 J of kinetic energy. (b) Dependence of the measured SQUID signal on the crack area initiated by an impact on the reverse side. (From Ref. [91], with permission.)

eddy currents are excited in the plate and the sensor scan line traversed across the center of the impact, depends on the area of damage visible on the *opposite* side of the sample [91].

Even though the currents in the excitation coils can be made considerably larger than those in the SQUID NDE of metals, the much smaller conductance of CFRP means that the excited currents and thus the SQUID signal are much smaller. Used in the unscreened laboratory environment with high levels of electromagnetic interference, the CFRP x - y maps often exhibit spikes and anomalous fea-

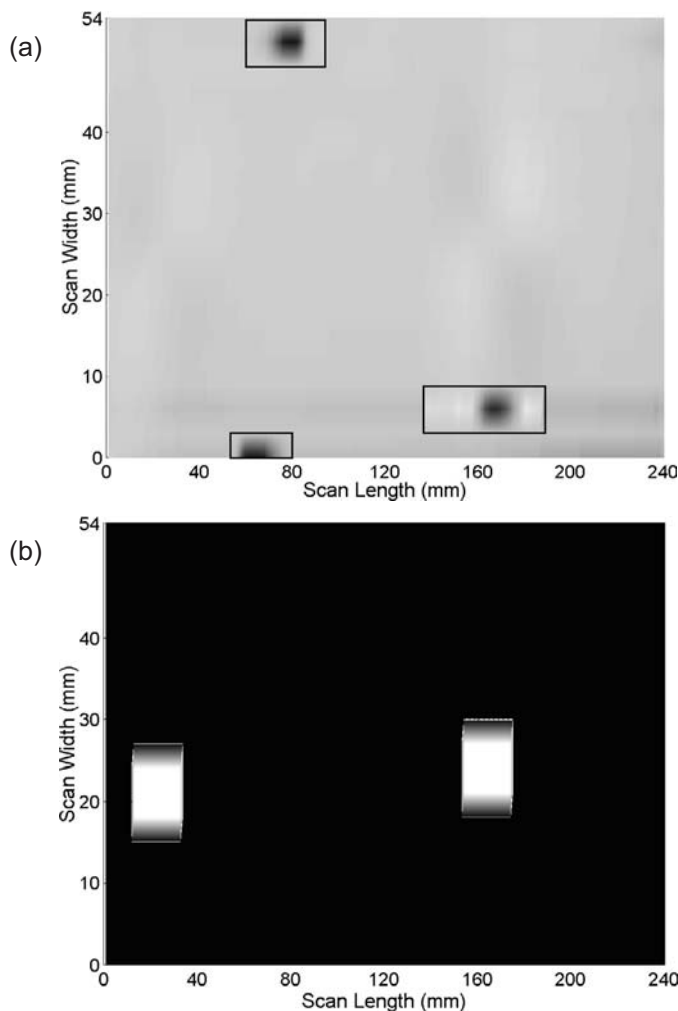


Fig. 13.17 (a) Data from a SQUID scan over a flawed CFRP plate in which high levels of background interference have caused spikes in the data (boxed). These obscure the signals arising from two defects. (b) Result of applying the neural network system to these data. Both defects are detected and their centers identified. (From Ref. [91], with permission.)

tures that obscure the real flaw signals. To overcome this difficulty, a neural network (NN) technique has been developed which, after appropriate training, recognizes characteristic flaw patterns. Neural networks are arrays of processing elements (neurons) that model the function of biological neural systems. Each node is connected to every node in the next layer by a series of weights. The weights are determined by training the network using as many as possible distinct patterns. Graham *et al.* [91] implemented a NN including preprocessing, feature extraction, normalization, pattern recognition, and classification steps. This system is very effective even when the flaw signals are considerably obscured by interference, as shown in Fig. 13.17.

13.6 Alternative Excitation Techniques

13.6.1

Light: SQUID Photoscanning

In addition to excitation by magnetic field (Section 13.3), electric current (Section 13.4), and electromagnetic induction (Section 13.5), the magnetic response field to be measured by the SQUID can be generated by other physical effects such as the photoeffect or the Seebeck effect, or by electrochemical corrosion. This section highlights some prominent examples of alternative excitation techniques.

In the NDE of semiconductors using photomagnetic detection [92, 93], laser light is focused onto the sample surface. If the photon energy exceeds the direct bandgap of the semiconductor, nonequilibrium charge carriers are generated. In the presence of a lateral doping gradient, the associated internal electric field separates the excited electron–hole pairs, resulting in photogenerated currents in the sample, which are detected by sensing their magnetic field using a SQUID magnetometer (Fig. 13.18). In contrast to the situation in SQUID microscopy, the spatial resolution is not determined by the size of the SQUID or the sample-to-SQUID spacing, but by the size of the excitation spot, the laser focus. It was possible to detect doping inhomogeneities in electronic-grade silicon, defects in photovoltaic device structures [94], the distribution of a photoinduced magnetic field from a p–n junction (Fig. 13.19), and the minority carrier diffusion length [95]. A spatial resolution of 1.3 μm was reported [96].

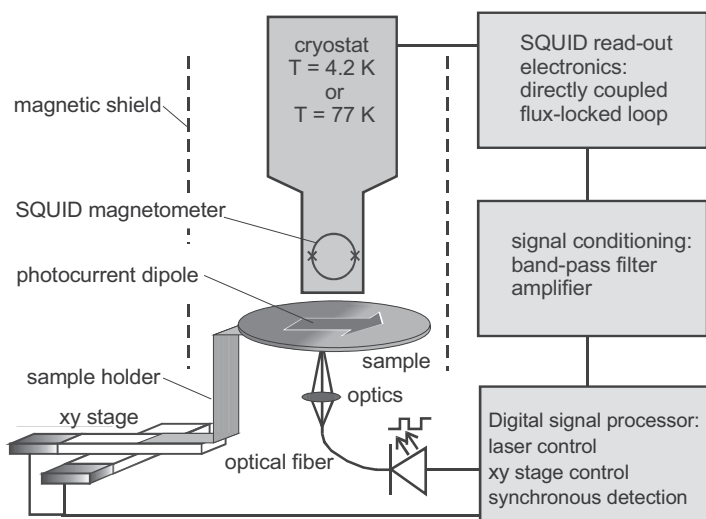


Fig. 13.18 Scheme of the SQUID photoscanning setup. (From Ref. [94], with permission.)

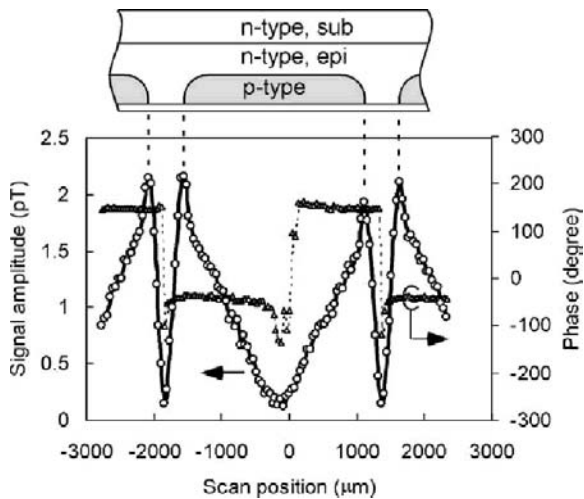


Fig. 13.19 Distribution of the photoinduced magnetic field and phase in a p–n junction. (From Ref. [95], with permission.)

13.6.2

Heat: Thermoelectric Method

Inclusions and other types of imperfection in nonmagnetic metals can be nondestructively detected by noncontacting magnetic measurements that sense the thermoelectric currents produced by directional heating and cooling of the specimen. The detectability of small and weak imperfections is ultimately limited by the intrinsic anisotropy and inhomogeneity of the material to be inspected.

It was demonstrated by Hinken and Tavrin [97] that self-referencing thermoelectric measurements can be done in an entirely noncontact way by using high-sensitivity magnetic detectors to sense the weak thermoelectric currents around inclusions and other types of inhomogeneities when the specimen is subjected to directional heating or cooling. Figure 13.20(a) depicts the principle of thermoelectric current generation according to the Seebeck effect. Figure 13.20(b) shows an example of aircraft turbine disc inspection. The rotating wheel is subjected to a cooling stream while the magnetic field is measured from the reverse side. The positions of segregations were readily determined from the SQUID signal.

Carreon *et al.* [98] investigated the spurious magnetic signature produced by the simplest type of macroscopic inhomogeneity when the material properties exhibit a linear spatial variation in the cross-section of a slender bar. An analytical method has been developed for calculating the normal and tangential magnetic fields produced by the resulting thermoelectric currents. Experimental results from a highly inhomogeneous artificial copper/brass sintered specimen were found to be in very good quantitative agreement with the theoretical predictions.

The noncontacting thermoelectric method can be used to characterize the prevailing residual stress in shot-peened specimens. This novel method is based on magnetic detection of local thermoelectric currents in the compressed near-surface layer of metals when a temperature gradient is established throughout the specimen. Besides the primary residual stress effect, the thermoelectric method is also sensitive to the secondary “material” effects of shot peening (local texture, increased dislocation density, hardening), but it is entirely insensitive to its “geometrical” byproduct, which is the rough surface topography. The experimental results in copper indicate that this method is more sensitive to residual stress effects than to the secondary material effects, but unequivocal separation of residual stress relaxation from the parallel decay of secondary cold-work effects is generally not feasible [99].

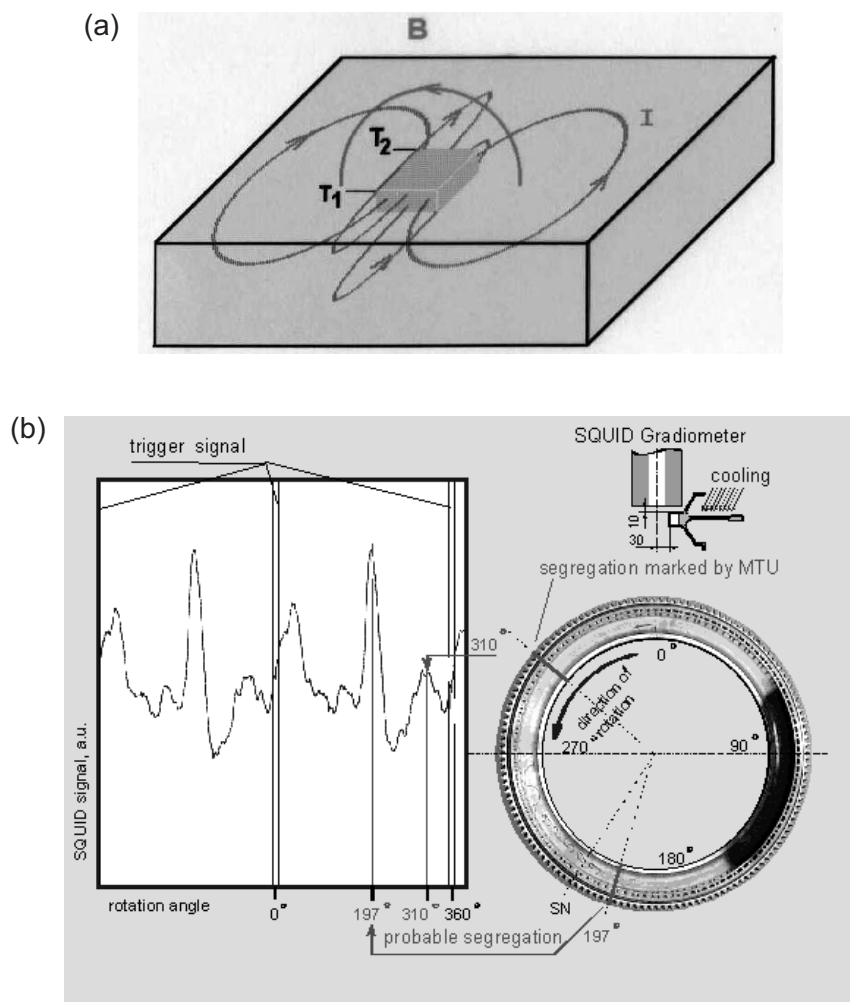


Fig. 13.20 The thermoelectric SQUID method. (a) An inclusion of one metal (dark gray) is embedded in a base material of another metal (light gray). If the temperatures T_1 and T_2 at their interfaces differ, a voltage develops across the interface region according to the Seebeck effect, giving rise to the

generation of a current I and a magnetic field B . (b) Aircraft turbine disc with segregations: photograph, measurement arrangement and measured magnetic signal. The test was performed from the reverse side. (From Ref. [97], with permission.)

13.6.3

Susceptometry

As ceramic and nonmetallic composite materials become increasingly popular in industry, especially in aircraft, techniques for monitoring their integrity are needed. SQUID susceptometry constitutes a promising alternative. Wikswo and co-workers demonstrated imaging of the susceptibility distribution of nonconducting materials [29] by measuring the spatial distribution of the magnetic field outside the specimen with a SQUID magnetometer, thus showing the applicability of this technique for NDE.

13.6.4

Tagging

For many nonconducting materials, the magnetic susceptibility is rather small, thus limiting the susceptibility imaging capability. The method of tagging the material with magnetic tracers, also called surface decoration, allows one to perform susceptibility analysis by means of a SQUID magnetometer with sufficient signal-to-noise ratio [100]. In surface decoration susceptometry, the nonmagnetic sample is marked by spreading a thin layer of a ferrofluid containing superparamagnetic tracer particles over its surface. Then, the sample is scanned with a susceptometer [31, 32]. An analysis of the resulting image allows the detection of very fine surface-breaking cracks. The material surface may also be decorated by ferromagnetic marker particles. In that case, it suffices to scan the remanent magnetic field by means of a magnetometer [30].

13.6.5

Corrosion

In contrast to standard eddy current testing (Section 13.5), which allows one to measure existing materials damage due to corrosion, it is possible to detect ongoing corrosion by measuring the magnetic fields caused by electrochemical ion currents of the oxidation process. Bellingham *et al.* [101] showed that the magnetic field of corrosion currents in aqueous metal–acid or metal–salt environments can be detected with a SQUID magnetometer. The SQUID was shown to be usable even for electrochemical cyclic voltammetry studies [102]. Hibbs *et al.* [103] designed a SQUID magnetometer especially for corrosion studies.

Wikswo *et al.* [33, 104] performed systematic studies of the time course of ongoing active corrosion on plate structures of 7075-T6 aluminum aircraft alloy samples in aqueous salt solution. They showed that the regions of anodal and cathodal activity change drastically over a 24 hour period. A magnetic imaging system for quantitative analysis of the rate of ongoing hidden corrosion in planar structures was designed and built [105]. Samples up to 0.28 m in size may be mounted on the scanner inside a magnetic shield. The magnetic fields generated by the currents of ongoing corrosion are scanned by a three-axis low- T_c SQUID

vector gradiometer. The SQUID system is considered to be a valuable laboratory tool for imaging the spatial distribution of hidden corrosion, for understanding the principles of ongoing hidden corrosion, and for the development of appropriate models for predicting the long-term behavior and rate of corrosion in occluded regions. At present, it seems unlikely that the technique can be extended to measurement of magnetic corrosion signals on aircraft because environmental magnetic field variations, magnetic components, or magnetic dirt on the samples give rise to spurious magnetic fields. In addition, thermoelectric currents or galvanic contact currents are usually much stronger than the weak currents due to ongoing corrosion in aircraft aluminum alloys.

13.7

Conclusion and Prospects

During the last two decades, numerous examples of the successful use of SQUIDs for NDE have been presented. In almost all cases, SQUID testing was superior to other “conventional” NDE techniques.

Particularly in the case of a number of aircraft NDE tasks, prototype SQUID systems were developed and tested in realistic industrial environments. The practical usability of mobile high- T_c SQUIDs in conjunction with the eddy current technique has been demonstrated using orientation-independent, simple, easy-to-use cryogenics (*e.g.*, a machine-cooler) under electromagnetically noisy conditions.

In close cooperations between developers, users, and often manufacturers of conventional techniques, prototype systems have been developed which are approaching the stage of industrial application and, in some cases, are already put to commercial use. In many other cases, the application-related SQUID development has led to significant improvements in conventional NDE equipment. Thus, the competition from SQUIDs has helped to push electromagnetic NDE to its fundamental limits, as given by Maxwell’s laws. In many cases, the limits in detectability of deep defects under field conditions is not given by sensor sensitivity but is rather imposed by the need to separate flaw signals from structural signatures with their variability range. The inherent nonuniqueness of the electromagnetic inverse problem makes it difficult to obtain an image of electromagnetic properties of the sample in the form of a tomography-like analysis.

Compared to conventional electromagnetic NDE devices, prototype SQUID systems have proved superior in performance in almost all cases. In some cases, such as the detection of inclusions in aircraft turbine discs, SQUIDs have been used commercially for routine inspections. In other cases, *e.g.*, aircraft wheel hub inspection, the industrial partners have refrained from commercialization for economic reasons. Taking into account the cost of developing the prototype into a commercial product and the size of the likely market, the cost was estimated to exceed the expected profit. The same holds true for magnetic flux leakage inspection of steel structures on oil platforms: although the feasibility has been clearly

demonstrated, the huge engineering effort required to make rugged a delicate SQUID system to the point at which it could be operated in the hostile environment of underwater structures was too elaborate to contemplate. In still other cases such as bridge inspection and magnetic particle detection, the SQUID competition led to progress in the development of NDE methodology. The improvements, for instance the subtleties of excitation and signal analysis, were successfully transferred to electromagnetic NDE using conventional induction coil, giant magnetoresistance (GMR), or fluxgate magnetometers, thereby diminishing the leading edge of SQUID NDE.

Evidently, the most important future development requirement is user-friendliness. The technical user wishes to have a "turnkey" system where he does not have to be concerned with the complex superconducting and cryogenic technology inside it. In addition, problem-adapted signal analysis techniques, such as the suppression of signals from undamaged rivets or bolts in aircraft testing, are key issues for widespread user acceptance. Successful industrial SQUID uses of NDE are expected provided that (1) the focus is laid on applications with unique SQUID advantages where the larger system cost is acceptable, (2) versatile signal interpretation tools are implemented, and (3) improved SQUID reliability and handling are attained. SQUID NDE groups worldwide are concentrating on these issues.

References

- 1 Donaldson, G.B. (1989) SQUIDs for everything else. In H. Weinstock and M. Nisenoff (eds.), *Superconducting Electronics*, Springer, Berlin, pp. 175–207.
- 2 Donaldson, G.B. (1996) The use of SQUIDs for NDE. In H. Weinstock (ed.), *SQUID Sensors, Fundamentals, Fabrication and Applications*, NATO ASI series E Vol. 329, Kluwer, Dordrecht, pp. 599–628.
- 3 Weinstock, H. and Nisenoff, M. (1985) Nondestructive evaluation of metallic structures using a SQUID gradiometer. In H.D. Hahlbohm and H. Lübbig (eds.), *SQUID'85, Proc. 3rd International Conference on Superconducting Quantum Devices*, deGruyter, Berlin, pp. 853–858.
- 4 Weinstock, H. and Nisenoff, M. (1986) Defect detection with a SQUID magnetometer. In D.O. Thompson and D.E. Chimenti (eds.), *Review of Progress in QNDE*, Vol. 5, Plenum Press, New York, pp. 699–704.
- 5 Bain, R.J.P., Donaldson, G.B., Evanson, S. and Hayward, G. (1985) SQUID gradiometric detection of defects in ferromagnetic structures. In H.D. Hahlbohm and H. Lübbig (eds.), *SQUID'85, Proc. 3rd International Conference on Superconducting Quantum Devices*, deGruyter, Berlin, pp. 841–846.
- 6 Bain, R.J.P., Donaldson, G.B., Evanson, S. and Hayward, G. (1987) Design and operation of SQUID-based planar gradiometers for NDT of ferromagnetic plates, *IEEE Trans. Magn.* 23, 473–476.
- 7 Capobianco, T.E., Moulder, J.C. and Fickett, F.R. (1986) Flaw detection with a magnetic field gradiometer. In D.W. Moore and G.A. Matzkanin (eds.), *Proc. 15th Symposium on NDE, NDE Testing Information Analysis Center, San Antonio*, p. 15.
- 8 Moulder, J.C. and Capobianco, T.E. (1987) Detection and sizing of surface flaws with a SQUID-based eddy current

- probe, *J. Res. Nat. Bureau Standards* **92**, 27–33.
- 9** Wikswo, J.P., van Egeraat, J.M., Ma, Y.P., Sepulveda, N.G., Staton, D.J., Tan, S. and Wijesinghe, R.S. (1990) Instrumentation and techniques for high resolution magnetic imaging. In A.F. Gmitro, P.S. Idell and I.J. LaHaie (eds.), *Digital Image Synthesis and Inverse Optics*, SPIE Proc. Vol. 1351, SPIE, Bellingham, pp. 438–471.
- 10** Wikswo, J.P. (1996) The magnetic inverse problem for NDE. In H. Weinstock (ed.), *SQUID Sensors, Fundamentals, Fabrication and Applications*, NATO ASI series E Vol. 329, Kluwer, Dordrecht, pp. 629–695.
- 11** Paulson, D.N., Fagaly, R.L., Toussaint, R.M. and Fischer, R. (1991) Biomagnetic susceptometer with SQUID instrumentation, *IEEE Trans. Magn.* **27**, 3249–3252.
- 12** Thomas, I.M., Ma, Y.P., Tan, S. and Wikswo, J.P. (1993) Spatial resolution and sensitivity of magnetic susceptibility imaging, *IEEE Trans. Appl. Supercond.* **3**, 1937–1940.
- 13** Tavrin, Y. and Hinken, J.H. (1998) First routine aircraft NDT with SQUID gradiometer. In B. Larsen (ed.), *Proc. 7th European Conference on Non-Destructive Testing*, ECNDT, Broendby, DK, pp. 3246–3253.
- 14** Tavrin, Y., Siegel, M. and Hinken, J.H. (1999) Standard method for detection of magnetic defects in aircraft engine discs using a HTS SQUID gradiometer, *IEEE Trans. Appl. Supercond.* **9**, 3809–3812.
- 15** Tavrin, Y., Zhang, Y., Wolf, W. and Braginski, A.I. (1994) A second-order SQUID gradiometer operating at 77K, *Supercond. Sci. Technol.* **7**, 265–268.
- 16** Wrobel, H., Tavrin, Y., Wenk, M. and Hinken, J.H. (2004) Fluxgate-Gradiometer für die hochauflösende Magnetometrie, *ZfP-Zeitung* **88**, 41–43.
- 17** Braginski, A.I., Krause, H.-J. and Vrba, J. (2000) SQUID magnetometers. In M.H. Francombe (ed.), *Handbook of Thin Film Devices*, Vol. 3, *Superconducting Film Devices*, Academic Press, San Diego, pp. 149–225.
- 18** Itozaki, H., Nagaishi, T., Toyoda, H. and Kugai, H. (1997) Detection of fine iron particles in high speed scrolled wire by high Tc SQUID, *IECE Trans. Electron. E80-C*, 1247–1251.
- 19** Evanson, S. (1989) A comparison of the performance of planar and conventional second-order gradiometers coupled to a SQUID for the NDT of steel plates, *IEEE Trans. Magn.* **25**, 1200–1203.
- 20** Sawade, G., Straub, J., Krause, H.-J., Bousack, H., Neudert, G. and Ehrlich, R. (1995) Signal analysis methods for remote magnetic examination of prestressed elements. In G. Schickert and H. Wiggenhauser (eds.), *Proc. Int. Symp. on NDT in Civil Engineering (NDT-CE)*, Vol. II, DGZfP, Berlin, pp. 1077–1084.
- 21** Scheel, H. (1997) Spannstahlbruchortung an Spannbetonbauteilen mit nachträglichem Verbund unter Ausnutzung des Remanenzmagnetismus, PhD thesis, D 83, Technical University Berlin (unpublished).
- 22** Sawade, G., Gampe, U. and Krause, H.-J. (1998) Non destructive examination of prestressed tendons by the magnetic stray field method. In J.H. Edwards, B. Gasper, P. Flewitt, B. Tomkins, P. Stanley and A. McLarty (eds.), *Proc. 4th Conf. on Engineering Structural Integrity Assessment*, Cambridge, UK, pp. 353–363.
- 23** Ghorbanpoor, A. (1998) Magnetic-based NDE of steel in prestressed and post-tensioned concrete bridges. In R.D. Medlock and D.C. Laffrey (eds.), *Proc. Structural Materials Technology III*, SPIE Vol. 3400, San Antonio, TX, pp. 343–347.
- 24** Sawade, G., Krause, H.-J., and Gampe, U. (1997) Non destructive examination of prestressed tendons by the magnetic stray field method. In M. T. Forde (ed.), *Proc. 7th International Conference on Structural Faults and Repair – 97*, Vol. I, Engineering Technical Press, Edinburgh, pp. 401–406.
- 25** Krause, H.-J., Wolf, W., Glaas, W., Zimmermann, E., Faley, M.I., Sawade, G., Mattheus, R., Neudert, G., Gampe, U. and Krieger, J. (2002) SQUID array for magnetic inspection of prestressed concrete bridges, *Physica C* **368**, 91–95.

- 26** Faley, M.I., Poppe, U., Urban, K., Zimmermann, E., Glaas, W., Halling, H., Bick, M., Krause, H.-J., Paulson, D.N., Starr, T. and Fagaly, R.L. (1999) Operation of the HTS dc-SQUID sensors in high magnetic fields, *IEEE Trans. Appl. Supercond.* **9**, 3386–3391.
- 27** Weinstock, H., Erber, T. and Nisenoff, M. (1985) Threshold of Barkhausen emission and onset of hysteresis in iron, *Phys. Rev. B* **31**, 1535–1553.
- 28** Banchet, J., Jouglar, J., Vuillermoz, P.-L., Waltz, P. and Weinstock, H. (1995) Evaluation of stress in steel via SQUID magnetometry. In D.O. Thompson and D.E. Chimenti (eds.), *Review of Progress in QNDE*, Vol. 14, Plenum Press, New York, pp. 1675–1682.
- 29** Wikswo, J.P., Ma, Y.P., Sepulveda, N.G., Tan, S., Thomas, I. and Lauder, A. (1993) Magnetic susceptibility imaging for nondestructive evaluation, *IEEE Trans. Appl. Supercond.* **3**, 1995–2002.
- 30** Hurley, D.C., Ma, Y.P., Tan, S. and Wikswo, J.P. (1993) Imaging of small defects in nonmagnetic tubing using a SQUID magnetometer, *Res. Nondestr. Eval.* **5**, 1–29.
- 31** Thomas, I.M., Ma, Y.P. and Wikswo, J.P. (1993) SQUID NDE: detection of surface flaws by magnetic decoration, *IEEE Trans. Appl. Supercond.* **3**, 1949–1952.
- 32** Clark, W.G. (1993) Magnetic particle tagging for improved material diagnostics. In C.A. Rogers and R.C. Rogers (eds.), *Proc. Recent Advances in Adaptive and Sensory Materials and Their Applications*, Technomic, Basel, pp. 274–284.
- 33** Li, D., Ma, Y.P., Flanagan, W.F., Lichten, B.D. and Wikswo J.P. (1996) Application of superconducting magnetometry in the study of aircraft aluminium alloy corrosion, *Corrosion* **52**, 219–231.
- 34** Li, D., Ma, Y.P., Flanagan, W.F., Lichten, B.D. and Wikswo, J.P. (1997) Detection of hidden corrosion of aircraft aluminium alloys by magnetometry using a SQUID, *Corrosion* **53**, 93–98.
- 35** Matthews, R., Kumar, S., Taussig, D.A., Whitecotton, B.R., Koch, R.H., Rozen, J.R. and Woeltgens, P. (1997) Corrosion measurements with HTS SQUID gradiometer. In H. Rogalla and D.H.A. Blank (eds.), *Applied Superconductivity 1997*, IoP Conference Series 158, Institute of Physics Publishing, Bristol, pp. 767–770.
- 36** Ewing, A.P., Ma, Y.P. and Wikswo, J.P. (1998) SQUID measurement, analysis and pattern recognition tool – Final report to KFA, Vanderbilt University, Dept. of Physics and Astronomy, Nashville, TN (unpublished).
- 37** Ma, Y.P. and Wikswo, J.P. (1998) private information (unpublished).
- 38** Ma, Y.P. and Wikswo, J.P. (1992) Detection of deep flaws inside a conductor using a SQUID magnetometer. In D.O. Thompson and D.E. Chimenti (eds.), *Review of Progress in QNDE*, Vol. 11, Plenum Press, New York, pp. 1153–1159.
- 39** Sepulveda, N.G., Staton, D.J. and Wikswo, J.P. (1992) A mathematical analysis of the magnetic field produced by flaws in two-dimensional current-carrying conductors, *J. Nondestr. Eval.* **11**, 89–101.
- 40** Wikswo, J.P., Ma, Y.P., Sepulveda, N.G., Staton, D.J., Tan, S. and Thomas, I.M. (1993) Superconducting magnetometry: a possible technique for aircraft NDE. In M.T. Valley, N.K. Grande and A.S. Kobayashi (eds.), *Nondestructive Testing of Aging Aircraft*, SPIE Proc. Vol. 2001, SPIE, Bellingham, pp. 164–190.
- 41** Ma, Y.P. and Wikswo, J.P. (1993) Imaging subsurface defects using a SQUID magnetometer. In D.O. Thompson and D.E. Chimenti (eds.), *Review of Progress in QNDE*, Vol. 12, Plenum Press, New York, pp. 1137–1143.
- 42** Podney, W.N. (1995) Eddy current evaluation of airframes using refrigerated SQUIDs, *IEEE Trans. Appl. Supercond.* **5**, 2490–2492.
- 43** v. Kreutzbrück, M., Mück, M. and Heiden, C. (1998) Simulations of eddy current distributions and crack detection algorithms for a SQUID based NDE system. In B. Larsen (ed.), *Proc. 7th European Conference on Non-Destructive Testing*, ECNDT, Broendby, DK, pp. 2513–2520.
- 44** Libby, H.L. (1971) *Introduction to Electromagnetic Nondestructive Test Methods*, Wiley-Interscience, New York.
- 45** Tavrin, Y., Krause, H.-J., Wolf, W., Glyantsev, V., Schubert, J., Zander, W.,

- Haller, A. and Bousack, H. (1996) Eddy current technique with HTS SQUID gradiometer for nondestructive evaluation of nonmagnetic metallic structures. In D. Dew-Hughes (ed.), *Applied Superconductivity 95*, IoP Conference Series No. 148, Institute of Physics Publishing, Bristol, pp. 1519–1520.
- 46** Buchanan, D.S., Crum, D.M., Cox, D. and Wikswo, J.P. (1989) MicroSQUID: a close-spaced four channel magnetometer. In S.J. Williamson, M. Hoke, G. Stroink and M. Kotani (eds.), *Advances in Biomagnetism*, Plenum Press, New York, pp. 677–679.
- 47** Cochran, A. and Donaldson, G.B. (1992) Improved techniques for structural NDT using SQUIDs. In H. Koch and H. Lübbig (eds.), *Superconducting Devices and their Applications*, Springer-Verlag, Berlin, pp. 576–580.
- 48** Lucía, M.L., Hohmann, R., Faley, M.I., Soltner, H., Krause, H.-J., Spörl, G., Binneberg, A., Wolf, W. and Bousack, H. (1997) Operation of HTS SQUIDs with a portable cryostat: a SQUID system in conjunction with eddy current technique for non-destructive Testing. *IEEE Trans. Appl. Supercond.* **7**, 2878–2881.
- 49** Ma, Y.P. and Wikswo, J.P. (1995) Techniques for depth-selective, low-frequency eddy current analysis for SQUID-based nondestructive testing. *J. NDE* **14**, 149–167.
- 50** Haller, A., Tavrin, Y. and Krause, H.-J. (1997) Eddy-current NDE by HTS SQUID gradiometer using rotating magnetic fields. *IEEE Trans. Appl. Supercond.* **7**, 2874–2877.
- 51** Haller, A., Tavrin, Y., Krause, H.-J., David, P. and Braginski, A.I. (1997) Eddy current tomography using rotating magnetic fields for deep SQUID-NDE. In H. Rogalla and D.H.A. Blank (eds.), *Applied Superconductivity 1997*, IoP Conference Series 158, Institute of Physics Publishing, Bristol, pp. 751–754.
- 52** Ma, Y.P. and Wikswo, J.P. (1998) SQUID magnetometers for depth-selective, oriented eddy current imaging. In D.O. Thompson and D.E. Chimenti (eds.), *Review of Progress in QNDE*, Vol. 17, Plenum Press, New York, pp. 1067–1074.
- 53** Yang, H.C., Jeng, J.T., Horng, H.E., Wang, S.Y., Hung, S.Y., Chen, J.C. and Chen, J.H. (2002) Noise characteristics of high- T_c $\text{YBa}_2\text{Cu}_3\text{O}_{7-y}$ SQUID gradiometers. *Physica C* **367**, 290–294.
- 54** Jeng, J.T., Horng, H.E., Yang, H.C., Chen, J.C. and Chen, J.H. (2002) Simulation of the magnetic field due to defects and verification using high- T_c SQUID. *Physica C* **367**, 298–302.
- 55** Horng, H.E., Jeng, J.T., Yang, H.C. and Chen, J.C. (2002) Evaluation of the flaw depth using high- T_c SQUID. *Physica C* **367**, 303–307.
- 56** v. Kreutzbrück, M. (2004) Unrivalled sensitivity – SQUIDs in NDT. In A.V. Narlikar (ed.), *High Temperature Superconductivity*, Vol. 2, Springer, Berlin, pp. 223–297.
- 57** Wikswo, J.P. (1995) SQUID magnetometers for biomagnetism and NDT: important questions and initial answers. *IEEE Trans. Appl. Supercond.* **5**, 74–120.
- 58** Cochran, S., Donaldson, G.B., Carr, C., McA. McKirdy, D., Walker, M.E., Klein, U., McNab, A. and Kuznik, J. (1995) Recent progress in SQUIDs as sensors for electromagnetic NDE. In R. Collins, W.D. Dover, J.R. Bowler and K. Miya (eds.), *Nondestructive Testing of Materials*, Studies in Applied Electromagnetics and Mechanics, Vol. 8, IOS Press, Amsterdam, pp. 53–64.
- 59** Ruosi, A., Valentino, M., Pepe, G., Mon-ebhurrun, V., Lesselier, D. and Duchêne, B. (2000) High Tc SQUIDs and eddy-current NDE: a comprehensive investigation from real data to modeling. *Meas. Sci. Technol.* **11**, 1639–1648.
- 60** Roth, B.J., Sepulveda, N.G. and Wikswo, J.P. (1989) Using a magnetometer to image a 2D current distribution. *J. Appl. Phys.* **65**, 361–372.
- 61** Podney, W.N. and Moulder, J.C. (1997) Electromagnetic microscope for deep, pulsed eddy current inspections. In D.O. Thompson and D.E. Chimenti (eds.), *Review of Progress in QNDE*, Vol. 16, Plenum Press, New York, pp. 1037–1044.
- 62** Krause, H.-J., Panaitov, G.I. and Zhang, Y. (2003) Conductivity tomography for non-destructive evaluation using pulsed eddy current with HTS SQUID magnet-

- ometer, *IEEE Trans. Appl. Supercond.* **13**, 215–218.
- 63** Spies, B.R. and Frischknecht, F.C. (1991) Electromagnetic sounding. In M.N. Nabighian (ed.), *Electromagnetic Methods in Applied Geophysics*, Vol. 2, *Application*, Society of Exploration Geophysicists, Tulsa, OK, pp. 285–425.
- 64** Panaitov, G., Krause H.-J. and Zhang, Y. (2002) Pulsed eddy current transient technique with HTS SQUID magnetometer for non-destructive evaluation, *Physica C* **372–376**, 278–281.
- 65** Tavrin, Y., Krause, H.-J., Wolf, W., Glyantsev, V., Schubert, J., Zander, W. and Bousack, H. (1996) Eddy current technique with high temperature SQUID for nondestructive evaluation of nonmagnetic metallic structures, *Cryogenics* **36**, 83–86.
- 66** Kuznik, J., Carr, C., Cochran, A., Morgan, L.N.C. and Donaldson, G.B. (1996) First order electronic gradiometry with simple HTS SQUIDs and optimised electronics. In D. Dew-Hughes (ed.), *Applied Superconductivity '95*, IoP Conference Series 148, Institute of Physics Publishing, Bristol, pp. 1499–1502.
- 67** Carr, C., McKirdy, D. McA., Romans, E.J., Donaldson, G.B. and Cochran, A. (1997) Electromagnetic nondestructive evaluation: moving HTS SQUIDs, including field nulling, and dual frequency measurements, *IEEE Trans. Appl. Supercond.* **7**, 3275–3278.
- 68** Carr, C., Romans, E.J., Macfarlane, J.C., Pegrum, C.M. and Donaldson, G.B. (1998) HTS dc SQUIDs for eddy current NDE in an unshielded environment, *Appl. Supercond.* **5**, 373–378.
- 69** Zhang, Y., Soltner, H., Krause, H.-J., Sodtke, E., Zander, W., Schubert, J., Grüneklee, M., Lomparski, D., Banzet, M., Bousack, H. and Braginski, A.I. (1997) Planar HTS gradiometers with large baseline, *IEEE Trans. Appl. Supercond.* **7**, 2866–2869.
- 70** Krause, H.-J., Hohmann, R., Soltner, H., Lomparski, D., Grüneklee, M., Banzet, M., Schubert, J., Zander, W., Zhang, Y., Wolf, W., Bousack, H., Braginski, A.I., Lucía, M.L., Zimmerman, E., Brandenburg, G., Clemens, U., Rongen, H., Halling, H., Faley, M.I., Poppe, U., Buschmann, H., Spörl, G., Binneberg, A. and Junger, M. (1997) Mobile HTS SQUID system for eddy current testing of aircraft. In D.O. Thompson and D.E. Chimenti (eds.), *Review of Progress in QNDE*, Vol. 16, Plenum Press, New York, pp. 1053–1060.
- 71** v. Kreutzbruck, M., Mück, M., Baby, U. and Heiden, C. (1998) Detection of deep lying cracks by eddy current SQUID NDE. In B. Larsen (ed.), *Proc. 7th European Conference on Non-Destructive Testing*, ECNDT, Broendby, DK, pp. 46–52.
- 72** v. Kreutzbruck, M., Allweins, K., Krause, H.-J., Gärtner, S. and Wolf, W. (2002) Defect detection of thick aircraft samples using HTS SQUID magnetometer, *Physica C* **368**, 85–90.
- 73** Krause, H.-J., Zhang, Y., Hohmann, R., Grüneklee, M., Faley, M.I., Lomparski, D., Maus, M., Bousack, H. and Braginski, A.I. (1997) Eddy current aircraft testing with mobile HTS-SQUID gradiometer system. In H. Rogalla and D.H.A. Blank (eds.), *Applied Superconductivity 1997*, IoP Conference Series 158, Institute of Physics Publishing, Bristol, pp. 775–780.
- 74** Grüneklee, M., Krause, H.-J., Hohmann, R., Maus, M., Lomparski, D., Banzet, M., Schubert, J., Zander, W., Zhang, Y., Wolf, W., Bousack, H., Braginski, A.I. and Faley, M.I. (1998) HTS SQUID system for eddy current testing of airplane wheels and rivets. In D.O. Thompson and D.E. Chimenti (eds.), *Review of Progress in QNDE*, Vol. 17, Plenum Press, New York, pp. 1075–1082.
- 75** Krause, H.-J., Hohmann, R., Grüneklee, M., Maus, M., Zhang, Y., Lomparski, D., Soltner, H., Wolf, W., Banzet, M., Schubert, J., Zander, W., Bousack, H. and Braginski, A.I. (1998) Aircraft wheel and fuselage testing with eddy current and SQUID. In B. Larsen (ed.), *Proc. 7th European Conference on Non-Destructive Testing*, ECNDT, Broendby, DK, pp. 296–303.
- 76** v. Kreutzbruck, M., Mück, M. and Heiden, C. (1999) Nondestructive testing of aircraft parts by SQUID based eddy current systems. In P. Di Barba and A. Savini (eds.), *Studies in Applied Electro-*

- magnetics and Mechanics*, Vol. 18, IOS Press, Amsterdam, pp. 257–260.
- 77** Krause, H.-J. and v. Kreutzbrück, M. (2002) Recent developments in SQUID NDE, *Physica C* **368**, 70–79.
- 78** Podney, W.N. and Murduck, J.M. (2001) Eddy current probe patterned in YBCO, *IEEE Trans. Appl. Supercond.* **11**, 1287–1290.
- 79** Carr C., Romans, E.J., Millar, A.J., Eulenburg, A., Donaldson, G.B. and Pegrum, C.M. (2001) First-order high-T_c single-layer gradiometers: parasitic effective area compensation and system balance, *IEEE Trans. Appl. Supercond.* **11**, 1367–1370.
- 80** Carr, C., Macfarlane, J.C. and Donaldson, G.B. (2002) The development of a fully portable cryocooled HTS SQUID NDE instrument, *Physica C* **372–376**, 259–262.
- 81** v. Kreutzbrück, M., Tröll, J., Mück, M. and Heiden, C. (1997) Experiments on eddy current NDE using HTS rf SQUIDs, *IEEE Trans. Appl. Supercond.* **7**, 3279–3282.
- 82** Hohmann, R., Maus, M., Lomparski, D., Grüneklee, M., Zhang, Y., Krause, H.-J., Bousack, H. and Braginski, A.I. (1999) Aircraft wheel testing with machine-cooled HTS SQUID gradiometer system, *IEEE Trans. Appl. Supercond.* **9**, 3801–3804.
- 83** Hohmann, R., Lomparski, D., Krause, H.-J., v. Kreutzbrück, M. and Becker, W. (2001) Aircraft wheel testing with remote eddy current using a HTS SQUID magnetometer, *IEEE Trans. Appl. Supercond.* **11**, 1279–1282.
- 84** Mück, M., Welzel, C., Gruhl, F., v. Kreutzbrück, M., Farr, A. and Schölz, F. (2002) Non-destructive testing of niobium sheets for superconducting resonators using an LTS SQUID system, *Physica C* **368**, 96–99.
- 85** Hatsukade, Y., Kasai, N., Kurosawa, M., Kawai, R., Takashima, H., Kojima, F. and Ishiyama, A. (2002) Detection of internal cracks and delamination in carbon-fiber-reinforced plastics using SQUID-NDI system, *Physica C* **372–376**, 267–270.
- 86** Valentino, M., Ruosi, A., Peluso, G. and Pepe, G.P. (2002) Structural health monitoring of materials by high critical temperature SQUID *Physica C* **372–376**, 201–208.
- 87** Ruosi, A., Valentino, M., Peluso, G. and Pepe, G.P. (2001) Analysis of low-velocity impact damage in reinforced carbon fiber composites by HTS-SQUID magnetometers, *IEEE Trans. Appl. Supercond.* **11**, 1172–1175.
- 88** Ruosi, A., Valentino, M., Lopresto, V. and Caprino, G. (2002) Magnetic response of damaged carbon fibre reinforced plastics measured by a HTS-SQUID magnetometer, *Compos. Struct.* **56**, 141–149.
- 89** Carr, C., Graham, D., Macfarlane, J.C. and Donaldson, G.B. (2003) SQUID-based nondestructive evaluation of carbon fibre reinforced polymer, *IEEE Trans. Appl. Supercond.* **13**, 196–199.
- 90** Hatsukade, Y., Aly-Hassan, M.S., Kasai, N., Takashima, H., Hatta H. and Ishiyama A. (2003) SQUID NDE method on damaged area and damage degree of defects in composite materials, *IEEE Trans. Appl. Supercond.* **13**, 207–210.
- 91** Graham D., Maas, P., Donaldson, G.B. and Carr, C. (2004) Impact damage detection in carbon fibre composites using HTS SQUIDs and neural networks, *NDT&E Int.* **37**, 565–570.
- 92** Beyer, J., Matz, M., Drung, D. and Schurig, Th. (1999) Magnetic detection of photogenerated currents in semiconductor wafers using SQUIDs, *Appl. Phys. Lett.* **74**, 2863–2865.
- 93** Beyer, J., Drung, D. and Schurig, T. (2001) SQUID photoscanning: an imaging technique for NDE of semiconductor wafers and devices based on photomagnetic detection, *IEEE Trans. Appl. Supercond.* **11**, 1162–1167.
- 94** Schurig, Th., Beyer, J., Drung, D., Ludwig, F., Lüdge, A. and Riemann, H. (2002) NDE of semiconductor samples and photovoltaic devices with high spatial resolution utilizing SQUID photoscanning, *IEICE Trans. Electron.* **E85-C**, 605–609.
- 95** Daibo, M., Shikoda A. and Yoshizawa, M. (2002) Non-contact evaluation of semiconductors using a laser SQUID microscope, *Physica C* **372–376**, 263–266.

- 96** Nikawa, K. (2002) Laser-SQUID microscopy as a novel tool for inspection, monitoring and analysis of LSI-chip defects: nondestructive and non-electrical contact technique, *IEICE Trans. Electron.* **E85-C**, 746–751.
- 97** Hinken, J.H. and Tavrin, Y. (2000) Thermoelectric SQUID method for the detection of segregations. In D.O. Thompson and D.E. Chimenti (eds), *Review of Progress in QNDE*, CP 509, American Institute of Physics, pp. 2085–2092.
- 98** Carreon, H., Lakshminarayanan, B., Faidi, W.I., Nayfeh, A.H. and Nagy, P.B. (2003) On the role of material property gradients in noncontacting thermoelectric NDE, *NDT & E Int.* **36**, 339–348.
- 99** Carreon, H., Nagy, P.B. and Blodgett, M.P. (2002) Thermoelectric nondestructive evaluation of residual stress in shot-peened metals, *Res. in Nondestr. Eval.* **14**, 59–80.
- 100** Jenks, W.G., Sadeghi, S.S.H. and Wikswo, J.P. (1997) SQUIDs for NDE, *J. Phys. D* **30**, 293–323.
- 101** Bellingham, J.G., MacVicar, M.L.A., Nissenoff, M. and Searson, P.C. (1986) Detection of magnetic fields generated by electrochemical corrosion, *J. Electrochem. Soc.* **133**, 1753–1754.
- 102** Jette, B.D. and MacVicar, M.L.A. (1991) SQUID magnetometry applied as a noninvasive electroanalytic chemical technique, *IEEE Trans. Magn.* **27**, 3025–3028.
- 103** Hibbs, A.D., Saeger, R.E., Cox, D.W., Aukerman, T.H., Sage, T.A. and Landis, R.S. (1992) A high-resolution magnetic imaging system based on a SQUID magnetometer, *Rev. Sci. Instrum.* **63**, 3652–3658.
- 104** Li, D., Ma, Y.P., Flanagan, W.F., Lichter, B.D. and Wikswo J.P. (1995) Detection of in-situ active corrosion by a SQUID magnetometer, *J. Min. Metals Mater.* **47**, 36–39.
- 105** Abedi, A., Feilenstein, J.J., Lucas, A.J. and Wikswo, J.P. (1999) A SQUID magnetometer system for quantitative analysis and imaging of hidden corrosion activity in aircraft aluminium structures, *Rev. Sci. Instrum.* **70**, 4640–4651.

14

SQUIDS for Geophysical Survey and Magnetic Anomaly Detection

T. R. Clem, C. P. Foley, M. N. Keene

| | | |
|----------|--|-----|
| 14.1 | Introduction | 483 |
| 14.2 | Magnetic Measurements in the Earth's Field | 484 |
| 14.2.1 | Introduction | 484 |
| 14.2.2 | Basic Principles of Magnetic Survey | 485 |
| 14.2.3 | The Principles of Tensor Gradiometers | 487 |
| 14.2.4 | Tensor Gradiometer Apparatus | 488 |
| 14.2.4.1 | Approaches to Tensor Gradiometer Systems | 488 |
| 14.2.4.2 | Intrinsic Gradiometers | 489 |
| 14.2.4.3 | Configured Gradiometers | 491 |
| 14.3 | Operation of SQUIDS in Real World Environments | 494 |
| 14.3.1 | SQUID Requirements for Unshielded Operation | 494 |
| 14.3.2 | Earth's Field Rejection | 496 |
| 14.3.3 | Environmental Magnetic Noise | 497 |
| 14.3.4 | Platform Noise | 497 |
| 14.3.5 | Mechanical Considerations | 498 |
| 14.4 | Data Acquisition and Signal Processing | 499 |
| 14.4.1 | Introduction | 499 |
| 14.4.2 | Data Acquisition | 499 |
| 14.4.3 | Survey Mapping | 500 |
| 14.4.4 | Point-by-Point Inversion | 500 |
| 14.4.5 | Localization using Time-Domain Windowed-Data Stochastic Approaches | 501 |
| 14.4.6 | Generalized Numerical Methods | 502 |
| 14.4.7 | Other Techniques | 503 |
| 14.5 | Geophysical Applications of SQUIDS | 504 |
| 14.5.1 | Introduction to Geophysical Prospecting | 504 |
| 14.5.2 | A Brief Historical Overview of SQUIDS in Geophysics | 508 |
| 14.5.3 | Laboratory Systems | 509 |
| 14.5.3.1 | Rock Magnetometers | 509 |
| 14.5.3.2 | Other SQUID-Based Systems for the Geophysics Laboratory | 513 |
| 14.5.4 | Field Systems | 513 |

- 14.5.4.1 Introduction 513
- 14.5.4.2 Transient Electromagnetics (TEM) 514
- 14.5.4.3 Ground-Based SQUID TEM 518
- 14.5.4.4 Airborne SQUID TEM 521
- 14.5.4.5 Tensor SQUID Gradiometers for Prospecting 523
- 14.5.4.6 Magnetotellurics and Radiometric Sounding 526
- 14.6 Magnetic Anomaly Detection Systems using SQUIDS 527
 - 14.6.1 MAD Detection Range 527
 - 14.6.2 The Superconducting Gradiometer/Magnetometer Sensor (SGMS) 529
 - 14.6.3 The High- T_c Three-Sensor Gradiometer 531
 - 14.6.4 The Global Feedback Gradiometer 532
 - 14.6.5 Other Systems 535
 - 14.7 Future Prospects 536

14.1 Introduction

There are many similarities and common requirements between systems for magnetic anomaly detection (MAD) in military hardware and the measurement of the magnetic properties of the Earth to explore for natural resources. For both applications, measurements are made of anomalies in the Earth's magnetic field that are caused by the presence of magnetic targets or sources. They both aim to determine the locations of magnetic sources and to classify them, preferably with the sensors on board a moving platform such as an aircraft or ship. Ideally, magnetic anomalies are classified from their measured magnetic moments to determine their physical size, shape, depth, and orientation. These common requirements have led to geophysics and defense adopting sensors and techniques developed for each other's applications. For example, geophysical airborne electromagnetics have been used in trials for bathymetry of the sea floor in turbid and shallow water (regions not suitable for traditional sonar techniques) [1], and fluxgates developed during World War II for aircraft guidance systems [2] are now standard magnetic sensors used in mineral exploration. The close relationship between MAD and exploration is epitomized by CAE Inc. and Geometrics Inc. who jointly own the patent for the standard sensors currently used for MAD and mineral exploration magnetics, the cesium vapor magnetometer [3].

There are also significant differences in the requirements for MAD and geophysical prospecting. MAD seeks specific-sized highly localized dipole sources, such as submarines and large ordnance, while geophysical prospecting targets are extended anomalies that can have a wide variety of configurations such as pipes, sheets, and compact targets. Whereas MAD needs a capability to track mobile sources, geophysical targets are always stationary. MAD only detects the magnetic moment of a source while geophysical exploration uses a range of electromagnetic techniques including the measurement of conductivity determined from actively inducing eddy currents in the Earth.

Unexploded ordnance (UXO) detection also adapts geophysical exploration techniques. Ranges of new techniques are under development to detect small and shallow magnetic anomalies. Various speculative techniques that are borrowed from active geophysical methods are being tested and modified by some research groups for UXO detection.

Because of the common use of far-field magnetic sensing techniques for MAD and geophysical exploration, it is little wonder that serious consideration has been given by both communities to the prospects for using SQUIDS to improve the effectiveness of their systems that are based on “conventional” magnetic sensors.

This chapter discusses the issues and principles that are universal to both geophysical prospecting and MAD. These include the operation of SQUIDS in the Earth’s magnetic field; the effects of motion on SQUID performance; schemes to overcome motion-induced noise; the improved information for both MAD and exploration by the measurement of tensors and vectors over standard scalar measurements; the use of magnetometers or gradiometers; the requirements for cryogenics in mobile systems; and methods of data acquisition and inversion of the measured data to provide information on the magnetic source from its distributed magnetic field as measured by a SQUID magnetometer or gradiometer.

14.2

Magnetic Measurements in the Earth’s Field

14.2.1

Introduction

In this section we treat MAD and airborne geophysical survey together and refer to them generically as *magnetic survey* unless a distinction between them is needed.

Magnetic surveys are well-established practices that have historically been developed utilizing conventional magnetometers, in particular optically pumped total field magnetometers (that measure a scalar total field) [3–5] as well as fluxgate magnetometers (that measure the three vector components of the magnetic field) [6, 7]. This is in contrast to the field of biomagnetism, for example, that was only made viable by the invention of the SQUID. It is not surprising that great interest has been shown in researching the potential of SQUIDS to improve the performance of magnetic survey sensors and instruments [8]. It is highly desirable for magnetic surveys to be conducted from platforms that are in motion, usually with six degrees of freedom in the Earth’s field. This is so that large areas can be covered in a short space of time (although there are several stationary applications for both MAD and geomagnetic surveys). For this reason magnetic sensors are required to have outputs that are invariant under motion, hence the use of scalar magnetometers or gradiometers rather than vector sensors. The vectorial characteristics and high sensitivity of SQUID magnetometers are thus a major drawback in magnetic survey applications, which must be overcome.

In terms of the research effort that has been put into developing SQUID-based systems for MAD, the military applications have had the most focus by far. Unfortunately, due to security classifications and censoring, much progress and work is unpublished. Since the mid-1980s there has been some relaxation on publishing constraints from several countries, but there is undoubtedly a good body of inter-

esting work that remains hidden. At least in the nonmilitary applications, it is clear that SQUIDS on moving platforms remain as experimental or highly specialized instruments that have not yet superseded conventional sensors despite several decades of research. This is mainly due to the problems in overcoming motion noise and achieving immunity to environmental interference. Chapter 7 (of volume I) gives a general discussion of these problems. As pointed out there, rotation in the Earth's field is the most difficult to overcome.

An idea of the scale of the motion noise problem is given when one considers that a SQUID magnetometer with $5.6 \text{ fT Hz}^{-1/2}$ noise floor, edgeways on to a $56\text{-}\mu\text{T}$ Earth field can subtend just $\sin\theta = \theta = 10^{-10}$ radians in one second before the motion is seen on the output. Even a first-order gradiometer with the same sensor noise floor (at the two points of measurement along the baseline) that is balanced to 1 part in 10^6 has a residual magnetometric response of $5.6 \text{ nT Hz}^{-1/2}$ and an allowable motion of 10^{-4} radians. Despite this considerable problem, much progress has been made to overcome motion-induced noise, and there is no reason to believe that it will not be completely solved in due course. Therefore, it is highly probable that SQUIDS will eventually become important sensors in all magnetic survey applications.

14.2.2

Basic Principles of Magnetic Survey

The far field of a magnetic object is, by definition, always of the form of a simple magnetic dipole moment, M , in which case its magnetic induction B at position r with respect to the object is

$$B = \frac{\mu_0}{4\pi} \left(\frac{3(M \cdot r)r}{r^5} - \frac{M}{r^3} \right) \quad [\text{T}]. \quad (14.1)$$

The magnetic field from a simple dipole falls off in all directions as $1/|r|^3$ and the severity of this dependence requires the use of highly sensitive magnetometers for useful detection ranges to be achieved. At close range, Eq. (14.1) does not usually apply because most large magnetic objects (targets) have complicated, individual magnetic structures that are not easily predictable, particularly if the target is physically larger than the range at which it is being measured. This can often be the case in geomagnetic prospecting. For ranges that are intermediate between these cases, quadrupole or higher order models are usually applicable and although these present tractable problems in classifying the target, the band of ranges over which they apply is very narrow so this regime is rarely considered.

Total-field magnetometers (also referred to as total magnetic intensity (TMI) magnetometers) measure the magnitude of the total magnetic field and are currently the accepted method for magnetic survey. The main advantage of this type of sensor over its vector counterpart is its insensitivity to rotation in the Earth's background field since total field is a scalar. If B_E and B_A denote the vector magnetic field of the Earth and of a magnetic anomaly respectively, and if $|B_A| \ll |B_E|$,

then the scalar signal observed by a total-field magnetometer (referenced to the Earth's field) is

$$B_T = |B_E + B_A| - |B_E| \equiv \frac{B_E \cdot B_A}{|B_E|} \quad [\text{T}]. \quad (14.2)$$

Note that, as a result of the right-hand approximation above, a total-field magnetometer does not actually measure the magnitude of the magnetic field anomaly, but measures the projection of that signal onto the Earth's field. This is shown in Figure 14.1 where a comparison is drawn between this and a three-axis vector magnetic measurement. From this comparison it is easy to see that whereas the magnitudes of B_E and $B_E + B_A$ are invariant under rotation of the sensor, the vec-

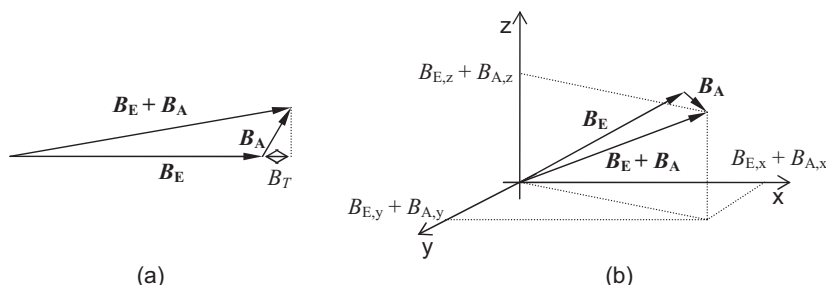


Fig. 14.1 A representation of the magnetic signals detected for a target, B_A , in the presence of the Earth's field, B_E , with (a) a total-field magnetometer (see Eq. (14.2)) and (b) for a three-axis *absolute* vector magnetometer such as a fluxgate. A three-axis *relative* vector magnetometer, such as a SQUID system with three orthogonal sensors that is cooled in the Earth's field, i.e., $\{B_{A,x}, B_{A,y}, B_{A,z}\}$.

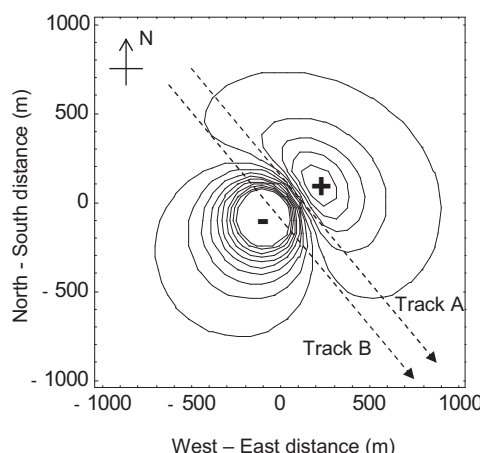


Fig. 14.2 Theoretical contour map, using (14.2) of the total field for a magnetic dipole with $M = \{4, 2, -3\} \text{ kA m}^2$ in an Earth's field of $\{0, 20, -50\} \mu\text{T}$ in the plane $\{0, 0, 300\} \text{ m}$. Track A represents the least favorable trajectory for detection and Track B is the most favorable.

tor components of these fields, shown in Figure 14.1(b), will vary considerably with rotation of the sensor's axes. This is the origin of *motion noise* in vector magnetometer systems, but total-field magnetometers are immune. A contour plot for total field calculated from Eq. (14.2) in a plane above a dipole is shown in Figure 14.2. The most common total-field magnetometers are based on the magnetic effects associated with atomic or nuclear resonance phenomena [3–5].

The total field can also be synthesized from three orthogonal vector magnetometers: $B = (B_x^2 + B_y^2 + B_z^2)^{1/2}$. This approach has been pursued using three-axis fluxgates as well as SQUID magnetometers, including the SQUID magnetometer reported in Ref. [9]. To date, this approach has had limited success due to the considerable difficulties in calibrating out all the errors. The main ones are:

- nonorthogonality between the sensors
- scaling mismatch between the three sensors
- offsets within each sensor
- nonlinearity in the sensors and their readout electronics
- crossfield effects, where vector magnetometers exhibit small responses to fields in their orthogonal direction
- crosstalk between sensors
- nonperfect angular dependence of the sensors, where the output of a sensor does not exhibit a perfect cosine response with respect to its angle to a uniform field.

Although it appears that SQUID- and fluxgate-synthesized total-field magnetometers may have similar performance to optically pumped sensors, this has not yet been robustly demonstrated.

14.2.3

The Principles of Tensor Gradiometers

In the following discussion we use the term “gradiometer” to refer to a first-order gradiometer as higher order sensors are very rare in magnetic survey applications. A magnetic gradiometer that is perfectly balanced, *i.e.*, with zero magnetometric response ($A_{\text{eff}} = 0$), will have an output that is free from direct motion noise when moved in a perfectly uniform field, and is therefore a suitable sensor for magnetic survey. A gradiometer may be configured from differencing two total-field magnetometers, separated by a baseline, and this configuration is often used for marine magnetic surveys. Another configuration is to use the difference between two vector magnetometers such as fluxgates or SQUIDS, again separated by a baseline. These are called *tensor gradiometers* because the baseline's direction and the field sensing direction are both fixed (usually confined on a parallel or orthogonal basis) within the same frame of reference so a particular tensor element is measured. This is not true for differenced total-field magnetometers where the field sensing direction is always in the Earth's field frame and the baseline is in the sensor's frame, and the two frames can rotate with respect to each other. The

(first-order) gradient of the magnetic field vector for a magnetic dipole is a second-order tensor with components G_{ij} given by

$$G_{ij} = \frac{\partial B_i}{\partial x_j} = -\frac{3\mu_0}{4\pi r^7} \left[\mathbf{M} \cdot \mathbf{r} \left(r_i r_j - r^2 \delta_{ij} \right) - r^2 \left(r_i M_j + r_j M_i \right) \right] \quad [\text{T m}^{-1}] \quad (14.3)$$

There are nine measurable first-order gradients but not all of them are independent. The Maxwell equation $\nabla \cdot \mathbf{B} = 0$ constrains the matrix G_{ij} to be traceless, *i.e.*, $G_{xx} + G_{yy} + G_{zz} = 0$, so only two out of the three leading-diagonal components are required to be measured if the full matrix is to be constructed. Furthermore, the Maxwell equation $\nabla \times \mathbf{H} = \mathbf{J}$ reduces to $\nabla \times \mathbf{H} = 0$ in free space and constrains the matrix G_{ij} to be symmetric, *i.e.*, $G_{ij} = G_{ji}$. There are therefore only five independent gradients in free space. Tensor gradiometer instruments are usually configured to measure the five independent gradients in airborne, land-based and most sea-based systems. (In undersea situations where substantial currents are flowing in the water, such as the corrosion currents from ships, eight gradients are required because G_{ij} will no longer be symmetric.)

It is a basic axiom of measurement theory for this class of problems that for each independent measurement that is taken one unknown may be eliminated. There are six unknowns in the dipole equations (14.1) and (14.3), $\mathbf{M} = \{M_x, M_y, M_z\}$ and $\mathbf{r} = \{x, y, z\}$, so measurements of the five independent gradients are not quite sufficient for a full solution. Early analytic inversion algorithms [11] solved for the bearing to the anomaly (two angles), the bearing of the dipole (two angles), and the quantity $|M|/r^4$. To separate $|M|$ and r^4 , a measurement from a different position is required so that \mathbf{r} is fixed by triangulation. Later techniques have largely overcome this difficulty and these are described in Section 14.4.

This ability to determine \mathbf{r} and \mathbf{M} from two measurements is highly advantageous, as this can be conducted by a single “fly past” along a straight-line track where all dipoles within a swath around the host platform that present sufficient signal-to-noise ratio (SNR) in the gradiometers will be located and classified. To achieve the same with a total field magnetometer requires the building of a contour map, similar to Figure 14.2, requiring systematic survey to magnetically map a whole area and then perform an analysis. Comparatively this is very time consuming and requires the dipole to be stationary whilst the survey is conducted. For land-based UXO surveys using total-field magnetometers and single-axis fluxgate gradiometers, this is the method most commonly used.

14.2.4

Tensor Gradiometer Apparatus

14.2.4.1 Approaches to Tensor Gradiometer Systems

A single-axis tensor gradiometer (defined by the field sensing direction and baseline being fixed within the same frame of reference) may be constructed in many different ways, but there are two distinct categories by which they may be classified. One of these is the “intrinsic” gradiometer where gradiometric measure-

ments are made with a single sensor (also called a “hardware gradiometer”), and the other is the “configured” gradiometer where two or more separated magnetometers are used and their outputs are processed, which consists of simple subtraction if the system is otherwise perfect, to determine the gradient. (Configured gradiometers are often called “electronic” or “software” gradiometers depending on whether the subtraction is done electronically or in software.) Many SQUID systems have been made within each of these categories.

Multiaxis gradiometers may be constructed from several single-axis sensors. For intrinsic gradiometers, one sensor per axis is required. With configured systems it is possible to use a magnetometer for more than one gradient measurement, *e.g.*, $\partial B_x/\partial x$ and $\partial B_x/\partial y$ can be measured with three magnetometers if they are mounted on an L-shaped baseline, the corner sensor’s output being used for both gradients. It is interesting to note that for a five-axis gradiometer, the independent gradients can be measured with a two-dimensional baseline structure, *e.g.*,

$$G_{ij} = \begin{pmatrix} \frac{\partial B_x}{\partial x} & \frac{\partial B_y}{\partial y} & \frac{\partial B_z}{\partial z} \\ - & \frac{\partial B_y}{\partial y} & \frac{\partial B_z}{\partial z} \\ - & - & - \end{pmatrix} [\text{T m}^{-1}] \quad (14.4)$$

can be built to occupy the $x-y$ plane and this is illustrated schematically in Figure 14.3. Here, the gradients are formed from the following differences $\partial B_x/\partial x \propto B_{x2}-B_{x1}$; $\partial B_y/\partial x \propto B_{y2}-B_{y1}$; $\partial B_z/\partial x \propto B_{z2}-B_{z1}$; $\partial B_y/\partial y \propto B_{y3}-B_{y1}$; and $\partial B_z/\partial y \propto B_{z3}-B_{z1}$. The constants of proportionality are the inverses of the baselines. Note that the B_{y1} and B_{z1} SQUIDs are utilized for measuring two different gradients.

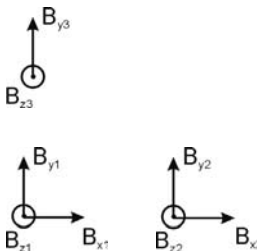


Fig. 14.3 A schematic representation of the practical arrangement for a five-axis tensor gradiometer on a two-dimensional baseline structure that is in the plane of the page. This arrangement will measure the tensor gradient components of Eq. (14.4). The arrows represent the sensing directions of the SQUIDs with the z-SQUIDs sensing perpendicular to the page.

14.2.4.2 Intrinsic Gradiometers

Intrinsic gradiometers measure the difference in the average field between two loops (or “pickup coils”) in a flux transformer. These may be connected serially (figure-of-eight) or in parallel, but for in-motion operation, serial connection is preferred because large shielding currents can flow in parallel-connected structures that can cause many problems. The big advantage that intrinsic gradiometers have over configured ones is that the process of subtraction between the two pickup coils within a flux transformer, by Kirchoff’s law, is perfectly linear at

low frequencies (provided the external field is low enough to prevent magnetic vortices entering the wire) and remains so over an enormous dynamic range.

Low- T_c flux transformers that are constructed from wire can be made into planar or axial gradiometers. Planar gradiometers measure the off-axis components of the gradient matrix G_{ij} ($i \neq j$) whereas axial ones are needed for the two required on-axis components, G_{ii} . These are described in detail in Chapters 1, 5, and 7 of volume I. Another important advantage is the circular cross-section of the wire, which has a favorable demagnetizing factor: strong field concentrations at the edges are therefore avoided. The main disadvantages of wire-wound systems is the difficulty in achieving good balance, because the two pickup loops have to be matched in area to a very high degree, and each loop must be highly planar to minimize sensitivity to fields in the plane of the coils. These difficulties are compounded by the crossover between the coils, the presence of the twisted wires to the SQUIDs, and any superconducting shielding the SQUIDs may have. The wire-wound approach is not an option for high- T_c devices because suitable wire is not available and neither is a superconducting connection method to the thin-film structures of high- T_c SQUIDs.

For planar gradiometers, thin-film devices significantly reduce the problems of balancing and planarization that are problematical with wire technology. The coils are photolithographically defined and can be very highly balanced. Furthermore, sacrificial superconducting tabs and tracks can be made on the substrate to fine-tune the balance by ablation. The SQUID may be fabricated on the same substrate, or a superconducting wire arrangement may be used for a more remote SQUID, although this introduces some of the problems with wire systems described above. The disadvantages of the thin-film approach are the requirements for large-area thin-film growth and patterning, the inability to make axial gradiometers, and the unfavorable demagnetization factor that leads to high concentrations of field at the film edges with a risk of flux penetration at weak spots.

The problem of the inability to make axial gradiometers has been addressed by using a planar gradiometer mounted at 45° to the basis of the mounting frame in order to measure a linear combination of the required axial gradient and a planar one. By correcting out the planar gradient contribution using a separate gradiometer that measures just the unwanted planar gradient, the pure axial component can be arrived at. The gradiometer has to be $\sqrt{2}$ longer than the others to achieve the same baseline and can be compromised by the compensation method, but nevertheless this has been shown to be successful [12].

A recent development of a hybrid flip-chip high- T_c SQUID which incorporates a gradiometric pickup coil made of bent flexible superconducting tape, on a hastalloy substrate, has been shown to measure the axial gradient G_{ii} achieving a balance of about 10^5 [13, 14]. Figure 14.4 shows a schematic layout for this hybrid axial gradiometer.

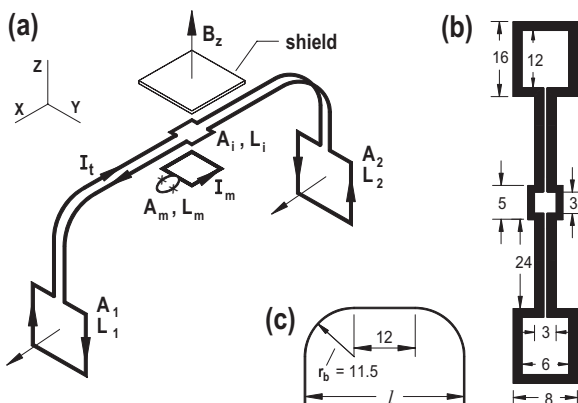


Fig. 14.4 The hybrid gradiometer constructed on flexible tape [13,14].
 (a) A SQUID magnetometer is inductively coupled to a bent symmetric flux transformer. A superconducting shield reduces the magnetometer response to B_z -fields. (b) The layout of the transformer in planar and (c) bent configuration. Dimensions are in mm.

14.2.4.3 Configured Gradiometers

The simplest configured gradiometer is made by using two magnetometers, separated by a baseline, and subtracting their outputs accurately. There are many formidable problems with doing this and we describe the main ones to highlight the issues rather than to suggest that this approach makes a practical gradiometer. The main problem is with meeting the high dynamic range requirement, ~ 180 dB for a SQUID system and ~ 120 dB for a fluxgate system (in a 1-Hz bandwidth). Digital subtraction (often referred to as a *software gradiometer*) is preferred over analog subtraction (*electronic gradiometer*) because it is more accurate, but this requires highly accurate digitization in the first place. Although 135 dB is now achievable with an ADC of 24 bits operating at ~ 23 -bit effective resolution, 180 dB is not yet achievable with slew rate or bandwidth sufficient for MAD and geophysics. Analog subtraction, on the other hand, places unreasonable demands on the matching of the two sensor electronics and the common-mode rejection ratio of the subtractor – overall 180 dB for the SQUID system – and this is too difficult. The residual common-mode signal after the subtraction stage (due to the limited common-mode rejection in the subtraction circuit) is directly equivalent in its effect to imbalance in the gradiometer. Another major difficulty is the (inevitable) difference in the non-linearity between the two sensors' electronics which are substantially more difficult to alleviate than linear errors. The wide dynamic range also requires a high slew rate, otherwise the field changes cannot be tracked properly.

A far better configuration is a three-sensor gradiometer (TSG) invented by Koch [15–17]. Here a third (reference) sensor is used between the two sensors that will form the gradiometer, as shown in Figure 14.5. The reference sensor measures

the average field between the other two and its output is fed back via an integrator and three identical coils, one surrounding each sensor. The reference sensor is held in a *field-locked-loop*, with its feedback field being equal and opposite to the external field. This same field is then applied equally to the other two sensors, thus the external field (common-mode field) is cancelled from the system. The outputs from the outer sensors are subtracted to form the gradiometer, but rather than experiencing the Earth's field, they each experience the error field from the feedback loop and any noise from the reference sensor or its electronics. These are a much lower level than the Earth's field so the requirements on the dynamic range, common-mode rejection, and slew rate of the subtraction stage are considerably relaxed. The feedback error and noise from the reference sensor are subtracted in the gradiometer. The reference sensor's integrated output is a measure of the Earth's magnetic field component in the gradiometer frame of reference, and this may be used in more sophisticated schemes to correct residual imbalance in the gradiometer as described in Section 7.7.4 of volume I.

This single-axis TSG offers great flexibility to measure any gradient component. Multiaxis gradiometers based on TSGs can share reference sensors and feedback circuits. For configuring a multiaxis gradiometer, multiple TSGs are not ideal

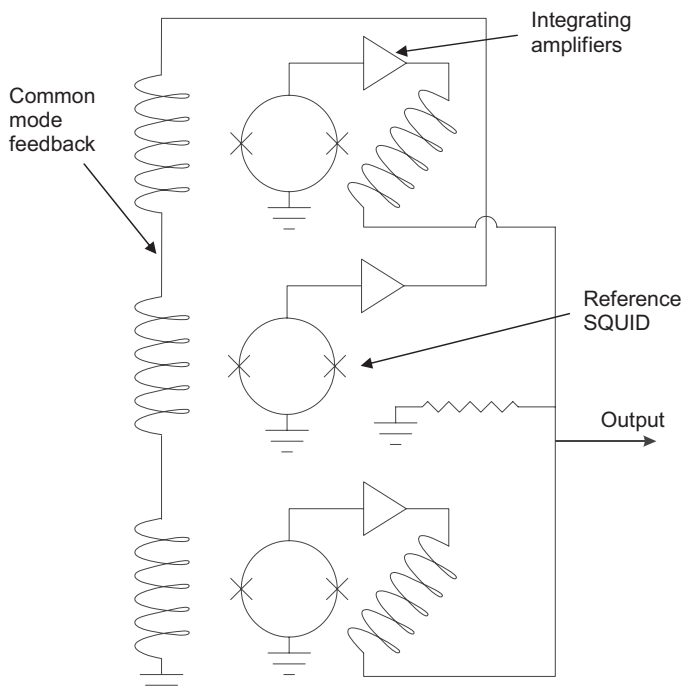


Fig. 14.5 The three-SQUID gradiometer [15–17] has a reference SQUID that feeds back to the outer SQUIDs as well as to itself, thus canceling changes in the uniform component of the ambient field. The system is fully sensitive to gradients that are measured by subtracting the flux-locked-loop outputs of the outer SQUIDs.

because the feedback coils from one gradiometer generate strong local time-varying gradients when in motion, which will be measured by neighboring gradiometers. Careful positioning of the sensors can reduce this problem. A high- T_c SQUID single-axis TSG has been successfully demonstrated [18] where a triaxial fluxgate was used as the reference sensor. This gradiometer is described in more detail in Section 14.6.3.

Another configured gradiometer for unshielded in-motion operation takes these ideas further and uses a scheme of “global feedback” to reduce the dynamic range and slew rate requirements [19, 20]. Here, the feedback to the gradient sensors from the field reference sensors is via three orthogonal Helmholtz coils that surround all the SQUIDs as shown in Figure 14.6. This ensures that strong local gradients are not formed within the gradiometer array. One way to consider this is that the magnetic field within the triaxial Helmholtz coils (and therefore over the whole gradiometer array) is locked to a constant value irrespective of any motion within the Earth's field. The SQUIDs in the array then have a much reduced, and now achievable, dynamic range requirement, the maximum field being the global feedback loop's error field and electronic noise. The magnetometers are then subtracted in pairs in the usual manner to enable gradient measurements to be made as well as to reject the residual error and noise signals from the global feedback coils. The gradiometer errors that are caused by miss-scaling, misalignment, and offsets are all linearly dependent and can then be compensated for by using adap-

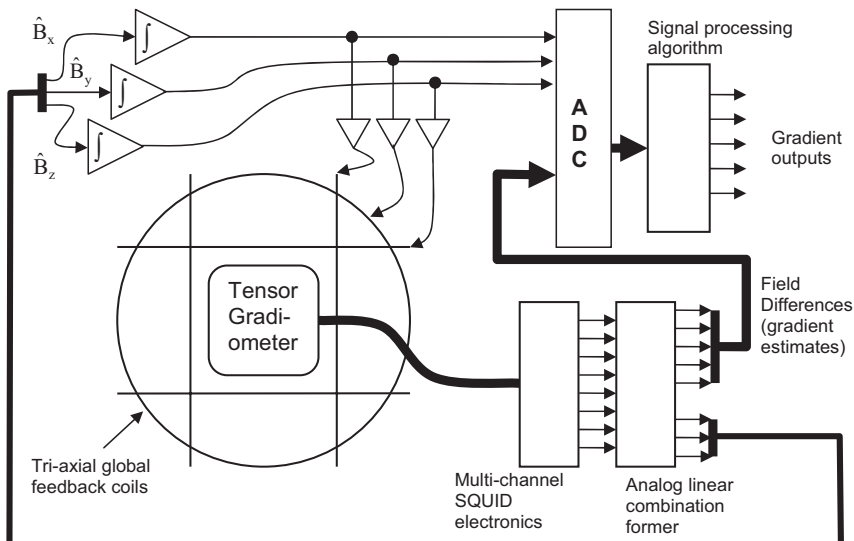


Fig. 14.6 A global feedback gradiometer system [19,20] actively cancels the three components of uniform field of a tensor-gradiometer array with triaxial Helmholtz coils. The analog linear combination former adds all SQUID outputs in the x-direction to feed back to the x-Helmholtz coil, and similarly for the y and z. It also forms the differences that are used as gradient measurements. The performance of a single axis proof-of-principle is shown in Figs. 14.18 and 14.19.

tive signal processing algorithms after the digitization stage. The reported gradiometer [19] does not use separate reference SQUIDS, but feeds back the sum of the x -facing SQUIDS to the x -coils and the similarly for the y and z directions. A system based on this principle is described in Section 14.6.4.

Most of the configured gradiometer schemes have also been used for fluxgate-based instruments [17, 21, 22]. However, with the introduction of very high-resolution ADCs (such as the Texas Instruments AD51210 and the Analog Devices AD7738), the full dynamic range of low-noise fluxgates operating in the Earth's field can now be directly digitized, removing the need for common-mode feedback and analog subtraction. (Mismatched nonlinearity between sensors is still a problem but this is more easily calibrated out with this approach.) There are no published reports of directly digitized configured fluxgate gradiometers so far, but some are known to be under construction.

14.3

Operation of SQUIDs in Real World Environments

14.3.1

SQUID Requirements for Unshielded Operation

For most SQUID applications, particularly where close-in sources are being examined, the magnetic and electric field environment is usually carefully controlled. This is achieved by shielding using mu-metal or eddy-current shields. Furthermore, such SQUID instruments tend to be operated within laboratory or hospital environments where ruggedness is not an important issue. In contrast, SQUID instruments for magnetic surveys cannot be magnetically shielded and must be rugged enough to be fielded under the same conditions as those to which other types of survey equipment are exposed.

It is difficult to operate a moving SQUID whilst it is fully exposed to the Earth's field. Even with the SQUID largely protected by the field feedback schemes discussed earlier, it is prudent to use design features that minimize both the hysteresis and the field that threads the Josephson junctions, because critical currents are field dependent. For high- T_c devices these problems are considerably worse than for low- T_c devices.

Hysteresis is caused by the entry of magnetic flux into the superconducting structures of the SQUIDs and flux transformers, as described in detail in Sections 5.5 and 5.6 (see in particular Refs. [23, 24]). It is clear from the research into hysteresis effects that it is difficult to operate low- T_c thin-film gradiometers without hysteresis errors if they are in motion when fully exposed to the Earth's field. For high- T_c materials the situation is far worse, but for systems with magnetic field feedback described in Section 14.2.4.2, the superconductors are highly protected from the Earth's field.

For thin-film SQUIDs, it is prudent to use fairly thick films, 0.5–1 μm , with steep smooth edge profiles. These measures minimize the demagnetizing factor,

reducing the field concentrations at the edges and the risk of flux lines entering to cause hysteresis. The superconductor linewidths should be minimized for the same reason. In thin-film flux transformer pickup coils, reducing the linewidth increases the coil inductance, which compromises coupling efficiency to the SQUID, so a design compromise has to be made. Large-area components such as SQUID washers can be patterned with slots or holes that relieve the field concentrations at the extremities of the devices [25]. However, there has been some discussion in the literature suggesting alternative approaches [26]. Protection of the Josephson junctions from external fields can be achieved by fabricating a superconducting shield on the chip. For high- T_c grain-boundary devices, junction widths must be less than 2 μm as the width of the junction determines its sensitivity to applied magnetic fields [27]. To ensure that the superconducting structures surrounding the junctions do not focus fields into them, the Josephson junction should be placed at distance of about 150–300 μm from the flux focuser [26]. Devices that are acceptable for unshielded use can be many times more expensive than other types of SQUID due to the special design features, film quality requirements, and comparatively lower yields.

The term *trial quality* refers to the requirement that the SQUID is stable in applied magnetic fields, *i.e.*, it demonstrates low levels of flux creep after a magnetic field is changed or removed. *Field removed* (FR) measurements are often used to assess the SQUID quality; these are described in Chapter 7. The behavior of the SQUID during FR noise measurements provides useful insights into the response of the SQUID's noise to changes in the magnetic field and helps with the understanding of the nature of excess noise.

Figure 14.7(a) shows the FR spectral field noise, which varies as $f^{-\beta}$. The exponent β is 1.0 for the data here but has been observed to vary from 0.5 to 1.5 for different SQUIDs in applied fields. Although the FR noise is time dependent, it is always smaller than *field applied* (FA) noise for the same applied field. Figure 14.7(b) shows an example of FA and FR flux noise for a 2-mm washer rf SQUID as a function of time for a field of 50 μT . The FR noise at 1 Hz decays following removal of the field. The same decay is not evident at 10 Hz, probably because at this frequency the excess noise is not much above the white noise floor of the device.

SQUID outputs may drift measurably following the removal of an applied field due to egress of magnetic flux from the SQUID body. The SQUID is a detector of its own magnetization. Figure 14.7(c) shows measurements of the output drift. It can be seen that the drift is approximately linear with $\log(t)$, a well-known characteristic of flux creep or thermally activated flux movement. Like flux noise, the creep rate is strongly dependent on the field magnitude but scarcely dependent on the length of time for which the field was applied. Minimal flux creep demonstrated during FR measurements is a defining parameter for a SQUID that can operate in the extreme conditions of airborne magnetometry.

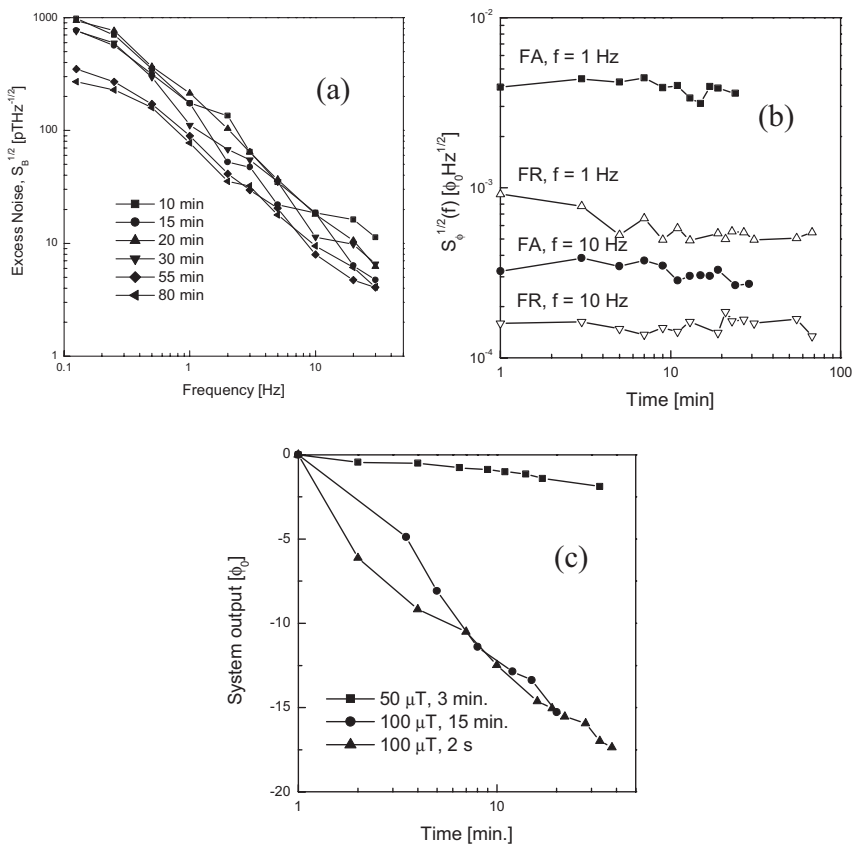


Fig. 14.7 (a) Zero-field cooled FR noise spectrum for a 2-mm rf washer SQUID at various times after removal of a 450- μT magnetic field. (b) Zero-field cooled spot noise measurements as a function of time interval after FA and FR measurements of a 50- μT magnetic field. (c) SQUID output drift under zero-field cooled FR conditions after the removal of 50- and 100- μT fields applied for various time lengths.

14.3.2 Earth's Field Rejection

The Earth's magnetic field can be approximated to first order as a large, time-invariant and spatially uniform magnetic field. This affects gradiometers by inducing motion noise caused by imbalance as described in detail earlier as well as by inducing hysteresis. Gradiometer imbalance is an issue that must be addressed through sensor design, system design and signal processing in accordance with the discussion in Chapter 7 and the systems concepts introduced in Section 14.2.4.

The Earth has a magnetic gradient of the order of $10\text{--}30 \text{ pT m}^{-1}$, arising from sources deep inside. Anomalous signals will therefore arise from rotation of a perfect gradiometer in the Earth's magnetic gradient. These gradients are directional, so that large signals may be measured in some channels of a tensor gradiometer, while the signals in the remaining channels may be two or three orders of magnitude smaller. Corrections can be made for these natural gradients in the signal processing stage, because the natural gradients have consistency over relatively long ranges compared to localized magnetic anomalies. The interested reader is referred to Ref. [28] for a more detailed discussion of this topic.

14.3.3

Environmental Magnetic Noise

Geomagnetic noise, *i.e.*, temporal variations in the Earth's field arising from ionospheric currents, is discussed in Ref. [29]. These variations occur nominally at levels from 10^{-3} to $10^{-1} \text{ nT Hz}^{-1/2}$ at 0.1 Hz, depending on the latitude and atmospheric electrical activity. The spatial scales are of the order of 100 km or greater. This phenomenon impacts the performance realizable by magnetometers, which could otherwise attain much greater detection ranges, but does not impact the performance of rigid gradiometers with short baselines.

Local variations in the Earth's field arise from geological sources within the Earth's outer crust (in contrast to the more uniform gradient field arising from sources deep inside the Earth) as well as from local surface features. These are referred to as geologic noise signals, and although they do not vary with time (except on geological timescales) they are manifest as a time-varying signal to a sensor that is passing them at speed. The magnitude of geologic signals may greatly exceed the Earth's field gradient in certain locales, notably in mountainous and rocky areas. Typical values of geologic noise range from 0.05 nT m^{-1} in low-gradient areas to in excess of 10 nT m^{-1} in high-gradient areas. In some cases, geology will be the source of false alarms if the spatial scales of the local geologic features are commensurate with the scales of targets of interest.

14.3.4

Platform Noise

In order to gain widespread acceptance of magnetic sensors, it is very desirable to provide system concepts in which the magnetic sensor can be operated onboard the primary platform. Such efforts involve designs to make the platform subsystems magnetically, electrically, and electronically quiet, and the implementation of platform noise compensation using auxiliary magnetic sensors and more sophisticated signal processing.

The ideal situation for operating sensitive magnetic sensors onboard moving platforms is to provide an environment in proximity to the sensor which is free of ferromagnetic material and free of large areas of nonferrous metal that become eddy-current sources under motion in the Earth's field. Furthermore, the sensor

should be distant from electrical and electronic equipment, power plants, electrical distribution paths, and propulsion systems. To the extent to which it is feasible, this philosophy leads to system configurations in which the sensor is operated in a magnetically sterile platform at a sufficient standoff from a primary vehicle towing the sensor package. This approach was used in the MADOM and MUDSS projects described in Section 14.6, where the sensor operated in an underwater fiberglass body towed behind a surface craft [30] and in airborne magnetometry and gradiometry for geophysical exploration [31, 32].

Successful operation of fluxgate gradiometers has been demonstrated inboard motorized underwater vehicles [21, 33]. This has been made possible by advanced adaptive data processing of the sensor outputs as well as advances in noise remediation techniques for the platforms (see Ref. [34] and references therein). Early high-sensitivity gradiometer measurements from a self-propelled unmanned underwater vehicle, (UUV) [21] used a purpose-built low-magnetic platform whereas later systems used modified standard vehicles [33, 35]. The platform noise was sufficiently low for these experiments to suggest that SQUIDS could potentially be operated sensitively from purpose-built UUVs or unmanned airborne vehicles (UAVs), although this has not yet been demonstrated in practice.

14.3.5

Mechanical Considerations

When designing a gradiometer for magnetic survey applications, it is important to ensure that proper consideration is given to the effects of vibration and other accelerations that the instrument will experience. For example, a gradiometer that is suspended from the top-plate of a cryostat by a thin-walled tube is likely to undergo pendulum motion under vibration, even though it is an acceptable configuration for a laboratory instrument. This can be overcome by securing the sensors at the base of the dewar with electrical connections made by free wires from the sensors to the dewar opening mounts as described in Ref. [36].

The very weak magnetic susceptibilities of cryogenic liquids, particularly if contaminated with oxygen, can cause signals if the liquid “sloshes” around the flux transformers. Preventing cryogen motion should therefore be addressed in the cryogenic design. This can be achieved by the introduction of cotton or glass wool into the dewar to act as a baffle. Temperature fluctuations within the cryogen can also be a problem, so consideration should be given to ensuring a constant pressure within the cryostat, particularly for airborne or underwater applications. A pressure regulator on the venting outlet of the dewar can control the gas pressure above the cryogen and hence keep the temperature stable. For high- T_c SQUIDs, this is particularly important as the Josephson junctions have far higher $\partial I_0/\partial T$ at 77 K than the low- T_c junctions at 4.2 K.

14.4

Data Acquisition and Signal Processing

14.4.1

Introduction

Localization and classification are the primary goals of magnetic survey. For some geophysical applications a magnetic map is retrospectively produced from the data that are collected during a survey. For MAD (and some other geophysical applications) the objective is to locate and classify anomalies in real-time or near real-time because some targets may move or time may be too limited to conduct high-density search patterns. To do this, algorithms that determine the magnetic moment M and location r from the measured gradients are required and these may be performed either analytically or numerically. These are commonly referred to as “inversion” algorithms in the context of MAD.

Two concepts of operation for magnetic anomaly localization and classification are usually considered. First, one would like to conduct searches over as wide an area as possible using systems that are airborne, underwater, or on the ground. For other cases, one may be interested in homing onto or tracking magnetic anomalies, which is more akin to “targeting” than to “survey.” In the former case, it is desirable to detect and process target signals at the longest possible range where the signal-to-noise ratios (SNRs) are very poor. In this situation statistical signal processing techniques, such as least-squares fitting of data collected in windows over a period of time would be considered in order to deduce r and M . In the other case, *i.e.* for targeting, one may need to update position estimates frequently as the sensor will not necessarily move smoothly; *e.g.*, for land-based operations over rough terrain or for diver-held underwater survey. In such cases, one would also consider the use of point-by-point or nonlinear numerical fitting techniques, although these generally require larger SNRs in order to be effective. In this section we describe mapping, point-by-point inversion, stochastic windowed-data techniques, and numerical fitting algorithms that have all been used to localize magnetic anomalies.

14.4.2

Data Acquisition

The general requirements for data acquisition are largely covered in Chapter 7. It should be noted that for magnetic surveys, data may be collected over long periods of time so a reliable data-recording apparatus with sufficient capacity to record an entire survey is required. Care should also be taken in the data transfer between the SQUID electronics output and the computer processor when these are physically separated by a large distance. This can be the case when the SQUIDs are in a towed body and the processor is in the main platform (boat or aircraft). Interference can be easily picked up on an analog link, particularly if it is single-ended.

Differential analog is better, *i.e.*, shielded balanced pairs, but if possible it is best to digitize immediately at the SQUID electronics and use a digital link.

14.4.3

Survey Mapping

This method is mostly employed in geomagnetic survey and can be applied for air-, sea-, or land-based measurements, although we will describe it in terms of airborne measurement. A survey aircraft would normally have a towed total-field magnetometer to escape from noise sources within the aircraft. It would typically fly along parallel lines, typically of 100–200 m separation at an altitude between 70 and 200 m, depending on the terrain, to cover the survey area. Magnetic data and positional telemetry of the aircraft are recorded simultaneously so the map can be accurately constructed. With this method, the magnetic data are continuous in the direction of flight but discrete in the perpendicular direction because of the sweep separation. For this direction the data are often interpolated to provide a smooth 2D map. The interpolated data may be displayed as contour maps, such as Figure 14.2, or more elaborately processed to resemble color relief maps. This method is excellent for “imaging” magnetic geological structures that are not small compared to the flying height or line separation; *i.e.* not in the simple dipole limit.

14.4.4

Point-by-Point Inversion

The remaining inversion techniques are all for locating anomalies that are in the simple dipole limit, *i.e.*, their physical size is much smaller than the detection range. The early work of Wynn *et al.* [11] analytically solves the inversion from five gradient measurements for the bearing to the target, the bearing of the target’s moment, and the scaled moment $|M|/r^4$. This can be done at any point in time because there are five measurements and five unknowns. With this method there are ambiguities because the sign of the bearings can not be determined, so four solutions result, only one of which is the real target. The three false solutions, “Wynn’s ghosts”, cannot be distinguished from the real solution within a single measurement. Wynn *et al.*’s analysis produced closed forms for the four solutions in terms of the eigenvalues and eigenvectors of the gradient tensor. This analytic approach was subsequently investigated by Wilson [39] who independently derived a simplified version that was equivalent to Wynn *et al.*’s treatment. Wilson also showed that gradient tensor measurements can be deduced from total-field gradiometer measurements, provided that multiple passes are made over the target from different directions.

To resolve the problem of separating M and r from the scaled moment, and rejecting the ghosts, measurement from another point in space is required. The real target is distinguished from ghost solutions because for the second measurement, one solution will coincide with one solution from the first measurement,

and three new unrelated ghosts are formed. The location may be obtained by triangulation, then \mathbf{M} can be deduced. However, this requires good navigational information to know the relative positions and orientations for the sensor at the two points.

More advanced point-by-point inversion algorithms exist that exploit the time rate of change of the gradient tensor. If the velocity of the sensor is known, the rate-tensor equation can be inverted [37] and the bearing vector common to this and the gradient-tensor inversion is unique. The different powers of range in the two systems of equations then lead to a unique range and moment vector. If the sensor velocity is not known, the gradient-tensor inversion and knowledge of the gradient-rate tensor lead to a unique solution for the bearing vector [38], allowing the sensor to be used for homing.

14.4.5

Localization using Time-Domain Windowed-Data Stochastic Approaches

This approach may be used for controlled survey sweeps where there may be multiple targets, but real-time analysis is not required. The basic concept of a time-domain windowed-data stochastic method is, first, to test the hypothesis that a dipole has been detected in a data window, then to estimate the values of \mathbf{r} and \mathbf{M} that best fit the time series data obtained from the gradiometer.

A simplified description of one specific model that has been developed and validated to detect, classify, and localize multiple stationary magnetic dipole targets is described in Ref. [40]. It considers a system carrying a magnetic sensor with five independent tensor gradiometer channels moving in a straight-line trajectory past targets at a constant speed. This model system also includes three orthogonal magnetometer channels used to cancel noise signals arising from gradiometer imbalance and platform noise sources: in particular for eddy currents that are induced in metallic structures near to the gradiometers by motion in the Earth's field. It is assumed that the gradiometer is operating in a magnetically quiet platform so that any noise above the intrinsic sensor noise consists only of imbalance and eddy-current signals that can effectively be compensated for.

The objective of this approach is to extract the dipole signals $G_{ij}^{(k)}(t)$ ($k = 1, 2, \dots, n$) for an unknown number n of dipole targets and then to determine the magnetic moments and the positions of the n targets. The model is applied to a window of data that is long enough to encompass the entire signal envelope from a target. One makes a rule-of-thumb estimate that the window length is twice the range of the most distant target that we expect to detect. The five output signals $\Gamma_i(t)$ ($i = 1, 2, \dots, 5$) from the five independent gradiometer channels and the three magnetic field components $B_j(t)$ ($j = 1, 2, 3$) are measured as a function of time over the data window as the sensor moves past the targets. (The time derivatives of field $\dot{B}_j(t)$ may be calculated from $B_j(t)$ for compensation of magnetic signals generated by eddy currents, if required.)

This model describes the signals $\Gamma_i(t)$ in the five gradiometer channels by the equations

$$\Gamma_i(t) = \sum_{j=1}^5 C_{ij} \left\{ \sum_{k=1}^n G_{jk}^{(k)} \right\} + a_i + \sum_{j=1}^3 \beta_{ij} B_j(t) + \sum_{j=1}^3 \gamma_{ij} \dot{B}_j(t) + S_i(t) \quad (14.5)$$

where C is the predetermined calibration matrix for the gradiometer, $S_i(t)$ is the uncompensated noise (setting the noise floor of the channel compensation parameters per channel), a_i is the channel bias, and β_{ij} and γ_{ij} are the balance and eddy-current vectors for channel i . An iterative analysis first estimates the values of a , β and γ (a total of 35 parameters) by minimizing the least-squares residual for the gradient signals. Next the model estimates the gradient signals for a magnetic source in the vicinity of the gradiometer by introducing a dipole at points in a discrete grid bounded in a region of space for which the model applies. A best-fit estimate of the dipole's magnetic moment vector at each grid point is obtained through a least-squares fit. The least-squares residuals obtained for the set of grid points are compared and the dipole that has the smallest residual is added to a target list. The algorithm then executes a gradient search to optimize estimates for a , β , and γ and for r and M of the dipole selected. The procedure is then repeated for a second target. Targets continue to be added provided their signals contribute substantially to the total signal power, otherwise the algorithm terminates. A version capable of target localization and classification in a single pass operating essentially in real time has been developed and successfully demonstrated in conjunction with the MADOM project described in Section 14.6.2.

14.4.6

Generalized Numerical Methods

These are not described well in the literature so far, but they have been used to good effect with various gradiometer systems [21, 41]. The numerical approach is computationally intense and has only been made practical in recent years by the high digital processing power of modern computer and DSP chips. A nonlinear least-squares fit algorithm may be used, such as those based on the elegant Levenberg–Marquardt method [42]. Here the dipole equations (14.1) and (14.3) are fitted to the measured data from the gradiometers to provide the inversion. The algorithm begins with a “virtual” dipole specified as a pre-determined starting condition, M_v and r_v . The gradients (and fields if appropriate) from these are used to calculate what would be measured in the gradiometers because the geometry of the gradiometer is known from its design. The algorithm then compares this with the actual measurements from the gradiometer and adjusts M_v and r_v to give a better fit in the next increment. When the fitting is complete, M_v and r_v are output as the best estimate of M and r and the residual is reported to provide an indicator of the confidence level of the inversion.

Numerical inversion has several powerful advantages. Data from an inertial navigation system may be directly input to the minimization as well as time series magnetic data. In this way the inversion may continually refine itself using historical data to provide unambiguous inversions. The first reported use of this method

[21] was successful in inverting using only a three-axis gradiometer, because in passing the target, the target is viewed from many different angles so the full tensor is gradually built up over time. (This did require an inertial navigation system with six degrees of freedom.) Another advantage is when, rather than using the gradient equation (14.3), the field equation (14.1) is used explicitly to form field differences over fixed baselines. In this case all higher order gradients are immediately accounted for in the inversion. This allows nearby dipoles to be tracked without the errors caused by second or higher order gradients. It is also possible that models other than dipoles, such as extended sources, multiple dipoles, or multipoles, can also be inverted provided that the system can access enough of the right information by its sensor configuration and motion behavior.

It is important that suitable starting conditions for the minimization are chosen when using numerical inversion to prevent minimizing to any of the many false minima in the cost function for the fit. Strategies, such as starting from several different points and taking a majority vote on the solution, can be effective for avoiding ghost solutions but this multiplies the computation time. Another option is to use an analytic point-by-point inversion to determine the start point or to use previously known reliable inversion solutions as the starting point for the next one, so targets are reliably tracked in real time. With modern DSP processors, over 30 inversions per second are possible so the process is essentially in real time to the operator. As with the point-by-point analytic inversions, good SNR in all channels is required for reliable results.

14.4.7

Other Techniques

Recently Heath *et al.* [43] have examined a number of inversion schemes for the magnetic gradient tensor. Numerical inversion schemes are generally iterative forward models, searching for a minimum difference between observation and model response as described above. A Monte Carlo approach was found to have the benefit of probing the solution space as broadly as possible, thus avoiding local minima, but it is inefficient. The Amoeba optimization method (Downhill Simplex [42]) was also tried and while efficient, runs the risk of becoming trapped in local minima especially when fitting more than a few parameters.

Schmidt *et al.* [44] used a combination of the Monte Carlo method with the Amoeba by running the Amoeba a number of times beginning with different initial parameters. This effectively combines the Monte Carlo and Amoeba approaches to optimize the efficiency and ensure the global minimum is found.

There are other schemes that are useful for magnetic anomalies that are more complicated than simple dipoles. A general scheme involves Euler deconvolution [45], and although this process was developed for the gravity tensor, it has been extended to the magnetic field tensor [44]. Using this method, the source geometry is contained in the structural index, n_E , which varies from 0 for a uniformly magnetized extensive stratum, such as a sill, to 3 for an isolated dipole. Quadru-

poles, although rare, have a structural index of 4. The general tensor Euler deconvolution is

$$x \frac{\partial B_x}{\partial x} + y \frac{\partial B_y}{\partial y} + z \frac{\partial B_z}{\partial z} = -n_E B_x \quad (14.6)$$

$$\begin{bmatrix} \frac{\partial B_x}{\partial x} & \frac{\partial B_x}{\partial y} & \frac{\partial B_x}{\partial z} \\ \frac{\partial B_y}{\partial x} & \frac{\partial B_y}{\partial y} & \frac{\partial B_y}{\partial z} \\ \frac{\partial B_z}{\partial x} & \frac{\partial B_z}{\partial y} & \frac{\partial B_z}{\partial z} \end{bmatrix} \begin{bmatrix} x - x_0 \\ y - y_0 \\ z - z_0 \end{bmatrix} = n_E \begin{bmatrix} B_x \\ B_y \\ B_z \end{bmatrix}. \quad (14.7)$$

Once the source geometry has been identified, the location and magnetic properties can be determined from the eigenvalues and eigenvectors of the magnetic tensor at judiciously selected points near to the source. Only a few tensor observations are required to furnish all the determinable information about a source, notwithstanding any fundamental nonuniqueness.

14.5

Geophysical Applications of SQUIDs

14.5.1

Introduction to Geophysical Prospecting

Geophysical prospecting is used to find natural commodities such as mineral deposits or oil. Mineral deposits cause variations (anomalies) in the physical properties of the rocks in which they occur. By observing these anomalies, the presence of the minerals may be deduced. The properties of interest include color, density, magnetic susceptibility, seismic velocity, radioactivity, resistivity, induced polarization effect, thermal conductivity, and temperature.

There are a variety of techniques used to measure these properties and they are listed in Table 14.1. This table lists the method, parameter measured, the characteristic physical property, the main cause of the anomaly, and the possible commodity detected.

Although one may assume that most of the mineral commodities that appear at the Earth's surface have already been discovered, new roads, receding glaciers, and trees falling over are exposing new outcrops. Furthermore some ore deposits such as gold are difficult to recognize at the surface. Breaking open a sample of the outcrop and examining the fresh face with further geochemical analysis or assay is still undertaken. The current challenge in commodities exploration is the discovery of commercially viable deposits under cover beneath shallow soils (thin overburden) that may be conducting or under oceans (that certainly are conduct-

Tab. 14.1 Geophysical techniques for prospecting.

| Method (A) active (P) passive | Parameter measured | Units | Characteristic physical property | Main cause of the anomaly | Application if direct detection | Application if indirect detection |
|-------------------------------------|--|----------------------------------|----------------------------------|---|---|--|
| Resistivity (A) | Resistance | Ω | Resistivity Conductivity | Conductive veins, sedimentary layers, volcanic intrusions, shear zones, faults, weatherings, hot waters | Massive nickel sulfides Oil shales, clays Geothermal reservoirs | Bulk material Base metals Coal and natural steam |
| Induced polarization (A) | Time domain: – chargeability – polarizability | Ionic-electronic Over voltage | | Conductive mineralizations: disseminated or massive (graphite, sulfides), clay | Conductive: – Sulfides – Oxides – Mn oxides | Associated minerals (zinc, gold, silver, tin, uranium, etc.) |
| | Frequency domain: frequency | | | | | |
| | Phase domain: phase shift | | | | | |
| Self potential (P) | Natural potential | mV | Conductivity Oxidizability | Massive conductive ores Graphite Electrofiltration Faults | Sulfides: – pyrite – pyrrhotite – copper Mn ore | Associated minerals (lead, gold, silver, zinc, nickel) |
| Telluric (P) | Relative ellipse area Ratios-apparent resistance | Ω | Conductance | Basin and range studies Conductance of sedimentary series Salt domes, geothermal | Structural studies, steam | Regional exploration – Oil – Gas |

Tab. 14.1 Continued.

| Method (A) active (P) passive | Parameter measured | Units | Characteristic physical property | Main cause of the anomaly | Application if direct detection | Application if indirect detection |
|--|--|--------------------------|--|---|--|---|
| Magnetotelluric (P) MT, AMT (A) CS-AMT | Resistivity Conductivity | | Conductive veins, sedimentary layers, shear zones, faults, weatherings, resistive basements, bedded ores | Massive sulfides Clays Natural steam | Shear zones General tectonics General structure Oil | Gas |
| Electromagnetic (A) | Phase difference Tilt angle Amplitude ratio Sampling of decay curve ($\partial V/\partial t$) induced in receiving coil by eddy currents In-phase, out-of-phase components | degrees Ω V | Electrical conductivity | Conductive mineralizations Surficial conductors Shear zones | Conductive: – sulfides – oxides Mn oxides | Kimberlites Associated minerals Ground follow up (lead, nickel), shear zones, weathered zones, conductivity maps |
| Magnetic (P, A) | Earth's magnetic field Vertical component, Z Total intensity Horizontal gradient Vertical gradient Tensor gradient | nT | Magnetic susceptibility | Contrasts of magnetization Magnetite content of the materials | Magnetite Pyrrhotite Titanomagnetite | Molybdenum Iron ore Chromite Copper ore Kimblerites Asbestos |
| | | $nT\text{ m}^{-1}$ | (gradient) | | | Geological mapping in terms of magnetic changes (basic rocks) and/or discontinuities inventory of mineral resources |

| Method (A) active (P) passive | Parameter measured | Units | Characteristic physical property | Main cause of the anomaly | Application if direct detection | Application if indirect detection |
|--|--|--------------|---|--|--|--|
| Gravity (P) | Gravity field | Milligal | Density | Deposits of heavy ores Salt domes (light) Basement rocks | Chromite Pyrite Chalcopyrite Lead | Placer configuration Karstic cavities Basement topography Structure Oil Gas |
| Gravity gradiometry | Eötvös (gradient) | | | | | |
| Radioactive (P) | Intensity and spectral composition of gamma rays | cps | radioactivity | Radioactive elements Uranium-Thorium ^{40}K | Uranium Thorium Phosphates | Ground follow up Geological structural mapping (differentiation in granites) |
| Seismic Refraction (A) | Travelling time of seismic waves | ms | Seismic wave velocity | Contrasts of velocity Markers at variable depth | Buried channels Faults | Tin, diamonds, heavy minerals |
| Seismic Reflection (A) | | | Dynamic modulus | Fissured rocks | Morphological traps | Natural stream |
| Thermometry (P) | Temperature | °C | Geothermal gradient and temperature | Abnormal flux of heat Thermal inertia of rocks | Basement topography | Uranium Natural stream Boron, sulfur Subterranean volcanism |

ing). Even more challenging is detection at depth where the target of interest is covered by a thick overburden or bedrock.

To find a new commodity, a range of exploration methods is used, normally selected from those listed in Table 14.1 on the basis of the anticipated geology, budget, and personal preference of the surveyors. It is important to note that no modern discovery of a geological commodity can be attributed to the use of a single exploration technique. Rather, the use of multiple methods with the fusion of resulting data is mandatory for reliable surveys.

The exploration process begins with wide-ranging airborne reconnaissance to discover an initial measurement anomaly. This is often undertaken by government bodies such as geophysical survey departments in order to encourage further exploration in their country. The data are made available for commodity companies to study and determine if there is a first suggestion that an ore or oil body lies below. These surveys typically use radiometrics, magnetics, transient electromagnetics, gravity gradiometry, seismology and optical spectroscopy with sweeps at 200 m line spacing and 100–200 m altitude. If an interesting anomaly is found in the data collected by one of the receivers, a more detailed exploration survey is undertaken with 50-m line spacing. At this stage, a range of geochemical and geological information is also collected and the data are fused together to develop a geological profile of the area using the inversions to determine the characteristics of the source. This helps the geologists determine what is buried beneath the surface.

If these results still show a potentially interesting target, a much more detailed ground survey is undertaken using gravity, electromagnetic, and electrical ionization potential techniques (*i.e.*, self potential and induced polarization) for mineral exploration or further seismology and controlled source electromagnetics (CSEM) for oil. If the remote sensing establishes the existence of a deposit, then sample cores are taken by drilling into the ground down to 500 – 1000 m for minerals or down to 5000 m for oil or gas. The sample soils and rocks are tested to determine the content and type of the minerals or hydrocarbons present to decide if the commodity is viable for exploitation. Even with all this information, it is difficult to accurately position a drill hole and many expensive mistakes are made. This is mainly due to the nonunique solutions possible when undertaking an inverse of the distributed fields being measured. In the following, we concentrate on mineral rather than oil measurements and exploration. Sensors commonly used for seismic and electromagnetic techniques such as induction coils, flux gates and geophones can also be used in bore holes to obtain improved signal-to-noise ratios and better resolution of the source. Some useful references on the methodology of mineral exploration can be found in Refs. [46–48].

14.5.2

A Brief Historical Overview of SQUIDs in Geophysics

Jim Zimmerman, the coinventor of the rf SQUID, saw the potential application of SQUIDs in geophysics [49] and measured fluctuations of the Earth's magnetic

field using a simple rf SQUID [50]. In 1980 Weinstock and Overton organized the first workshop that reviewed the use of SQUIDs for geophysics [8], identifying a wide variety of applications for SQUID systems to measure the magnetic fields and gradients that are the basic quantities characterized in electromagnetic methods of mineral exploration and the study of geophysics. In 1983 an extensive review on geophysical applications of SQUIDs outlined further potential uses in geophysics [51]. All this early work was based on low-temperature rf and dc SQUIDs.

The need for helium cooling in the field, along with difficult handling, insufficient slew rate, and the high cost of the devices and their associated electronics hindered the adoption of SQUIDs at that time. Nevertheless, the concept of remote referencing by Gamble *et al.* [52, 53], first introduced in their SQUID work, found a lasting place in the methodology of geophysics. This technique used SQUID magnetometers at two distant sites to measure fluctuations in the two orthogonal horizontal components of the magnetic field. The data obtained at each site were analyzed using the magnetic fields at the other site as a remote reference. This method makes surveying possible in regions of high cultural magnetic and electric noise, and has been used with other magnetometers such as cesium vapor magnetometers. It is standard practice in magnetotellurics and magnetic gradiometry.

During the 1980s, laboratory SQUID instruments were developed for measuring the paleomagnetic fields and susceptibilities of rocks. Suitable SQUID susceptometers are now commercially available and are instruments of choice for high-sensitivity measurements. During this decade, significant developments were also made in electromagnetics for mineral exploration involving transient electromagnetics (TEM) and magnetic tensor gradiometry. Progress with the TEM technique has continued since then, with new impetus following the discovery of high- T_c materials. More recently interest has been growing for new magnetic sensing techniques, in particular tensor gradiometry (SQUID and fluxgate) and configured SQUID total-field magnetometers.

14.5.3

Laboratory Systems

14.5.3.1 Rock Magnetometers

The Chinese discovered magnetism several thousand years ago by suspending stones on string threads and observing that some, the lodestones, always rotated to point in the same direction. Magnetism in more common rocks was recognized by the late 18th century by observing that they deflect a compass needle. In 1906 Brunhes [54] reported measurements of recent lava flows that were magnetized in the direction parallel to the Earth's magnetic field. This study initiated research in paleomagnetism, the study of magnetization of rocks in remote times for the purpose of geological dating. Paleomagnetic measurements of the magnetization direction and intensity indicate the position and strength of the geomagnetic pole

at the time of rock and sediment formation. Details of rock magnetism, paleomagnetism, and measurement techniques are given in Refs. [8, 55, 56]. This research has contributed substantially to our understanding of the Earth's geological history including the quantitative confirmation of continental drift, the discovery and determination of the history of magnetic reversals in the Earth's field over many epochs, and the motion of the Earth's magnetic poles.

Laboratory measurements of rock magnetism have also become an important technique for geophysics to help interpret magnetic survey data. The interpretation of survey data can be difficult, because of the inherent nonuniqueness of the inversion solutions that determine the geometry of the magnetic sources. Thus direct measurements of magnetic properties of the targeted rocks and sediments can add constraints to the inversion and help to resolve these ambiguities [57]. Reliable data can only be obtained by statistical analysis of a large number of samples that are collected in a survey area. One sample cannot indicate clearly the inclination, paleo-latitude, and average magnetic moment on the basis of a single measurement. A large number of samples and measurements is needed to obtain a true understanding of the magnetic history and current properties of the area under study.

The first paleomagnetic measurements used an astatic magnetometer [58], which consisted of two small magnets separated by a short distance and set with the magnetic moments in opposition to one another. The magnets were suspended by a torsion fiber and acted as a magnetic gradiometer. This gradiometer achieved a differential measurement limit of 10^{-3} A m $^{-1}$. During the 1960s, magnetometer sensitivities improved by spinning the rock specimen enabling the resultant oscillating signal to be amplified [59], but the rotation rate had to be high to generate suitable signal strengths. The high rotation rate caused problems with fragile specimens breaking up. Various spinning techniques were developed with the specimen located within or adjacent to a magnetic sensor, typically an induction coil of many turns. This approach, combined with improvements in electronic circuitry, achieved sensitivities of 10^{-5} A m $^{-1}$. The development of fluxgate magnetometers broadened the applicability of rock magnetism to sediment samples [60] due to improved sensitivity of the fluxgates and the feasibility to spin the rock specimen slowly [55, 61].

The advent of SQUID magnetometers in the 1970s provided improved sensitivity and speed of measurement [62]. Very weakly magnetized sediments such as limestone could now be measured quickly and easily for the first time. This began a new era in paleomagnetic studies. Low- T_c SQUIDs provided a sensitivity of 10^{-6} – 10^{-7} A m $^{-1}$. The company 2G Enterprises, established in 1981, is the most successful company to commercialize SQUID-based rock magnetometers. Based on the system of Goree and Fuller [62], the instrument consists of a pass-through SQUID magnetometer that can be used to measure small discrete samples and whole or half-split cores without the necessity of splitting or cutting the core into samples. To date, 102 of these systems operate in geophysics laboratories around the world, and about the same number again have been built and installed from a range of other companies. The main components of any SQUID-based rock mag-

netometer are the SQUID, cryogenics, control electronics, data logger, shielding, sample holder, and, for spinning rock magnetometers, the motor.

2G Enterprise's magnetometers employ three dc SQUIDs to measure orthogonal components of a sample's magnetic field. A photograph of the system and a schematic of its longitudinal section are shown in Figure 14.8. This system uses niobium SQUIDs with a white flux noise density of $5 \mu\Phi_0 \text{ Hz}^{-1/2}$ and a $1/f$ noise corner frequency at $<0.5 \text{ Hz}$. These are mounted inside the rock magnetometer's vacuum jacket near the bottom of the internal helium reservoir as shown in Figure 14.8(b). The magnetic field of the rock sample is coupled to the SQUIDs with flux transformers. There are three pickup coils, two for transverse measurements and one for the axial moment measurement.

Typical rock specimens consist of a section of a cylindrical core approximately 25 mm in diameter and length. Specimen volumes are about 10^4 mm^3 and typical

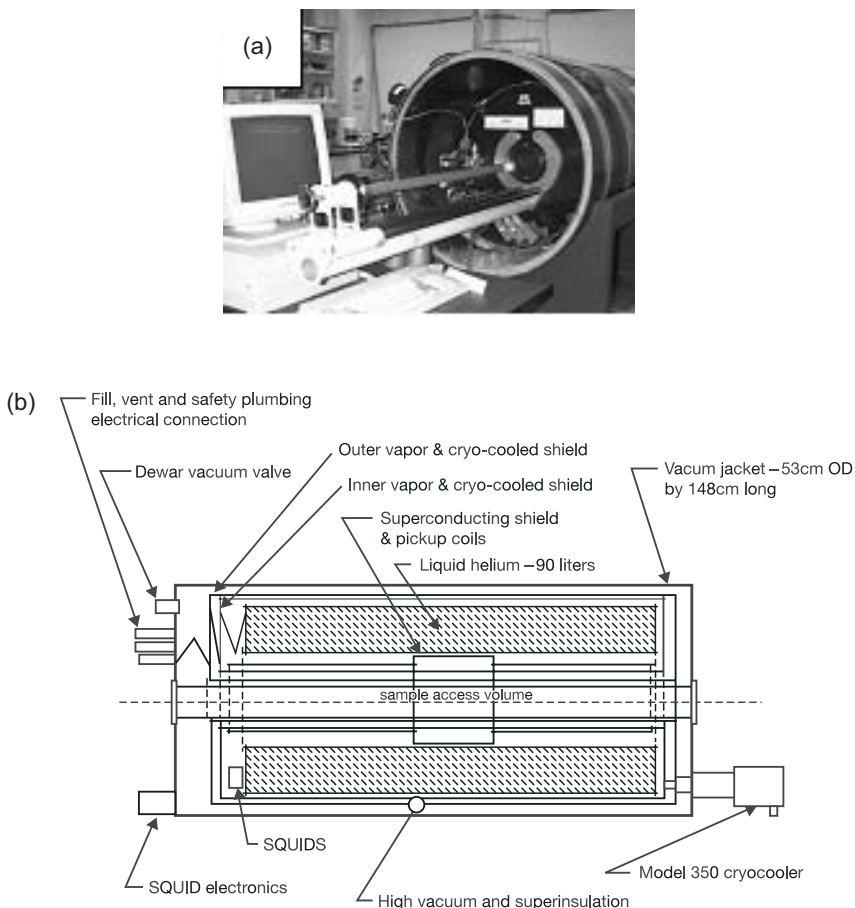


Fig. 14.8 (a) The loading view of a 2G low- T_c SQUID rock magnetometer and (b) a schematic of the 2G rock magnetometer configuration.
(Used with permission of W. Goree, 2G Enterprises.)

magnetization strengths range from 10^2 to 10^{-6} A m $^{-1}$. The sample access bore passes right through the cryostat to allow long rock and sediment cores to be passed through without sectioning. Successive measurements can be made at all positions along the core.

The 2G rock magnetometer has a resolution, when expressed in terms of magnetization, of less than 10^{-7} A m $^{-1}$ for a 10^4 -mm 3 sample volume. Equivalently, this can be expressed as a magnetic moment noise level of less than 10^{-12} A m $^{-1}$. To prevent extraneous magnetic noise in the system, the pickup coils and SQUIDS have superconducting shields placed around them. These provide frequency-independent attenuation factors up to 10^8 over the range of dc to 10 GHz.

An alternative to using superconducting shields has also been considered in rock magnetometers. A combination of three coaxially aligned mumetal cylinders ensures that the SQUIDS are always cooled in near-zero field. In this case, the shielding cylinders should be spaced according to the principles given by Ma and Wikswo [63]. If these are used within a Rubens coil [64] using active field suppression, a magnetic field attenuation factor of 10^6 can be achieved, although this will not be frequency independent, as discussed in Chapter 7. It is also possible to use Helmholtz coils with appropriate currents to cancel any geomagnetic or local laboratory noise. A comprehensive discussion of shielding for rock magnetometers is given in Ref. [61].

The successful adoption of SQUID-based systems required long liquid helium hold times. A heat load of only 28 mW will evaporate 1 liter of helium per day, and hence it is necessary that the helium dewar has a high thermal efficiency. A detailed discussion of cryostat insulation is given in Section 7.7.2. As an alternative to using cryogenic liquids, cooling engines could be used. However, cryocoolers generate static and fluctuating magnetic fields as well as mechanical vibrations. These can cause magnetic noise many orders of magnitude above the SQUID noise level. The 2G system is cooled in a hybrid fashion using liquid helium and a two-stage Gifford–McMahon cryocooler [65]. The cryocooler cools a thermal shield surrounding the liquid helium reservoir to 15 K, reducing the liquid loss rate. One thousand days of continuous operation can be achieved from a single 100-liter helium reservoir.

All moving parts in a rock magnetometer must be made from nonmagnetic materials to prevent unwanted magnetic interference. During the manufacture of the system components, contamination by ferrous material must be avoided. For example, the magnetic remanence of nonmetallic materials can increase from 10^{-6} A m $^{-1}$ to 10^{-4} A m $^{-1}$ if ferrous metal rather than ceramic or TiN-coated drill bits are used during manufacture [66].

“Spinner” rock magnetometers, in which the samples are rotated using a motor, have also been built. These have the advantage that only one sensor is required to obtain the magnetization in all three directions. Furthermore, if the sensors suffer from high $1/f$ noise, such as high- T_c SQUIDS or induction coil magnetometers, the rotation frequency can be chosen within the white noise region of the sensor. Spinning magnetometers require some form of phase detection as the phase of the signal generated by the rotating sample gives the direction of the magnetiza-

tion. This can be done by using a shaft encoder on the sample holder and a phase-sensitive detector at the output of the magnetometer. Reduction of the magnetic interference from the motor is usually achieved by good motor selection and having a sufficient separation from the sample.

Spinner rock magnetometers have been developed using high- T_c SQUIDs with the slow spinning of the rock specimen making up for the lower sensitivity compared to low- T_c SQUIDs and using the SQUID as the direct magnetic sensor rather than using a flux transformer. Measurement ranges of $10^1\text{--}10^{-5}\text{ A m}^{-1}$ have been achieved with a single high- T_c SQUID, three layers of mumetal shielding, and the sample rotated in a planetary motion to achieve the measurement of the three components of the magnetization [66].

14.5.3.2 Other SQUID-Based Systems for the Geophysics Laboratory

SQUID microscopes are also used in geophysics laboratories. The application of SQUID imaging to geophysical samples was first demonstrated by Thomas *et al.* [67] for high-resolution imaging of magnetic domains in single grains. Details of SQUID microscopes are discussed in Chapter 12. Susceptometers are another geophysics laboratory tool, which could provide detection of magnetic moments down to 10^{-11} A m^2 in very high and stable magnetic fields, up to 5 T, over a temperature range of 2–400 K. High magnetic field measurements of rocks can determine the nature and quantity of magnetic minerals and the presence of diamagnetism, paramagnetism, ferromagnetism, superparamagnetism, and the characteristic properties of ferromagnets such as their susceptibility and coercivity. Changes that occur through various environmental conditions, such as heating can also be studied. A detailed study of the methods of measuring high-field magnetic susceptibility is given in Ref. [61] and SQUID-based systems are discussed in Chapter 12.

14.5.4 Field Systems

14.5.4.1 Introduction

This section reviews the use of SQUID systems in the field for mineral exploration. These systems are primarily research instruments rather than established field equipment because fieldable SQUID technology is far less mature than the laboratory instruments such as the rock magnetometers described above. The success of a field SQUID system will be determined, first of all, by its ability to operate in the Earth's magnetic field. When SQUIDs experience large changing magnetic fields, a plethora of problems arise as detailed in Section 14.3 and in Chapter 7. However, good progress has been made toward using the superior sensitivity of SQUIDs to improve the performances of geophysical prospecting instrumentation. This section covers the most promising geophysical uses of SQUIDs in the field, the transient electromagnetics (TEM) method, TEM and magnetic tensor

gradiometry. The TEM technique can be deployed in either ground-based or airborne systems and is used to seek conductivity anomalies in the ground rather than magnetic anomalies. There is an important distinction between *active* and *passive* magnetic sensing in field systems. Active techniques, such as TEM, involve illuminating the target by actively providing a magnetic pulse or other “primary” excitation signal to induce a “secondary” response in the target, whereas passive techniques rely upon measuring the natural magnetic properties of the deposits, and their responses induced by natural, *e.g.*, atmospheric, excitations. Passive SQUID gradiometry in geophysics has also recently emerged in the quest to find magnetic deposits.

14.5.4.2 Transient Electromagnetics (TEM)

TEM is an exploration technique used to seek conducting ore bodies such as nickel, gold and silver metals and their compounds. Figure 14.9 shows schematics of airborne and ground TEM systems. The TEM technique uses a transmitter coil that emits a short magnetic pulse to set up electrical eddy currents in the ground that decay over time. A magnetometer measures the associated decaying “secondary” magnetic field. Once the decay is completed, the process repeats and the measured decays can be averaged to improve the SNR of the measurement. During the “off-time” period when the measurement is made, the response is divided into a number of channels each of a logarithmically increasing time period starting at about 100 μs in the early channels to longer times of about 300–1000 ms in the late channels. This is illustrated in Figure 14.9(c). The sensor output is averaged during the channel period and plotted. The early time channels show the response from shallower depths and the later time channels that from deeper soil or rock layers.

For ground-based TEM, the transmitter antenna coil is placed on the ground, as shown schematically in Figure 14.9(b), and the receiver is moved along a line, or both can be moved together. The airborne TEM method can only use a moving transmitter coil, schematically shown in Figure 14.9(a). The positions of the coils are recorded with the TEM data so a survey map may be constructed. The measurement of the decaying magnetic field is usually processed to derive the electrical conductivity of the ground as a function of depth, so a TEM survey is used to generate 3D conductivity maps. Figure 14.12 shows an example of a full map over a survey line. It displays the data of Figure 14.9(c), which is rotated 90°.

Where conducting anomalies occur, the decay of the secondary magnetic field will be slower than in the less well-conducting surroundings. This is manifest in the later stages of the decay curve, where the SNR is poorest, so high-sensitivity magnetometers are required.

TEM is a *pulse-induction* technique that was originally pioneered for metal detectors. This technique has two powerful advantages: (1) it has excellent transmitter rejection, because the frequency-independent measurements start after the transmitter has pulsed and (2) it is a broadband measurement technique, due to the pulses having a spread Fourier transform. The latter makes depth discrimination

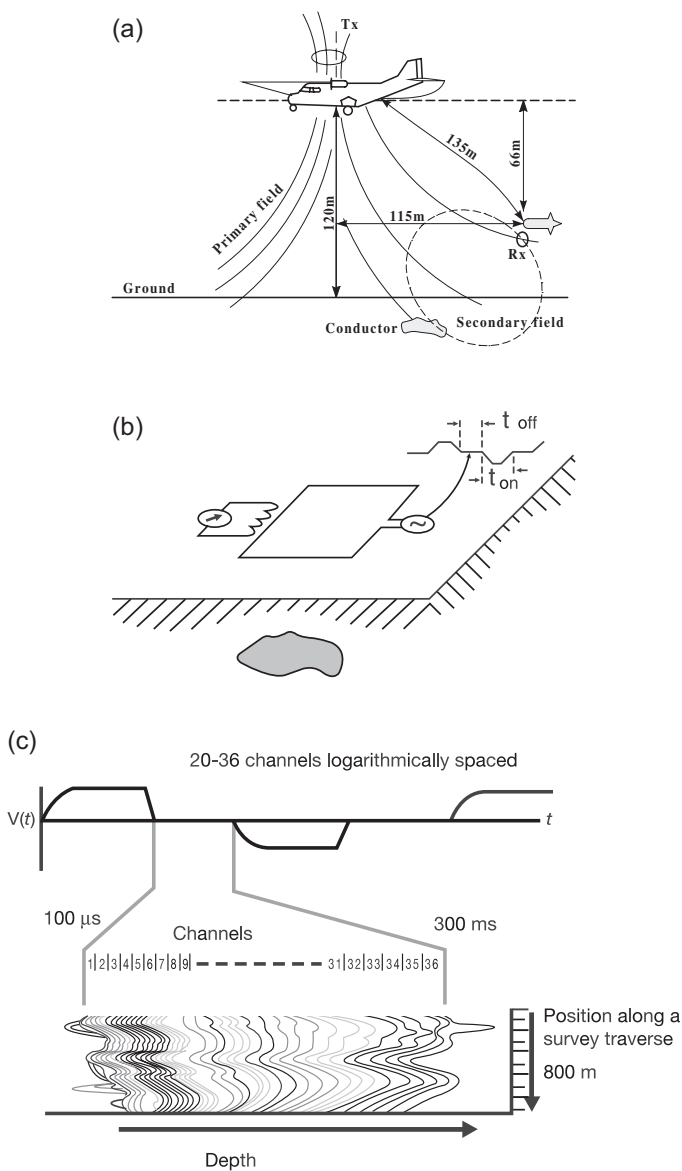


Fig. 14.9 A schematic of the system geometry for (a) airborne TEM and (b) ground-based TEM. A transmitter pulse, T_x , induces a current in a buried conducting ore body during the “on-time” of the pulse, t_{on} . The associated induced magnetic field is detected by a receiver, R_x , during the “off-time” of the pulse, t_{off} . (c) A schematic which shows the “off-time” period is divided into a number of channels. The sensor output is averaged during the

channel period and plotted. The early time channels show the response of shallower magnetic sources and the later time channels show the response of magnetic sources at deeper depths. A map can be constructed by moving the sensor along a line or “traverse” over the Earth’s surface giving a magnetic response at each position along the traverse for each channel (*i.e.*, different depths) of data.

possible, because the lower frequencies penetrate deeper into a conducting body than the higher ones. Therefore, these signals appear later in the decay. The disadvantage is that the measurement SNR decays rapidly in time with the signal (at a constant noise level), so the most interesting region from the point of view of resolving conductivity anomalies and looking deeper is compromised by poor SNR. Detailed information about TEM is given in Refs. [68–73]. There is a range of TEM transmitters and receivers available on the market, listed in Ref. [74].

Typically, induction coils are used as detectors. However, they measure $\partial B(t)/\partial t$ and the data must be integrated to recover $B(t)$. This limits the measurements in two ways. First, the SNR of an induction coil is proportional to frequency, so at low frequencies, *i.e.*, the longest decay times, the sensor loses performance. Therefore, not only does the signal decay with time but the detector's sensitivity does as well, compounding the SNR problem. The second disadvantage of measuring $\partial B(t)/\partial t$ and integrating is that the initial integration point is unknown and different initial boundary conditions can lead to many nonunique solutions.

It is clear that the direct measurement of $B(t)$ removes both of these difficulties. However, such a magnetometer would be required to have a lower noise floor than an induction coil at the lowest frequencies of interest. Only fluxgates or SQUIDs could potentially be used; optically pumped total-field magnetometers may be sensitive enough but they do not have bandwidth sufficient for active systems. For the deepest conductivity anomalies, SQUIDs are the only suitable sensors.

The four principal performance factors of a TEM system are: (1) the coupling of the transmitter field to the anomaly; (2) the anomaly's characteristics; (3) the sensor noise; and (4) the receiver's frequency response characteristics. The coupling of the transmitter field to the anomaly determines the magnitude of the response, *i.e.* the better the coupling the larger the initial size of the secondary field. The anomaly characteristics determine the way the induced currents decay and are recorded by a magnetometer differently than by an induction coil. This is particularly the case for regions where there is a conducting soil layer on top, the *conducting overburden*.

In a simple model [72], the target can be replaced by a conductive loop. In this case, the target current decays exponentially with the decay constant (τ) determined by the inductance L (dimensions) and resistance R of the loop, $\tau = L/R$. In most cases, a better assumption is that the response is made up of the superposition of a number of exponential decays with different time constants. While this distorts the decay from a true exponential, at *late times* the short- τ exponential decays will have become negligible and the decay should again approximate an exponential decay. The early signals due to low- τ mechanisms are from poorly conducting rock or soil overburdens or very small deposits of higher conductivity material. A significant measurement of exponential decay at later times is therefore indicative of a large volume of highly conducting material [73].

The decay of two special cases has been studied in greater detail [72]. These are (1) a conductive half space, representative of a uniform conductive Earth, and (2) a thin-layer conductor representative of a thin horizontal stratum. In both cases a

more accurate description of the expected decay of the induced currents is a power law. Expressions of the theoretical decays measured with magnetometers and coils are given in Table 14.2.

Table 14.2 Magnetometer and coil receiver TEM responses for two decay types. Note that the ratio of signals indicates that the magnetometer is superior for long time constant signals.

| | Magnetometer signal S_M | Coil receiver S_C | Ratio of signals S_M/S_C |
|-------------------|------------------------------|------------------------|-------------------------------|
| Exponential decay | $B e^{-t/\tau}$ | $(B/\tau) e^{-t/\tau}$ | τ |
| Power law decay | $B t^{-\rho}$ | $\rho B t^{-(\rho+1)}$ | t/ρ |

Although the response from a geophysical target is recorded differently by a SQUID than by coil receivers ($B(t)$ compared to $\delta B(t)/\delta t$), the ultimate performance is determined by the overall SNR of the system. The total noise of the system has four main contributors; receiver noise, cultural noise, atmospheric (sferics) and motion-induced noise. Receiver noise includes both the intrinsic noise of the detector (*e.g.*, SQUID) and its associated electronics. Sferics noise arises from naturally occurring background electromagnetic activity and is the ultimate limit to the performance of a TEM system. Cultural noise, *e.g.*, power line interference can be removed by filtering techniques, and stacking or averaging [75] to increase the SNR of the acquired data. Conventional receivers stack the data using simple averaging of all the waveforms recorded in the time series. (This is also known as *boxcar* filtering.) TEM receivers generally apply a tapered stacking filter in which several waveforms at the start and end of the stack are not considered with the same weighting as those in the bulk of the series. The tapered filter is designed to attenuate the coherent noise that occurs at frequencies other than the frequency at which the measurement is taken (usually 25–30 Hz) and its odd harmonics. With careful choice of the measurement frequency, coherent interference, such as power line harmonics, will reside in regions of the spectrum heavily attenuated by the tapered stacking filter [74].

Motion noise arises from changes in the magnetic signal due to motion of the receiver and transmitter in the Earth's magnetic field. This noise signal is many orders of magnitude larger than the fields associated with the induced target currents to be detected. Motion noise is very significant in airborne systems but is readily eliminated in ground-based systems. Noise due to wind effects, for example, can be reduced by the erection of screens.

14.5.4.3 Ground-Based SQUID TEM

High- T_c SQUID systems have been used as TEM receivers by several research groups and are listed in Table 14.3. Each of these groups has undertaken various experimental trials and several systems are available for purchase or hire. Currently there are about 10 TEM SQUID receivers in commercial use in Australia, Canada, the USA, Japan, China, and South Africa.

Tab. 14.3 Comparison of TEM high- T_c SQUID systems.

| | CSIRO ¹ [76] | FZ Julich ² [77] | IPHT Jena ³ [78] | Tristan ⁴ [79] | MMAJ ⁵ [80] |
|---|----------------------------|--------------------------------|--------------------------------|------------------------------|---------------------------|
| SQUID type | rf | rf | dc | dc | dc |
| Noise in field at 25 Hz (fT Hz ^{-1/2}) | 250 | 1,000 | 400 | 500 | 55 |
| Bandwidth (kHz) | 100 | 20 | 10 | 500 | 100 |
| Dynamic range (dB) | 110 | 130 | – | – | 93 |
| Slew rate (mT s ⁻¹) | 0.3–0.4 | 2 | 3 | – | 0.2 |
| Weight (kg) | 3 | 12 | 6.5 | 12.2 | 10 |
| Power (W/channel) | 1.8 | 3 | 1 | 50 ⁶ | 38 ⁶ |

¹ Commonwealth Scientific Industrial Research Organization

² Research Centre, Julich

³ Institute of High Physical Technologies

⁴ Tristan Technologies, San Diego

⁵ Metal and Mining Association of Japan

⁶ Units are (W) only

The first trial of a high- T_c SQUID system for ground-based TEM was undertaken in Australia in 1992 [76] using an rf SQUID with Quantum Design rf SQUID electronics and a traditional dewar and probe design. Since that time there have been many surveys conducted, see, *e.g.*, Refs. [77–81] and high- T_c SQUIDs are regularly used in the field, particularly for massive nickel sulfide deposits [76]. Wang *et al.* [81] outlined clearly the problems and prospects for SQUID TEM identifying slew rate, dynamic range, frequency response, and 1/ f noise as the main system characteristics that determine the performance of SQUID TEM systems.

Slew rate. For TEM applications, a high slew rate is necessary for the system to be able to follow the transmitter pulse and for the SQUID to remain in lock. Because the SQUID operates in a flux-locked loop, a large transient signal can cause the SQUID to go out of lock if the signal rate of change is too great. Although Wang *et al.* [81] recommended a slew rate of 5 mT s^{-1} , reliable systems have operated with slew rates of 2 mT s^{-1} [76–78]. It is also possible to adjust the transmitter pulse rise and decay time to reduce the need for excessively high slew rates.

Dynamic range. Ground-based TEM measurements are made at stationary points. Thermally cycling the SQUID at each point expels any trapped flux caught while moving the SQUID from one measurement station to the next. With heaters implemented, dynamic range is not an issue. Dynamic ranges between 93 and 130 dB are sufficient for ground-based TEM.

Frequency response. This parameter varies significantly between the various TEM SQUIDs developed, due to the variety of dewars used. The fiberglass dewars used in Refs. [77, 78] are known to limit the cut-off frequency. This is caused by the conducting properties of the superinsulation in fiberglass dewars. This insulation screens and distorts the external homogeneous magnetic fields at high frequencies. The effect becomes noticeable over 10 kHz. Also self-field effects due to metal near the SQUID contribute to reduced bandwidth. The CSIRO SQUID system [76] uses a glass dewar with optimized rf shielding and the MMAJ (Metal and Mining Association of Japan) SQUID system [80] uses a Styrofoam dewar, both achieving bandwidths of greater than 100 kHz. Unfortunately the MMAJ dewar has low hold times and increased noise due to rapid boil-off.

1/f noise. Ideally, the lowest possible $1/f$ noise devices are the most desirable for TEM SQUID measurements. While the geomagnetic background noise is quite high at low frequencies [72], it can be significantly exceeded by $1/f$ noise generated in changing magnetic fields, particularly due to flux creep and overall system drift.

TEM measurements have been undertaken in a range of different terrains (e.g., conducting or resistive soil regions). In some regions, responses are observed with polarity opposite to that expected. These negative responses are not well understood and have been attributed to inappropriate pulse schemes [82, 83] or induced polarization [84]. There is also the possibility that these responses are due to superparamagnetism in the soil, and they are survey-region dependent [85, 86]. Where this occurs, the SQUID systems should not be buried during measurement. However, when used on the surface windshields should be placed around the instruments [76, 77]. Figure 14.10 shows a SQUID response when buried and sitting on the soil at the same site.

As a technique, ground-based TEM has been successful in mineral exploration and has contributed to the discovery and delineation of several significant mineral deposits [87]. Although these instruments are currently based on inductive coil

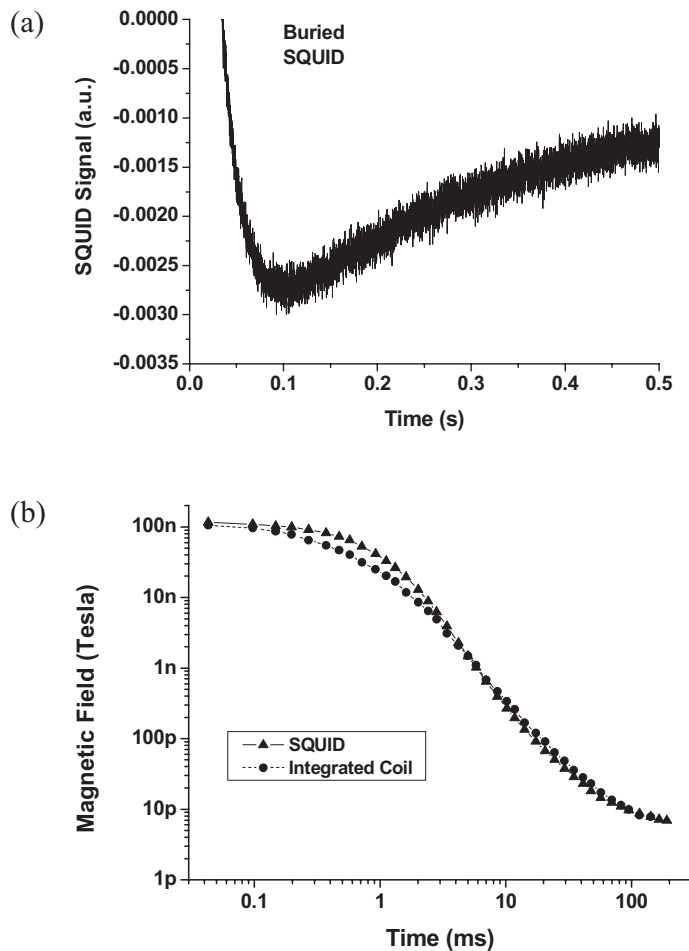


Fig. 14.10 The SQUID output response with time at a location where the surface soil has a strong magnetic moment when the SQUID is (a) buried and (b) sitting on the surface. Note that the buried SQUID has a negative offset.

magnetometers, SQUIDs have been shown to have some advantages over them. These are: (1) not requiring a high level of accuracy in the recording of primary field; (2) not requiring integration of the data during post processing because the B field is directly measured; and (3) having a lower noise floor at low frequencies to resolve deeper, larger anomalies. For these reasons, SQUIDs have an exciting future in ground-based TEM and are on their way to being adopted as mainstream options for exploration of highly conducting deep ore bodies.

14.5.4.4 Airborne SQUID TEM

The development of SQUID-based TEM for airborne application is in its early stages. Some research tests showing successful airborne operation are particularly encouraging [76, 88, 89] although a significant amount of further research and development is required. Table 14.4 summarizes the challenging required performance specification and that achieved by the CSIRO/BHP research system. [76, 89]. This system is used as an example for the following discussion.

Table 14.4 Airborne HTS SQUID magnetometer critical parameters.

| Parameter | Unit | Achieved to date [31] | Required specification |
|------------------|-------------------------|-----------------------|------------------------|
| Noise (1 KHz) | fT Hz ^{-1/2} | 350 | 40 |
| Noise (1 Hz) | fT Hz ^{-1/2} | 400 | 70 |
| 1/f noise corner | Hz | 40 | 1 |
| Bandwidth | MHz | 0.1 | 5 |
| Slew rate | $\Phi_0 \text{ s}^{-1}$ | 10^5 | 5×10^6 |
| Dynamic range | dB | 110 | 190 |

A schematic of the airborne TEM system is shown in Figure 14.9(a). A large transmitter coil is rigidly attached to the aircraft and the magnetometer is towed behind in a streamlined body called the *towed-bird*. The physical separation between the transmitter and magnetometer has several advantages. It reduces the direct transmit field seen by the sensor, reduces the signal returning from the aircraft's skin or airframe, and reduces the *platform noise* from the aircraft's systems (see Section 14.3.4). Furthermore, as the aircraft will be traveling at approximately 60 m s⁻¹, the sensor will be closer to the anomaly. All the separation distances shown in Figure 14.9(a) are typical examples. The difficulty when using vector magnetometers such as SQUIDs is that towed-birds are less stable in flight than aircraft.

In the CSIRO/BHP system, a transmitter pulse of about 14 A was passed through a single-turn induction coil around the wingtips of the aircraft (see Ref. [89] for details). The SQUID system was mounted in a towed-bird housing using a mechanical suspension, the details of which are given in Ref. [89]. The airborne noise spectrum is shown with the transmitter on and off in Figure 14.11. It can be seen that the effects of motion, which is responsible for the very large low-frequency noise, dominated the performance of this system. However, the detection of conductivity anomalies has been achieved, and an example of the data from an airborne survey using SQUIDs over a target in South Australia is shown in Figure 14.12.

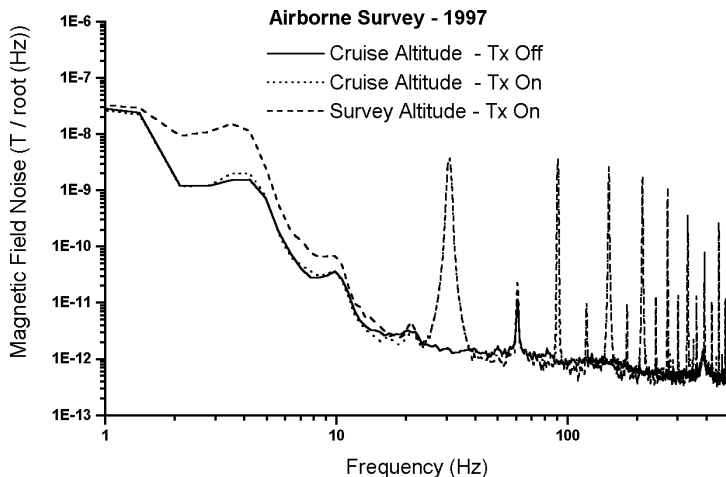


Fig. 14.11 Noise spectrum of an airborne SQUID system: at altitude with the transmitter off, at altitude with the transmitter on and at survey altitude with the transmitter on. Note the noise spikes due to 50-Hz power and the TEM transmitter operating at 30 Hz. At frequencies less than 20 Hz, the noise is dominated by motion of the system.

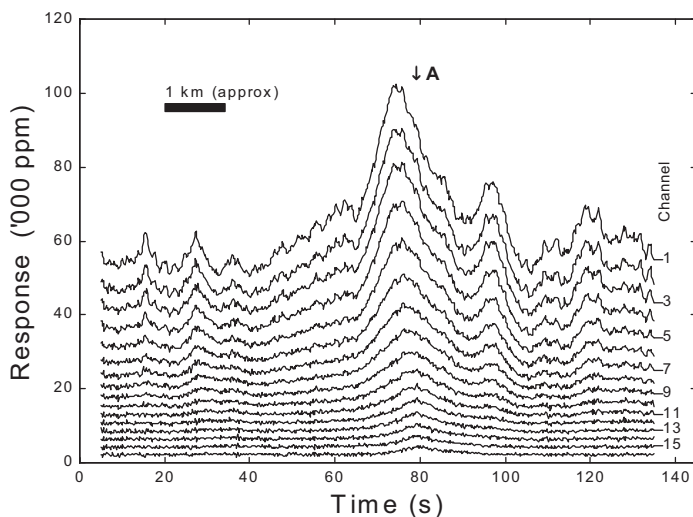


Fig. 14.12 An example of the SQUID response from an airborne magnetometer survey in South Australia. The units on the x-axis refer to the time at which the measurement was taken as the aircraft flew over the survey line. This is related to distance along the survey line by multiplying each value by the speed of the aircraft. A transmitter current pulse induces a current in a conducting ore body similarly to the ground-based TEM

method shown in Figure 14.9. "A" points to the position of the conducting anomaly of interest. The y-axis is the response of the SQUID magnetometer as expressed as a portion of the peak transmitter current pulse. The value of the peak transmitter current pulse, the speed of the aircraft and response units are proprietary. (Used with permission of BHP-Billiton Pty. Ltd.)

When designing an airborne SQUID TEM system it is important to ensure that the slew rate of the SQUID system is sufficient to be able to follow the pulse as it is turned off, and that the dynamic range of the SQUID is large enough so that the SQUID does not lose lock during operation. The CSIRO/BHP operators noted that the sensor noise increased as more and more magnetic flux became trapped in the SQUID over time. This can be overcome by the use of a heater arrangement to thermally cycle the SQUIDs while the aircraft turns. In addition to the many schemes outlined in Sections 14.2 and 14.3 that reduce the effects of motion noise, digital finite-impulse response filters can be applied to TEM SQUID receivers. These comb filters are related to the *B*-spline filters used in wavelet transforms. A digital tapered stacking filter was developed by MacNae *et al.* [75]. This filter technique for frequencies up to 25 Hz assisted in the elimination of low-frequency motion noise during airborne operation while not affecting the spatial resolution. The frequency response of filters and other details are given in Ref. [89].

Airborne SQUID TEM is at an early but promising stage. Although the system engineering challenges are substantially more difficult than for ground-based SQUID TEM, the airborne case is where the SQUID can potentially offer the largest advantage over conventional technology. This is because the extra vertical separation between the system and the conductivity anomalies means that the transmitter field is weaker at the anomalies (as it scales as $1/r^3$ in the dipole limit, see Eq. (14.1)), and the secondary field is measured at longer range, also scaling as $1/r^3$ in the dipole limit. If transmitter and anomaly are both in the dipole limit then the measured signal falls at a very severe $1/r^6$. Due to its superior low-frequency noise, the SQUID (once the motion noise is eliminated) appears to be the best sensor for this application.

14.5.4.5 Tensor SQUID Gradiometers for Prospecting

During the early stages of mineral exploration, it is mandatory to carry out magnetic surveys. The acquisition and processing of magnetic surveys using total field (total magnetic intensity, TMI,) data from airborne cesium vapor magnetometers have improved remarkably over the past decade. It is now possible to create high-quality magnetic images, similar to topographical maps, from survey data. Nevertheless, due to time constraints on surveys and the lack of magnetic tensor gradiometers, a lot of magnetic information is not yet accessed. It is possible to derive vector field components from suitably processed TMI data with high-density sampling; however, a more faithful representation of the vector field would be obtained by direct measurement. Unfortunately, the accuracy of direct measurements of the field vector is governed by motion noise, which for airborne platforms is so large that the theoretical derivation of the components from the TMI is actually preferable. These issues are discussed in more detail in Section 14.3.

Gradient measurements are preferable to vector field measurements for airborne survey from the point of view of motion noise rejection. Another advantage is they obviate the need for base stations, which are used for remote referencing to provide the corrections for diurnal variations. They also greatly reduce the need

for regional corrections, which are required when performing TMI surveys because of deeper crustal fields that are not of exploration interest or the normal (quasi-) latitudinal intensity variation of the global field. More information on this may be found in Refs. [90, 91]. Schmidt and Clark [92], who discussed design requirements of a tensor gradiometer, have calculated the required sensitivity and found it to be 0.01 nT m^{-1} . An instrument with this sensitivity would be able to detect the weakest geophysical structures, a vertical contact between two different paramagnetic rock faces with a susceptibility contrast of about 6×10^{-4} (dimensionless when in SI units) at a 100-m range.

CSIRO [93] and IPHT-Jena [94] reported initial trials both using configured axial gradiometers based on two SQUIDS mounted with a vertical separation and measuring the B_{zz} component of the Earth's magnetic field tensor. Both reports were on initial trials and development work is still underway. The effective noise levels achieved were $0.16\text{--}0.3 \text{ nT m}^{-1}$ RMS for a gradiometer with the two SQUIDS located within a single dewar with a baseline of 0.3 m [93] and 25 nT m^{-1} RMS for SQUIDS separated on a 1.2-m baseline (that flexed during the surveys reducing the balance) [94]. These may be compared to $0.1\text{--}0.5 \text{ nT m}^{-1}$ for a pair of cesium-vapor total field magnetometers separated by 1 m [93], so further progress is required. The SQUID noise was reported for both systems to be dominated by vibration with additional contributions from the multiplexed sampling arrangement used.

Further developments have continued with low- T_c gradiometry used in both helicopter trials [95] and fixed-wing aircraft trials [96]. The helicopter trials used a

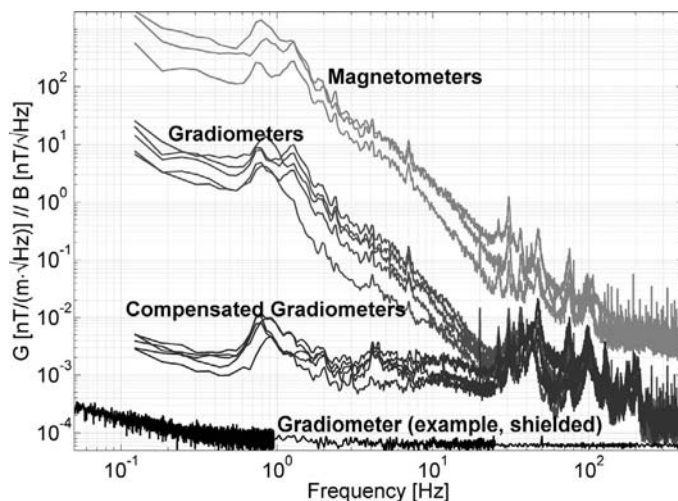


Fig. 14.13 Noise spectra of three magnetometers (triple used for balancing) and five-gradiometers (raw and after software balancing) on a flight line at about 1400 m above ground. The example of a shielded gradiometer spectrum shows the intrinsic noise [95]. These measurements can be used to determine all the nine components of the Earth's magnetic field gradient tensor. (Used with permission of R. Stolz and A. Chwala, IPHT, Jena.)

towed platform which carried the gradiometer constructed of planar gradiometers that achieved a gradient resolution after software balancing of better than $10 \text{ pT m}^{-1} \text{ Hz}^{-1/2}$ for frequencies above 0.1 Hz. Figure 14.13 shows the noise spectra of the gradiometer on a flight line at 700 m above the ground, with and without motion compensation, at rest in shielding and compared to the spectra reference magnetometers. To date, fixed-wing trial results have not been published. However, it is known that a full tensor gradient measurement was performed with software compensation using triaxial SQUID magnetometers providing data for the gradiometer's compensations [96]. Figure 14.14 shows how the LTS SQUID gradiometer was mounted on a fixed-wing aircraft in the tail boom and in a tow body of a helicopter.

SQUID system noise levels of the next generation of systems (that are currently under development) must improve significantly for the specification of 0.01 nT m^{-1} sensitivity to be achieved. This sensitivity requires a common mode rejection ratio of between 10^{-8} and 10^{-9} ; *i.e.*, the same as for the MAD applications. A rotating gradiometer described in Section 14.6.4 is being developed for this application.

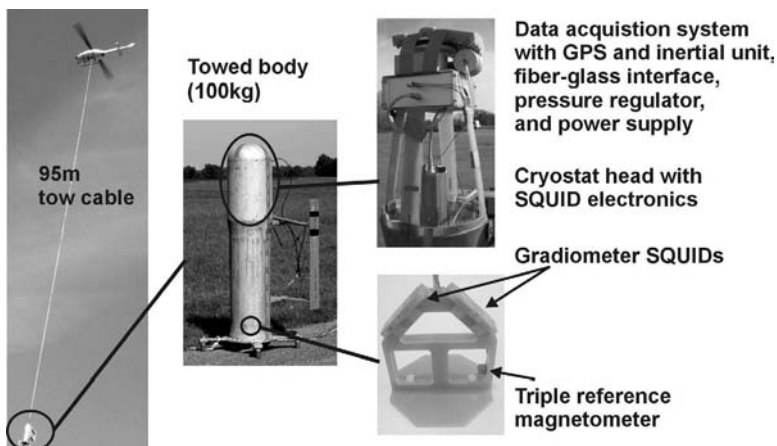


Fig. 14.14 Top: fixed-wing aircraft (Cessna Grand Caravan, the main type of aircraft used for airborne geophysical surveys) fitted with different generations of LTS SQUID-gradiometer systems in a tail boom. Bottom left: helicopter carrying the tow-body with the LTS SQUID gradiometer system, as depicted in the right-hand-side photographs [95,96]. (Used with permission of R. Stoltz and A. Chwala, IPHT, Jena.)

14.5.4.6 Magnetotellurics and Radiometric Sounding

Magnetotellurics (MT) is a passive remote sensing technique that can image the Earth's electrical conductivity distribution of the subsurface from measurements of the natural transient electric and magnetic field at the surface. Natural transient electromagnetic (EM) waves are generated in the Earth's atmosphere by a range of physical mechanisms such as sun spots (providing low-frequency signals), ionospheric resonances (intermediate-frequency signals), and thunderstorm activity (high-frequency signals). The low-frequency signals travel further into the earth than the high-frequency signals. By measuring the electric and magnetic fields at the Earth's surface and using advanced mathematical techniques to process the data one can detect, the electrical resistivity can be interpreted to create a map that can indicate the presence of oil, gas, and water [97] due to structures from depths of a few hundred meters to greater than 100 km. The time variations of the Earth's electric and magnetic fields at a site are recorded simultaneously over a wide range of frequencies. As already mentioned in Section 14.5.2, subtraction of correlated noise using a remote, distant reference is essential for obtaining usable signals [52, 53]. The signal variations are analyzed to obtain their spectra and apparent resistivities as a function of frequency. Interpretation consists of matching the computed apparent resistivity against frequency to responses calculated for simplified models.

Traditionally, large orthogonal induction coils are used to measure the magnetic components while electrodes buried in the ground provide the electrical field data. Because induction coils have very nonuniform frequency responses, a variety of optimized coils are required to achieve a uniform response over a wide frequency range. MT requires magnetic sensors with a bandwidth of 10^{-4} to 10^2 Hz which SQUIDs are clearly able to provide with the sensitivities necessary. Low- T_c SQUID systems have been used since the 1970s for MT surveys and are described in Refs. [98, 99] and more recently there have been reports on initial studies of using high- T_c and low- T_c devices [81, 100, 101]. Unfortunately adoption as a standard technique has not occurred for several reasons including the complications of using helium cryogenics in the field, drift, difficulties in recording very low frequency responses, dynamic range, and cost.

Controlled source audio magnetotellurics (CSAMT) is an extension of the MT technique with an artificial (active) source causing an electromagnetic response of the Earth to the excitation generated by a transmitter. For this technique, the transmitter is coupled to the earth electrically via electric dipole electrodes and magnetically via an antenna loop, so that CSAMT also measures three magnetic field components and two horizontal electrical components of the fields. The resistivity of the Earth is derived as a function of frequency, which is related to the depth into the ground where the signal originated [81]. For a SQUID system to demonstrate superior performance over induction coils for the measurement of the magnetic field components, a field resolution of the order of $10 \text{ ft Hz}^{-1/2}$ is required at the frequency range of several hundred hertz. To attain such resolution, the use of an optimized shielding-free flux transformer with a multturn input coil was suggested in Ref. [77]. Thus far, such resolution has been achieved

only with an rf SQUID and transformer in a magnetic shield [77]. To date there is no report of CSAMT field trials using SQUIDS.

Similar to MT, radiomagnetic sounding measures the conductivity of shallow subsoil down to a 10-m depth. Such measurements could be useful for ground water exploration and monitoring, soil foundation assessment, as well as environmental monitoring. Due to the skin effect, the penetration depth of an EM field depends on the frequency of the EM wave and the resistivity of the surface soil. For a horizontal plane EM wave, the skin depth determines the depth of investigation. Typical resistivities of unconsolidated and water-saturated sediments are in the range of 10 to 100 $\Omega \text{ m}$. For near-surface investigations, frequencies need to be in the range of 10 to 2000 kHz. This is much higher than for MT measurements. To cover this frequency and hence depth range, the passive EM method of radiomagnetic sounding (RMS) has been developed. RMS uses radio transmitter fields at discrete frequencies. To obtain the impedance, both the electric and magnetic fields must normally be measured. Early work by Meyer [102] has shown that it is possible to substitute the electrical measurement with measurement of the magnetic gradient. Unfortunately, calculations by Drung *et al.* [103] have shown that the ideal specification for such systems requires the balance and sensitivity of a biomagnetic gradiometer operating in a magnetically unshielded environment, $40\text{--}4000 \text{ fT m}^{-1}$ depending on transmitter strength, with the added requirement of a bandwidth of about 100 MHz. In practice, Drung *et al.* achieved $\sim 100 \text{ fT m}^{-1} \text{ Hz}^{-1/2}$ with an 11 MHz bandwidth and $5 \times 10^7 \Phi_0 \text{ s}^{-1}$ SQUID system [103]. The actual noise performance in the field was not stated, but 3.1% of the signal from a strong 990 kHz radio station was measured underground, favorably comparing with the theoretically estimated 3.5%.

The use of SQUIDs in MT, CSAMT and radiomagnetic sounding will occur only after the demonstration of superior performance over existing sensor technologies. Improvements in multilayer film quality, device fabrication, and transformer design may permit one to gradually achieve the field resolution and bandwidth required [77]. Also improved electronic system design is necessary to demonstrate a true broadband SQUID system for all ground-based geophysical prospecting methods.

14.6

Magnetic Anomaly Detection Systems using SQUIDS

14.6.1

MAD Detection Range

The selection of magnetic sensor for a given MAD application will largely depend on the requirement for detection range, which is in turn a function of the magnetic moments of the targets and of sensor sensitivities. Superconducting gradiometers and optically pumped total-field magnetometers provide the longest detection ranges for magnetic anomaly detection in mobile applications demon-

strated to date. From Eqs. (14.1) and (14.3), the signal strength of a magnetic dipole decreases for magnetometers and gradiometers as the third and fourth power of range, respectively. Nominal ranges of magnetometers and gradiometers as a function of magnetic moment are tabulated in Table 14.5. For this table, magnetometer and gradiometer sensitivities of $100 \text{ pT Hz}^{-1/2}$ and $3 \text{ pT m}^{-1} \text{ Hz}^{-1/2}$ at 0.1 Hz were selected. In both cases, these figures represent root mean square (RMS) values within the target's frequency passband and reflect detection with a 10 dB SNR. The magnetometer sensitivity reflects an environmental limitation on the measurement of magnetic field arising from temporal variations in geomagnetic field: the gradiometer sensitivity corresponds to the performance demonstrated by a reported SQUID system [12, 104]. In this comparison, the magnetometer has a greater detection range against targets with greater magnetic moment, while the gradiometer has greater range against targets with smaller magnetic moment. The detection ranges for these two sensors are approximately equal for a target with a moment of 10^5 A m^2 .

Table 14.5 Magnetic sensing swath width as a function of target moment.

| Target moment (A m^2) | Representative object | Magnetometer swath (m) | Gradiometer swath (m) |
|-------------------------------------|-------------------------------------|---------------------------|--------------------------|
| 1 | 105-mm artillery shell | 13 | 32 |
| 10^1 | 50-gallon oil drum | 27 | 56 |
| 10^2 | 2000-lb bomb | 60 | 100 |
| 10^3 | Automobile | 130 | 180 |
| 10^4 | Storage tank (10^2 m^3) | 270 | 320 |
| 10^5 | Diesel submarine | 590 | 560 |
| 10^6 | Bunker (10^4 m^3) | 1300 | 1000 |
| 10^7 | Industrial plant | 2800 | 1800 |

It is important to note when comparing gradiometers with total-field magnetometers that the detection ranges depend on the measurement's geometry. Usually a sensor's detection range performance is quoted only for the most favorable geometry. One can move a total-field magnetometer very close to a large dipole and not detect it if its track is along a null line of the total field distribution as shown in Figure 14.2. The same dipole can be sensed at long range if it is on the most favorable track with respect to the sensor. Single gradiometers also have nulls, so with either sensor the detection range for a single measurement can be anywhere between zero and the maximum. Multiaxis gradiometers have the big advantage that they are nearly omnidirectional so detection range is always close to the maximum.

14.6.2

The Superconducting Gradiometer/Magnetometer Sensor (SGMS)

In this section some example research systems for airborne and maritime MAD are described. There have been more systems built and tested than are described here, but this selection illustrates a variety of different design approaches. More details, representing the status of the mid-1990s, can be found in Ref. [12].

During the 1980s, a five-channel low- T_c tensor gradiometer, the superconducting gradiometer/magnetometer sensor (SGMS), was developed for mobile operations at the US Naval Surface Warfare Center [12, 104]. The SGMS demonstrated, for the first time, high sensitivity and rugged, robust, reliable performance of a helium-cooled, low critical temperature superconducting gradiometer operating onboard a towed underwater vehicle. This gradiometer has operated in sea tests conducted over a period of 17 years. Under some field conditions, it has attained sensitivities on the order of $1\text{--}3 \text{ pT m}^{-1} \text{ Hz}^{-1/2}$ at 0.1 Hz. A system concept that integrated SGMS with acoustic sensors was developed for enhanced sea mine detection under the Magnetic and Acoustic Detection of Mines (MADOM) project. The SGMS was demonstrated to provide effective and accurate localization and moment determination for single- and multitarget cases and to detect fully buried mines without any diminished performance arising from target burial. Moreover, the high effectiveness of magnetic and acoustic sensor fusion for false-alarm reduction was demonstrated.

The detection and classification capability developed for MADOM was tailored to the application of detecting and accurately mapping the locations of unexploded ordnance (UXO) in coastal regions under a project to develop and evaluate a mobile underwater debris survey system (MUDSS). A feasibility test in 1995 followed by an unscripted UXO survey in 1999 successfully demonstrated the effectiveness of the SGMS for UXO target detection [105, 106]. The example in Figure 14.15, obtained from data collected with the SGMS in MUDSS sea testing, demonstrates the basic capability. The motion-compensated gradiometer signals and the target location, moment magnitude, and orientation data obtained through signal processing are displayed. Figure 14.16 displays the magnetic target map for the 1999 MUDSS UXO survey. A total of 492 well-localized magnetic targets were detected during the survey with confidence levels exceeding the threshold value. Some 177 targets were located with magnetic moment magnitude in the correct range for a UXO target, $3\text{--}30 \text{ A m}^2$. The number of potential UXO targets was reduced from 177 to 135 by applying the enhanced classification criterion using vector-moment information. The 135 potential UXO targets are designated by dots on the map. A number of magnetic targets are highlighted. Targets T1 and T2 were test targets (a 500-lb and a 1000-lb bomb) laid to baseline system performance at the survey site. Other magnetic targets, designated T3-T20, detected both acoustically and magnetically and/or having a magnetic confidence level much greater than the threshold, were selected for separate diver inspection. Using a hand-held total-field magnetometer, divers successfully reacquired four targets, all buried, including a round steel plate (T10), a 0.15-m diameter pipe sec-

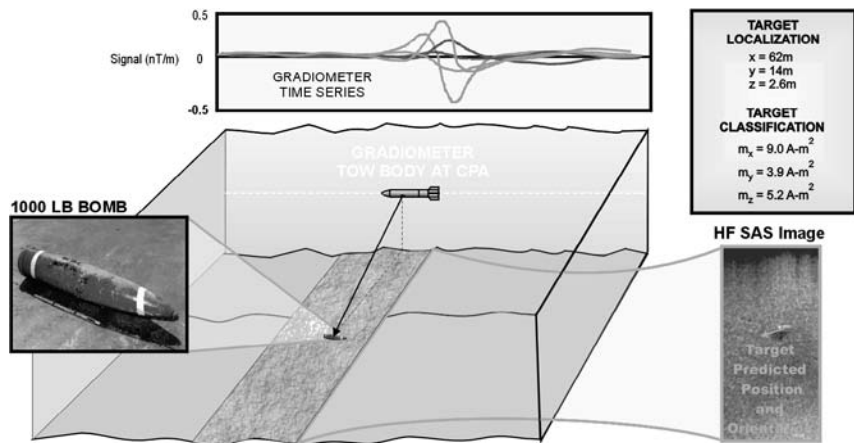


Fig. 14.15 Gradiometer housed in an under-water-towed vehicle moving in a straight-line tow past a 1000 lb bomb, 14 m to port and 3 m below the gradiometer at the closest point of approach. The time-series signals in a 45-m section of data for five gradiometer

channels are displayed on a pass near the bomb. The effectiveness of this signal processing is demonstrated by the accuracy of the location and orientation predictions, which are displayed superposed over an image from a synthetic-aperture sonar.

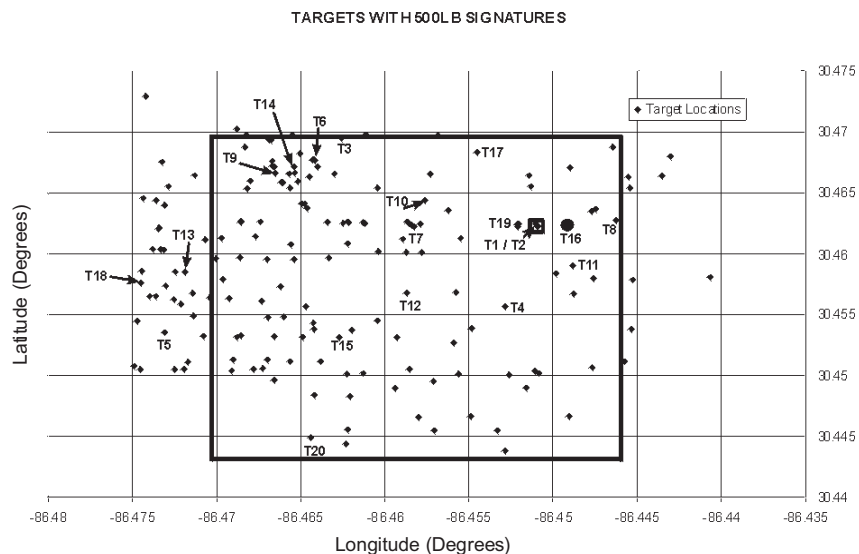


Fig. 14.16 Results from the 1999 MUDSS unsupervised magnetic survey. The 135 potential UXO targets are designated by dots on the map. A number of magnetic targets, T, are highlighted by numbers and commented on in the text.

tion, 0.9 m long (T13), a cylindrical iron object with dimensions similar to those of a 500-lb bomb (T16), and magnetic object (T19) not recovered and hence not identified. As the result of target burial and deteriorated acoustic and optical conditions at the survey site, the SGMS was the most useful sensor in this demonstration.

Combining different sensors that detect distinctly different target features is very desirable for effective classification [12, 105–107]. The application of two or more collocated sensors operating simultaneously in an essentially uncorrelated manner has the potential to reduce false alarms and to provide robust detection in a wide variety of background conditions. The fusion of a magnetic sensor with sonar provides such an alternative for underwater sensing. In Figure 14.15, note the positional and orientation accuracies obtained from the acoustic and magnetic sensors. In the MADOM sea testing, more than 98% of acoustically mine-like clutter was not magnetically mine-like. This promising process of sensor fusion is an integral part of the US Navy's ongoing buried mine hunting development program.

14.6.3

The High- T_c Three-Sensor Gradiometer

A prototype for a nitrogen-cooled high- T_c SQUID gradiometer using the TSG approach (see Section 14.2.4.3 and Figure 14.5) has been developed and evaluated for MAD [18]. The gradiometer consists of two three-axis high- T_c SQUID magnetometers that are each enclosed in a cube. These cubes are separated in the z direction and aligned to sense in the x , y , and z directions so the gradiometer measures G_{xz} , G_{yz} , and G_{zz} . Each cube is wound with three orthogonal Helmholtz pairs for the common-mode feedback, which is derived from a reference three-axis fluxgate magnetometer with its sense axes aligned to the x , y and z directions. This reference sensor measures the ambient Earth's magnetic field vector, and the appropriate feedback current is supplied to each Helmholtz coil pair to cancel the corresponding component of that field at the SQUID sensor. The Helmholtz coils for each direction are connected in series and controlled by negative feedback from the corresponding reference fluxgate magnetometer in the manner illustrated in Figure 14.5.

Using this method, the in-phase matching of the feedback fields at the two SQUID assemblies has been demonstrated to be within 4 parts in 1000 for all three axes. The quadrature components were maintained to within 1 part in 1000. Gradient sensitivity for this sensor when stationary was demonstrated to be $0.8 \text{ pT m}^{-1} \text{ Hz}^{-1/2}$ at 1 Hz. The power spectrum followed a $1/f$ power law at lower frequencies while operating stationary and unshielded in the Earth's magnetic field. Sensor noise under motions of order 1° was demonstrated to be $5 \text{ pT m}^{-1} \text{ Hz}^{-1/2}$ at 1 Hz, and the power spectrum followed a $f^{-3/2}$ law at lower frequencies.

14.6.4

The Global Feedback Gradiometer

Only a limited amount of information is available on this gradiometer that was developed for the UK Ministry of Defence [19, 20]. Its purpose was to demonstrate with a single-axis gradiometer that a high- T_c system can overcome the critical problems of motion noise and rf interference. A photograph of this system with global feedback coils is shown in Figure 14.17. The principle of motion noise rejection for global feedback gradiometers is described in Section 14.2.4.3 and Figure 14.6. The issue of RFI rejection is a minor concern for undersea systems where the conductivity of seawater is sufficiently high that rf cannot penetrate more than a meter below the surface; for airborne MAD it is a major issue. The global feedback gradiometer uses high- T_c dc SQUIDs with a modulation-based

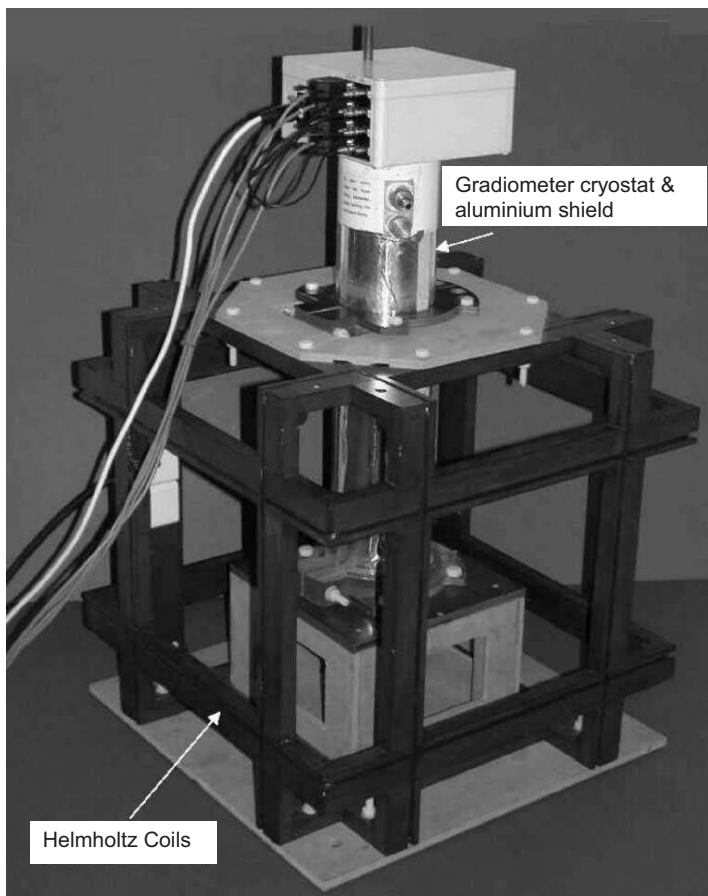


Fig. 14.17 The global feedback gradiometer from Ref. [20]. The coils have a side length of 0.5 m. (Courtesy of QinetiQ Ltd.)

readout scheme. Direct readout schemes were tried but found to be too susceptible to RFI and underwent too much drift whilst in motion. A thin conductive shield was also used around the dewar to prevent pickup through the flux transformers. The shield was carefully designed to provide sufficient rf shielding whilst not adding low-frequency magnetic noise caused by Johnson noise currents in the shield.

The system comprised two SQUIDs measuring the z -field separated by a 0.1-m baseline, and two orthogonal SQUIDs to measure the x and y fields. In other respects it is the same as depicted in Figure 14.6. The purpose of the signal-processing algorithm was to correct for scaling errors, alignment errors between the sensors in each gradiometer, offsets, and long-term drift. The linearly constrained least-squares-fit method was used for adaptive balancing. It is assumed that output signal Γ from the two electronically differenced z -sensing SQUIDs is represented by

$$\begin{aligned}\Gamma = & C_0(B_{z2} - B_{z1}) + C_1B_x + C_2B_y + C_3(B_{z1} + B_{z2}) \\ & + C_4T_x + C_5T_y + C_6(T_{z1} + T_{z2}) + C_7\end{aligned}\quad (14.8)$$

where C are coefficients to be determined; $B_{z2} - B_{z1}$ is the gradient estimation from subtracting the two z SQUIDs; $B_{x,y,z}$ are the external field components; and $T_{x,y,z}$ are field components inside the global coils as measured by the SQUIDs. An energy function is constructed from Eq. (14.8) which is minimized over time by adjusting coefficients C_1-C_7 whilst C_0 is constrained to unity. C_1 , C_2 , and C_3 correct for the overall magnetometric response of the system, *i.e.*, the overall balance, while C_4 , C_5 , and C_6 correct for imperfections in the global feedback coil system, *i.e.*, imperfect coil orthogonality and nonuniformity in the field: C_7 removes any offset.

This method of adaptive balancing is best suited to situations where magnetic anomalies are relatively rare. The gradiometer continually adapts to its environment over time, its adaptation rate being set slower than the minimum frequency component of the target's signals. This has several very powerful advantages for the system design and engineering. First, it removes the need to calibrate and to manually correct the balance: a difficult process that requires special low gradient facilities. Second, it considerably relaxes the requirements on the mechanical and thermal stability compared to fixed-balance systems. This is because the overall stability of the system (with regard to drift and balance) has only to be fixed to better than the adaptation time (typically 100–300 seconds) rather than the time between calibrations for non-adaptive systems (1–6 months). This has a big impact on the system costs as cryogenic dewars with less intricate mechanical engineering are needed. Third, the system does not have to be set up initially with high levels of balance. High intrinsic balance (*i.e.*, before computer compensation) lowers the values of the starting point of the coefficients C_1-C_7 in Eq. (14.8) and it has not been found to be advantageous to do so, provided the initial balance is not excessively poor.

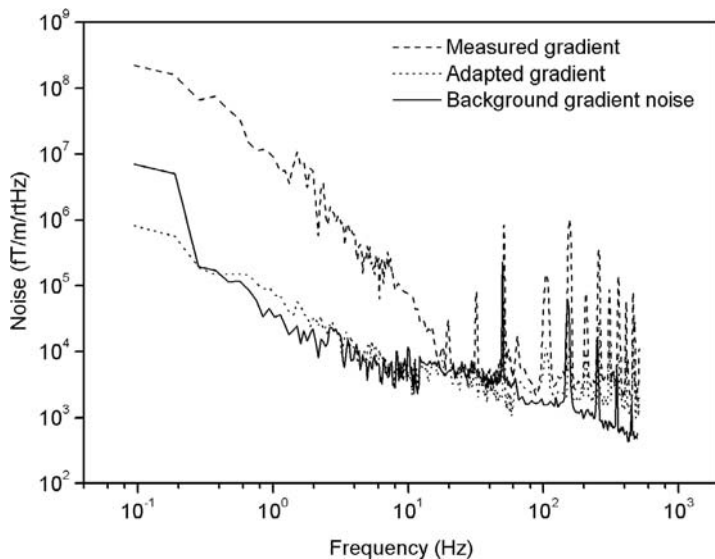


Fig. 14.18 The noise performance of the high- T_c global-feedback gradiometer with a 0.1 m baseline undergoing random $\pm 5^\circ$ rotations in pitch, yaw and heading whilst outdoors and unshielded. The “measured-gradient” spectrum is the signal with global-feedback

applied, and the ‘adapted gradient’ is after signal processing. The background trace was measured before and after the motion run with the gradiometer stationary. This demonstrates elimination of this level of motion noise at low frequencies.

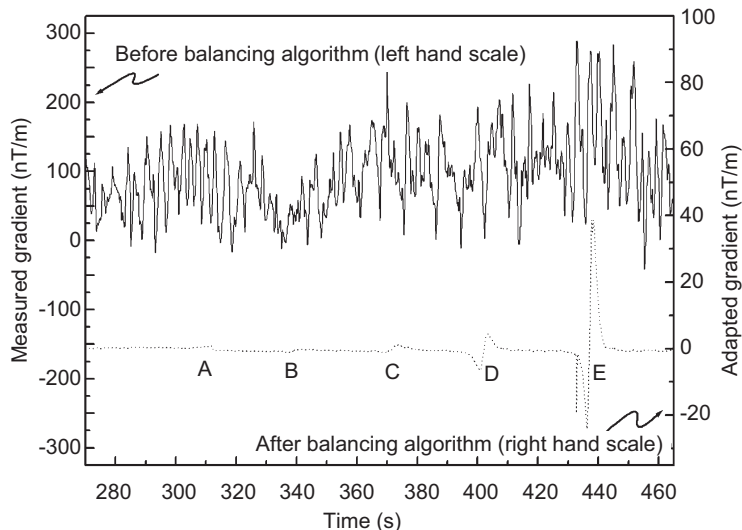


Fig. 14.19 Anomaly detection of five targets, A–E, using an in-motion high- T_c global feedback gradiometer from Ref. [20]. The upper trace is dominated by motion noise due to the mechanical and electronic imbalance under random rotations of $\pm 5^\circ$. The lower

dotted curve (right-hand scale) is the same data after the adaptive balancing algorithms, and shows five detections. The noise performance of this system is shown in Figure 14.18.

Figure 14.18 shows successful motion noise cancellation to the background gradient noise level, albeit in a magnetically noisy environment, when the gradiometer underwent random rotations of amplitude $\pm 5^\circ$ in three degrees of freedom. Figure 14.19 shows the effect of adaptive balancing on anomaly detections with the sensor in motion.

14.6.5 Other Systems

A three-axis low- T_c SQUID vector magnetometer was developed for airborne MAD of submerged vessels [9]. Signal processing was developed to synthesize magnetic total field precisely from the three orthogonal vector-component signals. The sensor was integrated into the tail boom of a P-3C, a fixed-wing aircraft, and during flight trials it detected a surface ship at a distance. Although no noise spectra are available for this sensor, the researchers stated that the residual noise under flight conditions was dominated by geological noise (see Section 14.3.3). This is suggestive of performance similar to or better than conventional optically pumped total-field magnetometers.

A new gradiometer concept is under development that uses three axial gradiometers constructed from a high- T_c SQUID flip-chipped onto a flexible tape pickup loop shown in Figure 14.4 [44]. Three of these sensor packages are rotated about separate axes at 45° to each other, as shown in Figure 14.20. As explained in Ref. [44], with this scheme it should be possible to obtain all the nine components of the magnetic field gradient tensor as well as the absolute value of the magnetic field vectors [13, 14]. A proof-of-concept system operated successfully in a field trial [44].

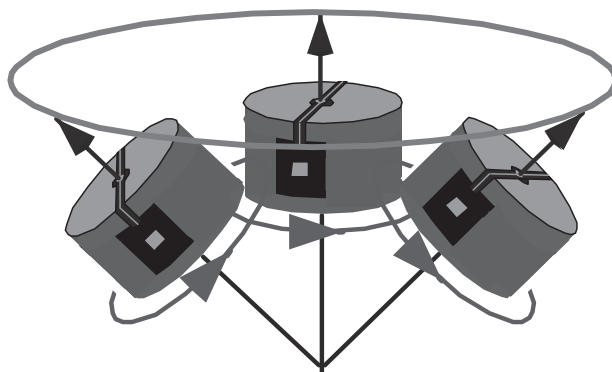


Fig. 14.20 A schematic of the rotating tensor-gradiometer instrument. Three gradiometers of the type shown in Figure 14.4 are mounted on rotating cylinders. The full tensor can in principle be measured in this way [44].

14.7

Future Prospects

SQUID systems operating in real environments to measure the field gradients of remote sources remain one of the most challenging aspects of SQUID research, particularly if the SQUIDS are in motion. For applications where the SQUIDS environment can be controlled, such as rock magnetometers, susceptometers, and magnetic microscopes, SQUIDS are now reasonably established for the high-sensitivity ends of their markets, although these markets are fairly small.

For field applications, where the sensor's magnetic environment cannot be controlled, acceptance has not yet occurred (although for ground-based TEM this is changing). In contrast to biomagnetism, which presently is not a practical proposition without SQUIDS, MAD and geophysical survey already have many well-established conventional magnetic sensors and techniques; SQUIDS will need to have clear functional advantages to supplant them. Fortunately, for both geophysical prospecting and MAD there are strong user requirements for better sensitivity and higher discrimination than current conventional systems can offer. To this end, several SQUID research systems for both geophysical and MAD survey applications have been built and tested in operation, and these have generally proved successful at demonstrating that SQUIDS can be used for these applications. However, with the exception of ground-based TEM for nickel sulfide exploration, such SQUID systems are not yet established as a first-choice technology for users.

To understand this, it is worth considering some of the main issues concerning the appropriateness of SQUIDS for field applications. Low- T_c SQUID gradiometers and magnetometers are more sensitive than high- T_c ones; even these are more sensitive than conventional sensors such as fluxgates and fieldable optically pumped magnetometers. The cost of the systems, as well as the operational difficulties in using them, decreases in the same order; low- T_c , high- T_c , then conventional. The environment places limits upon what can be measured in practice – the conductivity of soil in TEM measurement; the dynamo effect of sea waves in the Earth's field (*magnetohydrodynamic induction* [108]); geomagnetic noise; noise from magnetic sources in the host platform; geologic noise; and many others. These can limit the usable sensitivity of SQUIDS and, therefore, reduce the advantage of using them. The *benefit-improvement-to-price* ratio of using SQUIDS rather than conventional sensors is often not sufficiently favorable. In this context the term *benefit improvement* when using SQUIDS does not just refer to sensitivity but to the overall operational performance which is undermined by the inconvenience of running cryogenic systems and the fragility of the apparatus. Furthermore, the reliability and maturity of SQUID-based field systems is not yet sufficient either. For market acceptance, the benefit-improvement-to-price ratio must be increased.

Although a lot of research effort has been directed towards the SQUID sensor technology itself, comparatively little has been directed to overcoming the environmental limitations that curtail the effectiveness of field SQUID systems. There is much scope for progress in this area, particularly in the signal processing aspects, and a multidisciplinary approach will be needed to do this. Other improvements

will be needed as well. Cooling engines – if they can be magnetically quiet in future – will be far more acceptable than cryogenic liquids for most applications; the systems will have to be “turnkey” instruments whereby all setting up is done automatically; and the costs will have to drop. These measures will all act to increase the benefit-improvement-to-price ratio, making SQUID sensors more attractive to the markets. The use of SQUID sensors for ground-based TEM is beginning to become recognized as having such a worthwhile ratio. In some exploration contexts, such as in discovering nickel sulfide ore bodies, mining companies are making public announcements of their impending exploration using SQUID sensors. They do it to improve their share price by using innovative technology, which should reduce their future exploration costs by reducing the number of cores that have to be drilled.

Given all this, the future for fieldable SQUID instruments for geophysical exploration and MAD looks uncertain at this time. High expectations after the discovery of high- T_c materials led to a wave of optimism that improved sensors would be quickly fieldable. However, the perceived barrier of inconvenient cryogenics for low- T_c mobile systems was just one of a large number of technical difficulties that needed to be overcome; the remainder being as applicable to high- T_c as they are to low- T_c systems. Added to this, high- T_c systems have additional problems such as large 1/f noise and high hysteresis. Researchers in this area have certainly demonstrated that SQUIDs can be used in unshielded environments, but there is still much to do in the area of environmental cancellation and in making SQUID sensors rugged, practical, and easy to operate.

Despite this, unless there are surprising sensitivity improvements in room-temperature magnetometers, SQUIDs should eventually become adopted in the best field instruments, because there are real market needs for improved performance of magnetic survey equipment. This is already happening for ground-based TEM. Growing commercial operation of SQUID systems in Canada and Australia occurs without the involvement of researchers. These systems are already rugged and used regularly in difficult environments. Indeed, several SQUID-based systems have been in commercial use for nearly five years, making money for the contractors, the mining companies and even some for the researchers. More systems are being made, with the number in use growing at about three per year.

So far, there do not appear to be any fundamental technological *show-stoppers* that will prevent more widespread adoption of SQUIDs for field systems, although more technology progress is first needed.

References

- 1 Vrbancich, J., Fullagar, P.K., and Macnae, J. (2000) Bathymetry and seafloor mapping via one dimensional inversion and conductivity depth imaging of AEM, *Explor. Geophys.*, **31**, 603–610.
- 2 Vacquier, V. (1945) The Gulf absolute magnetometer, *Terr. Magn. Atmo. Elec.*, **50**, 91–104.
- 3 Ruddock, K. A., Slack, H. A., and Breiner, S. (1966) Method for determining depth and fall off rate of subterranean magnetic disturbances utilizing a plurality of magnetometers, U.S. Patent 3,263,161.
- 4 Cohen-Tannoudji, C., DuPont-Roc, J., Haroche, S., and Laloë, F. (1969) Detection of the static magnetic field produced by the oriented nuclei of optically pumped ^3He Gas, *Phys. Rev. Lett.* **22**, 758–760.
- 5 Bobb, L. C., Davis, J. P., Kuhlman, G., R. Slocum, R. E., and Swers, S. R. (2001) Advanced sensors for airborne magnetic measurements, in *Proc. 3rd International Conference on Marine Electromagnetics* (MARELEC 2001), Stockholm, Sweden, July 2001.
- 6 Primdahl, F. (1979) The fluxgate magnetometer, *J. Phys. E: Sci. Instrum.* **12**, 241–253.
- 7 Ripka, P. (1992) Review of fluxgate sensors, *Sensors and Actuators A* **33**, 129–141.
- 8 Weinstock, H. and Overton, W. C. (1981) SQUID Applications to Geophysics, *Proc. Workshop*, 2–4 June 1980, Soc. Explor. Geophys., Tulsa, OK.
- 9 Hirota, M., Furuse, T., Ebana, K., Kubo, H., Tsushima, K., Inaba, T., Shima, A., Fujinuma, M., and Tojyo, N. (2001) Magnetic detection of a surface ship by an airborne LTS SQUID MAD, *IEEE Trans. Appl. Supercond.* **11**, 884–887.
- 10 Schmidt, P. W. and Clark, D. A. (1998) The calculation of magnetic components and moments from TMI: a case study from the Tuckers igneous complex, Queensland, *Explor. Geophys.* **29**, 609–614.
- 11 Wynn, W. M., Frahm, C. P., Carroll, P. J., Clark, R. H., Wellhoner, J., and Wynn, M. J. (1975) Advanced superconducting gradiometer/magnetometer arrays and a novel signal processing technique, *IEEE Trans. Mag.* **11**, 701–707.
- 12 Clem, T. R., KeKlis, G. J., Lathrop, J. D., Overway, D. J., and Wynn, W. M. (1996) Superconducting magnetic gradiometers for mobile applications with an emphasis on ordnance detection, in *SQUID Sensors: Fundamentals, Fabrication and Applications*, H. Weinstock ed., Kluwer, pp. 517–568.
- 13 Bick, M., Leslie, K. E., Binks, R. A., Tilbrook, D. L., Lam, S. K. H., Gnanagaran, S., Du, J., and Foley, C. P. (2004) Axial high- T_c superconducting gradiometer with a flexible flux transformer, *Appl. Phys. Lett.* **84**, 5347–5349.
- 14 Tilbrook, D. L. (2004) The design of a new concept HTSC axial gradiometer, *Physica C* **407**, 1–9.
- 15 Koch, R. H., Rozen, J. R., Sun, J. Z., and Gallagher, W. J. (1993) Three SQUID gradiometer, *Appl. Phys. Lett.* **63**, 403–405.
- 16 Koch, R. H. (1992) Gradiometer having a magnetometer which cancels background magnetic field from other magnetometers, US Patent 5,122,744.
- 17 Koch, R. H., Keefe, G. A., and Allen, G. (1996) Room temperature three sensor magnetic field gradiometer, *Rev. Sci. Instrum.* **67**, 230–235.
- 18 Clem, T. R., Overway, D. J., Purpura, J. W., Bono, J. T., Koch, R. H., Rozen, J. R., Keefe, G. A., Willen, S., and Mohling, R. A. (2001) High- T_c SQUID gradiometer for mobile magnetic anomaly detection, *IEEE Trans. Appl. Supercond.* **11**, 871–875.
- 19 Keene, M. N., Exon, N. J., Humphreys, R. G., and Satchell, J. S. (1999) A HTS gradiometer for unshielded operation from moving platforms, *Extended Abstracts of the 1999 International Superconductive Electronics Conference (ISEC '99)*, Berkeley CA pp. 566–568.

- 20** Humphrey, K. P., Horton, T. J., and Keene, M. N. (2005) Detection of mobile targets from a moving platform using an actively shielded, adaptively balanced SQUID gradiometer, *IEEE Trans. Appl. Supercond.* **15**, 753–756.
- 21** Keene, M. N., Takel, S., Morrison, J., Exon, N. J., and Satchell, J. S., (1999) Magnetic sensing from unmanned underwater vehicles, *Proc. 2nd International Conference on Marine Electromagnetics (MARELEC 99)*, Brest, France, pp. 417–423.
- 22** Allen, G. I. and Wynn, W. M. (1999) Tensor fluxgate gradiometer development, ONR year end report, FY 1999 (#N0001498WX30244). Available in the public domain from the Office of Naval Research via their website (unpublished).
- 23** Sun, J. Z., Gallagher, and W. J., Koch, R. H. (1994) Initial-vortex-entry-related magnetic hysteresis in thin-film SQUID magnetometers, *Phys. Rev. B* **50**, 664–673.
- 24** Keene, M. N., Exon, N. J., Humphreys, R. G., and Chew, N. G. (1996) The influence of magnetic environments on high- T_c superconducting quantum interference device gradiometers, *J. Appl. Phys.* **79**, 8783–8791.
- 25** Dantsker, E., Tanaka, S., and Clarke, J., (1977) High- T_c superconducting quantum interference devices with slots or holes: low $1/f$ noise in ambient magnetic fields, *Appl. Phys. Lett.* **70**, 2037–2039.
- 26** Du, J., Tilbrook, D. L., Macfarlane, J. C., Leslie, K.E., and Ore, D. S. (2004) Noise performance of HTS solid and meshed DC SQUID magnetometers in external magnetic fields, *Physica C* **411**, 18–24.
- 27** Mitchell, E. E., Foley, C. P., Muller, K. H., and Leslie, K. E. (1999) Vortex penetration and hysteretic behavior of narrow planar Josephson junctions in a magnetic field, *Physica C* **321**, 219–230.
- 28** McCleod, M. G. (1967) A predicted geomagnetic field model for epoch 1990.0, NRL/FR/7442-92-9414, Naval Research Laboratory, Stennis Space Center, MS 39529-5004. (Available on request.).
- 29** Matsushita, S. and Campbell, W. H. (1967) *Introduction to Geomagnetic Phenomena*, Academic Press (2 volumes).
- 30** Summey, D. C., McCormick, J. F., and Carroll, P. J. (1999) Mobile underwater debris survey system (MUDSS), *Oceans 99, Marine Technologies Society and IEEE Oceanographic Engineering Society*, paper 2C3.
- 31** Foley, C. P., Leslie, K. E., Binks, R., Lewis, C., Murray, W., Sloggett, G. J., Lam, S., Sankrithyan, B., Savvides, N., Katzaros, A., Muller, K.H., Mitchell, E.E., Pollock, J., Lee, J., Dart, D.L., Barrow, R.R., Asten, M., Maddever, A., Panjkovic, G., Downey, M., Hoffman, C., and Turner, R. (1999) Field trials using HTS SQUID magnetometers for ground-based and airborne geophysical applications, *IEEE Trans. Appl. Supercond.* **9**, 3786–3792.
- 32** Chwala, A., Stoltz, R., Zakosarenko, V., Schultz, M., Oukhanski, N., and Meyer, H.-G. (2003) LTS SQUID gradiometer system for airborne geomagnetics, *Extended Abstracts Int. Supercond. Electron. Conf.*, 7–11 July 2003, Sydney, Australia, paper OTh4.
- 33** Lathrop, D. and Matthews, R. (2000) Development of a magnetic tensor gradiometer integration within an autonomous underwater vehicle, *Proc. SPIE* **4039**, 85–88.
- 34** Bono, J. T., Overway, D. J., Wynn, W. M. (2003) Magnetic sensor operation onboard a UUV: magnetic noise investigation using a total-field gradiometer, *MTS/IEEE Oceans 2003*, pp. 2018–2022.
- 35** Allen, G., Matthews, R., and Wynn, M. (2001) Mitigation of platform generated magnetic noise impressed on a magnetic sensor mounted in an autonomous underwater vehicle, *Proc. MTS/IEEE Oceans 2001*, p. 63.
- 36** Binks, R. A., Lee, J. B., and Turner, R. J. (1999) SQUID device such as magnetometer or magnetic gradiometer has SQUID housed in Dewar with regulating valve to maintain constant pressure and temperature, Patent WO 9905540.
- 37** Wynn, W. M. (1995) Magnetic dipole localization using the gradient rate tensor measured by a five-axis magnetic gradi-

- ometer with known velocity, Proc. SPIE **2496**, 357–367.
- 38** Wynn, W. M. (1999) Magnetic dipole localization with a tensor gradiometer: a rigorous analysis including relative motion, *Proc. 2nd International Conference on Marine Electromagnetics (MARELEC 99)*, Brest, France, pp. 295–303.
- 39** Wilson H. (1985) Analysis of the magnetic gradient tensor, *Defence Research Establishment Pacific: DREP Technical Memorandum 85-13*. Available on request from Defence Research Establishment Pacific FMO, Victoria, BC V0S 1B0, Canada (unpublished).
- 40** Vaizer, L., Lathrop, J., and Bono, J. (2004) Localization of magnetic dipole targets, *Proc. MTS/IEEE Oceans 2004*, 869–873.
- 41** Keene, M. N., and Satchell, J. S. (2002) Magnetic gradiometer incorporating global feedback, US Patent 6,339,328.
- 42** Press, W. H., Teukolsky, S. A., Vetterling, W. T., and Flannery, B. P. (1992) *Numerical Recipes in C: The Art of Scientific Computing*, 2nd edn, Cambridge University Press.
- 43** Heath, P., Heinson, G., and Greenhalgh, S. (2003) Some comments on potential field tensor data, *Preview* **85**, 26–30. (Preview is a periodical of Aust. Soc. of Explor. Geophys.).
- 44** Schmidt, P., Clark, D., Leslie, K., Bick, M., Tilbrook, D., and Foley, C.P. (2004) GETMAG: a SQUID magnetic tensor gradiometer, *Explor. Geophys.* **35**, 297–305.
- 45** Zhang, C., Mushayandev, M. F., Reid, A. B., Fairhead, J. D., and Odegard, M. E. (2000) Euler deconvolution of gravity tensor gradient data, *Geophysics* **56**, 512–520.
- 46** Rutter, H. (1998) Recent developments in electromagnetic and induced polarization methods applied to detailed exploration for mineral, *Exploration Workshop*, 12 June, Ballart, Victorian Chamber of Mines.
- 47** Dobrin, M. B. (1976) *Introduction to Geophysical Prospecting*, McGraw Hill, New York.
- 48** Van Blaricom, R. (1980) *Practical Geophysics for the Exploration Geologist*, Northwest Mining Association, Spokane, WA.
- 49** Kautz, R. L. (2001) Jim Zimmerman and the SQUID, *IEEE Trans. Appl. Supercond.* **11**, 1026–1031.
- 50** Zimmerman, J. E. and Campbell, W. H. (1975) Tests of cryogenic SQUID for geomagnetic field measurements, *Geophysics* **40**, 269–284.
- 51** Clarke, J. (1983) Geophysical Applications of SQUIDS, *IEEE Trans. Mag.*, **MAG-19**, 288–294.
- 52** Gamble, T. D., Goubau, W. M., and Clarke, J. (1979) Magnetotellurics with a remote reference, *Geophysics* **44**, 53–68.
- 53** Gamble, T. D., Goubau, W. M., and Clarke, J. (1979) Error analysis for remote reference magnetotellurics, *Geophysics* **44**, 959–968.
- 54** Brunhes, B. (1906) Recherches sur la direction d'aimantation des roches volcaniques, *J. Phys.* **5**, 705–724.
- 55** Collinson, D. W. (1983) *Methods in Rock Magnetism and Palaeomagnetism: Techniques and Instrumentation*, Chapman and Hall, New York.
- 56** Weeks, R., Laj, C., Endigoux, L., Fuller, M., Roberts, A., Manganna, R., Blanchard, E., and Goree, W. (1993) Improvements in long core measurements techniques: applications in palaeomagnetism and palaeoceanography, *Geophys. J. Int.* **114**, 651–662.
- 57** Clark, D. A. (1997) Magnetic petrophysical and magnetic petrology: aids to geological interpretation of magnetic surveys, *AGSO J. Aust. Geol. Geophys.* **17**, 83–103.
- 58** Blackett, P. M. S. (1952) A negative experiment relating to magnetism and the Earth's rotation, *Phil. Trans. R. Soc. Lond. A245*, 309–370.
- 59** Gough, D. I. (1964) A spinner magnetometer, *J. Geophys. Res.* **69**, 2455–2463.
- 60** Helbig, K. (1965) Optimum configuration for the measurement of the magnetic moment of samples of cubical shape using a fluxgate magnetometer, *J. Geomag. Geoelect.* **17**, 373–380.
- 61** Fuller, M. (1987) Experimental methods in rock magnetism and paleomagnetism, *Methods Exp. Phys.* **24**, 303–471.
- 62** Goree, W. S. and Fuller, M. (1976) Magnetometers using rf driven SQUIDS and

- their applications in rock magnetism and paleomagnetism, *Rev. Geophys. Space Phys.* **14**, 591–608.
- 63** Ma, Y. P. and Wikswo, J. P. (1991) Magnetic shield for wide bandwidth magnetic measurements for nondestructive testing and biomagnetism, *Rev. Sci. Instrum.* **62**, 2654–2681.
- 64** Rubens, S. M. (1945) Cube-surface coil for producing a uniform magnetic field, *Rev. Sci. Instrum.* **16**, 243–245.
- 65** Testard, D. A., and Locatelli, M. (1982) A hybrid cryogenic dewar, *Proc. ICEC 9*, G1-8.
- 66** Leslie, K. E., Binks, R. A., Lewis, C. J., Scott, M. D., Tilbrook, D. L., and Du J. (2001) Three component spinner magnetometer featuring rapid measurement times, *IEEE Trans. Appl. Supercond.* **11**, 252–255.
- 67** Thomas I. M., Moyer T. C., and Wikswo Jr., J. P. (1992) High-resolution magnetic-susceptibility imaging of geological thin-sections – pilot-study of a pyroclastic sample from the bishop tuff, California, USA, *Geophys. Res. Lett.* **19**, 2139–2142.
- 68** Spies, B. R. and Frischknecht, F. C. (1987) Electromagnetic sounding, *Soc. Expl. Geophys.* **2**, 285–425.
- 69** Spies, B. R. (1989) Depth Investigation in electromagnetic sounding methods, *Geophysics* **54**, 872–888.
- 70** Smith, R. S. and Balch, S. J. (2000) Robust estimation of the band limited inductive limit response from impulse response TEM measurements taken during the transmitter switch-off and the transmitter off-time: theory and an example from Voisey's bay, Labrador, Canada, *Geophysics* **65**, 476–481.
- 71** Liu, G. and Asten, M. (1992) A comparison of airborne and ground based transient EM systems in their resolving power against geological noise, *Explor. Geophys.* **23**, 197–200.
- 72** McCracken, K. G., Oristaglio, and M. L., Hohmann, G. W. (1986) A comparison of electromagnetic exploration systems, *Geophysics* **51**, 810–818.
- 73** Smith, R. S. and Annan, A. P. (1997) Advances in airborne time-domain EM technology, *Proc. Explor. 97: Fourth Decennial Int. Conf. Mineral Explor.*, Gubins, A.G. (ed.), pp. 497–504.
- 74** Elders, J. A. and Asten, M. W. (2003) A comparison of receiver technologies in borehole MMR and EM surveys, *Geophys. Prospect.* **52**, 85–96.
- 75** MacNae, J. C., Lamontane, Y., and West, G. F. (1984) Noise processing techniques for time domain EM systems, *Geophysics* **49**, 934–948.
- 76** Leslie, K. E., Binks, R. A., Foley, C. P., Thorn, R. G., Du, J., Mitchell, E. E., Lam, S. K. H., Lewis, C. J., Millar, C., and Osmond, R. T. (2003) Operation of a geophysical HTS SQUID system in sub-arctic environments, *IEEE Trans. Appl. Supercond.* **13**, 759–762.
- 77** Bick, M., Panaitov, G., Wolters, N., et al. (1999) A HTS rf SQUID vector magnetometer for geophysical exploration, *IEEE Trans. Appl. Supercond.* **9**, 3780–3785.
- 78** Chwala, A., Stoltz, R., Ramos, J., Schultze, V., Meyer, H.G., and Kretzschmar, D. (1999) An HTS Dc SQUID system for geomagnetic prospection, *Supercond. Sci. Technol.* **12**, 1036–1038.
- 79** Tristan Technologies Inc., 6185 Cornerstone Court East, Suite 106, San Diego, CA 92121, USA (www.tristantechologies.com), 2005 (unpublished).
- 80** Report summary on technical development of HTS SQUID geophysical system for mineral exploration, Nov. 2000, Metal Mining Association of Japan (unpublished).
- 81** Wang, S. G., Zhang, L. H., Wang, C. J., and Dai, Y. D. (1997) Application of high temperature superconducting quantum interference device in transient electromagnetic method for magnetotelluric soundings, *Physica C* **282–287**, 411–414.
- 82** Panaitov, G., Bick, M., Zhang, Y., et al. (2001) Effect of repetitive transmitter signals on SQUID response in geophysical TEM, *IEEE Trans. Appl. Supercond.* **11**, 888–891.
- 83** Panaitov, G., Bick, M., Zhang, Y., and Krause, H. J. (2002) Peculiarities of SQUID magnetometer applications in TEM, *Geophysics* **67**, 739–745.

- 84** Bishop, J. and Reid, J. (2003) Some positive thoughts about negative TEM responses, extended abstracts from *Aust. Soc. Explor. Geophys. 16th Geophys. Conf.*, Feb. 2003.
- 85** Spies, B. R. (2004) Discussion on "Peculiarities of SQUID magnetometer application in TEM", *Geophysics* **69**, 624–628.
- 86** Clark, D. A. and Schmidt, P. W. (1982) Theoretical analysis of thermomagnetic properties, low temperature hysteresis and domain structure of titanomagnetites, *Phys. Earth Planet. Int.* **30**, 300–316.
- 87** Osmond, R. T., Watts, A. M., Raven-shurst, W. R., Foley, C. P., and Leslie, K. E. (2002) Finding nickel from B field at Raglan—"To B or not dB", *CSEG Recorder* **27**, 44–47.
- 88** Foley, C.P., Leslie, K.E., and Binks, R.A., et al. (2002) Issues relating to airborne applications of HTS SQUIDS, *Supercond. Sci. Technol.* **12**, 1641–1645.
- 89** Lee, J.B., Dart, D.L., Turner, R.J., et al. (2002) Airborne TEM surveying with a SQUID magnetometer sensor. *Geophysics* **67**, 468–477.
- 90** Hood, P. (1980) Aeromagnetic gradiometry: superior geological mapping tool for mineral exploration programs, in *SQUID Applications to Geophysics*, Workshop proceedings, 2–4 June 1980, Soc. Explor. Geophysicists, pp. 72–77.
- 91** Fromm, W. E. (1952) The magnetic airborne detector, *Advances in Electronics*, Academic Press, New York, pp. 257–299.
- 92** Schmidt, P. W., and Clark, D. A. (2000) Advantages of measuring the magnetic gradient tensor, *Preview* **85**, 26–30.
- 93** Foley, C. P., Tilbrook, D. L., Leslie, K. E., Binks, R. A., Donaldson, G. B., Du, J., Lam, S. K., Schmidt, P. W., and Clark, D. A. (2001) Geophysical exploration using magnetic gradiometry based on HTS SQUIDS, *IEEE Trans. Appl. Supercond.* **11**, 1375–1378.
- 94** Zakosarenko, V., Chwala, A., Ramos, J., Stoltz, R., Schultze, V., Lütjen, H., Blume, J., Schüler, T., and Meyer, H. G. (2001) HTS Dc SQUID systems for geophysical prospection, *IEEE Trans. Appl. Supercond.* **11**, 896–899.
- 95** Stoltz, R., Zakosarenko, V., Schulz, M., Chwala, A., Fritzsch, L., Meyer, H.-G., and Köstlin, E.O. (2004) Magnetic full tensor SQUID gradiometer system for geophysical applications *SEG Technical Program Expanded Abstracts*, pp. 786–789.
- 96** Meyer, H.-G., Stoltz, R., Chwala, A., and Schultz, M. (2005) SQUID technology for geophysical exploration, *Phys. Stat. Sol. (c)* **2**, 1504–1509.
- 97** Cagniard, L. (1952) Basic theory of the magneto-telluric method of geophysical prospecting, *Geophysics* **18**, 605–635.
- 98** Vozoff, K. (1972) The magnetotelluric method in the exploration of sedimentary basins, *Geophysics* **37**, 98–141.
- 99** Clarke, J. and Goldstein, N. E. (1981) Magnetotelluric measurements, in Weinstock and H., Overton, W.C., Jr. (eds.), *SQUID Applications in Geophysics*, Soc. Expl. Geophys., pp. 49–60.
- 100** Dankster, E., Koelle, D., Miklich, A. H. et al. (1994) High T_c 3-axis Dc SQUID magnetometer for geophysical applications, *Rev. Sci. Instrum.* **65**, 3809–3813.
- 101** MacMillian, G., de Groot, P., Zhuravlev, Y., and Rassi, D. (1999) Study into the feasibility of SQUID sensors for use in geophysical exploration, *7th Int. Supercond. Electron. Conf.* pp. 166–168.
- 102** Meyer, J. (1966) Die magneto-tellurische Tiefensondierung und ihr erdmagnetisches Analogon, *Gerlands Beiträge zur Geophysik* **75**, 284–300.
- 103** Drung, D., Radic, T., Matz, H., Koch, H., Knappe, S., Menkel, J., and Burkhardt, H. (1997) A 2-channel wide band SQUID system for high frequency geophysical applications, *IEEE Trans. Appl. Supercond.* **7**, 3283–3286.
- 104** Clem, T. (1995) Superconducting magnetic sensors operating from a moving platform, *IEEE Trans. Appl. Supercond.* **5**, 2124–2130.
- 105** Lathrop, J. D., McCormick, J. F., Bernstein, P. J., Bono, J. T., Overway, D. J., Sammelmann, G. S., Chao, T. H., and Scott, K. C. (1996) Mobile underwater debris survey system (MUDSS) feasibility demonstration report, *UXO Forum 1996 Conference Proceedings*, PRC Environmental Management Inc., pp. 427–436.

- 106** Summey, D. C., McCormick, J. F., and Carroll, P. J. (1999) Mobile underwater debris survey system (MUDSS) Oceans 99, *Marine Technologies Society and IEEE Oceanographic Engineering Society*, paper 2C3.
- 107** Summey, D. C., and KeKlis, G. J. (1996) Fused airborne sensor technology, detection and remediation technologies for mines and minelike targets, *Proc. SPIE* **2765**, 226–232.
- 108** Weaver, J. T. (1965) Magnetic variations associated with ocean waves and swell, *J. of Geophys. Res.*, **70**, 1921–1929.

15

Gravity and Motion Sensors

Ho Jung Paik

| | | |
|--------|---|-----|
| 15.1 | Introduction | 546 |
| 15.2 | The Superconducting Accelerometer | 547 |
| 15.3 | Superconducting Transducer for Gravitational-Wave Detectors | 548 |
| 15.3.1 | Principle of Gravitational-Wave Detection | 548 |
| 15.3.2 | Superconducting Resonant Transducer | 551 |
| 15.4 | Superconducting Gravity Gradiometers (SGGs) | 554 |
| 15.4.1 | Principle of Gravity Gradiometry | 554 |
| 15.4.2 | In-Line-Component SGG | 555 |
| 15.4.3 | Cross-Component SGG | 559 |
| 15.5 | Applications of the SGG Technology | 563 |
| 15.5.1 | Precision Tests of the Laws of Gravity | 563 |
| 15.5.2 | Search for New Weak Forces | 569 |
| 15.5.3 | Gravity Mapping and Mass Detection | 571 |
| 15.5.4 | Gradiometer-Aided Inertial Navigation and Survey | 574 |
| 15.6 | Outlook | 575 |

15.1

Introduction

Sensitive superconducting gravity and motion sensors have been developed for gravitational wave detection, precision tests of the laws of gravity, and applications in geophysics, natural resource exploration, and inertial navigation. The Meissner effect, flux quantization, and SQUIDs are utilized, along with the enhanced mechanical stability of materials at cryogenic temperatures, to obtain gravitational-wave transducers with sensitivity approaching the quantum limit and to construct accelerometers with orders of magnitude improvement in sensitivity over their room-temperature counterparts.

To detect gravitational waves from nearby galaxies, a detector is required to resolve a change in the massive ($\geq 10^4$ kg) mechanical resonator amplitude smaller than 10^{-21} m in an integration time of ~ 0.01 s. To meet this requirement, Paik and Fairbank initiated in the early 1970s, at Stanford University, the development of a sensitive superconducting motion transducer, based on then emerging SQUID technology [1, 2]. Superconducting transducers have reached a displacement sensitivity of 10^{-19} m $\text{Hz}^{-1/2}$ by using commercially available dc SQUIDs. Exotic as this may look, it is still two orders of magnitude short of the sensitivity required for detection of gravitational waves of extragalactic origin. The gravitational-wave experiment imposes the most demanding requirement on the SQUID; both the flux and circulation current noise must approach the quantum limit while maintaining high coupling to the input circuit.

In 1975 Paik and his coworkers began applying the superconducting transducer technology to construct a superconducting gravity gradiometer (SGG) for precision gravity experiments. Three models of SGG with increasing complexity and sensitivity were developed at Maryland in the 1980s [3–5]. These instruments have been used to perform null tests of Newton's inverse-square law of gravitation in the laboratory [6, 7]. The exquisite sensitivities of superconducting accelerometers will enable other important fundamental physics experiments such as precision tests of the equivalence principle and searches for new forces weaker than gravity [8, 9]. With sensitivity improved by more than two orders of magnitude over conventional technologies, the SGG finds useful application in geophysical measurements, minerals prospecting, and inertial navigation. The great potential for practical applications has inspired many groups around the world to develop similar gravity gradiometer instruments.

In this chapter, we review the design, operating principles, and performance of superconducting gravity and motion sensors for different applications. Conditions that a gravitational-wave transducer must satisfy to approach the standard quantum limit are derived, with resulting requirements on the SQUID. Two types of SGGs that are respectively designed to detect diagonal and off-diagonal components of gravity gradient tensor are discussed. Then, applications of SGG technology in fundamental gravity experiments, airborne and spaceborne gravity surveying, mine and ordnance detection, and inertial navigation are discussed.

15.2

The Superconducting Accelerometer

Figure 15.1 shows a schematic of the basic superconducting accelerometer. The device consists of a superconducting test mass, a superconducting sensing coil, and a SQUID. The test mass may be suspended by a combination of a mechanical and magnetic spring, or by magnetic levitation alone. A persistent current is stored in the loop formed by the sensing coil and the SQUID input coil. A platform acceleration, or a gravity signal, displaces the test mass relative to the sensing coil, modulating its inductance. This induces a time-varying current in the loop, which is sensed by the SQUID.

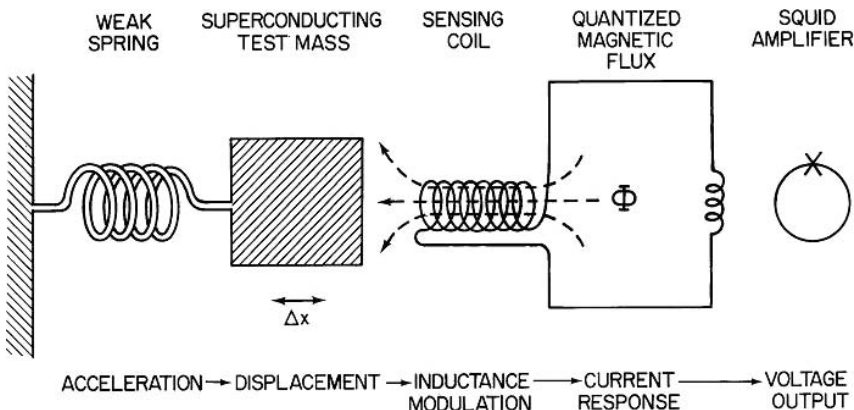


Fig. 15.1 Schematic of a superconducting accelerometer.

When the signal frequency ω is low compared to the resonance frequency ω_0 , the power spectral density of the intrinsic acceleration noise of a superconducting accelerometer can be shown [3] to be

$$S_a(f) = \frac{4}{m} \left[k_B T \frac{\omega_0}{Q} + \frac{\omega_0^2}{2\beta\eta} \varepsilon_c \right] , \quad (15.1)$$

where m , Q , and T are the mass, quality factor, and temperature of the resonating test mass, β is the electromechanical energy coupling constant, η is the energy coupling efficiency from the transducer circuit to the SQUID, ε_c is the coupled energy resolution of the SQUID,¹⁾ and $f = \omega/2\pi$. Equation (15.1) clearly exhibits the advantages of a superconducting accelerometer. As the device is cooled to liquid helium temperature ($T = 4.2$ K), T/Q is reduced typically by four orders of magnitude from its room-temperature value, and ε_c of a SQUID amplifier is by a similar ratio lower than the energy resolution of an FET amplifier. Further, since the persistent current provides the electromechanical coupling, the scale factor (the acceleration-to-voltage transfer function) of a superconducting accelerometer is extremely stable. Under a practical design, the two terms in (15.1) are usually comparable.

Here, “accelerometer” is used as a generic term encompassing all motion sensors. Due to the equivalence principle, gravity and platform acceleration cannot be distinguished by measuring the displacement of a *single* test mass relative to its platform. It requires a differential measurement between at least two test masses to separate out gravity from the platform acceleration, thus a gravity gradiometer. A single mass device may be called an “accelerometer,” a “seismometer,” or a “gravimeter,” depending on its use. Since the displacement of the test mass is obtained by simply integrating the acceleration twice, the device may also be used as a displacement sensor. In fact, the basic superconducting accelerometer described here has been used to detect displacements of liquid helium in superfluid helium experiments [10, 11].

15.3

Superconducting Transducer for Gravitational-Wave Detectors

15.3.1

Principle of Gravitational-Wave Detection

Gravitational waves are ripples in spacetime fabric that propagate at the speed of light. In analogy with electromagnetism, accelerated masses generate gravitational waves according to Einstein’s general relativity. The existence of gravitational waves has been demonstrated indirectly from the observed decrease in the orbital period of a binary pulsar in precise agreement with the value expected from gravitational-wave emission [12]. The principle of a gravitational-wave detector is shown in Figure 15.2. The hyperbolas represent force patterns on test masses resulting from a wave traveling into the page. If masses A and B are connected by a spring, the spring will be stretched and compressed as a gravitational

1) Here ε_c includes only the flux noise of the SQUID ($S_\phi/2k_b^2 L$) since the current noise contribution is generally negligible in the usual operation of the superconducting accelerometer where its electromechanical

energy coupling constant β (defined in Section 15.3.2) is small compared to unity. When β approaches unity, a contribution from the current noise must be added.

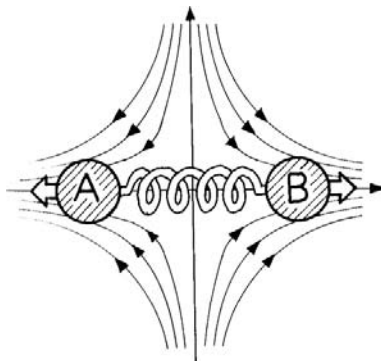


Fig. 15.2 Principle of a resonant-mass gravitational-wave detector.

wave passes by, absorbing energy from the wave [13]. In the absence of the spring, the gravitational wave will still cause a relative displacement between the two masses, which can be measured with an optical interferometer. A gravitational wave could therefore be detected by monitoring the energy it deposits into an elastic solid (resonant-mass antenna) or by measuring the resulting relative displacement between freely suspended mirrors (laser interferometer detector).

Practical considerations restrict the size of resonant-mass antennas to a few meters, severely limiting their sensitivity and frequency window. Laser interferometers have the advantage of being able to utilize a longer baseline and a wide bandwidth. This has led to the development of ground-based long-baseline laser interferometers [14] and a proposal for a space-based antenna, LISA (Laser Interferometer Space Antenna) [15]. Here we will restrict our discussion to the resonant-mass detectors where SQUID technology has made major contributions.

A gravitational-wave pulse is characterized by a “metric perturbation” h with a dominant frequency ω_S and duration τ_S , where h corresponds to the strain $\Delta L/L$ caused by the wave on the separation L between two free masses. For a short pulse with $\tau_S \approx 2\pi\omega_S^{-1}$, the energy that the gravitational wave deposits into a favorably oriented, noiseless, cylindrical antenna of effective mass M and length D becomes

$$E_S \approx \frac{2}{\pi^2} M \omega_S^2 (D h)^2. \quad (15.2)$$

The total intrinsic noise of the detector, referred to the input of the antenna, can be shown [16, 17] to be

$$E_N \approx k_B T_a \frac{\omega_a \tau}{Q_a} + k_B T_N \left[\frac{2(\zeta + \zeta^{-1})}{\beta_{21} \omega_S \tau} + \frac{\beta_{12} \omega_S \zeta \tau}{2} \right], \quad (15.3)$$

where ω_a , Q_a , and T_a are the resonance frequency, quality factor, and temperature of the antenna; β_{21} and β_{12} are the *forward* and *reverse* energy coupling coefficients of the transducer; ζ , T_N , and τ are a dimensionless impedance matching para-

meter, noise temperature, and integration time of the amplifier.²⁾ For a passive transducer, as is considered here, β_{21} and β_{12} are equal to β , the electromechanical energy coupling coefficient of the transducer.

Equation (15.3) shows that E_N comes from three terms: the Brownian motion noise and the two conjugate noise sources of the amplifier, the *forward* and *reverse action* noise of the amplifier. The Brownian motion noise can be made arbitrarily small, in principle, by reducing T_a/Q_a . The amplifier noise contribution can be minimized by choosing

$$\tau = \frac{2}{\beta\omega_S} \left(1 + \frac{1}{\zeta^2}\right)^{1/2}. \quad (15.4)$$

Substituting this into (15.3) leads to

$$E_N \approx \frac{2k_B T_a}{\beta Q_a} \left(1 + \frac{1}{\zeta^2}\right)^{1/2} + 2k_B T_N (1 + \zeta^2)^{1/2}. \quad (15.5)$$

In order to minimize E_N , one needs to satisfy three optimization conditions:

$$\zeta \leq 1, \quad \Delta\omega_S/\omega_S \approx \beta\zeta, \quad T_a/Q_a \ll \beta\zeta T_N, \quad (15.6)$$

where $\Delta\omega_S \approx \pi\tau^{-1}$ is the bandwidth of the detector. Thus a large $\beta\zeta$ allows for a large fractional bandwidth, which reduces the Brownian motion noise of the antenna. Therefore, if a near-unity $\beta\zeta$ could be achieved *without* sacrificing the bandwidth of the transducer, a *completely wideband* detector ($\Delta\omega_S \approx \omega_S$) could be realized in principle without compromising the signal-to-noise ratio.

When conditions (15.6) are satisfied, the total detector noise becomes amplifier-limited at $2k_B T_N$. A more rigorous theory [18] leads to the true amplifier limit of $k_B T_N$. Combining this with (15.2) leads to

$$h_{\min} \approx \left(\frac{5k_B T_N}{M\omega_S^2 D^2}\right)^{1/2}. \quad (15.7)$$

For *linear* (phase-preserving) amplifiers, T_N has a quantum limit [19]: $T_{N,QL} \approx \hbar\omega_S/k_B$. Thus the standard quantum limit of a typical cylindrical antenna with $M = 1200$ kg, $D = 3$ m, and $\omega_S/2\pi = 900$ Hz corresponds to $T_N \approx 0.04$ μK and $h_{\min} \approx 3 \times 10^{-21}$.

- 2) For a voltage amplifier, $\zeta \approx |Z_{22}|/R_{\text{opt}}$, where Z_{22} and R_{opt} are the output impedance of the transducer and the optimum source impedance of the amplifier. For a SQUID,

(15.3) remains valid if ζ is redefined as $\zeta \approx R_{\text{opt}}/|Z_{22} + j\omega L_i|$, where L_i is the inductance of the SQUID input coil.

15.3.2

Superconducting Resonant Transducer

A large antenna mass that increases E_S tends to make β very small, typically 10^{-6} – 10^{-5} for $M \geq 10^3$ kg. This is equivalent to there being an impedance mismatch by five to six orders of magnitude between the antenna output and the transducer electrical input. A standard technique of matching the impedance is by use of a *resonant* transducer [2]. The antenna with mass M is excited by the gravitational wave. If the resonance frequency of a small test mass m is tuned to that of the antenna, the antenna begins to drive this resonator, transferring the entire energy to the small mass, whose displacement then becomes $(M/m)^{1/2}$ times larger than the initial displacement of the antenna. The energy flows back and forth between the two masses with a beat period of $(2\pi/\omega_a)(M/m)^{1/2}$.

The resonant transducer thus improves the energy coupling β by the ratio of M/m , but with the bandwidth restricted by the beat frequency to $\Delta\omega_S \approx \omega_a(M/M)^{1/2}$. One is tempted to maximize m . However, this generally results in a reduction of β , thereby limiting the usable bandwidth $\Delta\omega_S$. To obtain the largest $\Delta\omega_S$, one must choose m_{opt} which satisfies

$$(\Delta\omega_S/\omega_S)_{\text{max}} \approx \beta(m_{\text{opt}})\zeta \approx \left(m_{\text{opt}}/M\right)^{1/2}. \quad (15.8)$$

The resonant transducer concept has been extended further by using a cascade of n resonators with geometrically decreasing masses [20, 21].

The superconducting resonant transducer for gravitational-wave experiments is identical to the basic accelerometer shown in Figure 15.1 except that in general two flat, pancake-shaped sensing coils, L_1 and L_2 , are used to sense both faces of the test mass. These coils are connected in parallel to the SQUID input coil, L_i , and a persistent current I_0 is stored in the loop formed by L_1 and L_2 . By a simple circuit analysis [2], one can show, in the limit where the parasitic stiffness due to the nonlinear inductance modulation can be ignored, that the resonance frequency is shifted from the uncoupled value ω_m according to

$$\omega_0^2 = \omega_m^2 + \frac{2}{1 + \gamma} \frac{B^2 S}{\mu_0 m d}, \quad (15.9)$$

where $\gamma \equiv L_i(L_1^{-1} + L_2^{-1})$, S is the average area of each sensing coil, d is the average gap between each pancake coil and the test mass, B is the magnetic field produced by I_0 , and μ_0 is the permeability of vacuum. From (15.9), we find

$$\beta = 1 - \left(\frac{\omega_m}{\omega_0}\right)^2 = \frac{2}{1 + \gamma} \frac{B^2 S}{\mu_0 m \omega_0^2 d}, \quad \beta_S = \frac{2k_i^2 \gamma}{(1 + \gamma)^2} \frac{B^2 S}{\mu_0 m \omega_0^2 d}, \quad (15.10)$$

where k_i is the coupling constant between L_i and the SQUID, and β_S is the coefficient defining the energy coupling to the SQUID. In practice, β and β_S assume slightly smaller values than given by (15.10) due to the parasitic stiffness arising from nonlinearities in the circuit.

The SQUID is characterized by three noise spectral densities: the flux noise $S_\phi(f)$, circulating current noise $S_J(f)$, and their correlation $S_{\phi J}(f)$. For optimized parameters, these noise spectral densities define [22]

$$\begin{aligned} T_N &\equiv \frac{\omega_S (S_\phi S_J - S_{\phi J}^2)^{1/2}}{2k_B}, \quad R_{\text{opt}} \equiv \omega_S M_i^2 \frac{(S_\phi S_J - S_{\phi J}^2)^{1/2}}{S_\phi}, \\ \zeta &\equiv \frac{R_{\text{opt}}}{\omega_S (L_p + L_i)}, \end{aligned} \quad (15.11)$$

where $M_i \equiv k_i(L_i L)^{1/2}$ is the mutual inductance between L_i and the SQUID loop inductance L , and $L_p \equiv (L_1^{-1} + L_2^{-1})^{-1}$ is the parallel combination of the sensing coil inductances. It is clear from (15.5) that, for gravitational-wave detection, minimizing both the flux and circulating current noise and maximizing the signal coupling are equally important. This imposes *very stringent* requirements for SQUID design.

When the SQUID is cooled to sufficiently low temperatures, typically a few tens of millikelvin, theory predicts that under optimum conditions it becomes a quantum-limited amplifier [23] (see also Chapter 8). In this limit, it is predicted that

$$T_N \approx \hbar \omega_S / k_B, \quad R_{\text{opt}} \approx k_i^2 \omega_S L_i / 3, \quad \zeta \approx k_i^2 \gamma / (1 + \gamma). \quad (15.12)$$

Thus, we find $\zeta \approx k_i^2 \eta$ and $\beta_S \approx \beta \zeta$. The optimization conditions (15.6) then lead to $k_i^2 \rightarrow 1$ and $\gamma \approx 1$. The second condition is easy to satisfy; however, $k_i^2 < 0.5$ is typical for low-noise dc SQUIDs due to the multistage transformers used. Substituting (15.12) into (15.5), one finds

$$E_N \approx \frac{4k_B T_a}{\beta k_i^2 Q_a} + 2\hbar \omega_S. \quad (15.13)$$

For the antenna thermal noise to be negligible compared to the SQUID noise, one should satisfy

$$\frac{T_a}{Q_a} \ll \beta k_i^2 \frac{\hbar \omega_S}{k_B}. \quad (15.14)$$

To reach the quantum limit without imposing a too demanding T_a/Q_a requirement on the antenna, βk_i^2 must be maximized.

Figure 15.3 shows a cross-sectional view of the superconducting transducer constructed at the University of Maryland. This transducer was originally fabricated for a 50-mK antenna then under construction at Stanford University but was retuned to ALLEGRO (A Louisiana Low-temperature Experiment and Gravitational Radiation Observatory), a 4-K antenna at Baton Rouge, Louisiana, after the Stanford project was closed [24]. The resonator is a centrally loaded diaphragm. The entire resonator is machined from a single block of high RRR (residual resistivity ratio)-grade niobium (Nb) and is heat-treated to obtain high mechanical and

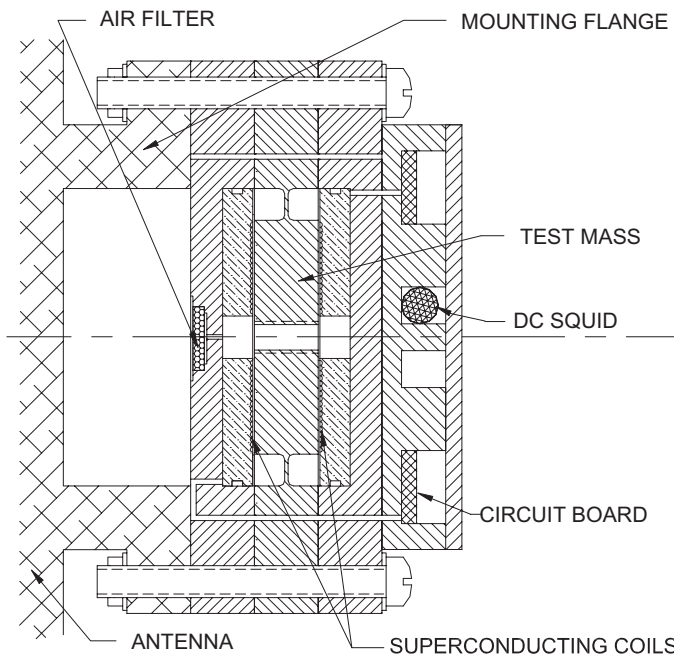


Fig. 15.3 Cross-section of a superconducting transducer.

electrical Q_s . Two Nb pancake coils are located close to the test-mass surfaces. The two sensing coils are connected in parallel to the input coil of a low-noise dc SQUID. Prior to assembly, the mating surfaces of the test mass and the pancake coils were lapped and chemically polished to reduce d to $\leq 25 \mu\text{m}$ and thus improve β . With $m = 0.62 \text{ kg}$, $S = 3.5 \times 10^{-3} \text{ m}^2$, $B = 0.14 \text{ T}$ ($< H_{c1}$ of Nb at 4.2 K), $\omega_0/2\pi = 900 \text{ Hz}$, $k_i^2 \approx 0.4$, and $\gamma \approx 1$, this transducer can achieve $\beta \approx 0.10$ and $\beta_S \approx 0.02$. For the antenna mass of $M = 1200 \text{ kg}$, this satisfies (15.8) and yields $\Delta\omega_S/\omega_S \approx 2\%$.

A dual dc SQUID system in which the output of the sensor SQUID is coupled to a second SQUID has been developed at the University of Maryland by Jin and Wellstood for applications in ultralow-temperature gravitational-wave detectors. The sensor SQUID with $L = 240 \text{ pH}$ is coupled to an input coil with $L_i = 0.84 \mu\text{H}$ through a two-stage transformer. The energy resolution of this SQUID was measured to be $\varepsilon = S_\phi/2L \approx 35\hbar$ at 50 mK [25]. The noise temperature of this SQUID estimated with Clarke-Tesche-Giffard theory [26] is $T_N \approx 1.2 \mu\text{K}$ at $f = 900 \text{ Hz}$.³⁾ With a loaded Q of the antenna $Q_a \geq 5 \times 10^6$, a 50-mK antenna with the Maryland transducer would have a sensitivity of $h_{\min} \approx 1.6 \times 10^{-20}$.

3) Upon integration with the transducer and cooling to 4.2 K, this SQUID exhibited a large excess circulation current noise, which

appears to be due to trapped flux in the thin-film transformer. This measurement is reported in Ref. [27].

Such a sensitivity would be sufficient to detect various astrophysical events occurring in our own galaxy. The event rate, however, may be only one in several years. To increase the event rate to several per year, it is necessary to improve the sensitivity to $h_{\min} \leq 10^{-21}$ and reach the Virgo cluster of galaxies, which is at a distance of ~ 15 Mpc (1 parsec = 3.09×10^{13} km). Such a sensitivity could be achieved in principle by cooling a massive ($M \geq 30$ tons) *spherical* antenna to an ultralow temperature ($T_a \leq 50$ mK) and coupling it through multimode transducers to a nearly quantum-limited SQUID [28, 29]. With the fractional bandwidth of each antenna approaching 10%, a xylophone of four detectors with varying diameter would cover several hundred hertz bandwidth with a sensitivity comparable to that of Advanced LIGO (Laser Interferometer Gravitational-wave Observatory), an advanced long-baseline laser interferometer under development [30, 31]. Unfortunately, the proposals to develop such large spherical detectors in USA and Italy have not been funded. At the time of writing, small prototype spherical antennas are undergoing tests in the Netherlands and Brazil [32, 33].

15.4

Superconducting Gravity Gradiometers (SCGs)

15.4.1

Principle of Gravity Gradiometry

In Newtonian physics, the gravity field is described by a scalar potential $\phi(x_i, t)$. Its second spatial derivatives form a gravity gradient tensor:

$$\Gamma_{ij} \equiv \partial^2 \phi / \partial x_i \partial x_j . \quad (15.15)$$

This tensor is symmetric by construction. Its trace is proportional to the local mass density ρ by Poisson's equation, which is a differential form of the inverse-square law:

$$\sum_i \Gamma_{ii} = \nabla^2 \phi = 4\pi G\rho . \quad (15.16)$$

In free space ($\rho = 0$), this trace must vanish. This leaves only *five* independent components for the tensor: two diagonal ("in-line") components and three off-diagonal ("cross") components.

An in-line-component gradiometer can be constructed by differencing signals between two *linear* accelerometers whose sensitive axes are aligned along their line of sight. In contrast, a cross-component gradiometer can be constructed by differencing signals between two concentric *angular* accelerometers whose moment arms are orthogonal to each other. The SGG offers the same benefits of operating at low temperatures as the superconducting accelerometer: low intrinsic noise and high scale factor stability.

Gravity gradiometers are usually operated in the dynamically noisy environment of a moving vehicle to detect very weak differential signals. Unlike in a gravitational-wave detector, passive vibration isolation is not possible because the signal frequencies for gradiometry are very low in general (≤ 0.1 Hz). Active isolation, or “platform stabilization,” can be applied to the angular degrees of freedom. It is difficult, however, to achieve active isolation in linear degrees of freedom since the required displacement may exceed the dimensions of the vehicle. Therefore, it is important to build into the device as high common-mode-rejection ratios as possible for both linear and angular accelerations.

In order to reject the common-mode acceleration along the sensitive axis, the scale factors of the component accelerometers must be matched precisely. This requires high stability of the scale factors. An SGG has *extremely stable* scale factors due to the enhanced mechanical stability of materials at low temperatures and the exceptional stability of the persistent currents used in the device.

With the scale factors perfectly matched, the gradiometer will still be sensitive to the transverse components of the acceleration due to misalignments of the sensitive axes. In an in-line-component gradiometer, linear and angular accelerations of the platform, \vec{a} and $\vec{\alpha}$, couple to the differential mode through departures from parallelism and concentricity of the sensitive axes of the component accelerometers, $\delta\hat{n}$ and $\delta\hat{\ell}$, respectively [3]:

$$\delta\Gamma_a = \frac{1}{\ell} \delta\hat{n} \cdot \vec{a}, \quad \delta\Gamma_\alpha = (\delta\hat{\ell} \times \hat{n}) \cdot \vec{\alpha}, \quad (15.17)$$

where \hat{n} and $\hat{\ell}$ are the unit vectors representing the sensitive axis and the line of sight between the two test masses, and ℓ is the baseline of the gradiometer. There are corresponding error sources in a cross-component device. A departure of the rotation axes from parallelism provides a coupling mechanism for angular acceleration, whereas an asymmetric mass distribution in each moment arm (a departure of the rotation axis from the mass symmetry axis) causes linear acceleration to couple to the gradiometer.

For an SGG, the mechanical stability of materials guarantees that $\delta\hat{n}$ and $\delta\hat{\ell}$ are stable. These error coefficients can therefore be measured once for all during the initial setup, multiplied by the proper acceleration components, and subtracted from the gradiometer output. By applying this “residual common-mode balance” [5], $\delta\hat{n}$ and $\delta\hat{\ell}$ can be reduced effectively to $\leq 10^{-7}$ and $\leq 10^{-9}$ for in-line and cross-component SGGs, respectively.

15.4.2

In-Line-Component SGG

Development of the in-line-component SGG was pioneered by Paik and his group at the University of Maryland [3–5]. Three models of increasing complexity and performance were constructed and tested.

Figure 15.4 shows a cross-sectional view of a component accelerometer of their Model II SGG [34]. The test mass weighing 1.2 kg is suspended by a pair of dia-

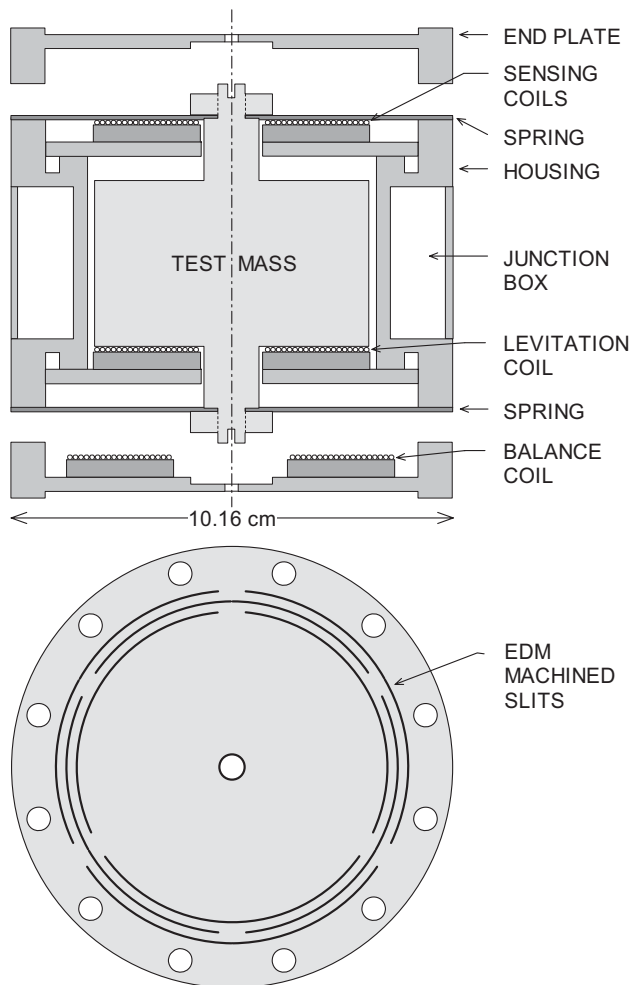


Fig. 15.4 Component accelerometer for an in-line-component SGG.

phragm flexures. The diaphragms have arc-like slits cut into them by wire EDM (electric discharge machining), so they act like a set of folded cantilevers. The natural frequency of the spring–mass system is 4.5 Hz. The differential and common-mode resonance frequencies increase to about 9 and 50 Hz, respectively, when magnetic flux is trapped in the circuits. The entire structure is machined from Nb. Six identical component accelerometers are mounted on six faces of a precision titanium (Ti) alloy cube, with the sensitive axes normal to the cube surfaces, to form a three-axis in-line-component SGG (see Figure 15.5).

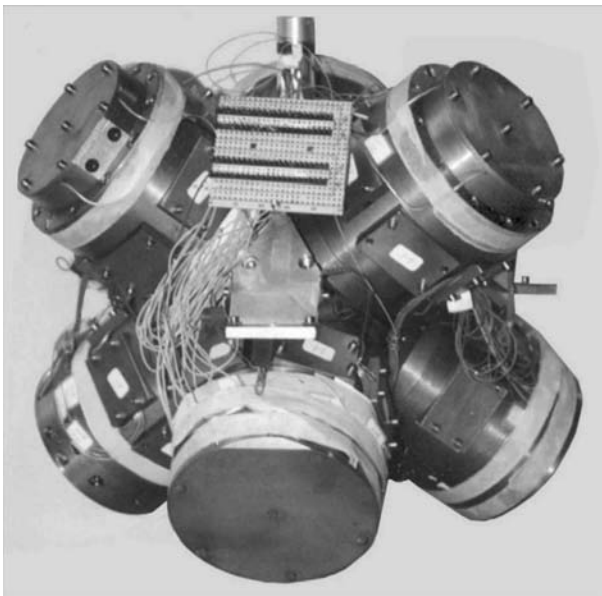


Fig. 15.5 The Maryland three-axis in-line-component SGG.

Figure 15.6 shows a schematic circuit diagram for one axis of the SGG. Two test masses on opposite faces of the mounting cube are connected by a superconducting circuit to form a gradiometer. The coils L_{Li} , L_{Bi} , and L_{Si} are coils wound in the pancake shape using Nb wire. The test masses are levitated against gravity by storing a persistent current I_L (using heat switch R_L) in the loop formed by L_{L1} and L_{L2} . The coils L_{S1} and L_{S2} are connected in parallel to a SQUID to form a sensing circuit. Each axis of the gradiometer has two circuits, although only one is shown for simplicity. In one circuit, the currents I_{S1} and I_{S2} are stored with the same sense (using heat switches R_{SS} and R_{SP}), as shown in the figure, to detect the differential acceleration, or the gravity gradient. In the other circuit, the direction of one of the currents is reversed so that the SQUID detects the common-mode acceleration. The coils L_{B1} and L_{B2} are connected in parallel to a transformer through which a force rebalance feedback can be applied. The currents I_{B1} and I_{B2} are stored (using heat switches R_{BS} and R_{BP}) to achieve a wideband balance by matching the resonance frequencies of the two accelerometers.

Signal differencing by means of stable persistent currents *before* detection is a unique feature of the SGG. This assures excellent *null stability* of the device, which in turn improves the overall common-mode rejection. Further, the SQUID sees only a small differential signal, thereby reducing the dynamic-range requirement on the amplifier and signal-processing electronics.

In an ideal gradiometer with perfectly matched spring constants, coil-to-test-mass gaps, and coil inductances, setting $I_{S2} = I_{S1}$ would give perfect rejection of the common-mode motion in the differential-mode output. In a real device, there

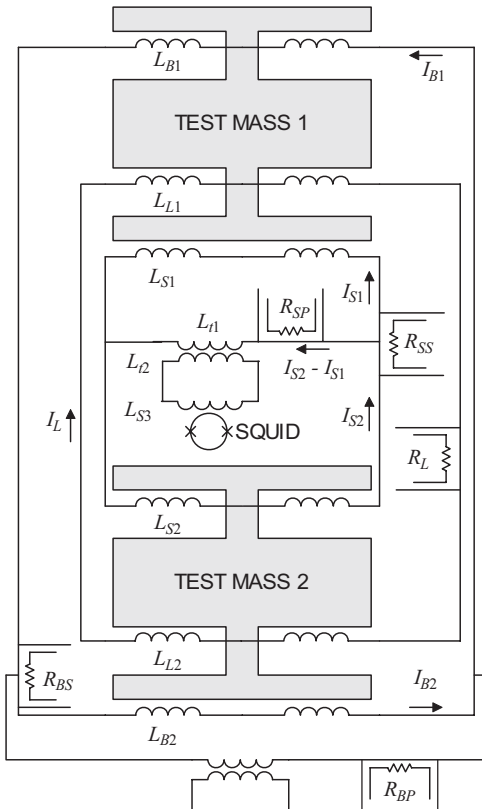


Fig. 15.6 Circuit diagram for an in-line-component SGG.

are mismatches and I_{S2}/I_{S1} is adjusted to maximize the common-mode rejection. The component of the linear acceleration parallel to the sensitive axis can be rejected precisely by this current adjustment. Components normal to the sensitive axis couple to the gradient output through misalignments of the sensitive axes, as described by (15.17). The misalignments are about 10^{-4} rad. The residual balance, described in the previous section, improves the common-mode rejection to $\geq 10^7$. The circuit containing L_{B1} and L_{B2} is used to provide an additional degree of freedom for signal balancing. Small currents in this circuit permit balancing over the entire frequency band of the SGG [34].

The power spectral density of the intrinsic gradient noise of the in-line-component SGG can be obtained [3, 34] from (15.1) by replacing m with $m/2$, the reduced mass for the differential mode, and by dividing $S_a(f)$ by ℓ^2 :

$$S_g(f) = \frac{8}{m\ell^2} \left[k_B T \frac{\omega_0}{Q} + \frac{\omega_0^2}{2\beta\eta} \epsilon_c \right] . \quad (15.18)$$

For Model II SGG, $m = 1.2 \text{ kg}$, $\ell = 0.19 \text{ m}$, $\omega_0/2\pi = 10 \text{ Hz}$, $Q = 10^6$, $T = 4.2 \text{ K}$, $\beta \approx \eta \approx 0.5$, $\varepsilon_c = (1 + 0.1 \text{ Hz}/f) 5 \times 10^{-31} \text{ J Hz}^{-1}$ (commercial dc SQUID). This gives an intrinsic white-noise level of $2 \times 10^{-3} \text{ E Hz}^{-1/2}$, where $1 \text{ E} \equiv 10^{-9} \text{ s}^{-2}$ is a unit of gravity gradient.

The actual noise spectrum obtained in the laboratory is shown in Figure 15.7. The white-noise level corresponds to $0.02 \text{ E Hz}^{-1/2}$, dominated by a displacement sensitivity of the instrument, the cause of which is not completely understood [34]. One possible source of this error is small distortion of the gradiometer housing caused by displacement-dependent forces from the leads. Below 0.1 Hz, a $1/f^\alpha$ power noise appears, but with an amplitude an order of magnitude higher than that expected from the SQUID $1/f$ noise. This excess low-frequency noise comes mainly from sensitivity to fluctuations in bath temperature. Without removing these additional errors, the SGG already represents three orders of magnitude improvement in sensitivity over the Bell gradiometer [35], the only operational room-temperature gravity gradiometer.

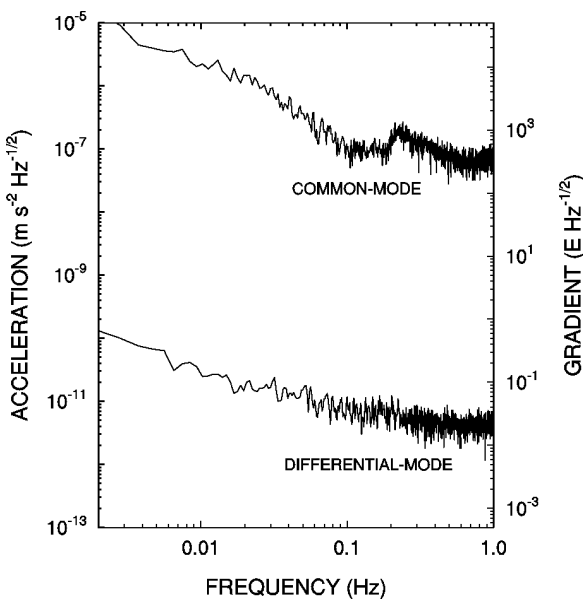


Fig. 15.7 Noise spectrum of the Maryland in-line-component SGG.

15.4.3

Cross-Component SGG

The in-line-component SGG has been developed primarily for laboratory and space applications. The achieved common-mode rejection of 10^7 is sufficient for these benign dynamic environments. However, for airborne applications for which the dynamic environment is much more hostile, the rejection must be improved to $\geq 10^9$.

A cross-component device can be designed to be inherently insensitive to linear accelerations by employing pivoted test masses whose mass moments are precisely balanced prior to assembly. Linear accelerations are further discriminated against by designing the pivot to be compliant only for the desired rotational acceleration, but stiff against the other degrees of freedom. The cross-component SGG based on this concept was pioneered by van Kann's group at the University of Western Australia [36].

Figure 15.8 shows a schematic of the Australian cross-component SGG [37]. The device consists of an orthogonal pair of pivoted test masses, or “moment arms” (A and B), which rotate in response to angular acceleration. Each moment arm (say, A) is equipped with three pairs of pancake coils in the plane of rotation. Two pairs of coils ($\theta_{A\pm}$, $F_{A\pm}$), sensitive to rotation, are placed symmetrically on

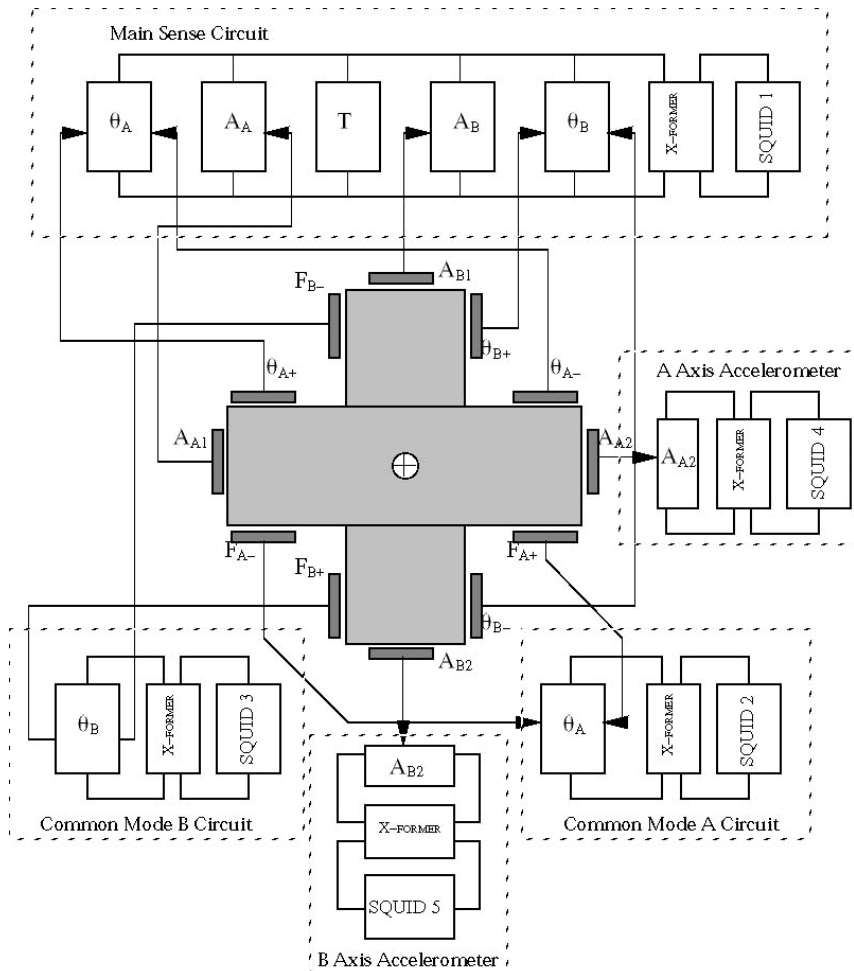


Fig. 15.8 Schematic of the Australian cross-component SGG.

either side of the long axis of the arm. A third pair of coils (A_{A1}, A_{A2}), sensitive only to translation, is located on the two ends of the moment arm. One of the pairs sensitive to rotation from one moment arm ($\theta_{A\pm}$) is connected with the corresponding pair from the other moment arm ($\theta_{B\pm}$) in a current differencing configuration to detect the differential angular acceleration. The other pairs of coils sensitive to rotation ($F_{A\pm}, F_{B\pm}$) are used to detect the common-mode angular acceleration. The coils sensitive to translation are used to remove linear acceleration errors from the gradiometer (A_{A1}, A_{B1}) and to detect the linear acceleration components (A_{A2}, A_{B2}), respectively.

By combining mass balance with error compensation, the Australian SGG achieved a rejection ratio of 10^9 for linear acceleration. Figure 15.9 shows the noise spectrum of this instrument obtained in the laboratory [38]. Above 10^{-2} Hz, the noise level corresponded to $1 \text{ E} \text{ Hz}^{-1/2}$. Below 10^{-2} Hz, the SGG exhibited a red noise with a $1/f^2$ power spectrum. Although the authors attributed this noise entirely to the intrinsic noise of the rf SQUID used, its $1/f^2$ power characteristic seems to indicate that it was from another source.

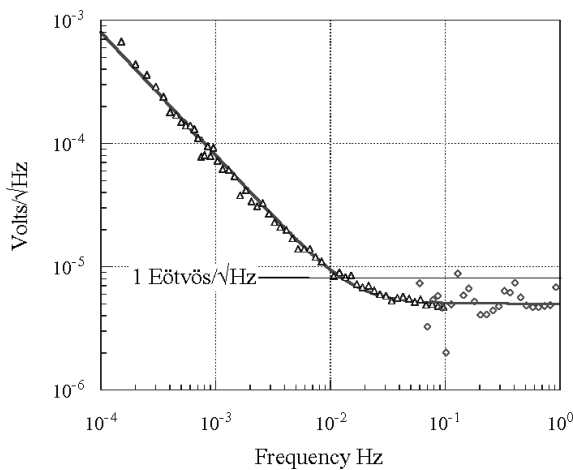


Fig. 15.9 Noise spectrum of the Australian cross-component SGG.

A cross-component SGG of a slightly different design is under development at the University of Maryland under the leadership of Moody [39]. Figure 15.10 shows the pivoted test mass (moment arm) and the housing for the Maryland cross-component SGG. The test mass/pivot structure is cut from a single block of Nb by wire EDM. Two component angular accelerometers on opposite faces of a Ti mounting cube, with their moment arms oriented orthogonal to each other, are connected together to form a single-axis SGG. Two superconducting circuits, as shown in Figure 15.11, are provided to detect the differential (cross-component gradient) and common-mode (angular acceleration) signals.

Superconducting angular accelerometers of a similar design have been tested extensively as components of the three-axis in-line-component SGG [40]. A photo-

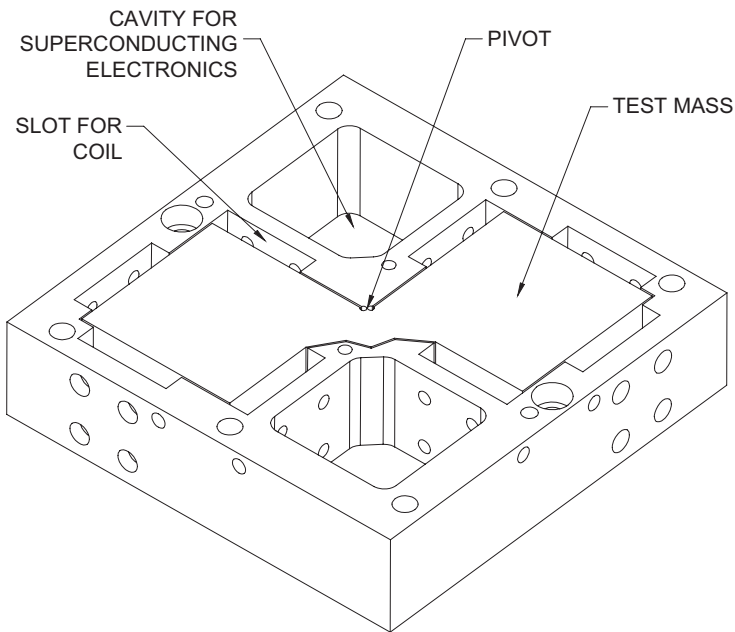


Fig. 15.10 Pivoted test mass and housing for the Maryland cross-component SGG.

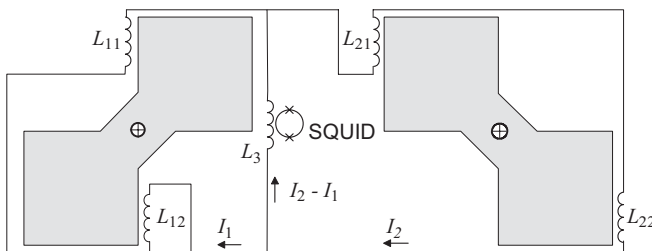


Fig. 15.11 Circuit diagram for a cross-component SGG.

graph of the angular accelerometer with the cover plate removed is shown in Figure 15.12. A semicircular shape of the test mass was chosen to provide pockets below the test mass for the SQUID sensor, transformer, heat switches, and high-current joints. The flexure pivot was defined by two 1.016-mm diameter holes at the ends of the cut. The minimum thickness of the bridge was 132 μm . These dimensions resulted in a resonance frequency of approximately 13.5 Hz. Although the test mass is limited to a small displacement range (<0.002 rad), the Nb in the region where the pivot is formed was replaced with a Ti alloy (Ti-6Al-4V) pin, which has a much higher yield strength. The pin, visible as the lighter circular region in Figure 15.12, is diffusion-bonded into the Nb disk.

At 4.2 K, the Q 's of the angular accelerometers were measured to be about 2.5×10^4 at a pressure of 8×10^{-4} torr. An analysis shows that these Q 's were lim-

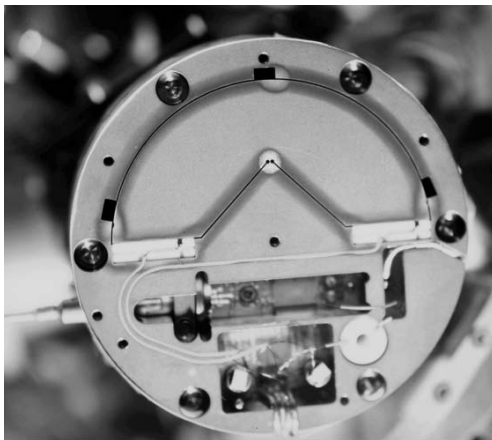


Fig. 15.12 A Maryland superconducting angular accelerometer.

ited by coupling to low- Q tilt modes of the suspension. An intrinsic Q of approximately 5×10^5 was required to produce the measured Q . This leads to a Brownian motion noise level of $1.4 \times 10^{-11} \text{ rad s}^{-2} \text{ Hz}^{-1/2}$ for frequencies well below the resonance frequency, which is an order of magnitude below the SQUID white-noise level. The lowest observed spectral density in the test environment was approximately $3 \times 10^{-9} \text{ rad s}^{-2} \text{ Hz}^{-1/2}$ at 0.01 Hz.

The intrinsic noise of a cross-component SGG can also be described by (15.18), if $m\ell^2$ is replaced by I , the moment of inertia of each test-mass arm [40]. The expected intrinsic noise of the University of Maryland device is $0.02 \text{ E Hz}^{-1/2}$, with a $1/f^z$ power noise below 0.1 Hz. The mass moments of each test mass have been balanced to 10^{-6} . A single-axis cross-component SGG, with a complete set of superconducting linear and angular accelerometers, has been assembled and is undergoing tests in the laboratory. To eliminate the need for transfer of liquid helium, the SGG has been integrated with a closed-cycle refrigerator, which is a dual-stage pulse-tube cryocooler.

15.5 Applications of the SGG Technology

15.5.1 Precision Tests of the Laws of Gravity

New weakly interacting particles have been proposed to solve remaining puzzles in particle physics, supergravity, and unified field theories. Many of these theories predict a departure from the gravitational inverse-square law in the form [41]:

$$\phi(r) = -\frac{GM}{r} \left[1 + \alpha \exp\left(-\frac{r}{\lambda}\right) \right], \quad (15.19)$$

where α and λ are the dimensionless strength and the range of the Yukawa potential. More recently, a suggestion came from higher-dimensional string theories that the inverse-square law may be violated at submillimeter distances [42].

Prior to the emergence of the SGG, most sensitive gravity experiments had been performed with torsion balances. A torsion balance is a cross-component gravity gradiometer with only one arm. Although the great compliance of the torsion fiber gives a superb sensitivity, the device suffers from its sensitivity to angular accelerations and to a certain degree of linear acceleration. The SGG is more versatile in design, is more sensitive, and rejects all components of the linear and angular accelerations of the platform.

The Poisson equation for the Newtonian potential, (15.16), suggests an interesting test of the inverse-square law: by summing the outputs of a three-axis in-line-component gradiometer in response to a locally generated time-varying gravity field, one can perform a *null* test of the inverse-square law [43]. Such a test has the advantage of being insensitive to source metrology errors although the detector must now satisfy stringent metrology requirements. Therefore, in principle, a geological source of arbitrary shape and density can be used to carry out a null test at large distances [44].

Paik and coworkers have carried out a series of laboratory tests of the inverse-square law using their SGG as a null detector [6, 7]. Figure 15.13 shows the source-detector configuration in their experiment. The source was a 1500-kg lead (Pb) pendulum suspended from the ceiling of the laboratory. The three-axis in-line-component SGG was used as the detector. The gradiometer was in the “umbrella orientation,” in which all three sensitive axes make the same angle, 54.7° , with respect to the vertical.

In order to match the scale factors for the three orthogonal gradients, the SGG was rotated about the vertical into three azimuthal positions separated by 120° , and each gradiometer output was summed over the three positions. The trace of the gradient tensor Γ_{ij} was therefore measured independently by each of the three

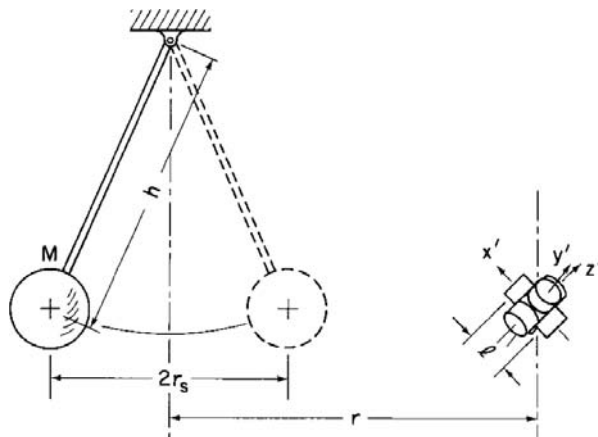


Fig. 15.13 Source-detector configuration for a meter-scale inverse-square law test.

single-axis gradiometers, allowing for a valuable crosscheck between the data. Data were collected and analyzed over 33 nights to obtain the final null result of $(0.58 \pm 3.10) \times 10^{-4}$ E. This null result was used to obtain upper limits of α as a function of λ . The strictest limit obtained was $\alpha = (0.9 \pm 2.3) \times 10^{-4}$ for $\lambda = 1.5$ m [7].

Figure 15.14 shows the 1σ error in α plotted as a function of λ . The shaded region is the excluded region of the parameter space set by previous experiments. Thus, the SGG experiment has improved the limit of the inverse-square law by more than an order of magnitude at a 1.5-m distance. In a new laboratory experiment under design, a long cylindrical shell could be used as a near-null source. This would reduce metrology errors and improve the limits of the inverse-square law to better than 1 part in 10^5 at $\lambda \approx 0.3$ m (the dotted line in the figure).

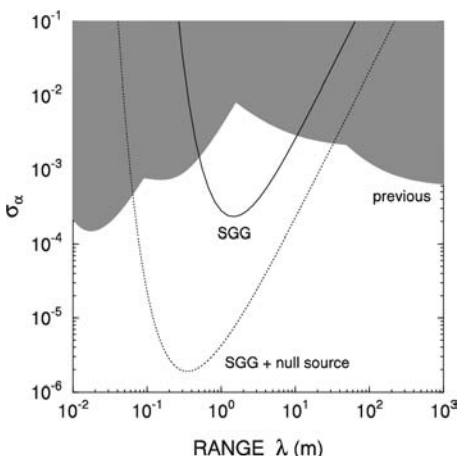


Fig. 15.14 1σ of the Yukawa potential obtained by the SGG experiment.

It is possible to extend the range of the test to $\lambda \geq 100$ m by moving the null detector horizontally with respect to a mountain, or up and down with respect to a plain or the ocean. A three-axis SGG in an eccentric Earth orbit would extend λ to 10^3 – 10^4 km [44]. In the opposite limit with $\lambda \leq 1$ mm, a null test could be performed by combining a Newtonian null source with a single-axis SGG [45].

New developments in string theories raise the possibility that there may be deviations from Newton's law between micrometer and millimeter length scales [42]. String theories can be consistently formulated only in nine spatial dimensions. Because the space we observe is three-dimensional, the extra dimensions must be hidden. It is possible to have dimensions that affect gravity but not elementary particles, which may be manifest as a violation of the inverse-square law at submillimeter distances. These developments represent the first prediction of a string theory that can be tested, and a discovery of such a deviation from the inverse-square law would be ground breaking. A null result would also be significant in that, in addition to extending the limits of Newton's law and general relativity, it will put constraints on the string scale and on the sizes of any possible extra dimension.

Figure 15.15 shows an expanded cross-section of the apparatus for a submillimeter inverse-square law experiment under preparation by Paik *et al.* [45] at the University of Maryland. To maximize the masses that can be brought to within 100 μm from each other, flat disk geometry is used for both the source and test masses. A circular tantalum (Ta) disk of a large diameter-to-thickness ratio forms an approximate null source of gravity, which produces nearly constant Newtonian fields with opposite signs on its two sides. Two disk-shaped Ta test masses are suspended on the two sides of the source mass and are coupled magnetically through superconducting sensing coils to form a superconducting differential accelerometer. Both the source and test masses are suspended by cantilever springs. As the source mass is driven sinusoidally along the symmetry axis, the violation signal should appear at the second harmonic.

To prevent a magnetic crosstalk, a superconducting shield is provided between the source mass and each test mass. To avoid direct mechanical coupling to the source motion through the distortion of the housing it causes, each test mass block is suspended from the housing by a cantilever spring. The sensitive axes of the two test masses are aligned by adjusting persistent currents in the alignment coils. The second harmonic signal detection also discriminates against the magnetic crosstalk and mechanical coupling.

Figure 15.16 shows the expected resolution (2σ) of the SGG experiment *versus* the existing limits for the inverse-square law at ranges below 1 mm. The line and the shaded region represent violations predicted by the string theory and the axion theory, respectively. (See Section 15.5.2 for a discussion of the axion.) At $\lambda = 100 \mu\text{m}$, the new experiment is expected to improve the resolution by four orders

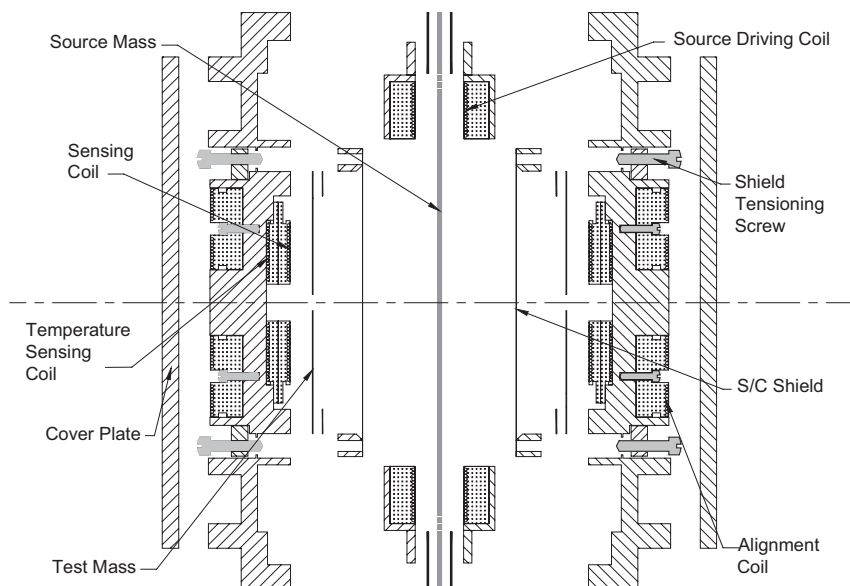


Fig. 15.15 Cross-section of a submillimeter inverse-square law experiment.

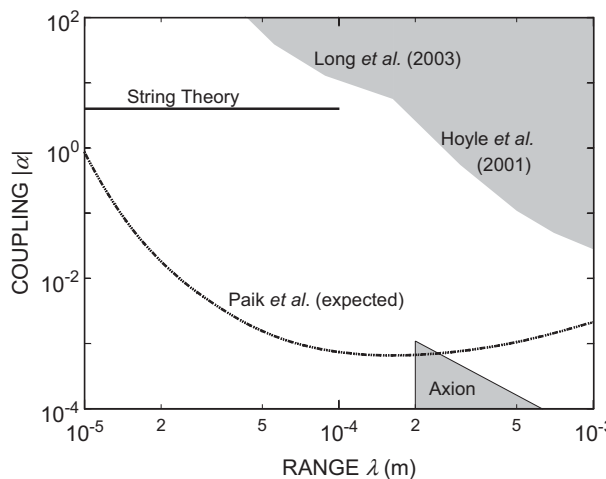


Fig. 15.16 Expected sensitivity (2σ) of the SGG experiment *versus* the existing limits.

of magnitude beyond the best limits obtained by a torsion balance experiment of Hoyle *et al.* [46] and a high-frequency resonator experiment of Long *et al.* [47]. The SGG experiment will probe the extra dimensions to below $10 \mu\text{m}$ and will be marginally sensitive to detect the axion with highest allowed coupling.

In zero- g , a very soft and stable suspension can be realized for the test masses by superconducting magnetic levitation. This eliminates the cumbersome mechanical springs and affords an opportunity to improve the sensitivity and align the sensitive axes magnetically. ISLES (Inverse-Square Law Experiment in Space), which has been proposed for the International Space Station (ISS), could improve the sensitivity by two orders of magnitude over the ground experiment by using levitated test masses [48]. With the improved sensitivity, ISLES would clearly detect a violation signal from the axion with the highest allowed strength.

The SGG technology enables other precision gravity experiments. General relativity predicts the existence of a “gravitomagnetic field,” which arises from a moving mass. GP-B (Gravity Probe-B), which was launched in April 2004, is searching for the effect of such a field on a spinning body, the “frame dragging” precession of superconducting gyros in an Earth orbit [49]. In GP-B, each of the four gyros is located inside a superconducting loop which is coupled to a dc SQUID. The spinning superconducting body produces a London moment⁴ and as the gyro precesses, the SQUID monitors the resulting time-varying magnetic flux in the loop.

An SGG in a polar orbit could detect the gravitomagnetic Riemann tensor component directly. In the geographic coordinate system, this field will appear as an off-diagonal component, with a strength of $8 \times 10^{-8} \text{ E}$ at a 650-km altitude. The

4) When a superconductor spins with an angular velocity $\vec{\Omega}$, a magnetic induction $\vec{B} = (2mc/e)\vec{\Omega}$ arises inside it due to the slippage of Cooper pairs with respect to the

lattice, where m and e are the electron mass and charge. The resulting magnetic moment of the superconductor is called “the London moment.”

Newtonian background would be removed by flying a two-axis in-line-component SGG, with one axis pointing northeast and the other northwest, and differencing the two signals [50]. With a gradiometer sensitivity of 10^{-5} E Hz $^{-1/2}$, which could be obtained by using levitated test masses, one could resolve the gravitomagnetic field to one part in 100 in a year. This is comparable to the expected resolution of GP-B and would give a valuable crosscheck to its result.

Superconducting differential accelerometers with magnetic levitation will also be used for STEP (Satellite Test of the Equivalence Principle), which is under development jointly by NASA (National Aeronautics and Space Administration) and ESA (European Space Agency) [8, 51]. In STEP, several pairs of nested cylindrical test masses, composed of different materials, are orbited around the Earth. One such pair is shown in Figure 15.17. The inner and outer test masses are carefully shaped to match their multipole moments up to octopole ($\ell = 3$) and their centers of mass are precisely matched to eliminate the sensitivity of the differential accelerometer to gravity gradients. Each test mass is suspended by a superconducting magnetic bearing and confined to move along its symmetry axis.

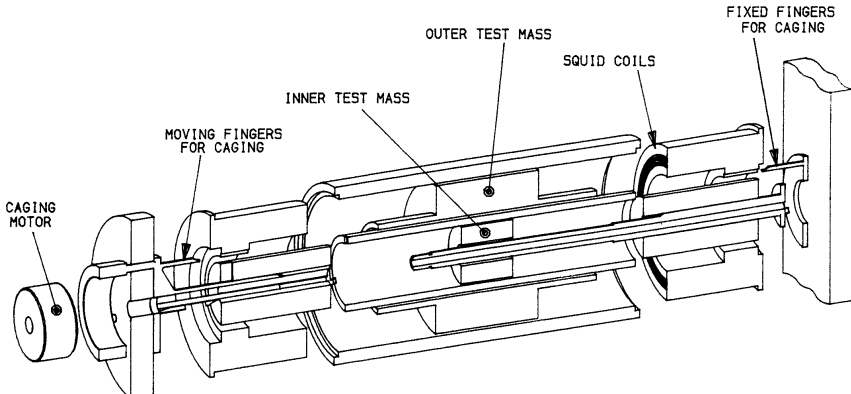


Fig. 15.17 Equivalence principle accelerometer on STEP.

If the equivalence principle were violated, the two masses in each pair would fall with different accelerations with respect to the Earth. With the test masses harmonically bound, the resulting differential acceleration becomes periodic at the frequency of rotation of the differential accelerometer with respect to the Earth. This differential acceleration signal is read out by a superconducting circuit similar to the one shown in Figure 15.6.

With design parameters of $m = 0.2$ kg, $\omega_0/2\pi = 3 \times 10^{-3}$ Hz, $Q = 10^6$, $T = 2$ K, $\beta = \eta = 0.5$, and $\varepsilon_c = (1 + 0.1 \text{ Hz}/f) 5 \times 10^{-31} \text{ J Hz}^{-1}$, (15.1) yields a differential acceleration sensitivity of $5 \times 10^{-15} \text{ m s}^{-2} \text{ Hz}^{-1/2}$ at a signal frequency of 10^{-3} Hz. Unlike the ground torsion balance experiments, which search for effects of a small horizontal component of the Earth's gravity, STEP accelerometers undergo a full gravitational acceleration by the Earth. This signal enhancement by a factor of 10^3 , combined with the exquisite sensitivity of the levitated superconducting acceler-

ometers, leads to the expected resolution of one part in 10^{18} in a few months, which is a five order of magnitude improvement over the best ground experiment [52].

15.5.2

Search for New Weak Forces

The tests of the inverse-square law and the equivalence principle discussed in the previous section also constitute searches for new forces since departures from these laws may be due to interactions mediated by new particles [41]. In this section, we discuss a superconducting accelerometer experiment that searches for a new type of force: spin–mass interaction.

The Standard Model of particle physics has had spectacular success in explaining all available data on the fundamental constituents of matter. However, one of the most important unresolved issues is the “strong CP problem”: namely, a violation of charge conjugation (C)–parity (P) symmetry has not been observed in strong interaction. Peccei and Quinn developed the most accepted explanation for this phenomenon three decades ago [53]. One of the most important results of the theory is the prediction of the existence of a new light-mass pseudoscalar particle, the “axion,” which mediates a short-range force between mass and intrinsic spin as well as between spins and between masses [54].

Axions, if they exist, would have been produced abundantly in the Big Bang. Being electrically neutral and interacting very weakly with matter, they would have decoupled from the rest of the universe early. The relic axion is therefore a very strong candidate for cold dark matter [55].

Searches for spin–mass interaction have been carried out by using a torsion balance [56], a SQUID susceptometer [57], and nuclear spin precession [58]. These experiments have set limits some ten orders of magnitude above the maximum theoretically allowed strength. A very different class of axion experiments relies on axion-to-photon conversion in a static B field, usually in a resonant cavity (see Chapter 8). Second-generation cavity detectors are currently in operation [59]. These experiments have the advantage that the existing technology is on the verge of probing the axion–photon coupling strength over an axion mass range of $1\text{--}10\,\mu\text{eV}$. However, because these experiments rely on the assumption that axions constitute a significant component of the galactic halo and are favorably distributed, a null result does not conclusively eliminate the Peccei–Quinn mechanism as the solution of the strong CP problem, nor does it imply absence of a spin–mass interaction mediated by virtual axions or other light-mass bosons.

A superconducting accelerometer search for spin–mass interaction was originally proposed by Speake as a coexperiment for STEP [51] and aimed at improving the spin–mass coupling by several orders of magnitude from the existing limit by using a superconducting linear differential accelerometer. Paik *et al.* [9] have proposed an improved version of this experiment by using a differential *angular* accelerometer. The advantage of an angular accelerometer is that it can be made inherently insensitive to linear accelerations by mass balance, analogous to a cross-com-

ponent SGG. Further, by employing magnetic levitation, the test masses can be made extremely compliant for rotational motion and thus a very high sensitivity can be achieved even in 1-g.

Figure 15.18 shows a vertical cross-section of the apparatus under construction. Each test mass is made out of Nb, and is nearly axisymmetric, consisting of a thin-walled cylindrical section inside a thin disk. A superconducting coil below each disk generates a field to levitate the mass. Four small pancake coils above each disk, located 90° apart around the symmetry axis, form circuits for measurement and control of the alignment. The cylindrical symmetry of the test masses is broken by a set of axial grooves on the inner surface, which form 16 ridges (see Figure 15.19 for a horizontal cross-section). A set of elongated pancake coils located near the ridges is used to detect the rotation of the test mass. The sensing current generates a restoring force, so the masses oscillate about their symmetry axis at a resonance frequency of $\sim 10^{-2}$ Hz.

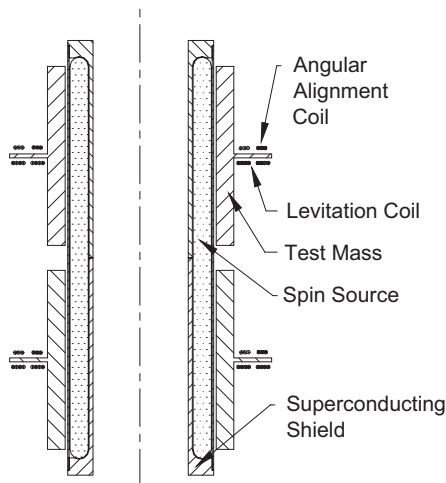


Fig. 15.18 Vertical cross-section of a spin–mass coupling experiment.

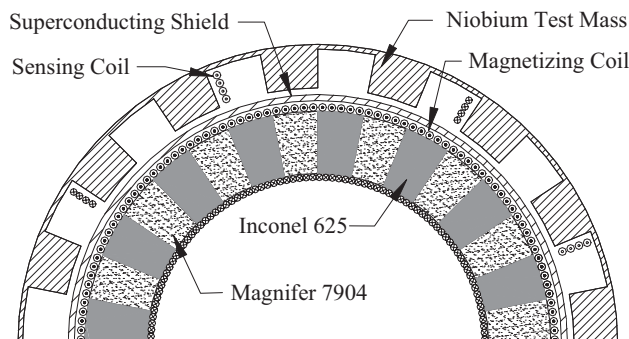


Fig. 15.19 Horizontal cross-section of a spin–mass coupling experiment.

The test masses fit over a cylindrical Nb shield. Inside the shield, concentric with the test masses, is a spin source formed from a hollow cylinder wrapped with a toroidal drive coil. A cross-section of the source and test mass is shown in Figure 15.19. Each shell is divided, in the azimuthal direction, into 32 sections of two alternating materials: Magnifer 7904, a soft ferromagnetic metal, and Inconel 625, a nonmagnetic metal. The magnetic field from Magnifer is forced to go through Inconel by the Nb shield. With this arrangement, a spin–mass coupling force produces a torque on the test mass. The source is driven at the differential-mode resonance frequency. This reduces the effect of amplifier noise to below the Brownian motion noise of the test masses. At a pressure of 3×10^{-8} torr, the intrinsic noise of the differential angular accelerometer becomes 3×10^{-14} rad s $^{-2}$ Hz $^{-1/2}$.

Construction of the spin source and the test masses has been completed. This experiment has the potential to approach the axion limit to within a few orders of magnitude. However, the search for a non-Newtonian mass–mass interaction appears to offer a much better chance of detecting the axion. Once the Maryland group realized this and saw also the possibility of searching for extra dimensions in a gravity experiment, it switched its main effort to the short-range inverse-square law test discussed in Section 15.5.1. Although the spin–mass experiment is inactive at the moment, it is included here to show the application of the SQUID motion sensing technology in the search for new weak forces.

15.5.3

Gravity Mapping and Mass Detection

In this section, we discuss the applications of the SGG for gravity surveying and mass detection. High-resolution (≤ 100 km) gravity maps are required to study geophysical processes that are responsible for shaping the Earth and the ocean. Even higher resolution maps (≤ 1 km) are needed to detect natural resources and hidden artificial objects. The latter include smuggled narcotics, camouflaged ordnance, tunnels, and underground bunkers.

The in-line-component SGG at the University of Maryland was developed with NASA support primarily for its application to gravity-mapping missions for the Earth and the planets. Mission studies have been conducted [60, 61] which showed that an SGG of a 10^{-3} E Hz $^{-1/2}$ sensitivity at an altitude of 250 km could resolve the Earth's gravity with a spatial resolution approaching 100 km in six months. This would be superior to the resolution expected from an alternative approach, a satellite-to-satellite tracking mission. Measuring second spatial derivatives of the potential, a gradiometer mission tends to be more sensitive to short-wavelength components of the Earth's harmonics than the alternative mission, which measures a first spatial derivative. However, without space-qualified cryo-coolers available, the duration of the SGG mission would be limited to about a year. Therefore, with a goal to monitor seasonal and annual gravity changes over five years, NASA selected a satellite-to-satellite tracking mission, called GRACE (Gravity Recovery And Climate Experiment), as the first gravity-mapping mission for the Earth [62].

A geodesy mission with an SGG has also been studied by ESA. Under ESA support, Oxford Instruments has demonstrated a magnetically levitated SGG [63] for future space applications. The design of this instrument is similar to that of the STEP equivalence principle accelerometers. A unique feature of this SGG is incorporation of superconducting coils for aligning the sensitive axes by means of persistent currents. This improves the common-mode rejection capability of the gradiometer and reduces the spacecraft control requirements. However, this is achieved at the expense of increasing the complexity of the device. This instrument is ideally suited for a quiet spacecraft environment. However, operating the magnetically levitated SGG in a noisy aircraft environment will be a great challenge due to the soft suspension, which amplifies nonlinearity errors.

Studies of various geophysical processes and exploration of petroleum and minerals require gravity data with a horizontal resolution down to several kilometers or below. Due to the attenuation of short-wavelength components of gravity with altitude, such a high-resolution map requires airborne or shipborne gravity survey. The development of an SGG at the University of Western Australia was supported by petroleum and mining industries interested in such applications. The University of Maryland effort to develop a cross-component SGG, which was supported by Sandia National Laboratories, was also motivated by the same applications. A cross-component gradiometer tends to be less sensitive than an in-line-component device but is more suitable for moving-base applications due to its superior acceleration rejection capability.

The expected noise performance of the University of Maryland cross-component SGG system for airborne survey is plotted in Figure 15.20, along with those of conventional gravimeters and the Gravity Gradiometer Survey System (GGSS) of Bell Aerospace [35]. An aircraft speed of 100 knots is assumed. The SGG performance was computed from the expected platform-limited noise of $1 \text{ E Hz}^{-1/2}$. The gravimeter and Bell gradiometer performances were estimated from their reported noise [35, 64]. The circle and square represent the actual performance

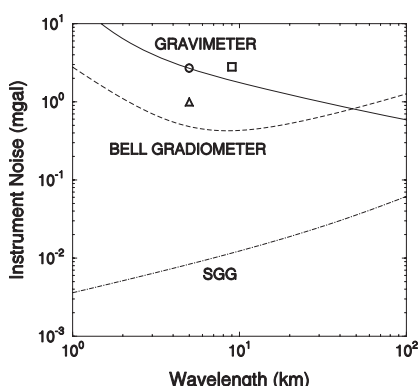


Fig. 15.20 Expected performance of the airborne SGG survey system.

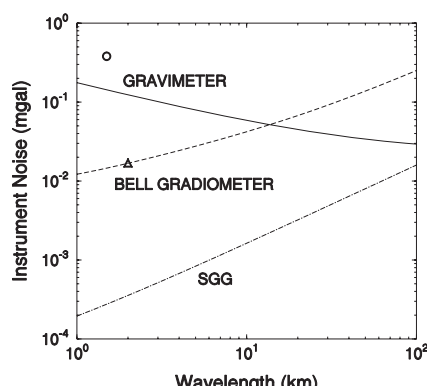


Fig. 15.21 Expected performance of the shipborne SGG survey system.

obtained with two different gravimeter systems [65, 66], and the triangle corresponds to the estimated error for a survey conducted with the GGSS [67].

The SGG is the only instrument that can provide a 0.1-mGal ($1 \text{ Gal} \equiv 1 \text{ cm s}^{-2}$) accuracy below 100 km. Further, the SGG performance keeps improving at wavelengths below 1 km due to its wide instrument bandwidth ($\sim 1 \text{ Hz}$). The instrument noise plotted in Figure 15.20 is not to be confused with the actual gravity recovery. At a finite altitude h , the gravity signal of a particular wavelength λ is attenuated by a factor $\exp(-2\pi h/\lambda)$. Therefore, it is essential to fly at a sufficiently low altitude in order to obtain a high-accuracy gravity map at short wavelengths.

Figure 15.21 compares the expected noise performance of the SGG survey system with those of the GGSS and gravimeters for shipborne gravity survey. A cruising speed of 10 knots is assumed. The performance curve of the Bell gradiometer was obtained by assuming that the noise is dominated by the intrinsic noise of the instrument, $10 \text{ E Hz}^{-1/2}$. The reported performance of the GGSS in the survey conducted in the Gulf of Mexico [68] is marked by a triangle. For the SGG and gravimeter noise, a factor of 10 improvement was assumed over the airborne case, which appears reasonable due to the quieter dynamic environment of the ship. The circle in the figure represents the reported performance of the BGM-3 sea gravity meter system [64]. The SGG improves the state of the art by 1.5 orders of magnitude at kilometer wavelengths.

An important feature of the accuracy *versus* wavelength curves of gravimeters and gravity gradiometers is that the slopes of the curves are different. While the accuracy of recovery by gravimeters improves as λ increases, gradiometers provide better accuracy at shorter λ 's within their bandwidth limit. This is because a gradiometer measures a higher derivative of the potential than a gravimeter, which makes it intrinsically more sensitive to shorter wavelength fluctuations. Thus, for a gradiometer with sensitivity 1 E and a gravimeter with sensitivity 0.1 mGal, the gradiometer has an increasing advantage in resolving density fluctuations at length scales below 6 km.

The high accuracy ($\leq 10^{-2}$ E) and high spatial resolution ($\leq 1 \text{ km}$) expected of the SGG makes it a prime candidate for a device that searches for hidden masses. However, in order to be able to detect hidden objects, a few very stringent conditions must be met. (1) Since the gravity gradient from a point mass falls off as $1/r^3$ with the distance r , even a sensitive SGG must be brought to a very close proximity to the suspected mass or void to have a reasonable signal-to-noise ratio. This may be difficult to accomplish for certain types of searches. (2) The density of the surrounding terrain must be reasonably uniform or well known, and must be sufficiently different from that of the suspected object. The second condition may be difficult to satisfy in a rugged mountain area, where the terrain effect is difficult to correct. However, if one could survey the same area repeatedly, a small change in gravity signature could be detected by differencing the gravity maps obtained at different times.

15.5.4

Gradiometer-Aided Inertial Navigation and Survey

Another field that will benefit from an SGG is inertial navigation and survey. GPS (Global Positioning System) navigation is rapidly taking over the field of navigation. However, inertial navigation will still be required for submarines, which cannot communicate with GPS and for aircraft in situations where the GPS system is disturbed.

An inertial navigation system (INS) generally consists of a triad of accelerometers and a sufficient number of gyroscopes (gyros). The gyros provide the instantaneous orientation of the accelerometers. The accelerometer outputs are integrated by an onboard computer and the data on the initial position and initial velocity are substituted to obtain the instantaneous position of the vehicle. Since the platform drifts and position errors grow with time due to random noise in the instruments, generally the position (and orientation) of the vehicle must be updated by communicating with ground stations or by using a GPS receiver. In the case of an inertial survey system (ISS), the vehicle is stopped occasionally to provide “zero velocity update,” which calibrates random gyro drift and other inertial system errors [69]. Communication with the outside world may not be possible for submarines and aircraft that are required to undergo autonomous navigation. Further, accelerometers measure platform acceleration plus local gravity field, as dictated by the equivalence principle. Hence the precision of inertial navigation is ultimately limited by the uncertainty in the Earth’s gravity field.

With a gradiometer on board, the platform drift can be eliminated by measuring the vertical deflection in real time. Assuming that the vehicle moves approximately in a horizontal plane with velocity \mathbf{v} , the components of the vertical deflection can be obtained from

$$\frac{\partial \phi}{\partial x} = \int (\Gamma_{xx} v_x + \Gamma_{xy} v_y) dt, \quad \frac{\partial \phi}{\partial y} = \int (\Gamma_{xy} v_x + \Gamma_{yy} v_y) dt. \quad (15.20)$$

To remove the gravity error completely, the integration can be extended to all three dimensions and the resulting gravity field can be subtracted from the accelerometer outputs. In order to perform this calculation in real time, a *tensor* gradiometer is needed.

A tensor gradiometer could be constructed by combining a three-axis in-line-component SGG with a three-axis cross-component SGG. The device would have six common-mode outputs, which correspond to the components of the linear and angular accelerations of the platform. Instead of using gyros, the angular acceleration outputs could be integrated to determine the orientation of the platform. Such a system would be a *total* gravity and motion sensing system. As a gravity survey system, it would measure all components of the gravity gradient tensor simultaneously as well as acceleration in all degrees of freedom, which could be used for platform control. As an inertial navigation or survey system, it would be a self-contained, gradiometer-aided INS or ISS.

15.6 Outlook

Superconducting accelerometer technology has enabled sensitive fundamental physics experiments. Laboratory models of two types of SGG have been developed. The potential benefits from airborne and shipborne SGG system in geophysics, resources exploration, and inertial navigation could be enormous.

A three-mode superconducting transducer integrated with a two-stage commercial SQUID is under development at the University of Maryland and Louisiana State University as the next-generation transducer for ALLEGRO. The noise temperature of a dual Quantum-Design dc SQUID at 4.2 K has been shown to be $T_N \approx 300 \hbar\omega_S/k_B$ [70], comparable to that of Wellstood's SQUID at the same temperature [27]. The double-SQUID arrangement requires a sophisticated feedback.

Recently, the possibility of instrumenting the entire Moon or the moons of Mars as sensitive gravitational-wave antennas has been suggested [71]. Superconducting accelerometers deployed on the surface could be tuned to the lowest quadrupole modes of these moons or could be operated as wideband detectors below these frequencies. The Martian-moon detector looks especially interesting because it will cover a new frequency window (≤ 0.3 Hz) that will be missed by both the ground detectors and LISA (Laser Interferometer Space Antenna), with a sufficient sensitivity ($h_{\min} \approx 10^{-22}$ Hz $^{-1/2}$) to detect many important astrophysical sources.

The cross-component SGG, which was originally developed for airborne gravity survey, has been reconfigured for applications in gradiometer-aided inertial navigation. The gradiometer has been integrated with a 4-K pulse-tube cryocooler and will be mounted on a stabilized platform. This program will demonstrate the operation of the SGG in a moving-base environment, which is hoped to lead to the development of a full SGG survey system.

At the moment, GP-B is orbiting the Earth, testing Einstein's prediction of gravitomagnetism. The STEP mission, which aims at improving the limits of the equivalence principle by five orders of magnitude, is under development jointly by NASA and ESA. The SGG inverse-square law experiment will begin in 2006 to probe extra dimensions down to several micrometers and search for the axion with unmatched sensitivity. It is easy to envision that motion sensors based on SQUID technology will continue to improve our knowledge of the basic laws of the universe and to enhance exploration, navigation, and other technologies.

References

- 1 Fairbank, W. M., Boughn, S. P., Paik, H. J., McAshan, M. S., Opfer, J. E., Taber, R. C., Hamilton, W. O., Pipes, B., Bernat, T. and Reynolds, J. M. (1974) Search for gravitational radiation using low-temperature techniques, in *Experimental Gravitation*, B. Bertotti (ed.), Academic Press, New York, pp. 294–309.
- 2 Paik, H. J. (1976) Superconducting tunable-diaphragm transducer for sensitive acceleration measurements, *J. Appl. Phys.* **47**, 1168–1178.
- 3 Chan, H. A. and Paik, H. J. (1987) Superconducting gravity gradiometer for sensitive gravity measurements: I. Theory, *Phys. Rev. D* **35**, 3551–3571.
- 4 Chan, H. A., Moody, M. V. and Paik, H. J. (1987) Superconducting gravity gradiometer for sensitive gravity measurements: II. Experiment, *Phys. Rev. D* **35**, 3572–3597.
- 5 Moody, M. V., Chan, H. A. and Paik, H. J. (1986) Superconducting gravity gradiometer for space and terrestrial applications, *J. Appl. Phys.* **60**, 4308–4315.
- 6 Chan, H. A., Moody, M. V. and Paik, H. J. (1982) Null test of the gravitational inverse square law, *Phys. Rev. Lett.* **49**, 1745–1748.
- 7 Moody, M. V. and Paik, H. J. (1993) Gauss's law test of gravity at short range, *Phys. Rev. Lett.* **70**, 1195–1198.
- 8 Worden, Jr., P. W. and Everitt, C. W. F. (1974) The gyroscope experiment: III. Tests of the Equivalence Principle of gravitational and inertial mass based on cryogenic techniques, in *Experimental Gravitation*, B. Bertotti (ed.) Academic Press, New York, pp. 381–402.
- 9 Paik, H. J., Moody, M. V. and Canavan, E. R. (1999) Search for axions using a superconducting differential angular accelerometer, in *Proc. 8th Marcel Grossmann Meeting on General Relativity*, T. Piran (ed.), World Scientific, Singapore, pp. 1197–1199.
- 10 Avenel, O. and Varoquaux, E. (1985) Observation of singly quantized dissipation events obeying the Josephson frequency relation in the critical flow of superfluid ^4He through an aperture, *Phys. Rev. Lett.* **55**, 2704–2707.
- 11 Packard, R. E. and Vitale, S. (1992) Principles of superfluid gyroscopes, *Phys. Rev. B* **46**, 3540–3549.
- 12 Taylor, J. H. (1994) Nobel Lecture: Binary pulsars and relativistic gravity, *Rev. Mod. Phys.* **66**, 711–719.
- 13 Weber, J. (1960) Detection and generation of gravitational waves, *Phys. Rev.* **117**, 306–313.
- 14 Ricci, F. and Brillet, A. (1997) A review of gravitational wave detectors, *Ann. Rev. Nucl. Part. Sci.* **47**, 111–156.
- 15 Faller, J. E. and Bender, P. L. (1984) A possible laser gravitational-wave experiment in space, in *Precision Measurements and Fundamental Constants II*, B. N. Taylor and W. D. Phillips (eds.), Natl. Bur. Stand. (US) Spec. Publ. 617, pp. 689–690.
- 16 Giffard, R. P. (1976) Ultimate sensitivity limit of a resonant gravitational wave antenna using a linear motion detector, *Phys. Rev. D* **14**, 2478–2486.
- 17 Paik, H. J. (1982) Unified theory of gravitational radiation detectors for pulses and monochromatic signals, in *Proc. 2nd Marcel Grossmann Meeting on General Relativity*, R. Ruffini (ed.), North-Holland, Amsterdam, pp. 1193–1209.
- 18 Price, J. C. (1987) Optimal design of resonant-mass gravitational wave antennas, *Phys. Rev. D* **36**, 3555–3570.
- 19 Heffner, H. (1962) The fundamental noise limit of linear amplifiers, *Proc. IRE* **50**, 1604–1608.
- 20 Richard, J.-P. (1984) Wide-band bar detectors of gravitational radiation, *Phys. Rev. Lett.* **52**, 165–167.
- 21 For a more complete treatment of the transducers for gravitational-wave detection, see Paik, H. J. (1995) Electromechanical transducers and bandwidth of resonant-mass gravitational-wave detectors, in *Gravitational Wave Experiments*, E. Coccia, G. Pizzella, and F. Ronga (eds.), World Scientific, Singapore, pp. 201–219.
- 22 Clarke, J. (1996) SQUID Fundamentals, in *SQUID Sensors: Fundamentals, Fabrication, and Applications*, Kluwer, Dordrecht, pp. 1–10.

- cation and Applications, H. Weinstock (ed.), Kluwer, Dordrecht, pp. 1–62.
- 23** Koch, R. H., Van Harlingen, D. J. and Clarke, J. (1981) Quantum noise theory for the dc SQUID, *Appl. Phys. Lett.* **38**, 380–382.
- 24** Geng, Z. K., Hamilton, W. O., Johnson, W. W., Mauceli, E., Merkowitz, S. M., Morse, A. and Solomonson, N. (1995) Operation of the ALLEGRO Detector at LSU, in *Gravitational Wave Experiments*, E. Coccia, G. Pizzella, and F. Ronga (eds.), World Scientific, Singapore, pp. 128–135.
- 25** Jin, I., Amar, A., Stevenson, T. R., Wellstood, F. C., Morse, A. and Johnson, W. W. (1997) 35 \hbar two-stage SQUID system for gravity wave detection, *IEEE Trans. Appl. Supercond.* **7**, 2742–2746.
- 26** Clarke, J., Tesche, C. D. and Giffard, R. P. (1979) Optimization of dc SQUID voltmeter and magnetometer circuits, *J. Low Temp. Phys.* **37**, 405–420.
- 27** Harry, G. M., Jin, I., Paik, H. J., Stevenson, T. R. and Wellstood, F. C. (2000) Two-stage superconducting-quantum-interference-device amplifier in a high-Q gravitational wave transducer, *Appl. Phys. Lett.* **76**, 1446–1448.
- 28** Wagoner, R. V. and Paik, H. J. (1977) Multi-mode detection of gravitational waves, in *Proc. Int. Symp. Experimental Gravitation*, B. Bertotti (ed.), Accademia Nazionale dei Lincei, Rome, pp. 258–265.
- 29** Johnson, W. W. and Merkowitz, S. M. (1993) Truncated icosahedral gravitational wave antenna, *Phys. Rev. Lett.* **70**, 2367–2370.
- 30** Coccia, E., Lobo, J. A. and Ortega, J. A. (1995) Proposed gravitational wave observatory based on solid elastic spheres, *Phys. Rev. D* **52**, 3735–3738.
- 31** Harry, G. M., Stevenson, T. R. and Paik, H. J. (1996) Detectability of gravitational wave events by spherical resonant-mass antennas, *Phys. Rev. D* **54**, 2409–2420.
- 32** Podt, M., Gottardi, L., de Waard, A., Frossati, G. and Flokstra, J. (2003) A spherical gravitational wave detector readout by nearly quantum limited SQUIDs, *Supercond. Sci. Technol.* **16**, 1531–1535.
- 33** Aguiar, O. D. et al. (2002) The status of the Brazilian spherical detector, *Class. Quantum Grav.* **19**, 1949–1953.
- 34** Moody, M. V., Paik, H. J. and Canavan, E. R. (2002) Three-axis superconducting gravity gradiometer for sensitive gravity experiments, *Rev. Sci. Instrum.* **73**, 3957–3974.
- 35** Jekeli, C. (1993) A review of gravity gradiometer survey system data analyses, *Geophys.* **58**, 508–514.
- 36** van Kann, F. J., Buckingham, M. J., Dransfield, M. H., Edwards, C., Mann, A. G., Matthews, R., Penny, R. D. and Turner, P. J. (1990) Laboratory tests of a mobile superconducting gravity gradiometer, *Physica B* **165**, 93–94.
- 37** Matthews, R. (2002) Mobile gravity gradiometry, Ph.D. thesis, University of Western Australia, Perth, Australia, unpublished.
- 38** van Kann, F. J., Buckingham, M. J., Edwards, C. and Matthews, R. (1994) Performance of a superconducting gravity gradiometer, *Physica B* **194–196**, 61–62.
- 39** Paik, H. J., Canavan, E. R. and Moody, M. V. (1997) Airborne/shipborne SGG survey system, in *Proc. Int. Symp. Kinematic Systems in Geodesy, Geomatics and Navigation*, M. E. Cannon and G. Lachapelle (eds.), University of Calgary, pp. 565–570.
- 40** Moody, M. V., Paik, H. J. and Canavan, E. R. (2003) Principle and performance of a superconducting angular accelerometer, *Rev. Sci. Instrum.* **74**, 1310–1318.
- 41** Adelberger, E. G., Heckel, B. R., Stubbs, C. W. and Rogers, W. F. (1991) Searches for new macroscopic forces, *Ann. Rev. Nucl. Part. Sci.* **41**, 269–320.
- 42** Antoniadis, I., Dimopoulos, S. and Dvali, G. (1998) Millimeter-range forces in superstring theories with weak-scale compactification, *Nucl. Phys. B* **516**, 70–82.
- 43** Paik, H. J. (1979) Null experiment to test the inverse square law of gravitation, *Phys. Rev. D* **19**, 2320–2324.
- 44** Chan, H. A. and Paik, H. J. (1984) Experimental test of a spatial variation of the Newtonian gravitational constant at large distances, in *Precision Measurements and Fundamental Constants II*, B.

- N. Taylor and W. D. Phillips (eds.), Natl. Bur. Stand. (US) Spec. Publ. 617, pp. 601–606.
- 45** Paik, H. J., Prieto, V. and Moody, M. V. (2004) Probing extra dimensions using a superconducting accelerometer, *J. Kor. Phys. Soc.* **45**, S104–S109.
- 46** Hoyle, C. D., Schmidt, U., Heckel, B. R., Adelberger, E. G., Gundlach, J. H., Kapner, D. J. and Swanson, H. E. (2001) Submillimeter tests of the gravitational inverse-square law: a search for “large” extra dimensions, *Phys. Rev. Lett.* **86**, 1418–1421.
- 47** Long, J. C., Chan, H. W., Churnside, A. B., Gulbis, E. A., Varney, M. C. M. and Price, J. C. (2003) Upper limits to submillimetre-range forces from extra space-time dimensions, *Nature* **421**, 922–925.
- 48** Paik, H. J., Moody, M. V. and Strayer, D. M. (2004) Short-range inverse-square law experiment in space, *Gen. Rel. Grav.* **36**, 523–537.
- 49** Everitt, C. W. F. (1974) The gyroscope experiment: I. General description and analysis of gyroscope performance, in *Experimental Gravitation*, B. Bertotti (ed.), Academic Press, New York, pp. 331–360.
- 50** Mashhoon, B., Paik, H. J. and Will, C. M. (1989) Detection of the gravitomagnetic field using an orbiting superconducting gravity gradiometer: Theoretical principles, *Phys. Rev. D* **39**, 2825–2838.
- 51** Blaser, J.-P., Bye, M., Cavallo, G. *et al.* (1993) Satellite Test of the Equivalence Principle (STEP), Phase A report to the European Space Agency, SCI (93) 4.
- 52** Su, Y., Heckel, B. R., Adelberger, E. G., Gundlach, J. H., Harris, M., Smith, G. L. and Swanson, H. E. (1994) New tests of the universality of free fall, *Phys. Rev. D* **50**, 3614–3636.
- 53** Peccei, R. D. and Quinn, H. R. (1977) CP conservation in the presence of pseudoparticles, *Phys. Rev. Lett.* **38**, 1440–1443.
- 54** Moody, J. E. and Wilczek, F. (1984) New macroscopic forces, *Phys. Rev. D* **30**, 130–138.
- 55** Turner, M. S. (1990) Windows on the axion, *Phys. Rep.* **197**, 67–97.
- 56** Ritter, R. C., Winkler, L. I. and Gillis, G. T. (1993) Search for anomalous spin-dependent forces with a polarized mass torsion pendulum, *Phys. Rev. Lett.* **70**, 701–705.
- 57** Ni, W.-T., Pan, S.-S., Yeh, H.-C., Hou, L.-S. and Wan, J. (1999) Search for an axion-like spin coupling using a paramagnetic salt with a dc SQUID, *Phys. Rev. Lett.* **82**, 2439–2442.
- 58** Youdin, A. N., Krause, Jr., D., Jagannathan, K., Hunter, L. R. and Lamoreaux, S. K. (1996) Limits on spin-mass couplings within the axion window, *Phys. Rev. Lett.* **77**, 2170–2173.
- 59** Bradley, R., Clarke, J., Kinion, D., Rosenberg, L. J., van Bibber, K., Matsuki, S., Mück, M. and Sikivie, P. (2003) Microwave cavity searches for dark-matter axions, *Rev. Mod. Phys.* **75**, 777–817.
- 60** Morgan, S. H. and Paik, H. J. (eds.) (1988) Superconducting Gravity Gradiometer Mission: II. Study Team technical report, NASA Technical Memorandum 4091.
- 61** McNutt, M., Paik, H. J., Bills, B. G. *et al.* (1996) Gravity for Earth, Ocean and Ice Dynamics (GEOID), ESSP mission proposal to NASA submitted in response to AO-96-MTPE-01.
- 62** Tapley, B. D. (1997) The gravity recovery and climate experiment (GRACE), *Suppl. EOS Trans. Am. Geophys. Union* **78**, 163.
- 63** Paik, H. J. and Lumley, J. M. (1996) Superconducting gravity gradiometers on STEP and GEM, *Class. Quantum Grav.* **13**, A119–A127.
- 64** Bell, R. E. and Watts, A. B. (1986) Evaluation of the BGM-3 sea gravity meter system onboard R/V Conrad, *Geophys.* **51**, 1480–1493.
- 65** Bell, R. E., Coakley, B. J. and Stemp, R. W. (1991) Airborne gravimetry from a small twin engine aircraft over the Long Island sound, *Geophys.* **56**, 1486–1493.
- 66** Brozena, J. M. and Peters, M. F. (1988) An airborne gravity study of eastern North Carolina, *Geophys.* **53**, 245–253.
- 67** Vasco, D. W. and Taylor, C. (1991) Inversion of airborne gravity gradient data, southwestern Oklahoma, *Geophys.* **56**, 90–101.

- 68** Biegert, E. K., Herring, A. Brett, J. *et al.* (1995) Comparisons of 3-D marine gravity gradiometry data and conventional marine gravity data survey in the Mississippi Canyon area, Gulf of Mexico, 1995 *Fall Meeting Abstracts*, American Geophysical Union.
- 69** Mueller, I. I. (1981) Keynote address: Inertial survey systems in the geodetic arsenal, in *Proc. 2nd Int. Symp. Inertial Technology for Surveying and Geodesy*, K.-P. Schwarz (ed.), Canadian Institute of Surveying, Ottawa, pp. 11–33.
- 70** Mezzena, R., Vinante, A., Falferi, P., Vitale, S., Bonaldi, M., Prodi, G. A., Cerdonio, M. and Simmonds, M. B. (2001) Sensitivity enhancement of Quantum Design dc superconducting quantum interference devices in two-stage configuration, *Rev. Sci. Instrum.* **72**, 3694–3698.
- 71** Paik, H. J. and Venkateswara, K. R. Y. (2004) Gravitational wave detection on the Moon and the moons of Mars, in *Proc. NASA/JPL Workshop on Physics for Planetary Exploration*, Solvang, California.

Appendix

Physical Constants, Abbreviations, and Symbols

This appendix lists physical constants, definitions of abbreviations (acronyms), and symbols of variables used in volumes I and II of the SQUID Handbook. General symbols, and those for SQUID devices, electronics, and systems generally remain the same throughout this Handbook and are listed first. However, applications of SQUIDs encompass multiple fields, each having its own terminology. The same symbol might have an entirely different meaning and definition, depending upon the application. Furthermore, abbreviations can be application-specific. Therefore, it is most effective to provide application-related listings separately for each chapter, that is, for each application field.

The general mathematical notation in volume II is in principle the same as in volume I. Vectors are represented in one of two ways, depending on the chapter. For example, the magnetic flux density (magnetic induction) vector can be represented by either \vec{B} or B ; in both cases the scalar value is B .

Physical Constants

| | |
|---|------------------------|
| $e = 1.6022 \times 10^{-19} \text{ C (A s)}$ | electron charge |
| $h = 6.6261 \times 10^{-34} \text{ J s}$ | Planck's constant |
| $\hbar = h/2\pi = 1.0546 \times 10^{-34} \text{ J s}$ | |
| $k_B = 1.3807 \times 10^{-23} \text{ J/K}$ | Boltzmann constant |
| $\varepsilon_0 = 8.8542 \times 10^{-12} \text{ A s/(V m)}$ | permittivity of vacuum |
| $\mu_0 = 4\pi \times 10^{-7} \text{ Vs/(A m)}$ | permeability of vacuum |
| $\Phi_0 \equiv h/2e = 2.0678 \times 10^{-15} \text{ Wb (Vs)}$ | flux quantum |

Abbreviations Used in Both Volumes

| | |
|-----|------------------------------|
| ac | alternating current |
| ADC | analog-to-digital converter |
| APF | additional positive feedback |

| | |
|------------------------------|---|
| BCF | bias current feedback |
| CFHX | counter-flow heat exchanger |
| CPR | current phase relation |
| DAC | digital-to-analog converter |
| dc | direct current |
| DLC | diamond-like carbon (thin-film etching mask of) |
| DROS | double relaxation oscillation SQUID |
| DSP | digital signal processor |
| EMI | electromagnetic interference |
| FA | field-applied |
| FEA | finite element analysis |
| FET | field-effect transistor |
| FLL | flux-locked loop |
| FR | field-removed |
| FWHM | full width at half-maximum |
| GBJ | grain boundary junction |
| GM | Gifford–McMahon |
| HTS | high-temperature superconductor/superconducting |
| HX | heat exchangers |
| I | insulator |
| ISJ | intrinsically shunted junction |
| JT | Joule–Thomson |
| LAO | LaAlO_3 |
| LSB | least significant bit |
| LTS | low-temperature superconductor/superconducting |
| MCG | magnetocardiography, magnetocardiogram |
| MEG | magnetoencephalography, magnetoencephalogram |
| MLI | superinsulation, or multilayer insulation |
| MRI | magnetic resonance imaging |
| MTTF | mean time to failure |
| MUSIC | multiple signal classification |
| N | normal conductor |
| NIS | normal–insulator–superconductor |
| NDE | nondestructive evaluation (of materials and structures) |
| NDT | nondestructive testing |
| PBCO | $\text{PrBa}_2\text{Cu}_3\text{O}_7$ |
| PECVD | plasma-enhanced chemical vapor deposition |
| $\text{PI}^{3/2}$ integrator | integrator with a gain slope of -30 dB/decade |
| PLD | pulsed laser deposition |
| PMMA | polymethyl methacrylate |
| RCSJ | resistively and capacitively shunted junction |
| rf | radio frequency |
| RIE | reactive ion etching |
| rms | root mean square |
| ROS | relaxation oscillation SQUID |

| | |
|-------|---|
| RRR | residual resistivity ratio |
| RSFQ | rapid single-flux quantum |
| RSJ | resistively shunted junction |
| RSJN | nonlinear resistive junction |
| RTS | random telegraph signal |
| S | superconductor |
| SAC | self-aligned contact |
| SIS | superconductor–insulator–superconductor (tunnel junction) |
| SNS | superconductor–normal conductor–superconductor (junction) |
| SHAD | second harmonic detection |
| SNAP | selective niobium anodization process |
| SNEAP | selective niobium etch and anodization process |
| SNEP | selective niobium etch process |
| SNIP | selective niobium insulation process |
| SNR | signal-to-noise ratio |
| SQUID | superconducting quantum interference device |
| SSP | signal space projection |
| STO | SrTiO_3 |
| TEM | transient electromagnetic (<i>e.g.</i> , geomagnetic exploration method) |
| TJM | tunnel junction microscopic |
| UHF | ultrahigh frequency |
| W | working point |
| YBCO | $\text{YBa}_2\text{Cu}_3\text{O}_7$ |
| YSZ | yttria-stabilized zirconia |
| ZBCP | zero bias conductance peak |
| ZES | zero energy state |
| ZFC | zero-field cooled |

General Symbols

| | |
|-----------------------|--------------------------------|
| \vec{A} | vector potential |
| \vec{B}, \mathbf{B} | magnetic flux density |
| B_0 | cooling field |
| C | capacitance |
| \vec{E}, \mathbf{E} | electric field |
| F_d | external driving force |
| f | frequency |
| \vec{H}, \mathbf{H} | magnetic field intensity |
| I | current |
| i | imaginary unit |
| L | inductance |
| \vec{M}, \mathbf{M} | magnetic moment, magnetization |

| | |
|-----------------------|--|
| M | mutual inductance |
| m | mass |
| Q | quality factor |
| R | resistance |
| \vec{r}, \mathbf{r} | spatial coordinate (of field point) |
| T | temperature |
| t | time |
| δ | electromagnetic skin depth (penetration depth) |
| ε | absolute permittivity |
| ε_r | relative permittivity |
| μ | absolute permeability |
| μ_r | relative permeability |
| ξ | friction coefficient |
| σ | electric conductivity |
| τ | relaxation time |
| $\vec{\Phi}, \Phi$ | magnetic flux |
| χ | magnetic susceptibility |
| ω | angular frequency |

Superconductors, General

| | |
|-------------------------|--|
| B_T | threshold field for vortex entry |
| $D(U)$ | distribution of activation energies for vortex motion |
| $H_c = B_c/\mu_0$ | thermodynamic critical field of superconductor |
| $H_{c1} = B_{c1}/\mu_0$ | lower critical field of type II superconductor |
| $H_{c2} = B_{c2}/\mu_0$ | upper critical field of type II superconductor |
| I_s | supercurrent |
| j_c | maximum supercurrent density |
| $j_{c,p}$ | depairing critical current density |
| j_s | supercurrent density |
| m_p | mass of Cooper pair |
| n_p | density of Cooper pairs |
| n_{p0} | density of Cooper pairs in the absence of a supercurrent |
| q_p | charge of Cooper pair |
| T_c | critical temperature of superconductor |
| v_p | velocity of Cooper pairs |
| a_{cp} | condensation energy per Cooper pair |
| Δ | energy gap for quasiparticle excitation |
| Δ_0 | maximum value of energy gap at $T = 0$ |
| κ | Ginzburg Landau parameter |
| λ_L | London penetration depth |
| ζ | Ginzburg Landau coherence length |

| | |
|--------------------|---|
| φ | phase of superconducting wave function |
| $\Psi(\vec{r}, t)$ | superconducting wave function |
| Ψ_0 | real amplitude of superconducting wave function |

Josephson Junctions

| | |
|---|---|
| A_J | cross-section of Josephson junction |
| A_{Jp} | parasitic area of Josephson junction |
| C | total capacitance of Josephson junction |
| C_{Jp} | parasitic capacitance of Josephson junction |
| $c_j \equiv C/A_J$ | capacitance per junction cross-section |
| $D(E)$ | distribution of activation energies |
| $E_J \equiv I_0\Phi_0/2\pi$ | Josephson coupling energy |
| $f_J \equiv \omega_J/2\pi = V/\Phi_0$ | Josephson frequency |
| $f_\delta \equiv -\partial u_j / \partial \delta$ | effective “force” (negative gradient) of tilted washboard potential |
| I | current through Josephson junction |
| I_0 | maximum supercurrent through Josephson junction |
| I_{ac} | amplitude of ac bias current |
| I_d | displacement current |
| I_N | noise current |
| I_{qp} | quasiparticle tunneling current |
| I_r | return critical current of hysteretic Josephson junction |
| $I_{th} \equiv I I_0 = 2\pi k_B T / \Phi_0$ | thermal noise current |
| $i \equiv I/I_0$ | normalized current through Josephson junction |
| $i_{ac} \equiv I/I_{ac}$ | normalized amplitude of ac bias current |
| $i_N \equiv I_N/I_0$ | normalized noise current |
| $i_r \equiv I/I_r$ | normalized return critical current |
| $j_0 \equiv I_0/A_J$ | maximum supercurrent density of Josephson junction |
| L_{jp} | parasitic inductance of Josephson junction |
| R | shunt resistance of Josephson junction |
| R_n | normal resistance of Josephson tunnel junction |
| $S_I(f), S_I(\omega)$ | power spectral density of current noise |
| $S_i(f), S_i(\omega)$ | power spectral density of normalized current noise |
| t_{eff} | magnetic thickness of Josephson junction |
| U | time-dependent voltage across Josephson junction |
| U_J | tilted washboard potential of Josephson junction |
| $u \equiv U/I_0 R$ | normalized time-dependent voltage across Josephson junction |
| $u_j \equiv U_J/E_J$ | normalized tilted washboard potential of Josephson junction |
| V | time-averaged voltage across Josephson junction |
| $V_c \equiv I_0 R$ | characteristic voltage of Josephson junction |
| V_{gap} | gap voltage |

| | |
|---|---|
| V_n | voltage of n th Shapiro step |
| V_r | return critical voltage of hysteretic Josephson junction |
| $\nu \equiv V/I_0 R$ | normalized time-averaged voltage across Josephson junction |
| $\beta_c = \frac{2\pi}{\Phi_0} I_0 R^2 C$ | Stewart–McCumber parameter |
| $\Gamma \equiv k_B T/E_1 = 2\pi k_B T/I_0 \Phi_0$ | noise parameter |
| δ | gauge invariant phase difference across Josephson junction |
| ΔI_n | height of n th Shapiro step |
| Δi_n | normalized height of n th Shapiro step |
| $\lambda_J = \sqrt{\Phi_0/2\pi\mu_0 j_0}$ | Josephson penetration depth |
| $\rho_J \equiv R \times A_J$ | resistance times junction cross-section |
| ρ_n | normal resistivity of Josephson junction |
| $\sigma(t, \delta, u)$ | probability density of finding system at point $[\delta, u]$ in phase space at the moment t |
| $\tau \equiv t \times \omega_c$ | normalized time |
| $\Omega_{ac} \equiv \omega_{ac}/\omega_c$ | normalized frequency of ac bias current |
| ω_{ac} | frequency of ac bias current |
| $\omega_c \equiv 2\pi V_c/\Phi_0$ | characteristic frequency of Josephson junction |
| $\omega_J \equiv 2\pi V/\Phi_0$ | Josephson frequency |
| $\omega_p \equiv 2\pi I_0/C\Phi_0$ | plasma frequency at zero bias current |
| $\omega_{p,i}$ | plasma frequency of Josephson junction |
| $\omega_{RC} \equiv 1/RC$ | frequency of RC circuit |

SQUIDs, General

| | |
|---|--|
| $A_{eff} = \Phi_s/B_a$ | effective area of SQUID |
| A_p | geometric area of the pickup coil |
| $A_{p,eff}$ | effective area of the pickup coil |
| A_R | parasitic area of junction shunt resistor |
| A_{spoke} | parasitic area of coplanar microstripline “spokes” in “wagon-wheel” magnetometer |
| a | outer dimension of pickup coil |
| B_a | external field applied to the pickup coil |
| $B_N = \sqrt{S_\phi}/A_{eff} = \sqrt{S_\phi^{(p)}}/A_p$ | magnetic field spectral resolution (field noise) |
| $B_\phi = \partial B/\partial \Phi = 1/A_{eff}$ | field sensitivity or field-flux conversion coefficient |
| b | gradiometer baseline |
| b_{sl} | length of slit in SQUID ring |

| | |
|--------------------------------------|--|
| C_{gp} | parasitic capacitance of groundplane over SQUID slit |
| C_p | parasitic capacitance across the SQUID inductance |
| C_R | parasitic capacitance of junction shunt resistor |
| C_x | capacitor of series $R_x C_x$ shunt across the input coil |
| C'_{strip} | input coil microstripline capacitance per unit length |
| D | mean diameter of wire-wound pickup coil |
| d | inner side length or diameter of SQUID hole or pickup coil, wire diameter of wire-wound pickup coil |
| F | coil factor for wire-wound pickup coils |
| f_c | $1/f$ noise corner frequency |
| $f_{\text{op}} = 0.3 I_0 R / \Phi_0$ | frequency corresponding to optimal SQUID operating point |
| f_s | microstripline resonant frequency of SQUID input coil |
| f_r | SQUID LC resonant frequency |
| f_w | SQUID washer resonant frequency |
| $G_{1,\Phi}$ | field gradient sensitivity, first-order gradiometer |
| $G_{2,\Phi}$ | field gradient sensitivity, second-order gradiometer |
| h | dielectric insulator thickness (also Planck's constant) |
| J | circulating current |
| J_s | current circulating in flux transformer |
| $j = J/I_0$ | normalized circulating current |
| k_i | input coil coupling constant |
| L | inductance of the SQUID ring |
| L_{cop} | inductance of coplanar microstripline |
| L_{dc} | effective SQUID inductance including screening effect of the input coil |
| $L_F = 2\pi k_B T / \Phi_0 I_0$ | fluctuation threshold inductance |
| L_g | geometric inductance |
| L_h | inductance of SQUID ring hole |
| L_i | input coil inductance |
| $L_{i,\text{eff}}$ | effective input coil inductance including screening effect of the SQUID loop |
| L_{kin} | kinetic inductance |
| L_{leads} | inductance of twisted pair leads |
| L_{loop} | inductance of a wire loop |
| L_p | inductance of pickup coil |
| L_{sl} | inductance of slit in SQUID ring |
| L_{spoke} | parasitic inductance of coplanar microstripline "spokes" in "wagon-wheel" magnetometer |
| L_{tot} | total inductance of SQUID ring |
| L'_{strip} | input coil microstripline inductance per unit length |
| l | length of input coil microstripline; length of wire-wound pickup coil |
| l_{eff} | effective length of input coil |
| M_i | mutual inductance between SQUID loop and input coil |

| | |
|---|--|
| N | number of turns in wire-wound pickup coil |
| N_i | number of turns in input coil |
| p | pitch of wire-wound pickup coil |
| R_x | damping resistor of series $R_x C_x$ shunt across the input coil |
| $S_B = S_\phi / A_{\text{eff}}^2 = B_N^2$ | power spectral density of magnetic field noise |
| $S_{G,1}$ | power spectral density of first-order gradiometer flux noise |
| $S_{G,2}$ | power spectral density of second-order gradiometer flux noise |
| S_I | power spectral density of current noise referred to SQUID input |
| S_r | power spectral density of radial vortex motion |
| S_T | power spectral density of temperature fluctuations |
| $S_\phi^{(p)}$ | power spectral density of flux noise |
| S_ϕ | power spectral density of flux noise referred to the pickup coil |
| s | input circuit screening factor |
| s_c | spacing between a pair of coplanar microstriplines |
| s_i | spacing between turns of input coil |
| $s_{\text{in}} = L_i / (L_i + L_p)$ | input coil screening factor |
| t | superconducting film thickness |
| t_i | film thickness of SQUID input coil |
| U_{SQUID} | SQUID potential |
| $u_{\text{SQUID}} = U_{\text{SQUID}} / E_J$ | normalized SQUID potential |
| w | superconducting film width |
| w_c | linewidth of coplanar microstripline |
| w_i | linewidth of input coil |
| w_p | linewidth of pickup coil |
| Z | microstripline impedance |
| Z_L | impedance of a microstripline termination |
| Γ_r | reflection coefficient at the termination of a microstripline |
| $\varepsilon = S_\phi / 2L$ | energy resolution |
| $\varepsilon_c = S_\phi / 2k_i^2 L = S_I L_i / 2$ | coupled energy resolution (spectral noise energy in input coil) |
| $\varepsilon^{(p)}$ | energy resolution referred to the pickup coil |
| $\lambda_{L,i}$ | London penetration depth of SQUID input coil |
| $\lambda_{L,w}$ | London penetration depth of SQUID washer |
| σ | probability density distribution |
| Φ_a | applied flux |
| $\Phi_N = \sqrt{S_\phi}$ | magnetic flux resolution (flux noise) |
| Φ_s | flux coupled into the SQUID by a pickup coil structure |

Φ_T
 $\phi_a = \Phi_a/\Phi_0$

total flux
normalized applied flux

Dc SQUID

| | |
|---|--|
| C | average junction capacitance |
| $e = s_\phi/2\Gamma\beta_L = eI_0R/2\Phi_0k_B T$ | normalized energy resolution |
| h | hysteresis parameter (degree of hysteresis in dc SQUID) |
| I | current through SQUID |
| I_0 | average junction critical current |
| I_b | SQUID bias current |
| I_c | critical current of SQUID |
| $i \equiv I/I_0$ | normalized current through SQUID |
| $M_{\text{dyn}} = R_{\text{dyn}}/V_\phi$ | current sensitivity of SQUID at working point |
| R | average junction resistance |
| R_d | damping resistor (shunting the SQUID inductance) |
| R_{dyn} | dynamic resistance of SQUID at working point |
| S_V | power spectral density of voltage noise |
| $s_\nu = S_V \frac{2\pi}{I_0 R \Phi_0}$ | normalized power spectral density of voltage noise |
| $s_\phi = s_\nu/v_\phi^2 = S_\phi \cdot 2_0 R / \Phi_0^3$ | normalized power spectral density of flux noise |
| U | time-dependent voltage across SQUID |
| $u \equiv U/I_0 R$ | normalized time-dependent voltage across SQUID |
| V | time-averaged voltage across SQUID |
| V_b | SQUID bias voltage |
| $\partial V / \partial \Phi_a$ | SQUID transfer coefficient |
| V_{pp} | peak-to-peak modulation of $V - \Phi_a$ characteristic |
| V_ϕ | SQUID transfer coefficient optimized with respect to bias current and flux |
| $v \equiv V/I_0 R$ | normalized time-averaged voltage across SQUID |
| $v_\phi = V_\phi \Phi_0 / I_0 R$ | normalized transfer function |
| \bar{X} | temporal average of quantity X |
| $a = L/4L_F$ | normalized SQUID inductance |
| a_C, a_I, a_R | asymmetry in junction capacitance, critical current, or resistance |
| a_L | asymmetry in SQUID loop inductance |
| $\beta_L \equiv \frac{2LI_0}{\Phi_0}$ | screening parameter of dc SQUID |
| $\gamma = R/R_d$ | damping parameter for shunted SQUID inductance |

| | |
|--|---|
| $\delta_+ \equiv (\delta_1 + \delta_2)/2$ | rotated coordinates for dc SQUID potential |
| $\delta I, \delta V, \delta\Phi_a$ | small change in current, voltage, or applied flux |
| δV^* | in-phase critical current or resistance fluctuation |
| $\delta\Phi^*$ | out-of-phase critical current or resistance fluctuation |
| Φ_b | SQUID bias flux |
| $\Phi_{\text{lin}} = V_{\text{pp}}/V_\Phi$ | linear flux range |

Rf SQUID

| | |
|--|--|
| C_M | matching capacitance |
| C_T | capacitance of tank circuit |
| I_{rf} | peak rf current in tank circuit |
| $i_{\text{rf}} = I_{\text{rf}} M 2\pi/\Phi_0$ | normalized rf current in tank circuit |
| $J_m(x)$ | Bessel functions of first kind of order m and variable x |
| $k = M/\sqrt{L L_T}$ | coupling coefficient between SQUID loop and tank circuit |
| L_T | inductance of tank circuit |
| M | mutual inductance between SQUID loop and tank circuit |
| $Q = R_T/\omega_0 L_T$ | quality factor of tank circuit (loaded) |
| Q_0 | unloaded quality factor of tank circuit |
| R_T | tank circuit impedance at resonance frequency (parallel resistance) |
| T_{eff} | effective noise temperature of the tank circuit, transmission line, and preamplifier lumped together |
| V_T | SQUID output voltage (peak rf voltage across tank circuit) |
| $\partial V_T / \partial \Phi_a$ | transfer function of rf SQUID |
| $v_T = V_T(k/\omega_{\text{rf}})\sqrt{L/L_T}2\pi/\Phi_0$ | normalized SQUID output voltage |
| $\langle X \rangle$ | statistical average of quantity X |
| Z | output impedance of rf SQUID |
| α | step tilting parameter |
| $\beta_{\text{rf}} \equiv \frac{2\pi L I_0}{\Phi_0} = \pi \beta_L$ | screening parameter of rf SQUID |
| λ | wave length |
| $\xi = (\omega_{\text{rf}} - \omega_0)/\omega_0$ | detuning of drive frequency from tank circuit resonant frequency |
| ρ | phase difference between rf bias current I_{rf} and SQUID output rf voltage V_T |
| $\Phi_{a,\text{rf}}$ | external applied rf flux |

| | |
|--|---|
| Φ_c | critical magnetic flux (for which a quantum transition takes place) |
| Φ_{EMI} | magnetic flux of electromagnetic interference |
| $\phi_{\text{a,rf}} = \Phi_{\text{a,rf}} / \Phi_0$ | normalized applied rf flux |
| $\omega_0 = 1 / \sqrt{L_{\text{T}} C_{\text{T}}}$ | tank circuit resonant frequency |
| $\omega_{\text{cut}} = R / L$ | SQUID cutoff frequency |
| $\omega_{\text{R}} = \omega_{\text{rf}} / \omega_{\text{cut}}$ | reduced operating frequency |
| $\omega_{\text{rf}} = 2\pi f_{\text{rf}}$ | frequency of rf bias current |

SQUID Electronics

| | |
|---|---|
| f_1 | unity-gain frequency of open feedback loop |
| $f_{1,\text{max}} = 1 / 4\pi t_{\text{d}}$ | maximum unity-gain frequency |
| f_2, f_2' | corner frequencies of two-pole integrator |
| $f_{3\text{dB}}$ | FLL bandwidth |
| $f_{3\text{dB,max}} = 0.18 / t_{\text{d}}$ | maximum FLL bandwidth |
| f_{APF} | cut-off frequency of APF circuit |
| f_b | bias reversal frequency |
| f_{clk} | clock frequency |
| f_{GBW} | gain-bandwidth product of feedback electronics |
| f_{mod} | modulation frequency |
| f_{peak} | frequency of peak in closed-loop frequency response |
| f_{RO} | relaxation oscillation frequency |
| G_{APF} | low-frequency small-signal voltage gain obtained with APF |
| $G_{\text{electronics}}$ | feedback electronics gain |
| G_{FLL} | closed-loop gain of FLL |
| G_{OL} | total gain of open feedback loop |
| $G_{\text{SQUID}} = V_{\Phi} M_{\text{f}} / R_{\text{f}}$ | SQUID gain |
| G_{Φ} | low-frequency small-signal flux gain in two-stage configuration |
| L_{amp} | input coil inductance of amplifier SQUID |
| L_{APF} | inductance of APF coil |
| L_{sh} | shunt inductance of ROS or DROS |
| I_{clk} | comparator clock current |
| I_{f} | feedback current |
| I_{in} | current in SQUID input coil |
| I_{out} | output current of voltage-biased SQUID |
| M_{amp} | mutual inductance between the amplifier SQUID and its input coil (in two-stage SQUID configuration) |
| M_{APF} | mutual inductance between APF coil and SQUID |
| M_{f} | mutual inductance between feedback coil and SQUID |
| R_{APF} | APF resistance |
| R_{b} | bias resistance |

| | |
|---|--|
| R_f | feedback resistance |
| R_{in} | real part of preamplifier input impedance |
| R_{sh} | shunt resistance of ROS or DROS |
| $S_{I,amp}$ | preamplifier current noise density |
| $S_{V,amp}$ | preamplifier voltage noise density |
| $S_{V,APF}$ | power spectral density of equivalent APF noise source |
| $S_{\phi,amp}$ | preamplifier flux noise contribution |
| $S_{\phi,FLL}$ | flux noise density in FLL mode |
| t_d | equivalent loop delay |
| V_0^*, V_ϕ^* | offset voltage and slope of straight-line fit to $V-\Phi_a$ characteristic |
| V_f | voltage across feedback resistor |
| V_{in} | preamplifier input voltage |
| V_{out} | output voltage |
| β_{APF} | APF feedback parameter |
| δI_{out} | small change in output current |
| δV_{out} | small change in output voltage |
| $\delta\Phi$ | deviation of flux in SQUID from value at working point (flux error) |
| $\delta\Phi_{n,pp}$ | peak-to-peak noise flux fed back into SQUID operated in FLL mode |
| $\delta\Phi_{pp}$ | peak-to-peak value of $\delta\Phi$ |
| Φ_{amp} | flux applied to amplifier SQUID |
| Φ_f | feedback flux |
| $\dot{\Phi}_f \equiv \partial\Phi_f/\partial t _{max}$ | system slew rate |
| $\dot{\Phi}_{f,max}$ | maximum system slew rate |
| Φ_{LSB} | LSB of digital SQUID referred to flux input |
| Φ_{nl} | nonlinear error flux |
| φ_{OL} | total phase of open feedback loop |

SQUID Systems

| | |
|-------|--|
| A | low-frequency noise constant of proportionality corresponding to the noise measured with gradiometer with baseline b |
| A | matrix constructed from matrix of rotation elements and sensor gains |
| A_E | area of an eddy current source |
| A_o | low-frequency noise constant of proportionality corresponding to the noise measured with gradiometer with baseline b_o |
| A_p | magnetometer coil area |

| | |
|--------------------------------------|---|
| a | sensor gain equal to the inverse of the field-to-flux conversion coefficient |
| α | matrix of rotation |
| $\alpha(t_n)$ | vector of noise space waveforms at time t_n |
| α_B | minimum allowed reference magnetometer gain devised not to increase balanced gradiometer white noise (equal to the inverse of the field-to-flux conversion coefficient) |
| α_k | sensor gain for component k , $k = 11, 12, 13, 22, 23$ (equal to the inverse of the field-to-flux conversion coefficient) |
| $\alpha_k(t_n)$ | component k of the vector of noise space waveforms at time t_n |
| α_r | sensor gain for reference magnetometers (equal to the inverse of the field-to-flux conversion coefficient) |
| B, B | field at a general position |
| \dot{B} | magnetic field slew rate in T/s |
| B_i^t | vector of magnetic field time samples for a component B_i |
| B_{low} | square root of low-frequency noise density |
| B_N | square root of total noise density |
| B_o, B_0 | field at the coordinate origin |
| B_{rms} | rms noise |
| B_p, B_{T1}, B_{T2} | total field acting on a magnetometer coil |
| B_w | square root of white noise density |
| $b(t_n)$ | vector of signal waveforms at time t_n |
| b, b, b_1, b_1, b_o, b_o | first-order gradiometer baseline |
| b_2, b_2, b_2', b_2' | second-order gradiometer baseline |
| b_3, b_3, b_3', b_3' | third-order gradiometer baseline |
| $b\delta G$ | gradiometer system white noise in 1-Hz bandwidth multiplied by the gradiometer baseline (includes SQUID and electronics noise, dewar noise, etc.) |
| $C_B, C_B = C_B $ | field common mode vector and its magnitude |
| C_{G1} | first gradient common mode vector |
| C_{G2} | second gradient common mode vector |
| C_o, C_o | "as made" field common mode vector and its magnitude |
| C_p | specific heat |
| C_R | required level of the field common mode vector balance |
| C_S | field common mode vector magnitude which would be induced by the eddy current object if it were superconducting |
| $D_{\text{mag}}, D_{\text{grd}}$ | dynamic range of magnetometer or gradiometer |
| $D_{\text{grd}}^C, D_{\text{grd}}^G$ | gradiometer dynamic range imposed by field common mode vector or by the environmental gradients |
| E | electric field intensity inside the shield |
| E_0 | intensity of the electric field |

| | |
|---|---|
| E_B , $E_B = E_B $ | field eddy current vector and its magnitude |
| E_{Gi} | i th gradient eddy current vector |
| E_R | required level of the field eddy current vector balance |
| f_E | characteristic frequency of an eddy current source |
| f_{\min} | minimum frequency of interest |
| f_o | onset of low-frequency noise measured with gradiometer with baseline b_o |
| f_{ob} | onset of low-frequency noise measured with gradiometer with baseline b |
| G , $G^{(1)}$, G , $G^{(1)}$ | first gradient tensor |
| $G^{(2)}$, $G^{(2)}$ | second gradient tensor |
| $G^{(3)}$, $G^{(3)}$ | third gradient tensor |
| G_{11} , G_{12} , G_{13} , G_{22} , G_{23} | first gradient tensor components |
| G_{111} , G_{112} , G_{113} , G_{122} , G_{123} , G_{222} , G_{223} | second gradient tensor components |
| G_E | first gradient tensor corresponding to the environmental gradients |
| G_i^t | vector of time samples of a component i of the first gradient tensor projection into the gradiometer baseline |
| $G(k)$ | gradiometer spatial transfer function |
| G_R | rotated first gradient tensors of the environmental gradient |
| $g^{(0)}$ | magnetometer (zeroth-order gradiometer) output |
| $g^{(1)}$ | first-order gradiometer output |
| $g^{(2)}$ | second-order gradiometer output |
| $g^{(3)}$ | third-order gradiometer output |
| $g_k^{(1)}$ | output of a first-order gradiometer component k , $k = 11, 12, 13, 22, 23$ |
| g_k^R | component k ($k = 11, 12, 13, 22, 23$) of the rotated first gradient tensor |
| g^m | measured output of first gradient tensor |
| g^R | output of all components of the rotated first gradient tensor |
| I | identity matrix |
| I_{cm} | common-mode current |
| I_{dm} | differential-mode current |
| K | number of channels |
| K_N | number of noise components |
| K_S | number of signal components |
| k | slope of low-frequency noise amplitude vs. frequency on log–log scale |

| | |
|--|---|
| k_s | spatial frequency |
| L_E | inductance of an eddy current source |
| $L_{\text{mag}}, L_{\text{grd}}$ | permitted magnetometer or gradiometer |
| | nonlinearity |
| M_E | mutual inductance between an eddy current source and a magnetometer coil |
| $M_{\text{source}}, M_{\text{dip}}, M_1, M_2, M_3$ | magnetic dipole moments |
| \mathbf{m} | $K \times N$ matrix of measurements |
| $\mathbf{m}_{\text{noise}}(t_n)$ | K -component vector of noise measurement at time t_n |
| N | number of time samples |
| N_{ave} | number of averages |
| n_{loc} | exponent in the field decay law with distance for a local anomaly |
| n_{reg} | exponent in the field decay law with distance for a regional anomaly |
| P | pressure |
| P_\perp | orthogonal projection operator |
| P_\parallel | parallel projection operator |
| \mathbf{p}, \mathbf{p}' | coil orientation vector |
| Q_{H1} | rejection of heat |
| Q_{H2} | associated heat |
| Q_L | heat of expansion |
| q | exponent that determines relationship between the system white noise in 1-Hz bandwidth and electronics bit resolution: $\delta B = 2^q \partial B$, $\delta G = 2^q \partial G$ (∂B , ∂G represent electronic bit resolution of magnetometer or gradiometer multiplied by baseline, in T) |
| R_g | effective volume (responsivity) |
| \mathbf{r}, r | distance from magnetometer or gradiometer to a source |
| r_b | distance normalized by three times the gradiometer baseline |
| r_i | reference outputs, $i = 1, 2, \dots$ |
| \mathbf{r}_{ref} | vector of reference outputs |
| S | synthetic system output |
| \mathbf{S} | vector of time samples of the synthetic system outputs |
| S_{cube} | shielding factor for a cube |
| S_{cylinder} | shielding factor for a cylinder |
| S_{sphere} | shielding factor for a sphere |
| $\ S \ _{\min}^{\text{adapt}}$ | signal vector norm determined by minimizing the system noise |

| | |
|------------------------------|--|
| $\ S\ _{\min}^{\text{grad}}$ | signal vector norm determined by requiring that the system be a gradiometer |
| T_H | environmental high temperature |
| T_L | environmental low temperature |
| t_1, t_2, t_i, t_k, t_n | time instances (time samples) |
| U | $K \times K_S$ matrix composed of signal column vectors |
| U_k | signal column vector, $k = 1, 2, \dots, K_S$ |
| $u_k(t_n)$ | component k of the signal space waveforms at time t_n |
| V | matrix composed of noise column vectors |
| V_k | K -component noise column vectors, $k = 1, 2, \dots, K_N$ |
| X | crosstalk matrix for first gradient tensor components |
| y_1 | vector of five independent components of a first gradient tensor |
| y_2 | vector of seven independent components of second gradient tensor |
| y_E | vector of independent components of the tensor G_E |
| Z_S | intrinsic impedance of a shield |
| Z_W | wave impedance of the incident energy |
| Z_{WB} | B -field component of the wave impedance |
| Z_{WE} | E -field component of the wave impedance |
| ΔB | field change applied to either a magnetometer coil, or a field difference between two first-order gradiometer coils |
| Δd | amplitude of translational vibrations |
| Δf | bandwidth of measurement |
| $\Delta \kappa$ | difference of the eddy current coupling constants between two gradiometer coils |
| $\partial B, b\partial G$ | electronic bit resolution of magnetometer or gradiometer multiplied by baseline (in T) |
| δB | magnetometer system white noise in 1-Hz bandwidth (includes SQUID and electronics noise, dewar noise, etc.) |
| $\delta t^{(1)}$ | maximum allowed time delay between channels determined by the requirement of negligible eddy current term |
| $\delta t^{(2)}$ | maximum allowed time delay between channels when the eddy current term is balanced out using constant coefficients |
| $\delta\Phi_B$ | flux resolution of magnetometer systems (contains SQUID system and electronics noise, dewar noise, or any other system noise) |
| $\delta\Phi_G$ | flux resolution of gradiometer systems (contains SQUID system and electronics noise, dewar noise, or any other system noise) |
| $\delta\Phi_r$ | flux resolution of reference magnetometers (contains SQUID system and electronics noise, dewar noise, or any other system noise) |

| | |
|--|--|
| ζ | strength of inequality for the reference magnetometer gain design |
| θ | amplitude of rotational vibrations |
| $\kappa, \kappa_1, \kappa_2$ | eddy current coupling constants |
| $\mu = (\partial T / \partial P)_H$ | Joule–Thomson coefficient |
| $v(t_n)$ | K-component vector of sensor noise at time t_n |
| ξ | vector of subtraction coefficients |
| ξ_i | component i of the subtraction coefficient |
| $\dot{\Phi}_{\text{grd}}^C, \dot{\Phi}_{\text{grd}}^G$ | gradiometer slew rates imposed by field common mode vector or by environmental gradients, in Φ_0/s |
| $\dot{\Phi}_{\text{mag}}, \dot{\Phi}_{\text{grd}}$ | magnetometer or gradiometer slew rates in Φ_0/s |
| φ_n | coefficient for a power law nonlinearity of n th order |
| Ψ | constant containing all orientation-dependent parts of the dipole equation |
| ψ | environmental noise attenuation |
| ψ_{grd} | environmental noise attenuation required for gradiometer operation |
| ψ_{mag} | environmental noise attenuation required for magnetometer operation |
| $\omega_E = 2\pi f_E$ | characteristic frequency of an eddy current source |

Chapter 8: SQUID Voltmeters and Amplifiers

Abbreviations

| | |
|---------|--|
| CDM | cold dark matter |
| CMB | cosmic microwave background |
| DFSZ | Dine–Fischler–Srednicki–Zhitnitsky |
| FIBRE | Fabry–Perot interferometer research experiment |
| fMUX | frequency-domain multiplexer |
| HEMT | high-electron-mobility transistor |
| HFET | heterojunction field-effect transistor |
| JFET | junction field-effect transistor |
| KSVZ | Kim–Shifman–Vainshtein–Zakharov |
| MMIC | millimeter integrated circuit |
| NASA | National Aeronautics and Space Administration |
| NEP | noise equivalent power |
| NMR | nuclear magnetic resonance |
| NQR | nuclear quadrupole resonance |
| RFSET | radio-frequency single-electron transistor |
| SCUBA-2 | submillimeter common user bolometer array 2 |
| SLUG | superconducting low-inductance undulatory galvanometer |
| TES | transition-edge sensor |
| UV | ultraviolet |
| WIMP | weakly interacting massive particle |

Symbols

| | |
|------------------|---|
| B_0 | Larmor magnetic field |
| B_p | prepolarizing field |
| b_{LC} | bandwidth of resonant filter in fMUX |
| C_0 | capacitance per unit length of microstrip |
| C_a | magnetic calorimeter absorber heat capacity |
| C_f | capacitor value for resonant filter in fMUX |
| C_h | detector heat capacity without feedback |
| C_i | series capacitance of input circuit of SQUID |
| C_j | tunnel junction capacitance |
| C_{\max} | largest capacitor value in fMUX |
| d | thickness of dielectric in microstrip |
| E_{\max} | saturation energy of TES calorimeter |
| eQ_e | nuclear quadrupole moment |
| f_{\max} | frequency response elbow of the TES = $1/2\pi\tau_{\text{eff}}$ |
| f_{\min} | minimum fMUX bias frequency |
| G | differential thermal conductivity = dP/dT |
| G_1 | signal geometric prefactor for magnetic calorimeter |
| G_P | power gain of amplifier |
| G_V | voltage gain of amplifier |
| h_t | height of magnetic calorimeter thermometer |
| I | nuclear angular momentum in units of \hbar |
| I_c | crosstalk current for fMUX crosstalk calculation |
| I_m | current in m th TES for fMUX crosstalk calculation |
| I_n | current in n th TES for fMUX crosstalk calculation |
| I_{TES} | current through TES |
| i_n | equivalent current noise referred to input coil of SQUID series array |
| J_ϕ | flux-to-current transfer coefficient of dc SQUID |
| J_ϕ^r | reduced flux-to-current transfer coefficient of dc SQUID |
| $J_N^r(\omega)$ | reduced current noise of dc SQUID |
| k_{ie} | effective coupling coefficient between SQUID and input circuit |
| L_0 | inductance per unit length of microstrip |
| L_f | inductor value for resonant filter in fMUX |
| L^r | reduced inductance of dc SQUID |
| L_s | stray inductance of flux transformer |
| L_T | total inductance of input circuit |
| l | dynamic input inductance of dc SQUID |
| l_{TES} | electrothermal feedback loop gain = $a_{\text{TES}} P_b / GT$ |
| M_0 | equilibrium magnetization of an ensemble of nuclear spins |
| M_t | magnetization of magnetic calorimeter thermometer |
| m_a | axion rest mass |
| m_I | nuclear magnetic quantum number |
| N | number of nuclei per unit volume |
| N_c | crosstalk noise current for fMUX crosstalk calculation |
| N_{col} | number of array columns multiplexed |

| | |
|-------------------|--|
| N_r | noise in TES for fMUX crosstalk calculation |
| N_{row} | number of array rows multiplexed |
| N_s | number of SQUIDs in SQUID array |
| n_a | number density of axions |
| P_b | background power on thermal detector |
| P_{bias} | bias power on thermal detector |
| P_{max} | saturation power of TES |
| P_o | optical power on thermal detector = $P_b + P_s$ |
| P_s | signal power on thermal detector |
| P_{tot} | total power on thermal detector = $P_o + P_{\text{bias}}$ |
| Q_f | quality factor of resonant filter in fMUX |
| \mathcal{R} | dynamic input resistance of dc SQUID |
| \mathcal{R}^r | reduced dynamic input resistance of dc SQUID |
| R_{bias} | value of bias resistor |
| R_d | tunnel junction dynamical resistance |
| R_i | series resistance of input circuit of SQUID |
| R_s | radius of sensor loop for magnetic calorimeter |
| R_{TES} | resistance of transition-edge sensor |
| R_{tot} | total resistance in series with fMUX resonant filter |
| r_t | radius of magnetic calorimeter thermometer |
| S_i | current responsivity of detector = dI_{TES}/dP |
| $S_j(f)$ | spectral density of current noise in dc SQUID loop |
| $S_v(f)$ | spectral density of voltage noise across dc SQUID |
| $S_{vj}(f)$ | cross spectral density of dc SQUID voltage and current noise |
| T_0 | base temperature of cryogenic system |
| T_1 | longitudinal relaxation time in NMR |
| T_2 | transverse relaxation time in NMR |
| T_2' | inhomogeneous lifetime in NMR |
| T_N | noise temperature of amplifier |
| T_Q | quantum-limited noise temperature of amplifier |
| T_s | system noise temperature |
| V_b | bias voltage across the TES |
| V_i | SQUID amplifier input voltage |
| $V_N(\omega)$ | voltage noise across dc SQUID |
| V_t | volume of magnetic calorimeter thermometer |
| V_{zz} | electric field gradient experienced by nucleus |
| V_{ϕ}^- | flux-to-voltage transfer function with negative feedback |
| V_{ϕ}^+ | flux-to-voltage transfer function with positive feedback |
| V_{ϕ}^r | reduced transfer coefficient of dc SQUID |
| $V_N^r(\omega)$ | reduced voltage noise across dc SQUID |
| w | width of microstrip |
| Z | dynamic input impedance of dc SQUID |
| Z_0 | characteristic impedance of microstrip |
| Z^r | reduced dynamic input impedance of dc SQUID |
| $Z_T(\omega)$ | total impedance of input circuit |

| | |
|---------------------|---|
| a_{TES} | logarithmic steepness of transition = $TdR_{\text{TES}}/R_{\text{TES}}dT$ |
| γ | gyromagnetic ratio |
| Δf | frequency spacing of carriers in fMUX |
| η | nuclear asymmetry parameter |
| μ | nuclear magnetic moment |
| μ_p | proton magnetic moment |
| τ_0 | time constant of detector with no electrothermal feedback |
| τ_d | magnetic calorimeter detector time constant |
| τ_e | spin echo time |
| τ_{eff} | time constant of detector including electrothermal feedback |
| τ_s | magnetic calorimeter sensor time constant |
| ω_0 | Larmor angular frequency |

Chapter 9: SQUIDs for Standards and Metrology

Abbreviations

| | |
|--------|---|
| acJE | alternating current Josephson effect |
| BIPM | Bureau International des Poids et Mesures |
| CCC | cryogenic current comparator |
| CIPM | Comité International des Poids et Mesures |
| CMN | cerium magnesium nitrate |
| CMR | colossal magnetoresistance |
| CODATA | Committee on Data for Science and Technology |
| ECCS | electron counting capacitance standard |
| ESR | electron spin resonance |
| FT | flux transformer |
| GMR | giant magnetoresistance |
| GUM | Guide to the Expression of Uncertainty in Measurement |
| IEEE | Institute of Electrical and Electronic Engineers |
| ITS-90 | International Temperature Scale, established in 1990 |
| JAVS | Josephson junction array voltage standard |
| JE | Josephson effect |
| JJA | Josephson junction array |
| LNE | Laboratoire National de Métrologie et d'Essais |
| METAS | Metrologie und Akreditierung Schweiz (Switzerland) |
| NIST | National Institute of Standards and Technology (USA) |
| NMI | National Metrology Institute |
| NMIJ | National Metrology Institute of Japan |
| NPL | National Physical Laboratory (UK) |
| PTB | Physikalisch Technische Bundesanstalt (Germany) |
| QHARS | quantum Hall array resistance standards |
| QHE | quantum Hall effect |
| QHRS | quantum Hall resistance standards |
| QMT | quantum metrological triangle |

| | |
|--------|--|
| SAW | surface acoustic wave |
| SET | single-electron transistor |
| SETSAW | single-electron transistor surface acoustic wave |
| SI | Système International d'Unités (International System of Units) |
| WBCO | waveguide beyond cut-off |

Symbols

| | |
|-------------------------------|---|
| a | mean radius of CCC torus |
| B_{Earth} | Earth's magnetic field |
| C | leakage capacitance of a CCC winding |
| C | Curie constant for a paramagnetic salt |
| F | Faraday constant |
| f_c | corner frequency representing lower limit of white noise |
| f_J | operation frequency of a JJA device |
| f_R | repetition frequency of a single measurement |
| f_{res} | resonant frequency of CCC winding |
| f_{SET} | operation frequency of a SET device |
| G | thermal conductance to a heat sink |
| G_{CCC} | gain of a CCC |
| G_L | loop gain of a CCC |
| $H_{\text{c}1}$ | lower critical field of a superconductor |
| J_0 | zeroth-order Bessel function |
| K_J | Josephson voltage–frequency constant |
| L_1 | self-inductance of primary winding of CCC |
| L_2 | self-inductance of secondary winding of CCC |
| L'_{CCC} | CCC effective inductance |
| l | CCC shield overlap length |
| N | Avogadro's constant |
| N_1 | number of turns of the primary winding of CCC |
| N_2 | number of turns of the secondary winding of CCC |
| N^{opt} | optimal number of turns |
| $P(\Phi_a)$ | reflected microwave power as a function of Φ_a |
| Q_X | elementary charge as realized by a quantum current standard |
| R_H | quantum Hall resistance |
| R_K | von Klitzing constant for QHE |
| $R_{\text{K-90}}$ | $= 25,812.807 \Omega$ the value assigned by the CIPM to the von Klitzing constant in 1990 |
| r | equivalent radius of tube |
| $S_{\text{CCC}}^{\text{opt}}$ | optimal sensitivity of CCC |
| S_I | power spectral density of current noise |
| S_n | electron spin detection sensitivity of a SQUID |
| $S_T(f)$ | power spectral density of temperature fluctuation |
| S_V | power spectral density of noise voltage |
| $S_{\Phi_{\text{ext}}}$ | power spectral density of external magnetic flux noise |
| $\langle T \rangle$ | mean temperature of a heat sink |

| | |
|--------------------------|--|
| T_c | Curie Weiss constant (magnetic ordering temperature) for a paramagnetic salt |
| V_J | voltage delivered by a Josephson junction array |
| $V_{\text{out}}(\Phi_a)$ | output voltage of a SQUID as a function of Φ_a |
| Δf | linewidth of the Josephson oscillation |
| ΔT^2 | mean square temperature fluctuations |
| δ | CCC gap thickness |
| δI | current resolution of CCC |
| δI_C^2 | power spectral density of the current noise |
| Φ_a | instantaneous magnetic flux applied to the SQUID ring |
| Φ_l | leakage flux through gap in CCC overlap |

Chapter 10: The Magnetic Inverse Problem

Abbreviations

| | |
|-----------|---|
| BEM | boundary element method |
| BSS | blind source separation |
| CG | conjugate gradient |
| ECG | electrocardiogram |
| EDM | electrical discharge machining |
| EMF | electromotive force |
| FEM | finite element method |
| FFT | fast Fourier transform |
| fICA | fast independent component analysis |
| FOCUSS | focal undetermined system solver |
| FT | Fourier transform |
| FT^{-1} | inverse Fourier transform |
| GCV | generalized cross-validation |
| GI | gastrointestinal |
| HC | Hosaka–Cohen (transformation) |
| ICA | independent component analysis |
| INFOMAX | information maximization |
| ISVD | integrated second vertical derivative |
| LCMV | linearly constrained minimum variance |
| LORETA | low-resolution electromagnetic tomography |
| LPF | low-pass filter function |
| MEM | maximum entropy of the mean |
| MFT | magnetic field tomography |
| MNLS | minimum norm least squares |
| MOI | magneto-optic imager |
| MSD | mean square deviation |
| MUSIC | multiple signal classification |
| NMR | nuclear magnetic resonance |

| | |
|---------|--|
| PCA | principal component analysis |
| PROMS | probabilistic reconstruction of multiple sources |
| SAM | synthetic aperture magnetometry |
| sLORETA | standardized low-resolution electromagnetic tomography |
| SOBI | second-order blind identification |
| SQUID | superconducting quantum interference device |
| SSP | signal space projection |
| SVD | singular-value decomposition |
| Voxel | volume element |

Symbols

| | |
|--|--|
| $\tilde{\mathbf{A}}$ | lead-field matrix |
| $\tilde{\mathbf{A}}$ | quadrupole tensor |
| $\tilde{\mathbf{A}}$ | gradiometer coil area |
| $\tilde{\mathbf{A}}^a$ | antisymmetric tensor |
| A^e | even moment of the multipole expansion |
| A_k | lead-field expansion coefficient |
| A^k | finite element coefficient |
| A^o | odd moment of the multipole expansion |
| A^p | even or odd moment of the multipole expansion |
| $\tilde{\mathbf{A}}^s$ | symmetric tensor |
| a | multipole coefficient |
| a | radius |
| a_i | coefficients in the signal space projection method |
| a^k | parameter of the interpolation function at the k th finite element |
| $\tilde{\mathbf{B}}$ | recovered magnetic field |
| $\tilde{\mathbf{B}}_p$ | perturbation in the magnetic field |
| b | boundary (line integral) |
| \vec{b} | multipole coefficient |
| $\tilde{\mathbf{b}}$ | Fourier transform of magnetic field |
| $\tilde{\mathbf{b}}$ | Fourier transform of recovered field using restricted deconvolution |
| $\tilde{\mathbf{b}}, \tilde{\mathbf{B}}$ | measured magnetic field vector |
| $\tilde{\mathbf{b}}_{el}$ | body surface potential vector |
| b^k | parameter of the interpolation function at the k th finite element |
| $\tilde{\mathbf{b}}_{mag}$ | magnetic field vector |
| C | functional minimized in the regularization method |
| $\tilde{\mathbf{C}}$ | rotation factor matrix |
| c | coefficient of the multipole expansion |
| c | normal component of the curl of a current-density distribution |
| c^k | parameter of the interpolation function at the k th finite element |
| d | thickness |
| d | gradiometer baseline |
| d^k | parameter of the interpolation function at the k th finite element |
| E | expectation operator |
| E | energy of a magnetic field |

| | |
|---------------|--|
| \vec{E} | electric field |
| \vec{E}^i | impressed voltage |
| F | current space |
| F | magnetic signal space |
| F | scalar field |
| F | generic two-dimensional function |
| F | current source and sink distribution in a sheet |
| F_G | stepwise or turns function of a gradiometer |
| F' | subspace of current space F |
| \vec{F} | vector field |
| \hat{F} | normalized stepwise function |
| \tilde{F} | spatio-temporal data matrix |
| F | Frobenius norm |
| f | weight function |
| f | Fourier transform of a generic function F |
| f | Fourier transform of a current source and sink distribution |
| f | second-order Taylor series approximation |
| f | multivariate probability density function |
| \vec{f} | gradient of the natural logarithm of a conductivity distribution |
| f_1 | Fourier transform of the x and y components of the stepwise function of an axial gradiometer |
| f_2 | Fourier transform of the z component of the stepwise function of an axial gradiometer |
| f_G | Fourier transform of the stepwise function of a gradiometer (gradiometer spatial frequency response) |
| f_G^l | pseudoinverse filter |
| f_{\max} | maximum temporal frequency |
| f_s | temporal sampling frequency |
| G | scalar Green's function |
| \vec{G} | vector Green's function |
| \tilde{G} | Green's function matrix |
| \tilde{G}_i | gain matrix |
| g | Fourier transform of a Green's function |
| H | integral equation kernel |
| H | turns function |
| \tilde{H} | hybrid gain matrix |
| h | sensor-to-sample distance |
| h | spatial filter transfer function or Fourier transform of a turns function |
| h | filter function associated with restricted deconvolution |
| h | Fourier transform of integral equation kernel |
| \tilde{I} | identity matrix |
| i | imaginary unit |
| \vec{J} | current density |
| \vec{J}^* | estimate of the current distribution |

| | |
|------------------------|---|
| \vec{J}_\perp | current perpendicular to a specific lead field |
| J_1 | Bessel function of first kind and first order |
| \vec{J}_c | continuous current component |
| \vec{J}_d | divergent current component |
| J_h | minimum eigenvalue |
| \vec{j} | impressed current density |
| \vec{J}_F | curl-free component of the impressed current density |
| \vec{J}_V | divergence-free component of the impressed current density |
| J^k | current distribution within the k th finite element |
| J_j^k | nodal values at the k th finite element |
| J^n | current distribution image at the n th step of the alternating projections algorithm |
| \tilde{J}^n | image at the n th step of the alternating projections algorithm |
| J_{PCA} | dipole fit error in the PCA method |
| J_r | cost function |
| \vec{J}^u | unknown current distribution |
| \vec{j} | Fourier transform of a current density \vec{J} |
| \hat{j} | Fourier transform of an approximate current image |
| j^n | Fourier transform of the current distribution image at the n th step of the alternating projections algorithm |
| $\text{jinc}(x)$ | $J_1(x)/x$ |
| $K_{3/2}$ | modified Bessel function of the second kind and order $3/2$ |
| K^i | secondary current sources |
| k | index (element) |
| k, \vec{k} | spatial frequency |
| k_c | cut-off spatial frequency |
| k_{LPF} | low-pass cut-off spatial frequency |
| k_{\max} | maximum spatial frequency |
| L | length of a square coil |
| \vec{L}^B | magnetic lead field |
| \vec{L}, \vec{L} | current lead field |
| \vec{M} | magnetization |
| \vec{M}_{eff} | effective magnetization |
| M_{pq} | mutual inductance between source element p and pickup coil q |
| M_{qp} | mutual inductance between pickup coil q and source element p |
| m | Fourier transform of a magnetization M |
| \vec{m} | magnetic dipole moment |
| \tilde{m} | time-dependent measured signal vector |
| N, n | number of turns in a gradiometer coil |
| \tilde{N} | model-measurement error matrix |
| N_j^k | j th interpolation function for the k th finite element |
| \hat{n} | normal to a surface S |
| \tilde{n} | noise vector |

| | |
|--|--|
| $\vec{p}, \tilde{\vec{p}}$ | current dipole moment |
| $\tilde{\vec{P}}^\perp, \tilde{\vec{P}}_\perp$ | orthogonal projection operator matrix |
| $\tilde{\vec{P}}_\parallel$ | parallel projection operator matrix |
| P_{ik} | element (i, k) of the weighted lead-field inner product matrix |
| P_n^m | associated Legendre polynomial |
| \vec{p} | dipole component vector |
| p_F | number of fixed dipoles |
| $p^{(n)}$ | magnitude of the n th multipole |
| p_R | number of rotating dipoles |
| \vec{Q} | dipole component vector |
| \tilde{R} | rank of hybrid gain matrix $\tilde{\vec{H}}$ |
| $\tilde{\vec{R}}_F$ | spatial autocorrelation matrix |
| r | radius, spherical coordinates |
| \vec{r} | spatial coordinate of source point |
| S | surface |
| S | electric or magnetic dipole source |
| S | generic time trace |
| $\tilde{\vec{S}}$ | source vector |
| $\tilde{\vec{S}}$ | scalar time-series matrix |
| S_j | boundary surfaces |
| s | source distribution |
| s | spectrum (Fourier transform) of a generic time trace S |
| \tilde{s}_i | elements of orthonormal basis spanning the magnetic signal space F |
| $\text{sinc}(x)$ | $\sin(\pi x)/\pi x$ |
| T | threshold |
| U | applied voltage |
| $\tilde{\vec{U}}$ | SVD decomposition matrix |
| V | electric scalar potential |
| $\tilde{\vec{V}}$ | SVD decomposition matrix |
| V_m | magnetic scalar potential |
| v, V | volume |
| v | scanning speed |
| v_j | volume element or voxel |
| W | window function |
| $\tilde{\vec{W}}$ | weighting matrix |
| w | Fourier transform of a window W |
| w | window in the frequency domain |
| w | weighting function |
| w | <i>a priori</i> probability density function |
| \tilde{w} | lead-field coefficient vector |
| \tilde{x} | moment vector |
| a | direction cosine |
| a | ratio of coil radii in a concentric planar gradiometer |

| | |
|--------------------------------|--|
| β | direction cosine |
| $\tilde{\Gamma}$ | lead-field inner product matrix |
| γ | pseudoinverse filter threshold |
| γ | direction cosine |
| Δ | scanning step size |
| δ | Dirac delta function |
| ε_0 | permittivity of free space |
| η | natural coordinate |
| θ | azimuthal angle, spherical coordinates |
| $\tilde{\Lambda}$ | eigendecomposition matrix |
| λ | regularization parameter |
| λ | eigenvalue |
| ξ | natural coordinate |
| ρ | electric charge density |
| ρ | radius, cylindrical coordinates |
| $\tilde{\Sigma}$ | SVD decomposition matrix |
| σ | conductivity distribution |
| Φ | magnetic flux |
| Φ' | truncated magnetic flux map |
| $\tilde{\Phi}$ | eigendecomposition matrix |
| ϕ, φ | Fourier transform of the magnetic flux |
| φ' | Fourier transform of the truncated magnetic flux map |
| ϕ | polar angle, spherical coordinates |
| χ | magnetic susceptibility |
| $\tilde{\chi}$ | susceptibility vector |
| Ψ | electric or magnetic scalar potential |
| Ψ^e | even unit potentials |
| Ψ^o | odd unit potentials |
| Ω | operator that measures the smoothness of a scalar field |
| $\ \cdot\ _2$ | L^2 norm |
| $\ \cdot\ _F$ | Frobenius norm |
| $\tilde{\mathfrak{I}}^k$ | vector current density at the k th finite element |
| $[\cdot]_z$ | z -component of the vector expression within square brackets |
| $\langle \cdot, \cdot \rangle$ | inner product |
| $+$ | pseudoinverse or Moore-Penrose inverse |
| $^\wedge$ | data estimate matrix of statistical quantities |
| $*$ | convolution in the space domain |
| \otimes | convolution in the frequency domain |
| \approx | resembles (<i>not</i> proportionality symbol) |

Chapter 11: Biomagnetism**Abbreviations**

| | |
|--------|--|
| AEF | auditory evoked fields |
| BEM | boundary element method |
| BER | basic electrical rhythm |
| BSPM | body surface potential mapping |
| CAD | coronary artery disease |
| CALM | continuously adjusted least squares method |
| CAM | current arrow maps |
| CAT | computed axial tomography |
| CMS | centers for Medicare and Medicaid services |
| CPT | current procedural terminologies |
| CSF | cerebrospinal fluid |
| CT | computed axial tomography |
| DICS | dynamic imaging of coherent sources |
| DPC | detection probability curve |
| DSP | digital signal processor |
| ECD | equivalent current dipole |
| ECG | electrocardiogram |
| EEG | electroencephalogram |
| EGG | electrogastrogram |
| ELISA | enzyme-linked immunosorbent assay |
| fAEF | fetal auditory evoked fields |
| fHRV | fetal heart rate |
| FIA | fluorescence dye immunoassay |
| fMCG | fetal magnetocardiogram |
| fMEG | fetal magnetoencephalogram |
| fMRI | functional magnetic resonance imaging |
| FOCUSS | focal underdetermined system solution |
| fVEF | fetal visually evoked fields |
| GH | genetic hemochromatosis |
| ICA | independent component analysis |
| LCD | liquid crystal display |
| LCMV | linearly constrained minimum variance beamformer |
| LED | light emitting diode |
| LORETA | low-resolution electromagnetic tomography |
| MARIA | magnetic relaxation immunoassay |
| MCE | minimum current estimation |
| MENG | magnetoenterogram |
| MFT | magnetic field tomography |
| MGG | magnetogastrogram |
| MI | myocardial infarction |
| mMCG | maternal magnetocardiogram |
| MMG | magnetomyogram |

| | |
|---------|--|
| MMM | magnetic marker monitoring |
| MNG | magnetoneurogram |
| MNLS | minimum norm least squares inverse |
| MSR | magnetically shielded room |
| MUSIC | multiple signal classification |
| NMR | nuclear magnetic resonance |
| PCA | principal component analysis |
| PET | positron emission tomography |
| RIA | radioisotope immunoassay |
| RMS | root mean square |
| ROI | region of interest |
| SAM | synthetic aperture magnetometry |
| SARA | SQUID array for reproductive assessment |
| SEF | somatosensory evoked fields |
| SIS | superconducting imaging surface |
| sLORETA | standardized low-resolution electromagnetic tomography |
| SNR | signal-to-noise ratio |
| SPECT | single-photon emission computed tomography |
| SPM | statistical parametric mapping |
| SSP | signal space projection |
| SSS | signal space separation |
| WPW | Wolf–Parkinson–White syndrome |

Symbols

| | |
|------------------|--|
| A_{ICA} | ICA mixing matrix |
| a, α | radius vector of a dipole |
| a_{nm} | internal spherical harmonic expansion coefficients |
| a_o, a_0 | radius vector for dipole q_0 |
| a_θ | radius vector for beamformer probe |
| B_{ICA} | ICA unmixing matrix |
| B_∞ | infinite-medium magnetic field |
| b_{nm} | external spherical harmonic expansion coefficients |
| b_o | first-order gradiometer baseline |
| b_{pln} | planar gradiometer baseline |
| b_{rad} | radial gradiometer baseline |
| C_m | data (measurement) covariance matrix |
| C_q | source covariance matrix |
| C_v | noise covariance matrix |
| d | sensor spacing |
| f_{\min} | minimum frequency of interest |
| f_0 | onset of low-frequency noise measured with gradiometer with baseline b_o |
| f_{00} | onset of low-frequency noise for magnetometers |
| f_{01} | onset of low-frequency noise for first-order gradiometer |
| f_{03} | onset of low-frequency noise for third-order gradiometer |

| | |
|------------------------------|---|
| HC | Hosaka–Cohen transformation |
| H_θ | gain matrix at θ |
| I | identity matrix |
| J | total current density |
| J^c | cellular average current |
| J^i | impressed current |
| J^p | primary source of biomagnetic field |
| J^v | volume current density |
| K | number of channels |
| k | slope of low-frequency noise |
| L | lead field matrix, forward solution per unit current dipole |
| L_{ij} | element of the lead field matrix |
| L_x | forward solution at voxel x |
| L_θ | forward solution at voxel θ |
| $L_{\theta 1}, L_{\theta 2}$ | forward solutions for two orthogonal components of a moment at θ |
| $\mathbf{m}, \mathbf{m}(t)$ | MEG measurement vector |
| $\hat{\mathbf{m}}$ | spherical harmonic expansion approximation to the MEG measurement |
| N | number of samples |
| N_{ave} | number of averages |
| N_{ext} | maximum external spherical harmonic expansion order |
| N_{int} | maximum internal spherical harmonic expansion order |
| N_Y | number of spherical harmonic terms |
| N_θ | sensor noise projected by beamformer from location θ |
| p_c | number of cortical dipoles |
| P_θ | beamformer power projected from location θ |
| q, \mathbf{q} | current dipole magnitude or vector |
| q_o | dipole moment |
| $q_{\theta 1}, q_{\theta 2}$ | two orthogonal components of q_o |
| $q_{\theta 1}, q_{\theta 2}$ | two orthogonal components of q_θ |
| R | sensor array diameter |
| r_{brain} | brain radius |
| r_{head} | head radius |
| $s(t)$ | source activity vector |
| $\hat{s}(t)$ | estimate of $s(t)$ |
| S_Y | matrix of spherical harmonic terms |
| V | electric potential |
| W | weighting matrix |
| W_{target} | beamformer weight matrix for target voxel |
| W_θ | beamformer weight matrix for location θ |
| X_Y | vector of spherical harmonic coefficients |
| Y_{nm} | spherical harmonic function |
| $\gamma_\theta(t)$ | spatial filter on location θ |
| \bar{y} | mean value of synthetic channel |
| Z_θ^2 | ratio of P_θ to N_θ |

| | |
|--------------------------|--|
| Δf | bandwidth of measurement |
| $\Delta\psi$ | SAM probe orientation relative to q_0 (in tangential plane) |
| θ | SAM probe parameter (either position, or position and orientation) |
| $v, v(t)$ | vector of sensor white noise |
| v, \mathbf{v} | one sensor white noise, or a vector of white noise for sensor array |
| $v_{\text{brain } b=26}$ | brain noise for radial gradiometers with 260 mm baseline |
| $v_{\text{brain } b=5}$ | brain noise for radial gradiometers with 50 mm baseline |
| $v_{\text{brain pln}}$ | brain noise for planar gradiometers with 16.5 mm baseline |
| v_w | one sensor white noise |
| σ_v | rms average of the standard deviations of the dipole reconstruction cluster along three principal directions |
| σ_y | standard deviation of synthetic channel |
| τ | relaxation time |
| Ψ | magnetic scalar potential |

Chapter 12: Measurements of Magnetism and Magnetic Properties of Matter

Abbreviations

| | |
|----------|---|
| AFM | atomic force microscope |
| AGM | alternating gradient magnetometer |
| ASIC | application-specific integrated circuit |
| IC | integrated circuit |
| MCM | multichip module |
| MFM | magnetic force microscope |
| MPMS | magnetic property measurement system (SQUID-MS from Quantum Design, Inc.) |
| PC | personal computer |
| QD | Quantum Design, Inc. |
| RSO | reciprocating sample option |
| SQUID-MS | SQUID magnetometer–susceptometer |
| STM | scanning tunneling microscope |
| VSM | vibrating sample magnetometer |
| VTS | variable-temperature susceptometer model from SHE Corp. |

Symbols

| | |
|-------|--|
| a | outer side length of square-washer SQUID loop (not same definition as in Vol. I) |
| B_n | rms magnetic field noise in a specified bandwidth (not same definition as in Vol. I) |
| B_x | component of magnetic field parallel to the surface being imaged in the scanning direction |
| B_z | component of magnetic field perpendicular to the surface being imaged |

| | |
|-------------|--|
| b_x, b_y | k -space x and y components of Fourier transformed magnetic field from a sample |
| d_i | thickness of a thin current-carrying layer |
| h | length of pixel in the x -direction, imaging step size (different from definition in Vol. I) |
| I_y | current in a sample wire that lies on the y -axis |
| J_n | rms noise in current density in each pixel of an image of source |
| J_x, J_y | currents obtained from a magnetic field image |
| j_x, j_y | x and y components of current density in a sample |
| | k -space x and y components of Fourier transformed current density in a sample |
| k | $\sqrt{k_x^2 + k_y^2}$, length of the spatial wave-vector |
| k_w | cut-off maximum wave-vector |
| k_x | x -component of the spatial wave-vector |
| k_y | y -component of the spatial wave-vector |
| M | sample magnetization |
| S/N | single pixel peak signal-to-noise ratio in a current density image |
| s | spatial resolution (not same definition as in Vol. I) |
| s_m | spatial resolution in a raw magnetic field image of a wire |
| x | scanning direction or distance in the sample plane |
| x' | recorded position when the sample is at true position x |
| z | separation between SQUID and sample surface |
| ΔB | error in a measurement of magnetic field |
| Δf | measurement bandwidth |
| Δx | error in the recorded position, $x' - x$ |
| λ | wavelength of magnetic field oscillating at frequency f (not same definition as in Vol. I) |
| Φ_n | rms flux noise in a specified bandwidth |
| χ_{ac} | complex magnetic susceptibility dM/dH |

Chapter 13: Nondestructive Evaluation of Materials and Structures Using SQUIDs

Abbreviations

| | |
|------|---|
| BEM | boundary element method |
| CFRP | carbon fiber-reinforced polymer |
| FDM | finite difference method |
| FEM | finite element method |
| GMR | giant magnetoresistance, or giant magnetoresistor |
| MFL | magnetic flux leakage |
| MR | magnetoresistance, or magnetoresistor |
| NN | neural network |

| | |
|-----|------------------------|
| PEC | pulsed eddy current |
| VIM | volume integral method |

Chapter 14: SQUIDs for Geophysical Survey and Magnetic Anomaly Detection

Abbreviations

| | |
|-------|---|
| CSAMT | controlled source audio magnetotellurics |
| CSEM | controlled source electromagnetics |
| MAD | magnetic anomaly detection |
| MADOM | Magnetic and Acoustic Detection of Mines (a US project) |
| MT | magnetotelluric |
| MUDSS | Mobile Underwater Debris Survey System (a US project) |
| RFI | radio frequency interference |
| RMS | radiometric sounding |
| SGMS | Superconducting Gradiometer/Magnetometer Sensor (a US project) |
| TMI | total magnetic intensity |
| TSG | three-SQUID (or sensor) gradiometer |
| UAV | unmanned airborne vehicle |
| UUV | unmanned underwater vehicle |
| UXO | unexploded ordnance |

Symbols

| | |
|------------------|--|
| B_A | field of a magnetic anomaly [T] |
| B_E | Earth's field [T] |
| B_T | scalar total field [T] referenced to the Earth's field |
| M | moment of a magnetic dipole [$A \text{ m}^2$] |
| M_v | virtual magnetic dipole moment variable in a numerical inversion algorithm [$A \text{ m}^2$] |
| r | displacement vector [m] |
| r_v | virtual displacement vector variable in a numerical inversion algorithm [m] |
| $T_{i,n}$ | field measurement inside a field-nulling coil |
| T_x | transmitter pulse current used in TEM [A] |
| t_{off} | time when the TEM transmitter current is turned off [s] |
| t_{on} | time when the TEM transmitter pulse is turned on [s] |
| R_x | magnetic field induced in a conductor by a TEM transmitter current pulse [T] |
| S_C | signal in a TEM coil detector |
| S_M | signal in a TEM magnetometer detector |
| Γ | measured signal from a gradiometer that contains errors |
| τ | time constant of decay in TEM measurement |

Chapter 15: Gravity and Motion Sensors

Abbreviations

| | |
|---------|--|
| ALLEGRO | A Louisiana Low-temperature Experiment and Gravitational Radiation Observatory |
| EDM | electric discharge machining |
| ESA | European Space Agency |
| GGSS | Gravity Gradiometer Survey System |
| GP-B | Gravity Probe-B |
| GPS | Global Positioning System |
| GRACE | Gravity Recovery and Climate Experiment |
| INS | inertial navigation system |
| ISLES | Inverse-Square Law Experiment in Space |
| ISS | International Space Station |
| ISS | inertial survey system |
| LIGO | Laser Interferometer Gravitational-wave Observatory |
| LISA | Laser Interferometer Space Antenna |
| NASA | National Aeronautics and Space Administration |
| RRR | residual resistivity ratio |
| SGG | superconducting gravity gradiometer |
| STEP | Satellite Test of the Equivalence Principle |

Symbols

| | |
|---|---|
| \ddot{a} | linear acceleration vector |
| C | charge conjugation |
| D | effective length of gravitational wave antenna |
| d | average gap between each pancake coil and test mass |
| $E \equiv 10^{-9} \text{ s}^{-2}$ | unit of gravity gradient |
| E_N | intrinsic energy noise of gravitational wave detector |
| E_S | signal energy of gravitational wave detector |
| G | gravitational constant |
| $\text{Gal} \equiv 1 \text{ cm s}^{-2}$ | unit of acceleration |
| h | dimensionless amplitude of gravitational waves (metric perturbation) |
| h | altitude of satellite |
| I_0 | persistent current stored in transducer sensing loop |
| $I_{\text{Li}}, I_{\text{Bi}}, I_{\text{Si}}$ | persistent current stored in levitation, balance, and sensing coil in SGG |
| L | separation between masses |
| L_1, L_2 | inductance of each sensing coil in transducer |
| $L_{\text{Li}}, L_{\text{Bi}}, L_{\text{Si}}$ | inductance of levitation, balance, and sensing coil in SGG |
| $L_p \equiv (L_1^{-1} + L_2^{-1})^{-1}$ | parallel combination of sensing coil inductances |
| ℓ | baseline of gradiometer |
| ℓ | order of multipole |

| | |
|--------------------------|--|
| $\hat{\ell}$ | unit vector representing line of sight between two test masses |
| M | effective mass of gravitational wave antenna |
| m | mass of transducer or accelerometer test mass |
| m | mass of electron |
| \hat{n} | unit vector representing sensitive axis of test mass |
| P | parity |
| Q_a | quality factor of gravitational wave antenna |
| R_{Li}, R_{Bi}, R_{Si} | heat switch resistance for levitation, balance, and sensing circuit in SGG |
| R_{opt} | optimum source impedance |
| S | average area of pancake-shaped sensing coils |
| $S_a(f)$ | power spectral density of acceleration noise |
| $S_J(f)$ | power spectral density of circulating current noise |
| $S_f(f)$ | power spectral density of gravity gradient noise |
| $S_{\phi J}(f)$ | correlation between $S_\phi(f)$ and $S_J(f)$ |
| T_a | temperature of gravitational wave antenna |
| T_N | noise temperature of SQUID |
| $T_{N,QL}$ | quantum-limited noise temperature of SQUID |
| Z_{22} | output impedance of transducer |
| | |
| a | dimensionless strength of Yukawa potential |
| \vec{a} | angular acceleration vector |
| β | electromechanical energy coupling constant |
| β_{12} | reverse energy coupling coefficient of transducer |
| β_{21} | forward energy coupling coefficient of transducer |
| β_S | electromechanical energy coupling constant to SQUID |
| Γ_{ij} | ij component of gravity gradient tensor |
| $\gamma \equiv L_i/L_p$ | ratio between SQUID input inductance and transducer output inductance |
| $\Delta\omega_S$ | bandwidth of gravitational wave detector |
| $\delta\hat{\ell}$ | misalignment of sensitive axes from concentricity |
| $\delta\hat{n}$ | misalignment of sensitive axes from parallelism |
| $\delta\Gamma_a$ | linear acceleration error in gravity gradiometer |
| $\delta\Gamma_a$ | angular acceleration error in gravity gradiometer |
| ζ | dimensionless impedance matching parameter of input circuit to SQUID |
| η | energy coupling efficiency from transducer circuit to SQUID |
| λ | range of Yukawa potential |
| λ | wavelength |
| ρ | mass density |
| τ | detector integration time |
| τ_s | pulse duration time |
| $\varphi(x_i, t)$ | gravitational potential |
| $\vec{\Omega}$ | angular velocity vector |

| | |
|------------|---|
| ω_0 | angular resonance frequency |
| ω_a | resonance frequency of gravitational wave antenna |
| ω_m | uncoupled resonance frequency before storing persistent current |
| ω_s | signal frequency |

Index

$1/f$ noise 113, 117–119, 416, 512, 519
 $1/f$ power law 531

a

absolute coil excitation 455
acceleration
 angular 555, 560–561, 564, 574
 common-mode 555, 557
 common-mode (angular) 561
 differential mode 557, 558, 568
 differential (angular) 561
 linear 555, 558, 560–561, 564, 569
 platform 547, 555, 564, 574
accelerometer
 angular 554, 561–563, 563, 569, 571
 differential 566, 568–569
 inertial navigation 574
 linear 554, 563, 569
 superconducting 546–548, 554 *ff.*,
 568–569, 575
ac susceptibility (SQUID) 405
 complex susceptibility 406
 quantum tunneling (in horse-spleen
 ferritin) 406
 superconducting transition (in
 RuSr₂GdCu₂O₈) 406
active field suppression 512
adaptive balancing 533
adaptive data processing 498
agarose gel (MRI, T_1 -weighed contrast)
 77–79
airborne
 reconnaissance 508
 survey 521 *ff.*, 572 *ff.*
 TEM 514, 521 *ff.*
aircraft component testing 224, 453,
 460–463
aliasing 180, 183, 220
alignment coil 566, 570

ALLEGRO (A Louisiana Low-temperature
Experiment and Gravitational Radiation
Observatory) 552
alternating gradient magnetometer (AGM)
 393
alternating projection 168, 195–197
amino acid (NMR) 62, 80
ammonium perchlorate (NMR) 63
Amoeba optimization method 503
Ampère's law 150, 152, 192
amplifier
 gravitational wave detector 550
 noise 550 *ff.*
 SQUID, rf
 intermediate frequency 20 *ff.*
 microstrip 20 *ff.*
 noise temperature 6, 10 *ff.*, 26
 quantum limit 18–20, 130, 552, 554
 radio frequency 5 *ff.*
 series array 17–18
 tuned 10 *ff.*
 untuned 12 *ff.*
 postamplifier 3, 14, 22, 26–27, 29, 31–32
 readout 7, 40
 ultra-low-current (CCC) 118
analog subtraction 491
analytic point-by-point inversion 503
anatomical image 75–76, 274–275, 337–339,
 351
anisotropy (magnetic, measurement) 398
apodizing, apodized 176, 178, 180, 198, 207
apparent conductivity 459
artifact (in or by)
 EEG 286, 314
 MCG 314
 SSP 253
 motion 299, 300, 303, 318
 eye blinks 303
 ocular 252

- signal 305
stimulation 287
- ASIC (application-specific integrated circuit imaging) 433
- astatic magnetometer 510
- asymmetry parameter (of nuclear charge distribution, NQR) 60, 62–63
- attenuation
high-frequency 127
factor 512
of gravity (with altitude) 572
magnetic field 184, 287, 512
neighbor channel 41
signal 348, 400
transformer 399
- auditory hallucinations 315
- axial gradiometer 204, 330, 490
- axion
detection, detector 3, 31, 81–82, 569
search for 569, 575
theory postulate 81–82, 566–567, 569
- b**
- bacteria (magnetic) 431
- bandwidth, SQUID 183, 273, 348, 363, 425, 436, 447, 518–519, 521, 526–527
- bandwidth, resonant mass transducer 551 *ff.*, 554 *ff.*
- Barkhausen emission 451
- baseline (of gradiometer) 198 *ff.*, 280 *ff.*, 358, 555
- basis function (in lead-field analysis) 214
- Bayesian inference 314
- beamformer
DICS 312
LCMV 246, 307 *ff.*
minimum norm 245–247
SAM 308 *ff.*
- Bell gradiometer (GGSS) 572 *ff.*
- bell pepper (MRI of) 75
- BEM (boundary-elements method) 216, 324, 458
- Bessel function 127, 181, 202
- bidomain model (of heart) 175–176, 239 *ff.*, 323
- biomagnetic image, imaging 254, 420, 430
- biopsy 81
- Biot–Savart law 145, 149 *ff.*, 168–171, 208 *ff.*, 225, 303
- blind deconvolution 168
- body surface potential mapping (BSPM) 321
- bolometer
conventional 46
- general 3, 32, 45
in astronomy 45
NIS junction 55
- TES
antenna-coupled 47
crosstalk (in multiplexing) 44
design 46–49
multiplexed operation 38, 44
performance 49
- bond detector (NMR) 72
- bone marrow (MRI of) 75
- boundary-element method (BEM) 216, 324, 458
- boxcar filtering 517
- brain model 286, 319
- brain noise 311
- bridge, mutual inductance 124
- bridge, resistance
(CCC – cryogenic current comparator) 101 *ff.*
- Brownian motion noise (see noise)
- BSPM (body surface potential mapping) 321
- B-spline filter (wavelet transform) 523
- c**
- calibration 117, 121–122, 502
- calorimeter
in astronomy 50–51
in laboratory 51
magnetic 53–54
NIS junction 55
SIS junction 54–55
- TES
design 51
general 3, 50–51
noise performance 52
- capacitive feedback 10, 14
- capillary tubes (helium flow) 397
- cardiac
action current 175
activation, excitation 165–167, 244, 322–324
arrhythmia 334
excitation waveform, model 323
imaging 175
injury current 336
ischemia 320, 335–337
tissue lesion 344
- cardiomagnetism 322
- carrier nulling (in frequency multiplexing) 42
- CAT (computed axial tomography) 275, 355
- CCC (cryogenic current comparator) bridge 101 *ff.*, 108–116, 118–122

- CDM (cold dark matter) 81, 569
 cesium vapor magnetometers 509, 523
 CG (conjugate gradient method) 210
 charge conjugation-parity inversion (CP) 82, 569
 charge density 153, 157
 chemical shift 69
 closed-cycle refrigerator 563
 CMB (cosmic microwave background) 45, 56
 cocaine hydrochloride (NQR) 62
 coil
 alignment 566, 570
 input 97 *ff.*, 129–130, 547, 551, 553
 levitation 99, 570
 pickup 6, 61, 65, 80, 102–105, 107–108,
 148, 151, 176–178, 197, 204 205, 210,
 215, 395
 saddle (in NMR, NQR spectrometer) 61,
 67, 73
 sensing 547, 547 *ff.*, 551–553, 566, 570
 inductance 495
 cold dark matter (CDM) 81, 569
 comb filter 523
 combinatorial library 430
 common-mode (SGG)
 angular acceleration 561
 balance 557
 rejection 557 *ff.*, 572
 rejection ratio 555, 561
 resonance frequency 556
 residual balance 558
 common mode (SQUID gradiometer)
 feedback 492–494, 531
 field 492
 rejection 491–492
 rejection ratio 491–492, 525
 signal 491
 computed axial tomography (CAT) 275, 355
 conducting overburden 516
 conductive half space 516
 conductive shield 533
 conductivity 150 *ff.*, 158, 188 *ff.*, 208, 226, 253
 conductivity maps 514
 configured gradiometer (see gradiometer)
 conjugate gradient (CG) method 210
 continuation (of magnetic field)
 downward or inward 143, 183 *ff.*, 207–208
 upward 143, 183–185, 206
 continuity equation 171, 218 *ff.*
 controlled source audio magnetotellurics
 (CSAMT) 526
 controlled source electromagnetics (CSEM)
 508
 convolution 151, 168–170, 198 *ff.*, 212, 224,
 231–232
 cooling fin (for microstrip amplifier) 31
 Cooper pair 131
 copper powder filter 29
 coronary artery disease (CAD) 336
 correlation time (in T_1 -weighed contrast,
 MRI) 78
 corrosion 218, 225, 449, 471–472
 cortex, cortical
 activity 307
 area 277
 cells 276–277
 change, hyperventilation 345
 current 276, 277
 dipole 302
 signal 276–278
 source 167
 surface 184, 275, 277, 286
 tissue, activated 278
 cosmic microwave background (CMB) 45, 56
 coupling coefficient or constant
 electromagnetic 105
 electromechanical energy 548 *ff.*
 quadrupole 61 *ff.*
 coupling energy efficiency 548
 covariance matrix 254, 302, 305, 309, 313
 CP (charge conjugation-parity inversion) 82,
 569
 CPT (current procedural terminology) code
 (see also reimbursement) 319
 creep, flux 495, 519
 cross-component gradient (SGG) 561
 cross-component SGG 559–563, 572
 cross-relaxation (between ^{14}N and ^1H , NMR)
 62
 cross spectral density (SQUID noise) 6, 12
 cryobattery 462
 cryocooled dewar 400
 cryocooler (see also refrigerator) 400, 512,
 571, 575
 cryogenic current comparator (CCC) 96,
 100–106, 108–116, 118–122
 cryogenic liquids 498
 cryogenic voltage comparator 101
 cryosurgery 81
 CSAMT (controlled source audio
 magnetotellurics) 526
 CSEM (controlled source electromagnetics)
 508
 cubic symmetry 60
 current
 axial 277

- arrow map (CAM) 332
 density 149 *ff.*, 165 *ff.*, 188–189, 194,
 209 *ff.*, 218 *ff.*, 232, 241, 253, 254
 dipole 150, 155 *ff.*, 181, 198, 208, 238, 288
 dipole density 154, 277, 278
 dipole, equivalent 203, 278, 303, 323, 349
 discontinuous 186 218, 221
 distribution 187 *ff.*, 302, 348–350
 distribution mapping 452
 eddy 146, 227, 443, 453, 483, 501, 514
 impressed 154 *ff.*, 211, 240, 254, 277
 ionic 274, 351–352
 primary 113, 278, 286, 323
 radial 286
 source 99, 109, 111, 113, 115–117, 121,
 131, 142 *ff.*
 tangential 286, 303, 310
 volume 277, 286, 297, 303, 356, 358
- current-injection tomography 188 *ff.*
 current-summing multiplexer 40
- d**
- dark matter 569
 data acquisition, processing (geophysical)
 499 *ff.*
 Dayem bridge 130
 dc-magnetometry (quasistatic) 342, 344–346
 decay constant (TEM) 516
 decay curve (TEM) 514
 deconvolution 144, 168, 177, 180, 197 *ff.*,
 223, 227
 demagnetization, organ 344
 dendrite (in brain cell) 276
 depolarization, ventricular 322
 depth-selective technique (NDE) 456
 detection at depth (mineral exploration) 508
 detection probability curve (DPC, in MEG)
 297
 detection ranges (MAD) 528
 detector, thermal 32 *ff.*
 dewar
 boil-off rate (LHe) 326, 408, 512
 cryocooled 396, 400–401
 cut-off frequency (TEM) 519
 elbow-shaped (MEG) 281–282
 helmet-shape (whole cortex MEG) 280–281
 inclined (LN_2) 330
 LN_2 (MCG) 328, 330–331
 MAD 498
 MCG 326
 MNG 327
 MRI 73
 NMR 68, 70
 noise 73, 279
 quasistatic MEG 344–345
 rock magnetometer 511
 safety 344
 SARA 300–301
 SQUID microscope 419
 twin (MCG) 328
 vacuum gap 281
 window (SQUID microscope) 409, 419
- DFSZ (Dine–Fischler–Srednicki–Zhmitinsky)
 model 82–83
 diamagnetic material 145–148, 230–231
 DICS (dynamic imaging of coherent
 sources) 312, 316
 differenced total-field magnetometers 487
 differential
 acceleration 568 *ff.*
 accelerometer 568 *ff.*
 excitation 455
 mode 556–557
 mode, cross-component gradient 561
 mode, resonance frequency 571
 digital tapered stacking filter 523
 dilution refrigerator 415, 425
 dipole
 current 150, 154 *ff.*, 181–182, 198, 208, 238
 current, density 277, 278
 current, equivalent 278, 203, 323, 349
 detection 501
 distribution, current 187 *ff.*, 307
 fitting 168, 208
 magnetic 141, 146, 152, 155, 162, 165,
 181, 203, 229, 233, 236, 242, 248, 403,
 528
 moment 141, 146, 155, 162, 165, 233, 236,
 248
 multiple 142, 167, 229, 234, 243–244
 signals 501–503
 source
 distributed 165–166, 243
 equivalent 323
 tracking 488
 direct readout scheme (SQUID) 533
 discontinuous current 186 218, 221
 displacement sensor 548
 distributed dipole source 165–166, 243
 distributed element model (microwave) 25
 diurnal variations 523
 DPC (detection probability curve, in MEG)
 297
 double-layer (model of cardiac activation)
 165–166, 176, 239, 244
 Downhill Simplex (method) 503

drift of SQUID output 495, 526

dynamic

imaging of coherent sources (DICS) 312, 316

input impedance 6, 9

input inductance 7

input resistance 7

nuclear polarization 69

range 280, 363, 519, 557

susceptibility 405

(see also ac susceptibility)

e

Earth's field 484–487, 492–494, 497, 501, 510, 536

ECG (electrocardiogram, electrocardiography) 210–211, 215–216, 238–241, 321

ECG lead 210

eddy current 145–146, 212, 226–227, 434, 443, 453, 483, 501, 514

eddy current imaging 434, 456, 459

edge field 223, 224

EDM (electric discharge machining) 556, 561

electric quadrupole moment 59–60

electrocardiogram, electrocardiography (ECG) 210–211, 215–216, 238–241, 321

electrogastrogram (EGG) 356–357

electromotive force (EMF) 153–154, 188

electronic gradiometer 489, 491

electrothermal feedback 33

eötvös unit or E 559

epilepsy 295, 302, 316

equivalence principle 546, 548, 568–569, 575

ergodic principle 127

ergometer, nonmagnetic 336

error

asymmetric multipole moments 568

calibration 487

field 492

localization 292, 297, 307

mass distribution, misalignment 555

mass imbalance 555,

Euler deconvolution 503

evoked fields

auditory 278, 318, 342

fetal 318–319

somatosensory 314

visual 318–319

exploration, geophysical (prospecting) 484, 504–508, 513 ff.

extra dimensions 565 ff., 571, 575

f

false-alarm reduction (MAD) 529

Faraday's law 69, 153

far-field magnetic sensing 484

fast Fourier transform (FFT) 169, 176, 207, 220

feedback (see also flux-locked loop)

current-nulling (external) 400

electronics 399, 425

error 492

loop 5, 281

FEM (finite-element method) 168, 216–226, 458

femtovoltmeter, SQUID 97–98

ferromagnetic material 145 ff.

fetal magnetocardiogram (fMCG) 339

fetal magnetoencephalogram (fMEG) 299, 318–319

FFT (fast Fourier transform) 169, 176, 207, 220

field integration 180, 197–198, 204, 206

field inversion spin echo 70

filter, filtering

adaptive 318

binomial (MCG) 334

B-spline (wavelet transform) 523

comb (TEM) 323

signal

MCG 328, 334

MEG 280, 303

MPMS 399–400

NDE 447

quasistatic MEG 342, 344

TEM 517, 523

spatial

general 168–170, 174, 182, 207, 224,

245, 253, 300, 305, 307 ff., 426–427,

432, 459

inverse 170, 199, 207, 209, 231, 459

pseudoinverse 202

tapered, stacking (TEM) 517, 523

finite difference method (FDM) 458

finite-element method (FEM) 168, 216–226, 458

fixed wing aircraft trials (geophysical prospecting) 524

flaw detection 446, 449, 460

flexible tape pickup loop 535

flip-chip (microstrip SQUID) 31

flip-chipped SQUID gradiometer 535

flux

creep 495, 519

focusing washer 18

- gate 508, 510
 gradiometer
 planar 197 *ff.*, 215, 224, 280 *ff.*, 288 *ff.*,
 304, 332
 radial 280 *ff.* 288 *ff.*, 304, 310–311, 332,
 352–353, 364
 magnetometer 357
 motion 394, 399–400, 402, 404, 406
 noise 106, 130, 394, 414–415, 546, 552
 penetration 490
 quantization 546
 quantum 3
 transformer 279, 288, 301, 489, 511
 flux-field deconvolution 177, 197 *ff.*
 flux-locked loop (see also feedback) 3, 21, 34,
 63, 70, 80,
 flux-to-current transfer function 6
 flux-to-voltage transfer coefficient 3, 6, 17,
 23, 97, 110, 398, 418
 fluxon (imaging) 430
 fMRI (magnetic resonance imaging,
 functional) 307, 320, 346
 focal undetermined system solver
 (FOCUSS) 248, 249, 306
 forearm (MRI) 75, 80
 forward problem 145 *ff.*, 191, 324, 337
 Fourier transform 169 *ff.*, 188, 193, 199, 204,
 214, 216, 220, 231, 232, 426, 514
 Fourier transform, fast (FFT) 169, 176, 207,
 220
 fractional-turn SQUID 414
 fragmentation index 334
 frame dragging 567
 Fredholm integral equation 209, 210
 free-induction decay (FID) 59, 76
 frequency-domain multiplexer 39–44
 frequency encoding 74
 frequency response, spatial 199 *ff.*
 frequency response, SQUID (TEM) 516 *ff.*
 full-width-half-maximum (FWHM) 9, 47, 52,
 58, 67
 fundamental constants
 Faraday 122
 Josephson 98
 Planck 99, 131
 Von Klitzing 112, 115
- g**
 gain matrix 249, 250–251
 gantry 279, 300, 326, 343
 gastrointestinal (GI) system, organs 166,
 356 *ff.*
 Gauss' law 152, 153
- generalized cross-validation (GCV) 209, 210
 generalized inverse 243, 244
 general relativity 548, 565, 567
 geologic, geomagnetic noise 497
 geophone 508
 geophysical exploration, prospecting 484,
 504–508, 513 *ff.*, 546, 572
 GGSS (Gravity Gradiometer Survey System)
 572–573
 ghost solution 503
 Gifford–McMahon (GM) cryocooler 400, 512
 global feedback
 coil system 533
 gradiometer 532–534
 scheme 493
 GP-B (gravity probe-B) 567 *ff.*, 575
 GPS (global positioning system) 574
 GRACE (Gravity Recovery and Climate
 Experiment) 571
 gradient, conjugate (CG) 210
 gradient, gravity 557, 568, 573
 gradiometer
 axial, see radial
 balance 533
 baseline 198 *ff.*, 280 *ff.*, 358, 555
 configured 489, 491–494, 524
 first-order 198–201, 301, 314, 487
 global feedback 532–534
 gravity (see gravity gradiometer)
 imbalance 491, 496
 intrinsic 489–491
 localization error 292
 multiaxis 489, 492, 528
 optical 341
 optimization of 398
 pickup coils 395
 planar 197 *ff.*, 215, 224, 280 *ff.*, 288 *ff.*, 304,
 330, 332, 490, 525
 radial 198, 204–206, 280 *ff.* 288 *ff.*, 304,
 310–311, 330, 332, 352–353, 364
 rigid mounting of 399
 second-order 395, 398, 403
 superconducting, gravity, see SGG
 tensor 487 *ff.*, 509, 523–525, 535
 theoretical response 403
 third-order 281, 292, 297, 314
 three-sensor 531
 vector-type 321
 gravimeter 548, 572 *ff.*
 gravitational wave 546, 548 *ff.*
 gravitational-wave detector
 antenna
 bandwidth 554

- cylindrical 549, 550
 noise 550, 552
 quality factor 549 *ff.*
 resonant mass 549, 551
 spherical 554
 space-based 549, 575
 bandwidth 549, 550, 551, 554
 in space 575
 inverse-square law 563
 laser interferometer 549, 554
 resonant-mass 549
 sensitivity 546, 553–554, 575
 superconducting transducer 546 *ff.*
- gravitomagnetism 575
 gravitomagnetic field 567–568
 gravity
 gradient tensor 557, 568, 573
 diagonal (“in-line”) components 547, 554
 general 554
 off-diagonal (“cross”) components 547,
 554
 trace measurement 564
 gradiometer, gradiometry
 cross-component 554, 564
 cross component (SGG) 559–561, 569,
 572, 574–575
 GGSS 573
 in geophysical exploration 508
 in-line component 554–555, 564, 572
 in-line component (SGG) 556, 558–559,
 561, 564, 568, 571, 574
 SGG 546, 554, 555, 559, 565, 567,
 571–575
 tensor 574
 map 571, 573
 mass detection 571 *ff.*
 meter 573 *ff.*
 survey 547, 571 *ff.*
- Green’s function 151, 168–171, 176, 180,
 195, 212, 214, 231, 232–234, 244, 248
- ground-based TEM 514 *ff.*
- gyromagnetic ratio 57, 62
- h**
- Hankel transform 181
 hardware (SQUID) gradiometers 489
 harmonic distortion 25
 HC (Hosaka-Cohen transformation) 168,
 192 *ff.*, 332–333
- heart rate variation (variability) 334, 339
 helicopter trials (geological prospecting) 524
 Helmholtz coil 73, 354, 512, 531
 Helmholtz decomposition 237, 238
- heterojunction field effect transistor (HFET)
 27, 29, 32
- heteronuclear spin system 72
 high-pass spatial filtering 195
 high-temperature (high- T_c) superconductor
 (HTS) 101, 103, 122–123, 186, 395
- high- T_c SQUID 5, 31, 69–70
 homogeneous broadening 58–59
 horse-spleen ferritin 406
 Hosaka–Cohen transformation (HC) 168,
 192 *ff.*, 332–333
- hot electron 30–31
 hybrid flip-chip gradiometer 490
 hyperpolarization 67
 hysteresis, magnetic 147–148
 hysteresis, SQUID 494–496
- i**
- ICA (independent component analysis) 245,
 251, 302, 314, 345
- ill-conditioned (expression, problem) 168,
 215, 235, 244, 249
- image effect (in magnetometer) 400
 image processing
 approach 177
 filter 426
 magnetic noise 426
 naïve near-field limit 428
 signal-to-noise ratio 427
 spatial resolution 427
 spatial resolution of raw magnetic image
 428
 standard magnetic inverse 426
 techniques 195
- imaging (see also magnetic imaging)
 biomagnetic (see also tomography) 420,
 430
- magnetic geological structures 500
 magnetization (see also SQUID
 microscope) 227 *ff.*
- immunoassay, magnetic 360
 impedance matching parameter 549
 impressed current 154 *ff.*, 211, 240, 254, 277
 impressed voltage 154
 inclusions (detection, NDE) 447, 463, 469
 independent component analysis (ICA) 245,
 251–252, 302, 314, 345
- induced motion noise 496
 induction coil 508, 510, 516
 inertial navigation 502, 546 *ff.*, 574 *ff.*
 inertial survey 574 *ff.*
- inhomogeneous broadening (NMR, spin
 echo) 59

- injury current (cardiac) 336
 in-line-component SGG 555 *ff.*
 input circuit (SQUID, in magnetometer/
 susceptometer) 399, 400
 integral equation (Fredholm) 209, 210
 integrated second vertical derivative method
 (ISVD) 184
 interference (magnetic and rf) 400, 409
 intermediate-frequency amplifier 20
 intermodulation distortion 25, 42
 interpolation function 214, 216–218, 220
 intrinsic balance 533
 intrinsic gradiometers 488–489
 intrinsic spin 569
 inverse (inversion) problem 139 *ff.*, 275,
 302, 313, 320, 357–358, 458, 472
 inverse spatial filter, filtering 170, 199, 207,
 209, 231, 459
 inverse-square law (see Newton's law of
 gravitation)
 inversion algorithms, techniques (in NDE,
 geophysical prospecting and MAD)
 426–428, 488, 500 *ff.*
 ionospheric resonances 526
 ischemic heart disease 336
 ISLES (Inverse-Square Law Experiment in
 Space) 567 *ff.*
 ISVD (integrated second derivative method)
 184
 iterative forward models 503
- j**
- J-coupling (scalar coupling, NMR) 72, 80
 Johnson noise 103, 106, 114, 400
 Josephson
 current-phase relationship 128
 frequency 8–9, 18–19
 junction 4, 6, 18, 22, 80, 99
 junction array 73, 116
 junction, Shapiro steps 98, 116
 voltage standard 98
 Joule–Thomson (JT) refrigerator 419, 463
- k**
- kinetic-inductance thermometer 55
 KSVZ (Kim–Shifman–Vainshtein–Zakharov)
 model 82
- l**
- LabView 426
 Laplace's equation 60, 142–143, 152–154,
 156, 159, 160, 168, 183, 184
 Laplacian 144, 154, 157, 253, 254, 307
- Larmor frequency 67, 72, 77, 80
 laser interferometer 549 *ff.*
 late time response (in TEM) 516
 law of Biot and Savart 145, 149 *ff.*, 168–171,
 208 *ff.*, 225, 303
 LCMV (linearly constrained minimum
 variance beamformer) 246, 307 *ff.*
 lead field 168, 210 *ff.*, 246–247, 302–306, 337
 least-squares
 fit, fitting 243, 502
 minimization 251
 solution 208, 235, 244, 247, 305
 Legendre polynomial 160
 Levenberg–Marquardt method 502
 levitation coil 99, 570
 liftoff 181 *ff.*, 198, 203, 205, 447, 453–454,
 460
 LIGO (Laser Interferometer Gravitational-
 wave Observatory) 554
 linear acceleration 555 *ff.*, 560 *ff.*
 linearly constrained minimum variance
 (LCMV) 246, 307 *ff.*
 LISA (Laser Interferometer Space Antenna)
 549, 575
 liver susceptometry 352–355
 localization of target 501
 London moment 567
 longitudinal magnetization 58
 longitudinal or spin-lattice relaxation time
 (T_1) 58 *ff.*
 LORETA (low resolution electromagnetic
 tomography) 245, 253–254, 307
 low-pass spatial filtering 176, 195
 lungs (MRI) 67
- m**
- machine learning 336
 MAD (magnetic anomaly detection, military)
 483 *ff.*, 499 *ff.*, 527 *ff.*
 MADOM (magnetic and acoustic detection of
 mines, a US project) 498, 502, 529
 magnet (see superconducting magnet)
 magnetic
 anisotropy measurement 398
 anomaly detection (MAD) 483 *ff.*, 499 *ff.*,
 527 *ff.*
 anomaly detection (NDE) 432–434, 442 *ff.*,
 451 *ff.*
 anomaly localization 499
 bacterium 431
 calorimeter 32, 53
 circuit 107
 dipole (see dipole, magnetic)

- dipole moment (see dipole, moment)
 field
 homogeneity 70
 intensity 147
 tomography (MFT) 245, 254
- flux leakage (MFL) 448
- imaging
 ASIC 433
 audio frequency 409
 cardiac 175, 337–338
 combinatorial library 430
 current 168, 174, 186, 189
 diamagnets 148
 eddy current 434
 field 169
 Fourier 172
 half-fluxons 430
 heart 430
 integrated circuit 174
 ink 429
 magnetization 227 *ff.*
 microwave 409
 multichip module 432
 paramagnets 148
 problem 144, 147 *ff.*
 resonance (MRI) 3, 56, 59, 61, 67,
 69–70, 73, 76, 80–81, 216, 237, 245,
 346, 351, 355
 source 337–338
 static field 409
 susceptibility 232
 vector sources 144
 windowing method 171 *ff.*, 204 *ff.*, 232
- intensity 485
- interference 400, 409, 512
- levitation 547, 567–568, 570, 572
- measurements (susceptibility,
 magnetization)
 ac susceptibility 405
 anisotropy 398
 ferromagnet (iron oxide) 395
 irreversible magnetization curves 398
 quantum tunneling (in horse-spleen
 ferritin) 406
 superconductor ($\text{RuSr}_2\text{GdCu}_2\text{O}_8$)
 406
- marker monitoring (MMM) 357–360
- microscopy (see also magnetic imaging and
 SQUID microscope) 409 *ff.*
- permeability 147
- potential
 scalar 152, 156–158, 230
 vector 160
- property measurement system (MPMS)
 395
- resonance imaging (see MRI)
- shield
 cylinder 331
 magnetically shielded room (MSR)
 342–343, 347, 358, 364
- survey, geophysical
 basic principles 484–487
 data acquisition 499–500
 data analysis 502–504
 equipment, instrument 494
 general 484
 gradiometry (tensor) 487–488
 localization 501–502
 mapping 500–501
 method 508 *ff.*
- susceptibility
 ac (measurement) 405
 Curie–Weiss law 124
 paramagnetic salt 124
 (quasistatic) measurement 352–354
 tomography 232, 235–237, 243
- target 501, 529
- tensor gradiometer 487, 509, 523–525, 535
- magnetics (for mineral exploration, survey)
 508
- magnetization
 detection 129
 distributed 146
 imaging 147, 227 *ff.*
 (in inverse problem) 141 *ff.*, 151,
 156 *ff.*, 184, 212, 229 *ff.*
 nucleus 57 *ff.*
 ferromagnet 395
 fractional 58 *ff.*
 longitudinal 58 *ff.*
 measurement 392 *ff.*
 paramagnetic material 53
 remanent, remnant 141, 145–148, 430
- magnetocardiogram, magnetocardiography
 (see MCG)
- magnetoencephalogram, magnetoencephalography (see MEG)
- magnetoenterogram, magnetoenterography
 (MENG) 356–357, 360
- magnetogastrogram, magnetogastrography
 (MGG) 356, 358, 360
- magnetometer, magnetometry
 alternating gradient (AGM) 393
 astatic 510
 localization error 292
 radial, SQUID 281–284, 288–289, 296, 304

- vector, SQUID 143, 215, 280, 296
 optical 341
 quasistatic
 rock 509, 511–512
 sensitivity 332
 system, multichannel SQUID 292, 294
 magnetometer-susceptometer (conventional) 392
 magnetometer-susceptometer (SQUID) 393
 ac susceptibility 405
 applications 395, 406
 commercial systems 394–395
 components 393, 397
 cryocooled (EverCool) 400
 gradiometer pickup coil 398
 history of development 394
 input circuit 399
 Magnetic Property Measurement System (MPMS) 395
 measurement accuracy 393, 403
 noise 404
 photo of MPMS 395
 sample chamber 397
 sample transport 397
 schematic cross-section 397
 schematic diagram 393
 SHE Variable Temperature Susceptometer (VTS) 394
 specification (table) 407
 superconducting magnet 398
 magnetoneurogram, magnetoneurography (MNG) 347–350
 magnetoresistive sensor 341
 magnetosome 431
 magnetotellurics (MT) 509, 526
 mapping area 180, 198, 206, 207
 mass detection 571
 maximum spatial frequency 180, 182, 183
 MCG (magnetocardiogram,
 magnetocardiography)
 action current imaging 175
 lead, lead field 211 *ff.*
 fetal 318
 inverse problem algorithm 237 *ff.*, 244 *ff.*,
 337–338
 multichannel system 324 *ff.*
 reference sensor, channel 327 *ff.*
 sensor array configuration 324–325
 sensor array optimization 215
 signal source 322–324
 stress testing 336
 system
 high-temperature 329–331
 low-temperature 325–329
 shielding-free 328–329
 versus ECG 238–241
 mean square deviation (MSD) 176, 220, 221
 mechanical vibrations 512
 MEG (magnetoencephalogram, magnetoencephalography)
 fetal (fMEG) 299, 318
 fMEG system 300–301
 integrated with MRI 81, 274
 inverse algorithms 245 *ff.*
 multichannel system, commercial 275,
 279 *ff.*
 noise cancellation 288, 301
 quasistatic 342–346
 reference sensor, channel 281, 283
 sensitivity (to cortical sources) 167
 sensor number 144
 whole-cortex 274, 279, 320
 Meissner effect 99, 103, 546
 MENG (magnetoenterogram, magnetoenterography) 356–357, 360
 metric perturbation 549
 metrological, metrology
 charged particle beams 122–123
 current
 resolution 103, 106, 108, 115, 118–119
 very low 115 *ff.*
 very high 121–122
 linking ampere, volt to SI mechanical units 98–100
 quantum metrological triangle 96,
 115–117
 resistance ratio 111 *ff.*
 rf attenuation 127–128
 single-spin detection 130
 thermometry 123 *ff.*
 universality of Josephson constant 98
 voltage 97, 101
 MGG (magnetogastrogram, magnetogastrography) 356, 358, 360
 microphonic response 35, 41, 393
 microscope, SQUID (see SQUID microscope)
 microstrip SQUID amplifier 3, 18–19, 25,
 29, 31, 81, 83
 mine and ordnance detection, mass
 detection 527 *ff.*, 547, 571
 mineral exploration by SQUID 513 *ff.*
 mineral oil (NMR) 70–72, 74
 minerals prospecting, SGG 546
 minimum norm method 208, 245–249, 254,
 302, 305–307, 320, 337
 mixing coefficient (junction noise) 18

- MMM (marker monitoring) 357–360
 MNG (magnetoneurogram, magnetoneurography) 347–350
 moment arm 560 *ff.*
 motion
 compensation 525
 - compensated gradiometer 529
 noise 485, 487, 517, 532
 noise cancellation 535
 operation 489
 sensor 546–548, 575
 motional narrowing (NMR, spin-spin interaction) 58
 moving platform 483, 497
 MPMS (magnetic property measurement system) 395
 MRI (magnetic resonance imaging)
 high-field (conventional) 56–57, 216, 237, 245, 346, 351, 355
 functional 307, 320, 346
 low-field
 2D pulse sequence 74–75
 3D imaging (tomography) 75–76
 early experiments 80
 frozen hyperpolarized ^{129}Xe 69
 integrated with MEG 81, 274
 liquid-state proton 69 *ff.*
 outlook 80–81
 (pre)polarization 69, 73–76
 setup 73–74
 spin echo 70–71
 T_1 -weighted contrast 76–79
 MSD (mean square deviation) 176, 220
 MSR (magnetically shielded room) 342–343, 347, 358, 364
 MT (magnetotellurics) 509, 526
 MUDSS (Mobile Underwater Debris Survey System, a US project) 498
 multiaxis gradiometer 489, 492, 528
 multichannel
 fMEG system 300–301
 MCG system 324 *ff.*
 MEG systems 279 *ff.*
 multichip module (imaging) 432
 multiple dipoles 142, 167, 229, 234, 243–244, 503
 multiple signal classification (MUSIC) 245, 249–251, 312, 320
 multiplexer (MUX), SQUID
 frequency-domain 39 *ff.*
 time-domain 35 *ff.*
 multipole 152, 159 *ff.*, 165, 236, 241, 242, 503
 multipole expansion 323
 multipole moment 162, 165, 207
 multiturn input coil 526
 mumetal shielding 512–513
 MUSIC (multiple signal classification) 249–251, 312, 320
 mutual inductance 5–6, 23, 97, 104–105, 110, 124, 127
 mutual inductance bridge 124
 myocardial infarction 334
- n**
- nanoparticle label 341, 360 *ff.*
 National Metrology Institute 117
 NDE (nondestructive evaluation)
 bridge, roof structure testing 449–452
 aircraft component testing 224, 453, 460–463
 corrosion testing 471–472
 current imaging 218 *ff.*, 426–428, 432–433
 eddy current technique 453 *ff.*
 examples 446–448
 excitation technique, alternative 467–470
 flux leakage technique 448 *ff.*
 history 443–444
 motivation 442
 niobium sheet testing 463–464
 PEC 456, 459
 principle 444–446
 fiber-reinforced polymer testing 464–467
 static current mapping 452–453
 susceptometry 471
 tagging 471
 NDT (nondestructive testing) see NDE
 near-field probe (microscopy) 414
 negative response (TEM) 519
 neural network (NN) 467
 Newton's (inverse-square) law of gravitation
 departure from 563, 569
 experiment (SGG) 575
 null test 546, 564–565
 short-range (submillimeter) test 566–567, 571
 NIS (normal-insulator-superconductor)
 tunnel junction 32, 55
 NMR (nuclear magnetic resonance)
 general 56–57, 80
 hyperpolarized ^{129}Xe 67 *ff.*
 J-coupling 72
 liquid-state proton (also MRI) 69 *ff.*
 mineral oil 71–72, 75
 prepolarization 69 *ff.*
 principle 57–59

- SQUID
 -detected 57, 61 *ff.*
 spectrometer 67–68
 trimethyl-phosphate 72–73
- noise
 1/f 416
 acceleration 547
 amplifier 550, 571
 below 1 Hz 342
 body (human) 358
 brain 291, 293, 296
 broadband 348
 Brownian motion 550, 563, 571
 bubbling helium 398
 cancellation 278–279, 281, 288, 292
 adaptive 283, 285
 gradiometer 292, 300
 circulating current 546, 552
 correlated 291, 296
 cultural 517
 dewar 73, 279
 energy 6, 30
 environmental 288–290, 292–294, 303,
 314, 320, 348
 environmental (vibrations, magnetic) 404
 excess 495
 forward action (amplifier) 550
 flux 106, 130, 394, 414–415, 546, 552
 geologic, geomagnetic 497
 GGSS 572–573
 gravimeter 572–573
 intrinsic 549, 558, 561, 563 *ff.*, 571 *ff.*
 in inverse problem 142 *ff.*
 Johnson 103, 106, 114, 400
 magnetic image 426
 magnetometer-susceptometer 399, 404
 magnet power supply 398
 position 416, 423
 red 561
 reduction (by averaging) 345
 remediation technique 49
 reverse action (amplifier) 550
 spectral density 563
 spectrum 111, 120, 496, 521–522, 559, 561
 SQUID 291–292, 296, 350, 552, 559
 spin 61, 64, 66
 superconducting accelerometer 547 *ff.*
 SGG 572–573
 superconducting magnet 404
 system (total) 517
 temperature 6, 10–13, 15, 17, 19–20,
 26–29, 31, 34, 66, 82–83, 553
 temperature, quantum limited 30, 31
- temperature fluctuations 498, 550, 553
 thermal 552
 thermometer 124, 126
 uncorrelated 288
 white 28, 118–119, 288, 292, 301, 313, 559,
 563
- non-adaptive systems 533
- nondestructive evaluation (see NDE)
- nondestructive testing (NDT) see NDE
- nonequilibrium detector (see also
 calorimeter) 54–55
- nonlinearity
 error (field detection) 487
 error (SGG) 572
 Josephson junction (quantum limit) 18
 nanovoltmeter (in CCC) 114
 sensor, electronics 487, 491, 494
 superconducting transducer 551
- nonuniqueness (in inverse problem) 142,
 144, 148, 208, 230, 508
- normal-insulator–superconductor (NIS)
 junction 32, 55
- NQR (nuclear quadrupole resonance)
¹⁴N nucleus
 cocaine hydrochloride 62–63
 ammonium perchlorate 63
 general 57, 80
 principle 59–61
 spin noise observation 64–66
- nuclear angular momentum 57
- nuclear dipole–dipole interaction 67
- nuclear magnetic resonance (see NMR)
- nuclear quadrupole resonance (see NQR)
- nuclear spin precession 569
- null detector 96, 100, 113–114, 116
- numerical fitting techniques 499
- numerical inversion 502–503
- Nyquist noise 4, 6, 9, 16, 26, 28
- o**
- octupole 165, 167
- Ohm's law 149, 153–154, 188, 226
- open-loop (SQUID operation) 3, 5
- optical pumping 67, 69
- optical spectroscopy 508
- organ demagnetization 344
- p**
- pacing catheter, nonmagnetic 338
- palaeomagnetic fields 509
- paramagnetic material 145–148, 228 *ff.*, 430
- parasitic capacitance 3, 7, 9, 15, 18–20
- Parseval's theorem 180

- particle detector 3
 pc (personal computer; in SQUID microscopy) 425
 PCA (principal component analysis) 251 *ff.*, 313
 PEC (pulsed eddy current method, in NDE) 456, 459
 pendulum motion 498
 peptide (NQR) 62, 80
 permeability, magnetic 147
 permittivity, electric 153
 persistent switch 398
 PET (positron emission tomography) 275, 346
 phantom 70, 74, 77, 79–80, 338, 353, 355, 358
 phase analysis (NDE) 456
 phase detection 512
 phase encoding 74–75
 photoscanning 467
 pickup coil 6, 61, 65, 80, 102–105, 107–108, 148, 151, 176–178, 197, 204 205, 210, 215, 395
 picovoltmeter, SQUID 4–5, 100–101
 planar gradiometer 197 *ff.*, 215, 224, 280 *ff.*, 288 *ff.*, 304, 330, 332, 490, 525
 platform noise 497–498, 501, 521
 platform subsystems 497
 point-by-point inversion 500
 point inversion algorithms 501
 Poisson's equation 142, 153 *ff.*
 positron emission tomography (PET) 275, 346
 postamplifier 3, 14, 22, 26–27, 29, 31–32
 potential
 electric, scalar 149 *ff.*, 158, 278, 286, 349
 electrostatic, scalar 153 *ff.*
 gravitational, scalar 554, 571–573
 magnetic, scalar 152 *ff.*, 294
 magnetic, vector 160
 Newtonian 564
 surface 324
 Yukawa 564
 powder pattern (NQR versus NMR) 63
 preferential continuation method 184
 pressure regulator 498
 Primakoff conversion 82
 primary current 113, 278, 286, 323
 principal component analysis (PCA) 245, 251 *ff.*, 313
 principle of reciprocity 212
 probability density function 213–214, 252
 pseudoinverse filter 202
 pulsed eddy current method (PEC, in NDE) 456, 459
 pulse-induction (technique, TEM) 514
 pyramidal cells (brain) 276
- q**
 Q-spoiler 80
 QHR (quantum Hall resistance) 100, 111–112
 quadrupole 152, 160 *ff.*, 241–243, 485, 504
 quadrupole coupling constant 61–63
 quantum
 effect 18
 Hall effect 96, 112
 Hall resistance (QHR) 100, 111–112
 information processing 129–130
 Langevin equation 18
 limit 546 *ff.*, 550 *ff.*
 metrological triangle 96, 115, 130–131
 quantum-limited amplifier 18–20, 130, 552, 554
 quasiparticle charge imbalance 3–4
 quasistatic limit (magnetic, electric field) 146, 154, 171, 188, 192, 230, 323
 quasistatic MEG 342–346
 quasistatic magnetometer (magnetometry) 342–346
 quench heater 398, 400, 404
- r**
 radio astronomy 20
 radio frequency (rf) amplifier, SQUID 5 *ff.*
 radio frequency single-electron transistor (RFSET) 3, 31
 radioactive seed (tumor therapy, MRI) 81
 radiomagnetic sounding 527
 radiometrics (for mineral exploration) 508
 radius (forearm bone) 75
 readout amplifier 7, 40
 real time tracking 503
 reciprocity principle 212
 reference sensor 283, 327 *ff.*, 491, 493, 531
 refrigerator (see also cryocooler)
 closed cycle 563
 dilution 415, 425
 GM 400–401, 512
 Joule-Thomson 419, 463
 pulse tube 563
 regularization (method, technique) 185, 209, 210, 244, 247, 249, 337

- reimbursement (health insurance), see also
 CPT (current procedural terminology)
 code 355
- remanent, remnant magnetization 141,
 145–148, 430
- remote referencing 509
- remote sensing 508
- repolarization, ventricular (heart) 322
- residual imbalance correction 492
- resistance measurement 118, 125
- resistance ratio 111
- resistor, cryogenic 100–101, 116
- resonant-mass antenna 549 *ff.*
- resonant transducer, superconducting 551 *ff.*
- resource exploration (see also mineral
 exploration by SQUID) 546, 572, 575
- reverse gain technique 24
- rf interference (RFI) 400, 409, 532
- RFI rejection 532–533
- RFSET (rf single electron transistor) 31–32
- Riemann tensor 567
- rock magnetometer 509, 511–512
- rotating frame 58–59
- rotating gradiometer 525
- rotation in the Earth's magnetic field 497
- RRR (residual resistivity ratio) -grade 552
- Ruben's coil 512
- s**
- saddle coil (in NMR, NQR spectrometer) 61,
 67, 73
- SAM (synthetic aperture magnetometry)
 246, 308 *ff.*
- sample chamber (of MPMS) 397
- sampling frequency, spatial 182–183, 205
- Satellite Test of the Equivalence Principle
 (STEP) 569, 572, 575
- scalar, magnetic potential 152 *ff.*, 294
- scalar coupling (*J*-coupling, NMR) 72, 80
- scanning speed (in imaging) 182, 183
- scanning SQUID microscope, microscopy
 (see also magnetic imaging, SQUID
 microscope) 409 *ff.*
- screening currents
- SQUID input circuit 400
 - superconducting shield 395
- search for hidden masses (see also MAD)
 573
- secondary source (current) 155, 157, 238
- second harmonic 25
- Seebeck effect 469
- seismology 508
- seismometer 548
- self-field effects 519
- sensitivity (SQUID in inverse problem) 167,
 176, 180, 182, 202, 207, 210, 226, 246, 239,
 246, 254, 554 *ff.*
- sensor
- primary 281, 288
 - reference 281, 353, 355, 358
- SET (single-electron transistor)
- current pump 131
 - current source 96, 115–116, 131
 - electron pump 96, 115, 117, 120–121, 131
 - measurement by CCC 119–121
- surface acoustic wave device 119, 131
- sferics noise (see geologic noise)
- SGG (superconducting gravity gradiometer)
 546, 554, 555, 559, 565, 567, 571–575
- SGMS (Superconducting Gradiometer/
 Magnetometer Sensor, a US project) 529
- Shannon sampling theorem 143
- SHE Variable Temperature Susceptometer
 (VTS) 394
- shield, shielding (magnetic)
- field stabilizing 394
 - high permeability 405
 - MSR 342–343
 - mumetal 512–513
 - screening currents 395
- superconducting (NbTi, niobium) 103,
 105, 118, 121–122, 394, 398, 400
- shot noise 26
- signal-processing (geophysical, MAD) 499 *ff.*,
 533
- signal space projection (SSP) 252–253, 304,
 324
- signal space separation (SSS) 292, 325, 345
- signal-to-noise ratio (SNR) 16, 29, 67, 69, 71,
 74, 81–82, 167, 182, 203, 210, 220, 221, 345,
 348–349, 353, 499, 508
- silent source 142, 160, 168, 210, 237, 239
- single electron transistor (see SET)
- single particle detection 97
- single spin detection 130
- single-photon emission computed
 tomography (SPECT) 275
- singular-value decomposition (SVD) 208,
 213, 215, 222, 235, 244, 249 *ff.*
- SIS (superconductor-insulator-
 superconductor) tunnel junction 20,
 54–55
- skin depth, effect 453–456, 459, 465, 527
- slew rate 519, 523
- SLUG (superconducting low-inductance
 undulatory galvanometer) 4

- SNR (signal-to-noise ratio) 16, 29, 67, 69, 71, 74, 81–82, 167, 182, 203, 210, 220, 221, 345, 348–349, 353, 499, 508
 software gradiometer 489, 491
 source
 dipolar 308, 345
 mass 566 *ff.*
 metrology error 564 *ff.*
 modeling, cardiac 323
 primary (biomagnetic field, see also current, primary) 277
 quadrupolar 277
 secondary (biomagnetic field) 277
 spin 571
 spatial
 blurring 142
 filter, filtering
 general 168–170, 174, 182, 207, 224, 245, 253, 305, 308
 inverse 170, 199, 207, 209, 231
 low-pass 142, 176, 195
 high pass 195
 frequency, maximum 180, 183
 frequency response 199 *ff.*
 resolution 169, 176, 180 *ff.*, 195, 207, 248, 427–428
 SPECT (single-photon emission computed tomography) 275
 spherical antenna 554 *ff.*
 spherical capacitor 160, 165–166, 168, 244
 spherical harmonic (function, theory) 159 *ff.*, 168, 294
 spin
 -1M2 nucleus 57
 echo 58–59, 70–71
 fluctuation 64–66
 -mass coupling, interaction 569 *ff.*
 noise 61, 64, 66
 spinner rock magnetometer 512
 spintronics 129
 SPM (statistical parametric map) 307
 spontaneous emission 64, 66
 SQUID
 amplifier 5 *ff.*
 amplifier, microstrip 20 *ff.*
 array 344, 358
 bandwidth 183, 273, 348, 363, 425, 436, 436, 447, 518–519, 521, 526–527
 behavior in applied magnetic fields 495
 channel 342, 360
 current metrology 99–100
 dc SQUID 97, 12, 116, 118–119, 130, 575
 dual dc SQUID 553, 575
 edge profile 494
 energy resolution 548, 553
 femtovoltmeter 97–98
 flat sensor array (grid) 325 *ff.* 344–347, 350
 gradiometer (see gradiometer)
 high- T_c 275, 320, 329–331, 348, 363–364,
 low- T_c 275, 283, 320, 348, 363
 microscope
 application 144, 429, 513
 bandwidth 409, 425,
 biomagnetic imaging 420
 cantilever-type (IBM) 419–420
 cryogenic refrigeration 419
 feedback 418
 figure of merit 416
 high- T_c 363–364, 417
 hinge mechanism 424
 imaging, mapping 180, 185
 immunoassays 364–365
 magnetic field resolution 414
 magnetic flux guide 417
 magnetic needle 412, 417
 magnetic shielding 418
 minimum detectable field 415
 performance 410
 position noise 416, 423
 principle 409 *ff.*
 proximity to sample 417
 scanning mechanism 422–423
 spatial resolution 413, 426
 technological advance 436
 upside down 422
 x-SQUID 417
 z-SQUID 417
 multiplexer
 frequency-domain 39 *ff.*
 time-domain 35 *ff.*
 open-loop (operation) 3, 5
 picovoltmeter 4–5, 100–101
 quantum-limit (amplifier) 18–20, 130, 552, 554
 readout (of thermal detectors) 32 *ff.*
 rf SQUID 126–127, 398, 495, 518, 527
 sensitivity (in inverse problem) 167, 176, 180, 182, 202, 207, 210, 226, 246, 239, 246, 254, 554 *ff.*
 series array 17, 19, 39, 43, 54
 square washer 3, 5, 20–21
 susceptometer, susceptometry (see also MPMS) 352 *ff.*, 392 *ff.*, 569
 voltmeter (see picovoltmeter)
 YBCO SQUID 101

- SSP (signal space projection) 252–253, 304, 324
- SSS (signal space separation) 292, 325, 345
- standard
- attenuation, rf 128
 - capacitance (SET) 115, 117
 - current, quantum (SET) 96, 115
 - QHR 96, 117
 - resistance, resistor 100, 101, 106, 111–113
 - secondary
 - resistance 112
 - voltage 101 - voltage (Josephson) 98, 116, 117
- Star Cryoelectronics (SQUID system) 425, 440
- statistical parametric map (SPM) 307
- STEP (Satellite Test of the Equivalence Principle) 569, 572, 575
- step size (in mapping) 180, 182–183, 206
- stimulation
- artifacts 287
 - auditory 345
 - cell 277
 - electric 347
 - equipment 287
 - peripheral nerve 347
 - sensory 344
 - tactile 287
 - vagus nerve 295
 - visual 287, 301
- stochastic method 501
- string theories 564*ff.*
- strong CP problem (see CP) 569*ff.*
- strong-field limit 148
- structural determination 62, 80
- subcutaneous fat (in forearm) 75
- sulcus (of cortex) 317
- superconducting
- accelerometer 547*ff.*, 568*ff.*, 575*ff.*
 - gravity gradiometer, see SGG
 - gyro 567
 - imaging-surface 283
 - magnet
 - cooling 398
 - field uniformity 398
 - flux motion in 404
 - NMR 56
 - persistent switch 398
 - power supply 398
 - quench heater 398
 - trapped flux 398 - penetration depth 21, 55
 - resonant transducer 551*ff.*
- shield 103, 105, 118, 121–122, 394, 398, 400
- shield, toroidal, overlapping 104–106
- transformer (CCC), winding ratio 109, 113–114, 116, 118–119
- transformer, flux 279, 288, 301, 393, 400, 414, 489, 511
- transition 125
- superconductor-insulator-superconductor (SIS) tunnel junction 20, 32, 54–55
- superinsulation 519
- superparamagnetism 361, 519
- supersymmetry, theory 81
- survey
- airborne 521*ff.*, 572*ff.*
 - gravity 571*ff.*
 - inertial 574*ff.*
 - mapping (geological) 500
- susceptibility
- ac (measurement) 405*ff.*
 - complex 406
 - horse-spleen ferritin 406–407
 - liver 353*ff.*
 - magnetic 147–149, 227, 230*ff.*, 243, 452
 - nonconducting material 471
 - rocks 509
 - sample holder 403
- susceptometer, susceptometry (see also MPMS) 351*ff.*, 392*ff.*, 471, 509, 513
- synthetic aperture magnetometry (SAM) 246, 308*ff.*
- t**
- T_1 (longitudinal or spin-lattice relaxation time)
- general 58*ff.*
 - T_1 -inversion recovery 78
 - T_1 -weighted contrast 59, 76, 79, 81
- T_2 (transverse or spin-spin relaxation time)
- 58*ff.*
- tachistoscopic reading 315
- tagging (magnetic tracers, NDE) 471
- tapered stacking filter 517
- target localization 502
- Taylor's series 160, 184, 193
- TEM (transient electromagnetics method) 456, 509, 513–514, 516*ff.*, 536–537
- tendon rupture 449
- tensor gradiometer 487–488, 523–525, 574*ff.*
- TES (transition-edge sensor) 32–33
- test mass 547*ff.*, 551*ff.*, 555*ff.*, 561*ff.*, 566*ff.*
- thermal detector 32*ff.*
- thermoelectric NDE method 469
- thermoelectric voltage 3–4

- thermometer
 kinetic inductance 55
 noise, Josephson linewidth 125
 noise, quantum-roulette 127
 primary 123, 126
- third harmonic 25
- thorax phantom 338
- three-sensor gradiometer (TSG) 491, 531
- threshold, thresholding (in spatial filtering)
 196, 202, 249
- time-domain multiplexer 35–36, 40, 43
- TMI (total magnetic intensity) 523
- tomography
 current-injection 188 *ff.*, 208, 227
 low-resolution electromagnetic (LORETA) 245, 253–254, 307
 magnetic field (MFT) 245, 254
 magnetic susceptibility 232, 235–237,
 243
 (methods in medicine) 275–276,
 (methods in NDE) 188 *ff.*, 459, 472
- torsion balance 564 *ff.*
- total-field magnetometer 485
- total magnetic intensity 523
- towed-bird 521
- towed body 498
- tracking magnetic anomalies (see also MAD)
 499
- transducer (gravitational wave detection)
 bandwidth 550
 general 546 *ff.*
 multimode 554
 principle 548 *ff.*
 superconducting resonant 551
- transfer function 169, 177, 179, 224
- transient electromagnetics method (TEM)
 456, 509, 513–514, 516 *ff.*, 536–537
- transformer, flux (superconducting) 279,
 288, 301, 393, 400, 414, 489, 511
- transition-edge sensor (TES) 32–33
- transverse (spin–spin) relaxation time (T_2)
 58 *ff.*
- trapped flux
 in magnet 398, 400, 404
 in SQUID 400
- TSG (three-sensor gradiometer) 491, 531
- tumor 79, 81
- tuned amplifier 12–14, 16, 20
- turns (stepwise) function 177, 199, 204, 206
- u**
- ulna (bone of forearm) 75
- uncertainty, Type A 119–121
- uncertainty, Type B 119
- uncompensated noise (localization) 502
- unexploded ordnance detection 483,
 529–531
- uniform conductive Earth 516
- uniform double-layer (cardiac excitation, see
 also bidomain model) 323
- unique solution 142, 168, 183, 189, 230, 237,
 254
- unit potential 160
- unmanned underwater vehicle 498
- unshielded (SQUID)
 in-motion operation 493
 MCG 328–329
 MEG 279–280, 311
 operation, general 494–495
- untuned amplifier 12–13, 15–16
- UXO (unexploded ordnance) 483, 488,
 529
- v**
- vacuum gap (in dewar) 281
- varactor diode 25, 29
- variable-temperature insert (of
 magnetometer) 393
- vector magnetometer 143, 215
- vibrating sample magnetometer (VSM)
 392
- vibration, effect of 498
- voltage noise 4–6, 11–12, 16–18
- voltage summing multiplexer 40
- voltmeter 3–5, 96
- volume conductor (MCG) 323
- volume current (MCG) 323
- volume-integral method (VIM) 458
- Von Klitzing constant RK 112, 115
- voxel 234, 235, 248
- w**
- Watt balance 99
- weak-field limit 148
- weight function 162, 214
- weighted averaging 306, 309, 348, 354,
 357, 361
- Weinstock's rule 435
- width of the junction 495
- WIMP (weakly interacting massive particle)
 50, 81
- window 174, 204, 206, 207
- windowing, method 171 *ff.*, 204 *ff.*, 232
- windshield 519
- wire-wound gradiometer 490

Wolff–Parkinson–White (WPW) syndrome

337

Wynn’s ghosts 500

x

x-SQUID (microscope geometry) 417

z

zero-point fluctuations 18

zero (in spatial frequency transfer function)

177, 179, 200–202, 206, 232

z-SQUID (microscope geometry) 417